UNIVERSITY OF SOUTHAMPTON
FACULTY OF PHYSICAL SCIENCES AND ENGINEERING
SCHOOL OF ELECTRONICS AND COMPUTER SCIENCE

Reduced-Complexity Communications System Design

by

Chao Xu
B. Eng., B.Sc.(Eng.), MSc.

A doctoral thesis report submitted in partial fulfilment of
the requirements for the award of Doctor of Philosophy
at the University of Southampton

May 2015

SUPERVISOR:
Professor Lajos Hanzo
FREng, FIEEE, FIEE, DSc, EIC IEEE Press
Chair of Communications, Signal Processing and Control Group
and
Dr Soon Xin Ng
PhD, SMIEEE, MIET, CEng, FHEA
Department of Electronics and Computer Science
University of Southampton
Southampton SO17 1BJ
United Kingdom

Dedicated to my parents, Professor Jingxia Zhang and Mr Zucheng Xu and to my grandparents who would have been proud to live to see this treatise.

UNIVERSITY OF SOUTHAMPTON

ABSTRACT

FACULTY OF PHYSICAL SCIENCES AND ENGINEERING
SCHOOL OF ELECTRONICS AND COMPUTER SCIENCE

Doctor of Philosophy

Reduced-Complexity Communications System Design

by Chao Xu

The technical breakthrough of Turbo Codes (TCs) initiated two decades of exciting developments leading to a suite of near-capacity techniques. It has been widely recognized that exchanging extrinsic information between the channel decoders and the modulated signal detectors assists communications systems in approaching their best possible performance potential that is predicted by the channel capacity. Nonetheless, in line with Moor's Law, as researchers inch closer and closer to the channel capacity, the complexity of the resultant communications systems is also significantly increased. In fact, soft-decision-aided signal detection conceived for Single-Input Single-Output (SISO), Single-Input Multiple-Output (SIMO) and Multiple-Input Multiple-Output (MIMO) schemes typically contribute a substantial fraction of the total complexity, especially when multiple received samples have to be jointly detected in order to combat the deleterious effect of channel fading. Against this background, in this treatise, we firstly propose a reduced-complexity design for the classic soft-decision-aided PSK/QAM detectors, and then these reduced-complexity design guidelines are applied to a variety of communications systems spanning from coherent to noncoherent, from uncoded to coded, and also from SISO to MIMO systems. Our aim is to reduce the computational complexity as much as possible, especially for complex near-capacity communications systems, while mitigating any performance loss imposed by our reduced-complexity design.

First of all, we commence from the family of basic coherent SISO/SIMO systems, where both uncoded and coded PSK/QAM schemes are considered. The channel coding assisted near-capacity systems design principles are introduced based on EXtrinsic Information Transfer (EXIT) charts. Furthermore, we observe that the Max-Log-MAP algorithm invoked for soft-decision-aided PSK/QAM detection aims for finding the maximum probabilities, which is similar to the action of hard-decision-aided detection of uncoded MPSK/QAM schemes. Therefore, we propose to link each *a priori* LLR to a reduced-size fraction of the channel's output signal constellations, so that the Max-Log-MAP algorithm may be operated at a reduced complexity. Moreover, the corresponding reduced-complexity Approx-Log-MAP algorithm is also conceived by compensating for the Max-Log-MAP algorithm's widely-used Jacobian approximation relying on a lookup table. Our performance results demonstrate that up to 41.6% and 72.6% complexity reductions are attained for soft-decision-aided Square 64QAM and Star 64QAM detectors, respectively, which is achieved *without any performance loss*. This complexity reduction is substantial, especially when the soft-decision-aided signal detectors are invoked several times during turbo detection.

Secondly, we proceed by conceiving reduced-complexity algorithms for the noncoherently detected DPSK schemes in both uncoded and coded SISO/SIMO systems. More explicitly, the DPSK transmitter modulates the data-carrying symbols onto the phase changes between consecutive transmitted symbols, so that the Conventional Differential Detection (CDD) may recover the source information by observing the phase change between every pair of consecutive received samples. However, the CDD aided DPSK suffers from a 3 dB performance penalty compared to its coherent counterpart. Moreover, an irreducible error floor occurs, when the CDD is employed in rapidly fluctuating fading channels. In order to mitigate this problem, Multiple-Symbol Differential Detection (MSDD) may be invoked in order to improve the DPSK performance by extending the observation window length from the CDD's $N_w = 2$ to $N_w \geq 2$. The price paid is that the MSDD complexity grows exponentially with $(N_w - 1)$ as a result of jointly detecting the $(N_w - 1)$ data-carrying symbols. As a remedy, the Decision-Feedback Differential Detection (DFDD) concept may be introduced in order to detect a single symbol based on previous decisions concerning the $(N_w - 2)$ data-carrying symbols in a MSDD window. However, the DFDD inevitably imposes a performance loss due to its inherent error propagation problem. In order to retain the optimal MSDD performance, the Multiple-Symbol Differential Sphere Detection (MSDSD) facilitates the MSDD by invoking a Sphere Decoder (SD). Against this background, we firstly propose to introduce a simple correlation operation into the hard-decision-aided MSDSD employing an arbitary number of Receive Antennas (RAs), so that the SD may visit the constellation points in a zigzag fashion for the case of uncoded DPSK SIMO systems. Furthermore, we propose a reduced-complexity Schnorr-Euchner search strategy for the soft-decision MSDSD employing an arbitrary number of RAs, so that the optimum candidate may be found by visiting a reduced-size subset of constellation points, and then the rest of the constellation points may be visited in a zig-zag fashion. Our simulation results demonstrate that up to 88.7% complexity reduction is attained for MSDSD $(N_w = 4)$ aided D16PSK. We have also proposed the near-optimum Approx-Log-MAP algorithm conceived for soft-decision-aided SD, which has not been disseminated in the open literature at the time of writing. Furthermore, the important subject of coherent versus noncoherent detection is discussed in the context of coded systems, which suggests that MSDSD aided DPSK is an eminently suitable candidate for turbo detection assisted coded systems operating at high Doppler frequencies.

Following this, a range of noncoherent detectors designed for non-constant modulus Differential QAM (DQAM) schemes are introduced for both uncoded and coded scenarios, where the open problem of MSDSD aided Differential QAM (DQAM) is solved. More explicitly, the MSDSD relies on the knowledge of channel correlation, which is determined both by the Doppler frequency and by the noise power. For DPSK, the transmitter's phases may form a unitary matrix, which may be separated from the channel's correlation matrix, so that a lower triangular matrix that is created by decomposion from the inverse of the channel's correlation matrix may be utilized in the context of sphere decoding. However, for DQAM, the transmitted symbol-amplitudes cannot form a unitary matrix, which implies that they have to be taken into account by the channel's correlation matrix. As a result, the symbol-amplitude-dependent channel correlation matrix only becomes

known, when all the symbol-amplitudes are detected. Furthermore, the classic DFDD solutions conceived for DQAM rely on the assumption of the channel's correlation matrix being independent of the symbol-amplitudes, which implies that these DFDD solutions are sub-optimal and they are not equivalent to the decision-feedback aided version of the optimum MSDD. To circumvent these problems, we prove that although the complete channel correlation matrix remains unknown, the associated partial channel correlation matrix may be evaluated with the aid of the SD's previous decisions as well as by relying on a single information-dependent symbol amplitude that may be readily found by the SD. As a benefit, we are able to invoke sphere decoding for both amplitude detection and phase detection in the context of MSDD aided DQAM. Furthermore, we have also improved the classic DFDD solutions conceived for DQAM by directly deriving them from the optimum MSDD. Moreover, we offer a unified treatment of diverse noncoherent detectors, including CDD, MSDD, MSDSD and DFDD for a variety of DQAM constellations that exist in the literature, including Differential Amplitude Phase Shift Keying (DAPSK), Absolute-Amplitude Differential Phase Shift Keying (ADPSK) and their twisted constellations. The reduced-complexity algorithms proposed for DPSK detection are also applied to DQAM detection in both uncoded and coded systems .

Last but not the least, we provide insights concerning the design of MIMO systems in both uncoded and coded scenarios, where two of the salient tradeoffs encountered in MIMO system design are investigated. Firstly, the tradeoff between the attainable multiplexing and diversity gain of MIMO schemes is discussed. More explicitly, the V-BLAST MIMO systems have a capacity that may even grow linearly with the number of antennas, but they are not designed for achieving a transmit diversity gain for combating the effects of fading. By contrast, the family of Space-Time Block Codes (STBCs) offers a benefical transmit diversity gain, but the STBCs cannot achieve the full MIMO capacity. In order to circumvent this problem, the Linear Dispersion Code (LDC) concept may be introduced to resolve this tradeoff, where a total number of N_Q modulated MPSK/QAM symbols are dispersed across both the N_T-element spatial domain and the N_P-element time domain of the transmission matrix. As a result, the LDC may attain both the full MIMO capacity and the full transmit diversity gain, provided that the parameters satisfy $N_Q \geq N_T N_P$. Nonetheless, since the STBC's orthogonality requirements are dropped by the LDC design, the LDC receiver has to employ the V-BLAST detectors in order to tackle the Inter-Antenna Interference (IAI). Hence a tradeoff between the performance attained and the complexity imposed is encountered, which explicitly manifests itself in the context of V-BLAST receiver design. More explicitly, on the one hand, it is well known that the ML detector and the SD are capable of achieving the best possible V-BLAST performance in uncoded systems, but their detection complexity may be potentially excessive, when employing a large number of Transmit Antennas (TAs). The optimum MAP V-BLAST detection complexity may become especially unaffordable, when the MIMO detector is invoked several times in the context of turbo detection in coded systems. On the other hand, linear V-BLAST receivers such as the classic MMSE receiver may be invoked in order to separate the superimposed parallel data streams. However, the residual IAI persisting after the linear interference-suppression filter

may still severely degrade the MIMO system's performance. Against this background, the Spatial Modulation (SM) concept may be introduced. Our goal is to ensure that the optimal ML MIMO detection performance may be achieved for SM at a substantially reduced complexity. More explicitly, the SM transmitter activates a single one out of N_T TAs in order to transmit a single modulated MPSK/QAM symbol. As a result, the SM receiver may aim for detecting the TA activation index and the modulated symbol index separately at a reduced complexity. Moreover, the concept of Space-Time Shift Keying (STSK) once again achieves a beneficial diversity gain, where a single one out of N_Q dispersion matrices is activated for dispersing a single modulated MPSK/QAM symbol. The STSK receiver may employ the low-complexity SM detectors in order to recover both the activated dispersion matrix index and the modulated symbol index. However, completely independently detecting the TA activation index and the modulated MPSK/QAM symbol imposes a performance loss on the SM receiver. This is because the potentially erroneous decisions concerning the TA activation index may mislead the MPSK/QAM demodulator into detecting the wrong symbol. In order to mitigate this problem, in this treatise, we have proposed reduced-complexity algorithms conceived both for hard-decision-aided SM detection and for soft-decision-aided SM detection, where the optimal SM performance is retained by taking into account the correlation between the TA activation index and the modulated MPSK/QAM symbol index. A range of other optimal and suboptimal SM detectors characterized in the literature are also summarized for the sake of comparison.

Declaration of Authorship

I, **Chao Xu**, declare that the thesis entitled **Reduced-Complexity Communications System Design** and the work presented in it are my own and has been generated by me as the result of my own original research. I confirm that:

- This work was done wholly or mainly while in candidature for a research degree at this University;
- Where any part of this thesis has previously been submitted for a degree or any other qualification at this University or any other institution, this has been clearly stated;
- Where I have consulted the published work of others, this is always clearly attributed;
- Where I have quoted from the work of others, the source is always given. With the exception of such quotations, this thesis is entirely my own work;
- I have acknowledged all main sources of help;
- Where the thesis is based on work done by myself jointly with others, I have made clear exactly what was done by others and what I have contributed myself;
- Parts of this work have been published.

Signed: ..... Date: .....

Acknowledgements

I would like to express my heartfelt gratitude to my supervisor, Professor Lajos Hanzo, who initiated me to the art of research. I have been working with Professor Hanzo since my MSc degree project, and he has been a faithful friend, a dedicated research collaborator, and a supportive supervisor. I am also grateful to my second supervisor Dr. Soon Xin Ng for his generous help and support whenever I was in need. Many thanks to Professor Lie-Liang Yang and Professor Sheng Chen for their kind guidance and assistance ever since my MSc study. I am also very grateful to Dr. Robert G. Maunder for his helpful advices.

I would like to thank all my colleagues in Southampton Wireless. It was a great pleasure to work in cooperation with Dr. Dandan Liang, Mr. Xin Zuo, Mr. Emmanuel Ternon, Dr. Hoang Anh Ngo and Dr. Hung Viet Nguyen on a variety of interesting research topics. Many thanks to Dr. Shaoshi Yang, Dr. Rong Zhang, Dr. Kent Cheung and Dr. Chen Dong for their constructive comments and suggestions. I also would like to especially thank Dr. Shinya Sugiura for his kind and helpful advice. I truly cherish my time doing research in Southampton, on which I will always look back with fond memories.

I would like to express my appreciation to the School of Electronics and Computer Science, University of Southampton for her financial support of my PhD study. I would also like to thank to IEEE Communications Society UK&RI Chapter for offering me the award of the 2008/2009 Best MSc Student in Broadband and Mobile Communication Networks, which greatly encouraged me at the outset of my PhD study. I would also like to express my heartfelt gratitude to the Chinese Scholarship Council for offering me the 2012 Chinese Government Award for Outstanding Self-Financed Student Abroad, which truly motivated me to finish my PhD thesis with enthusiasm and dedication.

I would like to express my heartfelt gratitude to my mother Professor Jingxia Zhang and my father Mr Zucheng Xu for their unconditional love and support. They have endured hardship in their lives so that I could have opportunities they themselves never had. I am their eyes, when I get to see more of the world. I thank them every time, when I achieve anything meaningful. They have both recently retired, but the good examples that they have set up for me will continue to guide me thoughout my career and life.

List of Publications

Journals:

1. **C. Xu**, S. X. Ng and L. Hanzo, ”Near-Capacity Irregular Convolutional Coded Cooperative Differential Linear Dispersion Codes Using Multiple-Symbol Differential Detection”, IEEE Signal Processing Letters, vol.18, no.3, pp.173-176, March 2011.

2. **C. Xu**, S. Sugiura, S. X. Ng and L. Hanzo, ”Reduced-Complexity Noncoherently Detected Differential Space-Time Shift Keying”, IEEE Signal Processing Letters, vol.18, no.3, pp.153-156, March 2011.

3. H. A. Ngo, **C. Xu**, S. Sugiura and L. Hanzo, ”Space-Time-Frequency Shift Keying for Dispersive Channels”, IEEE Signal Processing Letters, vol.18, no.3, pp.177-180, March 2011.

4. D. Yang, **C. Xu**, L. L. Yang and L. Hanzo, ”Transmit-Diversity-Assisted Space-Shift Keying for Colocated and Distributed/Cooperative MIMO Elements”, IEEE Transactions on Vehicular Technology, vol.60, no.6, pp.2864-2869, July 2011.

5. **C. Xu**, L. Wang, S. X. Ng and L. Hanzo, ”Multiple-Symbol Differential Sphere Detection Aided Differential Space-Time Block Codes Using QAM Constellations”, IEEE Signal Processing Letters, vol.18, no.9, pp.497-500, Sept. 2011.

6. **C. Xu**, S. Sugiura, S. X. Ng and L. Hanzo, ”Reduced-Complexity Soft-Decision Aided Space-Time Shift Keying”, IEEE Signal Processing Letters vol.18, no.10, pp.547-550, October 2011.

7. S. Sugiura, **C. Xu**, S. X. Ng and L. Hanzo, ”Reduced-Complexity Coherent Versus Non-Coherent QAM-Aided Space-Time Shift Keying”, IEEE Transactions on Communications, vol.59, no.11, pp.3090-3101, November 2011.

8. H. V. Nguyen, **C. Xu**, S. X. Ng and L. Hanzo, ”Non-Coherent Near-Capacity Network Coding for Cooperative Multi-User Communications”, IEEE Transactions on Communications, vol.60, no.10, pp.3059-3070, October 2012.

9. S. Sugiura, **C. Xu**, S. X. Ng and L. Hanzo, ”Reduced-Complexity Iterative-Detection-Aided Generalized Space-Time Shift Keying”, IEEE Transactions on Vehicular Technology, vol.61, no.8, pp.3656-3664, October 2012.

10. **C. Xu**, S. Sugiura, S. X. Ng and L. Hanzo, ”Spatial Modulation and Space-Time Shift Keying: Optimal Performance at a Reduced Detection Complexity”, IEEE Transactions on Communications, vol.61, no.1, pp.206-216, January 2013.

11. **C. Xu**, D. Liang, S. Sugiura, S. X. Ng and L. Hanzo, ”Reduced-Complexity Approx-Log-MAP and Max-Log-MAP Soft PSK/QAM Detection Algorithms”, IEEE Transactions on Communications, vol.61, no.4, pp.1415-1425, April 2013.

12. **C. Xu**, D. Liang, S. X. Ng and L. Hanzo, ”Reduced-Complexity Noncoherent Soft-Decision-Aided DAPSK Dispensing With Channel Estimation”, IEEE Transactions on Vehicular Technology, vol.62, no.6, pp.2633-2643, July 2013.

13. L. Wang, L. Li, **C. Xu**, D. Liang, S. X. Ng and L. Hanzo, ”Multiple-Symbol Joint Signal Processing for Differentially Encoded Single- and Multi-Carrier Communications: Principles, Designs and Applications”, IEEE Communications Surveys & Tutorial, vol.16, no.2, pp.689-712, Second Quarter 2014

14. H. V. Nguyen, **C. Xu**, S. X. Ng and L. Hanzo, ”Near-Capacity Wireless System Design”, *submitted to* IEEE Communications Surveys & Tutorial.

15. **C. Xu**, X. Zuo, S. X. Ng, R. G. Maunder and L. Hanzo, ”Reduced-Complexity Soft-Decision Multiple-Symbol Differential Sphere Detection”, *submitted to* IEEE Transactions on Communications.

Conferences:

1. **C. Xu**, S. Sugiura, S. X. Ng and L. Hanzo, ”Reduced-complexity noncoherently detected Differential Space-Time Shift Keying”, in Proceedings of IEEE Wireless Communications and Networking Conference (WCNC’11), pp.1505-1510, Cancun, Mexico, 28-31 March 2011.

2. **C. Xu**, S. X. Ng and L. Hanzo, ”Near-Capacity Irregular Convolutional Coded Cooperative Differential Linear Dispersion Codes Using Multiple-Symbol Differential Decoding Aided Non-Coherent Detection”, in Proceedings of IEEE International Conference on Communications (ICC’11), Kyoto, Japan, 5-9 June 2011.

3. H. V. Nguyen, **C. Xu**, S. X. Ng, J. L. Rebelatto, Y. Li and L. Hanzo, ”Near-Capacity Non-Coherent Network-Coding Aided Scheme for Cooperative Multi-User Communications,” in Proceedings of IEEE Vehicular Technology Conference (VTC’11 Fall), San Francisco, USA, 5-8 September 2011.

4. **C. Xu**, C. Liu, S. X. Ng and L. Hanzo, ”Multiple-Symbol Differential Sphere Decoding Aided Amplify-and-Forward Differential Space-Time Modulation”, in Proceedings of IEEE Vehicular Technology Conference (VTC’11 Fall), San Francisco, USA, 5-8 September 2011.

5. **C. Xu**, E. Ternon, S. Sugiura, S. X. Ng and L. Hanzo, ”Multiple-Symbol Differential Sphere Decoding Aided Cooperative Differential Space-Time Spreading for the Asynchronous CDMA Uplink”, in Proceedings of IEEE Global Communications Conference (GLOBECOM’11), Houston, USA, 5-9 December 2011.

6. S. Sugiura, **C. Xu** and L. Hanzo, ”Reduced-Complexity QAM-Aided Space-Time Shift Keying”, in Proceedings of IEEE Global Communications Conference (GLOBECOM 2011), Houston, USA, 5-9 December 2011.

7. **C. Xu**, D. Liang, S. Sugiura, S. X. Ng and L. Hanzo, ”Reduced-complexity Soft STBC detection”, in Proceedings of IEEE Global Communications Conference (GLOBECOM’12), pp.4217-4221, Anaheim, USA, 3-7 December 2012

8. **C. Xu**, D. Liang, S. Sugiura, S. X. Ng and L. Hanzo, ”Reduced-Complexity Soft-Decision Aided PSK Detection”, in Proceedings of IEEE Vehicular Technology Conference (VTC’12 Fall), Qubec City, Canada, September 2012

9. P. Zhang, S. Chen, **C. Xu**, J. Jiang, F. Jin and L. Hanzo, ”Joint Transmit and Receive Antenna Selection Aided Differential Space-Time Shift Keying Systems”, *submitted to* IEEE Global Communications Conference (GLOBECOM’15), San Deigo, 6-10 December 2015.

Strenuis Ardua Cedunt (The Heights Yield to Endeavour)

– University of Southampton Motto

Contents

Glossary

ADPSK	Absolute-Amplitude Differential Phase Shift Keying
ADPSK	Absolute-amplitude Differential Phase Shift Keying
AO	Amicable Orthogonal
AWGN	Additive White Gaussian Noise
BCH	Bose-Chaudhuri-Hocquenghem
BCJR	Bahl-Cocke-Jelinek-Raviv
BER	Bit Error Rate
BICM	Bit-Interleaved Coded Modulation
BICM-ID	Bit-Interleaved Coded Modulation concept relying on Iterative Decoding
BICM-ID	Bit-Interleaved Coded Modulation relying on Iterative Decoding
BLAST	Bell Laboratories Layered Space-Time
CCMC	Continuous-input Continuous-output Memoryless Channel
CDD	Conventional Differential Detection
CDMA	Code Division Multiple Access
CRB	Cramer-Rao Bound
CRR	Complexity-Reduction Ratio
CSI	Channel State Information
CW	Comparison Window
DAPSK	Differential Amplitude Phase Shift Keying
DCMC	Discrete-input Continuous-output Memoryless Channel
DFDD	Decision-Feedback Differential Detection
DPSK	Differential Phase Shift Keying
DQAM	Differential QAM
DQAM	Differential Quadrature Amplitude Modulation
ED	Euclidean Distance

EXIT	EXtrinsic Information Transfer
GSM	Generalized Spatial Modulation
GSSK	Generalized Space-Shift Keying
GSTSK	Generalized Space-Time Shift Keying
HCC	Hybrid Concatenated Coding
HDD-CDD	Hard-Decision-Directed CDD
HDD-MSDD	Hard-Decision-Directed MSDD
HDD-MSDSD	Hard-Decision-Directed MSDSD
HDD-MSDSD-IAP	Hard-Decision-Directed MSDSD using Iterative Amplitude/Phase processing
HR	Half-Rate
i.i.d.	independent and identically distributed
IAI	Inter-Antenna Interference
IRCC	IRregular Convolutional Code
ISI	Inter-Symbol Interference
LDC	Linear Dispersion Code
LDPC	Low-Density Parity Check
LF	Linear Filter
LLR	Log Likelihood Ratio
LP	Linear Prediction
LPD	Linear Prediction-based Detector
MAP	Max A Posteriori
MAP	Maximum A Posteriori
MF	Matched Filter
MIMO	Multiple-Input Multiple-Output
ML	Maximum-Likelihood
MLC	Multi-Level Coding
MLSE	Maximum Likelihood Sequence Estimation
MLSE	Maximum-Likelihood Sequence Estimation
MMSE	Minimum Mean Squared Error
MRC	Maximum Ratio Combining
MSDAD	Multiple Symbol Differential Amplitude Detection
MSDAD	Multiple-Symbol Differential Amplitude Detection
MSDASD	Multiple-Symbol Differential Amplitude Sphere Detection
MSDD	Multiple-Symbol Differential Detection

MSDD-IAP	MSDD using Iterative Amplitude/Phase processing
MSDPSD	Multiple Symbol Differential Phase Sphere Detection
MSDPSD	Multiple-Symbol Differential Phase Sphere Detection
MSDSD	Multiple-Symbol Differential Sphere Detection
MSDSD-IAP	MSDSD using Iterative Amplitude/Phase processing
MSE	Mean Squared Error
MUD	Multi-User Detection
MUD	Multi-User Detector
OF	Obejctive Function
PCC	Parallel Concatenated Code
PCC	Parallel Concatenated Coding
PDF	Probability Density Function
PED	Partial Euclidean Distance
PEP	Pairwise Error Probability
PSAM	Pilot Symbol Assisted Modulation
PSED	Pairwise Squared Euclidean Distance
QO	Quasi-Orthogonal
QS	Quasi-Static
RA	Receive Antenna
RS	Reed-Solomon
RSC	Recursive Convolutional Code
RTS	Repeated Tree Search
Rx-SD	Receiver-centric SD
SCC	Serial Concatenated Code
SCC	Serially Concatenated Coding
SD	Sphere Decoder
SDD-CDD	Soft-Decision-Directed CDD
SDD-MSDD	Soft-Decision-Directed MSDD
SDD-MSDSD	Soft-Decision-Directed MSDSD
SDD-MSDSD-IAP	Soft-Decision-Directed MSDSD using Iterative Amplitude/Phase processing
SDMA	Space-Division Multiple Access
SIC	Successive Interference Cancelling
SIMO	Single-Input Multiple-Output
SISO	Single-Input Single-Output

SM	Spatial Modulation
SOVA	Soft-Output Viterbi Algorithm
SSK	Space-Shift Keying
STBC	Space-Time Block Code
STM	Space-Time Modulation
STS	Single Tree Search
STSK	Space-Time Shift Keying
TA	Transmit Antenna
TADPSK	Twisted ADPSK
TC	Turbo Coding
TCM	Trellis Coded Modulation
TDAPSK	Twisted DAPSK
TS	Time Slot
TTIB	Transparent Tone-In-Band
Tx-SD	Transmitter-centric SD
URC	Unity Rate Code
VLSI	Very-Large-Scale Integration
ZF	Zero-Forcing

List of Symbols

General Rules for PSK

- A modulated MPSK symbol may be represented by $\{s^m = \exp(\frac{2\pi}{M}\check{m})\}_{m=0}^{M-1}$, where modulation index m is Gray coded version of the natural index $\check{m}$.
- The Gray coded index m may be directly translated to binary source bits combinations, i.e. we have $\text{dec2bin}(m) = b_1 b_2 \cdots b_{\text{BPS}}$.

General Rules for Square QAM

- A modulated Square MQAM symbol is constituted by a M_{Re}PAM $\{s_{\text{Re}}^{m_{\text{Re}}} = \frac{M_{\text{Re}}-2\check{m}_{\text{Re}}-1}{\sqrt{\beta}}\}_{m_{\text{Re}}=0}^{M_{\text{Re}}-1}$ for its real part and by a M_{Im}PAM $\{s_{\text{Im}}^{m_{\text{Im}}} = \frac{M_{\text{Im}}-2\check{m}_{\text{Im}}-1}{\sqrt{\beta}}\}_{m_{\text{Im}}=0}^{M_{\text{Im}}-1}$ for its imaginary part, i.e. we have $\{s^m = s_{\text{Re}}^{m_{\text{Re}}} + j s_{\text{Im}}^{m_{\text{Im}}}\}_{m=0}^{M-1}$.
- The QAM modulation index $m = \text{bin2dec}(b_1 \cdots b_{\text{BPS}}) = m_{\text{Im}} M_{\text{Re}} + m_{\text{Re}}$ and the PAM modulation indices $m_{\text{Re}} = \text{bin2dec}(b_{\text{BPS}_{\text{Im}}+1} \cdots b_{\text{BPS}})$ and $m_{\text{Im}} = \text{bin2dec}(b_1 \cdots b_{\text{BPS}_{\text{Im}}})$ are Gray coded natural indices $\check{m}$, $\check{m}_{\text{Re}}$ and $\check{m}_{\text{Im}}$, respectively.
- The normalization factor is given by $\beta = \frac{\sum_{\check{m}_{\text{Re}}=0}^{M_{\text{Re}}/2-1}\sum_{\check{m}_{\text{Im}}=0}^{M_{\text{Im}}/2-1}\left[(M_{\text{Re}}-2\check{m}_{\text{Re}}-1)^2+(M_{\text{Im}}-2\check{m}_{\text{Im}}-1)\right]}{M/4}$.

General Rules for Star QAM

- A modulated Star MQAM symbol is obtained by a M_PPSK phase $\{\Omega^p = \exp(j\frac{2\pi}{M_P}\check{p})\}_{p=0}^{M_P-1}$ multiplied by a M_A-level ring amplitude $\{\Gamma^a = \frac{\alpha^{\check{a}}}{\sqrt{\beta}}\}_{a=0}^{M_A-1}$, i.e. we have $\{s^m = \Gamma^a \Omega^p\}_{m=0}^{M-1}$.
- The modulation indices $m = \text{bin2dec}(b_1 \cdots b_{\text{BPS}}) = pM_A + a$, $p = \text{bin2dec}(b_1 \cdots b_{\text{BPS}_P})$ and $a = \text{bin2dec}(b_{\text{BPS}_P+1} \cdots b_{\text{BPS}})$ are Gray coded natural indices $\check{m}$, $\check{p}$ and $\check{a}$, respectively.
- The ring amplitude ratio is given by α, and the symbol power normalization factor is given by $\beta = \frac{\sum_{\check{a}=0}^{M_A-1}\alpha^{2\check{a}}}{M_A}$.

General Rules for Differential PSK (DPSK)

- The DPSK scheme maps BPS $= \log_2 M$ source bits $\{b_k\}_{k=1}^{\text{BPS}}$ to an MPSK symbol $x^m = \exp(j\frac{2\pi}{M}\check{m})$.
- The DPSK differential encoding processing is given by $s_n = x_{n-1}s_{n-1}$ commencing from $s_1 = 1$, where x_{n-1} and s_{n-1} denote the data-carrying symbol and the transmitted symbol, respectively.

General Rules for Differential Amplitude Phase Shift Keying (DAPSK)

- The DAPSK schemes are represented by the acronym of M-DAPSK(M_A,M_P).
- The DAPSK scheme aims to guarantee that all the transmitted symbols s_n are drawn from the same Star MQAM constellation. The differential encoding process is given by $s_n = x_{n-1}s_{n-1}$, which commences from $s_1 = \frac{1}{\sqrt{\beta}}$.
- The transmitted symbol s_n may be represented by a M_A-level ring amplitude $\Gamma_n = \frac{\alpha^{\mu_n}}{\sqrt{\beta}}$ combined with a M_P-PSK phase Ω_n as $s_n = \Gamma_n\Omega_n$. The data-carrying symbol x_n may be represented in the same way as $x_n = \gamma_n\omega_n$.
- A modulated data-carrying symbol is given by $x^m = \gamma^a\omega^p = \alpha^{[(\check{a}+\mu_{n-1}) \bmod M_A]-\mu_{n-1}} \cdot \exp(j\frac{2\pi}{M_P}\check{p})$, where the modulation indices $m = \text{bin2dec}(b_1 \cdots b_{\text{BPS}}) = pM_A + a$, $p = \text{bin2dec}(b_1 \cdots b_{\text{BPS}_P})$ and $a = \text{bin2dec}(b_{\text{BPS}_P+1} \cdots b_{\text{BPS}})$ are Gray coded natural indices $\check{m}$, $\check{p}$ and $\check{a}$, respectively.

General Rules for Absolute-Amplitude Differential Phase Shift Keying (ADPSK)

- The ADPSK schemes are represented by the acronym of M-ADPSK(M_A,M_P).
- The ADPSK scheme aims to guarantee that all the data-carrying symbols x_n are drawn from the same Star QAM constellation. In order to avoid having an unconstrained transmitted symbol power, the differential encoding process is given by $s_n = \frac{1}{|s_{n-1}|}x_{n-1}s_{n-1}$, which commences from $s_1 = \frac{1}{\sqrt{\beta}}$. As a result, the ADPSK scheme always has the absolute-amplitude of $\Gamma_n = |s_n| = |x_{n-1}| = \gamma_{n-1}$.
- The transmitted symbol may be represented as $s_n = \Gamma_n\Omega_n$, where Γ_n and Ω_n refer to the transmitted ring amplitude and the transmitted phase, respectively. Similarly, the data-carrying symbol may be represented as $x_n = \gamma_n\omega_n$, where γ_n and ω_n refer to the data-carrying ring amplitude and the data-carrying phase, respectively.

- A modulated data-carrying symbol is directly drawn from Star MQAM constellation associated with M_A ring amplitudes and M_PPSK phases as $x^m = \gamma^a \omega^p = \frac{\alpha^{\check{a}}}{\sqrt{\beta}} \cdot \exp(j\frac{2\pi}{M_P}\check{p})$.

General Rules for Twisted DAPSK (TDAPSK) and Twisted ADPSK (TADPSK)

- The TDAPSK schemes and the TADPSK schemes are represented by the acronyms of M-TDAPSK(M_A,M_P) and M-TADPSK(M_A,M_P), respectively.
- The data-carrying symbol is represented by $x_n = \gamma_n \omega_n \psi_n$, where the extra term of ψ_n is a ring-amplitude-dependent phase rotation of $\psi^a = \exp(j\frac{2\pi}{M}\check{a})$. As a result, the transmitted symbol is given by $s_n = \Gamma_n \Omega_n \Psi_n$, where Ψ_n refers to the accumulated ring-amplitude-dependent phase rotation.
- The TDAPSK scheme modulates the data-carrying symbol as $x^m = \gamma^a \omega^p \psi^a = \alpha^{[(\check{a}+\mu_{n-1}) \bmod M_A]-\mu_{n-1}} \cdot \exp(j\frac{2\pi}{M_P}\check{p}) \cdot \exp(j\frac{2\pi}{M}\check{a})$. The differential encoding process for TDAPSK is as same as that for DAPSK.
- The TADPSK scheme modulates the data-carrying symbol as $x^m = \gamma^a \omega^p \psi^a = \frac{\alpha^{\check{a}}}{\sqrt{\beta}} \cdot \exp(j\frac{2\pi}{M_P}\check{p}) \cdot \exp(j\frac{2\pi}{M}\check{a})$. Similarly, TADPSK invokes the same differential encoding process as ADPSK.

General Rules for DQAM Associated with Joint Mapping (DQAM$^{\mathbf{JM}}$)

- Instead of assigning the BPS$_P$ source information bits and the BPS$_A$ information bits to modulate the M_PPSK phase index and the M_A-level ring amplitude index separately, DQAM$^{\mathrm{JM}}$ joinly maps the ring amplitude and phase.
- The joint mapping for TDAPSK constellation is given by $x^m = \frac{\alpha^{[(\check{m} \bmod M_A)+\mu_{n-1}] \bmod M_A}}{\alpha^{\mu_{n-1}}} \cdot \exp(j\frac{2\pi}{M}\check{m})$, which may be termed as TDAPSK$^{\mathrm{JM}}$.
- Similarly, the joint mapping for TADPSK constellation is given by $x^m = \frac{\alpha^{(\check{m} \bmod M_A)}}{\sqrt{\beta}} \cdot \exp(j\frac{2\pi}{M}\check{m})$, which may be termed as TADPSK$^{\mathrm{JM}}$.
- All the BPS $= \log_2 M$ source information bits are assigned to encode the global modulation index $m = \mathrm{bin2dec}(b_1 \cdots b_{\mathrm{BPS}})$, which is Gray coded natural index $\check{m}$.

General Rules for V-BLAST

- The V-BLAST schemes are represented by the acroym of V-BLAST(N_T,N_R)-MPSK/QAM.

- A total of $N_Q = N_T$ modulated MPSK/QAM symbols are transmitted by the N_T transmit antennas during $N_P = 1$ symbol periods.
- The $(1 \times N_T)$-element V-BLAST transmission matrix is given by $\mathbf{S} = [\frac{s^{m_1}}{\sqrt{N_T}}, \cdots, \frac{s^{m_{N_T}}}{\sqrt{N_T}}]$, where the MPSK/QAM symbols are separately modulated as $\{s^{m_v} = \mathbb{M}(m_v)\}_{v=1}^{N_T}$.

General Rules for Space-Time Block Code (STBC)

- The STBC transmitter encodes the N_QBPS source bits into N_Q modulated MPSK/QAM symbols $\{s_q\}_{q=1}^{N_Q}$. During N_P symbol periods, the $(N_P \times N_T)$-element symbol-matrix transmitted from the N_T transmit antennas is given by $\mathbf{S} = \sqrt{P_t} G_{N_T}(\{s_q\}_{q=1}^{N_Q})$, where $G_{N_T}(\cdot)$ represents the STBC's space-time modulation arrangement.
- Alamouti's G2-STBC associated with $N_T = N_P = N_Q = 2$ is the only full-rate orthogonal STBC employing a complex-valued signal constellation, where the STBC's symbol rate is defined as $\overline{R} = N_Q/N_P$.
- Half-Rate(HR) STBCs relying on the Hurwitz-Radon orthogonal design are represented by the acroym of HR-GN_T-STBC, where we have $N_T = N_Q$ and $N_P = 2N_Q$ for the specific cases of N_T =2, 4 or 8. For the case of N_T not being a power of 2, the HR-GN_T-STBC transmission matrix may be obtained by taking the first N_T columns of the HR-G$2^{\lceil \log_2 N_T \rceil}$-STBC's codeword. Moreover, we have $N_P = 16 \times 16^{(N_T/8-1)}$ for N_T being bigger than 8 and being a power of 2.
- STBCs relying on the Amicable Orthogonal (AO) design are represented by the acroym of AO-GN_T-STBC. The AO-G2^ι-STBC's transmission matrix is formed from the AO-G$2^{\iota-1}$-STBC's codeword and an extra the $(\iota+1)$-th transmitted symbol, where ι denotes a positive integer that may start from $\iota = 1$. As a result, the AO-STBCs always have a reduced delay of $N_P = N_T$ for the cases of $N_T = 2^\iota$, and we also have $N_Q = \iota + 1$.
- The Quasi-Orthogonal(QO) STBCs are represented by the acroym of QO-GN_T-STBC, whose transmission matrix is formed by subgroups of orthogonal STBCs, so that the STBC's symbol rate may be improved but the STBC's orthogonality is compromised.

General Rules for Linear Dispersion Code (LDC)

- The LDC schemes are denoted by the acronyms of LDC(N_T,N_R,N_P,N_Q)-MPSK/QAM, where a total number of N_Q modulated MPSK/QAM symbols $\{s_q\}_{q=1}^{N_Q}$ are dispersed across both spatial domain and the time domain of the $(N_P \times N_T)$-element transmission matrix $\mathbf{S}$.
- The capacity-improving LDC scheme disperses the real and imaginary parts of modulated symbols separately as $\mathbf{S} = \sum_{q=1}^{N_Q} [\overline{\mathbf{A}}_q \Re(s_q) + j\overline{\mathbf{B}}_q \Im(s_q)]$, which may provide an improved capacity from the STBC while retaining the full diversity order.

- The capacity-achieving LDC scheme disperses the real and imaginary parts of modulated symbols jointly as $\mathbf{S} = \sum_{q=1}^{N_Q} \left[\overline{\mathbf{A}}_q s_q\right]$, which may achieve the full MIMO capacity while retaining the full diversity order, provided that the parameters satisfy $N_Q \geq N_T N_P$

General Rules for Spatial Modulation (SM)

- The SM schemes are represented by the acronym of SM(N_T,N_R)-MPSK/QAM.
- The SM transmitter assigns the first BPS $= \log_2 M$ source information bits to modulate a single MPSK/QAM symbol $s^m = \mathbb{M}(m)$, and the following BPS$_T$ $= \log_2 N_T$ bits are assigned to activate a single out of a total number of N_T transmit antennas.
- The $(1 \times N_T)$-element SM transmission matrix is given by $\mathbf{S} = [\underbrace{0 \ \cdots \ 0}_{v-1}, s^m, \underbrace{0 \ \cdots \ 0}_{N_T - v}]$.

General Rules for Space-Time Shift Keying (STSK)

- The STSK schemes are represented by the acronym of STSK(N_T,N_R,N_P,N_Q)-MPSK/QAM.
- The STSK transmitter activates a single out of a total number of N_Q dispersion matrices for dispersing a single MPSK/QAM symbol, so that the low-complexity SM detectors may be invoked at the STSK receiver.
- The $(N_P \times N_T)$-element STSK transmission matrix is given by $\mathbf{S} = \overline{\mathbf{A}}_q s^m$.

Special Symbols

α:	Ring amplitude ratio for Star MQAM.
β:	Normalization factor for a modulated MQAM symbol.
Γ_n:	A transmitted ring amplitude of a Star MQAM symbol or a DQAM symbol.
γ_n:	A data-carrying ring amplitude of a DQAM symbol.
Ω_n:	A transmitted M_PPSK phase of a Star MQAM symbol or a DQAM symbol.
ω_n:	A data-carrying M_PPSK phase of a DQAM symbol.
Ψ_n:	A transmitted ring-amplitude-dependent phase rotation of a DQAM symbol.
ψ_n:	A data-carrying ring-amplitude-dependent phase rotation of a DQAM symbol.
μ_n:	A transmitted ring amplitude index as in $\Gamma_n = \frac{\alpha^{\mu_n}}{\sqrt{\beta}}$ for DAPSK.
Δ_{v-1}:	The Partial Euclidean Distance (PED) increment evaluated by Sphere Decoder (SD).

σ^2_{MSE}: The Mean Squared Error (MSE).

Ξ_v: The determinant term in PED evaluated by MSDSD aided DQAM.

ξ_v: A constant determinant term that is introduced in order to guarantee that Ξ_v takes positive value.

a: The ring amplitude index for a Star MQAM symbol or a DQAM symbol.

$\mathbf{A}$: The $(N_w \times N_w)$-elements ring amplitudes matrix that is modelled by MSDD.

$\bar{\mathbf{A}}$: The MSDD's ring amplitudes matrix where the first ring amplitude Γ_1 is known.

$\{\overline{\mathbf{A}}\}_{q=1}^{N_Q}/\{\overline{\mathbf{B}}\}_{q=1}^{N_Q}$: The dispersion matrices that are used in MIMO schemes.

arg: Taking the argument.

$b_1 \cdots b_{\mathsf{BPS}}$: The source bits that are assigned to modulate a MPSK/QAM symbol.

$\widetilde{b}_1^m \cdots \widetilde{b}_{\mathsf{BPS}}^m$: The bits mapping arrangement corresponding to the specific constellation point s^m, where we have $(\widetilde{b}_1^m \widetilde{b}_2^m \cdots \widetilde{b}_{\mathrm{BPS}}^m) = \mathrm{dec2bin}(m)$.

$\mathsf{bin2dec}(\cdot)$: A function that converts binary bits to decimal integer.

BPS: The number of bits per symbol, i.e. we have $\mathrm{BPS} = \log_2 M$.

$\mathsf{BPS}_{\mathsf{Re}}/\mathsf{BPS}_{\mathsf{Im}}$: The number of bits per symbol that are assigned to modulate the real/imaginary part of a Square MQAM symbol, where we have $\mathrm{BPS} = \mathrm{BPS}_{\mathrm{Re}} + \mathrm{BPS}_{\mathrm{Im}}$.

$\mathsf{BPS}_A/\mathsf{BPS}_P$: The number of bits per symbol that are assigned to modulate the amplitude/phase of a Star MQAM symbol or a DQAM symbol, where we have $\mathrm{BPS} = \mathrm{BPS}_A + \mathrm{BPS}_P$.

$\mathbf{C}$: The channel correlation matrix that is often utilized by MSDD, MSDSD and DFDD.

$\widetilde{\mathbf{C}}$: The partial channel correlation matrix that is utilized by MSDSD aided DQAM.

C_{CCMC}: Capacity of Continuous-input Continuous-output Memoryless Channel.

C_{DCMC}: Capacity of Discrete-input Continuous-output Memoryless Channel.

$\mathsf{det}(\cdot)$: The determinant of a matrix.

$\mathsf{diag}(\cdot)$: A diagonal matrix using the input vector as its diagonal.

d^m: The probability metric that is facilitated by Log-MAP, Max-Log-MAP as well as Approx-Log-MAP according to the specific constellation point s^m.

$d^{m_{\mathsf{Re}}}_{\mathsf{Re}}/d^{m_{\mathsf{Im}}}_{\mathsf{Im}}$: The probability metrics that are associated with the real/imaginary part of a Square MQAM symbol.

d_v: The Partial Euclidean Distance (PED) evaluated by Sphere Decoder (SD).

$\mathsf{dec2bin}(\cdot)$: A function that converts decimal integer to binary bits.

$E(\cdot)$: The expectation of a random variable.

$exp(\cdot)$: The natural exponentiation of the elements.

f_d: The normalized Doppler frequency.

$\mathbf{H}_n$: The $(N_T \times N_R)$-element MIMO's Rayleigh fading channel matrix.

$\mathbf{H}$: The $(N_w \times N_R)$-element Rayleigh fading channels matrix that is modelled by MSDD.

$I(B;\Lambda)$: The mutual information between the variable B modelled for bit b and the variable Λ modelled for LLR L.

I_A: The *a priori* information.

I_E: The extrinsic information

$\mathbf{I}_N$: An identity matrix of size $N \times N$.

IR: Number of iterations between two turbo detected components.

j: The imaginary unit, where $j^2 = -1$.

$J_0(\cdot)$: The zeroth-order Bessel function of the first kind

$\mathsf{jac}(\cdot)$: The modified Jacobian algorithm that compares two numbers and produces an output according to a lookup table.

$\ln(\cdot)$: The natural logarithm of the elements.

$\log_a b$: The logarithm of b to base a.

$L(b)$: The Log Likelihood Ratio (LLR) of bit b.

$L_a(b)$: The *a priori* LLR of bit b.

$L_e(b)$: The extrinsic LLR of bit b.

$L_p(b)$: The *a posteriori* LLR of bit b.

$\mathbf{L}$: The lower triangular matrix that is decomposed from $\mathbf{L}\mathbf{L}^H = \mathbf{C}^{-1}$ that is often utilized by MSDD, MSDSD and DFDD.

$\widetilde{\mathbf{L}}$: The partial lower triangular matrix that is utilized by MSDSD aided DQAM.

M: The number of levels of a multi-level PSK/QAM scheme.

$M_{\mathsf{Re}}/M_{\mathsf{Im}}$: The number of levels of a PAM scheme that constitutes the real/imaginary part of a Square MQAM scheme, where we have $M = M_{\mathrm{Re}}M_{\mathrm{Im}}$.

M_A / M_P: The number of levels of a Star MQAM scheme's amplitude/phase, where we have $M = M_A M_P$.

m: Gray coded modulation index.

$m_{\mathsf{Re}} / m_{\mathsf{Im}}$: Gray coded M_{Re}PAM/M_{Im}PAM modulation index for the real/imaginary part of a Square MQAM scheme.

min/max: Comparing and taking the minimum/maximum candidate.

n: The subscript n of a symbol (e.g. the subscript n in s_n) indicates the time index.

N_{OL}: The number of observations that are overlapped by consecutive MSDD/MSDSD observation windows.

N_T: The number of transmit antennas.

N_R: The number of receive antennas.

N_Q: The number of symbols transmitted together by a MIMO (including STBC, SM, STSK, etc.) block.

N_P: The number of symbol periods (also termed as time slots) required by a MIMO transmission.

N_w: The observation window size for MSDD/MSDSD/DFDD.

$O(\cdot)$: Complexity order.

$\mathbf{O}$: The $(N_w \times N_w)$-elements ring-amplitudes-dependent phase rotations matrix that is modelled by MSDD aided DQAM.

$\bar{\mathbf{O}}$: The MSDD's ring-amplitudes-dependent phase rotations matrix where the first phase rotation Ψ_1 is known.

$p(\cdot)$: The probability of an event.

p: The PSK phase index for a Star MQAM symbol or a DQAM symbol.

$\mathbf{P}$: The $(N_w \times N_w)$-elements M_PPSK phases matrix that is modelled by MSDD aided DQAM.

$\bar{\mathbf{P}}$: The MSDD's M_PPSK phases matrix where the first M_PPSK phase Ω_1 is known.

R: The system's overall throughput.

R_c: The channel code's coding rate.

$\Re(\cdot)/\Im(\cdot)$: Taking the real/imaginary part of a complex number.

$\mathbf{R}_{\bar{H}\bar{H}}$: The fading channel correlation matrix.

$\mathbf{R}_{hh}$: The fading channel characteristic correlation matrix.

$\mathbf{R}_{VV}$: The AWGN correlation matrix.

$\mathbf{R}_{vv}$: The AWGN characteristic correlation matrix.

$\mathsf{rvec}(\cdot)$: A row vector formed by taking the rows of a matrix one-by-one.

s_n: A transmitted symbol for both coherent scheme and noncoherent scheme.

$\mathbf{S}$: The $(N_w \times N_w)$-element transmitted symbols matrix that is modelled by MSDD.

$\bar{\mathbf{S}}$: The MSDD's transmitted symbols matrix where the first transmitted symbol s_1 is known.

$T(\cdot)$: The transfer characteristic function of a soft-decision-aided decoder/demapper.

T_{QS}: The number of symbol periods in which the QS fading channel remains the same.

$\mathsf{Toeplitz}(\cdot)$: A symmetric Toeplitz matrix generated from the input vector.

$\mathsf{tr}(\cdot)$: Trace of a matrix.

$\mathbf{V}_n$: The AWGN matrix that is of the same size as the received signal matrix $\mathbf{Y}_n$.

$\mathbf{V}$: The $(N_w \times N_R)$-element AWGN matrix that is modelled by MSDD.

x_n: The data-carrying symbol for differential schemes.

$\mathbf{Y}_n$: The $(N_P \times N_R)$-element received signal matrix that models signal received by N_R receive antennas over N_P symbol periods.

$\mathbf{Y}$: The $(N_w \times N_R)$-element received signals matrix that is modelled by MSDD.

z_n: The decision variable for detecting a symbol.

Special Operations

$\|\cdot\|^2$: The Euclidean norm of a vector/matrix.

$(\cdot)^H$: The Hermitian transpose of a matrix.

$(\cdot)^T$: The transpose of a matrix.

$(\cdot)^*$: The conjugate of a complex symbol/vector/matrix.

$\lfloor\cdot\rceil$: Rounding a numerical value to its nearest integer.

$\lceil\cdot\rceil$: Rounding a numerical value to its nearest higher integer.

$\lfloor\cdot\rfloor$: Rounding a numerical value to its nearest lower integer.

$\angle z$: The angle of a complex value z.

$\sum$: The summation of all elements.

$\prod$: The product of all elements.

$\forall$: For all elements within a certain range.

$\int$: The integration function.

Chapter 1

Introduction

Wireless communication has been thriving throughout the information and telecommunication revolution of the last few decades. Driven by the growing demand for reliable wireless access, numerous advanced technologies have been developed. In line with Moor's Law, wireless communications systems have gradually become more and more complex. Fig. 1.1 offers a glimpse of a few key factors that directly affect wireless communications system design. The factors in the first category of system modelling seen in Fig. 1.1 play a fundamental role in efficient system planing and deployment. First of all, as the medium for reliable transmission, the channel characteristics have to be modelled before chosing the appropriate transmission scheme. To elaborate a little further, the effects of channel fading impose one of the most grave challenges in wireless communications systems. The path loss, which results in a substantial received signal power loss as a function of distance has to be tackled by robust power control [2–5]. The shadowing fading caused by large terrain features may either be compensated by the transmitter's power control or be mitigated by the employment of relays [6], which may forward the transmitter's signal to the desired receiver. For mitigating the effects of small-scale fading, which is often caused by signals received via different paths sometimes adding constructively or destructively, channel estimation [1] is required, so that the signals may be detected coherently. When the fading channel envelope fluctuates rapidly, differentially encoded schemes employing noncoherent receivers [7–9] may be invoked in order to avoid the effects of imperfect channel estimation and the pilot overhead. The factors found in the first category related to system modelling in Fig. 1.1 also include hardware-related configurations. For example, the number of antennas employed at the transmitter and at the receiver may explicitly determine the achievable capacity and influence the transceiver choices. Moreover, the multi-user scenario of Fig. 1.1 is also of critical importance. These system modelling concepts constitute the foundation of communications theory and they have been lavishly documented in textbooks, such as [2–5].

Once the system model is established, the communications system's transceiver design featured in Fig. 1.1 is centred around achieving the best possible performance at the lowest cost. The factors of the second category in Fig. 1.1 are all related to the attainable system performance, while the

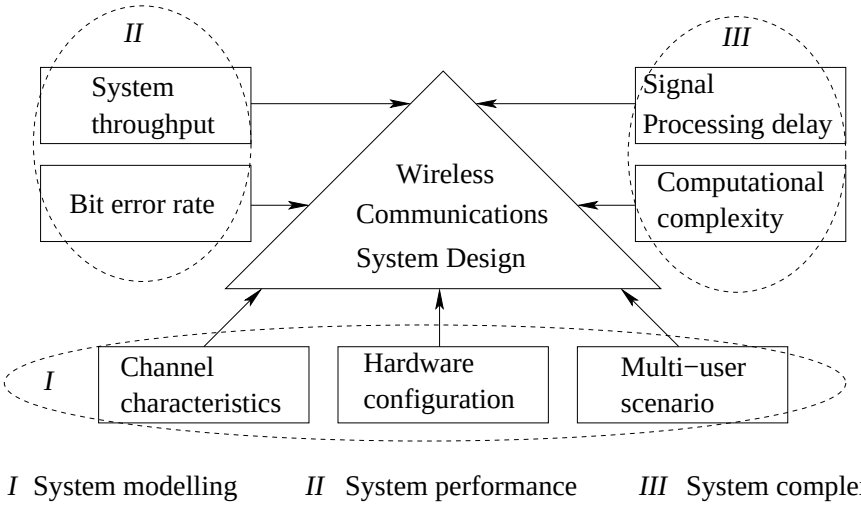

Figure 1.1: Factors affecting the design of wireless communications systems.

factors of the third category in Fig. 1.1 are related to the system's complexity. Unfortunately, there is invariably a tradeoff between the performance attained and the complexity imposed, since a complexity reduction is often associated with a performance degradation. As an example, the classic Multiple-Input Multiple-Output (MIMO) system is portrayed in Fig. 1.2, where both the transmitter and the receiver are equipped with multiple antennnas. The N_T Transmit Antenna (TA) elements independently transmit a total number of N_T modulated symbols, which are drawn from the MPSK constellation diagram. The N_T data streams are separately modulated and transmitted. They experience fading channels and arrive at the Receive Antenna (RA) elements simultaneously. As a result, the classic Maximum-Likelihood (ML) MIMO receiver [8] of Fig. 1.2 has to jointly consider all the N_T MPSK constellation diagrams in order to recover all data streams. As a result, the ML receiver has to examine a total number of M^{N_T} of MIMO signal combinations, which imposes a potentially excessive computational complexity. In order to mitigate this complexity problem, it is desirable to visit the individual MPSK constellation diagrams separately. However, in practice, Inter-Antenna Interference (IAI) is encountered, because the multiple data streams act as interference imposed on each other. An attractive option is to invoke a Sphere Decoder (SD) [10–12] as seen in Fig. 1.2, which only detects a single symbol at a time, while the previous decisions made by visiting other constellation diagrams are fed back in order to cancel out the known interference. The SD may continue to examine new constellation points of the next constellation diagram, until the search scope exceeds the SNR-dependent sphere radius. Therefore, the performance and complexity of SD is explicitly determined by the sphere radius, where the ML performance may be retained at the cost of the a high complexity, whilst visiting less candidates may result in a degraded performance. Another option is to mitigate the IAI by a Linear Filter (LF) [13–16], and then the individual constellation digrams may be visited completely separately, so that only a total of $N_T \times M$ constellation points have to be examined. Nonetheless, the residual IAI after LF may still severely degrade the MIMO system's performance.

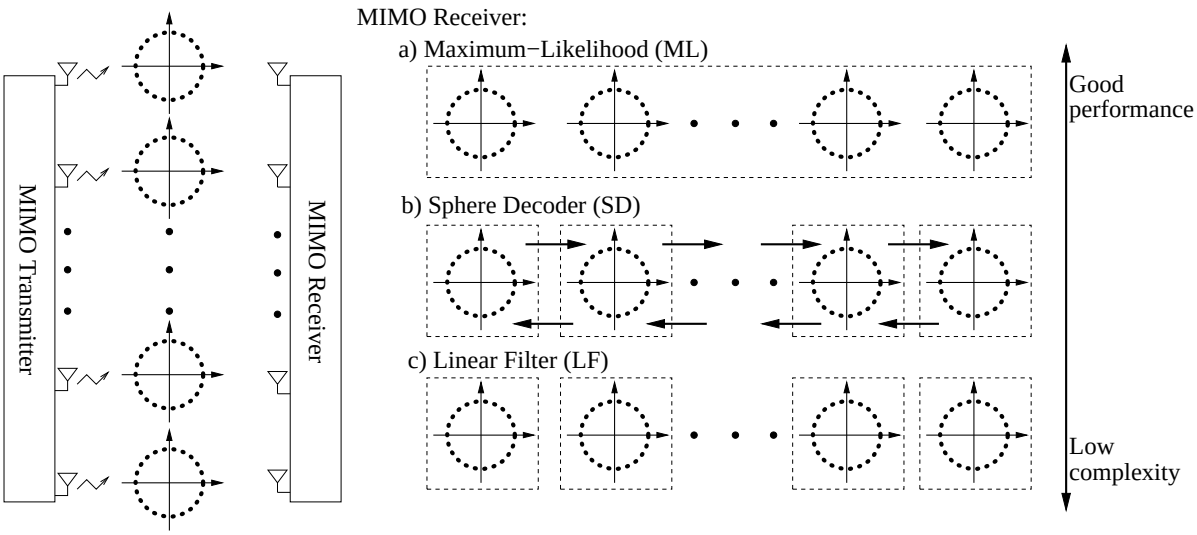

Figure 1.2: An example of striking a tradeoff between the performance attained and the complexity imposed by MIMO systems.

In this report, we focus our attention on the tradeoff between the performance and complexity. Our aim is to reduce the computational complexity as much as possible, especially for complex near-capacity communications systems, while mitigating any performance loss imposed by our reduced-complexity design. The basic idea of reduced-complexity design is illustrated by the example of SD seen in Fig. 1.2, where the complex detector may be decomposed into steps so that less decision candidates have to be considered, while the correlation between the detection steps should be carefully taken into account, so that the optimum performance may be retained.

1.1 A Historical Perspective on Near-Capacity Communications System Design

The communications theoretic capacity limit was established by Shannon [17] in the late 1940s, which quantified a channel's capacity as the maximum mutual information between the input signal and the output signal. Shannon proposed in Theorem 11 of [17] that the channel capacity, which is the maximum data rate that can be transmitted over the channel at an infinitesimally low error rate, can be achieved with the aid of channel coding at the unconstrained cost of delay and complexity. In the 1950s, the single-error correcting Hamming code was proposed in [18], while the convolutional coding concept was proposed by Elias [19]. Following this, the multiple error correcting Bose-Chaudhuri-Hocquenghem (BCH) code was proposed in [20–22]. Furthermore, the Maximum-Likelihood Sequence Estimation (MLSE) of convolutional codes was proposed by Viterbi [23] in 1967. This classic Viterbi algorithm was further interpreted by Forney [24] in 1973, and it was also applied to block codes by Wolf [25] in 1978. As a major milestone, the optimum Log-Max A Posteriori (MAP) decoding algorithm was proposed by Bahl *et al.* [26] in 1974, which is often referred to as the Bahl-Cocke-Jelinek-Raviv (BCJR) algorithm. More explicitly, the

BCJR Log-MAP algorithm aims for maximizing the *a posteriori* probability of $p(X|Y)$, where the variables X and Y model the input and the output signals of the wireless channel. By contrast, Viterbi's MLSE algorithm aims for maximizing the conditional probability $p(Y|X)$ of receiving Y upon sending X over the wireless channel. The pair of probabilities of $p(X|Y)$ and $p(Y|X)$ are only equivalent for equiprobable discrete sources. The BCJR Log-MAP algorithm was shown to be capable of achieving a lower Bit Error Rate (BER) in [26] than the Viterbi algorithm [23–25]. However, owing to the fact that the BCJR Log-MAP algorithm imposed a substantially higher computational complexity than the Viterbi ML algorithm, it had not attracted much attention until the revolutionary development of near-capacity system design emerging in the 1990s. Most notably, the BCJR Log-MAP algorithm was simplified by the approximation of $\ln\left[\sum_{\forall i}\exp(d^i)\right] \approx \max_{\forall i}\ d^i$ by Koch *et al.* [27] in 1990, which is often referred to as the Max-Lag-MAP algorithm, so that the computationally complex exponential operations may be avoided. Furthermore, Robertson *et al.* [28] proposed the near-optimum Approx-Log-MAP algorithm in 1995, which aimed for compensating the difference between the two terms of $\ln\left[\sum_{\forall i}\exp(d^i)\right]$ and $\max_{\forall i}\ d^i$ by invoking a lookup table.

On the voyage of persuing the near-capacity performance predicted by Shannon, the construction of powerful channel code became the greatest challenge. It was observed in [29] that the coding gain, which is the E_b/N_0-reduction provided by channel coding, grows linearly with the convolutional code's memory, but the associated decoding complexity grows exponentially. In order to mitigate this problem, the concept of concatenated codes [30] was introduced, where simple component codes were concatenated in order to construct a powerful channel code. The concatenated code concept was first proposed by Elias [31] in 1954, where an idealistic "error-free" performance predicted by Shannon's theory was shown to be possible. The concatenated code constituted by a convolutional code and a Reed-Solomon (RS) code stood out among the known candidates [30, 32, 33], which was capable of providing a performance that was only $2.0 \sim 3.0$ dB away from Shannon's capacity. In 1979, Battail *et al.* [34] proposed to place a interleaver between the component codes of a concatenated code, which was also referred to as a product code, so that the error bursts may be effectively interleaved. Battail *et al.* also suggested in [34] that the good performance of concatenated codes may be guaranteed if the component decoders can exchange their decisions. Inspired by the development of the Soft-Output Viterbi Algorithm (SOVA) and its application to concatenated codes developed by Hagenauer and Hoeher [35] in 1989, Lodge *et al.* [36] proposed in 1992 that the soft-decision-aided iterative decoding conceived for concatenated block codes inched closer to Shannon's capacity. This scheme was further improved by the same authors [37] in their ICC'93 paper, where the performance of half-rate channel coded BPSK transmitted over Additive White Gaussian Noise (AWGN) channels achieved an impressive closest ever 1.3 dB distance from Shannon capacity. It was also predicted by Lodge *et al.* [37] that the concatenated convolutional codes assisted by soft-decision-aided iterative decoding may provide an even better performance. At the same ICC conference in 1993, the groundbreaking Turbo Coding (TC) technique was independently proposed by Berrou *et al.* [38], where a low BER of

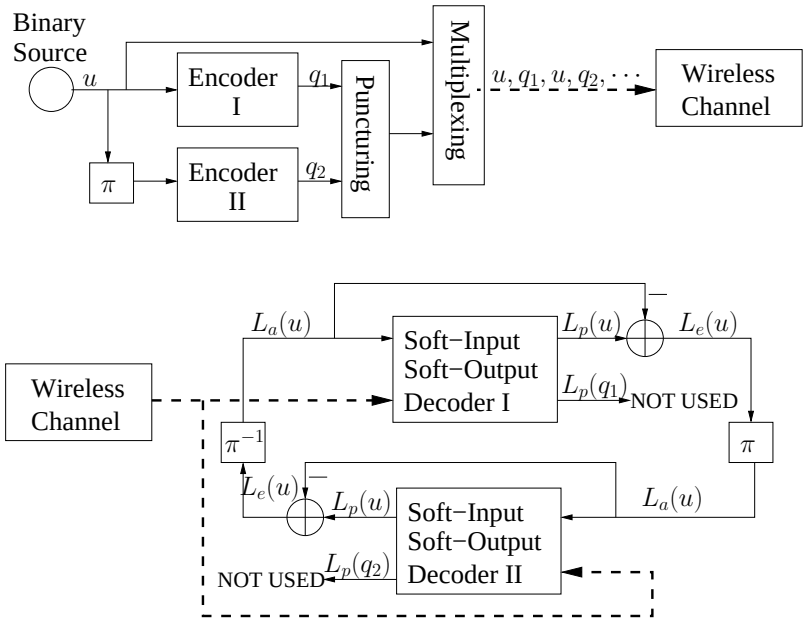

Figure 1.3: The schematic of a Parallel Concatenated Code (PCC) assisted by iterative decoding, which is adopted by Turbo Codes (TCs) [38, 39]. BPSK transmission over AWGN channels is assumed, unless otherwise stated.

10^{-5} was recorded at $E_b/N_0 = 0.7$ dB for half-rate channel coded BPSK transmitted over AWGN channel, which was achieved by the parallel concatenation of a pair of Recursive Convolutional Code (RSC) components exchanging their soft-bit information with the aid of iterative decoding, as previously predicted by Lodge *et al.* [36, 37].

Let us now elaborate a little further on TC and its revolutionary effect on channel coding science. The schematic of the Parallel Concatenated Code (PCC) adopted by TC [38, 39] is portrayed in Fig. 1.3. It can be seen in Fig. 1.3 that the information bits are encoded twice by a pair of component RSC encoders, where an interleaver is inserted between them in order to ensure that the bit-dependencies imposed by the two RSC codes are eliminated between them. At the receiver, the pair of component RSC decoders exchange their so-called extrinsic information[1] in order to achieve a near-capacity performance. The soft-bit processed by the soft-input soft-output decoders of Fig. 1.3 is in the form of Log Likelihood Ratio (LLR) [27, 35], where L_a, L_p and L_e represent the *a priori* LLR, *a posteriori* LLR and extrinsic LLR, respectively. BPSK transmission over an AWGN channel was assumed by the TC scheme of [38, 39]. However, it is straightforward to extend this scheme to more complex modulations, where an arbitrary modulator and a demodulator is placed before and after the wireless channel block of Fig. 1.3, respectively.

Following the groundbreaking invention of TC and considering that the block codes have relatively simple trellis structures [41], Pyndiah *et al.* [42] proposed to replace the convolutional codes of Fig. 1.3 by block codes, which also achieved a near-capacity performance [42, 43]. In [44],

[1]The terminology of extrinsic information stems from the fact that as a benefit of the interleaver, they are capable of providing an independent 'extended' source of information for each bit.

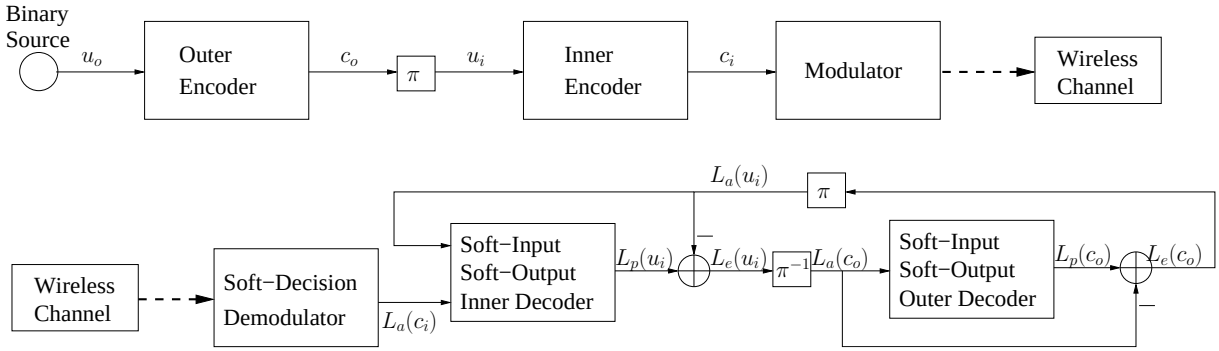

Figure 1.4: The schematic of Serial Concatenated Code (SCC) assisted by iterative decoding [40]. BPSK transmitting over AWGN channel is assumed unless otherwise stated.

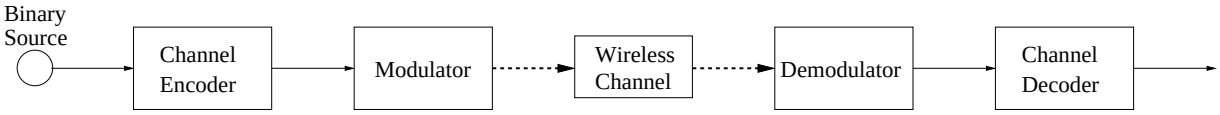

Figure 1.5: The schematic of a conventional communications system constituted by channel code and modulation.

Hagenauer *et al.* generalized PCC, where any combination of block and convolutional codes was deemed to be possible. Owing to the fact that the TC component decoders in Fig. 1.3 only updated the LLRs for the information bits, but not for the parity bits, an error floor was experienced for a limited number of decoding iterations, Benedetto *et al.* [40, 45] proposed the concept of Serial Concatenated Code (SCC). The schematic diagram of a SCC is depicted in Fig. 1.4. At the SCC encoder of Fig. 1.4, after interleaving the coded bits c_o that include both the information bits u_o and the parity bits q_o produced by the outer encoder, all bits become the input information bits u_i of the inner encoder. As a result, at the SCC decoder of Fig. 1.4, the extrinsic LLRs $L_e(u_i)$ produced by the inner decoder become the *a priori* LLRs $L_a(c_o)$ for the outer decoder after de-interleaving, while the extrinsic LLRs $L_e(c_o)$ produced by the outer decoder are transformed to be the *a priori* LLRs $L_a(u_i)$ for the inner decoder after interleaving. Therefore, unlike for the PCC of Fig. 1.3, the SCC component decoders of Fig. 1.4 exchange their extrinsic information based on the exact same binary bits without any puncturing.

The Low-Density Parity Check (LDPC) coding concept that was originally proposed by Galager [46] in 1962 was popularized by MacKay and Neal [47] in 1996, where a near-capacity performance was achieved by constructing sparse random parity check matrices and by iteratively improving the decoding performance [47–49]. Hence the LDPC concept preceded TC by 31 years.

In order to optimize the communications schemes, the modulation scheme, which defines the format of signal transmission and determines the effective throughput should also be taken into account. During their infancy, channel coding and modulation were treated as separate entities [4, 5], as portrayed by Fig. 1.5. The first attempt of jointly designing channel coding and modulation is

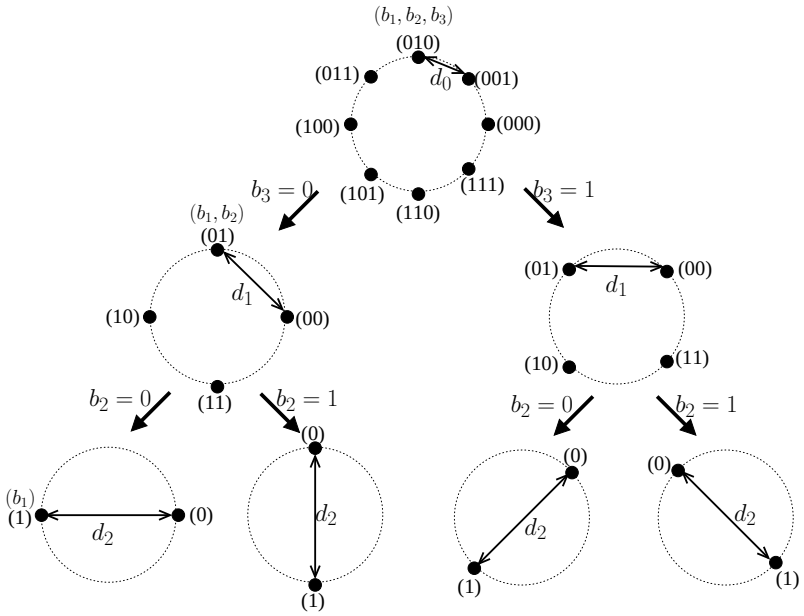

Figure 1.6: An example of 8PSK set partitioning for the Ungerboeck's Trellis Coded Modulation (TCM) of [50].

due to Mecklenburg *et al.* [51] in 1973, when the conventional Gray-labelling designed for modulation was revised in order to also impose bit-dependency on the channel coded source bits. As the benefit, the demodulator and the channel decoder act in liaison in order to jointly decide upon the modulated symbol. Inspired by this idea, Multi-Level Coding (MLC) was proposed by Imai and Hirakawa [52] in 1977, where the coded bits were mapped to the different - integrity protection - classes of multi-level modulus. The bits mapped to the lower-integrity modem sub-channels were protected by stronger channel codes, which were then detected first by the MLC scheme's multi-stage decoder followed by the other bits of the MLC scheme. In 1982, Ungerboeck [50] proposed the landmark concept of Trellis Coded Modulation (TCM), where the channel code's parity bits were accommodated by the modem by increasing the number of bits per symbol, because this required no bandwidth expansion for FEC. More explicitly, instead of using Gray-labelling for the modulated symbols, the TCM constellation diagram is divided into subsets by a techniqe referred to as set partitioning, where each bit determines a pair of subsets, and the Euclidean distance between the neighbouring constellation points within a subset is increased at every partitioning step. An example of 8PSK set partitioning [50] is portrayed by Fig. 1.6. Similar to the MLC of [52], the TCM of [50] assigned stronger component channel codes associated with longer memories to protect the bits associated with lower Euclidean distances. However, instead of invoking a multistage decoder as the MLC scheme [52], the TCM decoder was originally designed for relying on a single trellis for jointly deciding on all the information bits.

Inspired by the invention of MLC and TCM, a lot of research efforts had been dedicated to developing multi-dimensional constellations for TCM [53–55] in the 1980s, where instead of set-partitioning the constellation diagram of a single symbol, a block of data were mapped to higher di-

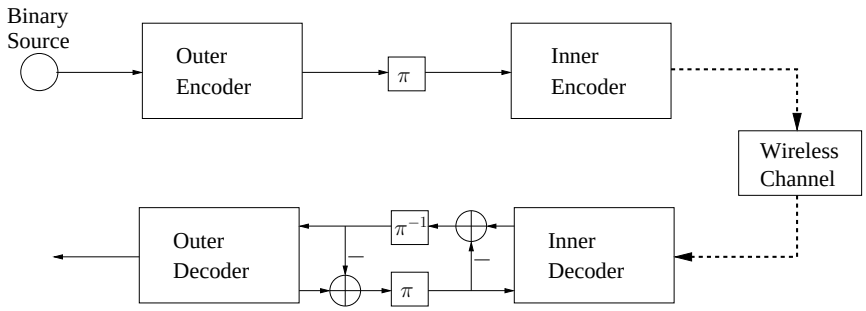

Figure 1.7: The schematic of generalized Serial Concatenated Code (SCC) assisted by iterative decoding.

mensional constellations, so that a beneficial coding gain was achieved by the joint channel coding and modulation design. However, as described in [56], the number of metrics to be calculated for the TCM decoder's trellis state transitions inevitably increases as the modulation-order increases. In order to mitigate the escalating complexity, the trellis construction of the TCM decoder was decomposed into lower-dimensional problems with the aid of multistage decoding [57–59] following the philosophy of the MLC receiver of [52].

A specific TCM scheme conceived for fading channels was conceived by Simon and Divsalar [60, 61] in 1988, where a symbol-based interleaver was proposed for separating the trellis-based channel encoder and the modulator at the TCM transmitter, while the corresponding symbol-based deinterleaver separated the demodulator and the channel decoder at the receiver. As a result, the channel code and modulation were once again separated into two entities. Despite the temporal correlation among the fading samples, the employment of interleaving/deinterleaving makes the fading channels more-or-less memoryless, so that the symbols along a given error event path may be considered to be independently faded. Moreover, it was observed in [60,61] that the TCM scheme's maximized Euclidean distance became less important in fading channels than in case of AWGN channels [62]. Against this background, the classic Bit-Interleaved Coded Modulation (BICM) arrangement was proposed by Zehavi [63] in 1992, which was further developed by Caire *et al.* [64]. It was proven in [63, 64] that the achievable time-diversity order of the BICM was determined by the minimum Hamming distance of the channel code. As a benefit of bit-based interleaving, every coded bits may be modulated to any modulation constellation point, and hence BICM is not designed for achieving the maximized free Euclidean distance of TCM. As a result, the TCM scheme still performs better than BICM in AWGN channels, but BICM outperforms TCM in fading channels, especially when the SNR is relatively high and hence the fading characteristics dominate the attainable performance. In order to further improve the performance of BICM, the landmark Bit-Interleaved Coded Modulation concept relying on Iterative Decoding (BICM-ID) was proposed by Li and Ritcey [65] in 1997. More explicitly, BICM-ID constitutes an instance of the generalized SCC portrayed in Fig. 1.7, where the channel code and the modulation scheme constitute the outer code and the inner code, respectively. The BICM-ID scheme was initially proposed for exchanging hard-decisions in [65,66] and then it was further developed for exchanging soft-bit decisions in [67]

SCC Systems	Inner code	Outer code
Serial concatenated channel code [40, 45]	Channel code	Channel code
LDPC codes [47–49]	Variable nodes	Check nodes
BICM-ID [65–68]	Modulation	Channel Code
Source-controlled channel decoding [69]	Channel code	Source code
Turbo equalization [70–72]	Equalization	Channel code
Turbo multiuser decoding [73–76]	Mutiuser transceiver	Channel code
Turbo-BLAST [13, 77, 78]	V-BLAST MIMO	Channel code
PCC Systems	**Component code I**	**Component code II**
Parallel concatenated channel code [38, 39, 42–44]	Channel code	Channel code
Turbo TCM (TTCM) [79]	TCM	TCM

Table 1.1: Examples of turbo detected concatenated codes.

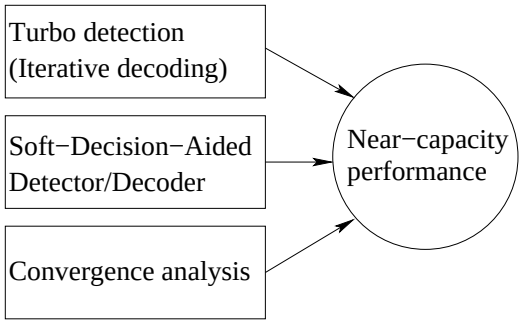

Figure 1.8: The key driving factors behind achieving a near-capacity performance.

with the aid of a turbo receiver. It was explicitly demonstrated in [68] that since the BICM-ID receiver's demodulator was capable of mapping any bit back to the constellation subset pairs with the aid of the *a priori* knowledge of all other bits, the free Euclidean distance was once again increased after the demodulator received feedback from the channel decoder, which assisted BICM-ID in outperforming TCM both in AWGN channels and in fading channels.

It was gradually realized by the community that the "turbo principle" [80] may in fact be extended to a variety of areas in order to achieve the full potential of different communications systems. The revolutionary development of near-capacity system design has attracted substantial research interest from the late 1990s onwards. A brief summary of turbo detected concatenated codes is offered in Table 1.1, which includes the areas of channel coding, source coding, equalization, multi-user detection, MIMO systems, etc.. The three driving factors behind near-capacity system design are summarized in Fig. 1.8. Clearly, in order to perform iterative decoding/turbo detection, the constituent detectors/decoders have to be revised both to be able to accept and to produce soft-bit LLRs, again, as summarized in Table 1.1. In this treatise, the terminologies of iterative decoding and turbo detection are used interchangeably in order to address the involvement of potentially any detector/decoder in iterative decoding. The last key factor in Fig. 1.8 that has not

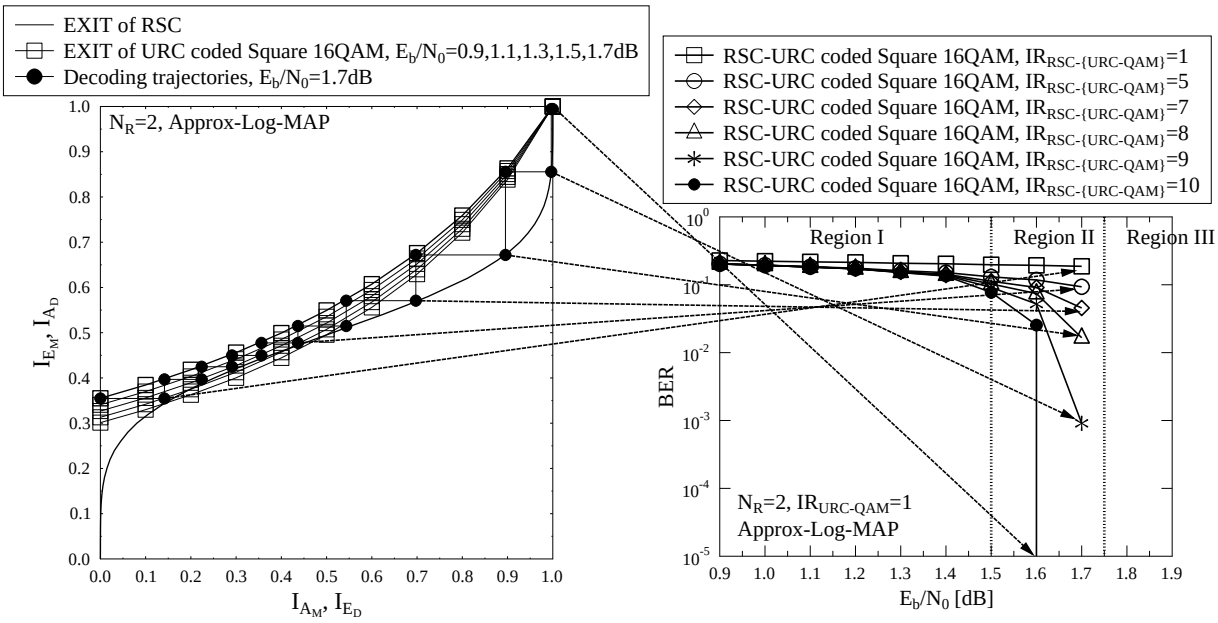

a) EXIT charts and decoding trajectories

b) BER performance

Figure 1.9: An example of EXIT charts analysis and BER performance of the RSC and URC coded Square 16QAM scheme. The Discrete-input Continuous-output Memoryless Channel (DCMC) capacity limit of this scheme is given by $E_b/N_0 = 0.1$ dB. A more powerful IRregular Convolutional Code (IRCC) may replace the RSC in order to further inch to the capacity limit. More details are offered in Chapter 2.

received much attention is the convergence analysis.

The BER versus E_b/N_0 performance curve of a near-capacity system may be generally divided into three regions according to the noise level. In the low SNR region, the component channel codes are unable to correct large bursts of errors. At a specific SNR, which is not much higher than the capacity limit, a "turbo cliff" or a "waterfall" may be observed as the BER curve drops rapidly, which is the result of decoding convergence. When the SNR is increased beyond this specific region, the BER is expected to become infinitesimally low. An example of such BER performance curve is shown in Fig. 1.9b. Owing to the fact that the asymptotic union bounds derived based on the distance properties of channel codes are only tight at high SNRs [40], this tool becomes less useful for predicting the performance of turbo detected concatenated codes, which generally operate at a relatively low SNR that is close to the capacity limit. Recall that the error performance of coded modulation at a low SNR associated with a high noise level is more related to the modem's Euclidean distance than to the channel code's Hamming distance. As a result, the modulation scheme's capacity limit itself may be regarded as a loose performance prediction of the decoding convergence. In general, a communications system may be considered to be capable of "near-capacity" operation, when a turbo-like performance is achieved, which may be interpreted as attaining decoding convergence at an SNR that is within 1.0 dB distance from the capacity limit, provided that optimum or near-optimum decoding/detecting algorithms are employed.

Naturally, the prediction of the BER curve's "turbo cliff" SNR is important for near-capacity

system design, but it is also important to optimize the number of iterations between the turbo detected component detectors/decoders so that no futile complexity wastage is imposed. In 1993, Moher [81] proposed to analyse the iterative convergence behavior with the aid of the cross-entropy metric, which was further developed to an iterative detection "stopping criterion" in [82]. The concept of cross-entropy allows us to keep track of the Probability Density Function (PDF) of the extrinsic LLRs produced by the component decoders, where decoding convergence is expected to occur, when the extrinsic LLR PDFs of the component decoders converge to the same decisions. Following this idea, Richardson *et al.* [48,49] proposed the density evolution concept for predicting the LDPC decoding convergence, where the belief propagation was also characterized by tracing the PDFs. Inspired by the development of density evolution, ten Brink [83] proposed the powerful tools of EXtrinsic Information Transfer (EXIT) charts in 1999, which visualized the convergence of turbo detection. More explicitly, the PDF of the extrinsic LLRs of a component decoder may be obtained by feeding Gaussian-distributed *a priori* LLRs [84, 85] to the decoder, so that the mutual information between the extrinsic LLRs and the source bits may be evaluated. As a benefit of iterative soft information exchanging between a pair of component decoders, the extrinsic information produced by a component decoder becomes the *a priori* information of another component decoder and vice versa. When the EXIT curves of two component decoders only intersect each other at the (1.0,1.0) point of the EXIT chart as seen in the example protrayed by Fig. 1.9a, decoding convergence is expected to occur. It can be seen in Fig. 1.9 that both the SNR and the number of iterations required for decoding convergence are accurately predicted by the EXIT charts. This technique was further extended for SCC in [86] and for PCC in [87, 88]. Furthermore, it was proposed in [89–91] that the mutual information may be calculated without having access to the source bits. As a result, the EXIT charts may be constructed "on-line", because as soon as new extrinsic LLRs become available at the receiver, they can be used for updating the current estimate of the mutual information [92].

This section is summarized by a list of major contributions on near-capacity system design, as presented in Tables 1.2-1.4. We will offer a more detailed discussion on this topic in Chapter 2, where a reduced-complexity design will be proposed for soft-decision-aided demodulators.

1.2 A Historical Perspective on Noncoherent Detection

The signal received at the output of a wireless communications channel typically contains a faded and noise-contaminated replica of the transmitted signal. In the classic AWGN channels, often a frequency offset of $\exp(j\theta)$ also corrupts the transmitted symbol s_n, so that the received symbol is given by $y_n = \exp(j\theta)s_n + v_n$, where v_n is the AWGN element. This frequency offset, which is the difference between the frequency of the received signal and the designed frequency of the receiver, is typically induced by numerous sources, such as the Doppler shift and the frequency difference of the heterodyning oscillators. Furthermore, in fading channels the frequency offset $\exp(j\theta)$ is replaced by a fading factor h_n, which may be a statistically random variable, because the signals

Table 1.2: Summary of major contributions on near-capacity system design (Part I).

Year	Author(s)	Topic	Contribution
1948	Shannon [17]	Capacity Theorem	Proposed that the channel capacity, which is the maximum data rate that can be transmitted over the channel at an infinitesimally low error rate, can be achieved with the aid of channel coding at the unconstrained cost of delay and complexity.
1950	Hamming [18]	Channel Code	Proposed the single-error correcting Hamming code.
1954	Elias [31]	Concatenated Code	Proposed the concatenated code concept, where an idealistic "error-free" performance predicted by Shannon's theory was shown to be possible.
1955	Elias [19]	Channel Code	Proposed the classic convolutional coding concept.
1959 $\sim$ 1960	Bose *et al.* [20–22]	Channel Code	Proposed the classic multiple-error correcting BCH code, which was named after the authors.
1967	Viterbi [23]	Decoding Algorithm	Proposed the Maximum Likelihood Sequence Estimation (MLSE) decoding algorithm of convolutional code, which was later termed as Viterbi algorithm [24] and was applied to block codes in [25].
1973	Mecklenburg *et al.* [51]	Coded Modulation	Proposed to jointly design channel coding and modulation, where the demodulator and the channel decoder act in liaison in order to jointly decide upon the modulated symbol.
1974	Bahl *et al.* [26]	Decoding Algorithm	Proposed the major milestone of the optimum Log-Max A Posteriori (MAP) decoding algorithm, which is also known as the BCJR algorithm named after the authors.
1977	Imai and Hirakawa [52]	Coded Modulation	Proposed Multi-Level Code (MLC), where the bits mapped to the lower-integrity modem sub-channels were protected by stronger channel codes, which were then detected first by the MLC scheme's multistage decoder followed by the other bits of the MLC scheme.
1979	Battail *et al.* [34]	Concatenated Code	Proposed to place a interleaver between the component codes of a concatenated code and proposed to exchange decisions between the component decoders.
1982	Ungerboeck [50]	Coded Modulation	Proposed the concept of Trellis Coded Modulation (TCM), which increased the constellation Euclidean distance by set-partitioning, while modulation and channel code were jointly designed by a single trellis.

Table 1.3: Summary of major contributions on near-capacity system design (Part II).

Year	Author(s)	Topic	Contribution
1988	Simon and Divsalar [60, 61]	Coded Modulation	Proposed to place a symbol-based interleaver between the channel code and the modulation for the TCM scheme conceived for fading channels.
1989	Hagenauer *et al.* [35]	Decoding Algorithm	Proposed to modify the Viterbi algorithm to be able to process soft-bit decisions, which is also known as the Soft-Output Viterbi Algorithm (SOVA) algorithm.
1990	Koch and Baier [27]	Decoding Algorithm	Proposed to simplify the BCJR Log-MAP algorithm by the approximation of $\ln\left[\sum_{\forall i}\exp(d^i)\right] \approx \max_{\forall i} d^i$ in order to avoid the computationally complex exponential operations, which is often referred to as the Max-Lag-MAP algorithm.
1992	Zehavi [63]	Coded Modulation	Proposed the classic Bit-Interleaved Coded Modulation (BICM), which replaced the TCM's symbol-based interleaver [60, 61] by a bit-based interleaver in order to improve the achievable time-diversity order of the BICM in fading channels.
1992	Lodge *et al.* [36]	Concatenated Code	Proposed the soft-decision-aided iterative decoding conceived for concatenated block codes that inched closer to Shannon's capacity, which was further improved by the authors in [37].
1993	Berrou *et al.* [38]	Concatenated Code	Proposed the groundbreaking Turbo Code (TC), which achieved a near-capacity performance by the parallel concatenation of a pair of RSCs exchanging their soft-bit decisions with the aid of iterative decoding. It was later summarized in detail by the authors in [39].
1995	Robertson *et al.* [28]	Decoding Algorithm	Proposed the near-optimum Approx-Log-MAP which compensated the difference between the BCJR Log-MAP [26] and the Max-Log-MAP [27] by invoking a lookup table.
1996	Hagenauer *et al.* [44]	Concatenated Code	Proposed to generalize the Parallel Concatenated Code (PCC), which included TC as an special case.
1996	Benedetto *et al.* [45]	Concatenated Code	Proposed to generalize the Searial Concatenated Code (SCC), which was later summarized in detail by the authors [40].

Table 1.4: Summary of major contributions on near-capacity system design (Part III).

Year	Author(s)	Topic	Contribution
1997 $\sim$ 1999	Li and Ritcey [65–67]	Coded Modulation	Proposed the Bit-Interleaved Coded Modulation concept relying on Iterative Decoding (BICM-ID), which improved BICM [63,64] by introducing iterative decoding between the demodulator and the channel decoder.
1999	ten Brink [83]	Convergence Analysis	Proposed the powerful tools of EXtrinsic Information Transfer (EXIT) charts, which visualized the extrinsic information exchanged in iterative decoding and accurately predicted both the SNR and the number of iterations required for decoding convergence.
2000	Divsalar *et al.* [93]	Concatenated code	Proposed to further place an Unity Rate Code (URC) as an intermediate component in the SCC, so that the error floor of the two-stage turbo detector may be eliminated by the resultant three-stage turbo detector.
2001	ten Brink [88]	Convergence Analysis	Extended EXIT charts to the PCC system design.
2004	Tuchler [86]	Convergence Analysis	Extended EXIT charts to the SCC system design, and proposed the IRregular Convolutional Code (IRCC) concept in order to inch closer to the capacity limit.
2009	Hanzo *et al.* [8]	Coded Modulation	Summarized guidelines for general near-capacity system design and offered design examples for a wide range of communications systems.

received from different paths may be superimposed either constructively or destructively. Against this background, a receiver is referred to as being "coherent", when the Channel State Information (CSI) of the frequency offset or the fading factor are assumed to be known at the receiver. This requirement of CSI knowledge at the receiver has inspired the development of channel estimation techniques.

Fig. 1.10 portrays two typical channel estimation examples. The preamble-based training assisted signal transmission of Fig. 1.10 is conceived for fading channels, which remain more-or-less time-invariant during a block of symbol periods. In this case, a sequence of training symbols that are known to both transmitter and receiver may be transmitted before the sequence of data symbols, so that the receiver may first recover the CSI knowledge by observing the faded and noise-contaminated training symbols, and then a coherent demodulator may be invoked for detecting the following data symbols with the aid of the CSI estimate. The training sequence design was proposed to maximize the capacity bound in [94–97]. In particular, in 2003, Hassibi and Hochwald [97] proposed a framework for appropriate time- and power- allocation between the

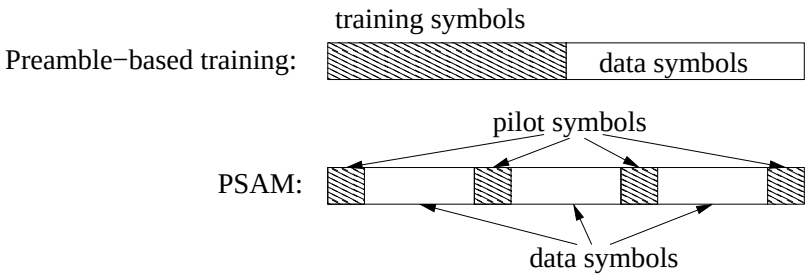

Figure 1.10: Examples of channel estimation techniques relying on preamble-based training and Pilot Symbol Assisted Modulation (PSAM).

training and data symbols based on the capacity lower bounds. They discovered that if the training symbols and the data symbols are assigned the same power, half of the channel's coherence time should be spent on training. However, if the power allocation is optimized by the capacity bounds, the number of neccessary training symbols may be set to the number of TAs. It was also observed in [97] that using training is optimal for obtaining accurate CSI estimation in the high SNR region in conjunction with a long coherence time, but channel estimation relying on training becomes suboptimal in the low SNR region. It was demonstrated in [98, 99] that the Mean Squared Error (MSE) lower bound of training is given by the Cramer-Rao Bound (CRB) of $CRB = N_0/N_{OW}$ in block fading, where N_{OW} represents the observation window length used for training symbols. This further confirms that channel estimation using training is challenging, when the noise power is high.

When the channel's coherence time is reduced and becomes comparable to the symbol period, a so-called rapidly fading channel is encountered, where the fading factor is generally considered to be different for each consecutive transmitted symbol. In this scenario, a beneficial solution is to insert a pilot tone into the spectrum of the transmitted signal, so that an estimate of the fading factor may be extracted at the receiver. This technique was proposed by McGeehan and Bateman [100] in 1984 termed as the Transparent Tone-In-Band (TTIB) solution. The design challenges of TTIB include an increased peak-to-average signal ratio, and the TTIB also has to carefully choose the position of the pilot tone in the signal specturm. In order to avoid this problem, the novel Pilot Symbol Assisted Modulation (PSAM) regime was proposed by Moher and Lodge [101] in 1989 and then theoretical analysed by Cavers [1] in 1991. As portrayed in Fig. 1.10, the PSAM scheme periodically transmits pilot symbols among data symbols, so that the receiver may interpolate the correlated fading envolope and phase by a Wiener filter that aims for the Minimum Mean Squared Error (MMSE) between the estimated CSI and the actual CSI. We will demonstrate in Sec. 3.4 that the PSAM scheme's MSE lower bound, which corresponds to the ideal case of the fading remaining constant over N_{OW} symbol observations, is given by $\sigma^2_{MSE-LB} = N_0/(N_0 + N_{OW})$, which is worse than that of the preamble-based training in the context of block fading. This channel estimation error expression implies that channel estimation is even more of a challenge in the low SNR region, when rapid fading is encountered. Moreover, as the Doppler frequency is increased, the PSAM scheme's pilot spacing has to be reduced in order to sample the fading channels more

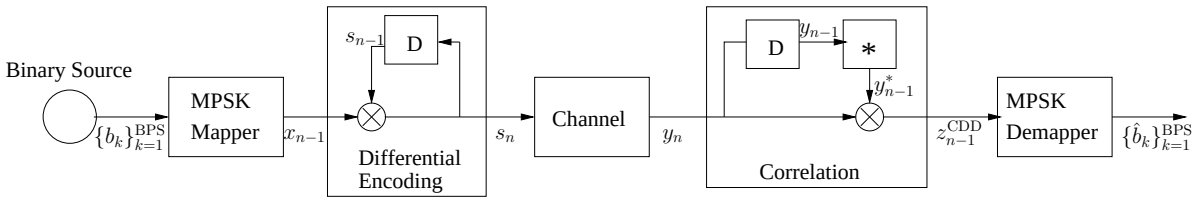

Figure 1.11: Schematic of a simple Differential Phase Shift Keying (DPSK) transceiver.

frequently. As a result, more transmission power has to be dedicated to the pilot symbols to the detriment of the data-carrying symbols.

As demonstrated in Sec. 1.1, turbo detected concatenated codes generally operate at a relatively low SNR that is close to the capacity limit, where accurate CSI knowledge is difficult to obtain. However, for coherent demodulators, researchers often assume having perfect CSI knowledge even in rapidly fading channels at low SNRs. However, realistic channel estimation always imposes a performance penalty that is more severe in coded systems than in uncoded systems. This is because the soft-decision-aided coherent demodulators relying on imperfect CSI will produce LLRs, which deviate from the true probabilities. Hence, the resultant exaggerated LLR values may become more and more difficult to correct by the channel decoder, as the number of iteration increases, which will be further discussed in more detail in Sec. 3.4.

Against this background, when the CSI knowledge is not assumed to be known at the receiver, "noncoherent" detection is encountered. The optimum noncoherent detection relies on Maximum Likelihood Sequence Estimation (MLSE), which jointly performs channel estimation and data detection. An early attempt of MLSE may be found in Kailath's work [102] in 1960. It was demonstrated in [102] that channel estimation may be tentatively performed for each possible combination of the data-carrying sequence, and then these combinations may be compared in order to make a final decision on the data-carrying sequence. This method was further augmented by Kailath [103] in the context of the "estimator-correlator" in 1969. However, as the message length increases, the complexity of MLSE inevitably increases exponentially. In order to circumvent this problem, Forney [104] proposed to invoke the Viterbi algorithm for MLSE in 1972, which relies on the early termination of the candidate evaluation process by ignoring those candidates that are unlikely to be the maximum likelihood solution. The aforementioned MLSE techniques were explicitly developed for frequency selective fading channels, where channel's memory was imposed onto the data transmission in the form of Inter-Symbol Interference (ISI). In 1979, Morley and Snyder [105] demonstrated that the MLSE may be capable of tackling any form of channel memory that may be imposed by either frequency selective channels or by time selective channels, such as correlated Rayleigh, Rician and lognormal fading. It was also demonstrated in [105] that the MLSE detection complexity, which is determined by the number of trellis states, grows exponentially with the channel's memory rather than with the message length, when using the Viterbi algorithm.

In order to eliminate channel estimation in noncoherent receivers, differentially encoded modu-

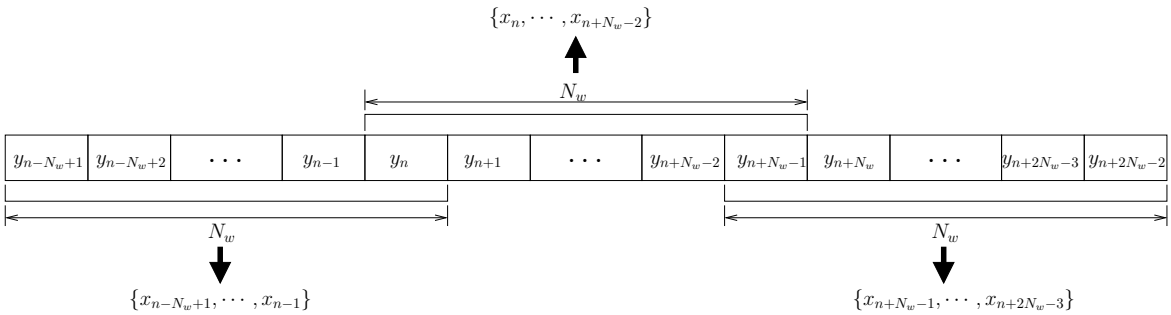

Figure 1.12: Schematic of Multiple-Symbol Differential Detection (MSDD) observations.

lated schemes may be employed. As an example, a simple Differential Phase Shift Keying (DPSK) transceiver is portrayed in Fig. 1.11. At the DPSK transmitter, the data-carrying MPSK symbol x_{n-1} is mapped onto the difference between the consecutive transmitted symbols as $s_n = x_{n-1}s_{n-1}$. In AWGN channels or in non-dispersive slow fading channels, the received signal seen in Fig. 1.11 may be expressed as $y_n = s_n h_n + v_n$, where h_n and v_n refer to the CSI and AWGN, respectively. As a result, the DPSK receiver of Fig. 1.11 may be capable of eliminating the need for channel esimation by the simple correlation operation of $z_{n-1} = y_n y^*_{n-1}$, which may be directly demapped to bits. This simple noncoherent detection, which detects a single symbol based on two observations may be termed as Conventional Differential Detection (CDD). The early development of DPSK may be found in Lawton's work [106, 107] in 1959-1960, where the effect of the constant phase rotation in AWGN channels is mitigated by the low-complexity transceiver portrayed in Fig. 1.11. However, it was demonstrated by Cahn [108] in 1959 that the CDD aided DPSK scheme suffers from a 3 dB performance penalty compared to its coherent MPSK counterpart assuming the idealistic perfect estimation of the frequency offset phase. Moreover, it was discovered by Bello and Nelin [109] in 1962 that an irreducible error floor occurs for DPSK, when the CDD, which was originally designed for AWGN channels, is directly employed in rapidly fluctuating fading channels.

The pragmatic approach to improve the performance of the noncoherently detected DPSK scheme for the sake of approaching the optimum MLSE performance is to increase the number of observations. In 1979, it was proposed by Masamura *et al.* [110] that the DBPSK's pair of data-carrying bits detected from three consecutive observations at the noncoherent receiver may be treated as an information bit and a parity bit. As a result, detecting DBPSK as a channel code may improve its performance in AWGN channels. Furthermore, Samejima *et al.* [111] extended the work in [110] to M-level DPSK and to more than three observations. Following this, the groundbreaking Multiple-Symbol Differential Detection (MSDD) conceived for DPSK operating in AWGN channels was proposed by Wilson *et al.* [112] in 1989 and then theoretically analysed by Divsalar and Simon [7] in 1990. As portrayed by Fig. 1.12, the MSDD extends the CDD's observation window from two to $N_w \geq 2$ observations, where a total number of $(N_w - 1)$ data-carrying symbols are jointly detected. The MSDD is a special case of MLSE, where the channel memory is assumed to span over N_w transmission intervals. Moreover, for the sake of simplicity,

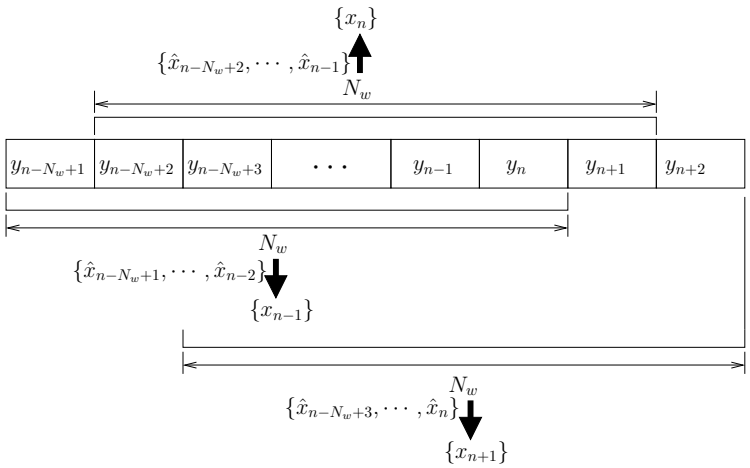

Figure 1.13: Schematic of the Decision-Feedback Differential Detection (DFDD) observations.

the MSDD assumes having a message length of N_w, which is the same as the channel memory, so that the employment of the Viterbi algorithm by the MLSE [104] may be avoided. Furthermore, the MSDD design conceived for DPSK was extended to Rayleigh fading channels by Ho and Fung [113] in 1992. As a further advance, the MSDD techniques developed for both DPSK and for Differential Quadrature Amplitude Modulation (DQAM) operating both in AWGN and Rayleigh fading channels were summarized by Divsalar and Simon [114] in 1994. It was demonstrated that the MSDD may be capable of reducing the 3 dB performance penalty both for AWGN channels and for slowly fluctuating fading channels [7, 112–114], while the CDD's error floor experienced in rapidly fading channels may also be mitigated by the MSDD [113, 114]. However, the major disadvantage of the MSDD is that its detection complexity increases exponentially with N_w. Given an M-level DPSK scheme, the MSDD complexity order imposed by detecting a single symbol is given by $O\left[M^{(N_w-1)}/(N_w-1)\right]$.

In order to further reduce the MSDD complexity, an efficient algorithm was conceived by Mackenthun [115] in 1994 for MSDD in AWGN channels, where a low detection complexity order of $O(\log N_w)$ was imposed by detecting a single symbol relying on tracing the phase changes over the N_w samples. This method may also be applied for reducing the MSDD complexity of DPSK operating in block fading channels. However, as discussed before, channel estimation for block fading channels is capable of maintaining a low estimation error that diminishes upon increasing SNR and the training window. Furthermore, it was also demonstrated by Chen *et al.* [116] that combining TC and channel estimation for DPSK in block fading may achieve a performance that is close to Shannon's capacity limit. By contrast, it is widely recognized that channel estimation remains a challenge for rapidly fading channels. Therefore, it is vitally important to implement MSDD in rapidly fading channels at an affordable complexity.

Similar to the MIMO scheme's ML detector portrayed in Fig. 1.2, the exponentially increasing MSDD complexity is the result of jointly detecting the $(N_w - 1)$ data-carrying symbols as seen in

Fig. 1.12. In order to separately visit the individual constellations, decision-feedback may be introduced, where a total of $(N_w - 2)$ data-carrying symbols are detected from the previous detection windows, while only a single unknown symbol has to be detected by the current detection window. This decision-feedback version of MSDD may be termed as Decision-Feedback Differential Detection (DFDD), which is portrayed in Fig. 1.13. The DFDD concept was originally proposed for DPSK operating in AWGN channels by Leib and Pasupathy [117] in 1988 and by Edbauer [118] in 1992, which were shown to be equivalent by Adachi and Sawahashi [119] in 1993. Leib [120] later confirmed in 1995 that the DFDD of [117] is equivalent to the MSDD of [7] operating in decision-feedback mode. The DFDD designed for DPSK was further extended to Rayleigh fading channels by Schober *et al.* [121] in 1999, which was derived from the MSDD of [113, 114]. Furthermore, the DFDD designed for DPSK was developed to be able to accept and produce soft-bit decisions by Lampe *et al.* [122] in 2001, so that the DFDD may be invoked in turbo detection. Another form of DFDD may be derived from linear prediction, where a channel sample is predicted by a low-pass filter based on the previous observations and decisions, so that coherent detection may be performed for the current symbol. This idea was originally introduced by Svensson [123] in 1994, which was tailored for DQPSK operating in fading channels. In 1999, Bin and Ho [124] further generalized the prediction-based DFDD to M-level DPSK, while Hoeher and Lodge [125] proposed the soft-decision-aided prediction-based DFDD for DPSK in fading channels. In 2000, Schober and Gerstacker [126] extended the prediction-based DFDD designed for DPSK to Ricean fading channels, and they proved that both MSDD-based DFDD [121, 122] and prediction-based DFDD employing the MMSE Wiener filter [123–125] are identical for DPSK operating both in AWGN and in Rayleigh fading channels. Furthermore, these two forms of DFDD also perform similarly in Ricean fading channels. The above DFDD solutions are capable of improving the CDD's performance by mitigating the error floor, when the fading fluctuates rapidly. Moreover, the DFDD complexity order is simply given by $O(M)$, because only a single symbol has to be detected at a time. However, the DFDD's imperfect decision feedback results in a performance loss compared to MSDD.

In order to retain the optimum MSDD performance, the concept of Multiple-Symbol Differential Sphere Detection (MSDSD) was proposed by Lampe *et al.* [127] in 2005, where the problem of optimizing the MSDD decision metric was transformed into a shortest-vector search problem [12], so that the SD may be invoked for MSDD. An example of the MSDSD conceived for DQPSK is portrayed in Fig. 1.14a. More explicitly, assuming that the SD's initial radius is set to be sufficiently large, and the SD index v may start from $v = 1$, for each SD index v, only M MPSK candidates have to be examined for detecting a single symbol. When the best candidate is chosen, the SD index v may be increased and the search may be repeated until $v = N_w$ is reached, where a valid MSDSD output is found and the SD's radius may be updated accordingly. Then the SD index v may be reduced, so that the next-best candidate may be examined. If no more valid candidates can be found within the SD's radius, the SD index v may be further reduced until reaching $v = 1$, where the sphere decoding process is terminated. As a result, the MSDSD complexity order imposed by

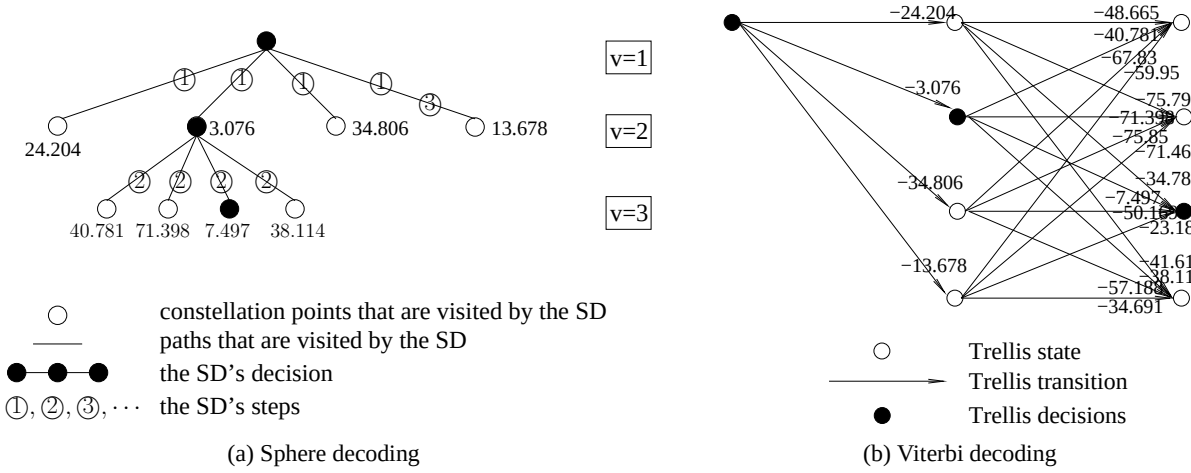

(a) Sphere decoding

(b) Viterbi decoding

Figure 1.14: Example of Multiple-Symbol Differential Sphere Detection (MSDSD) conceived for DQPSK recorded at SNR=10 dB, where we have $N_w = 3$, and its corresponding trellis decoding aided MSDD using the Viterbi algorithm. We note that all the likelihood metrics represented in the logarithmic domain that are calculated by the trellis have to be carefully modified for sphere decoding, so that the sphere decoder may only process non-negative values.

detecting a single symbol is lower bounded by $O(M)$. If the MSDSD is replaced by trellis decoding aided MSDD using the Viterbi algorithm as portrayed by Fig. 1.14b, the same optimum MSDD decisions may be obtained. The trellis seen in Fig. 1.14b is drawn according to the differential encoder's memory [125, 128], as seen in Fig. 1.11 instead of the channel's memory [129–131], so that the number of trellis states may be kept to a minimum. In general, the trellis decoding process may span over much more than just two time slots, as seen in Fig. 1.14b. Considering that except for the first time slot, there are always M trellis transition branches emerging from a particular current state, while there are always M transition braches merging into a particular next state, the average complexity order of the trellis-decoded MSDD imposed by detecting a single symbol is given by $O(M^2)$, which is higher than the MSDSD's lower bound. Inspired by the development of MSDSD, Pauli *et al.* [132] proposed the soft-decision-aided MSDSD for DPSK in 2006.

In summary, the links between the MIMO receivers of Fig. 1.2 and the noncoherent receivers introduced in this section are presented in Fig. 1.15, where the same performance-complexity tradeoff exists for both systems. In more details, both the MIMO's ML receiver and the noncoherent MSDD jointly detect multiple data-carrying symbols, so that the optimum performance may be achieved, albeit this imposes a high complexity. Both the MIMO's SD and the noncoherent MSDSD substantially reduce the original detection complexity by invoking a sphere decoder. Moreover, both the MIMO's linear filter based receiver and the noncoherent DFDD opt for separating the multiple data streams by employing a linear filter, which results in a low detection complexity, but a degraded performance.

If a higher bandwidth efficiency is pursued, the DQAM constellations may be considered.

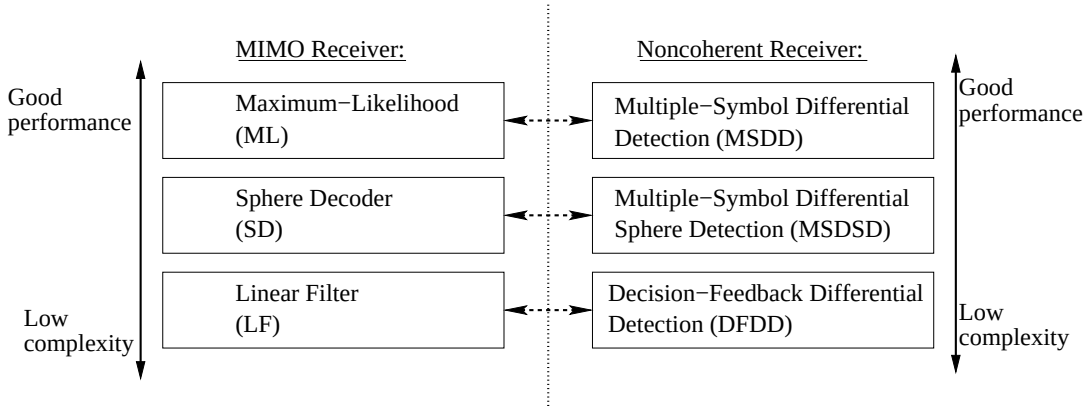

Figure 1.15: The links between MIMO receivers and noncoherent receivers.

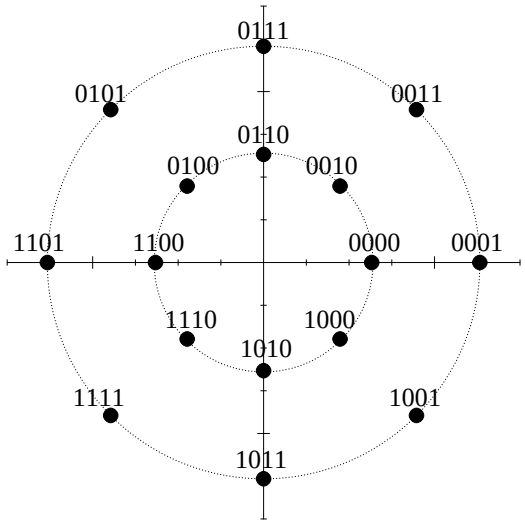

Figure 1.16: The constellation diagram of the data-carrying symbols of 16-Absolute-amplitude Differential Phase Shift Keying (16-ADPSK).

The early attempt to invoke differential encoding for QAM stems from Simon and Smith [133] in 1974, where they suggested that differential encoding may resolve the quadrant ambiguity of QAM transmission in the presence of a constant phase rotation in AWGN channels. This idea was implemented by Weber [134] in 1978, where part of the information bits were assigned to a differentially encoded phase. Furthermore, in 1982, Simon *et al.* [135] proposed a more general regime for the absolute-amplitude based DQAM scheme, where the transmitted phase was differentially encoded but the transmitted amplitude was the original data-carrying amplitude. This transmission regime [135], which was conceived for the maximum-minimum distance Square QAM constellation, was originally proposed to be detected noncoherently for recovering the data-carrying phase, but coherently recovering the data-carrying amplitude, required that the channel amplitude had to be estimated at the receiver. However, it was later discovered by Lampe and Schober [136] in 2001 that the equivalent differential encoding of the absolute-amplitude DQAM

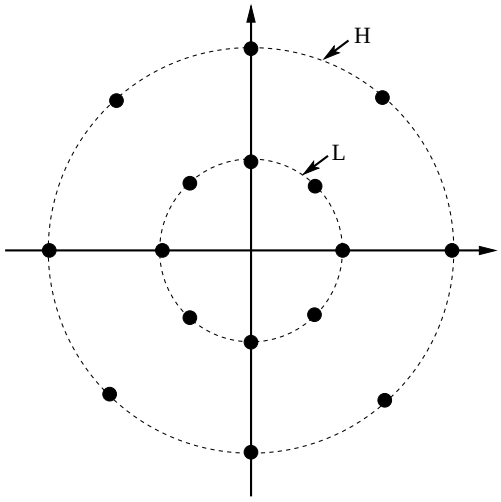

	$\|s_{n-1}\| = L$	$\|s_{n-1}\| = H$
$b_4 = 0$	$\|s_n\| = L$	$\|s_n\| = H$
$b_4 = 1$	$\|s_n\| = H$	$\|s_n\| = L$

"H" −− High amplitude ring
"L" −− Low amplitude ring

Figure 1.17: The constellation diagram of the transmitted symbols of 16-Differential Amplitude Phase Shift Keying (16-DAPSK), and its differential amplitude encoding lookup table.

may be represented by the revised expression of $s_n = \frac{1}{|s_{n-1}|} x_{n-1} s_{n-1}$, where the amplitude of the previous transmitted symbol $|s_{n-1}|$ is normalized, so that the amplitude of the next transmitted symbol $|s_n|$ becomes equal to the absolute amplitude of the data-carrying QAM symbol $|x_{n-1}|$. Lampe and Schober [136] adopted the absolute-amplitude DQAM regime for the Star QAM constellation, which may be termed as Absolute-amplitude Differential Phase Shift Keying (ADPSK). An example constellation diagram of the 16-ADPSK scheme's data-carrying symbols is portrayed in Fig. 1.16. For the ADPSK receiver, based on the revised differential encoding model of $s_n = \frac{1}{|s_{n-1}|} x_{n-1} s_{n-1}$, noncoherent detection may be invoked for both amplitude and phase detection. Considering CDD for ADPSK in block fading as an example, the received signal may be expressed as $y_n = s_n h_n + v_n = \frac{1}{|s_{n-1}|} x_{n-1} y_{n-1} + (v_n - \frac{1}{|s_{n-1}|} x_{n-1} v_{n-1})$, where $h_n = h_{n-1}$ and v_n refer to the block fading and AWGN factors, respectively. As a result, both the amplitude and phase of x_{n-1} may be recovered by the CDD with the aid of both the previous received sample y_{n-1} and the previous decision on $|s_{n-1}| = |x_{n-2}|$. It is worth noting that many QAM aided differential MIMO schemes [137–141] make use of this revised differential encoding model for dynamically constraining the transmitted symbol's amplitude.

As an alternative to ADPSK, the classic Differential Amplitude Phase Shift Keying (DAPSK) was proposed by Webb, Hanzo and Steele [142] in 1991. An example of 16-DAPSK is portrayed in Fig. 1.17. More explicitly, the 16-DAPSK scheme's first three bits are assigned to modulate the change in phase between two consecutive transmitted symbols, while the last bit is assigned to modulate the change in amplitude ring. It can be seen in Fig. 1.17 that in order to maintain a Star 16QAM constellation for the transmitted symbols, $b_4 = 0$ and $b_4 = 1$ determines whether the consecutive transmitted symbols' amplitude $|s_{n-1}|$ and $|s_n|$ should be retained or be toggled to its other legitimate value. In other words, if the DAPSK's differential encoding process is to be represented by $s_n = x_{n-1} s_{n-1}$, the transmitted symbols s_{n-1} and s_n are always drawn from the

classic Star QAM constellation. However, the specific constellation diagram of the data-carrying symbol x_{n-1} depends on the previously transmitted amplitude $|s_{n-1}|$. Considering the 16-DAPSK scheme of Fig. 1.17 as an example, if we have $|s_{n-1}| = L$, then $b_4 = 0$ and $b_4 = 1$ for modulating $|x_{n-1}|$ should enable the transitions of $L \rightarrow L$ and $L \rightarrow H$, respectively. However, if we have $|s_{n-1}| = H$, then the modulation of $|x_{n-1}|$ should enable the different amplitude transitions of $H \rightarrow H$ and $H \rightarrow L$ for $b_4 = 0$ and $b_4 = 1$, respectively. Nonetheless, the phase of 16-DAPSK's data-carrying symbol x_{n-1} is still drawn from the original 8PSK constellation diagram. It was proposed in [142] that the detection of DAPSK's data-carrying amplitude may be carried out by testing the amplitude change between consecutive received samples $|y_n|/|y_{n-1}|$, while the data-carrying phase may be detected by testing the phase change $\angle y_n - \angle y_{n-1}$. In summary, the fundamental difference between the ADPSK and the DAPSK is that the ADPSK aims for maintaining the mapping regime of a Star QAM constellation for the data-carrying symbols, while the DAPSK aims for maintaining a Star QAM constellation for the transmitted symbols.

The development of DAPSK has attracted a lot of research interests. The performance comparison between coherent QAM and CDD aided DAPSK was provided by Adachi and Sawahashi [143] and also by Chow *et al.* [144] in 1992. In 1995, Rohling and Engels [145] proposed the application of DAPSK in digital terrestrial video broadcasting, where the authors compared the performance of the CDD aided DAPSK to that of the coherent QAM in the presence of realistic channel estimation errors. Despite the satisfactory performance of CDD aided DAPSK in AWGN and block fading channels, it was observed by the authors [142] that the DAPSK performance degrades and eventually an error floor is formed, as the Doppler frequency is increased. It was suggested by the authors of [142] that both oversampling and channel coding may be invoked for mitigating this problem. We note that oversampling was also proposed for improving the performance of DPSK in rapidly fading channels [146, 147]. Moreover, it was observed by Chow *et al.* [148] in 1993 and then analysed by Chung [149] in 1997 that employing multiple RAs is capable of reducing the error floor of DAPSK in rapidly fading channels. Nonetheless, the optimum noncoherent detector of both the ADPSK and the DAPSK is the MSDD characterized by Divsalar and Simon [114] in 1994, which is capable of improving the performance of DQAM in different channel scenarios.

In order to mitigate the MSDD's exponentially increasing complexity, the prediction-based DFDD was proposed for 16-DAPSK operating in AWGN channels by Adachi and Sawahashi [150] in 1996, and then its amplitude detection was improved by Wei and Lin [151] in 1998. The MSDD-based DFDD was also proposed for 16-DAPSK for transmission over AWGN channels by Schober *et al.* [152] in 1998. Following this, the prediction-based DFDD designed for DAPSK communicating in fading channels was proposed by Gerstacker *et al.* [153] in 1999 and later it was improved by Schober *et al.* [154]. Notably, the prediction-based DFDD specifically conceived for ADPSK operating in fading channels was proposed by Lampe *et al.* [136] in 2001.

Inspired by the near-capacity performance achieved by turbo detection, soft-decision-aided DQAM detection has also been developed throughout the last two decades. May *et al.* [155] proposed Trellis decoded DQAM using the Viterbi algorithm in 1998, and then Fischer *et al.* [156]

invoked MSDD for DQAM in both multilevel coding and BICM in 2001. Moreover, Ishibashi *et al.* [157] proposed the low-complexity soft-decision-aided CDD concept conceived for DAPSK in Rayleigh fading channels, where the amplitude and phase are separately detected. However, no iteration was invoked between the channel decoder and the DQAM detector in these contributions. Liang *et al.* [158] proposed to employ the CDD for DAPSK relying on turbo detection in 2011, where the amplitude and phase are jointly detected. This soft-decision-aided CDD conceived for DAPSK was further streamlined by Xu *et al.* [159] in 2013, where the authors also discovered that completely separately detecting the DAPSK's amplitude and phase may impose a performance loss, which is more substantial in coded systems. Furthermore, in 2012, Wang and Hanzo [160] proposed a new arrangement for soft-decision-aided DAPSK detection. More explicitly, Wang and Hanzo [160] proposed to invoke MSDD and MSDSD for detecting the DAPSK's amplitudes and phases, which may be referred to as Multiple Symbol Differential Amplitude Detection (MSDAD) and Multiple Symbol Differential Phase Sphere Detection (MSDPSD), respectively. Given that the data-carrying amplitudes and phases are correlated, MSDAD and MSDPSD are capable of iteratively exchanging their decisions in order to achieve a near-optimum MSDD performance for DAPSK with the aid of *a priori* information gleaned from the channel decoder.

Against this background, solving the MSDD aided DQAM detection problem by sphere decoding is still an open problem, which also has been the gravest obstacle to offering a solution for MSDSD aided Differential MIMO schemes using QAM [137–141]. More explicitly, the MSDD [114] relies on the knowledge of channel correlation, which is determined by the Doppler frequency and the noise power. For DPSK, the transmitted phases may form a unitary matrix, which may be separated from the channel correlation matrix, so that a lower triangular matrix that is created by decomposion from the inverse of the channel's correlation matrix may be utilized in the context of sphere decoding [127, 132]. However, for DQAM, the transmitted symbol-amplitudes cannot form a unitary matrix, which implies that they have to be taken into account by the channel's correlation matrix. As a result, the symbol-amplitude-dependent channel correlation matrix only becomes known, when all the symbol-amplitudes are detected. This is the reason why Wang [160] invoked MSDD for amplitude detection. We note that without the assistance of channel coding, Wang's solution [160] may introduce an error floor for uncoded DAPSK schemes, because the MSDAD and the MSDPSD may exchange erroneous decisions. Furthermore, the DFDD conceived for DQAM operating in fading channels and documented in the existing literature [136, 153, 154] are all derived from the linear prediction filter, which is exactly the same as the linear prediction filter invoked by the DPSK detection scheme of [121, 122, 125]. This implies that these DFDD solutions are suboptimal and they are not equivalent to the decision-feedback version of MSDD. In this treatise, we will solve these problems for DQAM, including both ADPSK and DAPSK in Chapter 4 and Chapter 5 for coded and uncoded DQAM systems, respectively.

This section is summarized in form of a list of major contributions on noncoherent detection in Tables 1.5-1.7. We will continue by providing a detailed discussion on this topic from a technical perspective in Chapter 3 for noncoherent detection for DPSK and in Chapters 4 and 5 for

Table 1.5: Summary of major contributions on noncoherent detection (Part I).

Year	Author(s)	Topic	Contribution
1959-1960	Lawton [106, 107]	DPSK	Proposed that the constant phase rotation in AWGN channels may be mitigated by the simple DPSK transceiver.
1959	Cahn [108]	DPSK	Demonstrated that the CDD aided DPSK scheme suffers from a 3 dB performance penalty in AWGN channels compared to its coherent PSK assuming the idealistic perfect estimation of the frequency offset phase.
1960	Kailath [102]	MLSE	Proposed to jointly perform channel estimation and data detection, where channel estimation was tentatively performed for each possible combination of the data-carrying sequence, and then these combinations were compared in order to make a final decision on the data-carrying sequence.
1962	Bello and Nelin [109]	DPSK	Discovered that an irreducible error floor occurs, when the CDD that was originally designed for AWGN channels is employed in the rapidly fluctuating fading channels.
1972	Forney [104]	MLSE	Proposed to invoke the Viterbi algorithm for MLSE, which relies on the early termination of the candidate evaluation process by ignoring those candidates that are unlikely to be the maximum likelihood solution.
1979	Morley and Snyder [105]	MLSE	Proposed that with the aid of Viterbi algorithm, the MLSE complexity grows exponentially with the channel memory that imposed onto the data transmission in the form of Inter-Symbol Interference (ISI).
1982	Simon *et al.* [135]	DQAM	Proposed the absolute-amplitude DQAM scheme based on Square QAM constellation, where the transmitted phase was differentially encoded but the transmitted amplitude was the original data-carrying amplitude.
1988	Leib and Pasupathy [117]	DFDD (DPSK)	Proposed DFDD for DPSK operating in AWGN channels, which was later shown in [120] to be equivalent to the MSDD of [7] operating in decision-feedback mode.
1990	Divsalar and Simon [7]	MSDD (DPSK)	Proposed MSDD for DPSK operating in AWGN channels, which partially compensated the 3 dB performance penalty by observing more than two received samples.
1991	Webb, Hanzo and Steele [142]	DAPSK	Proposed DAPSK which differentially encodes both amplitude and phase, where the Star QAM constellation is maintained for all transmitted symbols.

Table 1.6: Summary of major contributions on noncoherent detection (Part II).

Year	Author(s)	Topic	Contribution
1992	Ho and Fung [113]	MSDD (DPSK)	Proposed MSDD for DPSK operating in Rayleigh fading channels, which mitigated the error floor in rapidly fluctuating fading channels.
1994	Divsalar and Simon [114]	MSDD (DPSK DQAM)	Summarized the MSDD techniques developed both for DPSK and for DQAM operating both in AWGN channels and in fading channels.
1994	Mackenthun [115]	MSDD (DPSK)	Proposed an efficient algorithm for MSDD aided DPSK operating in AWGN channels.
1996	Adachi *et al.* [150]	DFDD (DAPSK)	Proposed prediction-based DFDD for 16-DAPSK operating in AWGN channels.
1998	Schober *et al.* [152]	DFDD (DAPSK)	Proposed MSDD-based DFDD for 16-DAPSK for transmission over AWGN channels.
1999	Schober *et al.* [121]	DFDD (DPSK)	Proposed DFDD for DPSK operating in Rayleigh fading channels, which is derived from the MSDD of [113, 114].
1999	Bin and Ho [124]	DFDD (DPSK)	Proposed prediction-based DFDD for DPSK operating in Rayleigh fading channels, where a channel sample is predicted based on the previous decisions, so that coherent detection may be performed for the current symbol.
1999	Hoeher and Lodge [125]	DFDD (DPSK)	Proposed soft-decision-aided prediction-based DFDD for DPSK operating in fading channels, so that DFDD may be invoked in turbo detection.
2000	Schober and Gerstacker [126]	DFDD (DPSK)	Proved that both MSDD-based DFDD [121, 122] and prediction-based DFDD employing the MMSE Wiener filter [123–125] are identical for DPSK operating both in AWGN and in Rayleigh channels.
2001	Schober *et al.* [154]	DFDD (DAPSK)	Proposed prediction-based DFDD for 16-DAPSK communicating in fading channels.
2001	Lampe *et al.* [122]	DFDD (DPSK)	Proposed soft-decision-aided MSDD-based DFDD for DPSK operating in Rayleigh fading channels, where the DFDD was involved in turbo detection.
2001	Lampe and Schober [136]	DFDD (ADPSK)	Proposed the absolute-amplitude DQAM scheme based on the Star QAM constellation, and proposed prediction-based DFDD conceived for this ADPSK scheme.
2005	Lampe *et al.* [127]	MSDSD (DPSK)	Proposed MSDSD for DPSK operating in Rayleigh fading channels, which invoked a sphere decoder for MSDD.

Table 1.7: Summary of major contributions on noncoherent detection (Part III).

Year	Author(s)	Topic	Contribution
2005	Ishibashi *et al.* [157]	DAPSK	Proposed the low-complexity soft-decision-aided CDD conceived for DAPSK in Rayleigh fading channels, where the amplitude and phase are separately detected.
2006	Pauli *et al.* [132]	MSDSD (DPSK)	Proposed soft-decision-aided MSDSD for DPSK communicating in Rayleigh fading channels, so that MSDSD may be invoked in turbo detection.
2011	Liang *et al.* [158]	DAPSK	Proposed to invoke the CDD for DAPSK in turbo detection in 2011, where the amplitude and phase are jointly detected.
2012	Wang and Hanzo [160]	MSDSD (DAPSK)	Proposed to invoke MSDD and MSDSD for detecting the DAPSK's amplitudes and phases, which may be referred to as MSDAD and MSDPSD, respectively. The pair are capable of iteratively exchanging decisions in order to achieve a near-optimum MSDD performance in coded systems.
2013	Xu *et al.* [159]	DAPSK	Streamlined the soft-decision-aided CDD of [158], and discovered that completely separately detecting DAPSK's amplitude and phase may impose a performance loss, which is more substantial in coded systems.

noncoherent detection designed for uncoded and coded DQAM, respectively.

1.3 A Historical Perspective on Multiple-Input Multiple Output Schemes

Multiple-Input Multiple Output (MIMO) techniques have been one of the most vibrant areas in communications, where exciting progress has been made over the past two decades. The proposal of employing multiple antennas for a single user was motivated by its substantial capacity gain. In more details, the multiplexing-oriented MIMO concept was proposed by Paulraj and Kailath [161] in 1994, where a high data-rate transmission was carried out by splitting it into low data-rate signals transmitted by spatially separated Space-Division Multiple Access (SDMA) users. In order to pursue the multiplexing gain using co-located antennas, Foschini [162] proposed the groundbreaking layered space-time architecture in 1996, which was later termed as the Bell Laboratories Layered Space-Time (BLAST). In particular, the original encoding method proposed by Foschini [162] was diagonal-encoding, which may be termed as D-BLAST. As portrayed in Fig. 1.18a, the D-BLAST transmitter de-multiplexes a single data stream to N_T separate data streams, where channel coding and modulation may be performed either before or after the de-multiplexing, and then the N_T data streams of the N_T TAs are rotated in a round robin fashion, so that the code words are transmitted in diagonal layers. El-Gamal and Hammons [163] further extended this D-

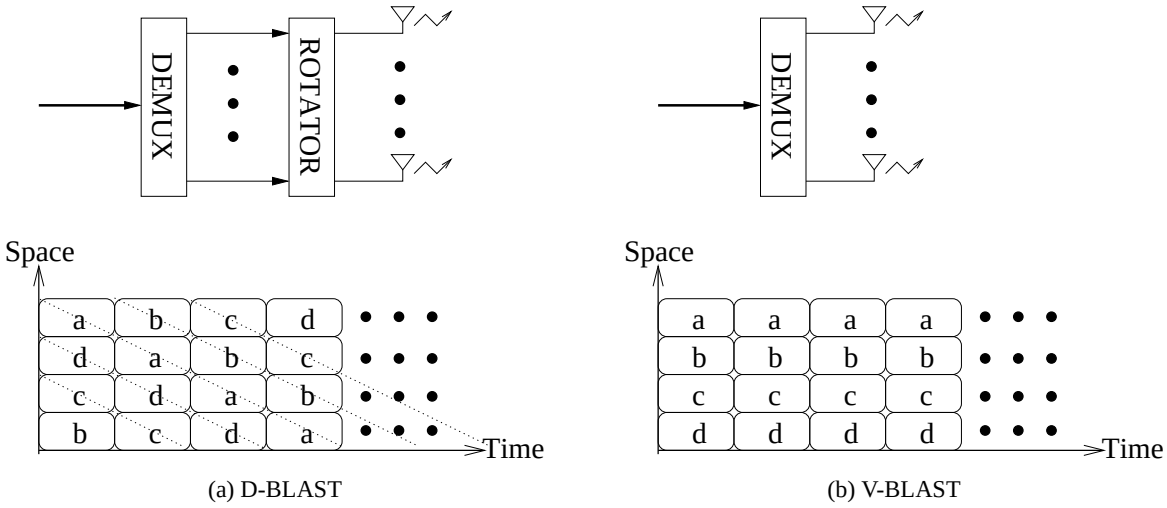

(a) D-BLAST (b) V-BLAST

Figure 1.18: Schematics of D-BLAST and V-BLAST.

BLAST structure in 2001, where each layer constitutes more than one consecutive diagonal lines. The benefit of D-BLAST's diagonal-encoding is that the signal components of a diagonal layer experience independent fading, which may lead to a potential temporal diversity gain.

In order to simplify the real-time implementation, in 1998, Wolniansky *et al.* [164] proposed V-BLAST that invokes vertical-encoding. As portrayed by Fig. 1.18b, the rotator of the D-BLAST was avoided by the V-BLAST transmitter. Owing to the fact that all the signals transmitted from N_T TAs are simultaneously received by N_R RAs, the same detection methods are shared by both D-BLAST and V-BLAST, which was exemplied in Fig. 1.2 at the beginning of this chapter. It was demonstrated in [162, 164] that both D-BLAST and V-BLAST may achieve an improved spectral efficiency that increases linearly with the number of antennas at realistic SNRs and error rates. It was further confirmed by Foschini and Gans [165] in 1998 and then by Telatar [166] in 1999 that compared to the family of Single-Input Multiple-Output (SIMO) systems where multiple antennas may only be used at the receiver, the BLAST MIMO systems have an ergodic capacity that may grow linearly, rather than logarithmically, with the number of antennas, provided that the BLAST MIMO system employs a large number of antennas and that both the input signals and the output signals are independent and identically Gaussian-distributed.

In order to exploit the full potential of BLAST MIMO systems and to approach the impressive capacity results, the BLAST receivers have to employ ML detection in uncoded systems, or the MAP detection in coded systems, which have to evaluate all M^{N_T} combinations of a total of N_T transmitted MPSK/QAM symbols [8]. This implies that the BLAST detection complexity increases exponentially with the number N_T of TAs, which may be particularly unaffordable, when the BLAST detector is invoked several times in turbo coded systems. In order to mitigate this problem, the BLAST schemes [162, 164] were originally proposed to employ the Multi-User Detector (MUD) of the classic Code Division Multiple Access (CDMA) systems [167, 168]. More

explicitly, in order to separate the N_T data streams impinging at the BLAST receiver, Linear Filter (LF) based receivers, such as Zero Forcing (ZF) and MMSE receivers may be invoked, where all the other data streams, i.e. the interferers, may be nulled when detecting a particular data stream. However, the LFs suffer from inevitable performance limitations, since ZF enhances the noise, while the MMSE receiver only minimizes, rather than eliminates, the interferers. In order to further improve the attainable performance, the decision-feedback techniques of [169–171], which have been widely used for equalization may be employed for cancelling an interfer from the BLAST scheme's received signal immediately after a data stream has been detected, so that the ensuing detection stages suffer less from the interference problem. Nonetheless, the LFs aided BLAST receivers generally suffer from a performance penalty compared to the optimum nonlinear BLAST detection, but the LF aided BLAST detection complexity becomes comparable to that of Single-Input Single-Output (SISO) or SIMO systems, because the constellation diagrams of the N_T data streams are visited completely separately.

In order to achieve a further improved performance in coded systems, the LFs may be revised to be able to both accept and produce soft-bit decisions. The first soft-decision-aided MMSE filter was proposed by Douillard *et al.* [70] for turbo equalization in 1995. However, in the presence of soft-bits, the *a priori* probabilities are no longer equal for all constellation points, which poses a major design challenge for the MMSE solution of coded systems. In order to solve this problem, the exact MMSE solution incorporating the non-constant *a priori* probabilities was derived for CDMA MUD by Wang and Poor [75] in 1999, and then this solution was invoked for turbo equalization by Tuchler *et al.* [72] in 2002 and finally for turbo BLAST by Sellathurai and Haykin [13] also in 2002.

In order to strike a performance-complexity tradeoff between the BLAST scheme's optimum detector and the LF-aided detectors, Damen *et al.* [172] proposed to apply sphere decoding for BLAST detection in 2000, where the ML performance may be retained at a substantially reduced complexity. As illustrated by Fig. 1.2, the SD visits the constellation diagrams one-by-one in order to find the best candidates that lie within the decoding radius, and then these constellation diagrams may be visited again by the SD in order to check for other possible candidates. The termination of SD is determined by the SNR-dependent sphere radius. The SD algorithms designed for BLAST detection were extensively documented by Damen *et al.* [10] in 2003. Inspired by the turbo codes, the first soft-decision-aided SD for BLAST was proposed by Hochwald and ten Brink [173], where a list of BLAST signal candidates was established by the hard-decision-aided SD and then the candidates in this list were processed by the MAP decoding algorithm. However, the *a priori* information gleaned from the channel decoder was not utlized for establishing the candidate-list in [173], which prevented it from achieving BLAST's full potential. In order to mitigate this problem, in 2004, Vikalo *et al.* [174] proposed the soft-decision-aided SD for BLAST, which incorporated the *a priori* information in sphere decoding. Furthermore, in 2008, Studer *et al.* [175] proposed the soft-output SD's Very-Large-Scale Integration (VLSI) implementation, where a single SD tree search was invoked just once for all the soft-bit decisions output for a

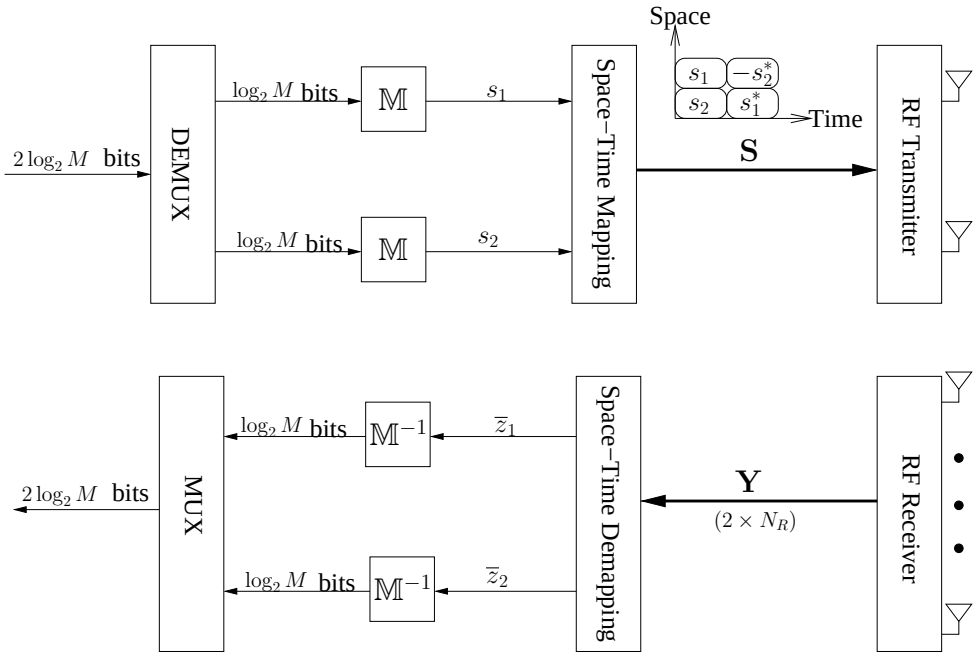

Figure 1.19: Schematic of Alamouti's G2 STBC transceiver.

BLAST detection block. Studer and Bolcskei further developed their work of [175] in [176] in 2010, where the *a priori* LLRs were once again incorporated into the SD's VLSI implementation.

The BLAST systems enjoy a beneficial multiplexing gain, where the system throughput may be N_T times higher than that of their SISO/SIMO counterparts using the same MPSK/QAM constellation. Alternatively, the mutliple TAs may be exploited for achieving a diversity gain, where multiple replicas of the modulated symbols may be transmitted by multiple TAs over multiple symbol periods, so that the receiver becomes capable of recovering the data-carrying symbols from several independently faded observations. This revolutionary invention was originally proposed by Alamouti [177] for the case of using $N_T = 2$ TAs in 1998, where the full transmit diversity was achieved by a SISO receiver at a low detection complexity. More explicitly, the transceiver of Alamouti's transmit diversity technique is portrayed in Fig. 1.19, where the space-time mapper forms a two-by-two unitary matrix from the $N_Q = 2$ independently modulated MPSK/QAM symbols, which are transmitted by $N_T = 2$ TAs over $N_P = 2$ symbol periods. Owing to the orthogonality provided by the unitary matrix design, the receiver of Fig. 1.19 is capable of decoupling the $N_Q = 2$ data streams without encountering BLAST's IAI problem. The class of transmit diversity techniques generated from orthogonal design has been termed as the set of Space-Time Block Code (STBC) arrangements. In particular, as the first member in the STBC family, Alamouti's scheme is often referred to as G2 STBC.

The gravest challenge of STBC design is to construct the unitary matrix from orthogonal design for any arbitrary number of TAs. Alamouti's G2 STBC has a unity normalized throughput of $\overline{R} = \frac{N_Q}{N_P} = 1$, which implies that its throughput is the same as that of its SISO/SIMO counterpart, when using the same MPSK/QAM constellation. Owing to its transmit diversity gain, Alamouti's

G2 STBC has a better BER performance than its BLAST MIMO and SIMO counterparts associated with the same system throughput. However, it was proven by Tarokh *et al.* [178] in 1999 that Alamouti's G2 STBC is the only full unity-rate code in the family of STBCs. Nonetheless, Tarokh *et al.* [178] discovered that full unity-rate real-valued STBCs do exist for N_T =2, 4 or 8, which may be generated by the Hurwitz-Radon theory [179, 180]. As a result, the class of Half-Rate (HR) STBCs may be obtained by vertically concatenating the real-valued STBC codeword and its conjugates, which forms the family of HR STBCs that are represented by the terminology of HR-GN_T-STBC for using N_T TAs. For the case of N_T not being a power of 2, the HR-GN_T-STBC transmission matrix may be obtained by taking the first N_T columns of the HR-G2$^{\lceil \log_2 N_T \rceil}$-STBC's codeword. Although the HR-GN_T-STBCs created for $N_T > 8$ were not explicitly constructed, Tarokh *et al.* [178] proved that such a design may impose a substantial transmission delay, which increases exponentially with N_T. For example, we have [178] $N_P = 16 \times 16^{(N_T/8-1)}$ for $N_T > 8$ and being a power of 2.

In order to improve the throughput of STBCs with $N_T > 2$, Ganesan and Stoica [181–183] invented the Amicable Orthogonal (AO) STBCs in 2001 according to the theory of amicable orthogonal design [179]. An AO STBC scheme having N_T TAs may be represented by the terminology of AO-GN_T-STBC. For the case of N_T being a power of 2 as $N_T = 2^\iota$, where ι denotes a positive integer, the AO-G2$^\iota$-STBC schemes have a reduced delay of $N_P = N_T$, and they also have $N_Q = \iota + 1$ transmitted symbols. More explicitly, the AO-G2$^\iota$-STBC's transmission matrix is constructed based both on the lower-level AO-G2$^{\iota-1}$-STBC's transmission matrix having ι symbols as well as on a an extra the $(\iota+1)$-th modulated symbol. Hence, the construction of AO-G2$^\iota$-STBCs may commence from $\iota = 1$, where the AO-STBC associated with $\iota = 1$ corresponds to Alamouti's G2 STBC. As a result, rate-3/4 STBCs associated with a reduced delay of $N_P = 4$ may be constructed for the AO-STBCs having $N_T = 3$ or $N_T = 4$, while half-rate STBCs associated with a reduced delay of $N_P = 8$ may be constructed for the AO-STBCs having $5 \leq N_T \leq 8$. However, owing to the fact that the AO-STBC's number of transmitted symbols N_Q only increases logarithmically with the number of TAs N_T as $N_Q = \lceil \log_2 N_T \rceil + 1$, the attainable throughput of AO-STBC is expected to be lower than the half-rate of $\overline{R} = \frac{1}{2}$ for $N_T > 8$.

Against this background, it has emerged that there is a tradeoff between the attainable multiplexing and diversity gain in MIMO system design. The development of STBCs was motivated by their improved BER performance, especially in the high SNR region, which is the benefit of their diversity gain. However, it was recognized by Sandhu and Paulraj [184] in 2000 that STBCs cannot achieve the full MIMO capacity except for a special case, which is Alamouti's G2-STBC system associated with a single RA, i.e. with $N_R = 1$. On the other hand, the BLAST systems have the full MIMO capacity, but they are not designed for achieving a transmit diversity gain for combating the effects of fading. This classic MIMO design tradeoff was quantified by Zheng and Tse [185] in 2003, where the relationship between the diversity gain d and the multiplexing gain r is given by $d = (N_T - r)(N_R - r)$, which portrays the diversity and multiplexing gains as rivals in MIMO system design.

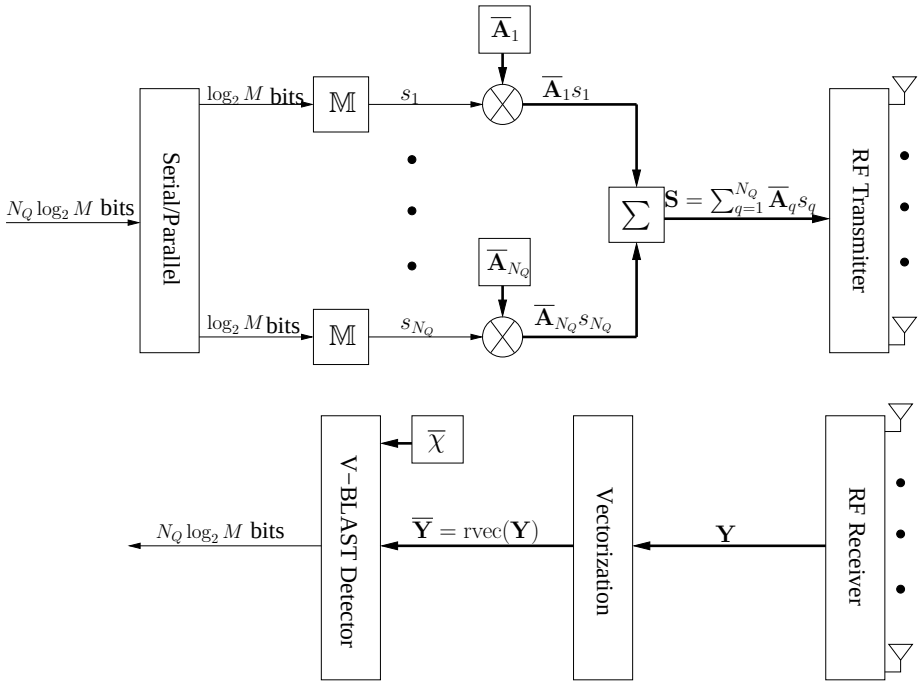

Figure 1.20: Schematic of the capacity-achieving LDC transceiver of [188].

If the STBC throughput is to be improved, the first step is to relax the orthogonality requirement. In the light of this principle, the concept of Quasi-Orthogonal (QO) STBC design was proposed by Jafarkhani [186] in 2001, where the QO STBC's transmission matrix is formed by subgroups of orthogonal STBCs. For the QO STBCs, the signals are orthogonal to each other within the subgroups, but they are not orthogonal to the signals from the other subgroups. As a result, the IAI problem resurfaces in the QO STBC design, and hence the signals that cannot be decoupled have to be jointly detected. It was suggested by Papadias and Foschini [187] in 2003 that linear MIMO receivers such as the MMSE detector or the ZF detector may be invoked for QO-STBC systems. However, this may not be an ideal solution, because the sub-optimal linear MIMO receivers may erode the performance advantage of the QO-STBC's diversity gain.

In 2002, Hassibi and Hochwald [189] proposed the new class of Linear Dispersion Code (LDC), which completely droped the STBC's orthogonality requirements in order to further improve the STBC capacity while retaining the full transmit diversity gain. In more details, the LDC's transmission matrix may be represented by $\mathbf{S} = \sum_{q=1}^{N_Q} \left[\overline{\mathbf{A}}_q \Re(s_q) + j\overline{\mathbf{B}}_q \Im(s_q)\right]$, where the real and imaginary parts of a total number of N_Q modulated MPSK/QAM symbols $\{s_q\}_{q=1}^{N_Q}$ are dispersed into both spatial and temporal dimensions by the dispersion matrices $\{\overline{\mathbf{A}}_q\}_{q=1}^{N_Q}$ and $\{\overline{\mathbf{B}}_q\}_{q=1}^{N_Q}$. The dispersion matrices are obtained from random search, where the capacity is maximized while the error probability is aimed to be minimized. Although the LDCs proposed by Hassibi and Hochwald [189] effectively improve the attainable STBC capacity, and the LDC may even outperform the STBC in certain scenarios, the full MIMO capacity still cannot be achieved by the LDC design of [189]. In order to further improve the LDC design, Heath and Paulraj [188] proposed in 2002 that jointly

dispersing the real and imaginary parts of the N_Q modulated MPSK/QAM symbols $\{s_q\}_{q=1}^{N_Q}$ may allow the LDC to achieve the full MIMO capacity, which results in a simplified form of the transmission matrix given by $\mathbf{S} = \sum_{q=1}^{N_Q} \left[\overline{\mathbf{A}}_q s_q\right]$. For the sake of clarity, the original LDC design proposed by Hassibi and Hochwald [189] is referred to as the capacity-improving LDC in this treatise, while the further optimized LDC design conceived by Heath and Paulraj [188] is termed as the capacity-achieving LDC, whose transceiver is portrayed in Fig. 1.20. We will demonstrate in Sec. 6.3.2.3 that the vectorization process seen in Fig. 1.20 may transform the LDC's received signal to a form that is equivalent to the received signal of a V-BLAST system equipped with N_Q TAs and $N_R N_P$ RAs, so that the classic V-BLAST detectors may be invoked for LDC detection. Owing to the fact that the dispersion matrices $\{\overline{\mathbf{A}}_q\}_{q=1}^{N_Q}$ are populated with random elements, they can be designed under the constraint of having a transmission delay of $N_P = N_T$, which is a more relaxed condition compared to the delay of STBCs [177, 178, 181–183]. Furthermore, it was demonstrated by Heath and Paulraj [188] that satisfying the condition of $N_Q \geq N_T N_P$ is required for the LDC to achieve the full MIMO capacity, which implies that the LDC throughput is flexibly adjusted and it may even be higher than that of its BLAST counterpart using the same MPSK/QAM constellations. Upon finding the MIMO matrix capable of achieving the full MIMO capacity, the random search for the capacity-achieving LDC of [188] may aim for minimizing the error probability. It was demonstrated by Heath and Paulraj [188] that powerful LDCs exist that are also capable of outperforming their STBC counterparts. The error probability of LDCs was further improved in [190–194], which also tackle the problem of having a diminishing distance between legitimate codewords, when aiming for the high-throughput LDC codeword generation. In general, the random search carried out for populating LDC matrix according to the original guidelines of [188] is capable of producing powerful LDCs that achieve both a full multiplexing gain and a full transmit diversity gain.

The development of LDC successfully resolves the diversity versus multiplexing tradeoff, where both full MIMO capacity and full diversity gain may be attained following the optimized codeword construction guidelines of [188], provided that the parameters satisfy $N_Q \geq N_T N_P$. However, the LDC design becomes a retrograde step for the tradeoff between the performance attained and the complexity imposed. As the STBC's orthogonality requirement is abandoned, the LDC receivers have to invoke conventional V-BLAST detectors in order to deal with the IAI problem. As discussed before, the performance versus complexity tradeoff has an even more significant impact on the family of coded systems. More explicitly, on one hand, optimal MIMO receivers exhibit a potentially excessive detection complexity, which may become especially unaffordable when the MIMO detector is invoked several times in the context of turbo detection. On the other hand, suboptimal receivers are at risk of producing over-confident output LLRs that deviate from the true probabilities, which cannot be readily corrected by the channel decoder.

Against this background, a newly-developed MIMO technique referred to as Spatial Modulation (SM) was proposed by Song *et al.* [195] in 2004, which is a modulated extension of a scheme proposed in 2001 by Chau and Yu [196]. Then SM was analysed by Mesleh *et al.* [197] in 2008.

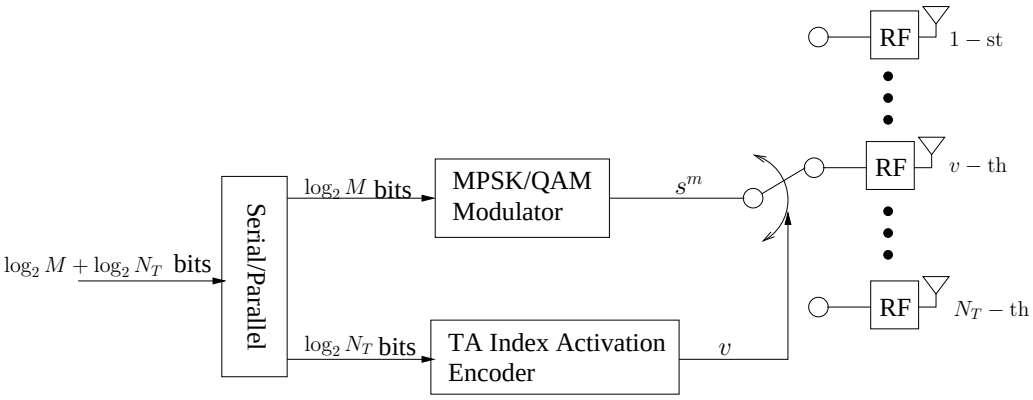

Figure 1.21: Schematic of the SM transmitter.

The SM transmitter is portrayed in Fig. 1.21, where $\log_2 M$ bits are assigned to modulate a single MPSK/QAM symbol by the MPSK/QAM modulator, while $\log_2 N_T$ bits are assigned to activate a single one out of N_T TA by the TA index activation encoder in order to transmit the single modulated MPSK/QAM symbol. It can be seen in Fig. 1.21 that only a single RF-chain associated with a TA is activated at a time, which effectively reduce the MIMO's transmission complexity. Moreover, one of the most important motivations behind the SM design is the hope that the TA activation index and the classic modulated symbol index may be separately detected, so that the optimal ML MIMO detection performance may be achieved for SM at a substantially reduced complexity. Therefore, Mesleh *et al.* [197] proposed a Maximum Ratio Combining (MRC) based SM detector, which firstly "decouples" the received signal to N_T matched filter output elements. Following this, the TA activation index may be detected by comparing the absolute values of the matched filter output elements, and then the classic MPSK/QAM demodulator may be invoked for demodulating the specific matched filter output element according to the detected TA activation index. As a result, the SM detector does not have to jointly detecting the N_T TA index candidates and the M modulated symbol candidates by evaluating a total of $N_T M$ combinations of SM signals. Instead, the N_T TA index candidates and the M modulated symbol candidates are evaluated separately, which reduces the SM detection complexity order from $O(N_T M)$ to $O(N_T + M)$. However, it was demonstrated by Jeganathan *et al.* [198] in 2008 that completely independently detecting the two indices results in an error floor, unless the fading channels are known and compensated at the transmitter by a precoder. This is because the erroneous TA activation index detection may mislead the MPSK/QAM demodulator into detecting the wrong symbol. As a remedy, Jeganathan *et al.* [198] streamlined the ML MIMO detector's calculations for SM, which takes advantage of the fact that the SM transmit vector contains $(N_T - 1)$ zero elements and a single non-zero element. As a benefit, the computational complexity imposed may be reduced by this simplification, but the detection complexity order remains $O(N_T M)$, where the N_T TA index candidates and the M modulated symbol candidates are still jointly evaluated. As a remedy, Space-Shift Keying (SSK) was proposed by Jeganathan *et al.* [199, 200] in 2008, where simply the TA activation index conveys the source information. However, the SSK schemes inevitably suffers from a capacity loss compared

to the SM schemes.

Inspired by this open problem, SM detector design has been developed in two major directions in the open literature. The first option is to develop the optimal SM ML detectors [201–204] endeavouring to reduce the complexity order of the simplified SM detector of [198] without imposing any performance loss. The second approach elaborated on in [141, 205–210] aims for improving the attainable performance of the sub-optimal MRC based SM detector of [197], but achieving the optimal ML SM performance is not guaranteed. In more details, for the optimum ML SM detection, in 2008, Yang and Jiao [201] proposed to invoke classic MPSK/QAM demodulators for all matched filter output elements first, and then the TA activation index detection was performed with the aid of the demodulated MPSK/QAM symbols. This method was also considered by Rajashekar *et al.* [204] in 2014, which was termed as the hard-limiter-based SM detector. Owing to the fact that in the absence of *a priori* information gleaned from a channel decoder, the hard-decision-aided MPSK/QAM demodulators may directly map the matched filter's output signal to the nearest MPSK/QAM constellation point. As a result, the hard-limiter-based SM detection has a low detection complexity order of $O(2N_T)$, which does not increase with the number of modulation levels M. However, this method cannot be directly applied to the soft-decision-aided SM detectors in coded systems, because the channel decoder is unaware of which constellation diagram is employed. As a result, the soft-decision-aided SM detectors have to evaluate and compare all the TA index and classic modulated symbol index combinations, when both the *a priori* information gleaned from the channel decoder and the matched filter output are taken into account, which increases the detection complexity order back to $O(N_T \times M)$.

In order to mitigate this problem, in 2013 Xu *et al.* [203] proposed a SM detector, which aims for reducing the SM detection search scope while maintaining the optimum detection capability. In more detail, by exploring the symmetry provided by the Gray-labelled MPSK/QAM constellation diagrams, the normalized matched filter output elements may be first partially demodulated, so that the correlation between the TA index and the classic modulated symbol index may be taken into account, when the TA index is detected. Following this, only a single MPSK/QAM demodulation action has to be carried out according to the already detected TA activation index. Based on these processing steps, this may be referred to as the reduced-scope SM detector. This method was then also applied to the soft-decision-aided SM detector of [203], which exploited the symmetry of the Gray-labelled constellation diagrams to perform the above mentioned reduced-scope MPSK/QAM demodulation. As a result, the reduced-scope SM detector [203] may achieve a substantial complexity reduction compared to the simplified SM detector of [198] without imposing any performance loss. We will further demonstrate in Chapter 6 that the reduced-scope SM [203] detection complexity is comparable to the hard-limiter-based SM [201, 204] detector of uncoded systems. Furthermore, it will be shown in Chapter 7 that the reduced-scope SM [203] detection is also capable of achieving a similaly substantial complexity reduction for coded SM systems, which is especially beneficial, when considering that the SM detector may be invoked several times in iterative turbo detection.

- Optimal ML SM detectors
  - Simplified ML SM detector [198]
  - Reduced−scope SM detector [203]
  - Hard−limiter−based SM detector [201,204]
- Suboptimal low−complexity SM detectors
  - Maximum Radio Combining (MRC)−based SM detector [197]
  - Normalized−MRC−based SM detector [205,206]
  - Signal−vector−based SM detector [207]
  - List−normalized−MRC−based SM detector [205,206,208]
  - Unity−constellation−power−based SM detector [141]
  - List−unity−constellation−power−based SM detector [209]
  - Distance−ordered−based SM detector [210]
- SD aided SM detectors [211−213]

Figure 1.22: Summary of hard-decision-aided SM detectors found in the open literature.

Considerable research efforts have also been dedicated to the family of sub-optimal low-complexity SM detectors in recent years. It was discovered and demonstrated by Guo *et al.* [205] in 2010 and by Naidoo *et al.* [206] in 2011 that the error performance of the TA activation index detection of the MRC based SM detector of [197] may be improved by normalizing the matched filter output signals by the fading norm, which leads to the concept of normalized-MRC-based SM detection. The so-called signal-vector-based SM detector proposed by Wang *et al.* [207] in 2012 operates based on the fact that the Square MQAM symbol does not change the direction of the received signal vector, which hence attains the same performance results as the normalized-MRC-based SM detectors. Furthermore, in order to avoid the situation of missing the optimum TA index candidate, the authors of [205, 206, 208] proposed to allow the TA activation index detector to produce a list of candidates, and then the MPSK/QAM demodulator may be invoked for all the TA indices in this list. This method may be termed as the List-normalized-MRC-based SM detector. Moreover, Sugiura *et al.* [141] conceived a unity-constellation-power-based SM detector in 2011, where a reduced number of non-negative constellation points associated with a unity constellation power are taken into account for the sake of achieving a more reliable TA index estimation. In 2012, Yang *et al.* [209] further improved the performance of the unity-constellation-power-based SM detector by invoking a list of TA indices as used in [205, 206, 208], which may be termed as the List-unity-constellation-power-based SM detector. The decision metrics used by the unity-constellation-power-based SM detector were further improved by Tang *et al.* [210] in 2013, which is termed as the distance-ordered-based SM detector.

In summary, the family-tree of optimal ML SM detectors and that of suboptimal low-complexity SM detectors is portrayed in Fig. 1.22. Since SM was motivated by implementing the optimal MIMO detectors at a reduced complexity, the aforementioned sub-optimal SM detectors may not be highly recommended for coded systems, because they are likely to produce unreliable LLRs, which

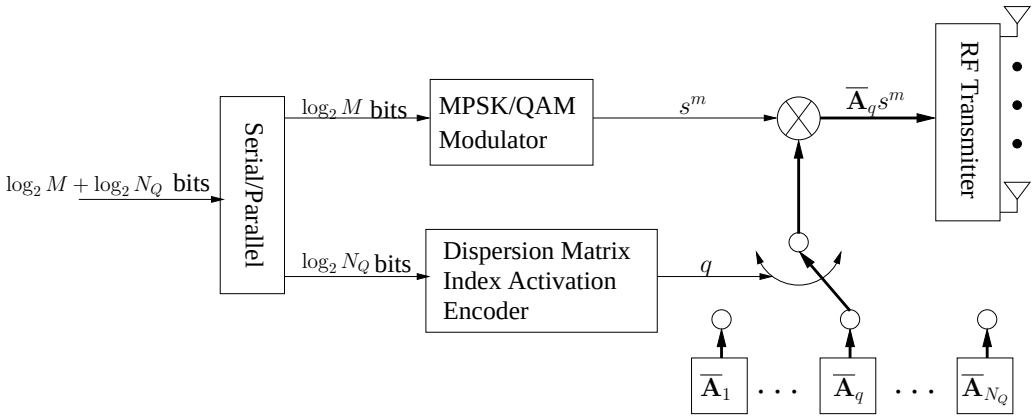

Figure 1.23: Schematic of the STSK transmitter.

fail to reflect the true probabilities. Moreover, we will demonstrate in Chapter 6 that these sub-optimal SM detectors do not have a significant complexity advantage over the reduced-complexity optimal SM detectors such as the hard-limiter-based SM detector [204] and the reduced-scope SM detector [203]. It is also worth mentioning that a sphere decoder was invoked for single-stream SM by Younis *et al.* [211–213], which exhibits a reduced complexity compared to the sphere decoder invoked by V-BLAST. However, it is widely recognized that the sphere decoder has an SNR-dependent detection complexity, which increases with the noise power [214, 215]. Therefore, the low-complexity optimum reduced-scope SM detector [203] may be perferred for coded systems, where an infinitesimally low BER may be achieved at a low SNR that is close to the capacity limit.

In order to be able to benefit from a transmit diversity gain, the concept of Space-Time Shift Keying (STSK) was proposed by Sugiura *et al.* [216] in 2010, which is a combination of SM and LDC. The schematic of the STSK transmitter is portrayed in Fig. 1.23, which evolved from the LDC transmitter of Fig. 1.20. In more detail, the STSK transmitter of Fig. 1.23 assigns $\log_2 M$ bits to modulate a single MPSK/QAM symbol by the MPSK/QAM modulator, while $\log_2 N_Q$ bits are assigned to the dispersion matrix index activation encoder in order to select a single one out of a total number of N_Q dispersion matrices. Then the modulated symbol s^m is dispersed into both spatial and temporal dimensions by the activated dispersion matrix $\overline{\mathbf{A}}_q$, so that the STSK transmission matrix seen in Fig. 1.23 is given by $\mathbf{S} = s^m \overline{\mathbf{A}}_q$. It was demonstrated by Sugiura *et al.* [216] that after vectorizing the STSK scheme's received signal matrix, the SM detectors may be invoked for detecting the STSK's dispersion matrix index and modulated symbol index. As a result, the SM may rely on a low-complexity single-stream ML detector derived from the optimum V-BLAST MIMO detector at a lower detection complexity. Similarly, STSK is also capable of effectively reducing the LDC's detection complexity. Although a beneficial transmit diversity gain is obtained, the STSK's disadvantage over the SM is that all the STSK transmitter's RF chains have to be activated at the same time, as seen in Fig. 1.23, which loses the SM's advantage of using a single RF chain at any symbol-instant, as seen in Fig. 1.21. In 2011, Sugiura *et al.* [217] proceeded to conceive the concept of Generalized Space-Time Shift Keying (GSTSK), where virtually all the

MIMO schemes including V-BLAST, STBC, LDC, SM and STSK are included in the framework of dispersion matrix-aided space-time modulation. Furthermore, in 2011, Basar *et al.* [218] arranged for achieving a transmit diversity gain for the original SM by activating more than one TAs in order to convey STBC codewords. This method has been further developed in [219–221] and all these schemes can be categorized under the framework of GSTSK according to the STBC's dispersion matrix expression. By contrast, Renzo *et al.* [222–224] conceived an STBC transmit diversity aided SM scheme by employing idealistic orthogonal shapping filters, while Yang [225] proposed to employ orthogonal frequency-hopping codes. These schemes are however beyond the scope of GSTSK and they impose extra stringent hardware requirements.

Considering the fact that there are always $(N_T - 1)$ zero elements and a single non-zero element in a SM's transmission vector, any pair of SM codewords will share a total number of $(N_T - 2)$ zero-element positions. As a result, the average pairwise Euclidean distance between SM codewords is lower than that of its V-BLAST counterpart, which implies that SM may have a higher pairwise symbol error probability than its V-BLAST counterpart. For this reason, it is not likely for SM to outperform V-BLAST at the same system throughput and under the same hardware and software conditions. Indeed, this would only be possible for SM systems, under the employment of extra hardware for creating transmit diversity techniques [224, 226, 227], orthogonal shapping filters [222,224,227], or when aiming for a reduced SM throughput [228] or when using more complex ML SM detectors while opting for suboptimal V-BLAST detectors [197, 204, 205, 212, 218]. In summary, the ubiquitous performance versus complexity tradeoff manifests itself in the context of V-BLAST and SM, which is also the case for the LDC and the STSK arrangements. However, we will demonstrate in Chapters 6 and 7 that although SM may not be capable of outperforming V-BLAST, the performance differences between them are almost negligible compared to the performance loss imposed by employing an MMSE detector for V-BLAST. The same claim is valid, when STSK is compared to LDC.

The capacity of SM was evaluated by Yang and Jiao [201], who confirmed that the SM capacity is higher than that of the SISO/SIMO systems, but the full MIMO capacity cannot be achieved by the family of SM systems. We will demonstrate under the same framework in Chapter 6 that STSK also suffers from the same capacity loss against LDC. In order to mitigate this problem, the GSTSK proposed by Sugiura *et al.* [217] advocates transmitting more than one symbols. However, considering SM as an example, if more than one TAs are activated to transmit different symbols, the problem of IAI resurfaces, unless STBC codewords are transmitted. In order to tackle this IAI problem, Wang *et al.* [226] and Sugiura *et al.* [229] proposed sub-optimal interference-suppression receivers for Generalized SM and for the GSTSK, respectively. However, these arrangements are not consistent with the SM/STSK motivation of relying on low-complexity optimum ML receiver design. Against this background, Fu *et al.* [230] and Younis *et al.* [231] proposed the a Generalized SM (GSM) design, where multiple activated TAs may transmit the same symbol. In this way, although the IAI problem is avoided, the capacity improvement provided by the GSM remains limited, because the ergodic capacity is only maximized, when the signals transmitted by multiple

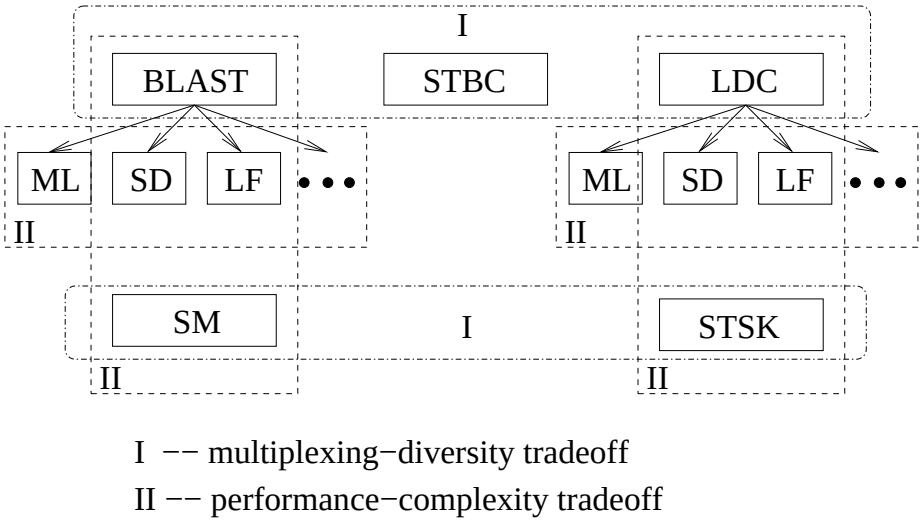

Figure 1.24: Key Multiple-Input Multiple Output (MIMO) schemes and the design tradeoffs that motivated their development.

TAs are independent and identically distributed (i.i.d.) [165, 166]. Therefore, the concept of a systematically normalized GSM/GSTSK arrangement that achieves an improved capacity without imposing IAI requires further research efforts.

It is worth noting that a comprehensive review paper on the recent development of SM was offered by Renzo *et al.* [227] and by Yang *et al.* [232].

Last but not least, the aforementioned milestones in MIMO development are summarized in Tables 1.8-1.10. We also summarize the key MIMO schemes and their relationships in Fig. 1.24. More explicitly, the first type of MIMO system design tradeoff is that between BLAST's multiplexing gain and STBC's diversity gain. The LDC design may resolve this tradeoff, provided that the parameters satisfy $N_Q \geq N_T N_P$. The second MIMO system design tradeoff manifests itself between the MIMO detectors conceived for tackling the IAI problem, hence strikes a performance versus complexity tradeoff. Furthermore, the concept of SM was motivated by the hope that the optimum MIMO detection may be implemented at a substantially reduced complexity. In reality, a slight performance loss is imposed by SM, which again, indicates the presence of the performance versus complexity tradeoff. The same performance versus complexity tradeoff exists between the LDC and the STSK family. Furthermore, since STSK provides a transmit diversity gain, the conventional multiplexing versus diversity tradeoff manifests itself between SM and STSK. The attainable capacity, BER performance and complexity will be at the centre of our further discussions on MIMO systems in Chapters 6 and 7.

Table 1.8: Summary of major contributions on MIMO schemes (Part I).

Year	Author(s)	Topic	Contribution
1994	Paulraj and Kailath [161]	MIMO	Proposed the concept of multiplexing-oriented MIMO, where a high data-rate transmission was carried out by splitting it into low data-rate signals transmitted by spatially separated SDMA users.
1996	Foschini [162]	BLAST	Proposed the concept of D-BLAST, where a single data stream is de-multiplexed and then rotated and transmitted by N_T co-located TAs, so that the multiplexing gain may be pursued for a single user.
1998	Wolniansky *et al.* [164]	BLAST	Proposed the concept of V-BLAST, which elimiates the D-BLAST transmitter's diagonal-encoding rotator in order to simplify the real-time implementation.
1998	Alamouti [177]	STBC	Proposed the transmit diversity technique for the case of $N_T = 2$, which is often referred to as Alamouti's G2 STBC.
1999	Telatar [166]	BLAST	Proved that the BLAST MIMO systems have an ergodic capacity that may grow linearly with the number of antennas, provided that the BLAST MIMO system employs a large number of antennas.
1999	Tarokh *et al.* [178]	STBC	Proved that Alamouti's G2 STBC is the only full unity-rate code in the family of STBCs, and proposed Half-Rate (HR) STBCs for any number of TAs according to the Hurwitz-Radon theory [179, 180].
2000	Damen *et al.* [172]	BLAST	Proposed to inoke a sphere decoder for BLAST in order to strike a performance-complexity tradeoff between the ML BLAST detector and the LF-aided detectors.
2000	Sandhu and Paulraj [184]	STBC	Demonstrated that STBCs cannot achieve the full MIMO capacity except for a single case, which is Alamouti's G2-STBC systems associated with $N_R = 1$.
2001	Jafarkhani [186]	STBC	Proposed the concept of Quasi-Orthogonal (QO) STBC, which relaxed the STBC's orthogonality requirement in order to improve the STBC throughput.
2001	Ganesan and Stoica [181–183]	STBC	Proposed Amicable Orthogonal (AO) STBCs for any number of TAs according to the theory of amicable orthogonal design [179], which reduced the transmission delay of HR-STBCs and achieved an improved normalized throughput of 3/4 for the AO-STBCs associated with $N_T = 3$ and 4.

Table 1.9: Summary of major contributions on MIMO schemes (Part II).

Year	Author(s)	Topic	Contribution
2002	Hassibi and Hochwald [189]	LDC	Proposed the capacity-improving LDC, which completely droped the STBC's orthogonality requirements in order to further improve the STBC capacity while retaining the full transmit diversity gain.
2002	Heath and Paulraj [188]	LDC	Proposed the capacity-achieving LDC, which simplified the LDC design of [189] so that both the full MIMO capacity and the full transmit diversity gain may be attained, provided that the parameters satisfy $N_Q \geq N_T N_P$.
2002	Sellathurai and Haykin [13]	BLAST	Proposed the exact MMSE solution incorporating the non-constant *a priori* probabilities for coded BLAST systems.
2003	Damen *et al.* [10]	BLAST	A comprehensive summary paper for the sphere decoding algorithms invoked by the uncoded BLAST systems.
2003	Zheng and Tse [185]	BLAST STBC	Quantified the classic MIMO design tradeoff between the attainable multiplexing and diversity gain.
2003	Hochwald and Brink [173]	BLAST	Proposed the first soft-decision-aided SD for BLAST, where a list of BLAST signal candidates was established by the hard-decision-aided SD and then the candidates in this list were processed by the MAP decoding algorithm.
2004	Vikalo *et al.* [174]	BLAST	Proposed the soft-decision-aided SD for BLAST, which incorporated the *a priori* information in sphere decoding.
2008	Studer *et al.* [175]	BLAST	Proposed the soft-output SD's VLSI implementation, which is further developed by the authors in [176], where the *a priori* LLRs are once again incorporated into the SD's VLSI implementation.
2008	Mesleh *et al.* [197]	SM	Analysed the SM that was firstly appeared in [195], where a single out of N_T TA is activated in order to transmit a single modulated MPSK/QAM symbol, so that a substantial complexity reduction may be achieved for the SM receiver by separately detecting the TA activation index and the classic modulated symbol index.
2008	Jeganathan *et al.* [198]	SM	Demonstrated that completely independently detecting the TA index and the modulated symbol index as seen in [197] resulted in an error floor. The authors further streamlined the ML MIMO detector's calculations for SM.

Table 1.10: Summary of major contributions on MIMO schemes (Part III).

Year	Author(s)	Topic	Contribution
2008	Jeganathan *et al.* [199, 200]	SM (SSK)	Proposed the concept of SSK, where simply the TA activation index conveys the source information.
2008	Yang and Jiao [201]	SM	Proposed to invoke demodulator before detecting the TA activation index, and demonstrated that the SM capacity is higher than that of the SISO/SIMO systems.
2010	Sugiura *et al.* [216]	STSK	Proposed the concept of STSK in order to be able to benefit from a transmit diversity gain for the SM techniques, where a single out of N_Q LDC's dispersion matrix is activated in order to disperse a single modulated MPSK/QAM symbol, so that the low-complexity SM detectors may be invoked by the STSK receiver.
2011	Basar *et al.* [218]	SM	Proposed to achieve a transmit diversity gain for the original SM by activating more than one TAs in order to convey STBC codewords.
2011	Sugiura *et al.* [217]	STSK	Proposed the concept of Generalized STSK (GSTSK), where virtually all the MIMO schemes including V-BLAST, STBC, LDC, SM and STSK are included in the framework of dispersion matrix-aided space-time modulation.
2013	Xu *et al.* [203]	SM STSK	Proposed the reduced-scope SM detector both for uncoded and coded SM systems, which reduced the detection search scope while maintaining the optimum detection capability. The correlation between the TA index and the modulated symbol index was taken into account when detecting the TA index, and then only a single MPSK/QAM demodulator was invoked according to the already detected TA index.
2014	Rajashekar *et al.* [204]	SM	Summarized the Yang and Jiao's [201] technique as the hard-limiter-based SM detector, which invoked classic MPSK/QAM demodulators for all matched filter output elements first, and then the TA activation index detection was performed with the aid of the already demodulated MPSK/QAM symbols. The hard-limiter-based SM detector cannot be directly applied to coded SM systems.
2014	Renzo *et al.* [227]	SM STSK	A comprehensive summary paper for the recent development of SM.

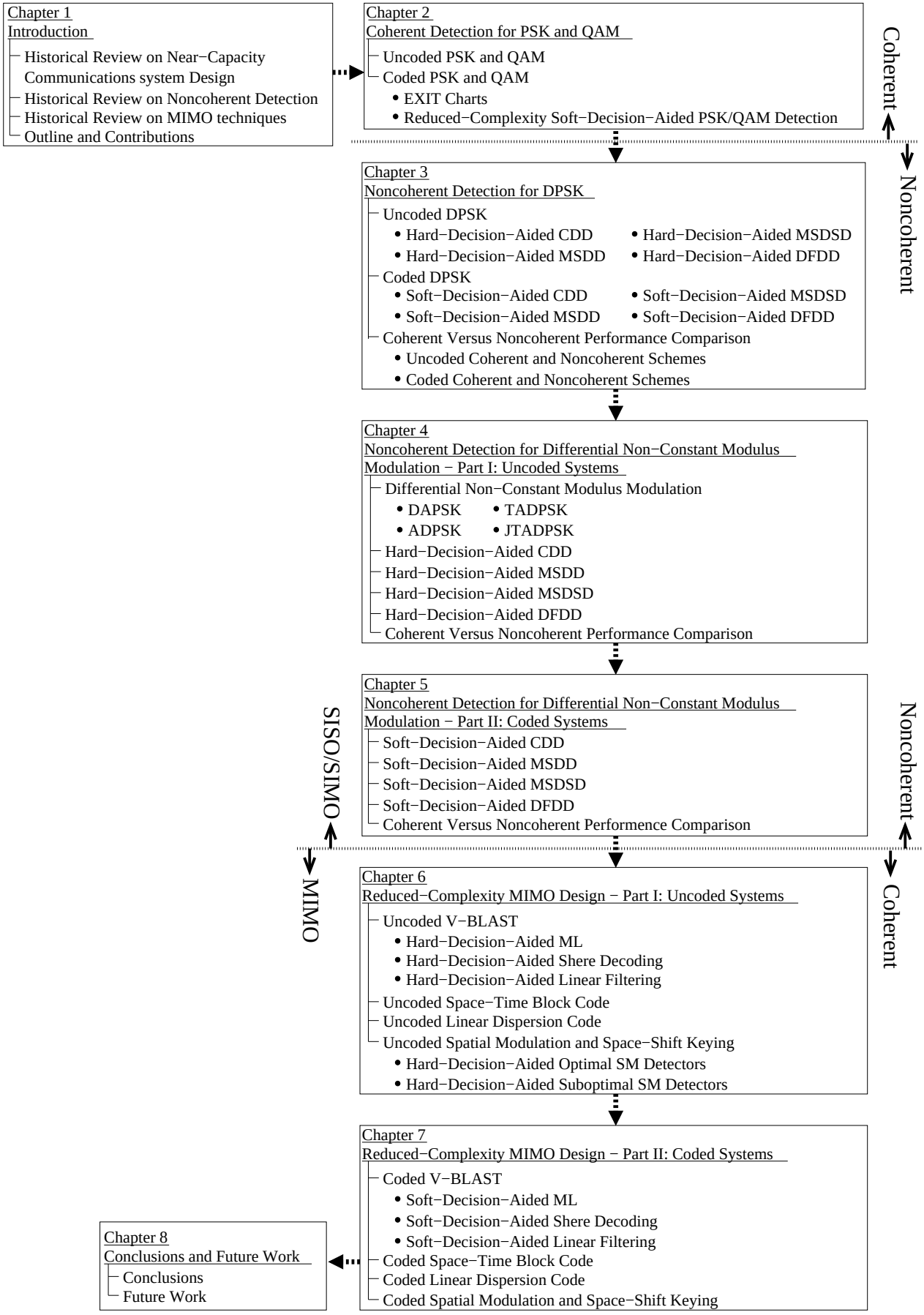

Figure 1.25: Outline of this treatise.

1.4 Outline and Novel Contributions

During my PhD study, I have authored and co-authored 14 journal papers as well as 9 conference papers. This report is written based on the 7 journal papers that I published as the first author. In more detail, my first journal publication was a near-capacity design for cooperative differential LDC using MSDD [233] in 2011, which covers the three main topics introduced in this chapter. Moreover, inspired by the open problem of how to separately detect the SM's TA index and modulated symbol index without imposing any performance loss, we discovered that the optimum SM detection capability may be retained if the TA index detector takes into account, which specific MPSK/QAM modulated symbol is transmitted. According to this carefully designed reduced-complexity algorithm, only a reduced number of constellation points has to be visited, and yet, no performance loss is imposed. We firstly proposed this method for the hard-decision-aided CDD and MSDSD conceived for Differential STSK [234] in 2011. Then we extended this work to soft-decision-aided STSK detection of [202] also in 2011. Furthermore, in the same year, we solved another open problem in the context of hard-decision-aided MSDSD conceived for Differential STBC using QAM in [235], where the channel's correlation matrix, which is determined by the QAM signal's non-constant modulus is solved step-by-step using a sphere decoder. Although this method successfully improved the performance of Differential STBC by using a sphere decoder, no theoretical proof was provided in this paper, and further modifications are still required for the family of coded systems. In 2013, we summarized our previous research efforts dedicated to reduced-complexity optimal SM/STSK detection in the context of both uncoded and coded systems in [203]. Moreover, we discovered that this reduced-complexity design, which was originally conceived for SM/STSK, may be applied to basic soft-decision-aided PSK/QAM detection [236], so that a wider range of communications systems may benefit from this reduced-complexity design. In the same year, we have applied this reduced-complexity design to soft-decision-aided CDD conceived for DAPSK in [159].

Instead of summarizing my publications according to their chronological order, in this report, a systematic approach is pursued along the road to reduced-complexity design by critically appraising the structure of communications systems, where the missing steps bridging the gap between my previous publications are conceived. The outline of the report is portrayed in Fig. 1.25, where the entire family of communications systems spanning from coherent to noncoherent, from uncoded to coded, and also from SISO/SIMO to MIMO systems is summarized.

In more details, the main body of the report commences from the basic coherent SISO/SIMO schemes, where the class of both uncoded and coded PSK/QAM schemes is introduced in Chapter 2. The near-capacity system design concept based on EXIT charts is also introduced in this chapter and our reduced-complexity design methodology is applied to soft-decision-aided PSK/QAM detectors, which is based on [236]. Chapter 3 moves on to conceiving noncoherent SISO/SIMO schemes both for uncoded and coded systems. A survey of noncoherent detectors designed for DPSK including CDD, MSDD, MSDSD and DFDD is provided, and our reduced-complexity

design philosophy is especially applied to the soft-decision-aided MSDSD conceived for coded DPSK. Moreover, a detailed comparison between coherent PSK using realistic imperfect channel estimation and its noncoherent counterpart is also offered in this chapter. In Chapter 4 and Chapter 5, the family of noncoherent detectors conceived for differential non-constant modulus modulation schemes is introduced for uncoded and coded scenarios, respectively. The separation between the uncoded system and the coded system is for the sake of arriving at manageable chapter length. In Chapter 4, the DQAM[2] constellations that exist in the literature including DAPSK, ADPSK, TADPSK, etc. are introduced and compared. Furthermore, the final steps of the theoretical proof of how to invoke a sphere decoder for DQAM detection is provided, and the MSDSD conceived for DQAM is proposed based on our theoretical analysis. Furthermore, the soft-decision-aided MSDSD was also proposed for coded DQAM in Chapter 5, where our reduced-complexity design is applied. Moreover, the comparison between coherent QAM and noncoherent DQAM is discussed in the context of both coded and uncoded systems in these two chapters. After introducing both the coherent and noncoherent SISO/SIMO schemes, Chapter 6 and Chapter 7 provide further insights concerning the design of MIMO systems. As the background of the recently proposed the family of SM and STSK arrangements, the development of MIMO techniques is summarized special emphasis on their capacity, performance and complexity analysis. Finally, our reduced-complexity SM/STSK detection techniques are detailed in Chapters 6 and 7 based on our publication of [203]. We leave our future deliberations on the class of noncoherent MIMO systems for our future work, as briefly discussed in Chapter 8.

Explicitly, the novel contributions offered by each chapter are summarized as follows:

Chapter 2: Coherent Detection for PSK and QAM

2.1) We observe that the Max-Log-MAP algorithm aided soft-detector aims for finding the maximum probabilities, which is similar to the action of hard-decision-aided detection of uncoded *M*PSK/QAM schemes. Therefore, after linking each *a priori* LLR to a reduced-size fraction of the channel's output signal constellations, the Max-Log-MAP algorithm may be operated at a reduced complexity.

2.2) Furthermore, the corresponding reduced-complexity Approx-Log-MAP algorithm is also conceived by compensating for the Max-Log-MAP algorithm's widely-used Jacobian approximation relying on a lookup table.

2.3) We have generalized our detection algorithms for different constellations, including *M*PSK, Square *M*QAM, Star *M*QAM and Cross *M*QAM. The symmetry exhibited by each Gray-labelled constellation diagram is the key to the detection complexity reduction.

2.4) Finally, we demonstrate the benefits of our solution in the context of a variety of turbo detected systems. The iteration gain achieved by the soft *M*PSK/QAM detectors results in a significant performance improvement. Furthermore, a substantial complexity reduction is achieved without any performance loss.

[2]We note that the terminology of non-constant modulus modulation and DQAM are exchangeable in this treatise.

Chapter 3: Noncoherent Detection for DPSK

3.1) We further extend the classic MSDSD aided uncoded DPSK [127] to the case of employing multiple RAs associated with $N_R \geq 1$, while maintaining a low complexity for the SD's Schnorr-Euchner [237] search strategy.

3.2) In order to compensate for the performance erosion imposed by the Max-Log-MAP algorithm, we propose to modify the output of the soft-decision-aided MSDSD conceived in [132], where multiple candidates may be produced by the SD so that the Approx-Log-MAP regime may be invoked.

3.3) When the *a priori* LLRs gleaned from a channel decoder are taken into account by the soft-decision-aided MSDSD of [132], the SD's Schnorr-Euchner [237] search strategy once again requires the sorting of all the M constellation points. In order to mitigate this problem, we proposed to adopt the reduced-complexity design proposed in Chapter 2 for the sorting algorithm, where the optimum candidate may be found by visiting a reduced-size subset of constellation points, and then the rest of the constellation points may be visited in a zig-zag fashion.

3.4) Furthermore, we provide a discussion on the important subject of coherent versus noncoherent detection. More explicitly, numerous channel estimation techniques are capable of acquiring accurate CSI knowledge at the coherent receiver, when the fading channels fluctuate relatively slowly. However, as the Doppler frequency increases, the coherent receivers relying on realistic imperfect CSI suffer from an inevitable performance loss. We will demonstrate that this problem becomes particularly serious for soft-decision-aided coherent detectors, because they are likely to produce extrinsic inaccurate LLRs.

Chapter 4: Noncoherent Detection for Differential Non-Constant Modulus Modulation – Part I: Uncoded Systems

4.1) We prove that although the complete channel correlation matrix required by the MSDD conceived for DQAM remains unknown until all the transmitted symbol amplitudes have been detected, its partial channel correlation matrix may be evaluated with the aid of the SD's previous decisions as well as a single information-dependent symbol amplitude that may be readily found by the SD. As a benefit, we are able to invoke sphere decoding for both amplitude detection and phase detection for MSDD aided DQAM.

4.2) As a solution to the open problem of MSDSD aided DQAM, a DFDD derived from an MSDD/MSDSD and a Linear Prediction Detection (LPD) relying on blind channel estimation are developed for uncoded DQAM schemes. We demonstrate that the DFDD regime and the LPD aided DQAM solution operating in Rayleigh fading channels are also equivalent, similarly to the trend we observe for the DFDD aided DPSK technique summarized in [121, 125]. As expected, the revised DFDD proposed in this chapter outperforms the DFDD aided DQAM solution of [136, 153, 154].

4.3) We provide a detailed study on the family of DQAM constellations based on the existing literature. A variety of noncoherent detectors, including CDD, MSDD, MSDSD and DFDD are tailored for different DQAM schemes, and their pros as well as cons exhibited in different scenarios are suggested. We provide a quantitative performance comparison between coherent QAM using realistic channel estimation and DQAM using noncoherent detection in the context of uncoded systems.

Chapter 5: Noncoherent Detection for Differential Non-Constant Modulus Modulation – Part II: Coded Systems

5.1) First of all, the soft-decision-aided MSDD conceived for coded DQAM is introduced in this chapter. Since the first transmitted symbol's ring amplitude within an observation window may be treated either as a variable, or a known quantity based on previous decisions or alternatively as a known term based on the *a priori* information gleaned from a channel decoder, three types of soft-decision-aided MSDDs including the original MSDD, the Hard-Decision-Directed MSDD (HDD-MSDD) and the Soft-Decision-Directed MSDD (SDD-MSDD) are treated in this chapter.

5.2) Secondly, the soft-decision-aided MSDSD conceived for coded DQAM is proposed in this chapter, where sphere decoding is invoked for both constellation ring amplitude detection and phase detection. According to the MSDD arrangements, the soft-decision-aided MSDSD may also be implemented in form of a HDD-MSDSD and SDD-MSDSD. Moreover, both the Max-Log-MAP and Approx-Log-MAP regimes are implemented by the soft-decision-aided MSDSD designed for coded DQAM, where the Approx-Log-MAP proposed for MSDSD aided DPSK in Chapter 3 may be applied for coded DQAM detection.

5.3) Thirdly, since Gray-coded labelling is applied to the DQAM constellations, we propose to invoke the reduced-complexity design conceived for MSDSD aided DPSK in Chapter 3 also for the soft-decision-aided MSDSD conceived for coded DQAM. In this way, the complexity of the soft-decision-aided MSDSD may be substantially reduced without imposing any performance loss.

5.4) Fourthly, the soft-decision-aided MSDD-IAP conceived for coded DAPSK in [160] is revised for employment for all DQAM constellations. Based on the above-mentioned developments, we propose to carry out MSDAD with the aid of sphere decoding. Hence the terminology may be revised to Multiple-Symbol Differential Amplitude Sphere Detection (MSDASD). Since both ring amplitude detection and phase detection are carried out by SD, the terminology of MSDD-IAP may be revised to MSDSD-IAP, which may also be carried out with the aid of HDD-MSDSD-IAP and SDD-MSDSD-IAP, if required. Furthermore, the reduced-complexity design conceived for MSDSD aided DPSK in Chapter 3 may be directly applied to MSDPSD, so that the total number of constellation points visited by the MSDSD-IAP may be substantially reduced.

5.5) Furthermore, the soft-decision-aided DFDD conceived for coded DQAM is proposed in this chapter based on the hard-decision-aided DFDD regime introduced in Chapter 4. We will demonstrate that the proposed DFDD outperforms the suboptimal DFDD solutions of [136, 153, 154], because the latter assume having a channel correlation matrix, which is independent of the transmitted symbol amplitudes.

5.6) Last but not least, a quantitative performance study of soft-decision-aided noncoherent detectors conceived for coded DQAM is offered in this chapter and the most suitable design choices are recommended for different DQAM constellations. Furthermore, we also demonstrate that when the fading channels fluctuate rapidly, the soft-decision-aided HDD-MSDSD-IAP conceived for ADPSK may even outperform PSAM aided coherent QAM detection in a variety of channel coding assisted systems.

Chapter 6: Reduced-Complexity Design Applied to MIMO Schemes – Part I: Uncoded Systems

6.1) The tradeoff between the attainable diversity and multiplexing gain is discussed in the context of each MIMO scheme introduced in this chapter. The achieveable capacity and error probability are used as the fundamental metrics of quantifying the associated tradeoff. We demonstrate that although this tradeoff exemplied by that between V-BLAST and STBC may be resolved by the LDC design, but it still exists between the newly-developed reduced-complexity MIMO systems of SM and STSK, which leaves room for further investigations.

6.2) The importance of the tradeoff between the performance attained and complexity imposed is stressed in the context of MIMO system designs throughout this chapter. This tradeoff persists both for the classic V-BLAST and LDC receiver design, but it is also the key motivation of SM and STSK.

6.3) Altough the development of SM and STSK is motivated by their potentially low detection complexity, it was demonstrated in [198] that completely independently detecting the TA activation index and the modulated MPSK/QAM symbol imposes a performance loss on the SM receiver. In order to mitigate this problem, in this chapter, we summarize the wide-ranging facets of reduced-complexity hard-decision-aided SM detector design based on our previous publications [141, 202, 203, 234], where the optimal SM performance was retained by taking into account the correlation between the TA activation index and the MPSK/QAM modulation index. A range of other optimal and suboptimal SM detectors found in the literature [141, 204–213] are also summarized for the sake of comparison.

Chapter 7: Reduced-Complexity Design Applied to MIMO Schemes – Part II: Coded Systems

7.1) We demonstrate the benefits of the reduced-complexity design proposed for the soft-decision-aided MPSK/QAM demodulators of Chapter 2 in the context of both channel coded V-BLAST systems as well as channel coded STBC systems. This contribution is based on our publication [236].

7.2) Similar to the soft-decision-aided MSDSD conceived for DPSK introduced in Chapter 3, the reduced-complexity SD previously proposed for MSDSD in Chapter 3 is applied for the soft-decision-aided V-BLAST detector, when MPSK constellations are employed.

7.3) We further exploit the reduced-complexity SM detector design proposed in Chapter 6 also for channel coded SM and STSK systems. In more details, the maximum *a posteriori* probability that is required by the Max-Log-MAP algorithm may be obtained by partially relying on the reduced-complexity soft-decision-aided MPSK/QAM demodulators before deciding the SM's TA activation index, where the correlation between the modulated symbol index and the TA index is taken into account, so that the detected TA index always corresponds to the MAP solution. This contribution is based on our publications [202, 203].

Chapter 2

Coherent Detection for PSK and QAM

2.1 Introduction

The significant technical breakthrough of Turbo Coding (TC) was proposed in [38, 39]. More explicitly, as portrayed by Fig. 2.1a, the transmitter encodes the source bits twice by a pair of component RSC encoders, with an interleaver between their inputs to ensure that the two encoders fed with sequences that are independent of each other. As a result, the pair of RSC decoders at the receiver of Fig. 2.1b may be capable of exchanging their extrinsic information, so that a substantial performance improvement may be achieved by this so-called turbo detection process. Tutorial for TC may be found in [238, 239].

Ever since the development of TC, the iterative decoding of concatenated codes has inspired numerous researchers to aim for achieving a near-capacity performance in diverse system contexts [2, 8, 239]. It was observed in [8, 240, 241] that a variety of commonly used modulation schemes also impose dependency among the source bits and hence their demodulators may be appropriately modified to be able to process soft-values which can be exchanged with the soft-input channel decoders in the context of turbo detection. As an example, Fig. 2.2a shows that the source bits are encoded twice by a RSC encoder and transmitted by a MIMO modulator. At the receiver, the inner receiver component, namely the RSC decoder of the conventional turbo detection of Fig. 2.1b is replaced by a MIMO demodulator, as seen in Fig. 2.2b.

Moreover, the concept of EXtrinsic Information Transfer (EXIT) charts was proposed in [88] for analyzing the convergence behaviour of turbo detection. Furthermore, in order to eliminate the error floor often observed in two-component concatenated codes, it was proposed in [93, 242] that a further Unity Rate Code (URC) may be incorporated as shown in Fig. 2.3a, so that an infinitesimally low BER may be achieved by the resultant three-stage turbo detector of Fig. 2.3b. Furthermore, the IRregular Convolutional Code (IRCC) concept [86, 243] was proposed for replacing the regular convolutional codes, where the area between the EXIT curve of the outer IRCC and that of the inner amalgamated URC and demodulator block was minimized. As a result, a vanishingly low

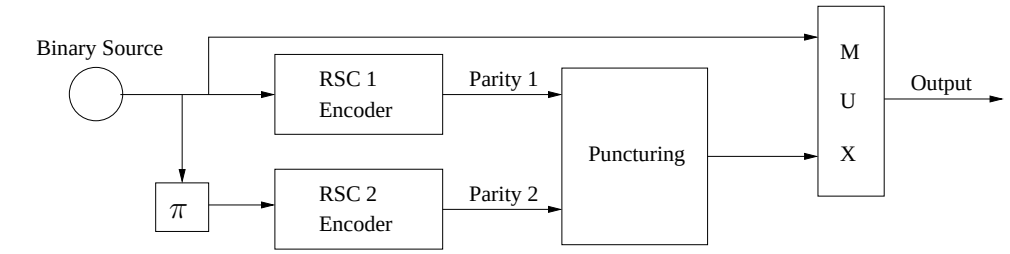

(a) Turbo code encoder

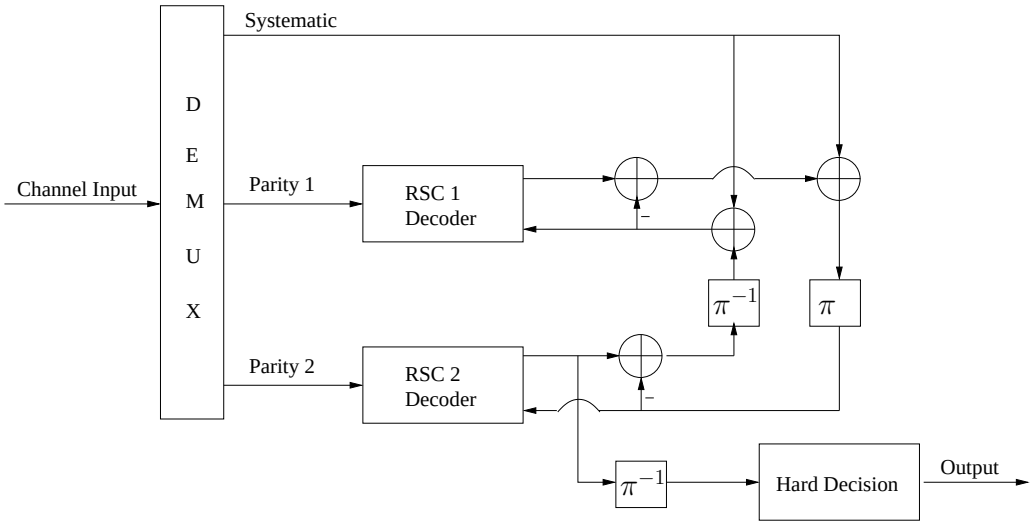

(b) Turbo code decoder

Figure 2.1: The schematic of turbo code.

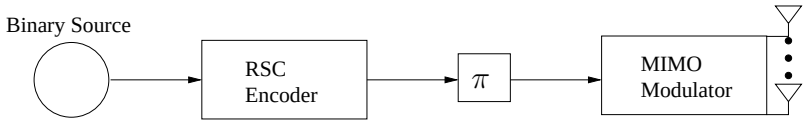

(a) RSC coded MIMO transmitter

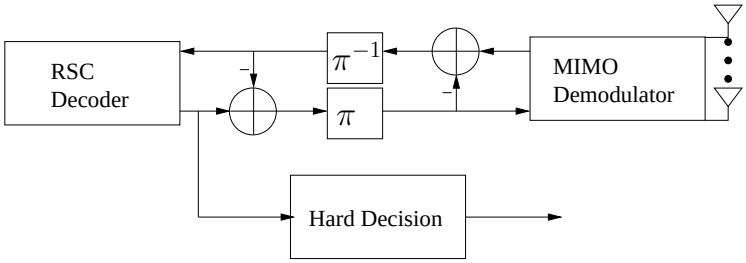

(b) Turbo detected RSC-MIMO receiver

Figure 2.2: The schematic of a turbo detected RSC coded MIMO system.

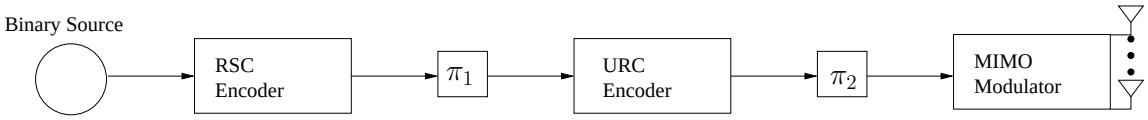

(a) RSC-URC coded MIMO transmitter

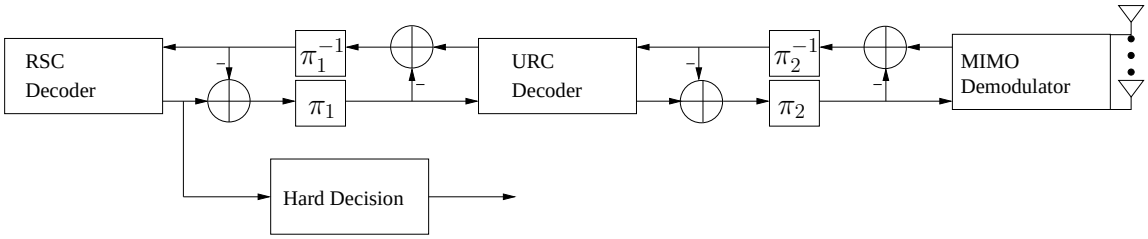

(b) Turbo detected RSC-URC-MIMO receiver

Figure 2.3: The schematic of a turbo detected RSC and URC coded MIMO system.

BER may be achieved at a near-capacity SNR [17, 244].

As researchers inch closer and closer to the channel capacity, the complexity of the resultant communication systems is also increased. In fact, soft-decision-aided MIMO demodulator as seen in Figs. 2.2b and 2.3b typically contributes a substantial fraction of the total complexity. In order to circumvent this problem, a soft-decision-aided Sphere Decoder (SD) assisted multiple-stream MIMO systems (e.g. V-BLAST [162]) was proposed in [173, 174, 176], where the total number of constellation points visited by the MIMO demodulator may be significantly reduced by the SD's tree-search. On the other hand, often low-complexity linear MIMO receivers (e.g. MMSE receiver) [13, 14, 75] may be employed for separating the superimposed parallel data streams. Similarly, the parallel streams of orthogonal STBC schemes [177, 178] may be readily transformed into an equivalent single-stream form, as a benefit of the orthogonal space-time code design. As a result, when the conventional MPSK/QAM detector is invoked either by the MIMO's linear receivers or by the STBC receivers, the detection complexity is on the order of $O(M)$ instead of $O(M^Q)$, where Q represents the number of symbols transmitted together.

Since the family of classic MPSK/QAM detectors is of salient significance in virtually all communication systems, the detection algorithms conceived for MPSK/QAM demodulation are revisited in this chapter. From a historical point of view, the methods introduced in [245–247] may be capable of reducing the soft MPSK/QAM detection complexity from the order of $O(M)$ to $O(\log_2 M)$, where the approxmiated LLR values are efficiently evaluated on a bit-by-bit basis. However, these early contributions on bit-metric generation did not consider the *a priori* LLRs produced by a channel decoder. This is because the detection of the Gray-labelled low-order PSK/QAM schemes (e.g BPSK/QPSK and Square 16QAM) generally produce near-horizontal curves in the EXIT charts [86, 88], which means that exchanging information between the soft MPSK/QAM detector and the channel decoder may have a negligible benefit. However, at the time of writing, high-order MPSK/QAM schemes are routinely utilized in commercialized systems. For example, Square 64QAM and Square 256QAM have been included in the ITU-R IMT Advanced

4G standards [248] and in IEEE 802.11ac [249], respectively. As the number of modulation levels M increases, the soft MPSK/QAM detectors become capable of producing an improved iteration gain. Therefore, a significant performance improvement is attained, once the *a priori* LLRs have been taken into account by the soft MPSK/QAM detector. However, since the soft MPSK/QAM detectors are required to process both the *a priori* LLRs and the channel's output signal, conventionally all the M symbol probabilities corresponding to all M constellation points have to be evaluated and compared. Against this background, in this chapter, a reduced-complexity design conceived for generalized soft-deicision-aided MPSK/QAM demodulation is proposed, where only a reduced-size subset of the MPSK/QAM constellation points is taken into account for producing a single soft-bit output. In more detail, the novel contributions of this chapter are as follows:

1. We observe that the Max-Log-MAP algorithm aims for finding the maximum probabilities, which is similar to the action of hard-decision-aided detection of uncoded MPSK/QAM schemes. Therefore, after linking each *a priori* LLR to a reduced-size fraction of the channel's output signal constellations, the Max-Log-MAP algorithm may be operated at a reduced complexity.

2. Furthermore, the corresponding reduced-complexity Approx-Log-MAP algorithm is also conceived by compensating for the Max-Log-MAP algorithm's widely-used Jacobian approximation relying on a lookup table.

3. We have generalized our detection algorithms for different constellations, including MPSK, Square MQAM, Star MQAM and Cross MQAM. The symmetry exhibited by each Gray-labelled constellation diagram is the key to the detection complexity reduction.

4. Finally, we demonstrate the benefits of our solution in the context of a variety of turbo detected systems. The iteration gain achieved by the soft MPSK/QAM detectors results in a significant performance improvement. Furthermore, a substantial complexity reduction is achieved without any performance loss.

The remainder of this chapter is organized as follows. The PSK and QAM constellations and their low-complexity hard-decision-aided detection methods in uncoded system are reviewed in Sec. 2.2. The soft-decision-aided PSK/QAM detection in coded system is introduced in Sec. 2.3, where the effective tool of EXIT chart is also thoroughly discussed. The proposed reduced-complexity soft-decision-aided PSK/QAM detection is presented in Sec. 2.4, while the chapter conclusions are offered in Sec. 2.5.

2.2 Uncoded PSK and QAM

In this section, the hard-decision-aided detectors conceived for uncoded MPSK/QAM schemes are reviewed first. Gray-labelled constellations are assumed throughout this chapter. Naturally, there

are many other constellation labelling schemes in the existing literatures [86, 250], but the reasons for choosing Gray-labelling in this work may be deemed to be twofold. First of all, the adjacent constellation points mapped according to the Gray code only differ by one bit, which results in the best performance in uncoded systems [2, 3]. This also implies a higher starting point for the EXIT-curves of soft-decision-aided MPSK/QAM detectors in coded systems in their EXIT charts [86,88], when initially no *a priori* LLRs are available from the outer channel decoder. Secondly, considering Square MQAM as an example, a Gray encoder labels the real and the imaginary parts of a Square MQAM symbol separately, where two separate bits respectively determine the polarities of the real and the imaginary parts of the Square MQAM symbol. This constellation mapping symmetry provided by Gray-labelling is the key to a low detection complexity both for the uncoded and for the coded MPSK/QAM detectors. We will elaborate on these features in the following sections.

2.2.1 Hard-Decision-Aided PSK Detection

The MPSK transmitter firstly maps BPS $= \log_2 M$ source binary bits to a phasor index $m =$ bin2dec$(b_1 \cdots b_{\text{BPS}})$[1], which modulates a MPSK phasor $\{s^m = \exp(j\frac{2\pi}{M}\check{m})\}_{m=0}^{M-1}$, where the phasor index m is mapped to the Gray coded index $\check{m}$. The constellation diagrams of Gray-labelled MPSK schemes including BPSK, QPSK, 8PSK and 16PSK are portrayed in Fig. 2.4.

For a Single-Input Multiple-Output (SIMO) system, the signal received by the N_R Receive Antennas (RAs) may be expressed as:

$$\mathbf{Y}_n = s_n \mathbf{H}_n + V_n, \tag{2.1}$$

where s_n denotes the transmitted MPSK symbol, while the $(1 \times N_R)$-element vectors $\mathbf{Y}_n$, $\mathbf{H}_n$ and $\mathbf{V}_n$ refer to the received signal vector, the Rayleigh fading channel vector and the Additive White Gaussian Noise (AWGN) vector, which has a zero mean and a variance of N_0, respectively.

The optimum Maximum A Posteriori (MAP) detector aims for maximizing the *a posteriori* probability according to Bayes' law [251] as:

$$p(s^m|\mathbf{Y}_n) = \frac{p(\mathbf{Y}_n|s^m)p(s^m)}{\sum_{\forall s^m \in \mathbf{s}} p(\mathbf{Y}_n|s^m)p(s^m)}, \tag{2.2}$$

where according to the received signal model of Eq. (2.1), the conditional probability of receiving $\mathbf{Y}_n$ given that s^m was transmitted may be expressed as:

$$p(\mathbf{Y}_n|s^m) = \frac{1}{(\pi N_0)^{N_R}} \exp\left(-\frac{\|\mathbf{Y}_n - s^m \mathbf{H}_n\|^2}{N_0}\right), \tag{2.3}$$

while we have constant *a priori* probabilities $\{p(s^m) = \frac{1}{M}\}_{m=0}^{M-1}$ upon assuming that the transmitted symbol s_n is equiprobable. As a result, the ML detection may be formulated as:

$$\hat{s}_n = \arg \min_{\forall s^m \in \mathbf{s}} \|\mathbf{Y}_n - s^m \mathbf{H}_n\|^2, \tag{2.4}$$

[1] In this report, "bin2dec" denotes the function that converts binary bits to decimal integers, while its inverse function "dec2bin" converts a decimal integer to bits.

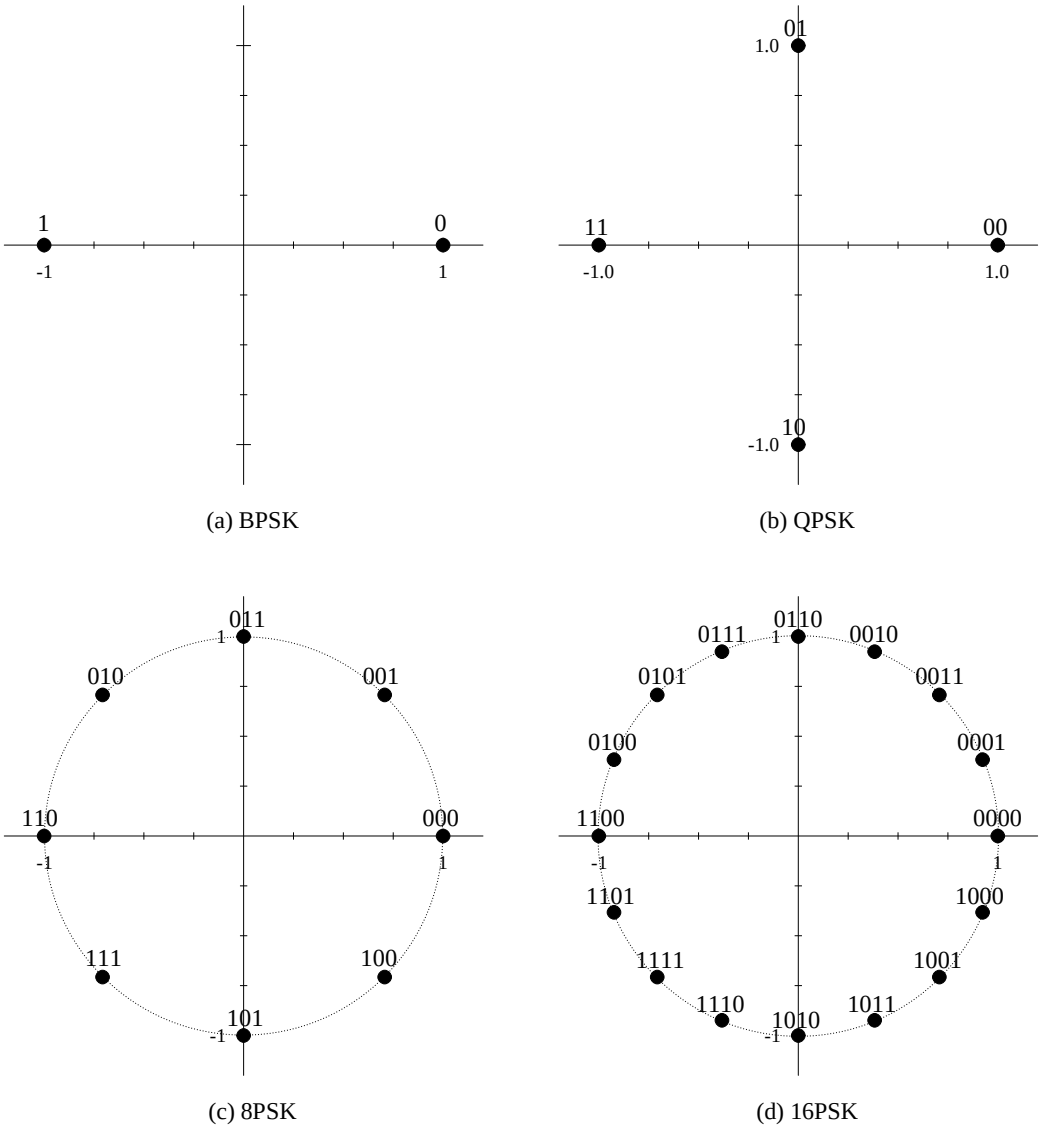

(a) BPSK (b) QPSK

(c) 8PSK (d) 16PSK

Figure 2.4: Constellation Diagrams of Gray-labelled *M*PSK schemes including BPSK, QPSK, 8PSK and 16PSK.

where **s** indicates the *M*PSK symbol set, while the coherent receiver assumes a perfect knowledge of the fading channel vector $\mathbf{H}_n$. The Euclidean norm calculation of Eq. (2.4) leads to the decision variable of:

$$z_n = \mathbf{Y}_n \mathbf{H}_n^H. \tag{2.5}$$

Therefore, the vector-by-vector based ML detection of Eq. (2.4) may be simplified to be operated on a symbol-by-symbol basis, which is expressed as:

$$\hat{s}_n = \arg \min_{\forall s^m \in \mathbf{S}} |z_n - s^m|^2. \tag{2.6}$$

In order to show the equivalence between Eq. (2.4) and Eq. (2.6), we further extend the decision

metric of Eq. (2.4) as:

$$\begin{aligned}\|\mathbf{Y}_n - s^m\mathbf{H}_n\|^2 &= \text{tr}\left[(\mathbf{Y}_n - s^m\mathbf{H}_n)(\mathbf{Y}_n - s^m\mathbf{H}_n)^H\right] \\ &= \|\mathbf{Y}_n\|^2 + |s^m|^2 \cdot \|\mathbf{H}_n\|^2 - \left[(s^m)^*\mathbf{Y}_n\mathbf{H}_n^H + s^m\mathbf{H}_n\mathbf{Y}_n^H\right] \\ &= \|\mathbf{Y}_n\|^2 + |s^m|^2 \cdot \|\mathbf{H}_n\|^2 - 2\Re\left[(s^m)^*\mathbf{Y}_n\mathbf{H}_n^H\right],\end{aligned} \tag{2.7}$$

while the decision metric of Eq. (2.6) may be extended as:

$$\begin{aligned}|z_n - s^m|^2 &= |z_n|^2 + |s^m|^2 - [(s^m)^*z_n + s^m z_n^*] \\ &= |z_n|^2 + |s^m|^2 - 2\Re[(s^m)^*z_n] \\ &= |z_n|^2 + |s^m|^2 - 2\Re\left[(s^m)^*\mathbf{Y}_n\mathbf{H}_n^H\right].\end{aligned} \tag{2.8}$$

Observe in Eq. (2.7) and Eq. (2.8) that $\|\mathbf{Y}_n\|^2$, $\|\mathbf{H}_n\|^2$ and $|z_n|^2$ are all invariant over the different candidates $\{s^m\}_{m=0}^{M-1}$, while we have $\{|s^m|^2 = 1\}_{m=0}^{M-1}$ for MPSK schemes. Therefore, minimizing $\|\mathbf{Y}_n - s^m\mathbf{H}_n\|^2$ and minimizing $|z_n - s^m|^2$ over all possible $\{s^m\}_{m=0}^{M-1}$ are equivalent.

Since only the phase of an MPSK symbol carries source information, the phase of the decision variable z_n in Eq. (2.5) may be directly used for detecting the phase of the transmitted symbol s_n. As a result, the symbol-by-symbol based MPSK demodulation of Eq. (2.6) may be further simplified to the following simple step:

$$\hat{s}_n = \exp(j\tfrac{2\pi}{M}\hat{m}), \quad \text{where } \hat{m} = \lfloor \tfrac{M}{2\pi}\angle z_n \rceil, \tag{2.9}$$

which is obtained from enforcing the equality of $z_n = s^m = \exp(j\frac{2\pi}{M}\check{m})$. Then, the resultant phasor index that is naturally given by $\frac{M}{2\pi}\angle z_n$ may be quantized to its nearest legitimate MPSK index $\hat{m} = \lfloor \frac{M}{2\pi}\angle z_n \rceil$.

2.2.2 Hard-Decision-Aided QAM Detection

In the family of bandwidth-efficient QAM schemes, Square QAM and Star QAM are the most popular candidates in a variety of communication systems. On one hand, Gray-labelled Square QAM generally enjoys a lower detection complexity owing to the fact that the real and the imaginary parts of a Square QAM symbol may be separately detected [2, 236]. Furthermore, a classic Square QAM scheme associated with an even number of BPS typically exhibits a better performance in uncoded systems because of its high minimum distance among all constellation points [2, 3, 141]. On the other hand, the Star QAM constellation is often employed in low-complexity non-coherent systems [136, 142, 154, 159] owing to its convenient separate amplitude-phase detection complexity. Moreover, Star QAM has also been shown to have a performance advantage in the recently proposed Space-Time Shift Keying (STSK) system context [141, 203]. We will further investigate these two QAM schemes in the following sections.

2.2.2.1 Square QAM

The square-shaped MQAM constellations were characterized in [2], and the constellation diagram of Square 16QAM is presented in Fig. 2.5a. More explicitly, at the transmitter, $\mathrm{BPS}_{\mathrm{Re}} = \log_2 M_{\mathrm{Re}}$ and $\mathrm{BPS}_{\mathrm{Im}} = \log_2 M_{\mathrm{Im}}$ numbers of bits are assigned to encode a M_{Re}PAM index $m_{\mathrm{Re}} = \mathrm{bin2dec}(b_{\mathrm{BPS}_{\mathrm{Im}}+1} \cdots b_{\mathrm{BPS}})$ and a M_{Im}PAM index $m_{\mathrm{Im}} = \mathrm{bin2dec}(b_1 \cdots b_{\mathrm{BPS}_{\mathrm{Im}}})$, respectively. As a result, a modulated Square MQAM symbol may be expressed as:

$$s^m = s_{\mathrm{Re}}^{m_{\mathrm{Re}}} + j s_{\mathrm{Im}}^{m_{\mathrm{Im}}} = \frac{M_{\mathrm{Re}} - 2\check{m}_{\mathrm{Re}} - 1}{\sqrt{\beta}} + j\frac{M_{\mathrm{Im}} - 2\check{m}_{\mathrm{Im}} - 1}{\sqrt{\beta}}, \tag{2.10}$$

where the normalization factor is given by:

$$\beta = \frac{\sum_{\check{m}_{\mathrm{Re}}=0}^{M_{\mathrm{Re}}/2-1} \sum_{\check{m}_{\mathrm{Im}}=0}^{M_{\mathrm{Im}}/2-1} \left[(M_{\mathrm{Re}} - 2\check{m}_{\mathrm{Re}} - 1)^2 + (M_{\mathrm{Im}} - 2\check{m}_{\mathrm{Im}} - 1)^2\right]}{M/4}, \tag{2.11}$$

while the PAM indices m_{Re} and m_{Im} are Gray coded $\check{m}_{\mathrm{Re}}$ and $\check{m}_{\mathrm{Im}}$, respectively. We note that $s_{\mathrm{Re}}^{m_{\mathrm{Re}}} = \Re(s^m)$ and $s_{\mathrm{Im}}^{m_{\mathrm{Im}}} = \Im(s^m)$ constitute the real and the imaginary part of a Square MQAM symbol, where the operations $\Re(\cdot)$ and $\Im(\cdot)$ take the real part and the imaginary part of a complex number, respectively. Their index relationship is given by $m = \mathrm{bin2dec}(b_1 \cdots b_{\mathrm{BPS}}) = m_{\mathrm{Re}} + m_{\mathrm{Im}} M_{\mathrm{Re}}$. Furthermore, the index ranges of m, m_{Re} and m_{Im} seen in Eq. (2.10) are given by $[0 \leq m \leq (M-1)]$, $[0 \leq m_{\mathrm{Re}} \leq (M_{\mathrm{Re}} - 1)]$ and $[0 \leq m_{\mathrm{Im}} \leq (M_{\mathrm{Im}} - 1)]$, respectively.

More specifically, when $\mathrm{BPS} = \mathrm{BPS}_{\mathrm{Re}} + \mathrm{BPS}_{\mathrm{Im}}$ is an even number, we have $\mathrm{BPS}_{\mathrm{Re}} = \mathrm{BPS}_{\mathrm{Im}} = \mathrm{BPS}/2$ and $M_{\mathrm{Re}} = M_{\mathrm{Im}} = \sqrt{M}$. As a result, the modulated Square MQAM symbol of Eq. (2.10) may be rewritten as:

$$s^m = s_{\mathrm{Re}}^{m_{\mathrm{Re}}} + j s_{\mathrm{Im}}^{m_{\mathrm{Im}}} = \frac{\sqrt{M} - 2\check{m}_{\mathrm{Re}} - 1}{\sqrt{\beta}} + j\frac{\sqrt{M} - 2\check{m}_{\mathrm{Im}} - 1}{\sqrt{\beta}}, \tag{2.12}$$

where the corresponding normalization factor is given by:

$$\beta = \frac{\sum_{\check{m}_{\mathrm{Re}}=0}^{\sqrt{M}/2-1} \left[(\sqrt{M} - 2\check{m}_{\mathrm{Re}} - 1)^2\right]}{\sqrt{M}/4}. \tag{2.13}$$

Furthermore, when BPS is an odd number, we have $\mathrm{BPS}_{\mathrm{Re}} = \mathrm{BPS}_{\mathrm{Im}} + 1 = (\mathrm{BPS}+1)/2$ and $M_{\mathrm{Re}} = 2M_{\mathrm{Im}} = \sqrt{2M}$, while the corresponding modulated Square MQAM symbol has to be represented by the general expression of Eq. (2.11). In fact, for the case of an odd BPS, it was shown in [252] that Cross-shaped MQAM constellations actually have a better performance compared to their Square MQAM counterparts.

For a QAM scheme, the received signal model and the vector-by-vector based ML detection may also be represented by Eq. (2.1) and Eq. (2.4). However, the symbol power $\{|s^m|^2\}_{m=0}^{M-1}$ is no longer a constant over different candidate QAM symbols. Therefore, we have to normalize the power of the decorrelating variable as:

$$\widetilde{z}_n = \mathbf{Y}_n \mathbf{H}_n^H / \|\mathbf{H}_n\|^2, \tag{2.14}$$

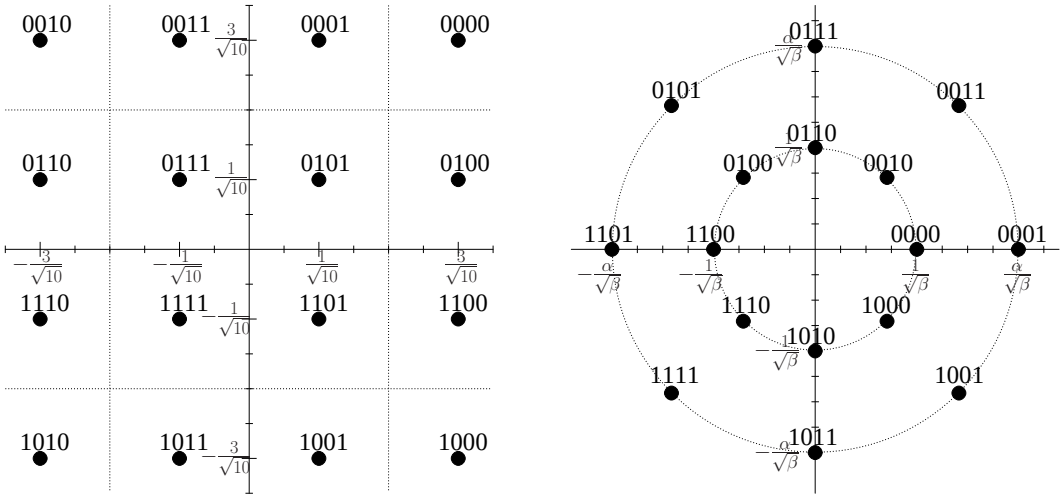

(a) Square 16QAM (b) Star 16QAM

Figure 2.5: Constellation Diagrams of Gray-labelled Square 16QAM and Star 16QAM.

so that the extension of Eq. (2.8) becomes:

$$|\widetilde{z}_n - s^m|^2 = |\widetilde{z}_n|^2 + |s^m|^2 - 2\Re\left[(s^m)^* \mathbf{Y}_n \mathbf{H}_n^H\right] / \|\mathbf{H}_n\|^2, \tag{2.15}$$

which is now equivalent to the vector-by-vector based ML detection metric of Eq. (2.7), because the fading channel's power $\|\mathbf{H}_n\|^2$ is a constant.

As a result, for a Square MQAM scheme, the real and the imaginary parts of $\widetilde{z}_n$ of Eq. (2.14) may be used for detecting the real and the imaginary part of s_n of Eq. (2.10), which may be expressed as:

$$\begin{aligned} \Re(\hat{s}_n) &= \frac{M_{\text{Re}} - 2\hat{\hat{m}}_{\text{Re}} - 1}{\sqrt{\beta}}, \\ \Im(\hat{s}_n) &= \frac{M_{\text{Im}} - 2\hat{\hat{m}}_{\text{Im}} - 1}{\sqrt{\beta}}, \end{aligned} \tag{2.16}$$

where the detected PAM indices are given by:

$$\begin{aligned} \hat{\hat{m}}_{\text{Re}} &= \max\left[\min\left(\lfloor q_{\text{Re}} \rceil, M_{\text{Re}} - 1\right), 0\right], \quad \text{where } q_{\text{Re}} = \left[M_{\text{Re}} - \sqrt{\beta}\Re(\widetilde{z}_n) - 1\right]/2, \\ \hat{\hat{m}}_{\text{Im}} &= \max\left[\min\left(\lfloor q_{\text{Im}} \rceil, M_{\text{Im}} - 1\right), 0\right], \quad \text{where } q_{\text{Im}} = \left[M_{\text{Im}} - \sqrt{\beta}\Im(\widetilde{z}_n) - 1\right]/2. \end{aligned} \tag{2.17}$$

Physically, Eq. (2.16) corresponds to the equalities of $\Re(\widetilde{z}_n) = s_{\text{Re}}^{m_{\text{Re}}}$ and $\Im(\widetilde{z}_n) = s_{\text{Im}}^{m_{\text{Im}}}$, and then quantizing the resultant indices q_{Re} and q_{Im} to their nearest legitimate PAM indices of $\hat{\hat{m}}_{\text{Re}}$ and $\hat{\hat{m}}_{\text{Im}}$, respectively.

2.2.2.2 Star QAM

A classic Star MQAM scheme [142, 155, 253] may encode the first $\text{BPS}_P = \log_2 M_P$ number of bits to a M_PPSK phasor index $p = \text{bin2dec}(b_1 \cdots b_{\text{BPS}_P})$, which modulates a M_PPSK phasor

$\{\Omega^p = \exp(j\frac{2\pi}{M_P}\check{p})\}_{p=0}^{M_P-1}$, where the index p is Gray coded $\check{p}$. The remaining $\text{BPS}_A = \log_2 M_A$ bits may be assigned for encoding a ring amplitude index $a = \text{bin2dec}(b_{\text{BPS}_P+1} \cdots b_{\text{BPS}})$, which corresponds to a specific ring amplitude of $\{\Gamma^a = \frac{\alpha^{\check{a}}}{\sqrt{\beta}}\}_{a=0}^{M_A-1}$, where the index a is Gray coded $\check{a}$, while α and β refers to the ring amplitude ratio and to the symbol power normalization factor, respectively. Furthermore, we have the modulation index $m = \text{bin2dec}(b_1 \cdots b_{\text{BPS}}) = a + pM_A$, which has the index range of $[0 \leq m \leq (M-1)]$. As a result, a modulated Star MQAM symbol may be represented by:

$$s^m = \Gamma^a \Omega^p = \frac{\alpha^{\check{a}}}{\sqrt{\beta}} \exp(j\frac{2\pi}{M_P}\check{p}), \tag{2.18}$$

where the symbol power normalization factor is given by:

$$\beta = \frac{\sum_{\check{a}=0}^{M_A-1} \alpha^{2\check{a}}}{M_A}. \tag{2.19}$$

It was shown in [155, 253] that for transmission over fading channels, Star MQAM schemes having an optimized ring ratio do not suffer from a substantial performance penalty compared to the classic Square MQAM schemes, despite their reduced Euclidean distance. For example, the twin-ring Star 16/32QAM associated with $\alpha = 2.0$ and the four-ring Star 64QAM associated with $\alpha = 1.4$ exhibit a performance close to their Square-QAM counterparts in Rayleigh fading channels. As an example, the constellation diagram of Star 16QAM is portrayed in Fig. 2.5b.

Similar to Square MQAM detection, the decision variable of $\widetilde{z}_n$ of Eq. (2.14) may be invoked for detecting the transmitted Star MQAM symbol of Eq. (2.18). In order to detect the phasor and the ring amplitude of a Star MQAM symbol separately, we return to the ML detection rule of Eq. (2.6), which may be simplified as:

$$\begin{aligned} \{\hat{\Gamma}_n, \hat{\Omega}_n\} &= \arg \min_{\forall \Gamma^a \in \mathbf{\Gamma}, \forall \Omega^p \in \mathbf{\Omega}} |\widetilde{z}_n - \Gamma^a \Omega^p|^2 \\ &= \arg \min_{\forall \Gamma^a \in \mathbf{\Gamma}, \forall \Omega^p \in \mathbf{\Omega}} (\Gamma^a)^2 - 2\Gamma^a \Re\left[(\Omega^p)^* \widetilde{z}_n\right]. \end{aligned} \tag{2.20}$$

If we define the local minimum metric of $\left\{(\Gamma^a)^2 - 2\Gamma^a \Re\left[(\Omega^p)^* \widetilde{z}_n\right]\right\}$ in Eq. (2.20) as the minimum over the set of M_PPSK phasors $\forall \Omega^p \in \mathbf{\Omega}$ only, then Eq. (2.20) may be transformed into:

$$\begin{aligned} \hat{\Omega}_n &= \arg \min_{\forall \Omega^p \in \mathbf{\Omega}} (\Gamma^a)^2 - 2\Gamma^a \Re\left[(\Omega^p)^* \widetilde{z}_n\right] \\ &= \arg \min_{\forall \Omega^p \in \mathbf{\Omega}} -2\Re\left[(\Omega^p)^* \widetilde{z}_n\right] \\ &= \arg \min_{\forall \Omega^p \in \mathbf{\Omega}} |\widetilde{z}_n - \Omega^p|^2, \end{aligned} \tag{2.21}$$

where a fixed ring amplitude is chosen from $\Gamma^a \in \mathbf{\Gamma}$. It can be seen in Eq. (2.21) that regardless of which ring amplitude $\{\Gamma^a\}_{a=0}^{M_A-1}$ is chosen, the optimum M_PPSK phasor can always be directly detected from $\widetilde{z}_n$, which may be explicitly expressed as the classic M_PPSK detection rule of:

$$\hat{\Omega}_n = \exp(j\frac{2\pi}{M_P}\hat{\check{p}}), \quad \text{where } \hat{\check{p}} = \lfloor \frac{M_P}{2\pi} \angle \widetilde{z}_n \rceil, \tag{2.22}$$

which is given by forcing the equality of $\angle \widetilde{z}_n = \frac{2\pi}{M_P}\check{p}$, and then rounding the resultant phasor index $\frac{M_P}{2\pi}\angle \widetilde{z}_n$ to its nearest legitimate M_PPSK phasor index. Furthermore, the global minimum in

Eq. (2.20) may be obtained by comparing all the local minima according to:

$$\begin{aligned}\hat{\Gamma}_n &= \arg \min_{\forall \Gamma^a \in \mathbf{\Gamma}} |\widetilde{z}_n - \Gamma^a \hat{\Omega}_n|^2 \\ &= \arg \min_{\forall \Gamma^a \in \mathbf{\Gamma}} (\Gamma^a)^2 - 2\Gamma^a \Re(\hat{\Omega}_n^* \widetilde{z}_n),\end{aligned} \tag{2.23}$$

where $\hat{\Omega}_n$ is obtained by Eq. (2.22). More specifically, for the case of twin-ring Star MQAM schemes, the last $\text{BPS}_A = 1$ bit which determines the ring amplitude may be detected according to Eq. (2.23) as:

$$\hat{b}_{\text{BPS}_P+1} = \begin{cases} 1, & \text{if } \Re(\hat{\Omega}_n^* \widetilde{z}_n) > \frac{\alpha+1}{2\sqrt{\beta}}, \\ 0, & \text{otherwise.} \end{cases} \tag{2.24}$$

Similarly, for the case of four-ring Star MQAM schemes, the last $\text{BPS}_A = 2$ bits which determine the ring amplitude may be detected according to Eq. (2.23) as:

$$\begin{aligned}\hat{b}_{\text{BPS}_P+1} &= \begin{cases} 1, & \text{if } \Re(\hat{\Omega}_n^* \widetilde{z}_n) > \frac{\alpha^2+\alpha}{2\sqrt{\beta}}, \\ 0, & \text{otherwise.} \end{cases} \\ \hat{b}_{\text{BPS}_P+2} &= \begin{cases} 1, & \text{if } \frac{\alpha+1}{2\sqrt{\beta}} < \Re(\hat{\Omega}_n^* \widetilde{z}_n) \leq \frac{\alpha^3+\alpha^2}{2\sqrt{\beta}}, \\ 0, & \text{otherwise.} \end{cases}\end{aligned} \tag{2.25}$$

Observe in Eq. (2.23) that the ML ring amplitude detection is completed with the aid of the detected phasor $\hat{\Omega}_n$. In fact, the Star MQAM detection process may be further simpified so that the ring amplitude and the phasor may be detected completely independently. More explicitly, as mentioned before, the M_PPSK phasor detection of Eq. (2.22) is given by forcing the equality of $\angle\widetilde{z}_n = \angle\Omega_n$. If we assume that the resultant phasor index is already a legitimate M_PPSK phasor index without the need of rounding, i.e. that we have $\hat{\tilde{p}} = \frac{M_P}{2\pi}\angle\widetilde{z}_n$ and hence $\angle\widetilde{z}_n = \angle\hat{\Omega}_n$, then the ring amplitude detection of Eq. (2.23) may be simplified as:

$$\begin{aligned}\hat{\Gamma}_n &= \arg \min_{\forall \Gamma^a \in \mathbf{\Gamma}} \left| |\widetilde{z}_n| \exp(j\angle\widetilde{z}_n) - \Gamma^a \hat{\Omega}_n \right|^2 \\ &= \arg \min_{\forall \Gamma^a \in \mathbf{\Gamma}} \left| |\widetilde{z}_n| - \Gamma^a \right|^2 \\ &= \arg \min_{\forall \Gamma^a \in \mathbf{\Gamma}} (\Gamma^a)^2 - 2\Gamma^a |\widetilde{z}_n|.\end{aligned} \tag{2.26}$$

Consequently, $\Re(\hat{\Omega}_n^* \widetilde{z}_n)$ seen in Eqs. (2.24) and (2.25) may all be replaced by $|\widetilde{z}_n|$. According to Eqs. (2.22) and (2.26), both the phase and the ring amplitude of a Star MQAM symbol are independently detected by $\angle\widetilde{z}_n$ and $|\widetilde{z}_n|$, respectively. In fact, this simplified method is detailed in [142], which relies on the aforementioned optimistic assumption of $\angle\widetilde{z}_n = \angle\hat{\Omega}_n$, and as a result this method does not have exactly the same detection capability as the ML Star MQAM detection of Eqs. (2.22) and (2.23). Nonetheless, the associated performance difference is negligible for coherent Star MQAM detection, which is evidenced by the performance results seen in Fig. 2.6. However, it is demonstrated in [159] that invoking completely independent amplitude-phase detection for noncoherent Star MQAM, which is also termed as Differential Amplitude-Phase Shift Keying (DAPSK), imposes a modest but non-negligible performance loss. We will further investigate this problem later in Chapter 4.

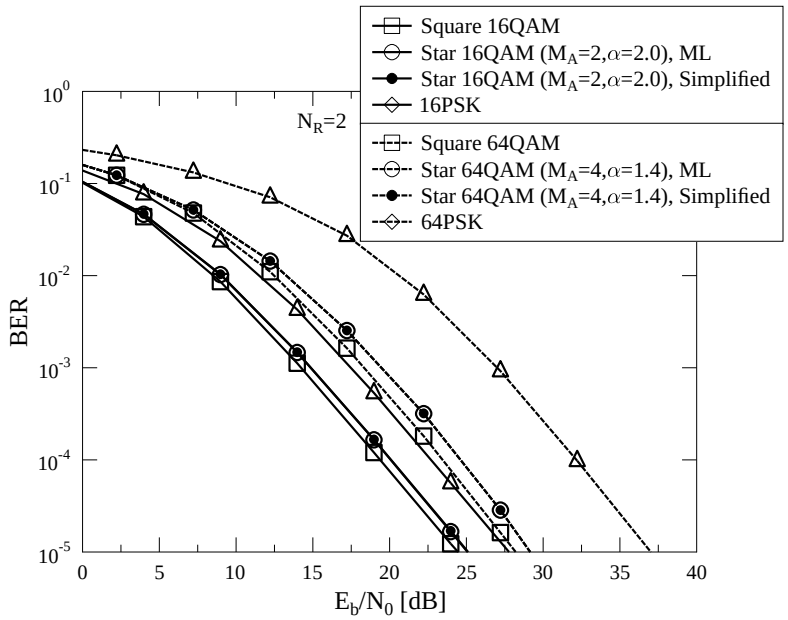

Figure 2.6: BER performance of Uncoded MPSK and Square/Star MQAM in Rayleigh fading channels, when $N_R = 2$ RAs are used. The ML Star MQAM detection is based on Eqs. (2.22) and (2.23), while the simplified Star MQAM detection is based on Eqs. (2.22) and (2.26).

The comparisons between MPSK and Square/Star MQAM constellations are characterized in Table 2.1. It can be seen that Square MQAM generally enjoys a higher minimum distance among its constellation points [2, 3, 141], which results in a superior performance, as demonstrated by Fig. 2.6. Furthermore, as suggested by [155, 253], Fig. 2.6 also verifies that for transmission over Rayleigh fading channels, Star MQAM schemes associated with optimized ring ratios are capable of achieving a comparable performance to their Square MQAM counterparts. Moreover, the minimum signal power $\min_{\forall s^m \in \mathbf{s}} |s^m|^2$ seen in Table 2.1 may also influence the performance of MPSK/QAM in certain communication systems (e.g. STSK of [141, 203]). We will further characterize this feature in Chapter 6.

2.3 Coded PSK and QAM

In this section, soft-decision-aided detectors conceived for coded MPSK/QAM schemes are investigated. The coded MPSK/QAM schemes considered in this section are not only assisted by powerful channel coding elements, but they are also detected with the aid of the powerful turbo principle [2, 8, 80, 239]. More explicitly, both the channel decoders and the MPSK/QAM detectors may be capable of receiving and producing soft-bit decisions, so that a near-capacity performance may be achieved by iteratively exchanging their decisions. Furthermore, we will introduce the theoretical principle and practical computation of EXIT charts [88], which constitute an effective tool conceived for designing different types of near-capacity systems.

	$\min_{\forall\{s^m \neq s^{m'}\}\in\mathbf{s}} \lvert s^m - s^{m'}\rvert$	$\min_{\forall s^m\in\mathbf{s}} \lvert s^m\rvert^2$
Square 16QAM	0.4	0.2
Star 16QAM ($M_A = 2$,$\alpha = 2$)	0.234	0.4
16PSK	0.152	1
Square 64QAM	0.0952	0.0476
Star 64QAM ($M_A = 4$,$\alpha = 1.4$)	0.0425	0.279
64PSK	0.0096	1

Table 2.1: Comparison of MPSK and Square/Star MQAM constellations.

2.3.1 Conventional Soft-Decision-Aided PSK/QAM Detection

The soft-bit decisions may be characterized in the form of Log Likelihood Ratios (LLRs) [27, 35] as:

$$\begin{aligned} L(b) &= \ln \frac{p(b=1)}{p(b=0)} \\ &= \ln \frac{p(b=1)}{1-p(b=1)}. \end{aligned} \tag{2.27}$$

The sign of the LLR $L(b)$ being positive or negative indicates that bit b is likely to be a logical 1 or a logical 0, respectively. Furthermore, the magnitude of $L(b)$ quantifies our confidence level concerning its sign. Explicitly, the higher the magnitude, the higher the possibility for bit b being either a logical 1 or a logical 0. Consequently, given a LLR value of $L(b)$, the corresponding probabilities of the bit b being 1 or 0 may be evaluated by:

$$\begin{aligned} p(b=1) &= \frac{e^{L(b)}}{1+e^{L(b)}}, \\ p(b=0) &= \frac{1}{1+e^{L(b)}}. \end{aligned} \tag{2.28}$$

The soft-decision-aided MPSK/QAM detectors aim for maximizing the *a posteriori* probability $p(s^m|\mathbf{Y}_n)$ of Eq. (2.2), given the conditional probability $p(\mathbf{Y}_n|s^m)$ expressed by Eq. (2.3), while the *a priori* probability $p(s^m)$ may now be obtained from a channel decoder[2]. More explicitly, according to Eq. (2.28), upon receiving the *a priori* LLRs $\{L_a(b_k)\}_{k=1}^{\mathrm{BPS}}$ from a channel decoder, the MPSK/QAM detector may evaluate the corresponding *a priori* probabilities for each constellation point $s^m \in \mathbf{s}$ as:

$$p(s^m) = \prod_{k=1}^{\mathrm{BPS}} \frac{\exp(\widetilde{b}_k^m L_a(b_k))}{1+\exp(L_a(b_k))}, \tag{2.29}$$

where $\{\widetilde{b}_k^m\}_{k=1}^{\mathrm{BPS}}$ refers to the bit-mapping arrangement for the specific constellation point $s^m \in \mathbf{s}$, where we have $(\widetilde{b}_1^m \cdots \widetilde{b}_{\mathrm{BPS}}^m) = \mathrm{dec2bin}(m)$. Taking QPSK of Fig. 2.4b as an example, the bit-mapping arrangements are given by $(\widetilde{b}_1^0\widetilde{b}_2^0 = 00)$,$(\widetilde{b}_1^1\widetilde{b}_2^1 = 01)$,$(\widetilde{b}_1^2\widetilde{b}_2^2 = 10)$ and $(\widetilde{b}_1^3\widetilde{b}_2^3 = 11)$ for the constellation points of $(s^0 = 1)$, $(s^1 = j)$, $(s^2 = -j)$ and $(s^3 = -1)$, respectively.

[2]For uncoded MPSK/QAM schemes in Sec. 2.2, the *a priori* probabilities $\{p(s^m)\}_{\forall s^m\in\mathbf{s}}$ are the same for all candidates as the transmitted symbol s_n is assumed to be equiprobable, i.e. we have $\{p(s^m) = \frac{1}{M}\}_{\forall s^m\in\mathbf{s}}$.

Furthermore, the resultant Log-MAP algorithm invoked by MPSK/QAM detection may be expressed as:

$$\begin{aligned} L_p(b_k) &= \ln \frac{\sum_{\forall s^m \in \mathbf{s}_{b_k=1}} p(s^m|\mathbf{Y}_n)}{\sum_{\forall s^m \in \mathbf{s}_{b_k=0}} p(s^m|\mathbf{Y}_n)} \\ &= \ln \frac{\sum_{\forall s^m \in \mathbf{s}_{b_k=1}} p(\mathbf{Y}_n|s^m)p(s^m)}{\sum_{\forall s^m \in \mathbf{s}_{b_k=0}} p(\mathbf{Y}_n|s^m)p(s^m)} \\ &= \ln \frac{\sum_{\forall s^m \in \mathbf{s}_{b_k=1}} \exp(d^m)}{\sum_{\forall s^m \in \mathbf{s}_{b_k=0}} \exp(d^m)} \\ &= L_a(b_k) + L_e(b_k), \end{aligned} \tag{2.30}$$

where $L_p(b_k)$ and $L_e(b_k)$ refer to the *a posteriori* LLR and to the extrinsic LLR produced by the MPSK/QAM detector, respectively, while $\mathbf{s}_{b_k=1}$ and $\mathbf{s}_{b_k=0}$ denote the MPSK/QAM subsets, when the specific bit b_k is fixed to 1 and 0, respectively. Furthermore, according to Eqs. (2.3) and (2.29), the probability metric $\{d^m\}_{m=0}^{M-1}$ seen in Eq. (2.30) is given by:

$$d^m = -\frac{\|\mathbf{Y}_n - s^m \mathbf{H}_n\|^2}{N_0} + \sum_{\bar{k}=1}^{\text{BPS}} \widetilde{b}_{\bar{k}}^m L_a(b_{\bar{k}}). \tag{2.31}$$

Taking QPSK constellation of Fig. 2.4b as an example, the four *a posteriori* probability metrics of Eq. (2.31) corresponding to the four QPSK constellation points $s^m \in \{1, j, -j, -1\}$ are given by:

$$\begin{aligned} d^0 &= -\frac{\|\mathbf{Y}_n - \mathbf{H}_n\|^2}{N_0}, \\ d^1 &= -\frac{\|\mathbf{Y}_n - j \cdot \mathbf{H}_n\|^2}{N_0} + L_a(b_2), \\ d^2 &= -\frac{\|\mathbf{Y}_n + j \cdot \mathbf{H}_n\|^2}{N_0} + L_a(b_1), \\ d^3 &= -\frac{\|\mathbf{Y}_n + \mathbf{H}_n\|^2}{N_0} + L_a(b_1) + L_a(b_2). \end{aligned} \tag{2.32}$$

As a result, the soft-decision-aided QPSK detector using the Log-MAP algorithm of Eq. (2.30) may produce the following soft-bit decisions:

$$\begin{aligned} L_p(b_1) &= \ln \frac{\exp(d^2) + \exp(d^3)}{\exp(d^0) + \exp(d^1)}, \\ L_p(b_2) &= \ln \frac{\exp(d^1) + \exp(d^3)}{\exp(d^0) + \exp(d^2)}. \end{aligned} \tag{2.33}$$

In practice, the Log-MAP algorithm of Eq. (2.30) imposes a potentially excessive detection complexity for high-order MPSK/QAM schemes, owing to its high-precision representation of probabilities. Therefore, when designing a low-complexity soft detector, the so-called Max-Log-MAP algorithm [27] may be invoked, which only considers the maxima of the d^m values in Eq. (2.31) associated with $\forall s^m \in \mathbf{s}_{b_k=1}$ and $\forall s^m \in \mathbf{s}_{b_k=0}$ respectively:

$$L_p(b_k) = \max_{\forall s^m \in \mathbf{s}_{b_k=1}} (d^m) - \max_{\forall s^m \in \mathbf{s}_{b_k=0}} (d^m). \tag{2.34}$$

$\|d^1 - d^2\|$	$\delta(\|d^1 - d^2\|)$
$\|d^1 - d^2\| > 3.7$	0
$2.25 < \|d^1 - d^2\| \leq 3.7$	0.05
$1.5 < \|d^1 - d^2\| \leq 2.25$	0.15
$1.05 < \|d^1 - d^2\| \leq 1.5$	0.25
$0.7 < \|d^1 - d^2\| \leq 1.05$	0.35
$0.43 < \|d^1 - d^2\| \leq 0.7$	0.45
$0.2 < \|d^1 - d^2\| \leq 0.43$	0.55
$\|d^1 - d^2\| \leq 0.2$	0.65

Table 2.2: Lookup table for the modified Jacobian algorithm [28, 239].

Since only the pair of maximum probability metrics are taken into account in Eq. (2.34), the Max-Log-MAP algorithm imposes a slight performance degradation. In order to compensate for this performance loss, the Approx-Log-MAP algorithm [28] was introduced as :

$$L_p(b_k) = \text{jac}_{\forall s^m \in \mathbf{s}_{b_k=1}} (d^m) - \text{jac}_{\forall s^m \in \mathbf{s}_{b_k=0}} (d^m), \tag{2.35}$$

where *jac* denotes the modified Jacobian algorithm, which may be expressed as [239]:

$$\text{jac}(d^1, d^2) = \max\ (d^1, d^2) + \delta(|d^1 - d^2|). \tag{2.36}$$

The addional term of $\delta(|d^1 - d^2|)$ in Eq. (2.36) takes into account the difference between d^1 and d^2 according to a lookup table, as demonstrated by Table 2.2 [28, 239]. Further details on these algorithms may be found in [239].

When MPSK is employed, as discussed in Sec. 2.2.1, the detector may be operated on a symbol-by-symbol basis, as seen in Eq. (2.6). Therefore, the probability metric evaluation of Eq. (2.31) may be simplified in the same way to:

$$d^m = -\frac{|z_n - s^m|^2}{N_0} + \sum_{\bar{k}=1}^{\text{BPS}} \widetilde{b}_{\bar{k}}^m L_a(b_{\bar{k}}), \tag{2.37}$$

where the decision variable z_n is given by Eq. (2.5), while the only differences between $-\frac{\|\mathbf{Y}_n - s^m \mathbf{H}_n\|^2}{N_0}$ in Eq. (2.31) and $-\frac{|z_n - s^m|^2}{N_0}$ in Eq. (2.37) are constants, which may be ignored by the division operation in the Log-MAP algorithm of Eq. (2.30).

Similarly, when MQAM is employed, the probability metric evaluation of Eq. (2.31) may be simplified to the same equation as Eq. (2.37), namely to:

$$d^m = -\frac{|\widetilde{z}_n - s^m|^2}{\widetilde{N}_0} + \sum_{\bar{k}=1}^{\text{BPS}} \widetilde{b}_{\bar{k}}^m L_a(b_{\bar{k}}), \tag{2.38}$$

with the difference that the decision variable $\widetilde{z}_n$ is given by Eq. (2.14), while the equivalent noise power is given by $\widetilde{N}_0 = N_0 / \|\mathbf{H}_n\|^2$.

To elaborate a little further, when Square MQAM is employed, the real and the imaginary parts of the constellation may be detected separately. As a result, the Square MQAM scheme's symbol probability metrics $\{d_{\text{Im}}^{m_{\text{Im}}}\}_{m_{\text{Im}}=0}^{M_{\text{Im}}-1}$ and $\{d_{\text{Re}}^{m_{\text{Re}}}\}_{m_{\text{Re}}=0}^{M_{\text{Re}}-1}$ are given by:

$$\begin{aligned} d_{\text{Im}}^{m_{\text{Im}}} &= -\frac{|\Im(\widetilde{z}_n) - s_{\text{Im}}^{m_{\text{Im}}}|^2}{\widetilde{N}_0} + \sum_{\bar{k}=1}^{\text{BPS}_{\text{Im}}} \widetilde{b}_{\bar{k}}^{m_{\text{Im}}} L_a(b_{\bar{k}}), \\ d_{\text{Re}}^{m_{\text{Re}}} &= -\frac{|\Re(\widetilde{z}_n) - s_{\text{Re}}^{m_{\text{Re}}}|^2}{\widetilde{N}_0} + \sum_{\bar{k}=\text{BPS}_{\text{Im}}+1}^{\text{BPS}} \widetilde{b}_{\bar{k}}^{m_{\text{Re}}} L_a(b_{\bar{k}}), \end{aligned} \tag{2.39}$$

where $\{s_{\text{Im}}^{m_{\text{Im}}}\}_{m_{\text{Im}}=0}^{M_{\text{Im}}-1}$ and $\{s_{\text{Re}}^{m_{\text{Re}}}\}_{m_{\text{Re}}=0}^{M_{\text{Re}}-1}$ refer to the M_{Im}PAM and M_{Re}PAM constellation sets for the imaginary part and the real part of the Square MQAM scheme, respectively.

2.3.2 EXtrinsic Information Transfer Charts

As more and more sophisticated concatenated codes are constructed for the sake of pursuing a near-capacity performance, one of the major design challenges is to predict and compare their E_b/N_0 convergence thresholds in order to choose the most appropriate channel coding and modulation parameters. Motivated by this challenge, researchers have focussed their attentions on characterizing the convergence behavior of turbo detection [48, 49, 85, 87, 88, 254]. In this section, we provide insights into the state-of-the-art EXtrinsic Information Transfer (EXIT) charts design tool [87, 88, 254], which effectively visualizes the flow of extrinsic information between the turbo detector components, so that their decoding convergence may be accurately predicted. We will introduce both their theoretical principles as well as the practical applications of EXIT charts.

2.3.2.1 Mutual Information and Transfer Characteristics

Let us assume that the data bits $b \in \{1, 0\}$ are equiprobable at the transmitter, i.e. we have $p(b = 1) = p(b = 0) = \frac{1}{2}$, while its corresponding LLR value L at the receiver is either a soft-valued input or a soft-valued output of a decoder/demapper. Then the mutual information between the random variables B and Λ modelling b and L respectively is given by [251]:

$$\begin{aligned} I(B;\Lambda) &= \sum_{b=1,0} \int_{-\infty}^{\infty} p(b,L) \log_2 \frac{p(b,L)}{p(b)p(L)} dL \\ &= \sum_{b=1,0} \int_{-\infty}^{\infty} p(L|b)p(b) \log_2 \frac{p(L|b)}{p(L|b=1)p(b=1) + p(L|b=0)p(b=0)} dL \\ &= \frac{1}{2} \sum_{b=1,0} \int_{-\infty}^{\infty} p(L|b) \log_2 \frac{2p(L|b)}{p(L|b=1) + p(L|b=0)} dL, \end{aligned} \tag{2.40}$$

where we have $p(b,L) = p(L|b)p(b)$ and $p(L) = \sum_{b=1,0} p(L|b)p(b)$ according to the definition of the joint probability and of the total probability, respectively. Furthermore, $p(L|b)$ may be obtained by evaluating the Probability Density Function (PDF) of the LLR L.

In order to investigate the flow of mutual information defined by Eq. (2.40) between the components of the receiver, the transfer characteristics of a decoder/demapper may be formulated

as [88, 92]:

$$I_E = T(I_A), \tag{2.41}$$

where the *a priori* information I_A and the extrinsic information I_E at the input and at the output of the transfer function T are given by $I(B;\Lambda_a)$ and $I(b;\Lambda_e)$ respectively according to Eq. (2.40), while Λ_a and Λ_e are random variables modelling L_a and L_e respectively.

The first step of obtaining I_E given I_A according to (2.41) is to generate a group of *a priori* LLRs L_a according to I_A. Then $I_E = I(B;\Lambda_e)$ may be evaluated according to Eq. (2.40), where the extrinsic LLRs L_e are obtained by feeding L_a to the decoder/demapper.

Let us assume that sufficiently long interleavers are employed between the concatenated components so that the LLRs exchanged by them may be deemed to be uncorrelated and Gaussian-distributed. Therefore, the LLR-generation based on the above-mentioned Gaussian distribution assumption may be performed as [88]:

$$L_a = \mu_A \cdot x + v \tag{2.42}$$

where v is a Gaussian random variable having a zero mean and a variance of σ_A^2, while we have $\mu_A = \frac{\sigma_A^2}{2}$. Furthermore, $x \in \{+1, -1\}$ in Eq. (2.42) is equivalent to source data bit $b \in \{1, 0\}$. Accordingly, the PDF of the *a priori* LLRs L_a generated by Eq. (2.42) is given by:

$$p(L_a|x) = \frac{1}{\sqrt{2\pi}\sigma_A} \exp\left[-\frac{(L_a - \frac{\sigma_A^2}{2}x)^2}{2\sigma_A^2}\right]. \tag{2.43}$$

The Gaussian PDF of (2.43) satisfies both the symmetry condition of $p(L_a|x) = p(-L_a|-x)$ and the consistency condition of $p(L_a|x=+1) = p(L_a|x=-1)e^{L_a}$. As a result, the mutual information of Eq. (2.40) may be rewritten for evaluating I_A as [88]:

$$\begin{aligned} I_A &= \frac{1}{2}\sum_{x=+1,-1}\int_{-\infty}^{\infty} p(L_a|x)\log_2\frac{2p(L_a|x)}{p(L_a|x=+1)+p(L_a|x=-1)}dL_a \\ &= 1 - \int_{-\infty}^{\infty} p(L_a|x=+1)\log_2\frac{p(L_a|x=+1)+p(L_a|x=-1)}{p(L_a|x=+1)}dL_a \\ &= 1 - \int_{-\infty}^{\infty} \frac{1}{\sqrt{2\pi}\sigma_A}\exp\left[-\frac{(L_a - \frac{\sigma_A^2}{2})^2}{2\sigma_A^2}\right]\log_2(1+e^{-L_a})dL_a, \end{aligned} \tag{2.44}$$

which may be simplified by an input-output relationship characterized by a function $J(\cdot)$ as:

$$I_A = J(\sigma_A), \tag{2.45}$$

where we have the input range of $\sigma_A \geq 0$ and output range of $0 \leq I_A \leq 1$. Furthermore, the function $J(\cdot)$ of Eq. (2.45) has the following properties:

$$\begin{aligned} \lim_{\sigma_A \to 0} J(\sigma_A) &= 0 \\ \lim_{\sigma_A \to \infty} J(\sigma_A) &= 1. \end{aligned} \tag{2.46}$$

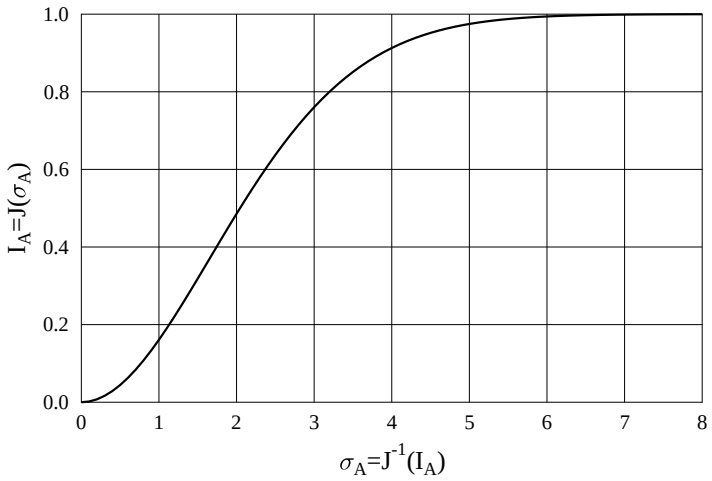

Figure 2.7: The function $J(\cdot)$ of Eq. (2.45).

Observe from Fig. 2.7 that the output I_A of function $J(\cdot)$ increases monotonically with respect to its input σ_A, hence its unique and unambiguous inverse function may be expressed as:

$$\sigma_A = J^{-1}(I_A). \tag{2.47}$$

Althougth the function $J(\cdot)$ and its inverse function $J^{-1}(\cdot)$ cannot be expressed in closed form [88], it is demonstrated in [255] that they can be approxmiated with negligible error as:

$$\begin{aligned} J(\sigma_A) &\approx \left(1 - 2^{-H_1 \sigma_A^{2H_2}}\right)^{H_3}, \\ J^{-1}(I_A) &\approx \left[-\frac{1}{H_1}\log_2(1 - I_A^{1/H_3})\right]^{1/(2H_2)}, \end{aligned} \tag{2.48}$$

where the parameters of $H_1 = 0.3073$, $H_2 = 0.8935$ and $H_3 = 1.1064$ were obtained by minimizing the squared difference between Eqs. (2.45) (2.47) and their approximations of Eq. (2.48).

Based on the previous discussions, we summarize the procedures of evaluating the transfer characteristics of Eq. (2.41) as:

Algorithm 2.1: EXIT module of Eq. (2.41)**.**

(1) For a specific *a priori* mutual information I_A, a group of *a priori* LLRs L_a may be generated according to Eq. (2.42), where the standard deviation σ_A of the Gaussian distribution is given by the inverse function of Eq. (2.47), i.e. we have $\sigma_A = J^{-1}(I_A)$.

(2) Upon feeding the generated soft-valued inputs L_a to the tested component decoder/demapper in the concatenated code, a group of extrinsic LLR outputs L_e may be obtained.

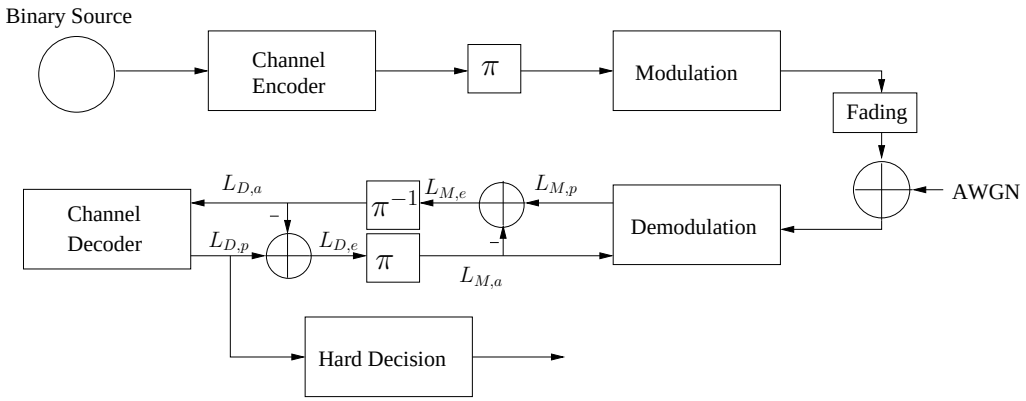

Figure 2.8: Schematics of a classic two-stage SCC.

(3) Finally, the extrinsic mutual information output of Eq. (2.41) may be computed according to Eq. (2.40) as:

$$I_E = \frac{1}{2} \sum_{b=1,0} \int_{-\infty}^{\infty} p(L_e|b) \log_2 \frac{2p(L_e|b)}{p(L_e|b=1) + p(L_e|b=0)} dL_e, \tag{2.49}$$

where the PDFs $p(L_e|b = 1)$ and $p(L_e|b = 0)$ may be obtained by evaluating the histograms of L_e [256] with respect to the source data bit being $b = 1$ and $b = 0$.

2.3.2.2 Concatenated Schemes

Concatenated schemes may be classified as Parallel Concatenated Coding (PCC), Serially Concatenated Coding (SCC) as well as Hybrid Concatenated Coding (HCC), where the latter combines both PCC and SCC [92]. The TC of Fig. 2.1 represents a classic PCC scheme, where the parity bits produced by the two RSC encoders are punctured at the transmitter, so that the two parallelly connnected RSC decoders of the receiver may process the parity bits of the upper and lower encoder alternatively. By contrast, the RSC coded MIMO arrangement of Fig. 2.2 exemplifies the popular SCC scheme, where the same number of bits are processed by both the RSC decoder and the MIMO demodulator at the receiver. Both the PCC and SCC schemes may be extended to have more than two component codes. As mentioned before, a URC is often incorportated in SCC as an intermediate component in order to eliminate the error floor of two-component SCC. The resultant three-stage SCC arrangement is demonstrated by Fig. 2.3. Furthermore, PCC may also be extended to multiple-stage turbo codes, as in [257, 258].

Let us consider the classic two-stage SCC of Fig. 2.8, where the pair of component codes may be classified as the inner and outer code. On one hand, the inner code typically processes both the channel's output and the *a priori* LLRs $L_{M,a}$, which are obtained by scrabbling the decoder's extrinsic LLRs $L_{D,e}$. On the other hand, the extrinsic LLRs of the inner code $L_{M,e}$ are de-interleaved

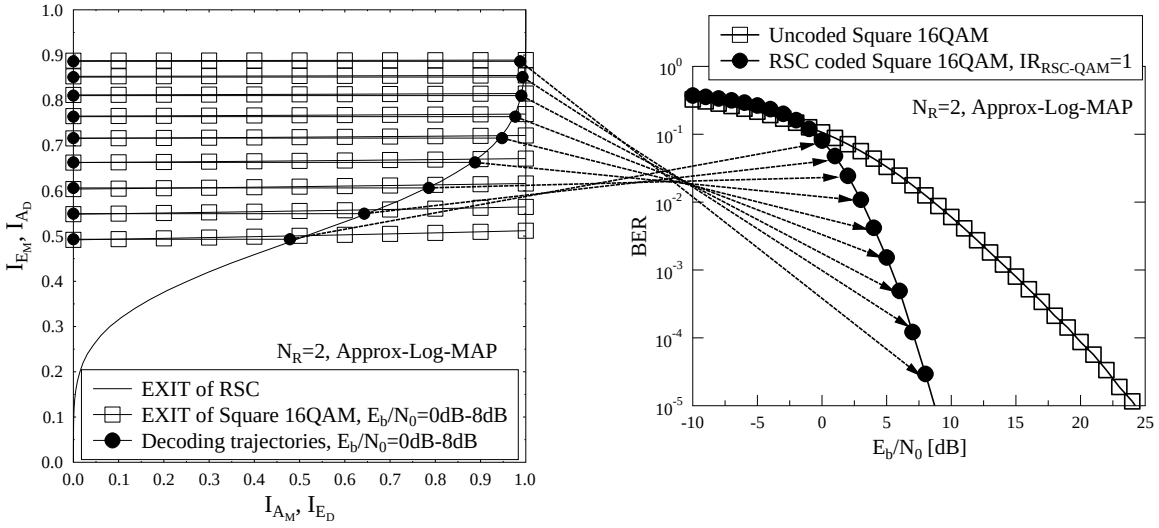

a) EXIT charts and decoding trajectories

b) BER performance

Figure 2.9: EXIT chart analysis and BER performance of the RSC coded Square 16QAM scheme of Fig. 2.8, where $N_R = 2$ RAs are employed. The corresponding simulation parameters are given by Table 2.3.

and fed to the decoder as *a priori* input $L_{D,a}$. Taking a RSC coded MPSK/QAM scheme as an example, the RSC decoder and the MPSK/QAM demodulator constitute the outer code and the inner code component, respectively. As a result, the mutual information transfer characteristics of the inner and the outer code may be expressed as:

$$\begin{aligned} I_{E_M} &= T_M(I_{A_M}, SNR), \\ I_{E_D} &= T_D(I_{A_D}), \end{aligned} \tag{2.50}$$

where the subscripts M and D refer to the demapper and decoder respectively, while naturally T_M of the inner code is a function of both the *a priori* information I_{A_M} and channel SNR.

The EXIT characteristics of both an inner Square 16QAM demapper introduced in Sec. 2.3.1 and of an outer RSC are portrayed in Fig. 2.9 a. The relationship between the SNR seen in Eq. (2.50) and the E_b/N_0 ratio seen in Fig. 2.9 is given by:

$$SNR\ (\text{dB}) = E_b/N_0 + \log_{10} R\ (\text{dB}), \tag{2.51}$$

where $R = R_c \cdot R_m$ refers to the overall throughput of the system, while R_c and R_m refer to the coding rate of the channel code and the modulation rate, respectively. The modulation rate is given by the number of bits per channel use which are mapped by the modulator, and we have $R_m =$ BPS for SISO/SIMO systems. Fig. 2.9a demonstrates that the intersections between the inner code's EXIT curve and the outer code's EXIT curve get closer to $I_{E_M} = I_{A_D} = 1.0$ as E_b/N_0 increases, which implies that the turbo detector's capability of enhancing our confidence in its input information gradually improves. The EXIT charts based performance prediction may be verified by the Monte-Carlo simulation based decoding trajectories and the BER performance curves, as seen

Modulation Scheme	MPSK/QAM defined in Sec. 2.2
Channel Model	SIMO channels ($N_T = 1, N_R \geq 1$) defined in Sec. 2.2
Channel Coding Scheme	Half-rate RSC associated with a constraint length of $K = 3$ and with a octal generator polynomial of $(G_r, G) = (7, 5)_8$
	Half-rate TC constituted by two half-rate RSCs and associated with the half-rate puncturing of the parity bits
	Unity-rate URC that serves as an intermediate code
	Half-rate IRCC introduced in Sec. 2.3.2.3
Number of iterations	$IR_{RSC-QAM}$ iterations between RSC decoder and QAM demapper
	IR_{TC} inner iterations between the two RSC decoders within a TC decoder
	IR_{TC-QAM} outer iterations between TC decoder and QAM demapper
	$IR_{URC-QAM}$ inner iterations between URC decoder and QAM demapper
	$IR_{RSC-\{URC-QAM\}}$ outer iterations between RSC decoder and the amalgamated URC-QAM decoder, where RSC may be replaced by IRCC
Frame Length	1,000,000 bits

Table 2.3: Simulation parameters of Sec. 2.3 and Sec. 2.4.

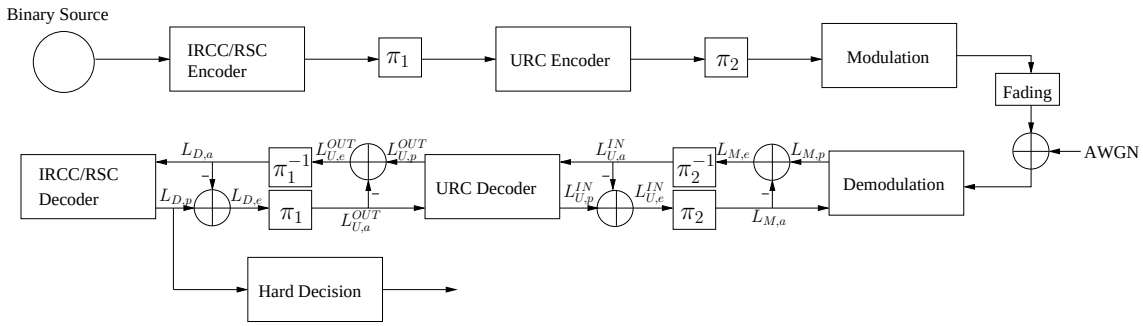

Figure 2.10: Schematics of a classic three-stage SCC.

in Fig. 2.9a and 2.9b. The corresponding simulation parameters are given by Table 2.3. Compared to the uncoded Square 16QAM scheme, the RSC coded Square 16QAM performs worse in the high-noise region of $E_b/N_0 < 0$ dB, because the channel code cannot correct bursts of errors that often occur in these hostile channel conditions. However, Fig. 2.9 shows that as predicted by the EXIT chart, the RSC coded Square 16QAM scheme gradually converges to a lower BER in the region of $E_b/N_0 > 0$ dB.

As demonstrated by Fig. 2.9a, perfect extrinsic information of $I_{E_D} = 1.0$ can only be safely achieved by the channel decoder, when perfect *a priori* information of $I_{A_D} = I_{E_M} = 1.0$ is provided by the demodulator, which requires an infinite SNR. This implies that a non-negligible BER exists, unless the inner code's EXIT curve and the outer code's EXIT curve only intersect at the (1.0,1.0) point. In order to achieve this goal, a URC may be introduced as an intermediate code as seen in Fig. 2.3, which equips the resultant concatenated scheme with a free distance of two that was shown to be the sufficient and neccessary condition for achieving an infinitesimally low BER [93,242]. For

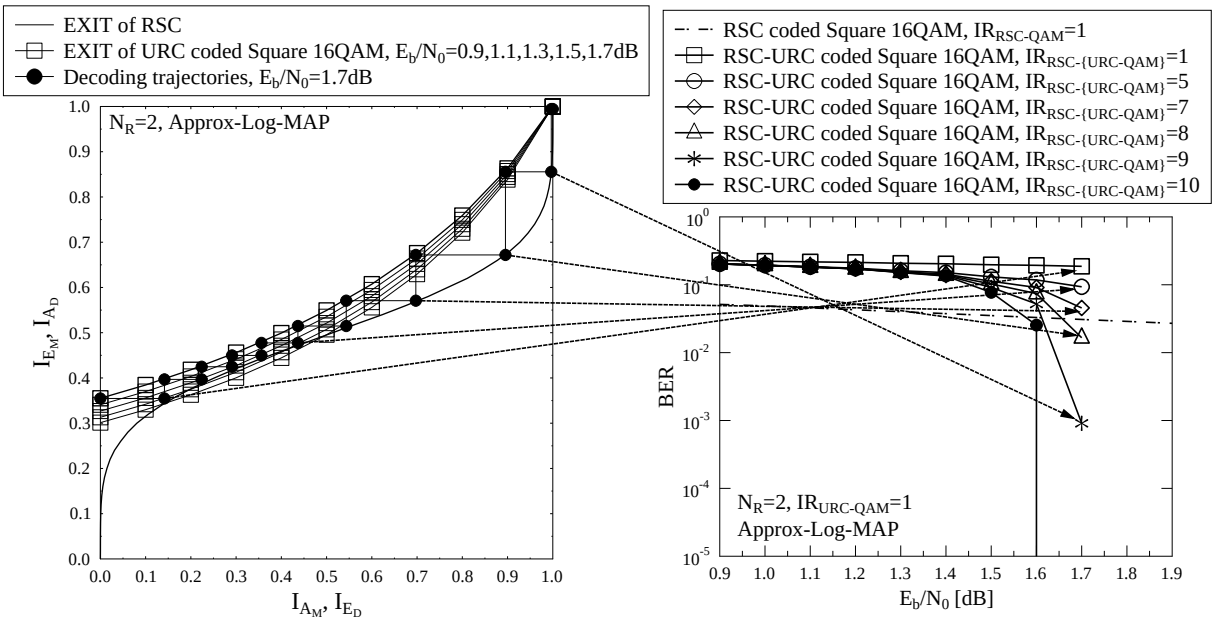

a) EXIT charts and decoding trajectories

b) BER performance

Figure 2.11: EXIT charts analysis and BER performance of the RSC and URC coded Square 16QAM scheme of Fig. 2.10, where $N_R = 2$ RAs are equipped. The corresponding simulation parameters are given by Table 2.3.

the three-stage turbo receiver of Fig. 2.10, the specific activation order of the component decoders is sometimes also referred to as scheduling in the related literature [255]. Moreover, in this treatise the terminology of 'activation order' is preferred to avoid confusion with 'scheduling' routinely used in resource-allocation. In order to simplify the receiver's analysis, the amalgamated URC and QAM decoder may be viewed as the amalgamated inner code, while the RSC as the outer code. The number of inner iterations may be set to $IR_{URC-QAM} = 1$ for the case of low-order PSK/QAM, whose demodulator does not exhibit a substantial iteration gain. It was also demonstrated in [233] that $IR_{URC-QAM} = 2$ is sufficient for the case of employing a modulation scheme (e.g. high-order PSK/QAM) which has a beneficial iteration gain, and only negligible performance improvements may be achieved upon increasing $IR_{URC-QAM}$ beyond 2.

Fig. 2.11 portrays the EXIT chart prediction as well as our Monte-Carlo simulation based performance results for a RSC and URC coded Square 16QAM scheme. It can be seen in Fig. 2.11a that an open tunnel emerges between the inner and outer codes' EXIT curves at $E_b/N_0 = 1.3$ dB, where the only intersection of the two curves is at the (1.0,1.0) point. More explicitly, the requirement for an open EXIT tunnel may be expressed as:

$$\begin{aligned} &T_M(I_{M_A}, SNR) > T_D^{-1}(I_{D_E}), \quad \text{when } I_{M_A} = I_{D_E} \in [0,1), \\ &T_M(I_{M_A}, SNR) = 1, \qquad\qquad\quad \text{when } I_{M_A} = I_{D_E} = 1. \end{aligned} \tag{2.52}$$

Since EXIT curves are obtained by averaging over numerous transmitted frames, the Monte-Carlo simulation based decoding trajectories are subject to small but potentially non-negligible deviations from the EXIT curves' prediction. As a result, it cannot be guaranteed that all Monte-Carlo simulation based decoding trajectories can get through the extremely narrow EXIT tunnel at $E_b/N_0 = 1.3$

dB seen in Fig. 2.11a. Nonetheless, Fig. 2.11b shows that an infinitesimally low BER is recorded at a slightly increased E_b/N_0 of 1.7 dB, which implies that all Monte-Carlo simulation based decoding trajectories recorded at $E_b/N_0 = 1.7$ dB can actually get through their open EXIT tunnels. An example of Monte-Carlo simulation based decoding trajectory recorded at $E_b/N_0 = 1.7$ is portrayed in Fig. 2.11a.

2.3.2.3 Capacity and Area Property

The concept of mutual information is popularly used for quantifying capacity. More explicitly, the Continuous-input Continuous-output Memoryless Channel (CCMC) capacity of the SIMO channels characterized in Eq. (2.1) is given by maximizing the mutual information between the channel's input and output signals as [17, 166]:

$$\begin{aligned} C^{CCMC}(SNR) &= \max_{p(s)} I(s;\mathbf{Y}) \\ &= \max_{p(s)} H(\mathbf{Y}) - H(\mathbf{Y}|s), \end{aligned} \tag{2.53}$$

where the operation $H(\cdot)$ evaluates the entropy of the random variable. Based on the Gaussian PDF $p(\mathbf{Y}|s)$ defined in Eq. (2.3), we have $H(\mathbf{Y}|s) = \log_2 \det[\pi e N_0 \mathbf{I}_{N_R}]$, where the operation $\det(\cdot)$ calculates the determinant of a matrix. Furthermore, it was suggested by Shannon [17, 166] that the maximum rate of Eq. (2.53) may be achieved when the input signal is also Gaussian distributed. Given a Gaussian-distributed input signal and Gaussian noise, the output signal is also Gaussian-distributed, and hence we have $H(\mathbf{Y}) = \log_2 \det\left[\pi e \left(\mathbf{H}^H\mathbf{H} + N_0\mathbf{I}_{N_R}\right)\right] = \log_2 (\pi e N_0)^{N_R} \left(1 + \frac{\|\mathbf{H}\|^2}{N_0}\right)$. In this way, the ergodic CCMC capacity, which defines the maximum rate of Eq. (2.53) averaged over all channel realizations, may be evaluated by [3, 17, 166]:

$$C^{\text{CCMC}}(SNR) = E\left[\log_2(1 + \eta \cdot \|\mathbf{H}\|^2)\right], \tag{2.54}$$

where SNR represents the logarithmic decibel scale of $\eta = \frac{1}{N_0}$, i.e. we have $SNR = 10\log_{10}\eta$ dB, while $\mathbf{H}$ refers to the randomly generated fading channel vector according to the received signal model of Eq. (2.1).

In practice, however, the modulated PSK/QAM symbols constitute a non-Gaussian channel input. As a result, the Discrete-input Continuous-output Memoryless Channel (DCMC) capacity represents the relevant performance bound, which is given by:

$$\begin{aligned} C^{DCMC}(SNR) &= \max_{p(s)} I(s;\mathbf{Y}) \\ &= \max_{\{p(s^m)\}_{m=0}^{M-1}} \sum_{m=0}^{M-1} \int p(s^m,\mathbf{Y}) \log_2 \frac{p(s^m,\mathbf{Y})}{p(s^m)p(\mathbf{Y})} d\mathbf{Y} \\ &= \max_{\{p(s^m)\}_{m=0}^{M-1}} \sum_{m=0}^{M-1} \int p(\mathbf{Y}|s^m)p(s^m) \log_2 \frac{p(\mathbf{Y}|s^m)}{\sum_{\bar{m}=0}^{M-1} p(\mathbf{Y}|s^{\bar{m}})p(s^{\bar{m}})} d\mathbf{Y}. \end{aligned} \tag{2.55}$$

The DCMC capacity of Eq. (2.55) is maximized, when the modulated PSK/QAM symbols are equiprobable, i.e. we have $\{p(s^m) = \frac{1}{M}\}_{m=0}^{M-1}$. According to the conditional PDF $p(\mathbf{Y}|s^m)$ given

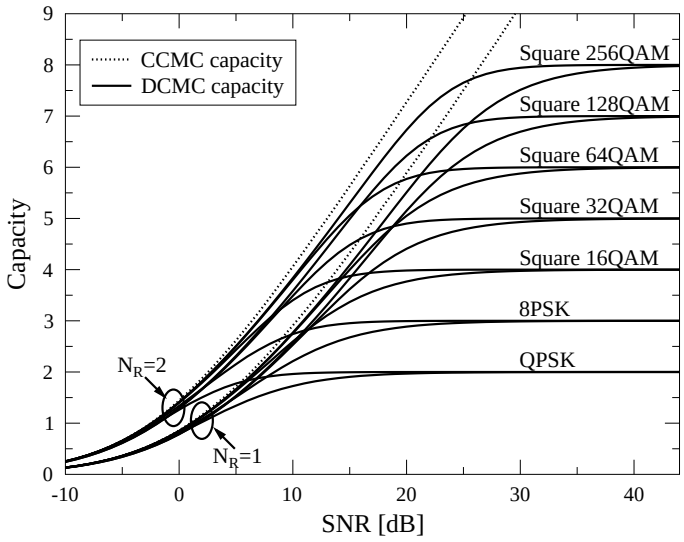

Figure 2.12: CCMC capacity and DCMC capability of MPSK/QAM schemes in SIMO fading channels characterized by Eq. (2.1).

by Eq. (2.3), Eq. (2.55) may be further simplified as [244]:

$$\begin{aligned} C^{DCMC}(SNR) &= \log_2 M - \frac{1}{M}\sum_{m=0}^{M-1}\int p(\mathbf{Y}|s^m)\log_2\frac{\sum_{\bar{m}=0}^{M-1} p(\mathbf{Y}|s^{\bar{m}})}{p(\mathbf{Y}|s^m)}d\mathbf{Y} \\ &= \text{BPS} - \frac{1}{M}\sum_{m=0}^{M-1} E\left\{\log_2\left[\sum_{\bar{m}=0}^{M-1}\exp\left(\frac{-\|(s^m - s^{\bar{m}})\mathbf{H} + \mathbf{V}\|^2 + \|\mathbf{V}\|^2}{N_0}\right)\right]\right\}, \end{aligned} \tag{2.56}$$

where $\mathbf{V}$ is an AWGN vector generated according to Eq. (2.1). According to Eq. (2.56), the maximum achievable rate of an MPSK/QAM scheme is given by:

$$C_{max}^{DCMC} = R_m. \tag{2.57}$$

Fig. 2.12 portrays both the CCMC and DCMC capacities of the MPSK/QAM schemes in Rayleigh fading channels. It can be seen that as the number of modulation levels M increases, the signal input to the channel becomes more Gaussian-like and hence a higher bandwidth efficiency is achieved. However, high-order QAM schemes require a higher SNR for their DCMC capacities to tend towards their C_{max}^{DCMC}, as evidenced by Fig. 2.12. Furthermore, it may be observed in Fig. 2.12 that the SNR required for achieving C_{max}^{DCMC} is reduced, when more RAs are employed.

Upon comparing the DCMC capacity definition of Eq. (2.55) and the extrinsic information of Eq. (2.49), it can be seen that Eq. (2.49) may be interpreted as a detection-directed rate estimation regime, where the input and output signals of the "channel" are the source bits and the detector's extrinsic output, respectively. This leads us to the so-called area property of EXIT chart [91, 259],

which relates the area under the EXIT curve of a MPSK/QAM demapper $\overline{A}_M(SNR)$ and the achievable DCMC capacity to each other as:

$$\begin{aligned}\overline{A}_M(SNR) &= \int_0^1 T_M(I_A, SNR)dI_A \\ &\approx \frac{C^{DCMC}(SNR)}{\text{BPS}},\end{aligned} \tag{2.58}$$

where the MAP detection algorithm is assumed to be used by the MPSK/QAM demapper, while the *a priori* LLRs fed to the MPSK/QAM demapper are assumed to be Gaussian-distributed.

Similarly, the area $\overline{A}_D$ under the EXIT curve of the channel decoder is related to the coding rate as:

$$\begin{aligned}\overline{A}_D &= \int_0^1 T_D(I_A)dI_A \\ &= 1 - \int_0^1 T_D^{-1}(I_E)dI_E \\ &\approx 1 - R_c.\end{aligned} \tag{2.59}$$

A variety of near-capacity systems have been designed in [8, 86, 88, 243, 260] by matching the EXIT curve shapes of the inner and outer codes, so that an open tunnel may be encountered at the lowest possible E_b/N_0. For the extreme situation of having an infinitesimally small open tunnel, there is supposed to be a perfect match between the EXIT curves of the inner and outer codes, which corresponds to $\overline{A}_M(SNR) \approx 1 - \overline{A}_D$, where the maximum achievable rate is attained according to Eqs. (2.58) and (2.59) as[3]:

$$C^{DCMC}(\overline{SNR}) = R_c \cdot R_m = R_c \cdot C_{max}^{DCMC}, \tag{2.60}$$

where $\overline{SNR}$ refers to the particular SNR which is required for the equality of Eq. (2.60). Let us now elaborate a little further on the situation of $SNR < \overline{SNR}$, where we have $C^{DCMC}(SNR) < C^{DCMC}(\overline{SNR})$, which implies that apparently the system's maximum throughput has not been achieved in full. Moreover, according to the area property of Eqs. (2.58) and (2.59), we have $\overline{A}_M(SNR) < 1 - \overline{A}_D$ at $SNR < \overline{SNR}$, which clearly contradicts with the conditions to be satisfied for having an open tunnel, as specified in Eq. (2.52). In other words, an error-free transmission at a SNR that is lower than $\overline{SNR}$ is not theoretically possible. By contrast, for $SNR > \overline{SNR}$, the modulation scheme's DCMC capacity may further increase, but the system's throughput remains at the full rate of $R = R_c \cdot R_m$. Therefore, a near-capacity system's design may aim for achieving an infinitesimally low BER at a SNR, which is supposed to be higher than $\overline{SNR}$, but at the same time it should be as close to $\overline{SNR}$ as possible, so that an error-free transmission may be achieved at the lowest possible SNR.

In order to approach to this goal, on the one hand, numerous researchers have focused their attention on how to design optimized modulation schemes so that their EXIT curves may match

[3] According to the requirements for having an open tunnel as expressed in Eq. (2.52), the maximum achievable rate specified in Eq. (2.60) can never be attained, because we shall always have $\overline{A}_M(SNR) > 1 - \overline{A}_D$.

the shape of the outer channel code's EXIT curve. This topic is widely known as bit-to-symbol mapping optimization for Bit-Interleaved Coded Modulation relying on Iterative Decoding (BICM-ID) [250, 260–264]. On the other hand, as the family of modulation schemes keeps evolving, especially in MIMO applications, it becomes more feasible to adjust the channel decoder's transfer characteristics, as seen in [86, 243, 265]. We only consider the latter case in this report.

The 17-point IRregular Convolutional Code (IRCC) proposed in [86] is a popular implementation of the aforementioned near-capacity design. More explicitly, the 17-point IRCC is constituted by 17 subcodes associated with code rates of $\{r_k = 0.1 + (k-1) \cdot 0.05\}_{k=1}^{17}$. These subcodes are constructed from a systematic half-rate memory-four mother code, which is defined by the octally represented generator polynomial of $(G_r, G) = (31, 27)_8$. Subcodes with higher rates are obtained by puncturing, while subcodes with lower rates are created by adding more generators and by puncturing. Given the appropriate weighting coefficients of $\{0 \leq \alpha_k \leq 1\}_{k=1}^{17}$, each subcode may encode $\alpha_k \cdot r_k \cdot N_c$ information bits to $\alpha_k \cdot N_c$ coded bits, where N_c refers to the frame length. The IRCC's coefficients have to satisfy the following two conditions:

$$\begin{aligned} \sum_{k=1}^{17} \alpha_k &= 1, \\ \sum_{k=1}^{17} \alpha_k r_k &= R_c. \end{aligned} \tag{2.61}$$

As a result, the transfer function of the outer IRCC may be characterized by the weighted superposition of the subcodes' mutual information transfer functions $\{T_{D,k}(I_A)\}_{k=1}^{17}$ as:

$$T_D(I_A) = \sum_{k=1}^{17} \alpha_k T_{D,k}(I_A), \tag{2.62}$$

where all subcodes are assumed to produce LLRs associated with symmetric and consistent PDFs. In summary, the IRCC's weighting coefficients may be obtained by minimizing the Mean Squared Error (MSE) between the mutual information transfer functions of the inner and the outer codes according to:

$$\{\alpha_k\}_{k=1}^{17} = \arg \min_{\{\alpha_k\}_{k=1}^{17}} \int_0^1 |T_D(I) - T_M^{-1}(I, SNR)|^2 dI. \tag{2.63}$$

We note that the search formulated in Eq. (2.63) may start with the maximum achievable rate's $\overline{SNR}$. If the resultant weighting coefficients cannot produce an EXIT curve for the outer code that matches the inner code's EXIT curve sufficiently well, then SNR shall be increased and Eq. (2.63) is repeatedly evaluated, until a valid group of weighting coefficients of $\{\alpha_k\}_{k=1}^{17}$ is obtained.

Fig. 2.13 portrays the EXIT chart prediction and Monte-Carlo simulation based performance of an IRCC and URC coded Square 16QAM scheme. The 17-point IRCC's coefficients evaluated from Eq. (2.63) are given by [0.0154826, 0, 0, 0, 0, 0, 0.661138, 0, 0, 0, 0, 0.106681, 0.151967, 0, 0, 0, 0.064775], which is closely matched to the EXIT curve of the amalgamated URC and QAM detector's EXIT curve at $E_b/N_0 = 0.6$ dB. Fig. 2.13b shows that an infinitesimally low BER is achieved by the IRCC coded scheme at $E_b/N_0 = 0.9$ dB, and the corresponding decoding trajectory is presented in Fig. 2.13a. Furthermore, it can be seen in Fig. 2.13b that the IRCC coded

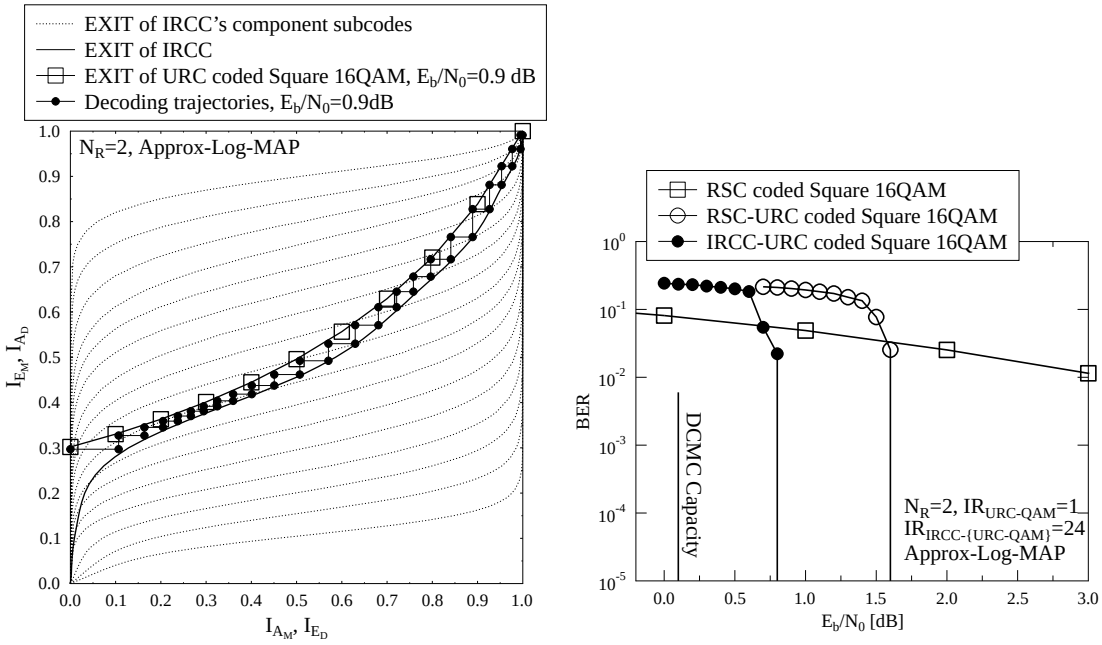

a) EXIT charts and decoding trajectories

b) BER performance

Figure 2.13: EXIT chart analysis and BER performance of the IRCC and URC coded Square 16QAM scheme of Fig. 2.10, where $N_R = 2$ RAs are used. The IRCC's coefficients are given by [0.0154826, 0, 0, 0, 0, 0, 0.661138, 0, 0, 0, 0, 0.106681, 0.151967, 0, 0, 0, 0.064775]. The corresponding simulation parameters are given by Table 2.3.

scheme outperforms the conventional RSC coded scheme by 0.8 dB, and its performance is only 0.7 dB away from the DCMC capacity limit.

2.3.2.4 Efficient Computation and Examination of EXIT Charts

If we assume that the PDF $p(L_e|b)$ of the extrinsic LLRs is symmetric and consistent, then the extrinsic information evaluation of Eq. (2.49) may be simplified by the following averaging method [86]:

$$\begin{aligned} I_E &= 1 - \int_{-\infty}^{\infty} p(L_e|x=+1)\log_2(1+e^{-L_e})dL_e \\ &= 1 - E_{x=+1}\left[\log_2(1+e^{-L_e})\right] \\ &\approx 1 - \frac{1}{N_c}\sum_{n=1}^{N_c}\left[\log_2(1+e^{-x[n]\cdot L_e[n]})\right], \end{aligned} \tag{2.64}$$

where $\{x[n]\}_{n=1}^{N_c}$ are equivalent to the source bits $\{b[n]\}_{n=1}^{N_c}$, while $\{L_e[n]\}_{n=1}^{N_c}$ represents the extrinsic LLRs produced by the demapper/decoder. It was discussed in [49, 86, 266] that the assumption of PDF symmetry may be granted, as long as the input PDFs including the PDFs of both *a priori* LLRs and of the channel's output signal are symmetric. Moreover, the assumption of PDF consistency should be valid all the time so that the LLR definition of Eqs. (2.27) and (2.28) may be guaranteed. Furthermore, we note that Eq. (2.64) is averaged over both $x = +1$ and $x = -1$ owing to the symmetry property.

It may be observed in Eq. (2.64) that the histograms $p(L_e|b=1)$ and $p(L_e|b=0)$ in Eq. (2.49) no longer have to be evaluated. However, the souce bits are assumed to be known for the evaluation of Eq. (2.64), which means that this method can only be used "off-line" namely, when the receiver can get access to the source bits. In order to circumvent this problem, an alternative computation method for the extrinsic information is presented in [89–91] as:

$$\begin{aligned} I_E &= H(X) - H(X|\Lambda_e) \\ &= 1 + p(x=+1|L_e)\log_2 p(x=+1|L_e) + p(x=-1|L_e)\log_2 p(x=-1|L_e) \\ &= 1 + E\left[\frac{e^{L_e}}{1+e^{L_e}}\log_2\left(\frac{e^{L_e}}{1+e^{L_e}}\right) + \frac{1}{1+e^{L_e}}\log_2\left(\frac{1}{1+e^{L_e}}\right)\right], \\ &\approx \frac{1}{N_c}\sum_{n=1}^{N_c}\left[\frac{e^{L_e[n]}}{1+e^{L_e[n]}}\log_2\left(\frac{2e^{L_e[n]}}{1+e^{L_e[n]}}\right) + \frac{1}{1+e^{L_e[n]}}\log_2\left(\frac{2}{1+e^{L_e[n]}}\right)\right], \end{aligned} \tag{2.65}$$

where we have $H(X) = 1$ because of the equiprobable source $x \in \{\pm 1\}$. With the aid of Eq. (2.65), the EXIT charts may be constructed "on-line", because as soon as new extrinsic LLRs become available at the receiver, they can be used for updating the current estimate of the mutual information [92].

As mentioned before, the efficient computation of Eqs. (2.64) and (2.65) is based on the important assumption of satisfying the symmetric condition of $p(L_e|x) = p(-L_e|-x)$ and the consistency condition of $p(L_e|x=+1) = p(L_e|x=-1)e^{L_e}$. If the symmetricity condition cannot be satisfied, the histogram-based Eq. (2.49) has to be invoked for evaluating I_E. However, if the consistency condition cannot be guaranteed, the LLR definition of Eq. (2.27) will be violated. Let us elaborate a little further here. The consistency condition of $p(L_e|b=1) = p(L_e|b=0)e^{L_e}$ leads to the following relationship:

$$L_e = \ln\frac{p(L_e|b=1)}{p(L_e|b=0)} = \ln\frac{p(b=1|L_e)}{p(b=0|L_e)}, \tag{2.66}$$

because we have $p(b|L_e) = \frac{p(L_e|b)p(b)}{\sum_{b=\{1,0\}} p(L_e|b)p(b)}$ according to Bayes' law [251], and we have $\{p(b) = 0.5\}_{b=\{1,0\}}$ for equiprobable source bits, the extrinsic LLRs satisfy the relationship defined by Eq. (2.66), their LLR values may be deemed as valid [49, 86, 266] according to the LLR definition of Eq. (2.27). Therefore, Eq. (2.66) may be used for testing the performance of virtually all soft-decision-aided demappers/decoders, and this method is termed as the LLR validity test in this treatise.

Let us consider the Square MQAM demodulator in conjunction with the Approx-Log-MAP algorithm of Eq. (2.35) and Max-Log-MAP algorithm of Eq. (2.34) as an example. It can be seen in Fig. 2.14a that Max-Log-MAP decoder introduces a performance loss, which is more noticeable as the number of modulation levels M increases, because more probability metrics of Eq. (2.39) are ignored by the Max-Log-MAP decoder of Eq. (2.34). Moreover, the accuracy of the extrinsic LLRs produced by the Square 256QAM demodulator using the Approx-Log-MAP and Max-Log-MAP algorithms are tested as portrayed in Fig. 2.14b, where the two PDFs $\{p(L_e|b)\}_{b=\{0,1\}}$ may be obtained by estimating the histograms of L_e, with the source bits being $b = \{0,1\}$. In other

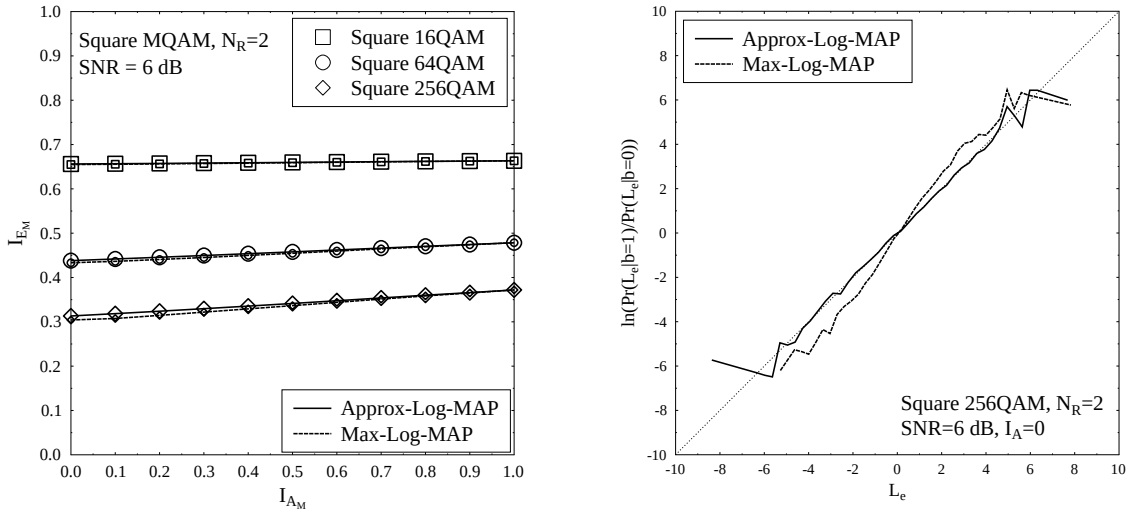

(a) EXIT charts

(b) LLR validity test

Figure 2.14: EXIT charts of Square MQAM demodulator using Approx-Log-MAP and Max-Log-MAP algorithms, as well as the LLR validity test for the Square 256QAM demodulator.

words, $\{p(L_e|b)\}_{b=\{0,1\}}$ scaled on the y-axis in Fig. 2.14b represents the magnitudes of the histograms' bins, while L_e scaled on the x-axis represents the locations of the histograms' bins. If $L_e = \ln\frac{p(L_e|b=1)}{p(L_e|b=0)}$ of Eq. (2.66) is statistically true, then the LLRs validity test is supposed to result in a diagonal line in Fig. 2.14b. However, as demonstrated by Fig. 2.14b, the LLRs of the Max-Log-MAP decoder suffer from a noticeable deviation, which implies that the Max-Log-MAP decoder's soft output is arguably less reliable than the LLRs produced by the Approx-Log-MAP algorithm.

Fig. 2.15a portrays our performance comparison between the Approx-Log-MAP and Max-Log-MAP algorithms, when they are invoked for Square 256QAM detection in a variety of coded systems, while the Monte-Carlo simulation based decoding trajectories are recorded in Fig. 2.15b. It can be seen that the performance difference between the Approx-Log-MAP and Max-Log-MAP decoders becomes more obvious for complex channel coding aided systems exemplified by the IRCC and URC schemes. We note that the modest performance loss imposed by the Max-Log-MAP decoder is generally expected and acceptable. Our comparison between the Approx-Log-MAP and Max-Log-MAP algorithms is only exemplified here in order to demonstrate the efficiency of the LLRs validity test. Generally speaking, if the L_e versus $\ln\frac{p(L_e|b=1)}{p(L_e|b=0)}$ plot of Fig. 2.14b severely deviates from the diagonal line, the demapper/decoder has to be carefully checked and revised so that reliable LLRs may be produced. Furthermore, if the demapper/decoder is a low-complexity sub-optimal one (e.g. the MMSE multi-user detector often produces less reliable LLRs), LLR post-processing [8] may be invoked for shaping the L_e versus $\ln\frac{p(L_e|b=1)}{p(L_e|b=0)}$ plot.

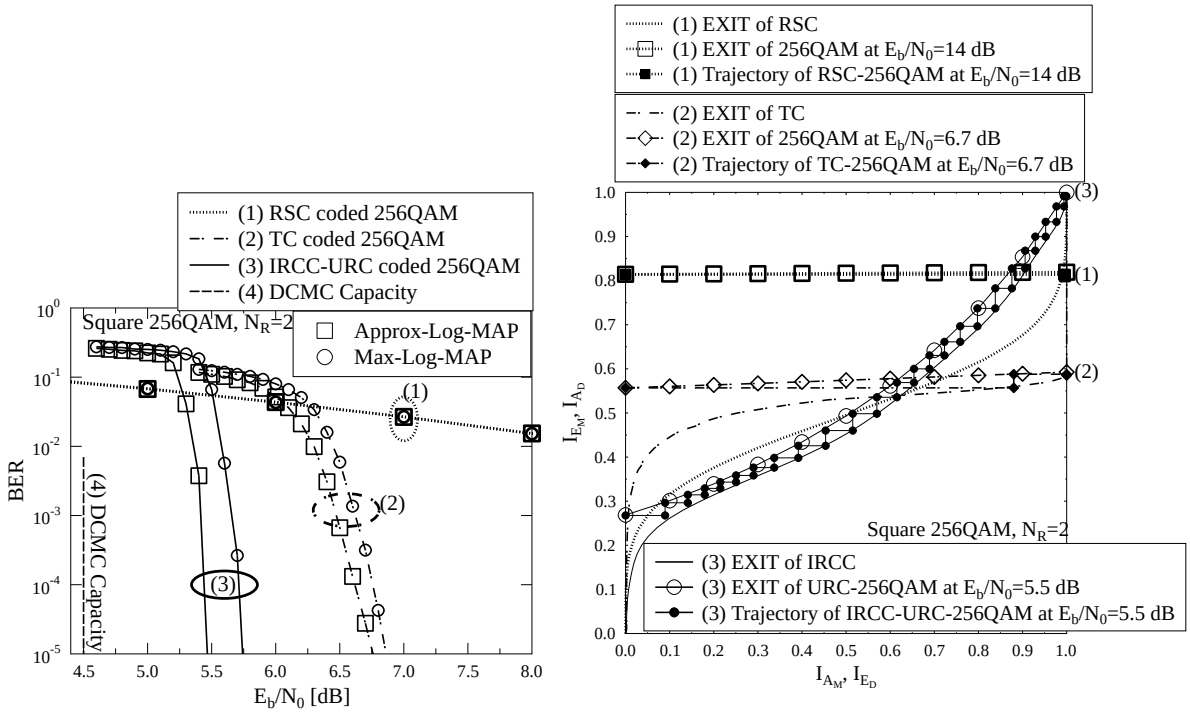

(a) BER performance

(b) Decoding trajectories

Figure 2.15: BER performance and decoding trajectories of RSC coded Square 256QAM ($IR_{RSC-QAM} = 2$), TC coded Square 256QAM ($IR_{TC} = 4$,$IR_{TC-QAM} = 2$) and IRCC-URC coded Square 256QAM ($IR_{URC-QAM} = 2$,$IR_{IRCC-\{URC-QAM\}} = 30$), where $N_R = 2$ RAs are equipped. The IRCC's coefficients are given by [0.0113078, 0, 0, 0, 0, 0.449189, 0.0859921, 0.0178352, 0, 0.129073, 0, 0.0962122, 0.103771, 0, 0.0184346, 0.0211703, 0.0670265]. The schematics of Figs. 2.8 and 2.10 are used.

2.4 Reduced-Complexity Coded PSK and QAM

After adapting the MPSK/QAM detectors of Sec. 2.2 for turbo detection according to [8, 240, 241], the receiver's complexity is inevitably increased as a result of iterative demodulation and decoding. To mitigate this problem, a new reduced-complexity design may be proposed for soft-decision-aided MPSK/QAM detectors, where only a reduced-size subset of the MPSK/QAM constellation points is taken into account for producing a single soft decision. In contrast to the soft-metric generation methods of [245–247], our reduced-complexity soft MPSK/QAM detectors retain their optimal unimpaired detection capabilities. We note that the reduced-complexity design introduced in this section is from our publication of [236].

2.4.1 Reduced-Complexity Soft-Decision-Aided Square QAM Detection

For producing a single soft-bit output, the conventional Max-Log-MAP algorithm of Eq. (2.34) as well as the Approx-Log-MAP algorithm of Eq. (2.35) have to estimate and compare all the M_{Re} and

M_{Im} probability metrics using Eq. (2.39) according to the M_{Re}PAM and M_{Im}PAM constellations, which forms the real part and the imaginary part of a Square MQAM symbol, respectively. In this section, we aim for reducing the detection complexity by reducing the number of constellation points that have to be visited.

First of all, let us extend the probability metric of the imaginary part in Eq. (2.39) as:

$$d_{\mathrm{Im}}^{m_{\mathrm{Im}}} = -\frac{|\Im(\widetilde{z}_n)|^2}{\widetilde{N}_0} - \frac{|s_{\mathrm{Im}}^{m_{\mathrm{Im}}}|^2}{\widetilde{N}_0} + \frac{2\Im(\widetilde{z}_n)s_{\mathrm{Im}}^{m_{\mathrm{Im}}}}{\widetilde{N}_0} + \sum_{\bar{k}=1}^{\mathrm{BPS}_{\mathrm{Im}}} \widetilde{b}_{\bar{k}}^{m_{\mathrm{Im}}} L_a(b_{\bar{k}}), \tag{2.67}$$

where $\left(-\frac{|\Im(\widetilde{z}_n)|^2}{\widetilde{N}_0}\right)$ is a constant for all the candidate variables $\{s_{\mathrm{Im}}^{m_{\mathrm{Im}}}\}_{m_{\mathrm{Im}}=0}^{M_{\mathrm{Im}}-1}$. Hence it may be ignored, because all the multiplicative constants may be eliminated by the division operation in the Log-MAP algorithm of Eq. (2.30). Therefore, Eq. (2.67) may be further simplified as:

$$d_{\mathrm{Im}}^{m_{\mathrm{Im}}} = \frac{s_{\mathrm{Im}}^{m_{\mathrm{Im}}}}{\overline{N}_0}\Im(\widetilde{z}_n) - \frac{|s_{\mathrm{Im}}^{m_{\mathrm{Im}}}|^2}{\widetilde{N}_0} + \sum_{\bar{k}=1}^{\mathrm{BPS}_{\mathrm{Im}}} \widetilde{b}_{\bar{k}}^{m_{\mathrm{Im}}} L_a(b_{\bar{k}}), \tag{2.68}$$

where we have $\left(\overline{N}_0 = \widetilde{N}_0/2\right)$. Let us now consider Square 16QAM as an example. Its detected constellation diagram is re-drawn in Fig. 2.16a for the sake of convenience. For the Square 16QAM scheme of Fig. 2.16a, the $M_{\mathrm{Im}} = 4$ imaginary metrics of Eq. (2.68) may be expressed as:

$$\begin{aligned}
d_{\mathrm{Im}}^{0} &= \tfrac{3\Im(\widetilde{z}_n)}{\sqrt{10}\cdot\overline{N}_0} - \tfrac{9}{10\widetilde{N}_0} &&= t_{\mathrm{Im}}^{G0} - \tfrac{4}{5\widetilde{N}_0} + C_{\mathrm{Im}},\\
d_{\mathrm{Im}}^{1} &= \tfrac{\Im(\widetilde{z}_n)}{\sqrt{10}\cdot\overline{N}_0} - \tfrac{1}{10\widetilde{N}_0} + L_a(b_2) &&= t_{\mathrm{Im}}^{G1} + L_a(b_2) + C_{\mathrm{Im}},\\
d_{\mathrm{Im}}^{2} &= -\tfrac{3\Im(\widetilde{z}_n)}{\sqrt{10}\cdot\overline{N}_0} - \tfrac{9}{10\widetilde{N}_0} + L_a(b_1) &&= -t_{\mathrm{Im}}^{G0} - \tfrac{4}{5\widetilde{N}_0} + C_{\mathrm{Im}},\\
d_{\mathrm{Im}}^{3} &= -\tfrac{\Im(\widetilde{z}_n)}{\sqrt{10}\cdot\overline{N}_0} - \tfrac{1}{10\widetilde{N}_0} + L_a(b_1) + L_a(b_2) &&= -t_{\mathrm{Im}}^{G1} + L_a(b_2) + C_{\mathrm{Im}},
\end{aligned} \tag{2.69}$$

where we relate the imaginary part of $\widetilde{z}_n$ to the corresponding soft-bit input $L_a(b_1)$ by defining the test-variables $\{t_{\mathrm{Im}}^{Gg}\}_{g=0}^{1}$ as:

$$\begin{aligned}
t_{\mathrm{Im}}^{G0} &= \tfrac{3\Im(\widetilde{z}_n)}{\sqrt{10}\cdot\overline{N}_0} - \tfrac{L_a(b_1)}{2},\\
t_{\mathrm{Im}}^{G1} &= \tfrac{\Im(\widetilde{z}_n)}{\sqrt{10}\cdot\overline{N}_0} - \tfrac{L_a(b_1)}{2},
\end{aligned} \tag{2.70}$$

while the constant in Eq. (2.69) is given by $\left[C_{\mathrm{Im}} = -\frac{1}{10\widetilde{N}_0} + \frac{L_a(b_1)}{2}\right]$. It may be observed in Eq. (2.69) that the only difference between d_{Im}^0 and d_{Im}^2 is the sign of t_{Im}^{G0}. Similarly, the only difference between d_{Im}^1 and d_{Im}^3 is the sign of t_{Im}^{G1}. Consequently, the maximum probability metrics of these two groups are given by:

$$\begin{aligned}
d_{\mathrm{Im}}^{G0} &= \max\{d_{\mathrm{Im}}^0, d_{\mathrm{Im}}^2\} = |t_{\mathrm{Im}}^{G0}| - \frac{4}{5\widetilde{N}_0} + C_{\mathrm{Im}},\\
d_{\mathrm{Im}}^{G1} &= \max\{d_{\mathrm{Im}}^1, d_{\mathrm{Im}}^3\} = |t_{\mathrm{Im}}^{G1}| + L_a(b_2) + C_{\mathrm{Im}}.
\end{aligned} \tag{2.71}$$

Therefore, the global maximum metric that is sought by the Max-Log-MAP algorithm of Eq. (2.34) may be obtained by:

$$d_{\mathrm{Im}}^{\max} = \max\left\{\begin{array}{l}\max\{d_{\mathrm{Im}}^0, d_{\mathrm{Im}}^2\}\\ \max\{d_{\mathrm{Im}}^1, d_{\mathrm{Im}}^3\}\end{array}\right\} = \max_{g=\{0,1\}} d_{\mathrm{Im}}^{Gg}. \tag{2.72}$$

As a result, instead of evaluating and comparing Eq. (2.68) $M_{\mathrm{Im}} = 4$ times in Eq. (2.69) according to the M_{Im}PAM constellation points, Eq. (2.72) is obtained by comparing a reduced number of

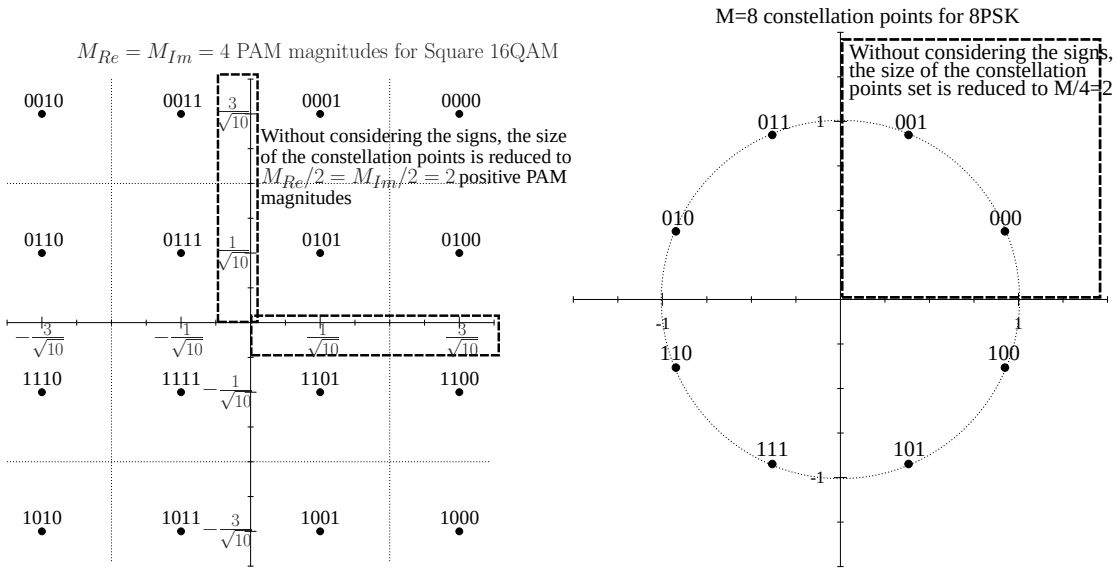

(a) Square 16QAM (b) Rotated 8PSK

Figure 2.16: The reduced-complexity soft-decision-aided MPSK/QAM detector's constellation diagrams. We deliberately rotate all the detected MPSK ($M \geq 4$) constellation diagrams and the detected Star MQAM constellation diagrams anti-clockwise by a phase of π/M and π/M_P, respectively, so that there are exactly $M/4$ constellation points in each quadrant.

$M_{\text{Im}}/2 = 2$ candidates according to having $M_{\text{Im}}/2$ positive PAM magnitudes, where the absolute value calculation eliminates the need for considering the signs, thanks to the Gray-labelled Square 16QAM constellation diagram of Fig. 2.16a.

Upon obtaining the maximum probability metric $d_{\text{Im}}^{\max}$ and the corresponding optimum group index $\hat{g}$ according to Eq. (2.72), the MAP hard-bit decisions may be produced accordingly as:

$$\hat{b}_1 = \begin{cases} 1, & \text{if } t_{\text{Im}}^{G\hat{g}} < 0 \\ 0, & \text{otherwise} \end{cases}, \quad \hat{b}_2 = \begin{cases} 1, & \text{if } \hat{g} = 1 \\ 0, & \text{otherwise} \end{cases}. \tag{2.73}$$

According to the maximum metric search of Eq. (2.72), the first two soft-bit decisions produced by the reduced-complexity Max-Log-MAP algorithm may be obtained as:

$$\begin{aligned} L_p(b_1) &= \max\{d_{\text{Im}}^2, d_{\text{Im}}^3\} - \max\{d_{\text{Im}}^0, d_{\text{Im}}^1\} \\ &= \max\{\ -t_{\text{Im}}^{G0} - \tfrac{4}{5\widetilde{N}_0},\ \ -t_{\text{Im}}^{G1} + L_a(b_2)\ \} - \max\{\ t_{\text{Im}}^{G0} - \tfrac{4}{5\widetilde{N}_0},\ \ t_{\text{Im}}^{G1} + L_a(b_2)\ \} \\ &= \begin{cases} d_{\text{Im}}^{\max} - \max\{\ t_{\text{Im}}^{G0} - \frac{4}{5\widetilde{N}_0},\ \ t_{\text{Im}}^{G1} + L_a(b_2)\ \}, & \text{if } \hat{b}_1 = 1 \\ \max\{\ -t_{\text{Im}}^{G0} - \frac{4}{5\widetilde{N}_0},\ \ -t_{\text{Im}}^{G1} + L_a(b_2)\ \} - d_{\text{Im}}^{\max}, & \text{otherwise} \end{cases}. \end{aligned} \tag{2.74}$$

$$\begin{aligned} L_p(b_2) &= \max\{d_{\text{Im}}^1, d_{\text{Im}}^3\} - \max\{d_{\text{Im}}^0, d_{\text{Im}}^2\} \\ &= d_{\text{Im}}^{G1} - d_{\text{Im}}^{G0} \\ &= |t_{\text{Im}}^{G1}| + L_a(b_2) - |t_{\text{Im}}^{G0}| + \frac{4}{5\widetilde{N}_0}. \end{aligned} \tag{2.75}$$

We note that the constant of C_{Im} may be deleted from $\{d_{\mathrm{Im}}^{m_{\mathrm{Im}}}\}_{m_{\mathrm{Im}}=0}^{M_{\mathrm{Im}}-1}$ of Eq. (2.69) as well as the following definitions for $\{d_{\mathrm{Im}}^{Gg}\}_{g=0}^{M_{\mathrm{Im}}/2-1}$ of Eq. (2.71) and $d_{\mathrm{Im}}^{\max}$ of Eq. (2.72), as the subtraction operations between two maxima in Eqs. (2.74) and (2.75) eliminates common constants.

Similarly, the corresponding Approx-Log-MAP algorithm may be obtained by compensating the error imposed by considering only the maximum in Eqs. (2.74) and (2.75) as:

$$L_p(b_1) = \mathrm{jac}\{\ -t_{\mathrm{Im}}^{G0} - \tfrac{4}{5\widetilde{N}_0},\ \ -t_{\mathrm{Im}}^{G1} + L_a(b_2)\ \} - \mathrm{jac}\{\ t_{\mathrm{Im}}^{G0} - \tfrac{4}{5\widetilde{N}_0},\ \ t_{\mathrm{Im}}^{G1} + L_a(b_2)\ \}, \quad (2.76)$$

$$L_p(b_2) = \Lambda(|t_{\mathrm{Im}}^{G1}|) + L_a(b_2) - \Lambda(|t_{\mathrm{Im}}^{G0}|) + \frac{4}{5\widetilde{N}_0}, \quad (2.77)$$

where we define the special case of the corrected Jacobian algorithm of Eq. (2.36) as:

$$\Lambda(|t|) = \mathrm{jac}(t, -t) = |t| + \delta(2|t|). \quad (2.78)$$

Based on the example of Square 16QAM detection, we summarize the Max-Log-MAP algorithm conceived for Square MQAM detection as follows:

Algorithm 2.2: Max-Log-MAP Algorithm for Square MQAM Detection.

(1) Define the test-variables, which relate $L_a(b_1)$ and $L_a\left(b_{\mathrm{BPS}_{\mathrm{Im}}+1}\right)$ to the imaginary and real parts of $\widetilde{z}_n$ as:

$$\begin{aligned} t_{\mathrm{Im}}^{Gg} &= \frac{A_{\mathrm{Im}}^{Gg}\Im(\widetilde{z}_n)}{\widetilde{N}_0} - \frac{L_a(b_1)}{2}, \\ t_{\mathrm{Re}}^{Gf} &= \frac{A_{\mathrm{Re}}^{Gf}\Re(\widetilde{z}_n)}{\widetilde{N}_0} - \frac{L_a\left(b_{\mathrm{BPS}_{\mathrm{Im}}+1}\right)}{2}, \end{aligned} \quad (2.79)$$

where $\{A_{\mathrm{Im}}^{Gg}\}_{g=0}^{M_{\mathrm{Im}}/2-1}$ and $\{A_{\mathrm{Re}}^{Gf}\}_{f=0}^{M_{\mathrm{Re}}/2-1}$ are the positive PAM magnitudes on the y-axis and x-axis of the Gray-labelled Square MQAM constellation diagram, respectively.

(2) Calculate the maximum probability metrics, which relates the rest of the *a priori* LLRs $\{L_a(b_{\bar{k}})\}_{\bar{k}=2}^{\mathrm{BPS}_{\mathrm{Im}}}$ and $\{L_a(b_{\bar{k}})\}_{\bar{k}=\mathrm{BPS}_{\mathrm{Im}}+2}^{\mathrm{BPS}}$ to the PAM magnitude indices g and f as:

$$\begin{aligned} d_{\mathrm{Im}}^{Gg} &= |t_{\mathrm{Im}}^{Gg}| + \textstyle\sum_{\bar{k}=2}^{\mathrm{BPS}_{\mathrm{Im}}} \widetilde{b}_{\bar{k}}^{Gg} L_a(b_{\bar{k}}) - \frac{(A_{\mathrm{Im}}^{Gg})^2}{\widetilde{N}_0}, \\ d_{\mathrm{Re}}^{Gf} &= |t_{\mathrm{Re}}^{Gf}| + \textstyle\sum_{\bar{k}=\mathrm{BPS}_{\mathrm{Im}}+2}^{\mathrm{BPS}} \widetilde{b}_{\bar{k}}^{Gf} L_a(b_{\bar{k}}) - \frac{(A_{\mathrm{Re}}^{Gf})^2}{\widetilde{N}_0}, \end{aligned} \quad (2.80)$$

where $\{\widetilde{b}_{\bar{k}}^{Gg}\}_{\bar{k}=2}^{\mathrm{BPS}_{\mathrm{Im}}}$ and $\{\widetilde{b}_{\bar{k}}^{Gf}\}_{\bar{k}=\mathrm{BPS}_{\mathrm{Im}}+2}^{\mathrm{BPS}}$ refer to the bit-mapping arrangements corresponding to the group indices g and f, where we have $[\widetilde{b}_2^{Gg} \cdots \widetilde{b}_{\mathrm{BPS}_{\mathrm{Im}}}^{Gg}] = \mathrm{dec2bin}(g)$ and $[\widetilde{b}_{\mathrm{BPS}_{\mathrm{Im}}+2}^{Gf} \cdots \widetilde{b}_{\mathrm{BPS}}^{Gf}] = \mathrm{dec2bin}(f)$.

(3) The global maximum probability metrics may be obtained by comparing all their local maxima as:

$$\begin{aligned} d_{\mathrm{Im}}^{\max} &= d_{\mathrm{Im}}^{G\hat{g}} = \max_{g\in\{0,\cdots,M_{\mathrm{Im}}/2-1\}} \left(d_{\mathrm{Im}}^{Gg}\right), \\ d_{\mathrm{Re}}^{\max} &= d_{\mathrm{Re}}^{G\hat{f}} = \max_{f\in\{0,\cdots,M_{\mathrm{Re}}/2-1\}} \left(d_{\mathrm{Re}}^{Gf}\right), \end{aligned} \quad (2.81)$$

where the optimum group indices $\hat{g}$ and $\hat{f}$ may be directly used for determining the MAP hard-bit decisions of $\{\hat{b}_k\}_{k=2}^{\mathrm{BPS}_{\mathrm{Im}}}$ and $\{\hat{b}_k\}_{k=\mathrm{BPS}_{\mathrm{Im}}+2}^{\mathrm{BPS}}$, i.e. we have $[\hat{b}_2 \cdots \hat{b}_{\mathrm{BPS}_{\mathrm{Im}}}] =$

dec2bin$(\hat{g})$ and $[\hat{b}_{\mathrm{BPS_{Im}}+2}\cdots\hat{b}_{\mathrm{BPS}}]$ = dec2bin$(\hat{f})$, respectively. Moreover, the first bit and the $(\mathrm{BPS_{Im}}+1)$-th bit may be determined by $\hat{b}_1 = (t_{\mathrm{Im}}^{G\hat{g}} < 0)$ and by $\hat{b}_{\mathrm{BPS_{Im}}+1} = (t_{\mathrm{Re}}^{G\hat{f}} < 0)$, respectively.

(4) For the first bit and the $(\mathrm{BPS_{Im}}+1)$-th bit, which determine the signs, the *a posteriori* LLRs are given by:

$$\begin{aligned} L_p(b_1) &= \max_{g\in\{0,\cdots,M_{\mathrm{Im}}/2-1\}} \left(d_{\mathrm{Im},b_1=1}^{Gg}\right) - \max_{g\in\{0,\cdots,M_{\mathrm{Im}}/2-1\}} \left(d_{\mathrm{Im},b_1=0}^{Gg}\right), \\ L_p(b_{\mathrm{BPS_{Im}}+1}) &= \max_{f\in\{0,\cdots,M_{\mathrm{Re}}/2-1\}} \left(d_{\mathrm{Re},b_{\mathrm{BPS_{Im}}+1}=1}^{Gf}\right) \\ &\quad - \max_{f\in\{0,\cdots,M_{\mathrm{Re}}/2-1\}} \left(d_{\mathrm{Re},b_{\mathrm{BPS_{Im}}+1}=0}^{Gf}\right), \end{aligned} \tag{2.82}$$

where the probability metrics of Eq. (2.80) have to be updated when the specific bit is set to be 1 or 0 as:

$$\begin{aligned} d_{\mathrm{Im},b_1=1}^{Gg} &= -t_{\mathrm{Im}}^{Gg} + \textstyle\sum_{\bar{k}=2}^{\mathrm{BPS_{Im}}} \widetilde{b}_{\bar{k}}^{Gg} L_a(b_{\bar{k}}) - \frac{(A_{\mathrm{Im}}^{Gg})^2}{\widetilde{N}_0}, \\ d_{\mathrm{Im},b_1=0}^{Gg} &= t_{\mathrm{Im}}^{Gg} + \textstyle\sum_{\bar{k}=2}^{\mathrm{BPS_{Im}}} \widetilde{b}_{\bar{k}}^{Gg} L_a(b_{\bar{k}}) - \frac{(A_{\mathrm{Im}}^{Gg})^2}{\widetilde{N}_0}. \end{aligned} \tag{2.83}$$

$$\begin{aligned} d_{\mathrm{Re},b_{\mathrm{BPS_{Im}}+1}=1}^{Gf} &= -t_{\mathrm{Re}}^{Gf} + \textstyle\sum_{\bar{k}=\mathrm{BPS_{Im}}+2}^{\mathrm{BPS}} \widetilde{b}_{\bar{k}}^{Gf} L_a(b_{\bar{k}}) - \frac{(A_{\mathrm{Re}}^{Gf})^2}{\widetilde{N}_0}, \\ d_{\mathrm{Re},b_{\mathrm{BPS_{Im}}+1}=0}^{Gf} &= t_{\mathrm{Re}}^{Gf} + \textstyle\sum_{\bar{k}=\mathrm{BPS_{Im}}+2}^{\mathrm{BPS}} \widetilde{b}_{\bar{k}}^{Gf} L_a(b_{\bar{k}}) - \frac{(A_{\mathrm{Re}}^{Gf})^2}{\widetilde{N}_0}. \end{aligned} \tag{2.84}$$

Moreover, for $L_p(b_1)$ and $L_p(b_{\mathrm{BPS_{Im}}+1})$ produced by Eq. (2.82), $d_{\mathrm{Im}}^{\max}$ and $d_{\mathrm{Re}}^{\max}$ of Eq. (2.81) may be utilized to replace one of their maxization operations. As a result, Eq. (2.82) may be simplified to:

$$\begin{aligned} L_p(b_1) &= \begin{cases} d_{\mathrm{Im}}^{\max} - \max_{g\in\{0,\cdots,M_{\mathrm{Im}}/2-1\}} \left(d_{\mathrm{Im},b_1=0}^{Gg}\right), & \text{if } \hat{b}_1 = 1 \\ \max_{g\in\{0,\cdots,M_{\mathrm{Im}}/2-1\}} \left(d_{\mathrm{Im},b_1=1}^{Gg}\right) - d_{\mathrm{Im}}^{\max}, & \text{otherwise} \end{cases}, \\ L_p(b_{\mathrm{BPS_{Im}}+1}) &= \begin{cases} d_{\mathrm{Re}}^{\max} - \max_{f\in\{0,\cdots,M_{\mathrm{Re}}/2-1\}} \left(d_{\mathrm{Re},b_{\mathrm{BPS_{Im}}+1}=0}^{Gf}\right), & \text{if } \hat{b}_{\mathrm{BPS_{Im}}+1} = 1 \\ \max_{f\in\{0,\cdots,M_{\mathrm{Re}}/2-1\}} \left(d_{\mathrm{Re},b_{\mathrm{BPS_{Im}}+1}=1}^{Gf}\right) - d_{\mathrm{Re}}^{\max}, & \text{otherwise} \end{cases}. \end{aligned} \tag{2.85}$$

(5) For the remaining $(\mathrm{BPS}-2)$ bits, which determine the magnitudes, the Max-Log-MAP algorithm is given by:

$$\begin{aligned} L_p(b_k) &= \max_{b_k=1} \left(d_{\mathrm{Im}}^{Gg}\right) - \max_{b_k=0} \left(d_{\mathrm{Im}}^{Gg}\right), \quad k \in \{2,\cdots,\mathrm{BPS_{Im}}\}, \\ L_p(b_k) &= \max_{b_k=1} \left(d_{\mathrm{Re}}^{Gf}\right) - \max_{b_k=0} \left(d_{\mathrm{Re}}^{Gf}\right), \quad k \in \{\mathrm{BPS_{Im}}+2,\cdots,\mathrm{BPS}\}, \end{aligned} \tag{2.86}$$

where the tentative indices set for $(g \in \{0,\cdots,M_{\mathrm{Im}}/2-1\})$ and $(f \in \{0,\cdots,M_{\mathrm{Re}}/2-1\})$ are halved to have set sizes of $M_{\mathrm{Im}}/4$ and $M_{\mathrm{Re}}/4$ when a specific bit b_k is fixed to 1 and 0, respectively. Taking Square 16QAM as an example, it was demonstrated in Eq. (2.75) that only $g = 1$ or $g = 0$ may be considered when b_2 is fixed to be 1 or 0, respectively.

Similar to Step (4), $d_{\text{Im}}^{\max}$ and $d_{\text{Re}}^{\max}$ of Eq. (2.81) may replace one of the maxization operations for each constituent equation of Eq. (2.86) as:

$$
\begin{aligned}
L_p(b_k) &= \begin{cases} d_{\text{Im}}^{\max} - \max_{b_k=0}\left(d_{\text{Im}}^{Gg}\right), & \text{if } \hat{b}_k = 1 \\ \max_{b_k=1}\left(d_{\text{Im}}^{Gg}\right) - d_{\text{Im}}^{\max}, & \text{otherwise} \end{cases}, \\
&\qquad k \in \{2, \cdots, \text{BPS}_{\text{Im}}\}, \\
L_p(b_k) &= \begin{cases} d_{\text{Re}}^{\max} - \max_{b_k=0}\left(d_{\text{Re}}^{Gf}\right), & \text{if } \hat{b}_k = 1 \\ \max_{b_k=1}\left(d_{\text{Re}}^{Gf}\right) - d_{\text{Re}}^{\max}, & \text{otherwise} \end{cases}, \\
&\qquad k \in \{\text{BPS}_{\text{Im}} + 2, \cdots, \text{BPS}\}.
\end{aligned}
\tag{2.87}
$$

The corresponding reduced-complexity Approx-Log-MAP algorithm conceived for general Square MQAM may be obtained by appropriately modifying Algorithm 2.2, where the max operation should be replaced by the Jacobian operation of Eq. (2.36), while the operation $(|t|)$ should be replaced by the special Jacobian operation $\Lambda(|t|)$ of Eq. (2.78). Furthermore, we note that the simplified *a posteriori* LLR evaluations of Eqs. (2.85) and (2.87) are not applicable to the Approx-Log-MAP algorithm because the maximum probability metrics $d_{\text{Im}}^{\max}$ and $d_{\text{Re}}^{\max}$ of Eq. (2.81) cannot replace the jac operation seen in Eq. (2.35). Accordingly, Step (3) may be deleted for the Approx-Log-MAP algorithm.

In the design of reduced-complexity soft-decision-aided QAM detection algorithms, we aim for a reduced-complexity order of $O(\log_2 M)$, i.e. each bit is detected independently. However, both the real part and the imaginary part of a Square MQAM symbol has $(\text{BPS}_{\text{Re}} - 1)$ and $(\text{BPS}_{\text{Im}} - 1)$ bits, which encode the PAM magnitudes together, hence they have to be jointly detected. As a result, when detecting the $(\text{BPS} - 2)$ bits which determine the magnitudes, the complexity order of Eq. (2.87) is given by $O(M_{\text{Im}}/4)$ and $O(M_{\text{Re}}/4)$ for detecting the imaginary part and the real part of a Square MQAM symbol, respectively. Furthermore, when detecting the two bits which determine the signs, the complexity order of Eq. (2.85) is given by $O(M_{\text{Im}}/2)$ and $O(M_{\text{Re}}/2)$ for detecting the imaginary and real parts of a Square MQAM symbol, respectively. It can be seen that the proposed algorithm exhibits a reduced complexity compared to the orignal complexity order of $O(M_{\text{Im}})/O(M_{\text{Re}})$ of Eq. (2.34), when using Eq. (2.39). We will demonstrate in the next section that the complexity reduction may even be more substantial, when the design portrayed in this section is applied to MPSK and Star/Cross constellation based MQAM schemes.

2.4.2 Reduced-Complexity Soft-Decision-Aided General PSK/QAM Detection

For Square MQAM schemes, the real part and the imaginary part of a transmitted symbol are encoded separately. By contrast, a high-order MPSK scheme associated with $(M > 4)$ encodes its phase, which means that the real and imaginary parts of a transmitted MPSK symbol are in fact en-

coded jointly. As a result, the jointly encoded bits in a MPSK symbol have to be detected together, which imposes a higher complexity. However, it can be seen in Algorithm 2.2 that as long as we have the symmetry provided by Gray-labelling, a similar reduced-complexity detection algorithm may be obtained. For the sake of achieving this goal, we have to rotate all the MPSK receiver's constellations (except BPSK) in [2] anti-clockwise by (π/M), so that there are exactly $M/4$ constellation points in each quadrant. The rotated 8PSK constellation is shown in Fig. 2.16b. Similarly, a Star MQAM receiver's constellation [155, 253] may be rotated anti-clockwise by a phase angle of (π/M_P). We note that the transmitted constellation diagrams of the MPSK and Star MQAM schemes may remain the same, but the MPSK scheme's detected constellation diagram is rotated, where z_n and s^m in Eq. (2.37) are replaced by $\bar{z}_n = z_n \exp(j\pi/M)$ and $\bar{s}^m = s^m \exp(j\pi/M)$. Similarly, the Star MQAM arrangement's detected constellation diagram may be rotated, where $\widetilde{z}_n$ and s^m in Eq. (2.38) are replaced by $\bar{z}_n = \widetilde{z}_n \exp(j\pi/M_P)$ and $\bar{s}^m = s^m \exp(j\pi/M_P)$, respectively.

In order to operate the Max-Log-MAP algorithm conceived for different PSK/QAM constellations at a reduced complexity, we extend the *a posteriori* probability metric of Eqs. (2.37) and (2.38)[4] as:

$$d^m = -\frac{|\bar{z}_n|^2}{\widetilde{N}_0} - \frac{|\bar{s}^m|^2}{\widetilde{N}_0} + \frac{\Re(\bar{z}_n)\Re(\bar{s}^m) + \Im(\bar{z}_n)\Im(\bar{s}^m)}{\overline{N}_0} + \sum_{\bar{k}=1}^{\text{BPS}} \widetilde{b}_{\bar{k}}^m L_a(b_{\bar{k}}), \tag{2.88}$$

where the constant of $\left(-\frac{|\widetilde{z}_n|^2}{\widetilde{N}_0}\right)$ may be ignored and we have $\overline{N}_0 = \widetilde{N}_0/2$. Let us now consider the detected 8PSK constellation of Fig. 2.16b as an example, where the eight metrics $\{d^m\}_{m=0}^7$ of Eq. (2.88) may be expressed as:

$$\begin{aligned} d^0 &= t_{\text{Re}}^{G0} + t_{\text{Im}}^{G0} + C_{\text{8PSK}}, \\ d^2 &= -t_{\text{Re}}^{G0} + t_{\text{Im}}^{G0} + C_{\text{8PSK}}, \\ d^4 &= t_{\text{Re}}^{G0} - t_{\text{Im}}^{G0} + C_{\text{8PSK}}, \\ d^6 &= -t_{\text{Re}}^{G0} - t_{\text{Im}}^{G0} + C_{\text{8PSK}}, \end{aligned} \tag{2.89}$$

$$\begin{aligned} d^1 &= t_{\text{Re}}^{G1} + t_{\text{Im}}^{G1} + L_a(b_3) + C_{\text{8PSK}}, \\ d^3 &= -t_{\text{Re}}^{G1} + t_{\text{Im}}^{G1} + L_a(b_3) + C_{\text{8PSK}}, \\ d^5 &= t_{\text{Re}}^{G1} - t_{\text{Im}}^{G1} + L_a(b_3) + C_{\text{8PSK}}, \\ d^7 &= -t_{\text{Re}}^{G1} - t_{\text{Im}}^{G1} + L_a(b_3) + C_{\text{8PSK}}, \end{aligned} \tag{2.90}$$

where we relate the real and imaginary parts of $\bar{z}_n$ to the corresponding soft bit input $L_a(b_2)$ and $L_a(b_1)$ by defining test-variables $\{t_{\text{Re}}^{Gg}\}_{g=0}^1$ and $\{t_{\text{Im}}^{Gg}\}_{g=0}^1$ as:

$$\begin{aligned} t_{\text{Re}}^{G0} &= \frac{\cos(\frac{\pi}{8})\Re(\bar{z}_n)}{\overline{N}_0} - \frac{L_a(b_2)}{2}, \\ t_{\text{Re}}^{G1} &= \frac{\sin(\frac{\pi}{8})\Re(\bar{z}_n)}{\overline{N}_0} - \frac{L_a(b_2)}{2}, \end{aligned} \tag{2.91}$$

[4]We note that MPSK's probability metric of Eq. (2.37) may be seen as a special case of the more general MQAM's expression of Eq. (2.38), where we have $\widetilde{N}_0 = N_0$ in Eq. (2.38) for the case of MPSK detection.

$$
\begin{aligned}
t_{\mathrm{Im}}^{G0} &= \frac{\sin(\frac{\pi}{8})\Im(\bar{z}_n)}{\overline{N}_0} - \frac{L_a(b_1)}{2}, \\
t_{\mathrm{Im}}^{G1} &= \frac{\cos(\frac{\pi}{8})\Im(\bar{z}_n)}{\overline{N}_0} - \frac{L_a(b_1)}{2},
\end{aligned}
\tag{2.92}
$$

while the constant $C_{8\mathrm{PSK}}$ is given by $\left[C_{8\mathrm{PSK}} = -\frac{1}{\overline{N}_0} + \frac{L_a(b_1)+L_a(b_2)}{2}\right]$. The eight probability metrics $\{d^m\}_{m=0}^{7}$ are arranged into two groups in Eqs. (2.89) and (2.90), where every four metrics are associated with the same constellation magnitudes. It can be seen that the four metrics formulated in Eq. (2.89) all contain three parts, i.e. they are $\pm t_{\mathrm{Re}}^{G0}$, $\pm t_{\mathrm{Im}}^{G0}$ and $C_{8\mathrm{PSK}}$. As a result, the maximum metric over the four candidates in Eq. (2.89) is given by a simple estimation:

$$
d^{G0} = \max_{m=\{0,2,4,6\}} d^m = |t_{\mathrm{Re}}^{G0}| + |t_{\mathrm{Im}}^{G0}| + C_{8\mathrm{PSK}}. \tag{2.93}
$$

Similarly, the maximum metric over the second group in Eq. (2.90) is given by:

$$
d^{G1} = \max_{m=\{1,3,5,7\}} d^m = |t_{\mathrm{Re}}^{G1}| + |t_{\mathrm{Im}}^{G1}| + L_a(b_3) + C_{8\mathrm{PSK}}. \tag{2.94}
$$

Therefore, the maximum *a posteriori* probability metric generated by the Max-Log-MAP algorithm is given by:

$$
\begin{aligned}
d^{\max} &= \max_{g=\{0,1\}} \left(d^{Gg}\right) \\
&= \max \left\{ \begin{array}{l} |t_{\mathrm{Re}}^{G0}| + |t_{\mathrm{Im}}^{G0}| + C_{8\mathrm{PSK}} \\ |t_{\mathrm{Re}}^{G1}| + |t_{\mathrm{Im}}^{G1}| + L_a(b_3) + C_{8\mathrm{PSK}} \end{array} \right\}.
\end{aligned}
\tag{2.95}
$$

Therefore, instead of evaluating and comparing Eq. (2.88) for a total number of $M = 8$ times in Eqs. (2.89) and (2.90), Eq. (2.95) only has to evaluate and compare a reduced number of ($M/4 = 2$) candidates in order to obtain $d^{\max}$. In other words, $d^{\max}$ of Eq. (2.95) is obtained without visiting all the eight 8PSK constellation points. In fact, only the two constellation points in the first quadrant are of interest, as demonstrated by Fig. 2.16b.

Upon obtaining the maximum probability metric $d^{\max}$ and the corresponding optimum group index $\hat{g}$ according to Eq. (2.95), the MAP hard-bit decisions may be produced as:

$$
\hat{b}_1 = \left\{ \begin{array}{ll} 1, & \text{if } t_{\mathrm{Im}}^{G\hat{g}} < 0 \\ 0, & \text{otherwise} \end{array} \right. , \quad \hat{b}_2 = \left\{ \begin{array}{ll} 1, & \text{if } t_{\mathrm{Re}}^{G\hat{g}} < 0 \\ 0, & \text{otherwise} \end{array} \right. , \tag{2.96}
$$

and we have $[\hat{b}_3 \cdots \hat{b}_{\mathrm{BPS}}] = \mathrm{dec2bin}(\hat{g})$. Furthermore, according to the maximum metric search demonstrated by Eq. (2.95), the reduced-complexity Max-Log-MAP algorithm may be formulated as:

$$
\begin{aligned}
L_p(b_1) &= d_{b_1=1}^{\max} - d_{b_1=0}^{\max} \\
&= \max \left\{ \begin{array}{l} |t_{\mathrm{Re}}^{G0}| - t_{\mathrm{Im}}^{G0} \\ |t_{\mathrm{Re}}^{G1}| - t_{\mathrm{Im}}^{G1} + L_a(b_3) \end{array} \right\} - \max \left\{ \begin{array}{l} |t_{\mathrm{Re}}^{G0}| + t_{\mathrm{Im}}^{G0} \\ |t_{\mathrm{Re}}^{G1}| + t_{\mathrm{Im}}^{G1} + L_a(b_3) \end{array} \right\} \\
&= \left\{ \begin{array}{ll} d^{\max} - \max\ \{\ |t_{\mathrm{Re}}^{G0}| + t_{\mathrm{Im}}^{G0},\ \ |t_{\mathrm{Re}}^{G1}| + t_{\mathrm{Im}}^{G1} + L_a(b_3)\ \}, & \text{if } \hat{b}_1 = 1 \\ \max\ \{\ |t_{\mathrm{Re}}^{G0}| - t_{\mathrm{Im}}^{G0},\ \ |t_{\mathrm{Re}}^{G1}| - t_{\mathrm{Im}}^{G1} + L_a(b_3)\ \} - d^{\max}, & \text{otherwise} \end{array} \right. .
\end{aligned}
\tag{2.97}
$$

$$
\begin{aligned}
L_p(b_2) &= d^{\max}_{b_2=1} - d^{\max}_{b_2=0} \\
&= \max \left\{ \begin{array}{l} -t^{G0}_{\mathrm{Re}} + |t^{G0}_{\mathrm{Im}}| \\ -t^{G1}_{\mathrm{Re}} + |t^{G1}_{\mathrm{Im}}| + L_a(b_3) \end{array} \right\} - \max \left\{ \begin{array}{l} t^{G0}_{\mathrm{Re}} + |t^{G0}_{\mathrm{Im}}| \\ t^{G1}_{\mathrm{Re}} + |t^{G1}_{\mathrm{Im}}| + L_a(b_3) \end{array} \right\} \\
&= \left\{ \begin{array}{ll} d^{\max} - \max \left\{ \; t^{G0}_{\mathrm{Re}} + |t^{G0}_{\mathrm{Im}}|, \;\; t^{G1}_{\mathrm{Re}} + |t^{G1}_{\mathrm{Im}}| + L_a(b_3) \; \right\}, & \text{if } \hat{b}_2 = 1 \\ \max \left\{ \; -t^{G0}_{\mathrm{Re}} + |t^{G0}_{\mathrm{Im}}|, \;\; -t^{G1}_{\mathrm{Re}} + |t^{G1}_{\mathrm{Im}}| + L_a(b_3) \; \right\} - d^{\max}, & \text{otherwise} \end{array} \right. .
\end{aligned} \tag{2.98}
$$

$$
\begin{aligned}
L_p(b_3) &= \max_{b_3=1} d^{Gg} - \max_{b_3=0} d^{Gg} \\
&= d^{G1} - d^{G0} \\
&= |t^{G1}_{\mathrm{Re}}| + |t^{G1}_{\mathrm{Im}}| + L_a(b_3) - |t^{G0}_{\mathrm{Re}}| - |t^{G0}_{\mathrm{Im}}|
\end{aligned} \tag{2.99}
$$

The constant $C_{8\mathrm{PSK}}$ in $\{d^m\}_{m=0}^{M-1}$ of Eqs. (2.89) and (2.90) as well as $\{d^{Gg}\}_{g=0}^{M/4-1}$ of Eqs. (2.93) and (2.94) and $d^{\max}$ of Eq. (2.95) may all be omitted.

Based on the example of 8PSK detection, we propose the reduced-complexity Max-Log-MAP algorithm conceived for general MPSK/QAM detection as follows:

Algorithm 2.3: Max-Log-MAP Algorithm for General MPSK/QAM Detection.

(1) Define the test-variables, which relates the first two *a priori* LLRs $L_a(b_2)$ and $L_a(b_1)$ to the real and imaginary parts of $\bar{z}_n$ as:

$$
\begin{aligned}
t^{Gg}_{\mathrm{Re}} &= \frac{A^{Gg}\Re(\bar{z}_n)}{\overline{N}_0} - \frac{L_a(b_2)}{2}, \\
t^{Gg}_{\mathrm{Im}} &= \frac{B^{Gg}\Im(\bar{z}_n)}{\overline{N}_0} - \frac{L_a(b_1)}{2},
\end{aligned} \tag{2.100}
$$

where $\{(A^{Gg}, B^{Gg})\}_{g=0}^{M/4-1}$ denote the coordinates of the rotated MPSK/QAM constellation points which are located in the first quadrant.

(2) Calculate the maximum probability metrics, which relates the rest of the *a priori* LLRs $\{L_a(b_{\bar{k}})\}_{\bar{k}=3}^{\mathrm{BPS}}$ to the magnitude index g as:

$$
d^{Gg} = |t^{Gg}_{\mathrm{Re}}| + |t^{Gg}_{\mathrm{Im}}| + \sum_{\bar{k}=3}^{\mathrm{BPS}} \widetilde{b}^{Gg}_{\bar{k}} L_a(b_{\bar{k}}) - \frac{(A^{Gg})^2 + (B^{Gg})^2}{\widetilde{N}_0}. \tag{2.101}
$$

where $\{\widetilde{b}^{Gg}_{\bar{k}}\}_{\bar{k}=3}^{\mathrm{BPS}}$ refers to the bit-mapping arrangement corresponding to the group index g, where we have $[\widetilde{b}^{Gg}_3 \cdots \widetilde{b}^{Gg}_{\mathrm{BPS}}] = \mathrm{dec2bin}(g)$.

(3) The global maximum probability metric $d^{\max}$ may be obtained by comparing all local maxima as:

$$
d^{\max} = d^{G\hat{g}} = \max_{g \in \{0,\cdots,M/4-1\}} d^{Gg}, \tag{2.102}
$$

where the optimum group index $\hat{g}$ may be directly used for determining the corresponding MAP hard-bit decisions, i.e. we have $\hat{b}_3 \cdots \hat{b}_{\mathrm{BPS}} = \mathrm{dec2bin}(\hat{g})$. Moreover, the first two hard-bit decisions may be obtained by $\hat{b}_1 = (t_{\mathrm{Im}\hat{g}} < 0)$ and $\hat{b}_2 = (t_{\mathrm{Re}\hat{g}} < 0)$, respectively.

(4) For the first two bits, which determine the signs, the *a posteriori* LLRs are given by:

$$\begin{aligned} L_p(b_1) &= \max_{g\in\{0,\cdots,M/4-1\}} \left(d^{Gg}_{b_1=1}\right) - \max_{g\in\{0,\cdots,M/4-1\}} \left(d^{Gg}_{b_1=0}\right), \\ L_p(b_2) &= \max_{g\in\{0,\cdots,M/4-1\}} \left(d^{Gg}_{b_2=1}\right) - \max_{g\in\{0,\cdots,M/4-1\}} \left(d^{Gg}_{b_2=0}\right), \end{aligned} \tag{2.103}$$

where the probability metrics of Eq. (2.101) have to be updated as:

$$\begin{aligned} d^{Gg}_{b_1=1} &= |t^{Gg}_{\mathrm{Re}}| - t^{Gg}_{\mathrm{Im}} + \textstyle\sum_{\bar{k}=3}^{\mathrm{BPS}} \widetilde{b}^{Gg}_{\bar{k}} L_a(b_{\bar{k}}) - \frac{(A^{Gg})^2+(B^{Gg})^2}{\widetilde{N}_0}, \\ d^{Gg}_{b_1=0} &= |t^{Gg}_{\mathrm{Re}}| + t^{Gg}_{\mathrm{Im}} + \textstyle\sum_{\bar{k}=3}^{\mathrm{BPS}} \widetilde{b}^{Gg}_{\bar{k}} L_a(b_{\bar{k}}) - \frac{(A^{Gg})^2+(B^{Gg})^2}{\widetilde{N}_0}. \end{aligned} \tag{2.104}$$

$$\begin{aligned} d^{Gg}_{b_2=1} &= -t^{Gg}_{\mathrm{Re}} + |t^{Gg}_{\mathrm{Im}}| + \textstyle\sum_{\bar{k}=3}^{\mathrm{BPS}} \widetilde{b}^{Gg}_{\bar{k}} L_a(b_{\bar{k}}) - \frac{(A^{Gg})^2+(B^{Gg})^2}{\widetilde{N}_0}, \\ d^{Gg}_{b_2=0} &= t^{Gg}_{\mathrm{Re}} + |t^{Gg}_{\mathrm{Im}}| + \textstyle\sum_{\bar{k}=3}^{\mathrm{BPS}} \widetilde{b}^{Gg}_{\bar{k}} L_a(b_{\bar{k}}) - \frac{(A^{Gg})^2+(B^{Gg})^2}{\widetilde{N}_0}. \end{aligned} \tag{2.105}$$

Moreover, $d^{\max}$ of Eq. (2.102) may replace one of the maxization operations in both equations of Eq. (2.103). Therefore, the evaluation of $L_p(b_1)$ and $L_p(b_2)$ of Eq. (2.103) may be simplified as:

$$\begin{aligned} L_p(b_1) &= \begin{cases} d^{\max} - \max_{g\in\{0,\cdots,M/4-1\}} \left(d^{Gg}_{b_1=0}\right), & \text{if } \hat{b}_1 = 1 \\ \max_{g\in\{0,\cdots,M/4-1\}} \left(d^{Gg}_{b_1=1}\right) - d^{\max}, & \text{otherwise} \end{cases}, \\ L_p(b_2) &= \begin{cases} d^{\max} - \max_{g\in\{0,\cdots,M/4-1\}} \left(d^{Gg}_{b_2=0}\right), & \text{if } \hat{b}_2 = 1 \\ \max_{g\in\{0,\cdots,M/4-1\}} \left(d^{Gg}_{b_2=1}\right) - d^{\max}, & \text{otherwise} \end{cases}. \end{aligned} \tag{2.106}$$

(5) For the following $(\mathrm{BPS}-2)$ bits which determine the magnitudes, the Max-Log-MAP algorithm is given by:

$$L_p(b_k) = \max_{b_k=1} \left(d^{Gg}\right) - \max_{b_k=0} \left(d^{Gg}\right), \quad k \in \{3,\cdots,\mathrm{BPS}\}, \tag{2.107}$$

where the tentative index set for $(g \in \{0,\cdots,M/4-1\})$ is halved to have a set size of $M/8$, when a specific bit b_k is fixed to 1 or 0. Taking 8PSK as an example, it was demonstrated in Eq. (2.99) that only $g=1$ or $g=0$ may be considered when b_3 is fixed to be 1 or 0, respectively.

Similar to Step (4), $d^{\max}$ of Eq. (2.102) may replace one of the maxizations in Eq. (2.107) as:

$$L_p(b_k) = \begin{cases} d^{\max} - \max_{b_k=0} \left(d^{Gg}\right), & \text{if } \hat{b}_k = 1 \\ \max_{b_k=1} \left(d^{Gg}\right) - d^{\max}, & \text{otherwise} \end{cases}, \quad k \in \{3,\cdots,\mathrm{BPS}\}. \tag{2.108}$$

The corresponding reduced-complexity Approx-Log-MAP algorithm may be obtained by replacing the max operation by the jac operation, and by replacing the operation $|t|$ by the $\Lambda(|t|)$, while Step (3) as well as Eqs. (2.106) and (2.108) may be omitted for Approx-Log-MAP.

When detecting the first two bits, Eq. (2.106) in Algorithm 2.3 has a detection complexity

order of $O(M/4)$, while Eq. (2.108) evaluated for detecting those specific $(\text{BPS}-2)$ bits has a detection complexity order of $O(M/8)$. They exhibit a substantially reduced complexity compared to the conventional detection complexity order $O(M)$, owing to the fact that the proposed detection algorithms visit a reduced-size fraction of the constellation points.

We note that when Algorithm 2.3 is invoked for MPSK detection, the constant $(\frac{(A^{Gg})^2+(B^{Gg})^2}{\widetilde{N}_0} = \frac{1}{\widetilde{N}_0})$ in Eqs. (2.101), (2.104) and (2.105) may be ignored. Furthermore, it was shown in [252] that Cross MQAM constellations actually have a better performance compared to Square MQAM schemes. We note that Algorithm 2.3 may be adopted for detecting Cross MQAM constellations without rotating its detected constellation diagram.

2.4.3 Performance Results

Let us now discuss our simulation results in this section. First of all, we classify the detection complexity into five categories, which are the number of real-valued multiplications, the number of real-valued additions, the number of comparisons, the number of table look-up operations with reference to Table 2.2 for the Approx-Log-MAP algorithm and the number of constellation points visited (which are equivalently termed as nodes). Therefore, the complexity of the conventional Square MQAM detection introduced in Sec. 2.3.1 and that of the reduced-complexity Square MQAM detection proposed in Algorithm 2.2 of Sec. 2.4.1 is compared in Table 2.4. We note that the practical implementation of detectors should be optimized to eliminate unnecessary calculations. For example, for the conventional Square MQAM detector, the decision variable $\widetilde{z}_n = \mathbf{Y}_n\mathbf{H}_n^H/\|\mathbf{H}_n\|^2$ of Eq. (2.39) only has to be evaluated once before invoking the Max-Log-MAP algorithm of Eq. (2.34) or the Approx-Log-MAP algorithm of Eq. (2.35). Similarly, for the reduced-complexity Square MQAM detection of Algorithm 2.2, the variables including $\{\frac{A_{\text{Im}}^{Gg}}{\widetilde{N}_0}\}_{g=0}^{M_{\text{Im}}/2-1}$, $\{\frac{A_{\text{Re}}^{Gf}}{\widetilde{N}_0}\}_{f=0}^{M_{\text{Re}}/2-1}$, $\{\frac{(A_{\text{Im}}^{Gg})^2}{\widetilde{N}_0}\}_{g=0}^{M_{\text{Im}}/2-1}$, $\{\frac{(A_{\text{Re}}^{Gf})^2}{\widetilde{N}_0}\}_{f=0}^{M_{\text{Re}}/2-1}$, $\{\sum_{\bar{k}=2}^{\text{BPS}_{\text{Im}}}\widetilde{b}_{\bar{k}}^{Gg}L_a(b_{\bar{k}})\}_{g=0}^{M_{\text{Im}}/2-1}$ and $\{\sum_{\bar{k}=\text{BPS}_{\text{Im}}+2}^{\text{BPS}}\widetilde{b}_{\bar{k}}^{Gf}L_a(b_{\bar{k}})\}_{f=0}^{M_{\text{Re}}/2-1}$ may all be computed before activating Algorithm 2.2.

Against this background, we can see in Table 2.4 that the Square MQAM detection complexity order is reduced from $O(M_{\text{Im}}+M_{\text{Re}})$ to $O(M_{\text{Im}}/2+M_{\text{Re}}/2)$ for all complexity categories, when the proposed Max-Log-MAP technique of Algorithm 2.2 and its corrected Approx-Log-MAP counterpart are invoked. This is expected, because Algorithm 2.2 only visits half of the overall constellation points, as demonstrated by Fig. 2.16a. We note that reducing the number of the detected constellation points is the most common technique of complexity reduction in communication systems. For example, the ML detection of a MIMO scheme equipped with N_T Transmit Antennas (TAs) and employing MPSK/QAM signalling has to consider a total number of M^{N_T} combinations of the constellation points, which is impractical for a large N_T and/or a high M. In order to mitigate the excessive complexity, Sphere Detection (SD) [173, 174, 176] and linear MIMO receivers (e.g. MMSE detector) [13, 14, 75] are capable of effectively reducing the number of constellation points that have to be visited by the MIMO detector. Compared to these popular solutions, our reduced-complexity design conceived for basic soft-decision-aided MPSK/QAM detection aims

	real-valued multiplications	real-valued additions	comparisons	Lookup Table 2.2	visited nodes
Conventional Approx-Log-MAP	$[(\text{BPS}_{\text{Im}}+2)M_{\text{Im}}$ $+(\text{BPS}_{\text{Re}}+2)M_{\text{Re}}$ $+6N_R+3]/\text{BPS}$	$[(3\text{BPS}_{\text{Im}}+2)M_{\text{Im}}+$ $(3\text{BPS}_{\text{Re}}+2)M_{\text{Re}}+$ $\text{BPS}+6N_R-3]/\text{BPS}$	$(\text{BPS}_{\text{Im}}M_{\text{Im}}+$ $\text{BPS}_{\text{Re}}M_{\text{Re}})/\text{BPS}$	$(\text{BPS}_{\text{Im}}M_{\text{Im}}+$ $\text{BPS}_{\text{Re}}M_{\text{Re}})/\text{BPS}$	$(M_{\text{Re}}$ $+M_{\text{Im}})$
Conventional Max-Log-MAP	$[(\text{BPS}_{\text{Im}}+2)M_{\text{Im}}$ $+(\text{BPS}_{\text{Re}}+2)M_{\text{Re}}$ $+6N_R+3]/\text{BPS}$	$[(\text{BPS}_{\text{Im}}+2)M_{\text{Im}}+$ $(\text{BPS}_{\text{Re}}+2)M_{\text{Re}}+$ $\text{BPS}+6N_R-3]/\text{BPS}$	$(\text{BPS}_{\text{Im}}M_{\text{Im}}+$ $\text{BPS}_{\text{Re}}M_{\text{Re}})/\text{BPS}$		$(M_{\text{Re}}$ $+M_{\text{Im}})$
Proposed Approx-Log-MAP	$[(\frac{\text{BPS}_{\text{Im}}}{2}+1)M_{\text{Im}}$ $+(\frac{\text{BPS}_{\text{Re}}}{2}+1)M_{\text{Re}}$ $+6N_R+6]/\text{BPS}$	$[(\frac{3\text{BPS}_{\text{Im}}}{2}+4)M_{\text{Im}}$ $+(\frac{3\text{BPS}_{\text{Re}}}{2}+4)M_{\text{Re}}+$ $\text{BPS}+6N_R-3]/\text{BPS}$	$[(\text{BPS}_{\text{Im}}+1)\frac{M_{\text{Im}}}{2}$ $+(\text{BPS}_{\text{Re}}+1)\frac{M_{\text{Re}}}{2}$ $]/\text{BPS}$	$[(\text{BPS}_{\text{Im}}+1)\frac{M_{\text{Im}}}{2}$ $+(\text{BPS}_{\text{Re}}+1)\frac{M_{\text{Re}}}{2}$ $]/\text{BPS}$	$(\frac{M_{\text{Re}}}{2}$ $+\frac{M_{\text{Im}}}{2})$
Proposed Max-Log-MAP	$[(\frac{\text{BPS}_{\text{Im}}}{2}+1)M_{\text{Im}}$ $+(\frac{\text{BPS}_{\text{Re}}}{2}+1)M_{\text{Re}}$ $+6N_R+6]/\text{BPS}$	$[(\frac{\text{BPS}_{\text{Im}}}{2}+2)M_{\text{Im}}$ $+(\frac{\text{BPS}_{\text{Re}}}{2}+2)M_{\text{Re}}+$ $\text{BPS}+6N_R-3]/\text{BPS}$	$[(\text{BPS}_{\text{Im}}+3)\frac{M_{\text{Im}}}{2}$ $+(\text{BPS}_{\text{Re}}+3)\frac{M_{\text{Re}}}{2}$ $+2+\text{BPS}]/\text{BPS}$		$(\frac{M_{\text{Re}}}{2}$ $+\frac{M_{\text{Im}}}{2})$

Table 2.4: Complexity (per bit) of soft-decision-aided Square MQAM detection. Conventional Max-Log-MAP and Approx-Log-MAP refer to Eqs. (2.34) and (2.35) using Eq. (2.39), while Proposed Max-Log-MAP and Approx-Log-MAP refer to Algorithm 2.2 and its Approx-Log-MAP correction.

for the same desirable objective, but no performance loss is imposed.

Similarly, Table 2.5 summarizes our complexity comparisons between the conventional QAM detection introduced in Sec. 2.3.1 and the reduced-complexity general MQAM detection techniques proposed in Algorithm 2.3 of Sec. 2.4.1. As expected, Table 2.5 demonstrates that the general MPSK/QAM detection complexity is reduced from $O(M)$ to $O(M/4)$, because only the $M/4$ constellation points residing in the first quadrant are visited by the Max-Log-MAP algorithm of Algorithm 2.3 and by its Approx-Log-MAP correction aided counterpart.

Furthermore, the complexity reductions achieved by Algorithms 2.2 and 2.3 are portrayed in terms of the total number of real-valued multiplications required for producing a single soft-bit output in Fig 2.17, where the Complexity-Reduction Ratio (CRR) may be defined as:

$$\text{CRR} = \frac{\text{Complexity of the conventional detector} - \text{Complexity of the proposed detector}}{\text{Complexity of the conventional detector}}. \tag{2.109}$$

In contrast to the Square MQAM results of Fig. 2.17a, Algorithm 2.3 conceived for general MPSK/QAM detection achieves a higher complexity reduction, as demonstrated in Fig. 2.17b. This is because the conventional Square MQAM detection presented in Sec. 2.3.1 already has a comparatively low detection complexity, owing to the fact that the real and imaginary parts of a Square MQAM symbol are detected separately. Nonetheless, Fig. 2.17 demonstrates that as the number of modulation levels M increases, the CRRs become more substantial, because the N_R-related complexity terms seen in Tables 2.4 and 2.5 contribute less to the overall complexity at higher M. It can be seen

	real-valued multiplications	real-valued additions	comparisons	Lookup Table 2.2	visited nodes
Conventional Approx-Log-MAP	$[(\text{BPS}+3)M$ $+6N_R+3]/\text{BPS}$	$[(3\text{BPS}+4)M+$ $\text{BPS}+6N_R-3]/\text{BPS}$	M	M	M
Conventional Max-Log-MAP	$[(\text{BPS}+3)M$ $+6N_R+3]/\text{BPS}$	$[(\text{BPS}+4)M+$ $\text{BPS}+6N_R-3]/\text{BPS}$	M		M
Proposed Approx-Log-MAP	$[(\text{BPS}+3)\frac{M}{4}+$ $6N_R+10]/\text{BPS}$	$[(3\text{BPS}+20)\frac{M}{4}+$ $\text{BPS}+6N_R-1]/\text{BPS}$	$[(\text{BPS}+2)\frac{M}{4}$ $]/\text{BPS}$	$[(\text{BPS}+2)\frac{M}{4}$ $]/\text{BPS}$	$M/4$
Proposed Max-Log-MAP	$[(\text{BPS}+3)\frac{M}{4}+$ $6N_R+10]/\text{BPS}$	$[(\text{BPS}+10)\frac{M}{4}+$ $\text{BPS}+6N_R-1]/\text{BPS}$	$[(\text{BPS}+4)\frac{M}{8}$ $+\text{BPS}+2]/\text{BPS}$		$M/4$

Table 2.5: Complexity (per bit) of soft-decision-aided General MQAM detection. Conventional Max-Log-MAP and Approx-Log-MAP refer to Eqs. (2.34) and (2.35) using Eq. (2.38), while Proposed Max-Log-MAP and Approx-Log-MAP refer to Algorithm 2.3 and its Approx-Log-MAP correction.

in Figs. 2.17a and 2.17b that the CRR achieved by Algorithms 2.2 and 2.3 approaches their upper bound of 50% and 75% respectively as M increases, because 50% and 75% of the constellation points have been avoided by the respective algorithms. Furthermore, the complexity reduction seen in both Fig. 2.17a and Fig. 2.17b is substantial, especially, when the soft MPSK/QAM detector is invoked several times in the aforementioned turbo detection applications.

As demonstrated by the EXIT charts of the Square MQAM schemes seen in Fig. 2.14a, the Square 16QAM detector has a near-horizontal EXIT curve. However, as the number of modulation levels M increases, the Square MQAM constellations involve more bits in jointly encoding the symbol magnitudes, which results in an improved iteration gain, as evidenced by Fig. 2.14a. Therefore, a performance loss may be imposed, when the QAM detectors do not take into account the *a priori* LLRs, as in the conventional bit metric generation methods presented in [245–247]. Fig. 2.18 further demonstrates that a significant performance improvement may be achieved, when the number of iterations between the Square 256QAM detector and the channel decoder is increased, which is only possible for the MQAM detectors introduced in Secs 2.3 and 2.4, which exhibit optimum detection capabilities.

The performance attained and the complexity imposed typically hinges on a tradeoff in communication systems design. Considering 32QAM as an example, Fig. 2.19a shows that Cross 32QAM and Star 32QAM outperform their Square 32QAM counterpart in the context of a variety of coded schemes. However, as demonstrated by Fig. 2.19b, the conventional Cross/Star 32QAM detection invoking Eq. (2.38) exhibits a substantially higher complexity compared to the conventional Square 32QAM detection relying on Eq. (2.39). Nonetheless, it can also be seen in Fig. 2.19b that the complexity difference between the Cross/Star 32QAM detection and the Square 32QAM detection is significantly reduced, when the proposed reduced-complexity algorithms are applied.

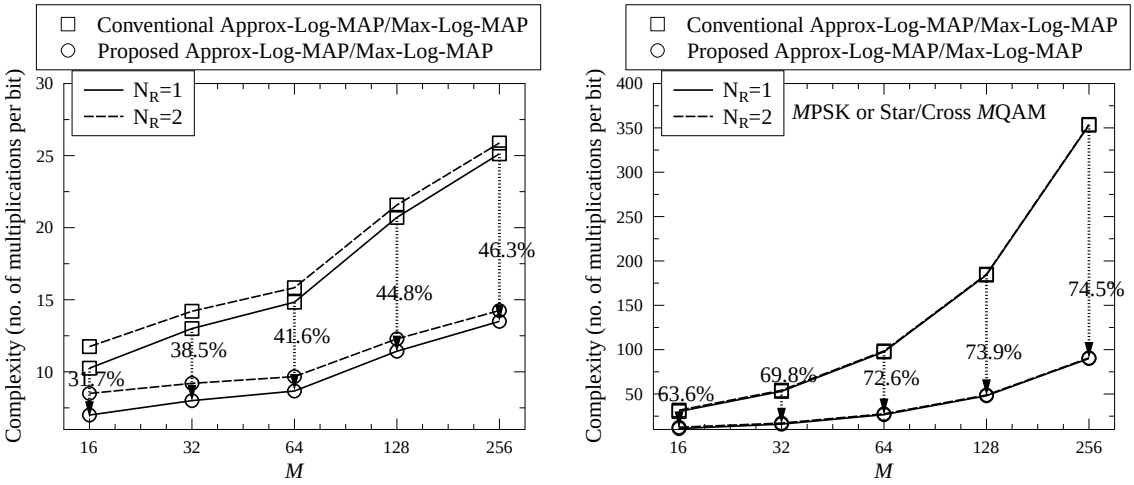

(a) Square MQAM

(b) MPSK or Star/Cross MQAM

Figure 2.17: Complexity (number of multiplications per bit) comparison between the conventional soft-decision-aided MPSK/QAM detection algorithms of Sec. 2.3.1 and the proposed reduced-complexity detection algorithms of Sec. 2.4. The Complexity Reduction Ratios (CRRs) achieved by the proposed detection algorithms are indicated on the figures.

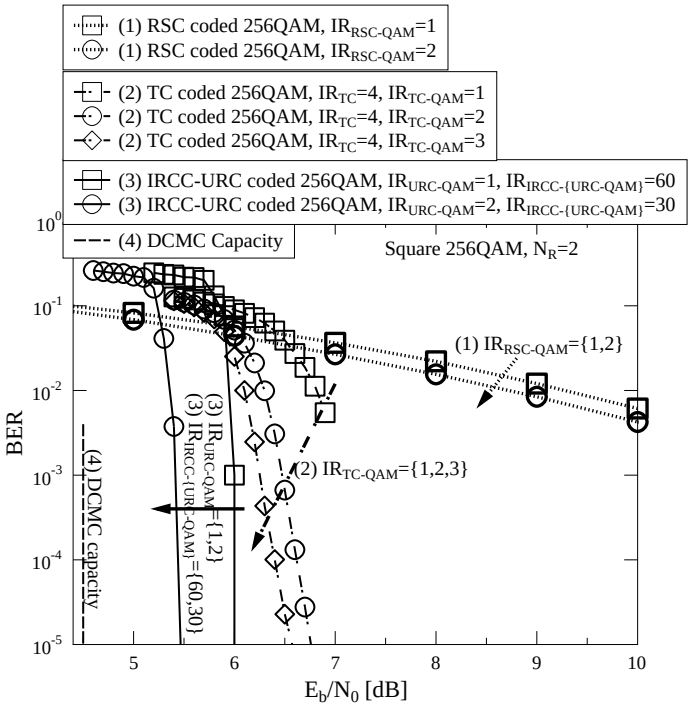

Figure 2.18: BER performance of a variety of coded Square 256QAM schemes ($N_R = 2$) associated with different number of iterations. For the case of $IR_{URC-QAM} = 1$, the IRCC's coefficients are given by [0.0106113, 0, 0, 0, 0, 0.105379, 0.547611, 0, 0, 0, 0, 0.138154, 0.126095, 0, 0, 0, 0.0721744]. The rest of the parameters are the same as those of Fig. 2.15. The corresponding schematics are portrayed in Figs. 2.8 and 2.10.

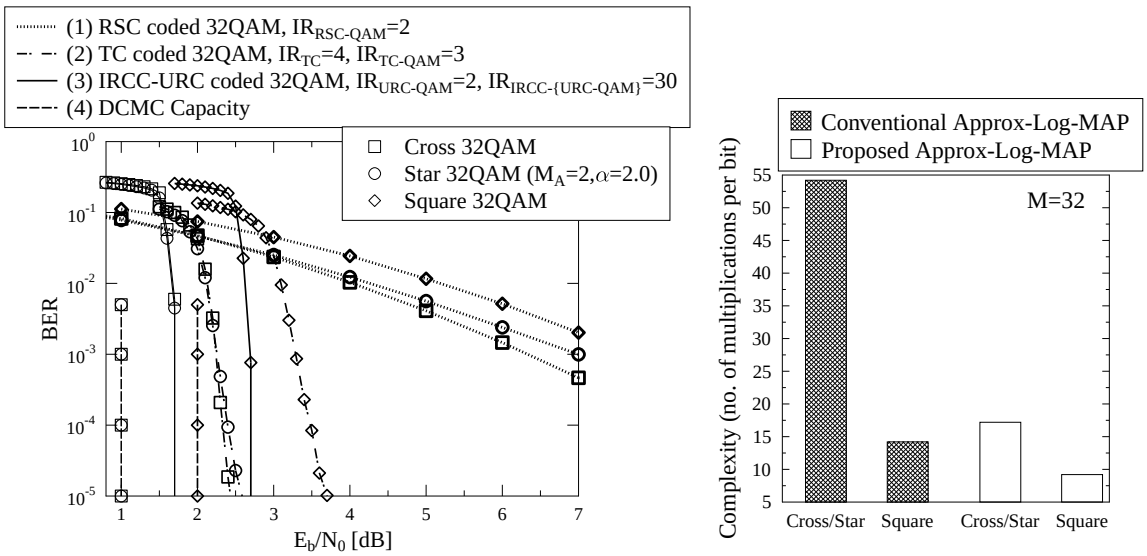

(a) BER performance

(b) Complexity comparison

Figure 2.19: The tradeoff between BER performance and complexity of Cross/Star/Square QAM schemes when they are invoked in a variety of coded system. The corresponding schematics are portrayed in Figs. 2.8 and 2.10.

2.5 Chapter Conclusions

In this chapter, the basic PSK and QAM modulation schemes in both coded systems and in uncoded systems are studied. Firstly, the constellations PSK and QAM and their hard-decision-aided low-complexity detectors are reviewed in Sec. 2.2. Secondly, the classic soft-decision-aided PSK/QAM detection algorithms are summaried in Sec. 2.3. Furthermore, both theoretical backgound and practical implementation of EXIT chart as well as the crucial role of EXIT chart in the near-capacity systems design are also thoroughly discussed in Sec. 2.3. Lastly, a new method of reducing the complexity of the soft-decision-aided PSK/QAM detection algorithms is proposed in Sec. 2.4. We demonstrate that the symmetry provided by Gray-labelled constellations enables the detector to only take into account a reduced subset of the constellation points, while the optimum detection capabilities are retained.

Among all the channel coded systems introduced in this chapter, the turbo coded schemes achieve a better performance than their RSC coded counterparts, while the IRCC and URC coded schemes are capable of achieving a performance that is closest to capacity, as discussed in Sec. 2.3.2 and verified by both Fig. 2.18 and Fig. 2.19a. However, the highest complexity is imposed by the IRCC-URC coded scheme, followed by the TC coded scheme and the RSC coded scheme. The tradeoff between the attainable performance and the complexity imposed is one of the most important considerations in communication systems. Moreover, owing to the fact that the real and imaginary parts of the Square MQAM constellation may always be separately detected, the detection complexity for Square MQAM is generally lower than that of other MPSK/QAM counterparts, which is exemplified by Fig. 2.19. An example of the complexity and performance tradeoffs sum-

Coded Scheme	At BER=10^{-5}
IRCC-URC coded Cross 32 QAM	$E_b/N_0 = 1.8$ dB
IRCC-URC coded Square 32 QAM	$E_b/N_0 = 2.8$ dB
TC coded Cross 32 QAM	$E_b/N_0 = 2.5$ dB
TC coded Square 32 QAM	$E_b/N_0 = 3.8$ dB
RSC coded Cross 32 QAM	$E_b/N_0 = 10$ dB
RSC coded Square 32 QAM	$E_b/N_0 = 11$ dB

Table 2.6: Summary table for the simulation results of Fig. 2.19, where $N_R = 2$ RAs are employed. The coded schemes are listed according to descending order of complexity. The E_b/N_0 results are recorded at a BER level of 10^{-5}.

marized according to the simulation results of Fig. 2.19 is presented in Table 2.6, where only the Cross 32QAM constellation and the Square 32QAM constellation seen in Fig. 2.19 are summarized. This is because the Star 32QAM schemes and their Cross 32QAM counterparts exhibit a similar performance and complexity. Table 2.6 demonstrates plausible trend that the performance attained may degrade as the system complexity is reduced.

The modulation and channel coding schemes introduced in this chapter constitute the most fundamental elements in communication systems. The algorithms of this chapter will be widely referred throughout this report. For example, the reduced-complexity soft PSK/QAM detectors proposed in this chapter may benefit a diverse variety of communication systems. As mentioned before, the linear MIMO receivers [13,14,75] as well as orthogonal STBC detectors [177,178] may directly invoke our proposed PSK/QAM detection algorithms. Similarly, linear receivers designed for beamforming [267] or for CDMA Multiple-User Detection (MUD) [75] that have a similar form to linear MIMO receivers may also employ our reduced-complexity PSK/QAM detection algorithms. Furthermore, noncoherent receivers [127, 132, 136, 154] for differential PSK/QAM schemes may also have their detection complexity reduced by applying our proposed method. We will continue to discuss some of the selected techniques in the following chapters.

Chapter 3

Noncoherent Detection for DPSK

3.1 Introduction

The coherent detection techniques introduced in Chapter 2 rely on the availability of Channel State Information (CSI) knowledge at the receiver. To elaborate a little further, when the fading channels remain constant over several transmission frame periods, which may be termed as Quasi-Static (QS) fading, accurate channel estimation becomes feasible with the aid of training based channel estimation [99, 268]. This Channel Estimator (CE) effectively takes samples of the fading channels envolope/phase by observing the received pilot samples, which are periodically sent by the transmitter and also known by the receiver. In order to avoid the associated system throughput reduction imposed by the pilot overhead, blind CEs allow the coherent receiver to process the received signal without known pilot samples [269, 270]. By contrast, semi-blind CEs rely on a significantly reduced number of pilot symbols [271, 272] but typically impose a high estimation complexity. It is demonstrated in [98] that the MSE between the fading channel matrix and its estimate at the coherent receiver may be minimized by the aforementioned three CEs in QS fading channels.

However, when the fading channel varies potentially for each consecutive transmitted symbol, which may be termed as rapid fading, the resultant inaccurate channel estimation may substantially deteriorate the coherent receiver's performance. More explicitly, as the Doppler frequency is increased, the Pilot Symbol Assisted Modulation (PSAM) [1] conceived for estimating the fading has to reduce the pilot spacing in order to sample the fading channels more frequently. This implies that more transmission power may be dedicated to the pilot symbols instead of the data-carrying symbols. Furthermore, as the temporal correlation between the fading samples becomes weaker, the accuracy of pilot-based channel estimation degrades, which may result in an unavoidable performance loss for all coherent schemes.

In order to mitigate this problem, low-complexity noncoherently detected differential schemes may be considered. More explicitly, Fig. 3.1 portrays the schematic of Differential Phase Shift Keying (DPSK) transmitter and its noncoherent receiver relying on Conventional Differential De-

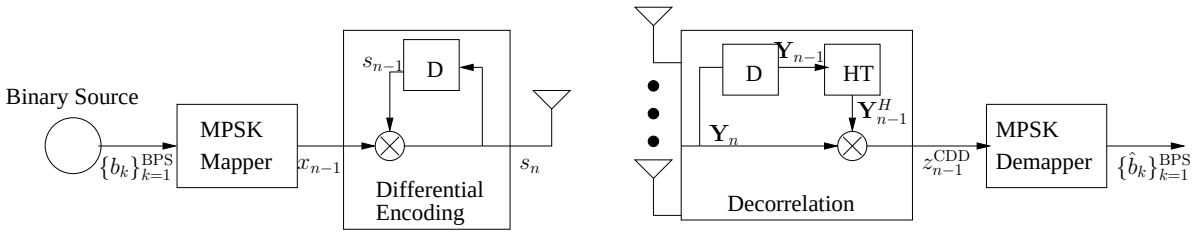

Figure 3.1: The schematic of DPSK transmitter and Conventional Differential Detection (CDD) aided DPSK receiver.

tection (CDD). The differential encoder of Fig. 3.1 modulates its data-carrying symbol x_{n-1} onto the phase changes between every pair of consecutive transmitted symbol, namely s_{n-1} and s_n. As a result, the CDD portrayed in Fig. 3.1 may recover the source information by observing the phase change between every pair of consecutive received samples $\mathbf{Y}_{n-1}$ and $\mathbf{Y}_n$. The family of DPSK schemes was originally proposed for avoiding false phase locking in AWGN channels [7, 115, 119, 273], and since then numerous noncoherent receivers have been developed to eliminate the need for channel estimation for transmission over fading channels.

In the absense of channel estimation, the CDD portrayed in Fig. 3.1 generally suffers from a 3 dB performance penalty, while upon increasing the Doppler frequency a pronounced irreducible error floor is formed. Hence Multiple-Symbol Differential Detection (MSDD) was proposed for DPSK in [7, 113, 114] in order to reduce the performance penalty imposed. Briefly, the MSDD observes N_w consecutive received samples $\{Y_{n-t}\}_{t=0}^{N_w-1}$ and makes a joint decision on (N_w-1) data-carrying symbols $\{x_{n-t}\}_{t=1}^{N_w-1}$. The price paid is that the MSDD complexity increases exponentially with N_w, because the (N_w-1) data-carrying symbols have a total number of $M^{(N_w-1)}$ joint combinations. In order to mitigate this problem, low-complexity Decision-Feedback Differential Detection (DFDD) was introduced based on two different approaches. The first approach proposed in [119, 121] makes use of the same decision metric as MSDD, where the first (N_w-2) data-carrying symbols $\{\hat{x}_{n-t}\}_{t=2}^{N_w-1}$ are detected as part of the previous DFDD windows, and the current DFDD window is only responsible for detecting a single symbol x_{n-1}. The second appoach proposed in [120, 121, 126] relies on blind channel estimation based on both the previous received samples $\{\mathbf{Y}_{n-t}\}_{t=1}^{N_w-1}$ as well as on the previous symbol decisions $\{\hat{x}_{n-t}\}_{t=2}^{N_w-1}$, and then the estimated fading channel is utilized for detecting the latest data-carrying symbol x_{n-1}. Interestingly, it was demonstrated in [121] that these DFDD methods are equivalent for DPSK operating in Rayleigh fading channels. However, the DFDD's imperfect decision feedback results in a performance loss compared to MSDD. In order to maintain the optimum MSDD performance at a reduced detection complexity, Multiple-Symbol Differential Sphere Detection (MSDSD) was proposed in [127], where the problem of optimizing the MSDD decision metric is transformed into a shortest-vector problem [12], so that the Sphere Decoder (SD) may be invoked for MSDD. This concept is reminiscent of the SD aided V-BLAST [10, 274–276] philosophy.

Similar to ML detection aided V-BLAST, MSDD jointly detects multiple independently faded

symbols, which implies that the MSDD's improved degree of freedom may result in a beneficial iteration gain, when the MSDD is invoked in turbo detection. Therefore, soft-decision-aided MSDD conceived for coded DPSK was proposed and analyzed in [114]. Similarly, soft-decision-aided DFDD was designed for coded DPSK schemes in [122,125,136]. Furthermore, soft-decision-aided MSDSD conceived for coded DPSK using the Max-Log-MAP detector was proposed in [132]. All these aforementioned developments facilitate the employment of turbo detection by exchanging extrinsic soft-information between the noncoherent detector and the channel decoder, which potentially facilitates attaining a near-capacity performance for coded DPSK systems. However, the objective of approaching the optimum noncoherent performance bound at a further reduced complexity continues to elude researchers at the time of writing. Our goal in this chapter is to provide a performance comparison between the coherent and noncoherent schemes at different Doppler frequencies in order to characterize their pros and cons in specific scenarios. Against this background, the novelty of this chapter may be summarized as follows:

1. We further extend the classic MSDSD aided uncoded DPSK [127] to the case of employing multiple Receive Antennas (RAs) $N_R \geq 1$, while maintaining a low complexity for the SD's Schnorr-Euchner [237] search strategy. More explicitly, the MSDSD conceived for multiple antennas aided differential schemes in [277] requires us to evaluate and sort all M constellation points for each SD index. A similar problem arises when we employ multiple RAs for MSDSD aided uncoded DPSK [127]. However, a simple decorrelating operation may be introduced before invoking the Schnorr-Euchner search strategy, so that the SD may first visit the specific constellation point that are near the decorrelated variable. Then the rest of the constellation points may be visited in a zig-zag fashion, if required, which is similar to the original case of $N_R = 1$ in [127].

2. As demonstrated in Sec. 2.3.2.4, the Max-Log-MAP algorithm imposes a modest, but non-negligible performance loss compared to the near-optimum Approx-Log-MAP algorithm. Therefore, we propose to modify the output of the soft-decision-aided MSDSD proposed in [132], where multiple candidates may be produced by the SD so that the Approx-Log-MAP may be implemented. Our simulation results demonstrate that the Approx-Log-MAP aided MSDSD matches the near-optimum detection capability of the Approx-Log-MAP aided MSDD.

3. When the *a priori* LLRs gleaned from a channel decoder are taken into account by the soft-decision-aided MSDSD in [132], the SD's Schnorr-Euchner [237] search strategy once again requires us to sort a total number of M probability metrics according to having M constellation points. This is because the channel decoder is unaware of the specific transmitted DPSK symbol, hence the decision variables that were used by the MSDSD for detecting the uncoded DPSK symbols cannot be directly employed for coded DPSK detection. However, as discussed in Chapter 2, a soft-decision-aided detector does not have to visit all constellation legitimate points for finding the optimum probability metric. Indeed, the reduced-complexity

design proposed in Chapter 2 may be adapted for the Schnorr-Euchner search strategy of MSDSD in [132], where the optimum candidate may be found by visiting a reduced-size subset of constellation points, and then the rest of the constellation points may be visited in a zig-zag fashion, if needed. Therefore, since the MSDSD proposed in [132] substantially reduces the MSDD complexity because of the SD's advantage of visiting a reduced number of constellation points within the sphere radius, our proposed MSDSD aided coded DPSK arrangement exhibits a further reduced detection complexity due to the fact that the number of constellation points visited by the SD is reduced.

4. Furthermore, we provide a discussion on the important subject of coherent versus noncoherent detection. More explicitly, numerous channel estimation techniques are capable of acquiring accurate CSI knowledge at the coherent receiver, when fading channels fluctuate relatively slowly. However, as the Doppler frequency increases, the estimated CSI may severely deviate from the true CSI. As a result, coherent receivers relying on realistic imperfect CSI suffer from an inevitable performance loss. We will demonstrate that this problem becomes particularly serious for soft-decision-aided coherent detectors, because they are likely to produce extrinsic LLRs exhibiting a poor integrity. This implies that the resultant LLRs may severely deviate from the LLR definition introduced in Sec. 2.3.2.4. We will confirm that coherent schemes may enjoy indeed, a substantial performance advantage in slowly fluctuating fading channels, while noncoherent schemes employing MSDSD may be deemed as a more suitable candidate for turbo detection aided coded DPSK systems operating at high Doppler frequencies.

The rest of this chapter is organized as follows. The noncoherent receivers conceived for uncoded DPSK are summarized in Sec. 3.2, where the CDD, MSDD, MSDSD and DFDD schemes are detailed. The soft-decision-aided noncoherent detectors conceived for coded DPSK are presented in Sec. 3.3, where both the Approx-Log-MAP aided MSDSD and the reduced-complexity MSDSD are proposed. Sec. 3.4 presents a summary of our performance comparisons between the coherent and noncoherent schemes. The Chapter is concluded in Sec. 3.5.

3.2 Uncoded DPSK

In this section, hard-decision-aided noncoherent detectors conceived for uncoded DPSK are introduced. The low-complexity CDD aided uncoded DPSK scheme is similar to the coherent detection aided uncoded MPSK arrangement introduced in Sec. 2.2. The CDD uses the previous received sample $\mathbf{Y}_{n-1}$ as a reference for detecting the data-carrying symbol x_{n-1}, which imposes a performance loss. The MSDD scheme improves the noncoherent receiver's performance by eliminating its error-floor encountered at high Doppler frequencies, albeit at the cost of an exponentially increasing complexity, as the detection-window width is increased. Fortunately, the MSDSD is capable of mitigating the excessive MSDD complexity without imposing any performance loss.

The DFDD is capable of bridging the gap between the coherent and noncoherent schemes, where blind channel estimation is performed with the aid of the previous received samples and previous decisions. However, DFDD still suffers from a potential error propagation problem, hence its performance is sub-optimal compared to the MSDD. We will continue by demonstrating these features in the following sections.

3.2.1 Hard-Decision-Aided CDD Conceived for Uncoded DPSK

The structure of a DPSK's transmitter and its CDD aided DPSK receiver is portrayed in Fig. 3.1. For an M-ary DPSK scheme, the transmitter firstly maps $\text{BPS} = \log_2 M$ source bits $\{b_k\}_{k=1}^{\text{BPS}}$ to an MPSK symbol $x^m = \exp(j\frac{2\pi}{M}\check{m})$, where the phasor index $m = \text{bin2dec}(b_1 \cdots b_{\text{BPS}})$ is the Gray-coded index $\check{m}$. Following MPSK mapping, the DPSK-related differential encoding operation of a single Transmit Antenna (TA) may be performed as:

$$s_n = \begin{cases} 1, & n = 1 \\ x_{n-1}s_{n-1}, & n > 1 \end{cases}, \tag{3.1}$$

where s_n is also drawn from the same MPSK constellation, as that introduced in Fig. 2.4 of Chapter 2. Furthermore, the signal received by the N_R RAs may also be modelled by Eq. (2.1).

If the Rayleigh fading channel is Quasi-Static (QS), i.e. we have $\mathbf{H}_n = \mathbf{H}_{n-1}$ over a block of T_{QS} symbol periods, then the received signal matrix of Eq. (2.1) may be further extended as:

$$\begin{aligned} \mathbf{Y_n} &= x_{n-1}s_{n-1}\mathbf{H}_n + \mathbf{V}_n \\ &= x_{n-1}(\mathbf{Y}_{n-1} - \mathbf{V}_{n-1}) + \mathbf{V}_n \\ &= x_{n-1}\mathbf{Y}_{n-1} + \widetilde{\mathbf{V}}_n, \end{aligned} \tag{3.2}$$

where the equivalent noise term $\widetilde{\mathbf{V}}_n = -x_{n-1}\mathbf{V}_{n-1} + \mathbf{V}_n$ is also Gaussian distributed with a zero mean and a variance of $2N_0$.

Similar to the low-complexity coherent MPSK detector of Eq. (2.4), the ML estimation of the data symbol x_{n-1} based on the equivalent received signal model of Eq. (3.2) may be formulated as [8]:

$$\begin{aligned} \hat{x}_{n-1} &= \arg \min_{x^m \in \mathbf{x}} \|\mathbf{Y}_n - x_{n-1}\mathbf{Y}_{n-1}\|^2 \\ &= \arg \min_{x^m \in \mathbf{x}} \left|z_{n-1}^{\text{CDD}} - x_{n-1}\right|^2, \end{aligned} \tag{3.3}$$

where the CDD decision variable is given by the decorrelating operation as:

$$z_{n-1}^{\text{CDD}} = \mathbf{Y}_n\mathbf{Y}_{n-1}^H. \tag{3.4}$$

Moreover, the differences between $\|\mathbf{Y}_n - x_{n-1}\mathbf{Y}_{n-1}\|^2 = \|\mathbf{Y}_n\|^2 + \|\mathbf{Y}_{n-1}\|^2 - 2\Re(x_{n-1}^*\mathbf{Y}_n\mathbf{Y}_{n-1}^H)$ and $\left|z_{n-1}^{\text{CDD}} - x_{n-1}\right|^2 = \left|z_{n-1}^{\text{CDD}}\right|^2 + |x_{n-1}|^2 - 2\Re(x_{n-1}^* z_{n-1}^{\text{CDD}})$ in Eq. (3.3) are all constants.

Upon obtaining the decision variable z_{n-1}^{CDD} of Eq. (3.4), the regular MPSK demapper of Eq. (2.9) may be formulated as:

$$\hat{x}_{n-1} = \exp(j\tfrac{2\pi}{M}\hat{\check{m}}), \quad \text{where } \hat{\check{m}} = \lfloor \tfrac{M}{2\pi}\angle z_{n-1}^{\text{CDD}} \rceil. \tag{3.5}$$

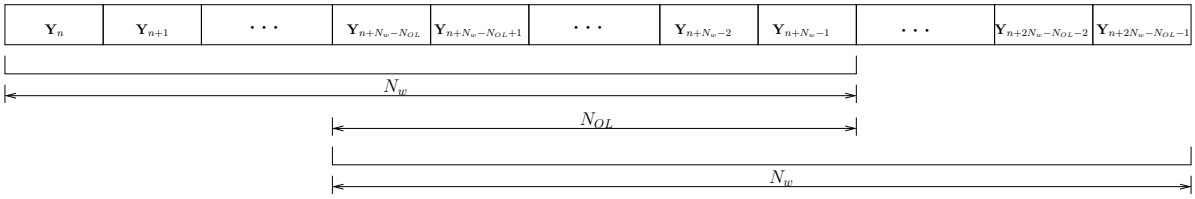

Figure 3.2: The arrangement of the observation windows.

Since the equivalent AWGN noise term $\widetilde{\mathbf{V}}_n$ in Eq. (3.2) has a doubled noise power of $2N_0$, the CDD aided DPSK scheme generally exhibits the widely-known 3 dB performance loss compared to its coherent counterpart in QS fading channels. Moreover, the continuous fading requires $\mathbf{H}_n \neq \mathbf{H}_{n-1}$, which introduces an even more severe performance loss for low-complexity CDD. Therefore, in the next section, we introduce the more advanced MSDD, which is capable of mitigating the error floor of CDD that is often encountered in rapidly fluctuating high-Doppler fading channels.

3.2.2 Hard-Decision-Aided MSDD Conceived for Uncoded DPSK

Again, MSDD aims for improving the performance of CDD by exploiting the temporal correlation of the fading channels over N_w observations. The observation windows are portrayed in Fig. 3.2, where N_{OL} denotes the number of samples that are overlapped by the consecutive observation windows. We normally have $N_{OL} = 1$ for MSDD, so that all the data symbols may be explicitly detected by MSDD.

Therefore, the N_w received signal blocks of Eq. (2.1) may be modelled by MSDD as [113, 114, 121, 127]:

$$\mathbf{Y} = \mathbf{S}\mathbf{H} + \mathbf{V}, \tag{3.6}$$

where the matrices are given by:

$$\begin{aligned} \mathbf{Y} &= \left[\mathbf{Y}_n^T, \mathbf{Y}_{n-1}^T, \cdots, \mathbf{Y}_{n-N_w+1}^T\right]^T, \quad \mathbf{S} = \text{diag}\left\{\left[s_n, s_{n-1}, \cdots, s_{n-N_w+1}\right]\right\}, \\ \mathbf{H} &= \left[\mathbf{H}_n^T, \mathbf{H}_{n-1}^T, \cdots, \mathbf{H}_{n-N_w+1}^T\right]^T, \quad \mathbf{V} = \left[\mathbf{V}_n^T, \mathbf{V}_{n-1}^T, \cdots, \mathbf{V}_{n-N_w+1}^T\right]^T. \end{aligned} \tag{3.7}$$

Without any confusion, we drop the time index n, and we always use the notations of the first MSDD window as:

$$\begin{aligned} \mathbf{Y} &= \left[\mathbf{Y}_{N_w}^T, \mathbf{Y}_{N_w-1}^T, \cdots, \mathbf{Y}_1^T\right]^T, \quad \mathbf{S} = \text{diag}\left\{\left[s_{N_w}, s_{N_w-1}, \cdots, s_1\right]\right\}, \\ \mathbf{H} &= \left[\mathbf{H}_{N_w}^T, \mathbf{H}_{N_w-1}^T, \cdots, \mathbf{H}_1^T\right]^T, \quad \mathbf{V} = \left[\mathbf{V}_{N_w}^T, \mathbf{V}_{N_w-1}^T, \cdots, \mathbf{V}_1^T\right]^T. \end{aligned} \tag{3.8}$$

We note that the matrices $\mathbf{Y}$, $\mathbf{H}$ and $\mathbf{V}$ are of size $(N_w \times N_R)$, while the transmitted signals matrix $\mathbf{S}$ has $(N_w \times N_w)$ elements. Furthermore, since the first transmitted symbol s_1 in $\mathbf{S}$ is a common phase rotation of the following symbols $\{s_t\}_{t=2}^{N_w}$, the MSDD's received signal model of Eq. (3.6)

may be rewritten as[1]:

$$\mathbf{Y} = \bar{\mathbf{S}}\bar{\mathbf{H}} + \mathbf{V}, \tag{3.9}$$

where the v^{th} diagonal element in $\bar{\mathbf{S}}$ is given by:

$$\bar{s}_v = s_v \cdot s_1^* = \begin{cases} 1, & n = 1 \\ x_{v-1}\bar{s}_{v-1} = \prod_{t=1}^{v-1} x_t, & n > 1 \end{cases}, \tag{3.10}$$

while the v^{th} row in $\bar{\mathbf{H}}$ is given by $\bar{\mathbf{H}}_v = s_1 \mathbf{H}_v$.

The MSDD aims for maximizing the following *a posteriori* probability over all candidates $\{\bar{\mathbf{S}}^i\}_{i=0}^{M^{(N_w-1)}-1}$:

$$p\left(\bar{\mathbf{S}}^i|\mathbf{Y}\right) = \frac{p\left(\mathbf{Y} \mid \bar{\mathbf{S}}^i\right) p(\bar{\mathbf{S}}^i)}{\sum_{\forall \bar{\mathbf{S}}^i} p\left(\mathbf{Y} \mid \bar{\mathbf{S}}^i\right) p(\bar{\mathbf{S}}^i)}, \tag{3.11}$$

where the *a priori* probability $\{p(\bar{\mathbf{S}}^i)\}_{i=0}^{M^{(N_w-1)}-1}$ may be assumed to be a constant of $\frac{1}{M^{(N_w-1)}}$ for the equiprobable variable $\{\bar{\mathbf{S}}^i\}_{i=0}^{M^{(N_w-1)}-1}$. Furthermore, the conditional probability $\{p\left(\mathbf{Y} \mid \bar{\mathbf{S}}^i\right)\}_{i=0}^{M^{(N_w-1)}-1}$ in Eq. (3.11) may be expressed as:

$$p\left(\mathbf{Y} \mid \bar{\mathbf{S}}^i\right) = \frac{\exp\left\{-\text{rvec}(\mathbf{Y}) \cdot \mathbf{R}_{YY}^{-1} \cdot [\text{rvec}(\mathbf{Y})]^H\right\}}{\pi^{N_R N_w} \det(\mathbf{R}_{YY})}, \tag{3.12}$$

where the operation $\text{rvec}(\mathbf{Y})$ forms a $(1 \times N_R N_w)$-element row vector by taking the rows of $\mathbf{Y}$ one-by-one. We note that the conditional probability $\{p(\mathbf{Y}_n|s^m)\}_{m=0}^{M-1}$ of Eq. (2.3) invoked by coherent receivers is given by the PDF of the Gaussian-distributed AWGN matrix $\mathbf{V}_n$ of Eq. (2.1). By contrast, the conditional probability $\{p\left(\mathbf{Y} \mid \bar{\mathbf{S}}^i\right)\}_{i=0}^{M^{(N_w-1)}-1}$ of Eq. (3.12) invoked by noncoherent receivers is given by the PDF of the multi-variate Gaussian-distributed MSDD's received signal matrix $\mathbf{Y}$ of Eq. (3.6), where the MSDD's Rayleigh fading matrix $\mathbf{H}$ of Eq. (3.6) (or equivalently $\bar{\mathbf{H}}$ of Eq. (3.9)) does not have to be known by noncoherent receivers [278].

The MSDD's received signal matrix $\mathbf{Y}$ of Eq. (3.9) is vectorized in Eq. (3.12) in order to form a vector of Gaussian-distributed variables. The equivalent signal model is given by:

$$\text{rvec}(\mathbf{Y}) = \text{rvec}(\bar{\mathbf{H}}) \cdot (\bar{\mathbf{S}} \otimes \mathbf{I}_{N_R}) + \text{rvec}(\mathbf{V}), \tag{3.13}$$

where the operation $\otimes$ represents the Kronecker product. As a result, the correlation matrix $\mathbf{R}_{YY}$ in Eq. (3.12) may be formulated as:

$$\begin{aligned} \mathbf{R}_{YY} &= \text{E}\left\{[\text{rvec}(\mathbf{Y})]^H \cdot \text{rvec}(\mathbf{Y})\right\} \\ &= \left[(\bar{\mathbf{S}}^i)^H \otimes \mathbf{I}_{N_R}\right] \text{E}\left\{[\text{rvec}(\bar{\mathbf{H}})]^H \cdot \text{rvec}(\bar{\mathbf{H}})\right\} \left(\bar{\mathbf{S}}^i \otimes \mathbf{I}_{N_R}\right) + \text{E}\left\{[\text{rvec}(\mathbf{V})]^H \cdot \text{rvec}(\mathbf{V})\right\} \\ &= \left[(\bar{\mathbf{S}}^i)^H \otimes \mathbf{I}_{N_R}\right] \left(\mathbf{R}_{\bar{H}\bar{H}} + \mathbf{R}_{VV}\right) \left(\bar{\mathbf{S}}^i \otimes \mathbf{I}_{N_R}\right), \end{aligned} \tag{3.14}$$

[1] We note that $\mathbf{Y}$ in Eq. (3.6) stores received signal vectors in a reverse order compared to the one seen in [127, 132]. As a result, the MSDSD introduced in the next section may detect the transmitted symbols according to their differential encoding order, i.e. we have $\bar{s}_v = x_{v-1}\bar{s}_{v-1}$, instead of detecting them backwards as $\bar{s}_v = x_v^*\bar{s}_{v+1}$ in [127, 132].

where the transmission matrix $\bar{\mathbf{S}}$ of Eq. (3.6) is a unitary matrix when DPSK is employed, hence we have $\{\bar{\mathbf{S}}^i(\bar{\mathbf{S}}^i)^H = \mathbf{I}_{\mathbf{N_w}}\}_{i=0}^{M^{(N_w-1)}-1}$. The fading channel's correlation matrix $\mathbf{R}_{\bar{H}\bar{H}}$ in Eq. (3.14) is given by:

$$\mathbf{R}_{\bar{H}\bar{H}} = \mathrm{E}\left\{[\mathrm{rvec}(\bar{\mathbf{H}})]^H \cdot \mathrm{rvec}(\bar{\mathbf{H}})\right\} = \mathbf{R}_{hh} \otimes \mathbf{I}_{N_R}, \tag{3.15}$$

where the fading channel's characteristic correlation matrix[2] $\mathbf{R}_{hh}$ may be expressed as:

$$\begin{aligned}\mathbf{R}_{hh} &= \mathrm{Toeplitz}([\ \rho_0 \quad \rho_1 \quad \cdots \quad \rho_{N_w-1}\ ]) \\ &= \begin{bmatrix} \rho_0 & \rho_1 & \cdots & \rho_{N_w-1} \\ \rho_1 & \rho_0 & \cdots & \rho_{N_w-2} \\ \vdots & \vdots & \ddots & \vdots \\ \rho_{N_w-1} & \rho_{N_w-2} & \cdots & \rho_0 \end{bmatrix}.\end{aligned} \tag{3.16}$$

The notation $\mathrm{Toeplitz}([\ \rho_0 \quad \rho_1 \quad \cdots \quad \rho_{N_w-1}\ ])$ refers to the symmetric Toeplitz matrix generated from the vector $[\ \rho_0 \quad \rho_1 \quad \cdots \quad \rho_{N_w-1}\ ]$. For the case of QS fading channels associated with $T_{QS} > N_w$, we have $\{\rho_v = 1\}_{v=0}^{N_w-1}$. For the case of continuous fading channels, we have $\{\rho_v = J_0(2\pi f_d \cdot v)\}_{v=0}^{N_w-1}$ according to the Rayleigh fading channel model characterized by Clarke [279] and Jakes [280], where $J_0(\cdot)$ is the zero-order Bessel function of the first kind, while f_d denotes the normalized Doppler frequency. In a mobile communication system, the normalized Doppler frequency characterizes the fading rate of the channels as:

$$f_d = \frac{v \cdot f_c}{c \cdot f_s}, \tag{3.17}$$

where v, f_c, c and f_s refer to the velocity of the mobile receiver, the carrier frequency, the speed of light and the sampling rate, respectively. As a result, the cross correlations $\{\rho_v\}_{v=1}^{N_w-1}$ in Eq. (3.15) may become relatively low in high-mobility scenarios, in which case the accurate channel estimation required by coherent receivers is severely challenged. Moreover, the AWGN correlation matrix $\mathbf{R}_{VV}$ in Eq. (3.21) is given by:

$$\mathbf{R}_{VV} = \mathrm{E}\left\{[\mathrm{rvec}(\mathbf{V})]^H \cdot \mathrm{rvec}(\mathbf{V})\right\} = \mathbf{R}_{vv} \otimes \mathbf{I}_{N_R}, \tag{3.18}$$

where the AWGN characteristic correlation matrix $\mathbf{R}_{vv}$ is simply given by:

$$\mathbf{R}_{vv} = N_0 \cdot \mathbf{I}_{\mathbf{N_w}}. \tag{3.19}$$

As a result, the correlation matrix $\mathbf{R}_{YY}$ of Eq. (3.14) may be expressed as:

$$\begin{aligned}\mathbf{R}_{YY} &= \left[(\bar{\mathbf{S}}^i)^H \otimes \mathbf{I}_{N_R}\right](\mathbf{C} \otimes \mathbf{I}_{N_R})\left(\bar{\mathbf{S}}^i \otimes \mathbf{I}_{N_R}\right) \\ &= \left[(\bar{\mathbf{S}}^i)^H \mathbf{C} \bar{\mathbf{S}}^i\right] \otimes \mathbf{I}_{N_R},\end{aligned} \tag{3.20}$$

where the channel's characteristic correlation matrix $\mathbf{C}$ is given by:

$$\mathbf{C} = \mathbf{R}_{hh} + \mathbf{R}_{vv}. \tag{3.21}$$

[2]We note that the fading channel's characteristic correlation matrix $\mathbf{R}_{hh}$ is a simplified representation of the fading channel's correlation matrix $\mathbf{R}_{\bar{H}\bar{H}}$. They are equal only when $N_R = 1$ RA is used as in [127, 132].

Therefore, the determinant of the correlation matrix $\mathbf{R_{YY}}$ seen in Eq. (3.12) is a constant of $\det(\mathbf{R}_{YY}) = \left\{\det\left[(\bar{\mathbf{S}}^i)^H \cdot \det(\mathbf{C}) \cdot \det(\bar{\mathbf{S}}^i)\right]\right\}^{N_R} = \det(\mathbf{C})^{N_R}$ for DPSK schemes.

In summary, the MSDD that maximizes the *a posteriori* probability of Eq. (3.11) may be formulated as:

$$\hat{\mathbf{S}} = \arg \min_{\forall \bar{\mathbf{S}}^i} \text{rvec}(\mathbf{Y}) \cdot \mathbf{R}_{YY}^{-1} \cdot [\text{rvec}(\mathbf{Y})]^H \tag{3.22a}$$

$$= \arg \min_{\forall \bar{\mathbf{S}}^i} [\text{vec}(\mathbf{Y}^H)]^H \cdot \left\{\left[(\bar{\mathbf{S}}^i)^H \mathbf{C}^{-1} \bar{\mathbf{S}}^i\right] \otimes \mathbf{I}_{N_R}\right\} \cdot [\text{vec}(\mathbf{Y}^H)] \tag{3.22b}$$

$$= \arg \min_{\forall \bar{\mathbf{S}}^i} [\text{vec}(\mathbf{Y}^H)]^H \cdot \text{vec}\left\{\mathbf{Y}^H \left[(\bar{\mathbf{S}}^i)^H \mathbf{C}^{-1} \bar{\mathbf{S}}^i\right]^T\right\} \tag{3.22c}$$

$$= \arg \min_{\forall \bar{\mathbf{S}}^i} \text{tr}\left\{\mathbf{Y}\mathbf{Y}^H \bar{\mathbf{S}}^i \mathbf{C}^{-1} (\bar{\mathbf{S}}^i)^H\right\} \tag{3.22d}$$

$$= \arg \min_{\forall \bar{\mathbf{S}}^i} \left\|\mathbf{L}(\bar{\mathbf{S}}^i)^H \mathbf{Y}\right\|^2. \tag{3.22e}$$

In more details, Eq. (3.22b) is obtained according to $(\mathbf{A} \otimes \mathbf{I})^{-1} = \mathbf{A}^{-1} \otimes \mathbf{I}$, and the operation $\text{vec}(\mathbf{Y}^H)$ forms a $(N_R N_w \times 1)$-element column vector by taking the columns in matrix $\mathbf{Y}^H$ one-by-one. Eq. (3.22c) is obtained according to $(\mathbf{B} \otimes \mathbf{I}) \cdot \text{vec}(\mathbf{A}) = \text{vec}(\mathbf{A}\mathbf{B}^T)$. Eq. (3.22d) is obtained according to $[\text{vec}(\mathbf{A})]^H \text{vec}(\mathbf{B}) = \text{tr}(\mathbf{A}^H \mathbf{B})$, while both $\bar{\mathbf{S}}^i$ and $\mathbf{C}$ are symmetric, i.e. we have $(\bar{\mathbf{S}}^i)^T = \bar{\mathbf{S}}^i$ and $\mathbf{C}^T = \mathbf{C}$. The relationships leading to these results may be found in [281]. Furthermore, the lower triangular matrix $\mathbf{L}$ in Eq. (3.22e) is obtained from the Cholesky decomposition of the inverted channel correlation matrix, i.e. we have $\mathbf{C}^{-1} = \mathbf{L}\mathbf{L}^H$.

Recall that both the coherent detection of Eq. (2.4) and CDD of Eq. (3.3) have a low-complexity of order $O(M)$ and their corresponding implementations of Eq. (2.9) and Eq. (3.5) directly search for the optimum constellation point, which is located closest to the decision variable. However, the MSDD of Eq. (3.22) imposes a high detection complexity of order $O(M^{(N_w-1)})$, where all candidates $\{\bar{\mathbf{S}}^i\}_{i=0}^{M^{(N_w-1)}-1}$ have to be visited and compared. Therefore, in order to mitigate the excessive MSDD complexity, MSDSD which incorporates SD into the MSDD of Eq. (3.22) is introduced in the next section.

3.2.3 Hard-Decision-Aided MSDSD Conceived for Uncoded DPSK

It is widely recognized that a V-BLAST MIMO system, which has N_T TAs for transmitting MPSK/QAM symbols has an exponentially increasing ML detection complexity of $O(M^{N_T})$. This trend is similar to that of the MSDD as a function of the window-width. Therefore, the SD that is often invoked for V-BLAST MIMO detection [10, 274–276] may be incorporated into the MSDD in order to substantially reduce the MSDD's complexity, while the optimum MSDD performance may still be retained, provided that the initial SD's search radius is initialized to a sufficiently large value. In

order to facilitate SD, the MSDD metric of Eq. (3.22) may be extended as:

$$\begin{aligned}\left\|\mathbf{L}^H\bar{\mathbf{S}}^H\mathbf{Y}\right\|^2 &= \sum_{v=1}^{N_w}\left\|\sum_{t=1}^{v} l_{N_w-t+1,N_w-v+1}\bar{s}_t^*\mathbf{Y}_t\right\|^2 \\ &= \sum_{v=1}^{N_w}\left\|\sum_{t=1}^{v}\bar{s}_t^*\mathbf{U}_{t,v}\right\|^2,\end{aligned} \tag{3.23}$$

where we define the vectors $\{\{\mathbf{U}_{t,v} = l_{N_w-t+1,N_w-v+1}\mathbf{Y}_t\}_{t=1}^{v}\}_{v=1}^{N_w}$ which are invariant over the variables $\{\bar{s}_v\}_{v=2}^{N_w}$, while the superscript $i \in \{0,\cdots,M^{(N_w-1)}-1\}$ for $\bar{\mathbf{S}}^i$ is omitted for notational convenience. Eq. (3.23) implies that MSDD may be regarded as a shortest-vector problem [12], which may be solved by SD [127]. More explicitly, the SD may be invoked to examine a limited, but high-probability decision candidate set $\{\bar{s}_v\}_{v=2}^{N_w}$, which falls into the decoding sphere as:

$$\sum_{v=1}^{N_w}\left\|\sum_{t=1}^{v}\bar{s}_t^*\mathbf{U}_{t,v}\right\|^2 \leq R^2, \tag{3.24}$$

where R refers to the SD's SNR-dependent radius. According to Eq. (3.24), we may define the Partial Euclidean Distance (PED) as [127]:

$$\begin{aligned}d_v &= \sum_{\bar{v}=1}^{v}\left\|\sum_{t=1}^{\bar{v}}\bar{s}_t^*\mathbf{U}_{t,\bar{v}}\right\|^2 \\ &= d_{v-1}+\Delta_{v-1},\end{aligned} \tag{3.25}$$

and the associated PED increment throughout the search as:

$$\begin{aligned}\Delta_{v-1} &= \left\|\sum_{t=1}^{v}\bar{s}_t^*\mathbf{U}_{t,v}\right\|^2 \\ &= \left\|\bar{s}_{v-1}^*\mathbf{U}_{v,v}+x_{v-1}\left(\sum_{t=1}^{v-1}\bar{s}_t^*\mathbf{U}_{t,v}\right)\right\|^2.\end{aligned} \tag{3.26}$$

Observe in Eqs. (3.25) and (3.26) that for a specific index v, all the previously tested transmitted symbols $\{\bar{s}_t\}_{t=1}^{v-1}$ have been decided, and the current SD search may opt for the best candidate for representing x_{v-1}, which is supposed to minimize Δ_{v-1}. In summary, the procedures of MSDSD may be summarized as [12]:

Algorithm 3.1: Procedures of Hard-Decision-Aided MSDSD Conceived for Uncoded DPSK.

(1) Initialize the SD's radius R to a sufficiently large value. For the initial SD index of $v=1$, the PED $d_1 = \|\bar{s}_1^*\mathbf{U}_{1,1}\|^2$ is a constant, which does not affect the search result, and hence we may fix $d_1 = 0$. Then the SD search may start with the index of $v=2$.

(2) When the SD visits a specific index v for the first time, the Schnorr-Euchner [237] search strategy is invoked, where the M hypothetical MPSK constellation points for x_{v-1} are

ordered according to the monotonically increasing values of Δ_{v-1} of Eq. (3.26). The first decision candidate for x_{v-1} is stored and the corresponding PED increment value Δ_{v-1} is used for updating PED d_v of Eq. (3.25).

(3) The SD increases the index v, and Step (2) is repeated. Once $v = N_w$ is reached, the radius is updated by $R = d_{N_w}$, and a valid $\bar{\mathbf{S}}$ is found. The SD may re-start its search with the decreased index of $v = N_w - 1$.

(4) When the SD visits a specific index v for the $(n_{v-1}+1)$-st time ($0 < n_{v-1} \leq (M-1)$), according to the previously defined Schnorr-Euchner search order, the $(n_{v-1}+1)$-st hypothetical MPSK constellation point candidate for x_{v-1} is visited, and then the corresponding Δ_{v-1} and d_v are updated.

(4.1) If the updated PED value d_v lies outside the sphere $d_v > R$ or if there is no more new candidate to be visited as specified by $n_{v-1} > (M-1)$, then the SD decreases its index v, and Step (4) is repeated.

(4.2) Otherwise, the SD increases its index v, and then Step (3) is repeated.

(5) The SD terminates when $v = 2$ is reached again without finding any other valid $\bar{\mathbf{S}}$ that lies inside the search sphere.

As demonstrated in Algorithm 3.1, the Schnorr-Euchner search strategy plays an essential role in MSDSD. To elaborate a little further, the Schnorr-Euchner search strategy tailored for MSDSD aided uncoded DPSK aims for finding the best phasor for x_{v-1}, which has the lowest PED increment value Δ_{v-1}, and then the remaining phasor candidates may be visited in a zig-zag fashion that their corresponding Δ_{v-1} value increases monotonically. When $N_R = 1$ RA is used, it was demonstrated in [127] that the best phasor index is given by $\check{m}_{v-1} = \lfloor p_{v-1} \rceil$, where we have $p_{v-1} = \frac{M}{2\pi}\angle(-\bar{s}^*_{v-1}\mathbf{U}_{v,v}/\sum_{t=1}^{v-1}\bar{s}^*_t\mathbf{U}_{t,v})$. If the phase index $\check{m}_{v-1}$ was rounded down from p_{v-1}, i.e. we have the condition of $p_{v-1} - \check{m}_{v-1} \geq 0$, then the SD visits the remaining phasors according to the steps of $\check{m}_{v-1} = \check{m}_{v-1} + 1$, $\check{m}_{v-1} = \check{m}_{v-1} - 2$, , $\check{m}_{v-1} = \check{m}_{v-1} + 3$, etc. By contrast, if the phase index $\check{m}_{v-1}$ was rounded up from p_{v-1}, i.e. we have the condition of $p_{v-1} - \check{m}_{v-1} < 0$, then the SD visits the remaining phasors according to the steps of $\check{m}_{v-1} = \check{m}_{v-1} - 1$, $\check{m}_{v-1} = \check{m}_{v-1} + 2$, $\check{m}_{v-1} = \check{m}_{v-1} - 3$, etc.

However, for the more general case of using $N_R > 1$ RAs, $\{\{\mathbf{U}_{t,v}\}_{t=1}^{v}\}_{v=1}^{N_w}$ in Eq. (3.26) become vectors. As a result, we cannot directly obtain p_{v-1} as we did for the case of $N_R = 1$ seen in [127]. In order to mitigate this problem, we further interpret the PED increment of Eq. (3.26) in the following form:

$$\Delta_{v-1} = \left\| \mathbf{Y}_{v-1}^{\text{MSDD}} - x_{v-1}\mathbf{H}_{v-1}^{\text{MSDD}} \right\|^2, \tag{3.27}$$

where the N_R-element vectors $\mathbf{Y}_{v-1}^{\text{MSDD}} = \bar{s}^*_{v-1}\mathbf{U}_{v,v}$ and $\mathbf{H}_{v-1}^{\text{MSDD}} = -\sum_{t=1}^{v-1}\bar{s}^*_t\mathbf{U}_{t,v}$ may be interpreted as the equivalent "received signal vector" and the equivalent "fading channel vector" for

detecting the variable x_{v-1}, because the PED increment Δ_{v-1} of Eq. (3.27) becomes similar to the specific form of the coherent detector's decision metric of Eq. (2.4). This leads us to the following MSDSD decision variable:

$$\begin{aligned} z_{v-1}^{\text{MSDSD}} &= -\vec{s}_{v-1}^{*}\mathbf{U}_{v,v}\left(\sum_{t=1}^{v-1}\vec{s}_{t}^{*}\mathbf{U}_{t,v}\right)^{H} \\ &= \mathbf{Y}_{v-1}^{\text{MSDD}}(\mathbf{H}_{v-1}^{\text{MSDD}})^{H}, \end{aligned} \tag{3.28}$$

which may be directly used for detecting x_{v-1}. More explicitly, similar to the case of $N_R = 1$ seen in [127], the best phasor index is given by $\acute{m}_{v-1} = \lfloor p_{v-1} \rceil$, where we have $p_{v-1} = \frac{M}{2\pi}\angle z_{v-1}^{\text{MSDSD}}$, and the Schnorr-Euchner search strategy may visit the remaining phasors in a zig-zag order according to the increasing value of $\overline{\Delta}_{v-1}$ of Eq. (3.27), which may be completed as:

$$\Delta_{v-1} = \overline{\Delta}_{v-1} + C_{v-1}, \tag{3.29}$$

where the equivalent PED increment is defined as:

$$\overline{\Delta}_{v-1} = -2\Re(x_{v-1}^{*} z_{v-1}^{\text{MSDSD}}), \tag{3.30}$$

while the constant C_{v-1} in Eq. (3.29) is given by:

$$C_{v-1} = \left\|\mathbf{Y}_{v-1}^{\text{MSDD}}\right\|^2 + \left\|\mathbf{H}_{v-1}^{\text{MSDD}}\right\|^2. \tag{3.31}$$

We note that comparing the various PED increments Δ_{v-1} of Eq. (3.26) is equivalent to comparing $\overline{\Delta}_{v-1}$ of Eq. (3.30) over the entire range of the variable x_{v-1}, which is also equivalent to comparing $\Delta'_{v-1} = |z_{v-1}^{\text{MSDSD}} - x_{v-1}|^2 = |z_{v-1}^{\text{MSDSD}}|^2 + |x_{v-1}|^2 + \overline{\Delta}_{v-1}$, where all the differences are constants.

An example of MSDSD aided DQPSK is portrayed in Fig. 3.3, which demonstrates that MSDSD is capable of acquiring the MSDD's ML result, while the total number of constellation points visited by MSDSD is substantially reduced compared to MSDD. Furthermore, the pseudo-code for hard-decision-aided MSDSD conceived for uncoded DPSK is summarized in Table 3.1, which was adapted and modified from [127] in order to accommodate the more general case of $N_R \geq 1$.

More explicitly, Fig. 3.3-a) shows that the "findBest" subfunction of Table 3.1 opts for obtaining the best phasor candidate by using the decision variable z_{v-1}^{MSDSD} of Eq. (3.28), when the SD visits the indices $v = 2$ and $v = 3$ for the first time in Step ① and Step ②, respectively. The SD radius is updated as $d = 7.497$, when the SD index reaches $v = N_w$ in Step ② of Fig. 3.3-a). Then the SD index is decreased to $v = 2$ in Step ③, and the second-best phasor candidate is obtained by the "findNext" subfunction of Table 3.1, which has a PED value of $d_2 = 13.678$ as seen in Fig. 3.3-a). Since this new PED value is higher than the SD radius, the SD decreases its index to $v = 1$ and terminates the search. It can be seen in Fig. 3.3-a) that the MSDSD does not visit all the MSDD candidates, but the SD output radius $d = 7.497$ is indeed the smallest amongst all the legitimate EDs at index $v = 3$. Fig. 3.3-b) further portrays the corresponding constellation points that are visited by the SD's Schnorr-Euchner search strategy in a zigzag fashion at SD index $v = 2$. Once again, the "findBest" subfunction of Table 3.1 is invoked for finding the best candidate, when the

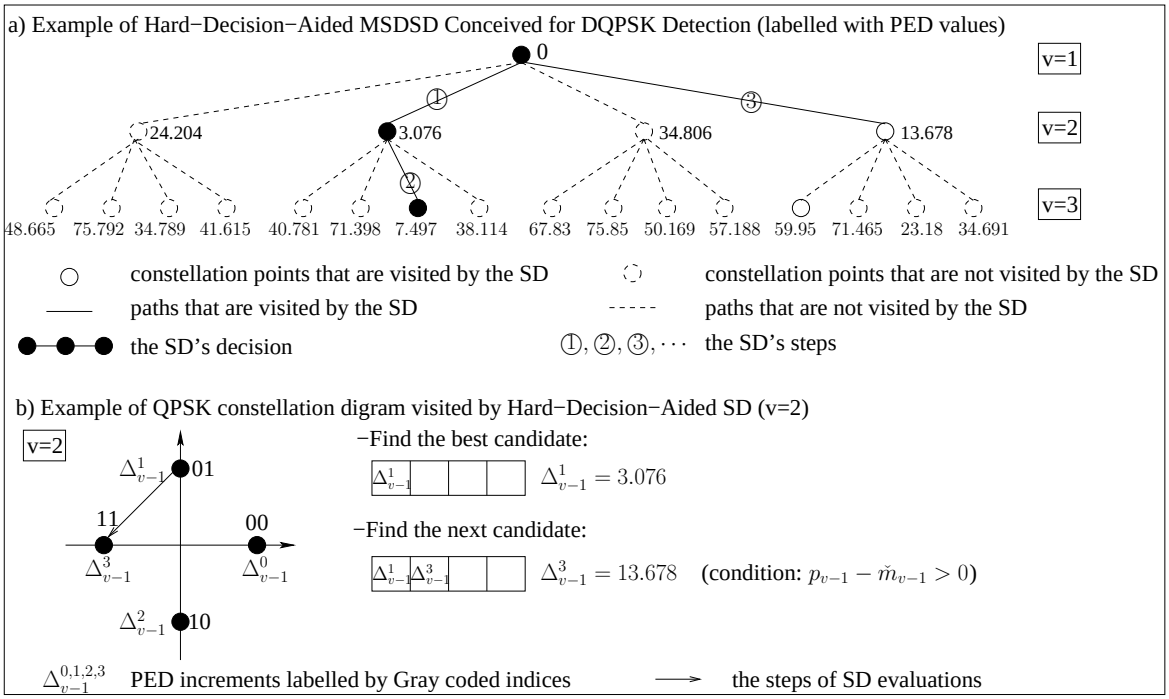

Figure 3.3: Example of hard-decision-aided MSDSD conceived for uncoded DQPSK recorded at SNR=10 dB, where we have $N_R = 2$ and $N_w = 3$. The MSDSD hard-decision-aided refers to Algorithm 3.1, which is detailed in the form of pseudo-code seen in Table 3.1.

SD visits index $v = 2$ for the first time, while the "findNext" subfunction is invoked to visit the next candidate, when the SD re-visits index $v = 2$. In this way, the SD does not have to visit all the constellation points.

It is worth noting that for the special case of $N_w = 2$, the channel's correlation matrix of Eq. (3.21) is given by:

$$\mathbf{C} = \begin{bmatrix} \rho_0 + N_0 & \rho_1 \\ \rho_1 & \rho_0 + N_0 \end{bmatrix}, \tag{3.32}$$

where we have $\rho_0 = 1$ and $\rho_1 \leq 1$. Therefore, according to Eq. (3.28), the MSDSD's decision variable for the special case of $N_w = 2$ is given by:

$$\begin{aligned} z_1^{MSDSD} &= -\mathbf{U}_{2,2}\mathbf{U}_{1,2}^H \\ &= -l_{1,1}l_{2,1}\mathbf{Y}_2\mathbf{Y}_1^H \\ &= \frac{\rho_1}{(1+N_0)^2 - \rho_1^2}\mathbf{Y}_2\mathbf{Y}_1^H. \end{aligned} \tag{3.33}$$

As a result, the angles of the MSDSD's decision variable z_1^{MSDSD} of Eq. (3.33) and of the CDD's decision variable $z_1^{CDD} = \mathbf{Y}_2\mathbf{Y}_1^H$ of Eq. (3.4) are exactly the same, owing to the fact that the factor $\frac{\rho_1}{(1+N_0)^2-\rho_1^2}$ in Eq. (3.33) is always positive in the presence of non-zero AWGN $N_0 > 0$. Therefore, as indicated by the pseudo-code of Table 3.1, CDD may be implemented as MSDSD associated with $N_w = 2$, where the MSDSD's decision variable of Eq. (3.33) only has to be evaluated once, while the findBest function in Table 3.1 only has to be evaluated once.

function: $[\{\hat{x}_{v-1}\}_{v=2}^{N_w}] = \textbf{MSDSD}(\{\{\mathbf{U}_{t,v}\}_{t=1}^{v}\}_{v=1}^{N_w}, M, N_w, R)$
requirements: Constellations set is given by$\{x^m \in \mathbf{x}\}_{m=0}^{M-1}$. We have $x^m = \exp(j\frac{2\pi}{M}\check{m})$, where m is Gray coded $\check{m}$. The SD's search radius R may be initialized to be a sufficiently large value.

$d_1 = 0$ //initialize PED
$\bar{s}_1 = 1$ //initialize the first transmitted symbol
$v = 2$ //initialize SD search index
$[\check{m}_{v-1}, \text{step}_{v-1}, n_{v-1}, z_{v-1}^{MSDSD}, C_{v-1}] = \textbf{findBest}(\{\mathbf{U}_{t,v}\}_{t=1}^{v}, \{\bar{s}_t\}_{t=1}^{v-1})$ //visit the best child node
loop
  $\Delta_{v-1} = C_{v-1} - 2\Re\left[\exp(-j\frac{2\pi}{M}\check{m}_{v-1}) \cdot z_{v-1}^{MSDSD}\right]$ //update Δ_{v-1} according to Eq. (3.29)
  $d_v = d_{v-1} + \Delta_{v-1}$ //update PED according to Eq. (3.25)
  if $d_v < R$
    $x_{v-1} = \exp(j\frac{2\pi}{M}\check{m}_{v-1})$ //update new child node
    $\bar{s}_v = x_{v-1}\bar{s}_{v-1}$
    if $v \neq N_w$
      $v = v + 1$ //move up index v
      $[\check{m}_{v-1}, \text{step}_{v-1}, n_{v-1}, z_{v-1}^{MSDSD}, C_{v-1}]$ //visit the best child node
        $= \textbf{findBest}(\{\mathbf{U}_{t,v}\}_{t=1}^{v}, \{\bar{s}_t\}_{t=1}^{v-1})$
    else
      $R = d_{N_w}$ //update SD radius
      $\{\hat{x}_{v-1}\}_{v=2}^{N_w} = \{x_{v-1}\}_{v=2}^{N_w}$ //update the optimum data symbols
      do
        if $v == 2$ **return** $\{\hat{x}_{v-1}\}_{v=2}^{N_w}$ **and exit** //terminate SD for the case of $N_w = 2$
        $v = v - 1$ //move down index v
      while $n_{v-1} == (M-1)$
      $[\check{m}_{v-1}, \text{step}_{v-1}, n_{v-1}] = \textbf{findNext}\,(\check{m}_{v-1}, \text{step}_{v-1}, n_{v-1})$ //visit the next child node
    end if
  else
    do
      if $v == 2$ **return** $\{\hat{x}_{v-1}\}_{v=2}^{N_w}$ **and exit** //terminate SD when $v = 2$ is reached
      $v = v - 1$ //move down index v
    while $n_{v-1} == (M-1)$
    $[\check{m}_{v-1}, \text{step}_{v-1}, n_{v-1}] = \textbf{findNext}\,(\check{m}_{v-1}, \text{step}_{v-1}, n_{v-1})$ //visit the next child node
  end if
end loop

subfunction: $[\check{m}_{v-1}, \text{step}_{v-1}, n_{v-1}, z_{v-1}^{MSDSD}, C_{v-1}] = \textbf{findBest}(\{\mathbf{U}_{t,v}\}_{t=1}^{v}, \{\bar{s}_t\}_{t=1}^{v-1})$

$\mathbf{Y}_{v-1}^{\text{MSDD}} = \bar{s}_{v-1}^{*}\mathbf{U}_{v,v}$ //update $\mathbf{Y}_{v-1}^{\text{MSDD}}$ according to Eq. (3.27)
$\mathbf{H}_{v-1}^{\text{MSDD}} = -(\sum_{t=1}^{v-1}\bar{s}_t^{*}\mathbf{U}_{t,v})$ //update $\mathbf{H}_{v-1}^{\text{MSDD}}$ according to Eq. (3.27)
$z_{v-1}^{MSDSD} = \mathbf{Y}_{v-1}^{\text{MSDD}}(\mathbf{H}_{v-1}^{\text{MSDD}})^{H}$ //update decision variable of Eq. (3.28)
$C_{v-1} = \|\mathbf{Y}_{v-1}^{\text{MSDD}}\|^2 + \|\mathbf{H}_{v-1}^{\text{MSDD}}\|^2$ //update the constant of Eq. (3.31)
$p_{v-1} = \frac{M}{2\pi}\angle z_{v-1}^{MSDSD}$ //update best child node
$\check{m}_{v-1} = \lfloor p_{v-1} \rceil$
$\text{step}_{v-1} = \text{sign}(p_{v-1} - \check{m}_{v-1})$ //store the step size for the next child node
$n_{v-1} = 0$

subfunction: $[\check{m}_{v-1}, \text{step}_{v-1}, n_{v-1}] = \textbf{findNext}\,(\check{m}_{v-1}, \text{step}_{v-1}, n_{v-1})$

$\check{m}_{v-1} = \check{m}_{v-1} + \text{step}_{v-1}$ //visit the next child node
$\text{step}_{v-1} = -\text{step}_{v-1} - \text{sign}(\text{step}_{v-1})$
$n_{v-1} = n_{v-1} + 1$

Table 3.1: Pseudo-code for Hard-Decision-Aided MSDSD Conceived for Uncoded DPSK.

It may be expected that for each SD index v, the distances between the hypothetical candidates' PED increment values Δ_{v-1} are sufficiently high in the high-SNR region, so that all the sub-optimal candidates' PED values d_v may lie outside the sphere $d_v > R$. Consequently, Steps (2)-(4) may not have to be repeated, which results in a prompt conclusion of the SD search. More specifically, if the SD may only visit a total of $(N_w - 1)$ constellation points, when the SD index increases from $v = 2$ to $v = N_w$, and provided that the SD may only visit a total number of $(N_w - 2)$ constellation points, when the SD index decreases from $v = (N_w - 1)$ back to $v = 2$, the MSDSD's complexity lower bound may be closely approached in the high-SNR region.

Compared to the exponentially increasing complexity of MSDD of Eq. (3.22), the MSDSD exhibits a substantially reduced linearly increasing complexity with respect to N_w at high SNRs. However, it is demonstrated in [214] that the average SD complexity obeys a polynomial function, often approximately a cubic function, while [215] demonstrates that the SD complexity still increases exponentially in the low SNR region. Therefore, in the next section, the classic DFDD that has a fixed linearly increasing detection complexity is discussed further.

3.2.4 Hard-Decision-Aided DFDD Conceived for Uncoded DPSK

The DFDD may also rely on the MSDD decision metric of Eq. (3.22). The symmetric matrix $\mathbf{F} = \mathbf{C}^{-1}$ that appeared in Eq. (3.22) equals to its own transpose $\mathbf{F}^T = \mathbf{F}$, which indicates that we have $\{\{f_{t,v} = f_{v,t}\}_{t=1}^{N_w}\}_{v=1}^{N_w}$. Consequently, the MSDD's Euclidean Distance (ED) of Eq. (3.22) may be extended as:

$$\begin{aligned} d &= \mathrm{tr}\left(\mathbf{F}\bar{\mathbf{S}}^H\mathbf{Y}\mathbf{Y}^H\bar{\mathbf{S}}\right) \\ &= \sum_{v=1}^{N_w}\left(\sum_{t=1}^{N_w} f_{N_w-v+1,N_w-t+1}\bar{s}_t^*\mathbf{Y}_t\right)\bar{s}_v\mathbf{Y}_v^H \\ &= \sum_{v=1}^{N_w} f_{N_w-v+1,N_w-v+1}\left\|\mathbf{Y}_v\right\|^2 + 2\Re\left(\sum_{v=1}^{N_w}\sum_{t=1}^{v-1} f_{N_w-v+1,N_w-t+1}\bar{s}_t^*\bar{s}_v\mathbf{Y}_t\mathbf{Y}_v^H\right), \end{aligned} \tag{3.34}$$

which may be simplified as:

$$d' = \Re\left(\sum_{v=1}^{N_w}\sum_{t=1}^{v-1} f_{N_w-v+1,N_w-t+1}\bar{s}_t^*\bar{s}_v\mathbf{Y}_t\mathbf{Y}_v^H\right). \tag{3.35}$$

Assuming that $\{\hat{\bar{s}}_v\}_{v=1}^{N_w-1}$ are known from the previous search decisions $\{\hat{x}_v\}_{v=1}^{N_w-2}$, only the single variable $\bar{s}_{N_w}$ has to be detected for the current decision x_{N_w-1}. As a result, the constant parts in d' that are associated with the index v that ranged from 1 to $(N_w - 1)$ may all be deleted, which leads to the DFDD decision formulated as [121]:

$$\begin{aligned} \hat{x}_{N_w-1} &= \arg\ \min_{x^m\in\mathbf{x}}\ \Re\left(\sum_{t=1}^{N_w-1} f_{1,N_w-t+1}\bar{s}_t^* x^m \bar{s}_{N_w-1}\mathbf{Y}_t\mathbf{Y}_{N_w}^H\right) \\ &= \arg\ \min_{x^m\in\mathbf{x}}\ -\Re\left[x^m(z_{N_w-1}^{\mathrm{DFDD}})^*\right] \\ &= \arg\ \min_{x^m\in\mathbf{x}}\ |z_{N_w-1}^{\mathrm{DFDD}} - x^m|^2, \end{aligned} \tag{3.36}$$

where the DFDD's decision variable is given by:

$$\begin{aligned} z_{N_w-1}^{\text{DFDD}} &= -\left[\left(\sum_{t=1}^{N_w-1} f_{1,N_w-t+1}\hat{\tilde{s}}_t^*\mathbf{Y}_t\right)\hat{\tilde{s}}_{N_w-1}\mathbf{Y}_{N_w}^H\right]^* \\ &= -\hat{\tilde{s}}_{N_w-1}^*\mathbf{Y}_{N_w}\left(\sum_{t=1}^{N_w-1} f_{1,N_w-t+1}\hat{\tilde{s}}_t^*\mathbf{Y}_t\right)^H. \end{aligned} \tag{3.37}$$

As a result, the optimum phasor index for $\hat{x}_{N_w-1}$ may be obtained by rounding the phase of $z_{N_w-1}^{\text{DFDD}}$ as:

$$\hat{x}_{N_w-1} = \exp(j\tfrac{2\pi}{M}\hat{m}), \quad \text{where } \hat{m} = \lfloor \tfrac{M}{2\pi}\angle z_{N_w-1}^{\text{DFDD}} \rceil, \tag{3.38}$$

which is similar to the low-complexity coherent detection of Eq. (2.9) and to the CDD detection of Eq. (3.5). According to Eqs. (3.37) and (3.38), the DFDD only detects a single variable x_{N_w-1} based on the previous decisions $\{\hat{\tilde{s}}_v\}_{v=1}^{N_w-1}$ within a DFDD window. Hence, the DFDD windows should be overlapped by $N_{OL} = (N_w - 1)$ observations according to Fig. 3.2, so that all data symbols may be explicitly detected.

Furthermore, compared to Eq. (3.28), the MSDSD's decision variable for x_{N_w-1} is given by:

$$\begin{aligned} z_{N_w-1}^{\text{MSDSD}} &= -\hat{\tilde{s}}_{N_w-1}^*\mathbf{U}_{N_w,N_w}\left(\sum_{t=1}^{N_w-1}\hat{\tilde{s}}_t^*\mathbf{U}_{t,N_w}\right)^H \\ &= -l_{1,1}\hat{\tilde{s}}_{N_w-1}^*\mathbf{Y}_{N_w}\left(\sum_{t=1}^{N_w-1} l_{N_w-t+1,1}\hat{\tilde{s}}_t^*\mathbf{Y}_t\right)^H, \end{aligned} \tag{3.39}$$

where we have $f_{1,N_w-t+1} = l_{1,1}l_{N_w-t+1,1}$ because of the relationship of $\mathbf{F} = \mathbf{L}\mathbf{L}^H$. As a result, the DFDD's decision variable $z_{N_w-1}^{\text{DFDD}}$ of Eq. (3.37) is equivalent to the MSDSD's decision variable $z_{N_w-1}^{\text{MSDSD}}$ associated with the SD index of $v = N_w$. This implies that DFDD may be simply implemented by MSDSD's subfunction findBest in Table 3.1, where only the optimum candidate associated with the fixed SD index of $v = N_w$ has to be known. Therefore, it may be expected that DFDD exhibits a substantially lower complexity than MSDSD, but DFDD may suffer from error propagation because of its idealized simplifying assumption of having a perfect decision-feedback $\{\hat{\tilde{s}}_v\}_{v=1}^{N_w-1}$.

Historically speaking, the literature has to a certain degree been dismissive of the family of noncoherent schemes. Nonetheless, it was demonstrated in [120, 121, 126] that a MMSE Linear Prediction (LP) based blind channel estimator is capable of providing a reference for coherently detecting the data symbols x_{N_w-1}, which was shown to be equivalent to DFDD [121]. Let us elaborate a little further here in order to bridge the gap between coherent and noncoherent schemes. First of all, the most recent received signal block within an observation window may be modelled as:

$$\begin{aligned} \mathbf{Y}_{N_w} &= s_{N_w}\mathbf{H}_{N_w} + \mathbf{V}_{N_w} \\ &\approx s_{N_w}\hat{\mathbf{H}}_{N_w} + \mathbf{V}_{N_w}, \end{aligned} \tag{3.40}$$

where the reference fading vector $\hat{\mathbf{H}}_{N_w}$ is output by a LP filter. More explicitly, the filter's output signal may be produced based on the previous received signal vectors $\{\mathbf{Y}_v\}_{v=1}^{N_w-1}$ as well as on the

previous decisions $\{\hat{s}_v\}_{v=1}^{N_w-1}$, which may be expressed as [120, 121, 126]:

$$\begin{aligned}\hat{\mathbf{H}}_{N_w} &= \sum_{v=1}^{N_w-1} \overline{w}_v \mathbf{Y}_v / \hat{s}_v, \\ &= \overline{\mathbf{w}}^T (\hat{\mathbf{S}}^{\bar{N}_w})^H \mathbf{Y}^{\bar{N}_w},\end{aligned} \tag{3.41}$$

where $\overline{\mathbf{w}} = [\overline{w}_{N_w-1}, \cdots, \overline{w}_1]^T$ represents the linear filter's taps, while the decision-feedback matrix $\hat{\mathbf{S}}^{\bar{N}_w}$ is given by the decisions concerning $\mathbf{S}$ of Eq. (3.8) eliminating element s_{N_w}, while $\mathbf{Y}^{\bar{N}_w}$ is given by $\mathbf{Y}$ of Eq. (3.8) eliminating $\mathbf{Y}_{N_w}$.

As a result, according to Eq. (3.40), the MSE Objective Function (OF) may be formulated as:

$$\begin{aligned}\sigma^2_{\text{MSE}} &= E\left\{ \left\| \mathbf{Y}_{N_w} - s_{N_w} \hat{\mathbf{H}}_{N_w} \right\|^2 \right\} \\ &= E\left\{ \left[\mathbf{H}_{N_w} + s^*_{N_w} \mathbf{V}_{N_w} - \overline{\mathbf{w}}^T (\hat{\mathbf{S}}^{\bar{N}_w})^H \mathbf{Y}^{\bar{N}_w} \right] \left[\mathbf{H}_{N_w} + s^*_{N_w} \mathbf{V}_{N_w} - \overline{\mathbf{w}}^T (\hat{\mathbf{S}}^{\bar{N}_w})^H \mathbf{Y}^{\bar{N}_w} \right]^H \right\} \\ &= 1 + N_0 - 2E\left\{ \mathbf{H}_{N_w} (\mathbf{Y}^{\bar{N}_w})^H \hat{\mathbf{S}}^{\bar{N}_w} \right\} \cdot \overline{\mathbf{w}} + \overline{\mathbf{w}}^T \cdot E\left\{ (\hat{\mathbf{S}}^{\bar{N}_w})^H \mathbf{Y}^{\bar{N}_w} (\mathbf{Y}^{\bar{N}_w})^H \hat{\mathbf{S}}^{\bar{N}_w} \right\} \cdot \overline{\mathbf{w}} \\ &= 1 + N_0 - 2\mathbf{e}^T_{N_w} \cdot \overline{\mathbf{w}} + \overline{\mathbf{w}}^T \cdot \mathbf{C}_{\mathbf{N_w-1}} \cdot \overline{\mathbf{w}},\end{aligned} \tag{3.42}$$

where the $(N_w - 1)$-element column vector $\mathbf{e}_{N_w}$ and the $(N_w - 1) \times (N_w - 1)$-element matrix $\mathbf{C}_{\mathbf{N_w-1}}$ are defined as components of the channel correlation matrix $\mathbf{C}$ of Eq. (3.21) as:

$$\mathbf{C} = \begin{bmatrix} \rho_0 + N_0 & \mathbf{e}^T_{N_w} \\ \mathbf{e}_{N_w} & \mathbf{C}_{\mathbf{N_w-1}} \end{bmatrix}. \tag{3.43}$$

The MMSE solution based on Eq. (3.42) is given by $\frac{\partial \sigma^2_{\text{MSE}}}{\partial \overline{\mathbf{w}}} = 0$, which leads to the classic Wiener-Hopf equation formulated as [125, 126, 136]:

$$\overline{\mathbf{w}} = \mathbf{C}^{-1}_{\mathbf{N_w-1}} \cdot \mathbf{e}_{N_w}, \tag{3.44}$$

where the partial channel correlation matrix $\mathbf{C}_{\mathbf{N_w-1}}$ is Hermitian and positive-definite. Furthermore, the MSE of Eq. (3.42) is now a constant, which is given by:

$$\begin{aligned}\sigma^2_{\text{MSE}} &= 1 + N_0 - \mathbf{e}^T_{N_w} \mathbf{C}^{-1}_{\mathbf{N_w-1}} \mathbf{e}_{N_w} \\ &= 1 + N_0 - \mathbf{e}^T_{N_w-1} \cdot \overline{\mathbf{w}}.\end{aligned} \tag{3.45}$$

Similar to the coherent receivers introduced in Chapter 2, the Linear Prediction-based Detector (LPD) aims for maximizing the *a posteriori* probability of:

$$p(x^m | \mathbf{Y}_{N_w}) = \frac{p(\mathbf{Y}_{N_w} | x^m) p(x^m)}{\forall_{x^m \in \mathbf{x}} p(\mathbf{Y}_{N_w} | x^m) p(x^m)}, \tag{3.46}$$

where the conditional probability of receiving $\mathbf{Y}_{N_w}$ with the aid of given x^m may be expressed as:

$$\begin{aligned}p(\mathbf{Y}_{N_w} | x^m) &= \frac{1}{\pi^{N_R} \cdot \sigma^2_{MSE}} \exp\left(- \frac{\| \mathbf{Y}_{N_w} - x^m s_{N_w-1} \hat{\mathbf{H}}_{N_w} \|^2}{\sigma^2_{MSE}} \right) \\ &\propto \frac{1}{\pi^{N_R} \cdot \sigma^2_{MSE}} \exp\left(-|z^{\text{LPD}}_{N_w-1} - x^m|^2 \right),\end{aligned} \tag{3.47}$$

while the candidates $\{x^m\}_{m=0}^{M-1}$ are assumed to be equiprobable, which is formulated as $\{p(x^m) = \frac{1}{M}\}_{m=0}^{M-1}$. Moreover, the new LPD decision variable in Eq. (3.47) is given by:

$$\begin{aligned} z_{N_w-1}^{\text{LPD}} &= s_{N_w-1}^* \mathbf{Y}_{N_w} (\hat{\mathbf{H}}_{N_w})^H / \sigma_{MSE}^2 \\ &= s_{N_w-1}^* \mathbf{Y}_{N_w} \left(\sum_{v=1}^{N_w-1} \overline{w}_v \hat{s}_v^* \mathbf{Y}_v \right)^H / \sigma_{MSE}^2. \end{aligned} \tag{3.48}$$

We note that the only differences between $-\|\mathbf{Y}_{N_w} - x^m s_{N_w-1} \hat{\mathbf{H}}_{N_w}\|^2 / \sigma_{MSE}^2 = -\|\mathbf{Y}_{N_w}\|^2 / \sigma_{MSE}^2 - \|\hat{\mathbf{H}}_{N_w}\|^2 / \sigma_{MSE}^2 + 2\Re\left\{ (x^m)^* s_{N_w-1}^* \mathbf{Y}_{N_w} (\hat{\mathbf{H}}_{N_w})^H \right\} / \sigma_{MSE}^2$ and $-|z_{N_w-1}^{\text{LPD}} - x^m|^2 = -|z_{N_w-1}^{\text{LPD}}|^2 - 1 + 2\Re\left\{ (x^m)^* z_{N_w-1}^{\text{LPD}} \right\}$ in Eq. (3.47) are the constants.

Furthermore, according to the channel correlation matrix interpreted by Eq. (3.43), the Hermitian matrix used by DFDD may be expressed based on the blockwise matrix inversion property [281] as:

$$\mathbf{F} = \mathbf{C}^{-1} = \begin{bmatrix} \epsilon & -\epsilon \cdot \mathbf{e}_{N_w}^T \cdot \mathbf{C}_{\mathbf{N_w-1}}^{-1} \\ -\epsilon \cdot \mathbf{C}_{\mathbf{N_w-1}}^{-1} \cdot \mathbf{e}_{N_w} & \mathbf{C}_{\mathbf{N_w-1}}^{-1} + \epsilon \cdot \mathbf{C}_{\mathbf{N_w-1}}^{-1} \cdot \mathbf{e}_{N_w} \cdot \mathbf{e}_{N_w}^T \cdot \mathbf{C}_{\mathbf{N_w-1}}^{-1} \end{bmatrix}, \tag{3.49}$$

where we have $\epsilon = \left(1 + N_0 - \mathbf{e}_{N_w}^T \cdot \mathbf{C}_{\mathbf{N_w-1}}^{-1} \cdot \mathbf{e}_{N_w}\right)^{-1} = (\sigma_{MSE}^2)^{-1}$. The first column of $\mathbf{C}^{-1}$ in Eq. (3.49) indicates that $[f_{2,1}, \cdots, f_{N_w,1}]^T = -\epsilon \overline{\mathbf{w}}$, which implies that we have $\{-\overline{w}_t / \sigma_{MSE}^2 = f_{N_w-t+1,1} = f_{1,N_w-t+1}\}_{t=1}^{N_w-1}$. As a result, the DFDD's decision variable $z_{N_w-1}^{\text{DFDD}}$ of Eq. (3.37) and the LPD's decision variable of $z_{N_w-1}^{\text{LPD}}$ of Eq. (3.48) are exactly the same for DPSK in Rayleigh fading channels. In other words, the DFDD introduced in this section may be regarded as either the low-complexity decision-feedback solution to MSDD or as a blind channel estimation aided data detector.

3.2.5 Performance Results for Uncoded DPSK

Let us now discuss our simulation results in this section. In order to retain the ML detection capability, all SDs implemented in this treatise are initialized with a sufficiently large sphere radius, so that MSDSD may achieve exactly the same ML performance as MSDD.

Similar to the performance results of the coherent receivers analyzed in Sec. 2.4, the detection complexities of CDD, MSDD, MSDSD and DFDD are characterized in Table 3.2. We note that unneccessary calculations are eliminated in practical implementations. For example, all the MPSK constellation points may be pre-stored so that the repeated calculations such as $\exp(-j\frac{2\pi}{M}\check{m}_{v-1})$ in line 6 of Table 3.1 may be avoided. It may be observed in Table 3.2 that CDD and DFDD exhibit a lower detection complexity compared to the ML MSDD/MSDSD. However, as discussed before, CDD and DFDD may be regarded as special cases of MSDD/MSDSD, while CDD and DFDD are expected to suffer from a performance penalty compared to MSDD/MSDSD. Moreover, Table 3.2 demonstrates that a substantial complexity reduction is achieved by MSDSD, where SD enables MSDD to visit a reduced number of constellation points, which are confined to a search sphere, as exemplied by Fig. 3.3.

	real-valued multiplications	real-valued additions	comparisons	visited nodes
CDD	$4N_R + 1$	$4N_R - 2$		1
MSDD	$(4N_w^3 + 4N_w^2 N_R + 2N_w N_R)$ $\times M^{(N_w-1)}/(N_w - 1)$	$[4N_w^3 + (4N_R - 2)N_w^2 - 1]$ $\times M^{(N_w-1)}/(N_w - 1)$	$M^{(N_w-1)}$ $\div(N_w - 1)$	$M^{(N_w-1)}$ $\div(N_w - 1)$
MSDSD (findBest)	$4N_R v + 6N_R + 1$	$4N_R v + 4N_R - 1$	1	1
MSDSD (findNext)		3	1	1
MSDSD (Lower Bound)	$N_w N_R + 8N_R + 13$ $+(\sum_{v=2}^{N_w} 4N_R v)/(N_w - 1)$ $+(2N_R - 8)/(N_w - 1)$	$4N_R + 14 - 13/(N_w - 1)$ $+(\sum_{v=2}^{N_w} 4N_R v)/(N_w - 1)$	7 $-5/(N_w - 1)$	$(2N_w - 3)$ $\div(N_w - 1)$
DFDD	$4N_w N_R + 2N_w + 4N_R - 1$	$2N_w N_R + 4N_R - 2$		1

Table 3.2: Complexity (per symbol) of hard-decision-aided noncoherent receivers for uncoded DPSK. CDD refers to Eq. (3.5). MSDD refers to Eq. (3.22). MSDSD refers to Algorithm 3.1, which is detailed in the form of pseudo-code seen in Table 3.1. DFDD refers to Eq. (3.38).

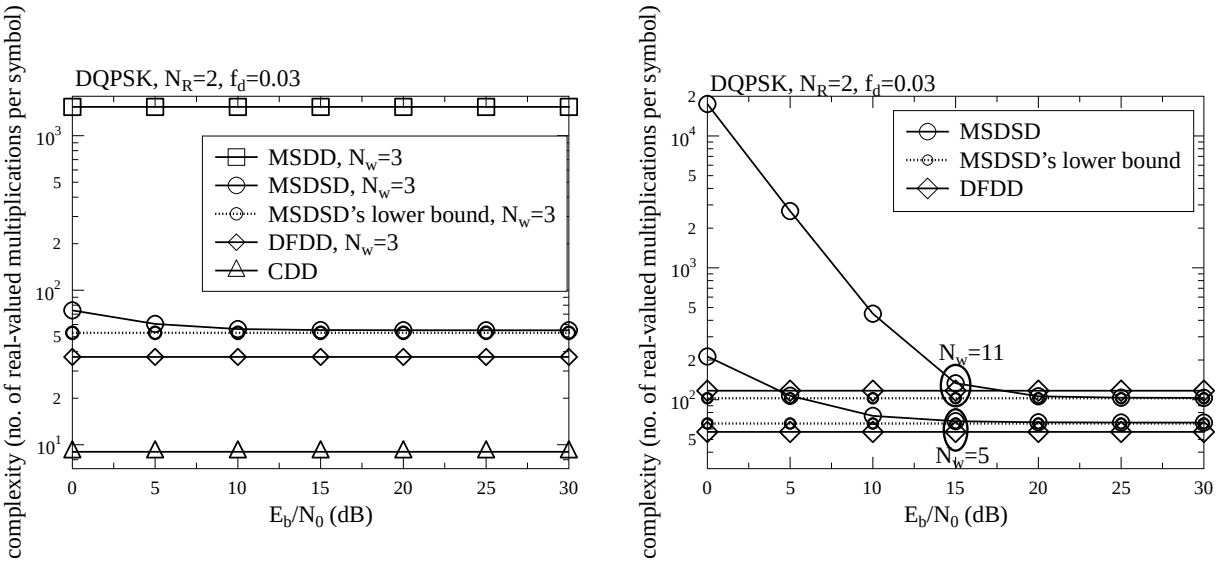

(a) MSDD/MSDSD/DFDD ($N_w = 3$) and CDD

(b) MSDSD and DFDD, $N_w = \{5, 11\}$

Figure 3.4: Complexity (number of real-valued multiplications per symbol) comparison between the noncoherent receivers conceived for uncoded DQPSK, where $N_R = 2$ RAs are employed, while the normalized Doppler frequency is given by $f_d = 0.03$. CDD refers to Eq. (3.5). MSDD refers to Eq. (3.22). MSDSD refers to Algorithm 3.1, which is detailed in the form of pseudo-code seen in Table 3.1. DFDD refers to Eq. (3.38).

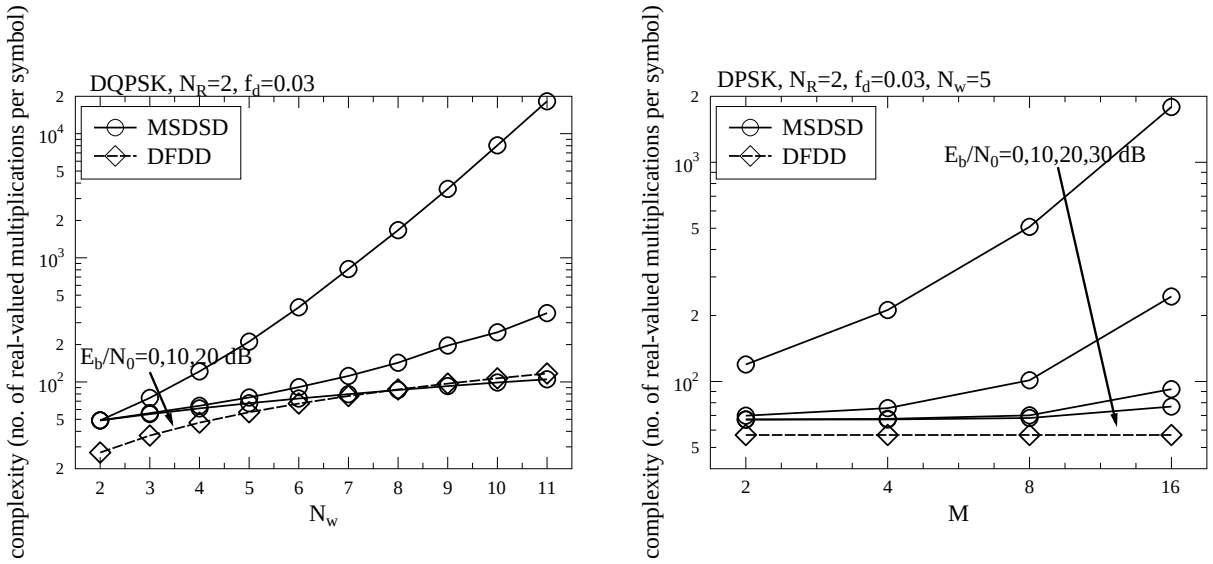

(a) $M = 4$, $N_w = \{2 \sim 11\}$ (b) $M = \{2, 4, 8, 16\}$, $N_w = 5$

Figure 3.5: Complexity (number of real-valued multiplications per symbol) comparison between MSDSD and DFDD aided uncoded DPSK, where $N_R = 2$ RAs are used, while the normalized Doppler frequency is given by $f_d = 0.03$. MSDSD refers to Algorithm 3.1, which is detailed in the form of pseudo-code seen in Table 3.1. DFDD refers to Eq. (3.38).

The complexity comparisons presented in Table 3.2 are further portrayed in Fig. 3.4, where the detection complexity is quantified in terms of the total number of real-valued multiplications required for detecting a single DPSK symbol. Fig. 3.4a shows that MSDD and CDD exhibit the highest and the lowest detection complexity, respectively. Furthermore, MSDSD substantially reduces the MSDD complexity, and the complexity of DFDD is even lower than that of MSDSD associated with $N_w = 3$. Furthermore, Fig. 3.4b presents our complexity comparison between MSDSD and DFDD. As expected, the SD of Algorithm 3.1 terminates sooner in the higher E_b/N_0 region, which results in the phenomenon seen in Fig. 3.4b, namely that the MSDSD complexity gradually converges to its lower bound, as E_b/N_0 increases. Furthermore, Fig. 3.4b demonstrates that the MSDSD's complexity lower bound is even lower than the DFDD complexity, when a long detection window of $N_w = 11$ is employed. This is because the DFDD's decision variable $z_{N_w-1}^{\text{DFDD}}$ of Eq. (3.37) has to be evaluated for each DFDD window, which only detects a single symbol. By contrast, the MSDSD decision variables $\{z_{v-1}^{\text{MSDSD}}\}_{v=2}^{N_w}$ of Eq. (3.28) have to be evaluated for detecting a total number of $N_w - 1$ symbols, where the complexity of evaluating z_{v-1}^{MSDSD} associated with a SD index of $v < N_w$ is generally lower than evaluating $z_{N_w-1}^{\text{DFDD}}$. Hence the overall average complexity (per symbol) of DFDD is higher than the MSDSD's (per symbol) complexity lower bound, when a long detection window is employed.

Fig. 3.5 further portrays the effects of detection window length N_w and of the number of modulation levels M on the MSDSD complexity and DFDD complexity. It can be seen in Fig. 3.5a that the MSDSD complexity still grows exponentially with N_w, when a low E_b/N_0 of 0 dB is encountered. However, in the high E_b/N_0 region, the MSDSD complexity trend becomes more linear with respect to N_w, which is similar to the DFDD complexity trend, as evidenced by Fig. 3.5a. Fur-

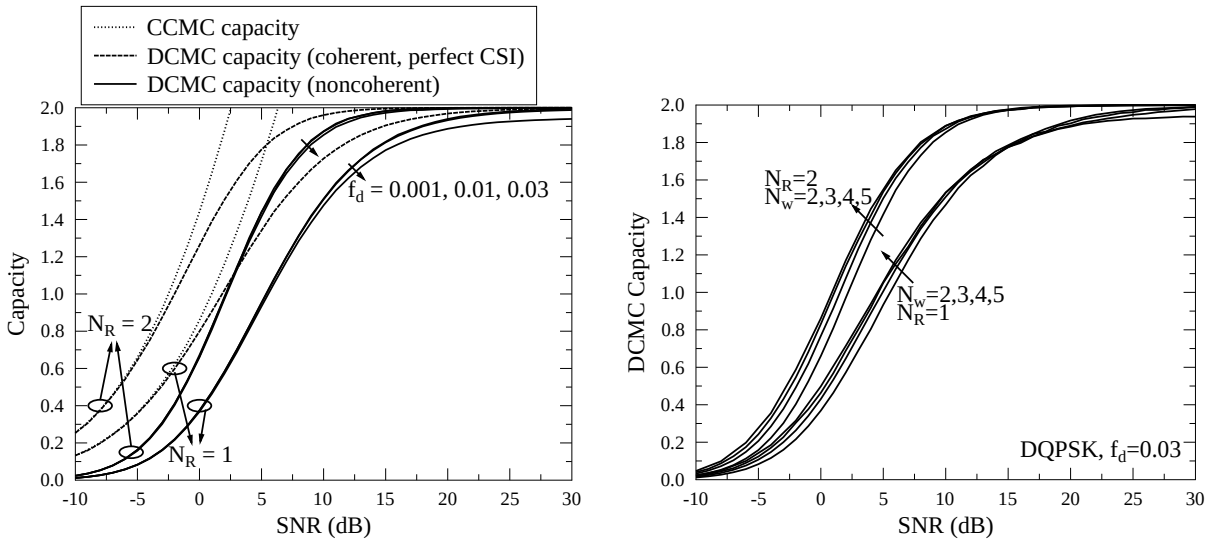

(a) $N_w = 2$, $f_d = \{0.001, 0.01, 0.03\}$

(b) $N_w = \{2, 3, 4, 5\}$, $f_d = 0.03$

Figure 3.6: CCMC capacity and DCMC capacity of DQPSK in Rayleigh fading channels, as evaluated from Eq. (2.54) and from Eq. (3.50), respectively.

thermore, it may be observed in Fig. 3.5a that the MSDSD complexity recorded at a high E_b/N_0 of 20 dB becomes lower than the DFDD complexity, as N_w increases. Moreover, as presented in Table 3.2, the MSDSD complexity lower bound and the DFDD complexity do not depend on the constellations set size M, because the hard-decision-aided detectors directly find the closest constellation point, as demonstrated by Table 3.2 and Eq. (3.38). Therefore, it can be seen in Fig. 3.5b that the MSDSD complexity becomes less dependent on M, as E_b/N_0 increases.

The capacity of noncoherent schemes is portrayed by Fig. 3.6. The CCMC capacity of the SIMO Rayleigh fading channels as well as the DCMC capacity of coherent schemes relying on perfect CSI are given by Eq. (2.54) and Eq. (2.56), respectively. Furthermore, the DCMC capacity of noncoherent schemes, which are modelled by Eq. (3.6), is given by:

$$
\begin{aligned}
C_{DCMC}^{MSDD} &= \max_{\{p(\bar{\mathbf{S}}^i)\}_{i=0}^{M^{(N_w-1)}-1}} \frac{\sum_{i=0}^{M^{(N_w-1)}-1} \int p(\mathbf{Y}|\bar{\mathbf{S}}^i) p(\bar{\mathbf{S}}^i) \log_2 \frac{p(\mathbf{Y}|\bar{\mathbf{S}}^i)}{\sum_{\tilde{i}=0}^{M^{(N_w-1)}-1} p(\mathbf{Y}|\bar{\mathbf{S}}^{\tilde{i}}) p(\bar{\mathbf{S}}^{\tilde{i}})} d\mathbf{Y}}{(N_w-1)} \\
&= \log_2 M - \frac{\sum_{i=0}^{M^{(N_w-1)}-1} \int p(\mathbf{Y}|\bar{\mathbf{S}}^i) \log_2 \frac{\sum_{\tilde{i}=0}^{M^{(N_w-1)}-1} p(\mathbf{Y}|\bar{\mathbf{S}}^{\tilde{i}})}{p(\mathbf{Y}|\bar{\mathbf{S}}^i)} d\mathbf{Y}}{(N_w-1)M^{(N_w-1)}} \\
&= \log_2 M - \frac{\sum_{i=0}^{M^{(N_w-1)}-1} \mathrm{E}\left\{ \log_2 \left[\sum_{\tilde{i}=0}^{M^{(N_w-1)}-1} \exp\left(- \left\| \mathbf{L}^H (\bar{\mathbf{S}}^{\tilde{i}})^H \mathbf{Y} \right\|^2 + \left\| \mathbf{L}^H (\bar{\mathbf{S}}^i)^H \mathbf{Y} \right\|^2 \right) \right] \middle| \bar{\mathbf{S}} = \bar{\mathbf{S}}^i \right\}}{(N_w-1)M^{(N_w-1)}},
\end{aligned}
\tag{3.50}
$$

where the lower triangular matrix $\mathbf{L}$ is defined in Eq. (3.22), while the samples for the received signal matrix $\mathbf{Y}$ are generated according to Eq. (3.9) as $\mathbf{Y} = \bar{\mathbf{S}}^i \bar{\mathbf{H}} + \mathbf{V}$. Similar to the evaluation of the coherent scheme's DCMC capacity of Eq. (2.56), the maximum mutual information of Eq. (3.50)

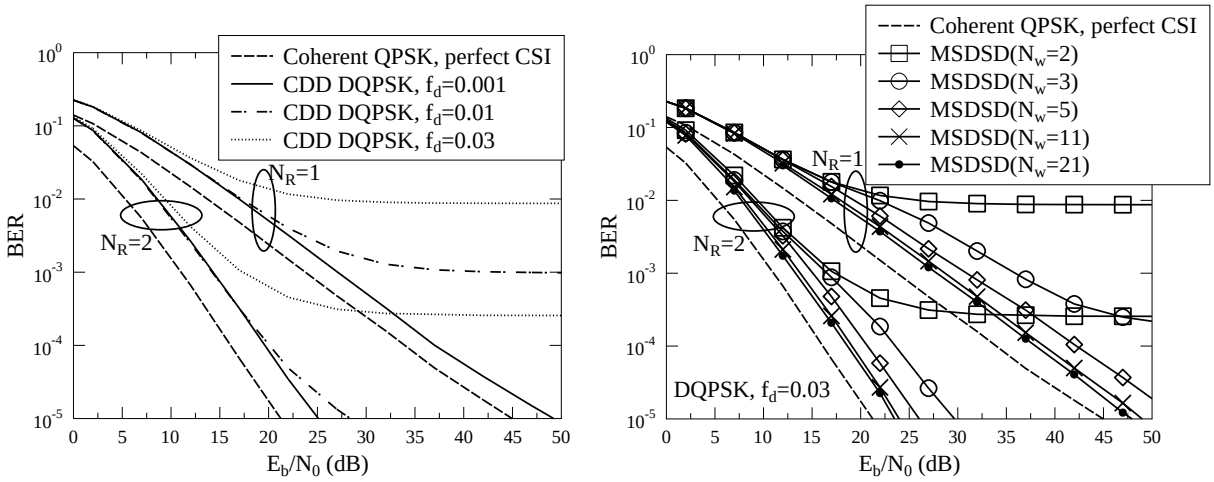

(a) $N_w = 2$, $f_d = \{0.001, 0.01, 0.03\}$

(b) $N_w = \{2, 3, 5, 11\}$, $f_d = 0.03$

Figure 3.7: BER performance of CDD and MSDSD aided DQPSK in Rayleigh fading channels, evaluated by Monte-Carlo simulation based on 10^7 samples. CDD refers to Eq. (3.5). MSDSD refers to Algorithm 3.1, which is detailed in the form of pseudo-code seen in Table 3.1.

is achieved when the combinations of transmitted symbols $\{\bar{\mathbf{S}}^i\}_{i=0}^{M^{(N_w-1)}-1}$ are equiprobable, i.e. we have $\{p(\bar{\mathbf{S}}^i) = \frac{1}{M^{(N_w-1)}}\}_{i=0}^{M^{(N_w-1)}-1}$.

It may be observed in Fig. 3.6a that there is a DCMC capacity gap between the noncoherent DQPSK and coherent QPSK relying on perfect CSI estimation. Furthermore, as expected, the DCMC capacity of noncoherent DQPSK decreases as the normalized Doppler frequency f_d increases, and the CDD assisted by $N_w = 2$ observations cannot achieve the full DQPSK DCMC capacity of $C_{max}^{DCMC} =$ BPS at $f_d = 0.03$ – not even at high SNRs, as evidenced by Fig. 3.6a. However, Fig. 3.6b demonstrates that the DCMC capacity of noncoherent schemes may be improved by increasing the observation window N_w. These capacity trends are verified by the BER performance trends of Fig. 3.7. Explicitly, it may be seen in Fig. 3.7a that CDD aided DQPSK suffers from an irreducible error floor, when the normalized Doppler frequency f_d is increased. Furthermore, it is demonstrated by Fig. 3.7b that the performance of noncoherent receivers recorded in rapidly fluctuating fading channels gradually approaches that of their coherent counterparts relying on perfect CSI estimation, as MSDSD window N_w increases, which is an explicit benefit of the MSDSD scheme.

As discussed in [277,282], Fig. 3.8a demonstrates that the symbols at the middle of the MSDSD window may be more reliably detected than those at its edges. This is because compared to the symbols located in the middle of the detection window, the symbols at the edges may benefit less from the detection of their surrounding symbols. As a result, the MSDSD's performance may be improved, if the detection windows are overlapped by more than one observations so that the symbols detected at the edges may be discarded, according to the MSDSD windows arrangement shown in Fig. 3.2. It is evidenced by Fig. 3.8b that the MSDSD associated with $N_{OL} = 3$ may be

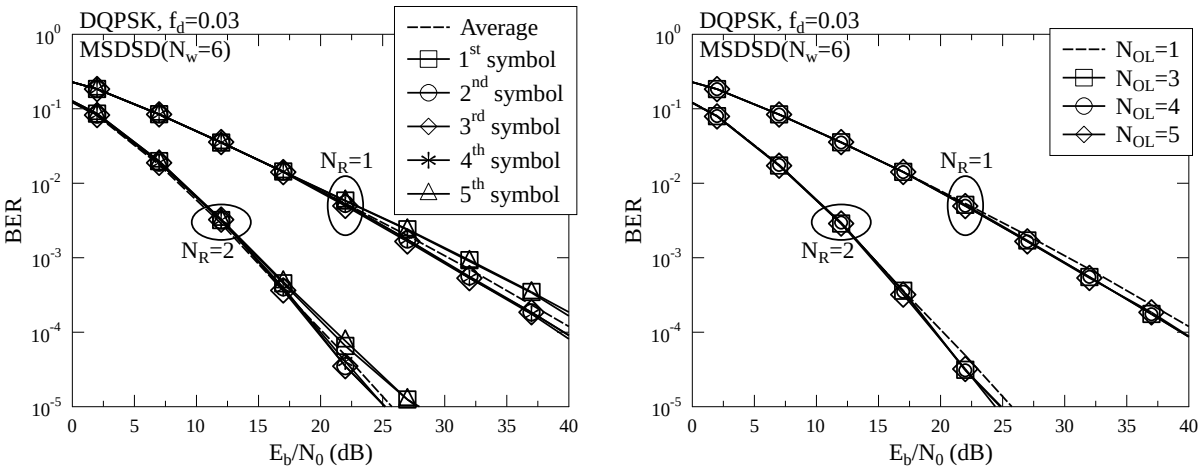

(a) $N_{OL} = 1$ (b) $N_{OL} = \{1, 3, 4, 5\}$

Figure 3.8: BER performance of MSDSD ($N_w = 6$) aided DQPSK in Rayleigh fading channels, where the normalized Doppler frequency is given by $f_d = 0.03$, which was evaluated by Monte-Carlo simulation based on 10^7 samples. MSDSD refers to Algorithm 3.1, which is detailed in the form of pseudo-code seen in Table 3.1.

sufficient to provide such performance improvement, and increasing N_{OL} beyond three does not provide any further advantage. Therefore, the MSDD/MSDSD associated with $N_{OL} = 3$ may be referred to as Subset MSDD/MSDSD for the rest of this thesis. More explicitly, when $N_{OL} = 3$ observations are overlapped by MSDSD window, there are two information symbols which are detected twice within the consecutive windows according to Fig. 3.2, and the ones located at the edges of the detection windows are discarded.

Fig. 3.9 presents our performance comparison between MSDSD and DFDD conceived for uncoded DPSK schemes. As expected, the hard-decision-aided MSDSD outperforms its DFDD counterpart, which is evidenced by Fig. 3.9. Furthermore, Fig. 3.9 shows that the performance difference between MSDSD and DFDD is relatively small in the low E_b/N_0 region. In fact, we will further demonstrate in Sec. 3.3 that the unreliable decisions utilized by DFDD at low E_b/N_0 values degrade the extrinsic LLR's reliability, which results in a more substantial performance difference between MSDSD and DFDD in coded DPSK systems.

3.3 Coded DPSK

In this section, soft-decision-aided noncoherent detectors conceived for coded DPSK are investigated. Firstly, we will introduce the MSDD appropriately modified for amalgamation with turbo detection [114]. Secondly, the soft-decision-aided MSDSD conceived for DPSK proposed in [132], which invokes the Max-Log-MAP algorithm is reviewed. Thirdly, we propose to modify the SD's output scenario in [132], so that the near-optimum Approx-Log-MAP algorithm may also be implemented by MSDSD. Fourthly, the reduced-complexity design proposed in Chapter 2 is applied to soft-decision-aided MSDSD, so that the MSDSD complexity may be further reduced with the aid

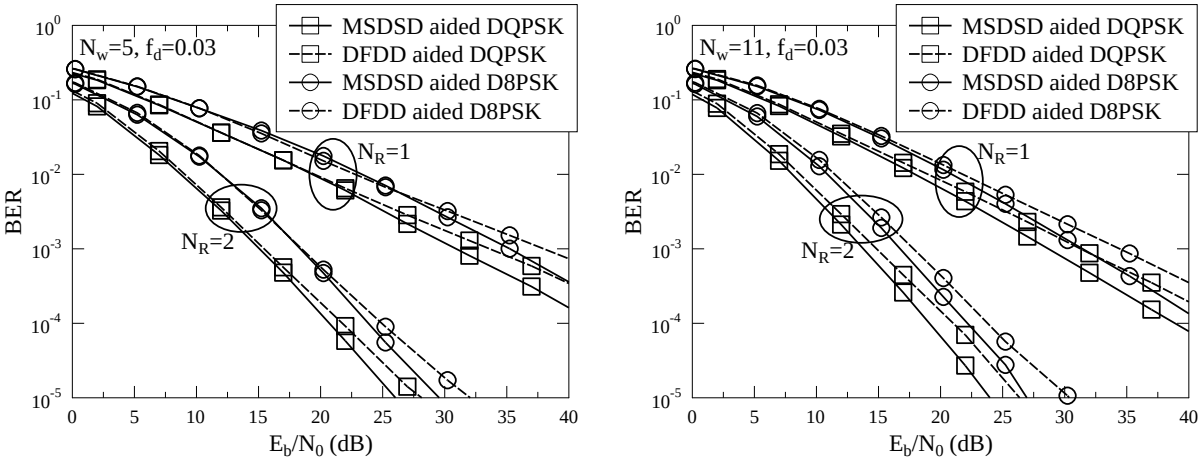

(a) $N_w = 5$ (b) $N_w = 11$

Figure 3.9: BER performance of MSDSD and DFDD aided DQPSK and D8PSK in Rayleigh fading channels, where the normalized Doppler frequency is given by $f_d = 0.03$, which was evaluated by Monte-Carlo simulation based on 10^7 samples. MSDSD refers to Algorithm 3.1, which is detailed in the form of pseudo-code seen in Table 3.1. DFDD refers to Eq. (3.38).

of visiting less constellation points. Lastly, the DFDD conceived for coded DPSK [122, 125, 136] is also presented. The detection capabilities of these noncoherent receivers are summarized and compared with the aid of the EXIT charts introduced in Sec. 2.3.2 in order to quantify and predict the performance of the noncoherent detectors presented in this section.

3.3.1 Soft-Decision-Aided CDD and MSDD Conceived for Coded DPSK

According to the *a posteriori* probability of Eq. (3.11), the optimum Log-MAP algorithm invoked by MSDD may be expressed as [27]:

$$\begin{aligned} L_p(b_k \mid \mathbf{Y}) &= \ln \frac{\sum_{\bar{\mathbf{S}}^i \in \bar{\mathbf{S}}_{b_k=1}} p\left(\mathbf{Y} \mid \bar{\mathbf{S}}^i\right) p\left(\bar{\mathbf{S}}^i\right)}{\sum_{\bar{\mathbf{S}}^i \in \bar{\mathbf{S}}_{b_k=0}} p\left(\mathbf{Y} \mid \bar{\mathbf{S}}^i\right) p\left(\bar{\mathbf{S}}^i\right)} \\ &= \ln \frac{\sum_{\bar{\mathbf{S}}^i \in \bar{\mathbf{S}}_{b_k=1}} \exp(d^i)}{\sum_{\bar{\mathbf{S}}^i \in \bar{\mathbf{S}}_{b_k=0}} \exp(d^i)} \\ &= L_a(b_k) + L_e(b_k), \end{aligned} \tag{3.51}$$

where $L_p(b_k \mid \mathbf{Y})$, $L_e(b_k)$ and $L_a(b_k)$ represent the *a posteriori* LLR and the extrinsic LLR produced by the soft MSDD as well as the *a priori* LLR gleaned from a channel decoder, respectively. Furthermore, $\bar{\mathbf{S}}^i$ denotes the i-th element in the MSDD signal set $\bar{\mathbf{S}}$, while $\bar{\mathbf{S}}_{b_k=1}$ and $\bar{\mathbf{S}}_{b_k=0}$ refer to the MSDD signal set $\bar{\mathbf{S}}$, when the specific bit b_k is set to 1 and 0, respectively. The probability metric $\{d^i\}_{i=0}^{M^{(N_w-1)}-1}$ seen in Eq. (3.51) is given by [8, 240, 241]:

$$d^i = -\left\| \mathbf{L}^H (\bar{\mathbf{S}}^i)^H \mathbf{Y} \right\|^2 + \sum_{\bar{k}=1}^{(N_w-1)\mathrm{BPS}} \widetilde{b}_{\bar{k}} L_a(b_{\bar{k}}), \tag{3.52}$$

where $\{\widetilde{b}_{\bar{k}}\}_{\bar{k}=1}^{(N_w-1)\mathrm{BPS}}$ denotes the bit mapping corresponding to the MSDD candidate $\mathbf{S}^i$. Similar to the soft-decision-aided coherent detection introduced in Sec. 2.3.1, the low-complexity Max-Log-MAP algorithm of Eq. (2.34) may be invoked for simplifying the Log-MAP aided MSDD of Eq. (3.51) as:

$$L_p(b_k \mid \mathbf{Y}) = \max_{\bar{\mathbf{S}}^i \in \bar{\mathbf{S}}_{b_k=1}} d^i - \max_{\bar{\mathbf{S}}^i \in \bar{\mathbf{S}}_{b_k=0}} d^i. \tag{3.53}$$

Furthermore, in order to compensate for the sub-optimum nature of the Max-Log-MAP algorithm, the Approx-Log-MAP algorithm of Eq. (2.35) may be invoked for MSDD as:

$$L_p(b_k \mid \mathbf{Y}) = \mathrm{jac}_{\bar{\mathbf{S}}^i \in \bar{\mathbf{S}}_{b_k=1}} d^i - \mathrm{jac}_{\bar{\mathbf{S}}^i \in \bar{\mathbf{S}}_{b_k=0}} d^i. \tag{3.54}$$

As demonstrated by Eq. (3.33), CDD is equivalent to MSDD/MSDSD associated with $N_w = 2$, which only has a single information symbol x_1 to detect. Therefore, according to the MSDD received signal model of Eq. (3.9), the probability metric of Eq. (3.52) may be revised for CDD as:

$$\begin{aligned} d^m &= -\|l_{2,2}\bar{s}_1^*\mathbf{Y}_1\|^2 - \|l_{2,1}\bar{s}_1^*\mathbf{Y}_1 + l_{1,1}(\bar{s}_1 x^m)^*\mathbf{Y}_2\|^2 + \sum_{\bar{k}=1}^{\mathrm{BPS}} \widetilde{b}_{\bar{k}} L_a(b_{\bar{k}}) \\ &= -\|l_{2,2}\mathbf{Y}_1\|^2 - |l_{2,1}|^2 \|\mathbf{Y}_1\|^2 - |l_{1,1}|^2 \|\mathbf{Y}_2\|^2 - 2\Re\left\{(x^m)^* l_{1,1} l_{2,1} \mathbf{Y}_2 \mathbf{Y}_1^H\right\} + \sum_{\bar{k}=1}^{\mathrm{BPS}} \widetilde{b}_{\bar{k}} L_a(b_{\bar{k}}), \end{aligned} \tag{3.55}$$

where $\left(-\|l_{2,2}\mathbf{Y}_1\|^2 - |l_{2,1}|^2 \|\mathbf{Y}_1\|^2 - |l_{1,1}|^2 \|\mathbf{Y}_2\|^2\right)$ is a constant over all the candidates $\{x^m\}_{m=0}^{M-1}$, and hence it may be deleted. When we have $N_w = 2$, the channel correlation matrix $\mathbf{C}$ of Eq. (3.21) is expressed by Eq. (3.32), and hence the inversion of the channel correlation matrix $\mathbf{F} = \mathbf{C}^{-1}$ is given by:

$$\mathbf{F} = \begin{bmatrix} f_{1,1}, & f_{1,2} \\ f_{2,1}, & f_{2,2} \end{bmatrix} = \begin{bmatrix} \frac{1+N_0}{(1+N_0)^2-\rho_1^2}, & -\frac{\rho_1}{(1+N_0)^2-\rho_1^2} \\ -\frac{\rho_1}{(1+N_0)^2-\rho_1^2}, & \frac{1+N_0}{(1+N_0)^2-\rho_1^2} \end{bmatrix}. \tag{3.56}$$

Therefore, according to the relationship of $\mathbf{C}^{-1} = \mathbf{L}\mathbf{L}^H$, we have $l_{1,1}l_{2,1} = f_{1,2} = -\frac{\rho_1}{(1+N_0)^2-\rho_1^2}$ in Eq. (3.55). Furthermore, the matrix norm calculation in Eq. (3.55) leads to the following decision variable:

$$z^{CDD} = \mathbf{Y}_2 \mathbf{Y}_1^H. \tag{3.57}$$

As a result, the CDD's probability metric may be represented by:

$$d^m = -\frac{\rho_1}{(1+N_0)^2-\rho_1^2} \cdot \left| z^{CDD} - x^m \right|^2 + \sum_{\bar{k}=1}^{\mathrm{BPS}} \widetilde{b}_{\bar{k}} L_a(b_{\bar{k}}). \tag{3.58}$$

The differences between Eq. (3.55) and Eq. (3.58) are all constants. Therefore, the MSDD algorithms of Eqs. (3.53) and (3.54) may be invoked for CDD using the probability metric of Eq. (3.58), where the MSDD signal set $\bar{\mathbf{S}}$ may be replaced by the MPSK constellation set $\mathbf{x}$ for detecting the single variable $\{x^m\}_{m=0}^{M-1}$.

As a special case, we have $\rho_0 = \rho_1 = 1$ in QS fading channels, and hence Eq. (3.58) becomes:

$$d^m = -\frac{\left| z^{CDD} - x^m \right|^2}{2N_0 + N_0^2} + \sum_{\bar{k}=1}^{\mathrm{BPS}} \widetilde{b}_{\bar{k}} L_a(b_{\bar{k}}), \tag{3.59}$$

which may also be expressed as:

$$d^m = -\frac{\|\mathbf{Y}_2 - x^m \mathbf{Y}_1\|^2}{2N_0 + N_0^2} + \sum_{\bar{k}=1}^{\text{BPS}} \widetilde{b}_{\bar{k}} L_a(b_{\bar{k}}), \tag{3.60}$$

where the equivalent noise power is given by $2N_0 + N_0^2 \approx 2N_0$ [158, 159].

3.3.2 Soft-Decision-Aided MSDSD Conceived for Coded DPSK

The Max-Log-MAP algorithm aims for finding the maximum probability metrics, which is similar to the action of hard-decision-aided detectors. Therefore, in order to invoke SD for the Max-Log-MAP algorithm, the maximization of Eq. (3.53) has to be revised for the sake of minimization, while the probability metrics should be guaranteed to have positive values. As a result, similar to the hard MSDD's decision metric of Eq. (3.23), the soft MSDD probability metric of Eq. (3.52) may be transformed into:

$$d = \sum_{v=1}^{N_w} \left\| \sum_{t=1}^{v} \bar{s}_t^* \mathbf{U}_{t,v} \right\|^2 - \sum_{v=2}^{N_w} \sum_{\bar{k}=(v-2)\text{BPS}+1}^{(v-1)\text{BPS}} \left[\widetilde{b}_{\bar{k}} L_a(b_{\bar{k}}) - \overline{C}_{a,\bar{k}}^{MSDSD} \right], \tag{3.61}$$

where the superscript $i \in \{0, \cdots, M^{(N_w-1)} - 1\}$ seen in Eq. (3.52) is deleted for the sake of convenience, while the polarity of Eq. (3.52) is altered. Furthermore, a constant of $\overline{C}_{a,\bar{k}}^{MSDSD} = \frac{1}{2}\left[|L_a(b_{\bar{k}})| + L_a(b_{\bar{k}})\right]$ is introduced in Eq. (3.61) so that all probability metrics have non-negative values, which may be verified by:

$$\begin{aligned} -\widetilde{b}_{\bar{k}} L_a(b_{\bar{k}}) + \frac{1}{2}\left[|L_a(b_{\bar{k}})| + L_a(b_{\bar{k}})\right] &= \begin{cases} -\widetilde{b}_{\bar{k}} L_a(b_{\bar{k}}) + L_a(b_{\bar{k}}), & \text{if } L_a(b_{\bar{k}}) \geq 0 \\ -\widetilde{b}_{\bar{k}} L_a(b_{\bar{k}}), & \text{if } L_a(b_{\bar{k}}) < 0 \end{cases} . \\ &= \begin{cases} L_a(b_{\bar{k}}), & \text{if } L_a(b_{\bar{k}}) \geq 0 \text{ and } \widetilde{b}_{\bar{k}} = 0 \\ -L_a(b_{\bar{k}}), & \text{if } L_a(b_{\bar{k}}) < 0 \text{ and } \widetilde{b}_{\bar{k}} = 1 \\ 0, & \text{otherwise} \end{cases} . \end{aligned} \tag{3.62}$$

We note that according to the LLR's definition of $L_a = \ln \frac{p(b=1)}{p(b=0)}$ seen in Eq. (2.27), the constant $\overline{C}_{a,\bar{k}}^{MSDSD}$ in Eq. (3.61) is formulated as $\overline{C}_{a,\bar{k}}^{MSDSD} = \ln \prod_{\bar{k}=(v-2)\text{BPS}+1}^{(v-1)\text{BPS}} \{1 + \exp\left[L_a(b_{\bar{k}})\right]\}$, which also guarantees that the ED of Eq. (3.61) is always non-negative. This constant was eliminated by the the division of the Log-MAP of Eq. (3.51) and by the subtraction of the Max-Log-MAP of Eq. (3.53). However, bringing back this constant for MSDSD as suggested by [132] introduces excessive calculations in logarithm domain. Therefore, we adopt the method in [176, 283], which uses a simple operation of $\overline{C}_{a,\bar{k}}^{MSDSD} = \frac{1}{2}\left[|L_a(b_{\bar{k}})| + L_a(b_{\bar{k}})\right]$ to guarantee a non-negative ED for SD as proven by Eq. (3.62).

As a result, the PED of soft-decision-aided MSDSD may be defined as [132]:

$$\begin{aligned} d_v &= \sum_{\bar{v}=2}^{v} \left\| \sum_{t=1}^{\bar{v}} \bar{s}_t^* \mathbf{U}_{t,\bar{v}} \right\|^2 - \sum_{\bar{v}=2}^{v} \sum_{\bar{k}=(\bar{v}-2)\text{BPS}+1}^{(\bar{v}-1)\text{BPS}} \left[\widetilde{b}_{\bar{k}} L_a(b_{\bar{k}}) - \overline{C}_{a,\bar{k}}^{MSDSD} \right] \\ &= d_{v-1} + \Delta_{v-1}, \end{aligned} \tag{3.63}$$

where the PED increment is given by:

$$\begin{aligned}\Delta_{v-1} &= \left\| \sum_{t=1}^{v} \bar{s}_t^* \mathbf{U}_{t,v} \right\|^2 - \sum_{\bar{k}=(v-2)\mathrm{BPS}+1}^{(v-1)\mathrm{BPS}} \left[\widetilde{b}_{\bar{k}} L_a(b_{\bar{k}}) - \overline{C}_{a,\bar{k}}^{MSDSD} \right] \\ &= \left\| \bar{s}_{v-1}^* \mathbf{U}_{v,v} + x^m \left(\sum_{t=1}^{v-1} \bar{s}_t^* \mathbf{U}_{t,v} \right) \right\|^2 - \sum_{\bar{k}_v=1}^{\mathrm{BPS}} \left[\widetilde{b}_{\bar{k}_v} L_a(b_{\bar{k}_v}) - \overline{C}_{a,\bar{k}_v}^{MSDSD} \right].\end{aligned} \tag{3.64}$$

For the sake of simplicity, when considering the symbol-based detection of Δ_{v-1}, the bit index subscript $\bar{k}_v$ is ranged from 1 to BPS in Eq. (3.64) according to the relationship of $\bar{k}_v = \bar{k} - (v-2)\mathrm{BPS}$.

As introduced in Sec. 3.2.3, the Schnorr-Euchner [237] search strategy may be invoked by MSDSD in order to effectively search for x_{v-1} according to Δ_{v-1} of Eq. (3.64). However, unlike the hard-decision-aided SD, the decision variable z_{v-1}^{MSDSD} of Eq. (3.28) cannot be directly used for finding the optimum MPSK phasor, because the *a priori* information $\left[\sum_{\bar{k}_v=1}^{\mathrm{BPS}} \widetilde{b}_{\bar{k}_v} L_a(b_{\bar{k}_v}) - \overline{C}_{a,\bar{k}_v}^{MSDSD}\right]$ is not included in z_{v-1}^{MSDSD}. In other words, the channel decoder is unaware of which particular MPSK constellation point (i.e. symbol) is considered, and hence the *a priori* LLRs obtained from it are not appropriately mapped to the received signal's constellation diagram. As a result, in order to implement the Schnorr-Euchner search strategy, the SD associated with a specific SD index v has to consider all MPSK constellation points for deciding upon x_{v-1} by evaluating and comparing a total of M PED increments Δ_{v-1}, which are given by Eq. (3.64).

In summary, the soft-decision-aided MSDSD conceived for DPSK is characterized by the pseudo-code in Table 3.3 [132], and it is exemplified for the cases of employing DQPSK and D8PSK constellations in Figs. 3.10 and 3.11, respectively. More explicitly, for the DQPSK detection example, Fig. 3.10-a) shows that the "sortDelta" subfunction of Table 3.3 has to evaluate and compare all $(M = 4)$ PED increment values of Eq. (3.64) by visiting all the $(M = 4)$ constellation points, when the SD visits the indices $v = 2$ and $v = 3$ for the first time in Step ① and Step ②, respectively. After a valid MSDSD solution is found at the SD index $v = 3$ in Step ② of Fig. 3.10-a), the SD radius is updated to the corresponding ED of $d = 7.28$. For Step ③ of Fig. 3.10-a), the SD decreases its index to $v = 2$ in order to visit the second-best candidate, whose PED value of $d_2 = 10.986$ turns out to be higher than the SD radius. Hence the SD index may be decreased to $v = 1$, which terminates the search in Fig. 3.10-a). Fig. 3.10-b) further portrays the corresponding constellation points that are visited by the SD's Schnorr-Euchner search strategy at SD index $v = 2$. Once again, the "sortDelta" subfunction of Table 3.3 is invoked for visiting and ranking all the constellation points.

The MSDSD algorithm of Table 3.3 is capable of finding both the global minimum d_{MAP} as well as the optimum constellation points $\{\hat{x}_{v-1}\}_{v=2}^{N_w-1}$, which may be translated into the hard-bit decisions of $\{b_k^{MAP}\}_{k=1}^{(N_w-1)\mathrm{BPS}}$. In order to produce soft-bit decisions, the Max-Log-MAP algorithm of Eq. (3.53) may be completed as:

$$L_p(b_k \mid \mathbf{Y}) = \begin{cases} -d_{MAP} + \bar{d}_{MAP}, & \text{if } b_k^{MAP} = 1 \\ -\bar{d}_{MAP} + d_{MAP}, & \text{if } b_k^{MAP} = 0 \end{cases}. \tag{3.65}$$

function: $[\{\hat{x}_{v-1}\}_{v=2}^{N_w}, d_{MAP}] = \textbf{Soft-MSDSD}(\{\{\mathbf{U}_{t,v}\}_{t=1}^{v}\}_{v=1}^{N_w}, \mathbf{P}, M, N_w, R)$

requirements: $\mathbf{P}$ is a $(N_w-1)\times M$ matrix with entries $\{\{P_{v-1,m+1} = \sum_{\tilde{k}_v=1}^{\text{BPS}} \widetilde{b}_{\tilde{k}_v} L_a(b_{\tilde{k}_v}) - \overline{C}_{a,\tilde{k}_v}^{MSDSD}\}_{v=2}^{N_w}\}_{m=0}^{M-1}$ in row $v-1$ and column $m+1$, where the constant $\overline{C}_{a,\tilde{k}_v}^{MSDSD}$ is defined in Eq. (3.61), while the bits mapping arrangement is given by $\{[\widetilde{b}_1, \cdots, \widetilde{b}_{\text{BPS}}] = \textbf{dec2bin}(m)\}_{m=0}^{M-1}$.

$d_1 = 0$ //initialize PED
$\bar{s}_1 = 1$ //initialize the first transmitted symbol
$v = 2$ //initialize SD search index
$[\{\Delta_{v-1}^{\overline{m}}\}_{\overline{m}=0}^{M-1}, \{x_{v-1}^{\overline{m}}\}_{\overline{m}=0}^{M-1}, n_{v-1}] = \textbf{sortDelta}(\{\mathbf{U}_{t,v}\}_{t=1}^{v}, \{\bar{s}_t\}_{t=1}^{v-1}, \mathbf{P})$ //sort all child nodes
loop
  $d_v = d_{v-1} + \Delta_{v-1}^{\overline{(n_{v-1})}}$ //update PED according to Eq. (3.63)
  if $d_v < R$
    $x_{v-1} = x_{v-1}^{\overline{(n_{v-1})}}$ //update new child node
    $\bar{s}_v = x_{v-1}\bar{s}_{v-1}$
    if $v \neq N_w$
      $v = v+1$ //move up index v
      $[\{\Delta_{v-1}^{\overline{m}}\}_{\overline{m}=0}^{M-1}, \{x_{v-1}^{\overline{m}}\}_{\overline{m}=0}^{M-1}, n_{v-1}]$ //sort all child nodes
        $= \textbf{sortDelta}(\{\mathbf{U}_{t,v}\}_{t=1}^{v}, \{\bar{s}_t\}_{t=1}^{v-1}, \mathbf{P})$
    else
      $R = d_{N_w}$ //update SD radius
      $\{\hat{x}_{v-1}\}_{v=2}^{N_w} = \{x_{v-1}\}_{v=2}^{N_w}$ //update the optimum data symbols
      do
        if $v == 2$ **return** $[\{\hat{x}_{v-1}\}_{v=2}^{N_w}, R]$ **and exit** //terminate SD for the case of $N_w = 2$
        $v = v-1$ //move down index v
      while $n_{v-1} == (M-1)$
      $n_{v-1} = n_{v-1} + 1$ //visit the next child node
    end if
  else
    do
      if $v == 2$ **return** $[\{\hat{x}_{v-1}\}_{v=2}^{N_w}, R]$ **and exit** //terminate SD when $v = 2$ is reached
      $v = v-1$ //move down index v
    while $n_{v-1} == (M-1)$
    $n_{v-1} = n_{v-1} + 1$ //visit the next child node
  end if
end loop

subfunction: $[\{\Delta_{v-1}^{\overline{m}}\}_{\overline{m}=0}^{M-1}, \{x_{v-1}^{\overline{m}}\}_{\overline{m}=0}^{M-1}, n_{v-1}] = \textbf{sortDelta}(\{\mathbf{U}_{t,v}\}_{t=1}^{v}, \{\bar{s}_t\}_{t=1}^{v-1}, \mathbf{P})$

for $m = 0$ **to** $(M-1)$ //visit all M child nodes
  $\Delta_{v-1}^{m} = \left\| \bar{s}_{v-1}^{*}\mathbf{U}_{v,v} + x^{m}(\sum_{t=1}^{v-1} \bar{s}_t^{*}\mathbf{U}_{t,v}) \right\|^2 - P_{v-1,m+1}$ //update PED increment according to Eq. (3.64)
end for
$[\{\Delta_{v-1}^{\overline{m}}\}_{\overline{m}=0}^{M-1}, \{x_{v-1}^{\overline{m}}\}_{\overline{m}=0}^{M-1}] = \textbf{sort}(\{\Delta_{v-1}^{m}\}_{m=0}^{M-1})$ //rank PED increments in increasing order
$n_{v-1} = 0$ //initialize child node counter

Table 3.3: Pseudo-code for conventional soft-decision-aided MSDSD.

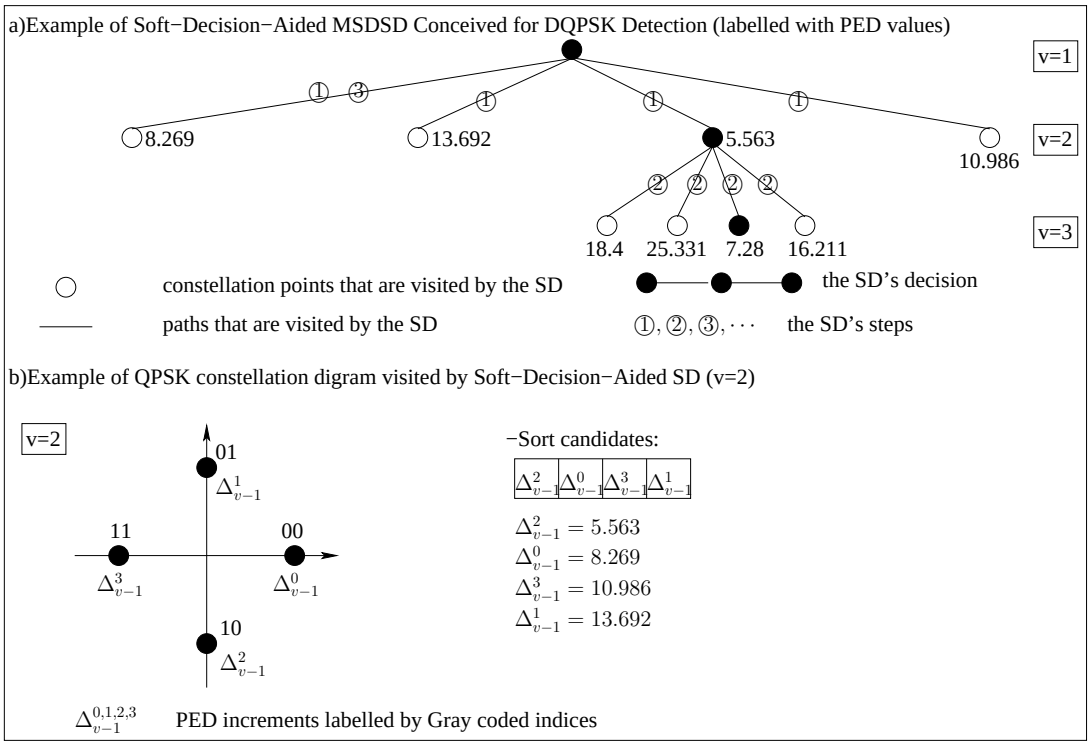

Figure 3.10: Example of soft-decision-aided MSDSD conceived for DQPSK, recorded at SNR=0 dB, where we have $I_A = 0.3$, $N_R = 2$ and $N_w = 3$. The soft-decision-aided MSDSD algorithm is detailed in the form of pseudo-code seen in Table 3.3.

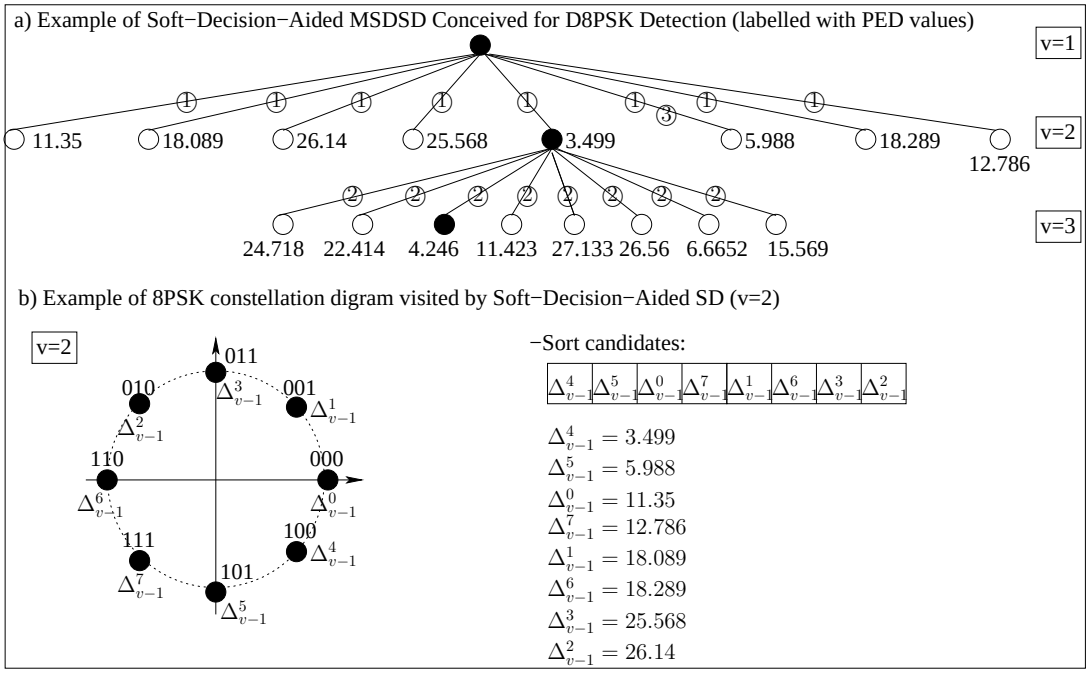

Figure 3.11: Example of soft-decision-aided MSDSD conceived for D8PSK, recorded at SNR=3 dB, where we have $I_A = 0.3$, $N_R = 2$ and $N_w = 3$. The soft-decision-aided MSDSD algorithm is detailed in the form of pseudo-code seen in Table 3.3.

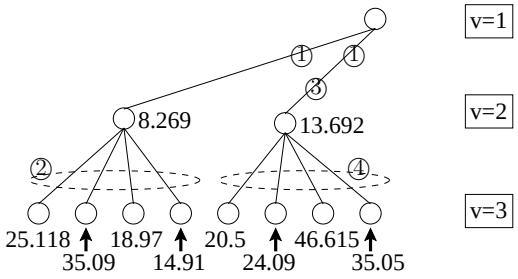

Figure 3.12: Example of the soft-decision-aided MSDSD conceived for DQPSK implementing Approx-Log-MAP, which invokes the SD seen in Fig. 3.10 with a fixed bit of $b_1 = 0$.

where $\bar{d}_{MAP}$ is obtained by invoking the MSDSD again for each soft-bit output, where the search space is halved by fixing the k-th bit b_k to be the flipped version of the MAP decision as $b_k = \bar{b}_k^{MAP}$. In summary, when the consecutive MSDSD windows are simply overlapped by $N_{OL} = 1$ observations, the MSDSD algorithm of Table 3.3 has to be invoked once first for finding the global MAP solution d_{MAP} in Eq. (3.65), and then it is invoked for an additional $(N_w - 1)\log_2 M$ number of times for finding the local MAP solutions $\bar{d}_{MAP}$ in Eq. (3.65), which may be referred to as the Repeated Tree Search (RTS). In this scenario, the MSDSD has to be invoked for an average number of $\frac{(N_w-1)\log_2 M+1}{(N_w-1)\log_2 M}$ times for producing a single soft-bit decision.

Alternatively, it's recently proposed in [175, 176] that the Single Tree Search (STS) [284] may opt to invoke the SD only once for obtaining all the EDs of d_{MAP} and $\bar{d}_{MAP}$ in Eq. (3.65), which may induce a potential performance loss. More explicitly, if the hypothesis bit-mapping arrangement for d_{MAP} is updated and changed, all the counter-hypothesis bit-mapping arrangements for $\bar{d}_{MAP}$ have to be changed accordingly. As a result, the previously dismissed candidates that obey the new bit-mapping cannot be taken into account again. As a remedy, the sub-optimal detector has to invoke the LLR correction method [176] for correcting the LLR results. Against this background, the RTS is suggested in this report. In fact, the STS's motivation of visiting a node at most once can still be accomplished by the RTS, where the previously visited nodes may be labelled so that the repeated calculations may be avoided by reading the previously evaluated PED metrics.

As long as the initial SD radius is set to be sufficiently large, as in [132], the Max-Log-MAP of Eq. (3.65) is realized with the aid of the MSDSD algorithm of Table 3.3, which retains the original detection capability of the Max-Log-MAP aided MSDD of Eq. (3.53). However, as demonstrated in Sec. 2.3.2.4, the Max-Log-MAP algorithm may impose a performance loss compared to the near-optimum Approx-Log-MAP. This performance loss is expected to be more substantial as MSDD/MSDSD window N_w increases. The reason for this degradation is that the Max-Log-MAP of Eq. (3.65) only considers the maximum probability metrics, which may hence ignore more candidates, as the window length increases. Hence the validity of the resultant *a posteriori* LLRs degrades. In order to mitigate this open problem, we propose the corresponding Approx-Log-MAP solution for MSDSD as follows:

Algorithm 3.2: Approx-Log-MAP Implemented by Soft-Decision-Aided MSDSD.

(1) Let us define the leaf nodes of a SD structure as the candidates associated with the SD index $v = N_w$. For example, the $M = 4$ candidates visited at the SD's step of ② in Fig. 3.10-a) as well as the $M = 8$ candidates visited at step ② in Fig. 3.11-a) are all leaf nodes. This leads us to the proposed change of the MSDSD output scenario. When the MSDSD algorithm is invoked for the first time, instead of just producing the global optimum d_{MAP} and the MAP hard-bit decisions $\{b_k^{MAP}\}_{k=1}^{(N_w-1)\text{BPS}}$, all the PED values of the leaf nodes $\{d_{CAN} = d_v\}_{\forall v=N_w}$ as well as all the corresponding hard-bit decisions $\{b_k^{CAN}\}_{k=1}^{(N_w-1)\text{BPS}}$ may also be recorded and produced. For example, the SD of Fig. 3.10-a) may produce both the MAP solution, which is represented by $d_{MAP} = 7.28$ and $\{b_k^{MAP}\}_{k=1}^{(N_w-1)\text{BPS}} = 1010$, as well as all the leaf nodes, which are represented by $\{d_{CAN}\} = \{18.4, 25.331, 7.28, 16.211\}$ and $\{b_k^{MAP}\}_{k=1}^{(N_w-1)\text{BPS}} = \{1000, 1001, 1010, 1011\}$. We note that the SD search strategy and its termination condition of Table 3.3 may remain unchanged.

(2) For each soft-bit output, the MSDSD algorithm is invoked again with a fixed bit $b_k = \bar{b}_k^{MAP}$. Similarly, whenever the SD visits index $v = N_w$, the resultant M leaf candidates $\{d_{CAN}^{b_k=\bar{b}_k^{MAP}}\}$ may all be recorded and produced. For example, when the SD of Fig. 3.10-a) is invoked again with a fixed bit $b_1 = 0$, the resultant SD structure is portrayed in Fig. 3.12, where the two sub-groups of leaf nodes $\{25.118, 35.09, 18.97, 14.91\}$ and $\{20.05, 24.09, 46.615, 35.05\}$ may be recorded as $\{d_{CAN}^{b_k=\bar{b}_k^{MAP}}\}$. We note that there may only be $M/2$ leaf candidates, when the fixed bit $b_k = \bar{b}_k^{MAP}$ is at the specific position in the range of $k \in \{(N_w-2)\text{BPS}+1, \cdots, (N_w-1)\text{BPS}\}$.

(3) Finally, the Max-Log-MAP solution of Eq. (3.65) may be appropriately revised for the Approx-Log-MAP algorithm as:

$$L_p(b_k) = \begin{cases} \text{jac}\,(-d_{CAN}) - \text{jac}\,(-d_{CAN}^{b_k=\bar{b}_k^{MAP}}), & \text{if } b_k^{MAP} = 1 \\ \text{jac}\,(-d_{CAN}^{b_k=\bar{b}_k^{MAP}}) - \text{jac}\,(-d_{CAN}), & \text{if } b_k^{MAP} = 0 \end{cases}. \tag{3.66}$$

We note that when the sizes of the two candidate groups $\{d_{CAN}\}$ and $\{d_{CAN}^{b_k=\bar{b}_k^{MAP}}\}$ are not the same, the size of the larger group may be reduced, so that ideally both groups disregard the same number of candidates. Ideally, any potential deviations introduced both by the jac $(-d_{CAN})$ and by jac $(-d_{CAN}^{b_k=\bar{b}_k^{MAP}})$ operations may be cancelled out. In practice, the SD's output candidates for $\{d_{CAN}\}$ and $\{d_{CAN}^{b_k=\bar{b}_k^{MAP}}\}$ are always constituted by either the sub-group of M leaf candidates or by the sub-group of $M/2$ leaf candidates. Therefore, for the larger-sized group, we may compare the best leaf candidates, which are supposed to have the minimum PED values in each sub-groups, and then we may delete the sub-groups associated with the highest locally best leaf candidate's PED value. For the example of Fig. 3.12, we may delete the sub-group of

$\{20.05, 24.09, 46.615, 35.05\}$, because the local best leaf candidates from each sub-group have the relationship of $20.05 > 14.91$. As a result, the Approx-Log-MAP of Eq. (3.66) may be implemented for the example seen in Figs. 3.10-a) and 3.12 as $L_p(b_1) = \text{jac}\left(-\{18.4, 25.331, 7.28, 16.211\}\right) - \text{jac}\left(-\{25.118, 35.09, 18.97, 14.91\}\right)$.

One may argue that the SD does not visit all the MSDD candidates, which means that the group sizes of $\{d_{CAN}\}$ and $\{d_{CAN}^{b_k=\bar{b}_k^{MAP}}\}$ seen in Eq. (3.66) may be smaller than the group sizes of $\bar{\mathbf{S}}^i \in \bar{\mathbf{S}}_{b_k=1}$ and $\bar{\mathbf{S}}^i \in \bar{\mathbf{S}}_{b_k=0}$ seen in Eq. (3.54). In other words, ideally, the Approx-Log-MAP of Eq. (3.54) may include all the MSDD candidates, but naturally the SD may only visit a subset of them. Nonetheless, as explained in Sec. 2.3.1, when the Approx-Log-MAP corrects the difference between two probability metrics of $|d^1 - d^2|$, only 8 values corresponding to $|d^1 - d^2|$ ranging between 0 and 3.7 may be taken into account, as demonstrated by Table 2.2. This implies that large differences of $|d^1 - d^2| > 3.7$ are inherently ignored by the Approx-Log-MAP. Therefore, we may assume that the leaf candidates ignored by the SD may also be ignored by the Approx-Log-MAP, so that no extra complexity is imposed on the SD by our proposed Approx-Log-MAP.

We note that for a better implementation, Step (2) may be executed for all $\text{BPS}(N_w - 1)$ fixed bits $\{b_k = \bar{b}_k^{MAP}\}_{k=1}^{\text{BPS}(N_w-1)}$ before proceeding to Step (3), so that all the leaf nodes visited by the repeated SD searches may be utilized in Step (3). As a result, $\{d_{CAN}\}$ in Eq. (3.66) may be replaced by $\{d_{CAN}^{b_k^{CAN}=b_k^{MAP}}\}$, and then both $\{d_{CAN}^{b_k^{CAN}=b_k^{MAP}}\}$ and $\{d_{CAN}^{b_k=\bar{b}_k^{MAP}}\}$ in Eq. (3.66) may include all the leaf nodes obtained from Steps (1) and (2) corresponding to the specific bit b_k being b_k^{MAP} and $\bar{b}_k^{MAP}$, respectively. We will demonstrate in Sec. 3.3.5 that our proposed Approx-Log-MAP aided MSDSD of Algorithm 3.2 is capable of matching the performance of the Approx-Log-MAP aided MSDD of Eq. (3.54).

3.3.3 Reduced-Complexity Soft-Decision-Aided MSDSD Conceived for Coded DPSK

It was demonstrated in Sec. 3.3.2 that the Schnorr-Euchner search strategy utilized by the soft-decision-aided MSDSD conceived for coded DPSK have to visit all MPSK constellation points in order to rank their PED increment values Δ_{v-1} of Eq. (3.64) in increasing order. However, since the MSDSD substantially reduces the MSDD complexity by visiting that specific subset of constellation points, which are confined to a search sphere, the MSDSD complexity may be further reduced by applying the algorithms proposed in Sec. 2.4, where the Schnorr-Euchner search strategy may visit a further reduced subset of the MPSK constellation points.

More explicitly, the PED increment Δ_{v-1} of Eq. (3.64) may be further extended to a form which

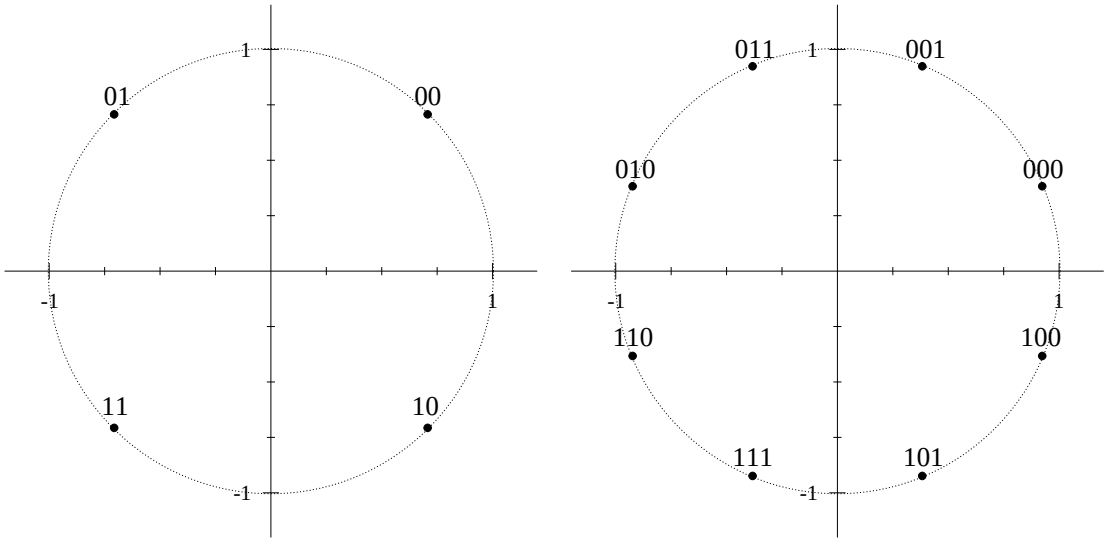

(a) Rotated QPSK (b) Rotated 8PSK

Figure 3.13: The rotated QPSK and 8PSK constellation diagrams, where we deliberately rotate all the detected MPSK ($M \geq 4$) constellation diagrams anti-clockwise by a phase of π/M, so that there are exactly $M/4$ constellation points in each quadrant.

is similar to the coherent detector's probability metric of Eq. (2.31) as follows:

$$\begin{aligned}\Delta_{v-1} &= \left\|\mathbf{Y}_{v-1}^{\text{MSDD}} - x_{v-1}\mathbf{H}_{v-1}^{\text{MSDD}}\right\|^2 - \sum_{\tilde{k}_v=1}^{\text{BPS}} \left[\widetilde{b}_{\tilde{k}_v} L_a(b_{\tilde{k}_v}) - \overline{C}_{a,\tilde{k}_v}^{MSDSD}\right] \\ &= -2\Re\left(\bar{x}_{v-1}^* \bar{z}_{v-1}^{MSDSD}\right) - \sum_{\tilde{k}_v=1}^{\text{BPS}} \widetilde{b}_{\tilde{k}_v} L_a(b_{\tilde{k}_v}) + \frac{L_a(b_1)+L_a(b_2)}{2} + \overline{C}_{v-1},\end{aligned} \tag{3.67}$$

where the N_R-element vectors $\mathbf{Y}_{v-1}^{\text{MSDD}} = \bar{s}_{v-1}^* \mathbf{U}_{v,v}$ and $\mathbf{H}_{v-1}^{\text{MSDD}} = -\sum_{t=1}^{v-1} \bar{s}_t^* \mathbf{U}_{t,v}$ are the same as the ones defined in Eq. (3.27). Furthermore, we deliberately rotate all the detected MPSK constellations (except for BPSK) anti-clockwise by (π/M) as seen in Sec. 2.4, i.e. we have $\bar{x}_{v-1} = x_{v-1} \cdot \exp\left(j\frac{\pi}{M}\right)$, so that there are exactly $M/4$ constellation points in each quadrant. The rotated constellation diagrams of QPSK and 8PSK are redrawn in Fig. 3.13 for the sake of convenience. Furthermore, the new decision variable $\bar{z}_{v-1}^{MSDSD}$ seen in Eq. (3.67) is given by:

$$\bar{z}_{v-1}^{MSDSD} = \mathbf{Y}_{v-1}^{\text{MSDD}} (\mathbf{H}_{v-1}^{\text{MSDD}})^H \cdot \exp\left(j\frac{\pi}{M}\right), \tag{3.68}$$

which is rotated anti-clockwise from the decision variable z_{v-1}^{MSDSD} of Eq. (3.28) by (π/M) for detecting $\bar{x}_{v-1}$, while the constant of $\overline{C}_{v-1}$ seen in Eq. (3.67) is given by:

$$\overline{C}_{v-1} = \left\|\mathbf{Y}_{v-1}^{\text{MSDD}}\right\|^2 + \left\|\mathbf{H}_{v-1}^{\text{MSDD}}\right\|^2 + \overline{C}_{a,v-1}^{MSDSD} - \frac{L_a(b_1)+L_a(b_2)}{2}, \tag{3.69}$$

and we have the constant $\overline{C}_{a,v-1}^{MSDSD} = \sum_{\tilde{k}_v=1}^{\text{BPS}} \overline{C}_{a,\tilde{k}_v}^{MSDSD}$. We note that $\overline{C}_{v-1}$ of Eq. (3.69) is invariant over all the different candidates $\bar{x}_{v-1}$ in Eq. (3.67).

As a result, comparing the M candidates $\{x^m\}_{m=0}^{M-1}$ according to their PED increment values Δ_{v-1} of Eq. (3.67) is equivalent to comparing the following equivalent PED increment metric over

all the variables $\bar{x}_{v-1}$ as:

$$\begin{aligned}\overline{\Delta}_{v-1} &= -2\Re\left(\bar{x}_{v-1}^{*}\bar{z}_{v-1}^{MSDSD}\right) - \sum_{\bar{k}_v=1}^{\text{BPS}} \widetilde{b}_{\bar{k}_v} L_a(b_{\bar{k}_v}) + \frac{L_a(b_1)+L_a(b_2)}{2} \\ &= -2\Re(\bar{x}_{v-1})\Re(\bar{z}_{v-1}^{MSDSD}) - 2\Im(\bar{x}_{v-1})\Im(\bar{z}_{v-1}^{MSDSD}) - \sum_{\bar{k}_v=1}^{\text{BPS}} \widetilde{b}_{\bar{k}_v} L_a(b_{\bar{k}_v}) + \frac{L_a(b_1)+L_a(b_2)}{2}.\end{aligned} \tag{3.70}$$

Considering the rotated QPSK constellation of Fig. 3.13a as an example, the four probability metrics $\{\overline{\Delta}_{v-1}^{m}\}_{m=0}^{M-1=3}$ of Eq. (3.70) corresponding to the $M=4$ rotated QPSK constellation points $\{\bar{x}^{m}\}_{m=0}^{M-1=3}$ may be expressed as:

$$\begin{aligned}
\overline{\Delta}_{v-1}^{0} &= -\sqrt{2}\Re(\bar{z}_{v-1}^{MSDSD}) - \sqrt{2}\Im(\bar{z}_{v-1}^{MSDSD}) + \tfrac{L_a(b_1)+L_a(b_2)}{2} && = -t_{v-1}^{Re} - t_{v-1}^{Im}, \\
\overline{\Delta}_{v-1}^{1} &= \sqrt{2}\Re(\bar{z}_{v-1}^{MSDSD}) - \sqrt{2}\Im(\bar{z}_{v-1}^{MSDSD}) - L_a(b_2) + \tfrac{L_a(b_1)+L_a(b_2)}{2} && = t_{v-1}^{Re} - t_{v-1}^{Im}, \\
\overline{\Delta}_{v-1}^{2} &= -\sqrt{2}\Re(\bar{z}_{v-1}^{MSDSD}) + \sqrt{2}\Im(\bar{z}_{v-1}^{MSDSD}) - L_a(b_1) + \tfrac{L_a(b_1)+L_a(b_2)}{2} && = -t_{v-1}^{Re} + t_{v-1}^{Im}, \\
\overline{\Delta}_{v-1}^{3} &= \sqrt{2}\Re(\bar{z}_{v-1}^{MSDSD}) + \sqrt{2}\Im(\bar{z}_{v-1}^{MSDSD}) - L_a(b_1) - L_a(b_2) + \tfrac{L_a(b_1)+L_a(b_2)}{2} && = t_{v-1}^{Re} + t_{v-1}^{Im},
\end{aligned} \tag{3.71}$$

where we associate the real and the imaginary parts of $\bar{z}_{v-1}^{MSDSD}$ with $L_a(b_2)$ and $L_a(b_1)$ respectively as:

$$\begin{aligned}
t_{v-1}^{Re} &= \sqrt{2}\Re(\bar{z}_{v-1}^{MSDSD}) - \frac{L_a(b_2)}{2}, \\
t_{v-1}^{Im} &= \sqrt{2}\Im(\bar{z}_{v-1}^{MSDSD}) - \frac{L_a(b_1)}{2}.
\end{aligned} \tag{3.72}$$

After assigning the *a priori* LLRs to the appropriate parts of $\bar{z}_{v-1}^{MSDSD}$, the only difference between the four candidate metrics $\{\overline{\Delta}_{v-1}^{m}\}_{m=0}^{M-1=3}$ in Eq. (3.71) is the polarity of t_{v-1}^{Re} and t_{v-1}^{Im}. This feature allows us to directly obtain the minimum metric by simply evaluating:

$$\overline{\Delta}_{v-1} = -|t_{v-1}^{Re}| - |t_{v-1}^{Im}|, \tag{3.73}$$

and then the ranking order of the rest of the candidates may be evaluated by comparing the two terms $|t_{v-1}^{Re}|$ and $|t_{v-1}^{Im}|$. In more detail, if we have the condition of $|t_{v-1}^{Re}| > |t_{v-1}^{Im}|$, then the SD may visit the remaining PED increments according to the steps of $\overline{\Delta}_{v-1} = -|t_{v-1}^{Re}| + |t_{v-1}^{Im}|$, $\overline{\Delta}_{v-1} = |t_{v-1}^{Re}| - |t_{v-1}^{Im}|$ and $\overline{\Delta}_{v-1} = |t_{v-1}^{Re}| + |t_{v-1}^{Im}|$. Otherwise, the remaining steps should be $\overline{\Delta}_{v-1} = |t_{v-1}^{Re}| - |t_{v-1}^{Im}|$, $\overline{\Delta}_{v-1} = -|t_{v-1}^{Re}| + |t_{v-1}^{Im}|$ and $\overline{\Delta}_{v-1} = |t_{v-1}^{Re}| + |t_{v-1}^{Im}|$.

As a result, this revised Schnorr-Euchner search strategy conceived for soft-decision-aided MSDSD assisted DQPSK does not have to compare all the $M=4$ child nodes in order to determine the order of the SD's search steps. Instead, the SD only has to visit the best candidate by evaluating $\overline{\Delta}_{v-1} = -|t_{v-1}^{Re}| - |t_{v-1}^{Im}|$, and also the value of $\text{sign}(|t_{v-1}^{Re}| - |t_{v-1}^{Im}|)$ has to be tested, if the SD visits a specific index v for the second time. Following this, the SD may zigzag through the remaining constellation points, which is carried out in a fashion similar to the strategy invoked by the hard-decision-aided MSDSD introduced in Sec. 3.2.3. The only difference is that as seen in Table 3.1 the hard-decision-aided MSDSD evaluates $\text{sign}(p_{v-1} - \lfloor p_{v-1} \rceil)$ for deciding the direction

function: $[\{\hat{x}_{v-1}\}_{v=2}^{N_w}, d_{MAP}] = \textbf{Soft-MSDSD-RC}(\{\{\mathbf{U}_{t,v}\}_{t=1}^{v}\}_{v=1}^{N_w}, \{\{L_a^{v-1,k}\}_{v=2}^{N_w}\}_{k=1}^{2}, \{\overline{C}_{a,v-1}^{MSDSD}\}_{v=2}^{N_w}, \{\{P_{v-1}^{g}\}_{g=0}^{M/4-1}\}_{v=2}^{N_w}, N_w, R)$

requirements: The *a priori* information on group index g is given by $\{\{P_{v-1}^{g} = \sum_{k=3}^{\text{BPS}} \widetilde{b}_k L_a^{v-1,k}\}_{g=0}^{M/4-1}\}_{v=2}^{N_w}$, where the bits mapping is given by $\{[\widetilde{b}_3 \cdots \widetilde{b}_{\text{BPS}}] = \textbf{dec2bin}(g)\}_{g=0}^{M/4-1}$.

```
1: d_1 = 0                                                          //initialize PED
2: s̄_1 = 1                                                          //initialize the first transmitted symbol
3: v = 2                                                            //initialize SD search index
4: (subfunction) findBest-DBPSK/findBest-DQPSK/findBest-DPSK        //find the best candidate
5: loop
6:    d_v = d_{v-1} + Δ̄_{v-1} + C̄_{v-1}                             //update PED according to Eq. (3.63)
7:    if d_v < R
8:       x_{v-1} = x^{m_{v-1}}                                      //update candidate data symbol
9:       s̄_v = x_{v-1} s̄_{v-1}.                                     //update candidate transmitted symbol
10:      if v ≠ N_w
11:         v = v + 1                                               //move up
12:         (subfunction) findBest-DBPSK/findBest-DQPSK/findBest-DPSK
13:      else
14:         R = d_{N_w}                                             //update SD radius
15:         {x̂_{v-1}}_{v=2}^{N_w} = {x_{v-1}}_{v=2}^{N_w}           //update the optimum data phasors
16:         do
17:            if v == 2 return [{x̂_{v-1}}_{v=2}^{N_w}, R] and exit //terminate SD for the case of N_w = 2
18:            v = v - 1                                            //move down
19:         while n_{v-1} == (M - 1)
20:       (subfunction) findNext-DBPSK/findNext-DQPSK/findNext-DPSK //find the next candidate for index v
21:      end if
22:   else
23:      do
24:         if v == 2 return [{x̂_{v-1}}_{v=2}^{N_w}, R] and exit    //terminate SD when v = 2 is reached
25:         v = v - 1                                               //move down
26:      while n_{v-1} == (M - 1)
27:      (subfunction) findNext-DBPSK/findNext-DQPSK/findNext-DPSK  //find the next candidate for index v
28:   end if
29: end loop
```

Table 3.4: Pseudo-code for reduced-complexity soft-decision-aided MSDSD conceived for coded DPSK.

subfunction: $[\overline{C}_{v-1}, \overline{\Delta}_{v-1}, m_{v-1}, n_{v-1}] = \textbf{findBest-DBPSK}(\{\mathbf{U}_{t,v}\}_{t=1}^{v}, \{\bar{s}_t\}_{t=1}^{v-1}, \{L_a^{v-1,k}\}_{k=1}, \overline{C}_{a,v-1}^{MSDSD})$

```
1: Y_{v-1}^{MSDD} = s̄*_{v-1} U_{v,v}                                  //update Y_{v-1}^{MSDD} according to Eq. (3.27)
2: H_{v-1}^{MSDD} = -(Σ_{t=1}^{v-1} s̄*_t U_{t,v})                     //update H_{v-1}^{MSDD} according to Eq. (3.27)
3: z̄_{v-1}^{MSDSD} = Y_{v-1}^{MSDD} (H_{v-1}^{MSDD})^H               //update decision variable of Eq. (3.28)
4: C̄_{v-1} = ||Y_{v-1}^{MSDD}||^2 + ||H_{v-1}^{MSDD}||^2 + C̄_{a,v-1}^{MSDSD} - 0.5 L_a^{v-1,1}   //update the constant of Eq. (3.69)
5: t_{v-1}^{Re} = ℜ(z̄_{v-1}^{MSDSD}) - 0.5 L_a^{v-1,1}
6: Δ̄_{v-1} = -|t_{v-1}^{Re}|                                          //update the optimum PED increment
7: m_{v-1} = (t_{v-1}^{Re} < 0)                                       //update the optimum candidate
8: n_{v-1} = 0                                                        //initialize child node counter
```

subfunction: $[\overline{\Delta}_{v-1}, m_{v-1}, n_{v-1}] = \textbf{findNext-DBPSK}(\overline{\Delta}_{v-1}, m_{v-1}, n_{v-1})$

```
1: Δ̄_{v-1} = -Δ̄_{v-1}          //the second child node is opposite to the optimum child node
2: m_{v-1} = 1 - m_{v-1}        //alter the optimum child node
3: n_{v-1} = n_{v-1} + 1        //update child node counter
```

Table 3.5: Pseudo-code for the subfunctions of the reduced-complexity soft-decision-aided MSDSD of Table 3.4, where DBPSK is employed.

subfunction: $[\overline{C}_{v-1}, |t^{Re}_{v-1}|, |t^{Im}_{v-1}|, \overline{\Delta}_{v-1}, m_{v-1}, n_{v-1}] =$ **findBest-DQPSK**$(\{\mathbf{U}_{t,v}\}_{t=1}^{v}, \{\bar{s}_t\}_{t=1}^{v-1}, \{L_a^{v-1,k}\}_{k=1}^{2}, \overline{C}_{a,v-1}^{MSDSD})$

1: $\mathbf{Y}_{v-1}^{\text{MSDD}} = \bar{s}^*_{v-1}\mathbf{U}_{v,v}$ //update $\mathbf{Y}_{v-1}^{\text{MSDD}}$ according to Eq. (3.27)
2: $\mathbf{H}_{v-1}^{\text{MSDD}} = -(\sum_{t=1}^{v-1} \bar{s}^*_t \mathbf{U}_{t,v})$ //update $\mathbf{H}_{v-1}^{\text{MSDD}}$ according to Eq. (3.27)
3: $\bar{z}_{v-1}^{MSDSD} = \mathbf{Y}_{v-1}^{\text{MSDD}}(\mathbf{H}_{v-1}^{\text{MSDD}})^H \cdot \exp\left(j\frac{\pi}{M}\right)$ //update decision variable of Eq. (3.68)
4: $\overline{C}_{v-1} = \left\|\mathbf{Y}_{v-1}^{\text{MSDD}}\right\|^2 + \left\|\mathbf{H}_{v-1}^{\text{MSDD}}\right\|^2 + \overline{C}_{a,v-1}^{MSDSD} - 0.5(L_a^{v-1,1} + L_a^{v-1,2})$ //update the constant of Eq. (3.69)
5: $t^{Re}_{v-1} = \sqrt{2}\Re(\bar{z}_{v-1}^{MSDSD}) - 0.5L_a^{v-1,2}$ //relate $L_a^{v-1,2}$ to real part of $\bar{z}_{v-1}^{MSDSD}$
6: $t^{Im}_{v-1} = \sqrt{2}\Im(\bar{z}_{v-1}^{MSDSD}) - 0.5L_a^{v-1,1}$ //relate $L_a^{v-1,1}$ to imag part of $\bar{z}_{v-1}^{MSDSD}$
7: $\overline{\Delta}_{v-1} = -|t^{Re}_{v-1}| - |t^{Im}_{v-1}|$ //update the optimum PED increment
8: $b_1 = (t^{Im}_{v-1} < 0)$ //update the optimum candidate
9: $b_2 = (t^{Re}_{v-1} < 0)$
10: $m_{v-1} =$ **bin2dec**$(b_1 b_2)$ //translate binary bits to decimal index
11: $n_{v-1} = 0$ //initialize child node counter

subfunction: $[\overline{\Delta}_{v-1}, m_{v-1}, n_{v-1}, \text{cd}_{v-1}] =$ **findNext-DQPSK**$(|t^{Re}_{v-1}|, |t^{Im}_{v-1}|, \overline{\Delta}_{v-1}, m_{v-1}, n_{v-1}, \text{cd}_{v-1})$

1: $n_{v-1} = n_{v-1} + 1$ //update child node counter
2: **switch** n_{v-1}
3: **case** 1: $b_1 b_2 =$ **dec2bin**(m_{v-1}) //translate decimal index to binary bits
4: $\text{cd}_{v-1} =$ **sign**$(|t^{Re}_{v-1}| - |t^{Im}_{v-1}|)$ //update the condition
5: **if** $\text{cd}_{v-1} == 1$ //the case of $|t^{Re}_{v-1}| > |t^{Im}_{v-1}|$
6: $\overline{\Delta}_{v-1} = -|t^{Re}_{v-1}| + |t^{Im}_{v-1}|$ //alter the imaginary part of the PED increment
7: $m_{v-1} =$ **bin2dec**$(\bar{b}_1 b_2)$ //alter b_1 in the optimum child node
8: **else** //the case of $|t^{Re}_{v-1}| < |t^{Im}_{v-1}|$
9: $\overline{\Delta}_{v-1} = |t^{Re}_{v-1}| - |t^{Im}_{v-1}|$ //alter the real part of the PED increment
10: $m_{v-1} =$ **bin2dec**$(b_1 \bar{b}_2)$ //alter b_2 in the optimum child node
11: **end if**
12: **break**
13: **case** 2: $\overline{\Delta}_{v-1} = -\overline{\Delta}_{v-1}$ //alter the decision made by the previous step
14: $m_{v-1} = 3 - m_{v-1}$
15: **break**
16: **case** 3: $b_1 b_2 =$ **dec2bin**(m_{v-1})
17: $\overline{\Delta}_{v-1} = |t^{Re}_{v-1}| + |t^{Im}_{v-1}|$ //alter the optimum child node
18: **if** $\text{cd}_{v-1} == 1$ $m_{v-1} =$ **bin2dec**$(\bar{b}_1 b_2)$ //alter b_1 in the decision made by the previous step
19: **else** $m_{v-1} =$ **bin2dec**$(b_1 \bar{b}_2)$ //alter b_2 in the decision made by the previous step
20: **break**
21: **end**

Table 3.6: Pseudo-code for the subfunctions of the reduced-complexity soft-decision-aided MSDSD of Table 3.4, where DQPSK is employed.

of SD's zigzag path, where we have $p_{v-1} = \frac{M}{2\pi}\angle z_{v-1}^{MSDSD}$, while the soft MSDSD aided DQPSK relies on the condition of $\text{sign}(|t^{Re}_{v-1}| - |t^{Im}_{v-1}|)$.

In more detail, the reduced-complexity soft-decision-aided MSDSD is summarized in the form of its pseudo-code in Table 3.4, where the simplified Schnorr-Euchner search strategy specifically tailored for the DBPSK and DQPSK schemes is given by Tables 3.5 and 3.6, respectively. Furthermore, Fig. 3.14 revisits the specific example of soft-decision-aided MSDSD conceived for DQPSK in Fig. 3.10, subject to the slight difference that the reduced-complexity algorithms of Tables 3.4 and 3.6 are invoked in Fig. 3.14.

More explicitly, it can be seen in Fig. 3.14-a) that the "findBest-DQPSK" subfunction of Table 3.6 opts for obtaining the best phasor candidate by simply evaluating $\overline{\Delta}_{v-1} = -|t^{Re}_{v-1}| - |t^{Im}_{v-1}|$ of Eq. (3.73), when the SD visits the indices $v = 2$ and $v = 3$ for the first time in Step ① and Step ②, respectively. The SD radius is updated as $d = 7.28$, when the SD index reaches $v = N_w$ in Step ② of Fig. 3.14-a). Then the SD index is decreased to $v = 2$ in Step ③, and the second-

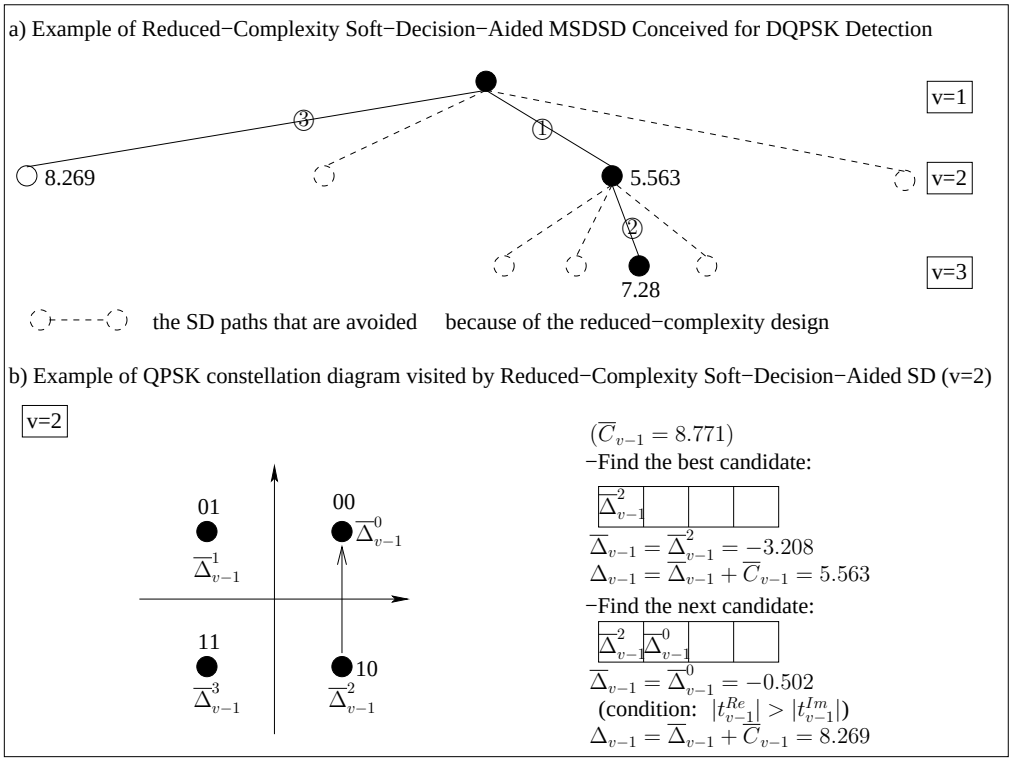

Figure 3.14: Example of soft-decision-aided MSDSD conceived for DQPSK, which corresponds to the example seen in Fig. 3.10, subject to the slight difference that the reduced-complexity algorithm of Tables 3.4 and 3.6 are invoked, instead of the conventional algorithm of Table 3.3.

best phasor candidate is obtained by the "findNext-DQPSK" subfunction of Table 3.6, which has a PED value of $d_2 = 8.269$ as seen in Fig. 3.14-a). Since this new PED value is higher than the SD radius, the SD decreases its index to $v = 1$ and terminates the search. As a result, the reduced-complexity MSDSD exemplified in Fig. 3.14-a) visits a reduced number of the constellation points compared to the conventional MSDSD exemplified in Fig. 3.10-a), yet the same SD result is arrived at. Fig. 3.14-b) further portrays the corresponding constellation points that are visited by the SD's Schnorr-Euchner search strategy in a zigzag fashion at SD index $v = 2$, which becomes similar to the zigzag constellation points visiting fashion seen in Fig. 3.3-b) for the hard-decision-aided DQPSK detection example.

Let us now consider the rotated 8PSK constellation portrayed by Fig. 3.15-b) as an example, where the $M = 8$ constellation points are arranged to $M/4 = 2$ groups, which are Group G0 of $\{\pm\cos(\frac{\pi}{8}) \pm j\sin(\frac{\pi}{8})\}$ and Group G1 of $\{\pm\sin(\frac{\pi}{8}) \pm j\cos(\frac{\pi}{8})\}$. Accordingly, their probability metrics $\{\overline{\Delta}^m_{v-1}\}^{M-1=7}_{m=0}$ of Eq. (3.70) may be expressed as:

$$\begin{aligned}
\overline{\Delta}^0_{v-1} &= -2\cos(\tfrac{\pi}{8})\cdot\Re(\bar{z}_{v-1}) - 2\sin(\tfrac{\pi}{8})\cdot\Im(\bar{z}_{v-1}) + \tfrac{L_a(b_1)}{2} + \tfrac{L_a(b_2)}{2} &&= -t^{Re0}_{v-1} - t^{Im0}_{v-1},\\
\overline{\Delta}^2_{v-1} &= 2\cos(\tfrac{\pi}{8})\cdot\Re(\bar{z}_{v-1}) - 2\sin(\tfrac{\pi}{8})\cdot\Im(\bar{z}_{v-1}) + \tfrac{L_a(b_1)}{2} - \tfrac{L_a(b_2)}{2} &&= t^{Re0}_{v-1} - t^{Im0}_{v-1},\\
\overline{\Delta}^4_{v-1} &= -2\cos(\tfrac{\pi}{8})\cdot\Re(\bar{z}_{v-1}) + 2\sin(\tfrac{\pi}{8})\cdot\Im(\bar{z}_{v-1}) - \tfrac{L_a(b_1)}{2} + \tfrac{L_a(b_2)}{2} &&= -t^{Re0}_{v-1} + t^{Im0}_{v-1},\\
\overline{\Delta}^6_{v-1} &= 2\cos(\tfrac{\pi}{8})\cdot\Re(\bar{z}_{v-1}) + 2\sin(\tfrac{\pi}{8})\cdot\Im(\bar{z}_{v-1}) - \tfrac{L_a(b_1)}{2} - \tfrac{L_a(b_2)}{2} &&= t^{Re0}_{v-1} + t^{Im0}_{v-1}.
\end{aligned} \tag{3.74}$$

$$\begin{aligned}
\overline{\Delta}_{v-1}^{1} &= -2\sin(\tfrac{\pi}{8})\cdot\Re(\bar{z}_{v-1}) - 2\cos(\tfrac{\pi}{8})\cdot\Im(\bar{z}_{v-1}) + \tfrac{L_a(b_1)}{2} + \tfrac{L_a(b_2)}{2} - L_a(b_3) &&= -t_{v-1}^{Re1} - t_{v-1}^{Im1} - L_a(b_3),\\
\overline{\Delta}_{v-1}^{3} &= 2\sin(\tfrac{\pi}{8})\cdot\Re(\bar{z}_{v-1}) - 2\cos(\tfrac{\pi}{8})\cdot\Im(\bar{z}_{v-1}) + \tfrac{L_a(b_1)}{2} - \tfrac{L_a(b_2)}{2} - L_a(b_3) &&= t_{v-1}^{Re1} - t_{v-1}^{Im1} - L_a(b_3),\\
\overline{\Delta}_{v-1}^{5} &= -2\sin(\tfrac{\pi}{8})\cdot\Re(\bar{z}_{v-1}) + 2\cos(\tfrac{\pi}{8})\cdot\Im(\bar{z}_{v-1}) - \tfrac{L_a(b_1)}{2} + \tfrac{L_a(b_2)}{2} - L_a(b_3) &&= -t_{v-1}^{Re1} + t_{v-1}^{Im1} - L_a(b_3),\\
\overline{\Delta}_{v-1}^{7} &= 2\sin(\tfrac{\pi}{8})\cdot\Re(\bar{z}_{v-1}) + 2\cos(\tfrac{\pi}{8})\cdot\Im(\bar{z}_{v-1}) - \tfrac{L_a(b_1)}{2} - \tfrac{L_a(b_2)}{2} - L_a(b_3) &&= t_{v-1}^{Re1} + t_{v-1}^{Im1} - L_a(b_3),
\end{aligned} \tag{3.75}$$

where the two real/imaginary terms are given by:

$$\begin{aligned}
t_{v-1}^{Re0} &= 2\cos(\frac{\pi}{8})\cdot\Re(\bar{z}_{v-1}) - \frac{L_a(b_2)}{2},\\
t_{v-1}^{Im0} &= 2\sin(\frac{\pi}{8})\cdot\Im(\bar{z}_{v-1}) - \frac{L_a(b_1)}{2},\\
t_{v-1}^{Re1} &= 2\sin(\frac{\pi}{8})\cdot\Re(\bar{z}_{v-1}) - \frac{L_a(b_2)}{2},\\
t_{v-1}^{Im1} &= 2\cos(\frac{\pi}{8})\cdot\Im(\bar{z}_{v-1}) - \frac{L_a(b_1)}{2}.
\end{aligned} \tag{3.76}$$

It can be seen in Eqs. (3.74) and (3.75) that the only difference between the four component probability metrics within each group is the polarity of the real/imaginary terms. As a result, the local minimum metrics of the $M/4 = 2$ groups may be obtained by:

$$\begin{aligned}
\overline{\Delta}_{v-1}^{G0} &= \min_{m\in\{0,2,4,6\}} \overline{\Delta}_{v-1}^{m} = -|t_{v-1}^{Re0}| - |t_{v-1}^{Im0}|,\\
\overline{\Delta}_{v-1}^{G1} &= \min_{m\in\{1,3,5,7\}} \overline{\Delta}_{v-1}^{m} = -|t_{v-1}^{Re1}| - |t_{v-1}^{Im1}| - L_a(b_3),
\end{aligned} \tag{3.77}$$

which are evaluated without invoking Eq. (3.70) for $M = 8$ times in Eqs. (3.74) and (3.75). Finally, the global minimum over $\{\overline{\Delta}_{v-1}^{m}\}_{m=0}^{M-1=7}$ of Eq. (3.70) may be simply obtained by comparing the two local minima as:

$$\overline{\Delta}_{v-1} = \min\ \{\overline{\Delta}_{v-1}^{G0}, \overline{\Delta}_{v-1}^{G1}\}. \tag{3.78}$$

In summary, for a generic high-order MPSK scheme ($M > 4$), we may firstly assign the M constellation points to $M/4$ groups of QPSK-like constellation points that are associated with the same magnitudes but different polarities, so that the local minimum metric for $\{\overline{\Delta}_{v-1}^{m}\}_{m=0}^{M-1}$ of Eq. (3.70) within each group is simply given by:

$$\overline{\Delta}_{v-1}^{Gg} = -\left|t_{v-1}^{Re_g}\right| - \left|t_{v-1}^{Im_g}\right| - \sum_{\tilde{k}=3}^{\mathrm{BPS}} \widetilde{b}_{\tilde{k}} L_a(b_{\tilde{k}}), \tag{3.79}$$

where the range for the group index is given by $g \in \{0, \cdots, M/4-1\}$, while the real and imaginary parts of $\bar{z}_{v-1}$ are associated with $L_a(b_2)$ and $L_a(b_1)$ respectively as follows:

$$\begin{aligned}
t_{v-1}^{Re_g} &= \overline{A}^{g}\cdot\Re(\bar{z}_{v-1}) - \frac{L_a(b_2)}{2},\\
t_{v-1}^{Im_g} &= \overline{B}^{g}\cdot\Im(\bar{z}_{v-1}) - \frac{L_a(b_1)}{2}.
\end{aligned} \tag{3.80}$$

The coordinates of the MPSK constellation points, which are located in the first quadrant may be denoted by $\{(A^g, B^g)\}_{g=0}^{M/4-1}$, and we have $\overline{A}^{g} = 2A^g$ as well as $\overline{B}^{g} = 2B^g$ in Eq. (3.80). As a result, the global minimum for $\{\overline{\Delta}_{v-1}^{m}\}_{m=0}^{M-1}$ of Eq. (3.70) may be simply given by:

$$\overline{\Delta}_{v-1} = \min_{g\in\{0,\cdots,M/4-1\}} \overline{\Delta}_{v-1}^{Gg}, \tag{3.81}$$

which is obtained by visiting a reduced-subset of $M/4$ constellation points that correspond to the $M/4$ local minima of Eq. (3.79).

We note that the procedures conceived for obtaining the minimum probability metric of Eq. (3.81) are similar to those for generic soft-decision-aided MPSK detection in Sec. 2.4. However, for the soft-decision-aided MSDSD, the Schnorr-Euchner search strategy also relies on the ranking order of constellation points. Against this background, we propose to complete the Schnorr-Euchner strategy by using a Comparison Window (CW). More explicitly, the CW is initialized to have $M/4$ local minima of Eq. (3.79), which correspond to local best candidates. Then the CW may choose the global best candidate which has the global minimum metric by invoking Eq. (3.81). This is the subfunction of "findBest-DPSK" for the Schnorr-Euchner search strategy tailored for MPSK ($M > 4$) in Table 3.7. Furthermore, when the SD re-visits a specific SD index v, the "findNext-DPSK" subfunction in Table 3.7 may offer the next constellation node. More explicitly, if previously a local minimum from Group G$\overline{g}$ is chosen as the global candidate, i.e. previously we have $\overline{\Delta}_{v-1} = \overline{\Delta}_{v-1}^{G\overline{g}}$ from Eq. (3.81), then Group G$\overline{g}$ has to visit a new local candidate in a zigzag fashion by comparing $|t_{v-1}^{Re\overline{g}}|$ and $|t_{v-1}^{Im\overline{g}}|$. Following this, the CW may once again update the new global candidate by invoking Eq. (3.81).

Fig. 3.15 portrays the D8PSK example of Fig. 3.11, where the reduced-complexity algorithms of Tables 3.4 and 3.7 are invoked. More explicitly, it can be seen in Fig. 3.15 that the "findBest-DPSK" subfunction in Table 3.7 may firstly initialize the CW by the $M/4 = 2$ local minima of Eq. (3.79) as $\overline{\Delta}_{v-1}^{G0} = -3.487$ and $\overline{\Delta}_{v-1}^{G1} = -0.998$, and then the CW invokes Eq. (3.81) in order to obtain the global candidate of $\overline{\Delta}_{v-1} = \overline{\Delta}_{v-1}^{G0} = -3.487$. Moreover, when the SD re-visits index $v = 2$ in Fig. 3.15, the "findNext-DPSK" in Table 3.7 may firstly update a new local candidate $\overline{\Delta}_{v-1}^{G0} = 4.364$ from Group G0 by visiting the QPSK-like constellation points in a zigzag fashion relying on the relationship between $|t_{v-1}^{Re0}|$ and $|t_{v-1}^{Im0}|$, and then the CW invokes Eq. (3.81) again in order to obtain the new global candidate of $\overline{\Delta}_{v-1} = \overline{\Delta}_{v-1}^{G1} = -0.998$. As a result, the reduced-complexity MSDSD exemplified in Fig. 3.15 visits a reduced subset of the constellation points compared to the conventional MSDSD exemplified in Fig. 3.11, yet the same SD result is arrived at.

Moreover, it is worth pointing out that the conventional MSDSD algorithm in [132] requires the Schnorr-Euchner search strategy to invoke a sorting algorithm, which was represented by the "qsort" function in the pseudo-code algorithm table of [132] and also in Table 3.3 of this report. As a result, all M constellation points $\{x^m\}_{m=0}^{M-1}$ are ranked according to an ascending order of the PED increment values $\{\Delta_{v-1}^m\}_{m=0}^{M-1}$, which is explicitly exemplified by Figs. 3.10 and 3.11. There are numerous sorting algorithms that may be suitable, such as Bubble sort, Timsort, Library sort [285, 286], etc., but the average number of comparisons required by these algorithms is as high as $O(M \log M)$. By contrast, the reduced-complexity MSDSD of Tables 3.5-3.7 does not require any sorting algorithms. As exemplified by Figs. 3.14 and 3.15, the proposed Schnorr-Euchner search strategy does not have to maintain the complete ranking order of constellation points, which dispenses with a considerable number of comparisons.

subfunction: $[\{|t_{v-1}^{Re_g}|\}_{g=0}^{M/4-1}, \{|t_{v-1}^{Im_g}|\}_{g=0}^{M/4-1}, \{\mathrm{CW}_{v-1}^{g}\}_{g=0}^{M/4-1}, \{\mathrm{CW}m_{v-1}^{g}\}_{g=0}^{M/4-1}, \{n_{v-1}^{g}\}_{g=0}^{M/4-1}, \overline{\Delta}_{v-1}, \overline{C}_{v-1}, m_{v-1}, n_{v-1}] = \textbf{findBest-DPSK}(\{\mathbf{U}_{t,v}\}_{t=1}^{v}, \{\bar{s}_t\}_{t=1}^{v-1}, \{L_a^{v-1,k}\}_{k=1}^{2}, \overline{C}_{a,v-1}^{MSDSD}, \{P_{v-1}^{g}\}_{g=0}^{M/4-1})$

$\mathbf{Y}_{v-1}^{\mathrm{MSDD}} = \bar{s}_{v-1}^{*}\mathbf{U}_{v,v}$ //update $\mathbf{Y}_{v-1}^{\mathrm{MSDD}}$ according to Eq. (3.27)

$\mathbf{H}_{v-1}^{\mathrm{MSDD}} = -(\sum_{t=1}^{v-1}\bar{s}_t^{*}\mathbf{U}_{t,v})$ //update $\mathbf{H}_{v-1}^{\mathrm{MSDD}}$ according to Eq. (3.27)

$\bar{z}_{v-1}^{MSDSD} = \mathbf{Y}_{v-1}^{\mathrm{MSDD}}(\mathbf{H}_{v-1}^{\mathrm{MSDD}})^{H} \cdot \exp\left(j\frac{\pi}{M}\right)$ //update decision variable of Eq. (3.68)

$\overline{C}_{v-1} = \|\mathbf{Y}_{v-1}^{\mathrm{MSDD}}\|^2 + \|\mathbf{H}_{v-1}^{\mathrm{MSDD}}\|^2 + \overline{C}_{a,v-1}^{MSDSD} - 0.5(L_a^{v-1,1} + L_a^{v-1,2})$ //update the constant of Eq. (3.69)

for g=0 **to** $(M/4-1)$

  $t_{v-1}^{Re_g} = \overline{A}^{g} \cdot \Re(\bar{z}_{v-1}^{MSDSD}) - 0.5L_a^{v-1,2}$ //relate $L_a^{v-1,2}$ to real part of $\bar{z}_{v-1}^{MSDSD}$

  $t_{v-1}^{Im_g} = \overline{B}^{g} \cdot \Im(\bar{z}_{v-1}^{MSDSD}) - 0.5L_a^{v-1,1}$ //relate $L_a^{v-1,1}$ to imag part of $\bar{z}_{v-1}^{MSDSD}$

  $\mathrm{CW}_{v-1}^{g} = -|t_{v-1}^{Re_g}| - |t_{v-1}^{Im_g}| - P_{v-1}^{g}$ //update the local minimum

  $b_1 = (t_{v-1}^{Im_g} < 0)$

  $b_2 = (t_{v-1}^{Re_g} < 0)$

  $\mathrm{CW}m_{v-1}^{g} = \textbf{bin2dec}(b_1 b_2 b_3 \cdots b_{\mathrm{BPS}})$ //we have $[b_3 \cdots b_{\mathrm{BPS}}] = \textbf{dec2bin}(g)$

  $n_{v-1}^{g} = 0$ //update child node counter for each group

end for

$[\overline{\Delta}_{v-1}, \hat{g}] = \textbf{min}(\{\mathrm{CW}_{v-1}^{g}\}_{g=0}^{M/4-1})$ //the global minimum is $\overline{\Delta}_{v-1} = \mathrm{CW}_{v-1}^{\hat{g}}$

$m_{v-1} = \mathrm{CW}m_{v-1}^{\hat{g}}$ //record the global optimum index

$n_{v-1} = 0$ //update global child node counter

subfunction: $[\{\mathrm{CW}_{v-1}^{g}\}_{g=0}^{M/4-1}, \{\mathrm{CW}m_{v-1}^{g}\}_{g=0}^{M/4-1}, \{n_{v-1}^{g}\}_{g=0}^{M/4-1}, \{\mathrm{cd}_{v-1}^{g}\}_{g=0}^{M/4-1}, \overline{\Delta}_{v-1}, m_{v-1}, n_{v-1}] = \textbf{findNext-DPSK}(\{|t_{v-1}^{Re_g}|\}_{g=0}^{M/4-1}, \{|t_{v-1}^{Im_g}|\}_{g=0}^{M/4-1}, \{P_{v-1}^{g}\}_{g=0}^{M/4-1}, \{\mathrm{CW}_{v-1}^{g}\}_{g=0}^{M/4-1}, \{\mathrm{CW}m_{v-1}^{g}\}_{g=0}^{M/4-1}, \{n_{v-1}^{g}\}_{g=0}^{M/4-1}, \{\mathrm{cd}_{v-1}^{g}\}_{g=0}^{M/4-1}, \overline{\Delta}_{v-1}, m_{v-1}, n_{v-1})$

$[b_1 \cdots b_{\mathrm{BPS}}] = \textbf{dec2bin}(m_{v-1})$ //obtain the previously tested child node

$\overline{g} = \textbf{bin2dec}(b_3 \cdots b_{\mathrm{BPS}})$ //update the previously tested group's index

$n_{v-1}^{\overline{g}}++$ //update child node counter

switch $n_{v-1}^{\overline{g}}$

  case 1: $\mathrm{cd}_{v-1}^{\overline{g}} = \textbf{sign}(|t_{v-1}^{Re_{\overline{g}}}| - |t_{v-1}^{Im_{\overline{g}}}|)$ //update the condition of group $\overline{g}$

    if $\mathrm{cd}_{v-1}^{\overline{g}} == 1$

      $\mathrm{CW}_{v-1}^{\overline{g}} = -|t_{v-1}^{Re_{\overline{g}}}| + |t_{v-1}^{Im_{\overline{g}}}| - P_{v-1}^{\overline{g}}$ //alter the imaginary part of local minimum

      $\mathrm{CW}m_{v-1}^{\overline{g}} = \textbf{bin2dec}(\bar{b}_1 b_2 b_3 \cdots b_{\mathrm{BPS}})$ //alter b_1 in the local optimum child node

    else

      $\mathrm{CW}_{v-1}^{\overline{g}} = |t_{v-1}^{Re_{\overline{g}}}| - |t_{v-1}^{Im_{\overline{g}}}| - P_{v-1}^{\overline{g}}$ //alter the real part of local minimum

      $\mathrm{CW}m_{v-1}^{\overline{g}} = \textbf{bin2dec}(b_1 \bar{b}_2 b_3 \cdots b_{\mathrm{BPS}})$ //alter b_2 in the local optimum child node

    end if

    break

  case 2: $\mathrm{CW}_{v-1}^{\overline{g}} = -\overline{\Delta}_{v-1} - 2P_{v-1}^{\overline{g}}$ //alter the second child node

    $\mathrm{CW}m_{v-1}^{\overline{g}} = \textbf{bin2dec}(\bar{b}_1 \bar{b}_2 b_3 \cdots b_{\mathrm{BPS}})$ //alter both b_1 and b_2 in the previous decision

    break

  case 3: $\mathrm{CW}_{v-1}^{\overline{g}} = |t_{v-1}^{Re_{\overline{g}}}| + |t_{v-1}^{Im_{\overline{g}}}| - P_{v-1}^{\overline{g}}$ //alter the local optimum child node

    if $\mathrm{cd}_{v-1}^{\overline{g}} == 1$ $\mathrm{CW}m_{v-1}^{\overline{g}} = \textbf{bin2dec}(\bar{b}_1 b_2 b_3 \cdots b_{\mathrm{BPS}})$ //alter b_1 in the previous decision

    else $\mathrm{CW}m_{v-1}^{\overline{g}} = \textbf{bin2dec}(b_1 \bar{b}_2 b_3 \cdots b_{\mathrm{BPS}})$ //alter b_2 in the previous decision

    break

end switch

$\overline{\Delta}_{v-1} = \inf$ //initialize global minimum

for $g = 0$ **to** $(M/4-1)$

  if $\mathrm{CW}_{v-1}^{g} < \overline{\Delta}_{v-1}$ **and** $n_{v-1}^{g} <= 3$ //compare local minimums from un-full groups

    $\overline{\Delta}_{v-1} = \mathrm{CW}_{v-1}^{g}$ //update global minimum

    $m_{v-1} = \mathrm{CW}m_{v-1}^{g}$

  end if

end for

$n_{v-1} = n_{v-1} + 1$ //update global child node

Table 3.7: Pseudo-code for the subfunctions of the reduced-complexity soft-decision-aided MSDSD of Table 3.4, where DPSK ($M > 4$) is employed.

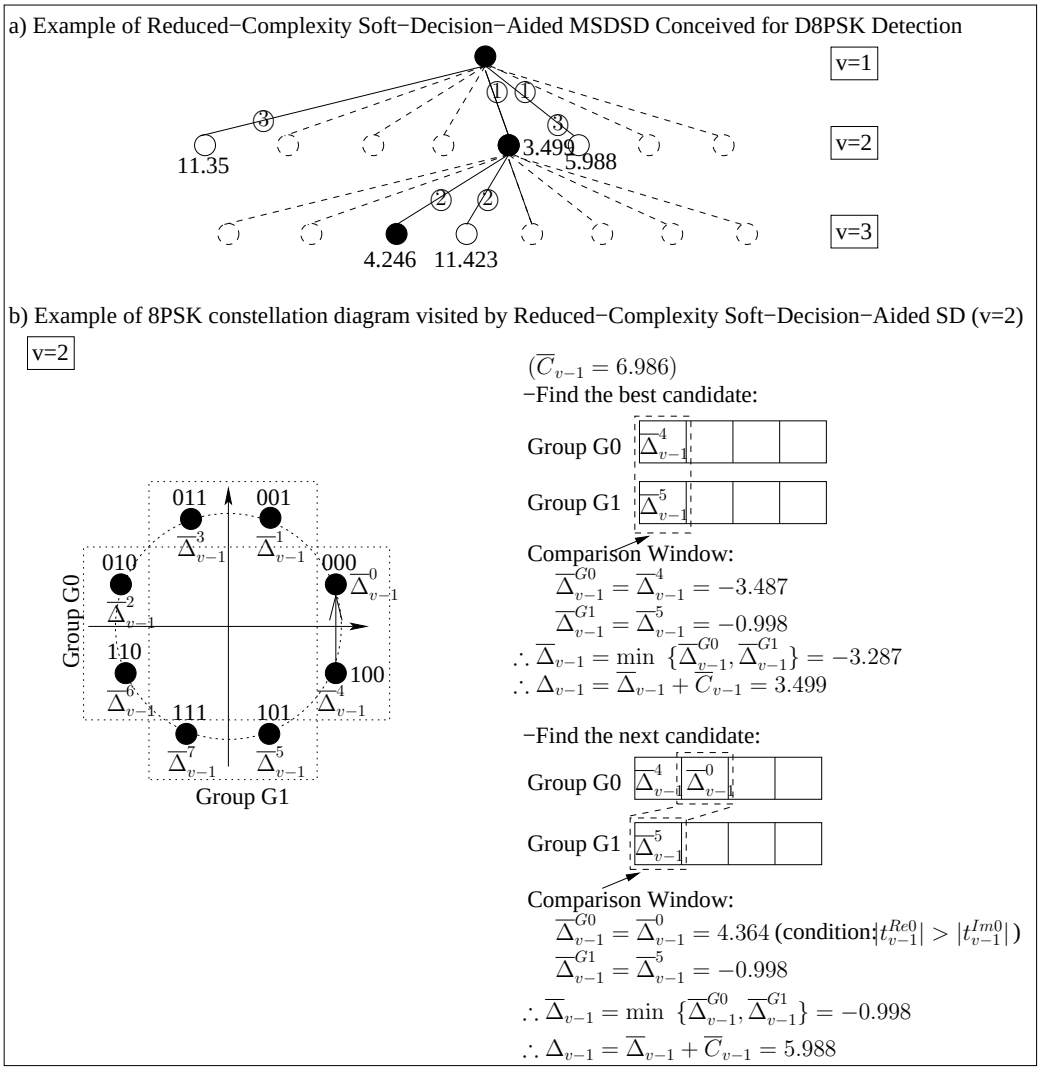

Figure 3.15: Example of the soft-decision-aided MSDSD conceived for D8PSK, which corresponds to the example seen in Fig. 3.11, subject to the slight difference that the reduced-complexity algorithms of Tables 3.4 and 3.7 are invoked, instead of the conventional algorithm of Table 3.3.

Furthermore, the Approx-Log-MAP proposed in Sec. 3.3.2 may also be straightforwardly applied to the reduced-complexity soft-decision-aided MSDSD of this section, where the simplified Schnorr-Euchner strategy of Tables 3.5-3.7 can be invoked for all SD indice satisfying $v < N_w$. However, the original Schnorr-Euchner strategy of [132] has to be invoked for the specific SD index $v = N_w$, because all the leaf nodes at $v = N_w$ have to be recorded and produced for the Approx-Log-MAP.

3.3.4 Soft-Decision-Aided DFDD Conceived for Coded DPSK

According to Eq. (3.36), the differences between the hard-decision aided DFDD metric $|z_{N_w-1}^{\text{DFDD}} - x^m|^2$ and the hard-decision assisted MSDD metric tr $\left(\mathbf{F}\bar{\mathbf{S}}^H\mathbf{Y}\mathbf{Y}^H\bar{\mathbf{S}}\right)$ are all constants, where previous

decisions $\{\hat{\bar{s}}_v\}_{v=1}^{N_w-1}$ are utilized for replacing all variables, except for $\bar{s}_{N_w}$ in the MSDD metric. As a result, for soft-decision-aided DFDD, the MSDD probability metric of Eq. (3.52) may be simplified to [122, 125, 136]:

$$d^m = -\left|z^{DFDD} - x^m\right|^2 + \sum_{\bar{k}=1}^{\text{BPS}} \widetilde{b}_{\bar{k}} L_a(b_{\bar{k}}), \tag{3.82}$$

where the DFDD decision variable z^{DFDD} is given by Eq. (3.37), and the subscript $(N_w - 1)$ of $z_{N_w-1}^{DFDD}$ in Eq. (3.37) is deleted for the sake of simplicity, because only a single variable x_{N_w-1} has to be detected within a DFDD window. Furthermore, the *a priori* LLRs of the previous decisions $\sum_{\bar{k}=1}^{(N_w-2)\text{BPS}} \widetilde{b}_{\bar{k}} L_a(b_{\bar{k}})$ seen in the MSDD probability metric expression of Eq. (3.52) is ignored in the DFDD probabilty metric of Eq. (3.82), because the common constant may be ignored both by the Max-Log-MAP algorithm of Eq. (3.53) and by the Approx-Log-MAP algorithm of Eq. (3.54).

In order to further simplify the DFDD symbol metric of Eq. (3.82), it was proposed in [122] that bit-metric based DFDD may be invoked. More explicitly, a universal maximum probability based on the *a priori* LLRs is given by a simple single-step evaluation as:

$$\hat{d}_{max} = -\left|z^{DFDD} - \hat{x}\right|^2 + \sum_{\bar{k}=1}^{\text{BPS}} \hat{b}_{\bar{k}} L_a(b_{\bar{k}}), \tag{3.83}$$

where $\hat{x}$ is modulated by $\{\hat{b}_{\bar{k}}\}_{\bar{k}=1}^{\text{BPS}}$, which are determined by the polarities of the *a priori* LLRs as $\{\hat{b}_{\bar{k}} = [L_a(b_{\bar{k}}) > 0]\}_{\bar{k}=1}^{\text{BPS}}$. For each single soft-bit output, the complete Max-Log-MAP algorithm is given by:

$$L_p(b_k \mid \mathbf{Y}) = \begin{cases} \hat{d}_{max} - \hat{d}'_{max}, & \text{if } \hat{b}_k = 1 \\ \hat{d}'_{max} - \hat{d}_{max}, & \text{if } \hat{b}_k = 0 \end{cases}, \tag{3.84}$$

where $\hat{d}'_{max}$ is given by replacing $\hat{x}$ in Eq. (3.83) by $\hat{x}'$ that is modulated by the same decisions $\{\hat{b}_{\bar{k}}\}_{\bar{k}\neq k}$, except that the specific bit $\hat{b}_k$ is flipped, i.e. we have $b_k \neq \hat{b}_k$. It can be seen that a total of only $(\log_2 M + 1)/\log_2 M$ probability metrics have to be estimated by the bit-metric based DFDD for producing a single soft-bit output, instead of evaluating and comparing the M metrics of Eq. (3.82) as required by the symbol-metric based DFDD.

However, we will demonstrate in Sec. 3.3.5 that the bit-metric based DFDD of Eq. (3.84) imposes a severe degradation on the LLR accuracy, which in turn results in a substantial BER performance penalty. In order to mitigate this problem, the reduced-complexity probability metric calculation of Algorithm 2.3 introduced in Sec. 2.4.2 may be directly applied to the DFDD using the symbol-metric of Eq. (3.82) without inflicting any performance loss. More explicitly, Algorithm 2.3 may be invoked, where the equivalent noise power is given by $\overline{N_0} = \frac{1}{2}$, while the decision variable is given by either $\bar{z}_n = z^{DFDD}$ for DBPSK or by $\bar{z}_n = z^{DFDD} \exp(j\frac{\pi}{M})$ for generic DPSK associated with $M \geq 4$.

3.3.5 Performance Results for Coded DPSK

We further discuss our simulation results in this section. As observed for the hard-decision-aided MSDSD, the SD radius of the soft-decision-aided MSDSD should be initialized to be sufficiently

	real-valued multiplications	real-valued additions	comparisons	visited nodes
CDD	$M + (3M + 4N_R)$/BPS	$M + 1 + (3M + 4N_R - 2)$/BPS	M	M
CDD (Algorithm 2.3)	$M/4 + (M/2 + 4N_R + 6)$/BPS	$M/4 + 1 + (7M/4 + 4N_R)$/BPS	$M/8 + 1 + (M/2 + 2)$/BPS	$M/4$
MSDD	$(4N_w^3 + 4N_w^2 N_R + 2N_w N_R) \times M^{(N_w-1)}/[\text{BPS}(N_w - 1)] + M^{(N_w-1)}$	$[4N_w^3 + (4N_R - 2)N_w^2 - 1] \times M^{(N_w-1)}/[\text{BPS}(N_w - 1)] + M^{(N_w-1)}$	$M^{(N_w-1)} \div [\text{BPS}(N_w - 1)]$	$M^{(N_w-1)}$
MSDSD's sortDelta	$(4N_R v + 6N_R)M$	$(4N_R v + 2N_R)M$	$O(M \log M)$	M
MSDSD's findBest-DBPSK	$4N_R v + 8N_R$	$4N_R v + 4N_R$	2	1
MSDSD's findNext-DBPSK	0	2	0	1
MSDSD's findBest-DQPSK	$4N_R v + 8N_R + 7$	$4N_R v + 4N_R + 6$	4	1
MSDSD's findNext-DQPSK	≤ 1	≤ 4	≤ 3	1
MSDSD's findBest-DPSK	$4N_R v + 8N_R + M + 4$	$4N_R v + 4N_R + 3M/2 + 2$	$5M/4$	$M/4$
MSDSD's findNext-DPSK	≤ 3	≤ 7	$\leq M/2 + 2$	1
DFDD	$M + (4N_R N_w + 2M)$/BPS	$M + (4N_R N_w - 4N_R + 4M - 2)$/BPS	M	M
DFDD (Algorithm 2.3)	$M/4 + (4N_R N_w + 7)$/BPS	$M/4 + 1 + (4N_R N_w - 4N_R + 7M/4 + 4)$/BPS	$M/8 + 1 + (M/2 + 4)$/BPS	$M/4$
DFDD (bit metric)	2BPS + 3 + $(4N_R N_w + 1)$/BPS	2BPS + 6 + $(4N_R N_w - 4N_R + 1)$/BPS	2	BPS + 1

Table 3.8: Complexity (per soft-bit output) of soft-decision-aided noncoherent detectors conceived for coded DPSK using the Max-Log-MAP algorithm. CDD and MSDD refer to the Max-Log-MAP of Eq. (3.53) using Eq. (3.58) and Eq. (3.52), respectively, where Algorithm 2.3 proposed in Sec. 2.4.2 may be applied for reducing the CDD complexity. The MSDSD's Schnorr-Euchner search strategy subfunctions are given by Tables 3.3 and 3.5-3.7. DFDD and bit-metric based DFDD are given by Max-Log-MAP using Eq. (3.82) and by Eq. (3.84), respectively, where Algorithm 2.3 may also be invoked for DFDD.

large, so that the full-search based MSDD's detection capability may be retained. This is especially important for the soft-decision-aided MSDSD presented in this section, because any erosion of the detector's capability may result inaccurate LLRs, which implies that the performance of the resultant suboptimal detectors cannot be accurately predicted by the EXIT charts introduced in Sec. 2.3.2.4. Furthermore, we note that the simulation parameters used in this section are the same as those in Table 2.3, except that the coherent modulation scheme is replaced by the DPSK scheme discussed in this chapter.

The detection complexities of Max-Log-MAP aided CDD, MSDD, MSDSD and DFDD conceived for coded DPSK schemes are summarized in Table 3.8. For CDD, MSDD and DFDD, the Approx-Log-MAP and Max-Log-MAP algorithms generally impose the same number of real-valued multiplications, but the Approx-Log-MAP algorithm needs more additions and comparisons, when relying on the lookup table of Table 2.2. Similarly, for a MSDSD's subfunction of Tables 3.3-3.7, the Approx-Log-MAP and Max-Log-MAP algorithms also have the same number of multiplications, but the Approx-Log-MAP algorithm may invoke the subfunctions of findNext-DBPSK, findNext-DQPSK and findNext-DPSK of Tables 3.5-3.7 a higher number of times compared to the Max-Log-MAP in order to take into account more leaf nodes candidates. This results in an overall complexity increase in all categories. Moreover, we note that some unneccessary calculations may be eliminated. For example, the expression $\{0.5L_a^{v-1,1}\}_{\forall v}$ and $\{0.5L_a^{v-1,2}\}_{\forall v}$ may be cal-

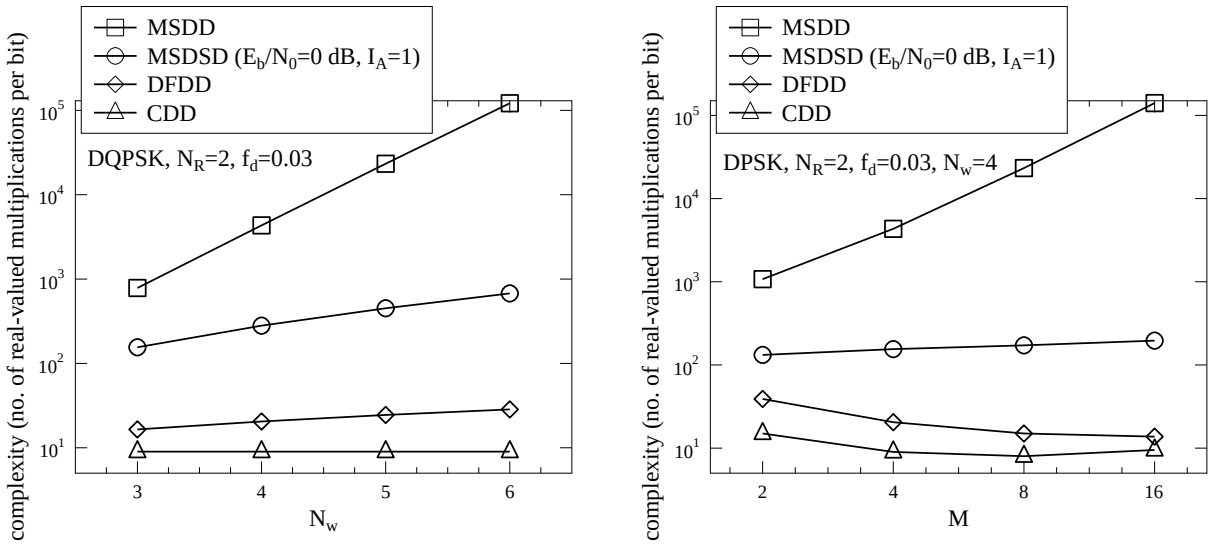

(a) $M = 4$,$N_w = \{3,4,5,6\}$ (b) $M = \{2,4,8,16\}$,$N_w = 4$

Figure 3.16: Complexity (number of real-valued multiplications per soft-bit output) comparison between the noncoherent detectors conceived for coded DPSK using the Max-Log-MAP algorithm, where $N_R = 2$ RAs are used, while the normalized Doppler frequency is given by $f_d = 0.03$.

culated before invoking the MSDSD's subfunctions. Furthermore, the function of $[b_1 \cdots b_{\text{BPS}}] =$ **dec2bin**(m) may be implemented by using a pre-stored lookup table for bit-mapping, while its inverse function $m =$ **bin2dec**$(b_1 \cdots b_{\text{BPS}}) = b_1 \cdot 2^{\text{BPS-1}} + b_2 \cdot 2^{\text{BPS-2}} + \cdots + b_{\text{BPS}-1} \cdot 2 + b_{\text{BPS}}$ may require a total number of $(BPS - 1)$ multiplications as well as $(BPS - 1)$ additions.

The detection complexity comparison of CDD, MSDD, MSDSD and DFDD conceived for coded DPSK is further characterized by Fig. 3.16 in terms of the total number of real-valued multiplications *per soft-bit output*, where the Max-Log-MAP algorithm is invoked. We note that Algorithm 2.3 is applied to both CDD and DFDD, while the MSDSD utilizes the reduced-complexity algorithm of Table 3.4. It may be seen in Fig. 3.16 that the MSDD and CDD exhibit the highest and the lowest detection complexities, respectively, while the DFDD complexity is lower than the MSDSD complexity. Moreover, it is demonstrated by Fig. 3.16b that the DFDD complexity and CDD complexity *per soft-bit output* decreases, as M increases. More explicitly, the application of Algorithm 2.3 may effectively reduce both CDD complexity and the DFDD complexity from $O(M)$ to $O(M/4)$, where we have $M/4 \leq$ BPS for low-order modulation schemes associated with $M \leq 16$. As a result, the complexities of the CDD and DFDD *per soft-bit output* may be reduced, as M grows as long as we have $M \leq 16$.

The complexity of the conventional MSDSD algorithm of Table 3.3 and that of the reduced-complexity MSDSD algorithm of Tables 3.4 and 3.6 conceived for coded DQPSK are compared in Fig. 3.17 in terms of the total number of real-valued multiplications of each algorithm. It is demonstrated by Fig. 3.17a that the complexities of both soft-decision-aided MSDSD algorithms

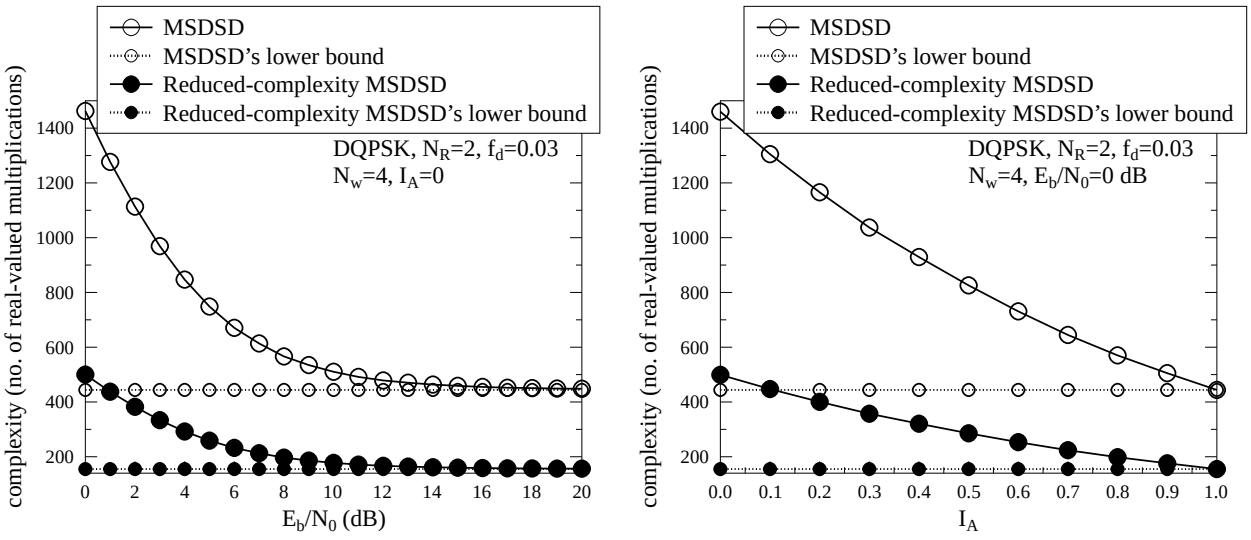

(a) $E_b/N_0 = 0 \sim 20$ dB, $I_A = 0$

(b) $E_b/N_0 = 0$ dB, $I_A = 0 \sim 1$

Figure 3.17: Complexity (number of real-valued multiplications) comparison between the conventional MSDSD algorithm of Table 3.3 and the reduced-complexity MSDSD algorithm of Tables 3.4 and 3.6 for coded DQPSK, where $N_R = 2$ RAs are used, while the normalized Doppler frequency is given by $f_d = 0.03$.

converge to their lower bounds as E_b/N_0 increases, which is exactly the same as that of the hard-decision-aided MSDSD presented in Sec. 3.2.5. Furthermore, it is evidenced by Fig. 3.17b that even at a low E_b/N_0 of 0 dB, the complexities of both soft-decision-aided MSDSD algorithms may also be reduced to their respective lower bounds, as I_A increases. Therefore, we may conclude that MSDSD based search conceived for coded DPSK terminates earlier, with when provided higher *a priori* information.

Fig. 3.17 demonstrates that the proposed MSDSD algorithm of Table 3.4 substantially reduces the complexity of the conventional MSDSD of Table 3.3. The CRRs defined by Eq. (2.109) achieved by our reduced complexity design are futher summarized in Fig. 3.18, where the complexity difference between the Approx-Log-MAP and Max-Log-MAP algorithms is also portrayed. It was discussed in Sec. 3.3.2 that all the SD's child nodes associated with the index $v = N_w$ which are also referred to as leaf nodes have to be taken into account by the Approx-Log-MAP Algorithm 3.2. As a result, Fig. 3.18 demonstrates that the Approx-Log-MAP algorithm exhibits a higher complexity than the Max-Log-MAP for the proposed MSDSD algorithm of Table 3.4, because the Max-Log-MAP algorithm is not required to visit all the leaf nodes, as exemplified by Figs. 3.14 and 3.15. Nonetheless, Fig. 3.18a shows that a significant complexity reduction of up to $CRR = 48.0\%$ is achieved by the Approx-Log-MAP algorithm aided MSDSD of Table 3.4, where the MSDSD window is increased up to $N_w = 6$ for coded DQPSK detection. Moreover, it may be seen in Fig. 3.18b that a substantial complexity reduction of up to $CRR = 52.2\%$ is achieved by the Approx-Log-MAP algorithm aided proposed MSDSD associated with $N_w = 4$, where the

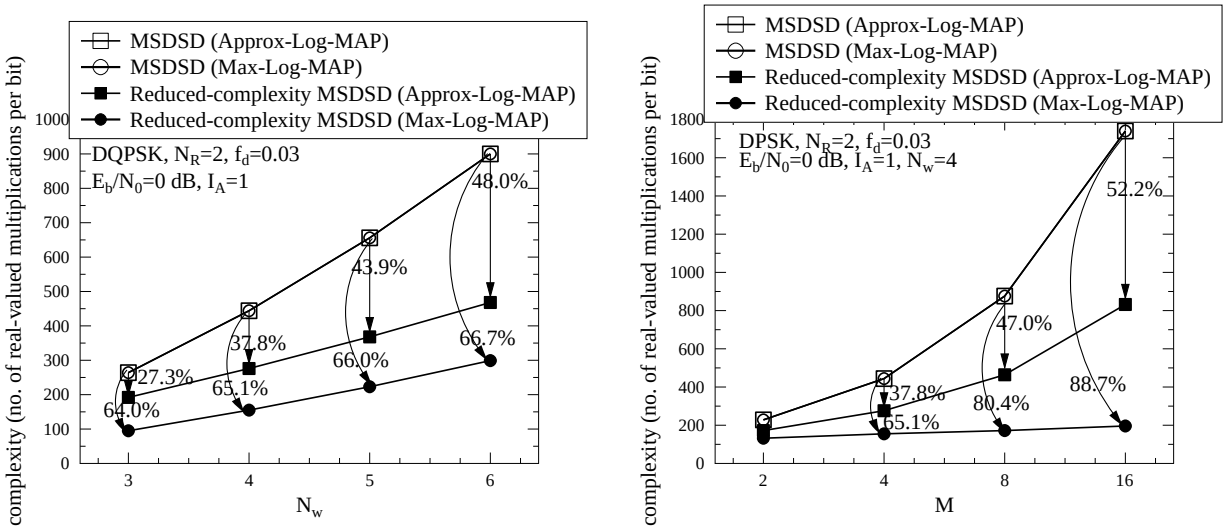

(a) $M = 4$, $N_w = \{3, 4, 5, 6\}$ (b) $M = \{2, 4, 8, 16\}$, $N_w = 4$

Figure 3.18: Complexity-Reduction Ratio (CRR) achieved by the reduced-complexity MSDSD algorithm of Table 3.4 compared to the conventional MSDSD algorithm of Table 3.3 recorded at $E_b/N_0 = 0$ dB and $I_A = 1$, where $N_R = 2$ RAs are employed, while the normalized Doppler frequency is given by $f_d = 0.03$.

number of modulation levels is increased to $M = 16$. Furthermore, Fig. 3.18 demonstrates that the proposed MSDSD of Table 3.4 achieves even more substantial CRRs when the Max-Log-MAP algorithm is invoked, where the complexity reductions are up to $CRR = 66.7\%$ and $CRR = 88.7\%$ for the two scenarios presented in Fig. 3.18a and Fig. 3.18b, respectively. We note that the complexity reductions achieved by the proposed soft-decision-aided MSDSD are especially substantial, when the MSDSD is iteratively invoked several times by the turbo detected systems, such as the TC coded scheme of Fig. 2.8 as well as the IRCC-URC coded scheme of Fig. 2.10.

In order to further investigate the performance of MSDSD, the EXIT charts of coded DPSK employing both the Approx-Log-MAP aided and the Max-Log-MAP algorithms assisted MSDSD are portrayed in Fig. 3.19. It can be seen in Fig. 3.19a that the performance of MSDSD aided DQPSK improves, as N_w increases. Moreover, Fig. 3.19a shows that the EXIT curves of CDD aided DQPSK are horizontal, because Gray labelling does not impose any bit-dependency during the QPSK bit-to-symbol mapping. However, the MSDSD observes multiple independently faded symbols and as a result, the attainable iteration gain is improved as N_w increases, as evidenced by Fig. 3.19a. Fig. 3.19b further demonstrates that the performance of MSDSD decays, as the number of modulation levels M increases, but a higher iteration gain is obtained by employing a higher M. Furthermore, as the iteration gain improves with N_w and M, the performance advantage of the Approx-Log-MAP Algorithm 3.2 compared to the Max-Log-MAP algorithm becomes more obvious, as seen in Fig. 3.19. It is further demonstrated by Fig. 3.20 that the LLR accuracy of Max-Log-MAP suffers from an obvious deviation from the LLR definition of Eq. (2.27) for both the cases of MSDSD aided DQPSK and D16PSK associated with $N_w = 4$. We note that when

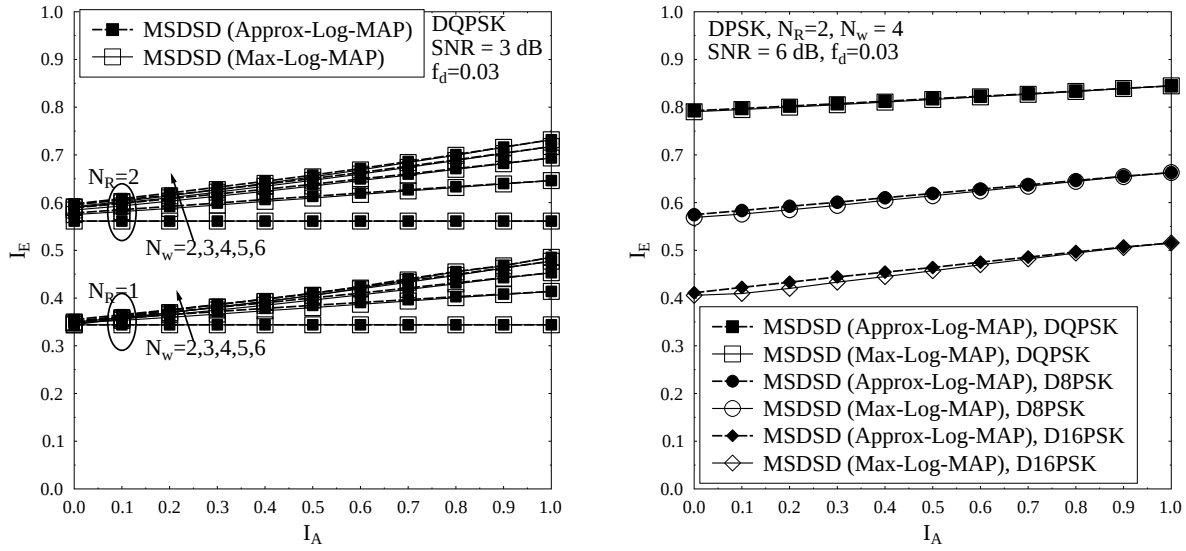

(a) $M = 4$,$N_w = \{2, 3, 4, 5, 6\}$ (b) $M = \{4, 8, 16\}$,$N_w = 4$

Figure 3.19: EXIT charts of coded DPSK employing Approx-Log-MAP aided and Max-Log-MAP aided MSDSD, where the reduced-complexity MSDSD algorithm of Table 3.4 is invoked.

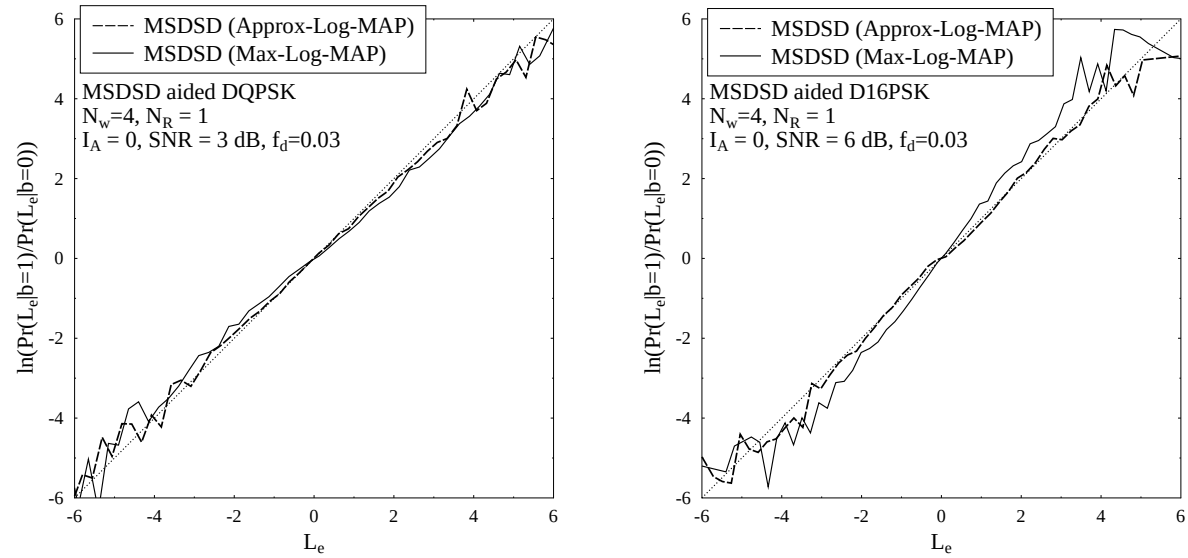

(a) DQPSK (b) D16PSK

Figure 3.20: LLR accuracy test for coded DQPSK and D16PSK employing both Approx-Log-MAP aided and Max-Log-MAP aided MSDSD, where the reduced-complexity MSDSD algorithm of Table 3.4 is invoked.

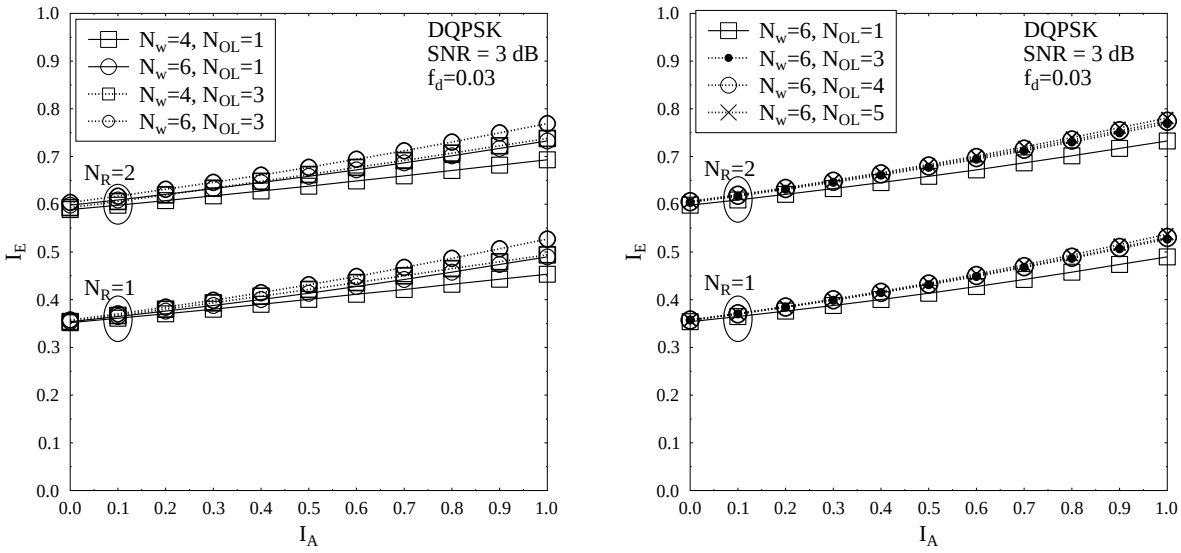

(a) $N_w = \{4, 6\}$, $N_{OL} = \{1, 3\}$

(b) $N_w = 6$, $N_{OL} = \{1, 3, 4, 5\}$

Figure 3.21: EXIT charts of coded DQPSK using Approx-Log-MAP aided DQPSK, where the number of overlapped observations between consecutive MSDSD windows N_{OL} is varied.

there is a beneficial iteration gain, the Max-Log-MAP algorithm may impose an undesirable performance loss, because many valuable candidates are overlooked by the Max-Log-MAP algorithm as M and N_w increase. By contrast, Fig. 3.20 demonstrates that the proposed Approx-Log-MAP Algorithm 3.2 may successfully improve the MSDSD's extrinsic LLR accuracy.

Recall from Sec. 3.2.5 that the symbols located at the centre of the MSDSD window may be detected more reliably than the ones at the edges. Similarly, Fig. 3.21a demonstrates that subset-based MSDSD associated with $N_{OL} = 3$ improves the performance of soft-decision-aided MSDSD with the aid of overlapping three observations amongst the consecutive windows, where the pair of data symbols detected at the edge of MSDSD window may be dropped. Moreover, Fig. 3.21b shows that further increasing N_{OL} beyond three does not provide any further benefit.

The BER performance of TC coded as well as IRCC-URC coded DPSK schemes employing MSDSD is portrayed in Fig. 3.22, while the corresponding Monte-Carlo simulation based staircase-shaped decoding trajectories are recorded in the EXIT charts of Fig. 3.23. For TC coded DQPSK and TC coded D16PSK, it may be seen both in Fig. 3.22a and Fig. 3.22b that MSDSD associated with $N_w = 4$ substantially improves the performance of MSDSD associated with $N_w = 2$, which is the case of CDD, and the subset-MSDSD previously discussed in Sec. 3.2.5 provides a further performance improvement. Furthermore, IRCC-URC coded DQPSK and D16PSK schemes employing subset-MSDSD achieve a near-capacity performance in Fig. 3.22a and Fig. 3.22b, respectively. Fig. 3.23 also evidences that the Approx-Log-MAP aided MSDSD Algorithm 3.2 generally outperform its Max-Log-MAP based counterpart. This performance advantage of the Approx-

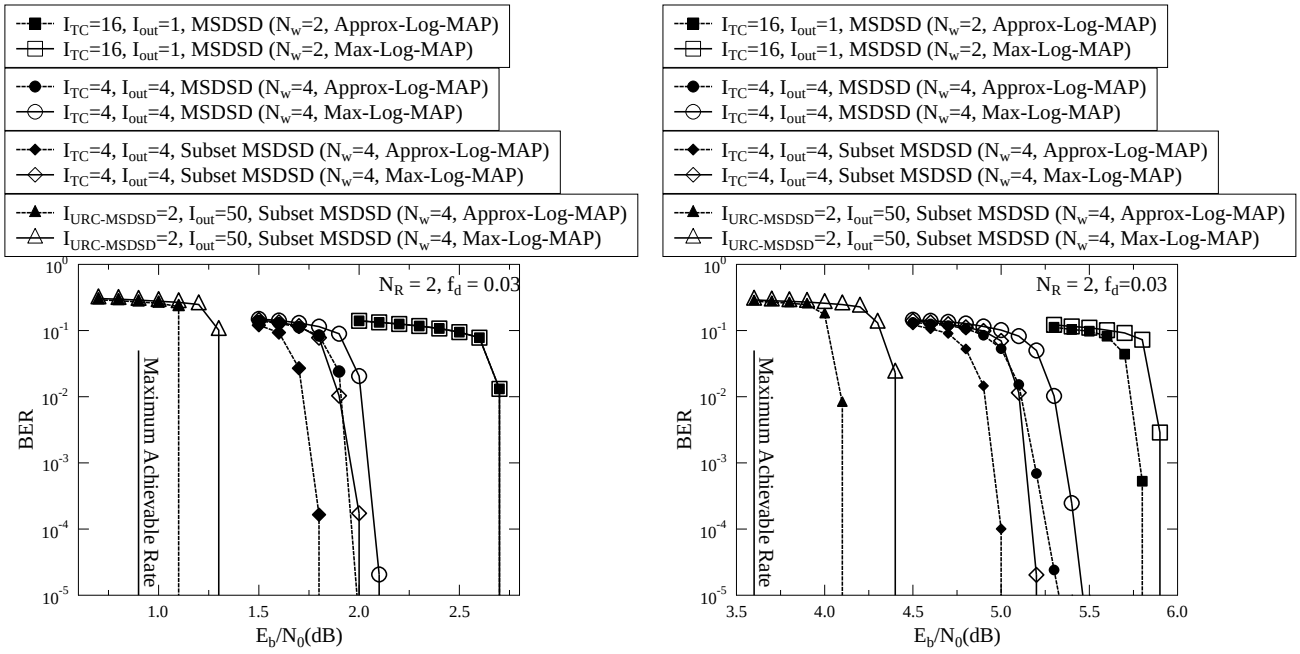

(a) DQPSK (b) D16PSK

Figure 3.22: BER performance of TC/IRCC-URC coded DPSK employing MSDSD, where the reduced-complexity MSDSD algorithm of Table 3.4 is invoked, while we have $N_R = 2$ and $f_d = 0.03$.

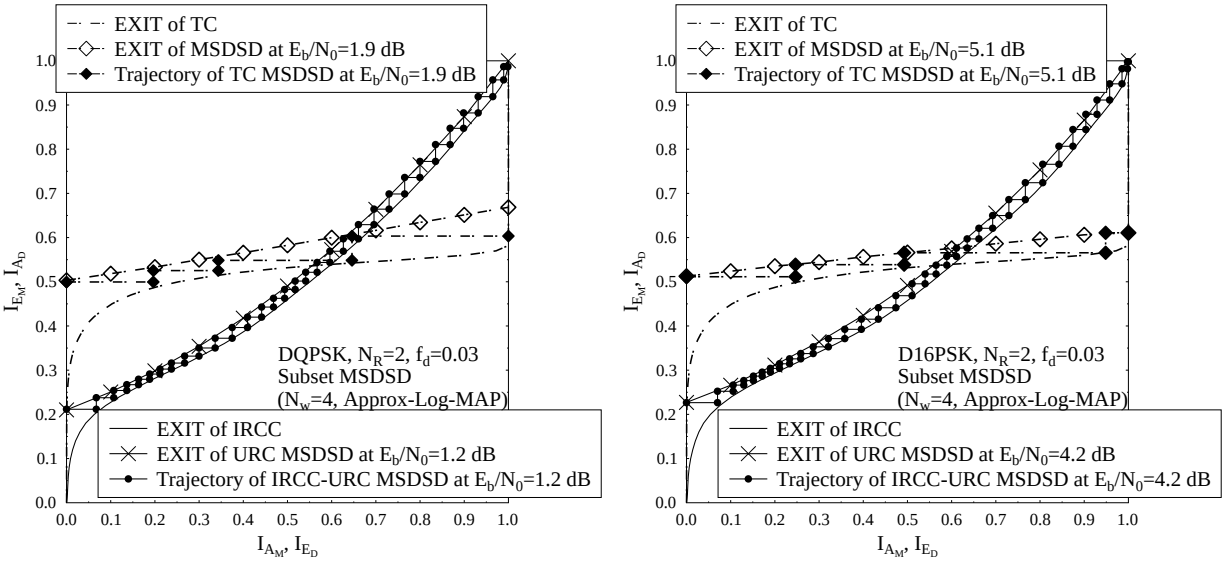

(a) DQPSK (b) D16PSK

Figure 3.23: EXIT charts and decoding trajectories of TC/IRCC-URC coded DPSK employing subset MSDSD associated with $N_w = 4$, where where the reduced-complexity MSDSD algorithm of Table 3.4 is invoked, while we have $N_R = 2$ and $f_d = 0.03$.

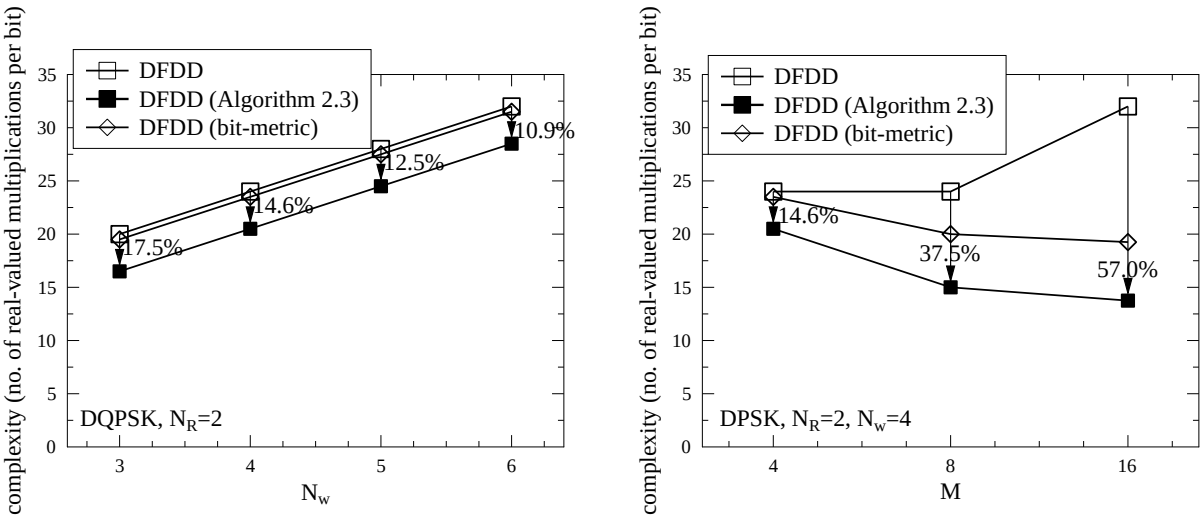

(a) $M = 4$, $N_w = \{3, 4, 5, 6\}$ (b) $M = \{4, 8, 16\}$, $N_w = 4$

Figure 3.24: Complexity comparison between symbol-metric based DFDD using Eq. (3.82), bit-metric based DFDD of Eq. (3.84) as well as the reduced-complexity symbol-metric based DFDD, where Algorithm 2.3 is applied.

Log-MAP algorithm is especially significant for the case of MSDSD ($N_w = 4$) aided D16PSK, as seen in Fig. 3.23b, because among a total number of $M^{N_w-1} = 4096$ MSDD candidates, only two maximum probability metrics associated with bit 1 and bit 0 are taken into account by the Max-Log-MAP, which results in an inevitable performance erosion.

The detection complexity of Max-Log-MAP aided DFDD using Eq. (3.82) and that of this symbol-metric based DFDD using Algorithm 2.3 are compared in Fig. 3.25 in terms of the total number of real-valued multiplications *per soft-bit output*, where the complexity of the bit-metric based DFDD of Eq. (3.84) is also portrayed as benchmark. As mentioned before, the application of Algorithm 2.3 may substantially reduce the symbol-metric based DFDD's complexity, namely from $O(M)$ to $O(M/4)$. This is achieved without any performance loss, while the bit metric based DFDD's complexity order is given by $O(\text{BPS})$, where we have $M/4 \leq \text{BPS}$ for low-order modulation schemes associated with $M \leq 16$. As a result, Fig. 3.25 demonstrates that the symbol-metric based DFDD using Algorithm 2.3 exhibits an even lower complexity than the bit-metric based DFDD of Eq. (3.84), provided that we have $M \leq 16$. Furthermore, it is demonstrated by Fig. 3.24b that a substantial complexity reduction of up to $CRR = 57.0\%$ may be achieved by applying Algorithm 2.3 to DFDD ($N_w = 4$), as the modulation order increases to $M = 16$.

Fig. 3.25a portrays a performance comparison amongst the CDD, DFDD and MSDSD with the aid of EXIT charts. It may be seen in Fig. 3.25a that as expected, the symbol-metric based DFDD improves the CDD's performance, but the DFDD's performance remains inferior to that of MSDSD. Moreover, it is also demonstrated by Fig. 3.25a that the bit-metric based DFDD performs poorly at low I_A values, yet it has the highest extrinsic information I_E when provided with the perfect *a priori* information of $I_A = 1$. Based on this feature, it was proposed in [122] that the

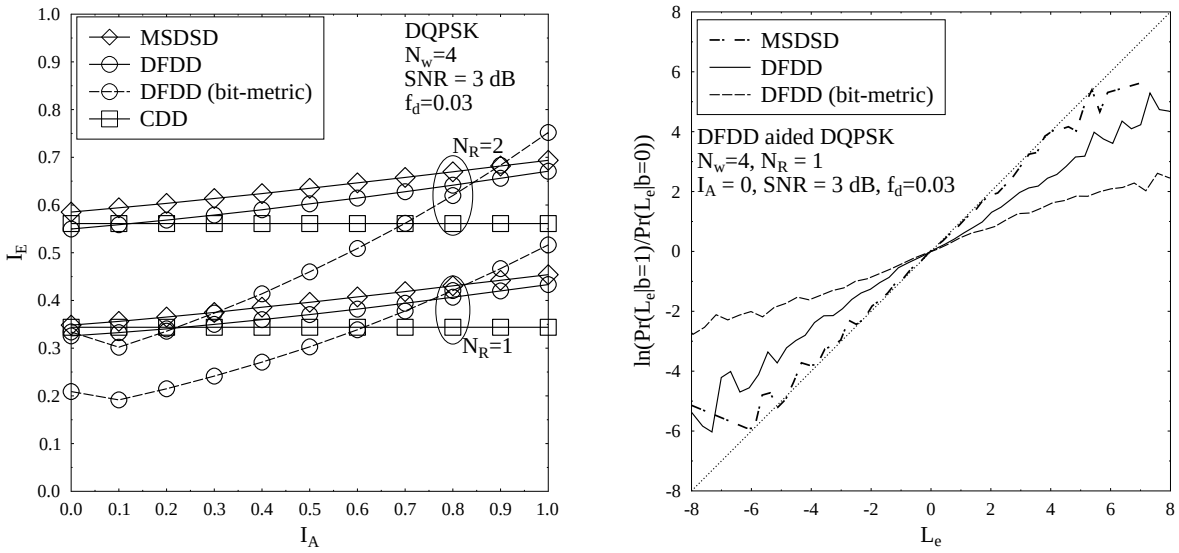

(a) EXIT charts

(b) LLR validity test

Figure 3.25: EXIT charts and LLR validity test of symbol-metric based DFDD using Eq. (3.82) and bit-metric based DFDD of Eq. (3.84) in comparison to MSDSD, where the Approx-Log-MAP algorithm is applied.

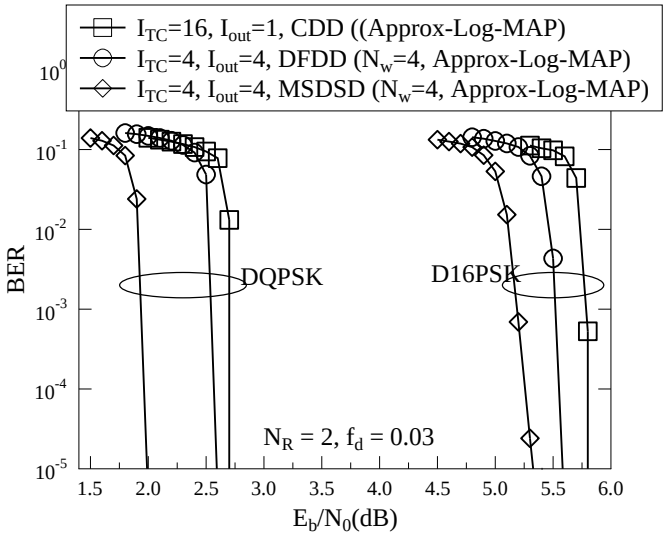

Figure 3.26: BER performance of TC coded DPSK employing the Approx-Log-MAP algorithm aided CDD, DFDD and MSDSD, where we have $N_R = 2$ and $f_d = 0.03$. The CDD refers to the Approx-Log-MAP of Eq. (3.54) using Eq. (3.58). The MSDSD using the Approx-Log-MAP of Algorithm 3.2 invokes the Schnorr-Euchner search strategy subfunctions of Tables 3.5-3.7. The DFDD is given by the Approx-Log-MAP using Eq. (3.82).

CDD may be invoked when there is little or no *a priori* information. However, as demonstrated by Fig. 3.25b, the bit-metric based DFDD's output LLRs accuracy exhibits a severe deviation from the LLR definition of Eq. (2.27). As a result, it is difficult to predict, when the noncoherent receiver should be switched from CDD to bit-metric based DFDD. In summary, since the symbol-metric based DFDD using Algorithm 2.3 exhibits a lower detection complexity without imposing any performance loss on the DFDD, the employment of bit-metric based DFDD may be avoided for low-order DPSK schemes associated with $M \leq 16$.

The BER performance of the CDD, DFDD and MSDSD aided TC coded DPSK schemes is portrayed in Fig. 3.26. As the EXIT charts correctly predicted in Fig. 3.25a, the DFDD performs better than CDD, but MSDSD achieves a more substantial performance improvement compared to both CDD and DFDD, as evidenced by Fig. 3.26.

3.4 Coherent Versus Noncoherent Performance Comparison

Reliable transmission over rapidly fluctuating fading channels is a challenging task. On one hand, for a coherent scheme, the pilot-spacing has to be reduced in order to sample the fading channels, which implies that more transmission power has to be assigned to the pilot symbols, and the coherent receiver's performance may degrade as a result of imperfect CSI knowledge. On the other hand, although a differential detection scheme may eliminate the need for CSI knowledge at the noncoherent receiver, a high-complexity detector such as MSDSD may have to be employed in order to attain an adequate performance. In order to elaborate on this important issue, we firstly introduce the concept of channel estimation conceived for continuous fading, and then discuss the pros and cons of coherent versus noncoherent schemes. Our aim is to identify the most appropriate scenarios for employing coherent and noncoherent schemes, respectively.

3.4.1 Preliminaries of Pilot Symbol Assisted Modulation [1]

Let us briefly focus our attention on the classic Pilot Symbol Assisted Modulation (PSAM) scheme proposed by Cavers in [1]. The schematic of PSAM is portrayed in Fig. 3.27. In more detail, pilot symbols are inserted into the transmitted symbols stream, where the pilot spacing is specified by N_{PS}. If we define a PSAM frame as N_{PS} transmitted symbols commencing with a pilot, a transmitted symbol s_n may be represented by $s_{v,t}$, where we have the PSAM frame index of $v \geq 1$ and symbol index of $1 \leq t \leq N_{PS}$, while the transmission frame index is given by $n = (v-1)N_{PS} + t$. The pilot symbols $\{s_{v,1}\}_{\forall v}$ are known by the receiver, and the data symbols $\{\{s_{v,t}\}_{t=2}^{N_{PS}}\}_{\forall v}$ are modulated MPSK/QAM signals. Therefore, the received signal model of Eq. (2.1) may be rewritten as:

$$\mathbf{Y}_{v,t} = s_{v,t}\mathbf{H}_{v,t} + \mathbf{V}_{v,t}. \tag{3.85}$$

In order to estimate the fading channel matrix $\{\mathbf{H}_{v,t}\}_{t=2}^{N_{PS}}$ for detecting $\{s_{v,t}\}_{t=2}^{N_{PS}}$, an observation window size of N_{OW} is established utilizing the nearby received pilot samples. In order to guarantee

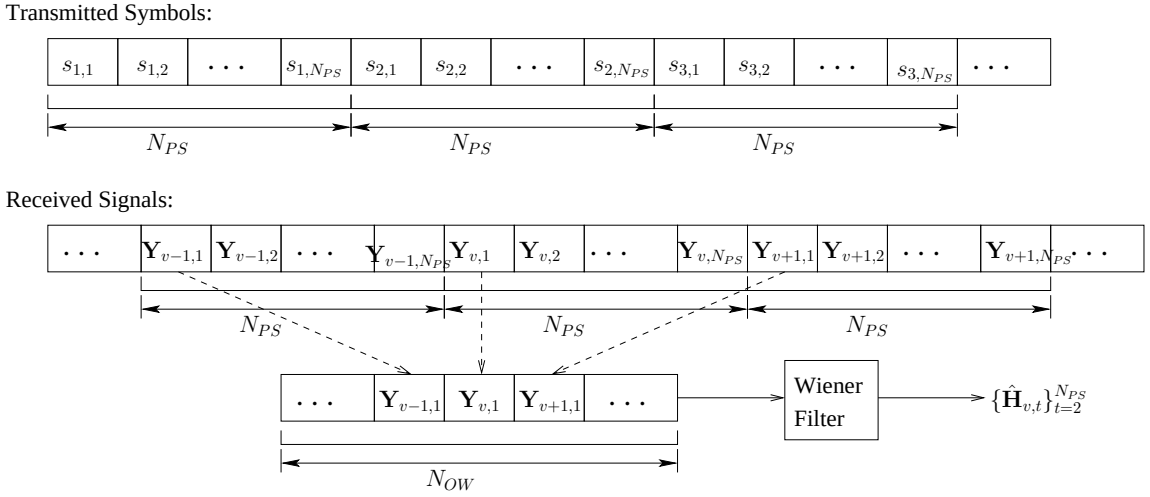

Figure 3.27: The schematic of Pilot Symbol Assisted Modulation (PSAM).

a multiplicative channel gain factor for each detected symbol interpolation may be invoked as:

$$\begin{aligned}\hat{\mathbf{H}}_{v,t} &= \sum_{\bar{v}=-N_{OW}^{a}}^{N_{OW}^{b}} w_{\bar{v},t}\mathbf{Y}_{v+\bar{v},1}/s_{v+\bar{v},1} \\ &= \sum_{\tilde{v}=1}^{N_{OW}} w_{\tilde{v},t}\mathbf{Y}_{v-N_{OW}^{a}-1+\tilde{v},1}/s_{v-N_{OW}^{a}-1+\tilde{v},1},\end{aligned} \tag{3.86}$$

where the observation window boundaries are given by $N_{OW}^{a} = \lfloor \frac{N_{OW}}{2} \rfloor - 1$ and $N_{OW}^{b} = \lfloor \frac{N_{OW}+1}{2} \rfloor$. Furthermore, Eq. (3.86) may be modelled in matrix form as:

$$\hat{\mathbf{H}}_{v,t} = \mathbf{w}_t^T (\mathbf{S}_v^{\text{PSAM}})^H \mathbf{Y}_v^{\text{PSAM}}, \tag{3.87}$$

where the filter taps are given by $\mathbf{w}_t = [w_{1,t}, w_{2,t}, \cdots, w_{N_{OW},t}]^T$, while the transmitted pilot symbols and received pilot samples are given by $\mathbf{S}_v^{\text{PSAM}} = \text{diag}\left\{[s_{v-N_{OW}^{a},1}, \cdots, s_{v,1}, \cdots, s_{v+N_{OW}^{b},1}]\right\}$ and $\mathbf{Y}_v^{\text{PSAM}} = [\mathbf{Y}_{v-N_{OW}^{a},1}^T, \cdots, \mathbf{Y}_{v,1}^T, \cdots, \mathbf{Y}_{v+N_{OW}^{b},1}^T]^T$, respectively.

The filter taps $\mathbf{w}_t$ seen in Eq. (3.87) may be optimized for minimizing the MSE between the filter output $\hat{\mathbf{H}}_{v,t}$ and $\mathbf{H}_{v,t}$. The corresponding MSE cost function may be formulated as:

$$\begin{aligned}\sigma_{MSE}^2 &= E\left\{\|\mathbf{H}_{v,t} - \hat{\mathbf{H}}_{v,t}\|^2\right\} \\ &= E\left\{\left[\mathbf{H}_{v,t} - \mathbf{w}_t^T(\mathbf{S}_v^{\text{PSAM}})^H\mathbf{Y}_v^{\text{PSAM}}\right]\left[\mathbf{H}_{v,t} - \mathbf{w}_t^T(\mathbf{S}_v^{\text{PSAM}})^H\mathbf{Y}_v^{\text{PSAM}}\right]^H\right\} \\ &= 1 - 2\mathbf{R}_{HY}^{\text{PSAM}}\mathbf{w}_t + \mathbf{w}_t^T\mathbf{R}_{YY}^{\text{PSAM}}\mathbf{w}_t.\end{aligned} \tag{3.88}$$

The auto-correlation matrix seen in Eq. (3.88) is given by:

$$\begin{aligned}\mathbf{R}_{YY}^{\text{PSAM}} &= E\{(\mathbf{S}_v^{\text{PSAM}})^H\mathbf{Y}_v^{\text{PSAM}}(\mathbf{Y}_v^{\text{PSAM}})^H\mathbf{S}_v^{\text{PSAM}}\} \\ &= \text{Toeplitz}([\rho_0, \rho_{N_{PS}}, \cdots, \rho_{(N_{OW}-1)N_{PS}}]) + N_0\mathbf{I}_{\mathbf{N_{OW}}}.\end{aligned} \tag{3.89}$$

Moreover, the cross-correlation matrix seen in Eq. (3.88) is given by:

$$\begin{aligned}\mathbf{R}_{HY}^{\text{PSAM}} &= E\{\mathbf{H}_{v,t}(\mathbf{Y}_v^{\text{PSAM}})^H\mathbf{S}_v^{\text{PSAM}}\} \\ &= [\rho_{N_{OW}^{a}N_{PS}+t-1}, \rho_{(N_{OW}^{a}-1)N_{PS}+t-1}, \cdots, \rho_{t-1}, \rho_{N_{PS}+1-t}, \cdots, \rho_{N_{OW}^{b}N_{PS}+1-t}].\end{aligned} \tag{3.90}$$

The MMSE solution based on Eq. (3.88) is given by $\frac{\partial \sigma_{MSE}^2}{\partial \mathbf{w}_t} = 0$, which leads to the classic Wiener-Hopf equation formulated as [1]:

$$\mathbf{w}_t = (\mathbf{R}_{YY}^{\text{PSAM}})^{-1}(\mathbf{R}_{HY}^{\text{PSAM}})^T. \tag{3.91}$$

As a result, the minimized MSE of Eq. (3.88) becomes a constant given by:

$$\sigma_{MSE}^2 = 1 - \mathbf{R}_{HY}^{\text{PSAM}}(\mathbf{R}_{YY}^{\text{PSAM}})^{-1}(\mathbf{R}_{HY}^{\text{PSAM}})^T. \tag{3.92}$$

It was demonstrated in [98, 99] that the MSE lower bound of pilot-training aided sequence-based channel estimation is given by the Cramer-Rao Bound (CRB). More explicitly, the pilot-training aided sequence-based channel estimator utilizes N_{OW} pilot samples at the beginning of each frame, and the fading channel is assumed to be Quasi-Static. The MSE of this estimation problem is lower-bounded by $E\{\|\mathbf{H} - \hat{\mathbf{H}}\|^2\} = 1/F(\mathbf{H})$, where $\mathbf{H}$ models the fading channel matrix that remains the same within the estimation frame, while the Fisher information function defined in [98,99] is given by $F(\mathbf{H}) = -E\left\{\frac{\partial^2 p(\mathbf{Y}|\mathbf{H})}{\partial \mathbf{H}^2}\right\}$. The PDF $p(\mathbf{Y}|\mathbf{H})$ is the same as $p(\mathbf{Y}_n|s^m)$ of Eq. (2.3), except that the pilot symbol s^m is known at the receiver, but the fading channel matrix $\mathbf{H}$ becomes unknown. Therefore, the CRB of the pilot-training sequence-based channel estimation is given by $CRB = N_0/N_{OW}$, which may decrease as the SNR and/or the pilot sequence length increased.

However, the PDF of Eq. (2.3) cannot be used for representing PSAM estimation, because the estimated fading channel matrix and the pilot samples are not located at the same position. Nonetheless, the lower bound of Eq. (3.92) may still be valid for the case of Quasi-Static fading, in which case the cross-correlation $\mathbf{R}_{HY}^{\text{PSAM}}$ becomes a vector of ones, and the eigenvalues of the auto-correlation matrix $\mathbf{R}_{YY}^{\text{PSAM}}$ are given by $(N_{OW} + N_0)$ once and N_0 for the remaining $(N_{OW} - 1)$ values. Therefore, as a result of eigendecomposition, the PSAM's MSE lower bound is given by [1]:

$$\sigma_{MSE-LB}^2 = 1 - \frac{N_{OW}}{N_0 + N_{OW}} = \frac{N_0}{N_0 + N_{OW}}. \tag{3.93}$$

The MSE lower bound of Eq. (3.93) is proportional to N_0 and $\frac{1}{N_{OW}}$, which implies that as either the SNR or N_{OW} increases, the channel estimation may become more accurate. Furthermore, we note that the throughput of a PSAM aided coherent detection aided scheme is given by:

$$R = \frac{\text{BPS}(N_{PS} - 1)}{N_{PS}}. \tag{3.94}$$

Therefore, according to the relationship $SNR\,(\text{dB}) = E_b/N_0 + \log_{10} R\,(\text{dB})$ specified in Eq. (2.51), the PSAM aided coherent scheme has to have a higher E_b/N_0 in order to maintain the same SNR level as a scheme assigning no power to the pilots. This verifies the fact that a fraction of $1/N_{PS}$ in transmitted symbol power is assigned to the pilots instead of data-carrying symbols.

3.4.2 Uncoded Coherent and Noncoherent Schemes

Let us now investigate the performance of an uncoded PSAM aided coherent receiver in comparison to uncoded noncoherent receivers. For the sake of simplicity, all the pilot symbols are configured to be $\{s_{v,1} = 1\}_{\forall v}$.

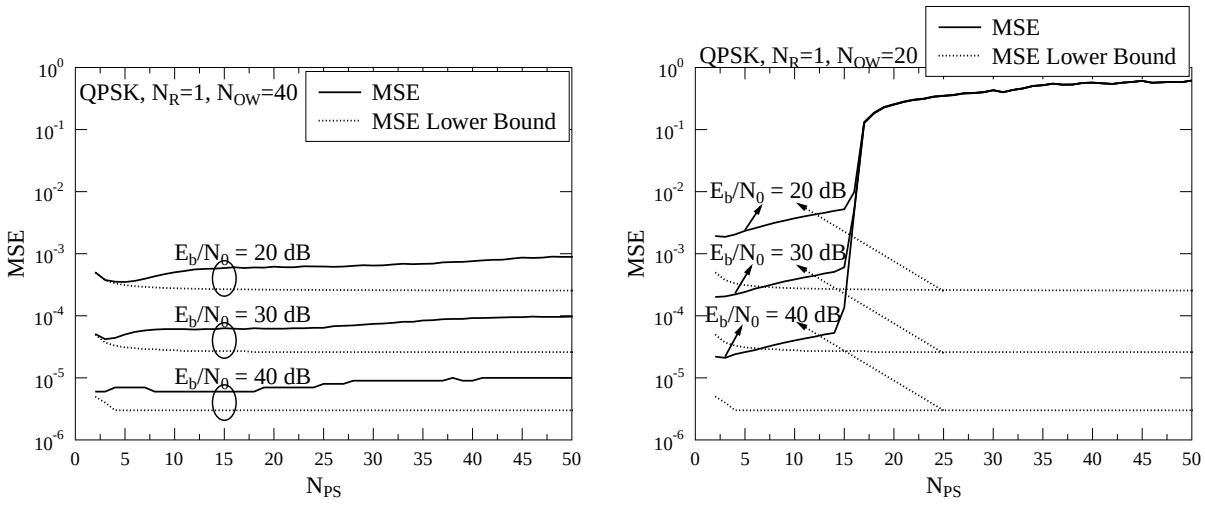

(a) $f_d = 0.001$ (b) $f_d = 0.03$

Figure 3.28: Effect of pilot spacing N_{PS} on PSAM aided QPSK associated with $N_R = 1$, where the observation window size N_{OW} is fixed. The MSE and the MSE lower bound are given by Eq. (3.92) and Eq. (3.93), respectively.

It is vitally important to choose the appropriate pilot spacing N_{PS} and observation window N_{OW} for PSAM at different normalized Doppler frequencies. Fig. 3.28 portrays the effect of N_{PS} on PSAM aided QPSK. It can be seen in Fig. 3.28 that the MSE grows with N_{PS}, as a result of sampling the fading channels less frequently. Furthermore, Fig. 3.28 shows that the MSE of Eq. (3.92) is closer to the lower bound of Eq. (3.93) at a low normalized Doppler frequency of $f_d = 0.001$, but it is hard for PSAM to approach the MSE lower bound, when the fading channel fluctuates more rapidly, as observed for the case of $f_d = 0.03$. Naturally, PSAM has to sample the fading channels above the Nyqust rate, which implies that $N_{PS} \leq \frac{1}{2f_d}$ is required. In reality, a substantially higher sampling rate is required, because the signal is faded and contaminated by noise. As a result, it can be seen in Fig. 3.28 that a lower N_{PS} is needed for a higher f_d. In the rest of this chapter, we choose $N_{PS} = 22$ and $N_{PS} = 12$ for the cases of $f_d = 0.001$ and $f_d = 0.03$, respectively.

Fig. 3.29 demonstrates the effect of observation window size N_{OW} on PSAM aided QPSK. As N_{OW} increases, more pilot samples are observed by the PSAM filter of Eq. (3.91), and hence a better estimation precision is recorded in Fig. 3.29. However, Fig. 3.29 shows that for the case of $f_d = 0.03$, increasing N_{OW} beyond 12 does not provide a further MSE improvement. This is because the correlation between the pilot sample and estimated sample is low, when their time indices are far apart at a high Doppler frequency. In the rest of this chapter, we opt for choosing $N_{OW} = 30$ and $N_{OW} = 12$ for the cases of $f_d = 0.001$ and $f_d = 0.03$, respectively.

The BER performance comparison between PSAM aided uncoded QPSK and a range of non-coherent detectors including CDD, MSDSD and DFDD aided uncoded DQPSK is portrayed in Fig. 3.30. It can be seen in Fig. 3.30a that MSDSD/DFDD does not provide any significant per-

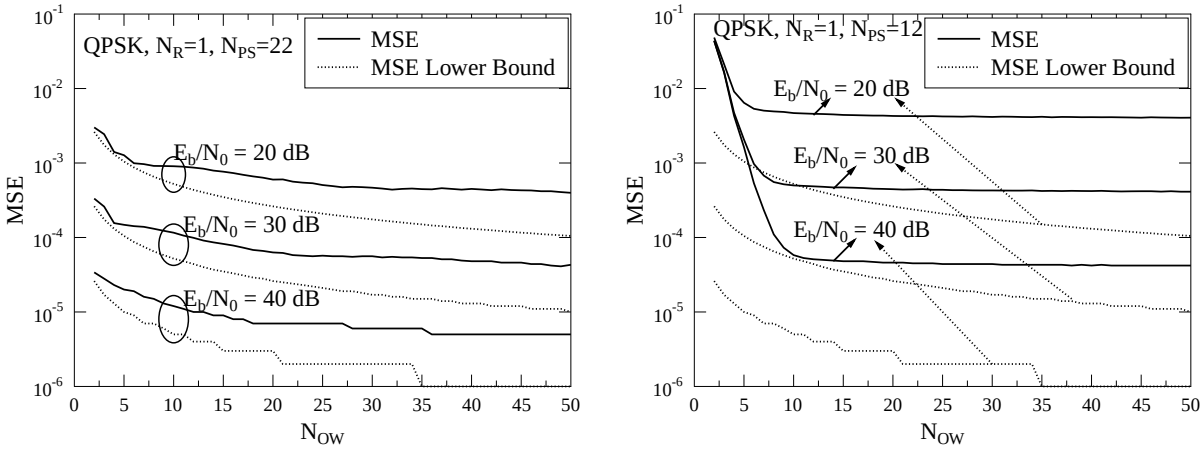

(a) $f_d = 0.001$ (b) $f_d = 0.03$

Figure 3.29: Effect of observation window size N_{OW} on PSAM aided QPSK associated with $N_R = 1$, where the pilot spacing N_{PS} is fixed. The MSE and the MSE lower bound are given by Eq. (3.92) and Eq. (3.93), respectively.

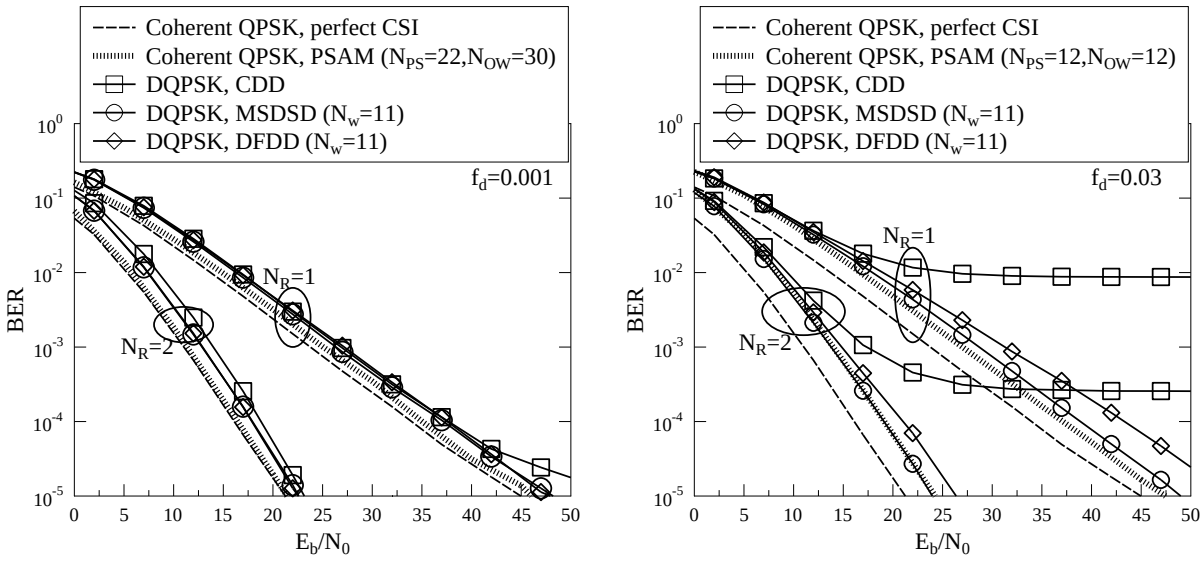

(a) $f_d = 0.001$ (b) $f_d = 0.03$

Figure 3.30: BER performance comparison between PSAM of Sec. 3.4.1 aided uncoded QPSK and noncoherent detectors including CDD, MSDSD and DFDD of Sec. 3.2 aided uncoded DQPSK.

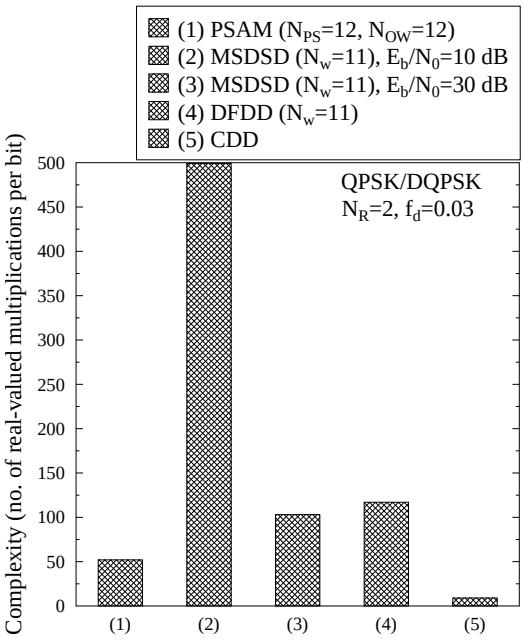

Figure 3.31: Complexity comparison between PSAM of Sec. 3.4.1 aided uncoded QPSK and noncoherent detectors including CDD, MSDSD and DFDD of Sec. 3.2 aided uncoded DQPSK, where we have $N_R = 2$ and $f_d = 0.03$.

formance improvement, when the fading channel fluctuates slowly, while PSAM aided QPSK performs close to the perfect CSI aided QPSK. However, Fig. 3.30b shows that MSDSD and DFDD provide a substantial performance improvement over CDD at the normalized Doppler frequency of $f_d = 0.03$. Furthermore, the performance gap between PSAM aided QPSK and perfect CSI aided QPSK becomes larger at $f_d = 0.03$, in which case the MSDSD aided DQPSK achieves a comparable performance to the realistic PSAM aided QPSK, as evidenced by Fig. 3.30b. This verifies that the MSDSD aided noncoherent scheme may be deemed to be a potent alternative to the coherent scheme, when the Doppler frequency is increased so that accurate CSI estimation becomes less feasible at the receiver.

Fig. 3.31 further compares the complexity of the PSAM aided coherent receiver to that of a variety of noncoherent receivers. Assuming that the channel characteristics f_d and E_b/N_0 remain the same during signal detection, the Wiener-Hopf equation of Eq. (3.91) is only required to be evaluated once, hence this one-off complexity contribution may be ignored. The complexity of PSAM only has to take into account the evaluation complexity of obtaining the filter output in Eq. (3.87) as well as the coherent detection complexity, which is the same as those summarized in Chapter 2. As expected, the complexity of PSAM is higher than that of CDD, but it is lower than that of MSDSD and DFDD, as demonstrated by Fig. 3.31. It can also be seen in Fig. 3.31 that MSDSD exhibits an excessive complexity at a low $E_b/N_0 = 10$ dB, which is an obvious disadvantange of MSDSD. Although the MSDSD complexity becomes five times lower at $E_b/N_0 = 30$ dB than at $E_b/N_0 = 10$ dB, it is still twice that of the PSAM complexity, as evidenced by Fig. 3.31.

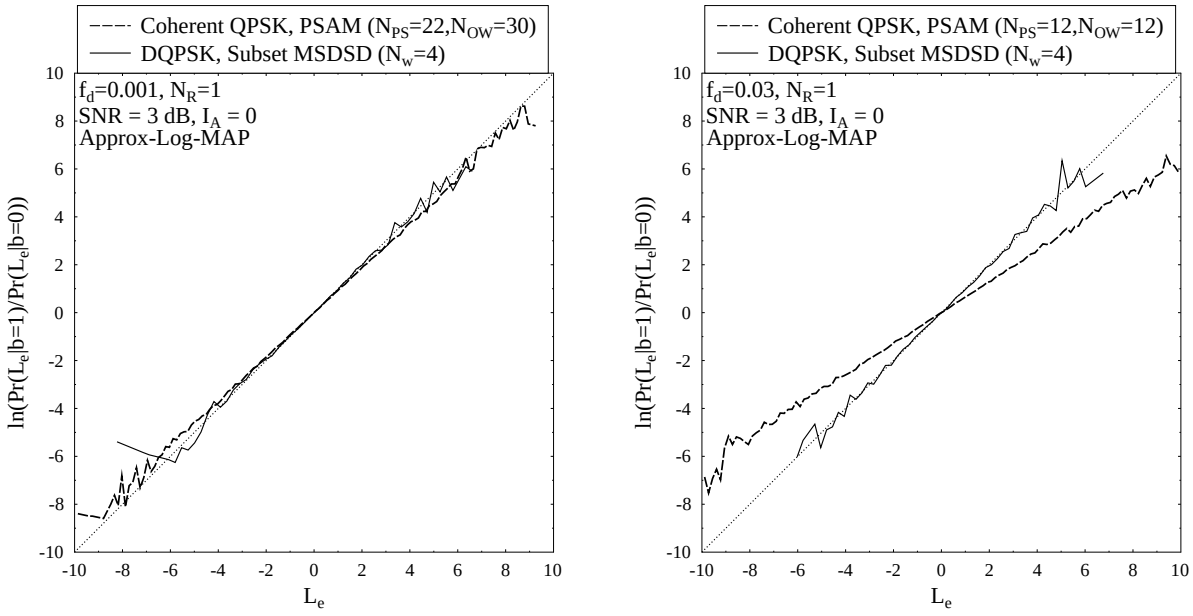

(a) $f_d = 0.001$ (b) $f_d = 0.03$

Figure 3.32: LLR accuracy test for PSAM of Sec. 3.4.1 aided coherent QPSK and for subset MSDSD of Sec. 3.3 aided DQPSK, where Approx-Log-MAP algorithm is invoked for both detectors, while $N_R = 1$ RA is equipped.

3.4.3 Coded Coherent and Noncoherent Schemes

It was demonstrated in the previous section that for uncoded systems, noncoherent detectors such as MSDSD impose a higher implementational complexity than coherent detectors, and yet they fail to provide a performance advantage when employing realistic channel estimation for the coherent detection. By contrast, in this section, we will demonstrate that MSDSD conceived for coded non-coherent schemes is capable of offering impressive performance benefits compared to its coherent counterpart relying on realistic imperfect CSI estimation in rapidly fluctuating fading channels.

First of all, let us compare the LLR accuracy test results for PSAM aided coherent QPSK and for the subset-MSDSD aided DQPSK in Fig. 3.32. As discussed in Sec. 2.3.2.4, the extrinsic LLRs produced by soft-decision-aided detector may be deemed to have adequate integrity only if they comply with the LLR definition of Eq. (2.66). It can be seen in Fig. 3.32a that both the PSAM aided coherent detector and the subset-MSDSD produce reliable extrinsic LLRs at a low normalized Doppler frequency of $f_d = 0.001$. However, Fig. 3.32b demonstrates that the soft-bits produced by the PSAM aided coherent detector deviates from the LLR definition, when the normalized Doppler frequency is increased to $f_d = 0.03$. This is because the coherent detectors introduced in Chapter 2 assumed perfect CSI knowledge at the receiver, which cannot be delivered by realistic channel estimation techniques, when the fading channel fluctuates rapidly unless joint iterative channel and data estimation is used and E_b/N_0 is sufficiently high. This problem will gravely affect the coherent scheme's performance in coded systems.

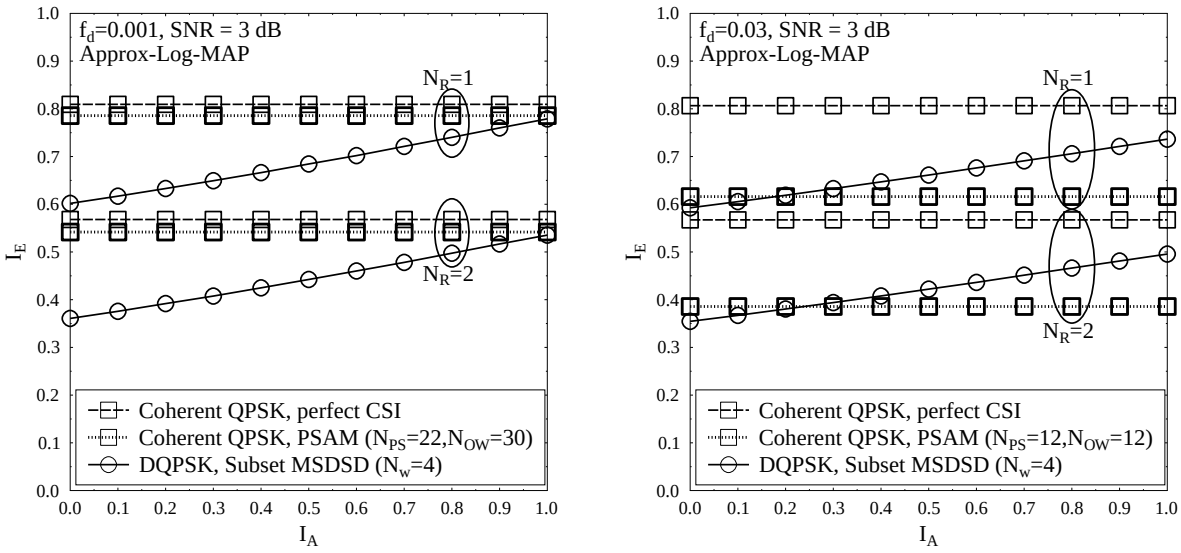

(a) $f_d = 0.001$ (b) $f_d = 0.03$

Figure 3.33: EXIT charts of coherent QPSK relying either on perfect CSI or on PSAM of Sec. 3.4.1 aided channel estimation and EXIT charts of subset-MSDSD ($N_w = 4$) of Sec. 3.3 aided DQPSK, where the Approx-Log-MAP algorithm is invoked for both the coherent QPSK detector and for the noncoherent subset-MSDSD.

Fig. 3.33 further examines the capability performance of coherent and noncoherent detectors using EXIT charts. As expected, Fig. 3.33 demonstrates that the imperfect channel estimation provided by realistic PSAM results in a performance loss for coherent receivers, which is quite substantial, when we have $f_d = 0.03$ in Fig. 3.33b. It may be further observed in Fig. 3.33b that PSAM aided coherent detectors produce higher extrinsic information I_E than the subset-MSDSD, when there is no *a priori* information, which verifies that PSAM aided coherent detection still has better performance for uncoded systems in this case. However, it can be seen in Fig. 3.33b that the area under the EXIT curve of the subset-MSDSD is considerably higher than that of the PSAM aided coherent detector, which implies that the subset-MSDSD may outperform the PSAM aided coherent scheme, when they rely on turbo detection at a high normalized Doppler frequency of $f_d = 0.03$.

For a low-complexity RSC coded system, Fig. 3.34 demonstrates that PSAM aided coherent PSK detectors outperform their subset-MSDSD aided DPSK counterparts, but the performance difference between the two schemes becomes smaller at $f_d = 0.03$. Recall from Fig. 3.33 that the PSAM aided coherent scheme exhibits horizontal EXIT curves. and for this reason the number of iterations between the RSC decoder and the detector is set to 1. As a result, in this RSC coded system design, the subset-MSDSD fail to achieve its full performance potential at $f_d = 0.03$, as predicted by the EXIT charts of Fig. 3.33b. More powerful channel coding is needed for MSDSD to demonstrate its advantage in rapidly fading channels.

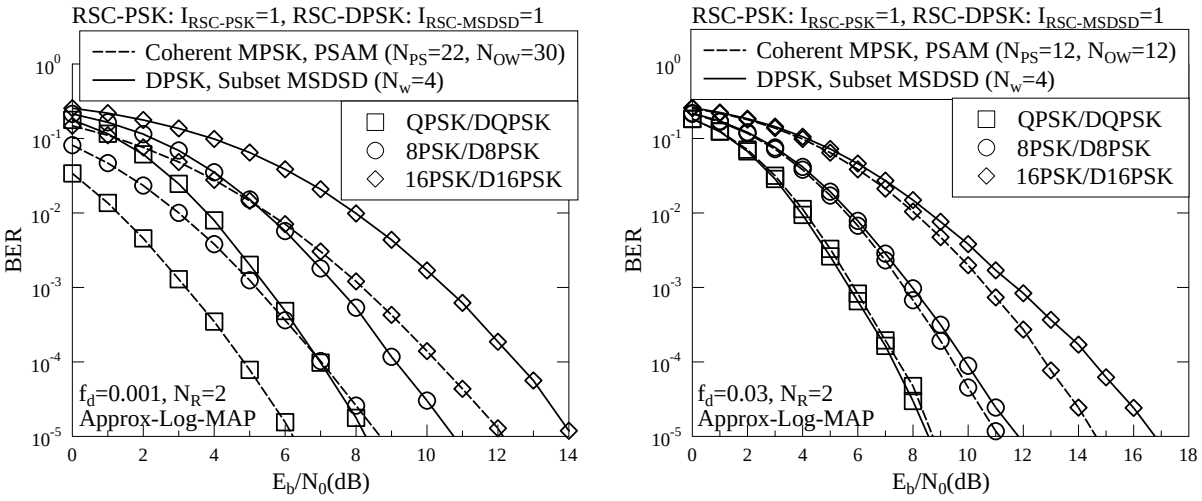

(a) $f_d = 0.001$ (b) $f_d = 0.03$

Figure 3.34: BER performance comparison between RSC coded PSAM of Sec. 3.4.1 aided coherent PSK and RSC coded subset-MSDSD of Sec. 3.3 aided DPSK, where the Approx-Log-MAP algorithm is invoked for both detectors, while $N_R = 2$ RAs are used. The number of iterations between the RSC decoder and the QPSK/DQPSK detector is set to $I_{RSC-QPSK} = I_{RSC-MSDSD} = 1$.

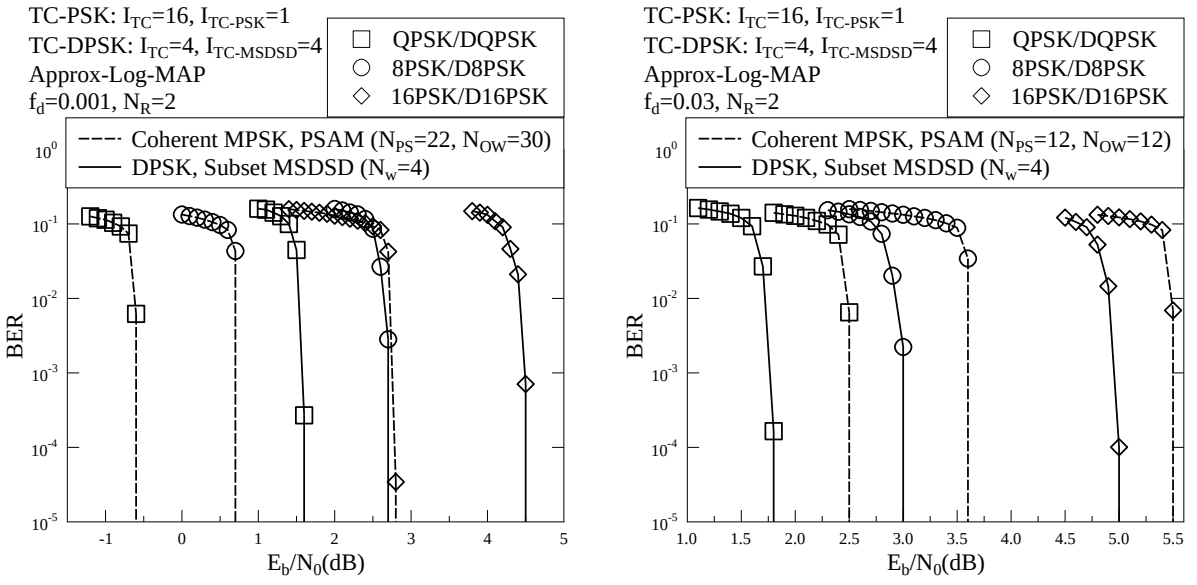

(a) $f_d = 0.001$ (b) $f_d = 0.03$

Figure 3.35: BER performance comparison between TC coded PSAM of Sec. 3.4.1 aided coherent PSK and TC coded subset-MSDSD of Sec. 3.3 aided DPSK, where the Approx-Log-MAP algorithm is invoked for both detectors, while $N_R = 2$ RAs are used. For TC coded PSK, the number of inner TC iterations and outer iterations are $I_{TC} = 16$ and $I_{TC-PSK} = 1$, respectively. For TC coded DPSK, we have $I_{TC} = 4$ and $I_{TC-MSDSD} = 4$.

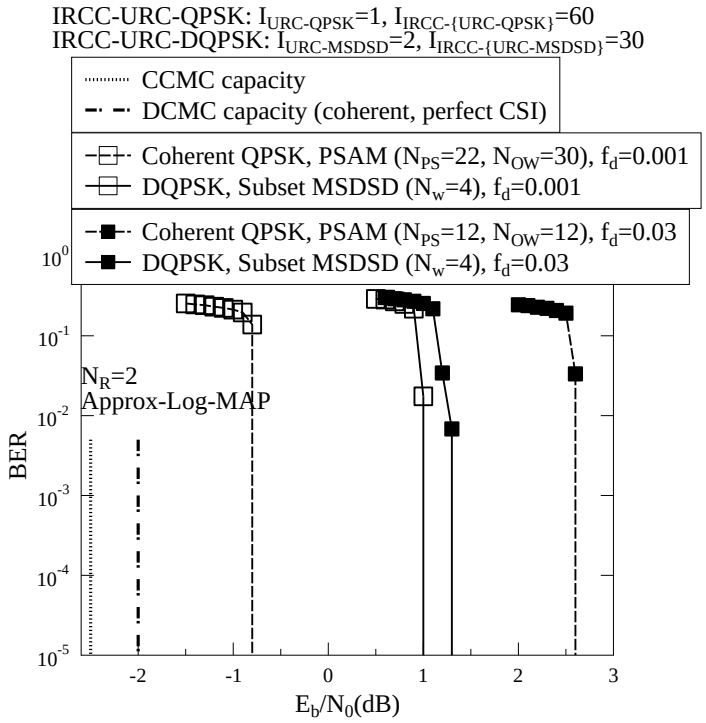

Figure 3.36: BER performance comparison between IRCC-URC coded PSAM of Sec. 3.4.1 aided coherent QPSK and IRCC-URC coded subset-MSDSD of Sec. 3.3 aided DQPSK, where the Approx-Log-MAP algorithm is invoked for both detectors, while $N_R = 2$ RAs are used. For IRCC-URC coded QPSK, we have $I_{URC-QPSK} = 1$ and $I_{IRCC-\{URC-QPSK\}} = 60$, while for IRCC-URC coded DQPSK, we have $I_{URC-MSDSD} = 2$ and $I_{IRCC-\{URC-MSDSD\}} = 30$.

Therefore, both the PSAM aided coherent receiver and the subset-MSDSD assisted noncoherent receiver are protected by TC coding, and their performance results are compared in Fig. 3.35. For TC coded PSK schemes, the number of inner TC iterations and outer iterations between the TC and the coherent detector are set to $I_{TC} = 16$ and $I_{TC-PSK} = 1$, respectively. For the TC coded DPSK scheme, the number of inner TC iterations and outer iterations between the TC and the subset-MSDSD are set to $I_{TC} = 4$ and $I_{TC-MSDSD} = 4$, respectively. According to this arrangement, both schemes may have exactly the same number of total turbo iterations. It can be seen in Fig. 3.35a that the PSAM aided coherent detector outperforms its subset-MSDSD counterpart, when we have $f_d = 0.001$. However, Fig. 3.35b demonstrates that the subset-MSDSD achieves a substantial performance advantage over the coherent detector using imperfect CSI in the context of the same TC coded system, when a rapidly fluctuating fading channel is specified by $f_d = 0.03$.

In order to further characterize the performance difference between the coherent and noncoherent receivers in near-capacity scenarios, Fig. 3.36 portrays the performance comparison between a PSAM aided coherent detector and the corresponding subset-MSDSD in the context of the IRCC-URC coded system of Fig. 2.10. The Monte-Carlo simulation based stair-case-shaped decoding trajectories for PSAM aided coherent receivers are recorded in the EXIT-chart of Fig. 3.37. First

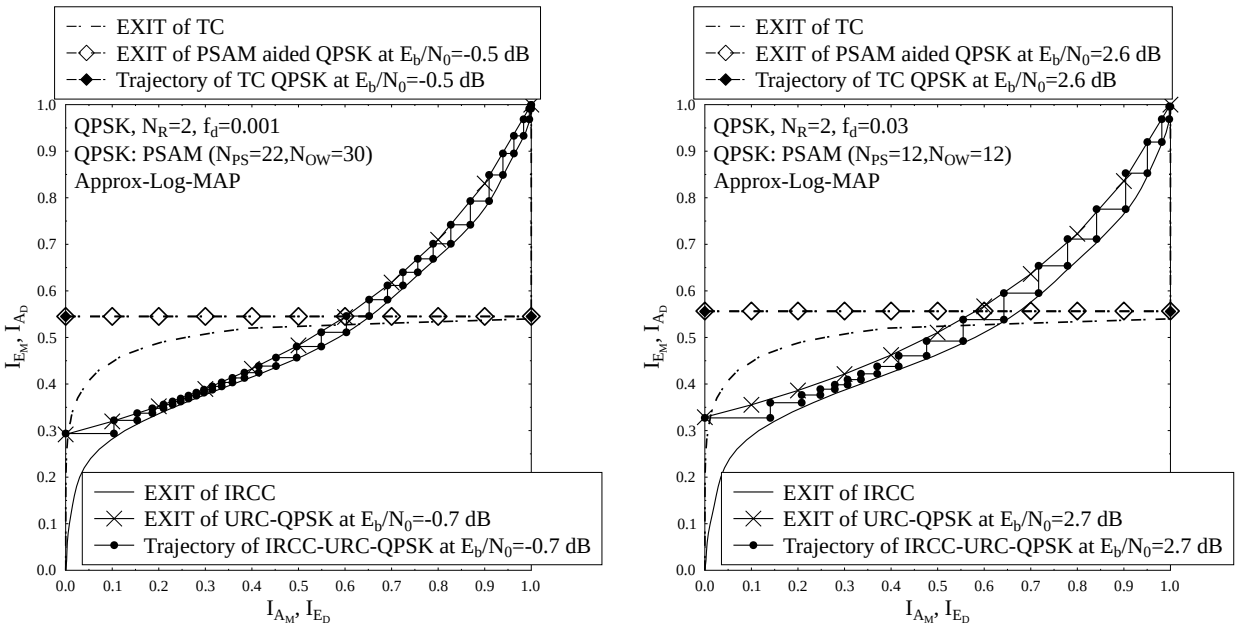

(a) $f_d = 0.001$ (b) $f_d = 0.03$

Figure 3.37: Decoding trajectories of TC coded and IRCC-URC coded PSAM of Sec. 3.4.1 aided coherent QPSK, where $N_R = 2$ RAs are employed.

of all, Fig. 3.36 shows that when the fading channel changes slowly as specified by $f_d = 0.001$, the IRCC-URC coded PSAM aided coherent QPSK scheme achieves a near-capacity performance, which is within 1.2 dB from the DCMC capacity. Hence it significantly outperforms its noncoherent counterpart. However, when the fading channel fluctuates more rapidly at $f_d = 0.03$, the coherent scheme's performance degrades substantially as a result of its less accurate CSI estimation, while the subset-MSDSD aided noncoherent scheme only suffers from a small deterioration in BER performance as f_d increases, which gives the noncoherent scheme a significant 1.4 dB performance advantage over its coherent counterpart at $f_d = 0.03$. Furthermore, the PSAM aided QPSK scheme requires a wider open EXIT tunnel for achieving decoding convergence to an infinitesimally low BER for the case of $f_d = 0.03$ in Fig. 3.37b compared to the case of $f_d = 0.001$ portrayed in Fig. 3.37a. This is because for the case of $f_d = 0.03$, the poor extrinsic LLR integrity of the PSAM aided coherent detector demonstrated in Fig. 3.32b deteriorates its performance. To elaborate a little further, it is very likely that soft-decision-aided detectors associated with a poor extrinsic LLR integrity may produce excessively large output LLR values. In this case, the more turbo iterations are invoked, the harder for the channel decoder to correct the corresponding errors. This is the reason why the TC coded PSAM aided QPSK scheme achieves decoding convergence to an infinitesimally low BER at a lower E_b/N_0 value than IRCC-URC coded scheme for the case of $f_d = 0.03$. Again, this is evidenced by Fig. 3.37b.

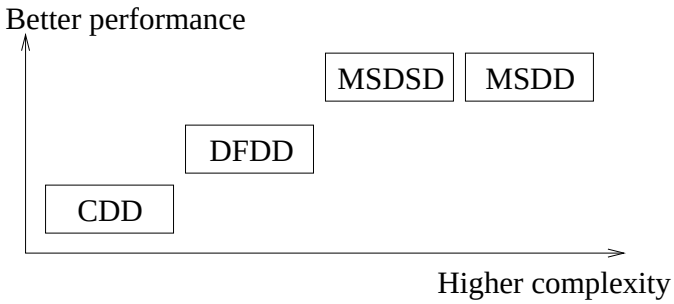

Figure 3.38: A summary on the family of noncoherent detectors in terms of performance and complexity.

3.5 Chapter Conclusions

In this chapter, we quantified the performance versus complexity trade-off of a variety of noncoherent receivers and the reduced-complexity design proposed for soft-decision-aided coherent detection in Chapter 2 was invoked for noncoherent detection in this chapter. For uncoded DPSK, we have demonstrated in Fig. 3.4 that the CDD of Sec. 3.2.1 exhibits a low detection complexity, but it was shown in Fig. 3.7 that the CDD also suffers from a severe performance penalty, especially in rapidly fluctuating fading channels. Observe in Fig. 3.7 that the MSDD aided uncoded DPSK of Sec. 3.2.2 eliminates the CDD's error floor encountered at a high Doppler frequency, and the MSDSD invokes SD in order to mitigate the excessive MSDD complexity. In Sec. 3.2.3 we proposed a novel decorrelating operation for hard-decision-aided MSDSD for ensuring that uncoded DPSK detection associated with $N_R > 1$ may still be carried out by the SD's Schnorr-Euchner search strategy without visiting all the M constellation points. Furthermore, the DFDD of Sec. 3.2.4 makes use of previous symbol decisions in order to reduce the complexity of evaluating and comparing the MSDD's decision metrics. We have demonstrated in Sec. 3.2.4 that this method is equivalent to blind channel estimation aided symbol detection. Although DFDD may also improve CDD's performance, we drewed in Fig. 3.9 that its detection capability is suboptimal compared to that of MSDD/MSDSD owing to the DFDD's error propagation problem. The family of noncoherent detectors characterized in terms of their performance versus complexity is summarized in Fig. 3.38.

The soft-decision-aided noncoherent detectors of Sec. 3.3 conceived for coded DPSK strike a similar tradeoff between their performance and complexity to that of the hard-decision-aided noncoherent detectors of Sec. 3.2. The soft-decision-aided MSDD attains the optimum performance for coded DPSK detection, but observe in Fig. 3.16 that its complexity is the highest. The CDD, which constitutes a special case of MSDD associated with $N_w = 2$ exhibits the lowest complexity for coded DPSK, but its performance is seen in Fig. 3.22 to be the poorest. The MSDSD using the Max-Log-MAP algorithm achieves exactly the same detection capability as the Max-Log-MAP aided MSDD as presented in Sec. 3.3.2, and the MSDD's complexity is significantly reduced by SD. In Sec. 3.3.2, we modified the output scenario of the soft-decision-aided SD, so that the near-optimum Approx-Log-MAP algorithm may be implemented with the aid of the MSDSD. Further-

Lower detection complexity:	PSAM		
Better performance in uncoded system:	$f_d = 0.001$	PSAM	
	$f_d = 0.03$	PSAM and MSDSD become comparable	
Better performance in coded system:	RSC-PSK/DPSK	$f_d = 0.001$	PSAM
		$f_d = 0.03$	PSAM
	TC-PSK/DPSK	$f_d = 0.001$	PSAM
		$f_d = 0.03$	MSDSD
	IRCC-URC-PSK/DPSK	$f_d = 0.001$	PSAM
		$f_d = 0.03$	MSDSD

Table 3.9: Summary of comparisons between PSAM aided coherent receiver and subset MSDSD aided noncoherent receiver based on the simulation results presented in Sec. 3.4.3.

more, in Sec. 3.3.3 a reduced-complexity design taylored for the Schnorr-Euchner search strategy of soft-decision-aided MSDSD conceived for coded DPSK was proposed. Explicitly, the detection candidate may be found by visiting a reduced-size subset of constellation points and then the rest of the constellation points may be visited in a zigzag fashion if needed. As a result, the MSDSD complexity is seen in Figs. 3.17 and 3.18 to be further reduced without any performance loss. Furthermore, in Sec. 3.3.4 soft-decision-aided DFDD is introduced as the decision-feedback aided version of MSDD/MSDSD. The DFDD's error propagation problem severely degrades its output extrinsic LLR's integrity as seem in Fig. 3.25b, hence its performance becomes sub-optimal compared to MSDD/MSDSD, as seen in Fig. 3.26.

Last, but not least, a discussion on coherent versus noncoherent detection was offered in Sec. 3.4. As representatives of the family of coherent and noncoherent detectors, the PSAM aided coherent receiver and the subset-MSDSD aided noncoherent receiver were compared in Table 3.9 based on our simulation results presented in Sec. 3.4. We have demonstrated that the MSDSD aided noncoherent receiver is more appropriate for coded system operating in the presence of rapidly fluctuating fading channels, especially when the number of iterations between the detector and the channel decoder is higher than one. The reason for this phenomenon is that it is particularly difficult for the channel estimation technique to acquire accurate CSI knowledge, when the Doppler frequency is high. As a result, the extrinsic LLRs produced by a coherent receiver relying on imperfect CSI may severely deviate from the valid LLR definition, and these high but inaccurate LLR values are hard to correct for the channel decoder. By contrast, MSDSD is capable of providing reliable extrinsic LLRs, even for high Doppler frequencies.

The classic noncoherent receivers studied in this chapter are all conceived for DPSK detection. In the next chapter, we will continue our discourse by solving a range of open problems in the field of noncoherent detection, when bandwidth efficient high-throughput schemes, such as Differential Amplitude Phase Shift Keying (DAPSK) are employed.

Chapter 4

Noncoherent Detection for Differential Non-Constant Modulus Modulation – Part I: Uncoded Systems

4.1 Introduction

Noncoherent detection of DPSK was introduced in Chapter 3, which is capable of mitigating the pilot overhead of coherent PSK detection for transmission over rapidly fluctuating fading channels. In order to improve the throughput of noncoherent DPSK systems, it is important to investigate the family of high-throughput differentially encoded non-constant modulus constellations as noncoherent QAM schemes. More explicitly, when bandwidth-efficient coherent QAM is employed, the Euclidean distances amongst the QAM constellation points is reduced, as the system throughput increases, which implies that any realistic channel estimation error degrades the performance of coherent QAM detection. For this reason, the noncoherent counterpart of differential non-constant modulus QAM schemes may be preferred, since no CSI knowledge is required at the noncoherent receivers. Similar to the performance results seen in Chapter 3, we will demonstrate in this chapter that differential non-constant modulus constellations may achieve comparable performance to their coherent QAM counterparts in uncoded systems, and we will further demonstrate in the next chapter that these noncoherent schemes may even outperform their coherent QAM counterparts in coded systems under specific conditions, despite their lower complexity.

Let us now focus our attention on the classic Star QAM constellation introduced in Chapter 2. As an installation of Star QAM, the popular Differential Amplitude Phase Shift Keying (DAPSK) [142, 149, 150, 154, 287] aim for guaranteeing that all transmitted symbols are drawn from the same Star QAM constellation. As a result, the changes between the ring amplitudes of the consecutive transmitted symbols are data-dependent. Considering the Star QAM constellation associated with $M_A = 2$ introduced in Sec. 2.2.2.2 as an example, the modulated data-dependent ring amplitudes

should either be drawn from the set of $\{1, \alpha\}$ or use the set of $\{1, \frac{1}{\alpha}\}$, when the previous transmitted symbol's ring amplitude is either $\frac{1}{\sqrt{\beta}}$ or $\frac{\alpha}{\sqrt{\beta}}$, respectively, so that the next transmitted symbol's ring amplitude is guaranteed to be drawn from the same Star QAM ring amplitudes set of $\{\frac{1}{\sqrt{\beta}}, \frac{\alpha}{\sqrt{\beta}}\}$.

However, it was argued in [136, 288] that the information carried by the DAPSK scheme's amplitude changes does not exhibit the best reliability, because the data-carrying magnitude such as $\frac{1}{\alpha}$ may even be much smaller than the smallest Star QAM ring amplitude given by $\frac{1}{\sqrt{\beta}}$, which may degrade the DAPSK scheme's achievable performance. Therefore, in addition to the classic Star QAM, the second solution to the differential non-constant modulus modulation problem is contributed by Absolute-amplitude Differential Phase Shift Keying (ADPSK), which was proposed in [136,288], where all the data-carrying symbols x_{n-1} are modulated onto classic Star QAM symbols. More explicitly, the ADPSK scheme's differential encoding for the transmitted symbols s_n is modelled by the revised expression of $s_n = \frac{1}{|s_{n-1}|} x_{n-1} s_{n-1}$, where the amplitude of the previous transmitted symbol $|s_{n-1}|$ is normalized, so that the amplitude of the next transmitted symbol $|s_n|$ is equal to the absolute amplitude of the data-carrying Star QAM symbol $|x_{n-1}|$. This transmission regime was originally conceived based on the Square QAM constellation in [135], which proposed to be detected noncoherently for recovering the data-carrying phase but coherently for recovering the data-carrying amplitude, meaning that the channel amplitude has to be estimated at the receiver. However, it was later revealed in [136, 288] that noncoherent detection may be invoked for both amplitude and phase detection for the absolute-amplitude Differential QAM (DQAM) schemes. Considering CDD in block fading as an example, the signal received at a single Receive Antenna (RA) may be expressed as $y_n = s_n h_n + v_n = \frac{1}{|s_{n-1}|} x_{n-1} y_{n-1} + (v_n - \frac{1}{|s_{n-1}|} x_{n-1} v_{n-1})$, where $h_n = h_{n-1}$ and v_n refer to the block fading and AWGN factors, respectively. As a result, the whole data-carrying symbol x_{n-1} including both its amplitude and phase may be recovered by the CDD with the aid of both the previous received sample y_{n-1} and the previous decision on $|s_{n-1}| = |x_{n-2}|$, while the unknown term of $(v_n - \frac{1}{|s_{n-1}|} x_{n-1} v_{n-1})$ may be treated as an equivalent AWGN term for the CDD. Statistically, the CDD's equivalent noise power of $(v_n - \frac{1}{|s_{n-1}|} x_{n-1} v_{n-1})$ is exactly twice the noise power of the original AWGN variable v_n, which results in the classic 3 dB performance difference between CDD aided DQAM and coherent QAM relying on perfect CSI in block fading channels.

It's worthy to note that the problem for using Square QAM constellation for modulating the data-carrying symbols x_{n-1} as suggested in [135] is that there would be no determined constellation set for the transmitted symbols s_n, which poses a major hardware difficulty. Considering Square 16QAM of Fig. 2.5a as an example, the data-carrying phases for $\angle x_{n-1}$ are given by $\{\arctan(1/3), \pi/4, \arctan(3)\}$ in the first quadrant and their projections in the other three quadrants, which divide the 2π phase circle space unevenly. This is different from, for example, a 16PSK constellation of Fig. 2.4d or a Star 16QAM constellation of Fig. 2.5b, which evenly divide the 2π phase circle space by a constant phase step of $\pi/16$ or $\pi/8$, respectively. As a result, if the absolute-amplitude DQAM scheme modulates the data-carrying symbols x_{n-1} according to the Square QAM constellation, then the differential encoding on phase, which is given

by ($\angle s_n = \angle x_{n-1} + \angle s_{n-1} \bmod 2\pi$), will result in $\angle s_n$ having irregular phases that can take any value from 0 to 2π. By contrast, the ADPSK scheme [136, 288] modulates the data-carrying symbols according to Star QAM constellation, which also results in the same Star QAM constellation for all the transmitted symbols s_n. In conclusion, the ADPSK schemes using the Star QAM constellation are easier to be implemented than the absolute-amplitude DQAM scheme using the Square QAM constellation. Nonetheless, it is still popular to employ the Square QAM constellations for Differential MIMO schemes as in [139–141], where the absolute-amplitude differential encoding method is invoked for dynamically restraining the transmitted symbols' amplitudes, while having a determined constellation diagram for the transmitted symbols is not a concern for these arrangements.

Moreover, it was also claimed in [136, 288] that a consistent ring-amplitude-dependent phase rotation may be applied to twist the constellation diagrams of DAPSK and ADPSK, so that the distances between the adjacent constellation points which are associated with different ring amplitudes may be increased. The resultant constellations are referred to as Twisted DAPSK (TDAPSK) and Twisted ADPSK (TADPSK), respectively. In order to simplify the discussions of the following sections, we may include DAPSK, TDAPSK, ADPSK and TADPSK as DQAM. Furthermore, all DQAM schemes may use the same form of notation, namely M-DQAM(M_A,M_P) to specify the number of their modulation levels.

Naturally, the employment of data-dependent ring amplitudes complicate the process of noncoherent detection. Since the ring amplitude and the phase are separately modulated, the CDD aided DAPSK proposed in [142], which independently detects the amplitude and phase exhibits a low detection complexity. However, it was noted in [159] that completely independently detecting the ring amplitude and the phase may impose a potential performance loss, which is especially significant in channel coded systems. Nevertheless, it was demonstrated in [159] that the optimum detection capability may be retained, when the ring amplitude's detection is assisted by the phase detection, and the detection complexity remains low as long as the subset of candidate ring amplitudes and that of candidate phases are separately visited.

Furthermore, the MSDD aided DQAM technique was proposed in [114] in order to compensate for the CDD's performance loss in the absence of CSI estimation. However, the appealing performance of DQAM in [114] is achieved at the cost of a substantial MSDD complexity. At the time writing, the implementation of MSDD by sphere decoding in the context of DQAM detection is still an open problem. Let us now elaborate a little further here in order to underline this predicament. The MSDD/MSDSD of DPSK [113, 127, 132] requires us to estimate the inversion of the received signal's correlation matrix $\mathbf{R}_{YY} = \mathrm{E}\left\{[\mathrm{rvec}(\mathbf{Y})]^H \cdot \mathrm{rvec}(\mathbf{Y})\right\}$. If the MSDD models the received signals as $\mathbf{Y} = \mathbf{SH} + \mathbf{V}$, where $\mathbf{S}$, $\mathbf{H}$ and $\mathbf{V}$ model the transmitted symbols, the Rayleigh fading channels and the AWGN, respectively, then the received signal's correlation matrix may be expressed as $\mathbf{R}_{YY} = \left(\mathbf{S}^H\mathbf{CS}\right)$, where $N_R = 1$ RA is assumed to be used, as detailed in [127, 132]. Moreover, the channel's correlation matrix is statistically known as $\mathbf{C} = \mathbf{R}_{hh} + \mathbf{R}_{vv}$, where the fading channel's correlation matrix is given by $\mathbf{R}_{hh} = \mathrm{Toeplitz}([\ \rho_0 \quad \rho_1 \quad \cdots \quad \rho_{N_w-1}\ ])$, while

the AWGN correlation matrix is given by $\mathbf{R}_{vv} = N_0 \cdot \mathbf{I}_{\mathbf{N_w}}$, as defined in [127, 132]. The notation Toeplitz($[\ \rho_0 \quad \rho_1 \quad \cdots \quad \rho_{N_w-1}\ ]$) refers to the symmetric Toeplitz matrix generated from the vector $[\ \rho_0 \quad \rho_1 \quad \cdots \quad \rho_{N_w-1}\ ]$, while $\{\rho_t\}_{t=0}^{N_w-1}$ refers to the time correlation between the fading samples. Owing to the fact that the transmitted symbol matrix $\mathbf{S}$ is unitary, the inversion of the received signal's correlation matrix is given by $\mathbf{R}_{YY}^{-1} = \left(\mathbf{S}^H\mathbf{C}^{-1}\mathbf{S}\right)$. Consequently, it was demonstrated in [127, 132] that the unique structure of the lower triangular matrix $\mathbf{L}$, which is the result of the decomposition $\mathbf{C}^{-1} = \mathbf{L}\mathbf{L}^H$ may facilitate sphere decoding for MSDSD aided DPSK. By contrast, for the case of MSDD aided DQAM, the transmitted symbol matrix is given by $\mathbf{S} = \mathbf{A}\mathbf{P}$, where $\mathbf{A}$ and $\mathbf{P}$ refer to the transmitted ring amplitudes and the transmitted phases, respectively. Naturally, the matrix $\mathbf{P}$ of phases is a unitary matrix, but the matrix $\mathbf{A}$ of ring amplitudes is not. As a result, the inversion of the received signal's correlation matrix is now given by $\mathbf{R}_{YY}^{-1} = \left(\mathbf{P}^H\mathbf{C}^{-1}\mathbf{P}\right)$ for the case of DQAM, where the channel's correlation matrix of $\mathbf{C} = \mathbf{A}^H \cdot \mathbf{R}_{hh} \cdot \mathbf{A} + \mathbf{R}_{vv}$ remains unknown until all the ring amplitudes in $\mathbf{A}$ are detected, which is the most substantial stumbling block in the way of offering a sphere decoding solution to the problem of DQAM ring amplitude detection.

Nonetheless, a low-complexity soft-decision-aided MSDD using Iterative Amplitude/Phase processing (MSDD-IAP) was proposed for coded DAPSK in [160], where the MSDD is invoked for ring amplitude detection, while the MSDSD is employed for phase detection. Then these two detectors may iteratively exchange their decisions in order to improve the overall performance. As expected, its complexity still grows exponentially with the MSDD window width N_w in the context of ring amplitude detection. Moreover, although the soft-decision-aided MSDD-IAP of [160] is capable of achieving a near-optimum MSDD performance for coded DAPSK schemes, its performance still suffers from an error floor when the MSDD-IAP is applied to uncoded DAPSK schemes. The reason for this is that without the aid of channel coding, the MSDD used for ring amplitude detection and the MSDSD conceived for phase detection may exchange erroneous decisions, which triggers the problem of error propagation.

Therefore, solving the MSDD aided DQAM detection problem by sphere decoding is still an open problem at the time of writing, which has been the most substantial obstacle in the way of offering a solution for MSDSD aided Differential MIMO schemes using QAM [137–141]. Furthermore, the DFDD was conceived for DQAM detection in [136, 153, 154], which relies on the assumption of the channel's correlation matrix $\mathbf{C}$ being independent of symbol-amplitude. The resultant DFDD solutions are no longer equivalent to MSDD relying on feedback decisions, which is in direct contrast to the case of DPSK detection [119–121, 121, 126]. Hence the DFDD proposed in [136, 153, 154] is sub-optimal.

As another fact worthnoting, is that the noncoherent detectors characterized in the open literatures have been conceived for specific differential non-constant modulus modulation schemes, among which the DAPSK detection [114, 142, 153, 154, 157, 159, 160] and the ADPSK detection [136, 288] are the most popular topics. No wide-ranging survey of noncoherent detectors exists in the open literature that may include CDD, MSDD, MSDSD and DFDD conceived for vir-

tually all DQAM constellations including DAPSK, TDAPSK, ADPSK and TADPSK. This paucity of knowledge hampers the application of DQAM schemes in a realistic communication systems. Against this background, the novel contributions of this chapter are as follows:

1. We observe that although the $(N_w \times N_w)$-element channel correlation matrix $\mathbf{C}$ has a total number of $M_A^{N_w}$ candidates, a $(v \times v)$-element partial channel correlation matrix $\widetilde{\mathbf{C}}_\mathbf{v}$ that may be evaluated with the aid of the SD's previous decisions only has M_A candidates according to the single variable detected by the SD associated with index v. We prove that the $(v \times v)$-element lower triangular matrix $\widetilde{\mathbf{L}}_\mathbf{v}$ that is directly generated by the decomposition of $\widetilde{\mathbf{C}}_\mathbf{v} = \widetilde{\mathbf{L}}_\mathbf{v}\widetilde{\mathbf{L}}_\mathbf{v}^H$ is always exactly the same as the sub-matrix of the $(N_w \times N_w)$-element lower triangular matrix $\mathbf{L}$, and hence sphere decoding may be carried out based on the partial lower triangular matrices $\{\widetilde{\mathbf{L}}_\mathbf{v}\}_{v=2}^{N_w}$ without the knowledge of all DQAM ring amplitudes. The optimum MSDD performance may be retained, provided that the sphere decoder radius is initialized to be sufficiently large, while the potentially excessive MSDD complexity may be substantially reduced by invoking sphere decoding.

2. With the advent of solving the open problem of MSDSD aided DQAM detection, both a DFDD derived from MSDD and a DFDD derived from prediction-based blind channel estimation are separately developed for uncoded DQAM schemes. We demonstrate that the MSDD-based DFDD and the prediction-based DFDD are equivalent for DQAM detection in Rayleigh fading channels. As expected, the enhanced DFDD proposed in this chapter outperforms the DFDD aided DQAM of [136, 153, 154].

3. We provide an indepth study of the family of DQAM constellations, commencing from those found in the existing literature. A variety of noncoherent detectors including CDD, MSDD, MSDSD and DFDD are adapted for employment in DQAM schemes, and their pros as well as cons are discussed in different scenarios. Finally, the performance comparison of DQAM schemes is carried out in this chapter for uncoded systems, while in the next chapter for channel coded systems.

The rest of this chapter is organized as follows. The DQAM constellations seen in the existing literature are studied and summarized in Sec. 4.2. The hard-decision-aided CDD and MSDD conceived for uncoded DQAM detection are introduced in Secs. 4.3 and 4.4, respectively. The hard-decision-aided MSDSD is proposed for uncoded DQAM detection in Sec. 4.5. Furthermore, for the DQAM schemes which separately modulate their data-dependent ring amplitude and data-carrying M_PPSK phase, a reduced-complexity MSDSD is proposed in Sec. 4.5.3, whose sphere decoder may separately visit the ring amplitude subset and the phase subset. Finally, hard-decision-aided DFDD conceived for uncoded DQAM is presented in Sec. 4.6, while Sec. 4.7 provides a summary of performance results characterizing the class of uncoded DQAM schemes. Our conclusions are offered in Sec. 4.8.

The hard-decision-aided CDD conceived for uncoded DAPSK introduced in Sec. 4.3 is based

on our publication of [159]. Furthermore, the hard-decision-aided MSDSD conceived for uncoded DQAM proposed in Sec. 4.5 is a generalized extension of our publication [235].

4.2 Differential Non-Constant Modulus Modulation

In this section, we focus our attention on the family of DQAM constellations. The DAPSK and the ADPSK, which adopt the classic Star QAM constellation, are reviewed in Secs. 4.2.1 and 4.2.2, respectively. The twisted constellations are introduced in Sec. 4.2.3, where the distances between the adjacent constellation points associated with different ring amplitudes are increased by simply imposing a ring-amplitude-dependent phase rotation. Furthermore, Sec. 4.2.4 offers a discussion on the DQAM constellations that jointly modulate the data-carrying M_A-level ring amplitude and the data-carrying M_PPSK phase.

4.2.1 Differential Amplitude Phase Shift Keying (DAPSK)

Similar to the differential encoding regime of DPSK seen in Eq. (3.1), the differential encoding process conceived for DAPSK is formulated as [142, 158, 159, 287]:

$$s_n = \begin{cases} \frac{1}{\sqrt{\beta}}, & \text{if } n = 1, \\ x_{n-1} s_{n-1}, & \text{if } n > 1, \end{cases} \tag{4.1}$$

where the normalization factor is given by $\beta = \frac{\sum_{\mu=0}^{M_A-1} \alpha^{2\mu}}{M_A}$ [159] and α refers to the ring ratio [158, 253, 289]. Note that in Rayleigh fading channels, the advantageous choices of ring ratios are $\alpha = 2.0$ for two-ring DAPSK [253, 289] and $\alpha = 1.4$ for four-ring DAPSK [155], respectively. In the absence of any better alternative, we will continue to use these optimized ring ratios throughout this chapter.

The basic notations that are shared by all DQAM schemes are summarized in Table 4.1. Specifically, the DAPSK's data-carrying symbol x_{n-1} in Eq. (4.1) may be represented by a M_A-level ring amplitude γ_{n-1} combined with an M_PPSK phase ω_{n-1} as:

$$x_{n-1} = \gamma_{n-1} \omega_{n-1}. \tag{4.2}$$

Similarly, the DAPSK's transmitted symbol s_n in Eq. (4.1) may also be represented by a M_A-level ring amplitude Γ_n combined with an M_PPSK phase Ω_n as:

$$s_n = \Gamma_n \Omega_n. \tag{4.3}$$

As a result, the DAPSK's differential encoding process of Eq. (4.1) may be applied to the ring amplitude as:

$$\Gamma_n = \gamma_{n-1} \Gamma_{n-1}. \tag{4.4}$$

Similarly, the differential encoding on the DAPSK phase is given by:

$$\Omega_n = \omega_{n-1} \Omega_{n-1}. \tag{4.5}$$

data-carrying amplitude:	γ_{n-1}
data-carrying phase:	ω_{n-1}
data-carrying symbol:	x_{n-1}

(a) Notations for data-carrying symbol

transmitted amplitude:	Γ_n
transmitted phase:	Ω_n
transmitted symbol:	s_n

(b) Notations for transmitted symbol

Table 4.1: Basic notations that are shared by all DQAM schemes.

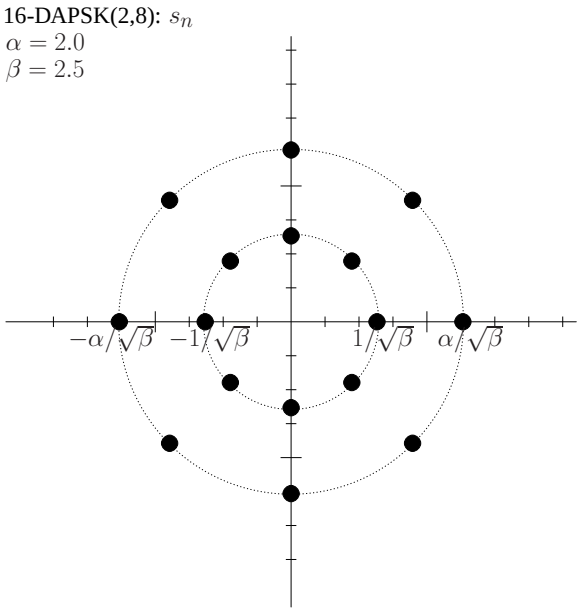

Figure 4.1: Constellation diagrams for the transmitted symbols of the 16-DAPSK(2,8) scheme.

$b_1b_2b_3$	ω_{n-1}	Ω_n
000	1	Ω_{n-1}
001	$\exp(j\frac{\pi}{4})$	$\exp(j\frac{\pi}{4})\Omega_{n-1}$
010	$\exp(j\frac{3\pi}{4})$	$\exp(j\frac{3\pi}{4})\Omega_{n-1}$
011	$\exp(j\frac{\pi}{2})$	$\exp(j\frac{\pi}{2})\Omega_{n-1}$
100	$\exp(j\frac{7\pi}{4})$	$\exp(j\frac{7\pi}{4})\Omega_{n-1}$
101	$\exp(j\frac{3\pi}{2})$	$\exp(j\frac{3\pi}{2})\Omega_{n-1}$
110	$\exp(j\pi)$	$\exp(j\pi)\Omega_{n-1}$
111	$\exp(j\frac{5\pi}{4})$	$\exp(j\frac{5\pi}{4})\Omega_{n-1}$

Table 4.2: Example of differential encoding applied to the 16-DAPSK(2,8) scheme's data-carrying phase and transmitted phase.

Let us consider the example of the classic 16-DAPSK(2,8) scheme, which employs the Star 16QAM constellation for all the transmitted symbols, as portrayed in Fig. 4.1. More explicitly, the 16-DAPSK(2,8) scheme maps a total number of $(\text{BPS} = \log_2 M = 4)$ source information bits to the data-carrying symbol x_{n-1} of Eq. (4.2). For the 16-DAPSK(2,8) scheme's phase, the first $(\text{BPS}_P = \log_2 M_P = 3)$ bits are assigned to a data-carrying 8PSK symbol ω_{n-1}, and then the transmitted phase Ω_n may be obtained by the differential encoding process of Eq. (4.5), which is summarized in Table 4.2. It can be seen that the 16-DAPSK(2,8) scheme's differential encoding process related to the phase is exactly the same as that of the DPSK scheme that was previously introduced in Sec. 3.2.

Following this, the 16-DAPSK(2,8) scheme's last $(\text{BPS}_A = \log_2 M_A = 1)$ bit is assigned to modulate the change in the consecutive transmitted ring amplitudes, which is summarized in Table 4.3. Explicitly, $b_4 = 0$ and $b_4 = 1$ determines whether the consecutive transmitted symbols' ring amplitude Γ_{n-1} and Γ_n should remain unchanged or be altered, respectively, while both Γ_{n-1} and Γ_n are drawn from the same two-ring Star 16QAM amplitude set $\{\Gamma_{n-1}, \Gamma_n\} \in \{\frac{1}{\sqrt{\beta}}, \frac{\alpha}{\sqrt{\beta}}\}$. As a result, according to the ring amplitude relationship of $\gamma_{n-1} = \frac{\Gamma_n}{\Gamma_{n-1}}$ defined by Eq. (4.4), there are two candidate sets for the data-carrying ring amplitude γ_{n-1} in Eq. (4.2), as summarized in Table 4.4. More explicitly, when we have $\Gamma_{n-1} = \frac{1}{\sqrt{\beta}}$, the source bit $b_4 \in \{0, 1\}$ is mapped to

b_4	$\Gamma_{n-1} = \frac{1}{\sqrt{\beta}}$	$\Gamma_{n-1} = \frac{\alpha}{\sqrt{\beta}}$
0	$\Gamma_n = \frac{1}{\sqrt{\beta}}$	$\Gamma_n = \frac{\alpha}{\sqrt{\beta}}$
1	$\Gamma_n = \frac{\alpha}{\sqrt{\beta}}$	$\Gamma_n = \frac{1}{\sqrt{\beta}}$

Table 4.3: Example of differential encoding applied to the 16-DAPSK(2,8) scheme's transmitted ring amplitudes.

b_4	γ_{n-1}	Γ_n
0	1	$\frac{1}{\sqrt{\beta}}$
1	α	$\frac{\alpha}{\sqrt{\beta}}$

(a) $\Gamma_{n-1} = \frac{1}{\sqrt{\beta}}$

b_4	γ_{n-1}	Γ_n
0	1	$\frac{\alpha}{\sqrt{\beta}}$
1	$\frac{1}{\alpha}$	$\frac{1}{\sqrt{\beta}}$

(b) $\Gamma_{n-1} = \frac{\alpha}{\sqrt{\beta}}$

Table 4.4: Example of differential encoding applied to the 16-DAPSK(2,8) scheme's data-carrying ring amplitude and transmitted ring amplitude.

$\gamma_{n-1} \in \{1, \alpha\}$. Furthermore, when we have $\Gamma_{n-1} = \frac{\alpha}{\sqrt{\beta}}$, the source bit $b_4 \in \{0, 1\}$ is mapped to $\gamma_{n-1} \in \{1, \frac{1}{\alpha}\}$. Therefore, the choice of the data-carrying ring amplitudes set for γ_{n-1} is explicitly determined by the previous transmitted ring amplitude $\Gamma_{n-1} = \frac{1}{\sqrt{\beta}}$.

As a result, there are also two constellation diagrams for the 16-DAPSK(2,8) scheme's data-carrying symbol $x_{n-1} = \gamma_{n-1}\omega_{n-1}$ of Eq. (4.2), which are portrayed in Fig. 4.2. In summary, for the classic 16-DAPSK(2,8) scheme, when we have $\Gamma_{n-1} = \frac{1}{\sqrt{\beta}}$ and $\Gamma_{n-1} = \frac{\alpha}{\sqrt{\beta}}$, the four source information bits should be mapped to the constellation diagrams of Fig. 4.2a and Fig. 4.2b, respectively, so that all transmitted symbols $\{s_n\}_{\forall n}$ of Eq. (4.1) are drawn from the same Star 16QAM constellation of Fig. 4.1.

Let us further extend the example of the 16-DAPSK(2,8) scheme to the generic M-DAPSK(M_A,M_P) scheme, where the ring amplitude γ_{n-1} and phase ω_{n-1} of the data-carrying symbol x_{n-1} of Eq. (4.2) are always separately encoded. More explicitly, the first $\text{BPS}_P = \log_2 M_P$ source information bits are assigned to modulate the data-carrying M_PPSK phase $\omega^p = \exp(j\frac{2\pi}{M_P}\check{p})$, where $p = \text{bin2dec}(b_1 \cdots b_{\text{BPS}_P})$ represents the Gray coded index $\check{p}$. Then the following $\text{BPS}_A = \log_2 M_A$ source information bits are assigned to the data-carrying ring amplitude γ_{n-1}, which has to guarantee that the next transmitted symbol s_n of Eq. (4.1) is drawn from the same Star QAM constellation as the previous transmitted symbol s_{n-1}. Therefore, on the basis of a pre-determined transmitted amplitude set $\{\Gamma_{n-1}, \Gamma_n\} \in \{\frac{\alpha^\mu}{\sqrt{\beta}}\}_{\mu=0}^{M_A-1}$ the data-carrying amplitudes γ_{n-1} may be modulated according to:

$$\gamma^a = \frac{\Gamma_n}{\Gamma_{n-1}} = \frac{\alpha^{\check{a}+\mu_{n-1} \bmod M_A}}{\alpha^{\mu_{n-1}}}, \tag{4.6}$$

where $a = \text{bin2dec}(b_{\text{BPS}_P+1} \cdots b_{\text{BPS}})$ is the Gray coded index $\check{a}$. It can be seen in Eq. (4.6) that the DAPSK data-carrying ring amplitude γ_{n-1} is not determined uniquely by the data-carrying index a, but it also depends on the previous transmitted ring amplitude index of μ_{n-1}, where we have $\Gamma_{n-1} = \frac{\alpha^{\mu_{n-1}}}{\sqrt{\beta}}$.

Therefore, the constellation set $\mathbf{x} = \{x^m\}_{m=0}^{M-1}$ of the data-carrying symbol x_{n-1} of Eq. (4.2)

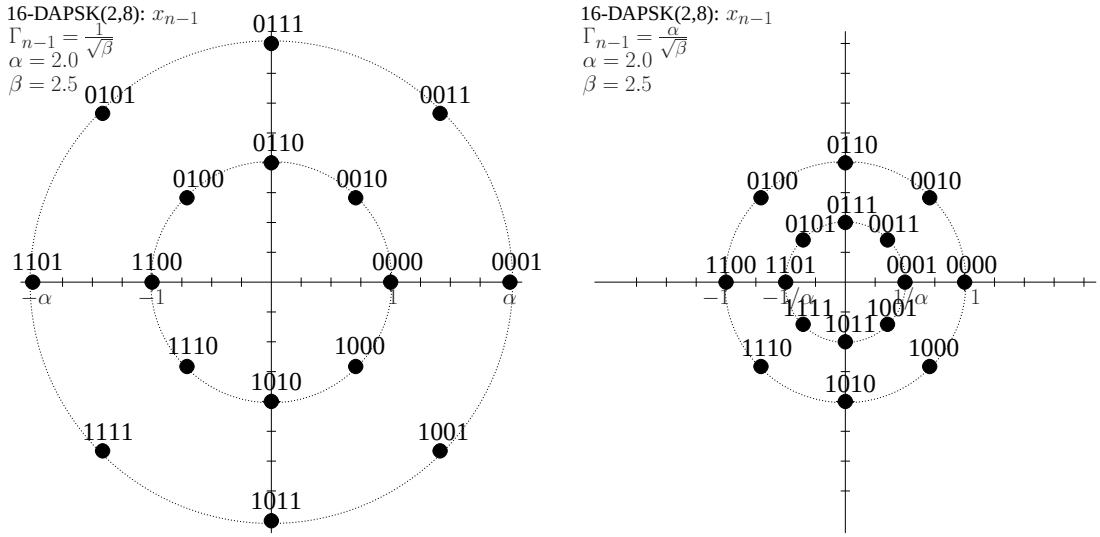

(a) $\Gamma_{n-1} = \frac{1}{\sqrt{\beta}}$ (b) $\Gamma_{n-1} = \frac{\alpha}{\sqrt{\beta}}$

Figure 4.2: Constellation diagrams for the data-carrying symbols of the 16-DAPSK(2,8) scheme.

is also supposed to be determined by the previous transmitted ring amplitude $\Gamma_{n-1} = \frac{\alpha^{\mu_{n-1}}}{\sqrt{\beta}}$. More explicitly, the modulation process of the DAPSK data-carrying symbol may be formulated as:

$$x^m = \gamma^a \omega^p = \alpha^{(\check{a}+\mu_{n-1} \bmod M_A)-\mu_{n-1}} \cdot \exp(j\frac{2\pi}{M_P}\check{p}), \tag{4.7}$$

where the data-carrying modulation index is $m = \text{bin2dec}(b_1 \cdots b_{\text{BPS}})$, while the index ranges of m, a and p are given by $[0 \leq m \leq (M-1)]$, $[0 \leq a \leq (M_A-1)]$ and $[0 \leq p \leq (M_P-1)]$, respectively. We note that the relationship between the modulation indices seen in Eq. (4.7) is given by $m = a + pM_A$, and the relationship between their modulation levels is given by $M = M_A M_P$.

4.2.2 Absolute-Amplitude Differential Phase Shift Keying (ADPSK)

The DAPSK introduced in Sec.4.2.1 relies on the same Star QAM constellation for all transmitted symbols s_n. Alternatively, it was proposed in [136,288] that all the data-carrying symbols x_{n-1} may be directly modulated as regular Star QAM symbols. As a result, if the differential encoding process of Eq. (4.1) is applied to this mechanism, the transmitted symbol's ring amplitude may become variable and unconstrained. In order to prevent this situation, the so-called absolute-amplitude is utilized in the alternative differential encoding process formulated as:

$$s_n = \begin{cases} \frac{1}{\sqrt{\beta}}, & \text{if } n = 1, \\ \frac{1}{|s_{n-1}|} x_{n-1} s_{n-1}, & \text{if } n > 1, \end{cases} \tag{4.8}$$

where the transmitted symbol's ring amplitude is dynamically normalized by $\frac{1}{|s_{n-1}|}$. More explicitly, for a generic M-ADPSK(M_A,M_P) scheme, the data-carrying quantity may still be represented by a M_A-level ring amplitude combined with a M_PPSK phase as $x_{n-1} = \gamma_{n-1}\omega_{n-1}$, which is in the

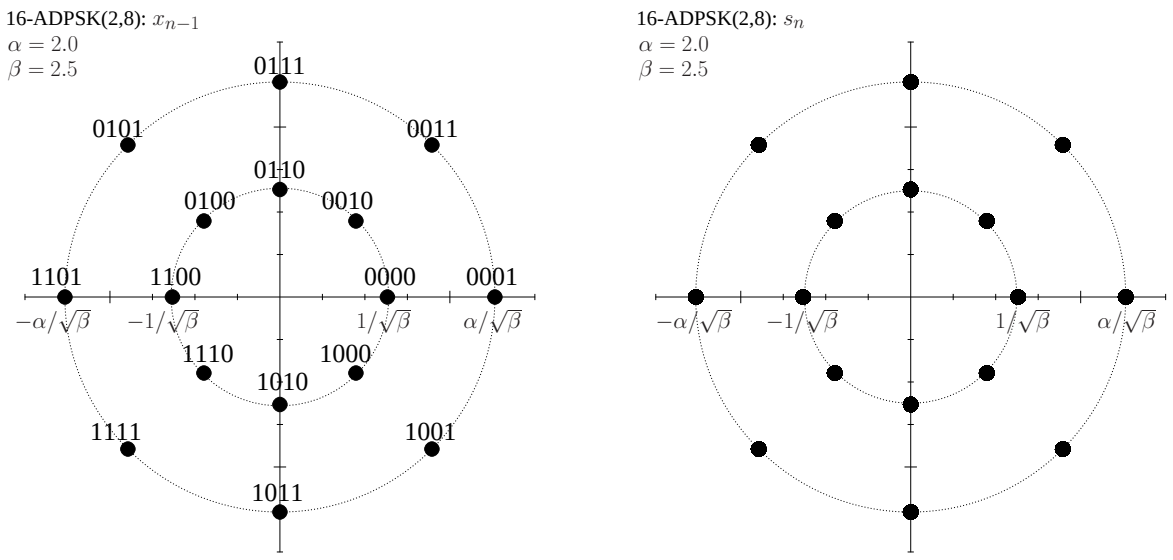

(a) Constellation set **x** for data-carrying symbols

(b) Constellation set **s** for transmitted symbols

Figure 4.3: Constellation diagrams for the 16-ADPSK(2,8) scheme.

same form as the DAPSK's data-carrying symbol of Eq. (4.2). Similarly, the ADPSK's transmitted symbol may also be represented by a M_A-level ring amplitude combined with a M_PPSK phase as $s_n = \Gamma_n \Omega_n$, which is in the same form as the DAPSK's transmitted symbol of Eq. (4.3). Therefore, according to Eq. (4.8), the ADPSK differential encoding applied to the phase is as same as the DAPSK of Eq. (4.5), i.e. we still have $\Omega_n = \omega_{n-1}\Omega_{n-1}$. However, there is no differential encoding on ring amplitude for the ADPSK. In fact, according to Eq. (4.8), the ADPSK always have the absolute-amplitude formulated as:

$$\Gamma_n = |s_n| = |x_{n-1}| = \gamma_{n-1}. \tag{4.9}$$

As a result, the data-carrying symbol x_{n-1} seen in Eq. (4.8) may be directly modulated as a Star QAM symbol as

$$x^m = \gamma^a \omega^p = \frac{\alpha^{\check{a}}}{\sqrt{\beta}} \exp(j\frac{2\pi}{M_P}\check{p}), \tag{4.10}$$

where the index ranges of m, a and p are given by $[0 \leq m \leq (M-1)]$, $[0 \leq a \leq (M_A-1)]$ and $[0 \leq p \leq (M_P-1)]$, respectively. More explicitly, the first $\text{BPS}_P = \log_2 M_P$ source information bits may be assigned to the data-carrying M_PPSK phase $\omega^p = \exp(j\frac{2\pi}{M_P}\check{p})$, where $p = \text{bin2dec}(b_1 \cdots b_{\text{BPS}_P})$ is Gray coded index $\check{p}$. Following this, the remaining $\text{BPS}_A = \log_2 M_A$ source information bits are assigned to the data-carrying Star QAM ring amplitude $\gamma^a = \frac{\alpha^{\check{a}}}{\sqrt{\beta}}$, where $a = \text{bin2dec}(b_{\text{BPS}_P+1} \cdots b_{\text{BPS}})$ is the Gray coded index $\check{a}$. The relationship between the modulation indices seen in Eq. (4.10) is given by $m = \text{bin2dec}(b_1 \cdots b_{\text{BPS}}) = a + pM_A$.

An example of the constellation diagram of the 16-ADPSK(2,8) scheme's data-carrying symbols and that of its transmitted symbols are portrayed by Fig. 4.3a and Fig. 4.3b, respectively. Moreover, the 16-ADPSK(2,8) scheme's differential encoding on phase is exactly as same as the case of the 16-DAPSK(2,8) scheme's phases summarized in Table 4.2. Furthermore, the 16-ADPSK(2,8)

b_4	γ_{n-1}	Γ_n
0	$\frac{1}{\sqrt{\beta}}$	$\frac{1}{\sqrt{\beta}}$
1	$\frac{\alpha}{\sqrt{\beta}}$	$\frac{\alpha}{\sqrt{\beta}}$

Table 4.5: Example of absolute-amplitude encoding applied to the 16-ADPSK(2,8) scheme's data-carrying ring amplitude and transmitted ring amplitude.

scheme's absolute-amplitude encoding is summarized in Table 4.5, where the data-carrying ring amplitude and the transmitted ring amplitude are always the same, as defined in Eq. (4.9).

Comparing to the 16-DAPSK(2,8) scheme's data-carrying symbol in Fig. 4.2, it can be seen in Fig. 4.3a that the ADPSK data-carrying symbol's constellation set no longer depends on the previous transmitted ring amplitude. Instead, the same Star QAM constellation is relied upon for all ADPSK's data-carrying symbols. Furthermore, the ADPSK transmitted symbols are also drawn from the same Star QAM constellation, as exemplified by Fig. 4.3b, which is facilitated by the differential encoding process of Eq. (4.8).

4.2.3 Twisted DAPSK (TDAPSK) and Twisted ADPSK (TADPSK)

As proposed in [136, 288], a ring-amplitude-dependent phase rotation of the DAPSK constellation and of the ADPSK constellation is capable of increasing the distance between the constellation points, which are located on different amplitude ring. Let us firstly consider a generic M-TDAPSK(M_A,M_P) scheme as an example of the so-called twisted modulation. The differential encoding process of TDAPSK is the same as that of DAPSK as specified by Eq. (4.1). However, the TDAPSK data-carrying symbol $x_{n-1} = \gamma_{n-1}\omega_{n-1}\psi_{n-1}$ contains the extra phase rotation term of ψ_{n-1}, which may be mapped by the data-carrying amplitude index as $\psi^a = \exp(j\frac{2\pi}{M}\check{a})$. Therefore, the modulation of the TDAPSK's data-carrying symbol x_{n-1} is now given by:

$$x^m = \gamma^a \omega^p \psi^a = \alpha^{(\check{a}+\mu_{n-1} \bmod M_A)-\mu_{n-1}} \exp(j\frac{2\pi}{M_P}\check{p}) \exp(j\frac{2\pi}{M}\check{a}). \tag{4.11}$$

As a result, the transmitted symbol s_n of the TDAPSK in Eq. (4.1) also contains an extra term of ring-amplitude-dependent phase rotation Ψ_n, i.e. we have $s_n = \Gamma_n\Omega_n\Psi_n$, where the differential encoding processes performed on the ring amplitude, M_PPSK phase and ring-amplitude-dependent phase rotation are given by $\Gamma_n = \gamma_{n-1}\Gamma_{n-1}$, $\Omega_n = \omega_{n-1}\Omega_{n-1}$ and $\Psi_n = \psi_{n-1}\Psi_{n-1}$, respectively.

Considering the 16-TDAPSK(2,8) scheme as an example, the twisted constellation diagrams of the data-carrying symbols are presented in Fig. 4.4, while the resultant constellation diagram for the transmitted symbols is portrayed in Fig. 4.5. It can be seen in Fig. 4.4a for 16-TDAPSK(2,8) that the distance between the constellation point labelled by source bits "0000" and "0001" is higher than for the case of 16-DAPSK(2,8) depicted in Fig. 4.2a. In fact, the distances between the constellation points associated with different amplitude rings are increased by twisted modulation, but the distances between the constellation points associated with the same amplitude ring remain unchanged.

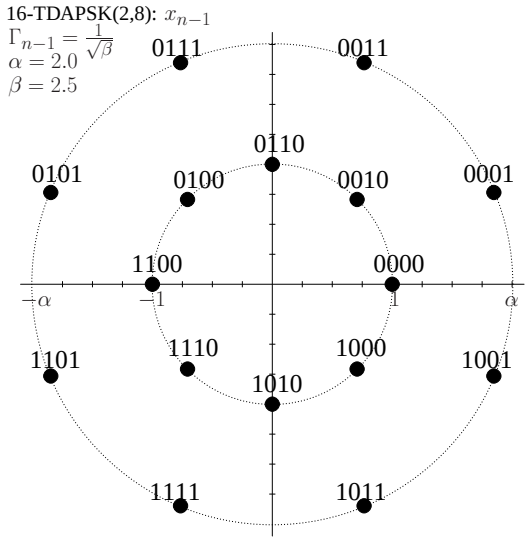

(a) $\Gamma_{n-1} = \frac{1}{\sqrt{\beta}}$

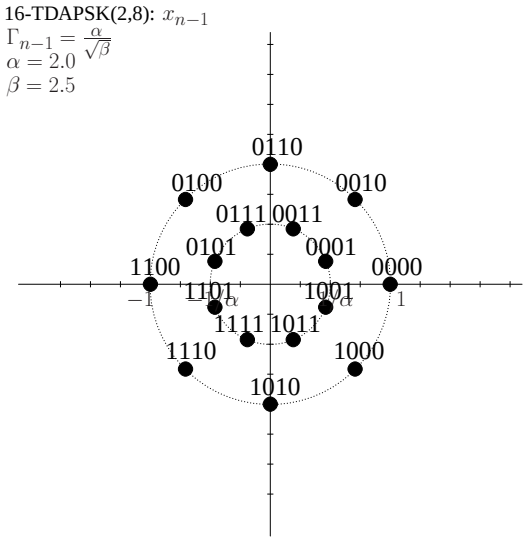

(b) $\Gamma_{n-1} = \frac{\alpha}{\sqrt{\beta}}$

Figure 4.4: Constellation diagrams for the data-carrying symbols of the 16-TDAPSK(2,8) scheme.

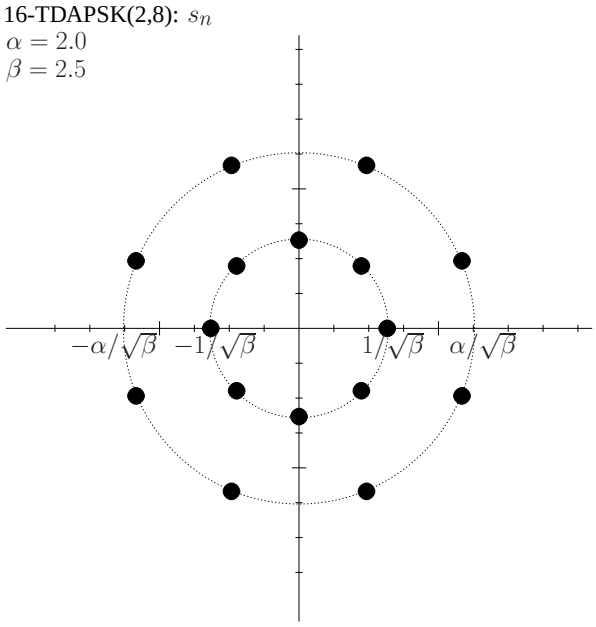

Figure 4.5: Constellation diagrams for the transmitted symbols of the 16-TDAPSK(2,8) scheme.

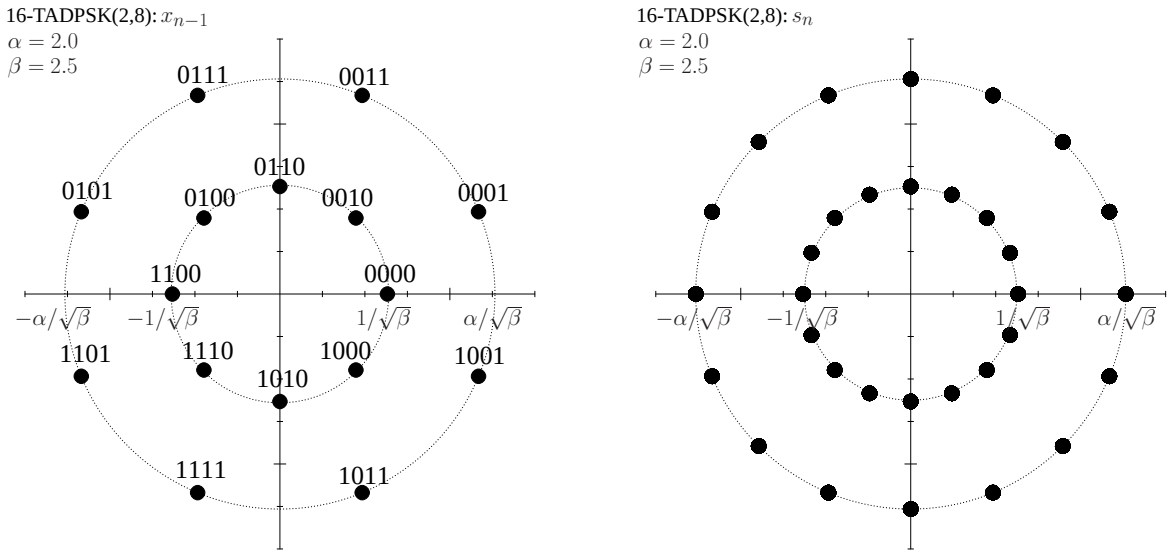

(a) Constellation set **x** for data-carrying symbols

(b) Constellation set **s** for transmitted symbols

Figure 4.6: Constellation diagrams for the 16-TADPSK(2,8) scheme.

Similarly, a generic M-TADPSK(M_A,M_P) scheme may be obtained by twisting the constellation of the generic M-ADPSK(M_A,M_P) scheme. The differential encoding process of TADPSK is the same as that of ADPSK formulated by Eq. (4.8). However, the modulation of the TADPSK data-carrying symbol $x_{n-1} = \gamma_{n-1}\omega_{n-1}\psi_{n-1}$ may be modified as:

$$x^m = \gamma^a \omega^p \psi^a = \frac{\alpha^{\check{a}}}{\sqrt{\beta}} \exp(j\frac{2\pi}{M_P}\check{p}) \exp(j\frac{2\pi}{M}\check{a}). \tag{4.12}$$

Therefore, the TADPSK transmitted symbol may be represented by $s_n = \Gamma_n \Omega_n \Psi_n$. According to Eq. (4.8), the differential encoding process is performed on both the M_PPSK phase term of $\Omega_n = \omega_{n-1}\Omega_{n-1}$ and on the ring-amplitude-dependent phase rotation term $\Psi_n = \psi_{n-1}\Psi_{n-1}$, but we still have the absolute-amplitude of $\Gamma_n = |s_n| = |x_{n-1}| = \gamma_{n-1}$ as specified by Eq. (4.9).

As an example, Fig. 4.6a and Fig. 4.6b portray the constellation diagram of both the 16-TADPSK(2,8) scheme's data-carrying symbols and of its transmitted symbols, respectively. It can be seen in Fig. 4.6b that each transmitted symbol's ring amplitude has $M = 16$ phase candidates, which results in an increased number of $M_A M = 32$ constellation points for the 16-TADPSK(2,8) scheme's transmitted symbol. However, we note that the TADPSK receiver is only required to decode the source information according to the M-point twisted Star QAM constellation such as for the example of the 16-TADPSK(2,8) seen in Fig. 4.6a, while the transmitted symbol's constellation exemplified in Fig. 4.6b does not influence the TADPSK detection.

Table 4.6 summarizes our comparison between DAPSK, ADPSK, TDAPSK and TADPSK in terms of their constellation distance. Since the minimum distance between the constellation points is determined by the adjacent constellation points located on the smallest amplitude ring, twisted modulation can only offer a small improvement on the average distance between all constellation points, as indicated by Table 4.6. We will demonstrate later that the small improvement offered by twisted modulation can barely provide any benefit in uncoded systems. However, since the ring-

	$\min_{\forall\{x^m \neq x^{m'}\}} \lvert x^m - x^{m'} \rvert$	$E_{\forall\{x^m \neq x^{m'}\}}\{\lvert x^m - x^{m'} \rvert\}$
16DAPSK(2,8)	0.382683	1.60486
16ADPSK(2,8)	0.484061	1.35334
16TDAPSK(2,8)	0.382683	1.60501
16TADPSK(2,8)	0.484061	1.35346
64DAPSK(4,16)	0.142194	1.58381
64ADPSK(4,16)	0.206137	1.29281
64TDAPSK(4,16)	0.142194	1.58383
64TADPSK(4,16)	0.206137	1.29282

Table 4.6: Comparison of DAPSK, ADPSK, TDAPSK and TADPSK constellations.

amplitude-dependent phase rotation imposes a correlation between the ring amplitude and phase, the iteration gain achieved by soft-decision-aided TDAPSK/TADPSK demodulator may be higher than that of their DAPSK/ADPSK counterparts, which implies that twisted modulation may offer certain performance advantages in coded systems, provided that appropriate coding schemes are used.

4.2.4 DQAM Associated with Joint Mapping on Ring Amplitude and Phase

All the aforementioned DQAM constellations including DAPSK, ADPSK, TDAPSK and TADPSK separately modulate the data-carrying M_A-level ring amplitude index $a = \text{bin2dec}(b_{\text{BPS}_P+1} \cdots b_{\text{BPS}})$ and the data-carrying M_PPSK phase index $p = \text{bin2dec}(b_1 \cdots b_{\text{BPS}_P})$. The rationale is that if the ring amplitude and the M_PPSK phase are encoded independently at the transmitter, they may be detected separately at the receiver, which results in a lower detection complexity of order $O(M_A + M_P)$.

By contrast, it was introduced in [136, 288] that the ring amplitude and the M_PPSK phase may be jointly modulated for DQAM, which may be represented in the form of DQAM$^{\text{JM}}$ in order to explicitly exploit the benefits of joint mapping. For example, the joint mapping conceived for the TDAPSK constellation of Eq. (4.11) may be expressed as:

$$x^m = \frac{\alpha^{[(\check{m} \bmod M_A)+\mu_{n-1}] \bmod M_A}}{\alpha^{\mu_{n-1}}} \exp(j\frac{2\pi}{M}\check{m}), \tag{4.13}$$

where all the $\text{BPS} = \log_2 M$ number of source bits are assigned to encode the global modulation index of $m = \text{bin2dec}(b_1 \cdots b_{\text{BPS}})$, which is the Gray coded index $\check{m}$. The resultant constellation may be referred to as TDAPSK$^{\text{JM}}$. Similarly, the joint mapping designed for TADPSK constellation of Eq. (4.12) may be formulated as:

$$x^m = \frac{\alpha^{(\check{m} \bmod M_A)}}{\sqrt{\beta}} \exp(j\frac{2\pi}{M}\check{m}), \tag{4.14}$$

which may now be referred to as TADPSK$^{\text{JM}}$.

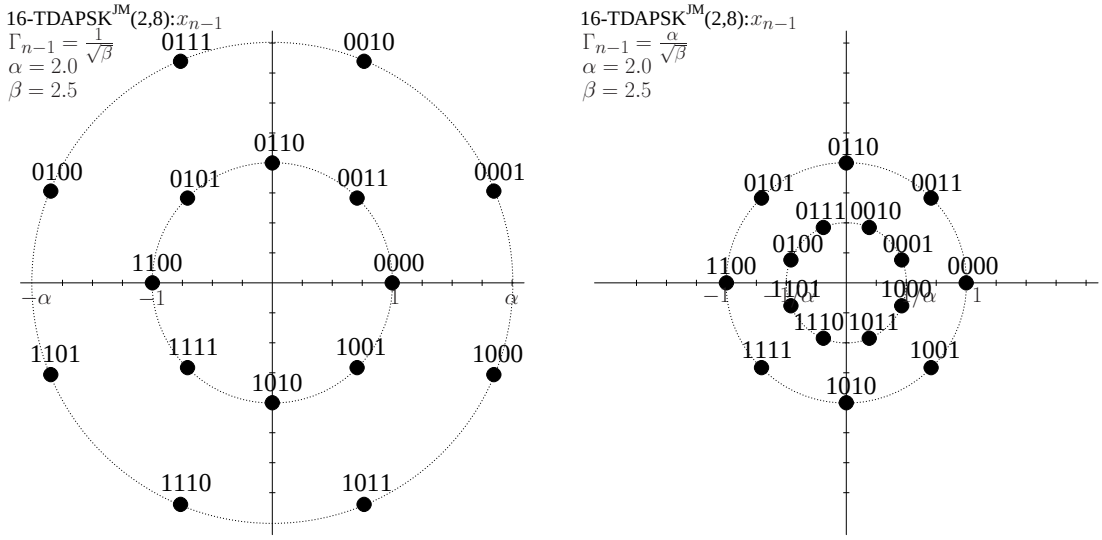

(a) $\Gamma_{n-1} = \frac{1}{\sqrt{\beta}}$ (b) $\Gamma_{n-1} = \frac{\alpha}{\sqrt{\beta}}$

Figure 4.7: Constellation diagrams for the data-carrying symbols of the 16-TDAPSK^{JM}(2,8) scheme.

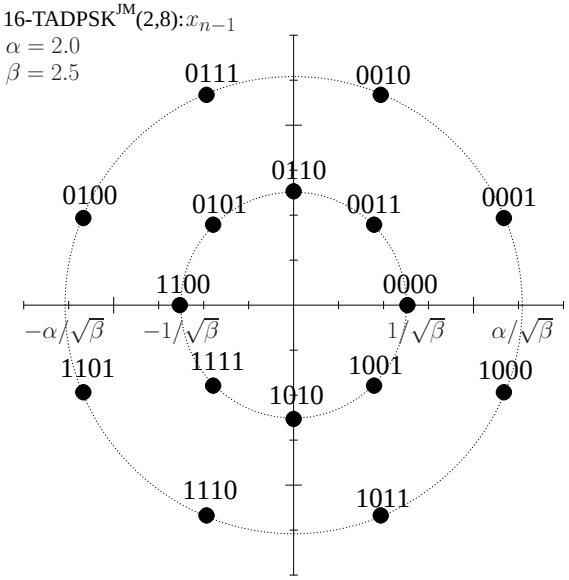

Figure 4.8: Constellation diagrams for the data-carrying symbols of the 16-TADPSK^{JM}(2,8) scheme.

	Data-Carrying Symbol	Example for Data-Carrying Symbol	Differential Encoding for Transmitted Symbol	Example for Transmitted Symbol
DAPSK	Eq. (4.7)	Fig. 4.2	Eq. (4.1)	Fig. 4.1
ADPSK	Eq. (4.10)	Fig. 4.3a	Eq. (4.8)	Fig. 4.3b
TDAPSK	Eq. (4.11)	Fig. 4.4	Eq. (4.1)	Fig. 4.5
TADPSK	Eq. (4.12)	Fig. 4.6a	Eq. (4.8)	Fig. 4.6b
TDAPSK^{JM}	Eq. (4.13)	Fig. 4.7	Eq. (4.1)	Fig. 4.5
TADPSK^{JM}	Eq. (4.14)	Fig. 4.8	Eq. (4.8)	Fig. 4.6b

Table 4.7: Summary of DQAM constellations and their examples.

An example of the constellation diagrams of the 16-TDAPSK^{JM}(2,8) scheme's data-carrying symbols are portrayed in Fig. 4.7. The constellation diagrams of the 16-TDAPSK^{JM}(2,8) scheme's transmitted symbols is as same as that of the 16-TDAPSK(2,8) scheme of Fig. 4.5. Moreover, an example of the constellation diagram of the 16-TADPSK^{JM}(2,8) scheme's data-carrying symbols is depicted by Fig. 4.8. Similarly, the constellation diagrams of the 16-TADPSK^{JM}(2,8) scheme's transmitted symbols is as same as that of the 16-TADPSK(2,8) scheme of Fig. 4.6b.

We note that owing to the fact that the DQAM^{JM} schemes including TDAPSK^{JM} and TADPSK^{JM} jointly modulate their ring amplitude and phase, the two variables have to be jointly detected at the DQAM^{JM} receiver, which implies that the complexity of DQAM^{JM} demodulation should be of order $O(M)$.

Furthermore, we would like to note that DQAM and its DQAM^{JM} counterpart which have the same constellation topology may achieve the same DCMC capacity despite their different mapping arrangements. This is similar to the situation of Gray and Anti-Gray mapping, as featured in [86, 250]. However, similarly, the iteration gain achieved by DQAM^{JM} may be higher than that of its DQAM counterpart in coded systems. This is because unlike DQAM schemes which encode their ring amplitude index and M_PPSK phase index separately using a Gray code, the joint mapping of DQAM^{JM} imposes a higher source bits dependency. Owing to this dependency, all the BPS number of source information bits have to be detected jointly by the DQAM^{JM} receiver. We will continue to discuss the pros and cons of these differential nonconstant modulus constellations in the following sections.

For the sake of clarification, this section is summarized by Table 4.7, where all the equations for DQAM constellations as well as all the figures for DQAM examples are listed. In the rest of this chapter, we will frequently refer to this table for the different DQAM constellations.

4.3 Hard-Decision-Aided CDD Conceived for Uncoded DQAM

Again, based on the assumption of Quasi-Static (QS) fading channels, where we have $\mathbf{H}_n = \mathbf{H}_{n-1}$ for a block of T_{QS} symbol periods, the received signal matrix of Eq. (2.1) may be further extended as:

$$\begin{aligned}\mathbf{Y}_n &= s_n \left(\mathbf{Y}_{n-1} - \mathbf{V}_{n-1}\right) / s_{n-1} + \mathbf{V}_n \\ &= \frac{s_n}{s_{n-1}} \mathbf{Y}_{n-1} + \widetilde{\mathbf{V}}_n,\end{aligned} \tag{4.15}$$

where the equivalent noise term $\widetilde{\mathbf{V}}_n = -\frac{s_n}{s_{n-1}}\mathbf{V}_{n-1} + \mathbf{V}_n$ has a zero mean and a variance of $(1 + \frac{\Gamma_n^2}{\Gamma_{n-1}^2})N_0$. For differentially encoded modulations, $\frac{s_n}{s_{n-1}}$ in Eq. (4.15) carrys source information. More explicitly, we have $\frac{s_n}{s_{n-1}} = x_{n-1}$ for DAPSK/TDAPSK based on Eq. (4.1), and we have $\frac{s_n}{s_{n-1}} = \frac{x_{n-1}}{\Gamma_{n-1}}$ for ADPSK/TADPSK based on Eq. (4.8). These two cases are considered separately in the following sections.

4.3.1 DAPSK and TDAPSK

First of all, let us introduce CDD aided DAPSK, which was investigated in our publication of [159]. Based on Eq. (4.15), the hard-decision-aided CDD conceived for uncoded DAPSK (e.g. the 16-DAPSK(2,8) constellation of Figs. 4.1-4.2) may be formulated as [142, 158, 159]:

$$\hat{x}_{n-1} = \arg \min_{\forall x^m \in \mathbf{x}(\hat{\Gamma}_{n-1})} \|\mathbf{Y}_n - x^m \mathbf{Y}_{n-1}\|^2, \tag{4.16}$$

where the constellation set for x_{n-1} is determined by the previous transmitted symbol's ring amplitude $\hat{\Gamma}_{n-1}$, where $\hat{\Gamma}_{n-1}$ may be fed back from previous CDD decision.

The demodulator of Eq. (4.16) operates on a vector-by-vector basis, where the detection complexity is expected to increase with N_R. As a remedy, Eq. (4.16) may be simplified to be operated on a symbol-by-symbol basis as:

$$\hat{x}_{n-1} = \arg \min_{\forall x^m \in \mathbf{x}(\hat{\Gamma}_{n-1})} |z_{n-1}^{CDD} - x^m|^2, \tag{4.17}$$

where the decision variable is given by:

$$z_{n-1}^{CDD} = \mathbf{Y}_n \mathbf{Y}_{n-1}^H / \|\mathbf{Y}_{n-1}\|^2. \tag{4.18}$$

The only differences between $\|\mathbf{Y}_n - x^m \mathbf{Y}_{n-1}\|^2 = \|\mathbf{Y}_n\|^2 + |x^m|^2 \|\mathbf{Y}_{n-1}\|^2 - 2\Re\left[(x^m)^* \mathbf{Y}_n \mathbf{Y}_{n-1}^H\right]$ of Eq. (4.16) and $|z_{n-1}^{CDD} - x^m|^2 = |z_{n-1}^{CDD}|^2 + |x^m|^2 - 2\Re\left[(x^m)^* z_{n-1}^{CDD}\right]$ of Eq. (4.17) are constants. Ideally, the decision variable z_{n-1}^{CDD} of Eq. (4.18) may be used for detecting the ring amplitude and phase of $x_{n-1} = \gamma_{n-1}\omega_{n-1}$ separately as:

$$\hat{\gamma}_{n-1} = \arg \min_{\forall \gamma^a \in \gamma(\hat{\Gamma}_{n-1})} \left| |z_{n-1}^{CDD}| - \gamma^a \right|^2, \tag{4.19a}$$

$$\hat{\omega}_{n-1} = \arg \min_{\forall \omega^p \in \omega} |z_{n-1}^{CDD} - \omega^p|^2, \tag{4.19b}$$

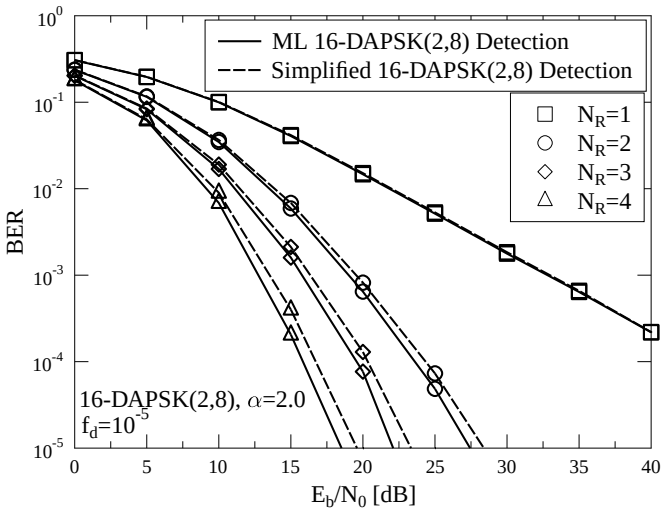

Figure 4.9: BER Performance comparison between the ML DAPSK detection of Eq. (4.16) and the simplified DAPSK detection of Eqs. (4.19a) and (4.19b).

For the special case of $N_R = 1$, we have $|z_{n-1}^{CDD}| = \frac{|y_n \cdot y_{n-1}^*|}{|y_{n-1}|^2} = \frac{|y_n|}{|y_{n-1}|}$ and $\angle z_{n-1}^{CDD} = \angle \frac{z_{n-1}^{CDD}}{|z_{n-1}^{CDD}|} = \angle \frac{y_n \cdot y_{n-1}^*}{|y_n \cdot y_{n-1}^*|} = \angle y_n - \angle y_{n-1}$. Therefore, Eqs. (4.19a) and (4.19b) are equivalent to the hard-decision-aided DAPSK detection introduced in [142].

However, the ML DAPSK detector of Eq. (4.16) and the simplified DAPSK detector of Eq. (4.19) do not have the same detection capability, as evidenced by Fig. 4.9, where the performance loss associated with detecting the ring amplitude and phase separately in Eqs. (4.19a) and (4.19b) becomes more significant as N_R increases. We also note that this performance difference is even more substantial for soft-decision-aided CDD conceived for coded DAPSK, as demonstrated in [159]. To elaborate a little further, the phase of a received DAPSK symbol may change the magnitudes along both the real and the imaginary axes of the received signal's constellation diagram, which implies that the detection of the DAPSK ring amplitude in fact relies on the detection of the DAPSK phase.

Therefore, in order to restore the ML DAPSK detector's detection capability, we return to Eqs. (4.16) and (4.17), which may be simplied as:

$$\begin{aligned} \{\hat{\gamma}_{n-1}, \hat{\omega}_{n-1}\} &= \arg \min_{\forall x^m \in \mathbf{x}(\hat{\Gamma}_{n-1})} |x^m|^2 - 2\Re\left[(x^m)^* z_{n-1}^{CDD}\right] \\ &= \arg \min_{\forall \gamma^a \in \gamma(\hat{\Gamma}_{n-1}),\ \forall \omega^p \in \omega} (\gamma^a)^2 - 2\gamma^a \Re\left[(\omega^p)^* z_{n-1}^{CDD}\right]. \end{aligned} \tag{4.20}$$

If we define the local minimum of the metric of $(\gamma^a)^2 - 2\gamma^a \Re\left[(\omega^p)^* z_{n-1}^{CDD}\right]$ in Eq. (4.20) as the minimum over the set of M_PPSK phases $\omega^p \in \omega$ only, then Eq. (4.20) may be transformed to:

$$\begin{aligned} \hat{\omega}_{n-1} &= \arg \min_{\forall \omega^p \in \omega} (\gamma^a)^2 - 2\gamma^a \Re\left[(\omega^p)^* z_{n-1}^{CDD}\right] \\ &= \arg \min_{\forall \omega^p \in \omega} -\Re\left[(\omega^p)^* z_{n-1}^{CDD}\right], \end{aligned} \tag{4.21}$$

where a fixed ring amplitude is chosen from the set of $\gamma^a \in \gamma(\hat{\Gamma}_{n-1})$. After deleting the constants

in Eq. (4.19b), it can be seen that Eq. (4.19b) and Eq. (4.21) are equivalent. Since the optimum phase is the same for all local minima associated with different γ^a, the phase detection process of DAPSK may be summarized as:

$$\hat{\omega}_{n-1} = \exp(j\frac{2\pi}{M_P}\check{p}_{n-1}), \quad \text{where } \check{p}_{n-1} = \lfloor \frac{M_P}{2\pi}\angle z_n^{CDD} \rceil. \tag{4.22}$$

Furthermore, the global minimum in Eq. (4.20) may now be obtained by comparing the local minima of the metrics, which may be expressed as:

$$\hat{\gamma}_{n-1} = \arg \min_{\forall \gamma^a \in \gamma(\hat{\Gamma}_{n-1})} (\gamma^a)^2 - 2\gamma^a \Re(\hat{\omega}_{n-1}^* z_{n-1}^{CDD}), \tag{4.23}$$

where $\hat{\omega}_{n-1}$ is obtained by Eq. (4.22). As a result, Eqs. (4.22) and (4.23) result in exactly the same detection capability as Eq. (4.16). We have arranged for both detectors to process the same channel output, and they always produce the same decisions. Moreover, Eqs. (4.22) and (4.23) separately evaluate the M_PPSK phase set and the ring amplitude set, hence a low DAPSK detection complexity is retained.

When the TDAPSK constellation (e.g. the 16-TDAPSK(2,8) constellation of Figs. 4.4-4.5) is employed, the phase of the data-carrying symbol is twisted by a ring-amplitude-dependent phase rotation. In order to retain the ML TDAPSK detection capability, Eqs. (4.16) and (4.17) may now be simplied to:

$$\{\hat{\gamma}_{n-1}, \hat{\omega}_{n-1}\} = \arg \min_{\forall \gamma^a \in \gamma(\hat{\Gamma}_{n-1}),\ \forall \omega^p \in \omega} (\gamma^a)^2 - 2\gamma^a \Re\left[(\omega^p \psi^a)^* z_{n-1}^{CDD}\right]. \tag{4.24}$$

The local minimum of the metric of $(\gamma^a)^2 - 2\gamma^a \Re\left[(\omega^p \psi^a)^* z_{n-1}^{CDD}\right]$ in Eq. (4.24), which is constituted by the minimum over the M_PPSK-related variable $\omega^p \in \omega$, is no longer independent of the candidate ring amplitudes $\gamma^a \in \gamma(\hat{\Gamma}_{n-1})$. In fact, the local minimum metric associated with a specific ring amplitude index a is given by:

$$\begin{aligned} \hat{\omega}_{n-1}^a &= \arg \min_{\forall \omega^p \in \omega} -\Re\left[(\omega^p \psi^a)^* z_{n-1}^{CDD}\right] \\ &= \exp(j\frac{2\pi}{M_P}\check{p}_{n-1}^a), \quad \text{where } \check{p}_{n-1}^a = \left\lfloor \frac{M_P}{2\pi}\angle\left[(\psi^a)^* z_n^{CDD}\right] \right\rceil. \end{aligned} \tag{4.25}$$

Naturally, there is a total number of M_A local minima corresponding to the local M_PPSK phases $\{\hat{\omega}_{n-1}^a\}_{a=0}^{M_A-1}$ of Eq. (4.25). Therefore, all the local minima may be compared in order to achieve the global minimum as:

$$\begin{aligned} \hat{\gamma}_{n-1} &= \arg \min_{\forall \gamma^a \in \gamma(\hat{\Gamma}_{n-1})} (\gamma^a)^2 - 2\gamma^a \Re\left[(\hat{\omega}_{n-1}^a \psi^a)^* z_{n-1}^{CDD}\right], \\ \hat{\omega}_{n-1} &= \hat{\omega}_{n-1}^{\hat{a}}, \end{aligned} \tag{4.26}$$

where the globally optimal ring amplitude index $\hat{a}$ corresponds to the globally optimal solution of $\hat{\gamma}_{n-1} = \gamma^{\hat{a}}$.

4.3.2 ADPSK and TADPSK

Let us continue by investigating the hard-decision-aided CDD conceived for uncoded ADPSK (e.g. the 16-ADPSK(2,8) constellation of Fig. 4.3) and TADPSK (e.g. the 16-TADPSK(2,8) constellation of Fig. 4.6). Similar to Eq. (4.16), the CDD aided ADPSK/TADPSK based on Eq. (4.8) is given by:

$$\hat{x}_{n-1} = \arg \min_{\forall x^m \in \mathbf{x}} \left\| \mathbf{Y}_n - \frac{x^m}{\hat{\Gamma}_{n-1}} \mathbf{Y}_{n-1} \right\|^2, \tag{4.27}$$

where the constellation set $\mathbf{x}$ for x_{n-1} is no longer determined by $\hat{\Gamma}_{n-1}$, nonetheless, $\hat{\Gamma}_{n-1}$ still has to be known from the previous CDD decisions for the sake of evaluating the decision metric of Eq. (4.27).

Similar to Eq. (4.17), the CDD aided ADPSK/TADPSK detection may be simplified to a symbol-by-symbol basis as:

$$\hat{x}_{n-1} = \arg \min_{\forall x^m \in \mathbf{x}} \left| z_{n-1}^{CDD} - \frac{x^m}{\hat{\Gamma}_{n-1}} \right|^2, \tag{4.28}$$

where the decision variable z_{n-1}^{CDD} is the same as the DAPSK decision variable defined by Eq. (4.18). The only differences between $\|\mathbf{Y}_n - \frac{x^m}{\hat{\Gamma}_{n-1}}\mathbf{Y}_{n-1}\|^2 = \|\mathbf{Y}_n\|^2 + \frac{|x^m|^2}{\hat{\Gamma}_{n-1}^2}\|\mathbf{Y}_{n-1}\|^2 - \frac{2}{\hat{\Gamma}_{n-1}}\Re\left[(x^m)^*\mathbf{Y}_n\mathbf{Y}_{n-1}^H\right]$ of Eq. (4.27) and $|z_{n-1}^{CDD} - \frac{x^m}{\hat{\Gamma}_{n-1}}|^2 = |z_n^{CDD}|^2 + \frac{|x^m|^2}{\hat{\Gamma}_{n-1}^2} - \frac{2}{\hat{\Gamma}_{n-1}}\Re\left[(x^m)^* z_n^{CDD}\right]$ of Eq. (4.28) are constants.

Furthermore, similar to the DAPSK detection of Eqs. (4.22) and (4.23), the CDD aided ADPSK may be simplied from Eq. (4.28) to separate phase and ring amplitude detection as:

$$\begin{aligned} \hat{\omega}_{n-1} &= \exp(j\frac{2\pi}{M_P}\check{p}_{n-1}), \quad \text{where } \check{p}_{n-1} = \lfloor \frac{M_P}{2\pi} \angle z_n^{CDD} \rceil, \\ \hat{\gamma}_{n-1} &= \arg \min_{\forall \gamma^a \in \gamma(\hat{\Gamma}_{n-1})} \frac{(\gamma^a)^2}{\hat{\Gamma}_{n-1}^2} - \frac{2\gamma^a}{\hat{\Gamma}_{n-1}} \Re(\hat{\omega}_{n-1}^* z_{n-1}^{CDD}), \end{aligned} \tag{4.29}$$

where the optimum detection capability of Eq. (4.28) is retained.

Moreover, similar to the TDAPSK detection of Eq. (4.26), the CDD aided TADPSK may be simplified from Eq. (4.28) to separate phase and ring amplitude detection as:

$$\begin{aligned} \hat{\gamma}_{n-1} &= \arg \min_{\forall \gamma^a \in \gamma(\hat{\Gamma}_{n-1})} \frac{(\gamma^a)^2}{\hat{\Gamma}_{n-1}^2} - \frac{2\gamma^a}{\hat{\Gamma}_{n-1}} \Re\left[(\hat{\omega}_{n-1}^a \psi^a)^* z_{n-1}^{CDD}\right], \\ \hat{\omega}_{n-1} &= \hat{\omega}_{n-1}^{\hat{a}}, \end{aligned} \tag{4.30}$$

where the locally optimal M_PPSK phases are given by:

$$\hat{\omega}_{n-1}^a = \exp(j\frac{2\pi}{M_P}\check{p}_{n-1}^a), \quad \text{where } \check{p}_{n-1}^a = \left\lfloor \frac{M_P}{2\pi} \angle \left[(\psi^a)^* z_n^{CDD}\right] \right\rceil. \tag{4.31}$$

4.3.3 TDAPSK$^{\text{JM}}$ and TADPSK$^{\text{JM}}$

When either the TDAPSK$^{\text{JM}}$ constellation (e.g. the 16-TDAPSK$^{\text{JM}}$(2,8) constellation of Fig. 4.7) or the TADPSK$^{\text{JM}}$ constellation (e.g. the 16-TADPSK$^{\text{JM}}$(2,8) constellation of Fig. 4.8) is employed, the ring amplitude and the M_PPSK phase of the data-carrying symbol are jointly encoded

as specified by Eqs. (4.13) and (4.14), respectively. Therefore, the ring amplitude and the M_PPSK phase have to be detected jointly for both TDAPSK$^{\text{JM}}$ and TADPSK$^{\text{JM}}$ by invoking Eq. (4.17) and Eq. (4.28), respectively, which results in a higher detection complexity. In more detail, the CDD complexity of DAPSK and ADPSK is of order $O(1+M_A)$, where the evaluation of the local minimum only requires visiting the closest M_PPSK phase by using the decision variable z_{n-1}^{CDD} of Eq. (4.18), while the global minimum is found by visiting all M_A ring amplitude candidates. Furthermore, the CDD complexity of both TDAPSK and TADPSK is of order $O(M_A+M_A)$, because the total number of local minima is now given by M_A. By contrast, the CDD of uncoded TDAPSK$^{\text{JM}}$ and TADPSK$^{\text{JM}}$ has the highest complexity order of $O(M)$, where all the M constellation points have to be visited in order to retain the globally optimum solution.

4.4 Hard-Decision-Aided MSDD Conceived for Uncoded DQAM

Similarly to the MSDD aided DPSK introduced in Sec. 3.2.2, the performance of differential non-constant modulus constellations may be improved by observing N_w received signal blocks of Eq. (2.1). Similarly to Eq. (3.6), for MSDD we may model the multiple received signal vectors as:

$$\begin{aligned}\mathbf{Y} &= \mathbf{SH} + \mathbf{V} \\ &= \mathbf{APOH} + \mathbf{V},\end{aligned} \tag{4.32}$$

where the corresponding matrices are given by:

$$\begin{aligned}
&\mathbf{Y} = \left[\mathbf{Y}_n^T, \mathbf{Y}_{n-1}^T, \cdots, \mathbf{Y}_{n-N_w+1}^T\right]^T, && \mathbf{S} = \text{diag}\left\{\left[s_n, s_{n-1}, \cdots, s_{n-N_w+1}\right]\right\}, \\
&\mathbf{H} = \left[\mathbf{H}_n^T, \mathbf{H}_{n-1}^T, \cdots, \mathbf{H}_{n-N_w+1}^T\right]^T, && \mathbf{V} = \left[\mathbf{V}_n^T, \mathbf{V}_{n-1}^T, \cdots, \mathbf{V}_{n-N_w+1}^T\right]^T, \\
&\mathbf{A} = \text{diag}\left\{\left[\Gamma_n, \Gamma_{n-1}, \cdots, \Gamma_{n-N_w+1}\right]\right\}, && \mathbf{P} = \text{diag}\left\{\left[\Omega_n, \Omega_{n-1}, \cdots, \Omega_{n-N_w+1}\right]\right\}, \\
&\mathbf{O} = \text{diag}\left\{\left[\Psi_n, \Psi_{n-1}, \cdots, \Psi_{n-N_w+1}\right]\right\}.
\end{aligned} \tag{4.33}$$

We note that the ring-amplitude-dependent phase rotation matrix $\mathbf{O}$ is taken into account in the MSDD model in order to include the constellation twisting actions of TDAPSK and TADPSK, while the matrix $\mathbf{O}$ is simply an identity matrix for the cases of DAPSK and ADPSK. Furthermore, with a little inaccuracy of notation, we drop the time index n for all MSDD windows as[1]:

$$\begin{aligned}
&\mathbf{Y} = \left[\mathbf{Y}_{N_w}^T, \mathbf{Y}_{N_w-1}^T, \cdots, \mathbf{Y}_1^T\right]^T, && \mathbf{S} = \text{diag}\left\{\left[s_{N_w}, s_{N_w-1}, \cdots, s_1\right]\right\}, \\
&\mathbf{H} = \left[\mathbf{H}_{N_w}^T, \mathbf{H}_{N_w-1}^T, \cdots, \mathbf{H}_1^T\right]^T, && \mathbf{V} = \left[\mathbf{V}_{N_w}^T, \mathbf{V}_{N_w-1}^T, \cdots, \mathbf{V}_1^T\right]^T, \\
&\mathbf{A} = \text{diag}\left\{\left[\Gamma_{N_w}, \Gamma_{N_w-1}, \cdots, \Gamma_1\right]\right\}, && \mathbf{P} = \text{diag}\left\{\left[\Omega_{N_w}, \Omega_{N_w-1}, \cdots, \Omega_1\right]\right\}, \\
&\mathbf{O} = \text{diag}\left\{\left[\Psi_{N_w}, \Psi_{N_w-1}, \cdots, \Psi_1\right]\right\}.
\end{aligned} \tag{4.34}$$

The MSDD's received signal matrix $\mathbf{Y}$, the MSDD's fading channel matrix $\mathbf{H}$ and the MSDD's AWGN matrix $\mathbf{V}$ are all of size $(N_w \times N_R)$. Moreover, the observed transmitted symbol matrix $\mathbf{S}$

[1] We note that $\mathbf{Y}$ in Eq. (4.32) stores received signal vectors in a reverse order compared to the one seen in [127, 132]. As a result, the MSDSD introduced in the next section may detect the transmitted symbols according to their differential encoding order, i.e. we have $\bar{\Omega}_v = \omega_{v-1}\bar{\Omega}_{v-1}$, instead of detecting them backwardly as $\bar{\Omega}_v = \omega_v^*\bar{\Omega}_{v+1}$ in [127, 132].

as well as the associated ring amplitude matrix $\mathbf{A}$, M_PPSK phase matrix $\mathbf{P}$ and the ring-amplitude-dependent phase rotation matrix $\mathbf{O}$ are all of size $(N_w \times N_w)$.

The first transmitted symbol's M_PPSK phase Ω_1 and the first ring-amplitude-dependent phase rotation Ψ_1 are constant with respect to the following M_PPSK phases $\{\Omega_t\}_{t=2}^{N_w}$ and phase rotation elements $\{\Psi_t\}_{t=2}^{N_w}$. Hence we have:

$$\mathbf{Y} = \bar{\mathbf{A}}\bar{\mathbf{P}}\bar{\mathbf{O}}\bar{\mathbf{H}} + \mathbf{V}, \tag{4.35}$$

where the v^{th} diagonal element in the M_PPSK matrix $\bar{\mathbf{P}}$ is given by:

$$\bar{\Omega}_v = \Omega_v \Omega_1^* = \begin{cases} 1, & n = 1 \\ \omega_{v-1}\bar{\Omega}_{v-1} = \prod_{t=1}^{v-1} \omega_t, & n > 1 \end{cases}, \tag{4.36}$$

while the v^{th} diagonal element in the ring-amplitude-dependent phase rotations matrix $\bar{\mathbf{O}}$ is given by:

$$\bar{\Psi}_v = \Psi_v \Psi_1^* = \begin{cases} 1, & n = 1 \\ \psi_{v-1}\bar{\Psi}_{v-1} = \prod_{t=1}^{v-1} \psi_t, & n > 1 \end{cases}. \tag{4.37}$$

As a result, the v^{th} row in $\bar{\mathbf{H}}$ is given by $\bar{\mathbf{H}}_v = \Omega_1 \Psi_1 \mathbf{H}_v$. There are a total of $M_P^{N_w-1}$ candidates for the M_PPSK phase matrix $\bar{\mathbf{P}}$. Moreover, the equivalent ring amplitude matrix $\bar{\mathbf{A}}$ in Eq. (4.35) depends on the ring amplitudes matrix $\mathbf{A}$ in Eq. (4.32), where the first transmitted ring amplitude Γ_1 is being decided with the aid of previous MSDD decisions, or it is treated as a separate variable. More specifically, for the DAPSK/TDAPSK constellations (e.g. the 16-DAPSK(2,8) constellation of Figs. 4.1-4.2 and the 16-TDAPSK(2,8) constellation of Figs. 4.4-4.5), which are differentially encoded according to Eq. (4.1), the v^{th} diagonal element in $\bar{\mathbf{A}}$ is given by:

$$\Gamma_v = \gamma_{v-1}\Gamma_{v-1} = \left(\prod_{t=1}^{v-1} \gamma_t\right) \Gamma_1. \tag{4.38}$$

By contrast, the ADPSK/TADPSK constellations (e.g. the 16-ADPSK(2,8) constellation of Fig. 4.3 and the 16-TADPSK(2,8) constellation of Fig. 4.6) rely on absolute data-carrying ring amplitudes according to the differential encoder of Eq. (4.8). Hence its v^{th} diagonal element in $\bar{\mathbf{A}}$ is given by:

$$\Gamma_v = \gamma_{v-1}. \tag{4.39}$$

Therefore, there is a total number of $M_A^{N_w-1}$ candidates for the ring amplitude matrix $\bar{\mathbf{A}}$ of Eq. (4.35). We note that the ring-amplitude-dependent phase rotation matrix $\bar{\mathbf{O}}$ is uniquely and unambiguously determined by the ring amplitudes $\bar{\mathbf{A}}$, i.e. $\bar{\mathbf{O}}$ is known as long as $\bar{\mathbf{A}}$ is detected.

In order to detect the ring amplitudes $\bar{\mathbf{A}}$ and M_PPSK phases $\bar{\mathbf{P}}$ from the MSDD's received signal matrix $\mathbf{Y}$ of Eq. (4.35), the MSDD aims for maximizing the following *a posteriori* probability:

$$\begin{aligned} p(\bar{\mathbf{A}}, \bar{\mathbf{P}}|\mathbf{Y}) &= \sum_{\forall \Gamma_1} p(\bar{\mathbf{A}}, \bar{\mathbf{P}}|\mathbf{Y}, \Gamma_1) p(\Gamma_1) \\ &= \sum_{\forall \Gamma_1} \frac{p(\mathbf{Y}|\bar{\mathbf{A}}, \bar{\mathbf{P}}, \Gamma_1) p(\bar{\mathbf{A}}) p(\bar{\mathbf{P}})}{\sum_{\forall \bar{\mathbf{A}}, \forall \bar{\mathbf{P}}} p(\mathbf{Y}|\bar{\mathbf{A}}, \bar{\mathbf{P}}, \Gamma_1) p(\bar{\mathbf{A}}) p(\bar{\mathbf{P}})} p(\Gamma_1), \end{aligned} \tag{4.40}$$

where $p(\Gamma_1)$, $p(\bar{\mathbf{A}})$ and $p(\bar{\mathbf{P}})$ refer to the *a priori* probabilities of Γ_1, $\bar{\mathbf{A}}$ and $\bar{\mathbf{P}}$, respectively, which may all be assumed to be equiprobable for hard-decision-aided MSDD. Hence we have $\left\{p(\Gamma_1) = \frac{1}{M_A}\right\}_{\forall \Gamma_1}$, $\left\{p(\bar{\mathbf{A}}) = \frac{1}{(M_A)^{N_w-1}}\right\}_{\forall \bar{\mathbf{A}}}$ and $\left\{p(\bar{\mathbf{P}}) = \frac{1}{(M_P)^{N_w-1}}\right\}_{\forall \bar{\mathbf{P}}}$, respectively. Furthermore, according to the MSDD received signal model of Eq. (4.35), the probability of receiving $\mathbf{Y}$ given $\bar{\mathbf{A}}$, $\bar{\mathbf{P}}$ and $\Gamma_1$is formulated as [113, 114, 127]:

$$p(\mathbf{Y}|\bar{\mathbf{A}}, \bar{\mathbf{P}}, \Gamma_1) = \frac{\exp\left\{-\text{rvec}(\mathbf{Y}) \cdot \mathbf{R}_{YY}^{-1}[\text{rvec}(\mathbf{Y})]^H\right\}}{\pi^{N_R N_w} \det(\mathbf{R}_{YY})}, \tag{4.41}$$

where the operation $\text{rvec}(\mathbf{Y})$ forms a $(1 \times N_R N_w)$-element row vector by taking the rows of $\mathbf{Y}$ one-by-one. The conditional probability $p(\mathbf{Y}|\bar{\mathbf{A}}, \bar{\mathbf{P}}, \Gamma_1)$ of Eq. (4.41) is given by the PDF of the multi-variate Gaussian-distributed MSDD's received signal matrix $\mathbf{Y}$ of Eq. (4.35) [278].

Similarly to the case of DPSK in Eq. (3.12), the MSDD received signal matrix $\mathbf{Y}$ of Eq. (4.35) is vectorized in Eq. (4.41) in order to form a vector of Gaussian-distributed variables. The equivalent MSDD received signal model now becomes:

$$\text{rvec}(\mathbf{Y}) = \text{rvec}(\bar{\mathbf{H}}) \cdot [(\bar{\mathbf{A}}\bar{\mathbf{P}}\bar{\mathbf{O}}) \otimes \mathbf{I}_{N_R}] + \text{rvec}(\mathbf{V}), \tag{4.42}$$

where the operation $\otimes$ represents the Kronecker product. As a result, the correlation matrix of the received signal $\mathbf{R}_{YY}$ seen in Eq. (4.41) may be expressed as:

$$\begin{aligned}
\mathbf{R}_{YY} &= \text{E}\left\{[\text{rvec}(\mathbf{Y})]^H \cdot \text{rvec}(\mathbf{Y})\right\} \\
&= \left[(\bar{\mathbf{O}}^H \bar{\mathbf{P}}^H \bar{\mathbf{A}}^H) \otimes \mathbf{I}_{N_R}\right] \text{E}\left\{[\text{rvec}(\bar{\mathbf{H}})]^H \cdot \text{rvec}(\bar{\mathbf{H}})\right\} [(\bar{\mathbf{A}}\bar{\mathbf{P}}\bar{\mathbf{O}}) \otimes \mathbf{I}_{N_R}] \\
&\quad + \text{E}\left\{[\text{rvec}(\mathbf{V})]^H \cdot \text{rvec}(\mathbf{V})\right\} \\
&= (\bar{\mathbf{O}}^H \bar{\mathbf{P}}^H \mathbf{C} \bar{\mathbf{P}} \bar{\mathbf{O}}) \otimes \mathbf{I}_{N_R},
\end{aligned} \tag{4.43}$$

where both $\bar{\mathbf{P}}$ and $\bar{\mathbf{O}}$ are unitary matrices. Moreover, the fading channel's correlation matrix $\text{E}\left\{[\text{rvec}(\bar{\mathbf{H}})]^H \cdot \text{rvec}(\bar{\mathbf{H}})\right\}$ seen in Eq. (4.43) was defined in Eq. (3.15), while the AWGN correlation matrix $\text{E}\left\{[\text{rvec}(\mathbf{V})]^H \cdot \text{rvec}(\mathbf{V})\right\}$ was defined in Eq. (3.18). Furthermore, the channel's characteristic correlation matrix $\mathbf{C}$ seen in Eq. (4.43) is given by:

$$\mathbf{C} = \bar{\mathbf{A}}^H \mathbf{R}_{hh} \bar{\mathbf{A}} + \mathbf{R}_{vv}, \tag{4.44}$$

where the fading characteristic correlation matrix $\mathbf{R}_{hh}$ and the AWGN characteristic correlation matrix $\mathbf{R}_{vv}$ were defined in Eq. (3.16) and Eq. (3.19), respectively, which are the same as in the case of DPSK using $N_R = 1$ in [127, 132]. We note that since the ring amplitude matrix $\bar{\mathbf{A}}$ is not a unitary matrix, it cannot be separated from the channel's characteristic correlation matrix $\mathbf{C}$, which is in contrast to $\bar{\mathbf{P}}$ and $\bar{\mathbf{O}}$ seen in Eq. (4.43). As a result, in contrast to Eq. (3.21) derived for the case of uncoded DPSK detection, $\bar{\mathbf{A}}^H \mathbf{R}_{hh} \bar{\mathbf{A}}$ seen in Eq. (4.44) is neither a constant matrix nor a Toeplitz matrix. This implies that for all the DQAM constellations, the channel's characteristic correlation matrix $\mathbf{C}$ of Eq. (4.44) does not become known until all the ring amplitudes in $\bar{\mathbf{A}}$ are detected, which is the most substantial stumbling block in the way of offering a sphere decoding solution to the DQAM ring amplitude detection problem.

In summary, once again, assuming that the ring amplitude matrix $\bar{\mathbf{A}}$, the phase matrix $\bar{\mathbf{P}}$ and the initial ring amplitude variable Γ_1 all represent equiprobable variables, the MSDD that maximizes the *a posteriori* probability of Eq. (4.40) may be formulated as:

$$\begin{aligned}\{\hat{\bar{\mathbf{A}}}, \hat{\bar{\mathbf{P}}}\} &= \max \ \ln\left[p(\bar{\mathbf{A}}, \bar{\mathbf{P}}|\mathbf{Y})\right] \\ &\approx \max_{\forall \Gamma_1} \ \max_{\forall \bar{\mathbf{A}}, \forall \bar{\mathbf{P}}} \ -\mathrm{tr}(\mathbf{Y}^H \bar{\mathbf{P}} \bar{\mathbf{O}} \mathbf{C}^{-1} \bar{\mathbf{O}}^H \bar{\mathbf{P}}^H \mathbf{Y}) - N_R \ln[\det(\mathbf{C})],\end{aligned} \tag{4.45}$$

where we have $\ln\left[\sum_{\forall d} \exp(d)\right] \approx \max_{\forall d} \ d$ [27], while the determinant of the correlation matrix $\mathbf{R}_{YY}$ seen in Eq. (4.41) is given by $\det(\mathbf{R}_{YY}) = \det(\mathbf{C})^{N_R}$ for the DQAM schemes. We note that Eq (4.45) is obtained following the same steps as illustrated in Eq. (3.22) and derived for the case of DPSK.

Furthermore, if the first transmitted ring amplitude $\hat{\Gamma}_1$ is fed back from the previous MSDD decisions, then a Hard-Decision-Directed MSDD (HDD-MSDD) may be simply formulated as:

$$\{\hat{\bar{\mathbf{A}}}, \hat{\bar{\mathbf{P}}}\} = \max_{\forall \bar{\mathbf{A}}, \forall \bar{\mathbf{P}}} \ -\mathrm{tr}(\mathbf{Y}^H \bar{\mathbf{P}} \bar{\mathbf{O}} \mathbf{C}^{-1} \bar{\mathbf{O}}^H \bar{\mathbf{P}}^H \mathbf{Y}) - N_R \ln[\det(\mathbf{C})]. \tag{4.46}$$

Then the newly detected $\hat{\Gamma}_{N_w}$ in $\hat{\bar{\mathbf{A}}}$ may be passed on to the next MSDD window. For the MSDD of Eq. (4.45), a total number of $M_A M^{N_w-1}$ candidates have to be evaluated and compared. For HDD-MSDD of Eq. (4.46), the total number of candidates is reduced to be M^{N_w-1}.

We note that both the MSDD of Eq. (4.45) and the HDD-MSDD of Eq. (4.46) are amenable to DAPSK and TDAPSK detection. However, both ADPSK and TADPSK which rely on having an absolute data-carrying ring amplitude can only employ the HDD-MSDD of Eq. (4.46). Let us consider MSDD aided ADPSK associated with $N_w = 2$ as an example. The channel's characteristic correlation matrix $\mathbf{C}$ of Eq. (4.44) becomes:

$$\mathbf{C} = \begin{bmatrix} \Gamma_1^2 + N_0, & \Gamma_1 \gamma_1 \rho_1 \\ \Gamma_1 \gamma_1 \rho_1 & \gamma_1^2 + N_0 \end{bmatrix}. \tag{4.47}$$

This implies that if both Γ_1 and γ_1 are random variables, then for example the combination of $[\Gamma_1 = \frac{1}{\sqrt{\beta}}, \gamma_1 = \frac{1}{\sqrt{\beta}}]$ and the combination of $[\Gamma_1 = \frac{\alpha}{\sqrt{\beta}}, \gamma_1 = \frac{\alpha}{\sqrt{\beta}}]$ will result in the same channel's characteristic correlation matrix $\mathbf{C}$, which imposes ambiguity for the data detection. Hence, for the cases of ADPSK/TADPSK, the first transmitted ring amplitude Γ_1 is supposed to be treated as a known term based on previous decision feedback and hence only the HDD-MSDD regime of Eq. (4.46) may be employed by the ADPSK/TADPSK detector.

Furthermore, it can be shown that the CDD introduced in Sec. 4.3 is equivalent to a suboptimal version of HDD-MSDD associated with $N_w = 2$. More explicitly, the HDD-MSDD of Eq. (4.46) may be formulated for the special case of $N_w = 2$ as:

$$\{\gamma_1, \omega_1\} = \min_{\forall \gamma_1, \forall \omega_1} \frac{(\Gamma_2^2 + N_0)\|\mathbf{Y}_1\|^2 + (\hat{\Gamma}_1^2 + N_0)\|\mathbf{Y}_2\|^2 - 2\hat{\Gamma}_1 \Gamma_2 \rho_1 \Re(\omega_1^* \psi_1^* \mathbf{Y}_2 \mathbf{Y}_1^H)}{\det(\mathbf{C})} + N_R \ln[\det(\mathbf{C})], \tag{4.48}$$

where $\hat{\Gamma}_1$ is obtained by decision feedback, while we have either $\Gamma_2 = \gamma_1 \hat{\Gamma}_1$ for the DAPSK/TDAPSK constellations (e.g. the 16-DAPSK(2,8) constellation of Figs. 4.1-4.2 and the 16-TDAPSK(2,8)

constellation of Figs. 4.4-4.5) or $\Gamma_2 = \gamma_1$ for the ADPSK/TADPSK constellations (e.g. the 16-ADPSK(2,8) constellation of Fig. 4.3 and the 16-TADPSK(2,8) constellation of Fig. 4.6). Let us now assume that the fading channel is quasi-static, i.e. we have $\rho_1 = 1$ in Eq. (4.48). Furthermore, the determinant $\det(\mathbf{C}) = (\hat{\Gamma}_1^2 + N_0)(\Gamma_2^2 + N_0) - \hat{\Gamma}_1^2\Gamma_2^2\rho_1^2$ in Eq. (4.48) is approaching zero as the noise power N_0 tends to zero, which implies that the variable γ_1 has a modest effect on the value of $\det(\mathbf{C})$ at high SNRs, and hence this term may be ignored by a sub-optimal solution. As a result, Eq, (4.48) may be further simplified for the idealistic simplifed situation of $\rho_1 = 1$ and $N_0 \approx 0$ as:

$$\{\gamma_1, \omega_1\} = \min_{\forall\gamma_1, \forall\omega_1} \|s_1\mathbf{Y}_2 - s_2\mathbf{Y}_1\|^2, \tag{4.49}$$

which may also be obtained based on the CDD's received signal model of Eq. (4.15), when dropping the time index n. Hence, we may conclude that the CDD introduced in Sec. 4.3 is equivalent to the special case of HDD-MSDD associated with $N_w = 2$ under the simplified idealistic situation of $\rho_1 = 1$ and $N_0 \approx 0$.

In summary, we have demonstrated that for MSDD aided DQAM, the channel's characteristic correlation matrix $\mathbf{C}$ of Eq. (4.44) is non-constant, which is in stark contrast to the MSDD/MSDSD aided DPSK scheme introduced in Chapter 3. Therefore, solving the detection problem associated with a non-constant $\mathbf{C}$ by a sphere decoder has been an open problem for MSDSD aided DQAM schemes. Hence, it has also been an obstacle in the way of offering a solution for MSDSD aided differential MIMO schemes using QAM [137–141]. Furthermore, since the DFDD aided DAPSK/ADPSK literature [136, 153, 154] tends to rely on the assumption of the channel's characteristic correlation matrix $\mathbf{C}$ being constant, the resultant DFDD solutions are no longer equivalent to those of the MSDD/MSDSD relying on feedback decisions. Hence their performance remains sub-optimal. We will continue by tackling these open problems in the following sections.

4.5 Hard-Decision-Aided MSDSD Conceived for Uncoded DQAM

In order to invoke SD for MSDD aided DQAM, we firstly have to rewrite the MSDD metric of Eq. (4.45), which may be referred to as the Euclidean Distance (ED). Specifically, our goal is to reformulate it as a summation of incremental metrics, so that the SD becomes capable of evaluating a single increment according to a single variable at a time. In other words, as suggested by the MSDSD aided DPSK in [127, 132], the Partial Euclidean Distance (PED) of $\{d_v = d_{v-1} + \Delta_{v-1}\}_{v=2}^{N_w}$ that may unambiguously restore the MSDD's ED has to be defined for SD. Secondly, the Schnorr-Euchner search strategy of [237] should be tailored for MSDSD aided DQAM. Thirdly, the detection of DQAM schemes that separately modulate their ring amplitude and phase may lead to a reduced-complexity search strategy, so that the reduced-cardinality subsets of ring amplitudes and M_PPSK phases may be separately visited. Let us now continue by providing further insights into these three areas.

4.5.1 Partial Euclidean Distance

First of all, the MSDD of Eq. (4.45) may be rewritten in form of the ED as:

$$\{\hat{\bar{\mathbf{A}}}, \hat{\bar{\mathbf{P}}}\} = \min_{\forall \Gamma_1} \left\{ \min_{\forall \bar{\mathbf{A}}, \forall \bar{\mathbf{P}}} \left\| \mathbf{L}^T \bar{\mathbf{O}}^H \bar{\mathbf{P}}^H \mathbf{Y} \right\|^2 + N_R \cdot \ln[\det(\mathbf{C})] \right\}, \tag{4.50}$$

where the lower triangular matrix $\mathbf{L}$ is derived from decomposition of $\mathbf{C}^{-1} = \mathbf{L}\mathbf{L}^T$. More explicitly, as a covariance matrix, $\bar{\mathbf{A}}^H \mathbf{R}_{hh} \bar{\mathbf{A}}$ of Eq. (4.44) is Hermitian positive-semidefinite, and hence $\mathbf{C} = \bar{\mathbf{A}}^H \mathbf{R}_{hh} \bar{\mathbf{A}} + N_0 \mathbf{I}_{\mathbf{N_w}}$ of Eq. (4.44) is Hermitian positive-definite. Furthermore, the matrix inversion $\mathbf{C}^{-1}$ also results in an Hermitian positive-definite matrix. Hence the lower triangular matrix $\mathbf{L}$ may be obtained by the Cholesky decomposition of $\mathbf{C}^{-1}$. As defined in Eq. (4.44), the channel's characteristic correlation matrix $\mathbf{C}$ is a variable determined by $\bar{\mathbf{A}}$ and Γ_1. As a result, $\mathbf{L}$ and $\ln[\det(\mathbf{C})]$ of Eq. (4.50) remain unknown, until the entire ring amplitude matrix $\bar{\mathbf{A}}$ is detected. In order to mitigate this problem, we conceive two propositions as follows:

Proposition 1: The first metric term $\left\| \mathbf{L}^T \bar{\mathbf{O}}^H \bar{\mathbf{P}}^H \mathbf{Y} \right\|^2$ seen in the ED of Eq. (4.50) may be represented as:

$$\begin{aligned} \left\| \mathbf{L}^T \bar{\mathbf{O}}^H \bar{\mathbf{P}}^H \mathbf{Y} \right\|^2 &= \sum_{v=1}^{N_w} \left\| \sum_{t=1}^{v} l_{N_w-t+1,N_w-v+1} \bar{\Psi}_t^* \bar{\Omega}_t^* \mathbf{Y}_t \right\|^2 \\ &= \| l_{N_w,N_w} \mathbf{Y}_1 \|^2 + \sum_{v=2}^{N_w} \left\| \sum_{t=1}^{v} l_{N_w-t+1,N_w-v+1} \bar{\Psi}_t^* \bar{\Omega}_t^* \mathbf{Y}_t \right\|^2, \end{aligned} \tag{4.51}$$

where the coefficients $\{\{l_{N_w-t+1,N_w-v+1}\}_{t=1}^{v}\}_{v=1}^{N_w}$ are elements in $\mathbf{L}$. It can be seen in Eq. (4.51) that for a specific index v, only a subset of the coefficients $\{l_{N_w-t+1,N_w-v+1}\}_{t=1}^{v}$ is required. More explicitly, the lower triangular matrix $\mathbf{L}$ in Eq. (4.50) may be expressed in the form of submatrices as:

$$\mathbf{L} = \begin{bmatrix} \widetilde{\mathbf{E}}_{\mathbf{v}} & \mathbf{0}_{N_w-v,v} \\ \widetilde{\mathbf{D}}_{\mathbf{v}} & \widetilde{\mathbf{L}}_{\mathbf{v}} \end{bmatrix}, \tag{4.52}$$

where the lower triangular submatrices $\widetilde{\mathbf{E}}_{\mathbf{v}}$ and $\widetilde{\mathbf{L}}_{\mathbf{v}}$ are of size $(N_w - v) \times (N_w - v)$ and $v \times v$, respectively, while the submatrix $\widetilde{\mathbf{D}}_{\mathbf{v}}$ and the *all-zero* submatrix $\mathbf{0}_{N_w-v,v}$ are of size $v \times (N_w - v)$ and $(N_w - v) \times v$, respectively. We will formally show below that for a specific SD index v, the coefficients $\{l_{N_w-t+1,N_w-v+1}\}_{t=1}^{v}$ may be taken from the submatrix $\widetilde{\mathbf{L}}_{\mathbf{v}}$ defined in Eq. (4.52), which may always be obtained by the Cholesky decomposition $\widetilde{\mathbf{L}}_{\mathbf{v}} \widetilde{\mathbf{L}}_{\mathbf{v}}^T = \widetilde{\mathbf{C}}_{\mathbf{v}}^{-1}$. Although $\mathbf{L}$ is unknown, the partial channel correlation matrix $\widetilde{\mathbf{C}}_{\mathbf{v}}$ may be evaluated with the aid of the SD's previous decisions concerning $\{\Gamma_t\}_{t=1}^{v-1}$ and a single variable Γ_v as:

$$\widetilde{\mathbf{C}}_{\mathbf{v}} = \begin{bmatrix} \Gamma_v^2 \rho_0 + N_0 & \Gamma_v \Gamma_{v-1} \rho_1 & \cdots & \Gamma_v \Gamma_1 \rho_{v-1} \\ \Gamma_{v-1} \Gamma_v \rho_1 & \Gamma_{v-1}^2 \rho_0 + N_0 & \cdots & \Gamma_{v-1} \Gamma_1 \rho_{v-2} \\ \vdots & \vdots & \ddots & \vdots \\ \Gamma_1 \Gamma_v \rho_{v-1} & \Gamma_1 \Gamma_{v-1} \rho_{v-2} & \cdots & \Gamma_1^2 \rho_0 + N_0 \end{bmatrix} = \begin{bmatrix} \Gamma_v^2 \rho_0 + N_0 & \widetilde{\mathbf{e}}_v^T \\ \widetilde{\mathbf{e}}_v & \widetilde{\mathbf{C}}_{\mathbf{v-1}} \end{bmatrix}, \tag{4.53}$$

where we have the $(v-1)$-element vector $\widetilde{\mathbf{e}}_v = [\Gamma_v \Gamma_{v-1} \rho_1, \ \cdots, \ \Gamma_v \Gamma_1 \rho_{v-1}]^T$.

Proof. Similar to the lower triangular matrix $\mathbf{L}$ expressed in Eq. (4.52), the Hermitian matrix $\mathbf{C}$ of Eq. (4.44) may be expressed in the form of submatrices as:

$$\mathbf{C} = \begin{bmatrix} \widetilde{\mathbf{A}}_{\mathbf{v}} & \widetilde{\mathbf{B}}_{\mathbf{v}}^{T} \\ \widetilde{\mathbf{B}}_{\mathbf{v}} & \widetilde{\mathbf{C}}_{\mathbf{v}} \end{bmatrix}, \tag{4.54}$$

where $\widetilde{\mathbf{A}}_{\mathbf{v}}$ and $\widetilde{\mathbf{B}}_{\mathbf{v}}$ are of size $(N_w - v) \times (N_w - v)$ and $v \times (N_w - v)$, respectively, while $\widetilde{\mathbf{C}}_{\mathbf{v}}$ was defined in Eq. (4.53). According to the blockwise matrix inversion property [290], the matrix inverse $\mathbf{C}^{-1}$ may be expressed as:

$$\mathbf{C}^{-1} = \begin{bmatrix} \widetilde{\mathbf{Q}}_{\mathbf{v}} & -\widetilde{\mathbf{Q}}_{\mathbf{v}}\widetilde{\mathbf{B}}_{\mathbf{v}}^{T}\widetilde{\mathbf{C}}_{\mathbf{v}}^{-1} \\ -\widetilde{\mathbf{C}}_{\mathbf{v}}^{-1}\widetilde{\mathbf{B}}_{\mathbf{v}}\widetilde{\mathbf{Q}}_{\mathbf{v}} & \widetilde{\mathbf{C}}_{\mathbf{v}}^{-1}\widetilde{\mathbf{B}}_{\mathbf{v}}\widetilde{\mathbf{Q}}_{\mathbf{v}}\widetilde{\mathbf{B}}_{\mathbf{v}}^{T}\widetilde{\mathbf{C}}_{\mathbf{v}}^{-1} + \widetilde{\mathbf{C}}_{\mathbf{v}}^{-1} \end{bmatrix}, \tag{4.55}$$

where $\widetilde{\mathbf{Q}}_{\mathbf{v}} = \left(\widetilde{\mathbf{A}}_{\mathbf{v}} - \widetilde{\mathbf{B}}_{\mathbf{v}}^{T}\widetilde{\mathbf{C}}_{\mathbf{v}}^{-\mathbf{1}}\widetilde{\mathbf{B}}_{\mathbf{v}}\right)^{-1}$ is a Hermitian matrix, because both $\widetilde{\mathbf{A}}_{\mathbf{v}}$ and $\widetilde{\mathbf{C}}_{\mathbf{v}}^{-1}$ are Hermitian matrices. According to $\mathbf{L}\mathbf{L}^{T} = \mathbf{C}^{-1}$, we have the following relationships based on Eqs. (4.52) and (4.55):

$$\widetilde{\mathbf{E}}_{\mathbf{v}}\widetilde{\mathbf{E}}_{\mathbf{v}}^{T} = \widetilde{\mathbf{Q}}_{\mathbf{v}}, \tag{4.56a}$$

$$\widetilde{\mathbf{D}}_{\mathbf{v}}\widetilde{\mathbf{E}}_{\mathbf{v}}^{T} = -\widetilde{\mathbf{C}}_{\mathbf{v}}^{-1}\widetilde{\mathbf{B}}_{\mathbf{v}}\widetilde{\mathbf{Q}}_{\mathbf{v}}, \tag{4.56b}$$

$$\widetilde{\mathbf{D}}_{\mathbf{v}}\widetilde{\mathbf{D}}_{\mathbf{v}}^{T} + \widetilde{\mathbf{L}}_{\mathbf{v}}\widetilde{\mathbf{L}}_{\mathbf{v}}^{T} = \widetilde{\mathbf{C}}_{\mathbf{v}}^{-1}\widetilde{\mathbf{B}}_{\mathbf{v}}\widetilde{\mathbf{Q}}_{\mathbf{v}}\widetilde{\mathbf{B}}_{\mathbf{v}}^{T}\widetilde{\mathbf{C}}_{\mathbf{v}}^{-1} + \widetilde{\mathbf{C}}_{\mathbf{v}}^{-1}, \tag{4.56c}$$

which leads to the following conclusions:

$$\widetilde{\mathbf{D}}_{\mathbf{v}} = -\widetilde{\mathbf{C}}_{\mathbf{v}}^{-1}\widetilde{\mathbf{B}}_{\mathbf{v}}\widetilde{\mathbf{E}}_{\mathbf{v}}, \tag{4.57a}$$

$$\widetilde{\mathbf{D}}_{\mathbf{v}}\widetilde{\mathbf{D}}_{\mathbf{v}}^{T} = \widetilde{\mathbf{C}}_{\mathbf{v}}^{-1}\widetilde{\mathbf{B}}_{\mathbf{v}}\widetilde{\mathbf{Q}}_{\mathbf{v}}\widetilde{\mathbf{B}}_{\mathbf{v}}^{T}\widetilde{\mathbf{C}}_{\mathbf{v}}^{-1}, \tag{4.57b}$$

$$\widetilde{\mathbf{L}}_{\mathbf{v}}\widetilde{\mathbf{L}}_{\mathbf{v}}^{T} = \widetilde{\mathbf{C}}_{\mathbf{v}}^{-1}. \tag{4.57c}$$

Therefore, the lower triangular submatrix $\widetilde{\mathbf{L}}_{\mathbf{v}}$ may be obtained from the Cholesky decomposition of $\widetilde{\mathbf{C}}_{\mathbf{v}}^{-1}$. □

Proposition 2: We propose that the second metric term $\ln[\det(\mathbf{C})]$ seen in the ED expression of Eq. (4.50) may be evaluated as:

$$\ln[\det(\mathbf{C})] = \ln\left(\Gamma_1^2\rho_0 + N_0\right) + \sum_{v=2}^{N_w} \ln[\left(\Gamma_v^2\rho_0 + N_0\right) - \widetilde{\mathbf{e}}_v^{T}\widetilde{\mathbf{C}}_{\mathbf{v-1}}^{-1}\widetilde{\mathbf{e}}_v]. \tag{4.58}$$

Proof. According to the Leibniz formula [290], the determinant of $\widetilde{\mathbf{C}}_{\mathbf{v}}$ in Eq. (4.53) may be evaluated by $\det(\widetilde{\mathbf{C}}_{\mathbf{v}}) = \det(\widetilde{\mathbf{C}}_{\mathbf{v-1}})[(\Gamma_v^2\rho_0 + N_0) - \widetilde{\mathbf{e}}_v^{T}\widetilde{\mathbf{C}}_{\mathbf{v-1}}^{-1}\widetilde{\mathbf{e}}_v]$. Therefore, the complete determinant term $\ln[\det(\mathbf{C})]$ may be calculated from the initial term that is associated with the index $v = 1$ as $\ln[\det(\widetilde{\mathbf{C}}_{\mathbf{1}})] = \ln\left(\Gamma_1^2\rho_0 + N_0\right)$, in addition to the summation of all incremental terms $\sum_{v=2}^{N_w} \ln[\left(\Gamma_v^2\rho_0 + N_0\right) - \widetilde{\mathbf{e}}_v^{T}\widetilde{\mathbf{C}}_{\mathbf{v-1}}^{-1}\widetilde{\mathbf{e}}_v]$. □

As a result, the MSDD's task of finding the minimum ED expressed in Eq. (4.50) may be solved

by a SD. In more detail, the SD's PED based on Eqs. (4.51) and (4.58) may be defined as:

$$\begin{aligned} d_v &= \|l_{N_w,N_w}\mathbf{Y}_1\|^2 + N_R \cdot \ln\left(\Gamma_1^2\rho_0 + N_0\right) + \sum_{\bar{v}=2}^{v}\left\|\sum_{t=1}^{\bar{v}} l_{N_w-t+1,N_w-\bar{v}+1}\bar{\Psi}_t^*\bar{\Omega}_t^*\mathbf{Y}_t\right\|^2 \\ &\quad + N_R \cdot \sum_{\bar{v}=2}^{v}\ln\left[\left(\Gamma_{\bar{v}}^2\rho_0 + N_0\right) - \widetilde{\mathbf{e}}_{\bar{v}}^T\widetilde{\mathbf{C}}_{\bar{\mathbf{v}}-\mathbf{1}}^{-1}\widetilde{\mathbf{e}}_{\bar{v}}\right] \\ &= d_{v-1} + \Delta_{v-1}. \end{aligned} \tag{4.59}$$

This implies that at each SD's tree-search parent node associated with index v, the SD may test the child nodes regarding their PED increment values Δ_{v-1} of Eq. (4.59), which is given by:

$$\begin{aligned} \Delta_{v-1} &= \left\|l_{N_w-v+1,N_w-v+1}\bar{\Psi}_{v-1}^*\bar{\Omega}_{v-1}^*\mathbf{Y}_v + \omega_{v-1}\psi_{v-1}\left(\sum_{t=1}^{v-1} l_{N_w-t+1,N_w-v+1}\bar{\Psi}_t^*\bar{\Omega}_t^*\mathbf{Y}_t\right)\right\|^2 + \Xi_v \\ &= \left\|\widetilde{l}_{1,1}\bar{\Psi}_{v-1}^*\bar{\Omega}_{v-1}^*\mathbf{Y}_v + \omega_{v-1}\psi_{v-1}\left(\sum_{t=1}^{v-1}\widetilde{l}_{v-t+1,1}\bar{\Psi}_t^*\bar{\Omega}_t^*\mathbf{Y}_t\right)\right\|^2 + \Xi_v, \end{aligned} \tag{4.60}$$

where the coefficients $\{\widetilde{l}_{v-t+1,1}\}_{t=1}^{v}$ are elements in the $(v \times v)$ lower triangular submatrix $\widetilde{\mathbf{L}}_{\mathbf{v}}$ defined in Eq. (4.52). According to Proposition 1, we always have $\{l_{N_w-t+1,N_w-v+1} = \widetilde{l}_{v-t+1,1}\}_{t=1}^{v}$. The previous ring amplitudes $\{\Gamma_t\}_{t=1}^{v-1}$ in $\widetilde{\mathbf{C}}_{\mathbf{v}}$ of Eq. (4.53) are known from previous SD search, and hence there is a total of M_A candidates for Γ_v, which determines M_A candidates for $\widetilde{\mathbf{L}}_{\mathbf{v}}$. The previous ring-amplitude-dependent phase rotations $\{\Psi_t\}_{t=1}^{v-1}$ and the variable term ψ_{v-1} are also uniquely and unambiguously determined by the previous decisions $\{\Gamma_t\}_{t=1}^{v-1}$ and the variable Γ_v, respectively. Moreover, the previous M_PPSK phases $\{\bar{\Omega}_t\}_{t=1}^{v-1}$ have also been decided by the previous SD steps. As a result, there are a total of M_P candidates for ω_{v-1} in Eq. (4.60). Furthermore, the determinant term Ξ_v in Eq. (4.60) is given by:

$$\Xi_v = N_R \cdot \ln\left[\left(\Gamma_v^2\rho_0 + N_0\right) - \widetilde{\mathbf{e}}_v^T\widetilde{\mathbf{C}}_{\mathbf{v}-\mathbf{1}}^{-1}\widetilde{\mathbf{e}}_v\right] - \xi_{v-1}. \tag{4.61}$$

In order to guarantee that all the PED increments of Eq. (4.60) have positive values, an extra constant ξ_{v-1} is introduced in Eq. (4.61), which is defined as:

$$\xi_{v-1} = \min_{\forall\{\Gamma_t\}_{t=1}^{v}} N_R \cdot \ln\left[\left(\Gamma_v^2\rho_0 + N_0\right) - \widetilde{\mathbf{e}}_v^T\widetilde{\mathbf{C}}_{\mathbf{v}-\mathbf{1}}^{-1}\widetilde{\mathbf{e}}_v\right]. \tag{4.62}$$

This constant is pre-evaluated and pre-stored before performing MSDSD. We note that adding a constant of $(\sum_{v=2}^{N_w} -\xi_{v-1})$ to the MSDD metric of Eq. (4.50) does not impose any performance difference. The only variable in the determinant term Ξ_v of Eq. (4.61) is Γ_v, and hence there are a total of M_A candidates for Ξ_v.

4.5.2 Schnorr-Euchner Search Strategy

In summary, the MSDSD algorithm [127, 132] summarized in Tables 3.1 and 3.3 may be invoked for DQAM detection based on the PED defined in Eq. (4.59). In fact, according to the Schnorr-Euchner [237] search strategy used by MSDSD, the SD associated with a specific index v has

subfunction:	$[\{\Delta_{v-1}^{\bar{m}}\}_{\bar{m}=0}^{M-1}, \{x_{v-1}^{\bar{m}}\}_{\bar{m}=0}^{M-1}, n_{v-1}] =$ **sortDelta**$(\{\mathbf{Y}_t\}_{t=1}^{v}, \{\hat{\Gamma}_t\}_{t=1}^{v-1}, \{\hat{\Psi}_t\}_{t=1}^{v-1}, \{\hat{\Omega}_t\}_{t=1}^{v-1})$
input:	$\{\mathbf{Y}_t\}_{t=1}^{v}$ refer to received signal vectors. $\{\hat{\Gamma}_t\}_{t=1}^{v-1}$, $\{\hat{\Psi}_t\}_{t=1}^{v-1}$ and $\{\hat{\Omega}_t\}_{t=1}^{v-1}$ are SD's previous decisions.
output:	$\{\Delta_{v-1}^{\overline{m}}\}_{\overline{m}=1}^{M}$ and $\{x_{v-1}^{\overline{m}}\}_{\overline{m}=1}^{M}$ are the sorted PED increments and their corresponding constellation points. n_{v-1} is SD's child node counter.
require:	$\{\widetilde{l}_{v-t+1,1}\}_{t=1}^{v}$ in Eq. (4.60) are taken from $\widetilde{\mathbf{L}}(\{\hat{\Gamma}_t\}_{t=1}^{v-1}, \Gamma_v) = \widetilde{\mathbf{L}}_{\mathbf{v}}$, which are pre-evaluated and pre-stored. $\Xi(\{\hat{\Gamma}_t\}_{t=1}^{v-1}, \Gamma_v) = \Xi_v$ in Eq. (4.60) are also pre-evaluated and pre-stored.

1:	**for** m=0 **to** $M-1$	//visit all M child nodes.
2:	(DAPSK/TDAPSK:) $\Gamma_v = \gamma_{v-1}^{a} \cdot \hat{\Gamma}_{v-1}$ (ADPSK/TADPSK:) $\Gamma_v = \gamma_{v-1}^{a}$	//visit $x_{v-1}^{m} = \gamma_{v-1}^{a} \cdot \omega_{v-1}^{p} \cdot \psi_{v-1}^{a}$.
3:	$\Delta_{v-1}^{m} = \|\widetilde{l}_{1,1}\hat{\Psi}_{v-1}^{*}\hat{\Omega}_{v-1}^{*}\mathbf{Y}_v + \omega_{v-1}^{p}\psi_{v-1}^{a}(\sum_{t=1}^{v-1}\widetilde{l}_{v-t+1,1}\hat{\Psi}_t^{*}\hat{\Omega}_t^{*}\mathbf{Y}_t)\|^2 + \Xi(\{\hat{\Gamma}_t\}_{t=1}^{v-1}, \Gamma_v)$	//evaluate PED increments of Eq. (4.60).
4:	**end for**	
5:	$n_{v-1} = 0$	//initialize child node counter.
6:	$[\{\Delta_{v-1}^{\bar{m}}\}_{\bar{m}=0}^{M-1}, \{x_{v-1}^{\bar{m}}\}_{\bar{m}=0}^{M-1}] =$ **sort**$(\{\Delta_{v-1}^{m}\}_{m=0}^{M-1})$	//sort PED increments in increasing order.

Table 4.8: Pseudo-code for the Schnorr-Euchner search strategy tailored for hard-decision-aided MSDSD conceived for uncoded DQAM.

to sort all the M candidates Δ_{v-1} of Eq. (4.60) according to their increasing values. Therefore, the MSDSD algorithm of [132] summarized in Table 3.3 should be invoked for hard-decision-aided MSDSD conceived for uncoded differential nonconstant modulus constellations, where the Schnorr-Euchner search strategy is summarized in Table 4.8.

Once again, we note that the subscript $m \in \{0, \cdots, M-1\}$ represents the data-carrying Gray coded constellation point indices which may be directly translated to binary source bits. Furthermore, the subscript $\overline{m} \in \{\overline{0}, \cdots, \overline{M-1}\}$ represents the constellation point index ordered according to the increasing values of PED increment Δ_{v-1}.

Similar to the pseudo-code presented in [132] and summarized in Table 4.8, the MSDSD may start with the initial PED $d_1 = 0$ for the sake of simplicity, but the Γ_1-related term $d_1 = \|l_{N_w,N_w}\mathbf{Y}_1\|^2 + N_R \cdot \ln\left(\Gamma_1^2\rho_0 + N_0\right)$ should be added to the SD's output radius before the ED comparisons carried out over Γ_1 in Eq. (4.50). Therefore, the complexity of the MSDSD algorithm of [132] relying on Eq. (4.50) using the PED increment Δ_{v-1} of Eq. (4.60) is lower-bounded by the order of $O\left[M_A \cdot M \cdot (N_w - 1)\right]$. Furthermore, when the first transmitted ring amplitude $\hat{\Gamma}_1$ is fed back from the previous MSDSD decision, then a Hard-Decision-Directed MSDSD (HDD-MSDSD) implementing the HDD-MSDD of Eq. (4.46) may be completed by using the same PED increment Δ_{v-1} of Eq. (4.60). Its complexity order is lower-bounded by $O\left[M \cdot (N_w - 1)\right]$.

It is worth noting that all the candidates of $\widetilde{\mathbf{L}}_{\mathbf{v}}$ and Ξ_v over $\{\Gamma_t\}_{t=1}^{v}$ seen in Eq. (4.60) may be pre-evaluated and pre-stored before MSDSD. There is a total number of $\sum_{v=1}^{N_w} M_A^v$ candidates for $\widetilde{\mathbf{L}}_{\mathbf{v}}$ and Ξ_v stored in memory. As a special case of DAPSK associated with $M_A = 1$, the DPSK schemes only have to evaluate and store a single candidate for the constant $\widetilde{\mathbf{L}}_{\mathbf{N_w}} = \mathbf{L}$ in memory. The memory required for storing $\widetilde{\mathbf{L}}_{\mathbf{v}}$ and Ξ_v is small compared to that of MSDD. Furthermore, the evaluation of $\widetilde{\mathbf{L}}_{\mathbf{v}}$ and Ξ_v should not be added to the MSDSD complexity, since they remain fixed as long as the constellation, the noise power N_0, the normalized Doppler frequency f_d and the MSDSD window length N_w are fixed.

4.5.3 Reduced-Complexity MSDSD Algorithm

When DQAM$^{\text{JM}}$ is employed, the Schnorr-Euchner search strategy of Table 4.8, which exhaustively visits and ranks all M constellation points is the only choice. However, a reduced-complexity search strategy should be conceived for detecting DQAM constellations including DAPSK, ADPSK, TDAPSK and TADPSK, which modulates the data-carrying ring amplitude and the data-carrying M_PPSK phase independently, with the motivation of visiting the subsets of both the ring amplitude and M_PPSK phase candidates separately. In order to achieve this goal, we separate the PED increment of Eq. (4.60) into two terms as:

$$\Delta_{v-1} = \Delta_{v-1}^{\Gamma} + \Delta_{v-1}^{\omega|\Gamma}, \tag{4.63}$$

where the ring-amplitude-related term is given by:

$$\Delta_{v-1}^{\Gamma} = \left\| \widetilde{l}_{1,1} \bar{\Psi}_{v-1}^{*} \bar{\Omega}_{v-1}^{*} \mathbf{Y}_v \right\|^2 + \left\| \sum_{t=1}^{v-1} \widetilde{l}_{v-t+1,1} \bar{\Psi}_{t}^{*} \bar{\Omega}_{t}^{*} \mathbf{Y}_t \right\|^2 + \Xi_v, \tag{4.64}$$

and Δ_{v-1}^{Γ} only has M_A candidates over the single variable Γ_v. Moreover, the M_PPSK-related term conditioned on the ring amplitude $\Delta_{v-1}^{\omega|\Gamma}$ in Eq. (4.63) is given by:

$$\begin{aligned} \Delta_{v-1}^{\omega|\Gamma} &= 2\Re\left[\widetilde{l}_{1,1} \bar{\Psi}_{v-1}^{*} \bar{\Omega}_{v-1}^{*} \mathbf{Y}_v \omega_{v-1}^{*} \psi_{v-1}^{*} \left(\sum_{t=1}^{v-1} \widetilde{l}_{v-t+1,1} \bar{\Psi}_{t}^{*} \bar{\Omega}_{t}^{*} \mathbf{Y}_t \right)^{H} \right] \\ &= -2\Re(\omega_{v-1}^{*} z_{v-1}^{\omega|\Gamma}), \end{aligned} \tag{4.65}$$

where the decision variable is formulated as:

$$\begin{aligned} z_{v-1}^{\omega|\Gamma} &= -\widetilde{l}_{1,1} \psi_{v-1}^{*} \bar{\Psi}_{v-1}^{*} \bar{\Omega}_{v-1}^{*} \mathbf{Y}_v \left(\sum_{t=1}^{v-1} \widetilde{l}_{v-t+1,1} \bar{\Psi}_{t}^{*} \bar{\Omega}_{t}^{*} \mathbf{Y}_t \right)^{H} \\ &= \mathbf{Y}_{v-1}^{\text{SD}} (\mathbf{H}_{v-1}^{\text{SD}})^{H}. \end{aligned} \tag{4.66}$$

The N_R-element vectors $\mathbf{Y}_{v-1}^{\text{SD}} = \widetilde{l}_{1,1} \psi_{v-1}^{*} \bar{\Psi}_{v-1}^{*} \bar{\Omega}_{v-1}^{*} \mathbf{Y}_v$ and $\mathbf{H}_{v-1}^{\text{SD}} = -\sum_{t=1}^{v-1} \widetilde{l}_{v-t+1,1} \bar{\Psi}_{t}^{*} \bar{\Omega}_{t}^{*} \mathbf{Y}_t$ seen in Eq. (4.66) may be interpreted as the equivalent "received signal vector" and the equivalent "fading channel vector" formulated for detecting the M_PPSK variable of ω_{v-1} in Eq. (4.65).

When the ring amplitude Γ_v is assumed to be fixed, the lower triangular matrix specific elements $\{\widetilde{l}_{v-t+1,1}\}_{t=1}^{v}$ and the ring-amplitude-dependent phase rotation ψ_{v-1} of Eq. (4.65) are given, hence there are M_P $\Delta_{v-1}^{\omega|\Gamma}$ candidates over the single variable ω_{v-1}. Therefore, given a specific ring amplitude candidate Γ_v, finding the local minimum $\Delta_{v-1}^{\omega|\Gamma}$ of Eq. (4.65) over all the M_P phase candidates of ω_{v-1} is equivalent to minimizing $|z_{v-1}^{\omega|\Gamma} - \omega_{v-1}|^2 = |z_{v-1}^{\omega|\Gamma}|^2 + 1 - 2\Re(\omega_{v-1}^{*} z_{v-1}^{\omega|\Gamma})$, where $|z_{v-1}^{\omega|\Gamma}|^2 + 1$ is a constant. As a result, the decision variable $z_{v-1}^{\omega|\Gamma}$ of Eq. (4.66) may be directly used for detecting the M_PPSK variable ω_{v-1}.

More explicitly, the locally optimum M_PPSK candidate associated with a specific ring amplitude Γ_v is directly given by $\omega_{v-1} = \exp(j\frac{2\pi}{M_P}\check{p})$, where $\check{p} = \lfloor \frac{M_P}{2\pi} \angle z_{v-1}^{\omega|\Gamma} \rceil$, and the remaining local M_PPSK candidates associated with the same Γ_v may be visited later in a zigzag fashion by the SD in

subfunction: $[\{\Delta_{v-1}^{\Gamma^a}\}_{a=0}^{M_A-1}, \{z_{v-1}^{\omega|\Gamma^a}\}_{a=0}^{M_A-1}, \{\check{p}_{v-1}^{a}\}_{a=0}^{M_A-1}, \{\text{step}_{v-1}^{a}\}_{a=0}^{M_A-1}, \{\Delta_{v-1}^{a}\}_{a=0}^{M_A-1}, \{n_{v-1}^{a}\}_{a=0}^{M_A-1}, \Delta_{v-1}, \hat{a}_{v-1}, n_{v-1}]$
$= \textbf{findBest}(\{\mathbf{Y}_t\}_{t=1}^{v}, \{\hat{\Gamma}_t\}_{t=1}^{v-1}, \{\hat{\Psi}_t\}_{t=1}^{v-1}, \{\hat{\Omega}_t\}_{t=1}^{v-1})$

output: $\{\Delta_{v-1}^{\Gamma^a}\}_{a=0}^{M_A-1}$, $\{z_{v-1}^{\omega|\Gamma^a}\}_{a=0}^{M_A-1}$, $\{\check{p}_{v-1}^{a}\}_{a=0}^{M_A-1}$, $\{\text{step}_{v-1}^{a}\}_{a=0}^{M_A-1}$, $\{\Delta_{v-1}^{a}\}_{a=0}^{M_A-1}$ and $\{n_{v-1}^{a}\}_{a=0}^{M_A-1}$ are local minimum parameters. Δ_{v-1}, $\hat{a}_{v-1}$ and n_{v-1} are global minimum parameters.

1: $\Delta_{v-1} = \inf$ //initialize Δ_{v-1} to be a sufficiently large number.
2: **for** $a = 0$ **to** $(M_A - 1)$ //visit all M_A local minimums.
3: (DAPSK/TDAPSK:) $\Gamma_v = \gamma_{v-1}^{a} \cdot \hat{\Gamma}_{v-1}$ //fix the specific Γ_v for $\widetilde{\mathbf{L}}_{\mathbf{v}}$ and Ξ_v.
(ADPSK/TADPSK:) $\Gamma_v = \gamma_{v-1}^{a}$
4: $\mathbf{Y}_{v-1}^{\text{SD}} = \widetilde{l}_{1,1}(\psi_{v-1}^{a})^{*}\hat{\Psi}_{v-1}^{*}\hat{\Omega}_{v-1}^{*}\mathbf{Y}_v$ //update$\mathbf{Y}_{v-1}^{\text{SD}}$ according to Eq. (4.66).
5: $\mathbf{H}_{v-1}^{\text{SD}} = -\sum_{t=1}^{v-1}\widetilde{l}_{v-t+1,1}\hat{\Psi}_t^{*}\hat{\Omega}_t^{*}\mathbf{Y}_t$ //update$\mathbf{H}_{v-1}^{\text{SD}}$ according to Eq. (4.66).
6: $\Delta_{v-1}^{\Gamma^a} = \|\mathbf{Y}_{v-1}^{\text{SD}}\|^2 + \|\mathbf{H}_{v-1}^{\text{SD}}\|^2 + \Xi(\{\hat{\Gamma}_t\}_{t=1}^{v-1}, \Gamma_v)$ //evaluate ring-amplitude-related term of Eq. (4.64).
7: $z_{v-1}^{\omega|\Gamma^a} = \mathbf{Y}_{v-1}^{\text{SD}}(\mathbf{H}_{v-1}^{\text{SD}})^{H}$ //evaluate M_PPSK-related decision variable of Eq. (4.66).
8: $\widetilde{p} = \frac{M_P}{2\pi}\angle z_{v-1}^{\omega|\Gamma^a}$ //update the local optimum M_PPSK candidate.
9: $\check{p}_{v-1}^{a} = \lfloor \widetilde{p} \rceil$
10: $\text{step}_{v-1}^{a} = \text{sign}(\widetilde{p} - \check{p}_{v-1}^{a})$ //store step size for the next child node.
11: $\Delta_{v-1}^{\omega|\Gamma^a} = -2\Re[\exp(-j\frac{2\pi}{M_P}\check{p}_{v-1}^{a}) \cdot z_{v-1}^{\omega|\Gamma^a}]$ //update local M_PPSK-related term of Eq. (4.65).
12: $\Delta_{v-1}^{a} = \Delta_{v-1}^{\Gamma^a} + \Delta_{v-1}^{\omega|\Gamma^a}$ //update local minimum.
13: **if** $\Delta_{v-1}^{a} < \Delta_{v-1}$ //update global minimum parameters.
14: $\Delta_{v-1} = \Delta_{v-1}^{a}$
15: $\hat{a}_{v-1} = a$ //update ring amplitude index.
16: **end if**
17: $n_{v-1}^{a} = 0$ //initialize M_PPSK counter.
18: **end for**
19: $n_{v-1} = 0$ //initialize child node counter.

subfunction: $[\{\check{p}_{v-1}^{a}\}_{a=0}^{M_A-1}, \{\text{step}_{v-1}^{a}\}_{a=0}^{M_A-1}, \{\Delta_{v-1}^{a}\}_{a=0}^{M_A-1}, \{n_{v-1}^{a}\}_{a=0}^{M_A-1}, \Delta_{v-1}, \hat{a}_{v-1}, n_{v-1}]$
$= \textbf{findNext}(\{\Delta_{v-1}^{\Gamma^a}\}_{a=0}^{M_A-1}, \{z_{v-1}^{\omega|\Gamma^a}\}_{a=0}^{M_A-1}, \{\check{p}_{v-1}^{a}\}_{a=0}^{M_A-1}, \{\text{step}_{v-1}^{a}\}_{a=0}^{M_A-1}, \{\Delta_{v-1}^{a}\}_{a=0}^{M_A-1}, \{n_{v-1}^{a}\}_{a=0}^{M_A-1}, \hat{a}_{v-1}, n_{v-1})$

1: $\hat{a} = \hat{a}_{v-1}$ //update the previously visited ring amplitude index
2: $n_{v-1}^{\hat{a}} = n_{v-1}^{\hat{a}} + 1$ //update the local child node counter
3: **if** $n_{v-1}^{\hat{a}} < M_P$ //visit the next local M_PPSK candidate associated with $\hat{a}$
4: $\check{p}_{v-1}^{\hat{a}} = \check{p}_{v-1}^{\hat{a}} + \text{step}_{v-1}^{\hat{a}}$
5: $\text{step}_{v-1}^{\hat{a}} = -\text{step}_{v-1}^{\hat{a}} - \text{sign}(\text{step}_{v-1}^{\hat{a}})$
6: $\Delta_{v-1}^{\hat{a}} = \Delta_{v-1}^{\Gamma_{\hat{a}}} - 2\Re[\exp(-j\frac{2\pi}{M_P}\check{p}_{v-1}^{\hat{a}}) \cdot z_{v-1}^{\omega|\Gamma_{\hat{a}}}]$
7: **end if**
8: $\Delta_{v-1} = \inf$
9: **for** $a = 0$ **to** $(M_A - 1)$ //update the next global child node
10: **if** $n_{v-1}^{a} < M_P$ **and** $\Delta_{v-1}^{a} < \Delta_{v-1}$
11: $\Delta_{v-1} = \Delta_{v-1}^{a}$
12: $\hat{a}_{v-1} = a$
13: **end if**
14: **end for**
15: $n_{v-1} = n_{v-1} + 1$ //update the global child node counter

Table 4.9: Pseudo-code for the reduced-complexity Schnorr-Euchner search strategy tailored for the hard-decision-aided MSDSD conceived for uncoded DQAM schemes which modulate the data-carrying ring amplitude and the data-carrying M_PPSK phase separately.

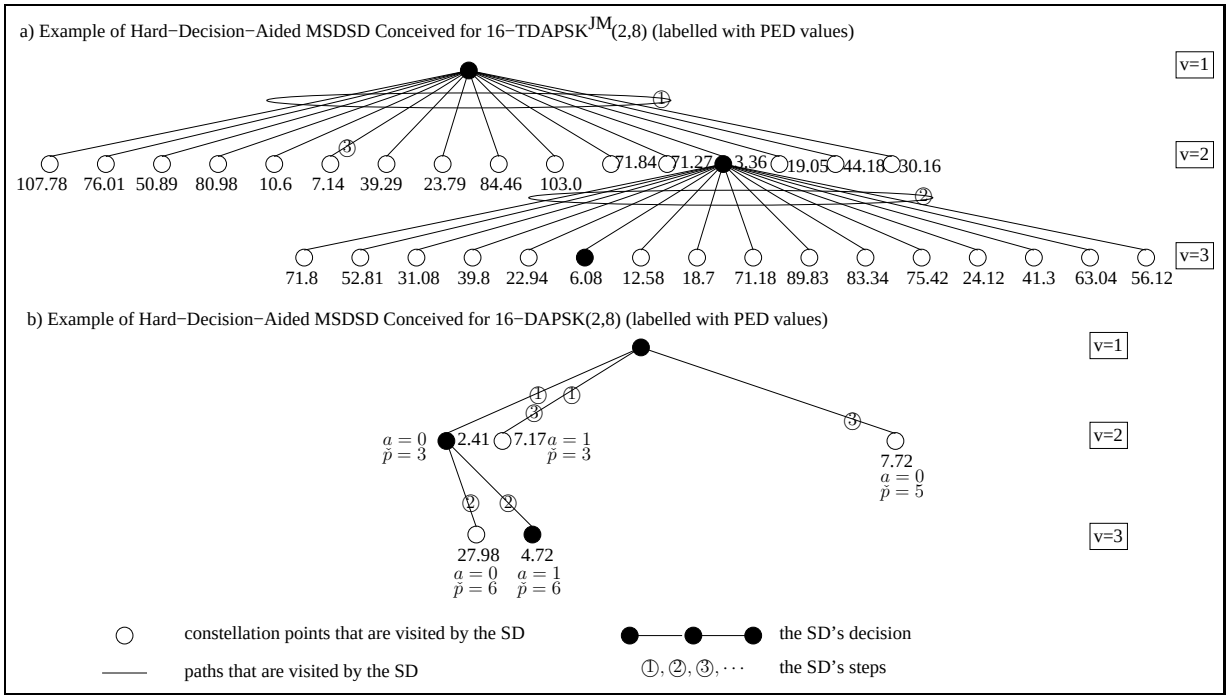

Figure 4.10: Example of hard-decision-aided MSDSD conceived for 16-TDAPSK$^{\text{JM}}$(2,8) and reduced-complexity hard-decision-aided MSDSD conceived for 16-DAPSK(2,8) recorded at SNR=15 dB, where we have $N_R = 2$ and $N_w = 3$.

the same way as the Schnorr-Euchner search strategy conceived for MSDSD aided uncoded DPSK seen in Table 3.1 and [127]. Once the local M_PPSK candidates related to each Γ_v have been determined by the SD, the globally minimum PED increment may be found by comparing the M_A local minimum candidates for Δ_{v-1} of Eq. (4.63) over the variable Γ_v. The detailed Schnorr-Euchner search strategy conceived for reduced-complexity MSDSD aided uncoded DQAM is summarized in form of its pseudo-code in Table 4.9, which is in a similar form to that of the strategy seen in Table 3.1 and [127] that was conceived for DPSK detection.

Observe in Table 4.9 that the "findBest" subfunction evaluates M_A PED increments for M_A candidate child nodes, while the "findNext" subfunction evaluates only a single new PED increment until all the local child nodes have been checked. Therefore, the reduced-complexity hard-decision-aided MSDSD using Table 4.9 has a complexity lower bound of $O\{M_A[M_A(N_w-1)+(N_w-2)]\}$. Furthermore, when the first transmitted ring amplitude of $\hat{\Gamma}_1$ is fed back from the previous MSDSD decisions, the HDD-MSDSD implementing the HDD-MSDD regime of Eq. (4.46) exhibits a complexity lower bound of $O\left[M_A(N_w-1)+(N_w-2)\right]$.

As mentioned, the reduced-complexity design introduced earlier in this section can only be applied to the constellations, which independently modulate the data-carrying ring amplitude and the data-carrying M_PPSK phase at the DQAM transmitter. As a result, when the DQAM schemes associated with joint bit-to-symbol mapping to the ring amplitude and phase are employed as introduced in Sec. 4.2.4, the conventional MSDSD using the Schnorr-Euchner search strategy of Table 4.8 may

exhibit a higher detection complexity, owing to the fact that all the M candidate child nodes have to be visited by the SD.

An example of the MSDSD aided 16-TDAPSK^{JM}(2,8) of Fig. 4.7 using the conventional Schnorr-Euchner search strategy of Table 4.8 is portrayed in Fig. 4.10-a). Specifically. Fig. 4.10-a) shows that for the MSDSD aided 16-TDAPSK^{JM}(2,8) detection, the "sortDelta" subfunction of Table 4.8 has to evaluate and compare all $(M = 16)$ PED increment values Δ_{v-1} of Eq. (4.60) by visiting all the $(M = 16)$ constellation points, when the SD visits the indices $v = 2$ and $v = 3$ for the first time in Step ① and Step ②, respectively. The PED $d_v = d_{v-1} + \Delta_{v-1}$ defined in Eq. (4.59) may be updated, when the SD increases or decreases its index v. After a valid MSDSD solution is found at the SD index $v = 3$ in Step ②, the SD radius is updated to the corresponding ED of $d = 6.08$. For Step ③, the SD decreases its index to $v = 2$ in order to visit the second-best candidate, whose PED value of $d_2 = 7.14$ turns out to be higher than the SD radius. Hence the SD index may be decreased to $v = 1$, which terminates the search.

By contrast, an example of the reduced-complexity MSDSD assisted 16-DAPSK(2,8) of Figs. 4.1-4.2 using the simplified Schnorr-Euchner search strategy of Table 4.9 is further portrayed in Fig. 4.10-b). In more detail, Fig. 4.10-b) shows that when the SD visits index $v = 2$ for the first time in Step ①, the "findBest" subfunction of Table 4.9 firstly evaluates the decision variables $\{z_{v-1}^{\omega|\Gamma^a}\}_{a=0}^{1}$ of Eq. (4.66) associated with the two ring amplitudes, and then the two locally best phase indices are directly given by $\{\check{p} = \lfloor \frac{M_P}{2\pi} \angle z_{v-1}^{\omega|\Gamma^a} \rceil\}_{a=0}^{1}$. The PED increments for these two locally best candidates associated with the ring amplitude index and the phase index of $(a = 0, \check{p} = 3)$ as well as those of $(a = 1, \check{p} = 3)$ are evaluated according to Eq. (4.63), and the candidate of $(a = 0, \check{p} = 3)$ is chosen as the best candidate for $v = 2$, which has the globally minimum PED value of $d_2 = 2.41$, where the PED value of $d_v = d_{v-1} + \Delta_{v-1}$ is updated according to Eq. (4.59). Then the SD may increase its index to $v = 3$ in Step ②, and the same "findBest" subfunction of Table 4.9 may be invoked. After a valid MSDSD solution is found at SD index $v = 3$ in Step ②, the SD radius is updated to the corresponding ED of $d = 4.72$. Following this, the SD index is decreased to $v = 2$, where the "findNext" subfunction of Table 4.9 may be invoked for checking the second-best candidate for $v = 2$. This also requires a local phase candidate for each ring amplitude index. Since the constellation point of $(a = 0, \check{p} = 3)$ was previously chosen as the globally optimum for $v = 2$, the next local phase candidate associated with the ring amplitude index $a = 0$ has to be visited in a zig-zag fashion. There are two adjacent phase candidates associated with the indices of $\check{p} = 3$ and $\check{p} = 5$ according to the constellation of Fig. 4.2. Since $\angle z_{v-1}^{\omega|\Gamma^0}$ is closer to the latter in this case, hence $(a = 0, \check{p} = 5)$ is the local candidate associated with $a = 0$. Furthermore, since $(a = 1, \check{p} = 3)$ was not selected by the SD for the globally best candidate, it can still be the local candidate for the second-best. In summary, the "findNext" subfunction of Table 4.9 may now find the second-best candidate by comparing the local candidates of $(a = 0, \check{p} = 5)$ and $(a = 1, \check{p} = 3)$, and the latter is chosen as a benefit of its lower PED value of $d_2 = 7.17$. However, this PED is already higher than the SD sphere radius. Therefore, the SD may further reduce its index to $v = 1$ and terminate its search.

In summary, the comparison example of Fig. 4.10 clearly demonstrates that given the same number of SD steps, the MSDSD aided 16-DAPSK(2,8) visits a considerably lower number of constellation points, compared to the MSDSD aided 16-TDAPSK^{JM}(2,8). We will continue to provide detailed discussions on the complexity and performance comparison between the different DQAM schemes in Sec. 4.7.

4.6 Hard-Decision-Aided DFDD Conceived for Uncoded DQAM

The DFDD aided uncoded DAPSK and ADPSK schemes have been conceived with a linear prediction based blind channel estimator in [136, 153, 154], which may also be termed as Linear Prediction-based Detection (LPD). However, the aforementioned contributions ignored the problem of having a symbol-amplitude-dependent channel correlation matrix, which is caused by the non-constant modulus of the constellation. Since we have solved this problem for MSDD/MSDSD, in this section, both a DFDD derived from the MSDD/MSDSD and a LPD derived from blind channel estimation will be developed. Similarly to the DFDD/LPD aided DPSK schemes of [121, 125] summarized in Chapter 3, we will demonstrate that the DFDD and LPD aided nonconstant modulus constellations operating in Rayleigh fading channels are also equivalent.

4.6.1 DFDD Derived from MSDD/MSDSD

As discussed in Sec. 3.2.4, DFDD may be regarded as a special case of MSDD/MSDSD. Specifically, given the decision-feedback for $(N_w - 2)$ data-carrying symbols, only a single data-carrying symbol has to be detected within an observation window. According to Eqs. (4.45) and (4.46), the MSDD Euclidean distance may be expressed as:

$$d = \mathrm{tr}(\mathbf{Y}^H \bar{\mathbf{P}} \bar{\mathbf{O}} \mathbf{F} \bar{\mathbf{O}}^H \bar{\mathbf{P}}^H \mathbf{Y}) + \ln[\det(\widetilde{\mathbf{C}}_{N_w-1})] + \widetilde{\Xi}_{N_w}, \tag{4.67}$$

where we define $\mathbf{F} = \mathbf{C}^{-1}$, while we have $\widetilde{\Xi}_{N_w} = \ln\left[(\Gamma_{N_w}^2 + N_0) - \widetilde{\mathbf{e}}_{N_w}^T \widetilde{\mathbf{C}}_{\mathbf{N_w-1}}^{-1} \widetilde{\mathbf{e}}_{N_w}\right]$. The constant ξ_{N_w} seen in Eq. (4.61) may be ignored by DFDD.

For DFDD, the previous $(N_w - 1)$ transmitted symbols' ring amplitudes $\{\hat{\Gamma}_t\}_{t=1}^{N_w-1}$, ring-amplitude-dependent phase rotations $\{\hat{\Psi}_t\}_{t=1}^{N_w-1}$ and the M_PPSK phases $\{\hat{\Omega}_t\}_{t=1}^{N_w-1}$ have been determined. Therefore, only the latest phase $\Omega_{N_w} = \omega_{N_w-1}\hat{\Omega}_{N_w-1}$ in $\bar{\mathbf{P}}$ and the latest ring amplitude Γ_{N_w} in $\mathbf{F}$ and $\widetilde{\Xi}_{N_w}$ have to be detected. The latest ring-amplitude-dependent phase rotation $\Psi_{N_w} = \psi_{N_w-1}\hat{\Psi}_{N_w-1}$ is also determined by the latest data-carrying ring amplitude γ_{N_w-1}, where we have $\Gamma_{N_w} = \gamma_{N_w-1}\hat{\Gamma}_{N_w-1}$ for DAPSK/TDAPSK and $\Gamma_{N_w} = \gamma_{N_w-1}$ for ADPSK/TADPSK. Owing to the fact that $\mathbf{F}$ is a Hermitian matrix, i.e. we have $\{f_{N_w-v+1,N_w-t+1} = f_{N_w-t+1,N_w-v+1}\}_{v,t=1}^{N_w}$,

Eq. (4.67) may be further extended as:

$$\begin{aligned} d &= \sum_{v=1}^{N_w} \left(\sum_{t=1}^{N_w} f_{N_w-v+1,N_w-t+1} \bar{\Psi}_t^* \bar{\Omega}_t^* \mathbf{Y}_t \right) \bar{\Omega}_v \bar{\Psi}_v \mathbf{Y}_v^H + \widetilde{\Xi}_{N_w} \\ &= \sum_{v=1}^{N_w-1} \left(\sum_{t=1}^{N_w-1} f_{N_w-v+1,N_w-t+1} \hat{\Psi}_t^* \hat{\Omega}_t^* \mathbf{Y}_t \right) \hat{\Omega}_v \hat{\Psi}_v \mathbf{Y}_v^H \\ &\quad + 2\Re \left(\sum_{t=1}^{N_w-1} f_{1,N_w-t+1} \Psi_{N_w}^* \Omega_{N_w}^* \hat{\Omega}_t \hat{\Psi}_t \mathbf{Y}_{N_w} \mathbf{Y}_t^H \right) + f_{1,1} \|\mathbf{Y}_{N_w}\|^2 + \widetilde{\Xi}_{N_w}, \end{aligned} \tag{4.68}$$

where the constant $\ln[\det(\widetilde{\mathbf{C}}_{N_w-1})]$ in Eq. (4.67) is ignored. According to the relationship of $\mathbf{F} = \mathbf{L}\mathbf{L}^T$, all elements in $\mathbf{F}$ may be represented by the combinations of elements in the lower triangular matrix $\mathbf{L}$ as:

$$f_{N_w-v+1,N_w-t+1} = \sum_{q=\max(v,t)}^{N_w} l_{N_w-v+1,N_w-q+1} l_{N_w-t+1,N_w-q+1}. \tag{4.69}$$

Furthermore, according to the proof of Propositions 1 and 2, both $\widetilde{\mathbf{C}}_{\mathbf{N_w-1}}$ in Eq. (4.53) and $\widetilde{\mathbf{L}}_{\mathbf{N_w-1}}$ in Eq. (4.52) are determined by the known ring amplitudes $\{\hat{\Gamma}_t\}_{t=1}^{N_w-1}$. Therefore, the specific elements $\left\{\{l_{N_w-v+1,N_w-t+1}\}_{t=v}^{N_w-1}\right\}_{v=1}^{N_w-1}$ are constants. As a result, Eq. (4.68) may be further simplified to:

$$\begin{aligned} d &= \sum_{v=1}^{N_w-1} \left(\sum_{t=1}^{N_w-1} l_{N_w-v+1,1} l_{N_w-t+1,1} \hat{\Psi}_t^* \hat{\Omega}_t^* \mathbf{Y}_t \right) \hat{\Omega}_v \hat{\Psi}_v \mathbf{Y}_v^H \\ &\quad + 2\Re \left(\sum_{t=1}^{N_w-1} l_{N_w-t+1,1} l_{1,1} \Psi_{N_w}^* \Omega_{N_w}^* \hat{\Omega}_t \hat{\Psi}_t \mathbf{Y}_{N_w} \mathbf{Y}_t^H \right) + l_{1,1}^2 \|\mathbf{Y}_{N_w}\|^2 + \widetilde{\Xi}_{N_w} \\ &= \left\| l_{1,1} \hat{\Psi}_{N_w-1}^* \hat{\Omega}_{N_w-1}^* \mathbf{Y}_{N_w} + \omega_{N_w-1} \psi_{N_w-1} \left(\sum_{t=1}^{N_w-1} l_{N_w-t+1,1} \hat{\Psi}_t^* \hat{\Omega}_t^* \mathbf{Y}_t \right) \right\|^2 + \widetilde{\Xi}_{N_w}, \end{aligned} \tag{4.70}$$

where a constant of $\sum_{v=1}^{N_w-1} \left[\sum_{t=1}^{N_w-1} (\sum_{q=\max(v,t)}^{N_w-1} l_{N_w-v+1,N_w-q+1} l_{N_w-t+1,N_w-q+1}) \hat{\Psi}_t^* \hat{\Omega}_t^* \mathbf{Y}_t \right] \hat{\Omega}_v \hat{\Psi}_v \mathbf{Y}_v^H$ is ignored. It can be seen that the DFDD metric of Eq. (4.70) is completely equivalent to the MSDSD's PED increment formulated in Eq. (4.60) associated with the index $v = N_w$. The difference between the MSDSD and the DFDD is that the DFDD windows are overlapped with $N_{OL} = (N_w - 1)$ observations, while only the best candidate for the last symbol within the window is detected by the DFDD.

Therefore, the DFDD aided DQAM$^{\text{JM}}$ constellations of Sec. 4.2.4 may be simply completed by the "sortDelta" subfunction in Table 4.8, and DFDD aided DQAM which separately modulates the ring amplitude and the M_PPSK phase may be implemented by the "findBest" subfunction of Table 4.9, where both subfunctions are supposed to be associated with a fixed index of $v = N_w$. We also note that Ξ_{N_w} in Tables 4.8 and 4.9 may be replaced by $\widetilde{\Xi}_{N_w}$ defined in Eq. (4.67) for DFDD.

4.6.2 DFDD Derived from Linear Prediction

It was demonstrated in [136, 153, 154] that the LPD aided DQAM may employ a blind channel estimator in order to perform coherent detection based on the estimated reference of fading channels.

Firstly, the most recent received signal block within an observation window is given by:

$$\begin{aligned}\mathbf{Y}_{N_w} &= s_{N_w}\mathbf{H}_{N_w} + \mathbf{V}_{N_w} \\ &\approx \Omega_{N_w}\Psi_{N_w}\mathbf{H}^{\text{ref}}_{N_w} + \mathbf{V}_{N_w},\end{aligned} \tag{4.71}$$

where the reference fading vector $\mathbf{H}^{\text{ref}}_{N_w}$ is output from a linear prediction filter, which observes the previous received signal vectors $\{\mathbf{Y}_v\}_{v=1}^{N_w-1}$ as well as the previous decisions $\{\hat{s}_v\}_{v=1}^{N_w-1}$. The input-output relationship of the linear prediction filter may be expressed as [125, 126, 136]:

$$\begin{aligned}\mathbf{H}^{\text{ref}}_{N_w} &= \sum_{v=1}^{N_w-1} \overline{w}_v \mathbf{Y}_v / (\hat{\Omega}_v \hat{\Psi}_v) \\ &= \overline{\mathbf{w}}^T (\hat{\mathbf{O}}^{\bar{N}_w})^H (\hat{\mathbf{P}}^{\bar{N}_w})^H \mathbf{Y}^{\bar{N}_w},\end{aligned} \tag{4.72}$$

where $\overline{\mathbf{w}} = [\overline{w}_{N_w-1}, \cdots, \overline{w}_1]^T$ represents the linear filter's taps, while the diagonal matrices $\hat{\mathbf{P}}^{\bar{N}_w}$ and $\hat{\mathbf{O}}^{\bar{N}_w}$ are given by the decisions on M_PPSK phases $\mathbf{P}$ and by the decisions on ring-amplitude-dependent phase rotations $\mathbf{O}$ of Eq. (4.32) eliminating Ω_{N_w} and Ψ_{N_w}, respectively. Moreover, $\mathbf{Y}^{\bar{N}_w}$ in Eq. (4.72) is given by the received signals $\mathbf{Y}$ of Eq. (4.32) eliminating $\mathbf{Y}_{N_w}$.

The LPD aims for minimizing the Mean Square Error (MSE), which is defined as:

$$\begin{aligned}\sigma^2_{\text{MSE}} &= \varepsilon\left\{\left\|\mathbf{Y}_{N_w}/(\Omega_{N_w}\Psi_{N_w}) - \mathbf{H}^{\text{ref}}_{N_w}\right\|^2\right\} \\ &= \varepsilon\left\{\left\|\Gamma_{N_w}\mathbf{H}_{N_w} + \Psi^*_{N_w}\Omega^*_{N_w}\mathbf{V}_{N_w} - \overline{\mathbf{w}}^T(\hat{\mathbf{O}}^{\bar{N}_w})^H(\hat{\mathbf{P}}^{\bar{N}_w})^H\mathbf{Y}^{\bar{N}_w}\right\|^2\right\} \\ &= \Gamma^2_{N_w} + N_0 - 2E\left\{\Gamma_{N_w}\mathbf{H}_{N_w}(\mathbf{Y}^{\bar{N}_w})^H\hat{\mathbf{P}}^{\bar{N}_w}\hat{\mathbf{O}}^{\bar{N}_w}\right\}\overline{\mathbf{w}} \\ &\qquad + \overline{\mathbf{w}}^T E\left\{(\hat{\mathbf{O}}^{\bar{N}_w})^H(\hat{\mathbf{P}}^{\bar{N}_w})^H\mathbf{Y}^{\bar{N}_w}(\mathbf{Y}^{\bar{N}_w})^H\hat{\mathbf{P}}^{\bar{N}_w}\hat{\mathbf{O}}^{\bar{N}_w}\right\}\overline{\mathbf{w}} \\ &= \Gamma^2_{N_w} + N_0 - 2\widetilde{\mathbf{e}}^T_{N_w}\overline{\mathbf{w}} + \overline{\mathbf{w}}^T\widetilde{\mathbf{C}}_{\mathbf{N_w-1}}\overline{\mathbf{w}},\end{aligned} \tag{4.73}$$

where the auto-correlation matrix $\widetilde{\mathbf{C}}_{\mathbf{N_w-1}}$ and cross-correlation vector $\widetilde{\mathbf{e}}_{N_w}$ are defined as submatrices of $\widetilde{\mathbf{C}}_{\mathbf{N_w}}$ in Eq. (4.53) associated with the index $v = N_w$.

As a result, the MMSE solution for $\frac{\partial\sigma^2_{\text{MSE}}}{\partial\overline{\mathbf{w}}} = 0$ based on the MSE σ^2_{MSE} defined in Eq. (4.73) is given by [125, 126, 136]:

$$\overline{\mathbf{w}} = \widetilde{\mathbf{C}}^{-1}_{\mathbf{N_w-1}}\widetilde{\mathbf{e}}_{N_w}, \tag{4.74}$$

where $\widetilde{\mathbf{e}}_{N_w}$ is determined by the unknown variable ring amplitude Γ_{N_w}. The resultant MSE is now simply given by:

$$\sigma^2_{\text{MSE}} = \Gamma^2_{N_w} + N_0 - \widetilde{\mathbf{e}}^T_{N_w}\widetilde{\mathbf{C}}^{-1}_{\mathbf{N_w-1}}\widetilde{\mathbf{e}}_{N_w}. \tag{4.75}$$

Given the reference $\mathbf{H}^{\text{ref}}_{N_w}$ defined in Eq. (4.71), the LPD may opt for maximizing the following *a posteriori* probability:

$$p(\Gamma_{N_w}, \Omega_{N_w}|\mathbf{Y}_{N_w}) = \frac{p(\mathbf{Y}_{N_w}|\Gamma_{N_w}, \Omega_{N_w})p(\Gamma_{N_w})p(\Omega_{N_w})}{\sum_{\forall\Gamma_{N_w},\forall\Omega_{N_w}} p(\mathbf{Y}_{N_w}|\Gamma_{N_w}, \Omega_{N_w})p(\Gamma_{N_w})p(\Omega_{N_w})}, \tag{4.76}$$

where the probability of receiving $\mathbf{Y}_{N_w}$ given Γ_{N_w} and Ω_{N_w} is formulated as:

$$p(\mathbf{Y}_{N_w}|\Gamma_{N_w}, \Omega_{N_w}) = \frac{1}{\pi\sigma^2_{MSE}}\exp\left(-\frac{\|\mathbf{Y}_{N_w} - \Omega_{N_w}\Psi_{N_w}\mathbf{H}^{\text{ref}}_{N_w}\|^2}{\sigma^2_{MSE}}\right). \tag{4.77}$$

Let us assume that the data-carrying ring amplitude γ_{N_w-1} and the M_PPSK variable ω_{N_w-1} are both equiprobable. Then the LPD may minimize the following decision metric:

$$\begin{aligned} d &= \frac{\|\mathbf{Y}_{N_w} - \Omega_{N_w}\Psi_{N_w}\mathbf{H}_{N_w}^{\text{ref}}\|^2}{\sigma_{MSE}^2} + \ln(\sigma_{MSE}^2) \\ &= \frac{\|\mathbf{Y}_{N_w} - \omega_{N_w-1}\psi_{N_w-1}\hat{\Psi}_{N_w-1}\hat{\Omega}_{N_w-1}(\sum_{t=1}^{N_w-1}\overline{w}_t\hat{\Psi}_t^*\hat{\Omega}_t^*\mathbf{Y}_t)\|^2}{\sigma_{MSE}^2} + \widetilde{\Xi}_{N_w} \\ &= \left\| l_{1,1}\hat{\Omega}_{N_w-1}^*\hat{\Psi}_{N_w-1}^*\mathbf{Y}_{N_w} - \omega_{N_w-1}\psi_{N_w-1}\left(\sum_{t=1}^{N_w-1} l_{1,1}\overline{w}_t\hat{\Psi}_t^*\hat{\Omega}_t^*\mathbf{Y}_t\right)\right\|^2 + \widetilde{\Xi}_{N_w}, \end{aligned} \tag{4.78}$$

where according to $\widetilde{\Xi}_{N_w}$ defined in Eq. (4.67) and σ_{MSE}^2 of Eq. (4.75), we have $\ln(\sigma_{MSE}^2) = \widetilde{\Xi}_{N_w}$. Furthermore, according to the proof of Proposition 1, $\widetilde{\mathbf{Q}}_{\mathbf{v}}$ defined in Eq. (4.55) associated with index $v = N_w - 1$ is given by $\widetilde{Q}_{N_w-1} = (\Gamma_{N_w}^2\rho_0 + N_0 - \widetilde{\mathbf{e}}_{N_w}^T\widetilde{\mathbf{C}}_{\mathbf{N_w-1}}^{-\mathbf{1}}\widetilde{\mathbf{e}}_{N_w})^{-1} = 1/\sigma_{MSE}^2$ and we also have $\widetilde{Q}_{N_w-1} = f_{1,1} = l_{1,1}^2$ as a benefit of the relationship of $\mathbf{F} = \mathbf{C}^{-1} = \mathbf{L}\mathbf{L}^T$. Therefore, the MSE may be rewritten as $\sigma_{MSE}^2 = 1/\widetilde{Q}_{N_w-1} = 1/l_{1,1}^2$, which results in the LPD decision metric presented in Eq. (4.78).

Furthermore, Eq. (4.55) indicates that $[f_{2,1}, \cdots, f_{N_w,1}]^T = -\widetilde{\mathbf{C}}_{\mathbf{N_w-1}}^{-\mathbf{1}}\widetilde{\mathbf{e}}_{N_w}\widetilde{Q}_{N_w-1} = -\widetilde{Q}_{N_w-1}\overline{\mathbf{w}}$, which implies that we have $\{f_{N_w-t+1,1} = -l_{1,1}^2\overline{w}_t\}_{t=1}^{N_w-1}$. Because of the relationship of $f_{N_w-t+1,1} = l_{N_w-t+1,1}l_{1,1}$, according to Eq. (4.69) we may conclude that $-l_{1,1}\overline{w}_t = l_{N_w-t+1,1}$. As a benefit, the LPD decision metric of Eq. (4.78) becomes the same as the DFDD decision metric of Eq. (4.70).

In summary, both the DFDD metric of Eq. (4.70) and the LPD metric of Eq. (4.78) are equivalent to the MSDSD's PED increment of Eq. (4.60) associated with the index of $v = N_w$. We hereby note that the DFDD is equivalent to a joint blind channel estimator and a data detector, where the previous $(N_w - 1)$ detected decisions of $\{\hat{\Gamma}_t\}_{t=1}^{N_w-1}$, $\{\hat{\Psi}_t\}_{t=1}^{N_w-1}$ and $\{\hat{\Omega}_t\}_{t=1}^{N_w-1}$ are used for estimating the N_w-th fading channel sample, and then the N_w-th transmitted symbol may be detected with the aid of the blindly estimated CSI reference. Therefore, MSDD/MSDSD may be viewed as an improved joint blind channel estimator and data detector, whose decision metric is equivalent to that of the DFDD/LPD. The difference between the MSDD/MSDSD and DFDD is that all the transmitted symbols $\{\Gamma_t\}_{t=2}^{N_w}$ and $\{\Omega_t\}_{t=2}^{N_w}$ within the observation window are detected together by MSDD/MSDSD in order to avoid the DFDD's problem of error propagation.

By contrast, the DFDD/LPD aided DAPSK/TDAPSK proposed in [153, 154] minimizes the following decision metric:

$$d = \left\| \mathbf{Y}_{N_w} - x_{N_w-1}\hat{s}_{N_w-1}\left[\sum_{t=1}^{N_w}\overline{w}_t\mathbf{Y}_t/(\hat{s}_t)\right]\right\|^2, \tag{4.79}$$

while DFDD/LPD aided ADPSK/TADPSK proposed in [136] minimizes the following decision metric:

$$d = \left\| \mathbf{Y}_{N_w} - \frac{x_{N_w-1}\hat{s}_{N_w-1}}{\hat{\Gamma}_{N_w-1}}\left[\sum_{t=1}^{N_w}\overline{w}_t\mathbf{Y}_t/(\hat{s}_t)\right]\right\|^2, \tag{4.80}$$

where the filter taps are given by $\overline{\mathbf{w}} = [\overline{w}_{N_w-1}, \cdots, \overline{w}_1]^T = \mathbf{C}_{\mathbf{N_w-1}}^{-\mathbf{1}}\mathbf{e}_{N_w}$, which are the same as the filter taps of DPSK detection as seen in [121, 125, 126] and as summarized in Sec. 3.2.4, i.e.

we have $\mathbf{C_{N_w-1}} = \text{toeplitz}([\rho_0, \cdots, \rho_{N_w-2}]) + N_0\mathbf{I_{N_w-1}}$ and $\mathbf{e}_{N_w} = [\rho_1, \cdots, \rho_{N_w-1}]^T$. Since the problem of symbol-amplitude-dependent channel correlation matrix is ignored in $\mathbf{C_{N_w-1}}$, this DFDD/LPD arrangement imposes a performance loss compared to our proposed DFDD/LPD. We will continue by comparing the performance difference between the noncoherent detectors in the following section.

4.7 Performance Results for Uncoded DQAM

In this section, the performance results of uncoded DQAM schemes are organized according to three different aspects. First of all, the achievable capacities of the DQAM constellations are evaluated and compared in Sec. 4.7.1. Secondly, the noncoherent detectors conceived for uncoded DQAM are examined in terms of their BER performance in Sec. 4.7.2. Last but not least, Sec. 4.7.3 offers a discussion on the complexity comparison a range of uncoded DQAM detectors.

4.7.1 Capacity Results

Let us firstly determine the DCMC capacity of the DQAM constellations. Similar to the DCMC capacity of the coherent schemes defined in Eq. (2.56) and to that of DPSK defined in Eq. (3.50), the DCMC capacity of differential nonconstant modulus constellations is given by:

$$\begin{aligned} C_{DCMC}^{MSDD} &= \max_{\{p(\bar{\mathbf{S}}^i)\}_{i=0}^{M^{(N_w-1)}-1}} \frac{\sum_{a=0}^{M_A-1}\sum_{i=0}^{M^{(N_w-1)}-1}\int p(\mathbf{Y}|\bar{\mathbf{S}}^i,\Gamma^a)p(\bar{\mathbf{S}}^i)p(\Gamma^a)\log_2\left[\frac{\sum_{\tilde{a}=0}^{M_A-1}p(\mathbf{Y}|\bar{\mathbf{S}}^i,\Gamma^{\tilde{a}})p(\Gamma^{\tilde{a}})}{\sum_{\tilde{a}=0}^{M_A-1}\sum_{\tilde{i}=0}^{M^{(N_w-1)}-1}p(\mathbf{Y}|\bar{\mathbf{S}}^{\tilde{i}},\Gamma^{\tilde{a}})p(\bar{\mathbf{S}}^{\tilde{i}})p(\Gamma^{\tilde{a}})}\right]}{(N_w-1)} \\ &= \frac{\sum_{a=0}^{M_A-1}\sum_{i=0}^{M^{(N_w-1)}-1}E\left\{\log_2\left[\frac{M^{(N_w-1)}\cdot\sum_{\tilde{a}=0}^{M_A-1}p(\mathbf{Y}|\bar{\mathbf{S}}^i,\Gamma^{\tilde{a}})p(\Gamma^{\tilde{a}})}{\sum_{\tilde{a}=0}^{M_A-1}\sum_{\tilde{i}=0}^{M^{(N_w-1)}-1}p(\mathbf{Y}|\bar{\mathbf{S}}^{\tilde{i}},\Gamma^{\tilde{a}})p(\Gamma^{\tilde{a}})}\right]\Big|\bar{\mathbf{S}}=\bar{\mathbf{S}}^i,\Gamma_1=\Gamma^a\right\}}{(N_w-1)M_AM^{(N_w-1)}}, \end{aligned} \tag{4.81}$$

where the conditions of $\bar{\mathbf{S}} = \bar{\mathbf{S}}^i$ and $\Gamma_1 = \Gamma^a$ indicate that the received signal matrix $\mathbf{Y}$ of the MSDD defined by Eq. (4.35) is obtained by sending the transmitted signal matrix $\bar{\mathbf{S}} = \bar{\mathbf{A}}\bar{\mathbf{P}}\bar{\mathbf{O}}$ determined by $\bar{\mathbf{S}}^i$ and Γ^a over Rayleigh fading channels. Furthermore, the conditional probability $p(\mathbf{Y}|\bar{\mathbf{S}}^i,\Gamma^a)$ in Eq. (4.81) is directly given by Eq. (4.41), while the maximum mutual information between the channel's discrete input and continuous output is given by equiprobable combinations of $\{p(\bar{\mathbf{S}}^i) = \frac{1}{M^{(N_w-1)}}\}_{i=0}^{M^{(N_w-1)}-1}$ and $\{p(\Gamma^a) = \frac{1}{M_A}\}_{a=0}^{M_A-1}$.

For the optimum MSDD aided DAPSK/TDAPSK, the first transmitted symbol's ring amplitude is treated as an equiprobable variable, i.e. we have $\{p(\Gamma^{\tilde{a}}) = p(\Gamma^{\bar{a}}) = \frac{1}{M_A}\}_{\forall\tilde{a},\forall\bar{a}}$. Therefore, the DCMC capacity of Eq. (4.81) may be revised for MSDD aided DAPSK/TDAPSK as:

$$C_{DCMC}^{MSDD-DAPSK} = \frac{\sum_{a=0}^{M_A-1}\sum_{i=0}^{M^{(N_w-1)}-1}E\left\{\log_2\left[\frac{M^{(N_w-1)}\cdot\sum_{\tilde{a}=0}^{M_A-1}p(\mathbf{Y}|\bar{\mathbf{S}}^i,\Gamma^{\tilde{a}})}{\sum_{\tilde{a}=0}^{M_A-1}\sum_{\tilde{i}=0}^{M^{(N_w-1)}-1}p(\mathbf{Y}|\bar{\mathbf{S}}^{\tilde{i}},\Gamma^{\tilde{a}})}\right]\Big|\bar{\mathbf{S}}=\bar{\mathbf{S}}^i,\Gamma_1=\Gamma^a\right\}}{(N_w-1)M_AM^{(N_w-1)}}. \tag{4.82}$$

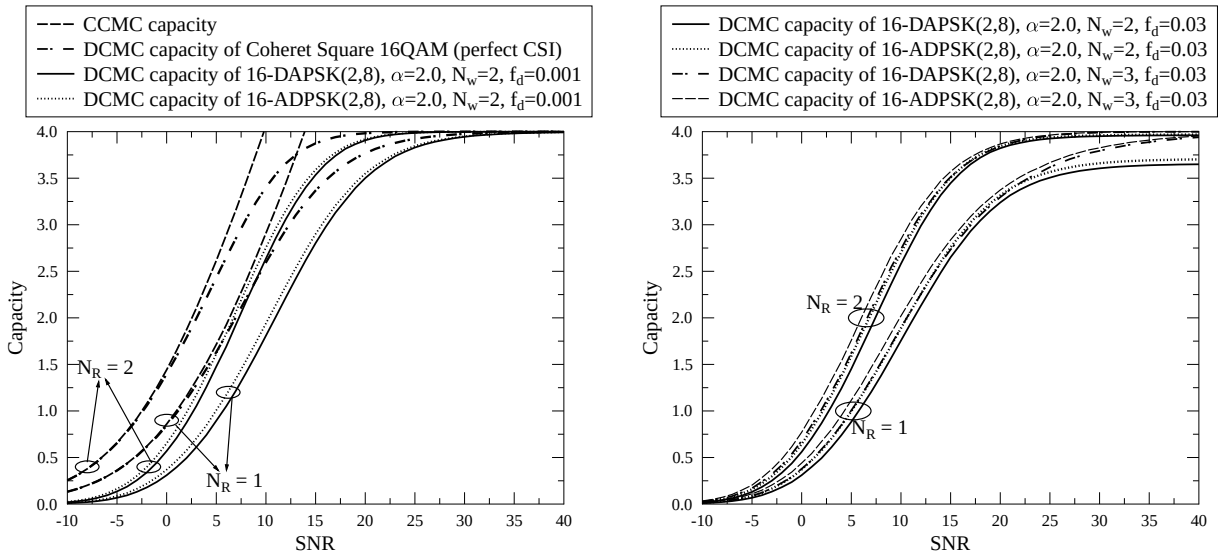

(a) $f_d = 0.001$ (b) $f_d = 0.03$

Figure 4.11: Capacity of MSDD aided 16-DAPSK(2,8) and HDD-MSDD aided 16-ADPSK(2,8).

By contrast, ADPSK and TADPSK can only employ HDD-MSDD, which means that the full DCMC capacity of HDD-MSDD aided ADPSK/TADPSK can only be achieved, when the *a priori* information on the first transmitted symbol's ring amplitude Γ_1 is available from decision feedback, i.e. we have $\{p(\Gamma^{\tilde{a}}) = p(\Gamma^{\bar{a}}) = 1\}_{\tilde{a}=\bar{a}=a}$ and $\{p(\Gamma^{\tilde{a}}) = p(\Gamma^{\bar{a}}) = 0\}_{\forall\tilde{a}\neq a,\forall\bar{a}\neq a}$. As a result, the DCMC capacity of Eq. (4.81) may be revised for HDD-MSDD aided ADPSK/TADPSK as:

$$C_{DCMC}^{HDD-MSDD-ADPSK} = \frac{\sum_{a=0}^{M_A-1}\sum_{i=0}^{M^{(N_w-1)}-1} E\left\{\log_2\left[\frac{M^{(N_w-1)}p(\mathbf{Y}|\bar{\mathbf{S}}^i,\Gamma^a)}{\sum_{i=0}^{M^{(N_w-1)}-1}p(\mathbf{Y}|\bar{\mathbf{S}}^i,\Gamma^a)}\right]\Big|\bar{\mathbf{S}}=\bar{\mathbf{S}}^i,\Gamma_1=\Gamma^a\right\}}{(N_w-1)M_A M^{(N_w-1)}}. \tag{4.83}$$

The DCMC capacities of DAPSK and ADPSK evaluated by Eqs. (4.82) and (4.83) are portrayed in Fig. 4.11. It can be seen in Fig. 4.11a that when accurate channel estimation is achieved in slowly fluctuating fading channels, coherent Square 16QAM may significantly outperform both noncoherent 16-DAPSK(2,8) and 16-ADPSK(2,8). However, when the normalized Doppler frequency is as high as $f_d = 0.03$, accurate channel estimation becomes unattainable. Under this condition, MSDD aided DAPSK and HDD-MSDD aided ADPSK may be preferred, owing to the fact that the noncoherent schemes do not require CSI knowledge, and their capacity may be further improved by increasing the MSDD window length, as demonstrated by Fig. 4.11b.

Moreover, it is also demonstrated in Fig. 4.11 that although both 16-ADPSK(2,8) and 16-DAPSK(2,8) may achieve their full DCMC capacity of BPS $= 4$ at a similarly high SNR, HDD-MSDD aided ADPSK is capable of achieving a higher capacity than MSDD assisted DAPSK before reaching their saturation points. This implies that both ADPSK and DAPSK may achieve a similar performance in uncoded systems, but HDD-MSDD aided ADPSK may outperform MSDD aided

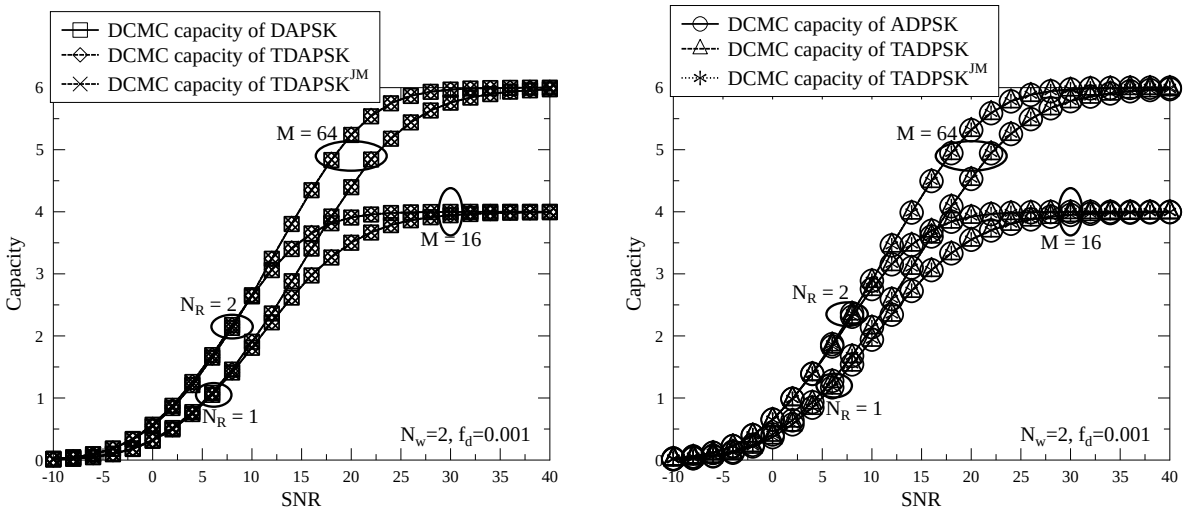

(a) DAPSK, TDAPSK and TDAPSK^{JM}

(b) ADPSK, TADPSK and TADPSK^{JM}

Figure 4.12: DCMC capacity comparison between DAPSK, ADPSK, and their twisted modulation counterparts.

DAPSK with the aid of channel coding.

Fig. 4.12 compares the DCMC capacities of DAPSK, ADPSK, and their twisted modulation counterparts. As expected, there is no capacity difference between DQAM and its DQAM^{JM} counterpart, as seen Fig. 4.12, because their different mapping arrangements do not change the achievable capacity. This trend is similar to the situation of the Gray and Anti-Gray mapping featured in [86, 250]. Furthermore, it can be seen in Fig. 4.12a that TDAPSK and TDAPSK^{JM} do not achieve any noticeable capacity improvement over DAPSK, while Fig. 4.12b demonstrates that ADPSK, TADPSK and TADPSK^{JM} also exhibit a similar capacity. We will demonstrate in the next section that although the twisted modulation schemes cannot provide any noticeable capacity improvement, their soft-decision-aided detectors are capable of producing an improved iteration gain in channel coded systems, owing to the fact that the data-carrying symbol's ring amplitude and phase are correlated in twisted modulation schemes. A higher iteration gain implies that the extrinsic information I_E becomes higher with the aid of perfect *a priori* information of $I_A = 1$, which is beneficial, provided that the appropriate coding scheme is invoked.

4.7.2 BER Performance Results

Let us now proceed to verify the capacity results presented in Figs. 4.11 and 4.12 with the aid of our BER performance results. Fig. 4.13 presents the BER performance of MSDSD and HDD-MSDSD aided uncoded DAPSK, while Fig. 4.14 portrays the BER performance of HDD-MSDSD aided uncoded ADPSK. It can be seen in Figs. 4.13 and 4.14 that the HDD-MSDSD associated with $N_w = 2$, which is shown to be equivalent to CDD, suffers from an error floor at $f_d = 0.03$.

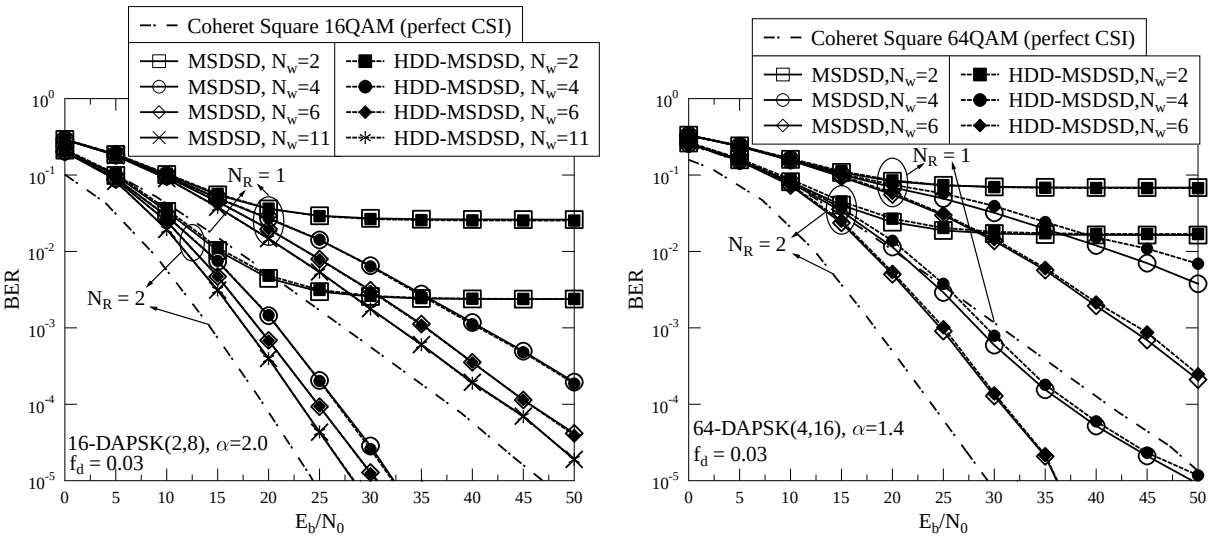

(a) 16-DAPSK(2,8) (b) 64-DAPSK(4,16)

Figure 4.13: BER performance of MSDSD and HDD-MSDSD aided DAPSK.

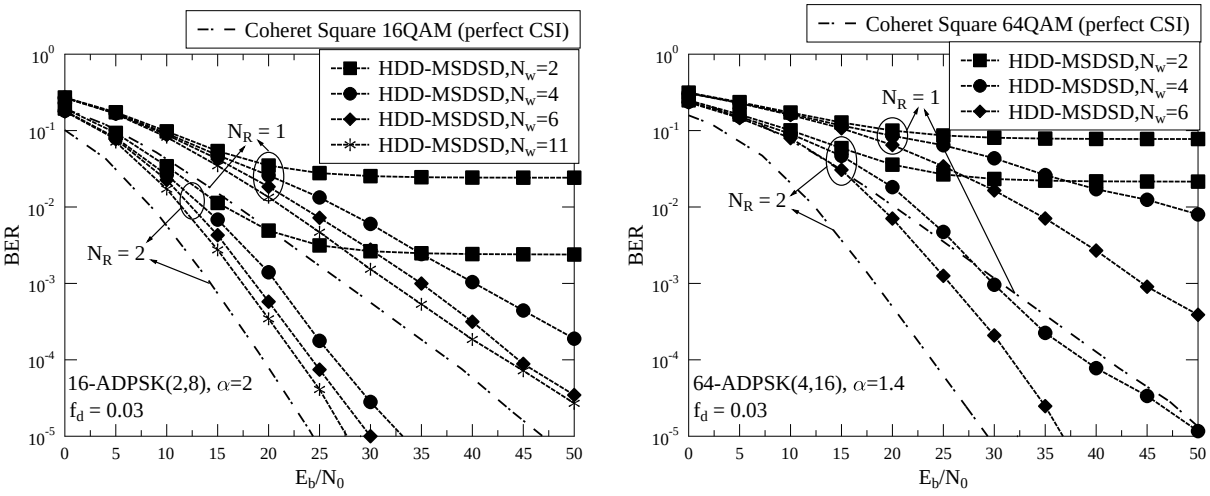

(a) 16-ADPSK(2,8) (b) 64-ADPSK(4,16)

Figure 4.14: BER performance of HDD-MSDSD aided ADPSK.

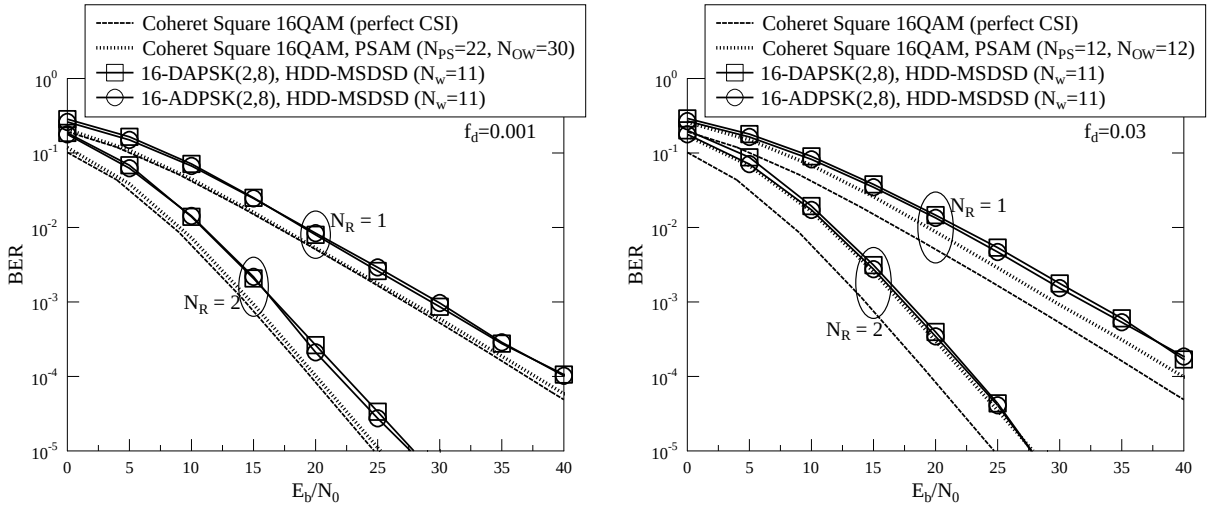

(a) $f_d = 0.001$ (b) $f_d = 0.03$

Figure 4.15: BER performance comparison between PSAM aided uncoded Square 16QAM and HDD-MSDSD aided uncoded 16-DAPSK/ADPSK(2,8).

This error floor is irreducible even at high E_b/N_0 values. Nonetheless, HDD-MSDSD mitigates the performance degradation of CDD and its performance gradually approaches that of the coherent scheme relying on idealistic perfect CSI within about 3 dB, as evidenced by Figs. 4.13 and 4.14. We will demonstrate later in this section that the coherent schemes cannot acquire accurate CSI, when the fading channels fluctuate as rapidly as specified by $f_d = 0.03$, which may result in an erosion of the performance advantage of coherent Square QAM over noncoherent DAPSK/ADPSK. Moreover, it is also demonstrated by Fig. 4.13 that HDD-MSDSD does not impose any significant performance loss on MSDSD, when employed for DAPSK detection. Therefore, the HDD-MSDSD is capable of facilitating both DAPSK detection and ADPSK detection in uncoded systems.

Fig. 4.15 provides a BER performance comparison between PSAM aided uncoded Square 16QAM and HDD-MSDSD aided uncoded DAPSK/ADPSK. Realistic imperfect channel estimation is performed by PSAM [1], which was introduced in Sec. 3.4.1. The PSAM parameters used for Fig. 4.15 are the same as those chosen in Sec. 3.4.2. It can be seen in Fig. 4.15a that when the fading channel fluctuates as slowly as specified by $f_d = 0.001$, PSAM is capable of providing accurate CSI estimation, which results in a small performance difference between coherent Square 16QAM using perfect CSI and coherent Square 16QAM using PSAM aided CSI. However, as the normalized Doppler frequency is increased to $f_d = 0.03$, the performance gap between PSAM aided coherent Square 16QAM and HDD-MSDSD assisted noncoherent DAPSK/ADPSK is significantly reduced, especially for the case of $N_R = 2$, as evidenced by Fig. 4.15b. In fact, we will demonstrate in the next chapter that the performance loss of coherent detectors caused by inaccurate CSI estimation becomes much more substantial in coded systems. Hence the soft-decision-aided MSDSD associated with a much smaller N_w conceived for coded DAPSK/ADPSK is capable of outperforming coded PSAM aided Square 16QAM, when the fading channels fluctuate rapidly.

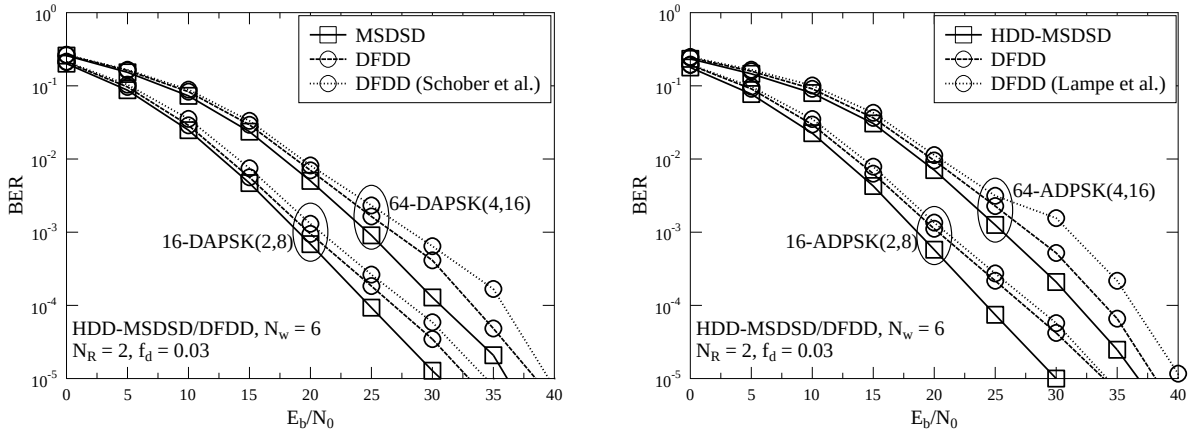

(a) DAPSK (b) ADPSK

Figure 4.16: BER performance of DFDD aided DAPSK and ADPSK. The performance of the DFDD (Schober et al.) conceived for DAPSK in [154] and the DFDD conceived for ADPSK (Lampe et al.) in [136] are also portrayed as benchmarks.

The reason is that the LLRs produced by the coherent detectors suffer from poor integrity and credibility, when the normalized Doppler frequency is high.

Fig. 4.16 portrays the BER performance of DFDD aided uncoded DAPSK/ADPSK. As demonstrated in Sec. 4.6, the proposed DFDD is a special case of the HDD-MSDSD, where only a single variable is detected based on the decision feedback for $(N_w - 2)$ observations within a DFDD window. As a result, the DFDD is also capable of mitigating the error floor that is often encountered by the CDD, when the fading channels fluctuate rapidly, but the HDD-MSDSD still appears to be superior to DFDD, as evidenced by Fig. 4.16. Furthermore, as expected, the DFDD that minimizes the decision metric of Eq. (4.79) as proposed in [154] imposes a performance loss on DAPSK detection, which is demonstrated by Fig. 4.16a. Similarly, the DFDD that aims for minimizing the decision metric of Eq. (4.80) as proposed in [136] also inflicts a performance degradation on ADPSK detection, as evidenced by Fig. 4.16b.

It was demonstrated in Fig. 4.15 that DAPSK and ADPSK may achieve a comparable performance in uncoded systems, which is consistent with the capacity results presented in Fig. 4.11, where both DAPSK and ADPSK achieve the saturation point of $\text{DCMC}^{\max} = \text{BPS}$ at a similar SNR. We note that as demonstrated by Fig. 4.11, the DCMC capacities of DAPSK and ADPSK are different in the low SNR region, which implies that their performance difference may become more distinct in coded systems. Furthermore, Fig. 4.17 presents a performance comparison between DAPSK and its twisted modulated counterparts. As expected, Fig. 4.17 shows that there is no significant performance difference between DAPSK and TDAPSK, which is also in line with the results of Fig. 4.12. However, Fig. 4.17 demonstrates that $\text{TDAPSK}^{\text{JM}}$ generally performs worse than DAPSK and TDAPSK in the context of uncoded systems. This is because the joint mapping of the ring amplitude and M_PPSK phase may result in an improved iteration gain for $\text{TDAPSK}^{\text{JM}}$

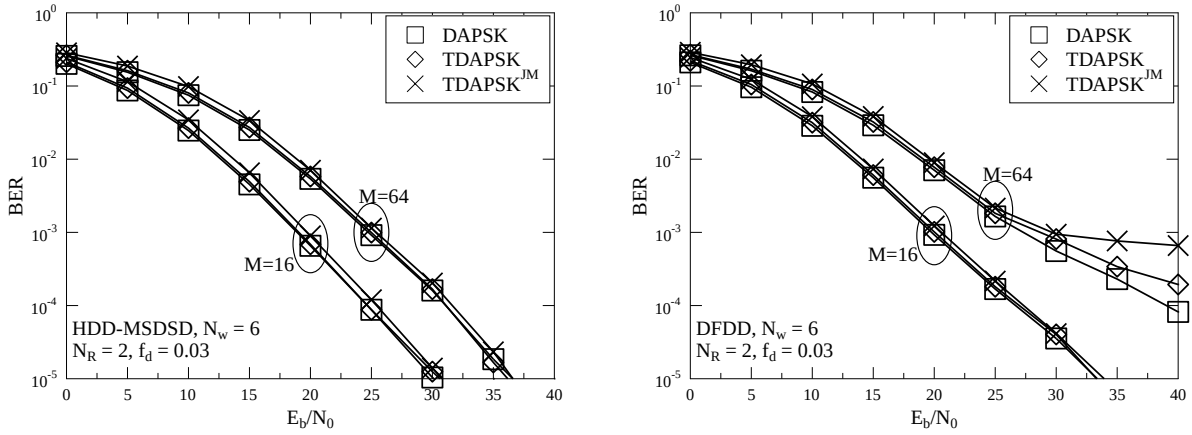

(a) HDD-MSDSD (b) DFDD

Figure 4.17: BER performance comparison between DAPSK, TDAPSK and TDAPSK$^{\text{JM}}$, where HDD-MSDSD and DFDD are employed.

	real-valued multiplications	real-valued additions	comparisons	visited nodes
CDD (TDAPSK$^{\text{JM}}$)	$6N_R + 2M + 2$	$6N_R + 3M - 3$	M	M
CDD (DAPSK)	$6N_R + 3M_A + 7$	$6N_R + M_A - 1$	M_A	M_A
HDD-MSDD (DAPSK/TDAPSK$^{\text{JM}}$)	$(12N_w^2 N_R + 4N_w N_R^2)M^{(N_w-1)}$	$[(12N_w - 6)N_w N_R + (4N_w - 2)N_R^2 + N_R + 2]M^{(N_w-1)}$	$M^{(N_w-1)}$	$M^{(N_w-1)}$
MSDSD's **sortDelta** (TDAPSK$^{\text{JM}}$)	$[(4N_R + 6)v + 6N_R + 5]M$	$(4N_R v + 2v + 2N_R - 1)M$	$O(M \log M)$	M
MSDSD's **findBest** (DAPSK)	$[(4N_R + 2)v + 8N_R + 7]M_A$	$(4N_R v + 4N_R)M_A$	M_A	M_A
MSDSD's **findNext** (DAPSK)	≤ 5	≤ 7	$\leq 2M_A + 1$	≤ 1

Table 4.10: Complexity summary of hard-decision-aided CDD/HDD-MSDD/HDD-MSDSD conceived for uncoded DAPSK and TDAPSK$^{\text{JM}}$.

in coded systems, which implies that TDAPSK$^{\text{JM}}$ detection may produce a lower extrinsic information I_E without *a priori* information i.e. at $I_A = 0$, but the extrinsic information I_E achieved by TDAPSK$^{\text{JM}}$ detection may be higher than that of DAPSK and TDAPSK in the presence of perfect *a priori* information of $I_A = 1$. According to this feature, it is expected that both DAPSK and TDAPSK outperform TDAPSK$^{\text{JM}}$ in uncoded systems, owing to the complete absence of the *a priori* information i.e. for $I_A = 0$. However, it may also be expected that TDAPSK$^{\text{JM}}$ is capable of outperforming both DAPSK and TDAPSK in coded systems, provided that the appropriate channel coding arrangement is selected. We will continue by exploring these features in the next chapter.

4.7.3 Complexity Comparison

As argued before, the data-carrying ring amplitude and the data-carrying M_PPSK phase candidate may be detected either separately or jointly, which depends on their source-bit mapping mechanisms introduced in Sec. 4.2. We provide here a complexity comparison between DAPSK and

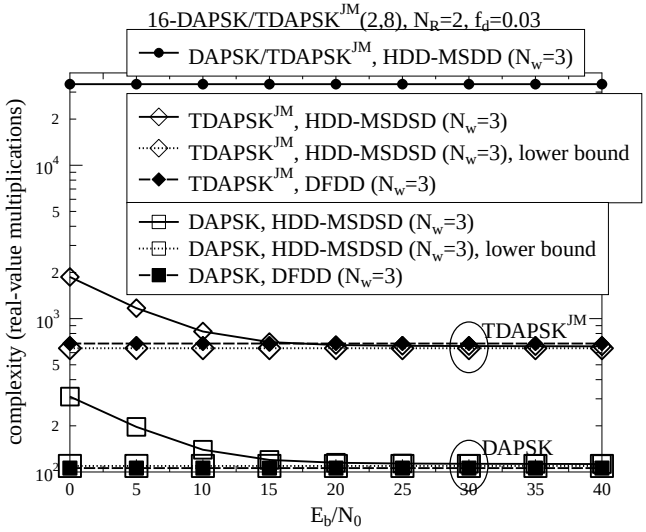

Figure 4.18: Complexity comparison between hard-decision-aided HDD-MSDD, HDD-MSDSD and DFDD associated with $N_w = 3$ conceived for 16-DAPSK(2,8) and 16-TDAPSK$^{\text{JM}}$(2,8), where we have $N_R = 2$ and $f_d = 0.03$.

TDAPSK$^{\text{JM}}$ as representatives of DQAM and DQAM$^{\text{JM}}$, respectively. In more detail, the complexities of CDD, HDD-MSDD and subfunctions of HDD-MSDSD for DAPSK and TDAPSK$^{\text{JM}}$ detection are summarized in Table 4.10, where different types of calculations are separately categorized. Naturally, unneccessary calculations have to be eliminated in practical implementations. For example, all the M_PPSK candidates may be stored so that the repeated calculations such as $\exp(-j\frac{2\pi}{M_P}\check{p}^a_{v-1})$ in line 11 of Table 4.9 may be avoided. Moreover, the DAPSK constellation does not have the amplitude-dependent phase rotation, and hence $\{\psi_t\}_{\forall t}$ and $\{\Psi_t\}_{\forall t}$ may be deleted from all DAPSK detectors.

It may be observed in Table 4.10 that CDD generally exhibits a low detection complexity, while the MSDD complexity may be excessively high. Furthermore, Table 4.10 demonstrates that the MSDSD's "sortDelta" subfunction for TDAPSK$^{\text{JM}}$ detection has a higher complexity order than the MSDSD's "findBest" and "findNext" subfunctions for DAPSK detection. We note that the "sortDelta" subfunction of Table 4.8 used for TDAPSK$^{\text{JM}}$ detection requires a sorting algorithm, where as exemplified by Fig. 4.10, all M constellation points $\{x^m\}_{m=0}^{M-1}$ are ranked according to the increasing order of PED increment values $\{\Delta^m_{v-1}\}_{m=0}^{M-1}$. There are numerous sorting algorithms (e.g. Bubble sort, Timsort, Library sort [285, 286], etc.), and the average number of comparisons required by these algorithms is as high as $O(M \log M)$. By contrast, the "findBest" and "findNext" subfunctions of Table 4.9 for DAPSK detection does not require any sorting algorithms. As exemplified by Fig. 4.10, the revised Schnorr-Euchner search strategy does not have to know the complete list of constellation points, which saves a considerable amount of computational complexity.

Fig. 4.18 provides a complexity comparison between HDD-MSDD, HDD-MSDSD and DFDD conceived for 16-DAPSK(2,8) and 16-TDAPSK$^{\text{JM}}$(2,8), where the detection complexity is quan-

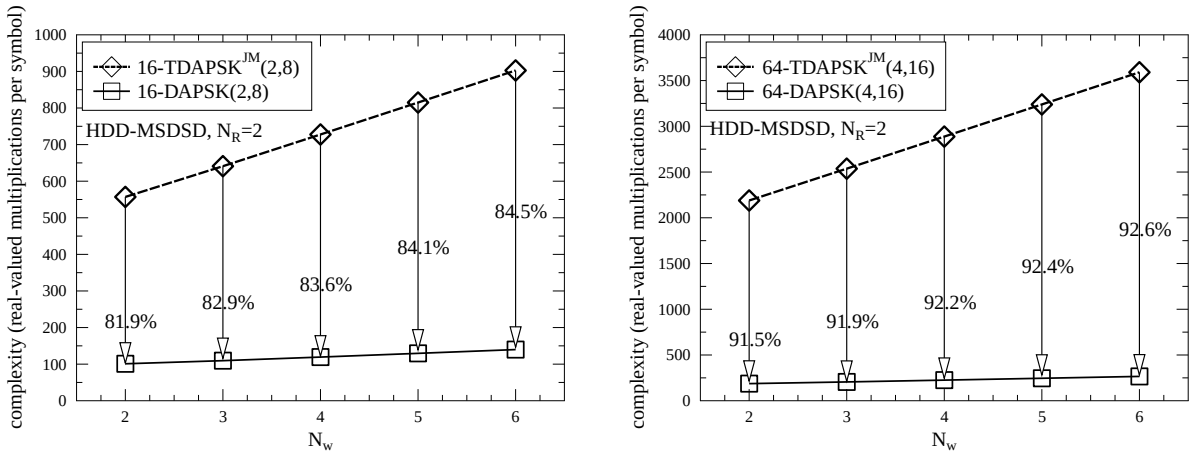

(a) $M = 16$ (b) $M = 64$

Figure 4.19: Complexity comparison between HDD-MSDSD's lower bounds associated with different N_w for DAPSK and TDAPSK$^{\text{JM}}$ detection, where we have $N_R = 2$ and $f_d = 0.03$. The Complexity Reduction Ratios (CRRs) achieved by DAPSK detection compared to TDAPSK$^{\text{JM}}$ detection are marked in figures.

tified in terms of the total number of real-valued multiplications required for detecting a single data-carrying symbol. It can be seen in Fig. 4.18 that the MSDSD introduced in Sec. 4.5 substantially reduces the excessive MSDD complexity, and as E_b/N_0 increases, the MSDSD complexity may converge to its lower bound, which is as low as the DFDD complexity. Furthermore, Fig. 4.18 evidences that compared to TDAPSK$^{\text{JM}}$ detection, both HDD-MSDSD and DFDD exhibit a significant complexity reduction for DAPSK detection.

In order to demonstrate the complexity reduction achieved by separately decoding the ring amplitude and the M_PPSK phase, a complexity comparison between HDD-MSDSD aided TDAPSK$^{\text{JM}}$ using Table 4.8 and HDD-MSDSD assisted DAPSK using Table 4.9 is portrayed by Fig. 4.19. The CRR marked in Fig. 4.19 was defined in Eq. (2.109). As expected, Fig. 4.19a demonstrates that HDD-MSDSD conceived for 16-DAPSK(2,8) achieves a substantial complexity reduction of up to 84.5% compared to 16-TDAPSK$^{\text{JM}}$(2,8) detection, while an even more significant complexity reduction of up to 92.6% is achieved by HDD-MSDSD conceived for 64-DAPSK(4,16), as evidenced by Fig. 4.19b.

4.8 Chapter Conclusions

In Sec. 4.2, we firstly surveyed a variety of bandwidth-efficient DQAM constellations found in the literature, and then their conventional hard-decision-aided CDD and MSDD solutions were summarized in Sec. 4.3 and Sec. 4.4, respectively. Furthermore, we have proposed the hard-decision-aided MSDSD conceived for uncoded DQAM in Sec. 4.5, which is capable of carrying out MSDD by

sphere decoding without imposing any performance loss. We have also revised the hard-decision-aided DFDD conceived for uncoded DQAM schemes in Sec. 4.6, which is equivalent to both the MSDD/MSDSD aided uncoded DQAM associated with decisions feedback and to the linear prediction based blind channel estimation aided coherent detection conceived for uncoded DQAM operating in Rayleigh fading channels.

We have demonstrated in this chapter that similar to uncoded DPSK, the differential noncon-stant modulus constellations may employ the popular noncoherent detectors including CDD, HDD-MSDD, HDD-MSDSD and DFDD. As demonstrated by Table 4.10 and Fig. 4.18, the CDD and the DFDD exhibit a low complexity, but the HDD-MSDSD may be preferred when the fading channels fluctuate rapidly, because Figs. 4.13 and 4.14 demonstrated that the HDD-MSDSD achieves the same detection capability as the HDD-MSDD, while the complexity of the HDD-MSDSD is substantially lower than that of the HDD-MSDD, as presented in Table 4.10 and in Fig. 4.18.

One may argue that DAPSK and ADPSK may be the preferred choices among the DQAM constellations in uncoded systems. We have demonstrated in Fig. 4.15 that DAPSK and ADPSK achieve a similar performance in uncoded systems, and Fig. 4.17 evidenced that the twisted modulated schemes cannot outperform their counterpart of DAPSK in uncoded systems. Considering that there are no ring-amplitude-dependent phase rotations for the DAPSK and ADPSK constellations, the noncoherent detectors for DAPSK and ADPSK may be more straightforward as all phase rotation terms may be deleted. Furthermore, we have demonstrated in Fig. 4.19 that the DQAM$^{\text{JM}}$ schemes exhibit higher detection complexity than the DQAM schemes, which separately modulate the data-carrying ring amplitude and the data-carrying M_PPSK phase. Moreover, the DQAM$^{\text{JM}}$ schemes also perform worse than their DQAM counterparts in uncoded systems, which was exemplified in Fig. 4.17.

In the next chapter, we will continue by investigating the performance features of different DQAM constellations in channel coded systems. The capacity difference between DAPSK and ADPSK will be explicitly reflected in the performance of coded schemes. The potential performance advantage of twisted modulated schemes may also be better observed, when channel coding is applied.

Chapter 5

Noncoherent Detection for Differential Non-Constant Modulus Modulation – Part II: Coded Systems

5.1 Introduction

In order to enhance the achievable error-free transmission for differential non-constant modulus modulations, the noncoherent detectors presented in Chapter 4 should be revised to be able to process soft-bit LLRs. Substantial research efforts have been invested in this area [114, 136, 153, 154, 160]. The classic soft-decision-aided MSDD conceived for coded DQAM is proposed in [114], where an appealing performance is achieved at the cost of the MSDD's exponentially increasing complexity. The typical constellation set size of DQAM is generally larger than that of DPSK, because M-ary DQAM tends to outperform M-ary DPSK for high values of M, which restricts the employment of DPSK to low M. Hence using MSDD is hardly affordable, especially when an increased observation window length is required for rapidly fluctuating fading channels. As a remedy, a low-complexity soft-decision-aided MSDD using Iterative Amplitude/Phase processing (MSDD-IAP) was proposed for coded DAPSK in [160]. More explicitly, the MSDD is invoked for ring amplitude detection, which may be referred to as the Multiple-Symbol Differential Amplitude Detector (MSDAD), while the MSDSD invoked for phase detection may be termed as Multiple-Symbol Differential Phase Sphere Detector (MSDPSD). The MSDAD and the MSDPSD may iteratively exchange their decisions in order to improve the overall performance. Owing to the fact that the constellation set of DQAM's ring amplitude is smaller than its complete constellation set, the employment of MSDAD is more realistic for general DQAM detection than the MSDD. However, how to implement the MSDD using a sphere decoder for ring amplitude detection is an open problem at the time of writing.

Let us recall that the unique structure of the lower triangular matrix $\mathbf{L}$, which is generated by

the decomposition of the fading channel correlation matrix inverse $\mathbf{C}$ according to $\mathbf{C}^{-1} = \mathbf{L}\mathbf{L}^T$ facilitates the sphere decoding of MSDSD aided DPSK, as shown in [113, 127, 132]. However, for the case of MSDD aided DQAM, the fading channel correlation matrix $\mathbf{C}$ in fact depends on the DQAM ring amplitudes, as clearly demonstrated in [159]. This implies that the lower triangular matrix $\mathbf{L}$ required by the sphere decoder cannot be obtained, unless all the DQAM ring amplitudes are known. In Chapter 4, we proposed to tackle this problem by proving that the partial triangular matrix $\widetilde{\mathbf{L}}_{\mathbf{v}}$ defined in (4.52) may be obtained from decomposing the inversion of the partial channel correlation matrix $\widetilde{\mathbf{C}}_{\mathbf{v}}$ according to $\widetilde{\mathbf{C}}_{\mathbf{v}}^{-1} = \widetilde{\mathbf{L}}_{\mathbf{v}}\widetilde{\mathbf{L}}_{\mathbf{v}}^T$ in (4.57), which only requires the SD's previous decisions concerning the ring amplitudes and only contains a single ring amplitude variable for the SD to detect. Following this effort, in Sec. 5.3, we will propose soft-decision-aided MSDSD solutions for coded DQAM schemes, where sphere decoding may be invoked for both ring amplitude detection and phase detection.

Furthermore, as mentioned in Sec. 4.6, the DFDD aided DQAM proposed in [136, 153, 154] stipulates compromised assumption namely that the channel correlation matrix $\mathbf{C}$ is a constant that is independent of symbol-amplitude, and hence these soft-decision-aided DFDD solutions are sub-optimal. In Sec. 5.4, we will further develop the soft-decision-aided DFDD conceived for DQAM of Sec. 4.2, which is also equivalent to the MSDD/MSDSD scheme of Sec. 5.3 associated with decisions feedback.

We summarize the novel contributions provided by this chapter as follows:

1. First of all, the soft-decision-aided MSDD conceived for coded DQAM is introduced in Sec. 5.2. As we demonstrated in Sec. 4.4, the first transmitted symbol's ring amplitude Γ_1 within an observation window may be treated either as an unknown variable by the MSDD or as a known term obtained from the previous decisions feedback provided by the HDD-MSDD of Sec. 4.4. In coded systems, we may still have both MSDD and HDD-MSDD for coded DQAM detection, and yet a new Soft-Decision-Directed MSDD (SDD-MSDD) may be developed for coded DQAM schemes, where the previous decisions on Γ_1 are in the form of *a priori* probabilities instead of hard-bit decisions. We will demonstrate for diverse DQAM schemes that SDD-MSDD may achieve the optimum detection capability for the DAPSK/TDAPSK schemes of Sec. 4.2, while HDD-MSDD may attain a competent performance for ADPSK/TADPSK at the cost of a lower detection complexity.

2. Secondly, the soft-decision-aided MSDSD conceived for coded DQAM is proposed in Sec. 5.3, where sphere decoding is invoked for both ring amplitude detection and phase detection. According to the MSDD arrangements, the soft-decision-aided MSDSD may also be further implemented in the forms of HDD-MSDSD and SDD-MSDSD, where the suitable choices for the different DQAM schemes are the same as for the previously discussed MSDD arrangements, namely SDD-MSDSD for DAPSK/TDAPSK and HDD-MSDSD for ADPSK/TADPSK. Moreover, both the Max-Log-MAP and Approx-Log-MAP algorithms may be invoked by the soft-decision-aided MSDSD, HDD-MSDSD and SDD-MSDSD conceived for coded DQAM,

where the Approx-Log-MAP of Algorithm 3.2, which was proposed for MSDSD aided DPSK may be applied for coded DQAM detection.

3. Thirdly, since Gray-coded labelling is applied to the DQAM constellations, we propose to apply the reduced-complexity design conceived in Sec. 3.3.3 for MSDSD aided DPSK also to the soft-decision-aided MSDSD conceived for coded DQAM. More explicitly, thanks to the constellation symmetry of Gray labelling, the SD does not have to visit all the constellation points for obtaining the best candidate. Instead, only the constellation points located in the first quadrant have to be visited, and then the rest of the constellation points may be later visited by the SD in a zigzag pattern if required, where the new metric values may be simply obtained by toggling the polarities of the metrics calculated for the constellation points of the first quadrant. In this way, the complexity of the soft-decision-aided MSDSD may be substantially reduced without imposing any performance loss.

4. Fourthly, the soft-decision-aided MSDD-IAP conceived for coded DAPSK in [160] is revised in order to make it applicable to all DQAM constellations, which map the bits to the data-carrying ring amplitude index and to the data-carrying M_PPSK index separately. We propose to implement the MSDAD in [160] by sphere decoding, and hence the terminology may be revised to Multiple-Symbol Differential Amplitude Sphere Detection (MSDASD). Since both ring amplitude detection and phase detection are carried out by SD, the terminology of MSDD-IAP may be revised to MSDSD-IAP, which may also be implemented as HDD-MSDSD-IAP and SDD-MSDSD-IAP, if required. Furthermore, the reduced-complexity design conceived for MSDSD aided DPSK in Sec. 3.3.3 may be directly applied to the MSDPSD, so that the total number of constellation points visited by the MSDSD-IAP may be substantially reduced. We will demonstrate that the MSDSD-IAP designed for coded DAPSK and HDD-MSDSD-IAP conceived for coded ADPSK are capable of achieving their respective near-optimum MSDD performance at a substantially reduced detection complexity.

5. Furthermore, the soft-decision-aided DFDD is conceived for coded DQAM in Sec. 5.4 based on the hard-decision-aided DFDD introduced in Sec. 4.6. We will demonstrate that the proposed DFDD outperforms the suboptimal DFDD solutions of [136, 153, 154], which assume a constant fixed channel correlation matrix $\mathbf{C}$ that is independent of symbol-amplitude.

6. Last but not least, a survey of the performance results of soft-decision-aided noncoherent detectors conceived for coded DQAM is offered in this chapter, and suitable design choices are suggested for different DQAM constellations. The capacity of DQAM is more closely approached with the aid of channel coding. Furthermore, we also demonstrate that when the fading channels fluctuate rapidly, the soft-decision-aided HDD-MSDSD-IAP conceived for ADPSK may even outperform PSAM aided coherent QAM detection in a variety of channel coding assisted systems.

The rest of this chapter is organized as follows. The soft-decision-aided MSDD conceived for

general coded DQAM detection is presented in Sec. 5.2. The soft-decision-assited MSDSD is proposed in Sec. 5.3 for coded DQAM, which highlights the principles of the MSDSD algorithm, the reduced-complexity MSDSD algorithm, the MSDD-IAP generalized for all DQAM constellations, which modulate the ring amplitude index and the M_PPSK phase index separately and the reduced-complexity MSDSD-IAP. The soft-decision-aided DFDD conceived for coded DQAM is proposed in Sec. 5.4. Furthermore, our performance results are presented in Sec. 5.5, and the chapter conclusions are offered in Sec. 5.6.

5.2 Soft-Decision-Aided MSDD Conceived for Coded DQAM

According to the MSDD scheme of Fig. 1.12, the *a posteriori* probability of Eq. (4.40) derived for the optimum Log-MAP algorithm [27, 240, 241] and invoked by MSDD may be represented by:

$$\begin{aligned} L_p(b_k|\mathbf{Y}) &= \ln \frac{\sum_{\forall\Gamma_1} \sum_{\forall\bar{\mathbf{S}}\in\bar{\mathbf{S}}_{b_k=1}} p(\bar{\mathbf{S}}|\mathbf{Y})}{\sum_{\forall\Gamma_1} \sum_{\forall\bar{\mathbf{S}}\in\bar{\mathbf{S}}_{b_k=0}} p(\bar{\mathbf{S}}|\mathbf{Y})} \\ &= \ln \frac{\sum_{\forall\Gamma_1} \sum_{\forall\bar{\mathbf{S}}\in\bar{\mathbf{S}}_{b_k=1}} p(\mathbf{Y}|\bar{\mathbf{S}},\Gamma_1) p(\bar{\mathbf{S}}) p(\Gamma_1)}{\sum_{\forall\Gamma_1} \sum_{\forall\bar{\mathbf{S}}\in\bar{\mathbf{S}}_{b_k=0}} p(\mathbf{Y}|\bar{\mathbf{S}},\Gamma_1) p(\bar{\mathbf{S}}) p(\Gamma_1)} \\ &= \ln \frac{\sum_{\forall\Gamma_1} \sum_{\forall\bar{\mathbf{S}}\in\bar{\mathbf{S}}_{b_k=1}} \exp\{d(\Gamma_1,\bar{\mathbf{S}})\}}{\sum_{\forall\Gamma_1} \sum_{\forall\bar{\mathbf{S}}\in\bar{\mathbf{S}}_{b_k=0}} \exp\{d(\Gamma_1,\bar{\mathbf{S}})\}}, \end{aligned} \tag{5.1}$$

where the subsets $\bar{\mathbf{S}}_{b_k=1}$ and $\bar{\mathbf{S}}_{b_k=0}$ refer to the MSDD combination sets associated with $\bar{\mathbf{S}} = \bar{\mathbf{A}}\bar{\mathbf{P}}\bar{\mathbf{O}}$ of Eq. (4.35), with the specific bit b_k being fixed to 1 and 0, respectively. We may assume that the first transmitted symbol's ring amplitude Γ_1 is random uniformly distributed according to $\{p(\Gamma_1) = \frac{1}{M_A}\}_{\forall\Gamma_1}$, because Γ_1 does not carry any source information and it is not aimed for detection. As a result, the probability metric $d(\Gamma_1,\bar{\mathbf{S}})$ seen in Eq. (5.1) may be expressed as:

$$d(\Gamma_1,\bar{\mathbf{S}}) = -\mathrm{tr}(\mathbf{Y}^H\bar{\mathbf{P}}\bar{\mathbf{O}}\mathbf{C}^{-1}\bar{\mathbf{O}}^H\bar{\mathbf{P}}^H\mathbf{Y}) - \ln[\det(\mathbf{C})] + \sum_{\bar{k}=1}^{(N_w-1)\mathrm{BPS}} \widetilde{b}_{\bar{k}} L_a(b_{\bar{k}}), \tag{5.2}$$

where $\{\widetilde{b}_{\bar{k}}\}_{\bar{k}=1}^{(N_w-1)\mathrm{BPS}}$ denotes the bit mapping corresponding to the MSDD candidate $\bar{\mathbf{S}}$ of Eq. (4.35), while $\{L_a(b_{\bar{k}})\}_{\bar{k}=1}^{(N_w-1)\mathrm{BPS}}$ denotes the *a priori* LLRs gleaned from a channel decoder. The low-complexity Max-Log-MAP algorithm may be invoked by the MSDD for the sake of simplifying the Log-MAP of Eq. (5.1), and it is given by [27]:

$$L_p(b_k|\mathbf{Y}) = \max_{\forall\Gamma_1} \max_{\forall\bar{\mathbf{S}}\in\bar{\mathbf{S}}_{b_k=1}} d(\Gamma_1,\bar{\mathbf{S}}) - \max_{\forall\Gamma_1} \max_{\forall\bar{\mathbf{S}}\in\bar{\mathbf{S}}_{b_k=0}} d(\Gamma_1,\bar{\mathbf{S}}), \tag{5.3}$$

which imposes a performance loss, owing to the fact that only the maximum probability metrics are taken into account. In order to compensate for the sub-optimum nature of the Max-Log-MAP algorithm, the near-optimum Approx-Log-MAP algorithm may be formulated as [28, 239]:

$$L_p(b_k|\mathbf{Y}) = \mathrm{jac}_{\forall\Gamma_1}\, \mathrm{jac}_{\forall\bar{\mathbf{S}}\in\bar{\mathbf{S}}_{b_k=1}}\, d(\Gamma_1,\bar{\mathbf{S}}) - \mathrm{jac}_{\forall\Gamma_1}\, \mathrm{jac}_{\forall\bar{\mathbf{S}}\in\bar{\mathbf{S}}_{b_k=0}}\, d(\Gamma_1,\bar{\mathbf{S}}), \tag{5.4}$$

where jac denotes the corrected Jacobian algorithm of Eq. (2.36). We note that a total number of $M_A M^{(N_w-1)}$ candidates have to be evaluated and compared by the MSDD using either the

Log-MAP algorithm of Eq. (5.1), or the Max-Log-MAP of Eq. (5.3) or alternatively, the Approx-Log-MAP algorithm of Eq. (5.4).

For uncoded systems, the so-called HDD-MSDD of Eq. (4.46) may conveniently facilitate the first transmitted symbol's ring amplitude Γ_1 by feeding back the previous hard-bit decisions. For coded systems, however, we may utilize soft-decisions, which may lead us to the optimum Soft-Decision-Directed MSDD (SDD-MSDD). In more detail, instead of assuming that Γ_1 is an equiprobable variable, the *a priori* probabilities $\{p(\Gamma_1)\}_{\forall\Gamma_1}$ may be obtained from the previous MSDD window. Therefore, the probability metric seen in Eq. (5.2) may be modified to take $\{p(\Gamma_1)\}_{\forall\Gamma_1}$ into account as:

$$d(\Gamma_1, \bar{\mathbf{S}}) = -\text{tr}(\mathbf{Y}^H \bar{\mathbf{P}} \bar{\mathbf{O}} \mathbf{C}^{-1} \bar{\mathbf{O}}^H \bar{\mathbf{P}}^H \mathbf{Y}) - \ln[\det(\mathbf{C})] + \sum_{\bar{k}=1}^{(N_w-1)\text{BPS}} \widetilde{b}_{\bar{k}} L_a(b_{\bar{k}}) + \ln[p(\Gamma_1)]. \quad (5.5)$$

Once all the probability metrics $\{d(\Gamma_1, \bar{\mathbf{S}})\}_{\forall\Gamma_1, \forall\bar{\mathbf{S}}}$ of Eq. (5.5) have been evaluated for producing soft-bit decisions, the probability of the last transmitted symbol's ring amplitude $p(\Gamma_{N_w})$ may be updated according to the Log-MAP, to the Max-Log-MAP or to the Approx-Log-MAP as:

$$\begin{aligned} \ln\left[p(\Gamma_{N_w})\right] &= \ln\left\{ \sum_{\forall\bar{\mathbf{A}} \in \langle \forall\Gamma_1, \Gamma_{N_w} \rangle} \exp\left[d(\Gamma_1, \bar{\mathbf{S}})\right] \right\} \\ &\approx \max_{\forall\bar{\mathbf{A}} \in \langle \forall\Gamma_1, \Gamma_{N_w} \rangle} d(\Gamma_1, \bar{\mathbf{S}}) \\ &\approx \text{jac}_{\forall\bar{\mathbf{A}} \in \langle \forall\Gamma_1, \Gamma_{N_w} \rangle} d(\Gamma_1, \bar{\mathbf{S}}). \end{aligned} \quad (5.6)$$

In Eq. (5.6), the ring amplitudes transmitted both at the start of the MSDD window and at the end of the MSDD window may represent trellis states $\langle \Gamma_1, \Gamma_{N_w} \rangle$, while the data-carrying ring amplitudes $\bar{\mathbf{A}}$ govern the state transition. As a result, all possible initial states $\forall\Gamma_1$ and all possible transitions $\forall\bar{\mathbf{A}}$ that lead to the specific trellis termination state of Γ_{N_w} have to be taken into account for evaluating $\ln\left[p(\Gamma_{N_w})\right]$, as seen in Eq. (5.6).

As an example, the SDD-MSDD invoking the Approx-Log-MAP algorithm is summarized in the form of its psudo-code in Table 5.1, which demonstrates that updating $\{\ln\left[p(\Gamma_1)\right]\}_{\forall\Gamma_1}$ according to Eq. (5.6) does not impose any significant amount of extra complexity. We note that the original MSDD invoking the Approx-Log-MAP algorithm may be implemented by the pseudo-code presented in Table 5.1, where the probability metric evaluation in line 4 may be replaced by Eq. (5.2), while the lines 1,5,6,9 conceived for the state probability update may be deleted accordingly. Similarly to the MSDD, a total of $M_A M^{(N_w-1)}$ candidates have to be evaluated and compared by the SDD-MSDD.

Moreover, similar to the uncoded system of Sec. 4.4, the HDD-MSDD may also be invoked for coded nonconstant modulus constellations. Once a hard-decision concerning $\hat{\Gamma}_1$ is determined from the previous MSDD window, the HDD-MSDD associated with a known $\hat{\Gamma}_1$ only has to test $M^{(N_w-1)}$ candidates. However, for coded systems, the HDD-MSDD only works reliably for ADPSK/TADPSK. More explicitly, for ADPSK/TADPSK, the most recent transmitted symbol's ring amplitude Γ_{N_w} of each MSDD block is given by the most recent data-carrying symbol's ring

Function: $[\{L_p(b_k)\}_{k=1}^{(N_w-1)\text{BPS}}] = \textbf{SDD-MSDD}(\mathbf{Y}, \{L_a(b_k)\}_{k=1}^{(N_w-1)\text{BPS}})$

Requirements: As long as the normalized Doppler frequency f_d and noise power N_0 are known, all the $M_A M^{N_w-1}$ candidates for the variable $\mathbf{C}^{-1}$ and $\ln[\det(\mathbf{C})]$ may be evaluated according to Eq. (4.44) and stored in memory before calling this function.

All the M^{N_w-1} combinations of bits mapping $\{[\widetilde{b}_1 \cdots \widetilde{b}_{(N_w-1)\text{BPS}}] = \textbf{dec2bin}(i)\}_{i=0}^{M^{N_w-1}-1}$ determining MSDD candidate $\bar{\mathbf{S}} = \bar{\mathbf{A}}\bar{\mathbf{P}}\bar{\mathbf{O}}$ of Eq. (4.35) may also be pre-stored.

$\{\ln[p(\Gamma_{N_w})] = -\inf\}_{\forall\Gamma_{N_w}}$ //initialize the termination states

for $\mu_1 = 0$ **to** $M_A - 1$ //evaluate all initial states $\Gamma_1 = \frac{\alpha^{\mu_1}}{\sqrt{\beta}}$

  for $i = 0$ **to** $M^{N_w-1} - 1$ //evaluate all data-carrying MSDD candidates

    $d(\Gamma_1, \bar{\mathbf{S}}) = -\text{tr}(\mathbf{Y}^H\bar{\mathbf{P}}\bar{\mathbf{O}}\mathbf{C}^{-1}\bar{\mathbf{O}}^H\bar{\mathbf{P}}^H\mathbf{Y}) - \ln[\det(\mathbf{C})] + \sum_{\bar{k}=1}^{(N_w-1)\text{BPS}} \widetilde{b}_{\bar{k}} L_a(b_{\bar{k}}) + \ln[p(\Gamma_1)]$ //update probability metrics according to Eq. (5.5)

    (DAPSK/TDAPSK:) $\Gamma_{N_w} = \Gamma_1 \sum_{t=1}^{N_w-1} \gamma_t$ //evaluate state transition

    (ADPSK/TADPSK:) $\Gamma_{N_w} = \gamma_{N_w-1}$

    $\ln[p(\Gamma_{N_w})] = \text{jac}\{\ln[p(\Gamma_{N_w})], d(\Gamma_1, \bar{\mathbf{S}})\}$ //update the termination state according to Eq. (5.6)

  end for

end for

$\{\ln[p(\Gamma_{N_1})] = \ln[p(\Gamma_{N_w})]\}_{\forall\Gamma_{N_1}}$ //update $\{p(\Gamma_{N_1})\}_{\forall\Gamma_{N_1}}$ for the next window

for $k = 1$ **to** $(N_w - 1)$BPS //produce soft-bit decisions

  $\zeta_1 = -\inf$

  $\zeta_0 = -\inf$

  for $\mu_1 = 0$ **to** $M_A - 1$ //visit all candidate Γ_1

    for $i = 0$ **to** $M^{N_w-1} - 1$ //visit all candidate $\bar{\mathbf{S}}$

      if $\widetilde{b}_k = 1$ //we have $[\widetilde{b}_1 \cdots \widetilde{b}_{(N_w-1)\text{BPS}}] = \textbf{dec2bin}(i)$

        $\zeta_1 = \text{jac}\,[\zeta_1, d(\Gamma_1, \bar{\mathbf{S}})]$

      else

        $\zeta_0 = \text{jac}\,[\zeta_0, d(\Gamma_1, \bar{\mathbf{S}})]$

      end if

    end for

  end for

  $L_p(b_k) = \zeta_1 - \zeta_0$ //output the a posteriori LLR for b_k

end for

Table 5.1: Pseudo-code for SDD-MSDD invoking the Approx-Log-MAP algorithm.

amplitude as $\Gamma_{N_w} = \gamma_{N_w-1}$, which directly becomes Γ_1 of the next MSDD block. By contrast, for DAPSK/TDAPSK, the most recent transmitted symbol's ring amplitude depends on all data-carrying symbol's ring amplitudes since we have $\Gamma_{N_w} = \left(\prod_{t=1}^{N_w-1} \gamma_t\right) \Gamma_1$, where all the MSDD decisions are made for the data-carrying symbols' ring amplitudes $\{\gamma_t\}$, rather than for $\{\Gamma_t\}$. This implies that the MSDD decisions concerning $\Gamma_{N_w} = \gamma_{N_w-1}$ are more reliable for ADPSK/TADPSK than the corresponding MSDD decisions on $\Gamma_{N_w} = \left(\prod_{t=1}^{N_w-1} \gamma_t\right) \Gamma_1$ of DAPSK/TDAPSK. This problem does not affect the hard-decision-aided MSDD/MSDSD conceived for DAPSK/TADPSK in uncoded systems, but the soft-decision-aided MSDD requires better LLR integrity. We will further characterize this feature in terms of our performance results in Sec. 5.5.

As a special case, the soft-decision-aided CDD may be implemented by the MSDD associated with $N_w = 2$. According to the hard-decision-aided CDD of Eq. (4.48), the MSDD metric of

Eq. (5.2) may be extended for CDD as:

$$\begin{aligned} d(\Gamma_1, x_1) &= -\mathrm{tr}(\mathbf{Y}^H \bar{\mathbf{P}} \bar{\mathbf{O}} \mathbf{C}^{-1} \bar{\mathbf{O}}^H \bar{\mathbf{P}}^H \mathbf{Y}) - \ln[\det(\mathbf{C})] + \sum_{\bar{k}=1}^{\mathrm{BPS}} \widetilde{b}_{\bar{k}} L_a(b_{\bar{k}}) \\ &= -\frac{(\Gamma_2^2 + N_0)\|\mathbf{Y}_1^2\|^2 + (\Gamma_1^2 + N_0)\|\mathbf{Y}_2^2\|^2 - 2\Gamma_1\Gamma_2\rho_1 \Re(\omega_1^* \psi_1^* \mathbf{Y}_2 \mathbf{Y}_1^H)}{\det(\mathbf{C})} \\ &\quad - \ln[\det(\mathbf{C})] + \sum_{\bar{k}=1}^{\mathrm{BPS}} \widetilde{b}_{\bar{k}} L_a(b_{\bar{k}}), \end{aligned} \tag{5.7}$$

where only $x_1 = \gamma_1 \omega_1 \psi_1$ carries source information, while the determinant of the channel correlation matrix associated with $N_w = 2$ is given by $\det(\mathbf{C}) = (\Gamma_2^2 \rho_0 + N_0)(\Gamma_1^2 \rho_0 + N_0) - \Gamma_1^2 \Gamma_2^2 \rho_1^2$. Explicitly, we have $\Gamma_2 = \gamma_1 \Gamma_1$ for DAPSK/TDAPSK or $\Gamma_2 = \gamma_1$ for ADPSK/TADPSK. Furthermore, CDD may also be implemented in the forms of Soft-Decision-Directed CDD (SDD-CDD) and Hard-Decision-Directed CDD (HDD-CDD), as special cases of the SDD-MSDD and HDD-MSDD of this section, respectively, where the observation window length is fixed to be the minimum of $N_w = 2$. We also note that soft-decision-aided CDD conceived for DAPSK was proposed in [157–159] for the case of Quasi-Static Rayleigh fading channels, which are expected to experience a performance loss in continuously fading channels.

5.3 Soft-Decision-Aided MSDSD Conceived for Coded DQAM

In this section, we propose to implement the soft-decision-aided MSDD introduced in Sec. 5.2 by invoking sphere decoding, and we dedicate substantial efforts to reducing the MSDSD complexity. In more detail, based on the development of the hard-decision-aided MSDSD conceived for uncoded DQAM in Sec. 4.5, the principles of the MSDSD algorithm designed for coded DQAM detection are formulated in Sec. 5.3.1. Following this, a reduced-complexity MSDSD algorithm is proposed in Sec. 5.3.2 in order to reduce the number of constellation points visited by the SD, which is achieved by exploring the symmetry of the Gray labelling. In Sec. 5.3.3, the efficient MSDD-IAP proposed in [160] is generalized for all DQAM constellations, which modulate the ring amplitude index and the M_PPSK phase index separately. Furthermore, the reduced-complexity MSDSD-IAP is proposed in Sec. 5.3.4, where sphere decoding is invoked for ring amplitude detection, while the reduced-complexity design proposed for soft-decision-aided MSDSD conceived for coded DPSK in Sec. 3.3.3 is applied to M_PPSK phase detection.

5.3.1 MSDSD Algorithm

Similar to the soft-decision-aided MSDSD for DPSK detection of Sec. 3.3.2, SD may be invoked for MSDD aided DQAM using the Max-Log-MAP algorithm of Eq. (5.3), where the maximization has to be converted to minimization, while the probability metrics should be guaranteed to have positive values. Therefore, according to the hard-decision-aided MSDSD's PED of Eq. (4.59) and to the PED increment of Eq. (4.60), the MSDD probability metric of Eq. (5.3) may be transformed

to:

$$d = \sum_{v=1}^{N_w} \left\| \sum_{t=1}^{v} l_{N_w-t+1,N_w-v+1} \bar{\Psi}_t^* \bar{\Omega}_t^* \mathbf{Y}_t \right\|^2 + \ln[\det(\mathbf{C})] + (\sum_{v=2}^{N_w} -\xi_{v-1}) - \sum_{v=2}^{N_w} \left[\sum_{\bar{k}=(v-2)\text{BPS}+1}^{(v-1)\text{BPS}} \widetilde{b}_{\bar{k}} L_a(b_{\bar{k}}) - \ln \overline{C}_A^{v-1} \right], \tag{5.8}$$

where the constant of $\xi_{v-1} = \min_{\forall\{\Gamma_t\}_{t=1}^{v}} \ln\left[(\Gamma_v^2\rho_0 + N_0) - \widetilde{\mathbf{e}}_v^T \widetilde{\mathbf{C}}_{\mathbf{v-1}}^{-1} \widetilde{\mathbf{e}}_v\right]$ defined in Eq. (4.62) and the constant of $\overline{C}_A^{v-1} = \prod_{\bar{k}=(v-2)\text{BPS}+1}^{(v-1)\text{BPS}} \{1 + \exp[L_a(b_{\bar{k}})]\}$ are artificially added in order to maintain a positive ED. Moreover, the elements $\{\{l_{N_w-t+1,N_w-v+1}\}_{t=1}^{v}\}_{v=1}^{N_w}$ are from the lower triangular matrix $\mathbf{L}$ defined in Eq. (4.50).

As a result, the MSDSD's PED based on Eq. (5.8) is given by:

$$\begin{aligned} d_v &= \|l_{N_w,N_w}\mathbf{Y}_1\|^2 + \ln\left(\Gamma_1^2\rho_0 + N_0\right) + \sum_{\bar{v}=2}^{v} \left\| \sum_{t=1}^{\bar{v}} l_{N_w-t+1,N_w-\bar{v}+1} \bar{\Psi}_t^* \bar{\Omega}_t^* \mathbf{Y}_t \right\|^2 \\ &\quad + \sum_{\bar{v}=2}^{v} \ln\left[\left(\Gamma_{\bar{v}}^2\rho_0 + N_0\right) - \widetilde{\mathbf{e}}_{\bar{v}}^T \widetilde{\mathbf{C}}_{\bar{\mathbf{v}}-\mathbf{1}}^{-1} \widetilde{\mathbf{e}}_{\bar{v}}\right] - \sum_{\bar{v}=2}^{v} \xi_{\bar{v}-1} \\ &\quad - \sum_{\bar{v}=2}^{v} \left[\sum_{\bar{k}=(\bar{v}-2)\text{BPS}+1}^{(\bar{v}-1)\text{BPS}} \widetilde{b}_{\bar{k}} L_a(b_{\bar{k}}) - \ln \overline{C}_A^{\bar{v}-1} \right] \\ &= d_{v-1} + \Delta_{v-1}. \end{aligned} \tag{5.9}$$

According to Propositions 1 and 2 of Sec. 4.5, the PED increment Δ_{v-1} seen in Eq. (5.9) may be defined as:

$$\Delta_{v-1} = \left\| \widetilde{l}_{1,1} \bar{\Psi}_{v-1}^* \bar{\Omega}_{v-1}^* \mathbf{Y}_v + \omega_{v-1}\psi_{v-1} \left(\sum_{t=1}^{v-1} \widetilde{l}_{v-t+1,1} \bar{\Psi}_t^* \bar{\Omega}_t^* \mathbf{Y}_t \right) \right\|^2 + \Xi_v - \left[\sum_{\bar{k}_v=1}^{\text{BPS}} \widetilde{b}_{\bar{k}_v} L_a(b_{\bar{k}_v}) - \ln \overline{C}_A^{v-1} \right], \tag{5.10}$$

where the determinant term Ξ_v is defined by Eq. (4.61), while the coefficients $\{\widetilde{l}_{v-t+1,1}\}_{t=1}^{v}$ are elements in the $(v \times v)$ lower triangular submatrix $\widetilde{\mathbf{L}}_\mathbf{v}$ defined in Eq. (4.52). Once again, according to Proposition 1 in Sec. 4.5, we always have $\{l_{N_w-t+1,N_w-v+1} = \widetilde{l}_{v-t+1,1}\}_{t=1}^{v}$. We note that for the symbol-based detection of Δ_{v-1}, the bit index subscript $\bar{k}_v$ in Eq. (5.10) ranges from 1 to BPS according to the relationship of $\bar{k}_v = \bar{k} - (v-2)\text{BPS}$.

Therefore, the SD algorithm proposed in [132] and summarized in Table 3.3 may be invoked for soft-decision-aided MSDSD conceived for coded DQAM, where the Schnorr-Euchner search strategy using the PED increment of Eq. (5.10) is summarized in Table 5.2. It can be seen that the SD associated with index v has to order all the M candidate child nodes by evaluating and comparing their PED increments $\{\Delta_{v-1}^m\}_{m=0}^{M-1}$ according to their ascending order. The sorting algorithm may involve an average of $O(M \log M)$ comparisons [285, 286].

We note that the SD algorithm may commence from the initial PED $d_1 = 0$ for the sake of simplicity, but the Γ_1-related term $d_1 = \|l_{N_w,N_w}\mathbf{Y}_1\|^2 + \ln\left(\Gamma_1^2\rho_0 + N_0\right)$ seen in Eq. (5.9) should

Subfunction: $[\{\Delta_{v-1}^{\bar{m}}\}_{\bar{m}=0}^{M-1}, \{x_{v-1}^{\bar{m}}\}_{\bar{m}=0}^{M-1}, n_{v-1}] =$ **sortDelta**$(\{\mathbf{Y}_t\}_{t=1}^{v}, \{\hat{\Gamma}_t\}_{t=1}^{v-1}, \{\hat{\Psi}_t\}_{t=1}^{v-1}, \{\hat{\Omega}_t\}_{t=1}^{v-1}, \{L_a^{v-1,k}\}_{k=1}^{\text{BPS}}, \ln \overline{C}_A^{v-1})$

Requirements: $\{\widetilde{l}_{v-t+1,1}\}_{t=1}^{v}$ in Eq. (5.10) are taken from $\widetilde{\mathbf{L}}(\{\hat{\Gamma}_t\}_{t=1}^{v-1}, \Gamma_v) = \widetilde{\mathbf{L}}_{\mathbf{v}}$, which are pre-evaluated and pre-stored. $\Xi(\{\hat{\Gamma}_t\}_{t=1}^{v-1}, \Gamma_v) = \Xi_v$ in Eq. (5.10) are also pre-evaluated and pre-stored.

1: **for** m=0 **to** $M-1$	//visit all M child nodes.
2: (DAPSK/TDAPSK:) $\Gamma_v = \gamma_{v-1} \cdot \hat{\Gamma}_{v-1}$	//visit $x_{v-1}^m = \gamma_{v-1} \cdot \omega_{v-1} \cdot \psi_{v-1}$.
(ADPSK/TADPSK:) $\Gamma_v = \gamma_{v-1}$	
3: $\Delta_{v-1}^m = \|\widetilde{l}_{1,1}\hat{\Psi}_{v-1}^*\hat{\Omega}_{v-1}^*\mathbf{Y}_v + \omega_{v-1}\psi_{v-1}(\sum_{t=1}^{v-1}\widetilde{l}_{v-t+1,1}\hat{\Psi}_t^*\hat{\Omega}_t^*\mathbf{Y}_t)\|^2$ $+\Xi(\{\hat{\Gamma}_t\}_{t=1}^{v-1}, \Gamma_v) - \sum_{k=1}^{\text{BPS}}\widetilde{b}_k L_a^{v-1,k} + \ln \overline{C}_A^{v-1}$	//evaluate PED increments of Eq. (5.10).
4: **end for**	
5: $[\{\Delta_{v-1}^{\bar{m}}\}_{\bar{m}=0}^{M-1}, \{x_{v-1}^{\bar{m}}\}_{\bar{m}=0}^{M-1}] =$ **sort**$(\{\Delta_{v-1}^m\}_{m=0}^{M-1})$	//rank PED increments in increasing order.
6: $n_{v-1} = 0$	//initialize child node counter.

Table 5.2: Pseudocode for the Schnorr-Euchner search strategy tailored for the SD algorithm of Table 3.3, when it's invoked for soft-decision-aided MSDSD conceived for coded DQAM.

be added to the SD's output radius before the associated ED comparison over the different values of Γ_1, as seen in the Max-Log-MAP formula of Eq. (5.3). Therefore, the optimum ED is given by $d_{MAP} = \max_{\forall \Gamma_1}\left(\max_{\forall \bar{\mathbf{A}}, \bar{\mathbf{P}}} d\right)$, where $\left(\max_{\forall \bar{\mathbf{A}}, \bar{\mathbf{P}}} d\right)$ is found by the SD, while the corresponding MAP hard-bit decisions $\{b_k^{MAP}\}_{k=1}^{(N_w-1)BPS}$ are also obtained along with d_{MAP}. Therefore, the Max-Log-MAP formula of Eq. (5.3) may be completed according to:

$$L_p(b_k) = \begin{cases} -d_{MAP} + \bar{d}_{MAP}, & \text{if } b_k^{MAP} = 1 \\ -\bar{d}_{MAP} + d_{MAP}, & \text{if } b_k^{MAP} = 0 \end{cases}. \tag{5.11}$$

The second term of the probability metric in Eq. (5.11) namely $\bar{d}_{MAP}$ is obtained by invoking the SD for each soft-bit decision $L_p(b_k)$, where the specific bit b_k is fixed to be the toggled MAP decision $\bar{b}_k^{MAP}$, where we have $\bar{d}_{MAP} = \max_{\forall \Gamma_1}\left(\max_{\forall \{\bar{\mathbf{A}}, \bar{\mathbf{P}}\}_{b_k = \bar{b}_k^{MAP}}} d\right)$. Furthermore, we note that Eq. (5.11) may be revised according to Algorithm 3.2, so that the near-optimum Approx-Log-MAP algorithm may also be invoked by the MSDSD aided DQAM.

In summary, for detecting each MSDD/MSDSD window, the MSDSD aided DQAM introduced in this section may invoke the SD for a total number of $M_A \cdot [1 + (N_w - 1)\text{BPS}]$ times. Consequently, the total of visited nodes is reduced from $M_A \times M^{(N_w-1)}$ as required by the MSDD to a lower bound of $\{M_A \times (N_w - 1) \times M + M_A \times (N_w - 1) \times \text{BPS} \times [(N_w - 2) \times M + M/2]\}$, as necessitated by the MSDSD.

Moreover, the SDD-MSDD of Table 5.1 may also be implemented in form of Soft-Decision-Directed MSDSD (SDD-MSDSD), where the Γ_1-related term added to the SD's output radius seen in Eq. (5.9) has to take into account the *a priori* probabilities concerning Γ_1 namely $p(\Gamma_1)$ as $d_1 = \|l_{N_w,N_w}\mathbf{Y}_1\|^2 + \ln\left(\Gamma_1^2\rho_0 + N_0\right) + \ln[p(\Gamma_1)]$. In order to obtain the *a priori* probabilities of $\{\ln[p(\Gamma_1)]\}_{\forall \Gamma_1}$, the SD's output EDs may be utilized for evaluating the *a posteriori* probabilities of Γ_{N_w} according to the Max-Log-MAP and Approx-Log-MAP algorithms as:

$$\begin{aligned} \ln[p(\Gamma_{N_w})] &\approx \max_{\forall \hat{\mathbf{A}} \in \langle \forall \Gamma_1, \Gamma_{N_w} \rangle} d(\Gamma_1, \hat{\bar{\mathbf{S}}}) \\ &\approx \text{jac}_{\forall \hat{\mathbf{A}} \in \langle \forall \Gamma_1, \Gamma_{N_w} \rangle} d(\Gamma_1, \hat{\bar{\mathbf{S}}}), \end{aligned} \tag{5.12}$$

where we have $\{d(\Gamma_1, \hat{\mathbf{S}}) = \max_{\forall \bar{\mathbf{A}}, \bar{\mathbf{P}}} d\}_{\forall \Gamma_1, \forall \hat{\mathbf{A}}}$ and the corresponding transitions $\{\hat{\mathbf{A}}\}$ are output by each of the $M_A \cdot [1 + (N_w - 1)\text{BPS}]$ number of SD search operations. Following this, the *a posteriori* probabilities $\{\ln[p(\Gamma_{N_w})]\}_{\forall \Gamma_{N_w}}$ of Eq. (5.12) may become the *a priori* probabilities $\{\ln[p(\Gamma_1)]\}_{\forall \Gamma_1}$ for the next MSDSD window. Apart from the extra term of $\{\ln[p(\Gamma_1)]\}_{\forall \Gamma_1}$, the SDD-MSDSD may proceed in the exact by the same way, as the MSDSD.

Similarly, the HDD-MSDD may also be implemented in form of the HDD-MSDSD, where a decision concerning Γ_{N_w} may be obtained according to the SD search for $\left(\max_{\forall \bar{\mathbf{A}}, \bar{\mathbf{P}}} d\right)$, given a specific $\hat{\Gamma}_1$ value. We note that the first transmitted symbol's ring amplitude $\hat{\Gamma}_1$ is known from previous decision feedback. Therefore, the HDD-MSDSD may also produce the *a posteriori* LLRs in the same way as the MSDSD, except that the comparisons over the different Γ_1 values for obtaining d_{MAP} and $\bar{d}_{MAP}$ in Eq. (5.11) may be eliminated, and there is no need to evaluate the Γ_1-related term $d_1 = \|l_{N_w,N_w}\mathbf{Y}_1\|^2 + \ln\left(\Gamma_1^2\rho_0 + N_0\right)$ for HDD-MSDSD.

5.3.2 Reduced-Complexity MSDSD Algorithm

It was proposed in Sec. 3.3.3 that by exploring the constellation symmetry provided by the M_PPSK scheme's Gray-coded labelling, the number of constellation points visited by the SD's Schnorr-Euchner search strategy may be reduced for the soft-decision-aided MSDSD conceived for coded DPSK detection. In this section, we propose to apply the same reduced-complexity design to the soft-decision-aided MSDSD conceived for coded DQAM. The resultant reduced-complexity soft-decision-aided MSDSD proposed in this section is applicable to a range of constellations, including DAPSK, TDAPSK, ADPSK and TADPSK, which modulate the data-carrying M_A-level ring amplitude index $a = \text{bin2dec}(b_{\text{BPS}_P+1} \cdots b_{\text{BPS}})$ and the data-carrying M_PPSK phase index $p = \text{bin2dec}(b_1 \cdots b_{\text{BPS}_P})$ separately, since their M_PPSK detection may be performed in the same way as the DPSK detection of Sec. 3.3.3.

First of all, let us extend the PED increment of Eq. (5.10) so that the ring-amplitude-related term and the M_PPSK-related term may be separated as:

$$\Delta_{v-1} = \widetilde{\Delta}_{v-1} + \overline{\Delta}_{v-1}, \tag{5.13}$$

where the ring amplitude-related term $\widetilde{\Delta}_{v-1}$ derived from Eq. (5.10) is given by:

$$\widetilde{\Delta}_{v-1} = \left\| \widetilde{l}_{1,1} \bar{\Psi}^*_{v-1} \bar{\Omega}^*_{v-1} \mathbf{Y}_v \right\|^2 + \left\| \sum_{t=1}^{v-1} \widetilde{l}_{v-t+1,1} \bar{\Psi}^*_t \bar{\Omega}^*_t \mathbf{Y}_t \right\|^2 + \ln \overline{C}_A^{v-1} + \Xi_v - \frac{L_a(b_1) + L_a(b_2)}{2}, \tag{5.14}$$

which is invariant over the M_PPSK parameter ω_{v-1} in Eq. (5.10). Furthermore, the M_PPSK-related term $\overline{\Delta}_{v-1}$ seen in Eq. (5.13) is given by:

$$\begin{aligned} \overline{\Delta}_{v-1} &= -2\Re\left[(\omega'_{v-1})^* z'_{v-1}\right] - \sum_{\bar{k}_v=1}^{\text{BPS}} \widetilde{b}_{\bar{k}_v} L_a(b_{\bar{k}_v}) + \frac{L_a(b_1) + L_a(b_2)}{2} \\ &= -2\Re(\omega'_{v-1})\Re(z'_{v-1}) - 2\Im(\omega'_{v-1})\Im(z'_{v-1}) - \sum_{\bar{k}_v=1}^{\text{BPS}} \widetilde{b}_{\bar{k}_v} L_a(b_{\bar{k}_v}) + \frac{L_a(b_1) + L_a(b_2)}{2}, \end{aligned} \tag{5.15}$$

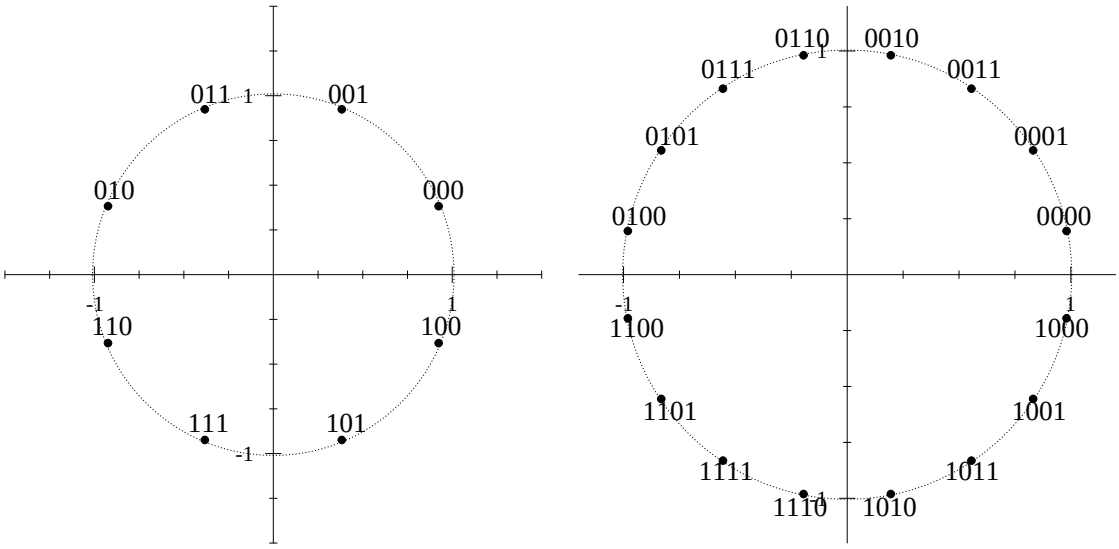

(a) Rotated 8PSK (b) Rotated 16PSK

Figure 5.1: Constellation diagrams for detecting 8PSK and 16PSK. We deliberately rotate all the detected M_PPSK constellations of Fig. 2.4 (except the special case of $M_P = 2$) anti-clockwise by (π/M_P), so that there are exactly $M_P/4$ constellation points in each quadrant.

where we deliberately rotate all the detected M_PPSK constellations[1] (except for the special case of $M_P = 2$) anti-clockwise by (π/M_P) as seen in [159, 236]. Explicitly, we invoke $\omega'_{v-1} = \omega_{v-1} \cdot \exp\left(j\frac{\pi}{M_P}\right)$, so that there are exactly $(M_P/4)$ PSK phases in each quadrant. The corresponding examples of rotated 8PSK and rotated 16PSK constellation diagrams are portrayed in Fig. 5.1. As a result, the M_PPSK-related decision variable z'_{v-1} used for detecting the variable ω'_{v-1} seen in Eq. (5.15) is given by:

$$\begin{aligned} z'_{v-1} &= -\widetilde{l}_{1,1}\psi^*_{v-1}\bar{\Psi}^*_{v-1}\bar{\Omega}^*_{v-1}\mathbf{Y}_v\left(\sum_{t=1}^{v-1}\widetilde{l}_{v-t+1,1}\bar{\Psi}^*_t\bar{\Omega}^*_t\mathbf{Y}_t\right)^H \cdot \exp\left(j\frac{\pi}{M_P}\right) \\ &= \mathbf{Y}^{\mathrm{SD}}_{v-1}(\mathbf{H}^{\mathrm{SD}}_{v-1})^H \cdot \exp\left(j\frac{\pi}{M_P}\right), \end{aligned} \tag{5.16}$$

which is rotated from the decision varible $z^{\omega|\Gamma}_{v-1}$ of Eq. (4.66), and we have the N_R-element equivalent "received signal vector" $\mathbf{Y}^{\mathrm{SD}}_{v-1} = \widetilde{l}_{1,1}\psi^*_{v-1}\bar{\Psi}^*_{v-1}\bar{\Omega}^*_{v-1}\mathbf{Y}_v$ and the N_R-element equivalent "fading channel vector" $\mathbf{H}^{\mathrm{SD}}_{v-1} = -\sum_{t=1}^{v-1}\widetilde{l}_{v-t+1,1}\bar{\Psi}^*_t\bar{\Omega}^*_t\mathbf{Y}_t$ for detecting the phase variable of ω'_{v-1}.

When a specific ring amplitude candidate Γ_v is fixed, ranking the M_P candidates of ω'_{v-1} according to their PED increment values Δ_{v-1} of Eq. (5.13) is equivalent to comparing the values of the PSK-related local PED increment $\overline{\Delta}_{v-1}$ of Eq. (5.15). For M_PPSK phase detection, an example of reduced-complexity soft-decision-aided MSDSD conceived for coded DQPSK may be found in Sec. 3.3.3. For a generic differential nonconstant modulus constellation, we may consider

[1] We note that only the detected M_PPSK constellation diagrams are rotated at the receiver. The encoding process introduced in Sec. 4.2 remains unchanged.

the M constellation points as $M/4$ groups of QPSK-like constellation points that are associated with the same magnitudes but different polarities. As a result, the local minimum within each group is simply given by:

$$\overline{\Delta}_{v-1}^{g} = -\left|t_{v-1}^{Re_g}\right| - \left|t_{v-1}^{Im_g}\right| - \sum_{\widetilde{k}_v=3}^{\mathrm{BPS}} \widetilde{b}_{\widetilde{k}_v} L_a(b_{\widetilde{k}_v}). \tag{5.17}$$

where the real and the imaginary part of z'_{v-1} are associated with $L_a(b_2)$ and $L_a(b_1)$, respectively, as:

$$\begin{array}{ll} t_{v-1}^{Re_g} & = 2A^{\overline{g}} \cdot \Re(z'_{v-1}) - \frac{L_a(b_2)}{2}, \\ t_{v-1}^{Im_g} & = 2B^{\overline{g}} \cdot \Im(z'_{v-1}) - \frac{L_a(b_1)}{2}. \end{array} \tag{5.18}$$

The specific coordinates of the M_PPSK phases ω'_{v-1} of Eq. (5.15) which are located in the first quadrant are given by $\{(A^{\overline{g}}, B^{\overline{g}})\}_{\overline{g}=0}^{M_P/4-1}$, that are used in Eq. (5.18). We note that there are a total number of $M_P/4$ PSK phases in the first quadrant, but there are $M/4$ constellation points in the first quadrant. More explicitly, for each data-carrying constellation point, its source bit-mapping for a specific group index seen in Eq. (5.17) is given by $\{\widetilde{b}_{\widetilde{k}}\}_{\widetilde{k}=3}^{\mathrm{BPS}}$, where the relationship between the group index $g = \mathrm{bin2dec}(\widetilde{b}_3 \cdots \widetilde{b}_{\mathrm{BPS}})$, the PSK phase group index $\overline{g} = \mathrm{bin2dec}(\widetilde{b}_3 \cdots \widetilde{b}_{\mathrm{BPS}_P})$ and the ring amplitude index $a = \mathrm{bin2dec}(\widetilde{b}_{\mathrm{BPS}_P+1} \cdots \widetilde{b}_{\mathrm{BPS}})$ is given by $\{\{g = \overline{g} \cdot M_A + a\}_{\overline{g}=0}^{M_P/4-1}\}_{a=0}^{M_A-1}$. As a result, the globally minimum PED increment of Eq. (5.13) is given by:

$$\Delta_{v-1} = \min_{\forall g} \overline{\Delta}_{v-1}^{g} + \widetilde{\Delta}_{v-1}^{a}, \tag{5.19}$$

where both the M_PPSK-related term of $\overline{\Delta}_{v-1}^{g}$ and the ring amplitude-related term of $\widetilde{\Delta}_{v-1}^{a}$ are determined by the group index g.

In order to obtain a legitimate child node associated with the PED increment Δ_{v-1} when the SD visits index v, a Comparion Window (CW) may be introduced for the Schnorr-Euchner search strategy. At the beginning, the CW stores the local minimum of the PED increments $\{\overline{\Delta}_{v-1}^{g} + \overline{C}_{v-1}^{a}\}_{g=0}^{M/4-1}$ from all groups and produces the global minimum according to Eq. (5.19), which is represented by the "findBest" subfunction of Table 5.3. To find the next tentative child node, CW has to visit the next child node within the group which is the one that produced the previous global child node. A group may be marked 'completed' when all its four QPSK-like child nodes have been tested using a zigzag pattern. By contrast, each incomplete group may provide a local child node candidate in the CW, and the CW may choose the specific global child node, which has the minimum metric. This strategy is represented by the "findNext" subfunction of Table 5.4.

Compared to the Schnorr-Euchner algorithm conceived for the hard-decision-aided MSDSD summarized in Table 4.9, it is more difficult for the soft-decision-aided MSDSD to visit the constellation points in a zigzag pattern, when the *a priori* LLRs gleaned from a channel decoder are utilized, because the bit-based channel decoders are unaware of which particular modulation scheme is employed. In fact, for a DQAM constellation, the BPS_A bits mapped to the ring amplitude and the $BPS_P - 2$ bits mapped to the M_PPSK magnitudes joinly determine the constellation magnitudes in the first quadrant. As a result, in order to maintain the optimum performance, a total

Subfunction: $[\{|t_{v-1}^{Re_g}|\}_{g=0}^{M/4-1}, \{|t_{v-1}^{Im_g}|\}_{g=0}^{M/4-1}, \{\widetilde{\Delta}_{v-1}^{a}\}_{a=0}^{M_A-1}, \{\mathrm{CW}_{v-1}^{g}\}_{g=0}^{M/4-1}, \{\mathrm{CW}m_{v-1}^{g}\}_{g=0}^{M/4-1}, \{n_{v-1}^{g}\}_{g=0}^{M/4-1}, \Delta_{v-1}, m_{v-1}, n_{v-1}] = \textbf{findBest}(\{\mathbf{Y}_t\}_{t=1}^{v}, \{\hat{\Gamma}_t\}_{t=1}^{v-1}, \{\hat{\Psi}_t\}_{t=1}^{v-1}, \{\hat{\Omega}_t\}_{t=1}^{v-1}, \{L_a^{v-1,k}\}_{k=1}^{\mathrm{BPS}}, \ln \overline{C}_A^{v-1})$

Input: $\{\mathbf{Y}_t\}_{t=1}^{v}$, $\{\hat{\Gamma}_t\}_{t=1}^{v-1}$, $\{\hat{\Psi}_t\}_{t=1}^{v-1}$, $\{\hat{\Omega}_t\}_{t=1}^{v-1}$, $\{L_a^{v-1,k}\}_{k=1}^{\mathrm{BPS}}$ and $\ln \overline{C}_A^{v-1}$ are required for evaluating z'_{v-1} of Eq. (5.16) and $\{\widetilde{\Delta}_{v-1}^{a}\}_{a=0}^{M_A-1}$ of Eq. (5.14).

Output: $\{|t_{v-1}^{Re_g}|\}_{g=0}^{M/4-1}$ and $\{|t_{v-1}^{Im_g}|\}_{g=0}^{M/4-1}$ are defined in Eq. (5.18). $\{\mathrm{CW}_{v-1}^{g}\}_{g=0}^{M/4-1}$ and $\{\mathrm{CW}m_{v-1}^{g}\}_{g=0}^{M/4-1}$ store local minima and their corresponding constellation point indices, respectively. $\{n_{v-1}^{g}\}_{g=0}^{M/4-1}$ refers to local child node counter for each group. Δ_{v-1} and m_{v-1} are the global minimum PED increment and its corresponding constellation point index. n_{v-1} refers to global child node counter.

Requirements: Coordinates of M_PPSK phases which are located in the first quadrant are given by $\{(A^{\overline{g}}, B^{\overline{g}})\}_{\overline{g}=0}^{M_P/4-1}$. For the sake of simplicity, the doubled coordinate values $\{(\overline{A^{\overline{g}}}, \overline{B^{\overline{g}}})\}_{\overline{g}=0}^{M_P/4-1}$ are pre-stored, where we have $\{\overline{A^{\overline{g}}} = 2A^{\overline{g}}\}_{\forall \overline{g}}$ and $\{\overline{B^{\overline{g}}} = 2B^{\overline{g}}\}_{\forall \overline{g}}$. We define the *a priori* knowledge of group index as $\{P^g = \sum_{k=3}^{\mathrm{BPS}} \widetilde{b}_k L_a^{v-1,k}\}_{g=0}^{M/4-1}$.

1: **for** $a = 0$ **to** $M_A - 1$
2: (DAPSK/TDAPSK:) $\Gamma_v = \gamma_{v-1}^{a} \cdot \hat{\Gamma}_{v-1}$ //fix the specific Γ_v for $\widetilde{\mathbf{L}}_{\mathbf{v}}$ and Ξ_v
(ADPSK/TADPSK:) $\Gamma_v = \gamma_{v-1}^{a}$
3: $\mathbf{Y}_{v-1}^{\mathrm{SD}} = \widetilde{l}_{1,1} \psi_{v-1}^{*} \bar{\Psi}_{v-1}^{*} \bar{\Omega}_{v-1}^{*} \mathbf{Y}_v$ //evaluate $\mathbf{Y}_{v-1}^{\mathrm{SD}}$ according to Eq. (5.16)
4: $\mathbf{H}_{v-1}^{\mathrm{SD}} = -\sum_{t=1}^{v-1} \widetilde{l}_{v-t+1,1} \bar{\Psi}_t^{*} \bar{\Omega}_t^{*} \mathbf{Y}_t$ //evaluate $\mathbf{H}_{v-1}^{\mathrm{SD}}$ according to Eq. (5.16)
5: $z'_{v-1} = \mathbf{Y}_{v-1}^{\mathrm{SD}} (\mathbf{H}_{v-1}^{\mathrm{SD}})^H \cdot \exp\left(j\frac{\pi}{M_P}\right)$ //evaluate M_PPSK-related decision varible of Eq. (5.16)
6: $\widetilde{\Delta}_{v-1}^{a} = \|\mathbf{Y}_{v-1}^{\mathrm{SD}}\|^2 + \|\mathbf{H}_{v-1}^{\mathrm{SD}}\|^2 + \ln \overline{C}_A^{v-1} + \Xi_v - \frac{L_a^{v-1,1} + L_a^{v-1,2}}{2}$ //evaluate ring-amplitude-related term of Eq. (5.14)
7: **for** $\overline{g} = 0$ **to** $M_P/4 - 1$
8: $g = \overline{g} \cdot M_A + a$ //update group index
9: $|t_{v-1}^{Re_g}| = |\overline{A^{\overline{g}}} \cdot \Re(z'_{v-1}) - \frac{L_a^{v-1,2}}{2}|$ //associate $\Re(z'_{v-1})$ to $L_a^{v-1,2}$ as defined in Eq. (5.18)
10: $|t_{v-1}^{Im_g}| = |\overline{B^{\overline{g}}} \cdot \Im(z'_{v-1}) - \frac{L_a^{v-1,1}}{2}|$ //associate $\Im(z'_{v-1})$ to $L_a^{v-1,1}$ as defined in Eq. (5.18)
11: $\mathrm{CW}_{v-1}^{g} = -|t_{v-1}^{Re_g}| - |t_{v-1}^{Im_g}| - P^g + \widetilde{\Delta}_{v-1}^{a}$ //update local minimum of each group
12: $b_1 = (t_{v-1}^{Im_g} < 0)$ //update local optimum child node index
13: $b_2 = (t_{v-1}^{Re_g} < 0)$
14: $\mathrm{CW}m_{v-1}^{g} = \textbf{bin2dec}(b_1 b_2) \cdot M/4 + g$ //recall that we have $[b_3 \cdots b_{\mathrm{BPS}}] = \textbf{dec2bin}(g)$
15: $n_{v-1}^{g} = 0$ //initialize child node counter for each group
16: **end for**
17: **end for**
18: $[\Delta_{v-1}, \hat{g}] = \textbf{min}(\{\mathrm{CW}_{v-1}^{g}\}_{g=0}^{M/4-1})$ //update global minimum
19: $m_{v-1} = \mathrm{CW}m_{v-1}^{\hat{g}}$ //initialize global optimum child node index
20: $n_{v-1} = 0$ //update global child node counter

Table 5.3: Pseudo-code for the Schnorr-Euchner search strategy tailored for the reduced-complexity soft-decision-aided MSDSD conceived for coded DQAM (Part I).

Subfunction: $[\{\mathrm{CW}_{v-1}^{g}\}_{g=0}^{M/4-1}, \{\mathrm{CW}m_{v-1}^{g}\}_{g=0}^{M/4-1}, \{n_{v-1}^{g}\}_{g=0}^{M/4-1}, \{\mathrm{cd}_{v-1}^{g}\}_{g=0}^{M/4-1}, \Delta_{v-1}, m_{v-1}, n_{v-1}]$
$= \textbf{findNext}(\{|t_{v-1}^{Re_g}|\}_{g=0}^{M/4-1}, \{|t_{v-1}^{Im_g}|\}_{g=0}^{M/4-1}, \{\widetilde{\Delta}_{v-1}^{a}\}_{a=0}^{M_A-1}, \{\mathrm{CW}_{v-1}^{g}\}_{g=0}^{M/4-1}, \{\mathrm{CW}m_{v-1}^{g}\}_{g=0}^{M/4-1}, \{n_{v-1}^{g}\}_{g=0}^{M/4-1}, \{\mathrm{cd}_{v-1}^{g}\}_{g=0}^{M/4-1}, \Delta_{v-1}, m_{v-1}, n_{v-1})$

1:	$b_1 \cdots b_{\mathrm{BPS}} = \textbf{dec2bin}(m_{v-1})$	//obtain the previously tested child node
2:	$\hat{a} = \textbf{bin2dec}(b_{\mathrm{BPS}_P+1} \cdots b_{\mathrm{BPS}})$	//previously tested group's amplitude index
3:	$\hat{g} = \textbf{bin2dec}(b_3 \cdots b_{\mathrm{BPS}_P}) \cdot M_A + \hat{a}$	//update previously tested group's index
4:	$n_{v-1}^{\hat{g}} + +$	//update child node counter
5:	**switch** $n_{v-1}^{\hat{g}}$	
6:	**case** 1: $\mathrm{cd}_{v-1}^{\hat{g}} = \textbf{sign}(|t_{v-1}^{Re_{\hat{g}}}| - |t_{v-1}^{Im_{\hat{g}}}|)$	//update the condition of group $\hat{g}$
7:	**if** $\mathrm{cd}_{v-1}^{\hat{g}} == 1$	//the case of $|t_{v-1}^{Re_{\hat{g}}}| > |t_{v-1}^{Im_{\hat{g}}}|$
8:	$\mathrm{CW}_{v-1}^{\hat{g}} = -|t_{v-1}^{Re_{\hat{g}}}| + |t_{v-1}^{Im_{\hat{g}}}| - P^{\hat{g}} + \widetilde{\Delta}_{v-1}^{\hat{a}}$	//alter the imaginary part of the local minimum
9:	$\mathrm{CW}m_{v-1}^{\hat{g}} = \textbf{bin2dec}(\bar{b}_1 b_2) \cdot M/4 + \hat{g}$	//alter b_1 in the mapping of the local optimum
10:	**else**	
11:	$\mathrm{CW}_{v-1}^{\hat{g}} = |t_{v-1}^{Re_{\hat{g}}}| - |t_{v-1}^{Im_{\hat{g}}}| - P^{\hat{g}} + \widetilde{\Delta}_{v-1}^{\hat{a}}$	//alter the real part of the local minimum
12:	$\mathrm{CW}m_{v-1}^{\hat{g}} = \textbf{bin2dec}(b_1 \bar{b}_2) \cdot M/4 + \hat{g}$	//alter b_2 in the mapping of the local optimum
13:	**end if**	
14:	**break**	
15:	**case** 2: $\mathrm{CW}_{v-1}^{\hat{g}} = -\overline{\Delta}_{v-1} - 2P^{\hat{g}} + 2\widetilde{\Delta}_{v-1}^{\hat{a}}$	//alter decision made in Case 1
16:	$\mathrm{CW}m_{v-1}(\hat{g}) = \textbf{bin2dec}(\bar{b}_1 \bar{b}_2) \cdot M/4 + \hat{g}$	
17:	**break**	
18:	**case** 3: $\mathrm{CW}_{v-1}^{\hat{g}} = |t_{v-1}^{Re_{\hat{g}}}| + |t_{v-1}^{Im_{\hat{g}}}| - P^{\hat{g}} + \widetilde{\Delta}_{v-1}^{\hat{a}}$	//alter the local optimum child node
19:	**if** $\mathrm{cd}_{v-1}^{\hat{g}} == 1$ $\mathrm{CW}m_{v-1}^{\hat{g}} = \textbf{bin2dec}(\bar{b}_1 b_2) \cdot M/4 + \hat{g}$	//alter b_1 in the mapping decision maded in Case 2
20:	**else** $\mathrm{CW}m_{v-1}^{\hat{g}} = \textbf{bin2dec}(b_1 \bar{b}_2) \cdot M/4 + \hat{g}$	//alter b_2 in the mapping decision maded in Case 2
21:	**break**	
22:	**end switch**	
23:	$\Delta_{v-1} = \inf$	//initialize global minimum
24:	**for** $g = 0$ **to** $M/4 - 1$	
25:	**if** $\mathrm{CW}_{v-1}^{g} < \Delta_{v-1}$ **and** $n_{v-1}^{g} < 4$	//compare local minimums from un-full groups
26:	$\Delta_{v-1} = \mathrm{CW}_{v-1}^{g}$	//update global minimum
27:	$m_{v-1} = \mathrm{CW}m_{v-1}^{g}$	//update global child node
28:	**end if**	
29:	**end for**	
30:	$n_{v-1} + +$	//update global child node counter

Table 5.4: Pseudo-code for the Schnorr-Euchner search strategy tailored for the reduced-complexity soft-decision-aided MSDSD conceived for coded DQAM (Part II).

of $2^{(BPS_A+BPS_P-2)} = M/4$ groups have to be evaluated and compared within the CW. Nonetheless, up to 75% of the child nodes are avoided by our reduced-complexity design in the soft MSDSD, as verified by the examples portrayed in Fig. 5.2. It can be seen in Fig. 5.2 that with the same number of SD steps, the soft-decision-aided MSDSD for 16-DAPSK(2,8) detection using the Schnorr-Euchner algorithm of Tables 5.3 and 5.4 visits a substantially reduced number of constellation points compared to the soft-decision-aided MSDSD aided 16-TDAPSK$^{\mathrm{JM}}$(2,8) detector of Table 5.2.

More explicitly, Fig. 5.2-a) shows that for the MSDSD aided 16-TDAPSK$^{\mathrm{JM}}$(2,8) detection, the "sortDelta" subfunction of Table 5.2 has to evaluate and compare all $(M = 16)$ PED increment values Δ_{v-1} of Eq. (5.10) by visiting all the $(M = 16)$ constellation points, when the SD visits the indices $v = 2$ and $v = 3$ for the first time in Step ① and Step ②, respectively. The PED $d_v = d_{v-1} + \Delta_{v-1}$ defined in Eq. (5.9) may be updated, when the SD increases or decreases its index v. After a valid MSDSD solution is found at the SD index $v = 3$ in Step ②, the SD radius is

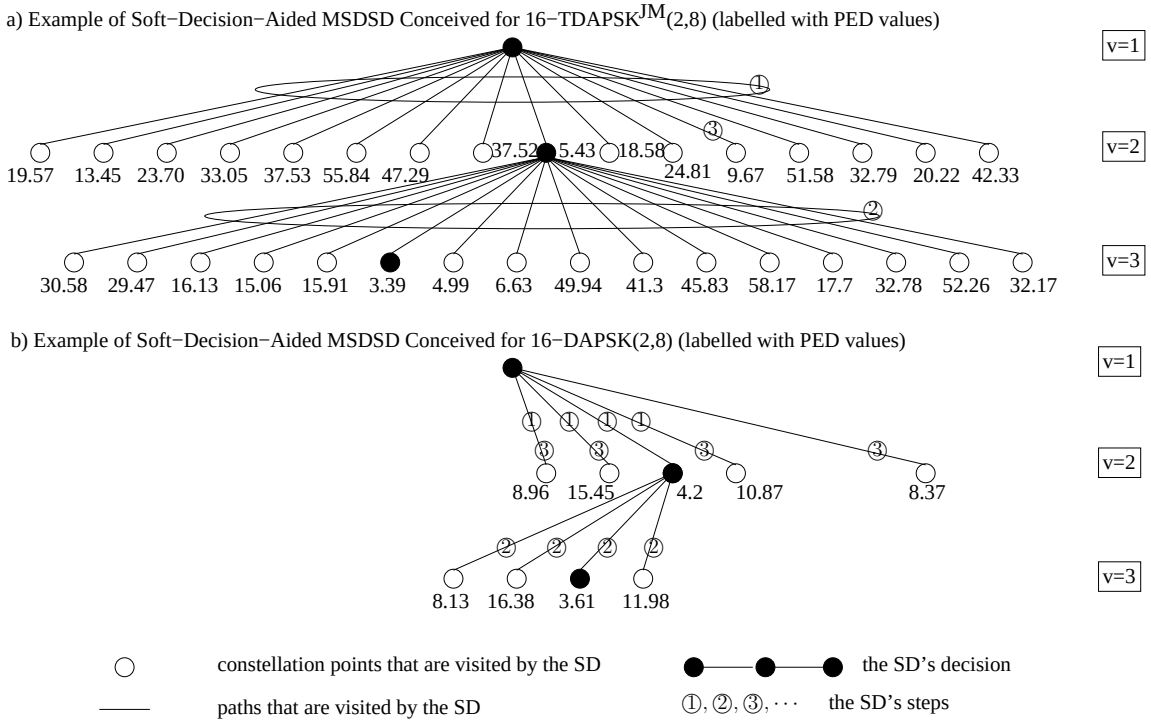

Figure 5.2: Example of soft-decision-aided MSDSD for 16-TDAPSK$^{\text{JM}}$(2,8) detection invoking the Schnorr-Euchner search strategy of Table 5.2 in comparison to soft-decision-aided MSDSD for 16-DAPSK(2,8) detection invoking Tables 5.3 and 5.4, which are recorded at SNR=9 dB, $f_d = 0.03$ and $I_A = 0.3$, where we have $N_R = 2$ and $N_w = 3$.

updated to the corresponding ED of $d = 3.39$. For Step ③, the SD decreases its index to $v = 2$ in order to visit the second-best candidate, whose PED value of $d_2 = 9.67$ turns out to be higher than the SD radius. Hence the SD index may be decreased to $v = 1$, which terminates the search.

By contrast, for the reduced-complexity MSDSD aided 16-DAPSK(2,8) detection, Fig. 5.2-b) shows that when the SD visits index $v = 2$ for the first time in Step ①, the "findBest" subfunction of Table 5.3 firstly evaluates the $M_A = 2$ ring amplitude-related PED increment values $\{\widetilde{\Delta}_{v-1}^{a}\}_{a=0}^{M_A-1}$ of Eq. (5.14) and the $M/4 = 4$ local minima $\{\overline{\Delta}_{v-1}^{g}\}_{g=0}^{M/4-1}$ of Eq. (5.17) for the phase-related PED increment values $\overline{\Delta}_{v-1}$ of Eq. (5.15). As a result, a total of $M/4 = 4$ nodes are visited in Step ① of Fig. 5.2-b), where the optimum PED at $v = 2$ is given by $d_2 = d_1 + \Delta_1 = 4.2$ according to the maximum PED increment value for Δ_1 evaluated by Eq. (5.19). Similarly, when the SD visits index $v = 3$ for the first time in Fig. 5.2-b), a total of $M/4 = 4$ nodes are visited by the "findBest" subfunction of Table 5.3, and then the SD radius is updated to $d = 3.61$ in Step ①. Moreover, when the SD visits the index $v = 2$ for the second time in Step ③ of Fig. 5.2-b), the "findNext" subfunction of Table 5.4 firstly visits a new child node having $d_2 = 8.37$ in the group which previously produced $d_2 = 4.2$ in Step ②, and then the global minimum is updated to $d_2 = 8.37$ according to Eq. (5.19). However, this PED is already higher than the SD sphere radius. Therefore, the SD may further reduce its index to $v = 1$ and terminate its search.

In summary, the conventional Schnorr-Euchner search strategy of Table 5.2 has to visit all the

constellation points in order to find the best candidate for the SD to visit first and then a sorting algorithm [285, 286] is required for ranking the priorities of the remaining constellation points, in order to assit the next decision candidate that the SD may visit later. By contrast, only the constellation points located in the first quadrant are visited by the "findBest" subfunction of Table 5.3, while then the rest of the constellation points may be visited by the "findNext"subfunction of Table 5.4 in a zigzag-pattern, as and when required by the SD, where their PED increment metric values may be simply obtained by toggling the polarities of those evaluated by "findBest". There is no need for invoking any sorting algorithm. As a result, the reduced-complexity MSDSD algorithm of Tables 5.3 and 5.4 is capable of skipping up to 75% of the total number of constellation points visited by the SD compared to the MSDSD algorithm of Table 5.2, which is clearly exemplified in Fig. 5.2.

As a result, for the sake of detecting the symbols of a MSDSD window, the total number of nodes visited is reduced to a lower bound of $\{M_A \times [(N_w - 1) \times M/4 + (N_w - 2)] + M_A \times (N_w - 1) \times \text{BPS} \times [(N_w - 1) \times M/4 + (N_w - 2)]\}$, where the subfunctions "findBest" and "findNext" of Tables 5.3 and 5.4 are invoked at least $(N_w - 1)$ and $(N_w - 2)$ times, respectively, for completing a SD search.

5.3.3 MSDD-Iterative Amplitude/Phase Algorithm

It is widely recognized that the MSDD complexity of DQAM detection may be significantly reduced, if the ring amplitudes and phases may be separately detected. However, it was demonstrated in the previous sections that completely independently detecting the ring amplitude and the phase may lead to a performance loss. It was proposed in [160] that a MSDD using Iterative Amplitude/Phase processing (MSDD-IAP) is capable of achieving a near-optimum performance for coded DAPSK detection, while the detection complexity may be subtantially reduced, since reduced subsets of ring amplitudes and M_PPSK phase candidates are visited separately.

More explicitly, a MSDD is conceived for ring amplitude detection, which is termed as Multiple-Symbol Differential Amplitude Detection (MSDAD), and similarly, a MSDSD is dedicated for M_PPSK phase detection, which is termed as Multiple-Symbol Differential Phase Sphere Detection (MSDPSD). The MSDAD and the MSDPSD may iteratively exchange their decisions in order to improve the overall performance. We will demonstrate in Sec. 5.5.2 that although the performance of uncoded DQAM using MSDD-IAP still suffers from an irreducible error floor, its soft-decision-aided coded counterpart may indeed approach the optimum performance in the low-SNR region.

First of all, let us generalize the steps of MSDD-IAP using the Max-Log-MAP algorithm proposed in [160] for all DQAM constellations, which modulate the ring amplitude index and the M_PPSK phase index separately as follows:

Algorithm 5.1: Procedures of Soft-Decision-Aided MSDD-IAP Conceived for Coded DQAM Using Max-Log-MAP.

(1) An initial estimate of the M_PPSK phases in the matrix $\bar{\mathbf{P}}$ of Eq. (4.35) may be obtained by the CDD introduced in Sec. 4.3.

(2) Upon obtaining $\hat{\bar{\mathbf{P}}}$ in Step (1) above, an estimate of the first transmitted symbol's ring amplitude Γ_1 and the ring amplitudes matrix $\bar{\mathbf{A}}$ of Eq. (4.35) may be obtained by the MSDAD as:

$$\left\{\hat{\Gamma}_1, \hat{\bar{\mathbf{A}}}\right\} = \arg \max_{\forall \Gamma_1} \max_{\forall \bar{\mathbf{A}}} d(\Gamma_1, \bar{\mathbf{A}}, \hat{\bar{\mathbf{P}}}), \tag{5.20}$$

where the MSDAD metric $d(\Gamma_1, \bar{\mathbf{A}}, \hat{\bar{\mathbf{P}}})$ is given by the MSDD metric of Eq. (5.2) associated with a fixed M_PPSK phase matrix $\hat{\bar{\mathbf{P}}}$, and it may be represented as:

$$d(\Gamma_1, \bar{\mathbf{A}}, \hat{\bar{\mathbf{P}}}) = -\text{tr}(\mathbf{Y}^H \hat{\bar{\mathbf{P}}} \bar{\mathbf{O}} \mathbf{C}^{-1} \bar{\mathbf{O}}^H \hat{\bar{\mathbf{P}}}^H \mathbf{Y}) - \ln[\det(\mathbf{C})] + \sum_{v=2}^{N_w} \sum_{\bar{k}=(v-2)\text{BPS}+\text{BPS}_P+1}^{(v-1)\text{BPS}} \widetilde{b}_{\bar{k}} L_a(b_{\bar{k}}). \tag{5.21}$$

The channel correlation matrix $\mathbf{C}$ and the ring-amplitude-induced phase rotations $\bar{\mathbf{O}}$ in Eq. (5.21) are determined by the ring amplitude variables Γ_1 and $\bar{\mathbf{A}}$. There are a total of $M_A^{N_w}$ MSDAD metric candidates in Eq. (5.20).

(3) After estimating $\hat{\Gamma}_1$, $\hat{\bar{\mathbf{A}}}$ and $\hat{\bar{\mathbf{O}}}$ in Step (2) above, the channel correlation matrix $\hat{\mathbf{C}}$ is determined accordingly. As a result, the estimate of the M_PPSK candidates may be improved according to:

$$\begin{aligned} \hat{\bar{\mathbf{P}}} &= \arg \max_{\forall \bar{\mathbf{P}}} d(\hat{\Gamma}_1, \hat{\bar{\mathbf{A}}}, \bar{\mathbf{P}}) \\ &= \arg \min_{\forall \bar{\mathbf{P}}} d^{MSDPSD}, \end{aligned} \tag{5.22}$$

where the MSDPSD metric is given by the toggled MSDD metric of Eq. (5.2) associated with the fixed ring amplitudes $\hat{\Gamma}_1$, $\hat{\bar{\mathbf{A}}}$ and $\hat{\bar{\mathbf{O}}}$ as:

$$\begin{aligned} d^{MSDPSD} &= -d(\hat{\Gamma}_1, \hat{\bar{\mathbf{A}}}, \bar{\mathbf{P}}) \\ &= \left\| \hat{\mathbf{L}}^T \hat{\bar{\mathbf{O}}}^H \bar{\mathbf{P}}^H \mathbf{Y} \right\|^2 - \sum_{v=2}^{N_w} \left[\sum_{\bar{k}=(v-2)\text{BPS}+1}^{(v-2)\text{BPS}+\text{BPS}_P} \widetilde{b}_{\bar{k}} L_a(b_{\bar{k}}) - \ln \overline{C}_A^{\omega_{v-1}} \right]. \end{aligned} \tag{5.23}$$

The lower triangular matrix $\hat{\mathbf{L}}$ in Eq. (5.22) is decomposed from $\hat{\mathbf{L}}\hat{\mathbf{L}}^H = \hat{\mathbf{C}}^{-1}$, and the M_PPSK-related constant $\overline{C}_A^{\omega_{v-1}} = \prod_{\bar{k}=(v-2)\text{BPS}+1}^{(v-2)\text{BPS}+\text{BPS}_P} \{1 + \exp[L_a(b_{\bar{k}})]\}$ aims for guaranteeing that the MSDPSD metric of Eq. (5.23) always has positive values. Moreover, the determinant term $\ln[\det(\mathbf{C})]$ in Eq. (5.2) becomes a constant for M_PPSK detection, and hence it is eliminated from the MSDPSD metric of Eq. (5.23). As mentioned before, the MSDPSD invokes SD for solving Eq. (5.22), which is the same as the MSDSD aided DPSK proposed in [127, 132] and summarized by Table 3.3.

(4) In order to achieve a near-optimum MSDD performance, Steps (2) and (3) above may be repeated IR_{AP} times. Finally, the soft-bit decisions may be made by the MSDAD as:

$$L_p(b_k) = \max_{\forall \Gamma_1} \max_{\forall \{\bar{\mathbf{A}}\}_{b_k=1}} d(\Gamma_1, \bar{\mathbf{A}}, \hat{\bar{\mathbf{P}}}) - \max_{\forall \Gamma_1} \max_{\forall \{\bar{\mathbf{A}}\}_{b_k=0}} d(\Gamma_1, \bar{\mathbf{A}}, \hat{\bar{\mathbf{P}}}), \tag{5.24}$$

where the bit index range is specified as $\{\{L_p(b_k)\}_{k=(v-2)\text{BPS}+\text{BPS}_P+1}^{(v-1)\text{BPS}}\}_{v=2}^{N_w}$. Furthermore, the M_PPSK-related soft-bit decisions may be produced by the MSDPSD as:

$$\begin{aligned} L_p(b_k) &= \max_{\forall \{\bar{\mathbf{P}}\}_{b_k=1}} d(\hat{\Gamma}_1, \hat{\bar{\mathbf{A}}}, \bar{\mathbf{P}}) - \max_{\forall \{\bar{\mathbf{P}}\}_{b_k=0}} d(\hat{\Gamma}_1, \hat{\bar{\mathbf{A}}}, \bar{\mathbf{P}}), \\ &= \begin{cases} -d_{MAP}^{MSDPSD} + \bar{d}_{MAP}^{MSDPSD}, & \text{if } b_k^{MAP} = 1 \\ -\bar{d}_{MAP}^{MSDPSD} + d_{MAP}^{MSDPSD}, & \text{if } b_k^{MAP} = 0 \end{cases}, \end{aligned} \tag{5.25}$$

where $d_{MAP}^{MSDPSD} = \min_{\forall \bar{\mathbf{P}}} d^{MSDPSD}$ may be obtained by Eq. (5.22) in Step (3), while $\bar{d}_{MAP}^{MSDPSD}$ is obtained by invoking the SD again for each soft-bit decision $\{\{L_p(b_k)\}_{k=(v-2)\text{BPS}+1}^{(v-2)\text{BPS}+\text{BPS}_P}\}_{v=2}^{N_w}$, when the specific bit b_k is fixed to be the flipped MAP decision, i.e. the SD is invoked to obtain $\bar{d}_{MAP}^{MSDPSD} = \min_{\forall \{\bar{\mathbf{P}}\}_{b_k=\bar{b}_k^{MAP}}} d^{MSDPSD}$.

As a result, the MSDD-IAP reduces the total number of nodes visited by the MSDD from $M_A \cdot M^{(N_w-1)}$ to a lower bound of $(N_w-1)M_P + IR_{AP}[M_A^{N_w} + (N_w-1)M_P] + (N_w-1)\text{BPS}_P[(N_w-2)M_P + M_P/2]$, where the SD is invoked IR_{AP} times by the MSDPSD for the sake of determining the final decisions on $\hat{\bar{\mathbf{P}}}$, and then the SD has to be further invoked $(N_w-1)\text{BPS}_P$ times in Eq. (5.25) for producing the M_PPSK-related soft-bit decisions. It can be seen that the MSDD-IAP complexity associated with ring amplitude detection still grows exponentially as N_w increases, because the SD was not invoked for MSDAD.

5.3.4 Reduced-Complexity MSDSD-Iterative Amplitude/Phase Algorithm

As we demonstrated in Sec. 4.5, the effects of the amplitude-dependent channel correlation matrix $\mathbf{C}$ may be eliminated with the aid of incremental steps. This implies that the MSDAD problem of MSDD-IAP [160] may also be solved by SD, which may be referred to as Multiple-Symbol Differential Amplitude Sphere Detection (MSDASD). More explicitly, the PED of Eq. (5.9) may be revised for MSDAD's metric of Eq. (5.21) as:

$$\begin{aligned} d_v^{MSDASD} &= \|l_{N_w,N_w}\mathbf{Y}_1\|^2 + \ln\left(\Gamma_1^2\rho_0 + N_0\right) + \sum_{\bar{v}=2}^{v} \Delta_{\bar{v}-1}^{MSDASD} \\ &= d_{v-1}^{MSDASD} + \Delta_{v-1}^{MSDASD}, \end{aligned} \tag{5.26}$$

where the PED increment is given by:

$$\Delta_{v-1}^{MSDASD} = \left\| \widetilde{l}_{1,1} \hat{\bar{\Psi}}_{v-1}^{*} \hat{\bar{\Omega}}_{v-1}^{*} \mathbf{Y}_v + \hat{\omega}_{v-1} \psi_{v-1} \left(\sum_{t=1}^{v-1} \widetilde{l}_{v-t+1,1} \hat{\bar{\Psi}}_{t}^{*} \hat{\bar{\Omega}}_{t}^{*} \mathbf{Y}_t \right) \right\|^2 + \Xi_v - \left[\sum_{\bar{k}_v=\mathrm{BPS}_P+1}^{\mathrm{BPS}} \widetilde{b}_{\bar{k}_v} L_a(b_{\bar{k}_v}) - \ln \overline{C}_A^{\gamma_{v-1}} \right]. \tag{5.27}$$

All the transmitted symbols' M_PPSK phases $\{\hat{\bar{\Omega}}_t\}_{\forall t}$ and their data-carrying M_PPSK candidates $\{\hat{\omega}_{v-1}\}_{\forall v}$ seen in Eq. (5.27) are known from the already determined phase matrix $\hat{\bar{\mathbf{P}}}$, while the constant of $\overline{C}_A^{\gamma_{v-1}} = \prod_{\bar{k}_v=\mathrm{BPS}_P+1}^{\mathrm{BPS}} \left\{1 + \exp\left[L_a(b_{\bar{k}_v})\right]\right\}$ ensures that all PED increments of Eq. (5.27) are positive. As a result, the MSDAD metric of Eq. (5.21) is given by the flipped MSDASD metric of Eq. (5.26) associated with the SD index $v = N_w$, i.e. we have $d(\Gamma_1, \bar{\mathbf{A}}, \hat{\bar{\mathbf{P}}}) = -d_{N_w}^{MSDASD}$. Therefore, the MSDAD of Eq. (5.20) may be explicitly implemented by the MSDASD as:

$$\begin{aligned} \left\{\hat{\Gamma}_1, \hat{\bar{\mathbf{A}}}\right\} &= \arg \max_{\forall \Gamma_1} \max_{\forall \bar{\mathbf{A}}} d(\Gamma_1, \bar{\mathbf{A}}, \hat{\bar{\mathbf{P}}}) \\ &= \arg \min_{\forall \Gamma_1} \min_{\forall \bar{\mathbf{A}}} d_{N_w}^{MSDASD}. \end{aligned} \tag{5.28}$$

The MSDASD using the PED of Eq. (5.26) may be implemented in the same way as the MSDSD algorithm of [132] and summarized in Table 3.3. The MSDASD may commence its action with the initial PED $d_1 = 0$ for the sake of simplicity, but the Γ_1-related term $d_1^{MSDASD} = \|l_{N_w,N_w} \mathbf{Y}_1\|^2 + \ln\left(\Gamma_1^2 \rho_0 + N_0\right)$ should be added to the SD's output radius before the EDs comparison over the legitimate Γ_1 values in Eq. (5.28). Finally, the ring amplitude-related soft-bit decisions of Eq. (5.24) may be carried out by the MSDASD as:

$$L_p(b_k) = \begin{cases} -d_{MAP}^{MSDASD} + \bar{d}_{MAP}^{MSDASD}, & \text{if } b_k^{MAP} = 1 \\ -\bar{d}_{MAP}^{MSDASD} + d_{MAP}^{MSDASD}, & \text{if } b_k^{MAP} = 0 \end{cases}, \tag{5.29}$$

where d_{MAP}^{MSDASD} is obtained by Eq. (5.28), while $\bar{d}_{MAP}^{MSDASD}$ may also be obtained by the MSDASD of Eq. (5.28), where b_k is fixed to be the flipped MAP decision $\bar{b}_k^{MAP}$ since we have $\bar{d}_{MAP}^{MSDASD} = \min_{\forall \Gamma_1} \min_{\forall \{\bar{\mathbf{A}}\}_{b_k=\bar{b}_k^{MAP}}} d_{N_w}^{MSDASD}$.

In summary, both the ring amplitude detection and the M_PPSK phase detection of Algorithm 5.1 may invoke the MSDSD algorithm. Hence this detector may now be termed as the MSDSD using Iterative Amplitude/Phase processing (MSDSD-IAP). Furthermore, as the MSDPSD used by the MSDD-IAP of Algorithm 5.1 always utilizes a fixed constant channel correlation matrix $\hat{\mathbf{C}}$, the reduced-complexity soft-decision-aided MSDSD conceived for the coded DPSK and proposed in Sec. 3.3.3 may be directly applied to the MSDPSD, which may result in a considerable reduction in the number of constellation points visited by the SD. Fig. 5.3 portrays an example of the comparison between the MSDD-IAP and the reduced-complexity MSDSD-IAP conceived for 64-DAPSK(4,16). It is evidenced by Fig. 5.3 that with the aid of sphere decoding, the MSDASD effectively reduces the number of ring amplitude candidates visited by the MSDAD, while with the aid of the reduced-complexity M_PPSK phase detection proposed in Sec. 3.3.3, the reduced-complexity MSDPSD also successfully reduces the number of M_PPSK candidates visited by the conventional MSDPSD.

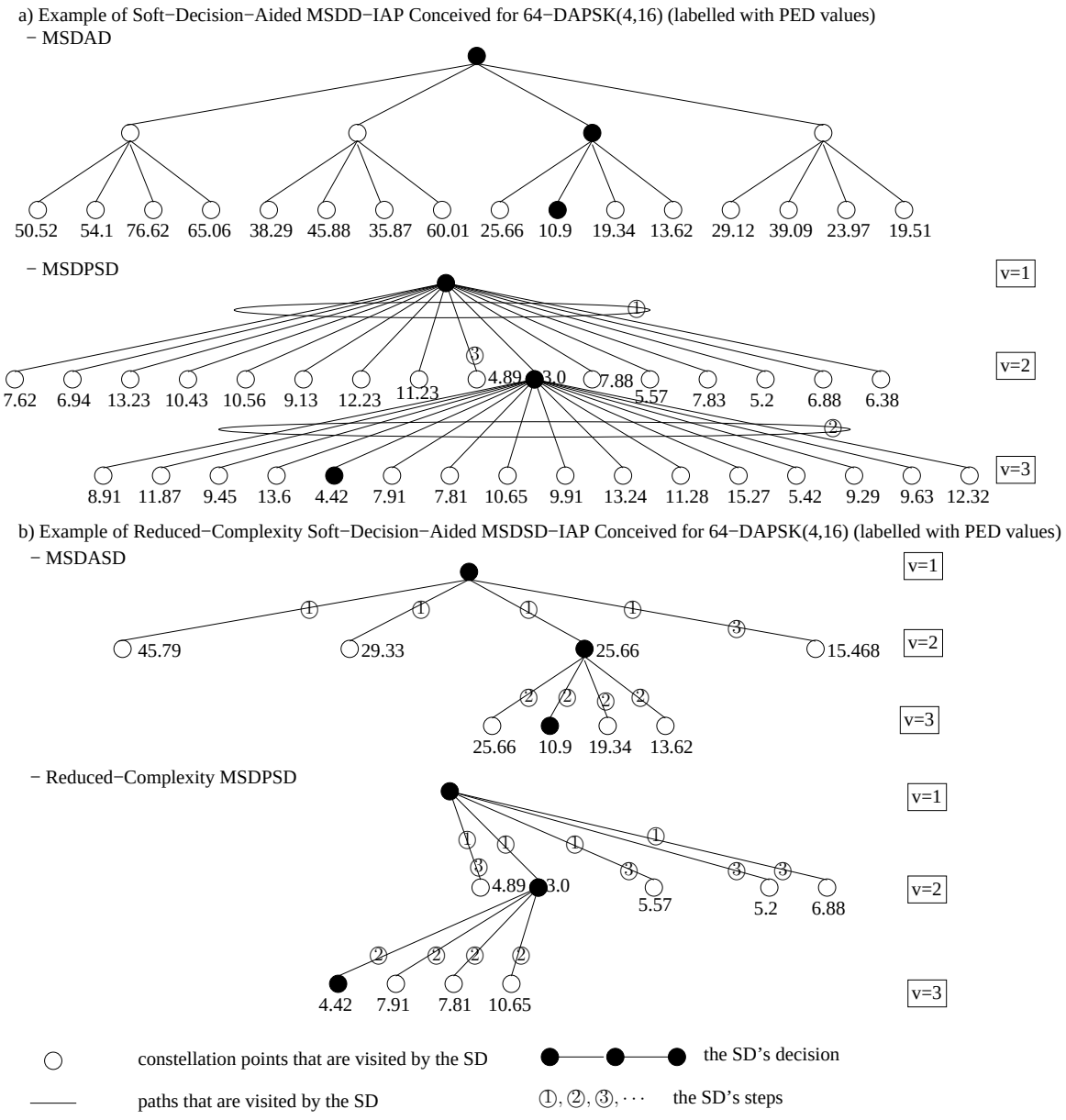

Figure 5.3: Example of comparison between soft-decision-aided MSDD-IAP and reduced-complexity soft-decision-aided MSDSD-IAP conceived for 64-DAPSK(4,16), recorded at SNR=9 dB, $f_d = 0.03$ and $I_A = 0.3$, where we have $N_R = 2$ and $N_w = 3$.

More explicitly, Fig. 5.3 a) shows that MSDAD of MSDD-IAP employs MSDD for the ring amplitude detection, which has to visit and compare all the $M_A^{N_w-1} = 16$ MSDD candidates for the 64-DAPSK(4,16) scheme in order to obtain the optimum solution having the ED of $d = 10.9$. By contrast, the MSDASD of the proposed MSDSD-IAP in Fig. 5.3 b) employs the SD for the ring amplitude detection, where only the $M_A = 4$ ring amplitude candidates are visited, when the SD visits the indices $v = 2$ and $v = 3$ for the first time in Step ① and Step ②, respectively. After the MSDASD of Fig. 5.3 b) has updated the SD radius of $d = 10.9$ in Step ②, the SD index is decreased to $v = 2$ and the second-best candidate having the PED value of $d_2 = 15.468$ is visited in Step ③. Since this new PED value is higher than the SD radius, the SD proceeds to decrease its index to $v = 1$ and terminates the search without visiting all the $M_A^{N_w-1} = 16$ MSDD candidates.

Moreover, MSDPSD of MSDD-IAP seen in Fig. 5.3 a) invokes the conventional soft-decision MSDSD algorithm of Table 3.3 in Sec. 3.3.2 for the 64-DAPSK(4,16) phase detection. As a result, the MSDPSD of Fig. 5.3 a) may invoke the "sortDelta" subfunction of Table 3.3 in order to evaluate and compare all $M_P = 16$ phase candidates, when the SD visits the indices $v = 2$ and $v = 3$ for the first time in Step ① and Step ②, respectively. The MSDPSD's SD radius is updated to $d = 4.42$ in Step ② of Fig. 5.3 a), and then the SD visits the second-best candidate at $v = 2$ in Step ③, which has a higher PED value of $d_2 = 4.89$ than the SD radius, hence the SD search is terminated. By contrast, the MSDPSD of the proposed MSDSD-IAP seen in Fig. 5.3 b) invokes the reduced-complexity MSDSD algorithm of Tables 3.4-3.7 in Sec. 3.3.3 for the 64-DAPSK(4,16) phase detection. Hence the MSDPSD of Fig. 5.3 b) may invoke the "findBest-DPSK" subfunction of Table 3.7, which only visits a reduced subset of $M_P/4 = 4$ phase candidates, when the SD visits the indices $v = 2$ and $v = 3$ for the first time in Step ① and Step ②, respectively. The SD radius of $d = 4.42$ is found by the MSDPSD of MSDSD-IAP in Fig. 5.3 b) in Step ②, which is the same as that found by the conventional MSDPSD of MSDD-IAP in Fig. 5.3 a). When the MSDPSD of Fig. 5.3 b) visits the index $v = 2$ for the second time, the "findNext-DPSK" subfunction of Table 3.7 is invoked to check the second-best candidate, which has a higher PED increment value and hence the SD decreases its index to $v = 1$ and terminates its search accordingly.

It may be readily shown that the total number of nodes visited by the reduced-complexity MSDSD-IAP is given by $(N_w - 1)M_P + IR_{AP}[(N_w - 1)M_A^2 + (N_w - 1)M_P/4 + (N_w - 2)] + (N_w - 1)\text{BPS}_A[(N_w - 2)M_A^2 + M_A^2/2] + (N_w - 1)\text{BPS}_P[(N_w - 2)M_P/4 + M_P/8 + (N_w - 2)]$. We note that the Approx-Log-MAP of Algorithm 3.2 proposed for soft-decision-aided MSDSD may be directly applied to the reduced-complexity MSDSD-IAP introduced in this section. Moreover, it is also straightforward to implement the SDD-MSDSD and HDD-MSDSD introduced in Sec. 5.3.1 as Soft-Decision-Directed MSDSD using Iterative Amplitude/Phase processing (SDD-MSDSD-IAP) and Hard-Decision-Directed MSDSD using Iterative Amplitude/Phase processing (HDD-MSDSD-IAP).

5.4 Soft-Decision-Aided DFDD Conceived for Coded DQAM

It was demonstrated in Sec. 4.6 that DFDD aided DQAM is equivalent to MSDSD aided DQAM associated with a fixed index of $v = N_w$, where the decision feedback based on the $(N_w - 2)$ data-carrying symbols are exploited for reducing the search-space, so that only a single variable has to be detected by the DFDD within an observation window. The consecutive DFDD windows are supposed to overlap by $N_{OL} = (N_w - 1)$ observations. Therefore, the DFDD aided DQAM using the Max-Log-MAP algorithm has the *a posteriori* LLRs of:

$$L_p(b_k) = \max_{\forall\{\gamma_{N_w-1},\omega_{N_w-1}\}b_k=1} d(\gamma_{N_w-1},\omega_{N_w-1}) - \max_{\forall\{\gamma_{N_w-1},\omega_{N_w-1}\}b_k=0} d(\gamma_{N_w-1},\omega_{N_w-1}), \quad (5.30)$$

where the DFDD scheme's decision metric is given by toggling the polarity of the MSDSD's PED increment Δ_{v-1} of Eq. (5.10) associated with the SD index $v = N_w$ as:

$$d(\gamma_{N_w-1},\omega_{N_w-1}) = -\left\| l_{1,1}\hat{\Psi}^*_{N_w-1}\hat{\Omega}^*_{N_w-1}\mathbf{Y}_{N_w} + \omega_{N_w-1}\psi_{N_w-1}\left(\sum_{t=1}^{N_w-1} l_{N_w-t+1,1}\hat{\Psi}^*_t\hat{\Omega}^*_t\mathbf{Y}_t\right)\right\|^2 - \widetilde{\Xi}_{N_w} + \sum_{\bar{k}=1}^{\mathrm{BPS}} \widetilde{b}_{\bar{k}} L_a(b_{\bar{k}}). \quad (5.31)$$

The variable ring amplitude γ_{N_w-1} determines $\{l_{N_w-t+1,1}\}_{t=1}^{N_w}$, ψ_{N_w-1} and $\widetilde{\Xi}_{N_w}$ in Eq. (5.31), where we have $\widetilde{\Xi}_{N_w} = \ln\left[(\Gamma^2_{N_w} + N_0) - \widetilde{\mathbf{e}}^T_{N_w}\widetilde{\mathbf{C}}^{-1}_{\mathbf{N_w-1}}\widetilde{\mathbf{e}}_{N_w}\right]$ as defined by the hard-decision-aided DFDD's ED of Eq. (4.67). The constant ξ_{N_w} in Ξ_{N_w} as well as the constant $\ln \overline{C}_A^{N_w-1}$ seen in Eq. (5.10) may be ignored by the DFDD. Moreover, the Approx-Log-MAP algorithm may also be conceived for the DFDD by replacing the max operations in Eq. (5.30) by the modified Jacobian algorithm jac defined by Eq. (2.36).

Furthermore, according to our experimental observation not documented here, the first transmitted ring amplitude Γ_1 of each DFDD window should still be treated as a separate variable for the case of DAPSK/TDAPSK detection in order to avoid the potential error propagation between DFDD windows. More explicitly, let us assume that a long frame of DAPSK/TADPSK symbols is transmitted and a transmitted ring amplitude at any position of the frame is given by $\Gamma_v = \Gamma_1\left(\prod_{t=1}^{v-1}\gamma_t\right)$, where Γ_1 refers to the first transmitted symbol's ring amplitude at the beginning of the transmission frame. It may be observed that any erroneous decisions concerning $\{\gamma_t\}_{\forall t}$ may degrade the decision reliablility concerning Γ_v, where Γ_v within the transmission frame may act as the first transmitted ring amplitude Γ_1 of a DFDD window. By contrast, we always have $\Gamma_v = \gamma_{v-1}$ for ADPSK/TADPSK schemes, where the potentially erroneous decision concerning γ_{v-1} would only affect a single DFDD window, i.e. there is no error propagation across the DFDD windows. Therefore, the *a posteriori* LLR of Eq. (5.31) derived for soft-decision-aided DFDD conceived for coded DAPSK/TDAPSK using the Max-Log-MAP algorithm may be revised as:

$$L_p(b_k) = \max_{\forall\,\Gamma_1}\ \max_{\forall\{\gamma_{N_w-1},\omega_{N_w-1}\}b_k=1} d(\Gamma_1,\gamma_{N_w-1},\omega_{N_w-1}) - \max_{\forall\,\Gamma_1}\ \max_{\forall\{\gamma_{N_w-1},\omega_{N_w-1}\}b_k=0} d(\Gamma_1,\gamma_{N_w-1},\omega_{N_w-1}), \quad (5.32)$$

so that the complete MSDSD's ED of Eq. (5.8) may be restored with the aid of decision feedback based on the $(N_w - 2)$ data-carrying symbols as:

$$\begin{aligned} d(\Gamma_1, \gamma_{N_w-1}, \omega_{N_w-1}) = & -\|l_{N_w,N_w}\mathbf{Y}_1\|^2 - \ln\left(\Gamma_1^2\rho_0 + N_0\right) - \sum_{v=2}^{N_w-1}\left\|\sum_{t=1}^{v} l_{N_w-t+1,N_w-v+1}\hat{\Psi}_t^*\hat{\Omega}_t^*\mathbf{Y}_t\right\|^2 \\ & - \left\|l_{1,1}\hat{\Psi}_{N_w-1}^*\hat{\Omega}_{N_w-1}^*\mathbf{Y}_{N_w} + \omega_{N_w-1}\psi_{N_w-1}\left(\sum_{t=1}^{N_w-1} l_{N_w-t+1,1}\hat{\Psi}_t^*\hat{\Omega}_t^*\mathbf{Y}_t\right)\right\|^2 \\ & - \sum_{v=2}^{N_w}\widetilde{\Xi}_v + \sum_{\bar{k}=1}^{\text{BPS}}\widetilde{b}_{\bar{k}}L_a(b_{\bar{k}}), \end{aligned} \tag{5.33}$$

where $\{\hat{\gamma}_t\}_{t=1}^{N_w-2}$, $\{\hat{\Psi}_t\}_{t=1}^{N_w-1}$ and $\{\hat{\Omega}_t\}_{t=1}^{N_w-1}$ are known from previous decisions, while the lower triangular matrix elements of $\{\{l_{N_w-t+1,N_w-v+1}\}_{t=1}^{v}\}_{v=1}^{N_w}$, as well as the determinant term $[-\ln\left(\Gamma_1^2\rho_0 + N_0\right) - \sum_{v=2}^{N_w}\widetilde{\Xi}_v]$ and the ring-amplitude-induced phase rotation variable ψ_{N_w-1} are determined by the variables of Γ_1 and γ_{N_w-1}. We note that the constant of $\sum_{v=2}^{N_w-1}[\sum_{\bar{k}=(v-2)\text{BPS}+1}^{(v-1)\text{BPS}}\widetilde{b}_{\bar{k}}L_a(b_{\bar{k}}) - \ln\overline{C}_A^{v-1}] - \ln\overline{C}_A^{N_w-1}$ in the MSDSD's ED of Eq. (5.8) is ignored for the DFDD metric of Eq. (5.33). In this way, the potentially erroneous decision concerning Γ_{N_w} made during the current DFDD window will not degrade the following DFDD windows. However, the soft-decision-aided DFDD conceived for the DAPSK/TDAPSK of Eq. (5.32) has a higher detection complexity than the soft-decision-aided DFDD conceived for the ADPSK/TADPSK of Eq. (5.30).

We note that the DFDD aided DQAM proposed in [136,153,154] ignored the problem of having a ring-amplitude-dependent channel correlation matrix. More explicitly, the DFDD decision metric of DAPSK/TDAPSK detection is given by [154]:

$$d(x_{N_w-1}) = -\frac{\left\|\mathbf{Y}_{N_w} - x_{N_w-1}\hat{s}_{N_w-1}\left[\sum_{t=1}^{N_w}\overline{w}_t\mathbf{Y}_t/(\hat{s}_t)\right]\right\|^2}{1 + N_0 - \mathbf{e}_{N_w}^T\overline{\mathbf{w}}} + \sum_{\bar{k}=1}^{\text{BPS}}\widetilde{b}_{\bar{k}}L_a(b_{\bar{k}}), \tag{5.34}$$

while that of ADPSK/TADPSK is given by [136]:

$$d(x_{N_w-1}) = -\frac{\left\|\mathbf{Y}_{N_w} - \frac{x_{N_w-1}\hat{s}_{N_w-1}}{\hat{\Gamma}_{N_w-1}}\left[\sum_{t=1}^{N_w}\overline{w}_t\mathbf{Y}_t/(\hat{s}_t)\right]\right\|^2}{1 + N_0 - \mathbf{e}_{N_w}^T\overline{\mathbf{w}}} + \sum_{\bar{k}=1}^{\text{BPS}}\widetilde{b}_{\bar{k}}L_a(b_{\bar{k}}), \tag{5.35}$$

where the decision-feedback filter taps are given by $\overline{\mathbf{w}} = [\overline{w}_{N_w-1}, \cdots, \overline{w}_1]^T = \mathbf{C}_{\mathbf{N_w-1}}{}^{-1}\mathbf{e}_{N_w}$, which are directly given by the filter taps of classic DPSK detection [121, 125, 126] as introduced in Chapter 3. We will demonstrate in the next section with the aid of our performance results that this sub-optimal DFDD evaluating the probability metrics of Eqs. (5.34) and (5.35) imposes a performance loss compared to the optimum DFDD using the probability metric of Eqs. (5.33) and (5.31).

5.5 Performance Results for Coded DQAM

In this section, we offer detailed comparisons of the soft-decision-aided noncoherent detectors conceived for coded DQAM schemes. Naturally, all noncoherent detectors may invoke either the

Approx-Log-MAP or Max-Log-MAP algorithms. Furthermore, similar to coded DPSK detection, all the classic detectors, including the CDD, MSDD, MSDSD and DFDD may be invoked also for coded DQAM detection. Moreover, the soft-decision-aided MSDD may be implemented as either MSDD, or HDD-MSDD or alternatively as SDD-MSDD, while the soft-decision-aided MSDSD may also be implemented as either MSDSD, or as HDD-MSDSD or alternatively as SDD-MSDSD. Furthermore, for the DQAM constellations, which map the bits to the data-carrying ring amplitude index and to the data-carrying M_PPSK phase index separately, the soft-decision-aided MSDSD may be carried out by either the MSDSD-IAP, or by the HDD-MSDSD-IAP or indeed also by the SDD-MSDSD-IAP.

Let us recall that as we demonstrated in Sec. 5.2, the CDD is a special case of the MSDD associated with $N_w = 2$. Moreover, the MSDSD may retain the MSDD's detection capability, as long as the initial SD's radius is set to be sufficiently large. Therefore, in this section, we focus our attention on the performance of both the MSDSD and of the DFDD. In more detail, the performance of MSDSD employing the Approx-Log-MAP and Max-Log-MAP algorithms is presented in Sec. 5.5.1. The different MSDSD arrangements are compared and discussed in Sec. 5.5.2 for a variety of coded DQAM schemes, so that the most appropriate MSDSD implementation for each DQAM constellation may be suggested. Sec. 5.5.3 provides performance comparisons between different coded DQAM schemes employing their respective MSDSD arrangements. The MSDSD complexity results are presented in Sec. 5.5.4. Moreover, the performance results the soft-decision-aided DFDD conceived for coded DQAM are portrayed in Sec. 5.5.5. Last but not least, our performance comparison between PSAM aided Square QAM and MSDSD aided DQAM in a variety of coded systems is demonstrated in Sec. 5.5.6.

5.5.1 Performance of MSDSD Employing Approx-Log-MAP and Max-Log-MAP

The EXIT charts of both DAPSK employing MSDSD and of ADPSK relying on HDD-MSDSD are portrayed in Fig. 5.4, where both the Approx-Log-MAP and Max-Log-MAP algorithms are invoked. First of all, in terms of the MSDSD performance, it can be clearly seen in Fig. 5.4a that the DAPSK detection capability improves, as MSDSD window length N_w is increased, which is reflected both by the increased area under the EXIT curves and by the improved iteration gain. This feature may also be seen in Fig. 5.4b for the case of HDD-MSDSD aided coded ADPSK detection. Furthermore, Fig. 5.4 demonstrates that the Approx-Log-MAP algorithm outperforms the Max-Log-MAP algorithm, which becomes more noticeable in the charts of Fig. 5.4 as the iteration gain improves with both N_w and M. This is because the Max-Log-MAP algorithm only takes into account the pair of maximum *a posteriori* probabilities associated with $b_k = 1$ and $b_k = 0$, which implies that some of the valuable probability candidates may be overlooked by the Max-Log-MAP algorithm, as N_w and M are increased.

Fig. 5.5 presents BER performance of both DAPSK employing MSDSD and of ADPSK relying on HDD-MSDSD in TC coded systems, where the Approx-Log-MAP and Max-Log-MAP

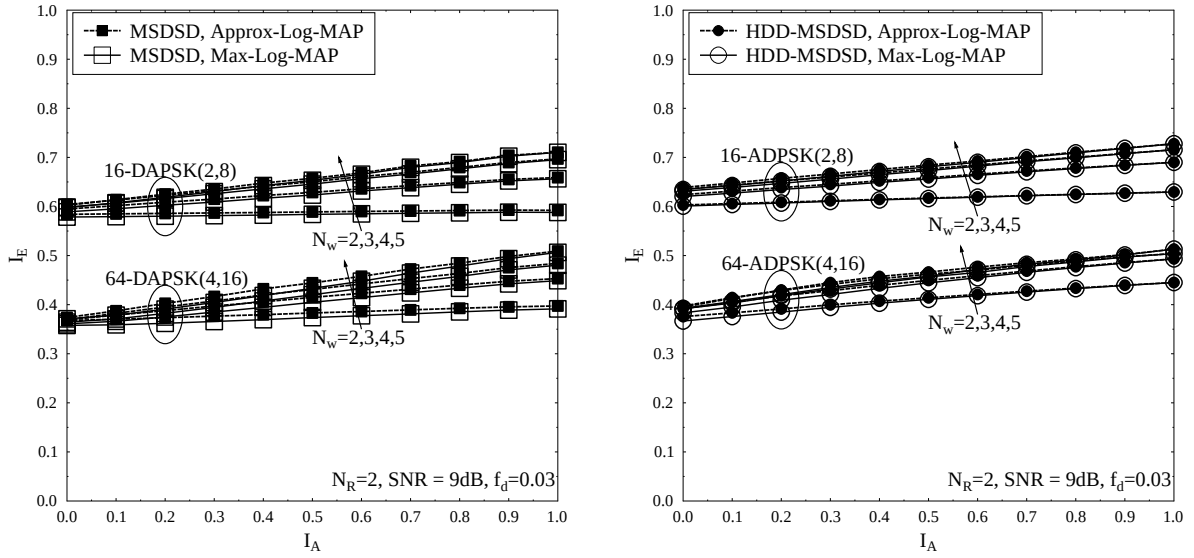

(a) DAPSK (b) ADPSK

Figure 5.4: EXIT charts of both DAPSK employing MSDSD and of its ADPSK counterpart relying on HDD-MSDSD recorded at SNR=9 dB and $f_d = 0.03$, where the Approx-Log-MAP and Max-Log-MAP algorithms are invoked, while $N_R = 2$ RAs are used.

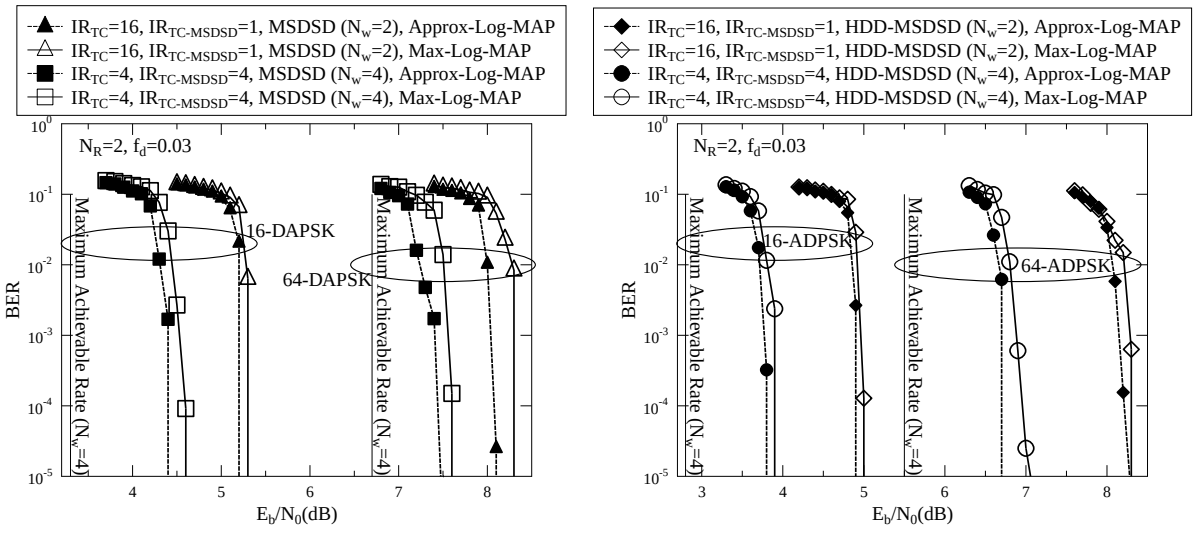

(a) TC coded DAPSK (b) TC coded ADPSK

Figure 5.5: BER performance of both DAPSK employing MSDSD and of its ADPSK counterpart relying on HDD-MSDSD in TC coded systems, where the Approx-Log-MAP and Max-Log-MAP algorithms are invoked. We have $f_d = 0.03$ and $N_R = 2$.

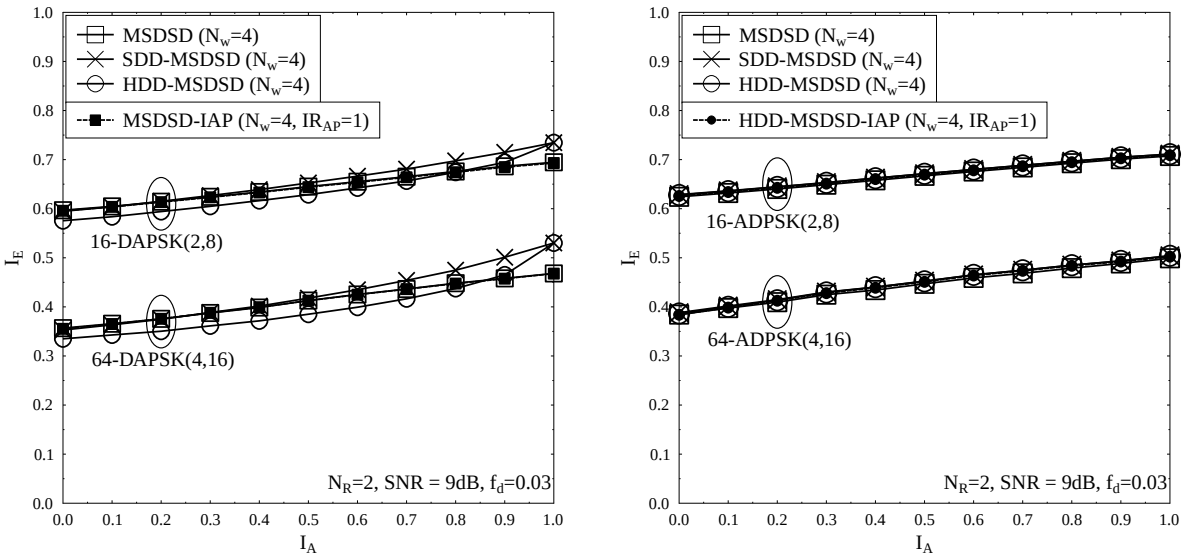

(a) DAPSK (b) ADPSK

Figure 5.6: EXIT charts of both DAPSK and of its ADPSK counterpart employing MSDSD, SDD-MSDSD and HDD-MSDSD recorded at SNR=9 dB and $f_d = 0.03$, where the Max-Log-MAP algorithm is invoked, while $N_R = 2$ RAs are used.

algorithms are invoked. It was demonstrated in Fig. 5.4 that increasing the MSDSD window length N_w beyond 4 only offers a limited performance improvement, hence $N_w = 4$ is chosen to represent the performance of MSDSD in Fig. 5.5. Moreover, we note that MSDD/MSDSD associated with $N_w = 2$ is equivalent to CDD. It is demonstrated by Fig. 5.5 that as the MSDSD window length is increased from $N_w = 2$ to $N_w = 4$, the system's performance is improved in Fig. 5.5a by $0.6 \sim 0.8$ dB for DAPSK employing MSDSD and by $1.1 \sim 1.5$ dB for ADPSK employing HDD-MSDSD, as seen in Fig. 5.5b. Furthermore, it is also demonstrated by Fig. 5.5 that the Approx-Log-MAP algorithm outperforms the Max-Log-MAP algorithm by $0.1 \sim 0.3$ dB, when they are invoked by DAPSK employing MSDSD and by ADPSK using HDD-MSDSD in TC coded systems. Since this performance difference is relatively small compared to the performance difference between different noncoherent detectors, the Max-Log-MAP algorithm is employed by all detectors in the following sections.

5.5.2 Comparison Amongst MSDSD Arrangements

In this section, we aim for identifying the best MSDSD arrangements for each DQAM constellation. Fig. 5.6 portrays the EXIT charts of DAPSK and ADPSK employing MSDSD, SDD-MSDSD and HDD-MSDSD. For the case of DAPSK recorded in Fig. 5.6a, when there is no *a priori* information associated with $I_A = 0$, SDD-MSDSD and MSDSD produce the same extrinsic information I_E, but the HDD-MSDSD's I_E output is lower. Moreover, when the full *a priori* information of $I_A = 1$ is provided for coded DAPSK detection, both SDD-MSDSD and HDD-MSDSD may achieve a

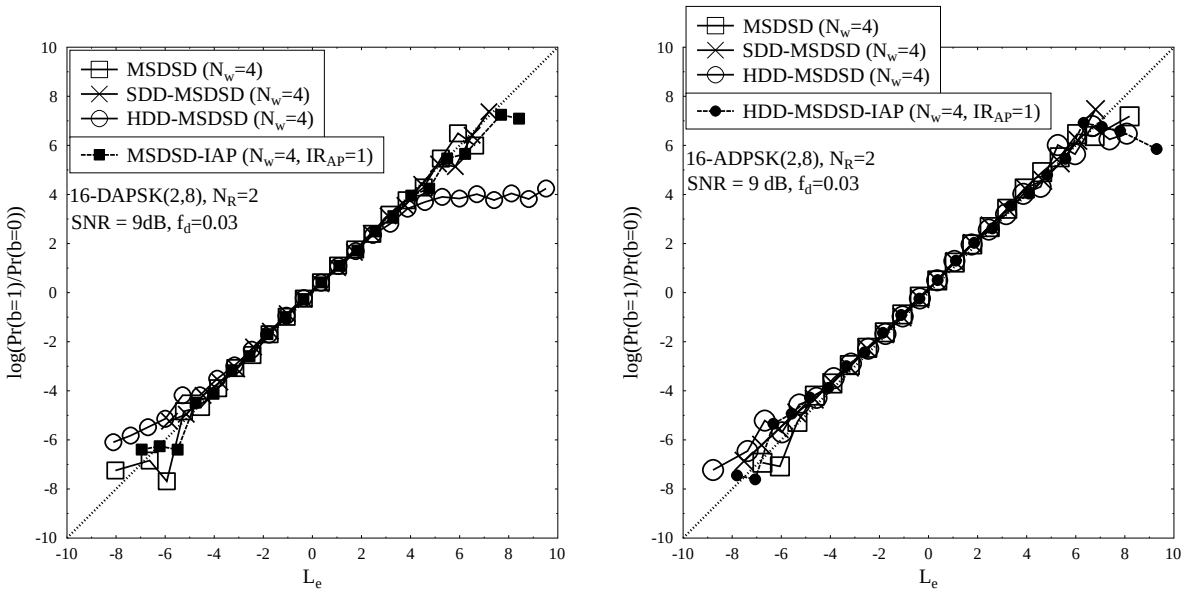

(a) 16-DAPSK(2,8)

(b) 16-ADPSK(2,8)

Figure 5.7: LLR validity test of both 16-DAPSK(2,8) and of its 16-ADPSK(2,8) counterpart employing MSDSD, SDD-MSDSD and HDD-MSDSD recorded at SNR=9 dB and $f_d = 0.03$, where the Max-Log-MAP algorithm is invoked, while $N_R = 2$ RAs are used.

higher I_E than MSDSD, as evidenced by Fig. 5.6a. In summary, Fig. 5.6a demonstrates that the SDD-MSDSD exhibits the optimum detection capability for coded DAPSK. However, considering that SDD-MSDSD has to produce a soft decision feedback, which only provides a marginal performance improvement in Fig. 5.6a, we opted for the MSDSD relying on the low-complexity iterative amplitude-phase detection aided MSDSD-IAP, since there is no noticeable performance difference between the MSDSD and the MSDSD-IAP associated with $IR_{AP} = 1$, as evidenced by Fig. 5.6a.

Furthermore, for the ADPSK of Fig. 5.6b, both SDD-MSDSD and HDD-MSDSD achieve a very similar detection capability as MSDSD. This is in contrast to the coded DAPSK detection portrayed by Fig. 5.6a. Let us hence elaborate a little further here. The DAPSK schemes differentially encode their ring amplitudes, so that we have $\{\Gamma_v = \left(\prod_{t=1}^{v-1} \gamma_t\right) \Gamma_1\}_{v=2}^{N_w}$ within an MSDSD observation window. This implies that the DAPSK detection may suffer from error propagation, where the potentially erroneous decision feedback concerning first ring amplitude Γ_1 and the potentially erroneous decisions concerning $\{\gamma_t\}_{\forall t}$ may degrade the accuracy of the following decisions. Therefore, the performance of DAPSK detection is highly dependent on how we treat Γ_1 by the different MSDSD arrangements. By contrast, the ADPSK schemes utilize the absolute data-carrying ring amplitude, where we have $\{\Gamma_v = \gamma_{v-1}\}_{v=2}^{N_w}$ within an MSDSD observation window. As a result, there is no error propagation in ADPSK detection, hence the different MSDSD arrangements exhibit a similar detection capability. Therefore, we may implement HDD-MSDSD by the low-complexity iterative amplitude-phase detection in form of the HDD-MSDSD-IAP for coded ADPSK detection, where HDD-MSDSD-IAP associated with $IR_{AP} = 1$ is also capable of achieving the near-optimum HDD-MSDSD performance, as demonstrated by Fig. 5.6b.

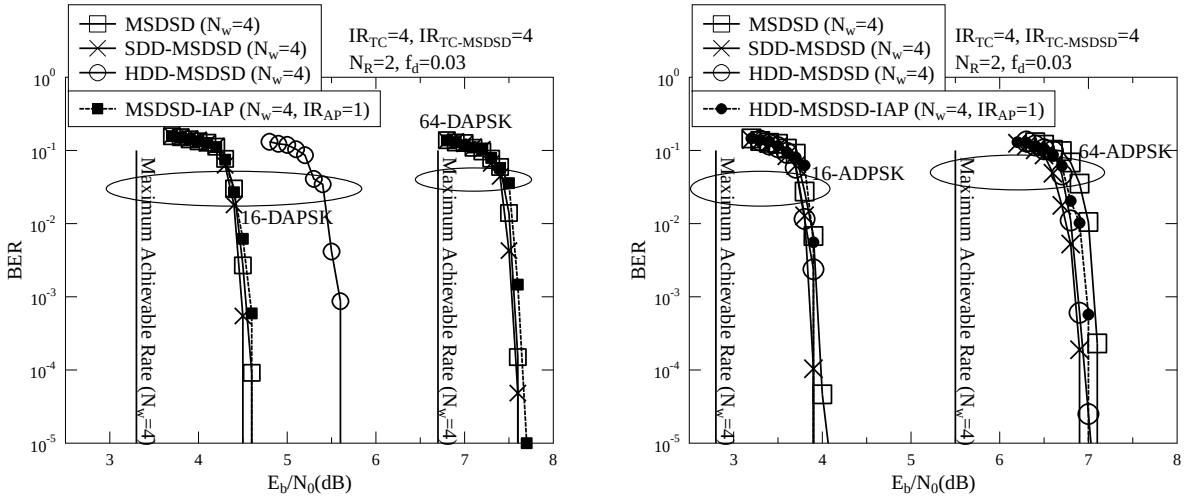

(a) TC coded DAPSK

(b) TC coded ADPSK

Figure 5.8: BER performance comparison of MSDSD, SDD-MSDSD and HDD-MSDSD when they are employed both for coded DAPSK detection and for its coded ADPSK detection counterpart in TC coded system, where the Max-Log-MAP algorithm is invoked, while we have $N_w = 4$, $f_d = 0.03$ and $N_R = 2$.

As a further insightful aspect, Fig. 5.7 presents the LLR validity test of both 16-DAPSK(2,8) and of 16-ADPSK(2,8) employing MSDSD, SDD-MSDSD and HDD-MSDSD. Fig. 5.7a shows that MSDSD, SDD-MSDSD and MSDSD-IAP are capable of producing reliable extrinsic LLRs that comply with the LLR definition of Eq. (2.27), but HDD-MSDSD's output LLRs exhibit poorer integrity for coded 16-DAPSK(2,8) detection, owing to its potential error propagation problem. Moreover, for the case of 16-ADPSK(2,8) detection, it is demonstrated by Fig. 5.7b that MSDSD, SDD-MSDSD, HDD-MSDSD and HDD-MSDSD-IAP are all competent soft-decision-aided non-coherent detectors that are capable of producing reliable extrinsic LLRs.

The BER performance of DAPSK and ADPSK employing different MSDSD arrangements in TC coded systems is portrayed by Fig. 5.8. In TC coded DAPSK systems, Fig. 5.8a demonstrates that MSDSD, SDD-MSDSD and MSDSD-IAP perform similarly, but HDD-MSDSD performs much worse than its counterparts. Hence the BER curve of TC coded 64-DAPSK(4,16) employing HDD-MSDSD cannot even be portrayed within our standard E_b/N_0 range. As mentioned in Sec. 5.2, it is advisable to avoid hard-decision-directed detection for coded DAPSK because of its error propagation problem. Furthermore, in TC coded ADPSK systems, the performance differences amongst MSDSD, SDD-MSDSD, HDD-MSDSD and HDD-MSDSD-IAP are all within 0.2 dB. Therefore, based on our observations gleaned from Figs. 5.6-5.8, we may now conclude that the soft-decision-aided MSDSD-IAP may be recommended for coded DAPSK detection, while the soft-decision-aided HDD-MSDSD-IAP may be suggested for coded ADPSK detection.

Although MSDSD-IAP and HDD-MSDSD-IAP have been shown to be competent arrangements in Fig. 5.8 for the coded DAPSK and ADPSK detection, respectively, Fig. 5.9 explicitly

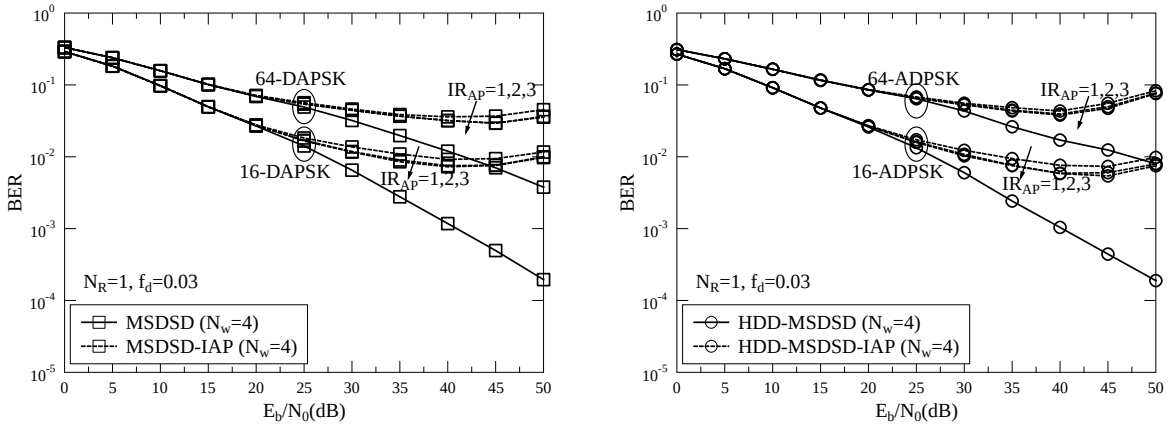

(a) DAPSK (b) ADPSK

Figure 5.9: BER performance of both uncoded DAPSK employing MSDSD-IAP and of its uncoded ADPSK counterpart employing HDD-MSDSD-IAP, where we have $f_d = 0.03$ and $N_R = 1$.

evidences that these detectors still suffer from irreducible error floors for uncoded DAPSK and ADPSK detection. The reason for this phenomenon is that without the assistance of channel coding, the MSDASD and the MSDPSD schemes may exchange erroneous decisions, which severely degrades the performance of MSDSD-IAP and HDD-MSDSD-IAP in uncoded systems. Therefore, the conventional hard-decision-aided HDD-MSDSD is recommended for uncoded DQAM schemes, as discussed in Chapter 4.

Let us now proceed by identifying the most appropriate MSDSD arrangements both for coded TDAPSK and TADPSK detection. Similarly to DAPSK, TDAPSK also differentially encodes the ring amplitudes, hence HDD-MSDSD should still be avoided for coded TDAPSK detection. Therefore, similar to coded DAPSK detection, we opt for implementing MSDSD by the low-complexity iterative amplitude-phase detection in the form of MSDSD-IAP for coded TDAPSK detection, which is characterized by the EXIT charts of Fig. 5.10a. However, in contrast to the EXIT charts of coded DAPSK seen in Fig. 5.6a, the EXIT charts of coded TDAPSK shown in Fig. 5.10a demonstrate that MSDSD-IAP associated with $IR_{AP} = 1$ clearly suffers from a performance loss compared to MSDSD. Upon increasing IR_{AP}, MSDSD-IAP may become capable of producing the same I_E as MSDSD with the aid of perfect *a priori* information of $I_A = 1$, but its performance gap at $I_A = 0$ cannot be compensated, as evidenced by Fig. 5.10a. The EXIT charts of coded TADPSK detection seen in Fig. 5.10b show a similar trend, where a performance gap persists between HDD-MSDSD and HDD-MSDSD-IAP. The reason for this performance gap is that the twisted modulations - including TDAPSK and TADPSK - introduce a ring-amplitude-induced phase rotation, which implies that the potentially erroneous ring amplitude detection may impose a false phase rotation upon the M_PPSK phase detection process. This error propagation can only be mitigated, when the perfect *a priori* information of $I_A = 1$ is supplied, which is demonstrated by the EXIT

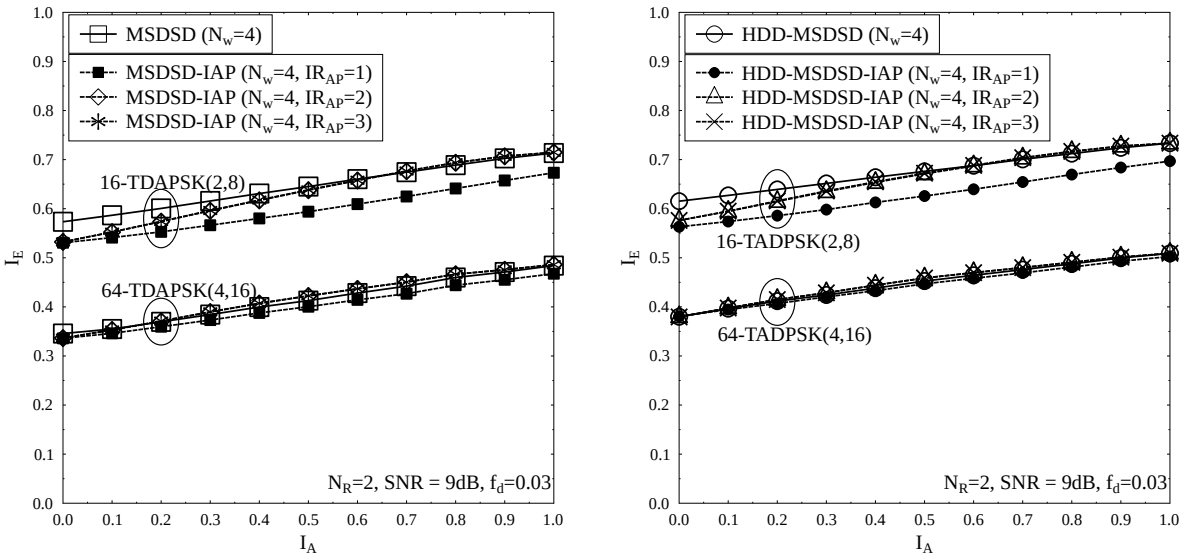

(a) TDAPSK

(b) TADPSK

Figure 5.10: EXIT charts of both TDAPSK employing MSDSD-IAP and of its TADPSK HDD-MSDSD-IAP counterpart recorded at SNR=9 dB and $f_d = 0.03$, where Max-Log-MAP is invoked, while $N_R = 2$ RAs are equipped.

charts of Fig. 5.10. It can also be seen in Fig. 5.10 that the performance difference between the MSDSD and MSDSD-IAP counterpart for coded TDAPSK detection and that of the HDD-MSDSD and HDD-MSDSD-IAP version for coded TADPSK detection become much less significant, as the number of modulation levels is increased to $M = 64$. This is because the ring-amplitude-induced phase rotation becomes smaller as M increases, which implies that the potentially erroneous phase rotation of M_PPSK detection imposed by the ring amplitude detection process may become less significant.

The specific characteristics of coded TDAPSK and TADPSK detection demonstrated by the EXIT charts of Fig. 5.10 are further verified both by the LLRs validity test of Fig. 5.11 and by the BER performance of Fig. 5.12. In more detail, it is demonstrated by Fig. 5.11 that the extrinsic LLRs produced by both MSDSD-IAP invoked for coded TDAPSK detection and by HDD-MSDSD-IAP used for coded TADPSK detection suffer from a severe deviation from the LLR definition of Eq. (2.27). Furthermore, the BER performance of Fig. 5.12a confirms that there is a significant performance gap between the MSDSD and MSDSD-IAP based coded TDAPSK detection, which becomes especially obvious for the 16-TDAPSK(2,8) scheme of Fig. 4.4. By increasing IR_{AP}, the performance of MSDSD-IAP conceived for coded TDAPSK detection may be improved, but the performance gap between the MSDSD and MSDSD-IAP schemes cannot be effectively compensated, as demonstrated by Fig. 5.12a. Similarly, Fig. 5.12b shows that for coded TADPSK detection, HDD-MSDSD-IAP also imposes a performance loss on HDD-MSDSD, which becomes especially substantial for the 16-TADPSK(2,8) scheme, and this performance loss cannot be completely compensated by increasing IR_{AP}.

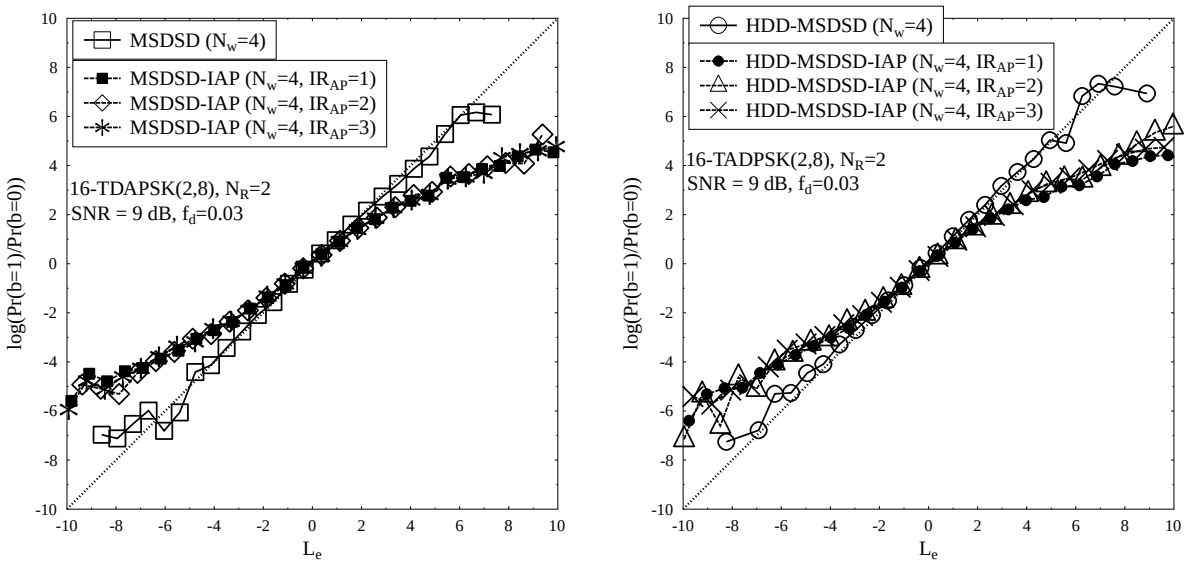

(a) 16-TDAPSK(2,8)

(b) 16-TADPSK(2,8)

Figure 5.11: LLR validity test of both 16-TDAPSK(2,8) employing MSDSD-IAP and of its 16-ADPSK(2,8) HDD-MSDSD-IAP counterpart recorded at SNR=9 dB and $f_d = 0.03$, where the Max-Log-MAP algorithm is invoked, while $N_R = 2$ RAs are used.

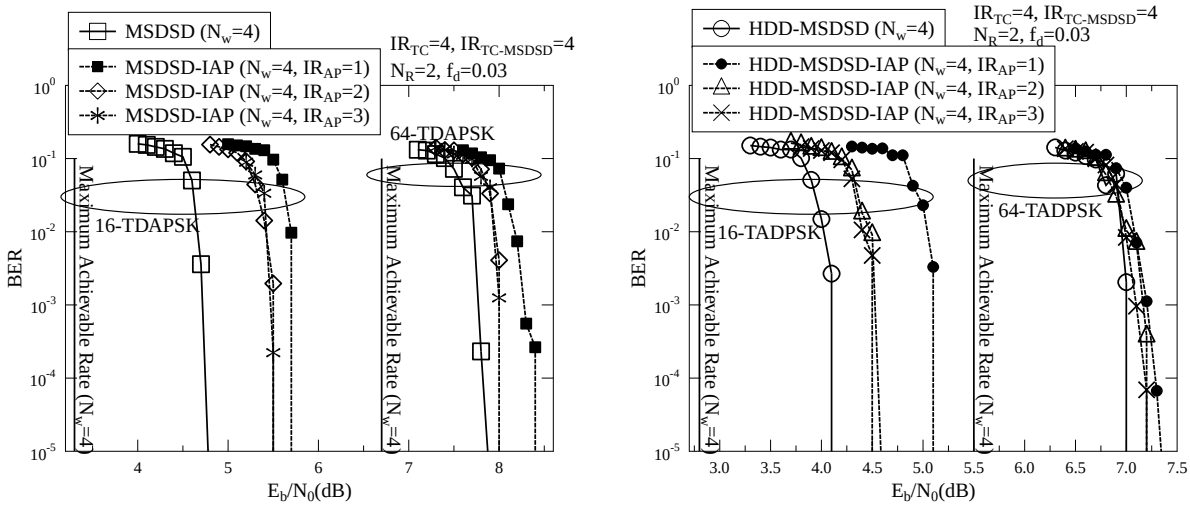

(a) TC coded TDAPSK

(b) TC coded TADPSK

Figure 5.12: BER performance of both TC coded TDAPSK employing MSDSD-IAP and of its TC coded TADPSK HDD-MSDSD-IAP counterpart, where the Max-Log-MAP algorithm is invoked, while we have $N_w = 4$, $f_d = 0.03$ and $N_R = 2$.

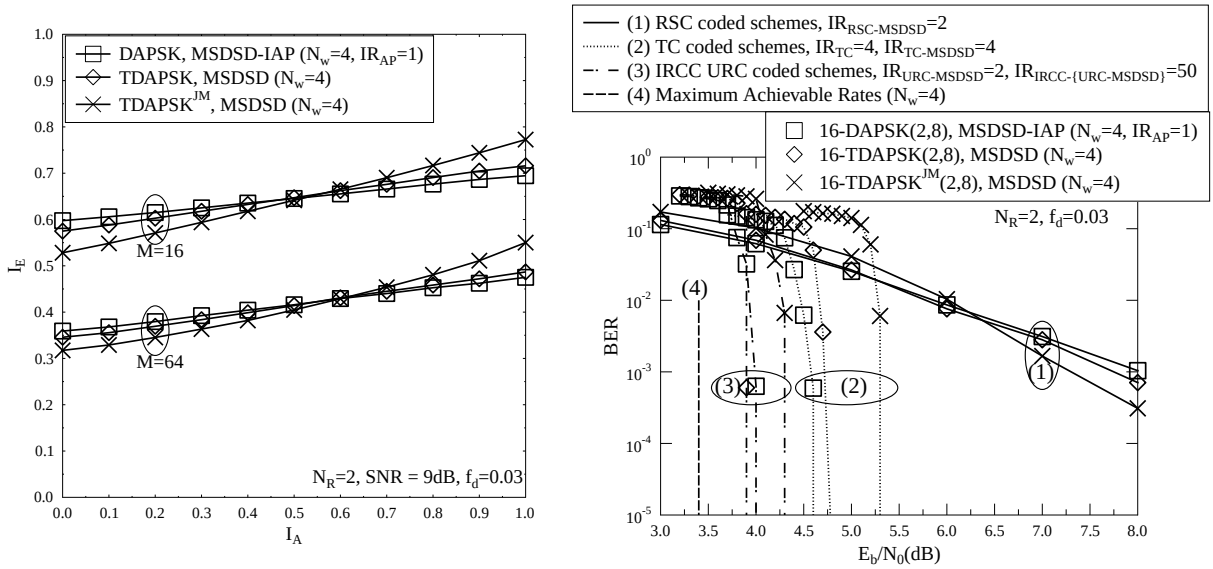

(a) EXIT charts

(b) BER performance

Figure 5.13: EXIT charts and BER performance comparison between coded DAPSK, TDAPSK and TDAPSK^{JM}, where the Max-Log-MAP algorithm is invoked, while we have $N_w = 4$, $f_d = 0.03$ and $N_R = 2$.

In summary, we may suggest that the soft-decision-aided MSDSD is the suitable choice for coded TDAPSK detection, while the soft-decision-aided HDD-MSDSD is the suitable choice for coded TADPSK detection. Naturally, TDAPSK^{JM} and TADPSK^{JM} cannot invoke iterative amplitude-phase detection, owing to the fact that all DQAM^{JM} constellations jointly map the bits to the data-carrying ring amplitude and phase. Therefore, the soft-decision-aided MSDSD may be recommended for coded TDAPSK^{JM} detection, because TDAPSK^{JM} differentially encodes the ring amplitudes as DAPSK and TDAPSK. Moreover, the soft-decision-aided HDD-MSDSD may be advocated for coded TADPSK^{JM} detection, where TADPSK^{JM} relies on absolute data-carrying ring amplitudes in the same form as ADPSK and TADPSK.

5.5.3 Comparison Between DQAM Constellations

In this section, we comparatively study the different DQAM constellations in the context of both TC coded systems, RSC coded systems as well as in IRCC and URC coded near-capacity systems. We would like to link the BER performance in this section to the DQAM capacity results of Fig. 4.12 presented in Sec. 4.7.1. Furthermore, different soft-decision-aided MSDSD arrangements are employed for different DQAM constellations according to the suggestions discussed in Sec. 5.5.2, so that each DQAM scheme may achieve its best attainable performance at the lowest possible detection complexity.

First of all, since DAPSK, TDAPSK and TDAPSK^{JM} employ the same differential encoding process of Eq. (4.1), these three DQAM constellations are compared in Fig. 5.13, where MSDSD-IAP is employed for coded DAPSK detection, while MSDSD is invoked for coded TDAPSK and

TDAPSK^{JM} detection. It was demonstrated in Fig. 4.12a that DAPSK, TDAPSK and TDAPSK^{JM} may achieve the same DCMC capacity, but Fig. 4.17 also shows that DAPSK and TDAPSK perform better than TDAPSK^{JM} in uncoded systems, regardless, whether HDD-MSDSD or DFDD is employed. By observing the EXIT charts of Fig. 5.13a, it may be confirmed that coded DAPSK detection is capable of producing the highest I_E, when there is no *a priori* information, but both TADPSK and TDAPSK^{JM} are capable of producing a higher iteration gain, where the steepest curve of coded TDAPSK^{JM} detection produces both the lowest I_E at $I_A = 0$ and the highest I_E at $I_A = 1$. Nonetheless, Fig. 5.13a shows that DAPSK, TDAPSK and TDAPSK^{JM} exhibits the same achievable rate, where the areas under the EXIT curves of the above-mentioned three counterparts are always the same. This verifies the capacity results presented in Fig. 4.12a.

Our BER performance comparison of DAPSK, TDAPSK and TDAPSK^{JM} in a variety of coded systems is portrayed by Fig. 5.13b, while the Monte-Carlo simulation based decoding trajectories of coded DAPSK detection are recorded in Fig. 5.16a, as an example. It is demonstrated in Fig. 5.13b that TDAPSK^{JM} outperforms its counterparts of DAPSK and TDAPSK in RSC coded system, while DAPSK performs better than TDAPSK and TDAPSK^{JM} in TC coded system. This is because that the steep EXIT curve of TDAPSK^{JM} matches better the EXIT curve shape of RSC, while the less steep EXIT curve of DAPSK matches better to the horizontal EXIT curve of TC. The shape matching between the EXIT curve of the inner demodulator and of the outer channel decoder minimizes the area of the open tunnel, which results in the best performance [86, 243]. Furthermore, Fig. 5.13b also shows that TDAPSK may outperform its counterparts of DAPSK and TDAPSK^{JM} in IRCC and URC coded near-capacity system. Essentially, all the three constellations have the same DCMC capacity, but TDAPSK and TDAPSK^{JM} exhibit a higher iteration gain than DAPSK, as demonstrated by Fig. 5.13a. Naturally, the improved iteration gain is beneficial, especially when turbo detection exchanges extrinsic information between the URC and MSDSD schemes. However, the number of iterations between the URC and MSDSD schemes is given by $IR_{URC-MSDSD} = 2$, which may not be sufficient for reaping the full benefit of the high iteration gain achieved by TDAPSK^{JM}, but unfortunately a higher number of iterations between the URC and MSDSD schemes may not be affordable because of the potentially excessive decoding complexity of the near-capacity system. Therefore, TDAPSK^{JM} performs even worse than DAPSK in IRCC and URC coded system, as evidenced by Fig. 5.13b.

In summary, DAPSK, TDAPSK and TDAPSK^{JM} attain their full potential in the context of different coded systems. In terms of the BER performance demonstrated by Fig. 5.13b, TDAPSK^{JM}, DAPSK and TDAPSK are the best choices for an RSC coded system, for an TC coded system and for an IRCC-URC coded system, respectively.

Secondly, our performance comparisons of ADPSK, TADPSK and TADPSK^{JM} employing the same differential encoding process of Eq. (4.8) are portrayed in Fig. 5.14. As suggested in Sec. 5.5.2, HDD-MSDSD-IAP is employed for coded ADPSK detection, while its HDD-MSDSD counterpart is used for coded TADPSK and TADPSK^{JM} detection. Similar to the EXIT chart based comparison of Fig. 5.13a, Fig. 5.14a also demonstrates that the twisted modulation of TADPSK

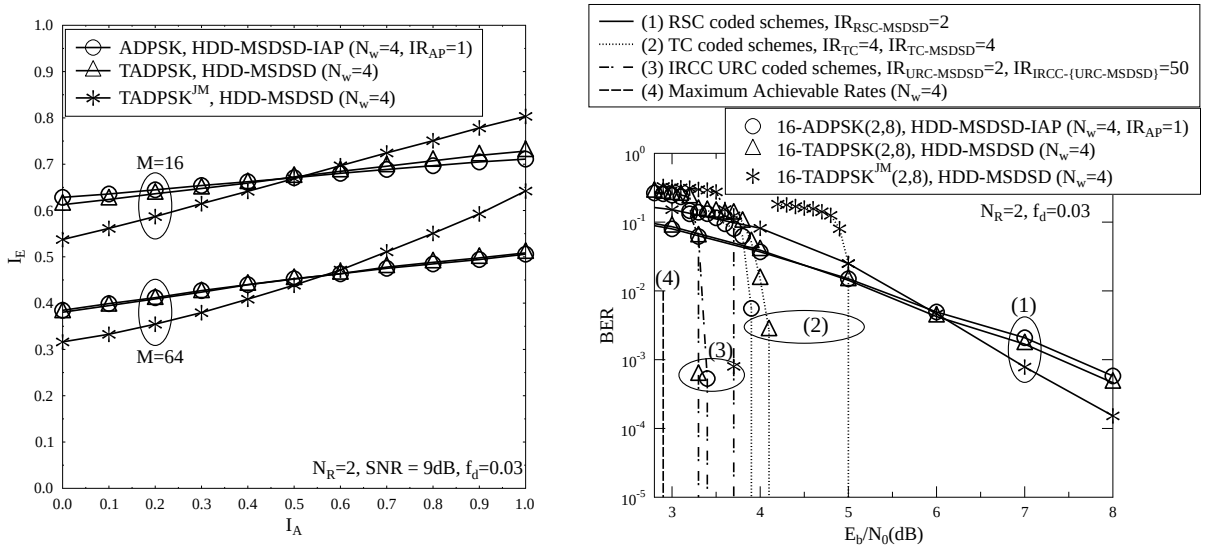

(a) EXIT charts

(b) BER performance

Figure 5.14: EXIT chart and BER performance comparison of coded ADPSK, TADPSK and TADPSK^{JM}, where the Max-Log-MAP algorithm is invoked, while we have $N_w = 4$, $f_d = 0.03$ and $N_R = 2$.

exhibits a slightly higher iteration gain than its original un-twisted DQAM constellation based ADPSK counterpart, while the joint amplitude and phase mapped twisted constellation of TADPSK^{JM} is capable of producing the highest iteration gain. The capacity results of Fig. 4.12b suggest that the ADPSK, TADPSK and TADPSK^{JM} constellations may achieve the same DCMC capacity, which is also confirmed by the EXIT charts of Fig. 5.14a, where the areas under the EXIT curves of the three counterparts are always the same.

Furthermore, Fig. 5.14b portrays our BER comparison of ADPSK, TADPSK and TADPSK^{JM}. As a further example, the decoding trajectories of coded ADPSK detection observed in a variety of coded systems are recorded in Fig. 5.16b. Once again, similar to the BER comparison of Fig. 5.13b, Fig. 5.14b further evidences that the joint mapped twisted modulation of TADPSK^{JM} outperforms its counterparts in the context of RSC coded systems. By contrast, the original un-twisted DQAM constellation of ADPSK is the best choice for TC coded systems, while the twisted modulation of TADPSK achieves the best performance in the IRCC and URC coded near capacity systems.

Having compared the un-twisted DQAM constellations to their twisted counterparts in Figs. 5.13 and 5.14, we may proceed to offer a comparison between the original DQAM constellations of DAPSK and ADPSK. Let us recall that DAPSK and ADPSK are conceived according to different design guidelines. As discussed in Sec. 4.2, the DAPSK constellation is a differential-amplitude DQAM scheme, which employs the differential encoding process of Eq. (4.1), where all the transmitted symbols including s_n and s_{n-1} in $s_n = x_{n-1}s_{n-1}$ of Eq. (4.1) are drawn from the same Star QAM constellation. By constrast, the ADPSK constellation is an absolute-amplitude DQAM scheme, which employs the differential encoding process of Eq. (4.8), where all the data-carrying

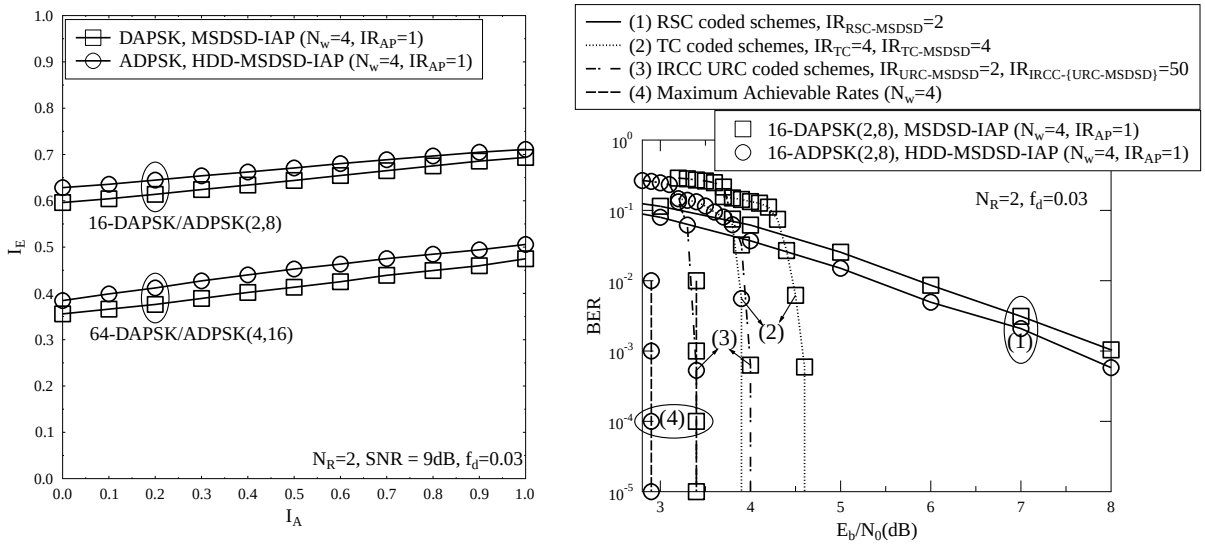

(a) EXIT charts (b) BER performance

Figure 5.15: EXIT chart and BER performance comparison between coded DAPSK and ADPSK, where the Max-Log-MAP algorithm is invoked, while we have $N_w = 4$, $f_d = 0.03$ and $N_R = 2$.

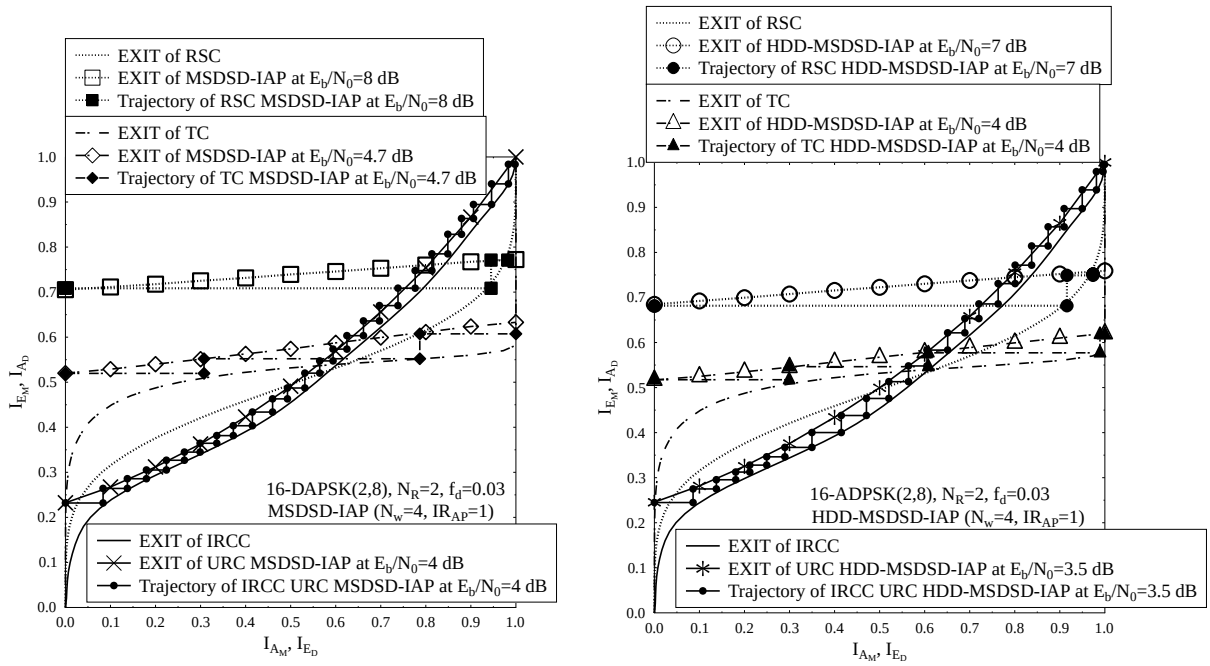

(a) 16-DAPSK(2,8) (b) 16-ADPSK(2,8)

Figure 5.16: EXIT chart and Monte-Carlo simulation based decoding trajectories of RSC/TC/IRCC-URC coded 16-DAPSK(2,8) employing MSDSD-IAP as well as its RSC/TC/IRCC-URC coded 16-ADPSK(2,8) based HDD-MSDSD-IAP counterpart, where the Max-Log-MAP algorithm is invoked, and we have $N_w = 4$, $f_d = 0.03$ and $N_R = 2$.

	real-valued multiplications	real-valued additions	comparisons	visited nodes
sortDelta	$[(4N_R + 2)v + 6N_R + \text{BPS} - 1]M$	$(4N_Rv + 2N_R + \text{BPS} + 1)M$	$O(M \log M)$	M
findBest	$[(4N_R + 2)v + 8N_R + 5]M_A + \text{BPS} \cdot M/2 + 2$	$(4N_Rv + 4N_R + 3)M_A + (\text{BPS} + 1)M/2$	$5M/4$	$M/4$
findNext	$\leq 2\text{BPS} - 2$	$\leq 2\text{BPS}$	$\leq 2 + M/2$	≤ 1

Table 5.5: Complexity summary of the subfunctions of soft-decision-aided MSDSD conceived for coded DAPSK detection.

symbols x_{n-1} are directly mapped to the Star QAM symbols. In order to avoid having an unconstrained transmitted symbol power, the ring amplitude normalization of $s_n = \frac{1}{|s_{n-1}|} x_{n-1} s_{n-1}$ seen in Eq. (4.8) results in the absolute-amplitude of $|s_n| = |x_{n-1}|$ for ADPSK. Against this background, the capacity results of Fig. 4.11 suggest that the ADPSK detection associated with effective decision-feedback may achieve a higher DCMC capacity than the DAPSK detection, but the BER results of Fig. 4.15 demonstrate that the performance advantage of ADPSK over DAPSK is negligible in uncoded systems.

However, in coded systems, the EXIT chart comparison of Fig. 5.15a clearly indicates that ADPSK outperforms DAPSK, where MSDSD-IAP and HDD-MSDSD-IAP are employed by coded DAPSK and ADPSK detection, respectively, according to the discussions of Sec. 5.5.2. Furthermore, the BER performance comparison of Fig. 5.15b explicitly demonstrates that 16-ADPSK(2,8) outperforms its 16-DAPSK(2,8) counterpart in all three of the RSC coded system, namely in the context of the TC coded system as well as in the IRCC and URC coded system. In conclusion, we may argue that ADPSK may be a better choice than DAPSK in coded systems, according to the performance comparisons seen in Fig. 5.15. Additionally, it would also be reasonable to choose the ADPSK's twisted modulated counterparts - including both TADPSK and TADPSK$^{\text{JM}}$ - to be employed in different coded systems, as discussed during the performance comparisons of Fig. 5.14.

5.5.4 Complexity Results for MSDSD

In this section, we present our complexity results for the soft-decision-aided MSDSD conceived for coded DQAM. Our complexity comparison amongst the MSDSD of Sec. 5.3.1, the reduced-complexity MSDSD algorithm of Sec. 5.3.2, the MSDD-IAP of Sec. 5.3.3 and the reduced-complexity MSDSD-IAP of Sec. 5.3.4 is firstly discussed in the context of coded DAPSK detection for demonstrating the efficiency of the proposed reduced-complexity design. Following this, the different DQAM constellations will be compared from a complexity perspective.

First of all, the complexities of the MSDSD's subfunctions presented in Sec. 5.3 are summarized in Table 5.5 for coded DAPSK detection, where the different types of calculations are separately categorized. We note that the DAPSK constellation does not have the amplitude-induced phase rotation, hence the $\{\psi_t\}_{\forall t}$ and $\{\Psi_t\}_{\forall t}$ contributions may be deleted from all DAPSK detectors. Furthermore, the subfunctions of MSDASD and MSDPSD constitute special cases of the subfunctions of MSDSD, where either the M_PPSK phases or the ring amplitudes are fixed. Ta-

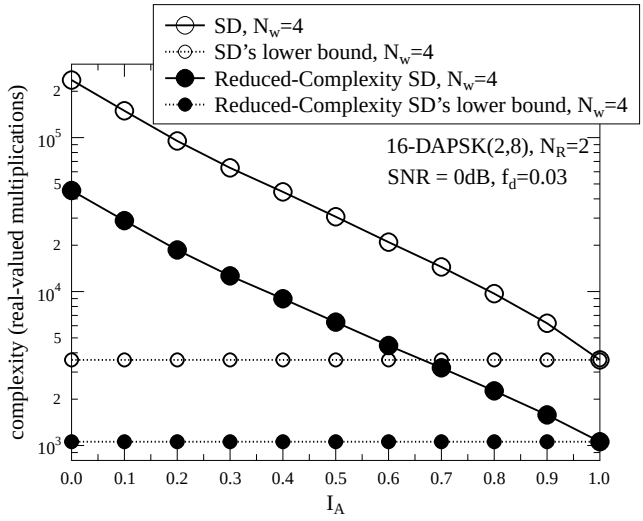

Figure 5.17: Complexity (number of real-valued multiplications) comparison between the SD algorithm using the subfunction "sortDelta" in Table 5.2 and the reduced-complexity SD algorithm using the subfunctions "findBest" and "findNext" of Tables 5.3 and 5.4. The results are recorded at SNR=0 dB and $f_d = 0.03$, where $N_R = 2$ RAs are used.

ble 5.5 demonstrates that the subfunction "sortDelta" of Table 5.2 has to visit all the M candidate constellation points and has to rank their priorities by invoking a sorting algorithm that generally involves $O(M \log M)$ comparisons [285,286]. By contrast, the subfunction "findBest" of Table 5.3 visits only the constellation points located in the first quadrant. Then the subfunction "findNext" of Table 5.4 may be called to further visit a new candidate constellation point by proceeding in zigzag-order. This is achieved by toggling the polarities of the metric evaluated by "findBest" of Table 5.3. In this way, the detection complexity of the subfunctions of "findBest" and "findNext" is lower than that of "sortDelta", as evidenced by Table 5.3.

The complexity of the SD algorithm of Table 3.3 invoking the subfunction "sortDelta" of Table 5.2 and that of Table 3.4 relying on the subfunctions "findBest" and "findNext" of Tables 5.3 and 5.4 are compared in Fig. 5.17 in terms of the total number of real-valued multiplications. First of all, it may be seen in Fig. 5.17 that the complexities of both soft-decision-aided SD algorithms converge to their lower bounds as I_A is increased from 0 to 1, even when the SNR is as low as 0 dB. Furthermore, Fig. 5.17 explicitly confirms that a significant complexity reduction is offered by invoking the reduced-complexity SD search strategy specified in Tables 5.3 and 5.4.

The complexity reductions achieved by our proposed MSDSD design are further quantified in Fig. 5.18 and Fig. 5.19 for coded 16-DAPSK(2,8) and for coded 64-DAPSK(4,16) detection, respectively. In more detail, Fig. 5.18a demonstrates that the reduced-complexity MSDSD algorithm of Sec. 5.3.2 offers a substantial 73.8% $\sim$ 80.7% complexity reduction compared to the conventional MSDSD algorithm of Sec. 5.3.1. In other words, a complexity reduction up a factor five is achieved without a performance reduction. As a result, the MSDSD complexity becomes as low as that of the MSDD-IAP. Let us recall that the MSDD-IAP proposed in [160] and summarized

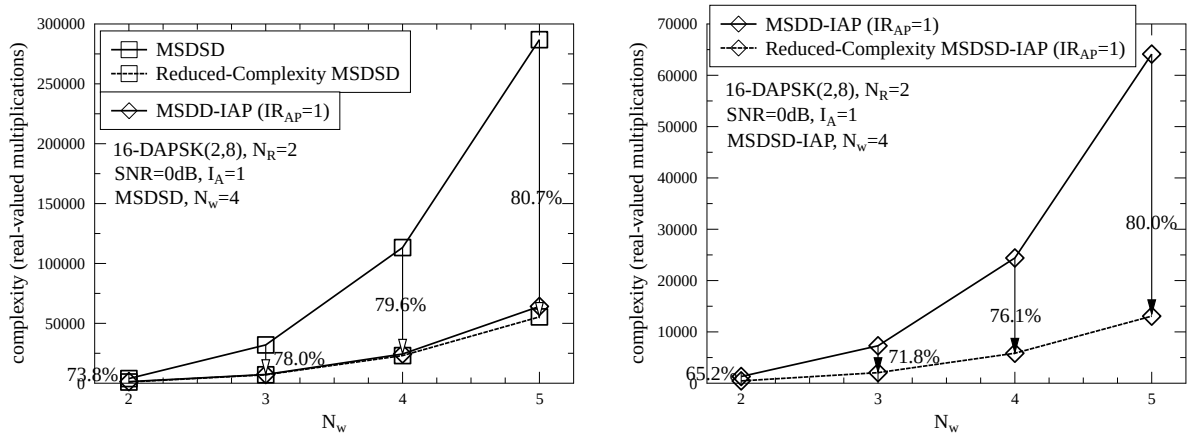

(a) MSDSD and reduced-complexity MSDSD

(b) MSDD-IAP and reduced-complexity MSDSD-IAP

Figure 5.18: Complexity (number of real-valued multiplications) comparison between MSDSD of Sec. 5.3.1, reduced-complexity MSDSD of Sec. 5.3.2, MSDD-IAP [160] of Sec. 5.3.3 and reduced-complexity MSDSD-IAP of Sec. 5.3.4 employed by coded 16-DAPSK(2,8). The results are recorded at SNR=0 dB and $f_d = 0.03$, where $N_R = 2$ RAs are equipped. The Complexity-Reduction Ratios (CRRs) of Eq. (2.109) achieved by the reduced-complexity design are indicated.

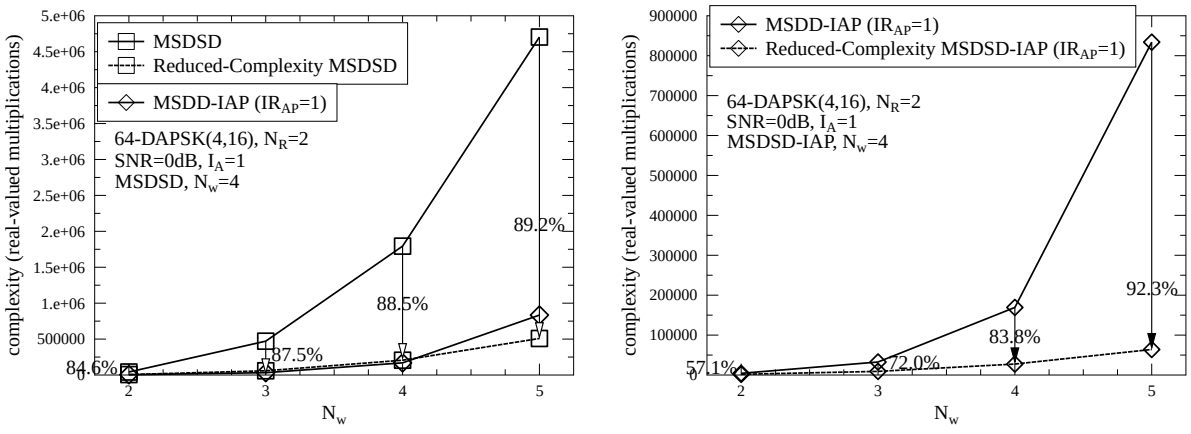

(a) MSDSD and reduced-complexity MSDSD

(b) MSDD-IAP and reduced-complexity MSDSD-IAP

Figure 5.19: Complexity (number of real-valued multiplications) comparison between MSDSD of Sec. 5.3.1, reduced-complexity MSDSD of Sec. 5.3.2, MSDD-IAP [160] of Sec. 5.3.3 and reduced-complexity MSDSD-IAP of Sec. 5.3.4 employed by coded 64-DAPSK(4,16). The results are recorded at SNR=0 dB and $f_d = 0.03$, where $N_R = 2$ RAs are equipped. The Complexity-Reduction Ratios (CRRs) of Eq. (2.109) achieved by the reduced-complexity design are indicated.

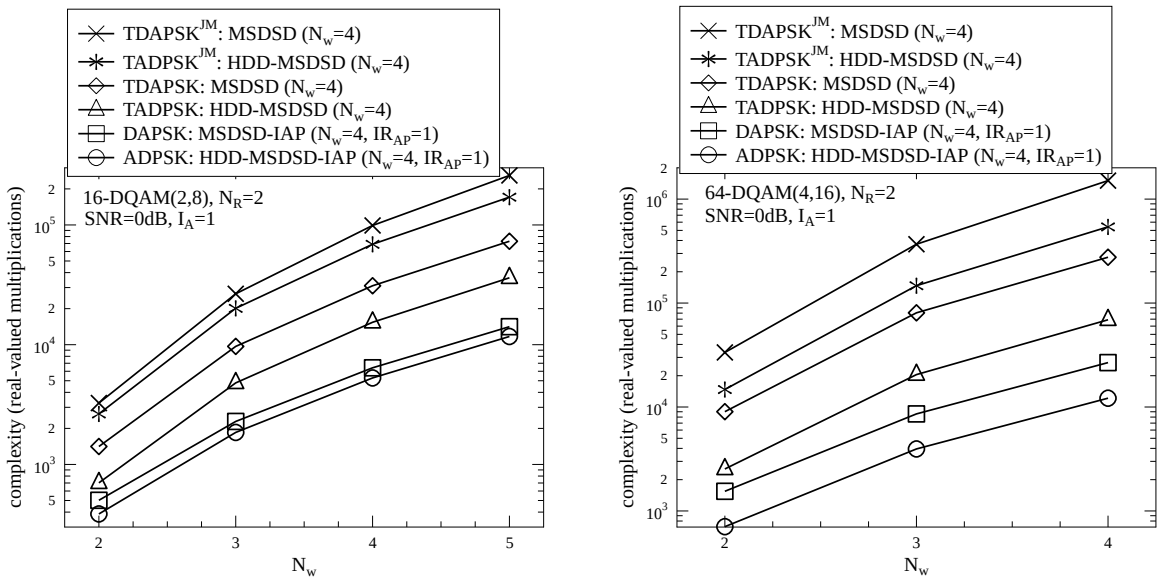

(a) 16-DQAM(2,8) (b) 64-DQAM(4,16)

Figure 5.20: Complexity (number of real-valued multiplications) comparison between DQAM schemes employing the different MSDSD arrangements of Sec. 5.5.2. The results are recorded at SNR=0 dB and $f_d = 0.03$, where $N_R = 2$ RAs are used.

in Sec. 5.3.3 exhibits a low detection complexity in Fig. 5.18a, because it separately carries out the ring amplitude detection and the M_PPSK phase detection by the MSDAD and by MSDPSD schemes, respectively, where only a single iteration associated with $IR_{AP} = 1$ is invoked between the MSDAD and MSDPSD schemes. Furthermore, Fig. 5.18b shows that the reduced-complexity MSDSD-IAP of Sec. 5.3.4 achieves an additional 65.2% $\sim$ 80.0% complexity reduction compared to the conventional MSDD-IAP of Sec. 5.3.3. Again, this corresponds to a complexity reduction of up to a factor five without a performance erosion. Similarly, it is also evidenced by Fig. 5.19 that for the case of coded 64-DAPSK(4,16) detection, 84.6% $\sim$ 89.2% complexity reduction is attained by the reduced-complexity MSDSD algorithm, which exhibits a similar detection complexity as MSDD-IAP, while the reduced-complexity MSDSD-IAP further cuts the complexity of MSDD-IAP by 57.1% $\sim$ 92.3%.

Therefore, as expected, the different MSDSD arrangments of Sec. 5.3 impose different levels of detection complexity. It is demonstrated by Fig. 5.18 and Fig. 5.19 that the reduced-complexity MSDSD-IAP of Sec. 5.3.4 associated with $IR_{AP} = 1$ may exhibit the lowest detection complexity, but as discussed in Sec. 5.5.2, only DAPSK and ADPSK benefit from the employment of MSDSD-IAP and HDD-MSDSD-IAP, respectively. Furthermore, Sec. 5.5.2 also suggests that TDAPSK and TADPSK benefit from using MSDSD and HDD-MSDSD relying on the reduced-complexity MSDSD algorithm introduced in Sec. 5.3.2. Moreover, TDAPSK$^{\text{JM}}$ and TADPSK$^{\text{JM}}$ may beneficially employ MSDSD and HDD-MSDSD according to the conventional MSDSD algorithm of Sec. 5.3.1, where all the BPS bits that are jointly mapped to the ring amplitude and to the M_PPSK phase have to be detected together in order to avoid any potential performance loss.

Fig. 5.20 provides our complexity comparison of the DQAM schemes which employ the dif-

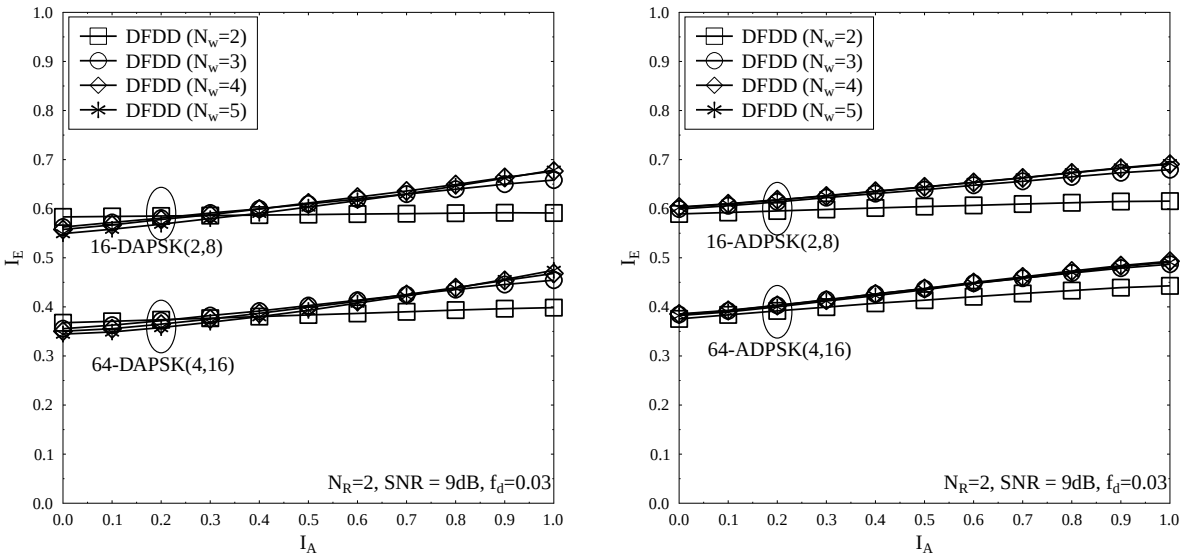

(a) DAPSK

(b) ADPSK

Figure 5.21: EXIT charts of DAPSK and ADPSK employing DFDD recorded at SNR=9 dB and $f_d = 0.03$, where the Max-Log-MAP algorithm is invoked, while $N_R = 2$ RAs are used.

ferent MSDSD arrangements of Sec. 5.5.2. It can be seen in Fig. 5.20 that the list of coded DQAM detection complexities ranging from high to low is given by TDAPSK^{JM}, TADPSK^{JM}, TDAPSK, TADPSK, DAPSK and ADPSK. This implies that the twisited modulations exhibit a higher detection complexity in coded systems than their original un-twisted counterparts, while joint mapping of bits to the ring amplitude and phase imposes the highest detection complexity. Moreover, Fig. 5.20 also shows that the HDD-MSDSD arrangements employed by the family of absolute-amplitude DQAM constellations - including ADPSK, TADPSK and TADPSK^{JM} which rely on the differential encoding process of Eq. (4.8) - generally exhibit a lower detection complexity than the MSDSD arrangements employed by their differential-amplitude DQAM counterparts of DAPSK, TDAPSK and TDAPSK^{JM}, which utilize the differential encoding process of Eq. (4.1).

5.5.5 Performance Results for DFDD

Let us now proceed with the performance characterization of the soft-decision-aided DFDD conceived for the coded DQAM detection scheme of Sec. 5.4. First of all, Fig. 5.21 portrays the EXIT charts of coded DAPSK and ADPSK employing DFDD. It can be seen that, the soft-decision-aided DFDD of Sec. 5.4 is capable of improving the CDD's performance for both DAPSK and ADPSK, but the additional improvements become negligible when the observation window length is increased beyond $N_w = 3$. We note that the DFDD arrangements of Sec. 5.4 are directly derived from the MSDD/MSDSD decision metric and hence DFDD associated with $N_w = 2$ is also equivalent to CDD.

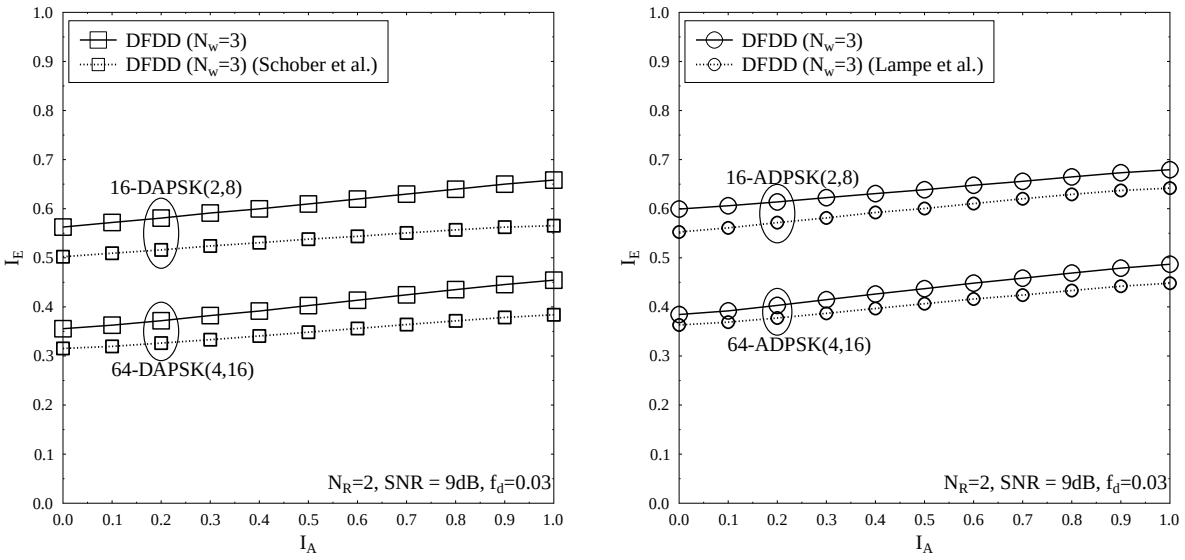

(a) DAPSK (b) ADPSK

Figure 5.22: EXIT charts of both DAPSK and of ADPSK employing DFDD recorded at SNR=9 dB and $f_d = 0.03$, where the Max-Log-MAP algorithm is invoked, and $N_R = 2$ RAs are used. The performance of the DFDD (Schober *et al.*) conceived for DAPSK in [154] and the DFDD conceived for ADPSK (Lampe *et al.*) in [136] are also portrayed as benchmarks.

Fig. 5.22 presents our EXIT chart comparison between the DFDD arrangements proposed in [136, 154] and those derived from the optimum MSDD/MSDSD, as presented in Sec. 5.4. As expected, since the DFDD arrangements of [136, 154] ignore the ring-amplitude-dependent nature of the nonconstant channel correlation matrix, a performance loss is imposed both on the coded DAPSK detection and on the ADPSK counterpart, as demonstrated by Fig. 5.22.

The BER performance of the MSDSD, of the DFDD of Sec. 5.4 and of the DFDD of [136, 154] are compared in Fig. 5.23, where they are employed by the TC coded DAPSK and ADPSK systems. As demonstrated by Fig. 5.23a, in TC coded DAPSK systems, the optimal MSDSD outperforms the DFDD presented in Sec. 5.4 by 0.5 dB, and the DFDD (Schober et al.) of [154] imposes a further substantial performance loss of 1.3 dB. Similar results can be observed in Fig. 5.23b, where HDD-MSDSD outperforms DFDD for the case of TC coded ADPSK by a moderate 0.3 dB, while the DFDD of Sec. 5.4 outperforms the DFDD (Lampe et al.) of [136] by a more substantial 1.4 dB.

5.5.6 Comparison Between Coherent and Noncoherent Detection

When the complex-valued fading envelope exhibits correlation, the Pilot Symbol Assisted Modulation (PSAM) technique proposed by Cavers [1] is capable of providing reliable but imperfect CSI estimation. It was demonstrated by Fig. 4.15 that although PSAM aided coherent QAM detection suffers from a performance erosion, when the normalized Doppler frequency is increased, uncoded

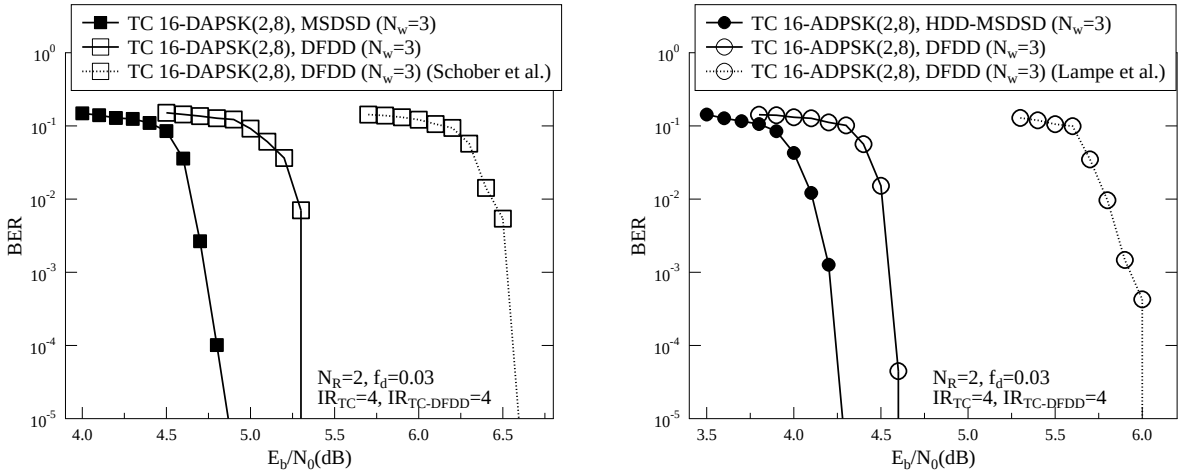

(a) TC coded DAPSK

(b) TC coded ADPSK

Figure 5.23: BER performance comparison of the MSDSD, of the DFDD of Sec. 5.4 and of the DFDD (Schober et al.) of [154], when they are invoked for coded DAPSK detection in TC coded systems. The DAPSK BERs of Fig. 5.23a may be contrasted to the BER comparison of the HDD-MSDSD, of the DFDD of Sec. 5.4 and of the DFDD (Lampe et al.) of [136], when they are employed for coded ADPSK detection in TC coded systems. We have $N_w = 3$, $f_d = 0.03$ and $N_R = 2$.

DQAM detection employing HDD-MSDSD is still outperformed by its coherent counterpart.

As discussed in Sec. 3.2.5, Subset MSDSD is capable of improving the MSDSD performance by a simple adjustment at the cost of an incremental complexity increase. More explicitly, as portrayed by Fig. 3.1, Subset MSDSD increases the number of overlapping samples of the adjacent observation windows to $N_{OL} = 3$, so that the less reliably detected data-carrying symbols located at the edge of each observation window may be discarded. Furthermore, it was suggested by Fig. 5.16 that ADPSK employing HDD-MSDSD-IAP may outperform its DAPSK counterpart, while Fig. 5.20 explicitly demonstrates that the coded ADPSK detection complexity is considered to be the lowest among that of the DQAM schemes. Therefore, in this section, ADPSK employing HDD-Subset MSDSD-IAP associated with $N_w = 4$ and $IR_{AP} = 1$ is employed as our representative noncoherent scheme in coded systems.

Fig. 5.24 compares PSAM aided coherent Square 16QAM detection and HDD-Subset MSDSD-IAP aided noncoherent 16-ADPSK(2,8) detection using EXIT charts. When the fading channels fluctuate slowly, as specified by $f_d = 0.001$ in Fig. 5.24a, the performance difference between coherent detectors either relying on perfect CSI or employing PSAM is small, and coherent Square 16QAM detection clearly outperforms noncoherent 16-ADPSK(2,8) detection in this scenario. However, as the normalized Doppler frequency increases to $f_d = 0.03$ in Fig. 5.24b, the performance gap between perfect CSI aided coherent detection and PSAM aided coherent detection becomes substantial, while the area under the EXIT curve of the ADPSK detection is considerably bigger than that of PSAM aided coherent detection, which implies that the noncoherent scheme

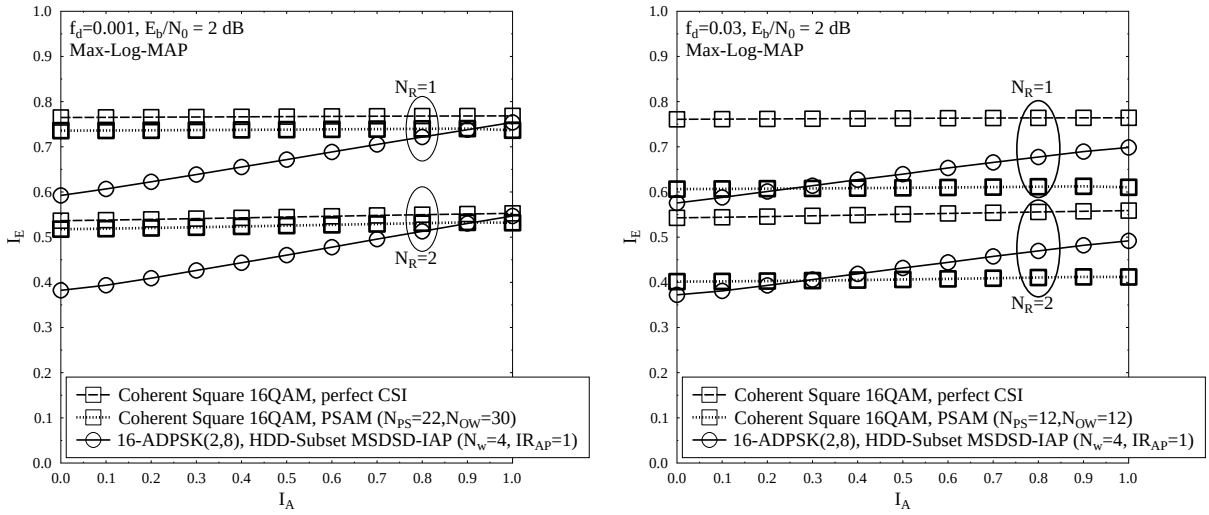

(a) $f_d = 0.001$ (b) $f_d = 0.03$

Figure 5.24: EXIT charts of PSAM aided Square 16QAM in comparison to 16-ADPSK(2,8) employing HDD-Subset MSDSD-IAP recorded at $E_b/N_0 = 2$ dB, where the Max-Log-MAP algorithm is invoked.

may outperform its coherent counterpart in coded systems, when turbo detection is invoked for exchanging extrinsic information between the channel decoder and the coherent or noncoherent demodulator.

Let us further examine the detection capabilities of the coherent and noncoherent detectors by carrying out the LLR validity test in Fig. 5.25. It can be seen in Fig. 5.25a that both the PSAM aided coherent 16QAM detector and the HDD-Subset MSDSD-IAP aided noncoherent 16-ADPSK(2,8) detector are capable of producing reliable extrinsic LLRs, provided that the fading channels fluctuate slowly. However, Fig. 5.25b shows that the extrinsic LLRs produced by the PSAM aided coherent 16QAM detector suffer from a severe deviation from the LLR definition of Eq. (2.66), when the normalized Doppler frequency is increased to $f_d = 0.03$. This is because the coherent detectors assume having perfect knowledge of the CSI, which is especially unrealistic when the fading channel fluctuates rapidly. This problem substantially affects the attainable performance of coherent detectors in coded systems, owing to the potential risk that the channel decoder may be fed with unreliable LLRs.

Finally, our BER performance comparison between the RSC/TC/IRCC-URC coded PSAM aided Square 16QAM and its 16-ADPSK(2,8) counterpart employing HDD-Subset MSDSD-IAP is portrayed in Fig. 5.26. As expected, when we have $f_d = 0.001$, PSAM aided coherent 16QAM outperforms HDD-Subset MSDSD-IAP assisted 16-ADPSK(2,8) in the RSC coded system, TC coded system as well as in the IRCC and URC coded system, as demonstrated by Fig. 5.26a. However, observe in the figure that when the fading channels fluctuate rapidly, as specified by $f_d = 0.03$, 16-ADPSK(2,8) exhibits an impressive performance advantage over coherently detected Square 16QAM. In summary, we may conclude that the soft-decision-aided MSDSD is capable of produc-

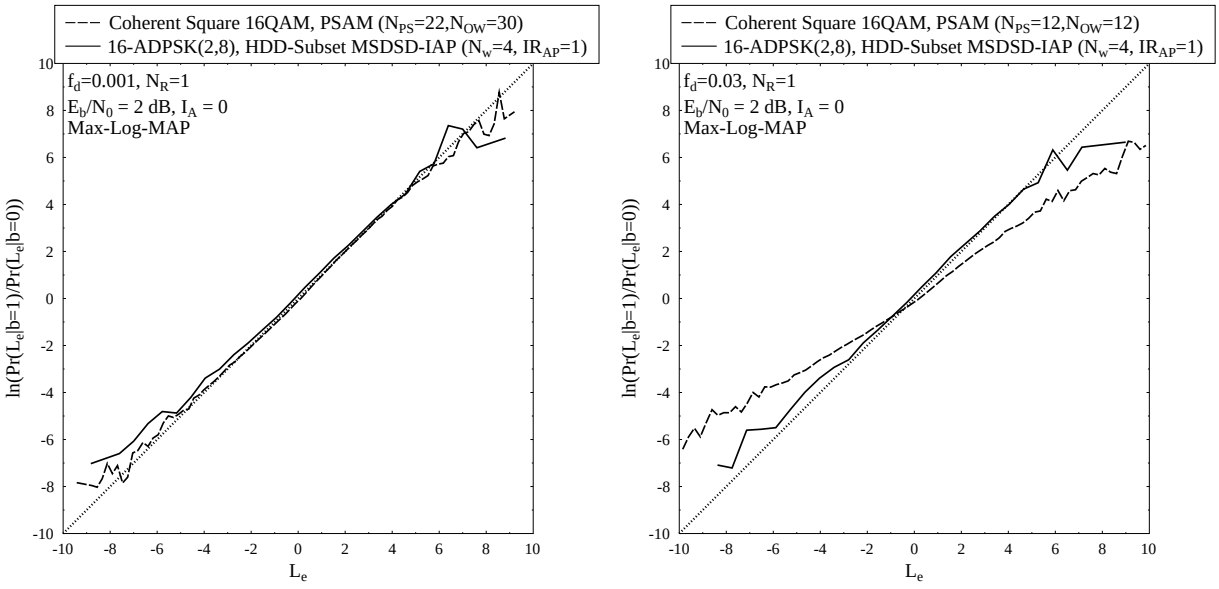

(a) $f_d = 0.001$ (b) $f_d = 0.03$

Figure 5.25: LLR validity test of PSAM aided Square 16QAM in comparison to 16-ADPSK(2,8) employing HDD-Subset MSDSD-IAP recorded at $E_b/N_0 = 2$ dB and $I_A = 0$, where the Max-Log-MAP algorithm is invoked.

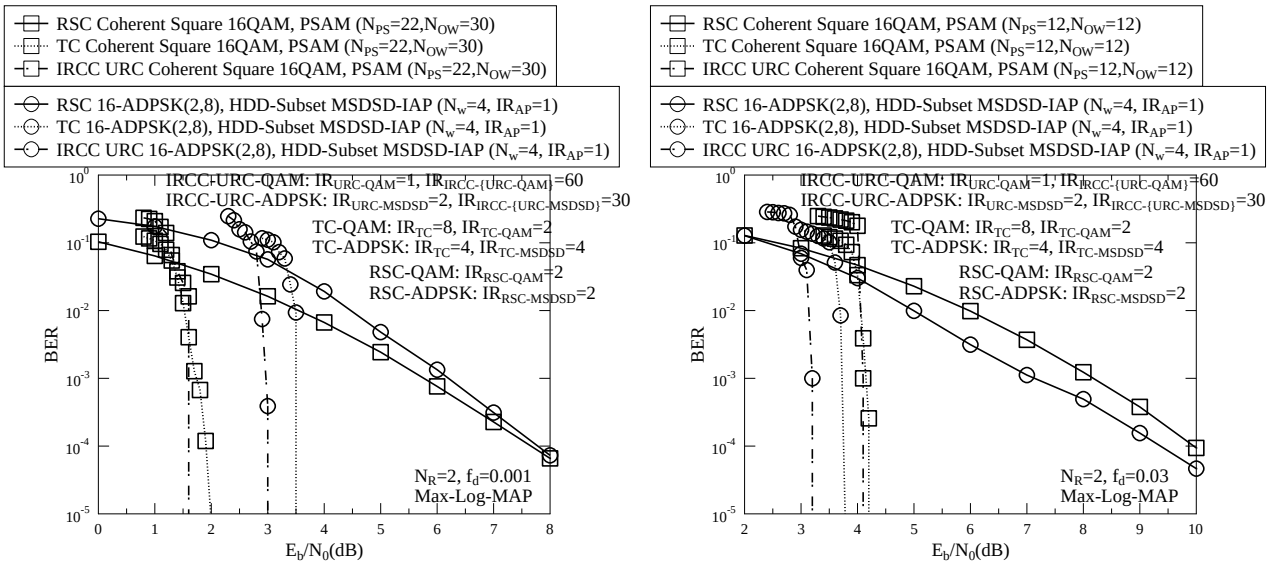

(a) $f_d = 0.001$ (b) $f_d = 0.03$

Figure 5.26: BER performance comparison between RSC/TC/IRCC-URC coded PSAM aided Square 16QAM and its 16-ADPSK(2,8) counterpart employing HDD-Subset MSDSD-IAP, where the Max-Log-MAP algorithm is invoked.

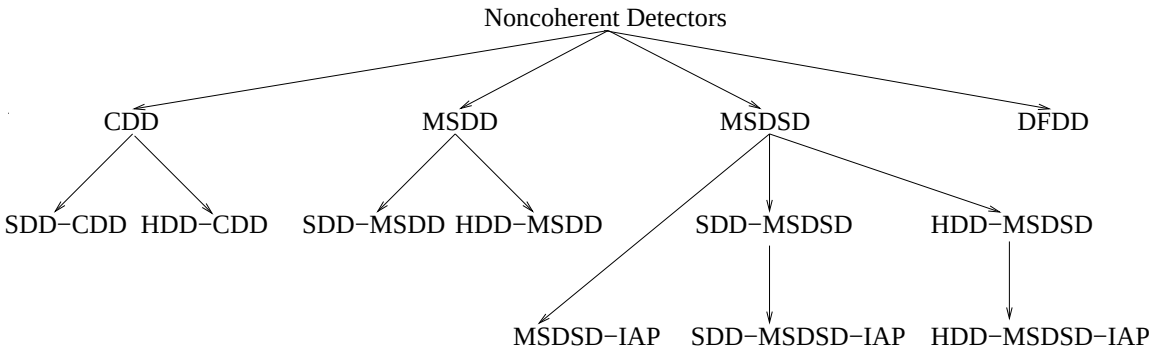

Figure 5.27: Summary of soft-decision-aided noncoherent detectors conceived for coded DQAM detection.

ing reliable extrinsic LLRs at any normalized Doppler frequencies and it exhibits a performance advantage over the coherent detector relying on realistic imperfect CSI, when the fading channels fluctuate rapidly.

5.6 Chapter Conclusions

In this chapter, we have developed the family of soft-decision-aided noncoherent detectors conceived for coded DQAM detection, which are briefly summarized in Fig. 5.27. Generally, the typical types of noncoherent detectors - including CDD, MSDD, MSDSD and DFDD - may be invoked for coded DQAM detection. The classic MSDD proposed in [114] was introduced in Sec. 5.2, which may be implemented in the forms of SDD-MSDD and HDD-MSDD for coded DQAM detection. The soft-decision-aided CDD arrangements - including CDD, SDD-CDD and HDD-CDD - may be considered to be equivalent to the corresponding MSDD arrangements associated with $N_w = 2$, as demonstrated in Sec. 5.2. The soft-decision-aided MSDSD conceived for coded DQAM detection was proposed in Sec. 5.3, where sphere decoding may be invoked for both the ring-amplitude detection and for the M_PPSK phase detection. The optimum MSDD detection capability may be retained by MSDSD, provided that the initial SD's radius is set to be sufficiently large, despite its reduced complexity. Furthermore, the soft-decision-aided DFDD conceived for coded DQAM was detailed in Sec. 5.4, and this solution was shown to be able to outperform the suboptimal DFDD solutions in [136, 153, 154], which assume a constant channel correlation matrix $\mathbf{C}$, which is independent of the variable ring-amplitudes of transmitted DQAM symbols.

We have dedicated substantial efforts to streamlining the MSDSD algorithm in Sec. 5.3 in order to maintain the MSDSD's performance at the lowest possible detection complexity. More explicitly, a reduced-complexity design was proposed in Sec. 3.3.3 for soft-decision-aided MSDSD conceived for coded DPSK, which was invoked for coded DQAM, where the total number of constellation points visited by the SD was reduced by exploring the symmetry provided by classic Gray labelling. Furthermore, we have generalized the MSDD-IAP proposed in [160] to all DQAM constellations, which map their bits to the data-carrying ring amplitude index and to the data-carrying M_PPSK

DAPSK	CDD	MSDD	MSDSD-IAP	DFDD
ADPSK	HDD-CDD	HDD-MSDD	HDD-MSDSD-IAP	DFDD
TDAPSK	CDD	MSDD	MSDSD	DFDD
TADPSK	HDD-CDD	HDD-MSDD	HDD-MSDSD	DFDD

Table 5.6: Summary of soft-decision-aided noncoherent detectors that are suggested for different DQAM constellations.

Better performance:	RSC-DQAM	ADPSK
	TC-DQAM	ADPSK
	IRCC-URC-DQAM	ADPSK
Lower detection complexity:	ADPSK	

Table 5.7: Summary of comparisons between coded DAPSK detection employing MSDSD-IAP and coded ADPSK detection employing HDD-MSDSD-IAP.

phase index separately. Since MSDD-IAP is capable of approaching the near-optimum MSDD performance for both coded DAPSK detection and coded ADPSK detection, we further reduced its detection complexity by invoking sphere decoding for ring amplitude detection and the reduced-complexity design of Sec. 3.3.3 for M_PPSK phase detection.

In order to simplify our discussions, in Table 5.6, we provide a summary of the set of soft-decision-aided noncoherent detectors recommended for different DQAM constellations, which emerged from our performance discussions of Sec. 5.5. In general, hard-decision-directed arrangements - including HDD-CDD, HDD-MSDD and HDD-MSDSD - can only be applied to ADPSK and TADPSK/TADPSK^{JM} in coded systems. They exhibit a lower detection complexity than their corresponding original counterparts, including CDD, MSDD and MSDSD that are applied to DAPSK and TDAPSK/TDAPSK^{JM}. Furthermore, MSDSD-IAP and HDD-MSDSD-IAP are recommended for coded DAPSK detection and coded ADPSK detection, respectively, which subtantially reduce the complexity of their original MSDSD and HDD-MSDSD.

The performance results of MSDSD are summarized in Table 5.7, where we observe that the RSC coded-, TC coded- as well as IRCC-and-URC coded ADPSK systems employing HDD-MSDSD-IAP detection is capable of achieving a better performance at a lower detection complexity than coded DAPSK detection employing MSDSD-IAP. Furthermore, as summarized in Table 5.7, TADPSK^{JM}, ADPSK and TADPSK constitute a better choice for RSC coded-, TC coded- as well as IRCC-and-URC coded systems, respectively, in terms of their BER performance. Amongst these the coded ADPSK detector imposes the lowest detection complexity. As discussed in Sec. 4.2, DAPSK and ADPSK are conceived according to different design guidelines, where DAPSK is a differential-amplitude DQAM scheme that invokes the differential encoding process of Eq. (4.1), while ADPSK is an absolute-amplitude DQAM scheme that employs the differential encoding process of Eq. (4.8). According to the performance results summarized in Tables 5.6-5.8, one may argue that ADPSK and its twisted constellations may be preferred over DAPSK. This discussion is beneficial, because the differential DQAM constellation using an absolute amplitude, such as ADPSK is also often applied to Differential MIMO schemes using QAM [139–141], where it is

Better performance:	RSC-DQAM	TADPSK^{JM}
	TC-DQAM	ADPSK
	IRCC-URC-DQAM	TADPSK
Lower detection complexity:	ADPSK	

Table 5.8: Summary of comparisons between coded ADPSK detection employing HDD-MSDSD-IAP as well as coded TADPSK/TADPSK^{JM} detection employing HDD-MSDSD.

more important to use the classic QAM constellation for the data-carrying symbols. The hard-decision-aided noncoherent detectors discussed in Chapter 4 and the soft-decision-aided noncoherent detectors explored in this chapter will be helpful for developing noncoherent receivers for Differential MIMO schemes, which is discussed in our future work of Sec. 8.2.6.

In the previous chapters, we have focused our attention on the reduced-complexity design of basic modulations, including both coherent and noncoherent schemes. As a further step, in the popular MIMO systems, where several symbols are transmitted together, the challenge of retaining the optimum performance at a low detection complexity becomes more difficult to tackle albeit it is of greater significance. We will carry on by investigating this topic in the following chapters.

Chapter 6

Reduced-Complexity MIMO Design – Part I: Uncoded Systems

6.1 Introduction

Multiple-Input Multiple-Output (MIMO) wireless communication systems, whose transmitter and receiver are both equipped with multiple antenna elements as portrayed by Fig. 6.1, provide an increased capacity [165,166,291] and/or improved transmission reliability [177,178,292]. It is widely recognized that the classic V-BLAST system [162] aims for an increased data rate by simultaneously transmitting independent data streams, while the family of Space-Time Block Code (STBC) [177, 178, 292] aims to achieve a diversity gain by transmitting redundant information so that the receiver may obtain several replicas of the faded data-carrying signals. Owing to the fact that V-BLAST cannot benefit from the STBC's transmit diversity gain, which combats the detrimental effects of fading channels, while that STBC is incapable of achieving the V-BLAST's full multiplexing gain because of the STBC's repetitive transmission, striking a compelling tradeoff between the multiplexing and diversity gain has inspired numerous research efforts [8].

In order to better understand this tradeoff, let us firstly introduce the two key mathematical measures used in MIMO system design, which are the achievable capacity and the error probability. As portrayed by Fig. 6.1, a typical MIMO system may employ N_T Transmit Antenna (TA) and N_R Receive Antenna (RA). Moreover, a transmission block of MIMO signals may be constituted by a total number of N_Q modulated MPSK/QAM symbols, and this transmission block may be transmitted over N_P symbol periods. Therefore, in the presence of the ubiquitous multipath fading as well as the Gaussian-distributed noise, the signal received by the N_R RAs over N_P Time Slot (TS) at the receiver may be modelled as:

$$\mathbf{Y} = \mathbf{SH} + \mathbf{V}, \tag{6.1}$$

where the $(N_P \times N_T)$-element matrix $\mathbf{S}$ and the $(N_P \times N_R)$-element matrix $\mathbf{Y}$ represent the input and output signals of the MIMO channels. Furthermore, the $(N_T \times N_R)$-element $\mathbf{H}$ in Eq. (6.1)

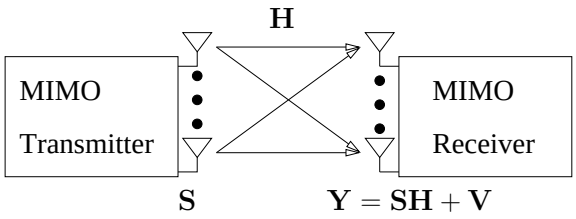

Figure 6.1: Schematic of MIMO transceiver.

MIMO Scheme	Transmitted Matrix	Parameters				
V-BLAST [162]	$\mathbf{S} = [s_1, \cdots, s_{N_T}]$	$N_T > 1$	$N_R \geq 1$	$N_P = 1$	$N_Q = N_T$	$R = N_T$BPS
G2-STBC [177]	$\mathbf{S} = \begin{bmatrix} s_1 & s_2 \\ -s_2^* & s_1^* \end{bmatrix}$	$N_T = 2$	$N_R \geq 1$	$N_P = 2$	$N_Q = 2$	$R =$ BPS
LDC [188]	$\mathbf{S} = \sum_{q=1}^{N_Q} \overline{\mathbf{A}}_q s_q$	$N_T > 1$	$N_R \geq 1$	$N_P > 1$	$N_Q \geq N_T N_P$	$R = \frac{N_Q \text{BPS}}{N_P}$
SM [197]	$\mathbf{S} = [\underbrace{0 \cdots 0}_{v-1}, s^m, \underbrace{0 \cdots 0}_{N_T - v}]$	$N_T > 1$	$N_R \geq 1$	$N_P = 1$	$N_Q = 1$	$R = \log_2 N_T +$ BPS
STSK [216]	$\mathbf{S} = \overline{\mathbf{A}}_q s_q$	$N_T > 1$	$N_R \geq 1$	$N_P > 1$	$N_Q \geq 1$	$R = \frac{\log_2 N_Q + \text{BPS}}{N_P}$

Table 6.1: A brief summary of the transmitted matrices and parameters of classic MIMO representatives.

models the MIMO's Rayleigh fading channels, which is assumed to be time-invariant over N_P symbol periods. The $(N_P \times N_R)$-element AWGN matrix $\mathbf{V}$ in Eq. (6.1) models the independent and identically distributed (i.i.d.) zero-mean Gaussian random variables with a common complex variance of N_0, whose PDF is given by:

$$p(\mathbf{V}) = p(\mathbf{Y}|\mathbf{S}^i) = \frac{1}{(\pi N_0)^{N_R N_P}} \exp(-\frac{\|\mathbf{Y} - \mathbf{S}^i\mathbf{H}\|^2}{N_0}), \tag{6.2}$$

where there are a total of I combinations $\{\mathbf{S}^i\}_{i=0}^{I-1}$ for the MIMO transmission matrix $\mathbf{S}$ in Eq. (6.1). The MIMO transmission matrices and parameters are briefly summarized in Table 6.1. The details of these classic MIMO schemes will be introduced later.

The CCMC capacity of the MIMO channels is given by maximizing the mutual information between the input signal and the output signal per channel use as [17]:

$$\begin{aligned} C^{CCMC}(SNR) &= \max_{p(\mathbf{S})} \frac{1}{N_P} I(\mathbf{S}; \mathbf{Y}) \\ &= \max_{p(\mathbf{S})} \frac{1}{N_P} H(\mathbf{Y}) - \frac{1}{N_P} H(\mathbf{Y}|\mathbf{S}). \end{aligned} \tag{6.3}$$

Based on the Gaussian PDF $p(\mathbf{V})$ of Eq. (6.2), we have $H(\mathbf{Y}|\mathbf{S}) = H(\mathbf{V}) = H\left[\text{rvec}(\mathbf{V})\right] = \log_2 \det\left[\pi e N_0 \mathbf{I}_{N_P N_R}\right]$, where the operation $\text{rvec}(\cdot)$ forms a row vector by concatenating the rows in a matrix one-by-one. For example, we have $\text{rvec}(\mathbf{V}) = [\mathbf{V}_{1,-} \ \cdots \ \mathbf{V}_{N_P,-}]$, where $\{\mathbf{V}_{t,-}\}_{t=1}^{N_P}$ refers to the t-th row in the AWGN matrix $\mathbf{V}$. Furthermore, in order to maximize the entropy $H(\mathbf{Y})$ in Eq. (6.3), both the input signal and the output signal have be Gaussian distributed. The received signal matrix $\mathbf{Y}$ of Eq. (6.1) may also be vectorized as $\text{rvec}(\mathbf{Y}) = \text{rvec}(\mathbf{S})\left(\mathbf{I}_{N_P} \otimes \mathbf{H}\right) + \text{rvec}(\mathbf{V})$, which results in $H(\mathbf{Y}) = H\left[\text{rvec}(\mathbf{Y})\right] = \log_2 \det\left\{\pi e \left[\frac{1}{N_T}\left(\mathbf{I}_{N_P} \otimes \mathbf{H}^H\right)\left(\mathbf{I}_{N_P} \otimes \mathbf{H}\right) + N_0 \mathbf{I}_{N_P N_R}\right]\right\}$.

We note that the autocorrelation of the input signals is given by $\mathrm{E}\left[\mathrm{rvec}(\mathbf{S})^H \mathrm{rvec}(\mathbf{S})\right] = \frac{1}{N_T}\mathbf{I}_{N_P N_T}$, which complies with the transmit power constraint of $\mathrm{E}\left\{\mathrm{tr}\left[\mathrm{rvec}(\mathbf{S})^H \mathrm{rvec}(\mathbf{S})\right]\right\} = N_P$. Therefore, the ergodic CCMC capacity of Eq. (6.3) that is averaged over all channel realizations is given by:

$$\begin{aligned} C^{CCMC}(SNR) &= \frac{1}{N_P}\mathrm{E}\left\{\log_2 \det(\mathbf{I}_{N_P N_R} + \frac{\eta}{N_T}\left[\mathbf{I}_{N_P} \otimes (\mathbf{H}^H\mathbf{H})\right]\right\} \\ &= \mathrm{E}\left[\log_2 \det(\mathbf{I}_{N_R} + \frac{\eta}{N_T}\mathbf{H}^H\mathbf{H})\right], \end{aligned} \tag{6.4}$$

where $SNR = 10\log_{10}\eta$ is the normalized signal-to-noise ratio $\eta = \frac{1}{N_0}$ represented on the logarithmic decibel scale. When the number of TAs grows towards infinity, the mutual information of Eq. (6.4) may be further extended as [165, 166]:

$$\begin{aligned} \lim_{N_T\to\infty} C^{CCMC}(SNR) &= \log_2 \det(\mathbf{I}_{N_R} + \eta\mathbf{I}_{N_R}) \\ &= N^{\min}\log_2(1+\eta), \end{aligned} \tag{6.5}$$

where we have $\lim_{N_T\to\infty}\mathrm{E}\left(\frac{1}{N_T}\mathbf{H}^H\mathbf{H}\right) = \mathbf{I}_{N_R}$, while $N^{\min} = \min(N_T, N_R)$ represents the minimum of the number of the TAs and RAs. It can be readily seen in Eq. (6.5) that as the number of antennas grows, the MIMO capacity grows linearly with $\min(N_T, N_R)$. Let us recall that the CCMC capacity of SIMO systems in Eq. (2.54) grows logarithmically with N_R. Therefore, compared to SIMO systems and also to SISO systems, the MIMO systems are capable of providing a higher data rate without requiring more signal bandwidth. We will demonstrate in Sec. 6.3.1 that the STBCs based on orthogonal design [177, 178, 293] and those relying on the so-called Amicable orthogonal design principle [181–183] cannot achieve the full MIMO capacity of Eq. (6.4), because their linear receivers operate based on the decoupled individual fading channels instead of relying on the original MIMO fading channels $\mathbf{H}$ exhibiting cross-coupling.

When the supposedly continuous Gaussian-distributed input signal is discretized for transmitting practical MPSK/QAM symbols, the CCMC capacity of Eq. (6.3) has to be replaced by the more realistic measure of DCMC capacity of [4, 8, 244]:

$$\begin{aligned} C^{DCMC}(SNR) &= \max_{\{p(\mathbf{S}^i)\}_{i=0}^{I-1}} \frac{1}{N_P}\sum_{i=0}^{I-1}\int p(\mathbf{S}^i,\mathbf{Y})\log_2\frac{p(\mathbf{S}^i,\mathbf{Y})}{p(\mathbf{S}^i)p(\mathbf{Y})}d\mathbf{Y} \\ &= \max_{\{p(\mathbf{S}^i)\}_{i=0}^{I-1}} \frac{1}{N_P}\sum_{i=0}^{I-1}\int p(\mathbf{Y}|\mathbf{S}^i)p(\mathbf{S}^i)\log_2\frac{p(\mathbf{Y}|\mathbf{S}^i)}{\sum_{\bar{i}=0}^{I-1}p(\mathbf{Y}|\mathbf{S}^{\bar{i}})p(\mathbf{S}^{\bar{i}})}d\mathbf{Y}. \end{aligned} \tag{6.6}$$

The DCMC capacity of Eq. (6.6) is maximized, when the MIMO transmission matrix candidates are equiprobable, i.e. we have $\{p(\mathbf{S}^i) = \frac{1}{I}\}_{i=0}^{I-1}$. Based on the PDF $p(\mathbf{Y}|\mathbf{S}^i)$ given by Eq. (6.2), the DCMC capacity of Eq. (6.6) may be further simplified as:

$$\begin{aligned} C^{DCMC}(SNR) &= \frac{1}{I\cdot N_P}\sum_{i=0}^{I-1}\mathrm{E}\left\{\log_2\left[\frac{I\cdot p(\mathbf{Y}|\mathbf{S}^i)}{\sum_{\bar{i}=0}^{I-1}p(\mathbf{Y}|\mathbf{S}^{\bar{i}})}\right]\right\} \\ &= R - \frac{1}{I\cdot N_P}\sum_{i=0}^{I-1}\mathrm{E}\left\{\log_2\left[\sum_{\bar{i}=0}^{I-1}\exp(\frac{-\|(\mathbf{S}^i-\mathbf{S}^{\bar{i}})\mathbf{H}+\mathbf{V}\|^2+\|\mathbf{V}\|^2}{N_0})\right]\right\}, \end{aligned} \tag{6.7}$$

where the MIMO throughput is given by $R = \frac{\log_2 I}{N_P}$, which is expected to be achieved by the DCMC capacity of $C^{DCMC}(SNR)$ in the high-SNR region.

In particular, the STBC throughput is given by $R = \frac{N_Q \text{BPS}}{N_P}$. It was demonstrated in [178] that Alamouti's G2-STBC associated with $N_T = N_P = N_Q = 2$ is the only full unity-rate orthogonal STBC employing a complex-valued signal constellation, where the STBC's normalized throughput is defined as $\overline{R} = N_Q/N_P$. When $N_T > 2$ is used for orthogonal STBC schemes, we always have $\overline{R} < 1$ for complex-valued signalling. Hence the orthogonal STBCs do not have the advantage of a higher data rate than SISO or SIMO schemes, albeit they have a diversity gain. By contrast, the V-BLAST's maximum achievable rate of Eq. (6.7) is given by $R = N_T$BPS, which is N_T times higher than that of the SIMO of Eq. (2.57). Again, the V-BLAST's feature of maximized MIMO throughput is often interpreted as *multiplexing gain*.

Nonetheless, a higher attainable capacity cannot guarantee a lower error probability. Let us now consider the average BER of a MIMO scheme, which is given by [223, 294, 295]:

$$\overline{P}_{e,bit} = \text{E}\left\{ \sum_{i=0}^{I-1} \sum_{\bar{i}=0, \bar{i}\neq i}^{I-1} \frac{d_H(i,\bar{i})}{I \log_2 I} p(\hat{\mathbf{S}} = \mathbf{S}^{\bar{i}} | \mathbf{S}^i) \right\}, \tag{6.8}$$

where $d_H(i,\bar{i})$ refers to the Hamming distance between the bit-mappings of $\mathbf{S}^i$ and $\mathbf{S}^{\bar{i}}$, which may be directly obtained by conveying the indices i and $\bar{i}$ back to $\log_2 I$ bits. Furthermore, the average Pairwise Error Probability (PEP) $\text{E}\left\{p(\mathbf{S}^i \to \mathbf{S}^{\bar{i}})\right\}$, which is the average probability $\text{E}\left\{p(\hat{\mathbf{S}} = \mathbf{S}^{\bar{i}} | \mathbf{S}^i)\right\}$ of choosing $\mathbf{S}^{\bar{i}}$ when $\mathbf{S}^i$ was transmitted, may be expressed as [3, 4, 296]:

$$\begin{aligned} \text{E}\left\{p(\mathbf{S}^i \to \mathbf{S}^{\bar{i}})\right\} &= \text{E}\left\{p\left(\|\mathbf{Y} - \mathbf{S}^{\bar{i}}\mathbf{H}\|^2 < \|\mathbf{V}\|^2\right)\right\} \\ &\leq \text{E}\left\{ Q\left[\sqrt{\frac{\left\|(\mathbf{S}^i - \mathbf{S}^{\bar{i}})\mathbf{H}\right\|^2}{2N_0}} \right] \right\}, \end{aligned} \tag{6.9}$$

where $Q(\cdot)$ represents the integral form of the Q-function. In order to find the ingredients that fundamentally determine the error probability, the average PEP of Eq. (6.9) may be further extended as [297–299]:

$$\text{E}\left\{p(\mathbf{S}^i \to \mathbf{S}^{\bar{i}})\right\} \leq \text{E}\left\{ \exp\left[-\frac{\left\|(\mathbf{S}^i - \mathbf{S}^{\bar{i}})\mathbf{H}\right\|^2}{4N_0} \right] \right\} \tag{6.10a}$$

$$\leq \left[\frac{1}{\det\left(\mathbf{I}_{N_T} + 0.25\eta\boldsymbol{\Delta}\right)} \right]^{N_R} \tag{6.10b}$$

$$\leq (0.25\eta)^{-\text{rank}(\boldsymbol{\Delta})\cdot N_R} \left[\prod_{k=1}^{\text{rank}(\boldsymbol{\Delta})} \lambda_k(\boldsymbol{\Delta}) \right]^{-N_R}, \tag{6.10c}$$

where we have $\boldsymbol{\Delta} = (\mathbf{S}^i - \mathbf{S}^{\bar{i}})^H(\mathbf{S}^i - \mathbf{S}^{\bar{i}})$. In more detail, firstly, Eq. (6.10a) is obtained by applying the Chernoff bound to Eq. (6.9). Secondly, Eq. (6.10b) may be obtained by transforming $\left\|(\mathbf{S}^i - \mathbf{S}^{\bar{i}})\mathbf{H}\right\|^2 = \left\|\left[\mathbf{I}_{N_R} \otimes (\mathbf{S}^i - \mathbf{S}^{\bar{i}})\right] \text{vec}(\mathbf{H})\right\|^2$ and taking the expectation over the fading channel matrix $\mathbf{H}$. We note that $\otimes$ denotes the Kronecker product, while the operation $\text{vec}(\cdot)$

forms a column vector by stacking the columns in the matrix one-by-one. For example, we have $\text{vec}(\mathbf{H}) = \left[\mathbf{H}_{-,1}^T \cdots \mathbf{H}_{-,N_R}^T\right]^T$, where $\{\mathbf{H}_{-,v}\}_{v=1}^{N_R}$ refers to the v-th column in $\mathbf{H}$. Lastly, Eq. (6.10c) is approximated in the high-SNR region of $\eta \gg 1$ by $\det(\mathbf{\Delta}) = \prod_{k=1}^{\text{rank}(\mathbf{\Delta})} \lambda_k(\mathbf{\Delta})$, where $\{\lambda_k(\mathbf{\Delta})\}$ refers to the k-th eigenvalue of matrix $\mathbf{\Delta}$, while $\text{rank}(\mathbf{\Delta})$ denotes the rank of matrix $\mathbf{\Delta}$.

As discussed in [297–299], Eq. (6.10c) suggests that there are two major factors that may minimize the error probability in the high-SNR region, which are often referred to as the rank criterion and the determinant criterion in the literature of analysing the MIMO systems' performance. In more detail, firstly, it may be observed in Eq. (6.10c) that the first term of $(0.25\eta)^{-\text{rank}(\mathbf{\Delta})\cdot N_R}$ decreases as the SNR increases.Furthermore, the rate of decline for the error probability, which may be interpreted as diversity order, is explicitly determined by $\text{rank}(\mathbf{\Delta}) \cdot N_R$. Therefore, this rank criterion indicates that the full MIMO diversity - which is the parlance used for representing the maximum attainable diversity order - is given by $\min(N_T, N_P) \cdot N_R$, where the full rank of $\mathbf{\Delta}$ is the minimum between N_T and N_P. Furthermore, when $\mathbf{\Delta}$ achieves full rank, the second term $\left[\prod_{k=1}^{\text{rank}(\mathbf{\Delta})} \lambda_k(\mathbf{\Delta})\right]^{N_R}$ in Eq. (6.10c) is a function of the determinant of $\mathbf{\Delta}$. As a result, this so-called determinant criterion indicates that a higher coding gain is achieved by maximizing the minimum determinant $\det(\mathbf{\Delta})$ over all legitimate combinations of $\mathbf{S}^i$ and $\mathbf{S}^{\tilde{i}}$. When Hadamard's inequality [281] is applied to the determinant term of Eq. (6.10c), it can be seen that the optimal condition is that of $\mathbf{\Delta}$ being unitary, which may be guaranteed by both the classic STBCs based on orthogonal design [177, 178, 293] and the STBCs relying on the Amicable orthogonal design criterion [181–183]. By contrast, it is plausible that the classic V-BLAST associated with $N_P = 1$ does not minimize the error probability, which is due to the fact that V-BLAST has neither transmit diversity - since we have $\min(N_T, N_P) = 1$ - nor has it unitary transmission matrices. The STBC's feature of minimizing the PEP in the high-SNR region according to the rank and determinant criteria is often referred to as *diversity gain*.

The tradeoff between the diversity gain $\overline{D}$ and the multiplexing gain $\overline{R} = \frac{N_Q}{N_P}$ is quantified as $\overline{D} = (N_T - \overline{R})(N_R - \overline{R})$ in [185], which portrays the diversity and multiplexing capability as rivals in MIMO systems design. As a breakthrough, the development of Linear Dispersion Code (LDC) [188, 189, 300] suceeded in perfectly accommodating this tradeoff. In more details, it was recognized in [184, 189, 301] that the STBC's orthogonal design prevents it from achieving the full MIMO capacity, albeit it facilitates an appealing simple separate detection of the MIMO streams. Therefore, without being constrained by the orthogonal design, the LDC of [189] proposed to randomly generate the so-called dispersion matrices $\{\overline{\mathbf{A}}_q\}_{q=1}^{N_Q}$ and $\{\overline{\mathbf{B}}_q\}_{q=1}^{N_Q}$, which disperse a total number of N_Q modulated MPSK/QAM symbols $\{s_q\}_{q=1}^{N_Q}$ across both spatial domain and the time domain of the transmission matrix $\mathbf{S} = \sum_{q=1}^{N_Q} \left[\overline{\mathbf{A}}_q \Re(s_q) + j\overline{\mathbf{B}}_q \Im(s_q)\right]$. The set of dispersion matrices that results in the highest CCMC capacity may be selected by a random search. The LDC of [189] was shown to have a higher CCMC capacity than orthogonal STBCs, but the full MIMO capacity was still not achieved. In order to solve this problem, the LDC transmission model was further simplifed in [188], which is summarized in Table 6.1, and it was shown in [188] that the full MIMO capacity may be achieved by this LDC design, provided that the parameters satisfy $N_Q \geq$

$N_T N_P$. Furthermore, as demonstrated in [188], the dispersion matrices $\{\overline{\mathbf{A}}_q\}_{q=1}^{N_Q}$ may be randomly generated, and the specific set, which results in the lowest error probability that requires full rank and the lowest determinant for $\mathbf{\Delta}$ may be selected from the random search. Consequently, the LDC may benefit from both V-BLAST's maximized multiplexing gain of $\overline{R} \geq N_T$ and from STBC's full diversity gain of $\overline{D} = \min(N_T, N_P) \cdot N_R$. The best LDCs generated from a sufficiently exhaustive random search are capable of outperforming both V-BLAST and STBC in MIMO systems.

There is an other arguably more important problem in MIMO system design, which is the tradeoff between performance and complexity. This tradeoff is also pertinent in the context of V-BLAST receiver design. On the one hand, it is well known that ML detector and Sphere Decoder (SD) [10–12, 173–176] are capable of achieving the optimum V-BLAST performance, but their detection complexity may be deemed excessively high. On the other hand, linear V-BLAST receivers [13, 14, 14–16] such as the classic MMSE receiver may separate the multiple data streams so that the family of low-complexity linear MPSK/QAM demodulators may be directly invoked for decoding each data stream, However, encountering a performance penalty is inevitable, as the interference between these data streams cannot be completely eliminated. This tradeoff also exists for the family of LDCs. We will demonstrate in Sec. 6.3.1 that all orthogonal STBCs may effectively separate the parallel data streams at the receiver without encountering the V-BLAST's inherent interference problem. However, since LDCs were proposed for overcoming the STBC's limitations of low data rate and high transmission delay, the STBC's orthogonality requirement is abandoned in LDC design. Hence the LDC receiver becomes more complex than that of the STBC's. In fact, the LDC may employ all V-BLAST detectors with the aid of low-complexity signal processing at the receiver, and as a result, the above-mentioned tradeoff between performance and complexity emerges once again.

It is worth noting that the family of suboptimal detectors designed for V-BLAST and LDC not only suffer from a performance penalty in uncoded systems, but they may also impose further constraints on the turbo detection of channel coded systems. As demonstrated in Chapter 2, the suboptimal detectors tend to produce unreliable soft output LLRs that fail to accurately represent the true probabilities and these flawed LLRs cannot be readily corrected by the channel decoder. In order to avoid this situation, numerous researchers designed MIMO schemes that may achieve the optimal ML detection capability at a reduced receiver complexity. For this reason, Spatial Modulation (SM) was proposed in [195–197], where a single one out of a total number of N_T TAs is activated to transmit a single modulated MPSK/QAM symbol, as presented in Table 6.1. A low-complexity SM receiver is capable of separately detecting the $\text{BPS}_T = \log_2 N_T$ bits used for TA activation and the $\text{BPS} = \log_2 M$ bits for classic modulation, so that its detection complexity order may be reduced from the conventional MIMO's $O(I)$ to $O(N_T + M)$. Furthermore, in order to benefit from a diversity gain, Space-Time Shift Keying (STSK) was proposed in [216], where a single one out of a total number of N_Q LDC dispersion matrices is activated for dispersing a single MPSK/QAM symbol, which is also shown in Table 6.1. It was demonstrated in [216] that the STSK receiver may employ SM detectors with the aid of low-complexity signal processing. The

transmit diversity design of SM can be found in [218–221], and they all can be categorized under the framework of Generalized Space-Time Shift Keying (GSTSK), as summarized in [217, 302].

In summary, against this background, we aim to offer the following novel discussions and contributions in this chapter:

1. The tradeoff between the attainable diversity and multiplexing gain is discussed in the context of each MIMO scheme introduced in this chapter. The mathematical measures of capacity and error probability are used in our analysis for quantifying this tradeoff. We demonstrate that although this tradeoff that famously manifests itself in the V-BLAST versus STBC context may be completely resolved by the LDC design, but it still exists for the family of reduced-complexity MIMO systems of SM and STSK, which leaves room for further investigations.

2. The importance of the tradeoff between performance and complexity is stressed in the context of MIMO systems design throughout this chapter. This tradeoff exists both for the classic V-BLAST and LDC as well as for the new SM and STSK. We demonstrate in this chapter that the performance differences between the MIMO schemes including V-BLAST, STBC, LDC, SM and STSK may vary depending on the different MIMO system setups, since the diversity-oriented MIMO schemes may loses their performance advantage, when an increased number of time slots N_P is required for the MIMO systems equipped with a high number of TAs N_T. But we will also demonstrate in the next chapter that these different MIMO schemes may perform similarly with the aid of channel coding, provided that they rely on their optimum detectors. Against this background, the design of MIMO transceivers that may achieve the optimum detection capability at a substantially reduced detection complexity is critically important for high-rate communication systems.

3. Altough the development of SM and STSK is motivated by their potentially low detection complexity, it was demonstrated in [198] that completely independently detecting the TA activation index and the modulated MPSK/QAM symbol imposes a performance loss to the SM receiver. In order to mitigate this problem, in this chapter, we summarize the reduced-complexity hard-decision-aided SM detector design based on our previous publications of [141, 202, 203, 234], where the optimal SM performance is retained by taking into account the correlation between the TA activation index and the MPSK/QAM classic modulated symbol index. A range of other optimal and suboptimal SM detectors exist in the literature [141, 204–213], which are also summarized for the sake of comparison.

The rest of this chapter is organized as follows. The classic V-BLAST transceiver design is introduced in Sec. 6.2. Both the STBC and LDC schemes involve signal processing in both the spatial domain and the time domain, hence they are referred to as Space-Time Modulation (STM) in Sec. 6.3. The newly developed SM and STSK arrangements are presented in Sec. 6.4. Our performance results derived for uncoded MIMO systems are summarized in Sec. 6.5, while our chapter conclusions are offered in Sec. 6.6.

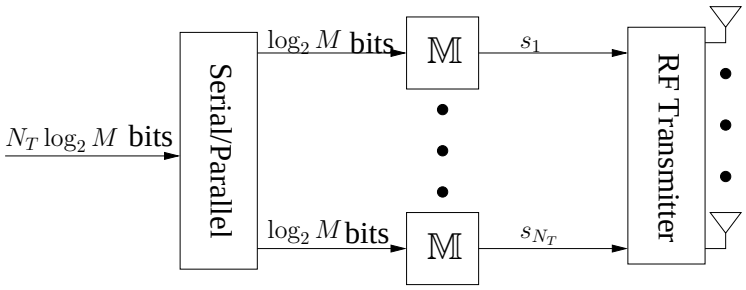

Figure 6.2: Schematic of V-BLAST transmitter.

The following notations are used throughout this chapter. The acronyms V-BLAST(N_T,N_R)-MPSK/QAM as well as SM(N_T,N_R)-MPSK/QAM refer to the V-BLAST scheme and to the SM scheme equipped with N_T TAs and N_R RAs. Furthermore, the LDC and STSK schemes are denoted by the acronyms of LDC(N_T,N_R,N_P,N_Q)-MPSK/QAM and STSK(N_T,N_R,N_P,N_Q)-MPSK/QAM, respectively, where N_P and N_Q represent the number of symbol periods per transmission block and the total number of dispersion matrices employed, respectively.

6.2 Uncoded V-BLAST

The classic V-BLAST MIMO, which multiplexes N_T data streams with the aid of N_T TAs, maximizes the MIMO capacity and throughput. This multiplexing gain of V-BLAST may be quantified in terms of the CCMC capacity of Eq. (6.4) and the DCMC capacity of Eq. (6.7), as analysed previously in Sec. 6.1. The challenge in V-BLAST system design is to deal with the Inter-Antenna Interference (IAI) at an affordable signal processing complexity, which clearly strikes a tradeoff between performance and complexity. In this section, first of all, the V-BLAST transceiver is introduced in Sec. 6.2.1, where the ML detection is shown to be capable of achieving the optimum performance at the great expense of a potentially excessive detection complexity. In order to mitigate this complexity, the SDs conceived for V-BLAST employing PSK and QAM are presented in Sec. 6.2.2 and Sec. 6.2.3, respectively. We proceed in Sec. 6.2.4 to demonstrate that low-complexity linear MPSK/QAM demodulators may be invoked by the V-BLAST receiver after the linear filters separate the multiplexed data streams. However, encountering a performance penalty is inevitable for these suboptimal linear V-BLAST receivers.

6.2.1 V-BLAST Transceiver

The schematic of a classic V-BLAST transmitter is portrayed by Fig. 6.2, where a total of $N_Q = N_T$ modulated symbols are transmitted by the N_T TAs during $N_P = 1$ symbol periods. Therefore, the

	MPSK	Square MQAM	Star MQAM
Modulation $s^m = \mathbb{M}(m)$	$s^m = \exp(j\frac{2\pi}{M}\check{m})$ m is Gray coded $\check{m}$	$s^m = s_{\text{Re}}^{m_{\text{Re}}} + j s_{\text{Im}}^{m_{\text{Im}}}$ $= \frac{M_{\text{Re}}-2\check{m}_{\text{Re}}-1}{\sqrt{\beta}} + j\frac{M_{\text{Im}}-2\check{m}_{\text{Im}}-1}{\sqrt{\beta}}$ m_{Re} and m_{Im} are Gray coded $\check{m}_{\text{Re}}$ and $\check{m}_{\text{Im}}$ $m = m_{\text{Re}} + M_{\text{Re}} m_{\text{Im}}$	$s^m = \Gamma^a \Omega^p = \frac{\alpha^{\check{a}}}{\sqrt{\beta}} \exp(j\frac{2\pi}{M_P}\check{p})$ a and p are Gray coded $\check{a}$ and $\check{p}$ $m = a + M_A p$
Demodulation $\hat{m} = \mathbb{M}^{-1}(z)$	$s^{\hat{m}} = \exp(j\frac{2\pi}{M}\check{m})$ $\check{m} = \lfloor \frac{M}{2\pi}\angle z \rceil$	$s^{\hat{m}} = \frac{M_{\text{Re}}-2\check{m}_{\text{Re}}-1}{\sqrt{\beta}} + j\frac{M_{\text{Im}}-2\check{m}_{\text{Im}}-1}{\sqrt{\beta}}$ $\check{m}_{\text{Re}} = \max\left[\min\left(\lfloor g_{\text{Re}} \rceil, M_{\text{Re}}-1\right), 0\right]$ $g_{\text{Re}} = \left[M_{\text{Re}} - \sqrt{\beta}\Re(z) - 1\right]/2$ $\check{m}_{\text{Im}} = \max\left[\min\left(\lfloor g_{\text{Im}} \rceil, M_{\text{Im}}-1\right), 0\right]$ $g_{\text{Im}} = \left[M_{\text{Im}} - \sqrt{\beta}\Im(z) - 1\right]/2$	$s^{\hat{m}} = \frac{\alpha^{\check{a}}}{\sqrt{\beta}} \exp(j\frac{2\pi}{M_P}\check{p})$ $\check{p} = \lfloor \frac{M_P}{2\pi}\angle z \rceil$ $\check{a} = \arg \min_{\forall \check{a}} \{(\frac{\alpha^{\check{a}}}{\sqrt{\beta}})^2$ $-(\frac{2\alpha^{\check{a}}}{\sqrt{\beta}})\Re\left[\exp(-j\frac{2\pi}{M_P}\check{p})z\right]\}$

Table 6.2: Summary of MPSK/QAM modulation and demodulation. The source information is carried by the classic modulated symbol index $m = \text{bin2dec}(b_1, \cdots, b_{\text{BPS}})$. The demodulation is operated based on a decision variable of z, i.e. we have $s^{\hat{m}} = \min_{\forall m} |z - s^m|^2$. More details may be found in Chapter 2.

$(1 \times N_T)$-element V-BLAST transmission matrix is given by:

$$\begin{aligned} \mathbf{S} &= \left[\begin{array}{ccc} s_1, & \cdots, & s_{N_T} \end{array} \right] \\ &= \left[\begin{array}{ccc} \frac{1}{\sqrt{N_T}} s^{m_1}, & \cdots, & \frac{1}{\sqrt{N_T}} s^{m_{N_T}} \end{array} \right], \end{aligned} \tag{6.11}$$

where the MPSK/QAM symbols are separately modulated as $\{s^{m_v} = \mathbb{M}(m_v)\}_{v=1}^{N_T}$. For the sake of convenience, the MPSK/QAM modulation and demodulation introduced in Chapter 2 are summarized in Table 6.2, and this table will be often utilized throughout this chapter.

Upon obtaining the $(1 \times N_R)$-element received signal matrix $\mathbf{Y}$ of Eq. (6.1), the Maximum-Likelihood (ML) detector may opt for maximizing the following *a posteriori* probability over the entire set of $I = M^{N_T}$ candidates $\{\mathbf{S}^i\}_{i=0}^{I-1}$ for the transmit vector $\mathbf{S}$ in Eq. (6.1) as:

$$p(\mathbf{S}^i|\mathbf{Y}) = \frac{p(\mathbf{Y}|\mathbf{S}^i)p(\mathbf{S}^i)}{\sum_{\forall \mathbf{S}^i} p(\mathbf{Y}|\mathbf{S}^i)p(\mathbf{S}^i)}, \tag{6.12}$$

where the *a priori* probability $\{p(\mathbf{S}^i)\}_{\forall \mathbf{S}^i}$ may be assumed to be a constant of $\frac{1}{M^{N_T}}$ for the equiprobable source symbols of an uncoded system. Furthermore, the conditional probability $\{p(\mathbf{Y}|\mathbf{S}^i)\}_{\forall \mathbf{S}^i}$ in Eq. (6.12) is given by the PDF of the $(1 \times N_R)$-element AWGN matrix $\mathbf{V}$ of Eq. (6.1), which was expressed by Eq. (6.2). Therefore, the ML aided V-BLAST detection may be expressed as:

$$\hat{\mathbf{S}} = \arg \min_{\forall \mathbf{S}^i} \|\mathbf{Y} - \mathbf{S}^i\mathbf{H}\|^2. \tag{6.13}$$

As a result, the V-BLAST scheme may achieve a high data rate of $R = N_T \log_2 M = N_T$BPS at a potentially excessive detection complexity, where the ML detection complexity order of Eq. (6.13) is given by $O(M^{N_T})$.

The reason for this high detection complexity is illustrated in Fig. 6.3. Although the N_T data streams defined in Eq. (6.11) are separately modulated and transmitted, they experience fading channels and arrive at the RAs simultaneously as expressed by Eq. (6.1). Therefore, for each individual data stream, all the other data streams impose interference, and hence the ML aided

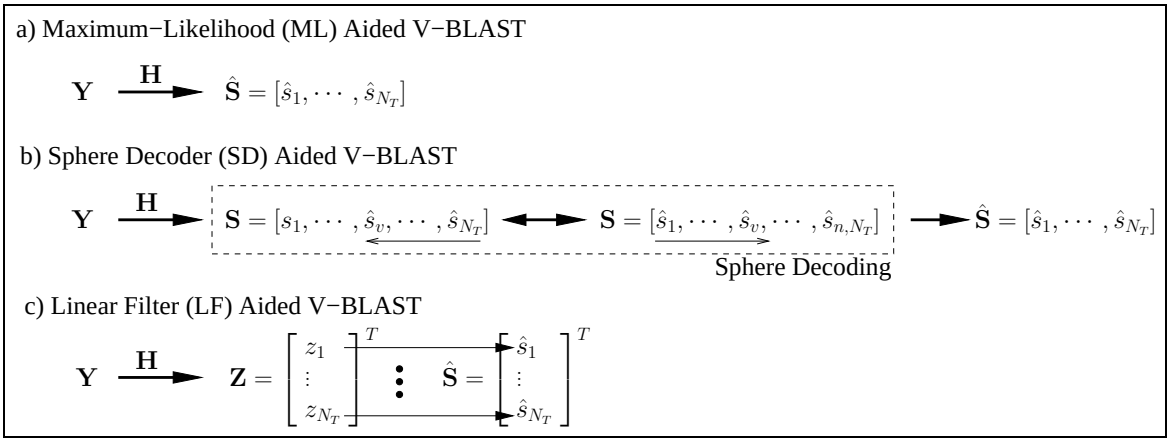

Figure 6.3: A simple demonstration of V-BLAST detection.

V-BLAST scheme of Eq. (6.13) has to detect the transmit vector $\mathbf{S}$ as a whole and consider all its possible combinations by exhaustive search, as portrayed by Fig. 6.3-a).

In order to mitigate this complexity problem, the detectors should search through each individual constellation diagram for detecting each data stream separately, rather than jointly. There are two ways of achieving this objective, as illustrated by Fig. 6.3-b) and c). The first option is to invoke the Sphere Decoder (SD) of [10–12], which only detects a single symbol s_v at a time, while the previous decisions concerning $\{\hat{s}_t\}_{\forall t>v}$ are invoked in order to cancel out the known interference. The potential error propogation problem caused by decision feedback may be avoided by confining the SD search to SNR-dependent decoding sphere. In more detail, the SD's search index v may be reduced to find a new legitimate candidate within this sphere, and it may also be increased. Eventually, the search is terminated, when there is no new candidate left for replacing the previous SD decisions within this sphere. Therefore, the SD aided V-BLAST is capable of retaining the optimum ML detection capability at a substantially reduced complexity, but its complexity may still be deemed as unaffordable, especially when the noise power is high and hence the sphere-radius is large. The SD search may be accelerated by manipulating the SD sphere radius, but the optimum decoding capability would inevitably become compromised.

The second option is to separate the multiple data streams by invoking a Linear Filter (LF), as portrayed by Fig. 6.3-c). The filter output is an N_T-element vector $\mathbf{Z}$, whose elements $\{z_v\}_{v=1}^{N_T}$ may be directly utilized for making decisions on the N_T individual data streams $\{\hat{s}_v\}_{v=1}^{N_T}$. In this way, the V-BLAST detection complexity order may become impressively low such as $O(N_T \cdot M)$. However, although the linear filters are generally conceived for reducing the interference, completely independently detecting the N_T data streams still results in a sub-optimal performance because of the interference residue. We will proceed to discuss the details of these V-BLAST detectors and their performance-complexity tradeoff in the rest of this section.

6.2.2 Hard-Decision-Aided SD Conceived for Uncoded V-BLAST Employing PSK

In order to invoke the SD, the V-BLAST receiver may apply the classic QR decomposition to $\mathbf{H}^H$ [173–176] as follows:

$$\mathbf{H}^H = \left[\begin{array}{c} \mathbf{Q}, \mathbf{Q}' \end{array} \right] \left[\begin{array}{c} \mathbf{U} \\ \mathbf{0} \end{array} \right], \tag{6.14}$$

where $\left[\begin{array}{c} \mathbf{Q}, \mathbf{Q}' \end{array} \right]$ is a $(N_R \times N_R)$-element unitary matrix, and the $(N_R \times N_T)$-element submatrix $\mathbf{Q}$ has orthogonal columns satisfying $\mathbf{Q}^H\mathbf{Q} = I_{N_T}$. Furthermore, $\mathbf{U}$ in Eq. (6.14) is a $(N_T \times N_T)$-element upper triangular matrix, while $\mathbf{0}$ refers to a $[(N_R - N_T) \times N_T]$-element all-zero matrix. It is a natural requirement that we have $N_R \geq N_T$, so that the QR decomposition of Eq. (6.14) may proceed. The generalized rank-deficient scenario of $N_R < N_T$ is discussed in [303–305]. For the sake of simplicity, we only consider the situation of $N_R \geq N_T$, which is generally compatible with the industrial MIMO standards [306,307]. According to Eq. (6.14), the $(N_T \times N_R)$-element fading channel matrix $\mathbf{H}$ may now be represented as:

$$\mathbf{H} = (\mathbf{QU})^H = \mathbf{LQ}^H, \tag{6.15}$$

where $L = \mathbf{U}^H$ is a $(N_T \times N_T)$-element lower triangular matrix. As a result, the received signal model of Eq. (6.1) may be modified as:

$$\mathbf{YQ} = \mathbf{SL} + \mathbf{VQ}, \tag{6.16}$$

where $\mathbf{VQ}$ has exactly the same statistics as the AWGN matrix $\mathbf{V}$. Therefore, the ML decision metric of Eq. (6.13), which may also be referred to as Euclidean Distance (ED), may be rewritten as:

$$\left\| \widetilde{\mathbf{Y}} - \mathbf{SL} \right\|^2 = \sum_{v=1}^{N_T} \left| \widetilde{Y}_v - \sum_{t=v}^{N_T} l_{t,v} s_t \right|^2. \tag{6.17}$$

The $(1 \times N_T)$-element vector $\widetilde{\mathbf{Y}} = \mathbf{YQ}$ in Eq. (6.17) is defined in Eq. (6.16), and $\{\widetilde{Y}_v\}_{v=1}^{N_T}$ are elements taken from $\widetilde{\mathbf{Y}}$. Furthermore, $\{\{l_{t,v}\}_{t=v}^{N_T}\}_{v=1}^{N_T}$ and $\{s_t\}_{t=v}^{N_T}$ in Eq. (6.17) are elements from the lower triangular matrix $\mathbf{L}$ defined in Eq. (6.15) and elements from the V-BLAST transmit vector $\mathbf{S}$ of Eq. (6.11), respectively.

The SD aims for finding the specific detection candidates that lie within the decoding sphere radius R, which is formulated as:

$$\left\| \widetilde{\mathbf{Y}} - \mathbf{SL} \right\|^2 < R^2. \tag{6.18}$$

This detection problem may be solved step-by-step. According to the ED of Eq. (6.17), the Partial Euclidean Distance (PED) evaluated by the SD may be defined as:

$$\begin{aligned} d_v &= \sum_{\bar{v}=v}^{N_T} \left| \widetilde{Y}_{\bar{v}} - \sum_{t=\bar{v}}^{N_T} l_{t,\bar{v}} s_t \right|^2 \\ &= d_{v+1} + \Delta_v, \end{aligned} \tag{6.19}$$

where the PED increment Δ_v is given by:

$$\begin{aligned}\Delta_v &= \left|\widetilde{Y}_v - \sum_{t=v}^{N_T} l_{t,v} s_t\right|^2 \\ &= \left|\left(\widetilde{Y}_v - \sum_{t=v+1}^{N_T} l_{t,v} s_t\right) - l_{v,v} s_v\right|^2 .\end{aligned} \tag{6.20}$$

The only variable in the PED increment of Eq. (6.20) is s_v, as elements $\{s_t\}_{t=v+1}^{N_T}$ are known from previous SD decisions.

For a SD based on the PED increment of Eq. (6.20), the Pohst searching strategy of [11, 308, 309] requires the SD to enumerate all candidates for s_v within the SNR-dependent decoding sphere, as defined by the condition of $d_v < R^2$. The Schnorr-Euchner search strategy of [12,237] efficiently refines the Pohst strategy, where the priorities of all the legitimate candidates for s_v are ranked according to the increasing order of their corresponding PED increment values Δ_v. Therefore, when the SD reaches a specific index v for the first time, the candidate associated with the highest priority is visited. Then, when the SD reaches v again for the m-th time, the candidate associated with the m-th highest priority should be visited. In this way, the SD always knows, which specific candidate should be examined without repeating the enumeration.

For MPSK signalling, the legitimate constellation points may be visited in a zigzag fashion. More explicitly, the PED increment of Eq. (6.20) may be further extended as:

$$\begin{aligned}\Delta_v &= \left|\widetilde{y}_v^{SD} - \widetilde{h}_v^{SD} s_v\right|^2 \\ &= \left|\widetilde{y}_v^{SD}\right|^2 + \frac{1}{N_T}\left|\widetilde{h}_v^{SD}\right|^2 - 2\Re\left(s_v^* \widetilde{z}_v^{SD}\right),\end{aligned} \tag{6.21}$$

where the equivalent "received signal" and "fading channel" associated with detecting s_v are given by $(\widetilde{y}_v^{SD} = \widetilde{Y}_v - \sum_{t=v+1}^{N_T} l_{t,v} s_t)$ and $(\widetilde{h}_v^{SD} = l_{v,v})$, respectively, while the decision variable is given by:

$$\widetilde{z}_v^{SD} = \widetilde{y}_v^{SD} (\widetilde{h}_v^{SD})^* . \tag{6.22}$$

As a result, detecting the MPSK variable s_v according to Eq. (6.21) becomes the same as that of generic MPSK detection. In other words, for the SD, the candidate MPSK constellation point associated with the highest priority is given by[1]:

$$\begin{aligned} s_v = \tfrac{1}{\sqrt{N_T}} \exp\left(j\tfrac{2\pi}{M}\check{m}_v\right), \quad \text{where} \quad & \check{m}_v = \lfloor p_v \rceil, \\ & p_v = \tfrac{M}{2\pi}\angle \widetilde{z}_v^{SD}. \end{aligned} \tag{6.23}$$

The remaining MPSK constellation points may be visited in a zigzag fashion by the SD. In more details, if the phasor index $\check{m}_v$ is rounded down from p_v, i.e. we have $\check{m}_v \leq p_v$, then the SD may visit the remaining constellation points according to the steps of $\check{m}_v = \check{m}_v + 1, \check{m}_v = \check{m}_v - 2$,

[1]The notation $\check{m}$ associated with superscript $(\check{\cdot})$ represents the natural constellation index, which directly links to the MPSK constellation point of $\exp\left(j\frac{2\pi}{M}\check{m}\right)$. We will also frequently use the notation of MPSK index m without superscript, which is Gray coded natural index $m = \text{Gray}(\check{m})$, and it may be directly translated from the source binary bits as $m = \text{bin2dec}(b_1 \cdots b_{\text{BPS}})$.

$\check{m}_v = \check{m}_v + 3$, etc. By contrast, for the case of $\check{m}_v > p_v$, the SD based steps of visiting constellation points are $\check{m}_v = \check{m}_v - 1$, $\check{m}_v = \check{m}_v + 2$, $\check{m}_v = \check{m}_v - 3$, etc.

The SD tree search may be performed either by breadth-first [310–312] or by depth-first approach [10, 12, 313]. The breadth-first tree search, which may also be termed as the K-best tree search, reduces the SD index from $v = N_T$ down to $v = 1$, where only K candidates associated with the higher priorities are retained at each level. The major advantage of the K-best approach is that the total number of nodes visited by the SD is constant, but K-best algorithm is unable to guarantee to spot the ML solution. The depth-first tree search, which is also popularly adopted by the MSDSD aided noncoherent detection introduced in the previous chapters, commence its search by decreasing the SD index from $v = N_T$ down to $v = 1$ as well, but only the best candidate is visited on each level. When the SD index of $v = 1$ is reached, the SD radius is shrunk to be consistent with the newly found contender candidate $\mathbf{S}$. Then the SD index is increased again in order to check if there is any other nodes that may lie inside the updated decoding sphere. If a new valid candidate is found within the sphere at any value of the SD index v, the SD index may decrement down towards $v = 1$ again. Otherwise, the search may terminate, once the SD index of $v = N_T$ is reached. Therefore, the depth-first tree search has a nonconstant complexity, but spotting the optimum ML solution may be only guaranteed, if the initial SD radius is set to be sufficiently large.

Similar to the MSDSD aided noncoherent detection introduced in Chapters 3-5, the depth-first tree search is recommended for SD aided V-BLAST detection in this chapter. Since the SD indices of V-BLAST detection are different from those of noncoherent detection, we re-summarize the pseudo-code of SD conceived for uncoded V-BLAST employing MPSK in Table 6.3. One may initialize the SD's input radius R as infinity in order to maintain the ML optimality. In practice, a possible choice of the initial SD radius R may be found from the statistical properties of the ED of Eq. (6.18) as [173]:

$$R^2 = JN_R N_0 - \mathbf{Y}\left[\mathbf{I}_{N_R} - \mathbf{H}^H(\mathbf{H}\mathbf{H}^H)^{-1}\mathbf{H}\right]\mathbf{Y}^H, \tag{6.24}$$

where an integer $J \geq 1$ may be selected in order to strike a tradeoff between the performance and complexity. Furthermore, it was demonstrated in [314] that both the selection of an SNR-dependent R and the potential SD search failure may be avoided by defining the intial SD radius R as the distance between the received signal and the MMSE solution formulated as:

$$R^2 = \|\mathbf{Y} - \mathbf{Y}^{MMSE}\|^2, \tag{6.25}$$

where the MMSE solution is given by:

$$\mathbf{Y}^{MMSE} = \mathbf{Y}(\mathbf{H}^H\mathbf{H} + N_0 N_T \mathbf{I}_{N_R})^{-1}\mathbf{H}^H. \tag{6.26}$$

The details of this MMSE solution will be elaborated on in Sec. 6.2.4.

Function: $[\hat{\mathbf{S}}] = \textbf{SD-MPSK}(\widetilde{\mathbf{Y}}, \mathbf{L}, M, N_T, R)$	
$d_{N_T+1} = 0$	//initialize PED
$v = N_T$	//initialize SD search index
$[\check{m}_v, \text{step}_v, n_v, \widetilde{z}_v^{SD}, C_v^{SD}] = \textbf{findBest}(\widetilde{Y}_v, \{l_{t,v}\}_{t=v}^{N_T}, \{s_t\}_{t=v+1}^{N_T})$	//visit the best child node
loop	
$\Delta_v = C_v^{SD} - \frac{2}{\sqrt{N_T}} \Re\left[\exp(-j\frac{2\pi}{M}\check{m}_v) \cdot \widetilde{z}_v^{SD}\right]$	//update Δ_v according to Eq. (6.21)
$d_v = d_{v+1} + \Delta_v$	//update PED according to Eq. (6.19)
if $d_v < R^2$	
$s_v = \frac{1}{\sqrt{N_T}} \exp(j\frac{2\pi}{M}\check{m}_v)$	//update new child node
if $v \neq 1$	
$v = v - 1$	//move down index v
$[\check{m}_v, \text{step}_v, n_v, \widetilde{z}_v^{SD}, C_v^{SD}] = \textbf{findBest}(\widetilde{Y}_v, \{l_{t,v}\}_{t=v}^{N_T}, \{s_t\}_{t=v+1}^{N_T})$	//visit the best child node
else	
$R^2 = d_1$	//update SD radius
$\hat{\mathbf{S}} = [s_1, \cdots, s_{N_T}]$	//update the optimum data symbols
do	
if $v == N_T$ **return** $\hat{\mathbf{S}}$ **and exit**	//terminate SD
$v = v + 1$	//move up index v
while $n_v == (M-1)$	
$[\check{m}_v, \text{step}_v, n_v] = \textbf{findNext}\,(\check{m}_v, \text{step}_v, n_v)$	//visit the next child node
end if	
else	
do	
if $v == N_T$ **return** $\hat{\mathbf{S}}$ **and exit**	//terminate SD
$v = v + 1$	//move up index v
while $n_v == (M-1)$	
$[\check{m}_v, \text{step}_v, n_v] = \textbf{findNext}\,(\check{m}_v, \text{step}_v, n_v)$	//visit the next child node
end if	
end loop	

Subfunction: $[\check{m}_v, \text{step}_v, n_v, \widetilde{z}_v^{SD}, C_v^{SD}] = \textbf{findBest}(\widetilde{Y}_v, \{l_{t,v}\}_{t=v}^{N_T}, \{s_t\}_{t=v+1}^{N_T})$	
$\widetilde{y}_v^{SD} = \widetilde{Y}_v - \sum_{t=v+1}^{N_T} l_{t,v} s_t$	//evaluate $\widetilde{y}_v^{SD}$ according to Eq. (6.21)
$\widetilde{h}_v^{SD} = l_{v,v}$	//evaluate $\widetilde{h}_v^{SD}$ according to Eq. (6.21)
$\widetilde{z}_v^{SD} = \widetilde{y}_v^{SD} (\widetilde{h}_v^{SD})^*$	//update decision variable of Eq. (6.22)
$C_v^{SD} = \left\|\widetilde{y}_v^{SD}\right\|^2 + \frac{1}{N_T}\left\|\widetilde{h}_v^{SD}\right\|^2$	//evaluate the constant in Eq. (6.21)
$p_v = \frac{M}{2\pi} \angle z_v^{MSDSD}$	//update the best child node
$\check{m}_v = \lfloor p_v \rceil$	
$\text{step}_v = \text{sign}(p_v - \check{m}_v)$	//store the step size for the next child node
$n_v = 0$	

Subfunction: $[\check{m}_v, \text{step}_v, n_v] = \textbf{findNext}\,(\check{m}_v, \text{step}_v, n_v)$	
$\check{m}_v = \check{m}_v + \text{step}_v$	//visit the next child node
$\text{step}_v = -\text{step}_v - \text{sign}(\text{step}_v)$	
$n_v = n_v + 1$	

Table 6.3: Pseudocode for hard-decision-aided SD conceived for uncoded V-BLAST employing MPSK.

6.2.3 Hard-Decision-Aided SD Conceived for Uncoded V-BLAST Employing Square QAM

It was suggested in [10, 172, 315] that the real part and the imaginary part of the Square QAM constellation should be separately visited by the SD. To this purpose, the received signal model of Eq. (6.1) has to be decoupled as:

$$\underbrace{\begin{bmatrix} \Re(\mathbf{Y}) & \Im(\mathbf{Y}) \end{bmatrix}}_{\overline{\mathbf{Y}}} = \underbrace{\begin{bmatrix} \Re(\mathbf{S}) & \Im(\mathbf{S}) \end{bmatrix}}_{\overline{\mathbf{S}}} \underbrace{\begin{bmatrix} \Re(\mathbf{H}) & \Im(\mathbf{H}) \\ -\Im(\mathbf{H}) & \Re(\mathbf{H}) \end{bmatrix}}_{\overline{\mathbf{H}}} + \underbrace{\begin{bmatrix} \Re(\mathbf{V}) & \Im(\mathbf{V}) \end{bmatrix}}_{\overline{\mathbf{V}}}, \tag{6.27}$$

where the $(1 \times 2N_R)$-element received signal vector $\overline{\mathbf{Y}}$, the $(1 \times 2N_T)$-element transmit signal vector $\overline{\mathbf{S}}$, the $(2N_T \times 2N_R)$-element fading matrix $\overline{\mathbf{H}}$ and the $(1 \times 2N_R)$-element AWGN matrix $\overline{\mathbf{V}}$ are all real-valued.

The V-BLAST receiver may now apply QR decomposition to $\overline{\mathbf{H}}^T$ as expressed in Eq. (6.14), so that the received signal matrix may be decomposed as:

$$\overline{\mathbf{H}} = \mathbf{L}\mathbf{Q}^T, \tag{6.28}$$

where $\mathbf{L}$ is a $(2N_T \times 2N_T)$-element real-valued lower triangular matrix, while the $(2N_R \times 2N_T)$-element real-valued matrix $\mathbf{Q}$ has orthogonal columns as $\mathbf{Q}^T\mathbf{Q} = \mathbf{I}_{2N_T}$. Similar to Eq. (6.14), $N_R \geq N_T$ is also assumed for V-BLAST employing Square QAM.

After applying the fading channel matrix decompostion of Eq. (6.28), the received signal model of Eq. (6.27) may be rewritten as:

$$\overline{\mathbf{Y}}\mathbf{Q} = \overline{\mathbf{S}}\mathbf{L} + \overline{\mathbf{V}}\mathbf{Q}, \tag{6.29}$$

where $\mathbf{Q}$ obtained from Eq. (6.28) does not change the statistics of the AWGN matrix $\overline{\mathbf{V}}$. Therefore, the ED of the ML detection of Eq. (6.13) may now be expressed as:

$$\left\| \widetilde{\overline{\mathbf{Y}}} - \overline{\mathbf{S}}\mathbf{L} \right\|^2 = \sum_{v=1}^{2N_T} \left(\widetilde{\overline{Y}}_v - \sum_{t=v}^{2N_T} l_{t,v}\overline{s}_t \right)^2, \tag{6.30}$$

where $\widetilde{\overline{\mathbf{Y}}} = \overline{\mathbf{Y}}\mathbf{Q}$ is defined in Eq. (6.29). By exploiting the structure of the lower triangular matrix $\mathbf{L}$, the PED utilized by the SD may be defined according to the ED of Eq. (6.30) as:

$$\begin{aligned} d_v &= \sum_{\bar{v}=v}^{2N_T} \left(\widetilde{\overline{Y}}_{\bar{v}} - \sum_{t=\bar{v}}^{2N_T} l_{t,\bar{v}}\overline{s}_t \right)^2 \\ &= d_{v+1} + \Delta_v, \end{aligned} \tag{6.31}$$

where the PED increment Δ_v is given by:

$$\begin{aligned} \Delta_v &= \left(\widetilde{\overline{Y}}_v - \sum_{t=v}^{2N_T} l_{t,v}\overline{s}_t \right)^2 \\ &= \left(\widetilde{y}_v^{SD} - \widetilde{h}_v^{SD}\overline{s}_v \right)^2. \end{aligned} \tag{6.32}$$

The equivalent "received signal" and "fading channel" associated with detecting the variable PAM symbol $\overline{s}_v$ in Eq. (6.32) are given by $(\widetilde{y}_v^{SD} = \widetilde{\overline{Y}}_v - \sum_{t=v+1}^{2N_T} l_{t,v}\overline{s}_t)$ and $(\widetilde{h}_v^{SD} = l_{v,v})$, respectively. In this section, we only consider the family of Square QAM constellations associated with an even BPS, hence both the real part and the imaginary part of the Square MQAM constellation are given by the same $\sqrt{M}$PAM constellation. We note that it is straightforward to extend the method advocated in this section to the case of Square QAM associated with an odd value of BPS.

The PED increment of Eq. (6.32) leads to a decision variable as:

$$\widetilde{z}_v^{SD} = \widetilde{y}_v^{SD} / \widetilde{h}_v^{SD}, \tag{6.33}$$

which may be directly used to visit the $\sqrt{M}$PAM constellation points in a zigzag fashion according to their Schnorr-Euchner search priorities, which are quantified as their PED increment values ranked in an increasing order. In particular, the best $\sqrt{M}$PAM candidate associated with the lowest PED increment value of Eq. (6.32) is given by:

$$\begin{aligned} \overline{s}_v = \tfrac{1}{\sqrt{N_T}} \cdot \tfrac{\sqrt{M}-2\check{m}_v-1}{\sqrt{\beta}}, \quad \text{where} \quad & \check{m}_v = \max\left[\min\left(q_v, \sqrt{M}-1\right), 0\right], \\ & q_v = \lfloor g_v \rceil, \\ & g_v = \tfrac{\sqrt{M}-\sqrt{N_T\cdot\beta}\cdot\widetilde{z}_v^{SD}-1}{2}. \end{aligned} \tag{6.34}$$

In contrast to the MPSK phase, which rotates a circle over an unlimited phase range, the index range of $\check{m}_v \in [0, \sqrt{M}-1]$ has to be enforced for Square QAM detection, as seen in the "findBest" subfunction of Table 6.4. According to the PED defined in Eq. (6.31) and to the best Schnorr-Euchner search candidate defined in Eq. (6.34), the SD conceived for uncoded V-BLAST employing MPSK in Table 6.3 may be adopted for the case of employing Square MQAM, but the following modifications have to be carried out:

1. The SD search should start with the index $v = 2N_T$ on line 2, and it may terminate with the index $v = 2N_T$ on lines 16 and 23 in Table 6.3 for Square QAM detection. Accordingly, the PED initialization may be modified as $d_{2N_T+1} = 0$ on line 1 in Table 6.3.

2. The subfunctions of "findBest" and "findNext" in Table 6.3 are modified for the case of Square MQAM detection in Table 6.4 according to Eqs. (6.32) and (6.34).

3. The PED increment on line 5 in Table 6.3 may be replaced by $\Delta_v = \left(\widetilde{y}_v^{SD} - \widetilde{h}_v^{SD}\overline{s}_v\right)^2$ according to Eq. (6.32) for Square QAM, where we have the symbol update of $\overline{s}_v = \frac{1}{\sqrt{N_T}} \cdot \frac{\sqrt{M}-2\check{m}_v-1}{\sqrt{\beta}}$.

In summary, with the aid of SD, the hard-decision-aided V-BLAST detection complexity may be lower bounded by $O(2N_T - 1)$ and by $O(4N_T - 1)$ for the case of MPSK and for the case of Square MQAM, respectively. For example, it can be seen in Table 6.3 that the "findBest" subfunction may be invoked at least N_T times, when the SD index is reduced from $v = N_T$ down to $v = 1$, while the "findNext" subfunction may be invoked at least $(N_T - 1)$ times when the SD index increases from $v = 2$ up to $v = N_T$.

Subfunction: $[\widetilde{y}_v^{SD}, \widetilde{h}_v^{SD}, \check{m}_v, \text{step}_v, n_v] = \textbf{findBest}(\widetilde{\widetilde{Y}}_v, \{l_{t,v}\}_{t=v}^{2N_T}, \{\bar{s}_t\}_{t=v+1}^{2N_T})$	
$\widetilde{y}_v^{SD} = \widetilde{\widetilde{Y}}_v - \sum_{t=v+1}^{2N_T} l_{t,v}\bar{s}_t$	//evaluate $\widetilde{y}_v^{SD}$ according to Eq. (6.32)
$\widetilde{h}_v^{SD} = l_{v,v}$	//evaluate $\widetilde{h}_v^{SD}$ according to Eq. (6.32)
$\widetilde{z}_v^{SD} = \widetilde{y}_v^{SD} / \widetilde{h}_v^{SD}$	//update decision variable of Eq. (6.33)
$g_v = \frac{\sqrt{M} - \sqrt{N_T \cdot \beta \cdot \widetilde{z}_v^{SD} - 1}}{2}$	//visit the best child node
$q_v = \lfloor g_v \rceil$	
$\check{m}_v = \max\left[\min\left(q_v, \sqrt{M}-1\right), 0\right]$	
$\text{step}_v = \text{sign}(g_v - q_v)$	//store the step size for the next child node
$n_v = 0$	

Subfunction: $[\check{m}_v, \text{step}_v, n_v] = \textbf{findNext}\,(\check{m}_v, \text{step}_v, n_v)$	
do	
$\quad \check{m}_v = \check{m}_v + \text{step}_v$	//visit the next child node
$\quad \text{step}_v = -\text{step}_v - \text{sign}(\text{step}_v)$	
while $(\check{m}_v < 0) \| \| (\check{m}_v > \sqrt{M}-1)$	//index range of $\check{m}_v \in [0, \sqrt{M}-1]$ has to be guaranteed
$n_v = n_v + 1$	

Table 6.4: Pseudocode for subfunctions of hard-decision-aided SD conceived for uncoded V-BLAST employing Square MQAM.

The SD complexity lower bounds can only be approached in the high-SNR region, where the ED differences between the candidates are large so that the optimum solution may be found without any ambiguity. However, it is also demonstrated in [214] that the average SD complexity is a polynomial function, which is often approximately cubic, while [215] demonstrates that the SD complexity is still exponential at low SNR region. Therefore, in the coming section, we further introduce LF aided V-BLAST receivers, which exhibit a detection complexity that may as low as single-antenna-based detection, but the sub-optimal performance is inevitable.

6.2.4 Hard-Decision-Aided Linear Filters Conceived for Uncoded V-BLAST

For low-complexity V-BLAST detection, LFs may be conceived for detecting the paralleled data-streams separately, while suppressing the interference as best as possible. More explicitly, under the idealized assumption of having perfect knowledge of the CSI, the basic Matched Filter (MF) output becomes [13]:

$$\mathbf{Z}^{MF} = \mathbf{Y}\mathbf{G}^{MF} = \mathbf{S}\mathbf{H}\mathbf{H}^H + \mathbf{V}\mathbf{H}^H, \tag{6.35}$$

where the $(N_R \times N_T)$-element MF weight matrix in Eq. (6.35) is given by $\mathbf{G}^{MF} = \mathbf{H}^H$. Furthermore, the v-th element in the $(1 \times N_T)$-element decision variable vector $\mathbf{Z}^{MF}$ of Eq. (6.35) is given by:

$$z_v^{MF} = s_v \|\mathbf{H}_{v,-}\|^2 + \sum_{\forall \bar{v} \neq v} s_{\bar{v}} \mathbf{H}_{\bar{v},-} (\mathbf{H}_{v,-})^H + \mathbf{V}(\mathbf{H}_{v,-})^H, \tag{6.36}$$

where the $(1 \times N_R)$-element vector $\mathbf{H}_{v,-}$ refers to the v-th row of fading matrix $\mathbf{H}$. It can be seen in Eq. (6.36) that the second term of $\sum_{\forall \bar{v} \neq v} s_{\bar{v}} \mathbf{H}_{\bar{v},-} (\mathbf{H}_{v,-})^H$ introduces severe interference. Without dealing with this interference term, directly demodulating the single symbol s_v by carrying out the operation $z_v^{MF} / \|\mathbf{H}_{v,-}\|^2$ according to Eq. (6.36) results in an irreducible error floor.

In order to mitigate this problem, the Zero-Forcing (ZF) detector aims for cancelling the interference term of the $(N_R \times N_T)$-element ZF weight matrix $\mathbf{G}^{ZF} = \mathbf{H}^H(\mathbf{H}\mathbf{H}^H)^{-1}$, so that the ZF

filter output is given by [14–16]:

$$\mathbf{Z}^{ZF} = \mathbf{Y}\mathbf{G}^{ZF} = \mathbf{S} + \widetilde{\mathbf{V}}, \tag{6.37}$$

where the $(1 \times N_T)$-element noise term $\widetilde{\mathbf{V}} = \mathbf{V}\mathbf{G}^{ZF}$ has an increased noise power of $\|\mathbf{G}^{ZF}\|^2 \cdot N_0$. The ZF's problem of noise enhancement may result in a severe performance contamination, especially in the low-SNR region.

The Minimum Mean Squared Error (MMSE) filter may further reduce the noise power by minimizing the Mean Squared Error (MSE), which is defined as the Euclidean distance between the MMSE filter output and the transmitted V-BLAST vector [13, 14, 16]. The MMSE filter output may be expressed as:

$$\mathbf{Z}^{MMSE} = \mathbf{Y}\mathbf{G}^{MMSE} = \mathbf{S}\mathbf{H}\mathbf{G}^{MMSE} + \mathbf{V}\mathbf{G}^{MMSE}, \tag{6.38}$$

where the $(N_R \times N_T)$-element MMSE weight matrix $\mathbf{G}^{MMSE}$ is conceived for minimizing the following MSE expression:

$$\begin{aligned}\sigma^2_{MSE} &= E\left(\|\mathbf{Z}^{MMSE} - \mathbf{S}\|^2\right) \\ &= \mathrm{E}\left\{\mathrm{tr}\left[(\mathbf{Y}\mathbf{G}^{MMSE} - \mathbf{S})^H(\mathbf{Y}\mathbf{G}^{MMSE} - \mathbf{S})\right]\right\} \\ &= \mathrm{tr}\left[(\mathbf{G}^{MMSE})^H\mathrm{E}\left(\mathbf{Y}^H\mathbf{Y}\right)\mathbf{G}^{MMSE}\right] - 2\Re\left\{\mathrm{tr}\left[(\mathbf{G}^{MMSE})^H\mathrm{E}\left(\mathbf{Y}^H\mathbf{S}\right)\right]\right\} + 1,\end{aligned} \tag{6.39}$$

where the auto-correlation matrix is given by $\mathrm{E}\left\{\mathbf{Y}^H\mathbf{Y}\right\} = \frac{1}{N_T}\mathbf{H}^H\mathbf{H} + N_0\mathbf{I}_{N_R}$, while the cross-correlation matrix is given by $\mathrm{E}\left\{\mathbf{Y}^H\mathbf{S}\right\} = \frac{1}{N_T}\mathbf{H}^H$. Therefore, the MMSE solution of $\frac{\partial\sigma^2_{\mathrm{MSE}}}{\partial\mathbf{G}^{MMSE}} = 0$ leads us to the MMSE weight matrix of:

$$\mathbf{G}^{MMSE} = \left(\mathbf{H}^H\mathbf{H} + N_0 \cdot N_T \cdot \mathbf{I}_{N_R}\right)^{-1}\mathbf{H}^H. \tag{6.40}$$

As a result, the v-th element in the MMSE filter output vector $\mathbf{Z}^{MMSE}$ of Eq. (6.38) may be rewritten as:

$$z_v^{MMSE} = s_v\mathbf{H}_{v,-}\mathbf{G}_{-,v}^{MMSE} + \sum_{\forall\bar{v}\neq v} s_{\bar{v}}\mathbf{H}_{\bar{v},-}\mathbf{G}_{-,v}^{MMSE} + \mathbf{V}\mathbf{G}_{-,v}^{MMSE}, \tag{6.41}$$

where the $(N_T \times 1)$-element vector $\mathbf{G}_{-,v}^{MMSE}$ denotes the v-th column of MMSE weight matrix $\mathbf{G}^{MMSE}$ of Eq. (6.40). Finally, the linear MPSK/QAM demodulator may be invoked for recovering the data-carrying modulation indices as:

$$\hat{m}_v = \mathbb{M}^{-1}(\widetilde{z}_v), \quad v = \{1, \cdots, N_T\}, \tag{6.42}$$

where we have $\widetilde{z}_v = \sqrt{N_T} \cdot z_v^{MMSE} \cdot (\mathbf{H}_{v,-}\mathbf{G}_{-,v}^{MMSE})^* / |\mathbf{H}_{v,-}\mathbf{G}_{-,v}^{MMSE}|^2$ according to Eq. (6.41).

It was proposed in [164, 316–320] that the interference cancellation techniques based on either ZF receivers or MMSE receivers may further improve the LF aided V-BLAST detection performance. Moreover, the interference nulling and cancelling proposed for Multi-User Detection (MUD) in CDMA systems [321–324] may be adopted by V-BLAST, since the V-BLAST scheme's multiple TAs may be considered to be equivalent to CDMA's multiple users. For example, the Successive Interference Cancelling (SIC) may opt for detecting the data streams one by

one from the strongest to the weakest. When the LF makes a decision concerning a single data stream, it may be remodulated and then subtracted from the received signal so that the remaining data streams may be detected successively, while having to cope with a reduced amount of interference. We note that the interference cancellation techniques still suffer from error propagation, which means that the optimum performance of ML detection and SD cannot be closely approached by the LF-based detection techniques.

6.3 Uncoded Space-Time Modulation

In this section, we offer further insights into the state-of-the-art STM schemes including both the family of STBCs and LDCs, whose signal processing is typically carried out both in the spatial domain and time domain. First of all, the classic STBCs are summarized in Sec. 6.3.1, where the code construction is introduced. Following this, we demonstrate that although orthogonal STBCs effectively minimize the error probability, they cannot achieve the full MIMO capacity. Therefore, the concept of LDC is described in Sec. 6.3.2 in order to resolve the tradeoff between the diversity gain and multiplexing gain.

6.3.1 Space-Time Block Coding

In order to better present the family of STBC techniques, we firstly summarize the general orthogonal design guideline in Sec. 6.3.1.1, followed by a general framework of low-complexity linear STBC receivers. Secondly, as the most important example, namely the full unity-rate STBC relying on a complex-valued orthogonal design is presented in Sec. 6.3.1.2. Following this, the STBCs relying on the half-rate Hurwitz-Radon orthogonal design are detailed in Sec. 6.3.1.3, and the STBCs that minimize the transmission delay by using the theory of Amicable orthogonal design are presented in Sec. 6.3.1.4. Lastly, the error probability and capacity of STBC schemes are analysed in Sec. 6.3.1.5.

6.3.1.1 General Orthogonal Design Guidelines

The schematic of orthogonal STBC transceivers is depicted in Fig. 6.4. An STBC transmitter firstly encodes the N_QBPS source bits into N_Q modulated MPSK/QAM symbols $\{s_q\}_{q=1}^{N_Q}$. During N_P symbol periods, the $(N_P \times N_T)$-element symbol-matrix transmitted from the N_T TAs may be formulated by:

$$\mathbf{S} = \sqrt{P_t} G_{N_T}(\{s_q\}_{q=1}^{N_Q}) \tag{6.43a}$$

$$= \sqrt{P_t} \sum_{q=1}^{N_Q} \left[\mathbf{A}_q \Re(s_q) + j\mathbf{B}_q \Im(s_q)\right], \tag{6.43b}$$

where $G_{N_T}(\cdot)$ represents the real and imaginary parts of the transmission matrix by dispersing the real and imaginary parts of the modulated MPSK/QAM symbols into the $(N_P \times N_T)$-element

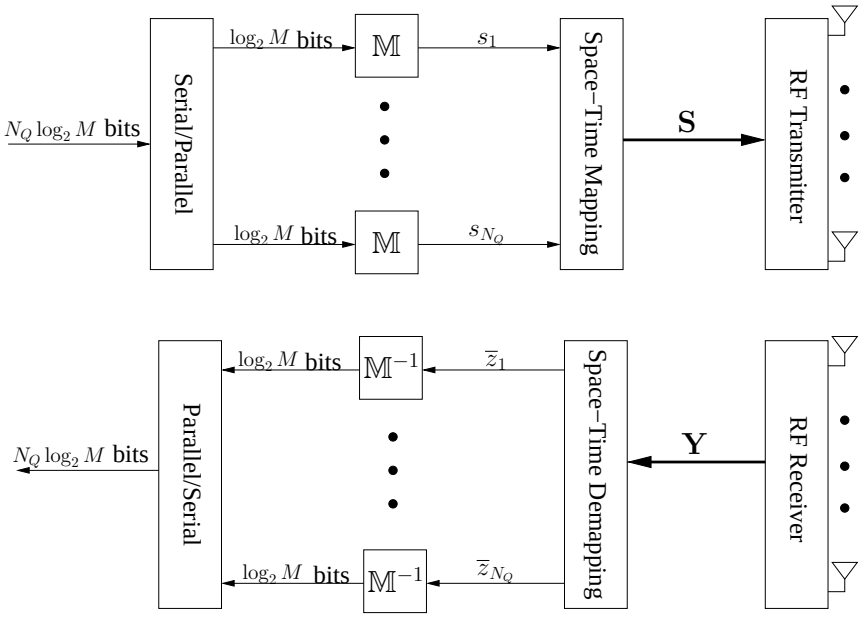

Figure 6.4: Schematic of an orthogonal STBC transceiver.

real-valued matrices $\{\mathbf{A}_q\}_{q=1}^{N_Q}$ and $\{\mathbf{B}_q\}_{q=1}^{N_Q}$, respectively, while the normalization factor P_t is introduced in order to guarantee satisfying the power constraint of $\mathrm{E}\left[\mathrm{tr}(\mathbf{S}^H\mathbf{S})\right] = N_P$.

We note that the V-BLAST transmission matrix of Eq. (6.11) may also be framed according to Eq. (6.43b). The corresponding dispersion matrices used for V-BLAST are given by:

$$\mathbf{A}_q = \mathbf{B}_q = [\underbrace{0 \cdots 0}_{q-1}, 1, \underbrace{0 \cdots 0}_{N_T-q}], \quad 1 \leq q \leq N_T, \tag{6.44}$$

where we have $N_T = N_Q$ and $N_P = 1$. Moreover, the power normalization factor is given by $P_t = \frac{1}{N_T}$. It can be seen in Eq. (6.44) that the V-BLAST transmission matrix is constructed in spatial domain only.

The objectives of the STBC design are two-fold: to minimize the error probability of Eq. (6.8) and to employ the low-complexity linear receiver portrayed in Fig. 6.4 without encountering the V-BLAST's inter-antenna interference problem. In order to achieve the former goal, the PEP of Eq. (6.9) should be minimized by achieving full diversity and maximizing the coding gain as presented in Eq. (6.10). In order to achieve the second objective, the MIMO's inter-antenna interference should be able to be cancelled out before invoking a linear MPSK/QAM demodulator at the receiver. Let us firstly consider the codeword difference formulated in the PEP upper bound of Eq. (6.10) according to the STBC transmission matrix of Eq. (6.43) as:

$$\begin{aligned} \mathbf{S}^i - \mathbf{S}^{\bar{i}} &= \sqrt{P_t} \sum_{q=1}^{N_Q} \left[\mathbf{A}_q \Re(s_q^i - s_q^{\bar{i}}) + j\mathbf{B}_q \Im(s_q^i - s_q^{\bar{i}}) \right] \\ &= \sqrt{P_t} G_{N_T}(\{s_q^i - s_q^{\bar{i}}\}_{q=1}^{N_Q}). \end{aligned} \tag{6.45}$$

Therefore, when Hadamard's inequality [281] is applied to the determinant term of Eq. (6.10c), it can be seen that the optimality condition is that $\mathbf{\Delta} = (\mathbf{S}^i - \mathbf{S}^{\bar{i}})^H(\mathbf{S}^i - \mathbf{S}^{\bar{i}})$ is unitary, which requires

that $\mathbf{S}^i - \mathbf{S}^{\bar{i}} = \sqrt{P_t} G_{N_T}(\{s_q^i - s_q^{\bar{i}}\}_{q=1}^{N_Q})$ have orthogonal columns. This reveals that in general, the STBC transmission matrix $\mathbf{S} = \sqrt{P_t} G_{N_T}(\{s_q\}_{q=1}^{N_Q})$ should always have orthogonal columns, which requires $N_P \geq N_T$. Furthermore, when the signal vectors transmitted by N_T TAs are orthogonal to each other, they are expected to be decoupled at the receiver without encountering the V-BLAST's IAI problem.

If we also take into account all the considerations including performance, cost and delay, the STBC from orthogonal design may be translated into the following stringent design requirements [8, 177, 178, 181–183, 293, 325]:

(R1) Full Unity-Rate Requirement: $N_P = N_Q$.

(R2) Delay Optimality Requirement: $N_P = N_T$.

(R3) Hardware Simplicity Requirement: all the elements in $G_{N_T}(\{s_q\}_{q=1}^{N_Q})$ of Eq. (6.43) should be taken from $\{0, \pm s_q, \pm s_q^*\}_{\forall q=1}^{N_Q}$.

(R4) Orthogonality Requirement: the transmission matrix of Eq. (6.43) should have orthogonal columns so that we have:

$$\mathbf{S}^H \mathbf{S} = \frac{N_P}{N_T} \frac{\sum_{q=1}^{N_Q} |s_q|^2}{N_Q} \mathbf{I}_{N_T}, \tag{6.46}$$

which complies with the power constraint of $\mathrm{E}\left[\mathrm{tr}(\mathbf{S}^H \mathbf{S})\right] = N_P$.

The first requirement (R1) results in the maximum attainable normalized throughput of $\overline{R} = \frac{N_Q}{N_P} = 1$, so that the employment of multiple TAs for STBC systems would not end up with a lower throughput than that of the SISO and SIMO systems. The second requirement (R2) minimizes the transmission delay while maintaining the transmit diversity order, which is given by $\min\{N_T, N_P\}$ according to Eq. (6.10c). The third requirement (R3) simplifies the hardware design of the RF amplifiers by minimizing the peak-to-average ratio. Lastly, the orthogonality requirement (R4) is the key both to the minimized error probability and to the low-complexity interference-free linear STBC receiver, where the multiple streams may be individually detected. For the sake of code construction, the orthogonality requirement (R4) may be further translated to the following requirements imposed on the dispersion matrices $\{\mathbf{A}_q\}_{q=1}^{N_Q}$ and $\{\mathbf{B}_q\}_{q=1}^{N_Q}$, which are three-fold:

$$\mathbf{A}_q^H \mathbf{A}_q = \mathbf{I}_{N_T}, \quad \mathbf{B}_q^H \mathbf{B}_q = \mathbf{I}_{N_T}, \quad \forall q \in \{1, \cdots, N_Q\}, \tag{6.47a}$$

$$\mathbf{A}_q^H \mathbf{A}_{\bar{q}} = -\mathbf{A}_{\bar{q}}^H \mathbf{A}_q, \quad \mathbf{B}_q^H \mathbf{B}_{\bar{q}} = -\mathbf{B}_{\bar{q}}^H \mathbf{B}_q, \quad \forall q \neq \bar{q} \in \{1, \cdots, N_Q\}, \tag{6.47b}$$

$$\mathbf{A}_q^H \mathbf{B}_{\bar{q}} = \mathbf{B}_{\bar{q}}^H \mathbf{A}_q, \quad \forall q \forall \bar{q} \in \{1, \cdots, N_Q\}. \tag{6.47c}$$

Let us now proceed to characterize the interference-free linear STBC receiver by further exploring the orthogonality requirement (R4). First of all, the STBC transmission matrix of Eq. (6.43)

may be expressed in the following alternative form:

$$\mathbf{S} = \sqrt{P_t} \sum_{q=1}^{N_Q} \left(\mathbf{D}_q^+ s_q + \mathbf{D}_q^- s_q^* \right), \tag{6.48}$$

where the alternative dispersion matrices in Eq. (6.48) are given by $\left\{ \mathbf{D}_q^+ = \frac{1}{2}(\mathbf{A}_q + \mathbf{B}_q) \right\}_{q=1}^{N_Q}$ and $\left\{ \mathbf{D}_q^- = \frac{1}{2}(\mathbf{A}_q - \mathbf{B}_q) \right\}_{q=1}^{N_Q}$. Following this, the matrix norm term in the probability $p(\mathbf{Y}|\mathbf{S})$ expression of Eq (6.2) may be extended as [325]:

$$\begin{aligned} \|\mathbf{Y} - \mathbf{SH}\|^2 &= \|\mathbf{Y}\|^2 - \mathrm{tr}(\mathbf{Y}^H \mathbf{SH}) - \mathrm{tr}(\mathbf{H}^H \mathbf{S}^H \mathbf{Y}) + \mathrm{tr}(\mathbf{H}^H \mathbf{S}^H \mathbf{SH}) \\ &= \|\mathbf{Y}\|^2 + \sum_{q=1}^{N_Q} \Big\{ -\sqrt{P_t}\mathrm{tr}\left[\mathbf{Y}^H \mathbf{D}_q^+ \mathbf{H} s_q + \mathbf{Y}^H \mathbf{D}_q^- \mathbf{H} s_q^* + \mathbf{H}^H (\mathbf{D}_q^+)^H \mathbf{Y} s_q^* + \mathbf{H}^H (\mathbf{D}_q^-)^H \mathbf{Y} s_q \right] \\ &\qquad + \frac{N_P \|\mathbf{H}\|^2}{N_T N_Q} |s_q|^2 \Big\} \\ &= \sum_{q=1}^{N_Q} \left(\frac{N_P \|\mathbf{H}\|^2}{N_T N_Q} |\overline{z}_q - s_q|^2 \right) + \varrho, \end{aligned} \tag{6.49}$$

where the decision variable is given by:

$$\overline{z}_q = \frac{N_T N_Q \sqrt{P_t}}{N_P \|\mathbf{H}\|^2} \mathrm{tr}\left[\mathbf{Y}^H \mathbf{D}_q^- \mathbf{H} + \mathbf{H}^H (\mathbf{D}_q^+)^H \mathbf{Y} \right], \tag{6.50}$$

and the constant is given by $\varrho = \|\mathbf{Y}\|^2 - \sum_{q=1}^{N_Q} \frac{N_P \|\mathbf{H}\|^2}{N_T N_Q} |\overline{z}_q|^2$. As a result, the conditional probability of receiving $\mathbf{Y}$, when $\mathbf{S}$ is transmitted in Eq (6.2) becomes:

$$p(\mathbf{Y}|\mathbf{S}) = \vartheta \prod_{q=1}^{N_Q} p(\overline{z}_q | s_q), \tag{6.51}$$

where the constant is given by $\vartheta = \frac{(\pi \overline{N}_0)^{N_Q}}{(\pi N_0)^{N_R N_P}} \exp(-\frac{\varrho}{N_0})$, so that the equivalent conditional probability of receiving $\overline{z}_q$, when s_q is transmitted may be expressed as:

$$p(\overline{z}_q | s_q) = \frac{1}{\pi \overline{N}_0} \exp\left(-\frac{|\overline{z}_q - s_q|^2}{\overline{N}_0} \right), \tag{6.52}$$

where the equivalent noise power is given by $\overline{N}_0 = \frac{N_T N_Q}{N_P \|\mathbf{H}\|^2} N_0$. The ML detector aims for maximizing the *a posteriori* probability $p(\mathbf{S}|\mathbf{Y})$ of Eq. (6.12), where the constant ϑ in Eq. (6.51) may be cancalled out by the division operation in Bayes' law seen in Eq. (6.12). Therefore, we may now conclude that the STBC may invoke a linear MPSK/QAM demodulator for recovering s_q from $\overline{z}_q$ without encountering the BLAST MIMO's IAI problem. More explicitly, the demodulation may be carried out as:

$$\hat{s}_q = \mathbb{M}^{-1}(\overline{z}_q), \quad \forall q \in \{1, \cdots, N_Q\}. \tag{6.53}$$

If the full unity-rate requirement (R1) is guaranteed in the STBC design, the equivalent noise power in the linear STBC receiver of Eq. (6.53) is given by $\overline{N}_0 = \frac{N_T}{\|\mathbf{H}\|^2} N_0 = \frac{1}{\left(\sum_{v=1}^{N_T} \|\mathbf{H}_{v,-}\|^2 \right) / N_T} N_0$, which

explicitly reveals the benefit of having diversity gain. Let us recall that the decision variable for a SIMO scheme associated with $N_P = N_Q = 1$ is given by $\widetilde{z}_q = \mathbf{Y}_{1,-}\mathbf{H}_{1,-}^H / \|\mathbf{H}_{1,-}\|^2$ as seen in Eq. (2.14), and the equivalent noise power is given by $\widetilde{N}_0 = \frac{1}{\|\mathbf{H}_{1,-}\|^2} N_0$. This implies that when the single TA experience a deep fade, the equivalent noise power of the SIMO demodulator may be amplified by the reduced divisor of $\|\mathbf{H}_{1,-}\|^2$. By contrast, the STBC's equivalent noise power encountered by the linear demodulator has the divisor of $\left(\sum_{v=1}^{N_T} \|\mathbf{H}_{v,-}\|^2\right) / N_T$, which is averaged over the fading samples gleaned from the N_T TAs. Therefore, an extra hardware requirement is imposed, when aiming for achieving the STBC's diversity gain potential, because we have to separate the multipe TAs sufficiently far apart, so that they will not experience a deep fade at the same time.

6.3.1.2 Full Unity-Rate Space-Time Block Code

When complex-valued high-throughput MPSK/QAM constellations are employed, it was proven in [178] that the only STBC satisfying all the requirements listed in Sec. 6.3.1.1 is Alamouti's G2-STBC [177], whose codeword is constructed by:

$$G_2(s_1, s_2) = \begin{bmatrix} s_1 & s_2 \\ -s_2^* & s_1^* \end{bmatrix}. \tag{6.54}$$

It can be seen in Eq. 6.54 that Alamouti's G2-STBC transmits $(N_Q = 2)$ modulated MPSK/QAM symbols by $(N_T = 2)$ TAs over $(N_P = 2)$ 'channel uses'. Therefore, the G2-STBC satisfies the full unity-rate requirement (R1), the delay optimal requirement (R2) and the transmitter's hardware requirement (R3) discussed in Sec. 6.3.1.1. Furthermore, we also have $[G_2(s_1, s_2)]^H G_2(s_1, s_2) = (|s_1|^2 + |s_2|^2)\mathbf{I}_2$ according to Eq. (6.54). Therefore, according to Eq. (6.43a), the G2-STBC's transmission matrix is given by:

$$\mathbf{S} = \frac{1}{\sqrt{2}} G_2(s_1, s_2), \tag{6.55}$$

since the power normalization factor in Eq. (6.43) is given by $P_t = \frac{1}{2}$, so that the orthogonality requirement (R4) in Sec. 6.3.1.1 may also be fully met. Moreover, the dispersion matrices designed for G2-STBC according to Eq. (6.43b) may be expressed as:

$$\mathbf{A}_1 = \begin{bmatrix} 1 & 0 \\ 0 & 1 \end{bmatrix}, \quad \mathbf{A}_2 = \begin{bmatrix} 0 & 1 \\ -1 & 0 \end{bmatrix}, \quad \mathbf{B}_1 = \begin{bmatrix} 1 & 0 \\ 0 & -1 \end{bmatrix}, \quad \mathbf{B}_2 = \begin{bmatrix} 0 & 1 \\ 1 & 0 \end{bmatrix}. \tag{6.56}$$

As expected, these dispersion matrices completely comply with the orthogonality requirement formulated in Eq. (6.47).

The signals received at the N_R RAs are modelled by Eq. (6.1), which may be further extended according to Eq. (6.54) as:

$$\begin{aligned} \mathbf{Y}_{1,-} &= \frac{s_1}{\sqrt{2}}\mathbf{H}_{1,-} + \frac{s_2}{\sqrt{2}}\mathbf{H}_{2,-} + V_{1,-}, \\ \mathbf{Y}_{2,-} &= -\frac{s_2^*}{\sqrt{2}}\mathbf{H}_{1,-} + \frac{s_1^*}{\sqrt{2}}\mathbf{H}_{2,-} + V_{2,-}, \end{aligned} \tag{6.57}$$

where the $(1 \times N_R)$-element row vector $\{\mathbf{Y}_{t,-}\}_{t=1}^{2}$ refers to the t-th row in the received signal matrix $\mathbf{Y}$ of Eq. (6.1), which models the signal received accross all N_R RAs during the t-th time slot. Similarly, the $(1 \times N_R)$-element AWGN row vector $\{\mathbf{V}_{t,-}\}_{t=1}^{2}$ is taken from the t-th row of the AWGN matrix $\mathbf{V}$ in Eq. (6.1). Furthermore, the $(1 \times N_R)$-element row vector $\{\mathbf{H}_{v,-}\}_{v=1}^{2}$ refers to the v-th row in the fading channel matrix $\mathbf{H}$ in Eq. (6.1), which models the fading samples received from the v-th TA by all N_R RAs.

Owing to the fact that the signal-vector transmitted from the two TAs are mutually orthogonal, the received signals of Eq. (6.57) may be decoupled without encountering any inter-antenna interference as [177]:

$$\begin{aligned} \overline{z}_1 &= \frac{\sqrt{2}(\mathbf{Y}_{1,-})(\mathbf{H}_{1,-})^H}{\|\mathbf{H}\|^2} + \frac{\sqrt{2}(\mathbf{H}_{2,-})(\mathbf{Y}_{2,-})^H}{\|\mathbf{H}\|^2} = s_1 + \frac{\sqrt{2}(\mathbf{V}_{1,-})(\mathbf{H}_{1,-})^H}{\|\mathbf{H}\|^2} + \frac{\sqrt{2}(\mathbf{H}_{2,-})(\mathbf{V}_{2,-})^H}{\|\mathbf{H}\|^2}, \\ \overline{z}_2 &= \frac{\sqrt{2}(\mathbf{Y}_{1,-})(\mathbf{H}_{2,-})^H}{\|\mathbf{H}\|^2} - \frac{\sqrt{2}(\mathbf{H}_{1,-})(\mathbf{Y}_{2,-})^H}{\|\mathbf{H}\|^2} = s_2 + \frac{\sqrt{2}(\mathbf{V}_{1,-})(\mathbf{H}_{2,-})^H}{\|\mathbf{H}\|^2} - \frac{\sqrt{2}(\mathbf{H}_{1,-})(\mathbf{V}_{2,-})^H}{\|\mathbf{H}\|^2}. \end{aligned} \tag{6.58}$$

Therefore, the G2-STBC receiver's decision on $\{\hat{s}_q\}_{q=1}^{2}$ may be directly obtained by demodulating the decision variables $\{\overline{z}_q\}_{q=1}^{2}$ in Eq. (6.58) as $\{\hat{s}_q = \mathbb{M}^{-1}(\overline{z}_q)\}_{q=1}^{2}$, and the equivalent noise power for the linear MPSK demodulators is given by $\overline{N}_0 = \frac{2}{\|\mathbf{H}\|^2}$.

We note that the decision variables $\{\overline{z}_q\}_{q=1}^{2}$ in Eq. (6.58) may also be obtained according to the general linear STBC receiver design of Eq. (6.50). In more details, according to Eq. (6.56), the equivalent dispersion matrices in the alternative transmitted signal model of Eq. (6.48) may be formulated for G2-STBC as:

$$\mathbf{D}_1^+ = \begin{bmatrix} 1 & 0 \\ 0 & 0 \end{bmatrix}, \quad \mathbf{D}_1^- = \begin{bmatrix} 0 & 0 \\ 0 & 1 \end{bmatrix}, \quad \mathbf{D}_2^+ = \begin{bmatrix} 0 & 1 \\ 0 & 0 \end{bmatrix}, \quad \mathbf{D}_2^- = \begin{bmatrix} 0 & 0 \\ -1 & 0 \end{bmatrix}. \tag{6.59}$$

As a result, the decision variables in Eq. (6.50) may be extended for G2-STBC as:

$$\begin{aligned} \overline{z}_1 &= \frac{\sqrt{2}}{\|\mathbf{H}\|^2}\text{tr}\left[\mathbf{Y}^H\mathbf{D}_1^-\mathbf{H} + \mathbf{H}^H(\mathbf{D}_1^+)^H\mathbf{Y}\right] = \frac{\sqrt{2}}{\|\mathbf{H}\|^2}\text{tr}\left[(\mathbf{Y}_{2,-})^H(\mathbf{H}_{2,-}) + (\mathbf{H}_{1,-})^H(\mathbf{Y}_{1,-})\right], \\ \overline{z}_2 &= \frac{\sqrt{2}}{\|\mathbf{H}\|^2}\text{tr}\left[\mathbf{Y}^H\mathbf{D}_2^-\mathbf{H} + \mathbf{H}^H(\mathbf{D}_2^+)^H\mathbf{Y}\right] = \frac{\sqrt{2}}{\|\mathbf{H}\|^2}\text{tr}\left[-(\mathbf{Y}_{2,-})^H(\mathbf{H}_{1,-}) + (\mathbf{H}_{2,-})^H(\mathbf{Y}_{1,-})\right]. \end{aligned} \tag{6.60}$$

It can be seen that the decision variables of Eq. (6.60) obtained according to the general STBC design of Eq. (6.50) are exactly the same as the ones presented in Eq. (6.58) obtained by observing the G2-STBC's received signal model of Eq. (6.57). This verifies that Alamouti's G2-STBC belongs to the family of orthognal STBCs, which not only minimizes the error probability, but it is also capable of employing low-complexity single-stream linear MPSK/QAM demodulators at STBC receiver without encountering the problem of inter-antenna interference.

6.3.1.3 Half-Rate Space-Time Block Code

When the family of real-valued constellations is considered, the orthogonal design satisfying the four requirements listed in Sec. 6.3.1.1 does exist for N_T =2, 4 or 8 [178], which may be solved by the Hurwitz-Radon theory of [179, 180]. We note that the conjugation operation $\{s_q^*\}_{q=1}^{N_Q}$ may be eliminated from the requirement (R3) of Sec. 6.3.1.1 for real-valued signalling, and only the dispersion matrices $\{\mathbf{A}_q\}_{q=1}^{N_Q}$ designed for dispersing real symbols are of concern in this scenario.

For $N_T = 2$ TAs, the real-valued orthogonal design $G_2^{\Re}(s_1, s_2)$ is the same as Alamouti's G2-STBC design of $G_2(s_1, s_2)$ seen in Eq. (6.54) without the conjugation operations. For the case of $N_T = 4$, the STBC from real-valued orthogonal design is given by [178]:

$$G_4^{\Re}(s_1, s_2, s_3, s_4) = \begin{bmatrix} s_1 & s_2 & s_3 & s_4 \\ -s_2 & s_1 & -s_4 & s_3 \\ -s_3 & s_4 & s_1 & -s_2 \\ -s_4 & -s_3 & s_2 & s_1 \end{bmatrix}. \tag{6.61}$$

For the case of $N_T = 8$, the STBC generated from real-valued orthogonal design is given by [178]:

$$G_8^{\Re}(s_1, s_2, s_3, s_4, , s_5, s_6, s_7, s_8) = \begin{bmatrix} s_1 & s_2 & s_3 & s_4 & s_5 & s_6 & s_7 & s_8 \\ -s_2 & s_1 & s_4 & -s_3 & s_6 & -s_5 & -s_8 & s_7 \\ -s_3 & -s_4 & s_1 & s_2 & s_7 & s_8 & -s_5 & -s_6 \\ -s_4 & s_3 & -s_2 & s_1 & s_8 & -s_7 & s_6 & -s_5 \\ -s_5 & -s_6 & -s_7 & -s_8 & s_1 & s_2 & s_3 & s_4 \\ -s_6 & s_5 & -s_8 & s_7 & -s_2 & s_1 & -s_4 & s_3 \\ -s_7 & s_8 & s_5 & -s_6 & -s_3 & s_4 & s_1 & -s_2 \\ -s_8 & -s_7 & s_6 & s_5 & -s_4 & -s_3 & s_2 & s_1 \end{bmatrix}. \tag{6.62}$$

In order to accommodate complex-valued MPSK/QAM symbols, the Half-Rate (HR)-G4-STBC may be obtained by vertically concatenating the STBC from real-valued orthogonal design and its conjugates as:

$$G_4(s_1, s_2, s_3, s_4) = \begin{bmatrix} G_4^{\Re}(s_1, s_2, s_3, s_4) \\ G_4^{\Re}(s_1, s_2, s_3, s_4)^* \end{bmatrix} = \begin{bmatrix} s_1 & s_2 & s_3 & s_4 \\ -s_2 & s_1 & -s_4 & s_3 \\ -s_3 & s_4 & s_1 & -s_2 \\ -s_4 & -s_3 & s_2 & s_1 \\ s_1^* & s_2^* & s_3^* & s_4^* \\ -s_2^* & s_1^* & -s_4^* & s_3^* \\ -s_3^* & s_4^* & s_1^* & -s_2^* \\ -s_4^* & -s_3^* & s_2^* & s_1^* \end{bmatrix}. \tag{6.63}$$

Furthermore, the HR-G3-STBC design of $G_3(s_1, s_2, s_3, s_4)$ may be constructed by taking the first three columns in $G_4(s_1, s_2, s_3, s_4)$. Similarly, the HR-G8-STBC may also be obtained by vertically concatenating $G_8^{\Re}(s_1, s_2, s_3, s_4, , s_5, s_6, s_7, s_8)$ and its conjugates as:

$$G_8(s_1, s_2, s_3, s_4, , s_5, s_6, s_7, s_8) = \begin{bmatrix} G_8^{\Re}(s_1, s_2, s_3, s_4, , s_5, s_6, s_7, s_8) \\ G_8^{\Re}(s_1, s_2, s_3, s_4, , s_5, s_6, s_7, s_8)^* \end{bmatrix}. \tag{6.64}$$

Accordingly, the HR-GN_T-STBC design of $G_{N_T}(s_1, s_2, s_3, s_4, , s_5, s_6, s_7, s_8)$ associated with $5 \leq N_T \leq 7$ may be constructed by taking the first N_T columns in $G_8(s_1, s_2, s_3, s_4, , s_5, s_6, s_7, s_8)$. For the sake of clarity, the parameters of these half-rate STBCs are summarized in Table 6.5.

It may be observed that all the HR-GN_T-STBCs associated with $3 \leq N_T \leq 8$ fail to meet the full unity-rate requirement (R1) of Sec. 6.3.1.1, resulting in a normalized throughput of $\overline{R} =$

HR-STBCs	NO. of TAs	NO. of channel uses	NO. of transmitted symbols
HR-G3-STBC	$N_T = 3$	$N_P = 8$	$N_Q = 4$
HR-G4-STBC	$N_T = 4$	$N_P = 8$	$N_Q = 4$
HR-G5-STBC	$N_T = 5$	$N_P = 16$	$N_Q = 8$
HR-G6-STBC	$N_T = 6$	$N_P = 16$	$N_Q = 8$
HR-G7-STBC	$N_T = 7$	$N_P = 16$	$N_Q = 8$
HR-G8-STBC	$N_T = 8$	$N_P = 16$	$N_Q = 8$

Table 6.5: A summary of the parameters of Half-Rate (HR) STBCs ($\overline{R} = \frac{N_Q}{N_P} = \frac{1}{2}$).

$\frac{N_Q}{N_P} = \frac{1}{2}$. Similarly, the delay optimal requirement (R2) becomes $N_P = 2N_Q$. However, the transmitter's hardware requirement (R3) is still satisfied by the half-rate STBCs. Furthermore, it may be observed that we always have $G_{N_q}(s_1, \cdots, s_{N_Q})^H G_{N_q}(s_1, \cdots, s_{N_Q}) = \sum_{q=1}^{N_Q} 2|s_q|^2 \mathbf{I}_{N_T}$ for $3 \leq N_T \leq 8$ according to the half-rate STBC design, hence the HR-STBC's transmission matrix of Eq. (6.43a) may be expressed as:

$$\mathbf{S} = \sqrt{\frac{N_P}{2N_T N_Q}} G_{N_T}(s_1, \cdots, s_{N_Q}), \tag{6.65}$$

since the power normalization factor of Eq. (6.43) is given by $P_t = \frac{N_P}{2N_T N_Q}$. As a result, the orthogonality requirement (R4) facilitating single-stream detection is fully satisfied by the half-rate STBCs. Therefore, the linear STBC receiver developed in Sec. 6.3.1.1 may also be applied to them. We note that no STBCs having $N_T > 8$ were explicitly constructed in the open literature, but it was proven in [178] that such a design may impose a substantial delay growing exponentially with N_T, which is given by $N_P = 16 \times 16^{(N_T/8-1)}$ for $N_T > 8$ with N_T being a power of 2.

6.3.1.4 Amicable Orthogonal Space-Time Block Code

In order to improve the throughput of STBCs associated with $N_T > 2$, it was demonstrated in [181–183] that rate 3/4 STBC exists for $N_T = 4$. More explicitly, the Amicable Orthogonal (AO)-G4-STBC obtained according to the theory of amicable orthogonal design [179] may be expressed as:

$$G_4^{\text{AO}}(s_1, s_2, s_3) = \begin{bmatrix} s_1 & s_2 & s_3 & 0 \\ -s_2^* & s_1^* & 0 & s_3 \\ -s_3^* & 0 & s_1^* & -s_2 \\ 0 & -s_3^* & s_2^* & s_1 \end{bmatrix}. \tag{6.66}$$

This AO-G4-STBC design complies with the delay optimal requirement of (R2), the transmitter's hardware requirement of (R3) and the orthogonality requirement of (R4), which are listed in Sec. 6.3.1.1. Moreover, an alternative form of AO-G4-STBC design was also presented in

AO-STBCs	NO. of TAs	NO. of channel uses	NO. of transmitted symbols
AO-G3-STBC	$N_T = 3$	$N_P = 4$	$N_Q = 3$
AO-G4-STBC	$N_T = 4$	$N_P = 4$	$N_Q = 3$
AO-G5-STBC	$N_T = 5$	$N_P = 8$	$N_Q = 4$
AO-G6-STBC	$N_T = 6$	$N_P = 8$	$N_Q = 4$
AO-G7-STBC	$N_T = 7$	$N_P = 8$	$N_Q = 4$
AO-G8-STBC	$N_T = 8$	$N_P = 8$	$N_Q = 4$

Table 6.6: A summary of the parameters of Amicable Orthogonal (AO) STBCs.

[178, 293] as:

$$\overline{G}_4^{\text{AO}}(s_1, s_2, s_3) = \begin{bmatrix} s_1 & s_2 & \frac{s_3}{\sqrt{2}} & \frac{s_3}{\sqrt{2}} \\ -s_2^* & s_1^* & \frac{s_3}{\sqrt{2}} & -\frac{s_3}{\sqrt{2}} \\ \frac{s_3^*}{\sqrt{2}} & \frac{s_3^*}{\sqrt{2}} & -\Re(s_1) + j\Im(s_2) & -\Re(s_2) + j\Im(s_1) \\ \frac{s_3^*}{\sqrt{2}} & -\frac{s_3^*}{\sqrt{2}} & \Re(s_2) + j\Im(s_1) & -\Re(s_1) - j\Im(s_2) \end{bmatrix}. \tag{6.67}$$

However, this alternative AO-G4-STBC does not obey the transmitter's hardware requirement of (R3) in Sec. 6.3.1.1, which implies that the linear region of the MIMO's amplifier has to be extended.

The AO-G4-STBC design of Eq. (6.66) is further extended for any values of N_T in [326–328]. In more details, if the number of TAs is a power of 2 as $N_T = 2^\iota$ for a positive integer of $\iota \geq 1$, the general AO-GN_T-STBC design may be formulated as:

$$G_{2^\iota}^{\text{AO}}(s_1, \cdots, s_{\iota+1}) = \begin{bmatrix} G_{2^{\iota-1}}^{\text{AO}}(s_1, \cdots, s_\iota) & s_{\iota+1}\mathbf{I}_{2^{\iota-1}} \\ -s_{\iota+1}^*\mathbf{I}_{2^{\iota-1}} & G_{2^{\iota-1}}^{\text{AO}}(s_1, \cdots, s_\iota)^H \end{bmatrix}. \tag{6.68}$$

It can be seen in Eq. (6.68) that if the AO-STBC design starts from $\iota = 1$ and $G_1^{\text{AO}}(s_1) = s_1$, then Alamouti's G2-STBC of Eq. (6.54) may be obtained from Eq. (6.68) as $G_2^{\text{AO}}(s_1, s_2) = G_2(s_1, s_2)$. Furthermore, based on the G2-STBC of Eq. (6.54), the AO-G4-STBC of Eq. (6.66) may also be constructed by Eq. (6.68). Similarly, for all the cases of AO-GN_T-STBC associated with $N_T = 2^\iota$, the STBC design requirements of (R2), (R3) and (R4) in Sec. 6.3.1.1 are satisfied.

For the scenarios of N_T not being a power of 2, the AO-GN_T-STBC design may be obtained by taking the first N_T columns of $G_{2^{\bar{\iota}}}^{\text{AO}}(s_1, \cdots, s_{\bar{\iota}+1})$, where we have $\bar{\iota} = \lceil \log_2 N_T \rceil$. These AO-STBCs do not obey the delay optimal requirement of (R2) in Sec. 6.3.1.1. Nonetheless, their transmission delay is still substantially lower than that of their HR-STBC counterparts discussed in Sec. 6.3.1.3. For example, the AO-G3-STBC and AO-G4-STBC have $N_P = 4$, while the AO-GN_T-STBC for $5 \leq N_T \leq 8$ have $N_P = 8$, which are halves of the parameters of the HR-STBCs seen in Table 6.5. The parameters of the AO-GN_T-STBC for $3 \leq N_T \leq 8$ are summarized in Table 6.6.

In summary, owing to the fact that we always have $G_{N_T}^{\text{AO}}(s_1, \cdots, s_{N_Q})^H G_{N_T}^{\text{AO}}(s_1, \cdots, s_{N_Q}) = \sum_{q=1}^{N_Q} |s_q|^2 \mathbf{I}_{N_T}$ according to Eq. (6.68), the AO-STBC transmission matrix may be expressed ac-

cording to Eq. (6.43a) as:

$$\mathbf{S} = \sqrt{\frac{N_P}{N_T N_Q}} G_{N_T}^{\text{AO}}(s_1, \cdots, s_{N_Q}), \tag{6.69}$$

where the power normalization factor seen in Eq. (6.43) is given by $P_t = \frac{N_P}{N_T N_Q}$. Since the transmission matrix of Eq. (6.69) satisfies the orthogonality requirement (R4) of Sec. 6.3.1.1, the linear STBC receiver developed in Sec. 6.3.1.1 may be directly invoked for the AO-STBCs.

Furthermore, the number of time slots N_P will not increase exponentially with N_T for the AO-STBC design according to Eq. (6.68), as opposed to the HR-STBCs in Sec. 6.3.1.3. However, it can be observed that the AO-STBCs associated with $5 \leq N_T \leq 7$ also have a normalized throughput of $\overline{R} = \frac{1}{2}$, which is exactly the same as that of their HR-STBCs counterparts of Sec. 6.3.1.3. Moreover, since the AO-STBC's number of transmitted symbols N_Q only increases logarithmically with N_T according to $N_Q = \lceil \log_2 N_T \rceil + 1$, the normalized throughput of AO-STBC is expected to be lower than $\overline{R} = \frac{1}{2}$ for $N_T > 8$.

6.3.1.5 Error Probability and Capacity of Space-Time Block Codes

In Sec. 6.3.1.1, we have discussed how the orthogonal design of STBCs may improve the performance of MIMO systems and how a simple low-complexity linear receiver may be employed for STBC schemes without encountering the BLAST MIMO's problem of inter-antenna interference. However, as demonstrated in the previous sections, the price paid is the reduced MIMO throughput. Except for the classic Alamouti G2-STBC that maintains the maximum attainable throughput of SISO/SIMO systems, the rest of the STBCs employing complex-valued MPSK/QAM constellations all have even lower throughputs. In fact, it was recognized in [184, 189, 301] that STBCs cannot achieve the full MIMO capacity except for a single special case, which is Alamouti's G2-STBC system associated with a single RA $N_R = 1$. Let us now elaborate a little further here on this issue, so that the multiplexing versus diversity tradeoff of MIMO system design may be better augmented.

It is shown by Eq. (6.51) that the STBC detection in fading channels may be transformed into decoupled MPSK/QAM detection in AWGN channels without any performance loss. Therefore, the STBC receiver operates based on the decoupled conditional probability $p(\overline{z}_q|s_q)$ of Eq. (6.52), which implies that the equivalent input/output relationship may now be formulated as:

$$\overline{z}_q = s_q + \overline{v}_q, \quad 1 \leq q \leq N_Q, \tag{6.70}$$

where $\overline{v}_q$ models a complex Gaussian variable having a zero mean and a variance of $\overline{N}_0 = \frac{N_T N_Q}{N_P \|\mathbf{H}\|^2} N_0$ according to Eq. (6.52). Considering that the average BER of Eq. (6.8) is approximated based on the evaluation of the PEP, which is only accurate in the high-SNR region, the error probability of the STBC in fading channels may be more closely evaluated by the performance of MPSK/QAM schemes in AWGN channels [2, 3], as summarized in Table 6.7.

It is worth noting that the STBCs that minimize the PEP's union bound of Eq. (6.10) have a dominant performance advantage in the high SNR region. For STBCs that require a high number

MPSK/QAM	Approximate Bit Error Probability
BPSK	$\overline{P}_{e,bit} = Q\left(\sqrt{\frac{2}{\overline{N}_0}}\right)$
QPSK	$\overline{P}_{e,bit} = Q\left(\sqrt{\frac{1}{\overline{N}_0}}\right)$
General MPSK	$\overline{P}_{e,bit} \approx \frac{2}{\text{BPS}} Q\left[\sqrt{\frac{2}{\overline{N}_0}}\sin(\frac{\pi}{M})\right]$
Square 16QAM	$\overline{P}_{e,bit} = \frac{3}{4}Q\left(\sqrt{\frac{1}{5\overline{N}_0}}\right) + \frac{1}{2}Q\left(3\sqrt{\frac{1}{5\overline{N}_0}}\right) - \frac{1}{4}Q\left(5\sqrt{\frac{1}{5\overline{N}_0}}\right)$
General MQAM	$\overline{P}_{e,bit} \approx \frac{4}{\text{BPS}} Q\left[\sqrt{\frac{3}{(M-1)\overline{N}_0}}\right]$

Table 6.7: A summary of the approximate bit error probability for STBC employing MPSK/QAM.

of time slots N_P, there is no guarantee that their performance - given the noise power normalized per channel use - can always be better than that of other MIMO schemes in the low-SNR region. We will continue this discussion in Sec. 6.5 related to our performance results.

According to the equivalent input/output relationship of Eq. (6.70), the maximized mutual information of STBC is given by:

$$\begin{aligned} C_{STBC}^{CCMC}(SNR) &= \max_{\{p(s_q)\}_{q=1}^{N_Q}} \frac{1}{N_P}\sum_{q=1}^{N_Q} I(s_q;\overline{z}_q) \\ &= \max_{\{p(s_q)\}_{q=1}^{N_Q}} \frac{1}{N_P}\sum_{q=1}^{N_Q} \left[H(\overline{z}_q) - H(\overline{z}_q|s_q)\right] \\ &= \frac{N_Q}{N_P}\text{E}\left[\log_2\left(1+\frac{N_P\|\mathbf{H}\|^2}{N_T N_Q}\eta\right)\right], \end{aligned} \tag{6.71}$$

where we have $H(\overline{z}_q|s_q) = \log_2\left[\pi e\left(\frac{N_T N_Q}{N_P\|\mathbf{H}\|^2}N_0\right)\right]$ and $H(\overline{z}_q) = \log_2\left[\pi e\left(1+\frac{N_T N_Q}{N_P\|\mathbf{H}\|^2}N_0\right)\right]$ according to $p(\overline{z}_q|s_q)$ of Eq. (6.52) and the assumption of Gaussian input PDFs $\{p(s_q)\}_{q=1}^{N_Q}$.

Considering a V-BLAST MIMO system equipped with N_T' and N_R' antennas operating at an SNR of η', the term of $\frac{\eta'}{N_T'}\mathbf{H}'^H\mathbf{H}'$ in the MIMO capacity of Eq. (6.4) can only be equal to the term of $\frac{N_P\|\mathbf{H}\|^2}{N_T N_Q}\eta$ in the STBC capacity of Eq. (6.71), when we have $N_T' = N_T N_R$, $N_R' = 1$ and $\eta' = \frac{N_R N_P}{N_Q}\eta$. In other words, the relationship between the STBC capacity and the V-BLAST MIMO capacity may be expressed as [184, 189, 301]:

$$\begin{aligned} C_{STBC}^{CCMC}(N_T, N_R, \eta) &= \frac{N_Q}{N_P} C_{MIMO}^{CCMC}(N_T N_R, 1, \frac{N_R N_P}{N_Q}\eta) \\ &\leq C_{MIMO}^{CCMC}(N_T, N_R, \eta), \end{aligned} \tag{6.72}$$

where the equality only holds, when we have $N_T = N_P = N_Q$ and $N_R = 1$, which may only be satisfied by Alamouti G2-STBC scheme equipped with a single RA of $N_R = 1$.

It becomes clear now that there is a tradeoff amongst the conflicting capacity, performance and complexity in MIMO systems design. More explicitly, the V-BLAST MIMO introduced in Sec. 6.2 achieves the maximum attainable MIMO throughput that is N_T times higher than a SISO/SIMO system throughput. By contrast, the STBC MIMO introduced in Sec. 6.3.1 minimizes the MIMO's

PEP bound and benefits from a low signal processing complexity at the receiver, but it cannot achieve the maximum achievable MIMO capacity. Motivated by improving the capacity limit of STBCs, we embark on introducing the concept of LDCs in the next section, which are capable of resolving the tradeoff between a diversity gain and a multiplexing gain.

6.3.2 Linear Dispersion Codes

In this section, we firstly introduce the family of Quasi-Orthogonal (QO)-STBCs [186, 187, 328–332] as the intermediate step for improving the STBC capacity, which can only be achieved by relaxing the orthogonality requirements detailed in Sec. 6.3.1.1. In Sec. 6.3.2.2, the STBC capacity is further improved by the high-rate LDC design philosophy of [189] proposing to randomly populate the dispersion matrices of Eq. (6.43) in order to find the specific set, which maximizes the CCMC capacity. However, we will also demonstrate in Sec. 6.3.2.2 that the LDCs of [189], which separately disperse the real and imaginary parts of the modulated symbols fail to achieve the maximum attainable MIMO capacity. In order to mitigate this problem, the set of so-called capacity-achieving LDCs proposed in [188, 300] are summarized in Sec. 6.3.2.3, where the MIMO capacity may be approached, while attaining a beneficial diversity gain.

6.3.2.1 Quasi-Orthogonal Space-Time Block Codes

In order to improve the attainable STBC throughput, the first step is to relax the orthogonality requirement of Sec. 6.3.1.1 at the cost of encountering IAI and hence requiring multi-stream detection. In the light of this principle, the concept of QO-STBC design was proposed in [186, 329]. In more details, provided that the number of TAs is a power of 2 according to $N_T = 2^\iota$ and ($\iota > 1$), the QO-STBC transmission codeword is constructed from the AO-STBC of Eq. (6.68) as [186, 328]:

$$G_{2^\iota}^{QO}(s_1, \cdots, s_{2\iota}) = \begin{bmatrix} G_{2^{\iota-1}}^{AO}(s_1, \cdots, s_\iota) & G_{2^{\iota-1}}^{AO}(s_{\iota+1}, \cdots, s_{2\iota}) \\ -G_{2^{\iota-1}}^{AO}(s_{\iota+1}, \cdots, s_{2\iota})^* & G_{2^{\iota-1}}^{AO}(s_1, \cdots, s_\iota)^* \end{bmatrix}. \tag{6.73}$$

It can be seen that the term $s_{\iota+1}\mathbf{I}_{2^{\iota-1}}$ that can only transmit a single modulated symbol in the context of the AO-STBC design of Eq. (6.68) is replaced by the term $G_{2^{\iota-1}}^{AO}(s_{\iota+1}, \cdots, s_{2\iota})$ that may transmit ι symbols in conjunction with the QO-STBC design of Eq. (6.73). As a result, for any number of TAs, the normalized throughput of QO-STBC is increased to $\overline{R} = \frac{2\bar{\iota}}{2^{\bar{\iota}}}$, where we have $\bar{\iota} = \lceil \log_2 N_T \rceil$.

It may be observed in Eq. (6.73) that we always have $\text{tr}\left[G_{2^\iota}^{QO}(s_1, \cdots, s_{2\iota})^H G_{2^\iota}^{QO}(s_1, \cdots, s_{2\iota})\right] = N_T(\sum_{q=1}^{N_Q} |s_q|^2)$. Therefore, the power normalization factor of Eq. (6.43a) is given by $P_t = \frac{N_P}{N_T N_Q}$, and the QO-STBC transmission matrix may be formulated as:

$$\mathbf{S} = \sqrt{\frac{N_P}{N_T N_Q}} G_{2^\iota}^{QO}(s_1, \cdots, s_{2\iota}), \tag{6.74}$$

so that the power constaint of $\text{E}\left[\text{tr}(\mathbf{S}^H\mathbf{S})\right] = N_P$ may be satisfied. However, the orthogonality requirement of (R4) in Sec. 6.3.1.1 cannot be satisfied, because the columns in $G_{2^{\iota-1}}^{AO}(s_1, \cdots, s_\iota)$

and the columns in $G_{2^{\iota-1}}^{AO}(s_{\iota+1}, \cdots, s_{2\iota})$ are not orthognal to each other, despite the fact that the columns are orthogonal within each transmission sub-group.

Let us consider the case of $N_T = 4$ as an example, where a full unity-rate of $\overline{R} = 1$ is achieved. According to the codeword construction of Eq. (6.73), the QO-G4-STBC transmission matrix of Eq. (6.74) is given by [186, 328]:

$$\mathbf{S} = \frac{1}{2}\begin{bmatrix} G_2(s_1, s_2) & G_2(s_3, s_4) \\ -G_2(s_3, s_4)^* & G_2(s_1, s_2)^* \end{bmatrix} = \frac{1}{2}\begin{bmatrix} s_1 & s_2 & s_3 & s_4 \\ -s_2^* & s_1^* & -s_4^* & s_3^* \\ -s_3^* & -s_4^* & s_1^* & s_2^* \\ s_4 & -s_3 & -s_2 & s_1 \end{bmatrix}. \tag{6.75}$$

Therefore, according to Eq. (6.75), the maximum throughput requirement (R1), the delay optimal requirement (R2) and the transmitter's hardware requirement (R3) listed in Sec. 6.3.1.1 are all satisfied by the QO-G4-STBC associated with $N_T = N_P = N_Q = 4$. However, the orthogonality requirement of (R4) in Sec. 6.3.1.1 is violated because:

$$\mathbf{S}^H\mathbf{S} = \begin{bmatrix} \frac{\sum_{q=1}^4 |s_q|^2}{4} & 0 & 0 & \frac{\Re(s_1 s_4^* - s_2 s_3^*)}{2} \\ 0 & \frac{\sum_{q=1}^4 |s_q|^2}{4} & -\frac{\Re(s_1 s_4^* - s_2 s_3^*)}{2} & 0 \\ 0 & -\frac{\Re(s_1 s_4^* - s_2 s_3^*)}{2} & \frac{\sum_{q=1}^4 |s_q|^2}{4} & 0 \\ \frac{\Re(s_1 s_4^* - s_2 s_3^*)}{2} & 0 & 0 & \frac{\sum_{q=1}^4 |s_q|^2}{4} \end{bmatrix} \tag{6.76}$$

is not a scaled identity matrix. As a result, the linear STBC receiver developed in Sec. 6.3.1.1 cannot be invoked for QO-STBC systems. Nonetheless, the QO-STBC receiver still has a lower detection complexity than the conventional MIMO receiver. More specifically, the decision metric of the ML MIMO detection of Eq. (6.13) may be extended for QO-G4-STBCs as:

$$\begin{aligned} \|\mathbf{Y} - \mathbf{SH}\|^2 = \|\mathbf{Y}\|^2 - \sum_{q=1}^4 \Re\left\{ \mathrm{tr}\left[\mathbf{Y}^H \mathbf{D}_q^+ \mathbf{H} + \mathbf{H}^H \left(\mathbf{D}_q^-\right)^H \mathbf{Y}\right] s_q - \frac{|s_q|^2}{4}\|\mathbf{H}\|^2 \right\} \\ + \Re(s_1 s_4^* - s_2 s_3^*)\Re\left[(\mathbf{H}_{1,-})(\mathbf{H}_{4,-})^H - (\mathbf{H}_{2,-})(\mathbf{H}_{3,-})^H\right], \end{aligned} \tag{6.77}$$

where the extra term of $\Re(s_1 s_4^* - s_2 s_3^*)\Re\left[(\mathbf{H}_{1,-})(\mathbf{H}_{4,-})^H - (\mathbf{H}_{2,-})(\mathbf{H}_{3,-})^H\right]$ introduces interference compared to the case of orthognal design in Eq. (6.49). In order to retain the ML detection capability of Eq. (6.13), the four symbols have to be detected in pairs as:

$$\begin{aligned} \{\hat{s}_1, \hat{s}_4\} = \arg \min_{\forall s_1, \forall s_4} \sum_{q=1\&q=4} \Re\left\{ \frac{|s_q|^2}{4}\|\mathbf{H}\|^2 - \mathrm{tr}\left[\mathbf{Y}^H \mathbf{D}_q^+ \mathbf{H} + \mathbf{H}^H \left(\mathbf{D}_q^-\right)^H \mathbf{Y}\right] s_q \right\} \\ + \Re(s_1 s_4^*)\Re\left[(\mathbf{H}_{1,-})(\mathbf{H}_{4,-})^H - (\mathbf{H}_{2,-})(\mathbf{H}_{3,-})^H\right], \\ \{\hat{s}_2, \hat{s}_3\} = \arg \min_{\forall s_2, \forall s_3} \sum_{q=2\&q=3} \Re\left\{ \frac{|s_q|^2}{4}\|\mathbf{H}\|^2 - \mathrm{tr}\left[\mathbf{Y}^H \mathbf{D}_q^+ \mathbf{H} + \mathbf{H}^H \left(\mathbf{D}_q^-\right)^H \mathbf{Y}\right] s_q \right\} \\ - \Re(s_2 s_3^*)\Re\left[(\mathbf{H}_{1,-})(\mathbf{H}_{4,-})^H - (\mathbf{H}_{2,-})(\mathbf{H}_{3,-})^H\right]. \end{aligned} \tag{6.78}$$

It was suggested in [187, 329] that linear MIMO receivers such as the MMSE detector or the ZF detector may be invoked for QO-STBC systems. However, this may not be an ideal solution because

the sub-optimal linear MIMO receivers fail to fully exploit QO-STBC's diversity gain. Moreover, a lot of research efforts [187, 328, 330–332] have been dedicated to improving both the capacity and the performance of QO-STBC designs by modifying the signal constellations. Nonetheless, the QO-STBC serves as an intermediate solution between the STBC and V-BLAST MIMO design, while the STBC's limitations imposed on the capacity and throughput have not been completely solved. In the following section, we continue by introducing the concept of LDC, which aims for systematically bridging the gap between the STBC and V-BLAST.

6.3.2.2 Capacity-Improving Linear Dispersion Codes

Motivated by the limitations of STBCs, the LDC concept was proposed in [189] in order to improve the STBC's capacity, while attaining the maximum achievable diversity order. First of all, the STBC's transmission matrix model of Eq. (6.43) may be rewritten for LDCs as:

$$\mathbf{S} = \sum_{q=1}^{N_Q} \left[\overline{\mathbf{A}}_q \Re(s_q) + j\overline{\mathbf{B}}_q \Im(s_q) \right], \tag{6.79}$$

where the dispersion matrices $\{\overline{\mathbf{A}}_q\}_{q=1}^{N_Q}$ and $\{\overline{\mathbf{B}}_q\}_{q=1}^{N_Q}$ are constructed according to our capacity-improving and diversity-maintaining requirements, which will be detailed later. Moreover, $\{s_q\}_{q=1}^{N_Q}$ represent modulated MPSK/QAM symbols, which are dispersed in both the spatial domain and time domain by the dispersion matrices of Eq. (6.79). We note that the transmission model of Eq. (6.79) may include both the STBC and V-BLAST schemes, where the dispersion matrices of Eq. (6.79) are normalized version of those introduced in Sec. 6.3.1.1, so that the power constraint of $\mathrm{E}\left[\mathrm{tr}(\mathbf{S}^H\mathbf{S})\right] = N_P$ may be satisfied.

In order to overcome the throughput disadvantage of STBCs, the number of transmitted symbols N_Q may be increased even beyond N_P, so that the V-BLAST throughput may be approached. Furthermore, the LDCs are still suggested to maintain $N_T = N_P$ in order to retain the maximum attainable transmit diversity order at the lowest transmission delay. According to the MIMO received signal model of Eq. (6.1), the LDC's signal received during the t-th time slot ($1 \leq t \leq N_P$) may be expressed as:

$$\mathbf{Y}_{t,-} = \sum_{q=1}^{N_Q} \left[\overline{\mathbf{A}}_q^{t,-} \mathbf{H} \Re(s_q) + j\overline{\mathbf{B}}_q^{t,-} \mathbf{H} \Im(s_q) \right] + \mathbf{V}_{t,-}, \tag{6.80}$$

where the $(1 \times N_R)$-element row vectors $\{\mathbf{Y}_{t,-}\}_{t=1}^{N_P}$ and $\{\mathbf{V}_{t,-}\}_{t=1}^{N_P}$ are taken from the received signal matrix $\mathbf{Y}$ and the AWGN matrix $\mathbf{V}$ in Eq. (6.1), respectively. Moreover, the $(1 \times N_T)$-element row vectors $\{\overline{\mathbf{A}}_q^{t,-}\}_{t=1}^{N_P}$ and $\{\overline{\mathbf{B}}_q^{t,-}\}_{t=1}^{N_P}$ are taken from the dispersion matrices of Eq. (6.79). Let us now decouple the real and imaginary parts of the received signal in Eq. (6.80) as:

$$\begin{aligned}
\Re(\mathbf{Y}_{t,-}) &= \sum_{q=1}^{N_Q} \left\{ \left[\Re(\overline{\mathbf{A}}_q^{t,-}) \Re(\mathbf{H}) - \Im(\overline{\mathbf{A}}_q^{t,-}) \Im(\mathbf{H}) \right] \Re(s_q) - \left[\Re(\overline{\mathbf{B}}_q^{t,-}) \Im(\mathbf{H}) + \Im(\overline{\mathbf{B}}_q^{t,-}) \Re(\mathbf{H}) \right] \Im(s_q) \right\} + \Re(\mathbf{V}_{t,-}), \\
\Im(\mathbf{Y}_{t,-}) &= \sum_{q=1}^{N_Q} \left\{ \left[\Re(\overline{\mathbf{A}}_q^{t,-}) \Im(\mathbf{H}) + \Im(\overline{\mathbf{A}}_q^{t,-}) \Re(\mathbf{H}) \right] \Re(s_q) + \left[\Re(\overline{\mathbf{B}}_q^{t,-}) \Re(\mathbf{H}) - \Im(\overline{\mathbf{B}}_q^{t,-}) \Im(\mathbf{H}) \right] \Im(s_q) \right\} + \Im(\mathbf{V}_{t,-}),
\end{aligned} \tag{6.81}$$

which leads to the following equivalent received signal model for the LDC of Eq. (6.79) as:

$$\widetilde{\mathbf{Y}} = \widetilde{\mathbf{S}} \cdot \widetilde{\chi} \cdot \widetilde{\mathbf{H}} + \widetilde{\mathbf{V}}, \tag{6.82}$$

where the matrices are given by:

$$\begin{aligned}
&\widetilde{\mathbf{Y}} = [\Re\{\text{rvec}(\mathbf{Y})\}, \Im\{\text{rvec}(\mathbf{Y})\}], \qquad \widetilde{\mathbf{S}} = \left[\Re(s_1), \cdots, \Re(s_{N_Q}), \Im(s_1), \cdots, \Im(s_{N_Q})\right], \\
&\widetilde{\chi} = \begin{bmatrix}
\Re\{\text{rvec}(\overline{\mathbf{A}}_1)\}, & \Im\{\text{rvec}(\overline{\mathbf{A}}_1)\} \\
\vdots & \vdots \\
\Re\{\text{rvec}(\overline{\mathbf{A}}_{N_Q})\}, & \Im\{\text{rvec}(\overline{\mathbf{A}}_{N_Q})\} \\
-\Im\{\text{rvec}(\overline{\mathbf{B}}_1)\}, & \Re\{\text{rvec}(\overline{\mathbf{B}}_1)\} \\
\vdots & \vdots \\
-\Im\{\text{rvec}(\overline{\mathbf{B}}_{N_Q})\}, & \Re\{\text{rvec}(\overline{\mathbf{B}}_{N_Q})\}
\end{bmatrix}, \qquad \widetilde{\mathbf{H}} = \begin{bmatrix}
\mathbf{I}_{N_P} \otimes \Re(\mathbf{H}) & \mathbf{I}_{N_P} \otimes \Im(\mathbf{H}) \\
-\mathbf{I}_{N_P} \otimes \Im(\mathbf{H}) & \mathbf{I}_{N_P} \otimes \Re(\mathbf{H})
\end{bmatrix}, \\
&\qquad\qquad\qquad\qquad\qquad\qquad \widetilde{\mathbf{V}} = [\Re\{\text{rvec}(\mathbf{V})\}, \Im\{\text{rvec}(\mathbf{V})\}].
\end{aligned} \tag{6.83}$$

If the fading channels are assumed to be known at the receiver, then the general ML MIMO detection may be reformulated for LDCs as:

$$\hat{\widetilde{\mathbf{S}}} = \arg \min_{\forall \widetilde{\mathbf{S}}^i} \|\widetilde{\mathbf{Y}} - \widetilde{\mathbf{S}}^i \cdot \widetilde{\chi} \cdot \widetilde{\mathbf{H}}\|^2, \tag{6.84}$$

where the equivalent dispersion matrix $\widetilde{\chi}$ is known to both the transmitter and receiver. According to the transmit power constraint, we always have $\text{tr}(\widetilde{\chi}^T \widetilde{\chi}) = 2N_P$. It is also worth noting that there is a total number of $I = M^{N_Q}$ combinations for the LDC codeword of $\{\widetilde{\mathbf{S}}^i\}_{i=0}^{I-1}$ in Eq. (6.84).

It can be seen in Eq. (6.82) that the equivalent LDC received signal model is the same as the V-BLAST received signal model of Eq. (6.1), where the LDC's equivalent fading channels matrix is given by $\widetilde{\chi} \cdot \widetilde{\mathbf{H}}$. Therefore, the LDC's ML detection of Eq. (6.94) may also be solved by the SD or by the sub-optimal linear V-BLAST detectors (e.g. MMSE/ZF) introduced in Sec. 6.2.

According to the LDC's input-output relationship of Eq. (6.82), the CCMC capacity of the LDC is given by:

$$\begin{aligned}
C_{LDC}^{CCMC}(SNR) &= \max_{p(\widetilde{\mathbf{S}})} \frac{1}{2N_P} H(\widetilde{\mathbf{Y}}) - \frac{1}{2N_P} H(\widetilde{\mathbf{Y}}|\widetilde{\mathbf{S}}) \\
&= \frac{1}{2N_P} \text{E}\left[\log_2 \det\left(\mathbf{I}_{2N_P N_R} + \eta \widetilde{\mathbf{H}}^T \widetilde{\chi}^T \widetilde{\chi} \widetilde{\mathbf{H}}\right)\right],
\end{aligned} \tag{6.85}$$

where the entropies are given by $H(\widetilde{\mathbf{Y}}) = \log_2 \det\left(\frac{\pi e}{2} \widetilde{\mathbf{H}}^T \widetilde{\chi}^T \widetilde{\chi} \widetilde{\mathbf{H}} + \frac{\pi e N_0}{2} \mathbf{I}_{2N_P N_R}\right)$ and $H(\widetilde{\mathbf{Y}}|\widetilde{\mathbf{S}}) = H(\widetilde{\mathbf{V}}) = \log_2 \det\left(\frac{\pi e N_0}{2} \mathbf{I}_{2N_P N_R}\right)$. We note that the CCMC capacity of virtually all MIMO schemes, whose transmission matrix may be expressed in the form of Eq. (6.79), may be evluated by Eq. (6.85).

Obviously, when $\widetilde{\chi}$ is a scaled unitary matrix formulated as:

$$\widetilde{\chi}^T \widetilde{\chi} = \frac{1}{N_T} \mathbf{I}_{2N_T N_P}, \tag{6.86}$$

the CCMC capacity of the LDC in Eq. (6.85) may achieve its highest possible value of:

$$C_{LDC}^{CCMC}(SNR) = \frac{1}{2N_P} \text{E}\left[\log_2 \det\left(\mathbf{I}_{2N_P N_R} + \frac{\eta}{N_T} \widetilde{\mathbf{H}}^T \widetilde{\mathbf{H}}\right)\right]. \tag{6.87}$$

Furthermore, it may be readily seen that the LDC's capacity of Eq. (6.87) may achieve the maximum MIMO capacity of Eq. (6.4), if and only if we have $\widetilde{\mathbf{H}}^T\widetilde{\mathbf{H}} = \mathbf{I}_{2N_P} \otimes (\mathbf{H}^H\mathbf{H})$. Unfortunately, this is only true when a single RA $N_R = 1$ is used. This is because the term of $\widetilde{\mathbf{H}}^T\widetilde{\mathbf{H}}$ in Eq. (6.87) may be extended as:

$$\widetilde{\mathbf{H}}^T\widetilde{\mathbf{H}} = \begin{bmatrix} \mathbf{I}_{N_P} \otimes \left[\Re(\mathbf{H}^T)\Re(\mathbf{H}) + \Im(\mathbf{H}^T)\Im(\mathbf{H})\right] & \mathbf{I}_{N_P} \otimes \left[\Re(\mathbf{H}^T)\Im(\mathbf{H}) - \Im(\mathbf{H}^T)\Re(\mathbf{H})\right] \\ \mathbf{I}_{N_P} \otimes \left[\Im(\mathbf{H}^T)\Re(\mathbf{H}) - \Re(\mathbf{H}^T)\Im(\mathbf{H})\right] & \mathbf{I}_{N_P} \otimes \left[\Re(\mathbf{H}^T)\Re(\mathbf{H}) + \Im(\mathbf{H}^T)\Im(\mathbf{H})\right] \end{bmatrix}, \tag{6.88}$$

which only becomes equal to $\mathbf{I}_{2N_P} \otimes (\mathbf{H}^H\mathbf{H})$, when we have $\Re(\mathbf{H}^T)\Im(\mathbf{H}) = \Im(\mathbf{H}^T)\Re(\mathbf{H})$ for $N_R = 1$. In summary, the relationship between the LDC capacity of Eq. (6.87) and the MIMO capacity of Eq. (6.4) may be expressed as $C_{LDC}^{CCMC}(SNR) \leq C_{MIMO}^{CCMC}(SNR)$, where the equality only holds for $N_R = 1$.

Nonetheless, the LDC capacity is expected to be higher than STBC capacity summarized in Sec. 6.3.1.5. Considering Alamouti's classic G2-STBC as an example, according to Eq. (6.56), the equivalent dispersion matrix $\widetilde{\chi}$ is given by:

$$\widetilde{\chi} = \begin{bmatrix} \frac{1}{\sqrt{2}} & 0 & 0 & \frac{1}{\sqrt{2}} & 0 & 0 & 0 & 0 \\ 0 & \frac{1}{\sqrt{2}} & -\frac{1}{\sqrt{2}} & 0 & 0 & 0 & 0 & 0 \\ 0 & 0 & 0 & 0 & \frac{1}{\sqrt{2}} & 0 & 0 & -\frac{1}{\sqrt{2}} \\ 0 & 0 & 0 & 0 & 0 & \frac{1}{\sqrt{2}} & \frac{1}{\sqrt{2}} & 0 \end{bmatrix}, \tag{6.89}$$

and it may be readily seen that it does not have orthogonal columns, since we have $\widetilde{\chi}^T\widetilde{\chi} \neq \frac{1}{2}\mathbf{I}_8$. We also note that it is straightforward to prove that the capacity of Alamouti's G2-STBC evaluated by Eq. (6.85) based on the equivalent LDC dispersion matrix of Eq. (6.89) is exactly the same as that calculated by Eq. (6.71).

In fact, in order to guarantee that the LDC's equivalent dispersion matrix $\widetilde{\chi}$ has orthogonal columns as specified by Eq. (6.86), we may have $N_Q \geq N_T N_P$. Considering that further increasing N_Q will inevitably reduce the codewords' difference $\|\mathbf{S}^i - \mathbf{S}^{\bar{i}}\|$, which degrades the PEP of Eq. (6.9), the LDC design is suggested to satisfy $N_Q = N_T N_P$. Owing to the earlier suggestion of $N_T = N_P$ recommended owing to its diversity and delay benefits, the LDC may achieve the throughput of $R = \frac{N_Q}{N_P}$BPS $= N_T$BPS, which is exactly the same as the V-BLAST throughput.

In summary, according to Eq. (6.86), the LDC dispersion matrix $\widetilde{\chi}$ may be randomly generated as a $(2N_Q \times 2N_Q)$-element unitary matrix scaled by $\frac{1}{\sqrt{N_T}}$, so that the CCMC capacity is maximized. Moreover, in order to also retain the maximum attainable diversity order, the randomly generated dispersion matrix should have a full rank for all $\mathbf{\Delta} = (\mathbf{S}^i - \mathbf{S}^{\bar{i}})^H(\mathbf{S}^i - \mathbf{S}^{\bar{i}})$ in Eq. (6.10c). Since it is also important to maximize the coding gain in Eq. (6.10c), the optimum LDC dispersion matrix chosen from random search should satisfy:

$$\max \ \{\det(\mathbf{\Delta})\}_{\min}, \tag{6.90}$$

where $\{\det(\mathbf{\Delta})\}_{\min}$ is the minimum determinant $\det(\mathbf{\Delta})$ among all legitimate $\mathbf{\Delta}$ values for a randomly generated $\widetilde{\chi}$. Further developments on LDC codeword generation may be found in

[190–194], which also tackle the problem of having a diminishing distance between legitimate codewords, when aiming for the high-throughput LDC codeword generation. Nonetheless, the random generation according to the above design guidelines is sufficiently effective for producing good LDCs that achieve both a multiplexing gain and a diversity gain.

6.3.2.3 Capacity-Achieving Linear Dispersion Codes

In order to achieve the maximum attainable MIMO capacity, it was proposed in [188] that the LDC's dispersion matrices in Eq. (6.79) should satisfy $\{\overline{\mathbf{A}}_q = \overline{\mathbf{B}}_q\}_{q=1}^{N_Q}$, just like the V-BLAST characterized in Eq. (6.44), so that the real and imaginary parts of the modulated MPSK/QAM symbols may be dispersed together as:

$$\mathbf{S} = \sum_{q=1}^{N_Q} \left[\overline{\mathbf{A}}_q s_q\right]. \tag{6.91}$$

In this way, the real and the imaginary parts of the received signal model do not have to be decoupled, as seen in Eq. (6.82). Instead, vectorizing the received MIMO signal matrix $\mathbf{Y}$ of Eq. (6.1) leads to the new received LDC signal model of:

$$\overline{\mathbf{Y}} = \overline{\mathbf{S}} \cdot \overline{\chi} \cdot \overline{\mathbf{H}} + \overline{\mathbf{V}}, \tag{6.92}$$

where the matrices are given by:

$$\overline{\chi} = \begin{bmatrix} \text{rvec}(\overline{\mathbf{A}}_1) \\ \vdots \\ \text{rvec}(\overline{\mathbf{A}}_{N_Q}) \end{bmatrix}, \quad \begin{aligned} &\overline{\mathbf{Y}} = \text{rvec}(\mathbf{Y}), \quad \overline{\mathbf{S}} = [s_1, \cdots, s_{N_Q}], \\ &\overline{\mathbf{H}} = \mathbf{I}_{N_P} \otimes \mathbf{H}, \quad \overline{\mathbf{V}} = \text{rvec}(\mathbf{V}). \end{aligned} \tag{6.93}$$

It can be seen that the new LDC's received signal model of Eq. (6.92) is equivalent to that of an V-BLAST system equipped with N_Q TAs and $N_R N_P$ RAs. Therefore, all the V-BLAST detectors introduced in Sec. 6.2 may be invoked for LDC detection, where the equivalent multiplexed transmitted symbol vector and the fading channel matrix of the V-BLAST system are given by $\frac{1}{\sqrt{N_Q}}\overline{\mathbf{S}}$ and $\sqrt{N_Q}\overline{\chi}\overline{\mathbf{H}}$, respectively. More specifically, the ML detection seen in Eq. (6.13) for V-BLAST may be invoked for LDC in the form of:

$$\hat{\overline{\mathbf{S}}} = \arg \min_{\forall \overline{\mathbf{S}}^i} \|\overline{\mathbf{Y}} - \overline{\mathbf{S}}^i \cdot \overline{\chi} \cdot \overline{\mathbf{H}}\|^2, \tag{6.94}$$

where the equivalent dispersion matrix $\overline{\chi}$ is known to both the transmitter and receiver, while there is a total number of $I = M^{N_Q}$ combinations for the LDC's transmission matrix $\{\overline{\mathbf{S}}^i\}_{i=0}^{I-1}$. The LDC transceiver is summarized in the schematic diagram of Fig. 6.5.

According to the new input-output relationship of Eq. (6.92), the CCMC capacity of the LDC model of Eq. (6.91) is given by:

$$\begin{aligned} C_{LDC}^{CCMC}(SNR) &= \max_{p(\overline{\mathbf{S}})} \frac{1}{N_P} H(\overline{\mathbf{Y}}) - \frac{1}{N_P} H(\overline{\mathbf{Y}}|\overline{\mathbf{S}}) \\ &= \frac{1}{N_P} \text{E}\left[\log_2 \det\left(\mathbf{I}_{N_P N_R} + \eta \overline{\mathbf{H}}^H \overline{\chi}^H \overline{\chi} \overline{\mathbf{H}}\right)\right], \end{aligned} \tag{6.95}$$

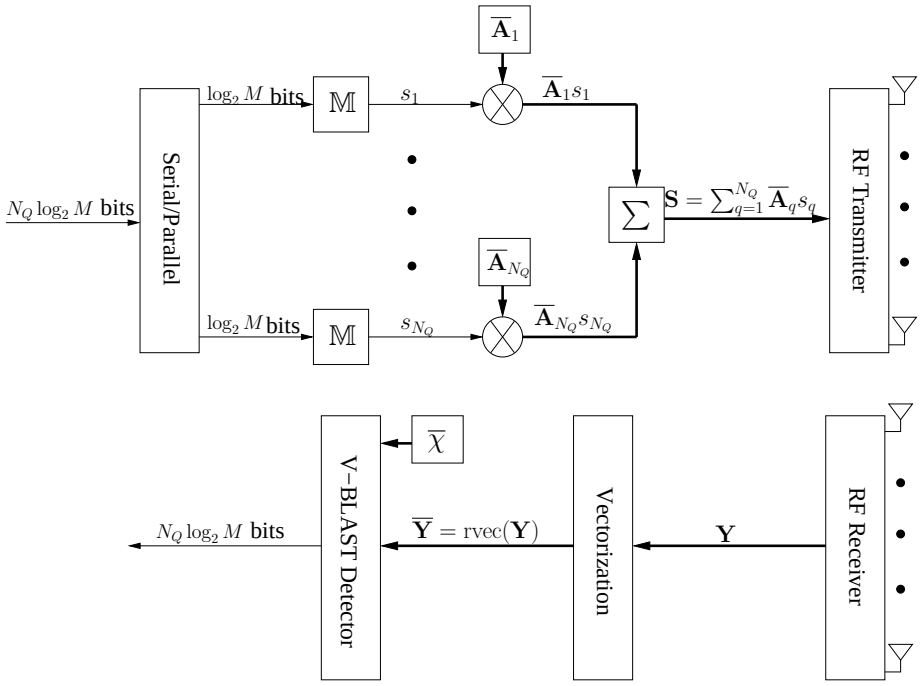

Figure 6.5: Schematic of the optimized LDC transceiver.

where the related entropies are given by $H(\overline{\mathbf{Y}}) = \log_2 \det\left(\pi e \overline{\mathbf{H}}^H \overline{\chi}^H \overline{\chi} \overline{\mathbf{H}} + \pi e N_0 \mathbf{I}_{N_P N_R}\right)$ and $H(\overline{\mathbf{Y}}|\overline{\mathbf{S}}) = H(\overline{\mathbf{V}}) = \log_2 \det\left(\pi e N_0 \mathbf{I}_{N_P N_R}\right)$. It can be seen in Eq. (6.95) that the CCMC capacity is maximized when the equivalent dispersion matrix $\overline{\chi}$ has orthogonal columns as represented by:

$$\overline{\chi}^H \overline{\chi} = \frac{1}{N_T} \mathbf{I}_{N_T N_P}, \tag{6.96}$$

which is scaled according to the power constraint of $\mathrm{E}\left[\mathrm{tr}(\mathbf{S}^H \mathbf{S})\right] = N_P$. As a result, the CCMC capacity of Eq. (6.95) becomes:

$$\begin{aligned} C_{LDC}^{CCMC}(SNR) &= \frac{1}{N_P} \mathrm{E}\left\{ \log_2 \det\left[\mathbf{I}_{N_P N_R} + \frac{\eta}{N_T} (\mathbf{I}_{N_P} \otimes \mathbf{H})^H (\mathbf{I}_{N_P} \otimes \mathbf{H}) \right] \right\} \\ &= \mathrm{E}\left[\log_2 \det(\mathbf{I}_{N_R} + \frac{\eta}{N_T} \mathbf{H}^H \mathbf{H}) \right], \end{aligned} \tag{6.97}$$

which is exactly the same as the full MIMO capacity of Eq. (6.4). Therefore, in order to avoid any ambiguity, the terminology of LDCs may generally refer to the capacity-achieving model of Eq. (6.91), rather than to the conventional model of Eq. (6.79).

We note that Eq. (6.96) requires $N_Q \geq N_T N_P$. Hence, for the case of full transmit diversity associated with $N_T = N_P$, $N_Q = N_T N_P$ leads to the LDC throughput being the same as the V-BLAST throughput of $R = N_T$BPS. Similar to the discussions in Sec. 6.3.2.2, the generation of LDCs may follow the guidelines of maximizing the CCMC capacity of Eq. (6.95) and of minimizing the PEP of Eq. (6.9), which may be summarized as:

(1) Randomly generate a unitary matrix χ of size $(N \times N)$, where we have $N = \max(N_Q, N_T N_P)$.

(a) If $N_Q > N_T N_P$ is required, the LDC dispersion matrix is given by taking the first $N_T N_P$ columns of the scaled unitary matrix as $\overline{\chi} = \frac{1}{\sqrt{N_T}}\chi \begin{bmatrix} \mathbf{I}_{N_T N_P} \\ \mathbf{0} \end{bmatrix}$, where $\mathbf{0}$ is a $(N_Q - N_T N_P) \times N_T N_P$-element all-zero matrix.

(b) If $N_Q = N_T N_P$ is required, the LDC's dispersion matrix is directly given by $\overline{\chi} = \frac{1}{\sqrt{N_T}}\chi$.

(c) If $N_Q < N_T N_P$ is required, the LDC's dispersion matrix is given by taking the first N_Q rows of the scaled unitary matrix as $\overline{\chi} = \sqrt{\frac{N_P}{N_Q}}\left[\mathbf{I}_{N_Q}, \mathbf{0}\right]\chi$, where $\mathbf{0}$ is a $N_Q \times (N_T N_P - N_Q)$-element all-zero matrix.

(2) Rank criterion: for the resultant $I = M^{N_Q}$ LDC codewords $\{\mathbf{S}^i\}_{i=0}^{I-1}$ of Eq. (6.91), having a full rank should be guaranteed for all combinations of $\mathbf{\Delta} = (\mathbf{S}^i - \mathbf{S}^{\bar{i}})^H(\mathbf{S}^i - \mathbf{S}^{\bar{i}})$ as $\text{rank}(\mathbf{\Delta}) = \min(N_T, N_P)$.

(3) Determinant criterion: The minimum determinant among all combinations of $\mathbf{\Delta}$ is given by $\{\det(\mathbf{\Delta})\}_{\min}$. The related random search may be conducted by repeating Steps (1) as well as (2), and the chosen one should maximize $\{\det(\mathbf{\Delta})\}_{\min}$.

It is worth emphasizing once again that the LDC's CCMC capacity is only maximized when $N_Q \geq N_T N_P$. Nonetheless, $N_Q < N_T N_P$ is acceptable in Step (1) for the sake of meeting specific system requirements, because a lower number of transmitted symbols N_Q normally leads to a higher Euclidean distance among the LDC codewords $\|\mathbf{S}^i - \mathbf{S}^{\bar{i}}\|^2$, which may minimize the PEP union bound of Eq. (6.9).

Furthermore, according to Hadamard's inequality, the determinant $\det(\mathbf{\Delta})$ is maximized when $\mathbf{\Delta}$ is unitary, which is the foundation of the orthogonal STBC design. It was proposed in [300] that the determinant criterion in the LDC design may be translated into making $\mathbf{\Delta}$ as close to unitary as possible, which may be quantified as minimizing the following two metrics:

$$d_1 = \sum_{q=1}^{N_Q} \kappa(\overline{\mathbf{A}}_q) = \sum_{q=1}^{N_Q} \|\overline{\mathbf{A}}_q^{-1}\| \cdot \|\overline{\mathbf{A}}_q\|, \tag{6.98a}$$

$$d_2 = \sum_{\forall q \neq \bar{q}} \|\overline{\mathbf{A}}_q^H \overline{\mathbf{A}}_{\bar{q}} + \overline{\mathbf{A}}_{\bar{q}}^H \overline{\mathbf{A}}_q\|, \tag{6.98b}$$

where the operation $\kappa(\cdot)$ refers to the condition number of the matrix [281], where we have $\kappa(\mathbf{A}) \geq 1$ and the equality only holds for unitary matrices. It can be readily seen that orthogonal codes may have $d_1 = N_Q$ and $d_2 = 0$. Moreover, it was also proposed in [8,333] that the determinant criterion of $\max\ \{\det(\mathbf{\Delta})\}_{\min}$ in the LDC design may be revised for the sake of maximizing the LDC's DCMC capacity of Eq. (6.7) in order to pursue an improved near-capacity performance. In fact, minimizing the PEP $\text{E}\left\{p\left(\|\mathbf{Y} - \mathbf{S}^{\bar{i}}\mathbf{H}\|^2 < \|\mathbf{V}\|^2\right)\right\} = \text{E}\left\{p\left[\|(\mathbf{S}^i - \mathbf{S}^{\bar{i}})\mathbf{H} + \mathbf{V}\|^2 < \|\mathbf{V}\|^2\right]\right\}$ of Eq. (6.9) would automatically result in minimizing the term $\exp(\frac{-\|(\mathbf{S}^i - \mathbf{S}^{\bar{i}})\mathbf{H} + \mathbf{V}\|^2 + \|\mathbf{V}\|^2}{N_0})$ in the DCMC capacity of Eq. (6.7). Consequently, the LDCs conceived for minimizing the PEP generally also have a maximized DCMC capacity.

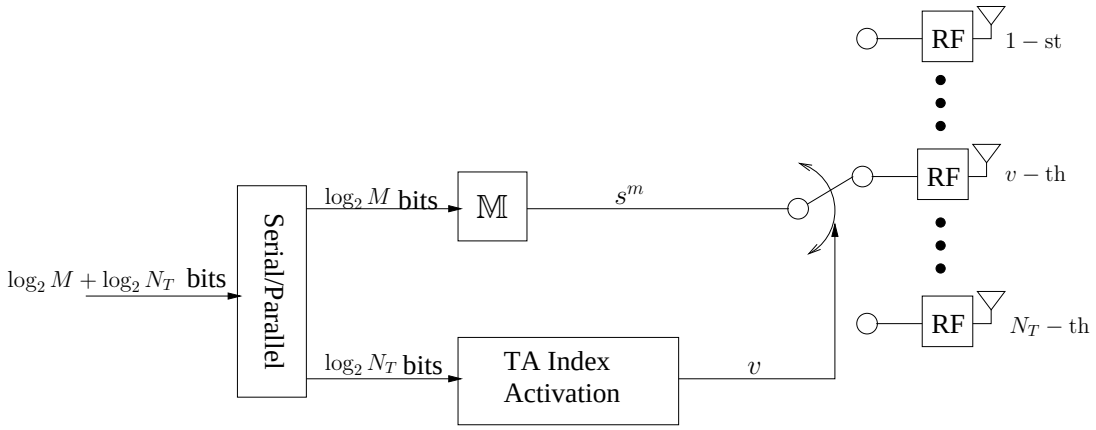

Figure 6.6: Schematic of the SM transmitter.

6.4 Uncoded Spatial Modulation and Space-Time Shift Keying

The development of LDCs has resolved the tradeoff between the diversity and multiplexing gain, but it is a retrograde step for the tradeoff between performance and complexity. Given that the STBC's orthogonality requirement is abandoned, the LDC receivers have to invoke V-BLAST-style multi-stream detectors, which may exhibit an excessive complexity, when aiming for attaining an optimal performance. Considering that the family of suboptimal V-BLAST detectors would not be deemed desirable, especially not in coded systems, because they tend to produce unreliable soft output LLRs that do not represent the true probabilities as demonstrated in Chapter 2, in this section, we focus our attention to the SM and STSK families, which are explicitly designed for low-complexity receivers. The development of SM is introduced in Sec. 6.4.1, and the STSK transceiver is introduced in Sec. 6.4.2, while their error probability and capacity are analysed in Sec. 6.4.3.

6.4.1 Spatial Modulation

The schematic of the SM transmitter is portrayed in Fig. 6.6. In more details, the first $\text{BPS} = \log_2 M$ bits are assigned to a single MPSK/QAM symbol $s^m = \mathbb{M}(m)$, while the following $\text{BPS}_T = \log_2 N_T$ source information bits are assigned to activate a single TA out of a total of N_T TAs. As a result, the $(1 \times N_T)$-element SM transmission vector may be expressed as [195–197]:

$$\mathbf{S} = [\underbrace{0 \ \cdots \ 0}_{v-1}, s^m, \underbrace{0 \ \cdots \ 0}_{N_T-v}]. \tag{6.99}$$

Based on the received MIMO signal model of Eq. (6.1), the full-search ML MIMO detection of Eq. (6.13) may also be invoked for SM. However, as it was demonstrated in Sec. 6.2 for V-BLAST, the MIMO detection complexity may increase exponentially with the throughput R. More explicitly, the complexity order of the MIMO detection of Eq. (6.13) is given by $O(I)$, where the total number of combinations is given by $I = 2^R$ for both V-BLAST and SM.

Owing to the fact that only a single TA is activated, opposed to V-BLAST, SM does not intro-

duce any IAI. Therefore, in order to conceive a single-antenna-based low complexity SM detector, the TA activation index and the classic modulated symbol index are suggested to be detected separately in [197], so that the complexity order of this so-called Maximum Ratio Combining (MRC) based SM detection may be reduced to $O(N_T + M)$. In more details, under the assumption of having perfect CSI knowledge at the receiver, the matched filter output may be recorded as:

$$\mathbf{Z} = \mathbf{Y}\mathbf{H}^H, \tag{6.100}$$

where the v-th element in the $(1 \times N_T)$-element vector $\mathbf{Z}$ is given by $\{z_v = \mathbf{Y}\mathbf{H}_{v,-}^H\}_{v=1}^{N_T}$, and the $(1 \times N_R)$-element vector $\{\mathbf{H}_{v,-}\}_{v=1}^{N_T}$ refers to the v-th row in $\mathbf{H}$. The MRC based SM detector may determine the TA activation index by comparing the absolute values of the elements in the matched filter's output vector $\mathbf{Z}$ as [197]:

$$\hat{v} = \arg \max_{\forall v \in \{1,\cdots,N_T\}} |z_v|. \tag{6.101}$$

Upon obtaining the TA activation index $\hat{v}$, the $\hat{v}$-th element in $\mathbf{Z}$ may be demodulated as:

$$\hat{m} = \mathbb{M}^{-1}(z_{\hat{v}}). \tag{6.102}$$

Therefore, the complexity order of MRC based SM detection is in fact given by $O(N_T + 1)$, where Eq. (6.102) directly maps $z_{\hat{v}}$ to the closest constellation point.

Unfortunately, as demonstrated in [198], the MRC based SM detection suffers from an irreducible error floor. It can be seen in Eq. (6.102) that the demodulator may be misled into detecting the wrong classic modulated symbol, if the TA activation index obtained in Eq. (6.101) is erroneous. In order to restore the ML detection capability, the simplified SM detector of [198] streamlines the ML MIMO detector of Eq. (6.13) as:

$$\begin{aligned} \hat{\mathbf{S}} &= \arg \min_{\forall m \in \{0,\cdots,M-1\}, \forall v \in \{1,\cdots,N_T\}} \|\mathbf{Y}\|^2 + \kappa_v^2 |s^m|^2 - 2\Re\left[(s^m)^* \mathbf{Y}\mathbf{H}_{v,-}^H\right] \\ &= \arg \min_{\forall m \in \{0,\cdots,M-1\}, \forall v \in \{1,\cdots,N_T\}} \kappa_v^2 |s^m|^2 - 2\Re\left[(s^m)^* z_v\right], \end{aligned} \tag{6.103}$$

where we have $\{\kappa_v = \|\mathbf{H}_{v,-}\|\}_{v=1}^{N_T}$, and the constant of $\|\mathbf{Y}\|^2$ is omitted from the MIMO decision metric of Eq. (6.13). As a benefit of having $(N_T - 1)$ zeros in the SM transmission vector of Eq. (6.99), the computational complexity of the SM detection of Eq. (6.103) is considerably lower than that of the conventional MIMO detection of Eq. (6.13). Nonetheless, the complexity order of the simplified SM detection of Eq. (6.103) is still given by $O(I)$.

When SM was first proposed as an alternative to V-BLAST MIMO, the most appealing feature of SM was its design objective of imposing a low receiver complexity. Therefore, in this section, we focus our attention on the strategically important subject of reduced-complexity SM detectors. The SM detector design has been developed in two directions in the open literature. The first option is to develop the optimal SM detection [201–204] that endeavours to reduce the complexity order of the simplified SM detection of Eq. (6.103) without imposing any performance loss. The second approach elaborated on in [141, 205–210] aims for improving the performance of the sub-optimal

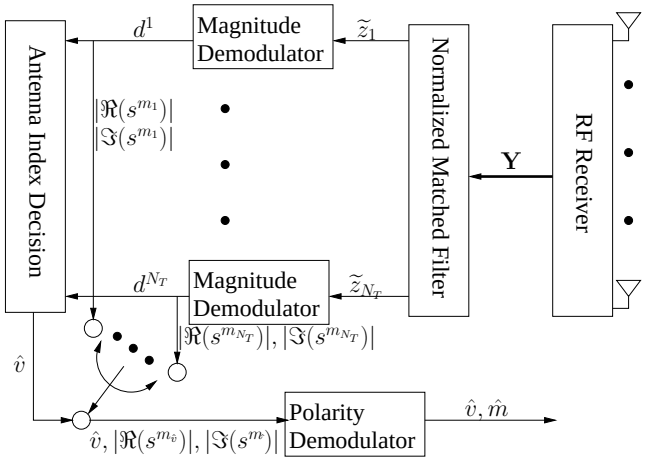

Figure 6.7: Schematic of the hard-decision-aided reduced-scope SM receiver.

MRC based SM detection of Eqs. (6.101) and (6.102), but attaining the optimal SM performance is not guaranteed.

For the optimal SM detectors, we firstly propose a hard-decision-aided reduced-scope SM detection in Sec. 6.4.1.1 by relying on our previous publications of [141, 202, 203, 234]. In more details, by exploring the symmetry provided by the Gray-labelled MPSK/QAM constellation diagrams, the normalized matched filter output elements may be first partially demodulated, so that the correlation between the TA index and the classic modulated symbol index may be taken into account, when the TA index is detected. The schematic of this reduced-scope SM receiver is portrayed by Fig. 6.7, where only the constellation points located in the first quadrant are visited by the "magnitude demodulator" before TA index detection, which leads to a reduced SM detection search scope. Following this, according to the already detected TA activation index, only a single MPSK/QAM demodulation has to be completed by the "polarity demodulator", which determines the quadrant of the demodulated symbol. The reduced-scope SM detection will be detailed in Sec. 6.4.1.1. Secondly, the recently proposed hard-decision-aided hard-limiter-based SM detection [204] is introduced in Sec. 6.4.1.2, where full classic demodulation is performed before the TA index detection, as depicted by Fig. 6.8. Owing to the fact that the linear MPSK/QAM demodulation complexity is quite low, as presented by Table 6.2, the hard-limiter-based SM detection complexity may not increase with the MPSK/QAM constellation size. We will demonstrate in Sec. 6.5 based on our performance results that the hard-limiter-based SM detection only exhibits a complexity advantage, when high-order PSK/QAM is employed. Furthermore, the hard-decision-aided SD that is specifically modified for SM [211–213] is also summarized in Sec. 6.4.1.3.

For the sub-optimal SM detectors, fist of all, the so-called normalized-MRC-based SM detection of [205–207] is introduced in Sec. 6.4.1.4, where the MRC's TA index detection is improved by normalizing the matched filter output $\{z_v\}_{v=1}^{N_T}$ obtained from Eq. (6.100). The terminology of List normalized-MRC based SM detection [205, 206, 208] will be introduced in Sec. 6.4.1.5, where instead of making a decision on the optimum TA index in Eq. (6.101), a list of possible TA indices

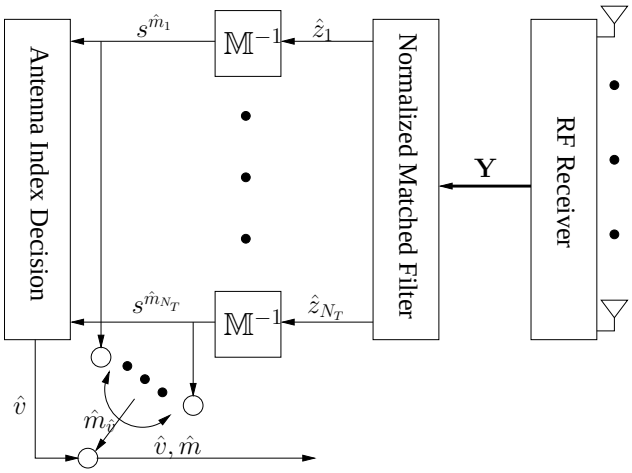

Figure 6.8: Schematic of the hard-decision-aided hard-limiter-based SM receiver. Its difference to Fig. 6.7 is that full classic demodulation is performed before the TA index detection, because the hard-decision-aided linear MPSK/QAM demodulation complexity is quite low in uncoded systems.

are recorded and then the optimum TA index may be decided after invoking the classic demodulator for all the TA index candidates in the list. Furthermore, the unity-constellation-power-based SM detection [141] will be presented in Sec. 6.4.1.6, which is capable of further improving the MRC's TA index detection of Eq. (6.101) by also taking into account all the non-negative MPSK/QAM constellation points, whose signal powers were normalized to unity. Accordingly, a List unity-constellation-power based SM detection algorithm [209] is also introduced in Sec. 6.4.1.6. Lastly, Sec. 6.4.1.7 describes the so-called distance-based-detection aided SM receiver [210], which establishes the TA index list based on the distances between the demodulated symbols and the matched filter output elements.

6.4.1.1 Hard-Decision-Aided Reduced-Scope-Based Optimal SM Detection

The reduced-scope SM detection [203] portrayed by Fig. 6.7 aims for restoring the ML detection capability of the MRC-based SM detection by separating the TA index and the classic modulated symbol index from the optimal SM detection of Eq. (6.103) without imposing any performance loss. First of all, we may further extend the optimal SM detection of Eq. (6.103) as:

$$\hat{\mathbf{S}} = \arg \max_{\forall v \in \{1,\cdots,N_T\}, \forall m \in \{0,\cdots,M-1\}} \Re(\widetilde{z}_v)\Re(s^m) + \Im(\widetilde{z}_v)\Im(s^m) - \kappa_v^2 |s^m|^2, \tag{6.104}$$

where we have $\{\widetilde{z}_v = 2z_v\}_{v=1}^{N_T}$. Let us now consider QPSK aided SM detection as an example. We deliberately rotate QPSK's detected constellation diagram anti-clockwise by $\pi/4$, so that there is only a single constellation point in each quadrant. As a result, the decision variable should be rotated as $z'_v = \widetilde{z}_v \exp(j\frac{\pi}{4})$, and the detected constellation points are given by $\{s'^m = s^m \exp(j\frac{\pi}{4})\}_{m=0}^{M-1} = \{\frac{1}{\sqrt{2}} + j\frac{1}{\sqrt{2}}, \frac{1}{\sqrt{2}} - j\frac{1}{\sqrt{2}}, -\frac{1}{\sqrt{2}} + j\frac{1}{\sqrt{2}}, -\frac{1}{\sqrt{2}} - j\frac{1}{\sqrt{2}}\}$. For a specific TA

index v, the maximum metric over all rotated QPSK constellations is given by:

$$d^v = \max \left\{ \begin{array}{ll} \frac{\Re(z'_v)}{\sqrt{2}} + \frac{\Im(z'_v)}{\sqrt{2}} - \kappa_v^2, & \frac{\Re(z'_v)}{\sqrt{2}} - \frac{\Im(z'_v)}{\sqrt{2}} - \kappa_v^2, \\ -\frac{\Re(z'_v)}{\sqrt{2}} + \frac{\Im(z'_v)}{\sqrt{2}} - \kappa_v^2, & -\frac{\Re(z'_v)}{\sqrt{2}} - \frac{\Im(z'_v)}{\sqrt{2}} - \kappa_v^2 \end{array} \right\} \tag{6.105a}$$

$$= \left| \frac{\Re(z'_v)}{\sqrt{2}} \right| + \left| \frac{\Im(z'_v)}{\sqrt{2}} \right| - \kappa_v^2. \tag{6.105b}$$

It can be seen in Eq. (6.105) that the four comparisons involving four metric evaluations of Eq. (6.105a) may be carried out by a single metric evaluation according to Eq. (6.105b). As a result, the optimum TA activation index $\hat{v}$ may be found by searching for the maximum metric over all the N_T candidates $\{d^v\}_{v=1}^{N_T}$, regardless of which particular QPSK symbol was transmitted. This may be expressed as:

$$\hat{v} = \arg \max_{\forall v \in \{1,\cdots,N_T\}} d^v. \tag{6.106}$$

Unlike the MRC-based detection of Eq. (6.101), the reduced-scope-based TA index detection of Eq. (6.106) is directly derived from the ML detection of Eq. (6.104), which does not impose any performance loss. Furthermore, upon finding the optimum TA index $\hat{v}$, QPSK demodulation may be concluded by directly testing the $\hat{v}$-th decision variable $z'_{\hat{v}}$ as:

$$\hat{b}_1 = \left\{ \begin{array}{ll} 1, & \text{if } \Im(z'_{\hat{v}}) < 0 \\ 0, & \text{otherwise} \end{array} \right. , \quad \hat{b}_2 = \left\{ \begin{array}{ll} 1, & \text{if } \Re(z'_{\hat{v}}) < 0 \\ 0, & \text{otherwise} \end{array} \right. . \tag{6.107}$$

Similarly, when Square 16QAM is employed, the maximum metrics $\{d^v\}_{v=1}^{N_T}$ seen in Eq. (6.104) may be obtained by testing both the real and the imaginary parts of the QAM constellation separately, which may be expressed as:

$$\begin{aligned} d_{\text{Re}}^{v,0} &= \max \left\{ \frac{1}{\sqrt{10}}\Re(\widetilde{z}_v) - \frac{1}{10}\kappa_v^2, \; -\frac{1}{\sqrt{10}}\Re(\widetilde{z}_v) - \frac{1}{10}\kappa_v^2 \right\} = \left| \frac{1}{\sqrt{10}}\Re(\widetilde{z}_v) \right| - \frac{1}{10}\kappa_v^2, \\ d_{\text{Re}}^{v,1} &= \max \left\{ \frac{3}{\sqrt{10}}\Re(\widetilde{z}_v) - \frac{9}{10}\kappa_v^2, \; -\frac{3}{\sqrt{10}}\Re(\widetilde{z}_v) - \frac{9}{10}\kappa_v^2 \right\} = \left| \frac{3}{\sqrt{10}}\Re(\widetilde{z}_v) \right| - \frac{9}{10}\kappa_v^2, \\ d_{\text{Im}}^{v,0} &= \max \left\{ \frac{1}{\sqrt{10}}\Im(\widetilde{z}_v) - \frac{1}{10}\kappa_v^2, \; -\frac{1}{\sqrt{10}}\Im(\widetilde{z}_v) - \frac{1}{10}\kappa_v^2 \right\} = \left| \frac{1}{\sqrt{10}}\Im(\widetilde{z}_v) \right| - \frac{1}{10}\kappa_v^2, \\ d_{\text{Im}}^{v,1} &= \max \left\{ \frac{3}{\sqrt{10}}\Im(\widetilde{z}_v) - \frac{9}{10}\kappa_v^2, \; -\frac{3}{\sqrt{10}}\Im(\widetilde{z}_v) - \frac{9}{10}\kappa_v^2 \right\} = \left| \frac{3}{\sqrt{10}}\Im(\widetilde{z}_v) \right| - \frac{9}{10}\kappa_v^2, \end{aligned} \tag{6.108}$$

where each one of them only has to be evaluated once. Furthermore, for a specific TA index v, the maximum metric is given by:

$$d^v = \max_{g \in \{0,1\}} d_{\text{Re}}^{v,g} + \max_{f \in \{0,1\}} d_{\text{Im}}^{v,f}, \tag{6.109}$$

where the optimum PAM magnitude index pairs $\hat{g}$ and $\hat{f}$ obtained for each $\{d^v\}_{v=1}^{N_T}$ may be recorded. There are a total of N_T pairs, hence they may be represented by $\{\hat{g}_v\}_{v=1}^{N_T}$ and $\{\hat{f}_v\}_{v=1}^{N_T}$. Based on Eq. (6.109), the TA activation index detection of Eq. (6.106) may be invoked, and then the second part of the Square 16QAM demodulation may be concluded as follows:

$$\begin{aligned} \hat{b}_1 &= \left\{ \begin{array}{ll} 1, & \text{if } \Im(\widetilde{z}_{\hat{v}}) < 0 \\ 0, & \text{otherwise} \end{array} \right. , \quad \hat{b}_2 = \left\{ \begin{array}{ll} 1, & \text{if } \hat{f}_{\hat{v}} = 1 \text{ for } d^{\hat{v}} \\ 0, & \text{otherwise} \end{array} \right. , \\ \hat{b}_3 &= \left\{ \begin{array}{ll} 1, & \text{if } \Re(\widetilde{z}_{\hat{v}}) < 0 \\ 0, & \text{otherwise} \end{array} \right. , \quad \hat{b}_4 = \left\{ \begin{array}{ll} 1, & \text{if } \hat{g}_{\hat{v}} = 1 \text{ for } d^{\hat{v}} \\ 0, & \text{otherwise} \end{array} \right. . \end{aligned} \tag{6.110}$$

(1) Define the metrics that test the real and imaginary parts separately as:
$$d_{\text{Re}}^{v,g} = \left|A_g \Re(\widetilde{z}_v)\right| - A_g^2 \kappa_v^2,$$
$$d_{\text{Im}}^{v,f} = \left|B_f \Im(\widetilde{z}_v)\right| - B_f^2 \kappa_v^2,$$
where $\{A_g\}_{g=0}^{M_{\text{Re}}/2-1}$ and $\{B_f\}_{f=0}^{M_{\text{Im}}/2-1}$ are the positive real PAM magnitudes on the x-axis and y-axis of Square MQAM constellation diagram, respectively. For Square MQAM associated with an even BPS, we have $M_{\text{Re}} = M_{\text{Im}} = \sqrt{M}$. For the case of BPS being an odd number, we have $M_{\text{Re}} = \sqrt{2M}$ and $M_{\text{Im}} = \sqrt{M/2}$.

(2) For a specific TA activation index v, the maximum metric over all Square MQAM constellations is given by testing the real and imaginary parts separately as:
$$d^v = \max_{g\in\{0,\cdots,M_{\text{Re}}/2-1\}} d_{\text{Re}}^{v,g} + \max_{f\in\{0,\cdots,M_{\text{Im}}/2-1\}} d_{\text{Im}}^{v,f},$$
where the optimum PAM magnitudes index pairs $\hat{g}$ and $\hat{f}$ obtained for each $\{d^v\}_{v=1}^{N_T}$ may be recorded as $\{\hat{g}_v\}_{v=1}^{N_T}$ and $\{\hat{f}_v\}_{v=1}^{N_T}$.

(3) The optimum TA activation index may be found by:
$$\hat{v} = \arg \max_{\forall v\in\{1,\cdots,N_T\}} d^v,$$
and then the corresponding $(\text{BPS}_T = \log_2 N_T)$ hard-bit decisions may be obtained by translating $\hat{v}$ back to binary bits as $[\hat{b}_{\text{BPS}+1}, \cdots, \hat{b}_{\text{BPS}+\text{BPS}_T}] = \text{dec2bin}(\hat{v}-1)$.

(4) The first bit and the $(\text{BPS}_{\text{Im}} + 1 = \log_2 M_{\text{Im}} + 1)$-th bit which determine the signs may be demodulated as:
$$\hat{b}_1 = \begin{cases} 1, & \text{if } \Im(\widetilde{z}_{\hat{v}}) < 0 \\ 0, & \text{otherwise} \end{cases}, \quad \hat{b}_{\text{BPS}_{\text{Im}}+1} = \begin{cases} 1, & \text{if } \Re(\widetilde{z}_{\hat{v}}) < 0 \\ 0, & \text{otherwise} \end{cases}.$$

(5) For the remaining $(\text{BPS} - 2)$ bits which determine the magnitudes, we have $[\hat{b}_{\text{BPS}_{\text{Im}}+2}, \cdots, \hat{b}_{\text{BPS}}] = \text{dec2bin}(\hat{g}_{\hat{v}})$ and $[\hat{b}_2, \cdots, \hat{b}_{\text{BPS}_{\text{Im}}}] = \text{dec2bin}(\hat{f}_{\hat{v}})$, where $\hat{g}_{\hat{v}}$ and $\hat{f}_{\hat{v}}$ are the specific PAM magnitude index pairs that are recorded for $d^{\hat{v}}$ in Step (2).

Table 6.8: Algorithm 6.1: Hard-decision-aided reduced-scope optimal SM detection, when Square MQAM is employed.

The specific index pair $\hat{f}_{\hat{v}}$ and $\hat{g}_{\hat{v}}$ are recovered from Eq. (6.109).

The reduced-scope optimal SM detection conceived for the case of employing Square MQAM is summarized in Table 6.8, while its detection complexity order is given by $O(M_{\text{Re}}N_T/2 + M_{\text{Im}}N_T/2)$. Furthermore, the reduced-scope optimal SM detection derived for the case of employing generic MPSK/QAM is summarized in Table 6.9, whose detection complexity order is given by $O(MN_T/4)$. We note that if the MPSK or Star MQAM constellations are rotated at the transmitter according to the instructions in Step (1) of Table 6.9, the rotation of the decision variable $\{\widetilde{z}_v\}_{v=1}^{N_T}$ may be omitted from the SM receiver's signal processing operations. A common rotation of all the MPSK/QAM constellation points does not change the performance results.

It can be seen in Tables 6.8 and 6.9 that the optimum TA index detection of Step (3) in both Algorithm 6.1 and 6.2 requires partial demodulation, which implies that although the classic modulated symbol index has not been explicitly detected before obtaining the TA activation index, the MPSK/QAM constellation points in the first quadrant are visited in Steps (1) and (2) of both Algorithm 6.1 and 6.2. However, we would like to stress that the full MPSK/QAM demodulation has not been invoked N_T times for determining the TA activation index, because after all, the TA index detection does not rely on the knowledge of which specific MPSK/QAM constellation point was transmitted. Instead, the correlation between the classic modulated symbol index and the TA index is carefully taken into accout. As a result, the complexity order of reduced-scope optimal SM

(1) Define the new test metrics as:
$$d^{v,g} = \left|A_g \Re(z'_v)\right| + \left|B_g \Im(z'_v)\right| - (A_g^2 + B_g^2)\kappa_v^2,$$
where $\{(A_g, B_g)\}_{g=0}^{M/4-1}$ denote the coordinates of the rotated MPSK/QAM constellation points in the first quadrant. The detector's rotated MPSK constellation points are $\{s'^m = s^m \exp(j\frac{\pi}{M})\}_{m=0}^{M-1}$, and the corresponding decision variables are $\{z'_v = \widetilde{z}_v \exp(j\frac{\pi}{M})\}_{v=1}^{N_T}$. For Star MQAM, the detector's rotated constellation points are $\{s'^m = s^m \exp(j\frac{\pi}{M_P})\}_{m=0}^{M-1}$, and hence we have $\{z'_v = \widetilde{z}_v \exp(j\frac{\pi}{M_P})\}_{v=1}^{N_T}$. In this way, there are exactly $M/4$ constellation points in each quadrant.

(2) For a specific TA activation index v, the maximum metric over all MPSK/QAM constellations is given by:
$$d^v = \max_{g\in\{0,\cdots,M/4-1\}} d^{v,g},$$
where the optimum constellation index $\hat{g}$ obtained for each $\{d^v\}_{v=1}^{N_T}$ may be recorded as $\{\hat{g}_v\}_{v=1}^{N_T}$.

(3) The optimum TA activation index may be found by:
$$\hat{v} = \arg \max_{v\in\{1,\cdots,N_T\}} d^v,$$
and then the corresponding $(\text{BPS}_T = \log_2 N_T)$ hard-bit decisions may be obtained by translating $\hat{v}$ back to binary bits as $[\hat{b}_{\text{BPS}+1}, \cdots, \hat{b}_{\text{BPS}+\text{BPS}_T}] = \text{dec2bin}(\hat{v} - 1)$.

(4) The first bit and the second bit, which determine the signs, may be demodulated as:
$$\hat{b}_1 = \begin{cases} 1, & \text{if } \Im(z'_{\hat{v}}) < 0 \\ 0, & \text{otherwise} \end{cases}, \quad \hat{b}_2 = \begin{cases} 1, & \text{if } \Re(z'_{\hat{v}}) < 0 \\ 0, & \text{otherwise} \end{cases}.$$

(5) For the remaining $(\text{BPS} - 2)$ bits which determine the magnitudes, we have $[\hat{b}_3, \cdots, \hat{b}_{\text{BPS}}] = \text{dec2bin}(\hat{g}_{\hat{v}})$, where $\hat{g}_{\hat{v}}$ is the specific group index recorded for $d^{\hat{v}}$ in Step (2).

Table 6.9: Algorithm 6.2: Hard-decision-aided reduced-scope optimal SM detection, when generic MPSK/QAM is employed.

detection is expected to be higher than that of the MRC-based suboptimal SM detection.

However, considering that the ML SM detection capability is retained, the reduced-scope optimal SM detection exhibits a subtantially lower detection complexity than the conventional optimal SM detection, espcially when either the number of modulation levels M or that of the TAs N_T increases. It is worth noting that all the computational complexity quantified in terms of the real-valued multiplications is imposed during Step (1) of both Algorithm 6.1 and 6.2, which implies that the practical complexity reduction ratio provided by the proposed algorithms may become substantial, since all the unneccessary calculations are avoided.

6.4.1.2 Hard-Decision-Aided Hard-Limiter-Based Optimal SM Detection

Due to the fact that detecting the TA index is generally much more computationally complex than demodulation, the hard-limiter-based optimal SM detection portrayed by Fig. 6.8 invokes the full MPSK/QAM demodulators first in order to obtain the optimum modulation indices for all candidate TA indices and then the TA index detection is performed with the aid of the demodulated MPSK/QAM symbols. This method was first advocated in [201] and further interpreted in [204].

Let us assume that a tentative TA activation index v is fixed, and then the SM detection of

Eq. (6.103) may be rewritten as:

$$\begin{aligned}\hat{m}_v &= \arg \min_{\forall m \in \{0,\cdots,M-1\}} \left(|\hat{z}_v - s^m|^2 - |\hat{z}_v|^2\right)\kappa_v^2 \\ &= \arg \min_{\forall m \in \{0,\cdots,M-1\}} |\hat{z}_v - s^m|^2 \\ &= \mathbb{M}^{-1}(\hat{z}_v),\end{aligned} \tag{6.111}$$

where the demodulator's decision variable is given by $\{\hat{z}_v = z_v/\kappa_v^2\}_{v=1}^{N_T}$. In this way, the optimum modulated symbol index $\hat{m}_v$ associated with all TA activation indices may be obtained by directly demapping $\hat{z}_v$ to the closest legitimate constellation point.

Upon obtaining the optimum constellation points for all candidate TA activation indices $\{s^{\hat{m}_v}\}_{v=1}^{N_T}$, the optimum TA index may be obtained based on Eq. (6.103) as:

$$\hat{v} = \arg \min_{\forall v \in \{1,\cdots,N_T\}} \left(\left|\hat{z}_v - s^{\hat{m}_v}\right|^2 - |\hat{z}_v|^2\right)\kappa_v^2 \tag{6.112}$$

and then the corresponding $(\text{BPS}_T = \log_2 N_T)$ hard-bit decisions may be obtained by translating $\hat{v}$ back to binary bits. Furthermore, the remaining $(\text{BPS} = \log_2 M)$ hard-bit decisions may be obtained by directly translating the specific modulated symbol index $\hat{m}_{\hat{v}}$ back to binary bits.

The hard-limiter-based optimal SM detection's complexity order is given by $O(N_T + N_T)$, where the demodulator has to be invoked N_T times before TA index detection. It can be seen that the detection complexity order does not grow with the number of modulation levels M, which is one of the most appealing advantages of hard-limiter-based optimal SM detection, espcially for the case of employing high-order MPSK/QAM schemes.

6.4.1.3 Hard-Decision-Aided SD Conceived for SM Detection

It was suggested in [211, 212] that the conventional MIMO detector's transmit search space in Eq. (6.13) may be reduced by the so-called Transmitter-centric SD (Tx-SD) as:

$$\{\hat{m}, \hat{v}\} = \arg \min_{\forall \{m,v\} \in \mathbb{S}} \left\|\mathbf{Y} - s^m \mathbf{H}_{v,-}\right\|^2, \tag{6.113}$$

where $\mathbb{S}$ denotes the Tx-SD search space. In more details, when MPSK is employed, the V-BLAST SD's PED increment of Eq. (6.20) may be simplified for SM Tx-SD as:

$$\left|\widetilde{Y}_v - l_{v,v} s_v\right|^2 < R^2, \tag{6.114}$$

because only one transmit TA is activated. Therefore, the PED increment of Eq. (6.114) defines a new search space for $\{m, v\}$, since only the candidates that lie inside the sphere have to be taken into account by the SM detection of Eq. (6.113).

Similarly, when Square MQAM is employed, the SD's PED increment of Eq. (6.32) may be simplified for SM as:

$$\left(\widetilde{\overline{Y}}_v - l_{v,v}\overline{s}_v\right)^2 < R^2, \qquad \forall v \in \{N_T + 1, \cdots, 2N_T\}, \tag{6.115a}$$

$$\left(\widetilde{\overline{Y}}_v - l_{v+N_T,v}\overline{s}_{v+N_T} - l_{v,v}\overline{s}_v\right)^2 < R^2, \quad \forall v \in \{1, \cdots, N_T\}. \tag{6.115b}$$

The new search space defined in Eq. (6.115) may be further reformulated as [211, 212]:

$$\frac{-R+\widetilde{\overline{Y}}_v}{l_{v,v}} < \overline{s}_v < \frac{R+\widetilde{\overline{Y}}_v}{l_{v,v}}, \qquad \forall v \in \{N_T+1, \cdots, 2N_T\}, \tag{6.116a}$$

$$\frac{-R+(\widetilde{\overline{Y}}_v - l_{v+N_T,v}\overline{s}_{v+N_T})}{l_{v,v}} < \overline{s}_v < \frac{R+(\widetilde{\overline{Y}}_v - l_{v+N_T,v}\overline{s}_{v+N_T})}{l_{v,v}}, \quad \forall v \in \{1, \cdots, N_T\}. \tag{6.116b}$$

This Tx-SD-defined search space may effectively reduce the SM detector's search space formulated in Eq. (6.113).

Furthermore, it was also proposed in [213] that the receive search space of the conventional MIMO detection of Eq. (6.13) may be reduced by the so-called Receiver-centric SD (Rx-SD) as:

$$\{\hat{m}, \hat{v}\} = \arg \max_{\forall\{m,v\}} \left\{ n(m,v) | \sum_{r=1}^{n(m,v)} |Y_r - s^m H_{v,r}|^2 < R^2 \right\}, \tag{6.117}$$

where Y_r refers to the signal received at the r-th RA, while $H_{v,r}$ models the fading channel spanning from the v-th TA to the r-th RA. The Rx-SD of Eq. (6.117) aims for finding the optimum pair $\{\hat{m}, \hat{v}\}$, which may maximize the counter $n(m,v)$. More explicitly, for a specific data-carrying index pair $\{m,v\}$, the following PED is examined:

$$d_r^{\{m,v\}} = d_{r-1}^{\{m,v\}} + |Y_r - s^m H_{v,r}|^2 < R^2. \tag{6.118}$$

If the PED $d_r^{\{m,v\}}$ lies inside the Rx-SD sphere specified by Eq. (6.118), the counter may be incremented according to $n(m,v) = n(m,v)+1$, and the Rx-SD index r may continue to be increased. Otherwise, the PED evaluation of Eq. (6.118) may be terminated, and the next index pair $\{m,v\}$ shall be examined. The sphere radius may be updated as $R^2 = d_{N_R}^{\{m,v\}}$, when the Rx-SD index reaches $r = N_R$. The Rx-SD tree search is supposed to be experienced by all the $I = N_T M$ candidates of the index pair $\{m,v\}$, but a reduced-complexity termination may be expected, when the sphere radius R is swiftly reduced in the high-SNR region. The optimum index pair $\{\hat{m}, \hat{v}\}$ seen in Eq. (6.117) is the one, which maximizes the counter $n_{\max} = \max_{\forall\{m,v\}} n(m,v)$ with the aid of the minimum final PED value as $\{\hat{m}, \hat{v}\} = \arg \min d_{n_{\max}}^{\{m,v\}}$.

As demonstrated in [211, 212], the Tx-SD of Eq. (6.113) and the Rx-SD of Eq. (6.118) may be combined as:

$$\{\hat{m}, \hat{v}\} = \arg \max_{\forall\{m,v\}\in \mathbb{S}} \left\{ n(m,v) | \sum_{r=1}^{n(m,v)} |Y_r - s^m H_{v,r}|^2 < R^2 \right\}, \tag{6.119}$$

where the transmit search space is limited within $\mathbb{S}$, while the receive search space is confined by the Rx-SD counter $n(m,v)$.

For the sake of discussion, it was thoroughly reviewed in [211–213] that as a benefit of the SM's specific feature of single TA activation, the SD conceived for SM exhibits a substantially reduced computational complexity compared to the SD conceived for conventional V-BLAST. Furthermore, the optimum SM performance may be attained by the SD, provided that the sphere radius is initialized to be sufficiently large. However, the SD complexity still remains SNR-dependent, since

its complexity the lower bound can only be reached in the high-SNR region. Moreover, it is important to note that the hard-limiter-based SM detection presented in Sec. 6.4.1.2 may be seen as a special case of the SD aided SM detection. This is because that the transmit search space associated with the classic modulated symbol index m is limited by minimizing the hard-limiter metric in Eq. (6.111), while the receive search space is reduced to a single-antenna-based scenario, since the hard-limiter-based SM detector examines the matched filter outputs $\{z_v\}_{v=1}^{N_T}$ instead of the received signals $\{Y_r\}_{r=1}^{N_R}$.

6.4.1.4 Hard-Decision-Aided Normalized-MRC-Based Suboptimal SM Detection

First of all, let us introduce the normalized matched filter output as:

$$\overline{\mathbf{Z}} = \mathbf{Y}\left(\overline{\mathbf{H}}\right)^H, \tag{6.120}$$

where each row in the normalized $(N_T \times N_R)$-element fading channels matrix $\overline{\mathbf{H}}$ is given by $\left\{\overline{\mathbf{H}}_{v,-} = \mathbf{H}_{v,-}/\kappa_v\right\}_{v=1}^{N_T}$, and the v-th element in the $(1 \times N_T)$-element normalized matched filter output vector $\overline{\mathbf{Z}}$ is given by $\{\overline{z}_v = \mathbf{Y}\overline{\mathbf{H}}_{v,-}^H = z_v/\kappa_v\}_{v=1}^{N_T}$.

It was demonstrated in [205–207] that a more accurate estimate of the TA activation index may be delivered by testing the normalized matched filter output of Eq. (6.120) instead of the direct matched filter output in the MRC based SM detection of Eq. (6.101). Therefore, the normalized-MRC-based SM detection may determine the TA index by :

$$\hat{v} = \arg \max_{\forall v \in \{1,\cdots,N_T\}} |\overline{z}_v|. \tag{6.121}$$

Upon obtaining the TA activation index $\hat{v}$, the linear MPSK/QAM demodulator of Eq. (6.111) may be invoked for detecting the classic modulated symbol index as:

$$\hat{m} = \mathbb{M}^{-1}(\overline{z}_{\hat{v}}/\kappa_{\hat{v}}). \tag{6.122}$$

Therefore, the complexity order of normalized-MRC-based SM detection is also given by $O(N_T + 1)$.

The so-called signal-vector-based detection proposed in [207] operates based on the fact that the Square MQAM symbol does not change the direction of the received signal vector $\mathbf{Y} = s^m\mathbf{H}_{v,-}$. The signal-vector-based detection's estimate of the TA activation index is given by:

$$\begin{aligned}\hat{v} &= \arg \min_{\forall v \in \{1,\cdots,N_T\}} \arccos\left(\frac{|\mathbf{Y}\mathbf{H}_{v,-}^H|}{\|\mathbf{Y}\|\|\mathbf{H}_{v,-}\|}\right) \\ &= \arg \min_{\forall v \in \{1,\cdots,N_T\}} \arccos\left(\frac{|\overline{z}_v|}{\|\mathbf{Y}\|}\right),\end{aligned} \tag{6.123}$$

which is in fact equivalent to the normalized-MRC-based estimation of Eq. (6.121), because $\arccos(\cdot)$ is a function that monotonically decreases with respect to its argument, and $\|\mathbf{Y}\|$ in Eq. (6.123) is a constant.

6.4.1.5 Hard-Decision-Aided List-Normalized-MRC-Based Suboptimal SM Detection

The normalized-MRC-based SM detection still suffers from the problem of imperfect TA index estimation. Therefore, to circumvent this, the List-normalized-MRC-based SM detection is introduced in [205, 206, 208], where a total of N_{List} TA indices are taken into account in order to avoid the situation of missing the optimum TA index candidate.

More explicitly, instead of selecting a single TA index in Eq. (6.121), a list of N_{List} possible TA candidates is compiled as:

$$[v_1, \cdots, v_{N_{\text{List}}}] = \arg \text{ sortD}_{\forall v \in \{1,\cdots,N_T\}} |\overline{z}_v|. \tag{6.124}$$

where the operation "sortD" sorts all the elements $\{|\overline{z}_v|\}_{v=1}^{N_T}$ in decreasing order. In the TA index list, v_1 represents the TA index associated with the highest metric $|\overline{z}_{v_1}|$, and $v_{N_{\text{List}}}$ associated with the lowest metric $|\overline{z}_{v_{N_{\text{List}}}}|$. We have $1 \leq N_{\text{List}} \leq N_T$, where the special cases of $N_{\text{List}} = 1$ and $N_{\text{List}} = N_T$ correspond to the normalized-MRC-based SM detection and to the optimum SM detection, respectively.

Following this, the demodulator may be invoked N_{List} times for all the candidates on the list as:

$$\hat{m}_{v_t} = \mathbb{M}^{-1}(\overline{z}_{v_t}/\kappa_{v_t}),\ 1 \leq t \leq N_{\text{List}}. \tag{6.125}$$

The TA activation index may now be confirmed by comparing the N_{List} candidates associated with their respective optimum classic modulated symbol indices according to Eq. (6.103) as:

$$\hat{v} = v_{\hat{t}} = \arg \min_{\forall t \in \{1,\cdots,N_{\text{List}}\}} \kappa_{v_t}^2 |s^{\hat{m}_{v_t}}|^2 - 2\kappa_{v_t} \Re\{(s^{\hat{m}_{v_t}})^* \overline{z}_{v_t}\}. \tag{6.126}$$

Then the classic modulated symbol index may be given by $\hat{m}_{v_{\hat{t}}}$, which is obtained from Eq. (6.125). The detected classic modulated symbol index as well as the detected TA activation index may now be translated back to bits. The complexity order of the List-normalized-MRC-based SM detector is given by $O(N_T + 2N_{\text{List}})$, where the demodulator has to be invoked N_{List} times in Eq. (6.125) before comparing the N_{List} candidates in Eq. (6.126).

As a further advance, it was proposed in [334, 335] that a classic modulated symbol index list may be introduced in order to strike a tradeoff between the performance and complexity of the demodulator. More explicitly, a list of constellation points is established for replacing the complete search space for $\{s^m\}_{m=0}^{M-1}$ of Eq. (6.103). In [334], all Square QAM constellations are partitioned into level-1 subsets as well as level-2 subsets, and only $N_{\text{List}-m1}$ constellation points in the level-1 subset and $N_{\text{List}-m2}$ constellation points in the level-2 subset are considered for the demodulation. In [335], the $3 \sim 5$ constellation points that surround the decision variable $\overline{z}_v/\kappa_v$ are considerred for demodulation. As summarized in Table 6.2, the hard-decision-aided MPSK/QAM demodulation may be implemented at a very low detection complexity, and hence the further discussion of sub-optimal modulation list establishment in [334, 335] may be avoided in uncoded systems. We note that the TA index list based SM detection of [205, 206] may be considered to represent the upper bound for [334, 335] in terms of both performance and complexity.

6.4.1.6 Hard-Decision-Aided Unity-Constellation-Power-Based Suboptimal SM Detection

The unity-constellation-power-based suboptimal SM detection is proposed in [141], where a total of $\widetilde{M}$ candidates of non-negative constellation points associated with unity constellation power $\{\widetilde{s}^{\widetilde{m}} = \frac{|\Re(s^m)|}{|s^m|} + j\frac{|\Im(s^m)|}{|s^m|}\}_{\widetilde{m}=1}^{\widetilde{M}}$ are taken into account for the sake of more reliable TA index estimation. In more details, the unity-constellation-power-based TA index detection is given by:

$$\hat{v} = \arg \max_{\forall v \in \{1,\cdots,N_T\}, \forall \widetilde{m} \in \{1,\cdots,\widetilde{M}\}} |\Re(\overline{z}_v)|\Re(\widetilde{s}^{\widetilde{m}}) + |\Im(\overline{z}_v)|\Im(\widetilde{s}^{\widetilde{m}}), \tag{6.127}$$

and then the demodulation regime of Eq. (6.122) may be invoked in order to detect the classic modulated symbol index. The complexity order of unity-constellation-power-based SM detection is given by $O(N_T\widetilde{M}+1)$. This method was shown to be especially beneficial [141] for Star MQAM detection, because when the constellation power is normalized, only a total of $(M_P/4+1)$ M_PPSK phase candidates focused in the first quadrant has to be considered.

In order to improve the TA index detection of Eq. (6.127), List-unity-constellation-power based SM detection was proposed in [209], which may follow the same procedures as the List-normalized-MRC-based SM detection of Sec. 6.4.1.5, except that the list establishment of Eq. (6.124) should use the metric of $|\Re(\overline{z}_v)|\Re(\widetilde{s}^{\widetilde{m}}) + |\Im(\overline{z}_v)|\Im(\widetilde{s}^{\widetilde{m}})$ in Eq. (6.127) instead of $|\overline{z}_v|$. As a result, the complexity order of List-unity-constellation-power-based SM detection is given by $O(N_T\widetilde{M} + 2N_{\text{List}})$.

6.4.1.7 Hard-Decision-Aided Distance-Ordered-Based Suboptimal SM Detection

The distance-ordered-based suboptimal SM detection of [210] performs classic symbol demodulation first, and then a list of candidate TA indices is established based on the Euclidean distances between the demodulated symbols and the decision variables.

More explicitly, the hard-limiter-based demodulator of Eq. (6.111) is invoked in order to identify the optimum classic modulated symbol indices $\{\hat{m}_v\}_{v=1}^{N_T}$ for all TA index candidates. Following this, the distance-based TA index list is established by:

$$[v_1, \cdots, v_{N_{\text{List}}}] = \arg \ \text{sortI}_{\forall v \in \{1,\cdots,N_T\}} \ |s^{\hat{m}_v} - \hat{z}_v|\kappa_v, \tag{6.128}$$

where the sorting operation "sortI" orders all the elements $\{|s^{\hat{m}_v} - \hat{z}_v|\kappa_v\}_{v=1}^{N_T}$ according to their increasing values. Therefore, the TA activation index detected from the list may be decided based on Eq. (6.103) as:

$$\hat{v} = v_{\hat{t}} = \arg \min_{\forall t \in \{1,\cdots,N_{\text{List}}\}} (\left|\hat{z}_{v_t} - s^{\hat{m}_{v_t}}\right|^2 - |\hat{z}_{v_t}|^2)\kappa_{v_t}^2. \tag{6.129}$$

Naturally, the classic modulated symbol index may be directly obtained by $\hat{m}_{v_{\hat{t}}}$. The complexity order of distance-ordered-based SM detection is given by $O(2N_T + N_{\text{List}})$.

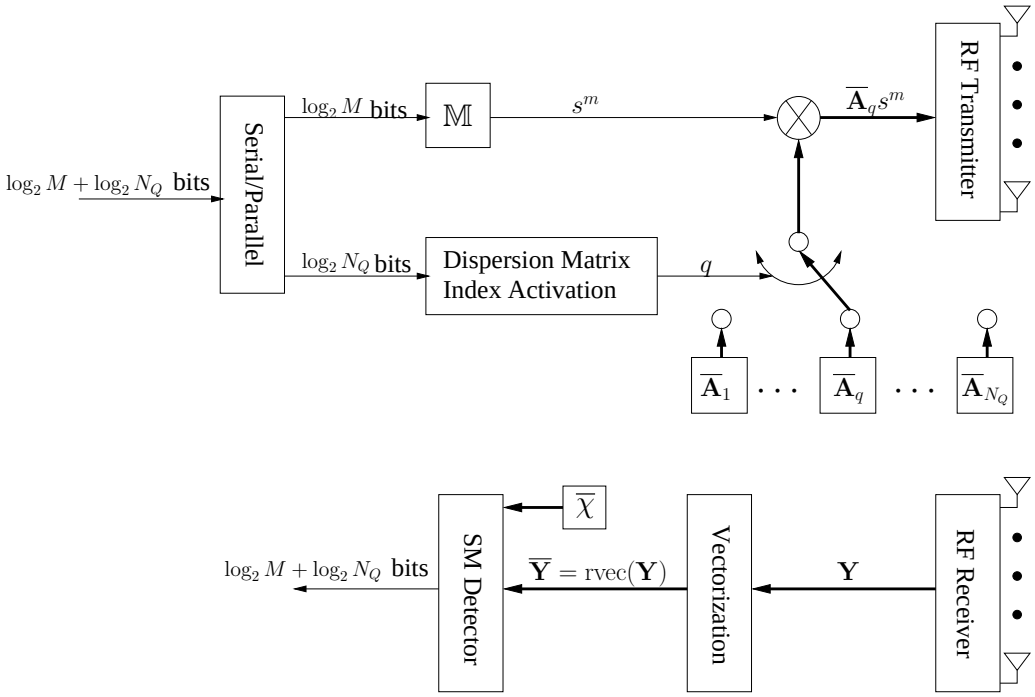

Figure 6.9: Schematic of the STSK transceiver, which relies on the LDC schematic of Fig. 6.5, but instead of a TA, a LDC matrix is activated.

6.4.2 Space-Time Shift Keying Transceiver

The concept of STSK was proposed in [216] as a combination of SM and LDC, so that a transmit diversity gain may be obtained by the family of SM-style low-complexity MIMO systems. The schematic of the STSK transceiver is portrayed in Fig. 6.9. The STSK transmitter is modified from the LDC transmitter of Fig. 6.5, where only a single one out of a total of N_Q dispersion matrices is selected for dispersing a single MPSK/QAM symbol. As a result, the $(N_P \times N_T)$-element STSK transmission matrix created from the LDC transmission matrix of Eq. (6.91) may be expressed as [216]:

$$\mathbf{S} = \overline{\mathbf{A}}_q s^m, \tag{6.130}$$

where the first $\text{BPS} = \log_2 M$ source information bits are assigned to modulate a single MPSK/QAM symbol $s^m = \mathbb{M}(m)$, while the following $\text{BPS}_Q = \log_2 N_Q$ source information bits are assigned to select a single dispersion matrix $\overline{\mathbf{A}}_q$ among a total number of N_Q candidates. There are a total of $(I = N_Q M)$ STSK codewords for Eq. (6.130), and the STSK throughput is given by $(R = \frac{\log_2 I}{N_P} = \frac{\text{BPS}+\text{BPS}_Q}{N_P})$, where the employment of N_P time slots is considered.

Similarly to the signal processing performed at the LDC receiver of Fig. 6.5, the STSK receiver presented in Fig. 6.9 firstly vectorizes the received MIMO signal model of Eq. (6.1) in order to form the received LDC signal model of Eq. (6.92), which is rewritten here for the sake of convenience:

$$\overline{\mathbf{Y}} = \overline{\mathbf{S}} \cdot \overline{\chi} \cdot \overline{\mathbf{H}} + \overline{\mathbf{V}}, \tag{6.131}$$

where the $(1 \times N_P N_R)$-element equivalent received signal matrix $\overline{\mathbf{Y}} = \text{rvec}(\mathbf{Y})$, the $(N_Q \times$

$N_P N_T)$-element equivalent dispersion matrix $\overline{\chi}$, the $(N_P N_T \times N_P N_R)$-element equivalent fading matrix $\overline{\mathbf{H}} = \mathbf{I}_{N_P} \otimes \mathbf{H}$ and the $(1 \times N_P N_R)$-element equivalent AWGN matrix $\overline{\mathbf{V}} = \text{rvec}(\mathbf{V})$ are all exactly the same as those of the LDC in Eq. (6.93). However, the $(1 \times N_Q)$-element equivalent STSK input signal vector in Eq. (6.131) is given by:

$$\overline{\mathbf{S}} = [\underbrace{0 \ \cdots \ 0}_{q-1}, s^m, \underbrace{0 \ \cdots \ 0}_{N_Q - q}], \tag{6.132}$$

which is in the same form as the SM input signal vector of Eq. (6.99). Therefore, according to the STSK received signal model of Eq. (6.131), a STSK(N_T,N_R,N_P,N_Q) scheme is equivalent to a SM system associated with N_Q TAs and $N_P N_R$ RAs, where the equivalent SM fading matrix is given by STSK's $\breve{\mathbf{H}} = \overline{\chi}\overline{\mathbf{H}}$, as defined in Eq. (6.131). As a result, all the SM detectors summarized in Sec. 6.4.1 may be invoked by the STSK receivers depicted in Fig. 6.9.

Since only a single dispersion matrix is activated, STSK loses the LDC's capacity advantage, which will be further discussed in Sec. 6.4.3. Nonetheless, the generation of the STSK's dispersion matrices may still rely on populating them with the aid of a random search, and then the specific dispersion matrix set that minimize the PEP of Eq. (6.9) may be selected. As discussed before, the PEP union bound of Eq. (6.10b) is minimized, when $\mathbf{\Delta} = (\mathbf{S}^i - \mathbf{S}^{\bar{i}})^H (\mathbf{S}^i - \mathbf{S}^{\bar{i}})$ is unitary, which is equivalent to the following requirements:

$$\overline{\mathbf{A}}_q^H \overline{\mathbf{A}}_q = \tfrac{N_P}{N_T} \mathbf{I}_{N_T}, \quad \forall q \in \{1, \cdots, N_Q\}, \tag{6.133a}$$

$$\overline{\mathbf{A}}_q^H \overline{\mathbf{A}}_{\bar{q}} = -\overline{\mathbf{A}}_{\bar{q}}^H \overline{\mathbf{A}}_q, \quad \forall q \neq \bar{q} \in \{1, \cdots, N_Q\}. \tag{6.133b}$$

We note that the first requirement of Eq. (6.133a) may be readily satisfied by directly generating the scaled unitary matrices for the case of $N_P \geq N_T$, while the second requirement of Eq. (6.133b) can only be approached by maximizing either the minimum determinant $\{\det(\mathbf{\Delta})\}_{\min}$ or the second metric $\sum_{\forall q \neq \bar{q}} \|\overline{\mathbf{A}}_q^H \overline{\mathbf{A}}_{\bar{q}} + \overline{\mathbf{A}}_{\bar{q}}^H \overline{\mathbf{A}}_q\|$ in Eq. (6.98) according to the suggestions in [300].

In more details, the generation of STSK may be summarized as:

(1) Randomly generate a group of N_Q unitary matrices $\{\widetilde{\mathbf{A}}_q\}_{q=1}^{N_Q}$ of size $(N \times N)$, where we have $N = \max(N_T, N_P)$.

   (a) If $N_P > N_T$ is required, the STSK dispersion matrices are given by taking the first N_T columns of the scaled unitary matrices as $\{\overline{\mathbf{A}}_q = \sqrt{\frac{N_P}{N_T}} \widetilde{\mathbf{A}}_q \begin{bmatrix} \mathbf{I}_{N_T} \\ \mathbf{0} \end{bmatrix}\}_{q=1}^{N_Q}$, where $\mathbf{0}$ is a $(N_P - N_T) \times N_T$-element all-zero matrix.

   (b) If $N_P = N_T$ is required, the STSK dispersion matrices are directly given by $\{\overline{\mathbf{A}}_q = \widetilde{\mathbf{A}}_q\}_{q=1}^{N_Q}$.

   (c) If $N_P < N_T$ is required, the STSK dispersion matrices are given by taking the first N_P rows of the scaled unitary matrices as $\{\overline{\mathbf{A}}_q = [\mathbf{I}_{N_P}, \mathbf{0}] \, \widetilde{\mathbf{A}}_q\}_{q=1}^{N_Q}$, where $\mathbf{0}$ is a $N_P \times (N_T - N_P)$-element all-zero matrix.

(2) Rank criterion: for the resultant $(I = N_Q M)$ STSK codewords $\{\mathbf{S}^i\}_{i=0}^{I-1}$ of Eq. (6.130), having a full rank should be guaranteed for all combinations of $\mathbf{\Delta} = (\mathbf{S}^i - \mathbf{S}^{\bar{i}})^H(\mathbf{S}^i - \mathbf{S}^{\bar{i}})$ as $\text{rank}(\mathbf{\Delta}) = \min(N_T, N_P)$.

(3) Determinant criterion: The minimum determinant among all combinations of $\mathbf{\Delta}$ is given by $\{\det(\mathbf{\Delta})\}_{\min}$. The related random search may be carried out by repeating Steps (1) and (2), while the chosen set should maximize $\{\det(\mathbf{\Delta})\}_{\min}$. For the sake of designing high-throughput STSK schemes, the chosen set may aim for maximizing $\sum_{\forall q \neq \bar{q}} \|\overline{\mathbf{A}}_q^H \overline{\mathbf{A}}_{\bar{q}} + \overline{\mathbf{A}}_{\bar{q}}^H \overline{\mathbf{A}}_q\|$ instead of determinant for the sake of faster random search termination.

When more than one dispersion matrices are allowed to be activated for the sake of achieving an increased throughput, the STSK scheme may be further developed to the concept of Generalized Space-Time Shift Keying (GSTSK), as presented in [217, 302], where both STSK and LDC constitute special cases of GSTSK. Furthermore, since LDC was proposed for generalizing both V-BLAST and STBC, GSTSK may include virtually all MIMO schemes. In more details, the dispersion matrix of V-BLAST is given by Eq. (6.44), while the dispersion matrix design of STBC was discussed in Sec. 6.3. The classic MIMO schemes of V-BLAST, STBC and LDC may all be deemed to be special GSTSK cases, which rely on activating all TAs. Moreover, SM may be considered to be a special case of STSK, where the SM dispersion matrices are given by:

$$\mathbf{A}_q = [\underbrace{0 \ \cdots \ 0}_{q-1}, 1, \underbrace{0 \ \cdots \ 0}_{N_T - q}], \ \ \forall q \in \{1, \cdots, N_T\}. \tag{6.134}$$

Furthermore, in [218–221], SM was improved for the sake of achieving a transmit diversity gain by activating more than one TAs in order to convey STBC codewords, which can be readily subsumed by the framework of GSTSK according to the STBC dispersion matrix design of Sec. 6.3. However, the orthogonal channels of STBC-aided transmit diversity were created either by employing the idealistic orthogonal shapping filters of [222–224] or the orthogonal frequency-hopping codes of [225]. These schemes no longer fit into the scope of GSTSK due to their additional hardware requirements. Moreover, when more than one classic modulated symbols are transmitted by GSTSK, the problem of IAI once again arises, unless orthogonal STBC codewords are transmitted. As a result, sub-optimal interference-rejecting receivers are proposed to be employed by the family of GSTSK receivers in [226, 229], which are less consistent with the SM/STSK motivation of low-complexity ML receiver designs. However, it was suggested in [230, 231] that the IAI may vanish, if the multiple activated TAs of the Generalized Spatial Modulation (GSM) opt for transmitting the same symbol. Further discussions on relaxing the GSM scheme's constraints concerning N_T may be found in [336–339].

Against this background, the concept of a GSM/GSTSK scheme that achieves an improved capacity without imposing IAI remains an open prospect, which we set aside for future work. In order to better prepare for this ambitious objective, we offer a discussion on the SM/STSK scheme's error probability and capacity, so that their strength and limitations may be better understood.

6.4.3 Error Probability and Capacity Analysis

The theoretical average BER of virtually all MIMO schemes is characterized by Eq. (6.8), where each PEP is bounded by Eq. (6.9). For the case of SM, the Pairwise Squared Euclidean Distance (PSED) that directly determines the PEP of Eq. (6.9) may be expressed as:

$$\|\mathbf{S}^i - \mathbf{S}^{\bar{i}}\|^2 = \begin{cases} |s^m|^2 + |s^{\bar{m}}|^2, & \text{Case 1: } v \neq \bar{v}, m \neq \bar{m} \\ 2|s^m|^2, & \text{Case 2: } v \neq \bar{v}, m = \bar{m} \\ |s^m - s^{\bar{m}}|^2, & \text{Case 3: } v = \bar{v}, m \neq \bar{m} \end{cases}, \tag{6.135}$$

where the SM codeword indices i and $\bar{i}$ represent the TA activation indices and the classic modulated symbol indices $\{v, m\}$ and $\{\bar{v}, \bar{m}\}$, respectively. The corresponding relationships are given by $(i = mN_T + v - 1)$ and $(\bar{i} = \bar{m}N_T + \bar{v} - 1)$. For the sake of comparison, the PSED of the V-BLAST scheme may be expressed in a similar form as:

$$\|\mathbf{S}^i - \mathbf{S}^{\bar{i}}\|^2 = \sum_{v=1}^{N_T} |s_v^i - s_v^{\bar{i}}|^2. \tag{6.136}$$

For the case of V-BLAST, the worst case of the minimum PSED that may maximize the PEP bound of Eq. (6.9) occurs, when the two V-BLAST codeword vectors $\mathbf{S}^i$ and $\mathbf{S}^{\bar{i}}$ only differ in a single element, which corresponds to SM's Case 3 in Eq. (6.135). However, any SM codeword has a total number of $(N_T - 1)$ zeros, which means that any two SM vectors $\mathbf{S}^i$ and $\mathbf{S}^{\bar{i}}$ in Eq. (6.135) share at least $(N_T - 2)$ zero elements. However, V-BLAST's pairwise codewords are often different in more than two elements for $(N_T > 2)$.

Moreover, since the throughput of V-BLAST is given by $R = N_T$BPS while that of SM by $R = \text{BPS}_T + \text{BPS}$, the SM system has to employ a higher-order MPSK/QAM constellation in order to match the throughput of the V-BLAST system equipped with the same number of N_T TAs. For example, a V-BLAST(4,N_T)-QPSK scheme has a throughput of $R = 8$, which requires the SM(4,N_R) system to employ a 64QAM scheme. As a result, the SM's PSED of Eq. (6.135) is substantially degraded owing to both the reduced constellation point powers and the reduced Euclidean distances between the constellation points.

For these reasons, SM is unlikely to outperform V-BLAST at the same system throughput under the same hardware and software conditions, albeit SM has a potential low-complexity advantage. Indeed, this would only be possible for SM systems, under the employment of extra hardware for creating transmit diversity techniques [224, 226, 227], orthogonal shapping filters [222, 224, 227], or when aiming for a reduced SM throughput [228] or when using more complex ML SM detectors while opting for suboptimal V-BLAST detectors [197, 204, 205, 212, 218]. In order to clarify this matter, we will provide a discussion on the performance and complexity tradeoff between V-BLAST and SM in Sec. 6.5, where the system requirements are the same for both of them.

It is also interesting to see in Eq. (6.135) that the SM's PEP experienced in some combinations is determined by constellation point power $\{|s^m|^2\}_{m=0}^{M-1}$, which is not the case for V-BLAST, as presented in Eq. (6.136). The same feature may also be observed in terms of the STSK's PSED,

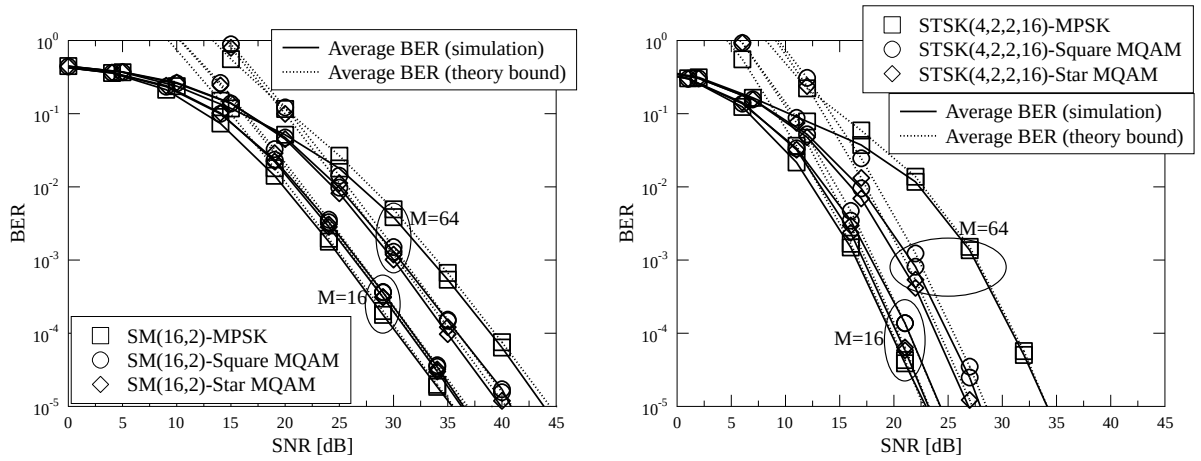

(a) SM employing MPSK/QAM

(b) STSK employing MPSK/QAM

Figure 6.10: Performance comparison between SM/STSK employing different MPSK/QAM constellations.

which may be expressed as:

$$\left\|\mathbf{S}^{i}-\mathbf{S}^{\bar{i}}\right\|^{2}=\begin{cases}\left\|\overline{\mathbf{A}}_{q}s^{m}-\overline{\mathbf{A}}_{\bar{q}}s^{\bar{m}}\right\|^{2}, & \text{Case 1: } q\neq\bar{q}, m\neq\bar{m}\\ \left\|\overline{\mathbf{A}}_{q}-\overline{\mathbf{A}}_{\bar{q}}\right\|^{2}\cdot|s^{m}|^{2}, & \text{Case 2: } q\neq\bar{q}, m=\bar{m}\\ \left\|\overline{\mathbf{A}}_{q}\right\|^{2}\cdot|s^{m}-s^{\bar{m}}|^{2}, & \text{Case 3: } q=\bar{q}, m\neq\bar{m}\end{cases}, \tag{6.137}$$

where the STSK codeword indices are formulated as $(i=mN_Q+q-1)$ and $(\bar{i}=\bar{m}N_Q+\bar{q}-1)$. It can be seen in both Eq. (6.135) and Eq. (6.137) that a higher value of $\min_{\forall s^m}|s^m|^2$ is required by Case 2, while a higher $\min_{\forall\{s^m\neq s^{m'}\}}|s^m-s^{m'}|$ value is required by Case 3 for both SM and STSK. These two requirements cannot be satisfied by the MPSK/QAM constellations at the same time.

Let us recall from Table 2.1 that Square MQAM exhibits the highest minimum constellation point distance of $\min_{\forall\{s^m\neq s^{m'}\}}|s^m-s^{m'}|$, but both MPSK and Star MQAM have a higher constellation point power of $\min_{\forall s^m}|s^m|^2$. Fig. 6.10 portrays our performance comparison between SM/STSK employing different MPSK/QAM constellations. It may be observed in Fig. 6.10 that for a lower modulation order of $M=16$, SM(16,2) and STSK(4,2,2,16) employing 16PSK perform even better than their Square 16QAM and Star 16QAM based counterparts, which is an explicit benefit of 16PSK's dominant advantage of having a higher constellation point power as seen in Table 2.1. However, as the number of modulation levels is increased to $M=64$, SM(16,2) and STSK(4,2,2,16) employing Star 64QAM perform the best, where the 64PSK's reduced constellation point distance of $\min_{\forall\{s^m\neq s^{m'}\}}|s^m-s^{m'}|$ shown in Table 2.1 severely degrades its performance in the concept of SM/STSK systems. We note that although MPSK and Star MQAM may exhibit a performance advantage of SM/STSK, the detection complexity for SM/STSK employing Square MQAM becomes the lowest, when the reduced-scope SM detector is employed, which was discussed in Sec. 6.4.1.1.

Even though its complexity advantage is attractive, SM and STSK fail to achieve the full MIMO capacity of Eq. (6.4). In more details, the SM's mutual information between the input and output

signals may be formulated as [201, 204]:

$$\begin{aligned} C_{SM}^{CCMC}(SNR) &= \max_{p(s^m),p(v)} I(\{s^m, v\}; \mathbf{Y}) \\ &= \max_{p(s^m)} I(s^m; \mathbf{Y}|v) + \max_{p(v)} I(v; \mathbf{Y}), \end{aligned} \tag{6.138}$$

where the input signal vector $\mathbf{S}$ is given by Eq. (6.99), while the output signal vector $\mathbf{Y}$ is given by Eq. (6.1). The first term in Eq. (6.138) represents a SIMO system's capacity, which is maximized, when the input is assumed to be a Gaussian-distributed continuous signal. This may be expressed as:

$$\begin{aligned} C_{SM,1}^{CCMC}(SNR) &= \max_{p(s^m)} I(s^m; \mathbf{Y}|v) \\ &= \frac{1}{N_T} \sum_{v=1}^{N_T} \log_2 \det \left(\mathbf{I}_{N_R} + \eta \mathbf{H}_{v,-}^H \mathbf{H}_{v,-} \right) \\ &= \frac{1}{N_T} \sum_{v=1}^{N_T} \log_2 (1 + \eta \|\mathbf{H}_{v,-}\|^2), \end{aligned} \tag{6.139}$$

where the entropy of the AWGN variable is given by $H(\mathbf{Y}|\{s^m, v\}) = H(\mathbf{V}) = \log_2 \det [\pi e N_0 \mathbf{I}_{N_R}]$, while that of the Gaussian-distributed output signal by $H(\mathbf{Y}|v) = \log_2 \det \left[\pi e (\mathbf{H}_{v,-}^H \mathbf{H}_{v,-} + N_0 \mathbf{I}_{N_R})\right]$. Furthermore, the second capacity term of Eq. (6.138) is also maximized by the Gaussian PDF of the output signal, which is given by:

$$p(\mathbf{Y}|v) = \frac{1}{\det(\pi \mathbf{R}_{YY|v})} \exp \left[-\mathbf{Y} \mathbf{R}_{YY|v}^{-1} \mathbf{Y}^H \right], \tag{6.140}$$

where provided that the v-th TA is active, the autocorrelation matrix of received signal $\mathbf{Y}$ is given by:

$$\mathbf{R}_{YY|v} = \mathrm{E} \left(\mathbf{Y}^H \mathbf{Y} | v \right) = \mathbf{H}_{v,-}^H \mathbf{H}_{v,-} + N_0 \mathbf{I}_{N_R}. \tag{6.141}$$

Therefore, the determinant term in Eq. (6.140) is given by:

$$\det(\pi \mathbf{R}_{YY|v}) = \pi^{N_R} N_0^{N_R} \det(\mathbf{I}_{N_R} + \eta \mathbf{H}_{v,-}^H \mathbf{H}_{v,-}) = \pi^{N_R} N_0^{N_R} (1 + \eta \kappa_v^2), \tag{6.142}$$

where we have $\kappa_v^2 = \|\mathbf{H}_{v,-}\|^2$, as defined in Eq. (6.103). As a result, the second capacity term of Eq. (6.138) may be further extended as:

$$\begin{aligned} C_{SM,2}^{CCMC}(SNR) &= \max_{p(v)} I(v; \mathbf{Y}) \\ &= \max_{p(v)} \int \int p(\mathbf{Y}|v) p(v) \log_2 \frac{p(\mathbf{Y}|v)}{p(\mathbf{Y})} dv d\mathbf{Y}, \end{aligned} \tag{6.143}$$

where the average output signal PDF is given by $p(\mathbf{Y}) = \int p(\mathbf{Y}|v) p(v) dv$, while the conditional PDF $p(\mathbf{Y}|v)$ is given by Eq. (6.140). Naturally, Eq. (6.143) is maximized, when the input PDF $p(v)$ is Gaussian. However, the TA activation index v is confined to the limited range of $(1 \leq v \leq N_T)$, which cannot be generalized by letting N_T tend to infinity. Therefore, we have to accept the fact that the TA activation index v can only be interpreted as a discrete input signal, and hence Eq. (6.143)

is maximized for equiprobable sources of $\{p(v) = \frac{1}{N_T}\}_{v=1}^{N_T}$ as:

$$\begin{aligned} C_{SM,2}^{CCMC}(SNR) &= \frac{1}{N_T}\sum_{v=1}^{N_T} \mathrm{E}\left\{\log_2 \frac{p(\mathbf{Y}|v)}{p(\mathbf{Y})}\right\} \\ &= \frac{1}{N_T}\sum_{v=1}^{N_T} \mathrm{E}\left\{\log_2 \frac{\frac{N_T}{1+\eta\kappa_v^2}\exp\left[-\mathbf{Y}\left(\mathbf{H}_{v,-}^H\mathbf{H}_{v,-}+N_0\mathbf{I}_{N_R}\right)^{-1}\mathbf{Y}^H\right]}{\sum_{\bar{v}=1}^{N_T}\frac{1}{1+\eta\kappa_{\bar{v}}^2}\exp\left[-\mathbf{Y}\left(\mathbf{H}_{\bar{v},-}^H\mathbf{H}_{\bar{v},-}+N_0\mathbf{I}_{N_R}\right)^{-1}\mathbf{Y}^H\right]}\right\}, \end{aligned} \tag{6.144}$$

where the statistically Gaussian output signal may be directly generated, given the sole input signal v as $\mathbf{Y} = \mathbf{H}_{v,-} + \mathbf{V}$, which was appropriately revised from Eq. (6.1).

For the case of STSK, the CCMC capacity may also be evaluated based on Eq. (6.138), where the equivalent fading channel of SM is given by $\breve{\mathbf{H}} = \overline{\chi}\overline{\mathbf{H}}$ according to the received signal vectorization of Eq. (6.131). Naturally, the STSK capacity has to be normalized by N_P owing to the employment of multiple time slots. Therefore, the SM's CCMC capacity of Eq. (6.138) may be revised for STSK as:

$$\begin{aligned} C_{STSK}^{CCMC}(SNR) &= \max_{p(s^m),p(q)} \frac{1}{N_P} I(\{s^m,q\};\overline{\mathbf{Y}}) \\ &= \max_{p(s^m)} \frac{1}{N_P} I(s^m;\overline{\mathbf{Y}}|q) + \max_{p(q)} \frac{1}{N_P} I(q;\overline{\mathbf{Y}}). \end{aligned} \tag{6.145}$$

The first part of Eq. (6.145) may be modified from Eq. (6.139) as:

$$C_{STSK,1}^{CCMC}(SNR) = \max_{p(s^m)} \frac{1}{N_P} H(\overline{\mathbf{Y}}|q) - \frac{1}{N_P} H(\overline{\mathbf{Y}}|\{s^m,q\}) \tag{6.146a}$$

$$= \frac{1}{N_P N_Q}\sum_{q=1}^{N_Q} \log_2 \det\left(\mathbf{I}_{N_P N_R} + \eta\overline{\mathbf{H}}^H\overline{\chi}_{q,-}^H\overline{\chi}_{q,-}\overline{\mathbf{H}}\right) \tag{6.146b}$$

$$= \frac{1}{N_P N_Q}\sum_{q=1}^{N_Q} \log_2\left(1+\eta\|\overline{\chi}_{q,-}\overline{\mathbf{H}}\|^2\right), \tag{6.146c}$$

where the related entropies are given by $H(\overline{\mathbf{Y}}|\{s^m,q\}) = H(\overline{\mathbf{V}}) = \log_2\det\left[\pi e N_0\mathbf{I}_{N_P N_R}\right]$ and $H(\overline{\mathbf{Y}}|q) = \log_2\det\left[\pi e(\breve{\mathbf{H}}_{q,-}^H\breve{\mathbf{H}}_{q,-}+N_0\mathbf{I}_{N_P N_R})\right]$ according to the STSK's equivalent received signal model of Eq. (6.131), while $\{\breve{\mathbf{H}}_{q,-}\}_{q=1}^{N_Q}$ and $\{\overline{\chi}_{q,-}\}_{q=1}^{N_Q}$ refer to the q-th row vectors obtained from $\breve{\mathbf{H}} = \overline{\chi}\overline{\mathbf{H}}$ and $\overline{\chi}$ of Eq. (6.131), respectively. Comparing Eq. (6.146b) to the LDC capacity of Eq. (6.95), it may be observed that the STSK capacity cannot reach the full MIMO capacity by forcing $\overline{\chi}_{q,-}^H\overline{\chi}_{q,-} = \mathbf{I}_{N_P N_T}$, because it requires that the elements of the dispersion matrix $\overline{\mathbf{A}}_q$ satisfy both $\{\{|\overline{A}_q^{t,v}|^2 = 1\}_{t=1}^{N_P}\}_{v=1}^{N_T}$ and $\{\{(\overline{A}_q^{\bar{t},\bar{v}})^*\overline{A}_q^{t,v} = 0\}_{\forall\bar{t}\neq t}\}_{\forall\bar{v}\neq v}$, which cannot be achieved. Comparing Eq. (6.146c) to Eq. (6.139), it may also be observed that the first term of the STSK capacity expression is smaller than that of the SM capacity. In more details, for the case of $N_P \geq N_T$, all STSK dispersion matrices may satisfy $\overline{\mathbf{A}}_q^H\overline{\mathbf{A}}_q = \frac{N_P}{N_T}\mathbf{I}_{N_T}$, as discussed in Sec. 6.4.2. Hence Eq. (6.146c) may be further extended as:

$$\begin{aligned} C_{STSK,1}^{CCMC}(\eta) &= \frac{1}{N_P N_Q}\sum_{q=1}^{N_Q}\log_2\left(1+\frac{N_P\eta}{N_T}\|\mathbf{H}\|^2\right) = \frac{1}{N_P}C_{SIMO}^{CCMC}(\frac{N_P\eta}{N_T},N_R N_P) \\ &< C_{SIMO}^{CCMC}(\eta,N_R) = C_{SM,1}^{CCMC}(\eta,N_R), \end{aligned} \tag{6.147}$$

where we have $\|\overline{\chi}_{q,-}\overline{\mathbf{H}}\|^2 = \|\overline{\mathbf{A}}_q\mathbf{H}\|^2$ according to Eq. (6.131). It is shown by Eq. (6.147) that the first term of the STSK capacity $C^{CCMC}_{STSK,1}(\eta)$ of Eq. (6.146) is equivalent to the SIMO system's capacity of Eq. (2.54) associated with the scaled SNR of $\frac{N_P\eta}{N_T}$ as well as with the increased number of N_RN_P RAs, which is normalized over N_P channel uses. Therefore, the first STSK capacity term $C^{CCMC}_{STSK,1}(\eta)$ of Eq. (6.146) is smaller than the first SM capacity term $C^{CCMC}_{SM,1}(\eta)$ of Eq. (6.139), which equals to the SIMO system's capacity of Eq. (2.54).

Finally, the second part of the STSK capacity of Eq. (6.145) may be obtained by modifying the SM's Eqs. (6.143) and (6.144) according to Eq. (6.131) as:

$$\begin{aligned} C^{CCMC}_{STSK,2}(SNR) &= \max_{p(q)} \frac{1}{N_PN_Q}\sum_{q=1}^{N_Q}\int p(\overline{\mathbf{Y}}|q)p(q)\log_2\frac{p(\overline{\mathbf{Y}}|q)}{p(\overline{\mathbf{Y}})}d\overline{\mathbf{Y}} \\ &= \frac{1}{N_PN_Q}\sum_{q=1}^{N_Q}\mathrm{E}\left\{\log_2\frac{\frac{N_Q}{1+\eta\kappa_q^2}\exp\left[-\overline{\mathbf{Y}}\left(\breve{\mathbf{H}}^H_{q,-}\breve{\mathbf{H}}_{q,-}+N_0\mathbf{I}_{N_PN_R}\right)^{-1}\overline{\mathbf{Y}}^H\right]}{\sum_{\tilde{q}=1}^{N_T}\frac{1}{1+\eta\kappa_{\tilde{q}}^2}\exp\left[-\overline{\mathbf{Y}}\left(\breve{\mathbf{H}}^H_{\tilde{q},-}\breve{\mathbf{H}}_{\tilde{q},-}+N_0\mathbf{I}_{N_PN_R}\right)^{-1}\overline{\mathbf{Y}}^H\right]}\right\}, \end{aligned} \tag{6.148}$$

where the STSK dispersion matrix selection is discretized similarly to the SM TA selection, and hence the mutual information $I(q;\overline{\mathbf{Y}})$ is maximized for the equiprobable source of $\{p(q)=\frac{1}{N_Q}\}_{q=1}^{N_Q}$, while we have $\{\kappa_q^2 = \|\breve{\mathbf{H}}_{q,-}\|^2\}$ for the STSK's equivalent received signal model of Eq. (6.131).

Since the first STSK capacity term of Eq. (6.146) is lower than the SIMO capacity, while the second STSK capacity term of Eq. (6.148) saturates according to $\max_{SNR} C^{CCMC}_{STSK,2}(SNR) = \frac{\mathrm{BPS}_Q}{N_P}$, the overall STSK capacity of Eq. (6.145) is expected to be lower than the SIMO system capacity in the high-SNR region.

6.5 Performance Results for Uncoded MIMO Systems

In this section, we provide simulation results for characterizing the pair of important MIMO design tradeoffs, namely the multiplexing versus diversity tradeoff as well as the performance versus complexity tradeoff.

6.5.1 The Multiplexing Versus Diversity Tradeoff

First of all, let us appraise the multiplexing versus diversity tradeoff that exist for conventional MIMO schemes, including V-BLAST, STBC and LDC. Fig. 6.11 presents our capacity comparison between the conventional MIMO schemes including V-BLAST, STBC and LDC. It can be seen in Fig. 6.11a that both V-BLAST and LDC achieve the highest MIMO capacity, as analysed in Sec. 6.1 and Sec. 6.3.2.3, respectively, but Alamouti's G2-STBC associated with $N_R = 2$ can only achieve the capacity of another V-BLAST system that is associated with $N_T = 4$ and $N_R = 1$ having a doubled SNR of 2η, which was explicitly discussed in Sec. 6.4.3. The MIMO's DCMC capacity of Eq. (6.7) often predicts the achievable performance. For this spirit, it can be seen in

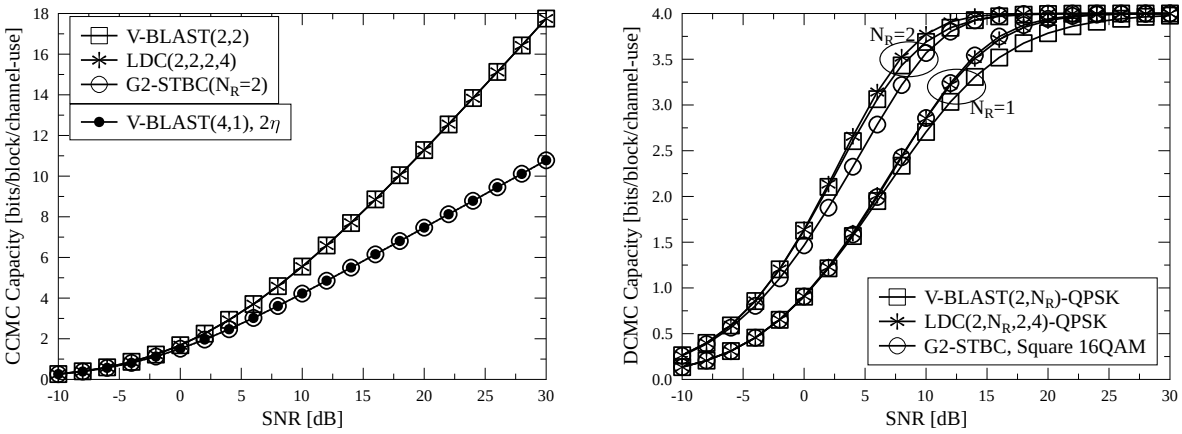

(a) CCMC Capacity

(b) DCMC Capacity

Figure 6.11: Capacity comparison between V-BLAST, Alamouti's G2-STBC and LDC, where $N_T = 2$ TAs are employed and the throughput is given by $R = 4$ bits/block/channel-use.

Fig. 6.11b that Alamout's G2-STBC and LDC achieve their full DCMC capacity quantified in terms of bits/block/channel-use at a lower SNR than V-BLAST for the case of $N_R = 1$, which confirms the beneficial transmit diversity gain of both STBC and LDC. However, when $N_R = 2$ RAs are used, Alamouti's G2 STBC exhibits a lower DCMC capacity in the low SNR region, as evidenced in Fig. 6.11b. We will augment the reasons for this feature later.

Fig. 6.12 portrays our performance comparison between V-BLAST, STBC and LDC associated with the same throughput of $R = 4$. It is evidenced by Fig. 6.12a that both LDC(2,2,2,4)-QPSK and Alamouti's G2-STBC ($N_R = 2$) employing Square 16QAM significantly outperform their multiplexing-oriented counterpart of V-BLAST(2,2)-QPSK, especially in the high SNR region. Furthermore, Fig. 6.12a demonstrates that LDC(2,2,2,4)-QPSK performs even slightly better than its STBC counterpart. Fig. 6.12b also shows that LDC(4,4,2,8)-QPSK is capable of outperforming both its multiplexing-oriented counterpart of V-BLAST(4,4)-BPSK and its STBC counterpart of HR-G4-STBC ($N_R = 4$) employing Square 256QAM for the case of $N_T = 4$.

However, it is also demonstrated by Fig. 6.12b that although HR-G4-STBC retains its full diversity order, its performance remains modest, unless the SNR is expected to be extremely high. This is because G4-STBC has a low normalized throughput of $\overline{R} = 0.5$, which requires us to employ a high-order 256QAM scheme in order to achieve the required system throughput. The orthogonal STBC design aims for achieving the lowest error probability at high SNRs, when the determinant term $\det(0.25\eta\Delta)$ dominants the divisor of the PEP in Eq. (6.10b). Since Δ is unitary as guaranteed by the STBC, it was shown in Table 6.7 that the number of modulation levels M is the only factor that affects the error probability in the low SNR region. This is also the reason why Alamouti's G2-STBC employing a higher-order 16QAM scheme associated with $N_R = 2$ cannot achieve the best DCMC capacity in the low SNR region of Fig. (6.11b).

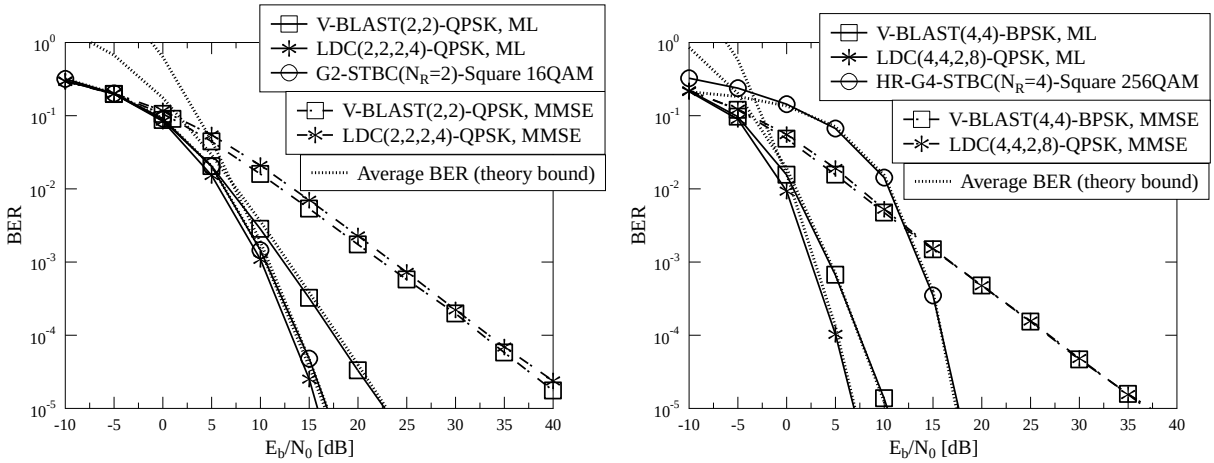

(a) $N_T = 2$, $N_R = 2$ (b) $N_T = 4$, $N_R = 4$

Figure 6.12: Performance comparison between V-BLAST, STBC and LDC associated with the same throughput of $R = 4$ bits/block/channel-use.

In summary, the LDC was shown in Fig. 6.11 to be able to achieve the V-BLAST's full MIMO capacity, and it is also capable of retaining the STBC's full diversity gain, hence offering the best performance, as shown in Fig. 6.12. Therefore, the LDC may resolves the tradeoff between the multiplexing and diversity gain in MIMO systems design, provided that the conditions of Eq. (6.96) as well as the rank and determinant criteria presented in Sec. 6.3.2.3 are satisfied. However, as demonstrated in Sec. 6.3.2.3, the LDC receivers have to employ the V-BLAST's ML detector, whose detection complexity grows exponentially with the system throughput. Furthermore, it is demonstrated by Fig. 6.12 that the low-complexity V-BLAST's MMSE detectors inevitably impose a severe performance loss.

6.5.2 The Performance Versus Complexity Tradeoff

Therefore, as discussed in Sec. 6.4, both SM and STSK constitute attractive design alternatives to multiplexing- and diversity-oriented MIMO schemes as a benefit of their lower detection complexity. Let us examine the capacity of SM and STSK first. Fig. 6.13a shows that SM(2,2) cannot achieve the V-BLAST(2,2)'s full MIMO capacity, but the SM capacity is evidently higher than that of both Alamouti's G2-STBC and of the SIMO system. By contrast, STSK(2,2,2,N_Q) performs poorly in terms of CCMC capacity, as seen in Fig. 6.13a, where the STSK capacity is seem to be even lower than the capacity of the SIMO system, as previously predicted in Sec. 6.4.3.

Fig. 6.13b demonstrates furthermore that Alamouti's G2-STBC approaches its full DCMC capacity at a lower SNR than the others for the case of $N_R = 1$. However, when $N_R = 2$ RAs are employed, both Alamouti's G2-STBC and STSK exhibit a lower DCMC capacity in the low SNR region, as evidenced by Fig. 6.13b. This is because both the diversity-oriented schemes have to employ higher-order modulations in order to achieve the same throughput, as their multiplexing-oriented counterparts.

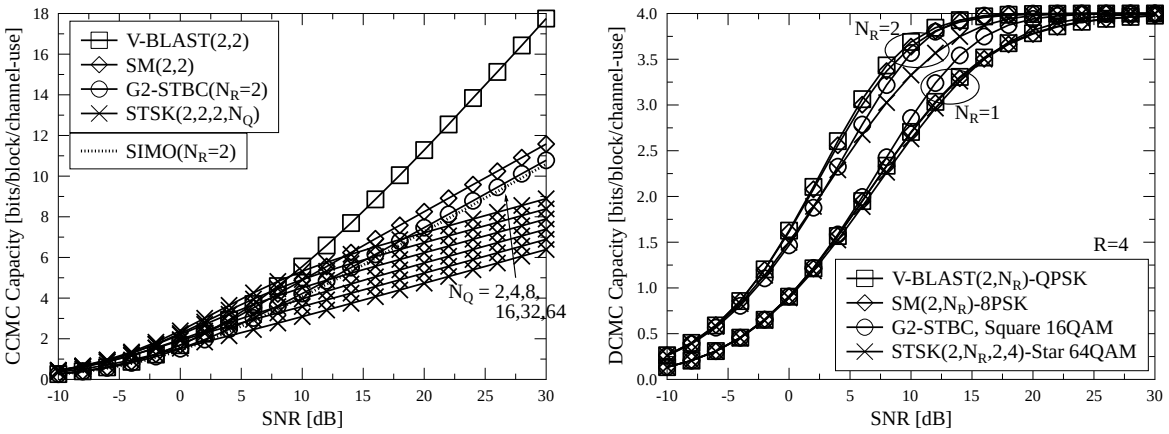

(a) CCMC Capacity

(b) DCMC Capacity

Figure 6.13: Capacity comparison between V-BLAST, SM, Alamouti's G2-STBC and STSK, where $N_T = 2$ TAs are employed.

Our BER performance comparison between V-BLAST, SM, STBC and STSK associated with the same throughput of $R = 4$ bits/block/channel-use is depicted in Fig. 6.14. Explicitly, it can be seen in Fig. 6.14a that when there is no receive diversity, SM(2,1)-8PSK performs slightly worse than V-BLAST(2,1)-QPSK, while STSK(2,1,2,4)-Star 64QAM has an improved performance as a benefit of its diversity gain, but Alamouti's G2-STBC employing Square 16QAM exhibits the best performance. However, Fig. 6.14a also shows that as N_R is increased, both the SM scheme and the V-BLAST scheme perform better at low SNRs, because the STSK and the G2-STBC arrangements have to employ high-order QAM in order to compensate for their throughput loss owing to utilizing N_P symbol periods. Similar trends may be observed in Fig. 6.14b for the case of $N_T = 4$. Explicitly, it is worth noting that the transmit diversity order of STSK(4,N_R,2,16)-16PSK is given by $\min(N_T, N_P) = 2$, which is lower than the full diversity order of HR-G4-STBC. The number of symbol periods N_P is flexibly adjustable for STSK, which results in a very flexible system design. More explicitly, the STSK associated with $N_P = N_T$ may achieve the full diversity order of $N_T N_R$, while a lower $N_P < N_T$ allows the STSK scheme to employ a lower-order modulation to be used for achieving the same system throughput, which may result in a better performance in the low SNR region.

Comparing the results of Fig. 6.12 and Fig. 6.14, it is essential to note that the performance loss imposed by employing SM instead of V-BLAST is significantly lower than that of employing a low-complexity linear MMSE receiver for V-BLAST in Fig. 6.12. The same trend prevails, when STSK is compared to LDC in Fig. 6.12. Therefore, the ultimate benefit of the SM and STSK systems lies on their complexity advantage.

Let us now elaborate a little further on the performance of MIMO systems associated with a higher number of antennas. Fig. 6.15 shows that the transmit diversity gain obtained by STSK only becomes advantageous, when there is no receive diversity owing to using $N_R = 1$ RA. As the number of RAs increases to $N_R = 2$, $N_R = 4$ and even to $N_R = 8$, the performance of

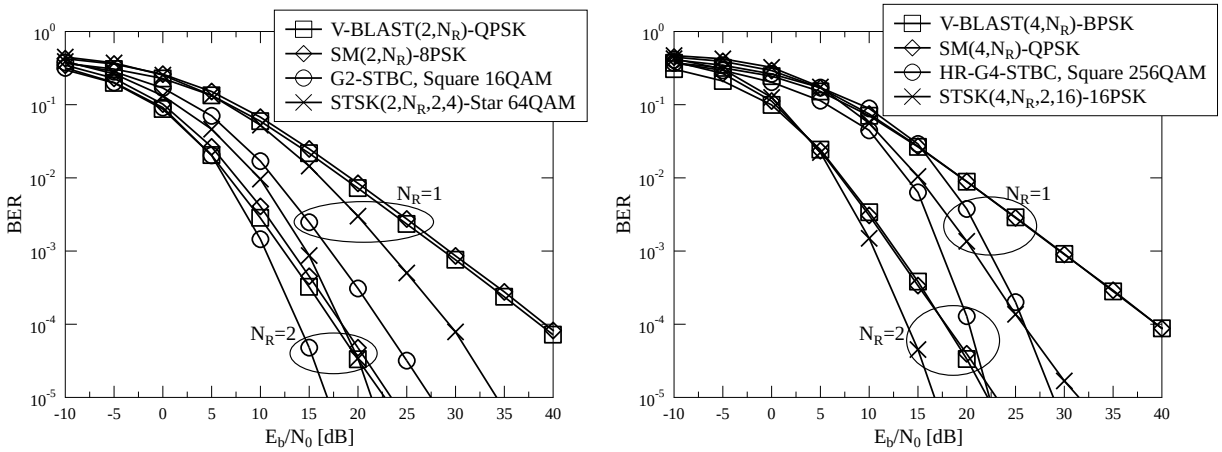

(a) $N_T = 2$ (b) $N_T = 4$

Figure 6.14: Performance comparison between V-BLAST, SM, STBC and STSK associated with the same throughput of $R = 4$ bits/block/channel-use.

Optimal SM Detectors	Complexity Order	Computational Complexity	Related Literatures
MIMO Detector (Eq. (6.13))	$O(N_T M)$	$(4N_T N_R + 2N_R)N_T M$	[3, 4, 8]
Simplified SM Detector (Eq. (6.103))	$O(N_T M)$	$6N_T N_R + 6N_T M$	[198]
Reduced-scope SM Detector (Tables 6.8 and 6.9)	MPSK: $O(N_T M/4)$	$(6N_R + M/2 + 2)N_T$	[202, 203, 234]
	Square MQAM: $O(N_T M_{Re}/2 + N_T M_{Im}/2)$	$(6N_R + M_{Re} + M_{Im} + 2)N_T$	
Hard-limiter-based SM Detector (Eqs. (6.111) and (6.112))	$O(2N_T)$	MPSK: $(6N_R + 9)N_T$	[201, 204]
		Square MQAM: $(6N_R + 11)N_T$	

Table 6.10: Summary of hard-decision-aided optimal SM detectors introduced in Sec. 6.4.1.

V-BLAST and SM becomes better and the performance difference between V-BLAST and SM is increased. This is because the high multiplexing gain of V-BLAST allows it to employ the low-order BPSK modulation for achieving the same throughput as SM and STSK employing higher-order modulation schemes. This important feature implies that altough STBC and STSK may be conceived for any arbitrary number of TAs, V-BLAST may be preferred for large-scale MIMO systems equipped with a large number of antennas at the base stations [227, 340–342]. SM may act as an alternative to V-BLAST at the cost of a slightly degraded performance achieved at a substantially reduced detection complexity.

In order to explicitly quantify the associated complexity versus performance tradeoffs, the optimal SM detectors and the suboptimal SM detectors introduced in Sec. 6.4.1 are summarized at a glance in Tables 6.10 and 6.11, respectively. The optimal SM detectors of Table 6.10 were developed for reducing the MIMO detection complexity, while maintaining their ML detection capability. By contrast, the suboptimal SM detectors of Table 6.11 aim for improving the performance of the MRC aided SM detector of [197], which is the problematic TA activation index detection. The associated computational complexity is summarized in terms of the total number of real-valued multiplications. It is assumed that all MPSK/QAM constellation points are stored in memory, so

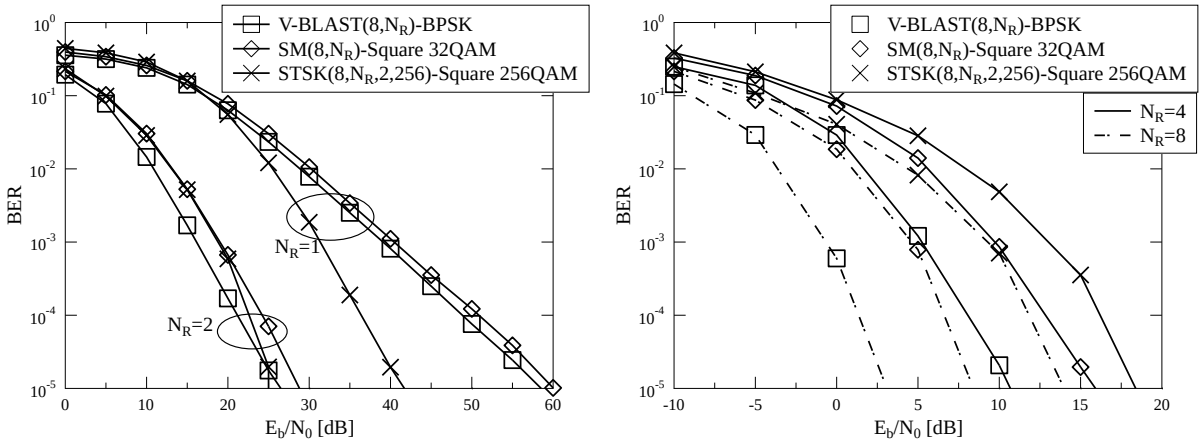

(a) $N_T = 8$, $N_R = \{1, 2\}$, $R = 8$

(b) $N_T = 8$, $N_R = \{4, 8\}$, $R = 8$

Figure 6.15: Performance comparison between V-BLAST, SM and STSK associated with a high number of TAs $N_T = 8$ and a higher throughput of $R = 8$ bits/block/channel-use.

that the unneccessary calculations of reconstructing the MPSK/QAM symbols based on their modulated constellation-point indices are eliminated. Hence, for example, the computational complexity of MPSK demodulation and that of Square MQAM demodulation seen in Table 6.2 is given by 2 and 4, respectively, where the complexity of the arctan function in $\angle z = \arctan\left[\Im(z)/\Re(z)\right]$ of the MPSK demodulation is ignored, because a look-up-table based stored input-output relationship is assumed in order to avoid the discussion of specific implementations.

Fig. 6.16 portrays our performance comparison between the different SM detectors, when they are invoked by the SM receivers and by the STSK receivers. It can be seen in Fig. 6.16a that both the normalized-MRC and List normalized-MRC detectors of Secs. 6.4.1.4 and 6.4.1.5 exhibit an error floor for SM detection, when there is no receive diversity gain owing to having $N_R = 2$, but their performance improves as N_R increases. It may also be observed in Fig. 6.16 that unity-constellation-power detector of Sec. 6.4.1.6 performs better than normalized-MRC detector and that the list-based detectors such as the List unity-constellation-power and List normalized-MRC detectors outperform their respective unity-constellation-power and normalized-MRC counterparts. In general, all optimal SM detectors of Table 6.10 achieve the same ML performance, while all suboptimal SM detectors of Table 6.11 impose a performance loss on both SM and STSK in Fig. 6.16 in a conceptually similar manner to the MMSE detector's performance loss inflicted upon V-BLAST as seen in Fig. 6.12.

Our detection complexity comparison of the different SM detectors is presented in Fig. 6.17. First of all, compared to the simplified SM detector of Eq. (6.103) proposed in [198], our reduced-scope SM detector conceived in Sec. 6.4.1.1 offers a substantial complexity reduction, which is as high as 84.3% for SM(N_T,1)-Square 16QAM ($1 \leq \text{BPS}_T \leq 4$) in Fig. 6.17a, and is up to 93.8% for SM(4,1)-MPSK/QAM ($1 \leq \text{BPS} \leq 6$), as seen in Fig. 6.17b. Furthermore, the hard-limiter-based SM detector proposed in [204] only provides a slightly lower complexity than the reduced-scope SM detector, when the number of modulation levels is as high as $M = 64$ in Fig. 6.17b. For the SM

Suboptimal SM Detectors	Complexity Order	Computational Complexity	Related Literatures
Maximum Ratio Combining (MRC) SM Detector (Eqs. (6.100)-(6.102))	$O(N_T+1)$	MPSK: $4N_R+2$ Square MQAM: $4N_R+4$	[197]
Normalized-MRC-based SM Detector (Eqs. (6.120)-(6.122))	$O(N_T+1)$	MPSK: $(6N_R+2)N_T+4$ Square MQAM: $(6N_R+2)N_T+6$	[205–207]
List normalized-MRC-based SM Detector (Eqs. (6.124)-(6.126))	$O(N_T+2N_{List})$	MPSK: $(6N_R+2)N_T+9N_{List}$ Square MQAM: $(6N_R+2)N_T+11N_{List}$	[205, 206, 208]
Unity-constellation-power based SM Detector (Sec. 6.4.1.6)	$O(N_T\widetilde{M}+1)$	MPSK: $(6N_R+2\widetilde{M}+2)N_T+4$ Square MQAM: $(6N_R+2\widetilde{M}+2)N_T+6$	[141]
List unity-constellation-power based SM Detector (Sec. 6.4.1.6)	$O(N_T\widetilde{M}+2N_{List})$	MPSK: $(6N_R+2\widetilde{M}+2)N_T+9N_{List}$ Square MQAM: $(6N_R+2\widetilde{M}+2)N_T+11N_{List}$	[209]
Distance-ordered-based SM Detector (Sec. 6.4.1.7)	$O(2N_T+N_{List})$	MPSK: $(6N_R+7)N_T+5N_{List}$ Square MQAM: $(6N_R+9)N_T+5N_{List}$	[210]

Table 6.11: Summary of hard-decision-aided suboptimal SM detectors introduced in Sec. 6.4.1.

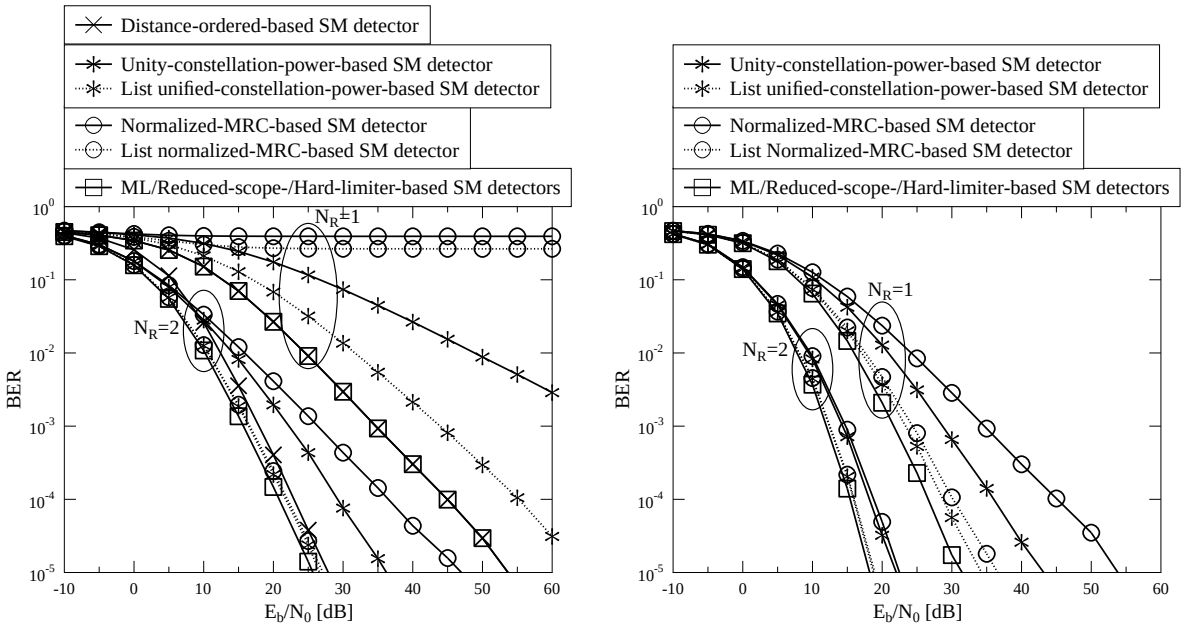

(a) SM(4,N_R)-Square 16QAM

(b) STSK(4,N_R,2,16)-Square 16QAM

Figure 6.16: Performance comparison between different SM detectors summarized in Sec. 6.4.1, when they are invoked by SM and STSK receivers.

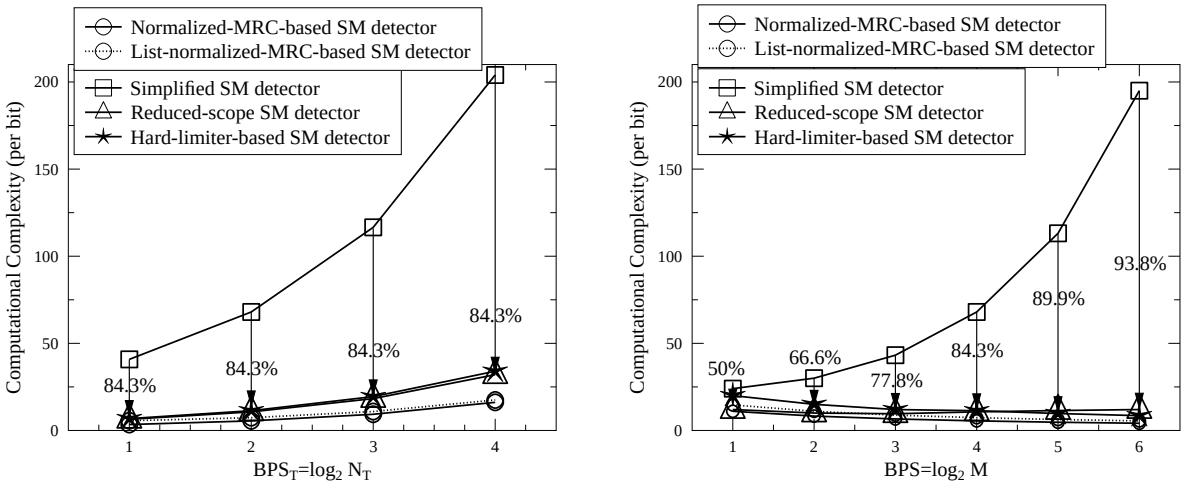

(a) SM(N_T,1)-Square 16QAM

(b) SM(4,1)-MPSK/Square MQAM

Figure 6.17: Complexity comparison between optimal and suboptimal SM detectors.

schemes employing a lower-order modulation scheme, our proposed reduced-scope SM detector exhibits a lower complexity. For the representatives of suboptimal SM detectors, it can be seen in Fig. 6.17 that the normalized-MRC and List normalized-MRC detectors do not show a significant complexity advantage. Considering their suboptimal performance quantified in Fig. 6.16, we may conclude that both our proposed reduced-scope SM detector and the hard-limiter-based SM detector are more attractive candidates in terms of offering a substantially reduced detection complexity, while maintaining the optimum SM performance.

In order to offer a quantitative complexity comparison between the conventional MIMO receivers designed for V-BLAST and STBC as well as the low-complexity optimal MIMO receivers conceived for SM and STSK, it is assumed that the fading channels do not change for a sufficiently long period of time, so that the MMSE filters taps of Eq. (6.38) adjusted for V-BLAST are not required to be updated frequently, while the fading channel powers $\{\kappa_v\}_{v=1}^{N_T}$ estimated by the SM detectors of Sec. 6.4.1 and the STSK scheme's equivalent fading matrix $\breve{\mathbf{H}} = \overline{\chi}\overline{\mathbf{H}}$ of Eq. (6.131) may also remain unchanged. Under this condition, it can be seen in Fig. 6.18 that the orthogonal STBC achieves the lowest detection complexity for both $N_T = 2$ and $N_T = 4$. It is also evidenced by Fig. 6.18 that the ML MIMO detector designed for V-BLAST exhibits the highest complexity, while the linear MMSE receiver successfully mitigates this complexity problem, at the cost of an eroded performance as seen in Fig. 6.12. Against this background, the SM detectors are capable of offering a complexity that is slightly higher than that of the MMSE receiver of V-BLAST, but still substantially lower than that of the ML MIMO detector of V-BLAST, as demonstrated by Fig. 6.18. Let us recall from Sec. 6.4.2 that the STSK receivers require extra signal processing, before being able to invoke the SM detectors. Therefore, it is shown by Fig. 6.18 that the STSK detection complexity is higher than the SM detection complexity. Nonetheless, considering that STSK is capable of offering a diversity gain for SM, as demonstrated by Fig. 6.14, the employment of STSK is beneficial, because its detection complexity is considerably lower than that of both the V-BLAST and

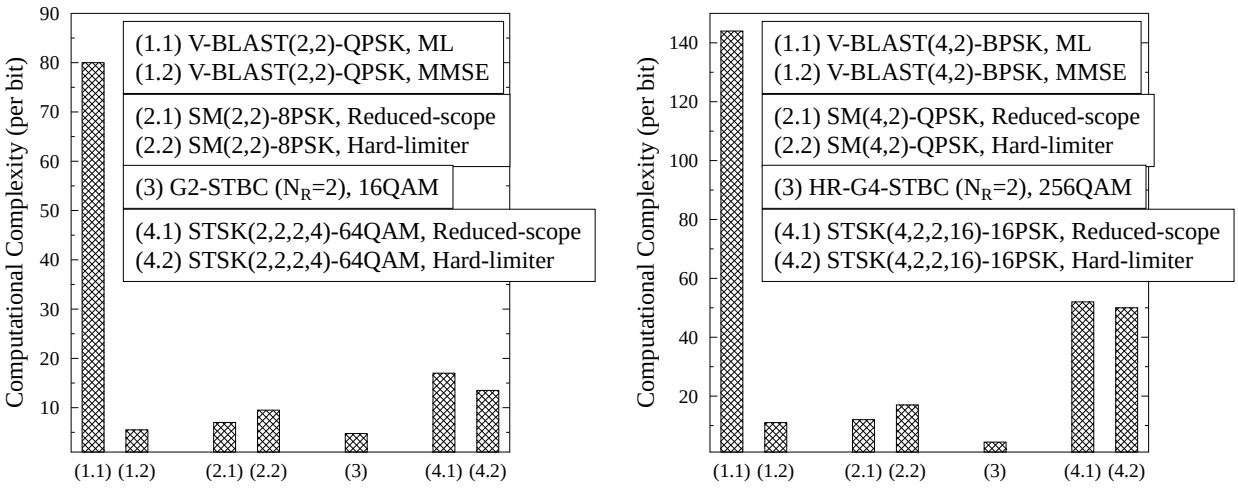

(a) $N_T = 2$, $N_R = 2$, $R = 4$ (b) $N_T = 4$, $N_R = 2$, $R = 4$

Figure 6.18: Complexity comparison between V-BLAST, SM, STBC and STSK associated with the same throughput of $R = 4$ bits/block/channel-use, where the fading channels are assumed to be constant, so that the same operations do not have to be repeated by the MIMO receivers.

the LDC receivers invoking the ML MIMO detector, as evidenced by Fig. 6.18.

6.6 Chapter Conclusions

In this chapter, two salient tradeoffs of MIMO system design were analysed. First of all, the conventional MIMO systems have to strike a tradeoff between the attainable multiplexing and diversity gain. Observe in Table 6.12 that both V-BLAST and LDC achieve the full MIMO capacity of Eq. (6.4) in Fig. 6.11, provided that the LDC's parameters satisfy $N_Q \geq N_T N_P$. Both V-BLAST and LDC are capable of achieving the full multiplexing gain of ($\overline{R} = \frac{R}{BPS} = N_T$), which leads to a high system throughput that is N_T times higher than that of a SISO and SIMO system. Furthermore, as documented in Table 6.12, both STBC and LDC may achieve the full diversity gain of $\overline{D} = N_T N_R$ as seen in Fig. 6.12, provided that a sufficiently high number of symbol periods $N_P \geq N_T$ are reserved for the STM transmission. Moreover, the LDC is capable of providing an even better performance than its STBC counterpart as exemplified by Fig. 6.12, because the LDC can employ low-order MPSK/QAM schemes for maintaining the same throughput as its STBC counterpart.

In summary, the LDCs of Sec. 6.3.2.3 constitute the only family of MIMO schemes, which allows us to avoid striking a tradeoff between the attainable multiplexing and diversity gains, as also evidenced by Figs. 6.11 and 6.12, provided that the conditions of Eq. (6.96) as well as the rank and

Full MIMO capacity:	V-BLAST, LDC
Full multiplexing gain ($\overline{R} = \frac{R}{BPS} = N_T$):	V-BLAST, LDC
High multiplexing gain ($\overline{R} = \frac{R}{BPS} > 1$):	SM, STSK
Full diversity gain ($\overline{D} = N_T N_R$):	STBC, LDC, STSK
Low PEP at high SNR region:	STBC, LDC, STSK
Low PEP at low SNR region when equipping a high number of RAs $N_R \gg 1$:	multiplexing schemes employing low-level MPSK/QAM
Employing low-complexity linear receivers without imposing a performance loss:	STBC, SM, STSK
Flexible MIMO systems design:	LDC, STSK

Table 6.12: A brief summary of the advantages of differet MIMO design.

determinant criteria presented in Sec. 6.3.2.3 are satisfied. More explicitly, observe in Fig. 6.11a that the LDC exhibits the same CCMC capacity as V-BLAST for $N_T = N_R = 2$. Furthermore, as seen in Fig. 6.11b and Fig. 6.12a, the LDC(2,2,2,4)-QPSK scheme outperforms its identical-throughput counterparts of G2-STBC Square 16QAM and V-BLAST(2,2)-QPSK schemes. Similarly, for $N_T = N_R = 4$, the LDC(4,4,2,8)-QPSK outperforms all the other identical-throughput arrangements of Fig. 6.12b.

The other MIMO system design tradeoff between performance and complexity is also of concern for conventional MIMO systems. Unfortunately, both V-BLAST and LDC suffer from a severe performance erosion when the low-complexity linear receivers of Sec. 6.2.4 are employed. Against this background, the tradeoff between the performance attained and the complexity imposed has inspired the development of SM and STSK, which are capable of retaining the optimal detection capability at a substantially reduced complexity, as evidenced by Figs. 6.16 and 6.17. We have demonstrated in Sec. 6.4.3 and confirmed by Figs. 6.14 and 6.15 that although SM may not be capable of outperforming V-BLAST, the performance difference between V-BLAST and SM is almost negligible compared to that imposed by employing MMSE detector for V-BLAST in Fig. 6.12. The same trends are observed in Figs. 6.14 and 6.15, when STSK is compared to LDC. We will demonstrate in Chapter 7 that the performance difference between these MIMO schemes may become relatively small when channel coding is applied. In this realistic scenario, SM and STSK will become more favoured, because they offer optimum detection capability, whilst the linear MMSE detectors of V-BLAST and LDC are prone to producing unreliable LLRs, which misinform the turbo detection in coded systems.

In Sec. 6.4.1.1, we have also proposed a novel hard-decision-aided reduced-scope SM detector based on our previous publications of [141, 202, 203, 234], which circumvent the problem of erroneous TA activation index detection by taking into account the correlation between the TA index and the classic modulated symbol index. The family of optimal and suboptimal SM detectors is characterized in Sec. 6.4.1 and summarized in Tables 6.10 and 6.11. Our conclusion is that the reduced-scope optimal SM detector [204] is a meritorious candidate for SM schemes employing low-order MPSK/QAM constellations, while the recently proposed hard-limiter-based optimal SM detector is preferred for SM schemes employing high-order MPSK/QAM constellations. In the

next chapter, we will continue by proposing a soft-decision-aided reduced-scope SM detector for the set of coded MIMO systems.

It is also shown in Table 6.12 that both LDC and STSK benefit from a flexible MIMO system design. They can be designed for any arbitrary number of antennas N_T and N_R, for any number of channel uses N_P and for any number of transmitted symbols N_Q. More particularly, when $N_P \geq N_T$ is satisfied, the full transmit diversity gain may be achieved by LDC and STSK, while decreasing N_P below N_T may also offer an increased system throughput. The major drawback of LDC and STSK is that although their transmission matrices are populated by a random generation process performed in a offline search, the transmitted signals are no longer classic MPSK/QAM symbols, which imposes an increased complexity on the power amplifiers at the transmitters.

The recent developments in the millimeter-wave band [227, 343, 344] allow us to use a high number of antennas, especially at the base stations [227, 340–342]. This opens an exciting prospect for low-complexity MIMO system design. However, both SM and STSK still have their own limitations. As demonstrated in Table 6.12, although SM and STSK are good candidates for striking a tradeoff between performance and complexity, the tradeoff between the attainable multiplexing and diversity gain arises again for SM and STSK. As discussed in Sec. 6.4.3 and demonstrated by Fig. 6.13, SM is not capable of achieving the full MIMO capacity, while the STSK capacity is even lower than the SIMO capacity in the high SNR region. This leaves room for further research on GSM and GSTSK [217, 302], where several symbols per channel use are transmitted. However, the problem of IAI resurfaces again for GSM and GSTSK, unless the STBC codewords are transmitted by multiple active TAs. As a result, sub-optimal interference-suppression aided receivers are proposed for GSTSK receivers in [226, 229], which however fail to satisfy the SM/STSK motivation of low-complexity ML receiver design. As a remedy, it was suggested in [230, 231] that the multiple activated TAs for GSM should transmit the same signal in order to eliminate the IAI. We leave the further discussions on the topic of GSM and GSTSK design for our future work.

Chapter 7

Reduced-Complexity MIMO Design – Part II: Coded Systems

7.1 Introduction

Inspired by the turbo principles [2,8,38,39,80,239], the hard-decision-aided conventional MPSK/QAM demodulators are revised to be able to accept soft-bit input and to produce soft-bit decisions [66, 240, 241, 345], so that the soft-decision-aided MPSK/QAM demodulator may iteratively interact with a channel decoder, as discussed in Chapter 2. The employment of a soft-decision-aided demodulator in turbo detection was shown to be fundamentally important for wireless communication systems to approach their capacity predictions [8, 86, 243].

It is straightforward to transform the hard-decision-aided ML MIMO detector of Eq. (6.13) into a soft-decision-aided Log-MAP MIMO detector, as seen in [8, 346], where the *a priori* LLRs gleaned from the channel decoder may be directly added to the MIMO decision metrics of Eq. (6.11). However, the beneficial exploitation of the *a priori* probabilities poses a major challenge in the context of reduced-complexity MIMO detectors, including the soft-decision-aided SD and MMSE detectors conceived for coded V-BLAST systems as well as the reduced-complexity design of soft-decision-aided SM detectors.

In more details, considering that an *a posteriori* LLR produced by a soft-decision-aided MIMO detector requires two *a posteriori* probabilities associated with the specific bit being 1 and 0, respectively, the hard-decision-aided SDs of Secs. 6.2.2 and 6.2.3 cannot directly deliver these soft-bit decisions. Therefore, it was proposed in [173] that the hard-decision-aided SD may be revised for generating a list of candidates that minimize the ML MIMO metric of Eq. (6.11). Then the two groups of candidates associated with the bit being 0 or 1 may be compared by the Max-Log-MAP algorithm or by the Approx-Log-MAP algorithm for evaluating the corresponding pair of output *a posteriori* probability metrics. However, owing to the fact that the *a priori* probabilities are not incorporated in the SD search, there is no guarantee that the optimal *a posteriori* MIMO probabil-

ity metrics can be found. Against this background, numerous research efforts [347–350] have been dedicated to improving the suboptimal soft-decision-aided SD. Following this, the optimum soft-decision-aided SD that invoked the depth-first algorithm and incorporated the *a priori* probabilities was proposed in [174]. This method was also adopted by the soft-decision-aided MSDSD [132] presented in Chapters 3 and 5. The optimum soft-decision-aided SD's PED increment is revised from its hard-decision counterpart by adding a non-negative *a priori* probability term to the PED increment, so that the output *a posteriori* probability becomes optimum for coded V-BLAST detection, as we will detail in Sec. 7.2.2.

In order to invoke low-complexity linear *M*PSK/QAM detectors for our V-BLAST receivers, the MMSE filter of Sec. 6.2.4 may be employed. The major challenge of tailoring the MMSE solution for coded V-BLAST detection is that the *a priori* probabilities are no longer identical for all constellation points. In order to solve this problem, the exact MMSE solution incorporating the candidate-dependent *a priori* probabilities was derived for turbo equalization in [70–72], for CDMA MUDs in [75, 76] and for linear V-BLAST receivers in [13, 77, 78]. The interference cancellation techniques of [351–353] may improve the MMSE receiver's performance in coded V-BLAST systems, but the additional complexity and the resultant problem of error propagation may further complicate the coded MIMO system's design.

For the sake of achieving a low detection complexity without compromising the optimum MIMO detection capability, in Sec. 7.4, we will propose reduced-complexity soft-decision-aided detectors for coded SM systems. It is not straightforward to revise the low-complexity hard-decision-aided SM detectors of Sec. 6.4 for coded systems. First of all, the substantial complexity reduction provided by the hard-limiter-based SM detection of Sec. 6.4.1.2 relies on the low-complexity implementation of hard-decision-aided *M*PSK/QAM demodulators. However, as demonstrated in Sec. 2.3, the soft-decision-aided *M*PSK/QAM demodulators cannot directly map the channel's output signal onto the *M*PSK/QAM constellation diagram, when the *a priori* LLRs gleaned from the channel decoder are taken into account. This is because the channel decoder is unaware of which *M*PSK/QAM modulation scheme is employed. More explicitly, the channel decoder invoking the BCJR Log-MAP algorithm [26–28, 239] relies on bit-based signal processing by accepting the *a priori* soft-bit LLRs from the demodulator and by producing the *a posteriori* LLRs for the demodulator, as depicted by Fig. 2.2. However, the soft-decision-aided demodulator has to rely on symbol-based signal processing, where both the channel's output signal as well as the *a priori* LLRs gleaned from the channel decoder have to be transformed back into modulated symbols according to the constellation diagram. As a result, all probability metrics corresponding to all constellation points have to be evaluated and compared in order to retain the optimum detection capability. Secondly, the sub-optimal hard-decision-aided SM detectors of Secs. 6.4.1.4-6.4.1.7 are not recommended for employment in coded SM systems. This is because these sub-optimal SM detectors may falsify the reliability of the output LLRs, which may fail to reflect the true *a posteriori* probabilities by producing LLRs having excessively high values. This flawed situation cannot be readily rectified by the channel decoder, as discussed in Sec. 2.3.2. The sub-optimal soft-decision-

aided SM detectors may also be found in [228, 354–357], where the beneficial *a priori* information is not exploited by the SM detectors.

We note that as previously demonstrated in Sec. 6.3.2.3, the LDC receiver may still invoke V-BLAST detectors in coded MIMO systems, and the STSK receiver may invoke soft-decision-aided SM detectors. Coded MIMO systems exhibit the same features as uncoded MIMO systems, including the tradeoff between the attainable multiplexing versus diversity gain as well as the tradeoff between the performance versus complexity, which were discussed in Chapter 6.

Against this background, in this chapter, we invoke the previously introduced reduced complexity design of Sec. 2.4, Sec. 3.3.3 and Sec. 6.4.1.1 to the soft-decision-aided MIMO detectors. The novel contributions of this chapter are as follows:

1. We demonstrate the benefits of the reduced-complexity design proposed in Sec. 2.4 for the soft-decision-aided MPSK/QAM demodulators in the context of both channel coded V-BLAST as well as channel coded STBC systems. More explicitly, the exact MMSE solution conceived for soft-decision-aided V-BLAST detection and the soft-decision-aided STBC detection relying on processing decoupled data streams are presented in the context of reduced-complexity soft-decision-aided MPSK/QAM detectors. This contribution is based on our publication [236].

2. Similar to the soft-decision-aided MSDSD conceived for DPSK in Chapter 3, the reduced-complexity SD previously proposed for MSDSD in Sec. 3.3.3 is now invoked for the soft-decision-aided V-BLAST detection, when MPSK constellations are employed[1]. More explicitly, by exploring the symmetry provided by the Gray-labelled MPSK constellation, the SD's Schnorr-Euchner search strategy becomes capable of visiting a reduced number of constellation points in a zig-zag fashion, without invoking any complex sorting algorithm. Meanwhile, the optimum SD capability is retained.

3. Furthermore, we apply the reduced-scope SM detector design of Sec. 6.4.1.1 to both channel coded SM and STSK systems. In more details, the maximum *a posteriori* probability required by the Max-Log-MAP algorithm may be obtained by tentatively invoking the reduced-complexity soft-decision-aided MPSK/QAM demodulators proposed in Sec. 2.4 before deciding on the SM's TA activation index, where the correlation between the classic modulated symbol index and the TA index is taken into account, so that the detected TA index is always the MAP solution. In this way, only a subset of the MPSK/QAM constellation points are visited, while the optimum SM detection capability is retained. Both the Approx-Log-MAP algorithm and the Max-Log-MAP algorithm are conceived for this soft-decision-aided SM detector design. This contribution is based on our publications [202, 203].

[1]The case of SD aided MQAM detection in coded V-BLAST systems is very different from our previous reduced-complexity design for SD aided MPSK detection. We demonstrate in this chapter the soft-decision-aided V-BLAST SD conceived for Square MQAM constellations, but the corresponding reduced complexity design is left to our future work.

The rest of this chapter is organized as follows. The coded V-BLAST system design is introduced in Sec. 7.2, where the reduced-complexity soft-decision-aided SD and MMSE receivers are discussed. Moreover, the reduced-complexity soft-decision-aided STBC detectors are presented in Sec. 7.3. Furthermore, the reduced-complexity SM detection design conceived for coded SM and STSK systems is proposed in Sec. 7.4. Our performance results recorded for coded MIMO systems are summarized in Sec. 7.5, while our chapter conclusions are offered in Sec. 7.6

7.2 Coded V-BLAST

As discussed in the previous section, there are numerous challenges in designing V-BLAST detectors for coded applications. In this section, we introduce a variety of soft-decision-aided V-BLAST detectors that are constructed from the hard-decision-aided V-BLAST detectors presented in Sec. 6.2. More explicitly, we are going to apply the previously proposed reduced complexity design of Sec. 3.3.3 and Sec. 2.4 to the family of soft-decision-aided SD and MMSE receivers conceived for coded V-BLAST systems. More explicitly, first of all, the optimum soft-decision-aided MAP V-BLAST detection is introduced in Sec. 7.2.1, which exhibits an excessive detection complexity. In order to mitigate this problem, the soft-decision-aided SDs conceived for MPSK and Square MQAM are presented in Secs. 7.2.2 and 7.2.3, respectively. Furthermore, in order to benefit from the linear MPSK/QAM detector's low complexity, the exact MMSE solution conceived for coded V-BLAST systems is derived in Sec. 7.2.4.

7.2.1 Soft-Decision-Aided Optimum MAP V-BLAST Detection

According to the received signal model of Eq. (6.1), the V-BLAST detector may aim for maximizing the *a posteriori* probability of Eq. (6.12) in the logarithmic domain, which may produce the *a posteriori* LLRs as [8, 27, 240, 241, 346]:

$$\begin{aligned} L_p(b_k) &= \ln \frac{\sum_{\forall \mathbf{S}^i \in \{\mathbf{S}^i\}_{b_k=1}} p(\mathbf{S}^i|\mathbf{Y})}{\sum_{\forall \mathbf{S}^i \in \{\mathbf{S}^i\}_{b_k=0}} p(\mathbf{S}^i|\mathbf{Y})} \\ &= \ln \frac{\sum_{\forall \mathbf{S}^i \in \{\mathbf{S}^i\}_{b_k=1}} p(\mathbf{Y}|\mathbf{S}^i) p(\mathbf{S}^i)}{\sum_{\forall \mathbf{S}^i \in \{\mathbf{S}^i\}_{b_k=0}} p(\mathbf{Y}|\mathbf{S}^i) p(\mathbf{S}^i)}, \end{aligned} \tag{7.1}$$

where the subsets $\{\mathbf{S}^i\}_{b_k=1}$ and $\{\mathbf{S}^i\}_{b_k=0}$ represent the V-BLAST combinations set for $\mathbf{S}$ of Eq. (6.11), when the specific bit b_k is fixed to be 1 and 0, respectively. There are a total number of $I = M^{N_T}$ combinations for $\mathbf{S}$ of Eq. (6.11). Furthermore, the conditional probability $p(\mathbf{Y}|\mathbf{S}^i)$ in Eq. (7.1) is given by Eq. (6.2). Let us assume that all source information bits are mutually independent. Then the *a priori* probabilities $\{p(\mathbf{S}^i)\}_{i=0}^{I-1}$ may be expressed as:

$$p(\mathbf{S}^i) = \prod_{\bar{k}=1}^{N_T \mathrm{BPS}} \frac{\exp\left[\widetilde{b}_{\bar{k}} L_a(b_{\bar{k}})\right]}{1 + \exp\left[L_a(b_{\bar{k}})\right]}, \tag{7.2}$$

where $\{L_a(b_k)\}_{k=1}^{N_T\text{BPS}}$ denote the *a priori* LLRs gleaned from a channel decoder, while $[\widetilde{b}_1 \cdots \widetilde{b}_{N_T\text{BPS}}] = \text{dec2bin}(i)$ refers to the bit mapping of V-BLAST to the signal $\mathbf{S}^i$. Therefore, the *a posteriori* LLRs produced the Log-MAP algorithm of Eq. (7.1), may be rewritten as:

$$L_p(b_k) = \ln \frac{\sum_{\forall \mathbf{S}^i \in \{\mathbf{S}^i\}_{b_k=1}} \exp(d^i)}{\sum_{\forall \mathbf{S}^i \in \{\mathbf{S}^i\}_{b_k=0}} \exp(d^i)}, \tag{7.3}$$

where the probability metric d^i in Eq. (7.3) is given by:

$$d^i = -\frac{\|\mathbf{Y} - \mathbf{S}^i\mathbf{H}\|^2}{N_0} + \sum_{\bar{k}=1}^{N_T\text{BPS}} \widetilde{b}_{\bar{k}} L_a(b_{\bar{k}}). \tag{7.4}$$

We note that the common constant of $\frac{1}{\prod_{\bar{k}=1}^{N_T\text{BPS}}\{1+\exp[L_a(b_{\bar{k}})]\}}$ in all V-BLAST combinations $\{\mathbf{S}^i\}_{i=0}^{I-1}$ of Eq. (7.2) is eliminated by the division operation in Eq. (7.1). The resultant extrinsic LLRs produced by the Log-MAP algorithm may be further expressed as $L_e(b_k) = L_p(b_k) - L_a(b_k)$.

In practice, the low-complexity Max-Log-MAP [27] algorithm may be invoked by the optimum V-BLAST detector relying on the simplified Obejctive Function (OF) of:

$$L_p(b_k) = \max_{\forall \mathbf{S}^i \in \{\mathbf{S}^i\}_{b_k=1}} d^i - \max_{\forall \mathbf{S}^i \in \{\mathbf{S}^i\}_{b_k=0}} d^i, \tag{7.5}$$

which imposes a performance loss owing to the fact that only the pair of maximum *a posteriori* probabilities associated with $b_k = 1$ and $b_k = 0$ are taken into account. In order to mitigate this problem, the so-called Approx-Log-MAP algorithm [28, 239] may be invoked by the optimum V-BLAST relying on the simplified OF of:

$$L_p(b_k) = \text{jac}_{\forall \mathbf{S}^i \in \{\mathbf{S}^i\}_{b_k=1}} d^i - \text{jac}_{\forall \mathbf{S}^i \in \{\mathbf{S}^i\}_{b_k=0}} d^i, \tag{7.6}$$

where the corrected Jacobian algorithm jac compensates for the inaccuracy imposed by the maximization operation of Eq. (7.5) by taking into account the difference between every pair of probability metrics, when their values are compared, which is demonstrated by Eq. (2.36).

The optimum V-BLAST detection introduced in this section requires us to evaluate and compare all $I = 2^{N_T\text{BPS}}$ combinations of MIMO signals, which imposes an unaffordable detection complexity. Therefore, as introduced in Sec. 6.2.1 for uncoded V-BLAST transceivers, the SD and the family of linear receivers may be introduced in order to visit all the N_T parallel MPSK/QAM constellation diagrams separately, so that the signal processing complexity may be reduced for coded V-BLAST systems.

7.2.2 Soft-Decision-Aided SD Conceived for Coded V-BLAST Employing PSK

In order to invoke SD for the Max-Log-MAP optimum V-BLAST detection, it may be observed in Eq. (7.5) that the Max-Log-MAP algorithm aims to find the maximum probability metric, which is similar to the action of the hard-decision-aided ML-optimum V-BLAST detection of Eq. (6.13).

Therefore, the problem of finding the maximum probability metric d^i of Eq. (7.4) may be transformed to the problem of searching for the minimum ED formulated as:

$$d = \frac{\sum_{v=1}^{N_T} \left| \widetilde{Y}_v - \sum_{t=v}^{N_T} l_{t,v} s_t \right|^2}{N_0} - \sum_{v=1}^{N_T} \left\{ \sum_{\bar{k}_v=1}^{\text{BPS}} \left[\widetilde{b}_{\bar{k}_v} L_a(b_{\bar{k}_v}) - \overline{C}_{a,\bar{k}_v}^{SD} \right] \right\}, \tag{7.7}$$

which is obtained by toggling the polarity of the probability metric d^i of Eq. (7.4). The first term in Eq. (7.7) is revised from the hard-decision-aided SD's ED of Eq. (6.17). We note that the SD aided V-BLAST employing MPSK operates based on the equivalent received signal model of Eq. (6.16) after the QR decomposition of Eq. (6.14). The $(N_R \times N_T)$-element submatrix $\mathbf{Q}$ has orthogonal columns satisfying $\mathbf{Q}^H\mathbf{Q} = I_{N_T}$, and hence it does not change the statistics of the AWGN matrix $\mathbf{V}$ in Eq. (6.16). The second term in Eq. (7.7) is revised from the *a priori* probability term of Eq. (7.4), where an extra constant $\overline{C}_{a,\bar{k}_v}^{SD} = \frac{1}{2}\left[|L_a(b_{\bar{k}_v})| + L_a(b_{\bar{k}_v})\right]$ is introduced in order to guarantee that the ED of Eq. (7.7) remains non-negative all the time [176, 283], which may be verified by:

$$\begin{aligned} -\widetilde{b}_{\bar{k}_v} L_a(b_{\bar{k}_v}) + \frac{1}{2}\left[|L_a(b_{\bar{k}_v})| + L_a(b_{\bar{k}_v})\right] &= \begin{cases} -\widetilde{b}_{\bar{k}_v} L_a(b_{\bar{k}_v}) + L_a(b_{\bar{k}_v}), & \text{if } L_a(b_{\bar{k}_v}) \geq 0 \\ -\widetilde{b}_{\bar{k}_v} L_a(b_{\bar{k}_v}), & \text{if } L_a(b_{\bar{k}_v}) < 0 \end{cases} . \\ &= \begin{cases} L_a(b_{\bar{k}_v}), & \text{if } L_a(b_{\bar{k}_v}) \geq 0 \text{ and } \widetilde{b}_{\bar{k}_v} = 0 \\ -L_a(b_{\bar{k}_v}), & \text{if } L_a(b_{\bar{k}_v}) < 0 \text{ and } \widetilde{b}_{\bar{k}_v} = 1 \\ 0, & \text{otherwise} \end{cases} . \end{aligned} \tag{7.8}$$

As a result, the maximization operation of the Max-Log-MAP of Eq. (7.5) is transformed into finding the optimal candidate that lies within the decoding sphere radius R, which is formulated as:

$$\frac{\sum_{v=1}^{N_T} \left| \widetilde{Y}_v - \sum_{t=v}^{N_T} l_{t,v} s_t \right|^2}{N_0} - \sum_{v=1}^{N_T} \left\{ \sum_{\bar{k}_v=1}^{\text{BPS}} \left[\widetilde{b}_{\bar{k}_v} L_a(b_{\bar{k}_v}) - \overline{C}_{a,\bar{k}_v}^{SD} \right] \right\} < R^2. \tag{7.9}$$

In order to solve Eq. (7.9) step by step, the SD may evaluate the PED according to the ED of Eq. (7.7) as:

$$\begin{aligned} d_v &= \frac{\sum_{\bar{v}=v}^{N_T} \left| \widetilde{Y}_{\bar{v}} - \sum_{t=\bar{v}}^{N_T} l_{t,\bar{v}} s_t \right|^2}{N_0} - \sum_{\bar{v}=v}^{N_T} \left\{ \sum_{\bar{k}_{\bar{v}}=1}^{\text{BPS}} \left[\widetilde{b}_{\bar{k}_{\bar{v}}} L_a(b_{\bar{k}_{\bar{v}}}) - \overline{C}_{a,\bar{k}_{\bar{v}}}^{SD} \right] \right\}, \\ &= d_{v+1} + \Delta_v, \end{aligned} \tag{7.10}$$

where the PED increment Δ_v is given by:

$$\begin{aligned} \Delta_v &= \frac{\left| \widetilde{Y}_v - \sum_{t=v}^{N_T} l_{t,v} s_t \right|^2}{N_0} - \sum_{\bar{k}_v=1}^{\text{BPS}} \left[\widetilde{b}_{\bar{k}_v} L_a(b_{\bar{k}_v}) - \overline{C}_{a,\bar{k}_v}^{SD} \right] \\ &= \frac{\left| \left(\widetilde{Y}_v - \sum_{t=v+1}^{N_T} l_{t,v} s_t \right) - l_{v,v} s_v \right|^2}{N_0} - \sum_{\bar{k}_v=1}^{\text{BPS}} \left[\widetilde{b}_{\bar{k}_v} L_a(b_{\bar{k}_v}) - \overline{C}_{a,\bar{k}_v}^{SD} \right]. \end{aligned} \tag{7.11}$$

It may be observed that the V-BLAST SD's PED increment of Eq. (7.11) is in the same form as the MSDSD's PED increment of Eq. (3.64). Therefore, in this chapter, the V-BLAST SD tree search

Function: $[\hat{\mathbf{S}}, d_{MAP}] = \textbf{SoftSD-MPSK}(\widetilde{\mathbf{Y}}, \mathbf{L}, \mathbf{P}, N_0, M, N_T, R^2)$

Requirements: $\mathbf{P}$ is a $(N_T \times M)$-element matrix with entries $\{\{P_{v,m+1} = \sum_{\bar{k}_v=1}^{\text{BPS}} \left[\widetilde{b}_{\bar{k}_v} L_a(b_{\bar{k}_v}) - \overline{C}_{a,\bar{k}_v}^{SD}\right]\}_{v=1}^{N_T}\}_{m=0}^{M-1}$, which is the *a priori* probability term in the PED increment of Eq. (7.11). The bits mapping arrangement is directly given by $\{[\widetilde{b}_1, \cdots, \widetilde{b}_{\text{BPS}}] = \textbf{dec2bin}(m)\}_{m=0}^{M-1}$.

```
1: d_{N_T+1} = 0                                                                          //initialize PED
2: v = N_T                                                                                //initialize SD search index
3: [{Δ_v^m}_{m=0}^{M-1}, {s_v^m}_{m=0}^{M-1}, n_v] = sortDelta(Ỹ_v, {l_{t,v}}_{t=v}^{N_T}, {s_t}_{t=v+1}^{N_T}, P_{v,m+1}, N_0)   //sort all child nodes
4: loop
5:    d_v = d_{v+1} + Δ_v^{n_v}                                                           //update PED of Eq. (7.10)
6:    if d_v < R^2
7:       s_v = s_v^{n_v}                                                                  //update new child node
8:       if v ≠ 1
9:          v = v − 1                                                                     //move down index v
10:         [{Δ_v^m}_{m=0}^{M-1}, {s_v^m}_{m=0}^{M-1}, n_v] = sortDelta(Ỹ_v, {l_{t,v}}_{t=v}^{N_T}, {s_t}_{t=v+1}^{N_T}, P_{v,m+1}, N_0)   //sort all child nodes
11:      else
12:         R^2 = d_1                                                                     //update SD radius
13:         Ŝ = [s_1, ··· , s_{N_T}]                                                      //update candidates
14:         do
15:            if v == N_T return [Ŝ, R^2] and exit                                       //terminate SD
16:            v = v + 1                                                                  //move up index v
17:         while n_v == (M − 1)
18:         n_v = n_v + 1                                                                //visit the next child node
19:      end if
20:   else
21:      do
22:         if v == N_T return [Ŝ, R^2] and exit                                        //terminate SD
23:         v = v + 1                                                                    //move up index v
24:      while n_v == (M − 1)
25:      n_v = n_v + 1                                                                   //visit the next child node
26:   end if
27: end loop
```

Subfunction: $[\{\Delta_v^m\}_{m=0}^{M-1}, \{s_v^m\}_{m=0}^{M-1}, n_v] = \textbf{sortDelta}(\widetilde{Y}_v, \{l_{t,v}\}_{t=v}^{N_T}, \{s_t\}_{t=v+1}^{N_T}, P_{v,m+1}, N_0)$

```
1: for m = 0 to (M − 1)                                                                   //visit all M child nodes
2:    s_v^m = s^m / sqrt(N_T)                                                             //visit the m-th child node
3:    Δ_v^m = |(Ỹ_v − Σ_{t=v+1}^{N_T} l_{t,v} s_t) − l_{v,v} s_v^m|^2 / N_0 − P_{v,m+1}   //update PED increment according to Eq. (7.11)
4: end for
5: [{Δ_v^m}_{m=0}^{M-1}, {s_v^m}_{m=0}^{M-1}] = sortI({Δ_v^m}_{m=0}^{M-1})                //rank PED increments in increasing order
6: n_v = 0                                                                                //initialize child node counter
```

Table 7.1: Pseudo-code for soft-decision-aided SD conceived for coded V-BLAST employing MPSK.

is also implemented by depth-first algorithm of [10,12,313] using the Schnorr-Euchner search strategy [237], as demonstrated in Sec. 3.3.2, so that the Max-Log-MAP optimum V-BLAST detection capability may be retained. Since the V-BLAST SD indices are different from those of the MSDSD, the pseudo-codes tailored for V-BLAST SD are summarized in Table 7.1. Similar to our discussion of Sec. 3.3.2 on soft-decision-aided MSDSD, the decision variable $\widetilde{z}_v^{SD}$ of Eq. (6.22) cannot be directly used to find the optimum MPSK phasor in coded V-BLAST systems, because the channel decoder is unaware of which MPSK constellation diagram is considered. Hence the *a priori* probability terms of $\sum_{\bar{k}_v=1}^{\text{BPS}} \left[\widetilde{b}_{\bar{k}_v} L_a(b_{\bar{k}_v}) - \overline{C}_{a,\bar{k}_v}^{SD}\right]$ are not appropriately mapped to the received signal's constellation diagram. As a result, the Schnorr-Euchner search strategy has to be implemented by enumerating and comparing all probability metrics corresponding to all MPSK constellation points, which is summarized by the subfunction "sortDelta" in Table 7.1.

Nonetheless, due to the similarity between the V-BLAST SD and MSDSD scheme, we propose to appropriately adapt our reduced-complexity design of Sec. 3.3.3 for our soft-decision-aided MSDSD to the soft-decision-aided SD of Table 7.1. More explicitly, the SD's PED increment of Eq. (7.11) may be further extended as:

$$\begin{aligned}\Delta_v &= \left|\widetilde{y}_v^{SD} - s_v^m \widetilde{h}_v^{SD}\right|^2 - \sum_{\bar{k}_v=1}^{\text{BPS}} \left[\widetilde{b}_{\bar{k}_v} L_a(b_{\bar{k}_v}) - \overline{C}_{a,\bar{k}_v}^{SD}\right] \\ &= -2\Re\left[(\bar{s}_v^m)^* \widetilde{z}_v^{SD}\right] - \sum_{\bar{k}_v=1}^{\text{BPS}} \widetilde{b}_{\bar{k}_v} L_a(b_{\bar{k}_v}) + \frac{L_a(b_1)+L_a(b_2)}{2} + \widetilde{C}_v^{SD},\end{aligned} \tag{7.12}$$

where the equivalent "received signal" and "fading factor" are given by $\widetilde{y}_v^{SD} = \frac{\widetilde{Y}_v - \sum_{t=v+1}^{N_T} l_{t,v} s_t}{\sqrt{N_0}}$ and $\widetilde{h}_v^{SD} = \frac{l_{v,v}}{\sqrt{N_0 N_T}}$, respectively. Similar to our discussions in Sec. 3.3.3, the MPSK constellation diagram (except BPSK) is rotated anti-clockwise by (π/M) at the receiver as $\{\bar{s}_v^m = s_v^m \exp(j\frac{\pi}{M})\}_{m=0}^{M-1}$, so that there are exactly $M/4$ constellation points in each quadrant. The new decision variable seen in Eq. (7.12) is then given by:

$$\widetilde{z}_v^{SD} = \widetilde{y}_v^{SD} (\widetilde{h}_v^{SD})^* \exp(j\frac{\pi}{M}). \tag{7.13}$$

We note that if the MPSK constellation diagram rotation of $\{\bar{s}_v^m = s_v^m \exp(j\frac{\pi}{M})\}_{m=0}^{M-1}$ is carried out at the V-BLAST transmitter, which implies that the rotated MPSK symbols $\{\bar{s}_v^m\}_{m=0}^{M-1}$ are transmitted instead of the original MPSK symbols $\{s_v^m\}_{m=0}^{M-1}$, the rotation term $\exp(j\frac{\pi}{M})$ in the decision variable calculation of Eq. (7.13) may be eliminated. Moreover, the constant $\widetilde{C}_v^{SD}$ seen in Eq. (7.12) is given by:

$$\widetilde{C}_v^{SD} = |\widetilde{y}_v^{SD}|^2 + |\widetilde{h}_v^{SD}|^2 + \sum_{\bar{k}_v=1}^{\text{BPS}} \overline{C}_{a,\bar{k}_v}^{SD} - \frac{L_a(b_1)+L_a(b_2)}{2}, \tag{7.14}$$

which is invariant over all MPSK candidates $\{\bar{s}_v^m\}_{m=0}^{M-1}$.

Therefore, the reduced-complexity design of Sec. 3.3.3 may be directly applied to soft-decision-aided V-BLAST SD. More explicitly, the subfunction "sortDelta" in Table 7.1 may be replaced by the subfunctions of "findBest" and "findNext" in Tables 3.5-3.7, where the MSDSD terms of $\mathbf{Y}_{v-1}^{MSDSD}$, $\mathbf{H}_{v-1}^{MSDSD}$, $\bar{z}_{v-1}^{MSDSD}$ and $\overline{C}_{v-1}^{MSDSD}$ may be respectively replaced by $\widetilde{y}_v^{SD}$, $\widetilde{h}_v^{SD}$, $\widetilde{z}_v^{SD}$ and $\widetilde{C}_v^{SD}$ in Eq. (7.12), while the MSDSD index $v-1$ may be replaced by V-BLAST SD index v. In this way, the soft-decision-aided V-BLAST SD may visit the MPSK constellation points in a zigzag fashion, in a similar manner to the hard-decision-aided V-BLAST SD, so that only a subset of constellation points have to be evaluated by the SD. Moreover, the sorting algorithm required by subfunction "sortDelta" in Table 7.1, whose complexity order may be as high as $O(M \log M)$ [285, 286], is avoided by the reduced complexity design.

In summary, with the aid of SD, the minimum ED d_{MAP} as well as the optimum V-BLAST candidate $\hat{\mathbf{S}}$ may be obtained. The optimum candidate $\hat{\mathbf{S}}$ may further be translated into hard-bit decisions $\{\hat{b}_k^{MAP}\}_{k=1}^{N_T \text{BPS}}$. In order to produce the soft-bit decisions according to the Max-Log-MAP algorithm of Eq. (7.5), the SD is invoked again for producing the second ED $\bar{d}_{MAP}$, where the search space is halved by fixing the k-th bit b_k to the flipped MAP decision as $b_k = \bar{b}_k^{MAP}$. In

summary, the Max-Log-MAP algorithm of Eq. (7.5) may be completed as:

$$L_p(b_k) = \begin{cases} -d_{MAP} + \bar{d}_{MAP}, & \text{if } b_k^{MAP} = 1 \\ -\bar{d}_{MAP} + d_{MAP}, & \text{if } b_k^{MAP} = 0 \end{cases}. \tag{7.15}$$

In this way, the SD has to be invoked $(N_T\text{BPS}+1)/(N_T\text{BPS})$ times for producing a single soft-bit output, which is often referred to as the Repeated Tree Search (RTS) [132, 284].

Recently, it was proposed in [175, 176] that a Single Tree Search (STS) [284] may avoid the RTS by establishing a list administration in the SD's tree search. In other words, the SD may only be invoked once for obtaining both d_{MAP} as well as a total number of N_TBPS EDs $\bar{d}_{MAP}$. The SD using STS may be implemented according to the following rules:

1. The list includes the MAP optimum ED hypothesis of d_{MAP} and a total of N_TBPS counter-hypothesis EDs $\bar{d}_{MAP}^{\bar{b}_k}$, which may be initialized to infinity. All the bit-mapping arrangements corresponding to the EDs in the list are recorded.

2. When a leaf node associated with the PED d_1 at the SD index of $v = 1$ is examined, if a new ED hypothesis is found and updated because we have $d_1 < d_{MAP}$, the former ED hypothesis becomes a new counter-hypothesis ED metric.

3. If the visited leaf node associated with the PED d_1 at the SD index of $v = 1$ is not a new ED hypothesis because of $d_1 > d_{MAP}$, the PED d_1 is a new counter-hypothesis ED metric.

4. A new counter-hypothesis ED metric has to be checked against at least one existing counter-hypothesis EDs. For example, considering a V-BLAST system associated with $N_T = 2$ employing QPSK, if the ED hypothesis d_{MAP} is associated with the bit-mapping arrangement of $[b_1 b_2 b_3 b_4] = [0000]$, the new counter-hypothesis ED metric associated with the bit-mapping arrangement of $[b_1 b_2 b_3 b_4] = [0101]$ has to be compared to both $\bar{d}_{MAP}^{\bar{b}_2}$ and $\bar{d}_{MAP}^{\bar{b}_4}$. The tested counter-hypothesis ED may be updated, when a case of $d_1 < \bar{d}_{MAP}^{\bar{b}_k}$ occurs.

5. A SD subtree may be prunned at index $1 < v < N_T$, if the PED d_v is higher than all the ED entries of d_{MAP} and $\bar{d}_{MAP}^{\bar{b}_k}$ in the list.

The downside of the STS is that the bit-mapping arrangements have to be recorded and traced along with the SD tree search. In fact, the STS's motivation of visiting a node at most once can also be accomplished by RTS, provided that the same SD tree is re-used when the SD search is invoked again. The extra requirement imposed on RTS is that the nodes that have previously been visited should be labelled, so that any repeated calculations may be avoided by reading the previously evaluated PED metrics. The labelling of SD nodes also requires extra memory, hence the choice between RTS and STS depends on the practical circuit design and implementation.

subfunction: $[\{\Delta_v^{\overline{m}}\}_{\overline{m}=0}^{\sqrt{M}-1}, \{s_v^{\overline{m}}\}_{\overline{m}=0}^{\sqrt{M}-1}, n_v] = \textbf{sortDelta}(\widetilde{\overline{Y}}_v, \{l_{t,v}\}_{t=v}^{2N_T}, \{s_t\}_{t=v+1}^{2N_T}, P_{v,m+1}, N_0)$	
1: **for** $m = 0$ **to** $(\sqrt{M}-1)$	//visit all $\sqrt{M}$ child nodes
2: $\quad \overline{s}_v^m = \frac{\overline{s}^m}{\sqrt{N_T}}$	//visit the m-th child node
3: $\quad \Delta_v^m = \frac{\left[\left(\widetilde{\overline{Y}}_v - \sum_{t=v+1}^{2N_T} l_{t,v}\overline{s}_t\right) - l_{v,v}\overline{s}_v^m\right]^2}{N_0} - P_{v,m+1}$	//update PED increment according to Eq. (7.18)
4: **end for**	
5: $[\{\Delta_v^{\overline{m}}\}_{\overline{m}=0}^{\sqrt{M}-1}, \{s_v^{\overline{m}}\}_{\overline{m}=0}^{\sqrt{M}-1}] = \textbf{sortI}(\{\Delta_v^m\}_{m=0}^{\sqrt{M}-1})$	//rank PED increments in increasing order
6: $n_v = 0$	//initialize child node counter

Table 7.2: Pseudo-code for soft-decision-aided SD conceived for coded V-BLAST employing Square MQAM.

7.2.3 Soft-Decision-Aided SD Conceived for Coded V-BLAST Employing Square QAM

As demonstrated in Sec. 6.2.3, when Square MQAM is employed for V-BLAST, the received signal model of Eq. (6.1) may be decoupled as seen in Eq. (6.27), so that the real and imaginary parts of the Square MQAM constellation may be detected separately. As a result, the ED of the soft-decision-aided V-BLAST SD of Eq. (7.7) may be revised for the case of Square MQAM as:

$$d = \frac{\sum_{v=1}^{2N_T}\left(\widetilde{\overline{Y}}_v - \sum_{t=v}^{2N_T} l_{t,v}\overline{s}_t\right)^2}{N_0} - \sum_{v=1}^{2N_T}\left\{\sum_{\bar{k}_v=1}^{\text{BPS}/2}\left[\widetilde{b}_{\bar{k}_v} L_a(b_{\bar{k}_v}) - \overline{C}_{a,\bar{k}_v}^{SD}\right]\right\}, \tag{7.16}$$

where the first term is revised from the hard-decision-aided SD's ED of Eq. (6.30). The equivalent received signal model is given by Eq. (6.29) after applying the QR decomposition of Eq. (6.28). The $(2N_R \times 2N_T)$-element real-valued matrix $\mathbf{Q}$ has orthogonal columns, yielding $\mathbf{Q}^T\mathbf{Q} = \mathbf{I}_{2N_T}$, hence it does not change the statistics of the AWGN matrix $\overline{\mathbf{V}}$ in Eq. (6.29). In this section, we only consider the Square MQAM constellations associated with an even BPS, although it is straightforward to extend this solution to the case of odd BPS.

In order to minimize the ED of Eq. (7.16) by SD, the PED may be expressed as:

$$\begin{aligned} d_v &= \frac{\sum_{\bar{v}=v}^{2N_T}\left(\widetilde{\overline{Y}}_{\bar{v}} - \sum_{t=\bar{v}}^{2N_T} l_{t,\bar{v}}\overline{s}_t\right)^2}{N_0} - \sum_{\bar{v}=v}^{2N_T}\left\{\sum_{\bar{k}_{\bar{v}}=1}^{\text{BPS}/2}\left[\widetilde{b}_{\bar{k}_{\bar{v}}} L_a(b_{\bar{k}_{\bar{v}}}) - \overline{C}_{a,\bar{k}_{\bar{v}}}^{SD}\right]\right\} \\ &= d_{v+1} + \Delta_v, \end{aligned} \tag{7.17}$$

where the PED increment Δ_v is given by:

$$\begin{aligned} \Delta_v &= \frac{\left(\widetilde{\overline{Y}}_v - \sum_{t=v}^{2N_T} l_{t,v}\overline{s}_t\right)^2}{N_0} - \sum_{\bar{k}_v=1}^{\text{BPS}/2}\left[\widetilde{b}_{\bar{k}_v} L_a(b_{\bar{k}_v}) - \overline{C}_{a,\bar{k}_v}^{SD}\right] \\ &= \frac{\left[\left(\widetilde{\overline{Y}}_v - \sum_{t=v+1}^{2N_T} l_{t,v}\overline{s}_t\right) - l_{v,v}\overline{s}_v\right]^2}{N_0} - \sum_{\bar{k}_v=1}^{\text{BPS}/2}\left[\widetilde{b}_{\bar{k}_v} L_a(b_{\bar{k}_v}) - \overline{C}_{a,\bar{k}_v}^{SD}\right]. \end{aligned} \tag{7.18}$$

Therefore, based on the PED increment of Eq. (7.18), the soft-decision-aided V-BLAST SD of Table 7.1 may be invoked for detecting Square MQAM symbols. Owing to the fact that the real and imaginary parts of the Square MQAM constellation are decoupled, the SD index of Table 7.1

should be starting and terminating at $v = 2N_T$ instead of $v = N_T$, and the constellation set size is given by $\sqrt{M}$ instead of M. The subfunction "sortDelta" in Table 7.1 is tailored for Square MQAM in Table 7.2, where $\{\bar{s}^m\}_{m=0}^{\sqrt{M}-1}$ are $\sqrt{M}$PAM symbols that constitute the real and imaginary parts of the Square MQAM constellation. The V-BLAST Max-Log-MAP algorithm obeys Eq. (7.15) following our discussions in Sec. 7.2.2.

The Schnorr-Euchner search strategy tailored for Square MQAM in Table 7.2 not only requires to visit all legitimate $\sqrt{M}$PAM constellation points, but it also invokes sorting algorithms for sorting the PED increments in ascending order. More efficient calculation methods may be found in [358–360], where the SD visits only a subset of $\sqrt{M}$PAM constellation points. However, these existing solutions only take into account the channel-output-related PED increment term, which is the hard-decision-aided SD metric. The *a priori* information is beneficial, especially for MIMO detectors, where the streams impose interference on each other. Therefore, it is desirable to simplify the Schnorr-Euchner search strategy of Table 7.2 without avoiding the *a priori* information, following the reduced complexity design proposed for MPSK constellations in Sec. 3.3.3. We will tailor the reduced complexity design for Square MQAM constellations in our future research.

7.2.4 Soft-Decision-Aided MMSE Receiver Conceived for Coded V-BLAST

Although SD may effectively reduce the MIMO system's detection complexity, its complexity is still substantially higher than linear MPSK/QAM receivers' detection complexity. Therefore, as discussed in the context of uncoded V-BLAST, linear filters such as the ZF and MMSE receivers may be conceived for decoupling the parallel data streams that are separately transmitted but amalgamated at the receiver. However, imposing a performance loss is inevitable due to the presence of interference amongst the data streams, hence a tradeoff between the performance attained and the complexity imposed has to be taken into account. In this section, we provide insights into the soft-decision-aided MMSE solution conceived for coded V-BLAST receivers.

If we directly revise the hard-decision-aided V-BLAST MMSE of Sec. 6.2.4 for employment in coded systems, the linear MPSK/QAM detection algorithms introduced in Sec. 2.3.1 may be invoked for detecting the decoupled data streams, where the symbol-by-symbol based *a posteriori* probability metrics are given by:

$$d^m = -\frac{\left|z_v^{MMSE} - s^m \mathbf{H}_{v,-}\mathbf{G}_{-,v}^{MMSE}/\sqrt{N_T}\right|^2}{N_0\|\mathbf{G}_{-,v}^{MMSE}\|^2} + \sum_{\bar{k}_v=1}^{\mathrm{BPS}} \widetilde{b}_{\bar{k}_v} L_a(b_{\bar{k}_v}). \tag{7.19}$$

The decision variable $\{z_v^{MMSE}\}_{v=1}^{N_T}$ is given by Eq. (6.41), while the MMSE filters taps $\{\mathbf{G}_{-,v}^{MMSE}\}_{v=1}^{N_T}$ are formulated in Eq. (6.40). When the fading channels envelope remains near-constant, the MMSE filters taps $\{\mathbf{G}_{-,v}^{MMSE}\}_{v=1}^{N_T}$ do not have to be updated. Therefore, the soft-decision-aided MPSK/QAM detection algorithms of Eqs. (2.30), (2.34) and (2.35) invoking Eq. (7.19) exhibit a low detection complexity. However, this simple mechanism does not deliver the exact MMSE solution [13, 77, 78] for coded V-BLAST systems, hence it suffers from a performance loss. In order

to mitigate this problem, we have to introduce the exact MMSE solution, which takes into account the *a priori* knowledge of the V-BLAST symbols.

Let us firstly assume that the v-th element s_v in the V-BLAST transmit signal vector of Eq. (6.11) has to be detected, while the remaining $N_T - 1$ signals are deemed to be interference. As a result, the received signal model of Eq. (6.1) may be further extended as:

$$\begin{aligned}\mathbf{Y} &= s_v \mathbf{H}_{v,-} + \sum_{\forall \bar{v} \neq v} s_{\bar{v}} \mathbf{H}_{\bar{v},-} + \mathbf{V} \\ &= s_v \mathbf{H}_{v,-} + \mathbf{S}^{\bar{v}} \mathbf{H}^{\bar{v}} + \mathbf{V},\end{aligned} \tag{7.20}$$

where the $[1 \times (N_T - 1)]$-element interference vector $\mathbf{S}^{\bar{v}} = [s_1, \cdots, s_{v-1}, s_{v+1}, \cdots, s_{N_T}]$ may be obtained by omitting the v-th element of the V-BLAST transmit signal vector $\mathbf{S}$ of Eq. (6.11), while the $[(N_T - 1) \times N_R]$-element fading matrix $\mathbf{H}^{\bar{v}} = \left[\mathbf{H}_{1,-}^T, \cdots, \mathbf{H}_{v-1,-}^T, \mathbf{H}_{v+1,-}^T, \cdots, \mathbf{H}_{N_T,-}^T\right]^T$ is obtained by omitting the v-th row in the fading matrix $\mathbf{H}$ of Eq. (6.1).

According to Eq. (7.20), the MMSE filter conceived for detecting s_v produces the following output signal:

$$\begin{aligned}\overline{z}_v^{MMSE} &= \mathbf{Y}\overline{\mathbf{G}}_v^{MMSE} \\ &= s_v \mathbf{H}_{v,-} \overline{\mathbf{G}}_v^{MMSE} + \mathbf{S}^{\bar{v}} \mathbf{H}^{\bar{v}} \overline{\mathbf{G}}_v^{MMSE} + \mathbf{V}\overline{\mathbf{G}}_v^{MMSE},\end{aligned} \tag{7.21}$$

where the $(N_R \times 1)$-element MMSE filter taps vector $\overline{\mathbf{G}}_v^{MMSE}$ aims for minimizing the interference term of $u_v = \mathbf{S}^{\bar{v}} \mathbf{H}^{\bar{v}} \overline{\mathbf{G}}_v^{MMSE}$ without increasing the noise power. In the presence of *a priori* LLRs, the residual interference term after MMSE filtering may be further mitigated by the following operations [13, 77, 78, 353]:

$$\begin{aligned}\check{z}_v^{MMSE} &= \overline{z}_v^{MMSE} - \hat{u}_v \\ &= \overline{z}_v^{MMSE} - \hat{\mathbf{S}}^{\bar{v}} \mathbf{H}^{\bar{v}} \overline{\mathbf{G}}_v^{MMSE},\end{aligned} \tag{7.22}$$

where $\hat{\mathbf{S}}^{\bar{v}} = \mathrm{E}(\mathbf{S}^{\bar{v}})$ referred to as the estimate of the interference vector. The t-th $(1 \leq t \leq N_T - 1)$ element $\hat{s}_t = \mathrm{E}(s_t)$ in $\hat{\mathbf{S}}^{\bar{v}}$ may be obtained from the *a priori* probabilities as [13, 72, 75]:

$$\begin{aligned}\hat{s}_t &= \frac{1}{\sqrt{N_T}} \sum_{m=0}^{M-1} s^m p(s_t = s^m) \\ &= \frac{1}{\sqrt{N_T}} \sum_{m=0}^{M-1} s^m \frac{\exp\left[\sum_{\tilde{k}=1}^{\mathrm{BPS}} \widetilde{b}_{\tilde{k}} L_a(b_{\tilde{k}})\right]}{\prod_{\tilde{k}=1}^{\mathrm{BPS}} \{1 + \exp\left[L_a(b_{\tilde{k}})\right]\}},\end{aligned} \tag{7.23}$$

where $\{\widetilde{b}_{\tilde{k}}\}_{\tilde{k}=1}^{\mathrm{BPS}}$ refers to the bit-mapping arrangement corresponding to the constellation point s^m.

The MMSE filter taps should be formulated by minimizing the OF constituted by the difference between the filter output $\check{z}_v^{MMSE}$ which was decontaminated from the interference and the target signal s_v as [13, 77, 78, 353]:

$$\begin{aligned}\mathrm{E}\left(|\check{z}_v^{MMSE} - s_v|^2\right) &= \mathrm{E}\left[|\mathbf{Y}\overline{\mathbf{G}}_v^{MMSE} - (\hat{u}_v + s_v)|^2\right] \\ &= (\overline{\mathbf{G}}_v^{MMSE})^H \mathrm{E}(\mathbf{Y}^H\mathbf{Y}) \overline{\mathbf{G}}_v^{MMSE} - (\overline{\mathbf{G}}_v^{MMSE})^H \mathrm{E}\left[\mathbf{Y}^H(\hat{u}_v + s_v)\right] \\ &\quad - \mathrm{E}\left[(\hat{u}_v + s_v)^* \mathbf{Y}\right] \overline{\mathbf{G}}_v^{MMSE} + \mathrm{E}(|\hat{u}_v + s_v|^2).\end{aligned} \tag{7.24}$$

From the MMSE filter's perspective, only the target signal s_v is an unknown variable, while the rest of the transmitted symbols $\{s_t\}_{t=1}^{N_T-1}$ in $\mathbf{S}^{\bar{v}}$ are assumed to be known that may be evaluated according to Eq. (7.23). As a result, the correlation between the interferring signals is given by:

$$\mathrm{E}(s_t^* s_{\bar{t}}) = \begin{cases} \hat{s}_t^* \hat{s}_{\bar{t}}, & t \neq \bar{t} \\ \mathrm{E}(|s_t|^2), & t = \bar{t} \end{cases}, \tag{7.25}$$

where the estimation of the interference power relies on:

$$\begin{aligned} \mathrm{E}(|s_t|^2) &= \frac{1}{N_T} \sum_{m=0}^{M-1} |s^m|^2 p(s_t = s^m) \\ &= \frac{1}{N_T} \sum_{m=0}^{M-1} |s^m|^2 \frac{\exp\left[\sum_{\bar{k}=1}^{\mathrm{BPS}} \widetilde{b}_{\bar{k}} L_a(b_{\bar{k}})\right]}{\prod_{\bar{k}=1}^{\mathrm{BPS}} \{1 + \exp\left[L_a(b_{\bar{k}})\right]\}}. \end{aligned} \tag{7.26}$$

As a special case, we have $\mathrm{E}(|s_t|^2) = \frac{1}{N_T}$ for MPSK constellations. Moreover, the correlation between the target signal s_v and the interference is simply given by $\{\mathrm{E}(s_v^* s_t) = 0\}_{t=1}^{N_T-1}$. As a result, the correlation of received signals $\mathbf{Y}$ in Eq. (7.24) is given by:

$$\begin{aligned} \mathrm{E}(\mathbf{Y}^H \mathbf{Y}) &= \frac{1}{N_T} \mathbf{H}_{v,-}^H \mathbf{H}_{v,-} + (\mathbf{H}^{\bar{v}})^H \mathrm{E}\left[(\mathbf{S}^{\bar{v}})^H \mathbf{S}^{\bar{v}}\right] \mathbf{H}^{\bar{v}} + N_0 \mathbf{I}_{N_R} \\ &= \frac{1}{N_T} \mathbf{H}_{v,-}^H \mathbf{H}_{v,-} + (\mathbf{H}^{\bar{v}})^H \left[(\hat{\mathbf{S}}^{\bar{v}})^H \hat{\mathbf{S}}^{\bar{v}} - \mathrm{diag}\left((\hat{\mathbf{S}}^{\bar{v}})^H \hat{\mathbf{S}}^{\bar{v}}\right) + \mathbf{R}_{|s|}^{\bar{v}}\right] \mathbf{H}^{\bar{v}} + N_0 \mathbf{I}_{N_R}, \end{aligned} \tag{7.27}$$

where the $[(N_T-1) \times (N_T-1)]$-element matrix $\mathbf{R}_{|s|}^{\bar{v}}$ refers to the estimate of the interference powers as $\mathbf{R}_{|s|}^{\bar{v}} = \mathrm{diag}\left[\mathrm{E}(|s_1|^2), \cdots, \mathrm{E}(|s_{v-1}|^2), \mathrm{E}(|s_{v+1}|^2), \cdots, \mathrm{E}(|s_{N_T}|^2)\right]$. Similarly, the cross-correlation in Eq. (7.24) may be further extended as:

$$\begin{aligned} \mathrm{E}\left[\mathbf{Y}^H(\hat{u}_v + s_v)\right] &= \frac{1}{N_T} \mathbf{H}_{v,-}^H + (\mathbf{H}^{\bar{v}})^H (\hat{\mathbf{S}}^{\bar{v}})^H \hat{u}_v \\ &= \frac{1}{N_T} \mathbf{H}_{v,-}^H + (\mathbf{H}^{\bar{v}})^H (\hat{\mathbf{S}}^{\bar{v}})^H \hat{\mathbf{S}}^{\bar{v}} \mathbf{H}^{\bar{v}} \overline{\mathbf{G}}_v^{MMSE}. \end{aligned} \tag{7.28}$$

Furthermore, the correlation of $(\hat{u}_v + s_v)$ in Eq. (7.24) is given by:

$$\mathrm{E}(|\hat{u}_v + s_v|^2) = \frac{1}{N_T} + (\overline{\mathbf{G}}_v^{MMSE})^H (\mathbf{H}^{\bar{v}})^H (\hat{\mathbf{S}}^{\bar{v}})^H \hat{\mathbf{S}}^{\bar{v}} \mathbf{H}^{\bar{v}} \overline{\mathbf{G}}_v^{MMSE}. \tag{7.29}$$

In summary, the MSE OF of Eq. (7.24) may be rewritten as:

$$\begin{aligned} \mathrm{E}\left(|\check{z}_v^{MMSE} - s_v|^2\right) &= (\overline{\mathbf{G}}_v^{MMSE})^H \Big\{ \frac{1}{N_T} \mathbf{H}_{v,-}^H \mathbf{H}_{v,-} + (\mathbf{H}^{\bar{v}})^H \left[(\hat{\mathbf{S}}^{\bar{v}})^H \hat{\mathbf{S}}^{\bar{v}} - \mathrm{diag}\left((\hat{\mathbf{S}}^{\bar{v}})^H \hat{\mathbf{S}}^{\bar{v}}\right) + \mathbf{R}_{|s|}^{\bar{v}}\right] \mathbf{H}^{\bar{v}} \\ &\quad + N_0 \mathbf{I}_{N_R} \Big\} \overline{\mathbf{G}}_v^{MMSE} - \frac{(\overline{\mathbf{G}}_v^{MMSE})^H \mathbf{H}_{v,-}^H}{N_T} - (\overline{\mathbf{G}}_v^{MMSE})^H (\mathbf{H}^{\bar{v}})^H (\hat{\mathbf{S}}^{\bar{v}})^H \hat{\mathbf{S}}^{\bar{v}} \mathbf{H}^{\bar{v}} \overline{\mathbf{G}}_v^{MMSE} \\ &\quad - \frac{\mathbf{H}_{v,-} \overline{\mathbf{G}}_v^{MMSE}}{N_T} + \frac{1}{N_T} \\ &= (\overline{\mathbf{G}}_v^{MMSE})^H \left\{ \frac{1}{N_T} \mathbf{H}_{v,-}^H \mathbf{H}_{v,-} + (\mathbf{H}^{\bar{v}})^H \left[\mathbf{R}_{|s|}^{\bar{v}} - \mathrm{diag}\left((\hat{\mathbf{S}}^{\bar{v}})^H \hat{\mathbf{S}}^{\bar{v}}\right)\right] \mathbf{H}^{\bar{v}} + N_0 \mathbf{I}_{N_R} \right\} \overline{\mathbf{G}}_v^{MMSE} \\ &\quad - \frac{(\overline{\mathbf{G}}_v^{MMSE})^H \mathbf{H}_{v,-}^H}{N_T} - \frac{\mathbf{H}_{v,-} \overline{\mathbf{G}}_v^{MMSE}}{N_T} + \frac{1}{N_T}. \end{aligned} \tag{7.30}$$

As a result, the MMSE solution of $\frac{\partial \mathrm{E}\left(|\tilde{z}_v^{MMSE}-s_v|^2\right)}{\partial \overline{\mathbf{G}}_v^{MMSE}}=0$ leads to the filter taps of:

$$\overline{\mathbf{G}}_v^{MMSE}=\left\{\mathbf{H}_{v,-}^H\mathbf{H}_{v,-}+N_T(\mathbf{H}^{\bar{v}})^H\left[\mathbf{R}_{|s|}^{\bar{v}}-\mathrm{diag}\left((\hat{\mathbf{S}}^{\bar{v}})^H\hat{\mathbf{S}}^{\bar{v}}\right)\right]\mathbf{H}^{\bar{v}}+N_TN_0\mathbf{I}_{N_R}\right\}^{-1}\mathbf{H}_{v,-}^H. \tag{7.31}$$

When there is no *a priori* information as represented by $I_A=0$, we have $\mathbf{R}_{|s|}^{\bar{v}}=\frac{1}{N_T}\mathbf{I}_{N_T-1}$ and $\hat{\mathbf{S}}^{\bar{v}}=\mathbf{0}_{1\times(N_T-1)}$, and the MMSE filter taps of Eq. (7.31) become:

$$\overline{\mathbf{G}}_v^{MMSE}=\left(\mathbf{H}^H\mathbf{H}+N_TN_0\mathbf{I}_{N_R}\right)^{-1}\mathbf{H}_{v,-}^H, \tag{7.32}$$

which is exactly the same as the hard-decision-aided MMSE solution of Eq. (6.40). By contrast, when perfect *a priori* information of $I_A=1$ is available, we have $\mathbf{R}_{|s|}^{\bar{v}}=\mathrm{diag}\left((\hat{\mathbf{S}}^{\bar{v}})^H\hat{\mathbf{S}}^{\bar{v}}\right)$, which results in the following MMSE filter taps:

$$\overline{\mathbf{G}}_v^{MMSE}=\left(\mathbf{H}_{v,-}^H\mathbf{H}_{v,-}+N_TN_0\mathbf{I}_{N_R}\right)^{-1}\mathbf{H}_{v,-}^H. \tag{7.33}$$

We note that the case of $I_A=1$ leads to the perfect estimation of the interference term $\hat{u}_v=\mathbf{S}^{\bar{v}}\mathbf{H}^{\bar{v}}\overline{\mathbf{G}}_v^{MMSE}$ of Eq. (7.22), which implies that the optimum MIMO detection capability may be achieved by the MMSE detector at $I_A=1$.

As a result, the interference-decontaminated MMSE filter output of Eq. (7.22) may now be rewritten as:

$$\tilde{z}_v^{MMSE}=s_v\mathbf{H}_{v,-}\overline{\mathbf{G}}_v^{MMSE}+(\mathbf{S}^{\bar{v}}-\hat{\mathbf{S}}^{\bar{v}})\mathbf{H}^{\bar{v}}\overline{\mathbf{G}}_v^{MMSE}+\mathbf{V}\overline{\mathbf{G}}_v^{MMSE}, \tag{7.34}$$

where the residual interference term $(\mathbf{S}^{\bar{v}}-\hat{\mathbf{S}}^{\bar{v}})\mathbf{H}^{\bar{v}}\overline{\mathbf{G}}_v^{MMSE}$ and the AWGN term $\mathbf{V}\overline{\mathbf{G}}_v^{MMSE}$ may be jointly considered as a Gaussian-distributed variable with a zero mean and a variance of $N_0^{MMSE}=\mathrm{E}\left[|(\mathbf{S}^{\bar{v}}-\hat{\mathbf{S}}^{\bar{v}})\mathbf{H}^{\bar{v}}\overline{\mathbf{G}}_v^{MMSE}+\mathbf{V}\overline{\mathbf{G}}_v^{MMSE}|^2\right]$, which may be further extended as [72, 75, 353, 361]:

$$\begin{aligned}
N_0^{MMSE}&=(\overline{\mathbf{G}}_v^{MMSE})^H\left\{(\mathbf{H}^{\bar{v}})^H\left[\mathrm{E}\left((\mathbf{S}^{\bar{v}})^H\mathbf{S}^{\bar{v}}\right)-(\hat{\mathbf{S}}^{\bar{v}})^H\hat{\mathbf{S}}^{\bar{v}}\right]\mathbf{H}^{\bar{v}}+N_0\mathbf{I}_{N_R}\right\}\overline{\mathbf{G}}_v^{MMSE}\\
&=(\overline{\mathbf{G}}_v^{MMSE})^H\left\{(\mathbf{H}^{\bar{v}})^H\left[\mathbf{R}_{|s|}^{\bar{v}}-\mathrm{diag}\left((\hat{\mathbf{S}}^{\bar{v}})^H\hat{\mathbf{S}}^{\bar{v}}\right)\right]\mathbf{H}^{\bar{v}}+N_0\mathbf{I}_{N_R}\right\}\overline{\mathbf{G}}_v^{MMSE}\\
&=(\overline{\mathbf{G}}_v^{MMSE})^H\left(\frac{1}{N_T}\mathbf{H}_{v,-}\right)^H-(\overline{\mathbf{G}}_v^{MMSE})^H\left(\frac{1}{N_T}\mathbf{H}_{v,-}^H\mathbf{H}_{v,-}\right)\overline{\mathbf{G}}_v^{MMSE}\\
&=\frac{1}{N_T}(\overline{\mathbf{G}}_v^{MMSE})^H(\mathbf{H}_{v,-})^H-\frac{1}{N_T}\left|(\overline{\mathbf{G}}_v^{MMSE})^H(\mathbf{H}_{v,-})^H\right|^2.
\end{aligned} \tag{7.35}$$

Finally, the linear soft-decision-aided MPSK/QAM detector of Sec. 2.3.1 may be invoked based on the equivalent received signal model of Eq. (7.34). The *a posteriori* probability metrics $\{d^m\}_{m=0}^{M-1}$ of Eq. (2.30) formulated in the Log-MAP algorithm, the Max-Log-MAP algorithm of Eq. (2.34) and the Approx-Log-MAP algorithm of Eq. (2.35) are given by:

$$d^m=-\frac{\left|\tilde{z}_v^{MMSE}-\frac{1}{\sqrt{N_T}}s^m\mathbf{H}_{v,-}\overline{\mathbf{G}}_v^{MMSE}\right|^2}{N_0^{MMSE}}+\sum_{\bar{k}=1}^{\mathrm{BPS}}\widetilde{b}_{\bar{k}}L_a(b_{\bar{k}}). \tag{7.36}$$

The calculation of the MMSE filter taps $\{\overline{\mathbf{G}}_v^{MMSE}\}_{v=1}^{N_T}$ of Eq. (7.31) specifically calculated for detecting all the V-BLAST symbols $\{s_v\}_{v=1}^{N_T}$ requires us to perform an matrix-element inversion

for a total number of N_T times, which may be excessive for practical implementations. Simplified matrix inversion techniques were proposed in [72, 362], but the matrix inversion still had to be carried out N_T times. Moreover, it was proposed in [353] that both $\mathbf{R}_{|s|}^{\bar{v}}$ and $\hat{\mathbf{S}}^{\bar{v}}$ may be estimated by averaging over all samples of a detection frame, so that the matrix inversion did not have to be updated for detecting each transmitted V-BLAST symbol. However, this method imposes a substantial performance loss. Against this background, a better choice is proposed in [78], where the matrix inversion only has to be performed once for detecting all the N_T transmitted V-BLAST symbols. In order to achieve this goal, let us firstly rewrite the MMSE filter taps $\overline{\mathbf{G}}_v^{MMSE}$ of Eq. (7.31) as:

$$\overline{\mathbf{G}}_v^{MMSE} = \left(\mathbf{Q} + e_v \mathbf{H}_{v,-}^H \mathbf{H}_{v,-}\right)^{-1} \mathbf{H}_{v,-}^H, \tag{7.37}$$

where the $(N_R \times N_R)$-element matrix $\mathbf{Q}$ is given by:

$$\mathbf{Q} = N_T \mathbf{H}^H \left[\mathbf{R}_{|s|} - \text{diag}\left(\hat{\mathbf{S}}^H \hat{\mathbf{S}}\right)\right] \mathbf{H} + N_T N_0 \mathbf{I}_{N_R}, \tag{7.38}$$

and we have $\mathbf{R}_{|s|} = \text{diag}[\text{E}(|s_1|^2), \cdots, \text{E}(|s_{N_T}|^2)]$ as well as $\hat{\mathbf{S}} = \text{E}(\mathbf{S}) = [\hat{s}_1, \cdots, \hat{s}_{N_T}]$, which are respectively revised from $\mathbf{R}_{|s|}^{\bar{v}}$ and $\hat{\mathbf{S}}^{\bar{v}}$ in Eq. (7.31). Moreover, the constant e_v in Eq. (7.37) is given by:

$$e_v = 1 - N_T \text{E}(|s_v|^2) + N_T |\hat{s}_v|^2. \tag{7.39}$$

According to the Sherman-Morrison formula of [363–365], the matrix inversion of Eq. (7.37) may be extended as:

$$\left(\mathbf{Q} + e_v \mathbf{H}_{v,-}^H \mathbf{H}_{v,-}\right)^{-1} = \mathbf{Q}^{-1} - \frac{e_v \mathbf{Q}^{-1} \mathbf{H}_{v,-}^H \mathbf{H}_{v,-} \mathbf{Q}^{-1}}{1 + e_v \mathbf{H}_{v,-} \mathbf{Q}^{-1} \mathbf{H}_{v,-}^H}. \tag{7.40}$$

As a result, the MMSE filter tap $\overline{\mathbf{G}}_v^{MMSE}$ of Eq. (7.37) may be further extended as [78]:

$$\begin{aligned} \overline{\mathbf{G}}_v^{MMSE} &= \mathbf{Q}^{-1} \mathbf{H}_{v,-}^H - \frac{e_v \mathbf{Q}^{-1} \mathbf{H}_{v,-}^H \mathbf{H}_{v,-} \mathbf{Q}^{-1} \mathbf{H}_{v,-}^H}{1 + e_v \mathbf{H}_{v,-} \mathbf{Q}^{-1} \mathbf{H}_{v,-}^H} \\ &= \widetilde{\mathbf{G}}_v^{MMSE} \widetilde{C}_v^{MMSE}, \end{aligned} \tag{7.41}$$

where the equivalent MMSE filter taps vector is given by:

$$\begin{aligned} \widetilde{\mathbf{G}}_v^{MMSE} &= \mathbf{Q}^{-1} \mathbf{H}_{v,-}^H \\ &= \left\{ N_T \mathbf{H}^H \left[\mathbf{R}_{|s|} - \text{diag}\left(\hat{\mathbf{S}}^H \hat{\mathbf{S}}\right)\right] \mathbf{H} + N_T N_0 \mathbf{I}_{N_R} \right\}^{-1} \mathbf{H}_{v,-}^H, \end{aligned} \tag{7.42}$$

while the constant $\widetilde{C}_v^{MMSE}$ is given by:

$$\begin{aligned} \widetilde{C}_v^{MMSE} &= 1 - \frac{e_v \mathbf{H}_{v,-} \widetilde{\mathbf{G}}_v^{MMSE}}{1 + e_v \mathbf{H}_{v,-} \widetilde{\mathbf{G}}_v^{MMSE}} \\ &= \frac{1}{1 + e_v \mathbf{H}_{v,-} \widetilde{\mathbf{G}}_v^{MMSE}}. \end{aligned} \tag{7.43}$$

We note that $\widetilde{\mathbf{G}}_v^{MMSE}$ of Eq. (7.42) may be obtained by simply retaining the v-th column of $\widetilde{\mathbf{G}}^{MMSE} = \mathbf{Q}^{-1} \mathbf{H}^H$. Hence the matrix inversion only has to be performed once for obtaining all the equivalent MMSE filter taps vectors $\{\widetilde{\mathbf{G}}_v^{MMSE}\}_{v=1}^{N_T}$.

It is maybe readily shown that using the equivalent MMSE filter taps vectors $\{\widetilde{\mathbf{G}}_v^{MMSE}\}_{v=1}^{N_T}$ of Eq. (7.42) instead of $\{\overline{\mathbf{G}}_v^{MMSE}\}_{v=1}^{N_T}$ of Eq. (7.31) does not change the MMSE detection results. More explicitly, the *a posteriori* probability metric d^m of Eq. (7.36) may be further extended as:

$$\begin{aligned} d^m &= -\frac{\left|\mathbf{Y}\widetilde{\mathbf{G}}_v^{MMSE}\widetilde{C}_v^{MMSE} - \hat{\mathbf{S}}^{\bar{v}}\mathbf{H}^{\bar{v}}\widetilde{\mathbf{G}}_v^{MMSE}\widetilde{C}_v^{MMSE} - \frac{1}{\sqrt{N_T}}s^m\mathbf{H}_{v,-}\widetilde{\mathbf{G}}_v^{MMSE}\widetilde{C}_v^{MMSE}\right|^2}{\left|\widetilde{C}_v^{MMSE}\right|^2(\widetilde{\mathbf{G}}_v^{MMSE})^H\left\{(\mathbf{H}^{\bar{v}})^H\left[\mathbf{R}_{|s|}^{\bar{v}} - \text{diag}\left((\hat{\mathbf{S}}^{\bar{v}})^H\hat{\mathbf{S}}^{\bar{v}}\right)\right]\mathbf{H}^{\bar{v}} + N_0\mathbf{I}_{N_R}\right\}\widetilde{\mathbf{G}}_v^{MMSE}} \\ &\quad + \sum_{\bar{k}=1}^{\text{BPS}}\widetilde{b}_{\bar{k}}L_a(b_{\bar{k}}) \\ &= -\frac{\left|\mathbf{Y}\widetilde{\mathbf{G}}_v^{MMSE} - \hat{\mathbf{S}}^{\bar{v}}\mathbf{H}^{\bar{v}}\widetilde{\mathbf{G}}_v^{MMSE} - \frac{1}{\sqrt{N_T}}s^m\mathbf{H}_{v,-}\widetilde{\mathbf{G}}_v^{MMSE}\right|^2}{(\widetilde{\mathbf{G}}_v^{MMSE})^H\left\{(\mathbf{H}^{\bar{v}})^H\left[\mathbf{R}_{|s|}^{\bar{v}} - \text{diag}\left((\hat{\mathbf{S}}^{\bar{v}})^H\hat{\mathbf{S}}^{\bar{v}}\right)\right]\mathbf{H}^{\bar{v}} + N_0\mathbf{I}_{N_R}\right\}\widetilde{\mathbf{G}}_v^{MMSE}} + \sum_{\bar{k}=1}^{\text{BPS}}\widetilde{b}_{\bar{k}}L_a(b_{\bar{k}}), \end{aligned} \tag{7.44}$$

which verifies that replacing $\overline{\mathbf{G}}_v^{MMSE}$ by $\widetilde{\mathbf{G}}_v^{MMSE}$ does not change the *a posteriori* probability metric d^m of Eq. (7.36). Finally, Eq. (7.44) may be simplified to:

$$d^m = -\frac{\left|\widetilde{z}_v^{MMSE} - s^m\right|^2}{\widetilde{N}_0^{MMSE}} + \sum_{\bar{k}=1}^{\text{BPS}}\widetilde{b}_{\bar{k}}L_a(b_{\bar{k}}), \tag{7.45}$$

where the decision variable is given by:

$$\widetilde{z}_v^{MMSE} = \left(\mathbf{Y}\widetilde{\mathbf{G}}_v^{MMSE} - \hat{\mathbf{S}}^{\bar{v}}\mathbf{H}^{\bar{v}}\widetilde{\mathbf{G}}_v^{MMSE}\right)/\widetilde{h}_v^{MMSE}, \tag{7.46}$$

while the equivalent fading factor $\widetilde{h}_v^{MMSE} = \frac{1}{\sqrt{N_T}}\mathbf{H}_{v,-}\widetilde{\mathbf{G}}_v^{MMSE}$ obtained from Eq. (7.44) is supposed to be a real number according to the MMSE receiver's equivalent noise power calculation of Eq. (7.35) [78]. Furthermore, the new equivalent noise power $\widetilde{N}_0^{MMSE}$ in Eq. (7.45) is given by:

$$\begin{aligned} \widetilde{N}_0^{MMSE} &= (\widetilde{\mathbf{G}}_v^{MMSE})^H\left\{(\mathbf{H}^{\bar{v}})^H\left[\mathbf{R}_{|s|}^{\bar{v}} - \text{diag}\left((\hat{\mathbf{S}}^{\bar{v}})^H\hat{\mathbf{S}}^{\bar{v}}\right)\right]\mathbf{H}^{\bar{v}} + N_0\mathbf{I}_{N_R}\right\}\widetilde{\mathbf{G}}_v^{MMSE}/(\widetilde{h}_v^{MMSE})^2 \\ &= \frac{(\widetilde{\mathbf{G}}_v^{MMSE})^H\mathbf{H}_{v,-}^H}{N_T(\widetilde{h}_v^{MMSE})^2} + \frac{\left[|\hat{s}_v|^2 - \text{E}(|s_v|^2)\right]\left|(\widetilde{\mathbf{G}}_v^{MMSE})^H\mathbf{H}_{v,-}^H\right|^2}{(\widetilde{h}_v^{MMSE})^2} \\ &= \frac{1}{\sqrt{N_T}\cdot\widetilde{h}_v^{MMSE}} + N_T\left[|\hat{s}_v|^2 - \text{E}(|s_v|^2)\right]. \end{aligned} \tag{7.47}$$

Considering that the V-BLAST MMSE receiver's *a posteriori* probability metric $\{d^m\}_{m=0}^{M-1}$ of Eq. (7.45) is in the same form as the general MPSK/QAM cases of Eqs. (2.37) and (2.38), the reduced-complexity soft-decision-aided MPSK/QAM detectors proposed in Sec. 2.4 may be directly invoked for the coded V-BLAST scheme's linear MMSE receiver, where $\widetilde{z}_n$ and $\widetilde{N}_0$ in Sec. 2.4 may be respectively replaced by $\widetilde{z}_v^{MMSE}$ of Eq. (7.46) and $\widetilde{N}_0^{MMSE}$ of Eq. (7.47).

7.3 Coded Space-Time Block Code

It was demonstrated in Sec. 6.3.1 that the STBCs, which comply with the orthogonality requirement may invoke the low-complexity linear MPSK/QAM receivers for detecting the decoupled

data streams without encountering V-BLAST's IAI problem. As a result, based on the decoupled conditional probability of receiving $\mathbf{Y}$ in Eq. (6.51) when the STBC codeword $\mathbf{S}$ is transmitted, the Log-MAP algorithm conceived for optimum MIMO detection in Eq. (7.1) may be simplified for optimum STBC detection as:

$$\begin{aligned} L_p(b_k) &= \ln \frac{\sum_{\forall s^m \in \{s^m\}_{b_k=1}} p(\overline{z}_q|s^m)p(s^m)}{\sum_{\forall s^m \in \{s^m\}_{b_k=0}} p(\overline{z}_q|s^m)p(s^m)} \\ &= \ln \frac{\sum_{\forall s^m \in \{s^m\}_{b_k=1}} \exp(d^m)}{\sum_{\forall s^m \in \{s^m\}_{b_k=0}} \exp(d^m)}, \end{aligned} \tag{7.48}$$

where the decoupled conditional probability $p(\overline{z}_q|s^m)$ is given by Eq. (6.52). Hence the *a posteriori* probability metric of Eq. (7.48) is given by:

$$d^m = -\frac{|\overline{z}_q - s^m|^2}{\overline{N}_0} + \sum_{\bar{k}=1}^{\text{BPS}} \widetilde{b}_{\bar{k}} L_a(b_{\bar{k}}). \tag{7.49}$$

The decision variable $\overline{z}_q$ and the equivalent noise power $\overline{N}_0$ are defined in Eq. (6.52). Therefore, the Log-MAP algorithm conceived for STBC detection in Eq. (7.48) produces the k-th soft-bit decision for the q-th STBC stream's transmitted symbol by visiting only a single MPSK/QAM constellation diagram.

Therefore, the Max-Log-MAP algorithm of Eq. (2.34) and the Approx-Log-MAP algorithm of Eq. (2.35) designed for a linear soft-decision-aided MPSK/QAM detector may also be directly invoked by the STBC receiver, where the *a posteriori* probability metric is given by Eq. (7.49). Furthermore, the reduced-complexity soft-decision-aided MPSK/QAM detectors proposed in Sec. 2.4 may also be applied to coded STBC detection, where $\widetilde{z}_n$ and $\widetilde{N}_0$ of Sec. 2.4 may be respectively replaced by $\overline{z}_q$ and $\overline{N}_0$ of Eq. (7.49)

As discussed in Sec. 6.3.1, the STBCs generated from orthogonal design cannot achieve the full MIMO capacity. Explicitly, the CCMC capacity of orthogonal STBCs was shown in Sec. 6.3.1.5 to be lower than the full MIMO capacity. Hence in practice the throughput of orthogonal STBCs can only achieve at most the SISO/SIMO system's throughput. Owing to this throughput loss, the STBC systems have to employ high-order MPSK/QAM constellations, when they are compared to V-BLAST systems at the same E_b/N_0 per channel use. Moreover, the employment of high-order MPSK/QAM results in a performance disadvantage, especially for MIMO systems employing more than two TAs.

In order to mitigate this problem, the attractive LDC scheme was introduced in Sec. 6.3.2, which are capable of achieving both the full MIMO capacity and the full STM diversity order. Hence the LDCs are capable of accommodating the multiplexing and diversity tradeoff of MIMO systems. However, the STBC's orthogonality requirement is abandoned in the context of LDC design. Hence the LDC receiver has to employ the high-complexity V-BLAST detectors, as shown in Sec. 6.3.2.3. In coded MIMO systems, LDC still has to employ the soft-decision-aided V-BLAST detectors of Sec. 7.2 based on the equivalent received signal model of Eq. (6.92). Therefore, the same performance versus complexity tradeoff is encountered in the context of coded MIMO system

design, where V-BLAST and LDC may compensate the STBC's throughput loss, but the V-BLAST and LDC receivers cannot employ low-complexity linear MPSK/QAM detectors without compromising their optimal detection capability.

7.4 Coded Spatial Modulation and Space-Time Shift Keying

As discused in Sec. 6.4.1, the SM's transmit signals vector of Eq. (6.99) only activates a single TA to transmit a modulated MPSK/QAM symbol. As a result, the matched filter output vector $\mathbf{Z} = \mathbf{Y}\mathbf{H}^H$ of Eq. (6.100) does not encounter the V-BLAST's IAI problem. Therefore, we may revise the general MIMO detector's *a posteriori* probability metric of Eq. (7.4) to be evaluated based on the matched filter output $\mathbf{Z}$ instead of the received signals $\mathbf{Y}$ as:

$$d^i = -\frac{\kappa_v^2|s^m|^2 - 2\Re\left[(s^m)^* z_v\right]}{N_0} + \sum_{\bar{k}=1}^{\log_2 I} \widetilde{b}_{\bar{k}} L_a(b_{\bar{k}}), \tag{7.50}$$

where we have $\{\kappa_v = \|\mathbf{H}_{v,-}\|\}_{v=1}^{N_T}$ as defined in Eq. (6.103), while $\{z_v\}_{v=1}^{N_T}$ are elements taken from $\mathbf{Z}$ of Eq. (6.100). The relationship between the SM index i, the TA activation index v and the classic modulated symbol index m is given by $i = v - 1 + mN_T$ according to the SM transceiver design in Sec. 6.4.1. The only difference between Eq. (7.4) and Eq. (7.50) is a constant of $-\frac{\|\mathbf{Y}\|^2}{N_0}$, which may be eliminated by the division operation of the Log-MAP of Eq. (7.3). Therefore, all general MIMO's detection algorithms including Log-MAP of Eq. (7.3), Max-Log-MAP of Eq. (7.5) and Approx-Log-MAP of Eq. (7.6) may invoke the probability metric of Eq. (7.50) instead of Eq. (7.4) for SM detection without imposing any performance loss.

The soft-decision-aided SM detection using Eq. (7.50) is the coded version of the conventional hard-decision-aided SM detection [198] of Eq. (6.103). There are a total number of $I = N_T M$ combinations for $\{d^i\}_{i=0}^{I}$, which means that the conventional soft-decision-aided SM detection still exhibits the general MIMO detection complexity order of $O(I)$. Therefore, we propose to further revise the reduced-scope SM detector for employment in coded systems, so that the soft-decision-aided SM detection complexity may be further reduced by visiting a reduced number of constellation points.

Similar to Eq. (6.104), the *a posteriori* probability metric of Eq. (7.50) may be extended as:

$$d^{v,m} = \frac{\Re(\widetilde{z}_v)\Re(s^m)}{N_0} + \frac{\Im(\widetilde{z}_v)\Im(s^m)}{N_0} - \frac{\kappa_v^2|s^m|^2}{N_0} + \sum_{\bar{k}=1}^{\log_2 I} \widetilde{b}_{\bar{k}} L_a(b_{\bar{k}}), \tag{7.51}$$

where we have $\{\widetilde{z}_v = 2z_v\}_{v=1}^{N_T}$. Let us firstly consider the Max-Log-MAP algorithm of Eq. (7.5), which may evaluate the *a posteriori* probability metrics according to Eq. (7.51). For the $\text{BPS}_T = \log_2 N_T$ bits that are assigned to modulate the TA activation index v, the soft-bit decisions produced by the Max-Log-MAP of Eq. (7.5) may be expressed as:

$$L_p(b_k) = \max_{\forall v \in \{1,\cdots,N_T\}_{b_k=1}} d^v - \max_{\forall v \in \{1,\cdots,N_T\}_{b_k=0}} d^v, \tag{7.52}$$

where $\{1, \cdots, N_T\}_{b_k=1}$ and $\{1, \cdots, N_T\}_{b_k=0}$ refer to the index set for v, when the specific bit $\{b_k\}_{k=\text{BPS}+1}^{\log_2 I}$ is fixed to 1 and 0, respectively. In order to produce the *a posteriori* LLR in Eq. (7.52), we have to obtain the maximum probability metric for each TA activation index v as:

$$d^v = \max_{\forall m \in \{0,\cdots,M-1\}} d^{v,m}. \tag{7.53}$$

Let us consider QPSK as an example. We deliberately rotate QPSK's detected constellation diagram anti-clockwise by $\pi/4$, so that there is only a single constellation point in each quadrant. As a result, the decision variable should be rotated as $z'_v = \widetilde{z}_v \exp(j\frac{\pi}{4})$, and the detected constellation points are given by $\{s'^m = s^m \exp(j\frac{\pi}{4})\}_{m=0}^{M-1} = \{\frac{1}{\sqrt{2}} + j\frac{1}{\sqrt{2}}, \frac{1}{\sqrt{2}} - j\frac{1}{\sqrt{2}}, -\frac{1}{\sqrt{2}} + j\frac{1}{\sqrt{2}}, -\frac{1}{\sqrt{2}} - j\frac{1}{\sqrt{2}}\}$[2]. Therefore, the maximum probability metric of Eq. (7.53) over four QPSK constellation points is given by:

$$\begin{aligned} d^v &= \max \left\{ \begin{array}{l} \frac{\Re(z'_v)}{\sqrt{2}N_0} + \frac{\Im(z'_v)}{\sqrt{2}N_0} - \frac{\kappa_v^2}{N_0} + p_v^a \\ -\frac{\Re(z'_v)}{\sqrt{2}N_0} + \frac{\Im(z'_v)}{\sqrt{2}N_0} + L_a(b_2) - \frac{\kappa_v^2}{N_0} + p_v^a \\ \frac{\Re(z'_v)}{\sqrt{2}N_0} - \frac{\Im(z'_v)}{\sqrt{2}N_0} + L_a(b_1) - \frac{\kappa_v^2}{N_0} + p_v^a \\ -\frac{\Re(z'_v)}{\sqrt{2}N_0} - \frac{\Im(z'_v)}{\sqrt{2}N_0} + L_a(b_1) + L_a(b_2) - \frac{\kappa_v^2}{N_0} + p_v^a \end{array} \right\} \\ &= \max \left\{ \begin{array}{l} t_{\text{Re}}^v + t_{\text{Im}}^v - \frac{\kappa_v^2}{N_0} + p_v^a \\ -t_{\text{Re}}^v + t_{\text{Im}}^v - \frac{\kappa_v^2}{N_0} + p_v^a \\ t_{\text{Re}}^v - t_{\text{Im}}^v - \frac{\kappa_v^2}{N_0} + p_v^a \\ -t_{\text{Re}}^v - t_{\text{Im}}^v - \frac{\kappa_v^2}{N_0} + p_v^a \end{array} \right\} + \frac{L_a(b_1) + L_a(b_2)}{2}, \end{aligned} \tag{7.54}$$

where the *a priori* probability metric for the TA activation index v is given by $p_v^a = \sum_{\bar{k}=\text{BPS}+1}^{\log_2 I} \widetilde{b}_{\bar{k}} L_a(b_{\bar{k}})$, while the two new variables associated with testing the real and imaginary parts separately are defined as:

$$\begin{aligned} t_{\text{Re}}^v &= \frac{\Re(z'_v)}{\sqrt{2}N_0} - \frac{L_a(b_2)}{2}, \\ t_{\text{Im}}^v &= \frac{\Im(z'_v)}{\sqrt{2}N_0} - \frac{L_a(b_1)}{2}. \end{aligned} \tag{7.55}$$

As a result, the maximum probability of Eq. (7.54) may be simply given by a one-step evaluation as:

$$d^v = |t_{\text{Re}}^v| + |t_{\text{Im}}^v| - \frac{\kappa_v^2}{N_0} + p_v^a, \tag{7.56}$$

where a constant of $\frac{L_a(b_1)+L_a(b_2)}{2}$ is discarded from Eq. (7.54), because this term may be eliminated by the subtraction in the Max-Log-MAP of Eq. (7.52). Therefore, instead of evaluating and comparing a total number of $M = 4$ probability metrics corresponding to all QPSK constellation points in Eq. (7.54), the calculation of Eq. (7.56) in fact only visits a single constellation point, which is located in the first quadrant.

[2]We note that if the QPSK constellation is rotated at the transmitter, the operation of $z'_v = \widetilde{z}_v \exp(j\frac{\pi}{4})$ may be eliminated at the SM receiver.

Similarly, when the Approx-Log-MAP of Eq. (7.6) is invoked for producing $\{L_p(b_k)\}_{k=\text{BPS}+1}^{\log_2 I}$, the maximum *a posteriori* probability metric of Eq. (7.56) may be reformulated as:

$$d^v = \Lambda(|t_{\text{Re}}^v|) + \Lambda(|t_{\text{Im}}^v|) - \frac{\kappa_v^2}{N_0} + p_v^a, \tag{7.57}$$

where the corrected Jacobian algorithm of $\Lambda(\cdot)$ is given by Eq. (2.78). As a result, the Approx-Log-MAP of Eq. (7.6) may be accomplished by using Eq. (7.57) as:

$$L_p(b_k) = \text{jac}_{\forall v \in \{1,\cdots,N_T\}_{b_k=1}} d^v - \text{jac}_{\forall v \in \{1,\cdots,N_T\}_{b_k=0}} d^v. \tag{7.58}$$

In summary, the detection algorithms of Eq. (7.52) and Eq. (7.58) only have to evaluate and compare the N_T *a posteriori* probability metrics $\{d^v\}_{v=1}^{N_T}$ of Eq. (7.56) and Eq. (7.57), respectively. Therefore, the SM-QPSK detection complexity order has been reduced from $O(N_T M)$ to $O(N_T)$ for detecting the $\text{BPS}_T = \log_2 N_T$ bits that are assigned to the TA activation index v.

For the $\text{BPS} = \log_2 M = 2$ bits that are assigned to encode the QPSK's classic modulated symbol index m, when a specific bit $\{b_k\}_{k=1}^2$ is set to 1 or 0 as required by the Max-Log-MAP of Eq. (7.5), the QPSK constellation set has to be updated. More specifically, when the first bit is set to be $b_1 = 1$ or $b_1 = 0$, the QPSK constellation set has to be updated as $\{\frac{1}{\sqrt{2}} - j\frac{1}{\sqrt{2}}, , -\frac{1}{\sqrt{2}} - j\frac{1}{\sqrt{2}}\}$ or $\{\frac{1}{\sqrt{2}} + j\frac{1}{\sqrt{2}}, -\frac{1}{\sqrt{2}} + j\frac{1}{\sqrt{2}}\}$, respectively. As a result, the Max-Log-MAP algorithm of Eq. (7.5) may be simplified for producing the first soft-bit decision as:

$$\begin{aligned} L_p(b_1) &= \max_{v\in\{1,\cdots,N_T\}} \left[\max_{m\in\{2,3\}} (d^{v,m})\right] - \max_{v\in\{1,\cdots,N_T\}} \left[\max_{m\in\{0,1\}} (d^{v,m})\right] \\ &= \max_{v\in\{1,\cdots,N_T\}} \left(|t_{\text{Re}}^v| - t_{\text{Im}}^v - \frac{\kappa_v^2}{N_0} + p_v^a\right) - \max_{v\in\{1,\cdots,N_T\}} \left(|t_{\text{Re}}^v| + t_{\text{Im}}^v - \frac{\kappa_v^2}{N_0} + p_v^a\right), \end{aligned} \tag{7.59}$$

where the imaginary term of $|t_{\text{Im}}^v|$ in Eq. (7.56) is replaced by $(-t_{\text{Im}}^v)$ and (t_{Im}^v), when b_1 is fixed to 1 and 0, respectively. Similarly, the second soft-bit decision is given by:

$$L_p(b_2) = \max_{v\in\{1,\cdots,N_T\}} \left(-t_{\text{Re}}^v + |t_{\text{Im}}^v| - \frac{\kappa_v^2}{N_0} + p_v^a\right) - \max_{v\in\{1,\cdots,N_T\}} \left(t_{\text{Re}}^v + |t_{\text{Im}}^v| - \frac{\kappa_v^2}{N_0} + p_v^a\right). \tag{7.60}$$

The complexity order of Eqs. (7.59) and (7.60) is given by $O(2N_T)$, where the TA index detector is invoked twice according to the updated QPSK constellation set, when the specific bit is fixed to 1 and 0.

Let us further consider the example of SM employing Square 16QAM. Owing to the fact that the real and the imaginary parts of the Square 16QAM constellation may be separately visited, the maximum probability metric for each TA index v of Eq. (7.56) may be rewritten as:

$$d^v = d_{\text{Re}}^v + d_{\text{Im}}^v + p_v^a. \tag{7.61}$$

The real term d_{Re}^{v} in Eq. (7.61) may be further extended as:

$$\begin{aligned} d_{\mathrm{Re}}^{v} &= \max \left\{ \begin{array}{ll} \frac{\Re(\widetilde{z}_v)}{\sqrt{10}N_0} + L_a(b_4) - \frac{\kappa_v^2}{10N_0}, & -\frac{\Re(\widetilde{z}_v)}{\sqrt{10}N_0} + L_a(b_3) + L_a(b_4) - \frac{\kappa_v^2}{10N_0}, \\ \frac{3\Re(\widetilde{z}_v)}{\sqrt{10}N_0} - \frac{9\kappa_v^2}{10N_0}, & -\frac{3\Re(\widetilde{z}_v)}{\sqrt{10}N_0} + L_a(b_3) - \frac{9\kappa_v^2}{10N_0} \end{array} \right\} \\ &= \max \left\{ \begin{array}{l} |t_{\mathrm{Re}}^{v,1}| + L_a(b_4) - \frac{\kappa_v^2}{10N_0}, \\ |t_{\mathrm{Re}}^{v,0}| - \frac{9\kappa_v^2}{10N_0} \end{array} \right\} + \frac{L_a(b_3)}{2} \\ &= \max \left\{ \begin{array}{l} d_{\mathrm{Re}}^{v,1}, \\ d_{\mathrm{Re}}^{v,0} \end{array} \right\} + \frac{L_a(b_3)}{2}, \end{aligned} \tag{7.62}$$

where the constant of $\frac{L_a(b_3)}{2}$ may be deleted, while the pair of test-variables are defined as:

$$\begin{aligned} t_{\mathrm{Re}}^{v,1} &= \frac{\Re(\widetilde{z}_v)}{\sqrt{10}N_0} - \frac{L_a(b_3)}{2}, \\ t_{\mathrm{Re}}^{v,0} &= \frac{3\Re(\widetilde{z}_v)}{\sqrt{10}N_0} - \frac{L_a(b_3)}{2}. \end{aligned} \tag{7.63}$$

Similarly, the imaginary term d_{Im}^{v} in Eq. (7.61) may be formulated as:

$$d_{\mathrm{Im}}^{v} = \max \left\{ \begin{array}{l} |t_{\mathrm{Im}}^{v,1}| + L_a(b_2) - \frac{\kappa_v^2}{10N_0}, \\ |t_{\mathrm{Im}}^{v,0}| - \frac{9\kappa_v^2}{10N_0} \end{array} \right\} = \max \left\{ \begin{array}{l} d_{\mathrm{Im}}^{v,1} \\ d_{\mathrm{Im}}^{v,0} \end{array} \right\}, \tag{7.64}$$

where the constant of $\frac{L_a(b_1)}{2}$ is discarded, while the pair of test-variables are defined as:

$$\begin{aligned} t_{\mathrm{Im}}^{v,1} &= \frac{\Im(\widetilde{z}_v)}{\sqrt{10}N_0} - \frac{L_a(b_1)}{2}, \\ t_{\mathrm{Im}}^{v,0} &= \frac{3\Im(\widetilde{z}_v)}{\sqrt{10}N_0} - \frac{L_a(b_1)}{2}. \end{aligned} \tag{7.65}$$

Therefore, for the Max-Log-MAP algorithm, the TA index detector of Eq. (7.52) may be invoked by utilizing the N_T *a posteriori* probabilities $\{d^v\}_{v=1}^{N_T}$ defined in Eq. (7.61), in order to produce the $(\mathrm{BPS}_T = \log_2 N_T)$ soft bit decisions $\{L_p(b_k)\}_{k=\mathrm{BPS}+1}^{\log_2 I}$. The complexity order is reduced from $O(N_T \cdot 16)$ to $O(N_T \cdot 4)$, where a total of four constellation points have been visited in Eqs. (7.62) and (7.64).

When the first bit b_1, which determines the sign of the imaginary part of a Square 16QAM symbol is fixed to 1 or 0, $\{|t_{\mathrm{Im}}^{v,1}|, |t_{\mathrm{Im}}^{v,0}|\}$ seen in Eq. (7.64) may be replaced by $\{-t_{\mathrm{Im}}^{v,1}, -t_{\mathrm{Im}}^{v,0}\}$ and $\{t_{\mathrm{Im}}^{v,1}, t_{\mathrm{Im}}^{v,0}\}$, respectively. More explicitly, the Max-Log-MAP produces the first soft bit as:

$$\begin{aligned} L_p(b_1) &= \max_{v \in \{1,\cdots,N_T\}} \left(d^{v,b_1=1} \right) - \max_{v \in \{1,\cdots,N_T\}} \left(d^{v,b_1=0} \right) \\ &= \max_{v \in \{1,\cdots,N_T\}} \left\{ d_{\mathrm{Re}}^{v} + \max \left[\begin{array}{ll} -t_{\mathrm{Im}}^{v,1} + L_a(b_2) - \frac{\kappa_v^2}{10N_0}, & -t_{\mathrm{Im}}^{v,0} - \frac{9\kappa_v^2}{10N_0} \end{array} \right] + p_v^a \right\} \\ &\quad - \max_{v \in \{1,\cdots,N_T\}} \left\{ d_{\mathrm{Re}}^{v} + \max \left[\begin{array}{ll} t_{\mathrm{Im}}^{v,1} + L_a(b_2) - \frac{\kappa_v^2}{10N_0}, & t_{\mathrm{Im}}^{v,0} - \frac{9\kappa_v^2}{10N_0} \end{array} \right] + p_v^a \right\}, \end{aligned} \tag{7.66}$$

where d_{Re}^{v} does not have to be estimated again. The complexity order of detecting $L_a(b_1)$ is given by $O(N_T \cdot 4)$.

When the second bit b_2 which determines the magnitude of the imaginary part of a Square 16QAM symbol is fixed to 1 or 0, Eq. (7.64) should be updated as $d_{\text{Im}}^{v} = d_{\text{Im}}^{v,1}$ or $d_{\text{Im}}^{v} = d_{\text{Im}}^{v,0}$, respectively. As a result, the second soft bit decision is given by:

$$L_p(b_2) = \max_{v\in\{1,\cdots,N_T\}} (d_{\text{Re}}^{v} + d_{\text{Im}}^{v,1} + p_v^a) - \max_{v\in\{1,\cdots,N_T\}} (d_{\text{Re}}^{v} + d_{\text{Im}}^{v,0} + p_v^a), \tag{7.67}$$

where there is no new variable to evaluate, i.e. only additions and comparisons are made in Eq. (7.67). The complexity order of detecting the second bit is given by $O(N_T \cdot 2)$.

Similarly, the third bit which determines the sign of the real part of a Square 16QAM symbol may be detected by the Max-Log-MAP algorithm as:

$$L_p(b_3) = \max_{v\in\{1,\cdots,N_T\}} \left(d_{\text{Re}}^{v,b_3=1} + d_{\text{Im}}^{v} + p_v^a\right) - \max_{v\in\{1,\cdots,N_T\}} \left(d_{\text{Re}}^{v,b_3=0} + d_{\text{Im}}^{v} + p_v^a\right), \tag{7.68}$$

where $d_{\text{Re}}^{v,b_3=1}$ and $d_{\text{Re}}^{v,b_3=0}$ are obtained by replacing $\{|t_{\text{Re}}^{v,1}|, |t_{\text{Re}}^{v,0}|\}$ seen in d_{Re}^{v} of Eq. (7.62) by $\{-t_{\text{Re}}^{v,1}, -t_{\text{Re}}^{v,0}\}$ and $\{t_{\text{Re}}^{v,1}, t_{\text{Re}}^{v,0}\}$, respectively.

Furthermore, the fourth bit, which modulates the magnitude of the real part of a Square 16QAM symbol may be detected as:

$$L_p(b_4) = \max_{v\in\{1,\cdots,N_T\}} (d_{\text{Re}}^{v,1} + d_{\text{Im}}^{v} + p_v^a) - \max_{v\in\{1,\cdots,N_T\}} (d_{\text{Re}}^{v,0} + d_{\text{Im}}^{v} + p_v^a), \tag{7.69}$$

where d_{Re}^{v} in Eq. (7.61) is replaced by $d_{\text{Re}}^{v,1}$ or $d_{\text{Re}}^{v,0}$ for $b_4 = 1$ or $b_4 = 0$, respectively.

Based on the examples of QPSK and Square 16QAM aided SM detection, we summarize the reduced-complexity Max-Log-MAP algorithm conceived for Square MQAM aided SM detection as:

Algorithm 7.1: Reduced-Complexity Max-Log-MAP Algorithm Conceived for Square MQAM Aided SM Detection.

(1) Define the variables testing the real and imaginary parts of the matched filter variable $\widetilde{z}_v$ separately as:

$$\begin{aligned} t_{\text{Im}}^{v,g} &= \frac{A_g \Im(\widetilde{z}_v)}{N_0} - \frac{L_a(b_1)}{2}, \\ t_{\text{Re}}^{v,f} &= \frac{A_f \Re(\widetilde{z}_v)}{N_0} - \frac{L_a(b_{\text{BPS}/2+1})}{2}, \end{aligned} \tag{7.70}$$

where $\{A_g\}_{g=0}^{M_{\text{Im}}/2-1}$ and $\{A_f\}_{f=0}^{M_{\text{Re}}/2-1}$ are the positive PAM magnitudes on the y-axis and x-axis of the Gray-labelled Square MQAM constellation diagram, respectively. As demonstrated in Chapter 2, for Square MQAM associated with an even BPS $= \log_2 M$, we have $M_{\text{Re}} = M_{\text{Im}} = \sqrt{M}$. For Square MQAM associated with an odd BPS, we have $M_{\text{Re}} = 2M_{\text{Im}} = \sqrt{2M}$.

(2) The *a posteriori* probability metric of a specific TA index v is given by:

$$d^v = d^v_{\mathrm{Re}} + d^v_{\mathrm{Im}} + p^a_v, \tag{7.71}$$

where the *a priori* probability metric for the TA index v is given by $p^a_v = \sum_{\bar{k}=\mathrm{BPS}+1}^{\log_2 I} \widetilde{b}_{\bar{k}} L_a(b_{\bar{k}})$. The corresponding bit-mapping arrangement for each TA index candidate may be directly obtained by $[\widetilde{b}_{\mathrm{BPS}+1}, \cdots, \widetilde{b}_{\log_2 I}] = \mathrm{bin2dec}(v-1)$. The real and imaginary terms of the probability metric are given by:

$$\begin{aligned} d^v_{\mathrm{Im}} &= \max_{g\in\{0,\cdots,M_{\mathrm{Im}}/2-1\}} \left(d^{v,g}_{\mathrm{Im}}\right), \\ d^v_{\mathrm{Re}} &= \max_{f\in\{0,\cdots,M_{\mathrm{Re}}/2-1\}} \left(d^{v,f}_{\mathrm{Re}}\right). \end{aligned} \tag{7.72}$$

The $M_{\mathrm{Im}}/2$ candidates of $\{d^{v,g}_{\mathrm{Im}}\}_{g=0}^{M_{\mathrm{Im}}/2-1}$ and the $M_{\mathrm{Re}}/2$ candidates of $\{d^{v,f}_{\mathrm{Re}}\}_{f=0}^{M_{\mathrm{Re}}/2-1}$ may be evaluated by:

$$\begin{aligned} d^{v,g}_{\mathrm{Im}} &= |t^{v,g}_{\mathrm{Im}}| + p^a_g - \frac{A^2_g \kappa^2_v}{N_0}, \\ d^{v,f}_{\mathrm{Re}} &= |t^{v,f}_{\mathrm{Re}}| + p^a_f - \frac{A^2_f \kappa^2_v}{N_0}, \end{aligned} \tag{7.73}$$

where the *a priori* probability metrics for group indices g and f are respectively given by $p^a_g = \sum_{\bar{k}=2}^{\mathrm{BPS}/2} \widetilde{b}_{\bar{k}} L_a(b_{\bar{k}})$ and $p^a_f = \sum_{\bar{k}=\mathrm{BPS}/2+2}^{\mathrm{BPS}} \widetilde{b}_{\bar{k}} L_a(b_{\bar{k}})$, while the bits-mapping arrangements $\{\widetilde{b}_{\bar{k}}\}_{\bar{k}=2}^{\mathrm{BPS}/2}$ and $\{\widetilde{b}_{\bar{k}}\}_{\bar{k}=\mathrm{BPS}/2+2}^{\mathrm{BPS}}$ may be obtained by respectively translating the group indices g and f to binary streams.

(3) The $\mathrm{BPS}_T = \log_2 N_T$ bits which determine the TA activation index v may be detected as:

$$L_p(b_k) = \max_{\forall v\in\{1,\cdots,N_T\}_{b_k=1}} d^v - \max_{\forall v\in\{1,\cdots,N_T\}_{b_k=0}} d^v, \quad k \in \{\mathrm{BPS}+1, \cdots, \log_2 I\}. \tag{7.74}$$

The TA activation index set $\forall v \in \{1, \cdots, N_T\}$ is reduced by half when the specific bit is fixed to be $b_k = 1$ or $b_k = 0$.

(4) The first bit and the $(\mathrm{BPS}/2+1)$-th bit which determine the signs may be detected as:

$$L_p(b_1) = \max_{v\in\{1,\cdots,N_T\}} \left(d^v_{\mathrm{Re}} + d^{v,b_1=1}_{\mathrm{Im}} + p^a_v\right) - \max_{v\in\{1,\cdots,N_T\}} \left(d^v_{\mathrm{Re}} + d^{v,b_1=0}_{\mathrm{Im}} + p^a_v\right), \tag{7.75}$$

$$\begin{aligned} L_p(b_{\mathrm{BPS}/2+1}) = &\max_{v\in\{1,\cdots,N_T\}} \left(d^{v,b_{\mathrm{BPS}/2+1}=1}_{\mathrm{Re}} + d^v_{\mathrm{Im}} + p^a_v\right) \\ &- \max_{v\in\{1,\cdots,N_T\}} \left(d^{v,b_{\mathrm{BPS}/2+1}=0}_{\mathrm{Re}} + d^v_{\mathrm{Im}} + p^a_v\right), \end{aligned} \tag{7.76}$$

where $d^{v,b_1=1}_{\mathrm{Im}}$ and $d^{v,b_1=0}_{\mathrm{Im}}$ may be obtained by replacing $\{|t^{v,g}_{\mathrm{Im}}|\}_{g=0}^{M_{\mathrm{Im}}/2-1}$ for evaluating d^v_{Im} in Step (2) by $\{-t^{v,g}_{\mathrm{Im}}\}_{g=0}^{M_{\mathrm{Im}}/2-1}$ and $\{t^{v,g}_{\mathrm{Im}}\}_{g=0}^{M_{\mathrm{Im}}/2-1}$, respectively, while $d^{v,b_{\mathrm{BPS}/2+1}=1}_{\mathrm{Re}}$ and $d^{v,b_{\mathrm{BPS}/2+1}=0}_{\mathrm{Re}}$ may be obtained by replacing $\{|t^{v,f}_{\mathrm{Re}}|\}_{f=0}^{M_{\mathrm{Re}}/2-1}$ for evaluating d^v_{Re} in Step (2) by $\{-t^{v,f}_{\mathrm{Re}}\}_{f=0}^{M_{\mathrm{Re}}/2-1}$ and $\{t^{v,f}_{\mathrm{Re}}\}_{f=0}^{M_{\mathrm{Re}}/2-1}$, respectively.

(5) The rest $(\mathrm{BPS}-2)$ bits which determine the real PAM magnitudes may be detected as:

$$\begin{aligned} L_p(b_k) = &\max_{v\in\{1,\cdots,N_T\}}\left[d_{\mathrm{Re}}^{v}+\max_{b_k=1}\ (d_{\mathrm{Im}}^{v,g})+p_v^a\right] \\ &-\max_{v\in\{1,\cdots,N_T\}}\left[d_{\mathrm{Re}}^{v}+\max_{b_k=0}\ (d_{\mathrm{Im}}^{v,g})+p_v^a\right], \\ &k\in\{2,\cdots,\mathrm{BPS}/2\}, \end{aligned} \tag{7.77}$$

$$\begin{aligned} L_p(b_k) = &\max_{v\in\{1,\cdots,N_T\}}\left[\max_{b_k=1}\ (d_{\mathrm{Re}}^{v,f})+d_{\mathrm{Im}}^{v}+p_v^a\right] \\ &-\max_{v\in\{1,\cdots,N_T\}}\left[\max_{b_k=0}\ (d_{\mathrm{Re}}^{v,f})+d_{\mathrm{Im}}^{v}+p_v^a\right], \\ &k\in\{\mathrm{BPS}/2+2,\cdots,\mathrm{BPS}\}. \end{aligned} \tag{7.78}$$

The total number of candidates for $\{d_{\mathrm{Im}}^{v,g}\}_{g=0}^{M_{\mathrm{Im}}/2-1}$ and that for $\{d_{\mathrm{Re}}^{v,f}\}_{f=0}^{M_{\mathrm{Re}}/2-1}$ are reduced by half when the specific bit is fixed to be $b_k=1$ or $b_k=0$.

When either a high-order MPSK ($M>4$) or a Star M-QAM scheme is employed, the real and imaginary parts of the matched filter output variable $\widetilde{z}_v$ cannot be detected separately. Therefore, similar to Algorithm 6.2, we summarize the reduced-complexity Max-Log-MAP algorithm conceived for general MPSK/QAM aided SM detection as:

Algorithm 7.2: Reduced-Complexity Max-Log-MAP Algorithm Conceived for General MPSK/QAM Aided SM Detection.

(1) Define the test-variables as:

$$\begin{aligned} t_{\mathrm{Im}}^{v,g} &= \frac{B_g\Im(z_v')}{N_0}-\frac{L_a(b_1)}{2}, \\ t_{\mathrm{Re}}^{v,g} &= \frac{A_g\Re(z_v')}{N_0}-\frac{L_a(b_2)}{2}, \end{aligned} \tag{7.79}$$

where $\{(A_g,B_g)\}_{g=0}^{M/4-1}$ denote the coordinates of the rotated MPSK/QAM constellation points in the first quadrant. The detector's rotated MPSK constellation points are $\{s'^m=s^m\exp(j\frac{\pi}{M})\}_{m=0}^{M-1}$, and the corresponding decision variables are $\{z_v'=\widetilde{z}_v\exp(j\frac{\pi}{M})\}_{v=1}^{N_T}$. For Star MQAM, the detector's rotated constellation points are $\{s'^m=s^m\exp(j\frac{\pi}{M_P})\}_{m=0}^{M-1}$, and hence we have $\{z_v'=\widetilde{z}_v\exp(j\frac{\pi}{M_P})\}_{v=1}^{N_T}$. In this way, there are exactly $M/4$ constellation points in each quadrant.

(2) The *a posteriori* probability metric of a specific TA index v is given by:

$$d^v=\left[\max_{g\in\{0,\cdots,M/4-1\}}(d^{v,g})\right]+p_v^a, \tag{7.80}$$

where the *a priori* probability metric for the TA index v is given by $p_v^a = \sum_{\tilde{k}=\text{BPS}+1}^{\log_2 I} \widetilde{b}_{\tilde{k}} L_a(b_{\tilde{k}})$, while the $M/4$ candidates of $\{d^{v,g}\}_{g=0}^{M/4-1}$ are evaluated by:

$$d^{v,g} = |t_{\text{Re}}^{v,g}| + |t_{\text{Im}}^{v,g}| + p_g^a - \frac{(A_g^2 + B_g^2)\kappa_v^2}{N_0}, \tag{7.81}$$

where the *a priori* probability metric for group index g is given by $p_g^a = \sum_{\tilde{k}=3}^{\text{BPS}} \widetilde{b}_{\tilde{k}} L_a(b_{\tilde{k}})$, while the bit-mapping arrangement $\{\widetilde{b}_{\tilde{k}}\}_{\tilde{k}=3}^{\text{BPS}}$ may be obtained by directly translating the group index g back to binary stream.

(3) The $\text{BPS}_T = \log_2 N_T$ bits which determine the TA activation index may be detected as:

$$L_p(b_k) = \max_{v \in \{1,\cdots,N_T\}_{b_k=1}} (d^v) - \max_{v \in \{1,\cdots,N_T\}_{b_k=0}} (d^v), \quad k \in \{\text{BPS}+1, \cdots, \log_2 I\}. \tag{7.82}$$

The TA activation index set $\forall v \in \{1, \cdots, N_T\}$ is reduced by half when the specific bit is fixed to be $b_k = 1$ or $b_k = 0$.

(4) The first two bits which determine the signs may be detected as:

$$\begin{aligned} L_p(b_1) &= \max_{v \in \{1,\cdots,N_T\}} (d^{v,b_1=1}) - \max_{v \in \{1,\cdots,N_T\}} (d^{v,b_1=0}), \\ L_p(b_2) &= \max_{v \in \{1,\cdots,N_T\}} (d^{v,b_2=1}) - \max_{v \in \{1,\cdots,N_T\}} (d^{v,b_2=0}). \end{aligned} \tag{7.83}$$

where $d^{v,b_1=1}$ and $d^{v,b_1=0}$ may be obtained by replacing $\{|t_{\text{Im}}^{v,g}|\}_{g=0}^{M/4-1}$ for evaluating d^v in Step (2) by $\{-t_{\text{Im}}^{v,g}\}_{g=0}^{M/4-1}$ and $\{t_{\text{Im}}^{v,g}\}_{g=0}^{M/4-1}$, respectively, while $d^{v,b_2=1}$ and $d^{v,b_2=0}$ may be obtained by replacing $\{|t_{\text{Re}}^{v,g}|\}_{g=0}^{M/4-1}$ for evaluating d^v in Step (2) by $\{-t_{\text{Re}}^{v,g}\}_{g=0}^{M/4-1}$ and $\{t_{\text{Re}}^{v,g}\}_{g=0}^{M/4-1}$, respectively

(5) The rest $(\text{BPS}-2)$ bits which determine the magnitude of the transmitted MPSK/QAM symbol may be detected as:

$$L_p(b_k) = \max_{v \in \{1,\cdots,N_T\}} \left[\max_{b_k=1} (d^{v,g})\right] - \max_{v \in \{1,\cdots,N_T\}} \left[\max_{b_k=0} (d^{v,g})\right], \; k \in \{3, \cdots, \text{BPS}\}. \tag{7.84}$$

The number of candidates for $\{d^{v,g}\}_{g=0}^{M/4-1}$ is reduced by half when a specific bit is fixed as $b_k = 1$ or $b_k = 0$.

The corresponding reduced-complexity Approx-Log-MAP algorithm conceived for SM detection may be obtained by appropriately modifying Algorithms 7.1 and 7.2, where the max operation should be replaced by the corrected Jacobian operation of jac defined in Eq. (2.36), while the absolute value calculation of $(|t|)$ should be replaced by the special corrected Jacobian algorithm of $\Lambda(|t|)$ of Eq. (2.36).

For the $\text{BPS}_T = \log_2 N_T$ bits assigned to the TA index, the 1PSK/BPSK/QPSK aided SM de-

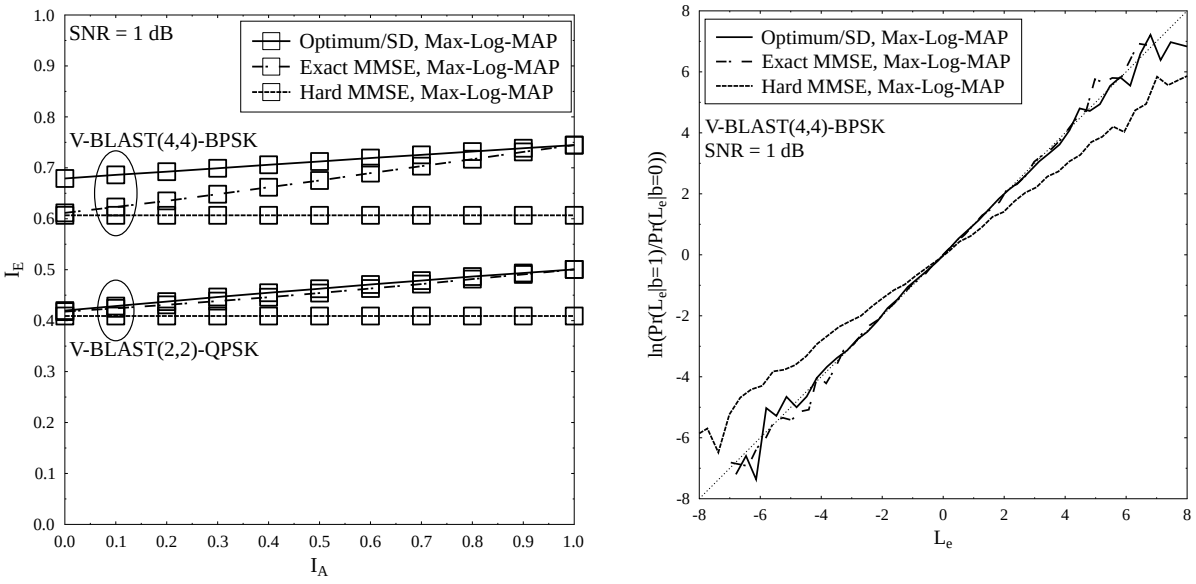

(a) EXIT charts

(b) LLR validity test

Figure 7.1: EXIT charts and LLR validity test for soft-decision-aided V-BLAST detectors, where the throughput is given by $R = 4$ bits/block/channel use.

tection operates at the complexity order lower bound of $O(N_T)$, while the Square MQAM aided SM detection of Algorithm 7.1 and the MPSK/QAM aided SM detection of Algorithm 7.2 have the complexity order of $O(\frac{M_{\text{Re}}}{2} \cdot N_T + \frac{M_{\text{Im}}}{2} \cdot N_T)$ and $O(\frac{M}{4} \cdot N_T)$, respectively. For the pair of specific bits, which determine the sign of the transmitted MPSK/QAM symbol, the BPSK/QPSK aided SM detection complexity is lower bounded by the order of $O(2N_T)$, while the Square MQAM aided SM detection complexity order and the general MPSK/QAM aided SM detection complexity order are given by $O(M_{\text{Re}} \cdot N_T)$ or $O(M_{\text{Im}} \cdot N_T)$ and $O(\frac{M}{2} \cdot N_T)$, respectively. For the remaining $(\text{BPS} - 2)$ bits, which determine the specific magnitudes of the MPSK/QAM symbols, the complexity order of the Square MQAM aided SM detection and that of the general MPSK/QAM aided SM detection are given by $O(\frac{M_{\text{Re}}}{2} \cdot N_T)$ or $O(\frac{M_{\text{Im}}}{2} \cdot N_T)$ and $O(\frac{M}{4} \cdot N_T)$, respectively. In summary, the Square MQAM aided SM detection of Algorithm 7.1 has a lower complexity compared to Algorithm 7.2, where the latter may be applied to high-order MPSK, Star MQAM and Cross MQAM aided SM schemes.

For coded STSK schemes, the soft-decision-aided SM detectors may all be invoked by the STSK receiver. According to the signal processing of Eq. (6.131), a STSK(N_T,N_R,N_P,N_Q) scheme may be transformed to a SM scheme associated with N_Q TAs and $N_P N_R$ RAs. The STSK detection complexity is expected to be higher than the SM detection complexity due to the extra signal processing operations in Eq. (6.131).

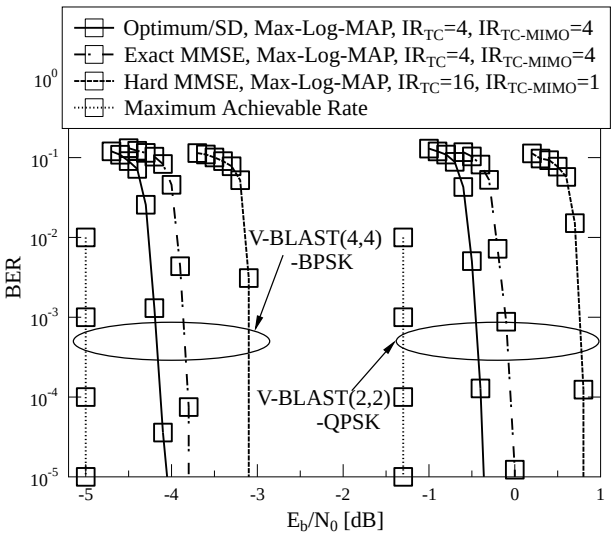

Figure 7.2: BER performance of half-rate TC coded V-BLAST associated with the same system throughput of $R_c R = 2$. The schematic of the TC coded systems is portrayed in Fig. 2.8, where the MIMO transmitter and the MIMO receiver may replace the conventional modulation and the demodulation blocks. The system parameters are given by Table 2.3.

7.5 Performance Results for Coded MIMO Systems

In this section, we provide performance results for a variety of coded MIMO systems. First of all, Figs. 7.1 and 7.2 portrays the performance of coded V-BLAST schemes, where the optimum detectors of Sec. 7.2.1, the SD of Sec. 7.2.2 that retains the optimum detection capability and the sub-optimal MMSE detectors of Sec. 7.2.4 are employed. We note that the "Hard MMSE" seen in Figs. 7.1 and 7.2 refers to the soft-decision-aided MPSK/QAM detectors invoking the probability metric of Eq. (7.19), which is directly derived from the hard-decision-aided V-BLAST MMSE of Sec. 6.2.4. Moreover, the "Exact MMSE" solution refers to the soft-decision-aided MPSK/QAM detectors invoking the probability metric of Eq. (7.45), which is obtained by taking into account the *a priori* LLRs for updating the MMSE filter taps, as derived in Sec. 7.2.4.

It can be seen in Fig. 7.1a that the "Hard MMSE" used for detecting V-BLAST signals employing BPSK/QPSK exhibits horizontal EXIT curves, while the optimum/SD aided V-BLAST detection benefits from a significant iteration gain. Furthermore, it was discussed in Sec. 7.2.4 that the exact MMSE solution associated with $I_A = 0$ is equivalent to the hard-decision-aided MMSE detector, while the exact MMSE solution associated with $I_A = 1$ is equivalent to the optimum V-BLAST detector, which is verified by Fig. 7.1a. Despite the associated performance loss, Fig. 7.1b shows that the "Hard MMSE" may produce unreliable LLRs, which deviate from the true probabilities. These unreliable LLRs cannot be readily corrected by the channel decoder, hence "Hard MMSE" is not recommended for turbo detection.

Fig. 7.2 further characterizes the performance of these soft-decision-aided V-BLAST detectors in the context of TC coded systems. In order to achieve an iteration gain, $IR_{TC} = 4$ inner itera-

tions are carried out within the TC and $IR_{TC-MIMO} = 4$ outer iterations are employed between the TC and MIMO receiver for MAP-optimum/SD V-BLAST detection and exact MMSE solution. Meanwhile, we have $IR_{TC} = 16$ and $IR_{TC-MIMO} = 1$, when "Hard MMSE" is employed, so that the turbo detection is configured to maintain the same total number of iterations. It can be seen in Fig. 7.2 that the MAP-optimum/SD V-BLAST detectors may achieve an excellent performance that is within 1.0 dB from the maximum achievable rate, which is the E_b/N_0 bound that has to be satisfied for achieving half of the full DCMC capacity of Eq. (6.6). By contrast, the low-complexity "Hard MMSE" imposes a substantial performance loss, as evidenced by Fig. 7.2. It is further demonstrated by Fig. 7.2 that the exact MMSE detector is capable of performing close to the optimum V-BLAST detector.

However, the soft-decision-aided exact MMSE detector of Sec. 7.2.4 is more complex than the hard-decision-aided MMSE of Sec. 6.2.4. More explicitly, we discussed in Sec. 7.2.4 that even when the fading channel envelope remains near-constant, the MMSE filter taps of Eq. (7.42) still have to be calculated by the matrix inversion of Eq. (7.42), because the *a priori* LLRs are updated by turbo detection. Moreover, the current versions of the SD and MMSE detectors of Secs. 7.2.2-7.2.4 only work for fully-loaded MIMO systems associated with $N_T \leq N_R$. For the rank-deficient MIMO systems associated with $N_T > N_R$, which are often encountered in realistic wireless communication systems, the SD is recommended for detecting N_R symbols, while the ML detector is invoked for the remaining symbols [303–305]. This complication may be avoided by using LDC instead of V-BLAST as discussed in Sec. 6.3.2.3, where we have the design-freedom to adjust the LDC arguments of N_P and N_Q in order to create an equivalent full-loaded MIMO system. However, considering that the LDC's dispersion matrices are randomly populated, the LDC transmitter may be required to transmit symbols that are not drawn from the classic MPSK/QAM constellations, which further complicates the hardware design of the related MIMO systems.

In order to overcome these limitations of the conventional MIMO systems design, it is desirable for the SM to implement its optimum detector at a reduced detection complexity. Let us firstly examine the performance of V-BLAST and SM together with STBC and STSK in the context of coded systems with the aid of the EXIT charts of Fig. 7.3 and the BER performance curves of Fig. 7.4. It can be seen in Fig. 7.3 that the STBC's orthogonal design results in a near-horizontal EXIT curve, similarly to a classic SISO scheme. By contrast, the V-BLAST, SM and STSK schemes exhibit a considerable iteration gain. For this reason, the number of iterations is set to $IR_{TC} = 4$ and $IR_{TC-MIMO} = 4$ for the TC coded V-BLAST, SM and STSK systems, while $IR_{TC} = 8$ and $IR_{TC-MIMO} = 2$ are used for the TC coded STBC systems. The BER performance of Fig. 7.4 shows that when there is no receive diversity, SM(2,1)-8PSK and SM(4,1)-QPSK perform worse than their respective V-BLAST counterparts of V-BLAST(2,1)-QPSK and V-BLAST(4,1)-BPSK in the context of the TC coded MIMO systems, but the STSK(2,1,2,4)-Square 64QAM and STSK(4,1,2,4)-Square 64QAM schemes offer a performance improvement over their SM counterparts, as a benefit of STSK's transmit diversity gain. It can be seen in Fig. 7.4a that the G2 STBC employing Square 16QAM exhibits the best performance amongst the TC coded MIMO systems,

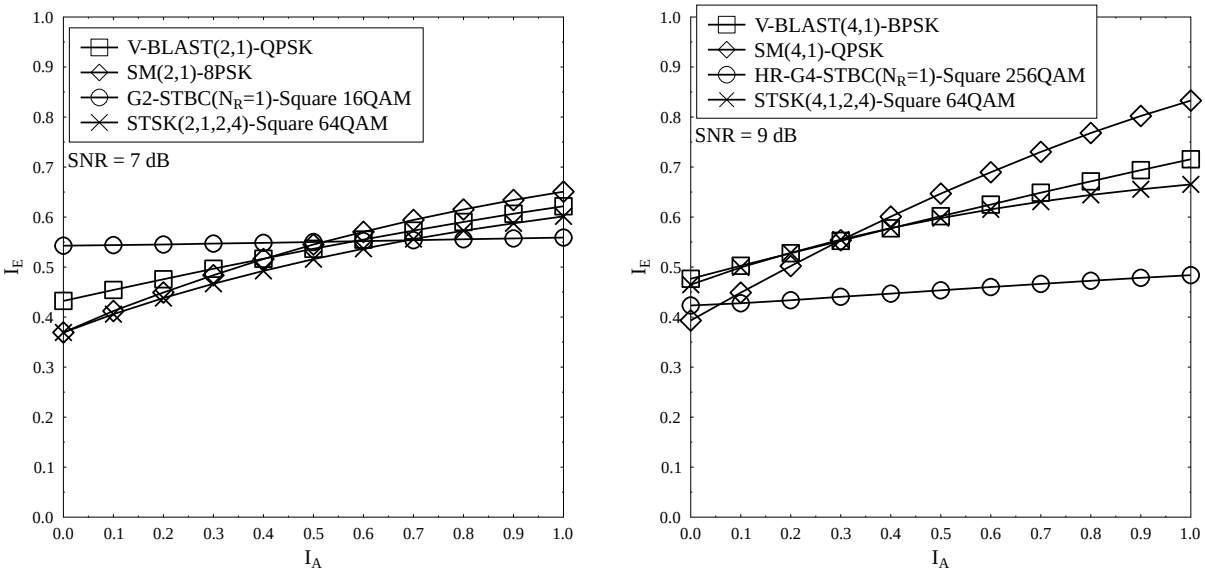

(a) $N_T = 2$ (b) $N_T = 4$

Figure 7.3: EXIT chart comparison of V-BLAST, SM, STBC and STSK associated with the same system throughput of $R_c R = 2$ bits/block/channel use.

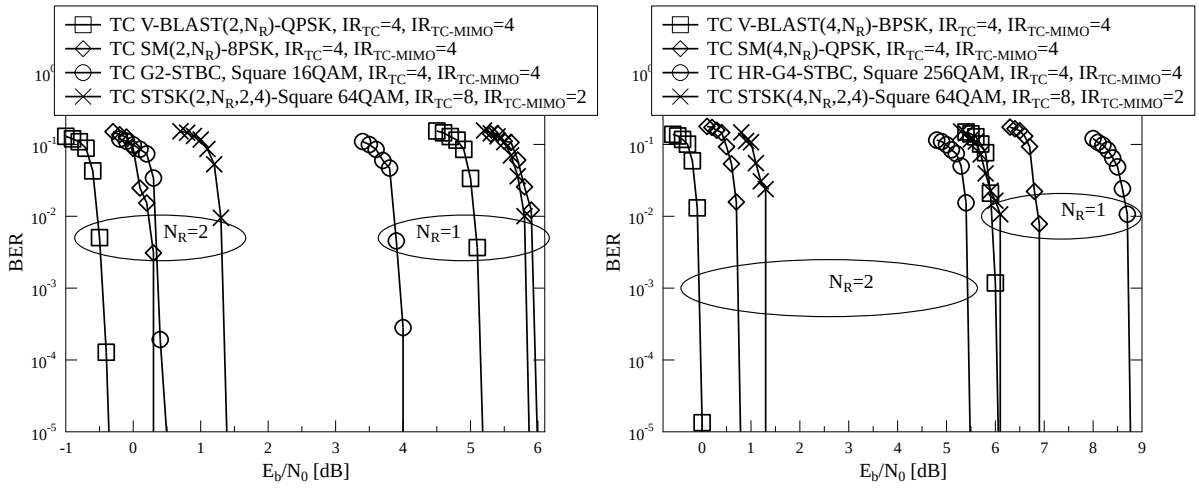

(a) $N_T = 2$ (b) $N_T = 4$

Figure 7.4: BER performance comparison between half-rate TC V-BLAST, SM, STBC and STSK associated with the same system throughput of $R_c R = 2$ bits/block/channel use. The schematic of the TC systems is portrayed in Fig. 2.8, and the system parameters are given by Table 2.3.

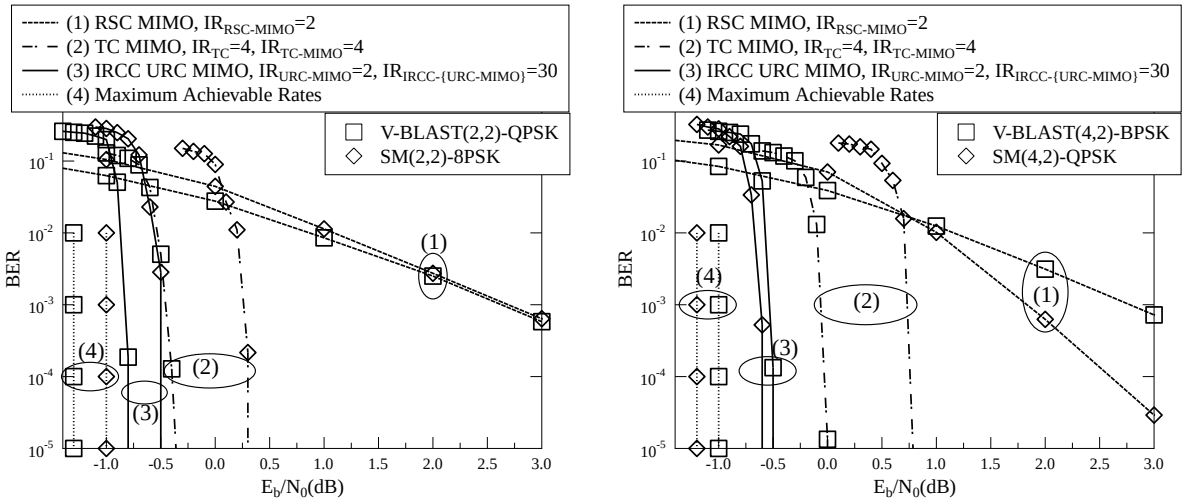

(a) $N_T = 2$ (b) $N_T = 4$

Figure 7.5: BER performance comparison between V-BLAST and SM in the context of RSC, TC and IRCC-URC coded systems associated with the same system throughput of $R_c R = 2$ bits/block/channel use. The schematics of the RSC coded systems, the TC coded systems and the IRCC-URC coded systems are portrayed in Fig. 2.2, Fig. 2.8 and Fig. 2.10, respectively. The system parameters are given by Table 2.3.

when we have $N_R = 1$. However, when all MIMO schemes benefit from a receive diversity gain owing to $N_R = 2$, V-BLAST(2,2)-QPSK performs the best in Fig. 7.4a, SM(2,2)-8PSK performs similarly to G2 STBC, while STSK(2,2,2,4)-Square 64QAM performs the worst. This is because the diversity-oriented STBC and STSK schemes have to employ higher order QAM arrangements in order to compensate for their throughput loss. Hence STBC and STSK generally perform worse at low SNRs than their V-BLAST and SM counterparts employing lower order MPSK/QAM, when all of them benefit from a diversity gain owing to employing $N_R > 1$. For the same reason, it may be observed in Fig. 7.4b that V-BLAST(4,2)-BPSK performs the best amongst the TC MIMO systems, while SM(4,2)-QPSK performs better than its STSK(4,2,2,4)-Square 64QAM counterpart. Furthermore, it can be seen that the TC half-rate G4 STBC arrangement performs the worst for both $N_R = 1$ and $N_R = 2$ in Fig. 7.4b, because it has to employ a high-order 256QAM scheme in order to provide the same system throughput, and its diversity advantage exhibited at high SNRs is eroded in channel coded systems operating at relatively low SNRs.

Although the EXIT charts of Fig. 7.3 predict a similar detection capability for V-BLAST and SM, the BER performance of Fig. 7.4 demonstrates that SM performs worse than V-BLAST by about 0.8 dB in TC MIMO systems associated with the same throughput of $R_c R = 2$ bits/block/channel use. As discussed in Chapter 2, TC associated with $IR_{TC} = 4$ exhibits a horizontal EXIT curve, which does not match well with the steep EXIT curves of V-BLAST and SM. In order to provide a more thorough comparison, Fig. 7.5 shows the BER performance of V-BLAST and SM in the context of RSC, TC and IRCC-URC coded systems, while the corresponding decoding trajectories are recorded in Fig. 7.6. It can be seen in Fig. 7.5a that RSC coded SM(2,2)-8PSK per-

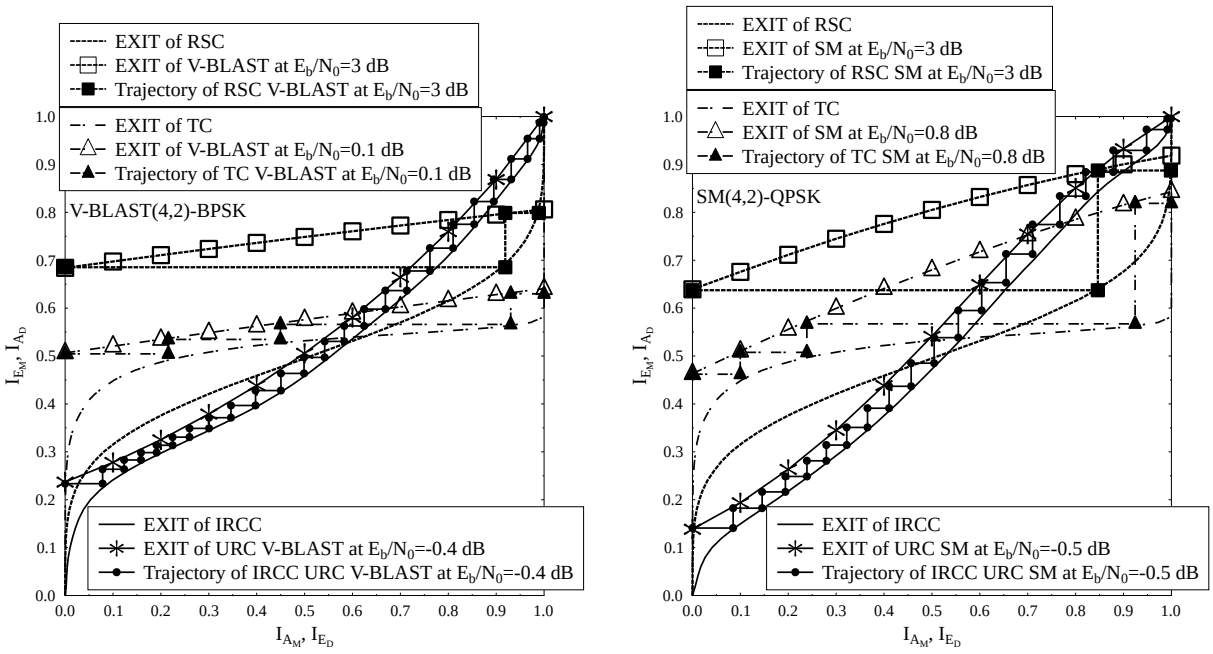

(a) V-BLAST(4,2)-BPSK

(b) SM(4,2)-QPSK

Figure 7.6: Decoding trajectories recorded for V-BLAST and SM in the context of RSC, TC and IRCC-URC coded systems associated with the same system throughput of $R_c R = 2$ bits/block/channel use.

forms very close to RSC coded V-BLAST(2,2)-QPSK, while the performance difference between the IRCC-URC coded SM(2,2)-8PSK and IRCC-URC coded V-BLAST(2,2)-QPSK arrangements is only 0.3 dB. Furthermore, Fig. 7.5b shows that RSC coded SM(4,2)-QPSK outperforms RSC coded V-BLAST(4,2)-BPSK. This is because SM(4,2)-QPSK exhibits a higher iteration gain than V-BLAST(4,2)-BPSK, as demonstrated by Figs. 7.3 and 7.6, which benefits its performance in the context of RSC coded systems, because the EXIT curve of the RSC decoder is much steeper than that of the TC decoder. For the same reason, IRCC-URC coded SM(4,2)-QPSK also slightly outperforms IRCC-URC coded V-BLAST(4,2)-BPSK, as evidenced by Fig. 7.5b. In summary, we may conclude that SM is capable of achieving a comparable performance to V-BLAST in coded systems, provided that the appropriate channel coding schemes are selected.

In Fig. 7.7, we quantify the computational complexity of the soft-decision-aided SM detectors considered in terms of the total number of real-valued multiplications. The conventional SM detectors invoke the Max-Log-MAP algorithm of Eq. (7.5) or the Approx-Log-MAP algorithm of Eq. (7.6) relying on the probability metric of Eq. (7.50). The reduced-complexity SM detectors invoke the proposed Algorithms 7.1 and 7.2 for implementing either the Max-Log-MAP or the Approx-Log-MAP regimes. We note that the calculations are carefully streamlined for the sake of offering a fair comparison. More specifically, $\{\kappa_v\}_{v=1}^{N_T}$ defined in Eq. (6.103) and $\{z_v\}_{v=1}^{N_T}$ of Eq. (6.100) are evaluated before calculating the probability metric of Eq. (7.50) for a total of $I = N_T M$ times for the detection algorithms, while the constellation power of $\{A_g^2\}_{g=0}^{M_{\text{Im}}/2-1}$ and $\{A_f^2\}_{f=0}^{M_{\text{Re}}/2-1}$ in Algorithm 7.1 as well as $\{A_g^2\}_{g=0}^{M/4-1}$ and $\{B_g^2\}_{g=0}^{M/4-1}$ in Algorithm 7.2 are as-

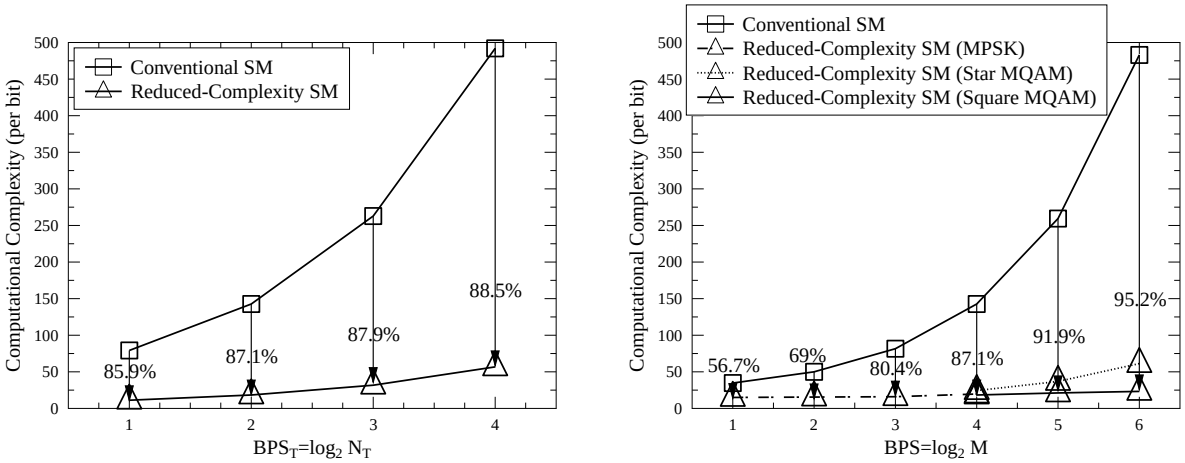

(a) SM(N_T,1)-Square 16QAM (b) SM(4,1)-MPSK/QAM

Figure 7.7: Complexity comparison between the conventional soft-decision-aided SM detection algorithms using the probability metric of Eq. (7.50) and the proposed reduced-complexity soft-decision-aided SM detection of Algorithms 7.1 and 7.2.

sumed to be stored before performing SM detection.

Owing to the zeros in the SM transmitted symbol vector of Eq. 6.99, the SM probability metric estimation of Eq. (7.50) is already less computationally complex than the MIMO probability metric estimation of Eq. (7.4). Nonetheless, Fig. 7.7 evidences a further substantial complexity reduction offered by the proposed algorithms, which is as high as 85.9% $\sim$ 88.5% for SM(N_T,1)-Square 16QAM employing different number of TAs from the set $N_T = \{2, 4, 8, 16\}$ in Fig. 7.7a and up to 56.7% $\sim$ 95.2% for SM(4,1) employing different MPSK/QAM constellations of $M = \{2, 4, 8, 16, 32, 64\}$ in Fig. 7.7b. We note that the SM schemes employing Square MQAM should be detected according to Algorithm 7.1, while the SM schemes employing MPSK or Star MQAM should be detected according to Algorithm 7.2. It is demonstrated by Fig. 7.7b that the detection complexity of SM employing Square MQAM is lower than that of employing Star MQAM, because the real and imaginary parts of the Square MQAM constellation may be separately visited. It is worth noting that the complexity reduction demonstrated in Fig. 7.7 is particularly beneficial for turbo detection assisted MIMO schemes, where the soft-decision-aided MIMO detector is invoked several times in order to achieve the best possible performance promised by the MIMO capacity predictions.

Fig. 7.8 further compares the computational complexities of different soft-decision-aided MIMO detectors. It can be seen in Fig. 7.8 that both the STBC and the STSK schemes exhibit a lower detection complexity than the conventional MIMO detector, but the SM detectors offer the lowest detection complexity in the context of coded MIMO systems. We note that in terms of the overall system complexity, the coded STBC system is the best, because the soft-decision-aided STBC detector has to be invoked for a lower number of times, albeit only, because it benefits to a lesser extent from the *a priori* information, which suggests to limit the number of iterations. Nonetheless, for both cases of $N_T = 2$ and $N_T = 4$ in Fig. 7.8, the SM detection complexity is as low as

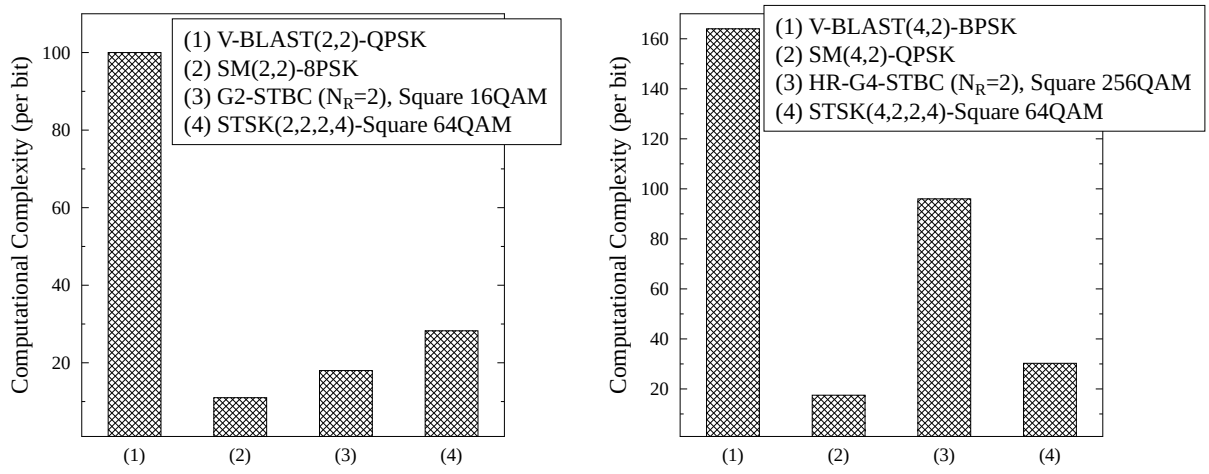

(a) $N_T = 2$, $N_R = 2$, $R = 4$ (b) $N_T = 4$, $N_R = 2$, $R = 4$

Figure 7.8: Complexity comparison between the soft-decision-aided detectors conceived for V-BLAST, SM, STBC and STSK associated with the same throughput of $R = 4$ bits/block/channel use, where the fading channel envelope is assumed to be constant for the duration of a channel use.

10% of the V-BLAST detection complexity, which offers a substantial reduction of both the signal processing complexity and the delay.

7.6 Chapter Conclusions

In this chapter, we provide insights into the tradeoff between the performance attained and the complexity imposed by coded MIMO system design. More explicitly, in order to achieve the best possible performance that is promised by the MIMO capacity predictions, the soft-decision-aided MIMO detector has to be invoked several times for turbo detection in the context of coded MIMO systems. In this scenario, the conventional optimum MAP V-BLAST detection complexity becomes excessive. In order to mitigate this problem, SD and MMSE detectors may be invoked in order to achieve an optimal or near-optimal V-BLAST detection capability in the context of coded MIMO systems. However, the state-of-the-art V-BLAST SD only works for full-loaded MIMO systems associated with $N_T \leq N_R$. For the rank-deficient MIMO systems associated with $N_T > N_R$, the extra signal processing complexity imposed by detecting the $N_T - N_R$ symbols also has to be taken into account. Moreover, the exact MMSE solution conceived for coded V-BLAST schemes has to be evaluated for each turbo iteration when the *a priori* LLRs are updated. In order to overcome these limitations, we demonstrate in Fig. 7.5 that the coded SM systems are capable of achieving a comparable performance to their V-BLAST counterparts, provided that the channel coding arrangements are appropriately selected. At the same time, the soft-decision-aided SM de-

tectors are capable of providing a substantial detection complexity reduction without imposing any performance loss on its optimum MAP detection.

The solutions conceived in this chapter reap the benefits of the complexity reduction proposed in the previous chapters. First of all, we demonstrate in Sec. 7.2.2 that the soft-decision-aided V-BLAST SD may be presented in a similar form to the soft-decision-aided MSDSD. Hence the reduced-complexity Schnorr-Euchner search strategy proposed in Sec. 3.3.3, which visits a reduced number of constellation points and avoids the extra complexity of a sorting algorithm, is applied to the soft-decision-aided V-BLAST SD in Sec. 7.2.2. Secondly, we demonstrate that the linear MIMO detectors including the soft-decision-aided V-BLAST MMSE detection of Sec. 7.2.4 and the soft-decision-aided orthogonal STBC detection of Sec. 7.3 may directly invoke the MPSK/QAM detectors of Sec. 2.3.1. Therefore, the reduced-complexity soft-decision-aided MPSK/QAM detection algorithms proposed in Sec. 2.4 are applied to linear MIMO receivers. Thirdly, based on the uncoded SM detection proposed in Sec. 6.4.1.1, we conceived reduced-complexity soft-decision-aided SM detection algorithms, which may retain the optimum detection capability, despite offering a substantial detection complexity reduction of up to over 90%, as seen in Fig. 7.7. The complexity reduction is particularly beneficial for coded MIMO systems, since the soft-decision-aided MIMO detectors have to be invoked several times. Furthermore, the optimality of SM detection is also important in the context of coded MIMO systems, because as demonstrated in Sec. 2.3.2 that any compromise concerning the detectors' optimality results in unreliable LLRs, which cannot be readily corrected by the channel decoder in coded MIMO systems.

Chapter 8

Conclusions and Future Research

In this chapter, a summary of the report is provided in Sec. 8.1, while a few future research suggestions are presented in Sec. 8.2.

8.1 Summary and Conclusions

8.1.1 Chapter 1: Introduction

In Chapter 1, the subjects related to this report are reviewed from a historical perspective. First of all, we summarized the consideration factors for wireless communications system design in Fig. 1.1, and we explicitly declared that the work in this report mainly deals with the tradeoff between performance and complexity. In order to better demonstrate this topic, an example of performance and complexity tradeoff that exists between the MIMO receivers including the ML, the SD and the LF was depicted in Fig. 1.2.

A historical perspective on near-capacity communications system design was offered in Sec. 1.1. As a brief summary, a historical chart for the major milestones is further portrayed in Fig. 8.1. Explicitly, Shannon [17] established the communications theory of capacity limit in 1949, which defined the maximum data rate that can be transmitted over the channel at the unconstrained cost of delay and complexity. Inspired by this promised capacity, a variety of channel coding schemes including Hamming code [18], convolutional code [19], BCH code [20–22] and LDPC code [46], which are still commonly used today, were developed in the 1950s and the 1960s. Following this, the classic decoding algorithms including the Viterbi algorithm [23–25] and the BCJR algorithm [26] were also proposed in the late 1960s and the early 1970s. In order to system-wise optimize the communications systems, the MLC [52] and the TCM [50] were proposed from the late 1970s, which started the era of joint channel coding and modulation design in [53–61] in the 1980s. Furthermore, the SOVA [35] proposed in 1989 improved the Viterbi algorithm by using soft-bits, while the Max-Log-MAP [27] proposed in 1990 further reduced the complexity of the

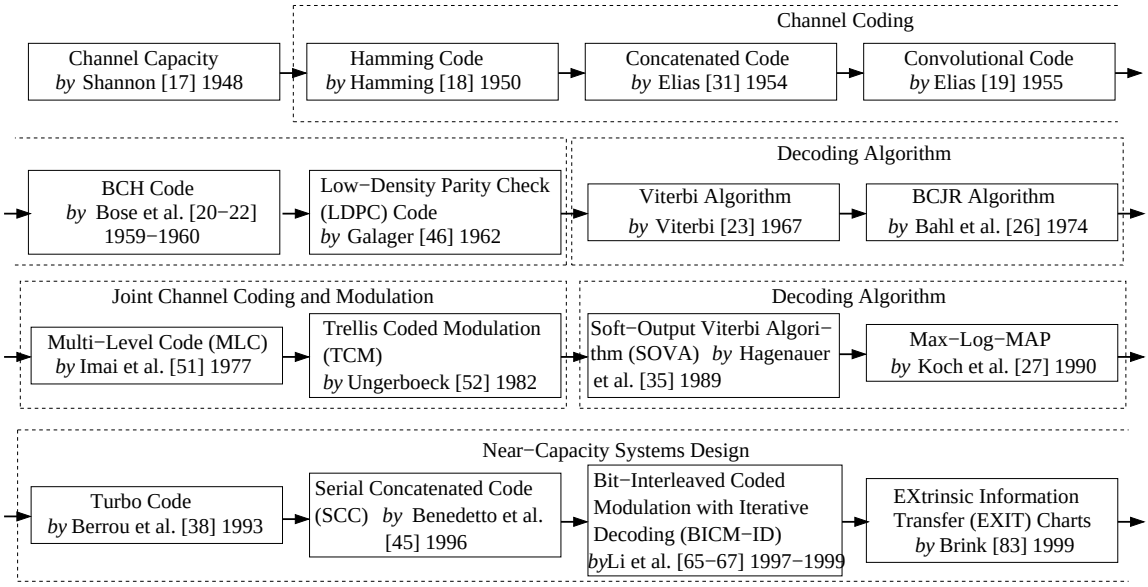

Figure 8.1: Historical chart for major milestones of near-capacity systems design.

BCJR algorithm. These improvements on decoding algorithm offered necessary preparations for the thrilling era of near-capacity systems design that opened by the invention of TC [38] in 1993. The PCC portrayed in Fig. 1.3 was generalized in [44] 1996, where any combination of block and convolutional codes was deemed to be possible, and the TC was included as a special case. In order to eliminate the PCC's puncturing, the SCC portrayed in Fig. 1.7 was generalized in [40, 45], where the SCC component detectors may exchange their decisions for the same binary bits. As an implementation of the SCC, the BICM-ID [65–67] proposed to follow the idea of breaking up channel coding and modulation, which was previously introduced by the BICM [63, 64], while iterative decoding between demodulator and channel decoder was adopted in order to achieve a system-wise near-capacity performance. The EXIT charts [83] offered an accurate and efficient tool for decoding convergence analysis as exemplied by Fig. 1.9, which has been used intensely in the near-capacity systems design [86–88, 92, 93] in the 21st century. In summary, the three key factors for achieving a near-capacity performance was depicted in Fig. 1.8, which are turbo detection (iterative decoding), soft-decision-aided detector/decoder and convergence analysis. The near-capacity system design and our proposed reduced-complexity soft-decision-aided PSK/QAM detectors were future presented in Chapter 2.

In Sec. 1.2, a historical perspective on noncoherent detection was provided. First of all, channel estimation for coherent schemes was introduced and exemplied in Fig. 1.10, which demonstrated that channel estimation becomes more difficult when the fading channels fluctuate rapidly. In order to eliminate the cost of channel estimation, the differential schemes and their noncoherent detectors have attracted a lot of research interests. Owing to the fact that the family of noncoherent detectors have been proposed over similar period of time, instead of portraying a historical chart, we summarize the noncoherent detectors including CDD, MSDD, MSDSD and DFDD into categories in Table 8.1. In more detail, after Lawton's early work on DPSK [106, 107], Cahn [108] found

	DPSK				DQAM			
CDD	Hard:	AWGN:	Lawton [106, 107]	1959	Hard:	AWGN:	Simon et al. [135]	1982
			Cahn [108]	1959		Fading:	Webb et al. [142]	1991
		Fading:	Bello et al. [109]	1962	Soft:	Fading:	Ishibashi et al. [157]	2005
							Liang et al. [158]	2011
MSDD	Hard:	AWGN:	Divsalar et al. [7]	1990	Hard/Soft:	AWGN/Fading:	Divsalar et al. [114]	1994
			Mackenthun [115]	1994				
		Fading:	Ho et al. [113]	1992				
	Soft:	Fading:	Divsalar et al. [114]	1994				
MSDSD	Hard:	Fading:	Lampe et al. [127]	2005				
	Soft:	Fading:	Pauli et al. [132]	2006	Soft:	Fading:	Wang et al. [160]	2012
DFDD	Hard:	AWGN:	Leib et al. [117]	1988	Hard:	AWGN:	Adachi et al. [150]	1996
	Hard:	Fading:	Schober et al. [121]	1999			Schober et al. [152]	1998
			Schober et al. [126]	2000	Hard:	Fading:	Gerstacker et al. [153]	1999
	Soft:	Fading:	Hoeher et al. [125]	1999			Schober et al. [154]	2001
			Lampe et al. [122]	2001	Soft:	Fading:	Lampe et al. [136]	2001

Table 8.1: Historical and technical summary of noncoherent receivers for differential schemes, where "Hard" and "Soft" refer to the hard-decision-aided detector and the soft-decision-aided detector, respectively.

in 1959 that the CDD aided DPSK scheme suffered from a 3 dB performance penalty in AWGN channels, while Bello et al. [109] found in 1962 that the CDD aided DPSK scheme suffered from an irreducible error floor in the rapidly fluctuating fading channels. Despite of the CDD's low complexity, the DPSK's performance limitations obstructed the development of differential scheme until the invention of DFDD [117] and MSDD [7] from the late 1980s. As portrayed by Fig. 1.12, the MSDD extends the CDD's observation window from two to $N_w \geq 2$, where a total number of $(N_w - 1)$ data-carrying symbols are jointly detected. Furthermore, the DFDD portrayed in Fig. 1.13 aims to detect a single data-carrying symbol based on the decision feedback of the previous $(N_w - 2)$ data-carrying symbols. Both MSDD and DFDD were originally proposed for DPSK in AWGN channels, and they have been further tailored for fading channels and further revised as soft-decision-aided detectors for coded systems as summarized in Table 8.1. Moreover, in order to reduce the MSDD complexity while maintaining the optimum performance, the MSDSD was proposed in [127, 132], where the SD was invoked. It was portrayed by Fig. 1.15 that the same performance and complexity tradeoff exists in both MIMO receivers design and noncoherent receivers design.

The noncoherent receivers conceived for DQAM schemes are also surveyed in Table 8.1. It can be seen in Table 8.1 that the development of CDD, MSDD and DFDD for DQAM also started from hard-decision-aided detection in AWGN channels, and then they have been extended to fading and coded scenarios. Nonetheless, the noncoherent receivers summarized in Table 8.1 were all conceived for specific DQAM constellations such as DAPSK or ADPSK. In other words, there is no systematic review of all noncoherent receivers for all DQAM constellations in open literatures at the

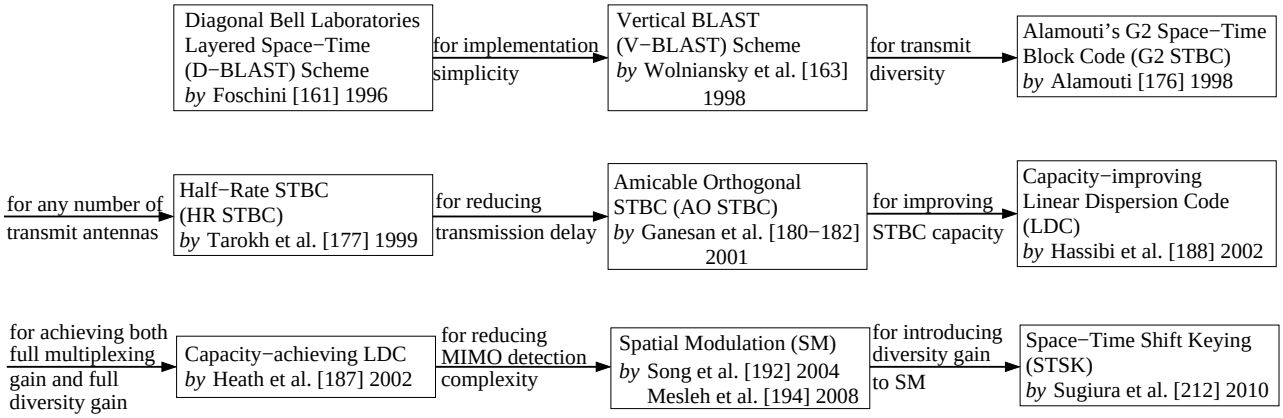

Figure 8.2: Historical chart for major milestones of Multiple-Input Multiple-Output (MIMO) schemes.

time of writing. Moreover, the MSDSD solution for DAPSK proposed by Wang et al. [160] invoked the SD only for the phase detection, and also an error floor was incurred in the absence of channel coding. Therefore, how to solve the DQAM's amplitude detection by the SD without compromising the MSDD performance remains another open problem at the time of writing. Furthermore, the DFDD solutions for DQAM summarized in Table 8.1 were all directly derived from the DPSK solutions, where the problem of non-constant DQAM amplitude was also ignored. These unsolved issues surveyed in Chapter 1 were aimed to be tackled in depth in the later technical chapters of Chapters 3-5 in this report.

In Sec. 1.3, a historical perspective on MIMO schemes is provided, and the major milesteones are summarized in the form of a historical chart in Fig. 8.2. The BLAST MIMO schemes [162, 164] proposed in the late 199s were illustrated in Fig. 1.18, where the multiple transmit antennas transmit independent data streams in order to achieve a potentially linearly increasing capacity [165, 166]. However, the multiple data streams that simultaneously arrived at the receiver have to be jointly detected by the ML detector if the full capacity potential of BLAST MIMO systems is pursued, which imposes an exponentially increasing detection complexity. In order to mitigate this problem, the BLAST MIMO schemes [162, 164] were originally proposed to employ the MUD of the CDMA systems [167, 168], where "nulling" and "cancelling" were in effect together for tackling the BLAST MIMO's interference problem. However, these low-complexity LF-based BLAST MIMO detectors cannot completely eliminate the interferences, which results in a sub-optimal performance. In order to balance the performance-complexity tradeoff, the SD was proposed to be invoked for the BLAST MIMO detection in [172–176].

Alternative to the BLAST MIMO's beneficial multiplexing gain, the revolutionary invention of Alamouti's G2 STBC [177] proposed in 1998 aims to pursue a transmit diversity gain in order to better combat fading. The schematics of the G2 STBC transceiver was portrayed in Fig. 1.19, where the $N_Q = 2$ symbols are redundantly transmitted by the $N_T = 2$ transmit antennas over the $N_P = 2$ time slots, so that the receiver may obtain replicas of the independently faded signals. Owing to the fact that the STBC transmission is in the form of unitary matrix constructed from

orthogonal design, the STBC receiver may decouple the multiple data streams without encountering the BLAST MIMO's interference problem. The Alamouti's G2 STBC has a unity symbol rate $\overline{R} = \frac{N_Q}{N_P} = 1$, which was proven to be the only full-rate STBC [178]. Nonetheless, HR STBCs associated with $\overline{R} = 0.5$ were proposed in [178] in 1999, which were constructed according to the Hurwitz-Radon theory [179, 180]. In order to achieve a higher symbol rate of $R = 3/4$ for $N_T = 3, 4$ and to reduce the HR STBC's transmission delay N_P, the AO STBCs [181–183] were invented in 2001 according to the theory of amicable orthogonal design [179].

Although the beneficial diversity gain is achieved, the STBC suffers from a throughput and capacity loss compared to the BLAST MIMO [184]. As a result, a classic tradeoff between multiplexing and diversity exists in MIMO systems design [185]. In order to improve the STBC capacity, the so-called capacity-improving LDC was proposed in [189] in 2002, which completely droped the STBC's orthogonality while retaining the full diversity gain by separately dispersing the real and imaginary parts of a total number of $N_Q \geq N_T N_P$ modulated MPSK/QAM symbols into both spatial and temporal dimensions. The so-called capacity-achieving LDC was further proposed in [188] in 2002, whose transceiver was portrayed by Fig. 1.20. The capacity-achieving LDC may retain both the full multiplexing gain and the full diversity gain by jointly dispersing the real and imaginary parts of the $N_Q \geq N_T N_P$ modulated MPSK/QAM symbols [188]. The development of LDC successfully solves the problem of diversity versus multiplexing tradeoff, but the performance versus complexity tradeoff once again emerges, as the LDC receivers have to employ the BLAST MIMO detectors because the STBC's orthogonality is abandoned by the LDC design.

Against this background, a newly-developed SM technique was firstly proposed in [195] in 2004, and it was re-introduced and analysed in [197] in 2008. The schematics of the SM transmitter was portrayed in Fig. 1.21, where a single out of N_T transmit antenna was activated to transmit a single modulated MPSK/QAM symbol. The motivations of the SM are twofold. Firstly, the SM transmitter may just employ a single RF chain, which reduces the MIMO's hardware complexity. Secondly, the optimum MIMO detection may be implemented by the SM at a substantially reduced complexity, where two parts of source information carried by the antenna activation index and the MPSK/QAM modulation index may be separately detected. In order to further introduce a diversity gain to the SM technique, the STSK scheme [216] was proposed in 2010. The schematics of the STSK portrayed by Fig. 1.23 was developed from the LDC's schematics of Fig. 1.20, where only a single LDC dispersion matrix was activated by the STSK, so that the low-complexity SM detector may be employed by the STSK receiver.

It can be seen from Fig. 8.2 that the research on MIMO techniques has been driven by two important tradeoffs since the late 1990s, which are the multiplexing and diversity tradeoff as well as the performance and complexity tradeoff. The key MIMO schemes and the two important design tradeoffs that motivated their development were summarized in Fig. 1.24. We further investigated these issues in Chapters 6 and 7. Furthermore, we surveyed the optimal and sub-optimal low-complexity SM detectors in Chapters 6 and 7, where our reduced-complexity optimal SM detection algorithms were also summarized based on our previous publications of [141, 202, 203, 234].

At the end of the first chapter, we demonstrated the outline and novel contributions of this report in Sec. 1.4. Explicitly, the outline of the report was portrayed by the block diagram of Fig. 1.25, which demonstrated that the communications systems were summarized from coherent to noncoherent, from uncoded to coded, and also from SISO/SIMO to MIMO in this report. Furthermore, the essence of this report is to apply our reduced-complexity design to these communications systems based on our previous publications of [159, 202, 203, 233–236]. The reduced-complexity design is demonstrated to be beneficial especially for coded systems, where a detector may be invoked several times by the turbo detection.

8.1.2 Chapter 2: Coherent Detection for PSK and QAM

In this chapter, the basic PSK and QAM modulation schemes in both uncoded and coded systems are studied. First of all, the Gray-labelled PSK/QAM constellations and their hard-decision-aided low-complexity detectors are reviewed in Sec. 2.2. More explicitly, the hard-decision-aided PSK/QAM detector may directly find the constellation point that is the closest to the channel's output signal based on the Gray-labelled PSK/QAM constellation diagram, which results in a low detection complexity for all the uncoded PSK/QAM schemes. We have also demonstrated that Square MQAM generally enjoys a higher minimum distance among its constellation points than its counterparts of Star MQAM and MPSK, as summarized in Table 2.1. As a result, Fig. 2.6 demonstrates that the Square MQAM exhibits a superior performance in the uncoded coherent systems.

Secondly, the classic soft-decision-aided PSK/QAM detection algorithms are summaried in Sec. 2.3, where the optimum Log-MAP, the low-complexity Max-Log-MAP and the near-optimum Approx-Log-MAP are introduced. Furthermore, the EXIT charts is introduced in Sec. 2.3.2 for analysing the convergence behaviour, when the soft-decision-aided PSK/QAM demodulation is invoked in turbo detection. Explicitly, in Sec. 2.3.2.1, the EXIT module is built in Algorithm 2.1 in order to evaluate the extrinsic information I_E that may be produced by a soft-decision-aided detector/decoder with given a specific amount of *a priori* information I_A, where I_E or I_A are the mutual information between the source binary bits and the detector/decoder's extrinsic LLRs L_e or *a priori* LLRs L_a, respectively. Following this, the transfer functions of both the inner code and the outer code of a concatenated scheme are drawn on the same EXIT charts in Sec. 2.3.2.2, where the BER performance and the required number of iterations may be efficiently predicted by the EXIT charts as exemplified in Fig. 2.9. It is also demonstrated in Sec. 2.3.2.2 that an infinitesimally low BER performance may be achieved by a concatenated scheme, when the EXIT curves of the inner and coder codes only intersect at the (1.0,1.0) point on the EXIT charts. The communications capacity theory is linked to the area property of EXIT charts in Sec. 2.3.2.3, where an infinitesimally low BER performance may be achieved at a SNR that is very close to the capacity limit when the area between the EXIT curves of the inner and coder codes is minimized, which is exemplifed by Fig. 2.13. The efficient computation for EXIT charts is further discussed in Sec. 2.3.2.4, where the extrinsic information I_E may be evaluated without the knowledge of the source information bits,

	$L_p(b_1)$	$L_p(b_2)\cdots L_p(b_{\mathrm{BPS}_{\mathrm{Im}}})$	$L_p(b_{\mathrm{BPS}_{\mathrm{Im}}+1})$	$L_p(b_{\mathrm{BPS}_{\mathrm{Im}}+2})\cdots L_p(b_{\mathrm{BPS}})$
Conventional	$O(M_{\mathrm{Im}})$	$O(M_{\mathrm{Im}})$	$O(M_{\mathrm{Re}})$	$O(M_{\mathrm{Re}})$
Proposed	$O(M_{\mathrm{Im}}/2)$	$O(M_{\mathrm{Im}}/4)$	$O(M_{\mathrm{Re}}/2)$	$O(M_{\mathrm{Re}}/4)$

Table 8.2: Complexity orders of the soft-decision-aided Square MQAM detectors. The conventional detection refers to the Max-Log-MAP of Eq. (2.34) and the Approx-Log-MAP of Eq. (2.35) using Eq. (2.39). The proposed detection refers to the reduced-complexity Max-Log-MAP of Algorithm 2.2 and its Approx-Log-MAP correction.

	$L_p(b_1)L_p(b_2)$	$L_p(b_3)\cdots L_p(b_{\mathrm{BPS}})$
Conventional	$O(M)$	$O(M)$
Proposed	$O(M/4)$	$O(M/8)$

Table 8.3: Complexity orders of the soft-decision-aided general MQAM detectors. The conventional detection refers to the Max-Log-MAP of Eq. (2.34) and the Approx-Log-MAP of Eq. (2.35) using Eq. (2.38). The proposed detection refers to the reduced-complexity Max-Log-MAP of Algorithm 2.3 and its Approx-Log-MAP correction.

provided that the PDFs of the extrinsic LLRs produced by a soft-decision-aided detector/decoder satisfy both the symmetric condition of $p(L_e|x) = p(-L_e|-x)$ and the consistency condition of $p(L_e|x=+1) = p(L_e|x=-1)e^{L_e}$. If the symmetricity condition cannot be satisfied, the EXIT charts has to be calculated with the aid of the source information bits, so that the PDFs $\{p(L_e|b)\}_{b=\{0,1\}}$ may be obtained by estimating the histograms of L_e with the source bits being $b = \{0,1\}$. However, if the consistency condition cannot be guaranteed, the LLR definition of $L_e = \ln\frac{p(L_e|b=1)}{p(L_e|b=0)}$ will be violated. Therefore, the LLR validity test is introduced in Fig. 2.14b in order to confirm that a soft-decision-aided detector/decoder is capable of producing reliable LLRs that obey the LLR definition. Otherwise, the unreliable LLR values may become unproportionately large after a few iterations, which may become difficult to correct in turbo detection.

As introduced in Sec. 2.3, the classic soft-decision-aided Square MQAM detection has a lower detection complexity than its counterparts of other PSK/QAM schemes, because the real and the imaginary parts of the Square MQAM constellation can always be separately detected. Nonetheless, the conventional Max-Log-MAP of Eq. (2.34) and the conventional Approx-Log-MAP of Eq. (2.35) have to estimate and compare all the M_{Re} and M_{Im} probability metrics using Eq. (2.39) according to the M_{Re}PAM and M_{Im}PAM constellations, when both the channel's output signal and the *a priori* information obtained from a channel decoder are taken into account by the soft-decision-aided Square MQAM detector. Similarly, the conventional soft-decision-aided PSK and general QAM detectors have to estimate and compare all the M probability metrics using Eq. (2.37) and Eq. (2.38), respectively. Against this background, we proposed the reduced-complexity PSK/QAM detection algorithms in Sec. 2.4 based on our publication of [236]. More explicitly, after linking each *a priori* LLR to a reduced-size fraction of the channel's output signal constellations,

only the positive PAM constellation points have to be visited by the proposed soft-decision-aided Square MQAM detection algorithm, which is exemplified by Fig. 2.16a and summarized by Algorithm 2.2. Similarly, for soft-decision-aided general PSK/QAM detection, only the constellation points located in the first quadrant have to be visited, which is exemplied by Fig. 2.16b and summarized by Algorithm 2.3. The complexity order reductions achieved by Algorithm 2.2 and Algorithm 2.3 are summarized in Table 8.2 and Table 8.3, respectively. We have demonstrated in Figs. 2.17a and 2.17b that the CRR achieved by Algorithms 2.2 and 2.3 approaches their upper bound of 50% and 75% respectively as M increases, because 50% and 75% of the constellation points have been avoided by the respective algorithms. This substantial complexity reduction is achieved without imposing any performance loss, which is beneficial especially when the soft-decision-aided PSK/QAM detector is invoked several times in turbo detection.

We have also demonstrated in the performance results of Figs. 2.18 and 2.19 that the turbo coded schemes achieve a better performance than their RSC coded counterparts, while the IRCC and URC coded schemes are capable of achieving a performance that is closest to capacity. However, the highest complexity is imposed by the IRCC-URC coded scheme, followed by the TC coded scheme and the RSC coded scheme.

8.1.3 Chapter 3: Noncoherent Detection for DPSK

The coherent detection techniques introduced in Chapter 2 rely on the availability of channel knowledge at the receiver. Alternatively, in this chapter, noncoherent detection for DPSK was investigated, where the reduced-complexity design was tailored for noncoherent receivers in both uncoded DPSK and coded DPSK systems.

The hard-decision-aided noncoherent receivers conceived for uncoded DPSK are introduced in Sec. 3.2. Explicitly, thanks to the DPSK's differential encoding of Eq. (3.1), the data-carrying MPSK symbol is mapped onto the phase change of the consecutive DPSK transmitted symbols. As a result, the channel estimation may be eliminated by the DPSK's noncoherent receivers, because the information may be recovered by observing the phase change of the consecutive received samples. The classic hard-decision-aided CDD conceived for uncoded DPSK is introduced in Sec. 3.2.1, where a single data-carrying symbol is recovered by observing two received signal samples. The CDD decision of Eq. (3.5) has a low detection complexity order of $O(1)$, where the closest constellation point is directly found based on the channel's output signal as the coherent MPSK detection of Eq. (2.9).

However, the low-complexity CDD suffers from a 3 dB performance penalty in slowly fluctuating fading channels compared to its coherent counterpart relying on perfect CSI estimation, and it also suffers from an irreducible error floor in rapidly fluctuating fading channels. In order to mitigate this problem, the hard-decision-aided MSDD conceived for uncoded DPSK is introduced in Sec. 3.2.2, which extends the CDD's observation window from two to $N_w \geq 2$ in order to further trace the fading channels' temporal memory for a longer period of time. As a result, the MSDD of

Eq. (3.22) has an exponentially increasing complexity order of $O(\frac{M^{N_w-1}}{N_w-1})$, where a total number of (N_w-1) data-carrying symbols have to be jointly detected by the MSDD.

As a remedy, the hard-decision-aided MSDSD conceived for uncoded DPSK is introduced in Sec. 3.2.3, where the SD is invoked in order to separately visit the constellation diagrams of the (N_w-1) data-carrying symbols. In this section, we further extend the classic MSDSD aided uncoded DPSK [127] to the case of employing multiple receive antennas $N_R \geq 1$, while maintaining a low complexity for the SD's Schnorr-Euchner [237] search strategy. More explicitly, the MSDSD conceived for multiple antennas aided differential schemes in [277] requires us to evaluate and sort all M constellation points for each SD index. A similar problem arises when we employ multiple receive antennas for MSDSD aided uncoded DPSK [127]. However, we propose to introduce a simple decorrelating operation, so that the MSDSD may still rely on the Schnorr-Euchner search strategy by first visiting the specific constellation point that are near the decorrelated variable. Then the rest of the constellation points may be visited in a zig-zag fashion, if required, which is similar to the original case of $N_R = 1$ in [127]. The MSDSD algorithm is summarized by Algorithm 3.1 and its pseudo-code is presented by Table 3.1, where the optimum MSDD solution is guaranteed to be found by the SD, provided that the SD's initial radius is set to be sufficiently large. The MSDSD complexity lower bound is given by $O(\frac{2N_w-3}{N_w-1})$, where the best constellation points are directly found based on the decorrelated variables when the SD index is increased from $v = 2$ to $v = N_w$ and then decreased from $v = (N_w-1)$ back to $v = 2$.

The MSDSD complexity lower bound can only be approached at high SNRs, and the MSDSD complexity may increase as the SNR decreases, because the SD terminates slower when the increased noise level reduces the distances between the noise contaminated received signal's constellation points. In order to further reduce the MSDSD complexity, the hard-decision-aided DFDD conceived for uncoded DPSK is introduced in Sec. 3.2.4. The DFDD in Sec. 3.2.4 is firstly introduced as the decision-feedback version of the MSDD/MSDSD, where only a single data-carrying symbol is aimed to be detected by the DFDD, as the remaining (N_w-2) data-carrying symbols in the MSDD/MSDSD decision metrics are obtained from the decision-feedback. Furthermore, the DFDD is also derived in an alternative prediction-based form in Sec. 3.2.4, which performs coherent detection for a single unknown DPSK symbol, where the estimated CSI sample is estimated and predicted by a MMSE Wiener filter based on the previous N_w-1 received signal samples and the previous decisions for the N_w-1 DPSK transmitted symbols. It is demonstrated in Sec. 3.2.4 that the MSDD/MSDSD-based DFDD and the prediction-based DFDD are equivalent for DPSK in Rayleigh fading channels. The DFDD decision of Eq. (3.38) also exhibits a low detection complexity order of $O(1)$, which is similar to the CDD.

The performance and complexity tradeoff between the hard-decision-aided noncoherent detectors is analysed in Sec. 3.2.5. It is demonstrated by Figs. 3.4-3.5 that the MSDD and the CDD exhibit the highest and the lowest detection complexities, respectively, while the DFDD complexity is generally lower than the MSDSD complexity. Moreover, it is demonstrated by Figs. 3.6-3.7 that the MSDD/MSDSD effectively improves the CDD's suboptimal performance, while Fig. 3.9 fur-

	CDD	MSDD	MSDSD	DFDD
Complexity order:	$O(1)$	$O(\frac{M^{N_w-1}}{N_w-1})$	Lower bound: $O(\frac{2N_w-3}{N_w-1})$	$O(1)$
Performance results:	3 dB penalty compared to MPSK, error floor in rapidly fading channels	Optimum	Optimum (when the SD radius is initialized to be sufficiently large)	better than the CDD but suboptimal to the MSDD/MSDSD

Table 8.4: Complexity orders and performance results of the hard-decision-aided noncoherent detectors conceived for uncoded DPSK in Sec. 3.2.

ther evidences that although both the MSDD/MSDSD and the DFDD may mitigate the CDD's error floor in rapidly fading channels, the MSDD/MSDSD outperforms its DFDD counterpart. The detection complexity orders of the hard-decision-aided noncoherent detectors conceived for uncoded DPSK and their performance results are summarized in Table 8.4.

The soft-decision-aided noncoherent receivers conceived for coded DPSK are introduced in Sec. 3.3. First of all, the soft-decision-aided MSDD and CDD are presented in Sec. 3.3.1, where the CDD is the special case of MSDD associated with $N_w = 2$. The soft-decision-aided MSDSD is investigated in Sec. 3.3.2. More explicitly, as proposed in [132], the Max-Log-MAP algorithm invoked by the MSDD aims for finding the maximum probabilities, which is similar to the action of the hard-decision-aided MSDD. Therefore, the polarity of the MSDD probability metric may be altered and the maximization of the Max-Log-MAP may be revised to be the minimization, so that the same SD algorithm used by the hard-decision-aided MSDSD may be adopted by the soft-decision-aided MSDSD. The major differences between the hard-decision-aided MSDSD of Sec. 3.2.3 and the soft-decision-aided MSDSD may be deemed as twofold. Firstly, the hard-decision-aided MSDSD's decorrelating variables cannot directly be used for finding the closest constellation point by the soft-decision-aided MSDSD, because the *a priori* information obtained from a channel decoder is not included. As a result, the soft-decision-aided MSDSD's Schnorr-Euchner search strategy once again requires us to sort a total number of M probability metrics by visiting all the M constellation points. The corresponding soft-decision-aided MSDSD algorithm is summarized as pseudo-code in Table 3.3. Secondly, the soft-decision-aided MSDSD algorithm of Table 3.3 has to be invoked $[(N_w-1)\log_2 M+1]$ / $[(N_w-1)\log_2 M]$ times for producing a single soft-bit output, because only a single minimized Euclidean distance may be obtained by invoking once the SD algorithm, but each Max-Log-MAP's soft-bit decision requires a pair of maximized probability metrics.

We have further proposed two improvements to the soft-decision-aided MSDSD in [132]. First of all, we propose to modify the output of the SD algorithm of Table 3.3, where multiple candidates may be produced by the SD so that the Approx-Log-MAP may be implemented. The corresponding Approx-Log-MAP algorithm implemented by the soft-decision-aided MSDSD is summarized in Algorithm 3.2 in Sec. 3.3.2. Secondly, in Sec. 3.3.3, the reduced-complexity design proposed in Chapter 2 is further revised for simplifying the Schnorr-Euchner search strategy used by the conventional soft-decision-aided MSDSD in [132], where the optimum candidate may be found by

visiting a reduced-size subset of constellation points, and then the rest of the constellation points may be visited in a zig-zag fashion, if needed. The corresponding soft-decision-aided MSDSD algorithm is summarized as pseudo-code in Tables 3.4-3.7. Moreover, it is worth pointing out that the conventional MSDSD in [132] requires the Schnorr-Euchner search strategy to invoke a sorting algorithm, where all the M constellation points are ranked according to their corresponding probability metrics. The average number of comparisons required by a sorting algorithm (e.g. Bubble sort, Timsort, Library sort [285, 286], etc.) may be as high as $O(M \log M)$. By contrast, the reduced-complexity Schnorr-Euchner search strategy of Tables 3.5-3.7 does not require any sorting algorithms.

The soft-decision-aided DFDD conceived for coded DPSK is introduced in Sec. 3.3.4. As the decision-feedback version of MSDD/MSDSD, the soft-decision-aided DFDD that aims to detect a single symbol based on the previous decisions on the $N_w - 2$ data-carrying symbols as seen in [122, 125, 136] may be termed as the symbol-metric based DFDD. Furthermore, the bit-metric based DFDD proposed in [122] is also introduced, where the probability metrics are evaluated based on the hard-decision-aided DFDD of Sec. 3.2.4. Although the bit-metric based DFDD may achieve a complexity reduction, a severe degradation on the LLR accuracy has also imposed. In order to mitigate this problem, we propose to apply the reduced-complexity soft-decision-aided PSK detection algorithm proposed in Chapter 2 to the symbol-metric based DFDD, where a substantial complexity reduction may be achieved without imposing any performance loss.

The performance and complexity tradeoff in coded DPSK systems is analysed in Sec. 3.3.5. Similar to Fig. 3.4 for uncoded DPSK, Fig. 3.16 demonstrates that the CDD and the MSDD exhibit the lowest and the highest detection complexities in coded DPSK systems, while the MSDSD complexity is higher than the DFDD complexity. Fig. 3.17 further shows that the complexity lower bound may be approached by the soft-decision-aided MSDSD given a high SNR and/or the full *a priori* information. Furthermore, Fig. 3.18a shows that a significant complexity reduction of up to $CRR = 66.7\%$ is achieved by the proposed MSDSD of Table 3.4, when the MSDSD window is increased up to $N_w = 6$ for coded DQPSK detection. Moreover, it may be seen in Fig. 3.18b that a substantial complexity reduction of up to $CRR = 88.7\%$ is achieved by the proposed MSDSD associated with $N_w = 4$, when the number of modulation levels is increased to $M = 16$. Figs. 3.19-3.22 further demonstrate that the soft-decision-aided MSDSD is capable of improving the CDD's performance for coded DPSK schemes. For the performance of DFDD, Figs. 3.24 and 3.25 evidence that the bit-metric based DFDD imposes a severe performance degradation without offering any significant complexity reduction. By contrast, it is demonstrated by Fig. 3.24b that a substantial complexity reduction of up to $CRR = 57.0\%$ may be achieved by applying Algorithm 2.3 to the symbol-metric based DFDD ($N_w = 4$), as the modulation order increases to $M = 16$, where no performance loss is imposed. Fig. 3.26 further demonstrates that the soft-decision-aided DFDD is also capable of improving the CDD's performance, but the soft-decision-aided MSDSD performs better than both DFDD and CDD.

In summary, the reduced-complexity design has been applied to the noncoherent receivers in

Novelty	Conventional method	Proposed improvement
The hard-decision-aided MSDSD for the case of employing $N_R \geq 1$ receive antennas.	The MSDSD conceived for multiple antennas in [277] requires us to sort all constellation points for each SD index. A similar problem arises when we employ $N_R \geq 1$ for MSDSD aided uncoded DPSK [127].	We propose to introduce a decorrelating operation, so that the Schnorr-Euchner strategy may simply visit the closest constellation point, and then the rest of the constellation points may be visited in a zig-zag fashion, if required, which is similar to the original case of $N_R = 1$ in [127].
The Approx-Log-MAP algorithm implemented by the soft-decision-aided MSDSD.	The MSDSD in [132] retains the detection capability of the Max-Log-MAP aided MSDD.	We propose to modify the output of the SD algorithm of [132], where multiple candidates may be produced by the SD so that the near-optimum Approx-Log-MAP may be implemented.
The reduced-complexity Schnorr-Euchner search strategy for the soft-decision-aided MSDSD.	When the *a priori* LLRs gleaned from a channel decoder are taken into account by the MSDSD in [132], the Schnorr-Euchner strategy once again requires us to visit and rank all the M constellation points for each SD index.	We proposed to simply the Schnorr-Euchner strategy in [132], where the optimum candidate is found by visiting a reduced-size subset of constellation points, and then the rest of the constellation points may be visited in a zig-zag fashion, if required. The sorting algorithm required by the conventional Schnorr-Euchner strategy in [132] may also be eliminated.
The reduced-complexity soft-decision-aided DFDD.	The bit-metric based DFDD [122] evaluate the probability metrics based on the hard-decision-aided DFDD of Sec. 3.2.4 in order to reduce the complexity of the symbol-metric based DFDD [122, 125, 136].	Since the bit-metric based DFDD [122] imposes a performance degradation, we propose to apply the reduced-complexity soft-decision-aided PSK detection algorithm proposed in Chapter 2 to the symbol-metric based DFDD, where a substantial complexity reduction may be achieved without imposing any performance loss.

Table 8.5: A brief summary of the proposed improvements to the noncoherent receivers conceived for DPSK in Chapter 3.

Chapter 3 from uncoded DPSK systems to coded DPSK systems. The proposed improvements to the noncoherent receivers are summarized in Table 8.5.

Last but by no means least, a discussion on the important subject of coherent versus noncoherent detection is offered in Sec. 3.4. When the fading channel varies potentially for each consecutive transmitted symbol, the accurate channel estimation may become more and more difficult as the Doppler frequency increases. Against this background, the classic PSAM [1] is introduced in Sec. 3.4.1, where the known pilot symbols are periodically transmitted through the fading channels. The receiver aims to recover the CSI knowledge by minimizing the MSE between the estimated fading sample and the objective fading sample, where the input signal to the MMSE filter is constituted by a window of received pilot observations. In Sec. 3.4.2, the realistic PSAM aided coherent PSK schemes are compared to their noncoherent DPSK counterparts in uncoded systems. First of all, the choice of pilot spacing and that of the MMSE filter's observation window length are discussed in Figs. 3.28-3.29, which evidence that more transmission power has to be dedicated to the pilot symbols, when the Doppler frequency is increased. Fig. 3.30 shows that the noncoherent receivers including the MSDSD associated with a long detection window of $N_w = 11$ can hardly provide any performance advantage over the PSAM aided coherent receivers in uncoded systems. Furthermore,

Fig. 3.31 demonstrates that although the noncoherent receiver of CDD exhibits a lower detection complexity than the PSAM aided coherent detection, both the MSDSD complexity and the DFDD complexity are higher than the PSAM complexity.

Although the noncoherent receivers fail to provide a performance advantage in uncoded systems, Sec. 3.4.3 further demonstrates that the noncoherent receivers may even outperform the realistic PSAM aided coherent schemes in coded systems, when the fading channels fluctuate rapidly, provided that the appropriate channel coding arrangement is selected. More explicitly, it is demonstrated by Fig. 3.32 that the LLRs produced by the PSAM aided coherent detector severely deviate from the true probabilities, when the Doppler frequency is increased. This is because that the coherent detectors alway rely on the idealistic assumption of perfect channel estimation, which cannot be delivered by the PSAM especially when the fading channels fluctuate rapidly. This problem may not affect the performance of the PSAM aided coherent scheme in uncoded systems seen in Sec. 3.4.2, but the unreliable LLRs will gravely affect the coherent scheme's performance in coded systems, because the high but inaccurate LLR values are hard to be corrected by the channel decoder after a few turbo iterations. By contrast, the soft-decision-aided MSDSD is always capable of providing reliable extrinsic LLRs, even for high Doppler frequencies, as seen in Fig. 3.32. As a result, although the PSAM aided coherent schemes still outperform their noncoherent counterparts in RSC, TC and IRCC-URC coded systems at a low normalized Doppler frequency of $f_d = 0.001$ as seen in Fig. 3.34a , Fig. 3.35a and Fig. 3.36, respectively, Fig. 3.35b and Fig. 3.36 evidence that the TC and IRCC-URC coded DPSK employing subset MSDSD are capable of even outperform their coherent counterparts, when the normalized Doppler frequency is increased to $f_d = 0.03$.

As representatives of the family of coherent and noncoherent detectors, the PSAM aided coherent receiver and the subset-MSDSD aided noncoherent receiver are compared in Table 3.9 based on our simulation results presented in Sec. 3.4.

8.1.4 Chapter 4: Noncoherent Detection for Differential Non-Constant Modulus Modulation – Part I: Uncoded Systems

Chapter 4 continues to investigate the noncoherent detection for differential non-constant modulus modulation, which is also referred to as the DQAM schemes in uncoded systems. A variety of DQAM constellations are surveyed in Sec. 4.2, which are also summarized in categories in Fig. 8.3. First of all, the classic DAPSK [142,158,159,287] is introduced in Sec. 4.2.1. The DAPSK invokes the conventional differential encoding process $s_n = x_{n-1}s_{n-1}$ of Eq. (4.1), which imposes the differential encoding on both amplitude and phase as expressed by Eq. (4.4) and Eq. (4.5), respectively. The DAPSK aims to guarantee that all the transmitted symbols s_n are drawn from the classic Star MQAM constellation. As a result, the choice of the constellation diagram for a DAPSK's data-carrying symbol x_{n-1} depends on the previous transmitted ring amplitude $\Gamma_{n-1} = |s_{n-1}|$. Considering the 16-DAPSK(2,8) as an example, the data-dependent ring amplitudes should either be drawn from the set of $\{1, \alpha\}$ or use the set of $\{1, \frac{1}{\alpha}\}$, when the previous transmitted ring am-

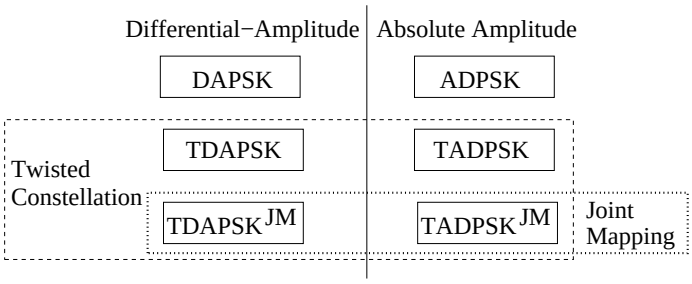

Figure 8.3: A summary of the DQAM constellations introduced in Sec. 4.2.

plitude is either $\frac{1}{\sqrt{\beta}}$ or $\frac{\alpha}{\sqrt{\beta}}$, respectively, so that the next transmitted symbol's ring amplitude is guaranteed to be drawn from the same Star QAM ring amplitudes set of $\{\frac{1}{\sqrt{\beta}}, \frac{\alpha}{\sqrt{\beta}}\}$. The differential encoding applied to the 16-DAPSK(2,8) scheme's ring amplitudes is exemplied in Tables 4.3 and 4.4, while the differential encoding on the 16-DAPSK(2,8) scheme's phases is summarized in Table 4.2, which is exactly the same as a D8PSK scheme. As a result, there are two constellation diagrams for the 16-DAPSK(2,8) scheme's data-carrying symbols x_{n-1}, which is drawn in Fig. 4.2, while the constellation for the 16-DAPSK(2,8) scheme's transmitted symbols s_n is guaranteed to be Star 16QAM, which is portrayed in Fig. 4.1. The modulation process for a generic M-DAPSK(M_A,M_P) scheme's data-carrying symbol is formulated in Eq. (4.7).

However, the information carried by the DAPSK scheme's ring amplitude changes may not exhibit the best reliability, because the data-carrying magnitude such as $\frac{1}{\alpha}$ may even be much smaller than the smallest Star QAM ring amplitude given by $\frac{1}{\sqrt{\beta}}$, which may degrade the achievable performance. Therefore, in addition to the classic DAPSK, the ADPSK [136, 288] is introduced in Sec. 4.2.2. The ADPSK directly modulate all the data-carrying symbols x_{n-1} as regular Star QAM symbols as formulated in Eq. (4.10). Moreover, the ADPSK utilizes the absolute-amplitude in the alternative differential encoding process $s_n = \frac{1}{|s_{n-1}|} x_{n-1} s_{n-1}$ of Eq. (4.8), which prevents the situation of having variable and unconstrained transmitted ring amplitudes. As a result, the ADPSK's differential encoding on phase is as same as that of the DAPSK, but the ADPSK always has the absolute amplitude of $\Gamma_n = |s_n| = |x_{n-1}| = \gamma_{n-1}$. For example, the constellation diagram of the 16-ADPSK(2,8) scheme's data-carrying symbols is drawn in Fig. 4.3a, which is the classic Star 16QAM constellation regardless of the previous transmitted ring amplitude. The constellation diagram of the 16-ADPSK(2,8) scheme's transmitted symbols is further shown in Fig. 4.3b, which is also the Star 16QAM constellation, thanks to the absolute-amplitude in the differential encoding process $s_n = \frac{1}{|s_{n-1}|} x_{n-1} s_{n-1}$ of Eq. (4.8).

As proposed in [136, 288], a ring-amplitude-dependent phase rotation of the DAPSK constellation and of the ADPSK constellation is capable of increasing the distance between the constellation points from different amplitude ring, which leads us to the twisted constellations of TDAPSK and TADPSK. The modulation of the TDAPSK's data-carrying symbols is formulated in Eq. (4.11). For example, the constellation diagrams of the 16-TDAPSK(2,8) scheme's data-carrying symbols

are portrayed in Fig. 4.4, where all the constellation points in the second amplitude ring are rotated anti-clockwisely by $\pi/8$. The TDAPSK still invokes the DAPSK's differential encoding process $s_n = x_{n-1}s_{n-1}$ of Eq. (4.1), and the example of the constellation diagram of the 16-TDAPSK(2,8) scheme's transmitted symbols is drawn in Fig. 4.5. Similarly, the modulation of the TADPSK's data-carrying symbols is formulated in Eq. (4.12), and the TADPSK still invokes the ADPSK's differential encoding process $s_n = \frac{1}{|s_{n-1}|}x_{n-1}s_{n-1}$ of Eq. (4.8). For example, the constellation diagrams of the 16-TADPSK(2,8) scheme's data-carrying symbols and transmitted symbols are shown in Fig. 4.6a and Fig. 4.6b, respectively. Since the minimum distance between the constellation points is determined by the adjacent constellation points located on the smallest amplitude ring, twisted modulation can only offer a small improvement on the average distance between all constellation points, which is represented in Table 4.6. However, since the amplitude-dependent phase rotation imposes a correlation between the amplitude and phase, it may be expected that the iteration gain achieved by soft-decision-aided TDAPSK/TADPSK demodulator may be higher than that of their DAPSK/ADPSK counterparts, which implies that twisted modulation may offer certain performance advantages in coded systems, provided that appropriate coding schemes are used.

The DQAM constellations including DAPSK, ADPSK, TDAPSK and TADPSK opt for separately modulating the amplitude and phase, which are aimed to be detected separately by their noncoherent receivers at a lower detection complexity. Alternatively, it was introduced in [136, 288] that the amplitude and the phase may be jointly modulated for DQAM, which may be referred to as the DQAM$^{\text{JM}}$ schemes. For example, the joint mapping conceived for the TDAPSK$^{\text{JM}}$ based on the constellation of TDAPSK is formulated in Eq. (4.13), while the joint mapping designed for TADPSK$^{\text{JM}}$ based on the constellation of TADPSK is formulated in Eq. (4.14). The constellation diagram of the 16-TDAPSK$^{\text{JM}}$(2,8) scheme's data-carrying symbols and that of the 16-TADPSK$^{\text{JM}}$(2,8) scheme's data-carrying symbols are depicted in Fig. 4.7 and Fig. 4.8, respectively. It may be expected that the DQAM and its DQAM$^{\text{JM}}$ counterpart may achieve the same DCMC capacity. However, owing to the further improved dependency between the modulated amplitude and phase, the DQAM$^{\text{JM}}$ arrangement may benefit from an improved iteration gain in the coded systems.

For the sake of clarification, the equations both for modulating and for differentially encoding as well as the figures for the example constellation diagrams are summarized in Table 4.7 for all DQAM constellations introduced in Sec. 4.2.

The hard-decision-aided CDD conceived for uncoded DQAM is introduced in Sec. 4.3. More explicitly, the CDD conceived for the differential-amplitude DQAM schemes which separately modulate the amplitude and phase is developed in Sec. 4.3.1. We demonstrate in Fig. 4.9 that completely independently detecting the DAPSK's ring amplitude and phase by Eqs. (4.19a) and (4.19b) as suggested by [142] may impose a performance loss. As a remedy, we propose to detect the DAPSK's phase first by Eq. (4.22), and then the detected phase may assist the ring amplitude detection by Eq. (4.23), which retains the optimum detection capability. Since the CDD decision variable of Eq. (4.18) may be directly used for finding the closest phase constellation point in

Eq. (4.22), the CDD aided DAPSK has a complexity order of $O(1 + M_A)$. By contrast, in the presence of the ring-amplitude-dependent phase rotation, the CDD aided TDAPSK has to find a total number of M_A phase candidates for M_A ring amplitudes in Eq. (4.25), and then the amplitude detection may be completed with the aid of the detected M_A phase candidates by Eq. (4.26). As a result, the CDD aided TDAPSK has a complexity order of $O(M_A + M_A)$. Similarly, the CDD conceived for the absolute-amplitude DQAM schemes which separately modulate the amplitude and phase is developed in Sec. 4.3.2. The CDD aided ADPSK of Eq. (4.29) also utilizes the decision variable to find the optimum phase first, and then the detected phase may be used for the amplitude detection, which results in a complexity order of $O(1 + M_A)$. Moreover, the CDD aided TADPSK of Eq. (4.30) requires to detect a total number of M_A phase candidates for the ring amplitude detection, which imposes a complexity order of $O(M_A + M_A)$. Furthermore, the CDD aided DQAM schemes which jointly modulate the amplitude and phase is introduced in Sec. 4.3.3, where the CDD for both TDAPSK$^{\text{JM}}$ and TADPSK$^{\text{JM}}$ has the highest complexity order of $O(M)$, because their amplitude and phase have to be jointly detected. The complexity orders of the CDD conceived for different DQAM constellations are summarized in Table 8.6.

The hard-decision-aided MSDD conceived for uncoded DQAM is developed in Sec. 4.4. The differences between the MSDD aided DPSK of Sec. 3.2.2 and the MSDD aided DQAM of Sec. 4.4 are three-fold. First of all, the MSDD aided DPSK models the transmitted symbols in a single $(N_w \times N_w)$-element unitary matrix $\mathbf{S}$ in Eq. (3.6), which is further replaced by $\bar{\mathbf{S}}$ in Eq. (3.9), where the first transmitted symbol in $\bar{\mathbf{S}}$ is simply fixed to $\bar{s}_1 = 1$ because it is a common phase rotation to all the following DPSK symbols. By contrast, the MSDD aided DQAM respectively models the transmitted ring amplitudes, phases and ring-amplitude-dependent phase rotations as separate $(N_w \times N_w)$-element matrices of $\mathbf{A}$, $\mathbf{P}$ and $\mathbf{O}$ in Eq. (4.32). They are further represented by $\bar{\mathbf{A}}$, $\bar{\mathbf{P}}$ and $\bar{\mathbf{O}}$ in Eq. (4.35), where the first transmitted symbol's ring amplitude, phase and ring-amplitude-dependent phase rotation are put aside. Secondly, for the MSDD aided DPSK, the channel's characteristic correlation matrix $\mathbf{C} = \mathbf{R}_{hh} + \mathbf{R}_{vv}$ of Eq. (3.21) is constant and known, where the fading channel's characteristic correlation matrix $\mathbf{R}_{hh}$ of Eq. (3.16) is determined by the time correlation between the fading samples, while the AWGN characteristic correlation matrix $\mathbf{R}_{vv}$ of Eq. (3.19) is determined by the noise power. However, for the MSDD aided DQAM, the channel's characteristic correlation matrix $\mathbf{C} = \bar{\mathbf{A}}^H \mathbf{R}_{hh} \bar{\mathbf{A}} + \mathbf{R}_{vv}$ of Eq. (4.44) is not a constant, where the ring amplitudes matrix $\bar{\mathbf{A}}$ is not a unitary matrix and hence it cannot be separated from $\mathbf{C}$. As a result, the channel's characteristic correlation matrix $\mathbf{C}$ of Eq. (4.44) does not become known until all the ring amplitudes in $\bar{\mathbf{A}}$ are detected, which is the most substantial stumbling block in the way of offering a sphere decoding solution to the DQAM ring amplitude detection problem. Thirdly, both the first transmitted phase in $\mathbf{P}$ and the first transmitted ring-amplitude-dependent phase rotation in $\mathbf{O}$ may be fixed to be 1 by $\bar{\mathbf{P}}$ and $\bar{\mathbf{O}}$ in Eq. (4.35) because they are common phase rotations for the following DQAM symbols, which is as same as the case of DPSK. However, the first transmitted ring amplitude has to be treated either as a separate variable or a known term based on the previous MSDD decision, which leads us to the two MSDD arrangements of the MSDD of Eq. (4.45) and the

HDD-MSDD of Eq. (4.46), respectively. We have also demonstrated that the differential-amplitude DQAM schemes may employ both MSDD and HDD-MSDD, but the absolute-amplitude DQAM scheme can only employ HDD-MSDD. The complexity order of the MSDD and HDD-MSDD conceived for different DQAM constellations are summarized in Table 8.6.

In Sec. 4.5, we proposed the hard-decision-aided MSDSD conceived for uncoded DQAM. In order to solve the MSDD's ED of Eq. (4.50) by a sphere decoder, firstly, the PED is developed in Sec. 4.5.1. More explicitly, both the lower triangular matrix $\mathbf{L}$ obtained from the decomposition of $\mathbf{C}^{-1} = \mathbf{L}\mathbf{L}^T$ and the determinant term of $\det(\mathbf{C})$ remain unknown, until the entire ring amplitude matrix $\bar{\mathbf{A}}$ is detected. In order to mitigate this problem, we proposed in Proposition 1 that although the $(N_w \times N_w)$-element $\mathbf{C}$ and $\mathbf{L}$ are unknown, the $(v \times v)$-element partial channel correlation matrix $\widetilde{\mathbf{C}}_\mathbf{v}$ may be evaluated with the aid of the SD's previous decisions concerning $\{\Gamma_t\}_{t=1}^{v-1}$ and a single variable Γ_v. We proved in Proposition 1 that for a specific SD index v, only the $(v \times v)$-element lower triangular submatrix $\widetilde{\mathbf{L}}_\mathbf{v}$ is required by the SD, which may be obtained from the Cholesky decomposition of $\widetilde{\mathbf{L}}_\mathbf{v}\widetilde{\mathbf{L}}_\mathbf{v}^T = \widetilde{\mathbf{C}}_\mathbf{v}^{-1}$. Furthermore, we proposed in Proposition 2 that the determinant in logarithm domain of $\ln[\det(\mathbf{C})]$ may also be written as a summation of incremental metrics by using the Leibniz formula, so that only a single variable Γ_v is required to be evaluated by the SD associated with index v. As a result, the PED of $\{d_v = d_{v-1} + \Delta_{v-1}\}_{v=2}^{N_w}$ that may unambiguously restore the MSDD's ED is formulated by Eq. (4.59).

Secondly, in Sec. 4.5.2, the MSDSD's Schnorr-Euchner search strategy is tailored for the DQAM constellations as pseudo-code in Table 4.8 based on the PED of Eq. (4.59), where the MSDSD algorithm of [132] summarized in Table 3.3 may be invoked for the hard-decision-aided MSDSD conceived for uncoded DQAM. As a result, the SD associated with a specific index v may sort all the M candidates Δ_{v-1} of Eq. (4.60) according to their increasing values, when the Schnorr-Euchner search strategy of Table 4.8 is employed. The resultant MSDSD implementing the MSDD of Eq. (4.45) and the resultant HDD-MSDSD implementing the HDD-MSDD of Eq. (4.46) have the complexity order lower bounds of $O(M_A \cdot M)$ and $O(M)$, respectively.

Thirdly, we further proposed the reduced-complexity MSDSD algorithm for the DQAM constellations of DAPSK, ADPSK, TDAPSK and TADPSK which separately modulate the amplitude and phase in Sec. 4.5.3. More explicitly, the PED increment Δ_{v-1} of Eq. (4.60) is separated into the ring-amplitude-related term Δ_{v-1}^{Γ} of Eq. (4.64) and the M_PPSK-related term conditioned on the ring amplitude $\Delta_{v-1}^{\omega|\Gamma}$ of Eq. (4.65) in Eq. (4.63). We propose to formulate a decision variable $z_{v-1}^{\omega|\Gamma}$ in Eq. (4.66), which may be directly used for visiting the M_PPSK phase candidates in a zig-zag fashion similar to the case of DPSK seen in Table 3.1 and [127]. As a result, given a specific ring amplitude candidate Γ_v, the local M_PPSK-related term $\Delta_{v-1}^{\omega|\Gamma}$ may be obstained without visiting all the M_P phase candidates, and then the global PED increment Δ_{v-1} of Eq. (4.60) may be found by comparing the M_A ring amplitude candidates with the aid of their local M_P phase decisions. The resultant reduced-complexity Schnorr-Euchner search strategy is summarized as pseudo-code in Table 4.9, where the MSDSD algorithm of [127] summarized in Table 3.1 may be invoked for the reduced-complexity hard-decision-aided MSDSD con-

	DAPSK	ADPSK	TDAPSK	TADPSK	TDAPSK^{JM}	TADPSK^{JM}
CDD	$O(1+M_A)$		$O(M_A+M_A)$		$O(M)$	
MSDD	$O\left(\frac{M_A M^{N_w-1}}{N_w-1}\right)$		$O\left(\frac{M_A M^{N_w-1}}{N_w-1}\right)$		$O\left(\frac{M_A M^{N_w-1}}{N_w-1}\right)$	
HDD-MSDD	$O\left(\frac{M^{N_w-1}}{N_w-1}\right)$					
MSDSD (Lower Bound)	$O\{M_A[M_A(N_w-1)+(N_w-2)]/(N_w-1)\}$		$O\{M_A[M_A(N_w-1)+(N_w-2)]/(N_w-1)\}$		$O(M_A \cdot M)$	
HDD-MSDSD (Lower Bound)	$O\{[M_A(N_w-1)+(N_w-2)]/(N_w-1)\}$				$O(M)$	
DFDD	$O(M_A)$				$O(M)$	

Table 8.6: Complexity orders of the hard-decision-aided noncoherent detectors conceived for uncoded DQAM schemes.

ceived for uncoded DQAM. The resultant complexity lower bounds of the reduced-complexity MSDSD and HDD-MSDSD are given by $O\{M_A[M_A(N_w-1)+(N_w-2)]/(N_w-1)\}$ and $O\{[M_A(N_w-1)+(N_w-2)]/(N_w-1)]$, respectively, which are also summarized in Table 8.6. For example, the MSDSD aided 16-TDAPSK^{JM}(2,8) and the MSDSD aided 16-DAPSK(2,8) are portrayed in Fig. 4.10, which demonstrates that the 16-DAPSK(2,8) scheme's MSDSD using the reduced-complexity Schnorr-Euchner search strategy of Table 4.9 is capable of visiting a substantially reduced number of constellation points.

Moreover, the hard-decision-aided DFDD conceived for uncoded DQAM is developed in Sec. 4.6. More explicitly, the DFDD conceived for DQAM in fading channels in the existing literatures [136, 153, 154] are all derived from the linear prediction filter that was originally conceived for the DPSK detection in [121, 122, 125]. This implies that these DFDD solutions are sub-optimal and they are not equivalent to the decision-feedback version of MSDD. As a remedy, first of all, we derive the DFDD from the MSDD's ED in Sec. 4.6.1. Since the DFDD utilizes the decision-feedback for (N_w-2) data-carrying symbols, only a single data-carrying symbol has to be detected within a DFDD observation window. As a result, all the metrics in the MSDD's ED which are related to the decision-feedback symbols become constant for the DFDD. After eliminating the constants, the DFDD decision metric of Eq. (4.70) becomes equivalent to the MSDSD's PED increment of Eq. (4.60) associated with the index $v = N_w$. Secondly, the prediction-based DFDD is derived in Sec. 4.6.2, where a CSI sample is estimated and predicted by a MMSE filter based on the previous (N_w-1) received signal samples and the decision-feedback for the (N_w-1) DQAM transmitted symbols, so that the next unknown data-carrying symbol may be detected coherently with the aid of the estimated CSI sample. It was proven in Sec. 4.6.2 that both the MSDSD-based DFDD metric of Eq. (4.70) and the prediction-based DFDD metric of Eq. (4.78) are once again equivalent to the MSDSD's PED increment of Eq. (4.60) associated with the index of $v = N_w$. The complexity orders of the DFDD conceived for different DQAM constellations are compared in Table 8.6.

The performance results for the uncoded DQAM schemes are presented in Sec. 4.7 according to three aspects, which are the capacity, the BER performance and the detection complexity. First

of all, the capacity results of the DQAM schemes are examined in Sec. 4.7.1. It is demonstrated by Fig. 4.11a that the noncoherent DQAM schemes of DAPSK/ADPSK exhibit a capacity loss compared to their coherent QAM counterpart relying on perfect CSI. When the fading channels fluctuate rapidly as specified by $f_d = 0.03$ in Fig. 4.11b, accurate channel estimation becomes difficult for the coherent QAM schemes, and hence the noncoherent DQAM may be perferred in this scenario, where the DAPSK capacity and the ADPSK capacity are effectively improved by the MSDSD and the HDD-MSDSD, respectively. It is also demonstrated by Fig. 4.11 that the ADPSK achieves a higher DCMC capacity than the DAPSK especially at low SNR region, which predicts a better performance for the ADPSK especially in coded systems. Moreover, it is further evidenced by Fig. 4.12 that the twisted modulations doesn't provide any noticeable capacity improvement over the original DAPSK/ADPSK.

In Sec. 4.7.2, the capacity results of Fig. 4.11b are confirmed by the BER performance results of Figs. 4.13 and 4.14, where the CDD's error floor in rapidly fluctuating fading channels is mitigated by the MSDSD for the DAPSK and by the HDD-MSDSD for the ADPSK. Moreover, it is evidenced by Fig. 4.13 that the HDD-MSDSD does not impose any significant performance loss on MSDSD for the DAPSK detection. Therefore, the HDD-MSDSD is capable of facilitating both DAPSK detection and ADPSK detection in uncoded systems. The BER performance of Fig. 4.15 further demonstrates that the performance gap between the coherent QAM scheme relying on realistic channel estimation technique of PSAM and the noncoherent DAPSK/ADPSK employing HDD-MSDSD is significantly reduced when the normalized Doppler frequency f_d and the number of receive antennas N_R are increased. Moreover, Fig. 4.16 evidences that our proposed DFDD in Sec. 4.6, which is equivalent to the decision-feedback version of the optimum MSDD/MSDSD, outperforms the conventional DFDD solutions in literatures [136, 154]. Furthermore, we have demonstrated in Fig. 4.15 that DAPSK and ADPSK achieve a similar performance in uncoded systems, and Fig. 4.17 further evidences that the twisted modulated schemes cannot outperform their counterpart of DAPSK in uncoded systems, where the joint mapping DQAM scheme of TDAPSK$^{\text{JM}}$ even imposes a slight performance loss.

The detection complexity results are offered in Sec. 4.7.3, where the complexities of the noncoherent detectors conceived for different DQAM schemes are summarized in Table 4.10 in details. Similar to the complexity summary of Table 3.8 for the DPSK detection, Table 4.10 also shows that the HDD-MSDD exhibits the highest detection complexity for the DQAM detection, followed by the HDD-MSDSD, the DFDD and the CDD, which is confirmed by Fig. 4.18. It is further evidenced by Figs. 4.18 and 4.19 that the reduced-complexity MSDSD algorithm proposed in Sec. 4.5.3 achieves a substantial complexity reduction compared to the conventional MSDSD algorithm developed in Sec. 4.5.2. More specifically, it is demonstrated by Fig. 4.19a that HDD-MSDSD conceived for 16-DAPSK(2,8) achieves a complexity reduction of up to 84.5% compared to 16-TDAPSK$^{\text{JM}}$(2,8) detection, while an even more significant complexity reduction of up to 92.6% is achieved by HDD-MSDSD conceived for 64-DAPSK(4,16), as evidenced by Fig. 4.19b.

Let us recall that the reduced-complexity MSDSD algorithm proposed in Sec. 4.5.3 can only be

employed by the DQAM constellations including DAPSK, ADPSK, TDAPSK and TADPSK which separately modulate the amplitude and phase. Therefore, we may suggest that the DAPSK and the ADPSK are perferred choices for uncoded DQAM systems, because their noncoherent detectors generally exhibit a lower complexity as demonstrated by Table 8.6 and Table 4.10, while their performance results are similar in the uncoded systems as evidenced by Fig. 4.15. Nonetheless, as predicted by the capacity results in Sec. 4.7.1, the performance difference between the DAPSK and the ADPSK may be increased in coded systems. Moreover, as introduced in the constellation design of Sec. 4.2, the twisted modulations and their joint mapping schemes may exhibit certain performance advantages in coded systems, where the dependency between the amplitude and phase is beneficial especially in turbo detection, provided that appropriate coding schemes are used.

8.1.5 Chapter 5: Noncoherent Detection for Differential Non-Constant Modulus Modulation – Part II: Coded Systems

In Chapter 5, the noncoherent detectors investigated in Chapter 4 are revised to be able to process soft-bit LLRs, so that they may be involved in turbo detection in coded DQAM systems. First of all, the soft-decision-aided MSDD conceived for coded DQAM is developed in Sec. 5.2. As we demonstrated in Chapter 4, the first transmitted symbol's ring amplitude Γ_1 within a observation window may be treated either as an unknown variable by the MSDD or as a known term obtained from the previous decisions feedback by the so-called HDD-MSDD. In coded systems, we still have both MSDD and HDD-MSDD for coded DQAM detection, and yet a new SDD-MSDD is also developed for coded DQAM schemes, where the previous decisions on Γ_1 are in the form of *a priori* probabilities instead of hard-bit decisions. All the decoding algorithms including the optimum Log-MAP, the low-complexity sub-optimum Max-Log-MAP and the near-optimum Approx-Log-MAP may be invoked for the three MSDD arrangements. As an example, the SDD-MSDD invoking Approx-Log-MAP is summarized as pseudocodes in Table 5.1, which demonstrates that updating the soft-decision feedback does not impose any appreciable amount of extra complexity. Moreover, the soft-decision-aided CDD conceived for coded DQAM is also presented in Sec. 5.2, which is implemented by the MSDD associated with the minimum observation window length of $N_w = 2$. The CDD may also be further implemented to be SDD-CDD and HDD-CDD as special cases of SDD-MSDD and HDD-MSDD, respectively. The complexity orders of the CDD and MSDD arrangements are summerized in Table 8.7.

The soft-decision-aided MSDSD arrangements conceived for coded DQAM are proposed in Sec. 5.3. First of all, based on the development of the hard-decision-aided MSDSD conceived for uncoded DQAM in Sec. 4.5, the principles of the MSDSD algorithm conceived for coded DQAM detection is proposed in Sec. 5.3.1. The MSDSD's PED is formulated in Eq. (5.9) based on the MSDD's ED of Eq. (5.8), and the Schnorr-Euchner search strategy tailored for the soft-decision-aided MSDSD conceived for coded DQAM is presented in the form of pseudocode in Table 5.2. Furthermore, both the SDD-MSDD and the HDD-MSDD may be implemented as the SDD-MSDSD and the HDD-MSDSD, respectively. Moreover, both the Max-Log-MAP and the

CDD $O(M_A M)$	SDD-CDD $O(M_A M)$	HDD-CDD $O(M)$
MSDD $O\left(\frac{M_A M^{N_w-1}}{N_w-1}\right)$	SDD-MSDD $O\left(\frac{M_A M^{N_w-1}}{N_w-1}\right)$	HDD-MSDD $O\left(\frac{M^{N_w-1}}{N_w-1}\right)$
MSDSD (lower bound) $O\{M_A M + M_A \text{BPS}[(N_w-2)M + \frac{M}{2}]\}$	HDD-MSDSD (lower bound) $O\{M_A M + M_A \text{BPS}[(N_w-2)M + \frac{M}{2}]\}$	HDD-MSDSD (lower bound) $O\{M + \text{BPS}[(N_w-2)M + \frac{M}{2}]\}$
Reduced-Complexity MSDSD (lower bound) $O\{\frac{M_A M}{4} + \frac{M_A(N_w-2)}{N_w-1} + M_A \text{BPS}[\frac{(N_w-1)M}{4} + (N_w-2)]\}$	Reduced-Complexity SDD-MSDSD (lower bound) $O\{\frac{M_A M}{4} + \frac{M_A(N_w-2)}{N_w-1} + M_A \text{BPS}[\frac{(N_w-1)M}{4} + (N_w-2)]\}$	Reduced-Complexity HDD-MSDSD (lower bound) $O\{\frac{M}{4} + \frac{(N_w-2)}{N_w-1} + \text{BPS}[\frac{(N_w-1)M}{4} + (N_w-2)]\}$
MSDD-IAP (lower bound) $O\{M_P + \frac{IR_{AP}M_A^{N_w}}{N_w-1} + IR_{AP}M_P + \text{BPS}_P[(N_w-2)M_P + \frac{M_P}{2}]\}$	SDD-MSDD-IAP (lower bound) $O\{M_P + \frac{IR_{AP}M_A^{N_w}}{N_w-1} + IR_{AP}M_P + \text{BPS}_P[(N_w-2)M_P + \frac{M_P}{2}]\}$	HDD-MSDD-IAP (lower bound) $O\{M_P + \frac{IR_{AP}M_A^{N_w-1}}{N_w-1} + IR_{AP}M_P + \text{BPS}_P[(N_w-2)M_P + \frac{M_P}{2}]\}$
Reduced-Complexity MSDSD-IAP (lower bound) $O\{M_P + IR_{AP}(M_A^2 + \frac{M_P}{4} + \frac{N_w-2}{N_w-1}) + \text{BPS}_A[(N_w-2)M_A^2 + \frac{M_A^2}{2}] + \text{BPS}_P[\frac{(N_w-2)M_P}{4} + \frac{M_P}{8} + (N_w-2)]\}$	Reduced-Complexity SDD-MSDSD-IAP (lower bound) $O\{M_P + IR_{AP}(M_A^2 + \frac{M_P}{4} + \frac{N_w-2}{N_w-1}) + \text{BPS}_A[(N_w-2)M_A^2 + \frac{M_A^2}{2}] + \text{BPS}_P[\frac{(N_w-2)M_P}{4} + \frac{M_P}{8} + (N_w-2)]\}$	Reduced-Complexity HDD-MSDSD-IAP (lower bound) $O\{M_P + IR_{AP}(M_A + \frac{M_P}{4} + \frac{N_w-2}{N_w-1}) + \text{BPS}_A[(N_w-2)M_A + \frac{M_A}{2}] + \text{BPS}_P[\frac{(N_w-2)M_P}{4} + \frac{M_P}{8} + (N_w-2)]\}$
DFDD (absolute-amplitude DQAM) $O(M)$	DFDD (differential-amplitude DQAM) $O(M_A M)$	

Table 8.7: Complexity orders of soft-decision-aided noncoherent detectors for coded DQAM in Chapter 5.

Approx-Log-MAP may be implemented by the soft-decision-aided MSDSD, HDD-MSDSD and SDD-MSDSD, where the Approx-Log-MAP of Algorithm 3.2 originally proposed for MSDSD aided DPSK may be applied for coded DQAM detection. The complexity order lower bounds of the soft-decision-aided MSDSD arrangements are summarized in Table 8.7, where the MSDD's exponentially increasing complexity is mitigated, because the sphere decoding is invoked for both ring amplitude detection and phase detection.

In Sec. 5.3.2, the reduced-complexity design originally proposed for the soft-decision-aided MSDSD conceived for coded DPSK in Sec. 3.3.3 is applied to the coded DQAM detection. More explicitly, the MSDSD's PED increment of Eq. (5.10) is splitted into the ring-amplitude-related term and the M_PPSK-related term, so that the decision variable of Eq. (5.16) may be utilized for detecting the M_PPSK phase. As introduced in Sec. 3.3.3, when the soft-decision-aided SD is invoked for phase detection, only the constellation points located in the first quadrant are required to be visited, and then the rest of the constellation points may be later visited in a zig-zag fashion by the SD if required. The reduced-complexity Schnorr-Euchner search strategy tailored for the soft-decision-aided MSDSD conceived for coded DQAM is presented in the form of pseudocode in Tables 5.3 and 5.4. Fig. 5.2 further portrays an example of the sphere decoding comparison between the 16-DAPSK(2,8) detection using the Schnorr-Euchner algorithm of Tables 5.3-5.4 and the 16-

TDAPSK^{JM}(2,8) detection invoking Table 5.2, where up to 75% of the child nodes are avoided to be visited by using the reduced-complexity Schnorr-Euchner algorithm. The complexity order lower bounds of the reduced-complexity soft-decision-aided MSDSD arrangements are summarized in Table 8.7.

The low-complexity soft-decision-aided MSDD-IAP that was originally proposed for coded DAPSK detection [160] is summarized and revised in Sec. 5.3.3, so that it may be employed by all DQAM constellations which modulate the ring amplitude and phase separately. More explicitly, the MSDD-IAP invokes the MSDD for ring amplitude detection, which may be referred to as the MSDAD, and it invokes the MSDSD for phase detection, which may be termed as the MSDPSD. The MSDAD and the MSDPSD iteratively exchange their decisions in order to improve the overall performance. The complexity order lower bound of the MSDD-IAP arrangements are summarized in Table 8.7. It can be seen that the MSDD-IAP complexity for ring amplitudes detection still grows exponentially as N_w increases, because the SD was not invoked for MSDAD.

Against this background, the reduced-complexity soft-decision-aided MSDSD-IAP is proposed in Sec. 5.3.4. The MSDSD-IAP implements the MSDAD for ring amplitude detection by SD, which may now be referred to as MSDASD. The MSDASD's PED of Eq. (5.26) is revised from the general MSDSD's PED of Eq. (5.9), where the phases are known from the decision feedback from the MSDPSD. Furthermore, the reduced-complexity soft-decision-aided MSDSD conceived for coded DPSK proposed in Sec. 3.3.3 may be directly applied to the MSDPSD, which may result in a considerable reduction in the number of constellation points visited by the SD. Fig. 5.3 portrays an example of the comparison between the MSDD-IAP and the reduced-complexity MSDSD-IAP conceived for 64-DAPSK(4,16), which evidences that both the number of ring amplitude candidates and that of phase candidates visited by the MSDD-IAP are effectively reduced by the proposed reduced-complexity MSDSD-IAP. The complexity order lower bounds of the MSDSD-IAP arrangements are summaried in Table 8.7.

Furthermore, the soft-decision-aided DFDD conceived for coded DQAM is proposed in Sec. 5.4 based on the hard-decision-aided DFDD introduced in Chapter 4. Especially, for the differential-amplitude DQAM schemes including DAPSK, TDAPSK and TDAPSK^{JM}, the first transmitted ring amplitude Γ_1 of each DFDD window should still be treated as a separate variable in order to evade the potential error propagation problem between DFDD windows. The complexity orders of the soft-decision-aided DFDD arrangements are also summarized in Table 8.7.

It can be seen in Table 8.7 that there are plenty of choices for the noncoherent detectors in coded DQAM systems. In Sec. 5.5 of performance results, the appropriate noncoherent detectors are suggested for different DQAM constellations, and the advantages of the noncoherent detectors in coded systems are discussed. First of all, the performance improvement provided by the MSDSD over the CDD is presented in Sec. 5.5.1. It is demonstrated by the EXIT charts of Fig. 5.4 that both the MSDSD conceived for DAPSK and the HDD-MSDSD conceived for ADPSK effectively improve the CDD's detection capability, which is reflected both by the increased area under the EXIT curves and by the improved beneficial iteration gain. Furthermore, the performance advantage of

the Approx-Log-MAP over the Max-Log-MAP becomes more noticeable, when the modulation level M and the MSDSD window length N_w are increased. These features evaluated by the EXIT charts of Fig. 5.4 are confirmed by the BER performance of Fig. 5.5.

Among all the MSDSD arrangements listed in Table 8.7, the most appropriate choices are suggested for different DQAM constellation in Sec. 5.5.2. In general, between the MSDSD arrangements of MSDSD, SDD-MSDSD and HDD-MSDSD introduced in Sec. 5.3.1, the SDD-MSDSD exhibits the best detection capability at the highest detection complexity. Therefore, the MSDSD or even the HDD-MSDSD may be preferred only if they can perform closely to the optimum SDD-MSDSD. The reduced-complexity MSDSD algorithm proposed in Sec. 5.3.2 is suggested to be applied to all the MSDSD arrangements of MSDSD, SDD-MSDSD and HDD-MSDSD, when the DQAM constellations including DAPSK, ADPSK, TDAPSK and TADPSK which separately modulate the amplitude and phase are employed. Furthermore, the iterative amplitude-phase detection algorithm proposed in Sec. 5.3.4 is suggested to be implemented for the MSDSD arrangements of MSDSD, SDD-MSDSD or HDD-MSDSD, provided that no noticeable performance loss is improved by separately detecting the amplitude and phase.

In order to suggest the most appropriate MSDSD choice, the performance results of the MSDSD arrangements are firstly compared by the EXIT charts of Fig. 5.6 for DAPSK and ADPSK. Secondly, the LLR reliability test of Fig. 5.7 further examines the reliability of the LLRs produced by the different MSDSD algorithms. Particularly, it is demonstrated by Fig. 5.7a that the LLRs produced by the HDD-MSDSD deviates from the LLR definition, when the DAPSK constellation is employed. This is because that the HDD-MSDSD introduces error propagation problem for the differential-amplitude DQAM constellations. Although this problem does not prevent the HDD-MSDSD from offering a good performance for the uncoded DAPSK detection as seen in Fig. 4.13, the coded DAPSK detection requires better LLR integrity, because the unreliable LLRs deteriorate the performance of the HDD-MSDSD in turbo detection. Thirdly, the BER performance results of Fig. 5.8 confirms the MSDSD suggestion, where the specific MSDSD arrangement that performs closely to the optimum SDD-MSDSD at the lowest possible detection complexity may be selected. As a result, the soft-decision-aided MSDSD-IAP associated with a single iteration of $IR_{AP} = 1$ between the MSDASD and the MSDPSD is suggested for the coded DAPSK detection based on Fig. 5.6a, Fig. 5.7a and Fig. 5.8a. Moreover, the soft-decision-aided HDD-MSDSD-IAP associated with $IR_{AP} = 1$ is selected for the coded ADPSK detection based on Fig. 5.6b, Fig. 5.7b and Fig. 5.8b.

It is worthy to note that although the MSDSD-IAP and the HDD-MSDSD-IAP are proven to be competent arrangements for coded DAPSK and ADPSK detection, respectively, Fig. 5.9 explicitly evidences that these detectors still suffer from irreducible error floors for uncoded DAPSK and ADPSK detection. The reason is that without the assistance of channel coding, the MSDASD and the MSDPSD may exchange erroneous decisions. Therefore, for uncoded DQAM schemes, the conventional hard-decision-aided HDD-MSDSD is suggested to be employed, as discussed in Chapter 4.

Similarly, the soft-decision-aided MSDSD is suggested for coded TDAPSK detection based on Fig. 5.10a, Fig. 5.11a and Fig. 5.12a. Moreover, the soft-decision-aided HDD-MSDSD is suggested for coded TADPSK detection based on Fig. 5.10b, Fig. 5.11b and Fig. 5.12b. The iterative amplitude and phase detection arrangements of MSDSD-IAP and HDD-MSDSD-IAP impose a performance loss for TDAPSK and TADPSK, respectively, which cannot be compensated by increasing IR_{AP}. The reason of this performance gap is that the twisted modulations of TDAPSK and TADPSK introduce a ring-amplitude-dependent phase rotation, which implies that the potential erroneous ring amplitude detection may impose a false phase rotation to the M_PPSK phase detection. Furthermore, TDAPSK$^{\text{JM}}$ and TADPSK$^{\text{JM}}$ naturally cannot invoke iterative amplitude-phase detection, because their amplitude and phase are jointly modulated. Therefore, the soft-decision-aided MSDSD may be suggested for coded TDAPSK$^{\text{JM}}$ detection, while the soft-decision-aided HDD-MSDSD may be suggested for coded TADPSK$^{\text{JM}}$ detection.

After selecting the most appropriate MSDSD arrangement for each DQAM constellation, the performance results of the different DQAM constellations employing MSDSD are further compared in Sec. 5.5.3 in order to also suggest the most appropriate DQAM constellation for each coded system. As predicted by Fig. 4.12, the twisted modulation and its counterpart associated with joint mapping do not offer any noticeable DCMC capacity improvement. Nonetheless, the improved bits dependency imposed by the increased correlation between the amplitude and phase may result in an improved iteration gain. These features are confirmed by the EXIT charts of Figs. 5.13a and 5.14a. Moreover, as the different levels of iteration gain leads to the varied results in different channel coded systems, Figs. 5.13b and 5.14b demonstrate that the original DQAM constellations of DAPSK and ADPSK perform better in TC coded systems, and the twisted constellations of TDAPSK and TADPSK are advantageous in IRCC-URC coded systems, while the joint mapping constellations of TDAPSK$^{\text{JM}}$ and TADPSK$^{\text{JM}}$ exhibit their performance advantage in RSC coded systems. Moreover, as predicted by Fig. 4.11, the absolute-amplitude DQAM scheme of ADPSK has a higher DCMC capacity than the differential-amplitude DQAM scheme of DAPSK. Although the ADPSK's capacity advantage does not come into effect in uncoded systems as shown by Fig. 4.15, it is demonstrated by Fig. 5.15 that the ADPSK employing the HDD-MSDSD-IAP outperforms the DAPSK employing the MSDSD-IAP in all of the three classic coded systems. As a result, we may conclude that the absolute-amplitude DQAM constellations of ADPSK, TADPSK and TADPSK$^{\text{JM}}$ are preferred over the differential-amplitude DQAM constellations of DAPSK, TDAPSK and TDAPSK$^{\text{JM}}$ in coded systems. Furthermore, the specific choice of the absolute-amplitude DQAM constellation depends on the employed channel coding schemes. This conclusion is summarized by Tables 5.7 and 5.8.

Sec. 5.5.4 delivers the complexity comparison between the different DQAM constellations employing MSDSD. First of all, Figs. 5.18a and 5.19a demonstrates that the reduced-complexity design proposed in Sec. 5.3.2 may successfully reduce the complexity of the conventional MSDSD of Sec. 5.3.1 to the similar level as the complexity of the MSDD-IAP of Sec. 5.3.3 associated with $IR_{AP} = 1$, where a substantial complexity reduction that is up to 89.2 is achieved, when the

64-DAPSK(4,16) is employed and its MSDSD window width is increased to $N_w = 5$. What's more, Figs. 5.18b and 5.19b further evidence that by invoking SD for amplitude detection and by applying the reduced-complexity design for phase detection, the MSDSD-IAP of Sec. 5.3.4 further offers a substantial complexity reduction for the MSDD-IAP of Sec. 5.3.3, which is up tp 92.3% for employing the 64-DAPSK(4,16) constellation, when the MSDSD window width is increased to $N_w = 5$. As a result, it is demonstrated by Fig. 5.20 that the twisted modulations of TDAPSK and TADPSK employing the reduced-complexity MSDSD algorithm of Sec. 5.3.2 exhibit a lower detection complexity than their joint mapping counterparts of TDAPSK$^{\text{JM}}$ and TADPSK$^{\text{JM}}$, while the original DQAM schemes of DAPSK and ADPSK employing the reduced-complexity MSDSD-IAP algorithm of Sec. 5.3.4 have a further lower complexity. Moreover, Fig. 5.20 also demonstrates that the abosulute-amplitude DQAM constellations generally have a lower detection complexity than their respective differential-amplitude DQAM counterparts, because the abosulute-amplitude DQAM constellations may employ the low-complexity HDD-MSDSD arrangement without encountering the error propagation problem. In summary, when the suitable MSDSD arrangements suggested in Sec. 5.5.2 are employed, the list of the DQAM constellations from the highest detection complexity to the lowest complexity is given by TDAPSK$^{\text{JM}}$, TADPSK$^{\text{JM}}$, TDAPSK, TADPSK, DAPSK and ADPSK.

The performance results for the DQAM employing DFDD in coded systems are further presented in Sec. 5.5.5. First of all, it is demonstrated by the EXIT charts of Fig. 5.21 that the ADPSK employing DFDD also outperforms its counterpart of DAPSK employing DFDD in coded systems, which is further confirmed by the BER performance of Fig. 5.22. Secondly, Fig. 5.22 also evidences that our DFDD solution presented in Sec. 5.4, which is the decision-feedback version of the optimum MSDD/MSDSD, outperforms the conventional DFDD solutions in literatures [136, 153, 154], which ignored the problem of non-constant channel correlation matrix.

Last but the most importantly, the performance of coherent QAM employing the realistic PSAM aided channel estimation and that of noncoherent DQAM employing MSDSD are compared in coded systems in Sec. 5.5.6. Specifically, when the fading channels fluctuate slowly as specified by $f_d = 0.001$, the PSAM is capable of delivering accurate CSI estimation for the coherent QAM detector. In this case, the soft-decision-aided coherent QAM detector may produce reliable LLRs as seen in Fig. 5.25a, and the performance of PSAM aided coherent QAM scheme outperforms its noncoherent counterpart of ADPSK employing HDD-Subet MSDSD-IAP in all the three of RSC/TC/IRCC-URC coded systems, as evidenced by Fig. 5.26a. However, when the fading channels fluctuate rapidly as specified by $f_d = 0.03$, Fig. 5.25b demonstrates that the LLRs produced by the coherent QAM detector become unreliable because of the inaccurate CSI estimation. As a result, it is demonstrated by Fig. 5.26b that the noncoherent ADPSK employing HDD-Subet MSDSD-IAP becomes capable of outperforming its coherent QAM counterpart in all the three of RSC/TC/IRCC-URC coded systems. In conclusion, similarly to the comparison between coherent PSK and noncoherent DPSK employing MSDSD in Sec. 3.4, the MSDSD aided DQAM may be deemed as the more appropriate choice for coded system operating in the presence of rapidly

fluctuating fading channels.

8.1.6 Chapter 6: Reduced-Complexity Design Applied to MIMO Schemes – Part I: Unoded Systems

In Chapter 6, the MIMO systems design is introduced to be centred at two classic design tradeoffs, which are the multiplexing and diversity tradeoff as well as the performance and complexity tradeoff. The multiplexing and diversity tradeoff, which may be analysed by the mathematical measures of capability and error probability introduced in Sec. 6.1, motivated the MIMO development from BLAST to STBC and LDC. Moreover, the performance and complexity tradeoff not only exists for the BLAST detectors including ML, SD and LF, but this tradeoff has also motivated the recently proposed SM and STSK. The rationale of MIMO system development has been reviewed from a historical perspective in Sec. 1.3, where the tradeoffs between the MIMO techniques are portrayed by Fig. 1.24. In this chapter, the development in the MIMO systems has further been presented from a technical perspective, and the reduced-complexity design has further been applied to the SM and STSK detection, so that the optimum MIMO detection capability may be retained at a substantially reduced detection complexity.

The classic V-BLAST is introduced in Sec. 6.2, where the full multiplexing gain is achieved. More explicitly, the proposal of the V-BLAST techniqe is motivated by its high CCMC capacity characterized by Eq. 6.3, which is achieved as the result of V-BLAST simultaneously transmitting N_T data streams by the N_T transmit antennas. However, the V-BLAST scheme does not benefit from a transmit diversity gain as indicated by the PEP of Eq. (6.10c), because the V-BLAST transmits each symbol by a single transmit antenna over a single time slot. Moreover, the V-BLAST receiver design presented in Sec. 6.2 focuses on the performance and complexity tradeoff, which is portrayed in Fig. 6.3. Owing to the fact that all the data streams arrive at the N_R receive antennas at the same time, the optimum ML detector introduced in Sec. 6.2.1 jointly detects a total number of N_T MPSK/QAM symbols, which imposes an exponentially increasing complexity of order $O(M^{N_T})$. As a remedy, the SD is invoked for V-BLAST employing MPSK in Sec. 6.2.2 in order to individually visit each MPSK constellation. The SD algorithm is summaried as pseudocode in Table 6.3, which is similar to the MSDSD aided DPSK of Table 3.1. Moreover, the SD conceived for V-BLAST employing Square MQAM is presented in Sec. 6.2.3, where the received signals are decoupled before invoking the SD in order to detect the real and imaginary parts of the Square MQAM constellation separately. On one hand, the performance of the SD aided V-BLAST may retain the optimum performance of the ML aided V-BLAST, provided that the initial SD radius is initialized to be sufficiently large. On the other hand, the complexity order lower bounds of the SD aided V-BLAST are now given by $O(2N_T - 1)$ and $O(4N_T - 1)$ for MPSK and Square MQAM, respectively. However, the SD complexity lower bounds can only be achieved at very high SNR region. In order to mitigate the SD's variable complexity, the LFs including ZF and MMSE are introduced in Sec. 6.2.4, where the amalgamated data streams are separated at the receiver. The detection complexity of the LF aided V-BLAST is the lowest, because the MPSK/QAM constel-

lations are visited completely separately. However, the LF aided V-BLAST imposes an inevitable performance loss, owing to the fact that the interference between the data streams is aimed to be minimized but cannot be completely eliminated.

Alternative to the multiplexing-oriented V-BLAST MIMO, the diversity-oriented STM MIMO schemes including STBC and LDC are introduced in Sec. 6.3. Generally speaking, the orthogonal STBC of Sec. 6.3.1 can achieve the full diversity gain, and the STBC receiver may decouple the received data streams without encountering the V-BLAST's interference problem. However, without the multiplexing gain, the STBC capacity is smaller than the full MIMO capacity. By contrast, the LDC of Sec. 6.3.2 may achieve both the full multiplexing gain and the full transmit diversity gain. However, in the absence of the STBC's orthogonal design, the LDC receiver has to invoke the V-BLAST detectors in order to tackle with the interference problem, which once again arises the performance and complexity tradeoff.

More explicitly, for the STBCs, the general orthogonal design is introduced in Sec. 6.3.1.1, where the most stringent orthogonal requirements for any STBCs associated with N_T transmit antennas, N_R receive antennas, N_Q transmitted symbols and N_P time slots are summarized. It is also demonstrated in Sec. 6.3.1.1 that owing to the orthogonal design, the STBC receiver is capable of decoupling the received signal so that the low-complexity MPSK/QAM demodulators may be invoked for separately detecting the independent data streams, where the V-BLAST's interference problem is not encountered. Following this, the only full-rate STBC of Alamouti's G2 [177] which achieves the unity symbol rate $\overline{R} = \frac{N_Q}{N_P} = 1$ for $N_T = 2$ is presented in Sec. 6.3.1.2. For the case of employing $N_T > 2$, the HR-STBC [178] designed based on the Hurwitz-Radon theory [179, 180] is introduced in Sec. 6.3.1.3. The HR-STBC can only achieve half symbol rate of $\overline{R} = 1/2$, and the number of time slots N_P required by the HR-STBC is as high as $N_P = 8$ for $N_T = 3, 4$ and $N_P = 16$ for $5 \leq N_T \leq 8$ as summarized in Table 6.5. What's more, it was proven in [178] that the HR-STBC may require a substantial N_P growing exponentially with N_T, which is given by $N_P = 16 \times 16^{(N_T/8-1)}$ for N_T being bigger than 8 and being a power of 2. In order to reduce the HR-STBC's transmission delay, the AO-STBC [181–183] based on the amicable orthogonal design [179] is introduced in Sec. 6.3.1.4. The AO-G2$^\iota$-STBC's transmission matrix is formed from the AO-G2$^{\iota-1}$-STBC's codeword and an extra the $(\iota+1)$-th transmitted symbol, as formulated by Eq. (6.68). As a result, the AO-STBCs have a reduced delay of $N_P = N_T$ for the cases of $N_T = 2^\iota$. However, owing to the fact that the AO-STBC's number of transmitted symbols N_Q only grows logarithmically with the number of antennas N_T as $N_Q = \lceil \log_2 N_T \rceil + 1$, the symbol rate of AO-STBC is expected to be lower than $\overline{R} = \frac{1}{2}$ for $N_T > 8$. In summary, the error probability and capacity analysis for STBC are presented in Sec. 6.3.1.5. Based on the PEP of Eq. (6.10c), the STBCs from orthogonal design may achieve the full diversity gain, and their approximate BERs are summarized in Table 6.7. However, it is proven by Eq. (6.72) that the STBC capacity is smaller or equal to the V-BLAST MIMO capacity, where the equality only holds for the Alamouti's G2-STBC equipped with a single receive antenna $N_R = 1$.

In order to improve the STBC capacity, the stringent orthogonal requirement has to be aban-

doned, which leads to the development of LDC presented in Sec. 6.3.2. More explicitly, the orthogonal requirement is firstly relaxed by the QO-STBC [186, 329] introduced in Sec. 6.3.2.1, which is formed by subgroups of orthogonal STBCs. As a result, the interference problem once gain emerges, and hence the signals that cannot be decoupled have to be jointly detected. Furthermore, the capacity-improving LDC [189] is introduced in Sec. 6.3.2.2, where the real and imaginary parts of a total number of N_Q modulated MPSK/QAM symbols $\{s_q\}_{q=1}^{N_Q}$ are dispersed into both spatial and temporal dimensions by the dispersion matrices $\{\overline{\mathbf{A}}_q\}_{q=1}^{N_Q}$ and $\{\overline{\mathbf{B}}_q\}_{q=1}^{N_Q}$. The randomly generated dispersion matrices are optimized for the transmission regime of $\mathbf{S} = \sum_{q=1}^{N_Q}\left[\overline{\mathbf{A}}_q\Re(s_q) + j\overline{\mathbf{B}}_q\Im(s_q)\right]$, so that the STBC capacity may be improved. What's more, the capacity-achieving LDC [188] is further introduced in Sec. 6.3.2.3, where the real and imaginary parts of the N_Q modulated MPSK/QAM symbols $\{s_q\}_{q=1}^{N_Q}$ are jointly dispersed by a group of dispersion matrices $\{\overline{\mathbf{A}}_q\}_{q=1}^{N_Q}$ as $\mathbf{S} = \sum_{q=1}^{N_Q}\left[\overline{\mathbf{A}}_q s_q\right]$, as depicted by Fig. 6.5. It is proven in Sec. 6.3.2.3 that the full BLAST MIMO capacity may be achieved by the LDC if the equivalent dispersion matrix $\overline{\chi}$ has orthognal columns as specified by Eq. (6.96), while the full STBC MIMO's diversity gain may also be retained if the equivalent dispersion matrix is generated according to the rank and determinant criteria derived from the PEP of Eq. (6.10c).

Although the LDC design has successfully solved the multiplexing and diversity tradeoff, the performance and complexity tradeoff once again emerges, because the V-BLAST detectors have to be invoked by the LDC receiver. This problem may further put a strain on the MIMO systems design in coded scenarios, because the optimum V-BLAST detection complexity may become especially unaffordable when the detector is invoked several times in turbo detection, while the sub-optimal V-BLAST detectors may produce unreliable LLRs, which are difficult to correct by the channel decoder. Against this background, the newly-developed SM [195–197] and STSK [216] are introduce in Sec. 6.4. The schematics of the SM transmitter is depicted in Fig. 6.6, where a single out of a total number of N_T transmit antenna is activated to transmit a single MPSK/QAM symbol. The advantages of the SM regime are twofold. Firstly, the SM transmitter has a lower handware implementation complexity compared to other MIMO schemes, because only a single RF chain is activated at one time. Secondly, in the absence of inter-antenna interference, the SM receiver may implement the MIMO ML detection at a substantially reduced complexity, where the antenna activation index and the MPSK/QAM modulation index are aimed to be separately detected. Moreover, in order to introduce a transmit diversity gain to the SM, the STSK transceiver of Fig. 6.9 opts to activate a single out of a total N_Q LDC's dispersion matrix to disperse a single MPSK/QAM symbol at the transmitter, so that the SM detector may be invoked by the STSK receiver in order to detect the dispersion matrix activation index and the modulation index separately. As a result, the STSK may implement the LDC detection also at a substantially reduced complexity.

However, the low-complexity SM receiver that was originally proposed in [197], which completely separately detects the antenna index and the modulation index from the matched filter output, suffers from an error floor in fading channels. This detection method is termed as the MRC-based suboptimal SM detection in Sec. 6.4.1. In order to mitigate this problem, the simplified SM

detection [198] streamlines the ML MIMO detection by eliminating the unneccessary calculations, as a benefit of having $(N_T - 1)$ zeros in the SM transmission vector. Nonetheless, this simplified method still jointly detect the antenna index and the modulation index, which does not reduce the ML MIMO detection complexity order. Against this background, we proposed a PFS-based optimal SM detection based on our previous publications of [141, 202, 203, 234] in Sec. 6.4.1.1, which is portrayed by Fig. 6.7. More explicitly, in order to take into account the correlation between the antenna index and the modulation index, the normalized matched filter output elements may be firstly partially demodulated for the sake of assisting the optimum antenna index detection, and then the specific matched filter element corresponding to the detected antenna index may be further fully demodulated in order to recover the modulation index. The PFS-based SM detection is directly derived from the optimum MIMO ML detection, where the number of visited constellation points is reduced thanks to the symmetry provided by Gray-labelled MPSK/QAM constellation diagrams. Therefore, no performance loss is imposed by the PFS-based SM detection, while the detection complexity order is substantially reduced. Moreover, an alternative low-complexity optimum SM detector, which was original proposed in [201] and then recently further implemented in [204], is also introduced in Sec. 6.4.1.2 as the HL-based SM detection, which is portrayed in Fig. 6.8. More explicitly, the HL-based optimum SM detector firstly fully demodulates all the normalized matched filter output elements, so that the antenna activation index may be optimally detected with the aid of N_T modulation index candidates, and then the optimum modulation index is automatically obtained after knowing the antenna index. Owing to the fact that the hard-decision-aided MPSK/QAM demodulator may directly map a matched filter output element to the nearest MPSK/QAM constellation point in uncoded systems, the HL-based SM detection may have a very low complexity that does not grow with modulation level M. It is worthy to note that the HL-based SM detection does not work in coded systems, which will be further discussed in details in the next chapter. Furthermore, a variety of suboptimal SM detectors in literatures [141, 205–210] are also introduced in Secs. 6.4.1.3-6.4.1.7, which aim to improve the suboptimal MRC-based SM detection, but the optimum SM detection capability cannot be retained.

The performance results for uncoded MIMO systems are summarized in Sec. 6.5. First of all, the conventional MIMO schemes of V-BLAST, STBC and LDC are compared in Figs. 6.11 and 6.12. It is confirmed by Fig. 6.11a that both V-BLAST and LDC may achieve the same full MIMO CCMC capacity, which is higher than the STBC's CCMC capacity. The DCMC capacity results of Fig. 6.11b and the BER performance results of Fig. 6.12 further evidence that the LDC can also retain the full diversity gain, which enables the LDC to outperforms both of its counterparts of V-BLAST and STBC. It is also demonstrated by Fig. 6.12 that a substantial performance loss is induced when the low-complexity linear MMSE detection is invoked for V-BLAST and LDC. Against this background, the performance results of V-BLAST and STBC are further compared to the low-complexity SM and STSK in Figs. 6.13-6.15. The capacity result of Fig. 6.13a shows that both the SM and the STSK cannot achieve the full MIMO CCMC capacity, where the SM still has a higher CCMC capacity than the STBC, but the STSK's CCMC capacity is even lower

than its counterpart of a SIMO system. Nonetheless, the DCMC capacity results of Fig. 6.13b and the BER performance results of Fig. 6.14a demonstrate that in the absence of receive diversity, Alamouti's G2 STBC performs the best, followed by its counterparts of STSK and V-BLAST, while the SM performs slightly worse than the V-BLAST. Moreover, owing to the fact that the HR-STBCs have to employ a higher level *M*PSK/QAM in order to compensate for their throughput loss, the HR-G4-STBC performs worse than its counterparts of V-BLAST and LDC in Fig. 6.12b, and it also performs worse than SM and STSK in Fig. 6.14b, unless when the SNR is extremely high. Similarly, Figs. 6.14 and 6.15 shows that the STSK's transmit diversity advantage also withers away, when the improved receive diversity gain is available for all MIMO schemes.

The complexities of the optimal SM detectors and those of the suboptimal SM detectors are summarized in Table 6.10 and Table 6.11, respectively. The BER performance results of Fig. 6.16 and the complexity results of Fig. 6.17 demonstrates that the suboptimal SM detectors [141, 205–210] summarized in Secs. 6.4.1.3-6.4.1.7 impose performance loses to the SM and STSK systems, which contrasts with the motivation of the SM, while the suboptimal SM detectors can only offer a slightly lower detection complexity than the low-complexity optimal PFS-based and HL-based SM detectors. Therefore, we may conclude that the PFS-based SM detector proposed based on our previous publications [141, 202, 203, 234] in Sec. 6.4.1.1 as well as the HL-based SM detector [201,204] introduced in Sec. 6.4.1.2 are better candidates for the uncoded SM systems, because they offer a substantially reduced detection complexity while maintaining the optimum SM detection capability.

In summary, it is evidenced by Fig. 6.18 that the optimal PFS-based and HL-based SM detectors exhibit a substantially lower detection complexity than the ML aided V-BLAST detection, and the performance loss imposed by employing SM instead of V-BLAST seen in Fig. 6.14 is significantly smaller than the performance loss of employing the linear MMSE detector for V-BLAST as seen in Fig. 6.12. The diversity-orient MIMO schemes of STBC and STSK also have lower detection complexities than the ML aided V-BLAST, as demonstrated by Fig. 6.18, but the transmit diversity gain is more advantageous in the MIMO systems which equipped with a smaller number of receive antennas N_R, as evidenced by Figs. 6.12, 6.14 and 6.15.

Last but not the least, Table 8.8 summarizes the pros and cons of the MIMO techniques introduced in this chapter, where both the multiplexing and diversity tradeoff as well as the performance and complexity tradeoff are reflected. In particular, it's worthy to note that the current form of the SD and LF aided V-BLAST detection introduced in Secs. 6.2.2-6.2.4 only works for full-loaded MIMO systems associated with $N_T \leq N_R$. For the overloaded MIMO systems associated with $N_T > N_R$, the extra signal processing complexity for detecting the $(N_T - N_R)$ symbols have to be taken into account [303–305]. By contrast, the SM does not have this hardware requirement, because there is no inter-antenna interference for the SM systems, and hence simply the ML MIMO detection is aimed to be implemented by the SM receiver at a reduced complexity. Furthermore, as indicated in Table 8.8, the SM has the unique advantage of employing a single RF chain at transmitter, which reduces the power consumption and eliminates the need for inter-antenna syn-

	Pros	Cons
BLAST	• Full multiplexing gain	○ No transmit diversity ○ Exponential complexity for ML detection ○ Variable complexity for SD ○ Inevitable performance loss for LF detection ○ Full-loaded requirement $N_T \leq N_R$ for SD and LF
STBC	• Full diversity gain • Low detection complexity	○ CCMC capacity lower than BLAST ○ Low system throughput ○ High transmission delay ○ Limited selection of transmission patterns
LDC	• Full multiplexing gain • Full diversity gain • Flexible transmission pattern	○ High complexity for ML detection ○ High performance loss for LF detection ○ Higher hardware requirements
SM	• Single RF chain at transmitter • Low receiver detection complexity • No full-loaded requirement	○ CCMC capacity lower than BLAST ○ No transmit diversity ○ Performance slightly worse than BLAST
STSK	• Full diversity gain • Low receiver detection complexity • Flexible transmission pattern	○ CCMC capacity lower than BLAST ○ High transmission delay ○ Higher hardware requirements

Table 8.8: The pros and cons of the MIMO techniques.

chronization. This SM's special feature does not shared by any other MIMO technique. Moreover, the LDC and the STSK have the advantage of flexible transmission pattern, because any combination of N_T, N_R, N_P and N_Q may all be accommodated. However, the LDC and the STSK also have the disadvantage of higher hardware requirements, because their transmitted symbols are no longer drawn from the classic MPSK/QAM constellations.

8.1.7 Chapter 7: Reduced-Complexity Design Applied to MIMO Schemes – Part II: Coded Systems

In this chapter, we have further revised the MIMO detectors in Chapter 6 to be able to accept and produce soft-bit decisions, so that the soft-decision-aided MIMO detector may be invoked in turbo detection. This chapter reaps the harvest of the complexity reduction design proposed in the previous chapters in order to implement the soft-decision-aided MIMO detectors at a reduced complexity. Interestingly, the interference that exists in the MIMO systems of V-BLAST and LDC improves the bit-dependency, which results in an improved iteration gain that is beneficial for turbo detection. Similarly, the correlation between the antenna activation index and the modulation index complicates the low-complexity SM detection design, but this correlation also imposes a beneficial iteration gain. Owing to these special features, it is important to further examine the tradeoff between multiplexing and diversity as well as the tradeoff between performance and complexity in the coded MIMO systems.

The coded V-BLAST scheme is firstly introduced in Sec. 7.2. More explicitly, it is straightfor-

ward to modify the hard-decision-aided ML V-BLAST detection of Eq. (6.13) to the soft-decision-aided V-BLAST detection invoking the Log-MAP, the Max-Log-MAP and the Approx-Log-MAP as presented in Sec. 7.2.1. Furthermore, similar to the MSDSD for DPSK in Sec. 3.3.2, the hard-decision-aided SD for V-BLAST employing *M*PSK introduced in Sec. 6.2.2 is revised for coded V-BLAST in Sec. 7.2.2, where the *a priori* probability obtained from a channel decoder is added to the SD's PED. The SD algorithm conceived for coded V-BLAST employing *M*PSK is summarized as pseudocode in Table 7.1. Moreover, we have also proposed to apply the reduced-complexity MS-DSD algorithm of Sec. 3.3.3 to the soft-decision-aided SD V-BLAST detection, when *M*PSK constellations are employed. The hard-decision-aided SD for V-BLAST employing Square *M*QAM introduced in Sec. 6.2.3 is also revised for coded V-BLAST in Sec. 7.2.3, where the Schnorr-Euchner search strategy is summarized as pseudocode in Table 7.2. Moreover, the exact MMSE solution that incorporates the *a priori* probabilities is derived in Sec. 7.2.4. The coded STBC is introduced in Sec. 7.3, where the data streams may still be decoupled without encountering the V-BLAST's interference problem thanks to the STBC's orthogonal design. Furthermore, we proposed to employ the reduced-complexity soft-decision-aided PSK/QAM detection algorithms of Sec. 2.4 for the linear receivers of both the MMSE aided V-BLAST detection and the STBC detection in Sec. 7.2.4 and Sec. 7.3, respectively, which is proposed based on our publication of [236].

The coded SM and STSK systems are investigated in Sec. 7.4. The major differences between the uncoded SM detection design presented in Sec. 6.4 and the coded SM detection design of Sec. 7.4 are twofold. First of all, the optimal HL-based SM detection of Sec. 6.4.1.2 cannot offer the substantial complexity reduction without performance loss in coded system. This is because that the soft-decision-aided *M*PSK/QAM demodulators cannot directly map the channel's output signal onto the *M*PSK/QAM constellation diagram, when the *a priori* LLRs gleaned from the channel decoder are taken into account. Secondly, the sub-optimal SM detectors in Secs. 6.4.1.4-6.4.1.7 are not suggested to be employed for coded SM systems. This is because that these sub-optmal SM detectors may jeopardize the reliability of the output LLRs, which may result in disproportionately large LLR values that are hard to be repaired by the channel decoder. Against this background, we propose to further apply the PFS-based SM detector design of Sec. 6.4.1.1 to coded SM and STSK systems in Sec. 7.4. More explicitly, the maximum *a posteriori* probability that is required by the Max-Log-MAP algorithm may be obtained by partially invoking the reduced-complexity soft-decision-aided *M*PSK/QAM demodulators proposed in Sec. 2.4 before deciding the SM's antenna activation index, where the correlation between modulation index and antenna index is taken into account, so that the detected antenna index is always the MAP solution. In this way, only a subset of the *M*PSK/QAM constellation points are visited while the optimum SM detection capability is retained. The resultant Max-Log-MAP algorithms are summarized as Algorithm 7.1 and 7.2 for the SM employing Square *M*QAM and *M*PSK, respectively. Furthermore, the required modifications for implementing the corresponding Approx-Log-MAP algorithms are also discussed in Sec. 7.4.

The performance results for coded MIMO systems are presented in Sec. 7.5. First of all, the performance comparison between the V-BLAST detectors is offered in Figs. 7.1 and 7.2. It is

demonstrated by the BER performance of Fig. 7.2 that the MMSE aided V-BLAST detection imposes a performance loss to the optimum V-BLAST detection in the TC coded systems. However, this performance loss has already been substantially reduced by the exact MMSE solution of Sec. 7.2.4, which is much smaller than the performance loss in the uncoded V-BLAST systems seen in Fig. 6.12. Secondly, the performance results between the conventional MIMO schemes of V-BLAST and STBC as well as the low-complexity MIMO schemes of SM and STSK are compared in Figs. 7.3-7.6. It is evidenced by the EXIT charts of Fig. 7.3 that all the three detectors of the V-BLAST, the SM and the STSK have a beneficial iteration gain, where the SM's iteration gain is even higher than the V-BLAST. As a result, although the V-BLAST detection capability is still slightly higher than the SM as evidenced by the EXIT chart of Fig. 7.3, their BER performance results depend on the channel coding arrangement employed, where the SM even slightly outperforms the V-BLAST in both RSC coded and IRCC-URC coded systems in Fig. 7.5b when $N_T = 4$ transmit antennas are used. The BER performance results of Figs. 7.4 and 7.5 demonstrate that the transmit diversity advantage of STBC and STSK also withers away, when the improved receive diversity gain is available for all MIMO schemes, which is similar to the uncoded MIMO performance results of Figs. 6.14 and 6.15. Thirdly, it is further confirmed by Fig. 7.7 that our proposed soft-decision-aided SM detection of Algorithms 7.1 and 7.2 offer a substantial complexity reduction for the coded SM detection, which is even as high as 95.2% for SM(4,1) employing 64QAM. Fourthly, the complexity results of V-BLAST, STBC, SM and STSK are compared in Fig. 7.8, which demonstrates that the complexity of optimum V-BLAST detection is still much more substantial than the STBC, the SM and the STSK in coded MIMO systems.

In summary, when we focus our attention on the comparison between V-BLAST and SM in coded MIMO systems, we may conclude that the SM may achieve a comparable performance to the V-BLAST at a substantially reduced detection complexity. The complexity reduction design is beneficial especially for coded MIMO systems, as the soft-decision-aided MIMO detectors are suggested to be invoked several times. Furthermore, the retained optimality for SM detection is also important for coded MIMO systems, because as demonstrated by Chapter 3 that any compromise on the detectors' optimality may results in unreliable LLRs, which are difficult to be corrected by channel decoder in coded MIMO systems.

8.2 Future Research Ideas

8.2.1 Reduced-Complexity Viterbi Decoding for Soft-Decision-Aided MSDD

In this report, we have highlighted the important role of the SD in the field of complexity and performance tradeoff in communications systems design. More explicitly, the MSDSD introduced in Chapter 3 is capable of retaining the MSDD performance at a substantially reduced complexity. Owing the the fact that the SD visits the individual MPSK constellations one-by-one, the MSDSD complexity is lower bounded by $O(M)$. However, this appealing complexity lower bound can only

be approached by the hard-decision-aided MSDSD at high SNR values in uncoded DPSK systems, as portrayed in Fig. 3.4, and it can only be approached by the soft-decision-aided MSDSD, when provided with the perfect *a priori* information of $I_A = 1$, as evidenced by Fig. 3.17. Despite of the idealistic complexity lower bound, it was demonstrated in [214] that the average SD complexity is in fact a polynomial function, often approximately cubic, while [215] demonstrated that the SD complexity is still exponential at low SNR values. This poses a problem for implementing the soft-decision-aided SDs in realistic communications systems, because the detectors/decoders have to work at relatively low SNR values which may even approach to the capacity limit in coded systems. In order to mitigate this problem, we have proposed a reduced-complexity soft-decision-aided MSDSD conceived for coded DPSK in Sec. 3.3.3, which aims to reduce the number of visited SD nodes by exploring the symmetry provided by the Gray-labelled constellation diagrams, when both the channel's output signal and the *a priori* information provided by channel decoder are taken into account. We have demonstrated in Fig. 3.18 that the resultant complexity reduction ratio is substantial, which may be even as high as up to over 80% of the conventional MSDSD complexity. This complexity reduction is beneficial especially in turbo detected DPSK receivers, when the soft-decision-aided MSDSD is invoked several times.

Nonetheless, the reduced-complexity soft-decision-aided MSDSD conceived for coded DPSK in Sec. 3.3.3 and also for coded DQAM in Sec. 5.3 still rely on the SD algorithm. This implies that the same problem of a SD complexity being variable over SNRs and I_As and also being especially high at low SNRs and low I_As [214, 215] still puts a strain on its realistic applications. Against this background, the Viterbi decoding aided MSDD [125, 128] may become an attractive alternative in coded DPSK and DQAM systems. As demonstrated in Fig. 1.14, both SD and Viterbi decoding may obtain the MSDD solution. However, except for the first time slot in the Viterbi decoding, there are always M transitions starting from a particular current state, while there are always M transitions merging to a particular next state, the average complexity order for the Viterbi-decoded MSDD is given by $O(M^2)$. The Viterbi decoding complexity is higher than the MSDSD's lower bound of $O(M)$, but it also is much lower than the cubic average SD complexity [214] and the exponential SD complexity at low SNRs [215].

A further proposal for implementing the Viterbi algorithm for the soft-decision-aided MSDD is that our reduce-complexity design may be able to further simplify the Trellis calculations. Considering the soft-decision-aided MSDSD conceived for coded DQPSK as an example, it was demonstrated in Eq. (3.71) that all the SD's PED increment values corresponding to the four QPSK constellation points may be represented as $(\pm t_{v-1}^{Re} \pm t_{v-1}^{Im})$. This feature allows us to directly obtain the minimum metric by simply evaluating $(-|t_{v-1}^{Re}| - |t_{v-1}^{Im}|)$, and the rest of the metrics are simply given by combinations of $\pm|t_{v-1}^{Re}|$ and $\pm|t_{v-1}^{Im}|$. Fig. 8.4a portrays an example of soft-decision-aided MSDSD conceived for DQPSK. Specifically, in Steps ① and ② of Fig. 8.4a, the SD directly obtains the minimum PED according to Eq. (3.63) as $(-|t_1^{Re}| - |t_1^{Im}| + \overline{C}_1 = 0.702)$ and $(d_1 - |t_2^{Re}| - |t_2^{Im}| + \overline{C}_2 = 3.437)$ for index $v = 2$ and index $v = 3$, respectively, where only a single constellation point is visited by each step. When the SD visits index $v = 2$ for the second time in

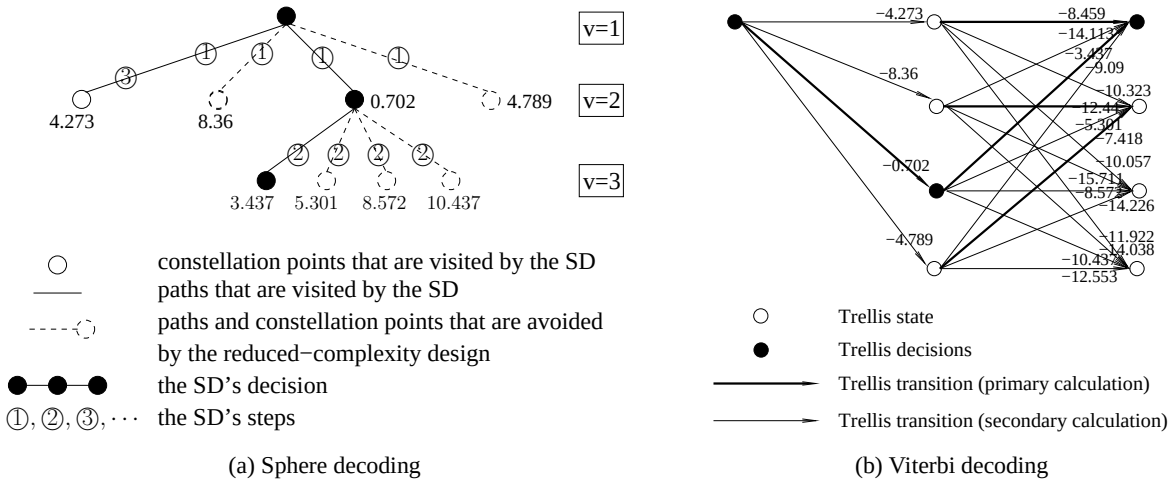

(a) Sphere decoding (b) Viterbi decoding

Figure 8.4: Example of soft-decision-aided MSDSD conceived for DQPSK, recorded at SNR=0 dB, where we have $I_A = 0.3$, $N_R = 2$ and $N_w = 3$, and its corresponding Viterbi implementation. We note that all the likelihood metrics in logarithm domain that are calculated by the Trellis are altered for sphere decoding, so that the sphere decoder may only process non-negative values.

Step ③ of Fig. 8.4a, the second-best candidate is simply given by $(-|t_1^{Re}| + |t_1^{Im}| + \overline{C}_1 = 4.273)$, where all of $|t_1^{Re}|$, $|t_1^{Im}|$ and $\overline{C}_1$ have already been calculated in Step ① so that no new entity is required to be evaluated.

The Viterbi decoding alternative to the MSDSD example of Fig. 8.4a is portrayed in Fig. 8.4b, which vitualizes how to apply the same reduced-complexity design to the Viterbi decoding. As the reduced-complexity algorithm eliminates unnecessary SD paths in Fig. 8.4a, none of the $M = 4$ transitions *starting from* a state can be deleted, because the Viterbi algorithm can only eliminate the transitions *merging to* the same state with lower metrics. Nonetheless, the same calculation reduction may be achieved by defining "primary calculations" and "secondary calculations". It can be seen in Fig. 8.4b that the primary calculations are corresponding to the SD's evaluation of the minimum PED, which now becomes $(-d_v + |t_{v-1}^{Re}| + |t_{v-1}^{Im}| - \overline{C}_1)$, while the secondary calculations corresponding to sub-optimum constellation candidates may be completed by altering the polarities of $|t_{v-1}^{Re}|$ and $|t_{v-1}^{Im}|$. In this way, it can be seen in Fig. 8.4b that for all the $M = 4$ transitions *starting from* a state, there is one primary calculation as well as three secondary calculations, where the major calculations are offloaded to the primary calculation. This method may be further extended to any DPSK and DQAM constellations, and it may be expected that up to 75% of the Viterbi decoding calculations may be streamlined by employing this reduced-complexity design.

8.2.2 Exact MMSE Solution for Soft-Decision-Aided DFDD

The soft-decision-aided DFDD conceived for DPSK in Sec. 3.3.4 directly uses the decision variable z^{DFDD} of Eq. (3.37) given by the hard-decision-aided DFDD, as suggested by [122, 125, 136].

In the absence of *a priori* LLRs, the hard-decision-aided DFDD in Sec. 3.2.4 always assumes that all combinations of data-carrying symbols are equiprobable, and the decision-feedback is based on the hard-bit output of the previous DFDD calculations. By employing the same decision variable z^{DFDD}, the soft-decision-aided DFDD tends to produce unreliable LLRs, as demonstrated in Fig. 3.25b, which deviate from the true probabilities, and these high but inaccurate LLR values are hard to correct for the channel decoder.

The exact MMSE solution incorporating the non-constant *a priori* probabilities was firstly derived for CDMA's MUD in [75, 76], and it is further derived for turbo equalization [70–72] and for turbo BLAST [13, 77, 78]. Therefore, it's beneficial to also propose the exact MMSE solution for the soft-decision-aided DFDD, so that the reliability of the produced LLRs may be improved in turbo detected coded DPSK systems.

Let us elaborate a little further here in order to steer our discussion towards a promising future research topic. The prediction-based DFDD introduced in Sec. 3.2.4 starts with the received signal model for $\mathbf{Y}_{N_w}$ in Eq. (3.40), where the reference fading vector $\hat{\mathbf{H}}_{N_w}$ estimated by a prediction filter is given by Eq. (3.41). Instead of utilizing the hard-bit DFDD decisions, the soft-decision-aided DFDD may produce the decision-feedback matrix $\hat{\mathbf{S}}^{\bar{N}_w}$ in Eq. (3.41) based on the previous soft-bit decisions. Similarly to the soft symbol estimation of Eq. (7.23) for turbo BLAST, the v-th element in $\hat{\mathbf{S}}^{\bar{N}_w}$ may now be evaluated according to:

$$\hat{s}_v = \mathrm{E}(s_v) = \hat{x}_{v-1}\hat{s}_{v-1}, \tag{8.1a}$$

$$\hat{x}_{v-1} = \mathrm{E}(x_{v-1}) = \sum_{m=0}^{M-1} x^m \frac{\exp\left[\sum_{\bar{k}=(v-2)\mathrm{BPS}+1}^{(v-1)\mathrm{BPS}} \widetilde{b}_{\bar{k}} L_a(b_{\bar{k}})\right]}{\prod_{\bar{k}=(v-2)\mathrm{BPS}+1}^{(v-1)\mathrm{BPS}} \{1+\exp[L_a(b_{\bar{k}})]\}}. \tag{8.1b}$$

In contrast to the decision-feedback matrix $\hat{\mathbf{S}}^{\bar{N}_w}$ used by the hard-decision-aided DFDD in Eq. (3.41), the soft symbols $\{\hat{s}_v\}_{v=1}^{N_w-1}$ of Eq. (8.1) in $\hat{\mathbf{S}}^{\bar{N}_w}$ are not regular MPSK symbols.

Similarly to the MSE of turbo BLAST in Eq. (7.24), the prediction-based DFDD's MSE of Eq. (3.42) may be formulated for coded DPSK systems as:

$$\begin{aligned}
\sigma^2_{\mathrm{MSE}} &= E\left\{\left\|\mathbf{Y}_{N_w} - s_{N_w}\hat{\mathbf{H}}_{N_w}\right\|^2\right\} \\
&= E\left\{\left\|\mathbf{H}_{N_w} + s^*_{N_w}\mathbf{V}_{N_w} - \overline{\mathbf{w}}^T(\hat{\mathbf{S}}^{\bar{N}_w})^H\mathbf{Y}^{\bar{N}_w}\right\|^2\right\} \\
&= 1 + N_0 - 2\mathrm{E}\left[\mathbf{H}_{N_w}(\mathbf{Y}^{\bar{N}_w})^H\right]\hat{\mathbf{S}}^{\bar{N}_w}\overline{\mathbf{w}} + \overline{\mathbf{w}}^T(\hat{\mathbf{S}}^{\bar{N}_w})^H\mathrm{E}\left[\mathbf{Y}^{\bar{N}_w}(\mathbf{Y}^{\bar{N}_w})^H\right]\hat{\mathbf{S}}^{\bar{N}_w}\overline{\mathbf{w}}.
\end{aligned} \tag{8.2}$$

The cross-correlation matrix in Eq. (8.2) may be evaluated by:

$$\mathrm{E}\left[\mathbf{H}_{N_w}(\mathbf{Y}^{\bar{N}_w})^H\right] = \mathrm{E}\left[\mathbf{H}_{N_w}(\hat{\mathbf{S}}^{\bar{N}_w}\mathbf{H}^{\bar{N}_w} + \mathbf{V}^{\bar{N}_w})^H\right] = \mathbf{e}^T_{N_w}(\hat{\mathbf{S}}^{\bar{N}_w})^H, \tag{8.3}$$

where $\mathbf{H}^{\bar{N}_w}$ and $\mathbf{V}^{\bar{N}_w}$ are respectively given by $\mathbf{H}$ and $\mathbf{V}$ in the MSDD received signal model of Eq. (3.6) eliminating the N_w-th row, while $\mathbf{e}_{N_w}$ was defined in Eq. (3.43). Moreover, the auto-

correlation matrix in Eq. (8.2) may be evaluated by:

$$\begin{aligned}\mathrm{E}\left[\mathbf{Y}^{\bar{N}_w}(\mathbf{Y}^{\bar{N}_w})^H\right] &= \mathrm{E}\left[(\hat{\mathbf{S}}^{\bar{N}_w}\mathbf{H}^{\bar{N}_w}+\mathbf{V}^{\bar{N}_w})(\hat{\mathbf{S}}^{\bar{N}_w}\mathbf{H}^{\bar{N}_w}+\mathbf{V}^{\bar{N}_w})^H\right] \\ &= \hat{\mathbf{S}}^{\bar{N}_w}\mathbf{R}_{hh}^{\bar{N}_w}(\hat{\mathbf{S}}^{\bar{N}_w})^H - \mathrm{diag}\left\{\left[|\hat{s}_{N_w-1}|^2,\cdots,|\hat{s}_1|^2\right]\right\} + \mathbf{I}_{N_w-1} + N_0\mathbf{I}_{N_w-1},\end{aligned} \tag{8.4}$$

where $\mathbf{R}_{hh}^{\bar{N}_w}$ is given by the fading's characteristic correlation matrix $\mathbf{R}_{hh}$ of Eq. (3.16) eliminating the N_w-th row and the N_w-th column, while the first term in Eq. (8.4) may be formulated as:

$$\hat{\mathbf{S}}^{\bar{N}_w}\mathbf{R}_{hh}^{\bar{N}_w}(\hat{\mathbf{S}}^{\bar{N}_w})^H = \begin{bmatrix} |\hat{s}_{N_w-1}|^2 & \hat{s}_{N_w-1}\hat{s}^*_{N_w-2}\rho_1 & \cdots & \hat{s}_{N_w-1}\hat{s}^*_1\rho_{N_w-2} \\ \hat{s}_{N_w-2}\hat{s}^*_{N_w-1}\rho_1 & |\hat{s}_{N_w-2}|^2 & \cdots & \hat{s}_{N_w-2}\hat{s}^*_1\rho_{N_w-3} \\ \vdots & \vdots & \ddots & \vdots \\ \hat{s}_1\hat{s}^*_{N_w-1}\rho_{N_w-2} & \hat{s}_1\hat{s}^*_{N_w-2}\rho_{N_w-3} & \cdots & |\hat{s}_1|^2 \end{bmatrix}. \tag{8.5}$$

Owing to the fact that the soft symbols $\{\hat{s}_v\}_{v=1}^{N_w-1}$ of Eq. (8.1) are not drawn from any regular MPSK constellations, the diagonal elements of $\hat{\mathbf{S}}^{\bar{N}_w}\mathbf{R}_{hh}^{\bar{N}_w}(\hat{\mathbf{S}}^{\bar{N}_w})^H$ have to be replaced by an identity matrix $\mathbf{I}_{N_w-1}$ in Eq. (8.4). For the sake of convenience, let us define the following soft symbol correlation matrix:

$$\mathbf{R}_{|s|}^{\bar{N}_w} = \hat{\mathbf{S}}^{\bar{N}_w}(\hat{\mathbf{S}}^{\bar{N}_w})^H = (\hat{\mathbf{S}}^{\bar{N}_w})^H\hat{\mathbf{S}}^{\bar{N}_w} = \mathrm{diag}\left\{\left[|\hat{s}_{N_w-1}|^2,\cdots,|\hat{s}_1|^2\right]\right\}. \tag{8.6}$$

Accordingly, the MSE of Eq. (8.2) may be extended as:

$$\sigma^2_{\mathrm{MSE}} = 1 + N_0 - 2\mathbf{e}^T_{N_w}\mathbf{R}_{|s|}^{\bar{N}_w}\overline{\mathbf{w}} + \overline{\mathbf{w}}^T\left[\mathbf{R}_{|s|}^{\bar{N}_w}\mathbf{R}_{hh}^{\bar{N}_w}\mathbf{R}_{|s|}^{\bar{N}_w} - (\hat{\mathbf{S}}^{\bar{N}_w})^H\mathbf{R}_{|s|}^{\bar{N}_w}\hat{\mathbf{S}}^{\bar{N}_w} + (N_0+1)\mathbf{R}_{|s|}^{\bar{N}_w}\right]\overline{\mathbf{w}}. \tag{8.7}$$

The MMSE solution of $\frac{\partial\sigma^2_{\mathrm{MSE}}}{\partial\overline{\mathbf{w}}} = 0$ leads to the classic Wiener-Hopf equation formulated as:

$$\overline{\mathbf{w}} = \left[\mathbf{R}_{|s|}^{\bar{N}_w}\mathbf{R}_{hh}^{\bar{N}_w}\mathbf{R}_{|s|}^{\bar{N}_w} - (\hat{\mathbf{S}}^{\bar{N}_w})^H\mathbf{R}_{|s|}^{\bar{N}_w}\hat{\mathbf{S}}^{\bar{N}_w} + (N_0+1)\mathbf{R}_{|s|}^{\bar{N}_w}\right]^{-1}\mathbf{R}_{|s|}^{\bar{N}_w}\mathbf{e}_{N_w}. \tag{8.8}$$

As a result, the MSE of Eq. (8.7) may be further simplified as:

$$\sigma^2_{\mathrm{MSE}} = 1 + N_0 - \mathbf{e}^T_{N_w}\mathbf{R}_{|s|}^{\bar{N}_w}\overline{\mathbf{w}}. \tag{8.9}$$

According to the *a posteriori* probability of Eq. (3.46), the probability metric of the soft-decision-aided DFDD of Eq. (3.82) may be revised for the exact MMSE solution as:

$$d^m = -\frac{\|\mathbf{Y}_{N_w} - x^m s_{N_w-1}\hat{\mathbf{H}}_{N_w}\|^2}{\sigma^2_{MSE}} + \sum_{\bar{k}=1}^{\mathrm{BPS}}\widetilde{b}_{\bar{k}}L_a(b_{\bar{k}}), \tag{8.10}$$

where the reference fading vector $\hat{\mathbf{H}}_{N_w}$ is estimated according to Eq. (3.41) using the revised weights vector $\overline{\mathbf{w}}$ of Eq. (8.8), while the MSE σ^2_{MSE} is given by Eq. (8.9).

However, we observe that the exact MMSE solution for DFDD has a particular problem of zero-feedback. Fig. 8.5 portrays this problem by a Trellis for the soft DQPSK symbol estimation based on Eq. (8.1). It can be seen in Fig. 8.5 that owing to the relationship of $\hat{s}_v = \hat{x}_{v-1}\hat{s}_{v-1}$ imposed by the differential encoding process, the probabilities for the transmitted DQPSK symbol s_v tends

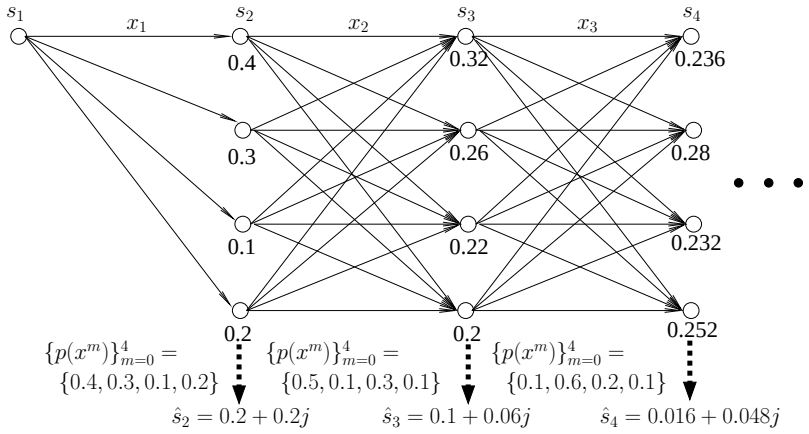

Figure 8.5: Example of probabilities update and soft DQPSK symbol estimation based on Eq. (8.1).

to be equiprobable as $\{p(s^m) \rightarrow 0.25\}_{m=0}^{M-1}$, which leads to the situation that the estimation on s_v tends to zeros as $(\hat{s}_v \rightarrow 0 + 0j)$. We note that this is not a problem for turbo BLAST of Sec. 7.2.4, because the BLAST's symbol probabilities do not accumulate like DPSK. Moreover, a near-zero interference symbol estimation for the MMSE BLAST detector simply results in no interference cancellation, which doesn't stop the MMSE detection. However, a near-zero symbol estimation for the DFDD implies no decision feedback, which leads to a near-zero channel estimation for $\hat{\mathbf{H}}_{N_w}$, and hence the DFDD cannot produce any valid results.

In order to mitigate this problem, the symbol esitmation of Eq. (8.1) may be replaced by the estimation on the entire decision matrix $\mathbf{S}^{\bar{N}_w}$ as:

$$\begin{aligned}\hat{\mathbf{S}}^{\bar{N}_w} = \mathrm{E}(\mathbf{S}^{\bar{N}_w}) &= \sum_{i=0}^{M^{N_w-2}-1} \mathbf{S}^{\bar{N}_w,i} p(\mathbf{S}^{\bar{N}_w} = \mathbf{S}^{\bar{N}_w,i}) \\ &= \sum_{i=0}^{M^{N_w-2}-1} \mathbf{S}^{\bar{N}_w,i} \frac{\exp\left[\sum_{\bar{k}=1}^{(N_w-2)\mathrm{BPS}} \widetilde{b}_{\bar{k}} L_a(b_{\bar{k}})\right]}{\prod_{\bar{k}=1}^{(N_w-2)\mathrm{BPS}} \{1 + \exp[L_a(b_{\bar{k}})]\}},\end{aligned} \tag{8.11}$$

where $\{\mathbf{S}^{\bar{N}_w,i}\}_{i=0}^{M^{N_w-2}-1}$ refers to all the combinations for the decision matrix $\mathbf{S}^{\bar{N}_w}$. As the benefit, Eq. (8.11) doesn't accumulate probabilities. Nonetheless, when the *a priori* information I_A is small, it is still very likely that $\hat{\mathbf{S}}^{\bar{N}_w}$ of Eq. (8.11) contains near-zero feedback symbols. As a remedy, we find that it is beneficial to define a probability threshold p_{th}. If the maximum decision-feedback probability $p_{max} = \max\ p(\mathbf{S}^{\bar{N}_w} = \mathbf{S}^{\bar{N}_w,i})$ for a DFDD window is smaller than the threshold probability, where we have $p_{max} < p_{th}$, it may be expected that $\hat{\mathbf{S}}^{\bar{N}_w}$ contains near-zeros feedback symbols. In this scenario, the decision-feedback matrix $\hat{\mathbf{S}}^{\bar{N}_w}$ should be estimated based on the hard-bit decisions rather than the soft-bit decisions.

Fig. 8.6 portrays a performance comparison between the conventional DFDD using Eq. (3.82) and the improved prediction-based DFDD using Eq. (8.10) derived according to the exact MMSE solution. It can be seen in Fig. 8.6a that the exact MMSE solution does not directly provide any improvement for EXIT charts, but Fig. 8.6b evidences that the exact MMSE solution indeed improves

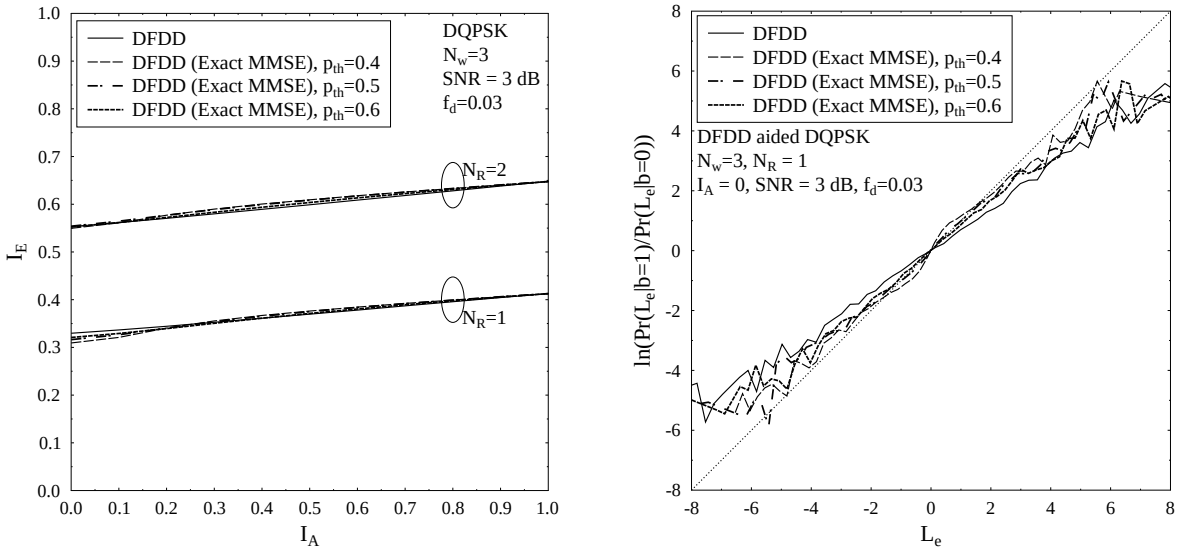

(a) EXIT charts

(b) LLR validity test

Figure 8.6: EXIT charts and LLR validity test of the conventional DFDD using Eq. (3.82) and the improved prediction-based DFDD using Eq. (8.10), which is derived according to the exact MMSE solution.

the LLRs reliability for the soft-decision-aided DFDD. This is beneficial especially for turbo detected coded DPSK systems, where the soft-decision-aided DFDD is invoked several times. In this case, if the DFDD continues to produce unreliable LLRs that deviate from the true probabilities, the high but inaccurate LLR values may become hard to correct for channel decoder after a few turbo iterations.

This exact MMSE solution may be further applied to improve the soft-decision-aided DFDD conceived for DQAM in Sec. 5.4.

8.2.3 Noncoherent Receivers for Square DQAM

Both the DAPSK, the ADPSK and their twisted counterparts of TDAPSK and TADPSK discussed in Chapters 4 and 5 are designed based on the Star QAM constellation. In fact, the first DQAM scheme appeared in literatures was the absolute-amplitude DQAM scheme designed based on the Square QAM constellation, which was proposed by Simon et al. [135] in 1982. However, the researchers have focused on noncoherent receivers conceived for the DAPSK [136, 142–145, 150, 152–154] and the ADPSK/TADPSK [136, 288] in recent years, whereas little progress has been made for the noncoherent receivers conceived for the Square DQAM scheme [135]. The reasons may be deemed to be twofold. First of all, the Square DQAM scheme in [135] was originally proposed to be detected noncoherently for recovering the data-carrying phase but coherently for recovering the data-carrying amplitude, meaning that the channel amplitude has to be estimated at the receiver. Secondly, when the absolute-amplitude differential encoding process of Eq. (4.8)

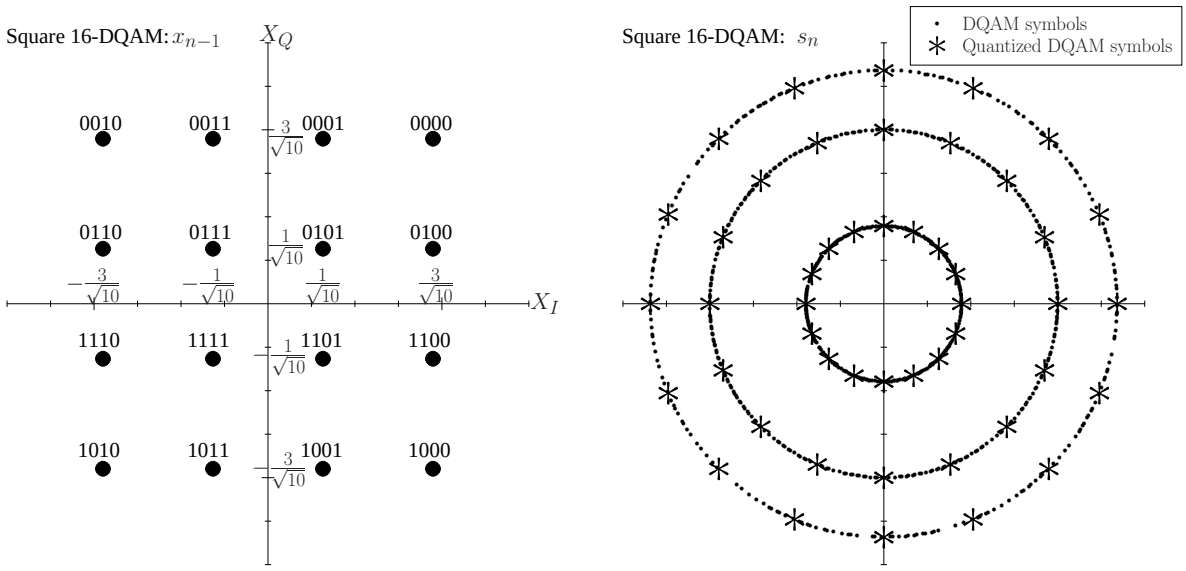

(a) Constellation set **x** for data-carrying symbols

(b) Constellation set **s** for transmitted symbols

Figure 8.7: Constellation diagrams for the Square 16-DQAM scheme.

is applied, there would be no determined constellation set for the Square DQAM's transmitted symbols s_n, which poses a major hardware difficulty.

More explicitly, if the Square 16QAM constellation of Fig. 8.7a is employed for DQAM's data-carrying symbols x_{n-1}, the data-carrying phases for $\angle x_{n-1}$ are given by $\{\arctan(1/3), \pi/4, \arctan(3)\}$ in the first quadrant and their projections in the other three quadrants, which divide the 2π phase circle space unevenly. This is different from, for example, a 16PSK constellation of Fig. 2.4d or a Star 16QAM constellation of Fig. 2.5b, which evenly divide the 2π phase circle space by a constant phase step of $\pi/16$ or $\pi/8$, respectively. As a result, if the absolute-amplitude differential encoding process of $s_n = \frac{1}{|s_{n-1}|} x_{n-1} s_{n-1}$ defined by Eq. (4.8) is applied, then the differential encoding on phase, which is given by $(\angle s_n = \angle x_{n-1} + \angle s_{n-1} \bmod 2\pi)$, will result in $\angle s_n$ having irregular phases that can take any value from 0 to 2π, which is exemplied by Fig. 8.7b.

However, it still can be expected that the Square DQAM scheme may be potentially beneficial if their implementation difficulties may be overcame. Let's recall the comparison between coherent Square and Star 16QAM by Fig. 8.8. It can be seen in Fig. 8.8a that the Star 16QAM achieves a slightly higher DCMC capacity at low SNR region, but the Square 16QAM achieves a slightly higher DCMC capacity at high SNR region. The optimum ring ratio of $\alpha = 2.0$ is employed for the two-ring Star 16QAM in Rayleigh fading channels [155, 253]. Furthermore, Fig. 8.8b demonstrates that the Square 16QAM has the appealing advantage of a lower detection complexity in coded systems. Owing to the fact that the real and imaginary parts of the Square QAM symbol may always be detected separately, the conventional Approx-Log-MAP algorithm of Eq. (2.35) using the Square QAM probability metric of Eq. (2.39) has a lower detection complexity that that using the Star QAM probability metric of Eq. (2.38). For the same reason, our proposed reduced-complexity soft-decision-aided Square QAM detection of Algorithm 2.2 also has a lower detection complexity than its Star QAM counterpart of Algorithm 2.3. Since both the ADPSK and the DAPSK are

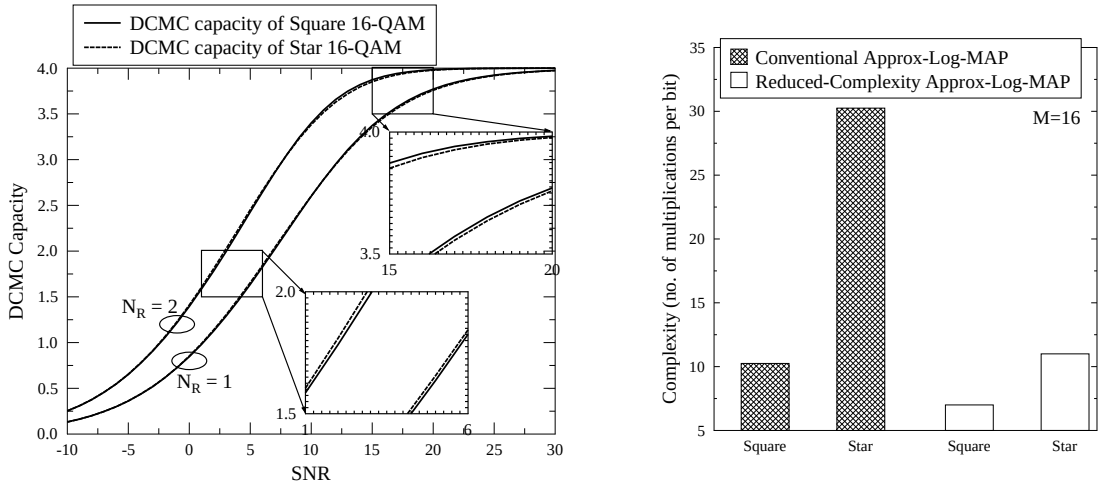

(a) DCMC capacity

(b) Complexity comparison

Figure 8.8: The DCMC capacity comparison between Square 16QAM of Fig. 2.5a and Star 16QAM of Fig. 2.5b and the detection complexity comparison between their soft-decision-aided detectors. The DCMC capacities are evaluated according to Eq. (2.56). The conventional QAM detection refers to the Approx-Log-MAP algorithm of Eq. (2.35) using the probability metrics of Eq. (2.39) and Eq. (2.38) for Square QAM and Star QAM, respectively. The reduced-complexity QAM detection refers to Algorithm 2.2 and 2.3.

the differential schemes conceived based on the Star QAM constellation, it would be beneficial to further explore the noncoherent receivers conceived for Square DQAM, so that the advantages of Square QAM in coherent systems may be further applied to noncoherent systems.

Let's elaborate a little further to demonstrate how to facilitate the implementation of the Square DQAM scheme. First of all, the Square DQAM scheme may modulate the data-carrying symbols according to the Square MQAM constellation as:

$$x^m = \frac{M_{\text{Re}} - 2\check{m}_{\text{Re}} - 1}{\sqrt{\beta}} + j\frac{M_{\text{Im}} - 2\check{m}_{\text{Im}} - 1}{\sqrt{\beta}}, \tag{8.12}$$

where the normalization factor β is given by Eq. (2.11). Explicitly, the first $\text{BPS}_{\text{Im}} = \log_2 M_{\text{Im}}$ source bits are assigned to modulate the imaginary modulation index $m_{\text{Im}} = \text{bin2dec}(b_1, \cdots, b_{\text{BPS}_{\text{Im}}})$, where m_{Im} is the Gray coded index $\check{m}_{\text{Im}}$. The following $\text{BPS}_{\text{Re}} = \log_2 M_{\text{Re}}$ source information bits are assigned to modulate the real modulation index $m_{\text{Re}} = \text{bin2dec}(b_{\text{BPS}_{\text{Im}}+1}, \cdots, b_{\text{BPS}})$, where m_{Re} is the Gray coded index $\check{m}_{\text{Re}}$. The relationship between the modulation indices is given by $m = \text{bin2dec}(b_1, \cdots, b_{\text{BPS}}) = m_{\text{Re}} + m_{\text{Im}} M_{\text{Re}}$, while the relationship between the modulation levels is given by $M = M_{\text{Re}} M_{\text{Im}}$. More specifically, when $\text{BPS} = \text{BPS}_{\text{Re}} + \text{BPS}_{\text{Im}}$ is an even number, we have $\text{BPS}_{\text{Re}} = \text{BPS}_{\text{Im}} = \text{BPS}/2$ and $M_{\text{Re}} = M_{\text{Im}} = \sqrt{M}$. Furthermore, when BPS is an odd number, we have $\text{BPS}_{\text{Re}} = \text{BPS}_{\text{Im}} + 1 = (\text{BPS}+1)/2$ and $M_{\text{Re}} = 2M_{\text{Im}} = \sqrt{2M}$.

In order to mitigate the problem of the irregular phases that result from the differential encoding process of Eq. (4.8), we have to quantize the Square DQAM symbols s_n before transmission.

Specifically, a 16PSK constellation is employed in Fig. 8.7b for quantizing each amplitude ring of the Square 16-DQAM symbols s_n. It may be expected that the quantization error may be reduced, when the quantization level is increased. As a result, instead of directly transmitting the differential encoder's output symbols s_n, the quantized Square DQAM symbols s'_n are transmitted, and hence the received signal model of Eq. (2.1) may be revised as:

$$\begin{aligned} \mathbf{Y}_n &= s'_n \mathbf{H}_n + \mathbf{V}_n \\ &= s_n \mathbf{H}_n + \mathbf{V}'_n, \end{aligned} \tag{8.13}$$

where the equivalent AWGN vector $\mathbf{V}'_n = \mathbf{V}_n - (s_n - s'_n)\mathbf{H}_n$ contains both the original AWGN vector $\mathbf{V}_n$ and the faded quantization error $(s_n - s'n)\mathbf{H}_n$, which are both unknown to the receiver. It's worthy to note that the quantization shall only be applied before Square DQAM signal transmission, so that the quantization error may not be accumulated through the differential encoding process of Eq. (4.8).

Owing to the fact that the differential encoding process of Eq. (4.8) is adopted by the Square DQAM scheme, the noncoherent receivers for Square DQAM are similar to those for any abosulute-amplitude DQAM schemes including ADPSK, TADPSK and JTADPSK$^{\text{JM}}$, where channel estimation is not required for both channel phase and amplitude. Let's consider the CDD conceived for Square DQAM as an example. The received signal model of Eq. (8.13) may be further extended as:

$$\begin{aligned} \mathbf{Y}_n &= \frac{x_{n-1}}{\Gamma_{n-1}} s_{n-1} \mathbf{H}_n + \mathbf{V}'_n \\ &= \frac{x_{n-1}}{\Gamma_{n-1}} \mathbf{Y}_{n-1} + \widetilde{\mathbf{V}}_n, \end{aligned} \tag{8.14}$$

where the fading is assumed to be constant as $\mathbf{H}_{n-1} = \mathbf{H}_n$, while the equivalent AWGN term is given by $\widetilde{\mathbf{V}}_n = \mathbf{V}'_n - \frac{x_{n-1}}{\Gamma_{n-1}} \mathbf{V}'_{n-1}$. As a result, the CDD aided Square DQAM may be formulated as same as the CDD aided ADPSK/TADPSK/JTADPSK$^{\text{JM}}$ in Eqs. (4.27) and (4.28) as:

$$\begin{aligned} \hat{x}_{n-1} &= \arg \min_{\forall x^m \in \mathbf{x}} \left\| \mathbf{Y}_n - \frac{x^m}{\hat{\Gamma}_{n-1}} \mathbf{Y}_{n-1} \right\|^2 \\ &= \arg \min_{\forall x^m \in \mathbf{x}} \left| z_{n-1}^{CDD} - \frac{x^m}{\hat{\Gamma}_{n-1}} \right|^2, \end{aligned} \tag{8.15}$$

where the decision variable is given by $z_n = \mathbf{Y}_n \mathbf{Y}_{n-1}^H / \|\mathbf{Y}_{n-1}\|^2$ as defined in Eq. (4.18). Furthermore, the previous Square DQAM symbol's amplitude $\hat{\Gamma}_{n-1} = |\hat{s}_{n-1}|$ is obtained from the previous CDD decision. Moreover, similar to the low-complexity coherent Square QAM detection of Eq. (2.17), the CDD aided Square DQAM of Eq. (8.15) may be further simplified as:

$$\begin{aligned} \hat{m}_{\text{Re}} &= \max\left[\min\left(\lfloor q_{\text{Re}} \rceil, M_{\text{Re}} - 1\right), 0\right], \quad \text{where } q_{\text{Re}} = \left[M_{\text{Re}} - \hat{\Gamma}_{n-1}\sqrt{\beta}\Re(z_{n-1}^{CDD}) - 1\right]/2, \\ \hat{m}_{\text{Im}} &= \max\left[\min\left(\lfloor q_{\text{Im}} \rceil, M_{\text{Im}} - 1\right), 0\right], \quad \text{where } q_{\text{Im}} = \left[M_{\text{Im}} - \hat{\Gamma}_{n-1}\sqrt{\beta}\Im(z_{n-1}^{CDD}) - 1\right]/2. \end{aligned} \tag{8.16}$$

In summary, all the noncoherent receivers introduced in Chapters 4 and 5 that are shared by the abosulute-amplitude DQAM schemes including ADPSK, TADPSK and TADPSK$^{\text{JM}}$ may be

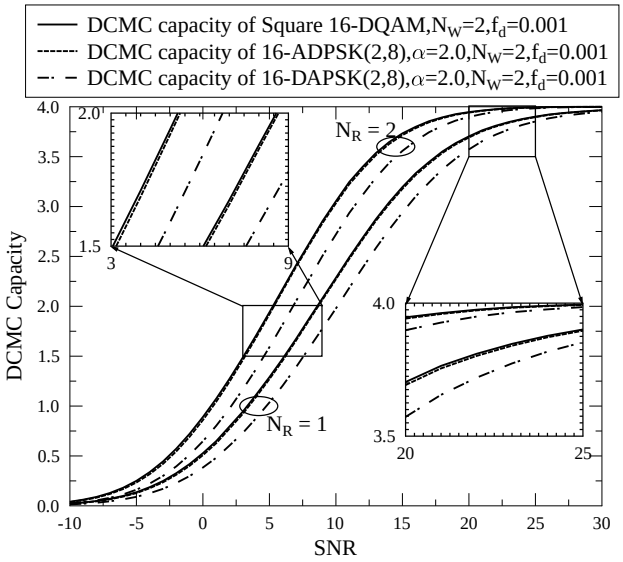

Figure 8.9: The DCMC capacity comparison between Square 16-DQAM of Fig. 8.7, 16-ADPSK(2,8) of Fig. 4.3 and 16-DAPSK(2,8) of Figs. 4.1-4.2. The DCMC capacities of Square 16-DQAM and that of 16-ADPSK(2,8) are evaluated by Eq. (4.83), while the DCMC capacity of 16-DAPSK(2,8) is evaluated by Eq. (4.82).

invoked for Square DQAM. Fig. 8.9 portrays the DCMC capacity comparison between the Square 16-DQAM of Fig. 8.7, the 16-ADPSK(2,8) of Fig. 4.3 and the 16-DAPSK(2,8) of Figs. 4.1-4.2. It can be seen in Fig. 8.9 that the 16-ADPSK(2,8) and the Square 16-DQAM respectively achieve the lowest and the highest DCMC capacities at all SNRs, although the DCMC capacity difference between the Square 16-DQAM and the 16-ADPSK(2,8) is not significant. This is similar to the capacity results for the coherent Square and Star 16QAM presented in Fig. 8.8a, and we may conclude that Square and Star QAM may achieve the similar capacity in both coherent and noncoherent systems.

Furthermore, specific reduced-complexity detection algorithms may be further conceived for the noncoherent receivers according to the Square DQAM constellation. It's worthy to note that both the CDD aided ADPSK of Eq. (4.29) and the CDD aided TADPSK of Eq. (4.30) have a low detection complexity that is similar to the CDD aided Square DQAM of Eq. (8.16). This is because that in uncoded systems, the linear noncoherent receivers such as CDD and DFDD may always directly map the channel's output signal to the nearest constellation point. However, in coded systems, the soft-decision-aided noncoherent detectors have to visit all the constellation points, when both the channel's output signal and the *a priori* information obtained from channel decoder are taken into account. Nonetheless, it may be expected that the soft-decision-aided noncoherent detectors conceived for Square DQAM may have a lower detection complexity than those for other DQAM schemes, because the Square DQAM detection may always be conducted separately for the real and imaginary parts of the constellation points in both uncoded and coded systems, which imposes a reduced complexity order of $O(M_{\mathrm{Re}} + M_{\mathrm{Im}})$ rather than $O(M)$.

8.2.4 Reduced-Complexity Design Applied to Generalized Spatial Modulation

As discussed in Sec. 6.4.3, one of the major disadvantage of the SM is its CCMC capacity loss compared to the V-BLAST, which is explicitly demonstrated by Fig. 6.13a. As the recent development in millimeter-wave band [227, 343, 344] enables the equipment of a large amount of antennas especially at base stations [227, 340–342], the V-BLAST's full MIMO CCMC capacity may even grow linearly with the number of antennas, as specified by Eqs. (6.3)-(6.5). By contrast, the SM's CCMC capacity of Eq. (6.138) can only grow logarithmically with the number of antennas, because the maximized mutual information between the antenna activation index and the received signal formulated by Eqs. (6.143)-(6.144) is upper bounded by $\log_2 N_T$.

Therefore, the antenna activation procedure portrayed by the SM schematics of Fig. 6.6 has to be modified in order to convey more information bits. From a historical point of view, the fractional bit encoded SM proposed in [336] allows the transmitter to employ any number of antennas N_T instead of requiring N_T being a power of 2. Specifically, when N_T is not a power of 2, the antenna activation index may opt to carry different numbers of information bits, where some antenna index candidates are encoded by $(\lfloor \log_2 N_T \rfloor)$ bits, while other candidates are encoded by $(\lfloor \log_2 N_T \rfloor + 1)$ bits. However, the variable number of bits assigned for antenna activation may lead to the error propagation problem, when the antenna index and the modulation index are detected separately at the SM receiver. As a remedy, the bit-padding method is introduced in [337], where an extra bit is padded at the end of the short codewords so that all antenna activation index candidates may convey the same number of $(\lfloor \log_2 N_T \rfloor + 1)$ bits.

The earliest effort to assign more bits to the antenna activation procedure is the Generalized Space-Shift Keying (GSSK) [199], where more than one transmitted antennas are activated. More explicitly, when a total number of n_t out of N_T transmit antennas are activated, the total number of possible combinations is given by the binomial coefficient of $\overline{U}_T = \binom{N_T}{n_t}$. As a result, the total number of bits that can be conveyed by GSSK is given by $\text{BPS}_T = \lfloor \log_2 \overline{U}_T \rfloor = \log_2 U_T$, where there are a total number of $U_T = 2^{\text{BPS}_T}$ GSSK codewords. Therefore, the SSK [200] is a special case of GSSK, where we have $n_t = 1$ and $U_T = N_T$. Furthermore, the Generalized Spatial Modulation (GSM) [231] may utilize the same antenna activation procedure of GSSK, while the same MPSK/QAM symbol that is modulated from $BPS = \log_2 M$ bits is transmitted by all the activated antennas, so that the GSM still has the advantage of no inter-antenna interference. As a result, the SM of Sec. 6.4.1 also becomes a special case of the GSM associated with $n_t = 1$ and $U_T = N_T$.

The total number of bits assigned to the antenna activation procedure is further optimized according to Hamming code in [338]. More explicitly, for a transmitter equipped with N_T antennas, the maximized number of bits that can be conveyed by the GSSK is simply given by N_T, where all the 2^{N_T} combinations between $[0, \cdots, 0]$ and $[1, \cdots, 1]$ are legitimate GSSK codewords. Specifically, the GSSK codeword of $[0, \cdots, 0]$ activates no antenna, while the GSSK codeword of $[1, \cdots, 1]$ activates all antennas. In this case, the minimum Hamming distance is given by

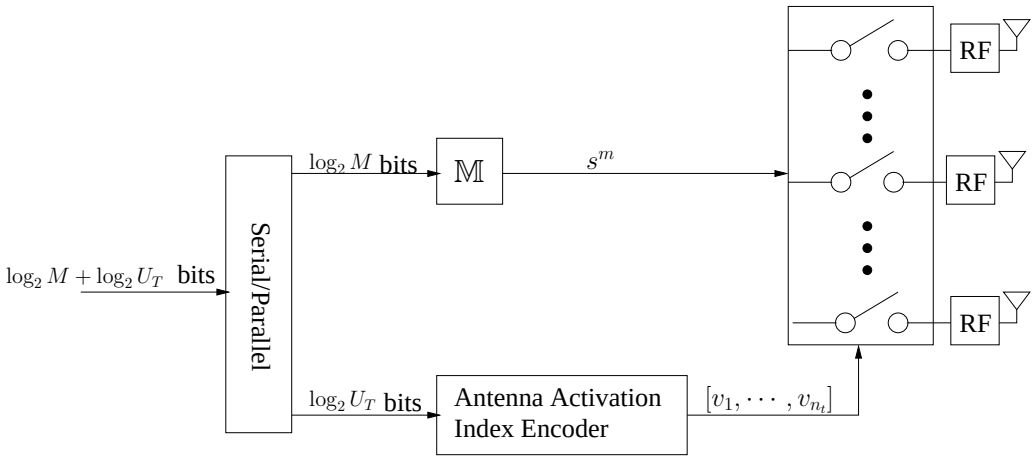

Figure 8.10: Schematic of the GSM transmitter.

$d_{min} = 1$. In order to improve d_{min}, the all-zero GSSK codeword of $[0, \cdots, 0]$ has to be eliminated. As a result, the remaining $2^{(N_T-1)}$ combinations can only convey $(N_T - 1)$ bits at most. In order to optimize this GSSK transmission, it is proposed in [338] that the Hamming code may be employed to guarantee the minimum Hamming distance of $d_{min} = 2$, where $(\text{BPS}_T = N_T - 1)$ bits are assigned for $(U_T = 2^{=N_T-1})$ GSSK codewords. This GSSK design is further applied to the GSM in [339]. For example, if the transmitted signals vector of the GSSK and the GSM may be represented by the STSK's dispersion process of $\mathbf{S} = \overline{\mathbf{A}}_q s^m$ in Eq. (6.130), then the GSSK/GSM dispersion matrices optimized by Hamming code for the case of $N_T = 4$ are given by:

$$\begin{aligned} &\overline{\mathbf{A}}_0 = [0,0,0,1], \quad \overline{\mathbf{A}}_1 = [0,0,1,0], \quad \overline{\mathbf{A}}_2 = [0,1,0,0], \quad \overline{\mathbf{A}}_3 = [0,1,1,1], \\ &\overline{\mathbf{A}}_4 = [1,0,0,0], \quad \overline{\mathbf{A}}_5 = [1,0,1,1], \quad \overline{\mathbf{A}}_6 = [1,1,0,1], \quad \overline{\mathbf{A}}_7 = [1,1,1,0]. \end{aligned} \tag{8.17}$$

For this case, a total number of $(\text{BPS}_T = 3)$ bits are assigned for $(U_T = 8)$ antenna activation arrangements.

Moreover, the GSM proposed in [226] opt to use the n_t out of N_T activated antennas to transmit n_t different MPSK/QAM symbols, so that the total number of bits conveyed by the GSM scheme may be increased to $\text{BPS}_T + n_t\text{BPS}$, where we have $\text{BPS}_T = \lfloor \log_2[\binom{N_T}{n_t}] \rfloor$. Similarly, the GSTSK proposed in [217, 302] also activates n_q out of N_Q dispersion matrices to disperse a total number of n_q different MPSK/QAM symbols. Naturally, the GSM of [226] has a higher capacity than the GSM of [231, 339]. However, the inter-antenna interference problem arises again for the GSM of [226] and also for the GSTSK of [217, 302]. As a remedy, the sub-optimal interference-suppressed receivers are proposed to be employed by the GSM and GSTSK receivers in [226, 229], which are not consistent with the SM/STSK motivation of low-complexity ML receiver design. Against this background, the preferred GSM arrangement for future research is the one conceived in [231, 339]. Ideally, in the absence of inter-antenna interference, the GSM and the corresponding GSTSK may invoke the low-complexity SM detectors summarized in Secs. 6.4 and 7.4.

To elaborate a little further, the schematic of the GSM of [231, 339] is portrayed in Fig. 8.10, where n_t out of N_T transmit antennas are activated to transmit a single MPSK/QAM symbol. The

SM transmission vector of Eq. (6.99) may be revised for GSM as:

$$\begin{aligned}\mathbf{S} = [\ \ 0 \cdots 0 \ \ s^m \ \ 0 \cdots 0 \ \ s^m \ \ \cdots\cdots \ \ s^m \ \ 0 \cdots 0].\\ \qquad\qquad\quad \uparrow \qquad\qquad \uparrow \qquad\qquad \uparrow \\ \qquad\qquad\quad v_1 \qquad\qquad v_2 \qquad\qquad v_{n_t}\end{aligned} \tag{8.18}$$

More explicitly, the GSM transmitter assigns $\text{BPS}_T = \log_2 U_T$ bits to modulate the antenna activation indices of $[v_1, v_2, \cdots, v_{n_t}]$, while $\text{BPS} = \log_2 M$ bits are assigned to modulate the MPSK/QAM modulation index m. Therefore, a total number of $\text{BPS}_T + \text{BPS}$ bits are conveyed by the GSM.

The GSM's signal received at N_R antennas may also be modelled by Eq. (6.1). In order to retain the ML detection capability, the decision metric of the ML MIMO detection of Eq. (6.13) may be extended for GSM as:

$$\begin{aligned}\|\mathbf{Y} - \mathbf{SH}\|^2 &= \left\| \mathbf{Y} - s^m \left(\sum_{t=1}^{n_t} \mathbf{H}_{v_t,-} \right) \right\|^2 \\ &= \|\mathbf{Y}\|^2 + |s^m|^2 \left\| \sum_{t=1}^{n_t} \mathbf{H}_{v_t,-} \right\|^2 - 2\Re \left[(s^m)^* \mathbf{Y} \left(\sum_{t=1}^{n_t} \mathbf{H}_{v_t,-} \right)^H \right].\end{aligned} \tag{8.19}$$

Compared with the SM detection of Eq. (6.103), the GSM detection of Eq. (8.19) also does not encounter the interference problem, because only a single MPSK/QAM symbol is transmitted. Nonetheless, for GSM, there are a total number of U_T combinations for antenna activation arrangements, which results in a total number of U_T combinations for $\left(\sum_{t=1}^{n_t} \mathbf{H}_{v_t,-}\right)$ in Eq. (8.19). Therefore, the matched filter output of Eq. (6.100) cannot be directly applied for the GSM detection. Instead, a $(U_T \times N_R)$-element equivalent fading matrix $\widetilde{\mathbf{H}}$ may be constructed, where the u-th row in $\widetilde{\mathbf{H}}$ is given by:

$$\widetilde{\mathbf{H}}_{u,-} = \sum_{t=1}^{n_t} \mathbf{H}_{v_t,-}. \tag{8.20}$$

The antenna activation indices of $[v_1, v_2, \cdots, v_{n_t}]$ are explicitly determined by the combination index u, and there are a total number of U_T combinations for all possible antenna activation arrangements. As a result, the $(1 \times U_T)$-element equivalent matched filter output vector may be obtained by:

$$\widetilde{\mathbf{Z}} = \mathbf{Y}\widetilde{\mathbf{H}}^H, \tag{8.21}$$

where the u-th element in $\widetilde{\mathbf{Z}}$ is given by $\widetilde{z}_u = \mathbf{Y}\widetilde{\mathbf{H}}^H_{u,-}$. In summary, the simplified SM detection of Eq. (6.103) may be revised for the GSM detection as:

$$\hat{\mathbf{S}} = \arg \min_{\forall m \in \{0,\cdots,M-1\}, \forall u \in \{1,\cdots,U_T\}} \widetilde{\kappa}_u^2 |s^m|^2 - 2\Re\left[(s^m)^* \widetilde{z}_u\right], \tag{8.22}$$

where the constant of $\|\mathbf{Y}\|^2$ in Eq. (8.19) is omitted, while we have $\{\widetilde{\kappa}_u = \|\widetilde{\mathbf{H}}_{u,-}\|\}_{u=1}^{U_T}$. In conclusion, the GSM detection of Eq. (8.22) is completely equivalent to the SM detection of Eq. (6.103), where the SM's antenna activation index v that is aimed to be detected from a total number of N_T

candidates is replaced by the GSM's antenna activation combination index u that is aimed to be detected from a total number of U_T candidates. Therefore, all the hard-decision-aided SM detectors in Sec. 6.4 and the soft-decision-aided SM detectors in Sec. 7.4 may be invoked for GSM detection.

There are also two hard-decision-aided suboptimal GSM detectors in literatures [230, 366] which may achieve a near-optimum performance in uncoded GSM systems. Moreover, it is demonstrated by [230,339] that the GSM may outperfoms the SM, but the simulation results in [231] show the contradiction results. Therefore, the capacity and performance comparison between the SM and the GSM in both uncoded and coded system are still await for future work.

8.2.5 Reduced-Complexity Design Applied to Soft-Decision-Aided SD Conceived for Coded V-BLAST Employing Square QAM

The soft-decision-aided SD conceived for coded V-BLAST employing Square QAM was introduced in Sec. 7.2.3. However, we didn't apply the reduced-complexity design to this scheme, because the reduced-complexity SD algorithm proposed in Sec. 3.3.3 is explicitly tailored for MPSK constellation. As a result, when Square MQAM constellation is used, the soft-decision-aided SD has to invoke the conventional Schnorr-Euchner searching strategy which is summarized as pseudocode in Table 7.2. It can be seen in Table 7.2 that all legitimate $\sqrt{M}$PAM constellation points have to be visited by the SD. Moreover, a sorting algorithm (Bubble sort, Timsort, Library sort, etc. [285, 286]) also has to be invoked for increasingly order the PED increments.

Some efficient calculation methods may be found in literatures [358–360], where the SD visits only a subset of $\sqrt{M}$PAM constellation points. However, these existing solutions simplifies the Schnorr-Euchner searching strategy by utilizing only the channel-output-related PED increment term, where the beneficial *a priori* information is not taken into account. The *a priori* information is beneficial especially for MIMO detectors, because the MIMO signals dependency is very high as they act as interference to each other. Against this background, we propose a future work to tailor the reduced complexity design for Square MQAM constellation.

To elaborate a little further, the PED increment of Eq. (7.18) may be firstly extended as:

$$\begin{aligned}\Delta_v &= \left(\widetilde{\overline{y}}_v^{SD} - \widetilde{\overline{h}}_v^{SD}\,\overline{s}_v\right)^2 - \sum_{\bar{k}_v=1}^{\mathrm{BPS}/2}\left[\widetilde{b}_{\bar{k}_v} L_a(b_{\bar{k}_v}) - \overline{C}_{a,\bar{k}_v}^{SD}\right] \\ &= \overline{\Delta}_v + \overline{C}_v,\end{aligned} \tag{8.23}$$

where the equivalent "received signal" and "fading factor" for detecting the $\sqrt{M}$PAM variable $\overline{s}_v$ are given by $\widetilde{\overline{y}}_v^{SD} = \frac{\widetilde{\overline{Y}}_v - \sum_{t=v+1}^{2N_T} l_{t,v}\overline{s}_t}{\sqrt{N_0}}$ and $\widetilde{\overline{h}}_v^{SD} = \frac{l_{v,v}}{\sqrt{N_0}}$, respectively. Moreover, comparing the $\sqrt{M}$ candidates for $\overline{s}_v$ according to their PED increment values Δ_v of Eq. (8.23) is equivalent to comparing the equivalent PED increment metrics $\overline{\Delta}_v$ as:

$$\overline{\Delta}_v = -2\overline{s}_v\overline{z}_v + \overline{\kappa}_v^2(\overline{s}_v)^2 - \sum_{\bar{k}_v=1}^{\mathrm{BPS}/2}\widetilde{b}_{\bar{k}_v} L_a(b_{\bar{k}_v}) + \frac{L_a(b_1)}{2}, \tag{8.24}$$

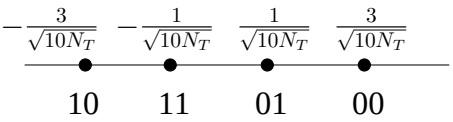

Figure 8.11: Constellation Diagrams of Gray-labelled 4PAM.

where we have $\overline{z}_v = \widetilde{\overline{y}}_v^{SD}\widetilde{\overline{h}}_v^{SD}$ and $\overline{\kappa}_v^2 = (\widetilde{\overline{h}}_v^{SD})^2$. As a result, the remnant constant term $\overline{C}_v$ in Eq. (8.23) that does not change over the variable $\overline{s}_v$ is given by:

$$\overline{C}_v = (\widetilde{\overline{y}}_v^{SD})^2 + \sum_{\bar{k}_v=1}^{\mathrm{BPS}/2} \overline{C}_{a,\bar{k}_v}^{SD} - \frac{L_a(b_1)}{2}. \tag{8.25}$$

Let us now consider the Square 16QAM constellation of Fig. 2.5a as an example, where both the real and imaginary parts of the Square 16QAM constellation are drawn from the same 4PAM constellation of Fig. 8.11. We note that the power normalization factor of $\sqrt{N_T}$ is imposed by the V-BLAST transmission vector of Eq. (6.11). As a result, the four probability metrics $\{\overline{\Delta}_v^m\}_{m=0}^{\sqrt{M}-1=3}$ of Eq. (8.24) corresponding to the $\sqrt{M}=4$ PAM constellation points in Fig. 8.11 may be expressed as:

$$\begin{array}{lll}
\overline{\Delta}_v^0 & = -\frac{6}{\sqrt{10N_T}}\overline{z}_v + \frac{9}{10N_T}\overline{\kappa}_v^2 + \frac{L_a(b_1)}{2} & = -t_v^{G0} + \frac{9}{10N_T}\overline{\kappa}_v^2, \\
\overline{\Delta}_v^1 & = -\frac{2}{\sqrt{10N_T}}\overline{z}_v + \frac{1}{10N_T}\overline{\kappa}_v^2 + \frac{L_a(b_1)}{2} - L_a(b_2) & = -t_v^{G1} + \frac{1}{10N_T}\overline{\kappa}_v^2 - L_a(b_2), \\
\overline{\Delta}_v^2 & = \frac{6}{\sqrt{10N_T}}\overline{z}_v + \frac{9}{10N_T}\overline{\kappa}_v^2 - \frac{L_a(b_1)}{2} & = t_v^{G0} + \frac{9}{10N_T}\overline{\kappa}_v^2, \\
\overline{\Delta}_v^3 & = \frac{2}{\sqrt{10N_T}}\overline{z}_v + \frac{1}{10N_T}\overline{\kappa}_v^2 - \frac{L_a(b_1)}{2} - L_a(b_2) & = -t_v^{G1} + \frac{1}{10N_T}\overline{\kappa}_v^2 - L_a(b_2),
\end{array} \tag{8.26}$$

where the testing variables are given by:

$$\begin{array}{l}
t_v^{G0} = \frac{6}{\sqrt{10N_T}}\overline{z}_v - \frac{L_a(b_1)}{2}, \\
t_v^{G1} = \frac{2}{\sqrt{10N_T}}\overline{z}_v - \frac{L_a(b_1)}{2}.
\end{array} \tag{8.27}$$

It can be seen in Eq. (8.26) that the 4PAM constellations may be arranged into two groups of $\{\pm\frac{1}{\sqrt{10N_T}}\}$ and $\{\pm\frac{3}{\sqrt{10N_T}}\}$ thanks to the symmetry provided by the Gray-labelling. As a result, instead of evaluating four PED increment values, the minimum probability metrics of these two groups are given by:

$$\begin{array}{l}
\overline{\Delta}_v^{G0} = -|t_v^{G0}| + \frac{9}{10N_T}\overline{\kappa}_v^2, \\
\overline{\Delta}_v^{G1} = -|t_v^{G1}| + \frac{1}{10N_T}\overline{\kappa}_v^2 - L_a(b_2).
\end{array} \tag{8.28}$$

Furthermore, the global minimum probability metric is simply given by:

$$\overline{\Delta}_v = \min\{\overline{\Delta}_v^{G0}, \overline{\Delta}_v^{G1}\}. \tag{8.29}$$

As a result, when the SD visits the specific index v for the first time, the minimum PED increment metric may be obtained by Eq. (8.29), which evaluates and compares two probability metrics of $\overline{\Delta}_v^{G0}$ and $\overline{\Delta}_v^{G1}$ instead of the four probability metrics of Eq. (7.18), where in fact only two constellation points are visited. Moreover, no sorting algorithm is required for obtaining Eq. (8.29), and the

$\boxed{1^{\text{st}}\text{ visit}}$ – Calculate $\{t_v^{Gg}\}_{g=0}^{1}$, $\{\overline{\Delta}_v^{Gg}\}_{g=0}^{1}$ and $\overline{C}_v$
– If $\overline{\Delta}_v^{G1} < \overline{\Delta}_v^{G0}$ and if $t_v^{G1} < 0$
• $\overline{s}_v = -\frac{1}{\sqrt{10N_T}}$
• $\Delta_v = \overline{\Delta}_v^{G1} + \overline{C}_v$

$\boxed{2^{\text{nd}}\text{visit}}$ – Update $\overline{\Delta}_v^{G1} = |t_v^{G1}| + \frac{1}{\sqrt{10N_T}}\overline{\kappa}_v^2 - L_a(b_2)$
– If $\overline{\Delta}_v^{G0} < \overline{\Delta}_v^{G1}$ and if $t_v^{G0} < 0$
• $\overline{s}_v = -\frac{3}{\sqrt{10N_T}}$
• $\Delta_v = \overline{\Delta}_v^{G0} + \overline{C}_v$

$\boxed{3^{\text{th}}\text{ visit}}$ – Update $\overline{\Delta}_v^{G0} = |t_v^{G0}| + \frac{9}{\sqrt{10N_T}}\overline{\kappa}_v^2$
– If $\overline{\Delta}_v^{G1} < \overline{\Delta}_v^{G0}$
• $\overline{s}_v = \frac{1}{\sqrt{10N_T}}$
• $\Delta_v = \overline{\Delta}_v^{G1} + \overline{C}_v$

$\boxed{4^{\text{th}}\text{ visit}}$ • $\overline{s}_v = \frac{3}{\sqrt{10N_T}}$
• $\Delta_v = \overline{\Delta}_v^{G0} + \overline{C}_v$

Figure 8.12: Example of the reduced-complexity Schnorr-Euchner searching strategy conceived for 4PAM constellation.

remaining constellation points may be visited in a zig-zag fashion if the SD visits the specific index v again.

Fig. 8.12 portrays an example of the proposed reduced-complexity Schnorr-Euchner searching strategy conceived for 4PAM constellation. More explicitly, when the SD visits the specific index v for the first time, the testing variables t_v^{G0} and t_v^{G1} of Eq. (8.27), the local minima $\overline{\Delta}_v^{G0}$ and $\overline{\Delta}_v^{G1}$ of Eq. (8.28) as well as the constant $\overline{C}_v$ of Eq. (8.25) have to be evaluated. According to Eq. (8.29), the global minimum $\overline{\Delta}_v$ may be obtained by simply comparing the local minima, where we have $\overline{\Delta}_v^{G1} < \overline{\Delta}_v^{G0}$ for the example shown in Fig. 8.12, and then the optimum constellation point that is corresponding to $\overline{\Delta}_v$ may also be obtained by testing the polarity of t_v^{G1}. If the SD visits the specific index v for the second time, the specific local minimum $\overline{\Delta}_v^{G1}$ has to be updated to its next candidate, because the optimum $\overline{\Delta}_v^{G1}$ was the output in the first step. Following this, the second-best global minimum and the corresponding constellation point may be obtained accordingly. This algorithm is repeated until all the constellation points have been checked at the SD's 4-th visit. The advantages of this reduced-complexity Schnorr-Euchner searching strategy are three-fold. First of all, all the calculations are off-loaded to the SD's 1-st visit, where only combinations and comparisons are made when the SD visits the specific index v again. Secondly, no sorting algorithm is required to be invoked for ranking all the constellation points according to their PED increment values. Instead, the constellation points are visited in a zig-zag fashion, which is similar to the case of hard-decision-aided MSDSD conceived for DPSK in [127]. Thirdly, given a higher SNR and/or a higher *a priori* information, the SD may terminate sonner by visiting each index v at most twice. As a result, the reduced-complexity Schnorr-Euchner searching strategy portrayed in Fig. 8.12 may

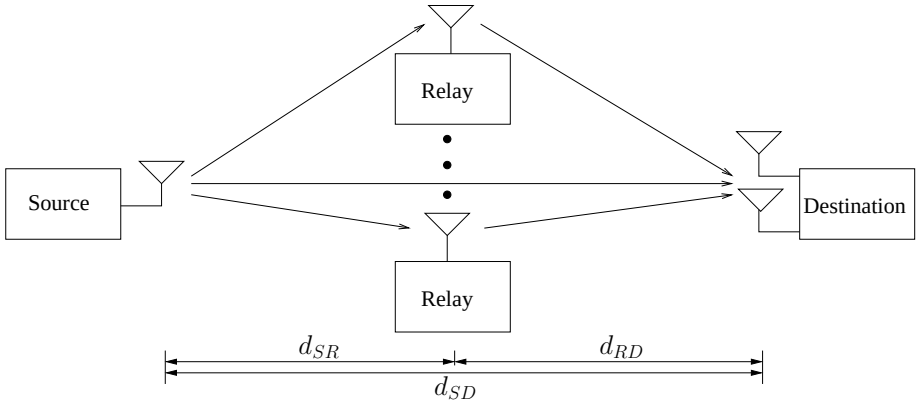

Figure 8.13: Schematics of a cooperative communication system.

visit a reduced number of constellation points, which is consistent with the motivation of the SD.

We leave it to our future work to further generalize the reduced-complexity Schnorr-Euchner searching strategy for the soft-decision-aided SD invoked by V-BLAST employing Square MQAM.

8.2.6 Reduced-Complexity Design Applied to Differential MIMO Schemes

In this report, we aim to apply the reduced-complexity design to the communication systems, which are are summarized from coherent to noncoherent, from uncoded to coded, and also from SISO/SIMO to MIMO. However, due to time and space limit, the differential MIMO schemes have to be left for future work. Many recently developed communication systems show growing interest for employing the Differential Space-Time Modulation (DSTM), which facilitates the signal processing in both the spatial and temporal dimensions, while the demanding requirement of accurate channel estimation is eliminated. For example, the cooperative communication systems [6, 367–369] opt to employ the single-element mobile stations to share their antennas, so that a Virtual Antenna Array (VAA) may be formed for MIMO transmission, where the distributed antennas typically experience uncorrelated fading. The schematics of a cooperative communication system is portrayed in Fig. 8.13. As a result, it becomes unrealistic for the relays and the destinations to estimate the channel of all VAA links, and hence the employment of DSTM may be perferred.

To elaborate a little further, the DSTM design starts with the following matrix-based differential encoding process:

$$\mathbf{S}_n = \begin{cases} \mathbf{S}_1, & n = 1 \\ \mathbf{X}_{n-1}\mathbf{S}_{n-1}, & n > 1 \end{cases}, \tag{8.30}$$

where the $(N_P \times N_P)$-element unitary matrix $\mathbf{X}_{n-1}$ carries the source information, while the $(N_P \times N_T)$-element transmission matrix $\mathbf{S}_n$ models the signal transmitted from the N_T transmit antennas over N_P symbol periods. The first DSTM scheme was proposed by Tarokh and Jafarkhani [370] in 1999, where the Differential STBC (DSTBC) based on the G2 STBC structure employing MPSK

signalling was conceived. More explicitly, the DSTBC in [370] proposed to employ the G2 STBC codeword of Eq. (6.54) for both the data-carrying matrix and the transmission matrix in Eq. (8.30), where the MPSK signalling can only be guaranteed for all the transmitted symbols in $\mathbf{S}_{n-1}$ and $\mathbf{S}_n$ because of the matrix-wise differential encoding of Eq. (8.30). In order to also retain the MPSK signalling for the data-carrying symbols in $\mathbf{X}_{n-1}$, Hughes [371] proposed the group code in 2000, where a throughput loss was induced. In 2001, Jafarkhani and Tarokh [372] further extend the DSTBC [370] to the case of employing multiple transmit antennas based on the general STBC structure of Sec. 6.3.1.3. Furthermore, the Differential LDC (DLDC) was proposed by Hassibi and Hochwald [138] in 2002, where the Cayley transform was invoked in order to guarantee that the data-carrying matrix $\mathbf{X}_{n-1}$ is always unitary. In 2003 and 2004, Hwang et al. [139] and Nam et al. [140] further proposed to employ QAM for the DSTBCs of [370] and [372], respectively. Moreover, Wang et al. [373] further suggested in 2005 that the high rate DLDCs may be generated by using gradient-ascend method. Oggier and Hassibi [374] suggested in 2007 that the high rate DLDCs may be constructed based on division algebra, so that the Cayley codes may be expressed in closed-form. As mentioned before, the DSTSK was proposed by Sugiura et al. [216] in 2010 together with the proposal of the STSK, while the DLDC's Cayley transformed was eliminated by our publication of [234] in 2011.

The noncoherent receivers conceived for SISO/SIMO schemes introduced in Chapter 3 have also been developed for the DSTM. More explicitly, the MSDD and the DFDD were firstly developed for the DSTM by Schober and Lampe [375] in 2002. Furthermore, Pauli and Lampe [376] proposed the MSDSD for DSTM employing MPSK in 2007. In 2011, the MSDSD for DSTBC employing MQAM was developed by our publication of [235], and then the reduced-complexity MSDSD conceived for DSTSK was proposed by our publication of [234]. Further research efforts for noncoherent DSTM detection may be deemed as three-fold. First of all, these aforementioned noncoherent receivers all rely on hard-bit decisions, and hence a thorough study on the the soft-decision-aided noncoherent detectors conceived for coded DSTM is still awaited for future efforts. Secondly, it was noted in [234,235] that owing to the matrix-based signal processing, the noncoherent DSTM detectors generally exhibit a higher complexity than their counterparts of noncoherent DPSK detectors. Therefore, a systematic reduced-complexity design is needed for the noncoherent DSTM detection. Thirdly, the recent development of massive MIMO [340, 341] demonstrated the interesting result that the linear MMSE MIMO detector may become near-optimum as the number of antennas employed grows substantially. As the accurate channel estimation may become difficult in massive MIMO systems, the employment of DSTM may become preferred. Against this background, one may predict that the optimum MSDD/MSDSD may become hardly affordable when a massive number of antennas are employed, and hence it is highly plausible that the DFDD, which is the equivalent of MMSE in noncoherent systems as demonstrated in Sec. 3.2.4 may become the preferred choice.

Bibliography

[1] J. K. Cavers, "An analysis of pilot symbol assisted modulation for Rayleigh fading channels," *IEEE Transactions on Vehicular Technology*, vol. 40, pp. 686–693, Nov. 1991.

[2] L. Hanzo, S. X. Ng, T. Keller, and W. Webb, *Quadrature Amplitude Modulation: From Basics to Adaptive Trellis-Coded, Turbo-Equalised and Space-Time Coded OFDM, CDMA and MC-CDMA Systems*. John Wiley & Sons, 2004.

[3] A. Goldsmith, *Wireless communications*. Cambridge University Press, 2005.

[4] J. G. Proakis, *Digital Communications*. New York: McGraw-Hill, 1995.

[5] B. Sklar, *Digital Communications*. Prentice-Hall, 1988.

[6] J. N. Laneman and G. W. Wornell, "Distributed space-time-coded protocols for exploiting cooperative diversity in wireless networks," *IEEE Transactions on Information Theory*, vol. 49, pp. 2415–2425, Oct. 2003.

[7] D. Divsalar and M. K. Simon, "Multiple-symbol differential detection of mpsk," *IEEE Transactions on Communications*, vol. 38, pp. 300–308, Mar. 1990.

[8] L. Hanzo, O. Alamri, M. El-Hajjar, and N. Wu, *Near-Capacity Multi-Functional MIMO Systems: Sphere-Packing, Iterative Detection and Cooperation*. John Wiley & Sons, May 2009.

[9] L. Hanzo, Y. Akhtman, L. Wang, and M. Jiang, *MIMO-OFDM for LTE, WiFi and WiMAX: Coherent versus Non-coherent and Cooperative Turbo Transceivers*. Wiley-IEEE Press, 2011.

[10] M. Damen, H. El-Gamal, and G. Caire, "On Maximum-Likelihood detection and the search for the closest lattice point," *IEEE Transactions on Information Theory*, vol. 49, pp. 2389–2402, Oct. 2003.

[11] E. Viterbo and J. Boutros, "A universal lattice code decoder for fading channels," *IEEE Transactions on Information Theory*, vol. 45, pp. 1639–1642, July 1999.

[12] E. Agrell, T. Eriksson, A. Vardy, and K. Zeger, "Closest point search in lattices," *IEEE Transactions on Information Theory*, vol. 48, pp. 2201–2214, Aug. 2002.

[13] M. Sellathurai and S. Haykin, "Turbo-BLAST for wireless communications: theory and experiments," *IEEE Transactions on Signal Processing*, vol. 50, pp. 2538–2546, Oct. 2002.

[14] A. J. Paulraj, D. A. Gore, R. U. Nabar, and H. Bolcskei, "An overview of MIMO communications - a key to gigabit wireless," *Proceedings of the IEEE*, vol. 92, pp. 198–218, Feb. 2004.

[15] D. Gore, R. W. Heath, and A. Paulraj, "On performance of the zero forcing receiver in presence of transmit correlation," in *Proceedings of IEEE International Symposium on Information Theory, 2002. (ISIT'02)*, 2002.

[16] D. Wubben, R. Bohnke, V. Kuhn, and K. D. Kammeyer, "MMSE extension of V-BLAST based on sorted QR decomposition," in *Proceedings of IEEE 58th Vehicular Technology Conference, 2003. (VTC'03-Fall)*, vol. 1, pp. 508–512, Oct. 2003.

[17] C. E. Shannon, "A mathematical theory of communication," *Bell Systems Technical Journal*, vol. 27, pp. 379–423, June 1948.

[18] R. W. Hamming, "Error detecting and error correcting codes," *Bell Systems Technical Journal*, vol. 29, no. 2, pp. 147–160, 1950.

[19] P. Elias, "Coding for noisy channels," *Proceedings of the Institute of Radio Engineers*, vol. 43, no. 3, pp. 356–356, 1955.

[20] A. Hocquenghem, "Codes correcteurs derreurs," *Chiffres*, vol. 2, pp. 147–156, Sept. 1959.

[21] R. C. Bose and D. K. Ray-Chaudhuri, "On a class of error correcting binary group codes," *Information and Control*, vol. 3, pp. 68–79, Mar. 1960.

[22] R. C. Bose and D. K. Ray-Chaudhuri, "Further results on error correcting binary group codes," *Information and Control*, vol. 3, pp. 279–290, Sept. 1960.

[23] A. J. Viterbi, "Error bounds for convolutional codes and an asymptotically optimum decoding algorithm," *IEEE Transactions on Information Theory*, vol. 13, pp. 260–269, Apr. 1967.

[24] G. D. Forney, "The Viterbi algorithm," *Proceedings of the IEEE*, vol. 61, pp. 268–278, Mar. 1973.

[25] J. K. Wolf, "Efficient Maximum Likelihood decoding of linear block codes using a Trellis," *IEEE Transactions on Information Theory*, vol. 24, pp. 76–80, Jan. 1978.

[26] L. Bahl, J. Cocke, F. Jelinek, and J. Raviv, "Optimal decoding of linear codes for minimizing symbol error rate," *IEEE Transactions on Information Theory*, vol. 20, pp. 284–287, Mar. 1974.

[27] W. Koch and A. Baier, "Optimum and sub-optimum detection of coded data disturbed by time-varying intersymbol interference," in *Proceedings of IEEE Global Telecommunications Conference (GLOBECOM'90)*, vol. 3, pp. 1679–1684, San Diego, USA, Dec. 1990.

[28] P. Robertson, E. Villebrun, and P. Hoeher, "A comparison of optimal and sub-optimal MAP decoding algorithms operating in the log domain," in *Proceedings of IEEE International Conference on Communications (ICC'95)*, vol. 2, pp. 1009–1013, Seattle, USA, June 1995.

[29] Y. Yasuda, K. Kashiki, and Y. Hirata, "High-rate punctured convolutional codes for soft decision Viterbi decoding," *IEEE Transactions on Communications*, vol. 32, pp. 315–319, Mar. 1984.

[30] G. D. Forney, *Concatenated Codes*. Cambridge: MIT press, 1966.

[31] P. Elias, "Error-free coding," *IRE Transactions on Information Theory*, vol. 4, pp. 29–37, Sept. 1954.

[32] A. Morello, G. Montorosi, and M. Visintin, "Convolutional and Trellis coded modulations concatenated with block codes for digital HDTV," in *Proceedings of International Workshop Digital Communications*, pp. 237–250, Tirennia, Italy, Sept. 1993.

[33] E. C. Posner, L. L. Rauch, and B. D. Madsen, "Voyager mission telecommunication firsts," *IEEE Communications Magazine*, vol. 28, pp. 22–27, Sept. 1990.

[34] G. Battail, M. Decouvelaere, and P. Godlewski, "Replication decoding," *IEEE Transactions on Information Theory*, vol. 25, pp. 332–345, May 1979.

[35] J. Hagenauer and P. Hoeher, "A Viterbi algorithm with soft-decision outputs and its applications," in *Proceedings of IEEE Global Telecommunications Conference (GLOBECOM'89)*, vol. 3, pp. 1680–1686, Dallas, USA, Nov. 1989.

[36] J. Lodge, P. Hoeher, and J. Hagenauer, "The decoding of multidimentional codes using separable MAP "filters"," in *Proceedings of 16th Biennial Symposium on Communications*, pp. 343–346, Queen's University, Kingston, Ontario Canada, May 1992.

[37] J. Lodge, R. Young, P. Hoeher, and J. Hagenauer, "Separable MAP "filters" for the decoding of product and concatenated codes," in *Proceedings of IEEE International Conference on Communications, 1993. (ICC'93)*, vol. 3, pp. 1740–1745, Geneva, May 1993.

[38] C. Berrou, A. Glavieux, and P. Thitimajshima, "Near Shannon limit error-correcting coding and decoding: Turbo-codes. 1," in *Proceedings of IEEE International Conference on Communications (ICC'93)*, vol. 2, pp. 1064–1070, Geneva, Switzerland, May 1993.

[39] C. Berrou and A. Glavieux, "Near optimum error correcting coding and decoding: Turbo-codes," *IEEE Transactions on Communications*, vol. 44, pp. 1261–1271, Oct. 1996.

[40] S. Benedetto, D. Divsalar, G. Montorsi, and F. Pollara, "Serial concatenation of interleaved codes: performance analysis, design, and iterative decoding," *IEEE Transactions on Information Theory*, vol. 44, pp. 909–926, May 1998.

[41] G. D. Forney, "Coset codes II: Binary lattices and related codes," *IEEE Transactions on Information Theory*, vol. 34, pp. 1152–1187, Sept. 1988.

[42] R. Pyndiah, A. Glavieux, A. Picart, and S. Jacq, "Near optimum decoding of product codes," in *Proceedings of IEEE Global Telecommunications Conference, 1994, (GLOBECOM '94)*, pp. 339–343, San Francisco, USA, Nov. 1994.

[43] R. M. Pyndiah, "Near-optimum decoding of product codes: block turbo codes," *IEEE Transactions on Communications*, vol. 46, pp. 1003–1010, Aug. 1998.

[44] J. Hagenauer, E. Offer, and L. Papke, "Iterative decoding of binary block and convolutional codes," *IEEE Transactions on Information Theory*, vol. 42, pp. 429–445, Mar. 1996.

[45] S. Benedetto and G. Montorsi, "Serial concatenation of block and convolutional codes," *Electronics Letters*, vol. 32, pp. 887–888, May 1996.

[46] R. G. Gallager, "Low-density parity-check codes," *IRE Transactions on Information Theory*, vol. 8, no. 1, pp. 21–28, 1962.

[47] D. J. C. MacKay and R. M. Neal, "Near Shannon limit performance of low density parity check codes," *Electronics Letters*, vol. 32, pp. 1645–, Aug. 1996.

[48] T. J. Richardson and R. L. Urbanke, "The capacity of low-density parity-check codes under message-passing decoding," *IEEE Transactions on Information Theory*, vol. 47, pp. 599–618, Feb. 2001.

[49] T. J. Richardson, M. A. Shokrollahi, and R. L. Urbanke, "Design of capacity-approaching irregular low-density parity-check codes," *IEEE Transactions on Information Theory*, vol. 47, pp. 619–637, Feb. 2001.

[50] G. Ungerboeck, "Channel coding with multilevel/phase signals," *IEEE Transactions on Information Theory*, vol. 28, pp. 55–67, Jan. 1982.

[51] P. Mecklenburg, W. Pehlert, and D. Sullivan, "Correction of errors in multilevel Gray coded data," *IEEE Transactions on Information Theory*, vol. 19, pp. 336–340, May 1973.

[52] H. Imai and S. Hirakawa, "A new multilevel coding method using error-correcting codes," *IEEE Transactions on Information Theory*, vol. 23, pp. 371–377, May 1977.

[53] A. R. Calderbank and N. J. A. Sloane, "Four-dimensional modulation with an eight-state trellis code," *AT&T Technical Journal*, vol. 64, pp. 1005–1018, May 1985.

[54] A. R. Calderbank and N. Sloane, "New trellis codes based on lattices and cosets," *IEEE Transactions on Information Theory*, vol. 33, pp. 177–195, Mar. 1987.

[55] L. F. Wei, "Trellis-coded modulation with multidimensional constellations," *IEEE Transactions on Information Theory*, vol. 33, pp. 483–501, July 1987.

[56] G. D. Forney, R. G. Gallager, G. Lang, F. M. Longstaff, and S. U. Qureshi, "Efficient modulation for band-limited channels," *IEEE Journal on Selected Areas in Communications*, vol. 2, pp. 632–647, Sept. 1984.

[57] G. J. Pottie and D. P. Taylor, "Multilevel codes based on partitioning," *IEEE Transactions on Information Theory*, vol. 35, pp. 87–98, Jan. 1989.

[58] A. R. Calderbank, "Multilevel codes and multistage decoding," *IEEE Transactions on Communications*, vol. 37, pp. 222–229, Mar. 1989.

[59] S. I. Sayegh, "A class of optimum block codes in signal space," *IEEE Transactions on Communications*, vol. 34, pp. 1043–1045, Oct. 1986.

[60] D. Divsalar and M. K. Simon, "The design of trellis coded MPSK for fading channels: performance criteria," *IEEE Transactions on Communications*, vol. 36, pp. 1004–1012, Sept. 1988.

[61] M. K. Simon and D. Divsalar, "The performance of trellis coded multilevel DPSK on a fading mobile satellite channel," *IEEE Transactions on Vehicular Technology*, vol. 37, pp. 78–91, May 1988.

[62] N. Seshadri and C. E. W. Sundberg, "Multilevel trellis coded modulations for the rayleigh fading channel," *IEEE Transactions on Communications*, vol. 41, pp. 1300–1310, Sept. 1993.

[63] E. Zehavi, "8-PSK trellis codes for a Rayleigh channel," *IEEE Transactions onCommunications*, vol. 40, pp. 873–884, May 1992.

[64] G. Caire, G. Taricco, and E. Biglieri, "Bit-interleaved coded modulation," *IEEE Transactions on Information Theory*, vol. 44, pp. 927–946, May 1998.

[65] X. Li and J. A. Ritcey, "Bit-interleaved coded modulation with iterative decoding," *IEEE Communications Letters*, vol. 1, pp. 169–171, Nov. 1997.

[66] X. Li and J. A. Ritcey, "Trellis-coded modulation with bit interleaving and iterative decoding," *IEEE Journal on Selected Areas in Communications*, vol. 17, pp. 715–724, Apr. 1999.

[67] X. Li and J. A. Ritcey, "Bit-interleaved coded modulation with iterative decoding," in *Proceedings of IEEE International Conference on Communications, 1999, (ICC'99)*, vol. 2, pp. 858–863, Vancouver, Canada, June 1999.

[68] X. Li, A. Chindapol, and J. A. Ritcey, "Bit-interleaved coded modulation with iterative decoding and 8-PSK signaling," *IEEE Transactions on Communications*, vol. 50, pp. 1250–1257, Aug. 2002.

[69] J. Hagenauer, "Source-controlled channel decoding," *IEEE Transactions on Communications*, vol. 43, pp. 2449–2457, Sept. 1995.

[70] C. Douillard, M. Jezequel, C. Berrou, D. Electronique, A. Picart, P. Didier, and A. Glavieux, "Iterative correction of intersymbol interference: Turbo equalization," *European transactions on telecommunications*, vol. 6, no. 5, pp. 507–511, 1995.

[71] M. Tuchler, R. Koetter, and A. C. Singer, "Turbo equalization: principles and new results," *IEEE Transactions on Communications*, vol. 50, pp. 754–767, May 2002.

[72] M. Tuchler, A. C. Singer, and R. Koetter, "Minimum mean squared error equalization using a priori information," *IEEE Transactions on Signal Processing*, vol. 50, pp. 673–683, Mar. 2002.

[73] M. Moher, "An iterative multiuser decoder for near-capacity communications," *IEEE Transactions on Communications*, vol. 46, pp. 870–880, July 1998.

[74] M. C. Reed, C. B. Schlegel, P. D. Alexander, and J. A. Asenstorfer, "Iterative multiuser detection for CDMA with FEC: near-single-user performance," *IEEE Transactions on Communications*, vol. 46, pp. 1693–1699, Dec. 1998.

[75] X. Wang and H. Poor, "Iterative (turbo) soft interference cancellation and decoding for coded CDMA," *IEEE Transactions on Communications*, vol. 47, pp. 1046–1061, July 1999.

[76] M. L. Honig, G. K. Woodward, and Y. Sun, "Adaptive iterative multiuser decision feedback detection," *IEEE Transactions on Wireless Communications*, vol. 3, pp. 477–485, Mar. 2004.

[77] M. Sellathurai and S. Haykin, "Turbo-BLAST: performance evaluation in correlated Rayleigh-fading environment," *IEEE Journal on Selected Areas in Communications*, vol. 21, pp. 340–349, Apr. 2003.

[78] C. Studer, S. Fateh, and D. Seethaler, "ASIC implementation of soft-input soft-output MIMO detection using MMSE parallel interference cancellation," *IEEE Journal of Solid-State Circuits*, vol. 46, pp. 1754–1765, July 2011.

[79] P. Robertson and T. Worz, "Bandwidth-efficient turbo trellis-coded modulation using punctured component codes," *IEEE Journal on Selected Areas in Communications*, vol. 16, pp. 206–218, Feb. 1998.

[80] J. Hagenauer, "The turbo principle: Tutorial introduction and state of the art," in *Proceedings of International Symposium on Turbo Codes and Related Topics*, 1997.

[81] M. Moher, "Decoding via cross-entropy minimization," in *Proceedings of IEEE Global Telecommunications Conference, 1993, (GLOBECOM'93)*, pp. 809–813 vol.2, Houston, USA, Nov. 1993.

[82] M. Moher and T. A. Gulliver, "Cross-entropy and iterative decoding," *IEEE Transactions on Information Theory*, vol. 44, pp. 3097–3104, Nov. 1998.

[83] S. ten Brink, "Convergence of iterative decoding," *Electronics Letters*, vol. 35, pp. 806–808, May 1999.

[84] S. Y. Chung, T. J. Richardson, and R. L. Urbanke, "Analysis of sum-product decoding of low-density parity-check codes using a Gaussian approximation," *IEEE Transactions on Information Theory*, vol. 47, pp. 657–670, Feb. 2001.

[85] H. El-Gamal and A. R. Hammons, "Analyzing the turbo decoder using the Gaussian approximation," *IEEE Transactions on Information Theory*, vol. 47, pp. 671–686, Feb. 2001.

[86] M. Tuchler, "Design of serially concatenated systems depending on the block length," *IEEE Transactions on Communications*, vol. 52, pp. 209–218, Feb. 2004.

[87] S. ten Brink, "Iterative decoding trajectories of parallel concatenated codes," in *Proceedings of the 3rd IEEE/ITG Conference on Source and Channel Coding*, pp. 75–80, Jan. 2000.

[88] S. ten Brink, "Convergence behavior of iteratively decoded parallel concatenated codes," *IEEE Transactions on Communications*, vol. 49, pp. 1727–1737, Oct. 2001.

[89] I. Land, P. Hoeher, and S. Gligorevic, "Computation of symbol-wise mutual information in transmission systems with log APP decoders and application to EXIT charts," in *Proceedings of International ITG Conference on Source and Channel Coding*, pp. 195–202, 2004.

[90] J. Kliewer, S. X. Ng, and L. Hanzo, "Efficient computation of EXIT functions for nonbinary iterative decoding," *IEEE Transactions on Communications*, vol. 54, pp. 2133–2136, Dec. 2006.

[91] A. Ashikhmin, G. Kramer, and S. ten Brink, "Extrinsic information transfer functions: model and erasure channel properties," *IEEE Transactions on Information Theory*, vol. 50, no. 11, pp. 2657–2673, 2004.

[92] L. Hanzo, R. G. Maunder, J. Wang, and L. Yang, *Near-Capacity Variable-Length Coding: Regular and EXIT-Chart-Aided Irregular Designs*. John Wiley & Sons, 2011.

[93] D. Divsalar, S. Dolinar, and F. Pollara, "Serial concatenated Trellis coded modulation with rate-1 inner code," in *Proceedings of IEEE Global Telecommunications Conference (GLOBECOM'00)*, vol. 2, pp. 777–782, San Francisco, USA, Nov. 2000.

[94] M. Medard, "The effect upon channel capacity in wireless communications of perfect and imperfect knowledge of the channel," *IEEE Transactions on Information Theory*, vol. 46, pp. 933–946, May 2000.

[95] S. Adireddy, T. Lang, and H. Viswanathan, "Optimal placement of training for frequency-selective block-fading channels," *IEEE Transactions on Information Theory*, vol. 48, pp. 2338–2353, Aug. 2002.

[96] T. Yoo and A. Goldsmith, "Capacity and power allocation for fading MIMO channels with channel estimation error," *IEEE Transactions on Information Theory*, vol. 52, pp. 2203–2214, May 2006.

[97] B. Hassibi and B. M. Hochwald, "How much training is needed in multiple-antenna wireless links?," *IEEE Transactions on Information Theory*, vol. 49, pp. 951–963, Apr. 2003.

[98] E. D. Carvalho and D. T. M. Slock, "Cramer-Rao bounds for semi-blind, blind and training sequence based channel estimation," in *Proceedings of First IEEE Signal Processing Workshop on Signal Processing Advances in Wireless Communications*, pp. 129–132, Paris, France, Apr. 1997.

[99] A. Vosoughi and A. Scaglione, "Everything you always wanted to know about training: guidelines derived using the affine precoding framework and the CRB," *IEEE Transactions on Signal Processing*, vol. 54, pp. 940–954, Mar. 2006.

[100] J. P. McGeehan and A. J. Bateman, "Phase-locked Transparent Tone-In-Band (TTIB): A new spectrum configuration particularly suited to the transmission of data over SSB mobile radio networks," *IEEE Transactions on Communications*, vol. 32, pp. 81–87, Jan. 1984.

[101] M. L. Moher and J. H. Lodge, "TCMP-a modulation and coding strategy for Rician fading channels," *IEEE Journal on Selected Areas in Communications*, vol. 7, pp. 1347–1355, Dec. 1989.

[102] T. Kailath, "Correlation detection of signals perturbed by a random channel," *IRE Transactions on Information Theory*, vol. 6, pp. 361–366, June 1960.

[103] T. Kailath, "A general likelihood-ratio formula for random signals in gaussian noise," *IEEE Transactions on Information Theory*, vol. 15, pp. 350–361, May 1969.

[104] G. Forney, "Maximum-likelihood sequence estimation of digital sequences in the presence of intersymbol interference," *IEEE Transactions on Information Theory*, vol. 18, pp. 363–378, May 1972.

[105] R. Morley and D. Snyder, "Maximum likelihood sequence estimation for randomly dispersive channels," *IEEE Transactions on Communications*, vol. 27, pp. 833–839, June 1979.

[106] J. G. Lawton, "Theoretical error rates of differentially coherent binary and kineplex data transmission systems," *Proceedings of the Institute of Radio Engineers*, vol. 47, no. 2, pp. 333–334, 1959.

[107] J. G. Lawton, "Investigation of digital data communication systems," *Cornell Aeronautical Lab.*, 1961.

[108] C. R. Cahn, "Performance of digital phase-modulation communication systems," *IRE Transactions on Communications Systems*, vol. 7, no. 1, pp. 3–6, 1959.

[109] P. Bello and B. D. Nelin, "The influence of fading spectrum on the binary error probabilites of incoherent and differentially coherent matched filter recievers," *IRE Transactions on Communications Systems*, vol. 10, pp. 160–168, June 1962.

[110] T. Masamura, S. Samejima, Y. Morihiro, and H. Fuketa, "Differential detection of MSK with nonredundant error correction," *IEEE Transactions on Communications*, vol. 27, pp. 912–918, June 1979.

[111] S. Samejima, K. Enomoto, and Y. Watanabe, "Differential PSK system with nonredundant error correction," *IEEE Journal on Selected Areas in Communications*, vol. 1, pp. 74–81, Jan. 1983.

[112] S. G. Wilson, J. Freebersyser, and C. Marshall, "Multi-symbol detection of M-DPSK," in *Proceedings of IEEE Global Telecommunications Conference and Exhibition (GLOBECOM'89)*, pp. 1692–1697 vol.3, Dallas, USA, Nov. 1989.

[113] P. Ho and D. Fung, "Error performance of multiple-symbol differential detection of PSK signals transmitted over correlated Rayleigh fading channels," *IEEE Transactions on Communications*, vol. 40, pp. 1566 –1569, Oct. 1992.

[114] D. Divsalar and M. K. Simon, "Maximum-likelihood differential detection of uncoded and Trellis coded amplitude phase modulation over AWGN and fading channels-metrics and performance," *IEEE Transactions on Communications*, vol. 42, pp. 76 –89, Jan. 1994.

[115] K. Mackenthun, "A fast algorithm for multiple-symbol differential detection of MPSK," *IEEE Transactions on Communications*, vol. 42, no. 234, pp. 1471–1474, 1994.

[116] R. R. Chen, R. Koetter, U. Madhow, and D. Agrawal, "Joint noncoherent demodulation and decoding for the block fading channel: a practical framework for approaching Shannon capacity," *IEEE Transactions on Communications*, vol. 51, pp. 1676–1689, Oct. 2003.

[117] H. Leib and S. Pasupathy, "The phase of a vector perturbed by Gaussian noise and differentially coherent receivers," *IEEE Transactions on Information Theory*, vol. 34, pp. 1491–1501, Nov. 1988.

[118] F. Edbauer, "Bit error rate of binary and quaternary DPSK signals with multiple differential feedback detection," *IEEE Transactions on Communications*, vol. 40, pp. 457–460, Mar. 1992.

[119] F. Adachi and M. Sawahashi, "Decision feedback multiple-symbol differential detection for M-ary DPSK," *Electronics Letters*, vol. 29, pp. 1385–1387, July 1993.

[120] H. Leib, "Data-aided noncoherent demodulation of DPSK," *IEEE Transactions on Communications*, vol. 43, no. 234, pp. 722–725, 1995.

[121] R. Schober, W. H. Gerstacker, and J. B. Huber, "Decision-feedback differential detection of MDPSK for flat Rayleigh fading channels," *IEEE Transactions on Communications*, vol. 47, pp. 1025–1035, July 1999.

[122] L. Lampe and R. Schober, "Iterative decision-feedback differential demodulation of bit-interleaved coded MDPSK for flat Rayleigh fading channels," *IEEE Transactions on Communications*, vol. 49, no. 7, pp. 1176–1184, 2001.

[123] A. Svensson, "Coherent detector based on linear prediction and decision feedback for DQPSK," *Electronics Letters*, vol. 30, pp. 1642–1643, Sept. 1994.

[124] L. Bin and P. Ho, "Data-aided linear prediction receiver for coherent DPSK and CPM transmitted over Rayleigh flat-fading channels," *IEEE Transactions on Vehicular Technology*, vol. 48, pp. 1229–1236, July 1999.

[125] P. Hoeher and J. Lodge, ""Turbo DPSK": iterative differential PSK demodulation and channel decoding," *IEEE Transactions on Communications*, vol. 47, pp. 837–843, June 1999.

[126] R. Schober and W. H. Gerstacker, "Decision-feedback differential detection based on linear prediction for MDPSK signals transmitted over Ricean fading channels," *IEEE Journal on Selected Areas in Communications*, vol. 18, pp. 391–402, Mar. 2000.

[127] L. Lampe, R. Schober, V. Pauli, and C. Windpassinger, "Multiple-symbol differential sphere decoding," *IEEE Transactions on Communications*, vol. 53, pp. 1981 – 1985, Dec. 2005.

[128] F. Adachi and M. Sawahashi, "Viterbi-decoding differential detection of DPSK," *Electronics Letters*, vol. 28, pp. 2196–2198, Nov. 1992.

[129] G. M. Vitetta and D. P. Taylor, "Viterbi decoding of differentially encoded PSK signals transmitted over Rayleigh frequency-flat fading channels," *IEEE Transactions on Communications*, vol. 43, pp. 1256–1259, Feb. 1995.

[130] F. Adachi, "Reduced state transition Viterbi differential detection of M-ary DPSK signals," *Electronics Letters*, vol. 32, pp. 1064–1066, June 1996.

[131] G. Colavolpe and R. Raheli, "Noncoherent sequence detection," *IEEE Transactions on Communications*, vol. 47, pp. 1376–1385, Sept. 1999.

[132] V. Pauli, L. Lampe, and R. Schober, ""Turbo DPSK" using soft multiple-symbol differential sphere decoding," *IEEE Transactions on Information Theory*, vol. 52, pp. 1385–1398, Apr. 2006.

[133] M. K. Simon and J. Smith, "Carrier synchronization and detection of QASK signal sets," *IEEE Transactions on Communications*, vol. 22, pp. 98–106, Feb. 1974.

[134] W. Weber, "Differential encoding for multiple amplitude and phase shift keying systems," *IEEE Transactions on Communications*, vol. 26, pp. 385–391, Mar. 1978.

[135] M. K. Simon, G. K. Huth, and A. Polydoros, "Differentially coherent detection of QASK for frequency-hopping systems–part I: Performance in the presence of a Gaussian noise environment," *IEEE Transactions on Communications*, vol. 30, pp. 158–164, Jan. 1982.

[136] L. Lampe and R. Schober, "Low-complexity iterative demodulation for noncoherent coded transmission over Ricean-fading channels," *IEEE Transactions on Vehicular Technology*, vol. 50, pp. 1481–1496, Nov. 2001.

[137] X. G. Xia, "Differentially en/decoded orthogonal space-time block codes with APSK signals," *IEEE Communications Letters*, vol. 6, pp. 150–152, Apr. 2002.

[138] B. Hassibi and B. M. Hochwald, "Cayley differential unitary space-time codes," *IEEE Transactions on Information Theory*, vol. 48, pp. 1485–1503, June 2002.

[139] C.-S. Hwang, S. H. Nam, J. Chung, and V. Tarokh, "Differential space time block codes using nonconstant modulus constellations," *IEEE Transactions on Signal Processing*, vol. 51, pp. 2955–2964, Nov. 2003.

[140] S. H. Nam, C. S. Hwang, J. Chung, and V. Tarokh, "Differential space time block codes using QAM for four transmit antennas," in *Proceedings of IEEE International Conference on Communications (ICC'04)*, vol. 2, pp. 952–956, July 2004.

[141] S. Sugiura, C. Xu, S. X. Ng, and L. Hanzo, "Reduced-complexity coherent versus noncoherent QAM-aided space-time shift keying," *IEEE Transactions on Communications*, vol. 59, pp. 3090–3101, Nov. 2011.

[142] W. T. Webb, L. Hanzo, and R. Steele, "Bandwidth efficient QAM schemes for Rayleigh fading channels," *IEE Proceedings I, Communications, Speech and Vision*, vol. 138, pp. 169–175, June 1991.

[143] F. Adachi and M. Sawahashi, "Performance analysis of various 16 level modulation schemes under Rayleigh fading," *Electronics Letters*, vol. 28, pp. 1579–1581, Aug. 1992.

[144] Y. C. Chow, A. R. Nix, and J. P. McGeehan, "Analysis of 16-APSK modulation in AWGN and Rayleigh fading channel," *Electronics Letters*, vol. 28, pp. 1608–1610, Aug. 1992.

[145] H. Rohling and V. Engels, "Differential amplitude phase shift keying (DAPSK)-a new modulation method for DTVB," in *Proceedings of IET International Broadcasting Convention, 1995, (IBC 95).*, pp. 102–108, Sept. 1995.

[146] W. C. Dam and D. P. Taylor, "An adaptive maximum likelihood receiver for correlated Rayleigh-fading channels," *IEEE Transactions on Communications*, vol. 42, pp. 2684–2692, Sept. 1994.

[147] G. M. Vitetta and D. P. Taylor, "Maximum likelihood decoding of uncoded and coded PSK signal sequences transmitted over Rayleigh flat-fading channels," *IEEE Transactions on Communications*, vol. 43, pp. 2750–2758, Nov. 1995.

[148] Y. C. Chow, A. R. Nix, and J. P. McGeehan, "Diversity improvement for 16-DAPSK in Rayleigh fading channel," *Electronics Letters*, vol. 29, pp. 387–389, Feb. 1993.

[149] C. Chung, "Differentially amplitude and phase-encoded QAM for the correlated Rayleigh-fading channel with diversity reception," *IEEE Transactions on Communications*, vol. 45, pp. 309–321, Mar. 1997.

[150] F. Adachi and M. Sawahashi, "Decision feedback differential detection of differentially encoded 16APSK signals," *IEEE Transactions on Communications*, vol. 44, pp. 416–418, Apr. 1996.

[151] R. Y. Wei and M. C. Lin, "Modified decision feedback differential detection for differentially encoded 16APSK signals," *Electronics Letters*, vol. 34, pp. 336–337, Feb. 1998.

[152] R. Schober, W. H. Gerstacker, and J. B. Huber, "Decision-feedback differential detection scheme for 16-DAPSK," *Electronics Letters*, vol. 34, pp. 1812–1813, Sept. 1998.

[153] W. H. Gerstacker, R. Schober, and J. B. Huber, "Decision-feedback differential detection for 16DAPSK transmitted over Rician fading channels," in *Proceedings of IEEE VTS 50th Vehicular Technology Conference (VTC'99-Fall).*, vol. 5, pp. 2515–2519, Amsterdam, Netherlands, Sept 1999.

[154] R. Schober, W. H. Gerstacker, and J. B. Huber, "Decision-feedback differential detection based on linear prediction for 16DAPSK signals transmitted over flat Ricean fading channels," *IEEE Transactions on Communications*, vol. 49, pp. 1339–1342, Aug. 2001.

[155] T. May, H. Rohling, and V. Engels, "Performance analysis of Viterbi decoding for 64-DAPSK and 64-QAM modulated OFDM signals," *IEEE Transactions on Communications*, vol. 46, pp. 182–190, Feb. 1998.

[156] R. F. H. Fischer, L. Lampe, and S. H. Muller-Weinfurtner, "Coded modulation for noncoherent reception with application to OFDM," *IEEE Transactions on Vehicular Technology*, vol. 50, pp. 910–919, July 2001.

[157] K. Ishibashi, H. Ochiai, and R. Kohno, "Low-complexity bit-interleaved coded DAPSK for Rayleigh-fading channels," *IEEE Journal on Selected Areas in Communications*, vol. 23, pp. 1728–1738, Sept. 2005.

[158] D. Liang, S. X. Ng, and L. Hanzo, "Soft-decision star-QAM aided BICM-ID," *IEEE Signal Processing Letters*, vol. 18, pp. 169–172, Jan. 2011.

[159] C. Xu, D. Liang, S. X. Ng, and L. Hanzo, "Reduced-complexity noncoherent soft-decision-aided DAPSK dispensing with channel estimation," *IEEE Transactions on Vehicular Technology*, vol. 62, pp. 2633–2643, Feb. 2013.

[160] L. Wang and L. Hanzo, "Low-complexity near-optimum multiple-symbol differential detection of DAPSK based on iterative amplitude/phase processing," *IEEE Transactions on Vehicular Technology*, vol. 61, pp. 894–900, Jan. 2012.

[161] A. J. Paulraj and T. Kailath, "Increasing capacity in wireless broadcast systems using distributed transmission/directional reception," *U.S. Patent No. 5,345,599. 6*, Sept. 1994.

[162] G. J. Foschini, "Layered space-time architecture for wireless communication in a fading environment when using multi-element antennas," *Bell Labs Technical Journal*, vol. 1, no. 2, pp. 41–59, 1996.

[163] H. El-Gamal and A. R. Hammons, "A new approach to layered space-time coding and signal processing," *IEEE Transactions on Information Theory*, vol. 47, pp. 2321–2334, Sept. 2001.

[164] P. W. Wolniansky, G. J. Foschini, G. D. Golden, and R. Valenzuela, "V-BLAST: an architecture for realizing very high data rates over the rich-scattering wireless channel," in *Proceedings of International Symposium on Signals, Systems, and Electronics, 1998. (ISSSE'98)*, pp. 295–300, Pisa, Italy, Sept. 1998.

[165] G. J. Foschini and M. J. Gans, "On limits of wireless communications in a fading environment when using multiple antennas," *Wireless Personal Communications*, vol. 6, no. 3, pp. 311–335, 1998.

[166] E. Telatar, "Capacity of multiantenna gaussian channels," *European transactions on telecommunications*, vol. 10, no. 6, pp. 585–595, 1999.

[167] Y. C. Yoon, R. Kohno, and H. Imai, "A spread-spectrum multiaccess system with cochannel interference cancellation for multipath fading channels," *IEEE Journal on Selected Areas in Communications*, vol. 11, pp. 1067–1075, Sept. 1993.

[168] A. L. C. Hui and L. Khaled, "Successive interference cancellation for multiuser asynchronous DS/CDMA detectors in multipath fading links," *IEEE Transactions on Communications*, vol. 46, pp. 384–391, Mar. 1998.

[169] C. A. Belfiore and J. H. Park, "Decision feedback equalization," *Proceedings of the IEEE*, vol. 67, pp. 1143–1156, Aug. 1979.

[170] J. Salz, "Optimum mean-square decision feedback equalization," *Bell System Technical Journal*, vol. 52, pp. 1341–1373, Oct. 1973.

[171] D. D. Falconer and G. J. Foschini, "Theory of minimum mean-square-error QAM systems employing decision feedback equalization," *Bell System Technical Journal*, vol. 52, pp. 1821–1849, Dec. 1973.

[172] O. Damen, A. Chkeif, and J. C. Belfiore, "Lattice code decoder for space-time codes," *IEEE Communications Letters*, vol. 4, pp. 161–163, May 2000.

[173] B. M. Hochwald and S. ten Brink, "Achieving near-capacity on a multiple-antenna channel," *IEEE Transactions on Communications*, vol. 51, pp. 389–399, Mar. 2003.

[174] H. Vikalo, B. Hassibi, and T. Kailath, "Iterative decoding for MIMO channels via modified sphere decoding," *IEEE Transactions on Wireless Communications*, vol. 3, pp. 2299–2311, Jan. 2004.

[175] C. Studer, A. Burg, and H. Bolcskei, "Soft-output sphere decoding: algorithms and VLSI implementation," *IEEE Journal on Selected Areas in Communications*, vol. 26, pp. 290–300, Feb. 2008.

[176] C. Studer and H. Bolcskei, "Soft-input soft-output single tree-search sphere decoding," *IEEE Transactions on Information Theory*, vol. 56, pp. 4827–4842, Sept. 2010.

[177] S. M. Alamouti, "A simple transmit diversity technique for wireless communications," *IEEE Journal on Selected Areas in Communications*, vol. 16, pp. 1451–1458, Oct. 1998.

[178] V. Tarokh, H. Jafarkhani, and A. R. Calderbank, "Space-time block codes from orthogonal designs," *IEEE Transactions on Information Theory*, vol. 45, pp. 1456–1467, July 1999.

[179] A. V. Geramita and J. Seberry, *Orthogonal Designs: Quadratic Forms and Hadamard Matrices*. Marcel Dekker, 1979.

[180] J. Radon, "Lineare scharen orthogonaler matrizen," *Abhandlungen aus dem Mathematischen Seminar der Universitat Hamburg*, vol. 1, Springer Berlin/Heidelberg, 1922.

[181] G. Ganesan and P. Stoica, "Space-time diversity using orthogonal and amicable orthogonal designs," *Wireless Personal Communications*, vol. 18, no. 2, pp. 165–178, 2001.

[182] G. Ganesan and P. Stoica, "Space-time block codes: a maximum SNR approach," *IEEE Transactions on Information Theory*, vol. 47, pp. 1650–1656, May 2001.

[183] G. Ganesan and P. Stoica, "Differential modulation using space-time block codes," in *Proceedings of The Thirty-Fifth Asilomar Conference on Signals, Systems and Computers*, vol. 1, pp. 236–240, Pacific Grove, USA, Nov. 2001.

[184] S. Sandhu and A. Paulraj, "Space-time block codes: a capacity perspective," *IEEE Communications Letters*, vol. 4, pp. 384–386, Dec. 2000.

[185] L. Zheng and D. N. C. Tse, "Diversity and multiplexing: a fundamental tradeoff in multiple-antenna channels," *IEEE Transactions on Information Theory*, vol. 49, pp. 1073–1096, May 2003.

[186] H. Jafarkhani, "A quasi-orthogonal space-time block code," *IEEE Transactions on Communications*, vol. 49, pp. 1–4, Jan. 2001.

[187] C. B. Papadias and G. J. Foschini, "Capacity-approaching space-time codes for systems employing four transmitter antennas," *IEEE Transactions on Information Theory*, vol. 49, pp. 726–732, Mar. 2003.

[188] R. W. Heath and A. J. Paulraj, "Linear dispersion codes for MIMO systems based on frame theory," *IEEE Transactions on Signal Processing*, vol. 50, pp. 2429–2441, Oct. 2002.

[189] B. Hassibi and B. M. Hochwald, "High-rate codes that are linear in space and time," *IEEE Transactions on Information Theory*, vol. 48, pp. 1804–1824, July 2002.

[190] B. A. Sethuraman, B. S. Rajan, and V. Shashidhar, "Full-diversity, high-rate space-time block codes from division algebras," *IEEE Transactions on Information Theory*, vol. 49, pp. 2596–2616, Oct. 2003.

[191] P. Elia, K. R. Kumar, S. A. Pawar, P. V. Kumar, and H. F. Lu, "Explicit space-time codes achieving the diversity-multiplexing gain tradeoff," *IEEE Transactions on Information Theory*, vol. 52, pp. 3869–3884, Sept. 2006.

[192] M. O. Damen, A. Tewfik, and J. C. Belflore, "A construction of a space-time code based on number theory," *IEEE Transactions on Information Theory*, vol. 48, pp. 753–760, Mar. 2002.

[193] H. E. Gamal and M. O. Damen, "Universal space-time coding," *IEEE Transactions on Information Theory*, vol. 49, pp. 1097–1119, May 2003.

[194] F. Oggier, G. Rekaya, J. C. Belfiore, and E. Viterbo, "Perfect space-time block codes," *IEEE Transactions on Information Theory*, vol. 52, pp. 3885–3902, Sept. 2006.

[195] S. Song, Y. Yang, Q. Xionq, K. Xie, B. J. Jeong, and B. Jiao, "A channel hopping technique I: theoretical studies on band efficiency and capacity," in *Proceedings of 2004 International Conference on Communications, Circuits and Systems, 2004. (ICCCAS'04)*, vol. 1, pp. 229–233, Chengdu, China, June 2004.

[196] Y. A. Chau and S. H. Yu, "Space modulation on wireless fading channels," in *Proceedings of IEEE VTS 54th Vehicular Technology Conference, 2001. (VTC'01 Fall)*, vol. 3, pp. 1668–1671, Atlantic City, USA, Oct. 2001.

[197] R. Y. Mesleh, H. Haas, S. Sinanovic, C. W. Ahn, and S. Yun, "Spatial modulation," *IEEE Transactions on Vehicular Technology*, vol. 57, pp. 2228–2241, July 2008.

[198] J. Jeganathan, A. Ghrayeb, and L. Szczecinski, "Spatial modulation: optimal detection and performance analysis," *IEEE Communications Letters*, vol. 12, pp. 545–547, Aug. 2008.

[199] J. Jeganathan, A. Ghrayeb, and L. Szczecinski, "Generalized space shift keying modulation for MIMO channels," in *Proceedings of IEEE 19th International Symposium on Personal, Indoor and Mobile Radio Communications, 2008. (PIMRC 2008)*, Cannes, France, Sept. 2008.

[200] J. Jeganathan, A. Ghrayeb, L. Szczecinski, and A. Ceron, "Space shift keying modulation for MIMO channels," *IEEE Transactions on Wireless Communications*, vol. 8, pp. 3692–3703, July 2009.

[201] Y. Yang and B. Jiao, "Information-guided channel-hopping for high data rate wireless communication," *IEEE Communications Letters*, vol. 12, pp. 225–227, Apr. 2008.

[202] C. Xu, S. Sugiura, S. X. Ng, and L. Hanzo, "Reduced-complexity soft-decision aided space-time shift keying," *IEEE Signal Processing Letters*, vol. 18, pp. 547–550, Oct. 2011.

[203] C. Xu, S. Sugiura, S. X. Ng, and L. Hanzo, "Spatial modulation and space-time shift keying: Optimal performance at a reduced detection complexity," *IEEE Transactions on Communications*, vol. 61, pp. 206–216, Feb. 2013.

[204] R. Rajashekar, K. V. S. Hari, and L. Hanzo, "Reduced-complexity ML detection and capacity-optimized training for spatial modulation systems," *IEEE Transactions on Communications*, vol. 62, pp. 112–125, Jan. 2014.

[205] M. Guo, C. Jia, and Y. Shen, "Detection algorithm for spatial modulation system under unconstrained channel," in *Proceedings of 2010 12th IEEE International Conference on Communication Technology (ICCT)*, pp. 458–461, Nanjing, China, Nov. 2010.

[206] N. R. Naidoo, H. J. Xu, and T. A.-M. Quazi, "Spatial modulation: optimal detector asymptotic performance and multiple-stage detection," *IET Communications*, vol. 5, pp. 1368–1376, July 2011.

[207] J. Wang, S. Jia, and J. Song, "Signal vector based detection scheme for spatial modulation," *IEEE Communications Letters*, vol. 16, pp. 19–21, Jan. 2012.

[208] J. Zheng, "Signal vector based list detection for spatial modulation," *IEEE Wireless Communications Letters*, vol. 1, pp. 265–267, Aug. 2012.

[209] P. Yang, Y. Xiao, L. Li, Q. Tang, and S. Li, "An improved matched-filter based detection algorithm for space-time shift keying systems," *IEEE Signal Processing Letters*, vol. 19, pp. 271–274, May 2012.

[210] Q. Tang, Y. Xiao, P. Yang, Q. Yu, and S. Li, "A new low-complexity near-ML detection algorithm for spatial modulation," *IEEE Wireless Communications Letters*, vol. 2, pp. 90–93, Feb. 2013.

[211] A. Younis, M. D. Renzo, R. Mesleh, and H. Haas, "Sphere decoding for spatial modulation," in *Proceedings of 2011 IEEE International Conference on Communications (ICC 2011)*, Kyoto, Japan, June 2011.

[212] A. Younis, S. Sinanovic, M. D. Renzo, R. Mesleh, and H. Haas, "Generalised sphere decoding for spatial modulation," *IEEE Transactions on Communications*, vol. 61, pp. 2805–2815, July 2013.

[213] A. Younis, R. Mesleh, H. Haas, and P. M. Grant, "Reduced complexity sphere decoder for spatial modulation detection receivers," in *Proceedings of 2010 IEEE Global Telecommunications Conference (GLOBECOM 2010)*, Miami, USA, Dec. 2010.

[214] B. Hassibi and H. Vikalo, "On the sphere-decoding algorithm I. expected complexity," *IEEE Transactions on Signal Processing*, vol. 53, pp. 2806–2818, Aug. 2005.

[215] J. Jalden and B. Ottersten, "On the complexity of sphere decoding in digital communications," *IEEE Transactions on Signal Processing*, vol. 53, pp. 1474–1484, Apr. 2005.

[216] S. Sugiura, S. Chen, and L. Hanzo, "Coherent and differential space-time shift keying: A dispersion matrix approach," *IEEE Transactions on Communications*, vol. 58, pp. 3219–3230, Nov. 2010.

[217] S. Sugiura, S. Chen, and L. Hanzo, "Generalized space-time shift keying designed for flexible diversity-, multiplexing- and complexity-tradeoffs," *IEEE Transactions on Wireless Communications*, vol. 10, pp. 1144–1153, Apr. 2011.

[218] E. Basar, U. Aygolu, E. Panayirci, and H. V. Poor, "Space-time block coded spatial modulation," *IEEE Transactions on Communications*, vol. 59, pp. 823–832, Mar. 2011.

[219] R. Rajashekar and K. V. S. Hari, "Modulation diversity for spatial modulation using complex interleaved orthogonal design," in *Proceedings of EEE Region 10 Conference*, Nov. 2012.

[220] D. Yang, C. Xu, L. L. Yang, and L. Hanzo, "Transmit-diversity-assisted space-shift keying for colocated and distributed/cooperative MIMO elements," *IEEE Transactions on Vehicular Technology*, vol. 60, pp. 2864–2869, July 2011.

[221] M. T. Le, V. D. Ngo, H. A. Mai, X. N. Tran, and M. D. Renzo, "Spatially modulated orthogonal space-time block codes with non-vanishing determinants," *IEEE Transactions on Communications*, vol. 62, pp. 85–99, Jan. 2014.

[222] M. D. Renzo and H. Haas, "Space shift keying (SSK-) MIMO over correlated Rician fading channels: Performance analysis and a new method for transmit-diversity," *IEEE Transactions on Communications*, vol. 59, pp. 116–129, Jan. 2011.

[223] D. M. Renzo, D. D. Leonardis, F. Graziosi, and H. Haas, "Space shift keying (SSK-) MIMO with practical channel estimates," *IEEE Transactions on Communications*, vol. 60, pp. 998–1012, Apr. 2012.

[224] M. D. Renzo and H. Haas, "On transmit diversity for spatial modulation MIMO: Impact of spatial constellation diagram and shaping filters at the transmitter," *IEEE Transactions on Vehicular Technology*, vol. 62, pp. 2507–2531, July 2013.

[225] L. L. Yang, "Signal detection in antenna-hopping space-division multiple-access systems with space-shift keying modulation," *IEEE Transactions on Signal Processing*, vol. 60, pp. 351–366, Jan. 2012.

[226] J. Wang, S. Jia, and J. Song, "Generalised spatial modulation system with multiple active transmit antennas and low complexity detection scheme," *IEEE Transactions on Wireless Communications*, vol. 11, pp. 1605–1615, Apr. 2012.

[227] M. D. Renzo, H. Haas, A. Ghrayeb, S. Sugiura, and L. Hanzo, "Spatial modulation for generalized MIMO: Challenges, opportunities, and implementation," *Proceedings of the IEEE*, vol. 102, pp. 56–103, Jan. 2014.

[228] R. Mesleh, M. D. Renzo, H. Haas, and P. M. Grant, "Trellis coded spatial modulation," *IEEE Transactions on Wireless Communications*, vol. 9, pp. 2349–2361, July 2010.

[229] S. Sugiura, C. Xu, S. X. Ng, and L. Hanzo, "Reduced-complexity iterative-detection-aided generalized space-time shift keying," *IEEE Transactions on Vehicular Technology*, vol. 61, pp. 3656–3664, Oct. 2012.

[230] J. Fu, C. Hou, W. Xiang, L. Yan, and Y. Hou, "Generalised spatial modulation with multiple active transmit antennas," in *Proceedings of IEEE GLOBECOM Workshops (GLOBECOME 2010)*, pp. 839–844, Miami, USA, Dec. 2010.

[231] A. Younis, N. Serafimovski, R. Mesleh, and H. Haas, "Generalised spatial modulation," in *Proceedings of The Forty Fourth Asilomar Conference on Signals, Systems and Computers (ASILOMAR 2010)*, pp. 1498–1502, Pacific Grove, USA, Nov. 2010.

[232] P. Yang, M. D. Renzo, Y. Xiao, S. Li, and L. Hanzo, "Design guidelines for spatial modulation," *IEEE Communications Surveys Tutorials*, vol. 17, pp. 6–26, Firstquarter 2015.

[233] C. Xu, S. X. Ng, and L. Hanzo, "Near-capacity irregular convolutional coded cooperative differential linear dispersion codes using multiple-symbol differential detection," *IEEE Signal Processing Letters*, vol. 18, pp. 173–176, Jan. 2011.

[234] C. Xu, S. Sugiura, S. X. Ng, and L. Hanzo, "Reduced-complexity noncoherently detected differential space-time shift keying," *IEEE Signal Processing Letters*, vol. 18, pp. 153 –156, Mar. 2011.

[235] C. Xu, L. Wang, S. X. Ng, and L. Hanzo, "Multiple-symbol differential sphere detection aided differential space-time block codes using QAM constellations," *IEEE Signal Processing Letters*, vol. 18, pp. 497–500, Sept. 2011.

[236] C. Xu, D. Liang, S. Sugiura, S. X. Ng, and L. Hanzo, "Reduced-complexity Approx-Log-MAP and Max-Log-MAP soft PSK/QAM detection algorithms," *IEEE Transactions on Communications*, vol. 61, pp. 1415–1425, Apr. 2013.

[237] C. P. Schnorr and M. Euchner, "Lattice basis reduction: Improved practical algorithms and solving subset sum problems," *Math. Programming*, vol. 66, pp. 181–191, 1994.

[238] B. Sklar, "A primer on turbo code concepts," *IEEE Communications Magazine*, vol. 35, pp. 94–102, Dec. 1997.

[239] L. Hanzo, T. Liew, B. Yeap, R. Tee, and S. X. Ng, *Turbo Coding, Turbo Equalisation and Space-Time Coding: EXIT-Chart-Aided Near-Capacity Designs for Wireless Channels*. John Wiley & Sons, 2011.

[240] S. ten Brink, J. Speidel, and R. H. Yan, "Iterative demapping for QPSK modulation," *Electronics Letters*, vol. 34, pp. 1459–1460, July 1998.

[241] S. ten Brink, J. Speidel, and R. H. Yan, "Iterative demapping and decoding for multilevel modulation," in *Proceedings of IEEE Global Telecommunications Conference (GLOBECOM'98)*, vol. 1, pp. 579–584, Sydney, Australia, Nov. 1998.

[242] H. M. Tullberg and P. Siegel, "Serial concatenated TCM with an inner accumulate code-Part I: maximum-likelihood analysis," *IEEE Transactions on Communications*, vol. 53, pp. 64–73, Jan. 2005.

[243] L. Kong, S. X. Ng, R. Tee, R. G. Maunder, and L. Hanzo, "Reduced-complexity near-capacity downlink iteratively decoded generalized multi-layer space-time coding using irregular convolutional codes," *IEEE Transactions on Wireless Communications*, vol. 9, pp. 684–695, Feb. 2010.

[244] S. X. Ng and L. Hanzo, "On the MIMO channel capacity of multidimensional signal sets," *IEEE Transactions on Vehicular Technology*, vol. 55, pp. 528–536, Mar. 2006.

[245] F. Tosato and P. Bisaglia, "Simplified soft-output demapper for binary interleaved COFDM with application to HIPERLAN/2," in *Proceedings of IEEE International Conference on Communications (ICC'02)*, vol. 2, pp. 664–668, 2002.

[246] K. Hyun and D. Yoon, "Bit metric generation for Gray coded QAM signals," *IEE Proceedings Communications*, vol. 152, pp. 1134–1138, Dec. 2005.

[247] L. Wang, D. Xu, and X. Zhang, "Low complexity bit metric generation for PAM signals based on nonlinear function," *Electronics Letters*, vol. 47, pp. 966–967, Aug. 2011.

[248] ITU-R, "Coexistence between IMT-2000 PCDMA-DS and IMT-2000 OFDMA TDD WMAN in the 2 500-2 690 mhz band operating in adjacent bands in the same area." [Online]. Available: `http://www.itu.int/pub/R-REP-M.2146-2009`, 2009.

[249] Qualcomm, "IEEE802.11ac: The next evolution of Wi-Fi standards." [Online]. Available: `http://www.qualcomm.com/media/documents/files/ieee802-11ac-the-next-evolution-of-wi-fi.pdf`, 2012.

[250] F. Schreckenbach, N. Gortz, J. Hagenauer, and G. Bauch, "Optimization of symbol mappings for bit-interleaved coded modulation with iterative decoding," *IEEE Communications Letters*, vol. 7, pp. 593–595, Dec. 2003.

[251] A. Leon-Garcia, *Probability and random processes for electrical engineering*. Addison-Wesley, 2nd Edition, 1994.

[252] P. K. Vitthaladevuni, M. S. Alouini, and J. C. Kieffer, "Exact BER computation for cross QAM constellations," *IEEE Transactions on Wireless Communications*, vol. 4, pp. 3039–3050, Nov. 2005.

[253] X. Dong, N. C. Beaulieu, and P. H. Wittke, "Error probabilities of two-dimensional M-ary signaling in fading," *IEEE Transactions on Communications*, vol. 47, pp. 352–355, Mar. 1999.

[254] S. ten Brink, "Design of serially concatenated codes based on iterative decoding convergence," in *Proceedings of the 2nd International Symposium on Turbo Codes and Related Topics*, pp. 319–322, Sept. 2000.

[255] F. Brannstrom, L. K. Rasmussen, and A. J. Grant, "Convergence analysis and optimal scheduling for multiple concatenated codes," *IEEE Transactions on Information Theory*, vol. 51, pp. 3354–3364, Sept. 2005.

[256] W. N. Venables and B. D. Ripley, *Modern applied statistics with S-PLUS*. New York: Springer-verlag, 1994.

[257] D. Divsalar and F. Pollara, "Multiple turbo codes for deep-space communications," *TDA Progress Report*, vol. 42, pp. 66–77, May 1995.

[258] S. Huettinger and J. Huber, "Design of multiple-turbo-codes with transfer characteristics of component codes," in *Proceedings of Conference on Information Sciences and Systems, (CISS'02)*, Mar. 2002.

[259] A. Ashikhmin, G. Kramer, and S. ten Brink, "Code rate and the area under extrinsic information transfer curves," in *Proceedings of IEEE International Symposium on Information Theory*, 2002.

[260] D. Divsalar, S. Dolinar, and F. Pollara, "Iterative turbo decoder analysis based on density evolution," *IEEE Journal on Selected Areas in Communications*, vol. 19, pp. 891–907, May 2001.

[261] F. Simoens, H. Wymeersch, H. Bruneel, and M. Moeneclaey, "Multidimensional mapping for bit-interleaved coded modulation with BPSK/QPSK signaling," *IEEE Communications Letters*, vol. 9, pp. 453–455, May 2005.

[262] S. Pfletschinger and F. Sanzi, "Error floor removal for bit-interleaved coded modulation with iterative detection," *IEEE Transactions on Wireless Communications*, vol. 5, pp. 3174–3181, Nov. 2006.

[263] N. S. Muhammad and J. Speidel, "Joint optimization of signal constellation bit labeling for bit-interleaved coded modulation with iterative decoding," *IEEE Communications Letters*, vol. 9, pp. 775–777, Sept. 2005.

[264] F. Schreckenbach and G. Bauch, "Bit interleaved coded irregular modulation," *European Transactions on Telecommunications*, vol. 17, no. 2, pp. 269–282, 2006.

[265] S. ten Brink, G. Kramer, and A. Ashikhmin, "Design of low-density parity-check codes for modulation and detection," *IEEE Transactions on Communications*, vol. 52, pp. 670–678, May 2004.

[266] I. Land, P. Hoeher, and U. Sorger, "Log-likelihood values and Monte Carlo simulation: Some fundamental results," in *Proceedings of International Symposium on Turbo Codes*, pp. 43–46, Sept. 2000.

[267] S. Tan, S. Chen, and L. Hanzo, "On multi-user EXIT chart analysis aided turbo-detected MBER beamformer designs," *IEEE Transactions on Wireless Communications*, vol. 7, pp. 314–323, Jan. 2008.

[268] M. Dong and L. Tong, "Optimal design and placement of pilot symbols for channel estimation," *IEEE Transactions on Signal Processing*, vol. 50, pp. 3055–3069, Dec. 2002.

[269] L. Tong, R. Liu, V. C. Soon, and Y.-F. Huang, "Indeterminacy and identifiability of blind identification," *IEEE Transactions on Circuits and Systems*, vol. 38, pp. 499–509, May 1991.

[270] L. Tong and S. Perreau, "Multichannel blind identification: from subspace to maximum likelihood methods," *Proceedings of the IEEE*, vol. 86, pp. 1951–1968, Oct. 1998.

[271] V. Buchoux, O. Cappe, E. Moulines, and A. Gorokhov, "On the performance of semi-blind subspace-based channel estimation," *IEEE Transactions on Signal Processing*, vol. 48, pp. 1750–1759, June 2000.

[272] E. D. Carvalho and D. T. M. Slock, "Blind and semi-blind FIR multichannel estimation: (global) identifiability conditions," *IEEE Transactions on Signal Processing*, vol. 52, pp. 1053–1064, Apr. 2004.

[273] M. Peleg and S. Shamai, "Iterative decoding of coded and interleaved noncoherent multiple symbol detected DPSK," *Electronics Letters*, vol. 33, pp. 1018–1020, June 1997.

[274] A. Chan and I. Lee, "A new reduced-complexity sphere decoder for multiple antenna systems," in *Proceedings of IEEE International Conference on Communications, 2002 (ICC'02)*, vol. 1, pp. 460–464, New York, USA, Apr. 2002.

[275] W. Zhao and G. B. Giarmakis, "Reduced complexity closest point decoding algorithms for random lattices," *IEEE Transactions on Wireless Communications*, vol. 5, pp. 101–111, Jan. 2006.

[276] D. Pham, K. R. Pattipati, P. K. Willett, and J. Luo, "An improved complex sphere decoder for V-BLAST systems," *IEEE Signal Processing Letters*, vol. 11, pp. 748–751, Sept. 2004.

[277] V. Pauli and L. Lampe, "Tree-search multiple-symbol differential decoding for unitary space-time modulation," *IEEE Transactions on Communications*, vol. 55, pp. 1567–1576, Aug. 2007.

[278] M. Schwartz, R. B. William, and S. Stein, *Communication systems and techniques*. John Wiley & Sons, 1995.

[279] R. H. Clarke, "A statistical theory of mobile radio reception," *Bell Labs Technical Journal*, vol. 47, pp. 957–1000, 1968.

[280] W. C. Jakes, *Microwave mobile communications*. John Wiley & Sons, 1975.

[281] D. S. Bernstein, *Matrix mathematics: theory, facts, and formulas*. Princeton University Press, 2009.

[282] V. Pauli, J. Huber, and L. Lampe, "Decision-feedback subset multiple-symbol differential detection for unitary space-time modulation," *IEEE Transactions on Vehicular Technology*, vol. 58, pp. 1022–1026, June 2009.

[283] S. Baro, J. Hagenauer, and M. Witzke, "Iterative detection of MIMO transmission using a list-sequential (LISS) detector," in *Proceedings of IEEE International Conference on Communications, 2003 (ICC'03)*, vol. 4, pp. 2653–2657, May 2003.

[284] J. Jalden and B. Ottersten, "Parallel implementation of a soft output sphere decoder," in *Proceedings of Thirty-Ninth Asilomar Conference on Signals, Systems and Computers, 2005.*, pp. 581–585, Oct. 2005.

[285] T. H. Cormen, C. E. Leiserson, R. L. Rivest, and C. Stein, *Introduction to algorithms*. The MIT press, 2001.

[286] M. A. Bender, M. Farach-Colton, and M. Mosteiro, "Insertion sort is O(n log n)," *Theory of Computing Systems*, vol. 39, no. 3, pp. 391–397, 2006.

[287] N. Svensson, "On differentially encoded star 16QAM with differential detection and diversity," *IEEE Transactions on Vehicular Technology*, vol. 44, pp. 586–593, Aug. 1995.

[288] R. Fischer, L. Lampe, and S. Calabro, "Differential encoding strategies for transmission over fading channels," *International Journal of Electronics and Communications*, vol. 54, no. 1, pp. 59–67, 2000.

[289] L. Lampe and R. Fischer, "Comparison and optimization of differentially encoded transmission on fading channels," in *Proceedings of International Symposium on PowerLine Communication and its Applications (ISPLC'99)*, 1999.

[290] D. S. Bernstein, *Matrix Mathematics: Theory, Facts, and Formulas (Second Edition)*. Princeton University Press, 2009.

[291] A. Goldsmith, S. A. Jafar, N. Jindal, and S. Vishwanath, "Capacity limits of MIMO channels," *IEEE Journal on Selected Areas in Communications*, vol. 21, pp. 684–702, June 2003.

[292] D. Gesbert, M. Shafi, D.-S. Shiu, P. Smith, and A. Naguib, "From theory to practice: An overview of MIMO space-time coded wireless systems," *IEEE Journal on Selected Areas in Communications*, vol. 21, pp. 281 – 302, Apr. 2003.

[293] V. Tarokh, H. Jafarkhani, and A. R. Calderbank, "Space-time block coding for wireless communications: performance results," *IEEE Journal on Selected Areas in Communications*, vol. 17, pp. 451–460, Mar. 1999.

[294] M. I. Irshid and I. S. Salous, "Bit error probability for coherent M-ary PSK systems," *IEEE Transactions on Communications*, vol. 39, pp. 349–352, Mar. 1991.

[295] M. D. Renzo and H. Haas, "A general framework for performance analysis of space shift keying (SSK) modulation for MISO correlated Nakagami-m fading channels," *IEEE Transactions on Communications*, vol. 58, pp. 2590–2603, Sept. 2010.

[296] S. Sugiura and L. Hanzo, "On the joint optimization of dispersion matrices and constellations for near-capacity irregular precoded space-time shift keying," *IEEE Transactions on Wireless Communications*, vol. 12, pp. 380–387, Jan. 2013.

[297] V. Tarokh, N. Seshadri, and A. R. Calderbank, "Space-time codes for high data rate wireless communication: performance criterion and code construction," *IEEE Transactions on Information Theory*, vol. 44, pp. 744–765, Mar. 1998.

[298] V. Tarokh, A. Naguib, N. Seshadri, and A. R. Calderbank, "Space-time codes for high data rate wireless communication: performance criteria in the presence of channel estimation errors, mobility, and multiple paths," *IEEE Transactions on Communications*, vol. 47, pp. 199–207, Feb. 1999.

[299] J. C. Guey, M. P. Fitz, M. R. Bell, and W.-Y. Kuo, "Signal design for transmitter diversity wireless communication systems over Rayleigh fading channels," *IEEE Transactions on Communications*, vol. 47, pp. 527–537, Apr. 1999.

[300] S. Sandhu and A. Paulraj, "Unified design of linear space-time block codes," in *Proceedings of IEEE Global Telecommunications Conference, 2001. (GLOBECOM'01)*, vol. 2, pp. 1073–1077, San Antonio, USA, Nov. 2001.

[301] C. Papadias, "On the spectral efficiency of space-time spreading schemes for multiple antenna CDMA systems," in *Proceedings of 33rd Asilomar Conference on Signals, Systems, and Computers.*, vol. 1, pp. 639–643, Pacific Grove, USA, Oct. 1999.

[302] S. Sugiura, S. Chen, and L. Hanzo, "A unified MIMO architecture subsuming space shift keying, OSTBC, BLAST and LDC," in *Proceedings of IEEE 72nd Vehicular Technology Conference Fall (VTC 2010-Fall)*, Ottawa, Canada, Sept. 2010.

[303] M. O. Damen, K. Abed-Meraim, and S. Burykh, "Iterative QR detection for BLAST," *Wireless Personal Communications*, vol. 19, no. 3, pp. 179–191, 2001.

[304] M. O. Damen, K. Abed-Meraim, and J. C. Belfiore, "A generalized lattice decoder for asymmetrical space-time communication architecture," in *Proceedings of IEEE International Conference on Acoustics, Speech, and Signal Processing, 2000. (ICASSP '00)*, vol. 5, pp. 2581–2584, Istanbul, Turkey 2000.

[305] M. O. Damen, K. Abed-Meraim, and J. C. Belfiore, "Generalised sphere decoder for asymmetrical space-time communication architecture," *Electronics letters*, vol. 36, no. 2, pp. 166–167, 2000.

[306] L. Hanzo, M. El-Hajjar, and O. Alamri, "Near-capacity wireless transceivers and cooperative communications in the MIMO era: Evolution of standards, waveform design, and future perspectives," *Proceedings of the IEEE*, vol. 99, pp. 1343–1385, Aug. 2011.

[307] Q. Li, G. Li, W. Lee, M. Lee, D. Mazzarese, B. Clerckx, and Z. Li, "MIMO techniques in WiMAX and LTE: a feature overview," *IEEE Communications Magazine*, vol. 48, pp. 86–92, May 2010.

[308] M. Pohst, "On the computation of lattice vectors of minimal length, successive minima and reduced bases with applications," *ACM Sigsam Bulletin*, vol. 15, no. 1, pp. 37–44, 1981.

[309] U. Fincke and M. Pohst, "Improved methods for calculating vectors of short length in a lattice, including a complexity analysis," *Mathematics of computation*, vol. 44, no. 170, pp. 463–471, 1985.

[310] K. Q. Wong, C. Y. Tsui, R. S. K. Cheng, and W. H. Mow, "A VLSI architecture of a K-best lattice decoding algorithm for MIMO channels," in *Proceedings of IEEE International Symposium on Circuits and Systems, 2002. (ISCAS'02)*, vol. 3, pp. 273–276, 2002.

[311] Z. Guo and P. Nilsson, "Algorithm and implementation of the K-best sphere decoding for MIMO detection," *IEEE Journal on Selected Areas in Communications*, vol. 24, pp. 491–503, Mar. 2006.

[312] M. Wenk, M. Zellweger, A. Burg, N. Felber, and W. Fichtner, "K-best MIMO detection VLSI architectures achieving up to 424 Mbps," in *Proceedings of 2006 IEEE International Symposium on Circuits and Systems, 2006. (ISCAS'06)*, May 2006.

[313] A. Burg, M. Borgmann, M. Wenk, M. Zellweger, W. Fichtner, and H. Bolcskei, "VLSI implementation of MIMO detection using the sphere decoding algorithm," *IEEE Journal of Solid-State Circuits*, vol. 40, pp. 1566–1577, July 2005.

[314] Q. Liu and L. Yang, "A novel method for initial radius selection of sphere decoding," in *Proceedings of IEEE 60th Vehicular Technology Conference, 2004. (VTC'04-Fall)*, vol. 2, pp. 1280–1283, Sept 2004.

[315] E. Telatar, "Capacity of multiantenna Gaussian channels," *European Transactions on Telecommunications*, vol. 10, no. 6, pp. 585–595, 1999.

[316] G. J. Foschini, G. D. Golden, R. A. Valenzuela, and P. W. Wolniansky, "Simplified processing for high spectral efficiency wireless communication employing multi-element arrays," *IEEE Journal on Selected Areas in Communications*, vol. 17, pp. 1841–1852, Nov. 1999.

[317] G. D. Golden, C. J. Foschini, R. Valenzuela, and P. W. Wolniansky, "Detection algorithm and initial laboratory results using V-BLAST space-time communication architecture," *Electronics Letters*, vol. 35, pp. 14–16, Jan. 1999.

[318] S. Loyka and F. Gagnon, "Performance analysis of the V-BLAST algorithm: an analytical approach," *IEEE Transactions on Wireless Communications*, vol. 3, pp. 1326–1337, July 2004.

[319] D. Wubben, R. Bohnke, J. Rinas, V. Kuhn, and K. D. Kammeyer, "Efficient algorithm for decoding layered space-time codes," *Electronics Letters*, vol. 37, pp. 1348–1350, Oct. 2001.

[320] A. Benjebbour, H. Murata, and S. Yoshida, "Comparison of ordered successive receivers for space-time transmission," in *Proceedings of IEEE VTS 54th Vehicular Technology Conference, 2001. (VTC'01-Fall)*, vol. 4, pp. 2053–2057 vol.4, Atlantic City, USA, Oct. 2001.

[321] M. K. Varanasi and B. Aazhang, "Multistage detection in asynchronous code-division multiple-access communications," *IEEE Transactions on Communications*, vol. 38, pp. 509–519, Apr. 1990.

[322] R. Kohno, H. Imai, M. Hatori, and S. Pasupathy, "Combinations of an adaptive array antenna and a canceller of interference for direct-sequence spread-spectrum multiple-access system," *IEEE Journal on Selected Areas in Communications*, vol. 8, pp. 675–682, May 1990.

[323] S. Moshavi, "Multi-user detection for DS-CDMA communications," *IEEE Communications Magazine*, vol. 34, pp. 124–136, Oct. 1996.

[324] S. Verdu, *Multiuser Detection*. Cambridge University Press, 1998.

[325] O. Tirkkonen and A. Hottinen, "Square-matrix embeddable space-time block codes for complex signal constellations," *IEEE Transactions on Information Theory*, vol. 48, pp. 384–395, Feb. 2002.

[326] W. Su and X. G. Xia, "On space-time block codes from complex orthogonal designs," *Wireless Personal Communications*, vol. 25, no. 1, pp. 1–26, 2003.

[327] X. B. Liang, "Orthogonal designs with maximal rates," *IEEE Transactions on Information Theory*, vol. 49, pp. 2468–2503, Oct. 2003.

[328] W. Su and X. G. Xia, "Signal constellations for quasi-orthogonal space-time block codes with full diversity," *IEEE Transactions on Information Theory*, vol. 50, pp. 2331–2347, Oct. 2004.

[329] C. B. Papadias and G. J. Foschini, "A space-time coding approach for systems employing four transmit antennas," in *Proceedings of IEEE International Conference on Acoustics, Speech, and Signal Processing, 2001. (ICASSP '01)*, vol. 4, pp. 2481–2484, Salt Lake City, USA, May 2001.

[330] N. Sharma and C. B. Papadias, "Improved quasi-orthogonal codes through constellation rotation," *IEEE Transactions on Communications*, vol. 51, pp. 332–335, March 2003.

[331] H. F. Lu and P. Y. Kumar, "A unified construction of space-time codes with optimal rate-diversity tradeoff," *IEEE Transactions on Information Theory*, vol. 51, pp. 1709–1730, May 2005.

[332] C. Yuen, Y. L. Guan, and T. T. Tjhung, "Quasi-orthogonal STBC with minimum decoding complexity," *IEEE Transactions on Wireless Communications*, vol. 4, pp. 2089–2094, Sept. 2005.

[333] N. Wu and L. Hanzo, "Near-capacity irregular-convolutional-coding-aided irregular precoded linear dispersion codes," *IEEE Transactions on Vehicular Technology*, vol. 58, pp. 2863–2871, July 2009.

[334] H. Xu, "Simplified maximum likelihood-based detection schemes for M-ary quadrature amplitude modulation spatial modulation," *IET Communications*, vol. 6, pp. 1356–1363, July 2012.

[335] H. Xu, "Simple low-complexity detection schemes for M-ary quadrature amplitude modulation spatial modulation," *IET Communications*, vol. 6, pp. 2840–2847, Nov. 2012.

[336] N. Serafimovski, M. D. Renzo, S. Sinanovic, R. Y. Mesleh, and H. Haas, "Fractional bit encoded spatial modulation (FBE-SM)," *IEEE Communications Letters*, vol. 14, pp. 429–431, May 2010.

[337] Y. Yang and S. Aissa, "Bit-padding information guided channel hopping," *IEEE Communications Letters*, vol. 15, pp. 163–165, Feb. 2011.

[338] R. Y. Chang, S. J. Lin, and W. H. Chung, "New space shift keying modulation with hamming code-aided constellation design," *IEEE Wireless Communications Letters*, vol. 1, pp. 2–5, Feb. 2012.

[339] J. M. Luna-Rivera, D. U. Campos-Delgado, and M. G. Gonzalez-Perez, "Constellation design for spatial modulation," in *Proceedings of The 2013 Iberoamerican Conference on Electronics Engineering and Computer Science*, pp. 71–78, 2013.

[340] T. L. Marzetta, "Noncooperative cellular wireless with unlimited numbers of base station antennas," *IEEE Transactions on Wireless Communications*, vol. 9, pp. 3590–3600, Nov. 2010.

[341] F. Rusek, D. Persson, B. K. Lau, E. G. Larsson, T. L. Marzetta, O. Edfors, and F. Tufvesson, "Scaling up MIMO: Opportunities and challenges with very large arrays," *IEEE Signal Processing Magazine*, vol. 30, pp. 40–60, Jan. 2013.

[342] E. Larsson, O. Edfors, F. Tufvesson, and T. Marzetta, "Massive MIMO for next generation wireless systems," *IEEE Communications Magazine*, vol. 52, pp. 186–195, Feb. 2014.

[343] Z. Pi and F. Khan, "An introduction to Millimeter-wave mobile broadband systems," *IEEE Communications Magazine*, vol. 49, pp. 101–107, June 2011.

[344] T. S. Rappaport, J. N. Murdock, and F. Gutierrez, "State of the art in 60-GHz integrated circuits and systems for wireless communications," *Proceedings of the IEEE*, vol. 99, pp. 1390–1436, Aug. 2011.

[345] X. Li and J. A. Ritcey, "Bit-interleaved coded modulation with iterative decoding using soft feedback," *Electronics Letters*, vol. 34, pp. 942–943, May 1998.

[346] A. Stefanov and T. M. Duman, "Turbo-coded modulation for systems with transmit and receive antenna diversity over block fading channels: system model, decoding approaches, and practical considerations," *IEEE Journal on Selected Areas in Communications*, vol. 19, pp. 958–968, May 2001.

[347] L. G. Barbero and J. S. Thompson, "Extending a fixed-complexity sphere decoder to obtain likelihood information for Turbo-MIMO systems," *IEEE Transactions on Vehicular Technology*, vol. 57, pp. 2804–2814, Sept. 2008.

[348] B. Dong, X. Wang, and A. Doucet, "A new class of soft MIMO demodulation algorithms," *IEEE Transactions on Signal Processing*, vol. 51, pp. 2752–2763, Nov. 2003.

[349] J. Boutros, N. Gresset, L. Brunel, and M. Fossorier, "Soft-input soft-output lattice sphere decoder for linear channels," in *Proceedings of IEEE Global Telecommunications Conference, 2003 (GLOBECOM '03)*, vol. 3, pp. 1583–1587, Dec. 2003.

[350] Y. L. C. Jong and T. J. Willink, "Iterative tree search detection for MIMO wireless systems," *IEEE Transactions on Communications*, vol. 53, pp. 930–935, June 2005.

[351] H. Lee, B. Lee, and I. Lee, "Iterative detection and decoding with an improved v-blast for mimo-ofdm systems," *IEEE Journal on Selected Areas in Communications*, vol. 24, pp. 504–513, Mar. 2006.

[352] K. Liu and A. M. Sayeed, "An iterative extension of BLAST decoding algorithm for layered space-time signals," *IEEE Transactions on Communications*, vol. 53, pp. 1754–1761, Oct. 2005.

[353] J. W. Choi, A. C. Singer, J. Lee, and N. I. Cho, "Improved linear soft-input soft-output detection via soft feedback successive interference cancellation," *IEEE Transactions on Communications*, vol. 58, pp. 986–996, Mar. 2010.

[354] E. Basar, U. Aygolu, E. Panayirci, and H. V. Poor, "New trellis code design for spatial modulation," *IEEE Transactions on Wireless Communications*, vol. 10, pp. 2670–2680, Aug. 2011.

[355] R. Mesleh, I. Stepan, H. Haas, and P. M. Grant, "On the performance of Trellis coded spatial modulation," in *Proceedings of International ITG Workshop on Smart Antennas*, Feb. 2009.

[356] S. U. Hwang, S. Jeon, S. Lee, and J. Seo, "Soft-output ML detector for spatial modulation OFDM systems," *IEICE Electronics Express*, vol. 6, no. 19, pp. 1426–1431, 2009.

[357] C. Vladeanu, A. Martian, A. F. Paun, and S. E. Assad, "A new ML detector for Trellis-coded spatial modulation using hard and soft estimates," in *Proceedings of 10th International Symposium on Electronics and Telecommunications (ISETC'12)*, pp. 143–146, Nov. 2012.

[358] B. Mennenga and G. Fettweis, "Search sequence determination for tree search based detection algorithms," in *Proceedings of IEEE Sarnoff Symposium, 2009 (SARNOFF '09)*, Princeton, USA, Mar. 2009.

[359] J. Ketonen, M. Myllyla, M. Juntti, and J. R. Cavallaro, "ASIC implementation comparison of SIC and LSD receivers for MIMO-OFDM," in *Proceedings of 42nd Asilomar Conference on Signals, Systems and Computers*, pp. 1881–1885, Pacific Grove, USA, Oct. 2008.

[360] J. Ketonen, M. Juntti, and J. R. Cavallaro, "Performance-complexity comparison of receivers for a LTE MIM-OFDM system," *IEEE Transactions on Signal Processing*, vol. 58, pp. 3360–3372, June 2010.

[361] H. V. Poor and S. Verdu, "Probability of error in MMSE multiuser detection," *IEEE Transactions on Information Theory*, vol. 43, pp. 858–871, May 1997.

[362] A. Tomasoni, M. Ferrari, D. Gatti, F. Osnato, and S. Bellini, "A low complexity turbo MMSE receiver for W-LAN MIMO systems," in *Proceedings of IEEE International Conference on Communications, 2006 (ICC'06)*, vol. 9, pp. 4119–4124, Istanbul, Turkey, June 2006.

[363] J. Sherman and W. J. Morrison, "Adjustment of an inverse matrix corresponding to changes in the elements of a given column or a given row of the original matrix," *Annals of Mathematical Statistics*, vol. 20, pp. 621–621, Jan. 1949.

[364] J. Sherman and W. J. Morrison, "Adjustment of an inverse matrix corresponding to a change in one element of a given matrix," *Annals of Mathematical Statistics*, pp. 124–127, 1950.

[365] W. H. Press, *Numerical recipes 3rd edition: The art of scientific computing*. Cambridge university press, 2007.

[366] T. Datta and A. Chockalingam, "On generalized spatial modulation," in *Proceedings of IEEE Wireless Communications and Networking Conference (WCNC'13)*, pp. 2716–2721, Shanghai, China, Apr. 2013.

[367] A. Sendonaris, E. Erkip, and B. Aazhang, "User cooperation diversity. part I. system description," *IEEE Transactions on Communications*, vol. 51, pp. 1927–1938, Nov. 2003.

[368] A. Sendonaris, E. Erkip, and B. Aazhang, "User cooperation diversity. part II. implementation aspects and performance analysis," *IEEE Transactions on Communications*, vol. 51, pp. 1939–1948, Nov. 2003.

[369] J. N. Laneman, D. N. C. Tse, and G. W. Wornell, "Cooperative diversity in wireless networks: Efficient protocols and outage behavior," *IEEE Transactions on Information Theory*, vol. 50, pp. 3062–3080, Dec. 2004.

[370] V. Tarokh and H. Jafarkhani, "A differential detection scheme for transmit diversity," *IEEE Journal on Selected Areas in Communications*, vol. 18, pp. 1169–1174, July 2000.

[371] B. L. Hughes, "Differential space-time modulation," *IEEE Transactions on Information Theory*, vol. 46, pp. 2567–2578, Nov. 2000.

[372] H. Jafarkhani and V. Tarokh, "Multiple transmit antenna differential detection from generalized orthogonal designs," *IEEE Transactions on Information Theory*, vol. 47, pp. 2626–2631, Sept. 2001.

[373] J. Wang, X. Wang, and M. Madihian, "Design of minimum error-rate Cayley differential unitary space-time codes," *IEEE Journal on Selected Areas in Communications*, vol. 23, pp. 1779–1787, Sept. 2005.

[374] F. Oggier and B. Hassibi, "Algebraic Cayley differential space-time codes," *IEEE Transactions on Information Theory*, vol. 53, pp. 1911–1919, May 2007.

[375] R. Schober and L. Lampe, "Noncoherent receivers for differential space-time modulation," *IEEE Transactions on Communications*, vol. 50, pp. 768–777, May 2002.

[376] V. Pauli and L. Lampe, "On the complexity of sphere decoding for differential detection," *IEEE Transactions on Information Theory*, vol. 53, pp. 1595–1603, Apr. 2007.

Subject Index

Author Index

C

D

E

F

G

H

L

M

N

O

P

Q

R

S

W

X

Y

Z